BRIDGE COLUMN FOOTING PERFORMANCE AND SEISMIC RETROFIT EVALUATION CONSIDERING SOIL-STRUCTURE INTERACTION

Final Report

SPR 830



Oregon Department of Transportation

BRIDGE COLUMN FOOTING PERFORMANCE AND SEISMIC RETROFIT EVALUATION CONSIDERING SOIL-STRUCTURE INTERACTION

SPR 830

by
Armin W. Stuedlein, Ph.D., PE (WA)
Professor, Oregon State University

Christopher C. Higgins, Ph.D., PE (NY)
Professor, Oregon State University

Ali Khosravi, Ph.D.
Assistant Professor, Auburn University

Lance Parson, M.S. and Logan McGinn, M.S.

for

Oregon Department of Transportation
Research Section
555 13th Street NE, Suite 1
Salem OR 97301

and

Federal Highway Administration
1200 New Jersey Avenue SE
Washington, DC 20590

June 2024

Technical Report Documentation Page

1. Report No. FHWA-OR-RD-24-11	2. Government Accession No.	3. Recipient's Catalog No.
4. Title and Subtitle Bridge Column Footing Performance and Seismic Retrofit Evaluation Considering Soil-Structure Interaction		5. Report Date June 2024 6. Performing Organization Code
7. Author(s) Armin W. Stuedlein, Christopher C. Higgins, Ali Khosravi, Lance Parson, M.S. and Logan McGinn		8. Performing Organization Report No.
9. Performing Organization Name and Address Oregon Department of Transportation Research Section 555 13th Street NE, Suite 1 Salem, OR 97301		10. Work Unit No. (TRAIS) 11. Contract or Grant No.
12. Sponsoring Agency Name and Address Oregon Dept. of Transportation Research Section 555 13th Street NE, Suite 1 Salem, OR 97301 Federal Highway Admin. 1200 New Jersey Avenue SE Washington, DC 20590		13. Type of Report and Period Covered Final Report 14. Sponsoring Agency Code

15. Supplementary Notes

16. Abstract: This project investigated a new seismic retrofitting technique for bridge column-footing substructure components considering the influence of soil-structure interactions (SSI). The seismic retrofitting technique uses titanium alloy bars to provide both confinement of the concrete column and a supplemental flexural tension load path. Laboratory and field tests of full-scale models of existing bridge column-footing assemblies were conducted. SSI were included in the laboratory tests using extruded polystyrene foam insulation to approximate the bearing strength and stiffness of some soils. SSI prevented failure of the retrofitted columns due to rocking of the foundation. Analytical studies were used to predict the overall response of the footing-column-soil systems for SSI including nonlinear finite difference models and nonlinear discrete spring models to allow parametric studies. Multi-column bents were modeled to predict system response which caused axial loads to vary in the columns during lateral loading. Field snap-back tests were conducted using a footing-column specimen in native Willamette Silt. Variations in response were observed with seasonal changes in soil conditions. The results demonstrate that interactions between column-footing-soil are significant to assessing the demands in the soil, footing, and column to optimally design the retrofit to achieve proper seismic performance of vintage reinforced concrete bridge substructures. A guideline for the analysis of rocking footings using the AASHTO-LRFD specifications was developed using sectional and strut-and-tie methods.

17. Key Words: Seismic, Soil-structure interaction, Retrofit, Titanium, Field testing, Full-scale testing, Laboratory testing, LRFD, Seasonal, Finite difference modeling, Non-linear modeling	18. Distribution Statement Copies available from NTIS, and online at www.oregon.gov/ODOT/TD/TP_RES/

19. Security Classification (of this report) Unclassified	20. Security Classification (of this page) Unclassified	21. No. of Pages 668	22. Price

SI* (MODERN METRIC) CONVERSION FACTORS

APPROXIMATE CONVERSIONS TO SI UNITS

Symbol	When You Know	Multiply By	To Find	Symbol
		LENGTH		
in	inches	25.4	millimeters	mm
ft	feet	0.305	meters	m
yd	yards	0.914	meters	m
mi	miles	1.61	kilometers	km
		AREA		
in^2	square inches	645.2	millimeters squared	mm^2
ft^2	square feet	0.093	meters squared	m^2
yd^2	square yards	0.836	meters squared	m^2
ac	acres	0.405	hectares	ha
mi^2	square miles	2.59	kilometers squared	km^2
		VOLUME		
fl oz	fluid ounces	29.57	milliliters	ml
gal	gallons	3.785	liters	L
ft^3	cubic feet	0.028	meters cubed	m^3
yd^3	cubic yards	0.765	meters cubed	m^3
~NOTE: Volumes greater than 1000 L shall be shown in m^3.				
		MASS		
oz	ounces	28.35	grams	g
lb	pounds	0.454	kilograms	kg
T	short tons (2000 lb)	0.907	megagrams	Mg
		TEMPERATURE (exact)		
°F	Fahrenheit	(F-32)/1.8	Celsius	°C

APPROXIMATE CONVERSIONS FROM SI UNITS

Symbol	When You Know	Multiply By	To Find	Symbol
		LENGTH		
mm	millimeters	0.039	inches	in
m	meters	3.28	feet	ft
m	meters	1.09	yards	yd
km	kilometers	0.621	miles	mi
		AREA		
mm^2	millimeters squared	0.0016	square inches	in^2
m^2	meters squared	10.764	square feet	ft^2
m^2	meters squared	1.196	square yards	yd^2
ha	hectares	2.47	acres	ac
km^2	kilometers squared	0.386	square miles	mi^2
		VOLUME		
ml	milliliters	0.034	fluid ounces	fl oz
L	liters	0.264	gallons	gal
m^3	meters cubed	35.315	cubic feet	ft^3
m^3	meters cubed	1.308	cubic yards	yd^3
		MASS		
g	grams	0.035	ounces	oz
kg	kilograms	2.205	pounds	lb
Mg	megagrams	1.102	short tons (2000 lb)	T
		TEMPERATURE (exact)		
°C	Celsius	1.8C+32	Fahrenheit	°F

*SI is the symbol for the International System of Measurement

ACKNOWLEDGEMENTS

The authors are grateful for support from the Oregon Department of Transportation through Grant SPR 830. The authors also thank Mr. Jeff Gent for technical support during the experiments, along with graduate students that assisted with various tasks throughout portions of this project including Madison Hall, Julie Li, Christopher Neumann, Ian Morrell, and Aaron Reedus. We also acknowledge the help of Mr. Besrat Alemu and Dr. Amalesh Jana who assisted with cross-hole testing and analysis.

DISCLAIMER

This document is disseminated under the sponsorship of the Oregon Department of Transportation and the United States Department of Transportation in the interest of information exchange. The State of Oregon and the United States Government assume no liability of its contents or use thereof.

The contents of this report reflect the view of the authors who are solely responsible for the facts and accuracy of the material presented. The contents do not necessarily reflect the official views of the Oregon Department of Transportation or the United States Department of Transportation.

The State of Oregon and the United States Government do not endorse products of manufacturers. Trademarks or manufacturers' names appear herein only because they are considered essential to the object of this document.

This report does not constitute a standard, specification, or regulation.

TABLE OF CONTENTS

EXECUTIVE SUMMARY XXXIX

1.0 INTRODUCTION 1

1.1 OVERVIEW 1

1.2 OBJECTIVES OF THIS RESEARCH 2

1.3 ORGANIZATION OF THIS REPORT 3

2.0 LITERATURE REVIEW 5

2.1 DEVELOPMENT OF ODOT SEISMIC DESIGN STANDARDS 5

2.2 ODOT BRIDGE DESIGN PHILOSOPHY 8

2.3 FAILURE MECHANISMS AND SEISMIC RETROFITTING OF BRIDGE COLUMNS 9

2.3.1 Contributing Parameters to Column Failure 11

2.3.2 Retrofit Strategies 17

2.4 TITANIUM ALLOY BARS (TIABS) RETROFIT APPROACH 29

2.4.1 Column-Footing Specimens 31

2.4.2 Retrofit Details 33

2.4.3 Experimental Verification through Large-Scale Testing 36

2.5 CONCEPT OF ROCKING FOUNDATION AND ITS EFFECT ON SEISMIC ASSESSMENT OF RETROFITTED BRIDGE COLUMN FOOTING SYSTEM 49

2.6 SOIL STRUCTURE INTERACTION: ROCKING FOUNDATIONS 53

2.6.1 Overview 53

2.6.2 Estimation of critical contact length (L_c) 58

2.6.3 Rocking Effects on Overall Performance of Bridge Column/ Footing Systems 59

2.7 SUMMARY 90

2.8 REFERENCES 94

3.0 REVIEW OF THE ODOT BRIDGE INVENTORY 105

3.1 COLUMN DIMENSIONS 106

3.2 REINFORCEMENT DETAILS 107

3.3 LONGITUDINAL SPLICE DETAIL 110

3.4 AXIAL LOAD 111

3.5 FOUNDATION DETAILS 114

3.6 FOUNDATION EMBEDMENT DEPTH 119

3.7 REFERENCES 120

4.0 NEW FORMULATION FOR ESTIMATING THE MOMENT CAPACITY OF ROCKING SHALLOW FOUNDATIONS RESTING ON PARTIALLY SATURATED SOIL 121

4.1 INTRODUCTION 121

4.2 UNIFIED METHODOLOGY FOR THE MOMENT CAPACITY OF ROCKING SHALLOW BRIDGE FOUNDATIONS UNDER VARYING SATURATION CONDITIONS 123

4.2.1 Concept of Foundation Rocking in Competent Soil Conditions 123

4.2.2 Moment Capacity of Rocking Shallow Foundations under Varying Saturation Conditions 126

4.3 APPLICATION TO UNSATURATED MOMENT CAPACITY 128

4.4 PARAMETRIC ANALYSIS: EFFECT OF VARYING SATURATION CONDITIONS ON MOMENT CAPACITY 134

4.4.1 Profiles of Soil Suction, Effective Saturation, and Suction Stress under Various Surface Flux Boundary Conditions 135

4.4.2 Effect of Soil Types, Groundwater Table Depth, and Flow Rates on the Moment Capacity 136

4.5 VALIDATION AGAINST FULL-SCALE EXPERIMENTS 139

4.6 DISCUSSION AND IMPLICATIONS FOR PRACTICE 147

4.7 CONCLUSION 147

4.8 REFERENCES 149

5.0 TITANIUM SEISMIC SUBSTRUCTURE RETROFIT TO ENABLE ROCKING OF BRIDGE FOUNDATIONS CONSIDERING SOIL-STRUCTURE INTERACTION: EXPERIMENTS AND NUMERICAL SIMULATIONS 155

5.1 INTRODUCTION 155

5.2 DETAILS OF THE EXPERIMENTAL FULL-SCALE SPECIMENS 156

5.2.1 Experimental Specimens and Vintage Structural Detailing 156

5.2.2 Titanium Alloy Bar Retrofit Details 157

5.2.3 Concrete and Epoxy Material Properties 160

5.2.4 Specimen Construction and Retrofit Installation 161

5.2.5 Soil Simulant to Enable Soil-Structure Interaction 162

5.3 FULL-SCALE LOADING TESTS OF VINTAGE AND RETROFITTED SPECIMENS 162

5.3.1 Instrumentation and Loading Protocol 162

5.3.2 Experimental Test Setup 162

5.3.3 Experimental Response of the Single Column-Footing Specimens 164

5.4 3D NUMERICAL STUDY OF FIXED AND ROCKING FOUNDATIONS FOR SINGLE- AND TWO-COLUMN BRIDGE SUBSTRUCTURES 169

5.4.1 Model Components and Boundary Conditions *169*
5.4.2 Calibration of Constitutive Models *173*
5.4.3 Pushover Response of the Single-Column-Footing Systems *178*
5.4.4 Parametric Study of Soil and Structural Characteristics on Rocking Responses *180*
5.5 NUMERICAL SIMULATION OF BRIDGE BENT SYSTEMS 186
5.5.1 OVERVIEW OF THE 3D NUMERICAL STUDY OF MULTI-COLUMN BRIDGE SUBSTRUCTURES *187*
5.5.2 3D Numerical Study of Multi-Column Bridge Bents *192*
5.6 DISCUSSION AND IMPLICATIONS FOR PRACTICE 198
5.7 CONCLUSIONS 199
5.8 REFERENCES 201
6.0 FULL-SCALE PERFORMANCE OF RETROFITTED REINFORCED CONCRETE COLUMNS INCLUDING SOIL-STRUCTURE INTERACTION: PART I 205
6.1 INTRODUCTION 205
6.2 EXPERIMENTAL PROGRAM 207
6.2.1 Specimen Design *207*
6.2.2 Retrofit Design *211*
6.2.3 Specimen Construction *213*
6.2.4 Material Properties *220*
6.2.5 Instrumentation *222*
6.2.6 Test Setup *223*
6.2.7 Loading Protocol *233*
6.3 EXPERIMENTAL OBSERVATIONS AND ANALYSIS 235
6.3.1 Observed Global Structural Behavior *235*
6.3.2 Force Displacement Responses *251*
6.3.3 Reinforcing Steel and TiAB Strains *264*
6.3.4 Soil-Structure Interaction *267*
6.3.5 Soil Simulant Model *278*
6.3.6 Post-Failure TiAB Retrofit *287*
6.3.7 Vintage Footing Performance *288*
6.4 CONCLUSIONS 295
6.5 REFERENCES 298
7.0 FULL-SCALE PERFORMANCE OF RETROFITTED REINFORCED CONCRETE COLUMNS INCLUDING SOIL-STRUCTURE INTERACTION: PART II 307
7.1 INTRODUCTION 307
7.2 EXPERIMENTAL PROGRAM 308

7.2.1 Subsurface Characterization of the Geotechnical Test Site....308
7.2.2 Column-Footing Specimens....318
7.2.3 Instrumentation....336
7.2.4 Test Setup....344
7.2.5 Loading Protocol....347
7.2.6 Summary of Section 7.2....350
7.3 EXPERIMENTAL OBSERVATIONS, RESULTS, AND ANALYSES....350
7.3.1 Shear Force-Displacement Responses....350
7.3.2 Correction of Column Shear Force for P-Δ Effects....351
7.3.3 Observed Global Structural Behavior....353
7.3.4 Reinforcing Steel and Titanium Alloy Bar Strains....371
7.3.5 Summary of Section 7.3....380
7.4 EXPERIMENTAL OBSERVATIONS AND ANALYSIS OF FIELD SNAP-BACK TESTS382
7.4.1 Overall Force-Deformation Response of Column-Footing Specimen to Snap-Back Tests....382
7.4.2 Reinforcing Steel Strains....401
7.4.3 Some Observations on the Response of Bearing Soils to Snap-Back Tests....410
7.4.4 Summary of Section 7.4....417
7.5 DEVELOPMENT OF A NONLINEAR SOIL-STRUCTURE-INTERACTION MODEL FOR ROCKING BRIDGE SUBSTRUCTURES AND PARAMETRIC STUDY....418
7.5.1 Development of Static-Force SSI Models Representative of Snap-Back Tests....418
7.5.2 Hysteretic Soil-Structure Interaction Model and Results....448
7.5.3 Summary of Section 7.5....464
7.6 SUMMARY AND CONCLUSIONS....465
7.6.1 Summary....465
7.6.2 Conclusions....465
7.7 REFERENCES....468
8.0 SUMMARY AND SUGGESTIONS FOR FUTURE RESEARCH....473
8.1 SUMMARY OF THIS REPORT....473
8.2 SUMMARY OF RECOMMENDATIONS FOR IMPLEMENTATION OF THIS RESEARCH....474
8.3 SUGGESTIONS FOR FUTURE RESEARCH....474
8.4 REFERENCES....476
APPENDIX A6.1: MATERIAL PROPERTIES....477
A6.1.1 CONCRETE....A6.1-1
A6.1.2 REINFORCING STEEL....A6.1-2

A6.1.3 TITANIUM ALLOY BARS A6.1-3
A6.1.4 SOIL SIMULANT A6.1-3
A6.1.5 BONDING EPOXY A6.1-6
A6.1.6 3D NUMERICAL SIMULATIONS OF EMBEDDED COLUMN-FOOTING SPECIMENS TO DEVELOP EQUIVALENT LATERAL EARTH PRESSURE-INDUCED SPRING STIFFNESS A6.1-7
APPENDIX A6.2: SENSOR NAMING CONVENTIONS AND PLACEMENT A6.2-1
A6.2.1 STRAIN GAUGE NAMING CONVENTION A6.2-2
A6.2.2 STRAIN GAUGE SENSOR LOCATIONS A6.2-3
A6.2.3 STRING POTENTIOMETER SENSOR LOCATIONS A6.2-11
APPENDIX A6.3: EXPERIMENTAL DATA FOR ALL TESTS REPORTED IN SECTION 6 ..... A6.3-1
A6.3.1 TEST 1 - SPECIMEN 1: COMPLETE RETROFIT WITH FOAM EMBEDMENT & SUBGRADE A6.3-2
A6.3.2 TEST 2 - SPECIMEN 2: COMPLETE RETROFIT WITH NO EMBEDMENT & FOAM SUBGRADE A6.3-12
A6.3.3 TEST 3 – SPECIMEN 3: VINTAGE WITH FOAM EMBEDMENT, SUBGRADE, & 150 KIP AXIAL LOAD A6.3-22
A6.3.4 TEST 4 – SPECIMEN 3: VINTAGE WITH FOAM EMBEDMENT, SUBGRADE, & 100 KIP AXIAL LOAD A6.3-30
A6.3.5 TEST 5 – SPECIMEN 3 -VINTAGE FAILURE WITH FOAM SUBGRADE & STEEL EMBEDMENT A6.3-38
A6.3.6 TEST 6 – SPECIMEN 3: VINTAGE TIAB LIGAMENT RETROFIT WITH FOAM SUBGRADE & STEEL EMBEDMENT A6.3-46
A6.3.7 TEST 7 – SPECIMEN 3: VINTAGE COMPLETE RETROFIT WITH FOAM SUBGRADE & STEEL EMBEDMENT A6.3-56
A6.3.8 TEST 8 – SPECIMEN 2: COMPLETE RETROFIT WITH TIED DOWN FOOTING A6.3-65
A6.3.9 COMPARISON PLOTS A6.3-79
APPENDIX A7.1: EXPERIMENTAL DATA FOR ALL TESTS REPORTED IN SECTION 7 ..... A7.1-1
A7.1.1 TEST 9 – S1: VINTAGE COLUMN WITH LIGAMENT AND SPIRAL RETROFIT, RESTRAINED FOOTING WITH RETROFIT A7.1-1
A7.1.2 TEST 10 – S2: VINTAGE COLUMN WITH LIGAMENT AND SPIRAL RETROFIT, RESTRAINED FOOTING WITH ADDITIONAL RETROFIT A7.1-7
A7.1.3 NOVEMBER 29TH SNAP-BACK TEST (F = 19.9 KN OR 4.48 KIP) A7.1-14
A7.1.4 DECEMBER 2ND SNAP-BACK TEST (F = 19.1 KN OR 4.34 KIP) A7.1-17

A7.1.5 DECEMBER 5TH SNAP-BACK TEST (F = 28.1 KN OR 6.32 KIP).....A7.1-20
A7.1.6 MAY 22ND SNAP-BACK TEST (F = 28.9 KN OR 6.50 KIP).....A7.1-23
A7.1.7 MAY 22ND SNAP-BACK TEST (F = 38.6 KN OR 8.67 KIP).....A7.1-26
APPENDIX A7.2: STRAIN TIME HISTORIES IN SOIL SIMULANT BELOW THE FOOTING OF TEST 2 – SPECIMEN 2 .....A7.1-1

LIST OF TABLES

Table 2.1: Oregon Seismic Activity (Nako et al. 2014). 8
Table 3.1 Sample calculation of axial load for a column in a 1950s bridge located in Springfield, Oregon. The values used in this calculation are based on the structural drawings for the bridge. 112
Table 4.1: Parameters used in the parametric study for different soil types. 135
Table 5.1: Comparison of different characteristics of the materials for the test specimens and the column-footing system representative of the bridge inventory. 158
Table 5.2: Characteristics of each of the simulations conducted for model validation.....172
Table 5.3: Summary of compression test results on the FOAMULAR® 1000 XPS foam (Shrestha 2019).....176
Table 5.4: Model parameters used to simulate the moment-curvature responses of the test column sections in LPILE. 177
Table 5.5: Case numbers and model parameters varied in the parametric study. 181
Table 5.6: Characteristics of the two-column bent system models. 188
Table 5.7: Model parameters used to simulate the moment-curvature responses of the test column sections in LPILE. 192
Table 6.1: Test specimen designation and test description. 208
Table 6.2: Compressive strength of concrete at 28 days. 221
Table 6.3: Compressive strength of concrete on the day of testing. 221
Table 6.4: Tensile strength of concrete on the day of testing. 221
Table 6.5: Results of tensile tests on reinforcing steel. 222
Table 6.6: Results of tensile tests on TiABs. 222
Table 6.7: Lateral displacement loading protocol (Shreshtha 2019). 234
Table 6.8: Summary of notable force-drift performance metrics.....258
Table 7.1: Summary of average SCPT results for locations of Specimen 4 and 5. 312
Table 7.2: Comparison of initial estimates of s_u based on correlations to LI and V_s.....314

Table 7.3: Summary of ICU triaxial strength tests on specimens of Upper Willamette Silt retrieved from the GEFRS (after Dickenson et al. 2006). 315

Table 7.4: Summary and comparison of s_u estimations from various correlations. 318

Table 7.5: Summary and comparison of ϕ' estimates from ICU tests and SCPT results..... 318

Table 7.6: Specimen Designations and Descriptions. 321

Table 7.7: Lateral Displacement Protocol (Modified from Shrestha 2019). 349

Table 7.8: Specimen Designations and Descriptions. 354

Table 7.9: Summary of results from structural tests on column-footing specimens. 381

Table 7.10: Summary of Snap-Back Tests Conducted 383

Table 7.11: Summary of the damped free vibration coefficients and parameters determined through the analyses of snap-back top drift histories. Note: An insufficient number of cycles was recorded during the 19.1 kN (4.34 kip) test to determine the damped parameters for positive cycles. They are therefore omitted. 397

Table 7.12: Comparison of the relative change in the damped free vibration parameters for the December 5th (F = 28.1 kN or 6.32 kips) and the May 22nd (F = 28.9 kN or 6.50 kips) snap-back tests. 398

Table 7.13: Summary of the damped free vibration coefficients and parameters determined through the analyses of the December 5th snap-back accelerometer history. Note: Acceleration is denoted by the variable, u. 400

Table 7.14: Number of cycles and corresponding shear strain representative of the May 22nd snap-back (F = 38.6 kN or 8.67 kip). 416

Table 7.15: Summary of seasonally dependent strength parameters and bearing capacities. 421

Table 7.16: Summary of inputs for nonlinear pressure-displacement relationships. 423

Table 7.17: Summary of UCS and axial load tests on soil simulant foam with varied strain rates, $\boldsymbol{\varepsilon}$. 439

Table 7.18: Summary of strain rates at the edge of the footing during Test 2 – S2. 443

Table 7.19: Summary of upper and lower bound estimates of E and σ_{ult} at the edge of the footing during Test 2 – S2 based on strain-rate, $\boldsymbol{\varepsilon}$, correlations from the UCS test data. 444

Table A6.1.1 – 28 Day Concrete Compressive Strength. A6.1-1

Table A6.1.2 – Day of Test Concrete Compressive Strength. A6.1-2

Table A6.1.3 – Day of Test Concrete Tensile Strength. A6.1-2

Table A6.1.4 – Tensile Test Results of #10M (#3) Steel Bars (after Shrestha 2019). A6.1-2

Table A6.1.5 – Tensile Test Results on the Reinforcing Steel A6.1-3

Table A6.1.6 – Tensile Test Results on TiABs. A6.1-3

Table A6.1.7 – Summary of Foam Compression Test Results (reported by Shrestha 2019). A6.1-5

Table A6.1.8 – Summary of calculated spring stiffnesses for the four simulation cases. A6.1-11

LIST OF FIGURES

Figure 2.1 Distribution of over 14000 earthquakes in the state of Oregon over the years of 1841 to 2002 (Nako et al. 2009). 5

Figure 2.2: A map of Oregon showing all active faults (Source: Compiled by Robert Langridge of University of Oregon) and the location of Cascade Subduction Zone. 7

Figure 2.3: Distribution of predominant types of materials used for bridge construction in Oregon (Nako et al. 2014). 9

Figure 2.4: Distribution of year of construction completion and bridge collapse potential relative to the year of construction (Nako et al. 2014). 10

Figure 2.5: Base Moment - Rotation along splice length responses for columns under axial load levels of (a) 0.1, (b) 0.2, and (c) 0.3 $A_g f'_c$ (A_g: gross area and f'_c: concrete compressive design strength at 28 days) (Melek and Wallace 2004). 12

Figure 2.6: Details of the model proposed by Mander et al. (1988): (a) Stress-strain model proposed for monotonic loading of confined and unconfined concrete, (b) Effectively confined core for circular hoop reinforcement, (c) Effectively confined core for rectangular hoop reinforcement. 15

Figure 2.7: Load variation with respect to column's (a) axial and (b) lateral displacements Razvi and Shaikh (2018). 16

Figure 2.8 : Seismic Retrofit Concepts (Nako et al. 2009). 18

Figure 2.9: Typical jacket configurations (a) full-height (continuous) jacket, (b) jacketing applied only in the potential plastic hinge regions, and (c) layered jacketing (Alvarez and Brena 2017). 19

Figure 2.10: Methods of FRP strengthening for RC columns: (a) wrapping of fabric, (b) partially wrapping with strips, (c) prefabricated jackets, (d) spiral rings, (e) automated winding, (f) resin infusion (Taranu et al. 2008). 19

Figure 2.11: Jacket configuration for the sample with pre-mold mortar block (Haroun and Elsanadedy 2005). 21

Figure 2.12: Lateral load-displacement relationships for the specimens with different lap-splice lengths (LS) of (ϕ: bar diameter): (a) 25ϕ, (b) 35ϕ, (c) 45ϕ, (d) continuous (1: Flexural crack, 2: Yielding of longitudinal bars, 3: Crack at the upper end of lap splices, 4: Spalling of concrete cover, and 5: Buckling of longitudinal bars) (Goksu et al. 2014). 22

Figure 2.13: Details of experiments by Chai et al. (2008): (a) Experimental test setup, and (b) hysteretic response of columns with starter bar and weak footing. 24

Figure 2.14: Hysteretic curves of the test specimens (AB-1: no retrofit; SJ: Oval shaped steel jacketing; FRP-MS: Oval shaped CFRP with 2 layers; FRP-4: CFRP with 4 layers; FRP-6: CFRP with 6 layers; FRP-8: CFRP with 8 layers;) (El Gawady et al. 2010). 26

Figure 2.15 : An example of external prestressing square RC columns (Saatcioglu and Yalcin 2003). 28

Figure 2.16: Effective confinement area in concrete columns with different cross sections (Campione et al. 2004). 30

Figure 2.17: The column formwork and reinforcing steel details (Shrestha 2019). 32

Figure 2.18: Retrofit details including the TiAB spiral and ligament (Shrestha 2019). 33

Figure 2.19: Anchorage details of TiAB components: (a) Straightened end of spiral TiAB and 90° anchorage hook, (b) TiAB ligament dimensions and details (Shrestha 2019). 35

Figure 2.20: TiAB retrofit processing (Shrestha 2019).....37

Figure 2.21: Typical setup with lateral and axial loading for lateral seismic tests on “short” column (Shrestha 2019). 39

Figure 2.22: The equivalent lateral load, expressed as column shear, versus drift response for the control columns (representatives of as-constructed bridge columns): (a) loading perpendicular to column face, and (b) loading 45° to column face (Shrestha 2019). 41

Figure 2.23: The equivalent lateral load, expressed as column shear, versus drift response for the control columns (representatives of as-constructed bridge columns) (a) control short square column, and (b) retrofitted short square column with 90° hooked ligament (Shrestha 2019). ..42

Figure 2.24: The equivalent lateral load, expressed as column shear, versus drift response for the control columns (representatives of as-constructed bridge columns) (a) retrofitted short square column with 90° hooked ligament, and (b) retrofitted short square column with 135° hooked ligament (Shrestha 2019). 44

Figure 2.25: The equivalent lateral load, expressed as column shear, versus drift response for the control columns (a) retrofitted short square column with no ligament, and (b) standard retrofitted short square column (Shrestha 2019). 45

Figure 2.26: The equivalent lateral load, expressed as column shear, versus drift response for the control columns (a) retrofitted short square column with stainless steel ligament, and (b) control short square column (Shrestha 2019). 47

Figure 2.27: Column retrofit design of the example bridge (Shrestha 2019). 49

Figure 2.28: (a) Footing moments and shears corresponding to elastic design forces; (b) Shear force in column/footing joint under seismic actions; and (c) actual earthquake inputs (with gray lines; Xiao et al. 1996). 50

Figure 2.29: The equivalent lateral load, expressed as column shear, versus drift response for (a) the retrofitted short square column with 90° hooked ligament on foam, and (b) fixed-base retrofitted short square column with 90° hooked ligament , (c) foam profile at the end of testing, (d) visual damage to top layer of XPS foam after removal of specimen (Shrestha 2019). 53

Figure 2.30: A schematic describing the concept of plastic hinge in bridge columns (Allmond 2014).....55

Figure 2.31: Columns and foundations of a one-story building that collapsed during the moderate 1999 Athens earthquake (Gazetas 2019; Sharma 2019). 56

Figure 2.32: Forces and displacements at footing–soil interface during combined loading (Hakhamaneshi 2014; Allmond 2014). 57

Figure 2.33: Comparison of the concepts of rocking foundation and hinging column in bridge column/footing systems (Allmond 2014). 58

Figure 2.34: Two variants of square columns and transverse members, with a bent with cantilevers on the left and integral bent on the right (Isaac Constant Bridge #697, Central Point, Oregon; Kramer 2004). 60

Figure 2.35: Examples of various monolithic concrete bridge piers along Interstate-5 (Kramer 2004). 61

Figure 2.36: Idealized failure mechanisms: (a) rocking foundation and column yielding at the top; (b)rocking foundation and pinned column (Deng et al. 2012). 62

Figure 2.37: Free-body diagram for a two-column bent system with abutments on the side of the bridge (Deng et al. 2012). 63

Figure 2.38: Experimental setup used by Deng et al. (2012): (a) 3D view; (b) an elevation view of the bridge model in transverse direction (note: L_f = 5.04 m for rocking bridge and L_f = 7.56 m for hinging-column bridge); (c) deck drift angles of models: (left) permanent; (right) peak. ...64

Figure 2.39: Simplified models assuming fixed-base conditions, for the longitudinal direction: (a) System A, considering a single pier; (b) System B, taking account of the contribution of the lateral stiffness of the abutment bearings; and (c) System C, also accounting for the rotational restraint provided by the torsional resistance of the deck acting in series with the transverse moment resistance provided by the system of bearings. 65

Figure 2.40: Response of bridge columns with different typologies (Anastasopoulos et al. 2015)...66

Figure 2.41: Experimental Details by Reinhardt et al. (2003): (a) Overall Test setup, (b) steel details for beam, (c) steel details of the as-built column, (c) elevation view of the retrofitted footings, and (d) plan view of the as-built footing. 68

Figure 2.42: Accumulated Force-Displacement Hysteresis Curve for (a) B2SA, (b) B2SR, (c) B2SF, Envelope of Accumulated Force-Displacement Hysteresis Curve for (d) B2SA, (e) B2SR, and (f) B2SF (Reinhardt et al. 2003). 69

Figure 2.43: Comparison of measured (a) average footing horizontal displacement and (b) rotations vs Lateral Force for the B2SA and B2SR specimens (Reinhardt et al. 2003). 70

Figure 2.44: Comparison of the performance of footing/columns systems designed based on different concepts of foundation rocking bridge and plastic hinging (a) Moment-rotation behavior of footing of rocking bridge (b) performance of column of hinging column bridge (c) performance of footing of hinging column bridge (Deng et al. 2012). 71

Figure 2.45: Model container and experimental setup with instrumentation for vertical push, slow cyclic lateral push and dynamic loading tests (Gajan et al. 2005). 73

Figure 2.46: Slow cyclic lateral push tests (a) sand, and (b) clay (Gajan et al. 2005). 74

Figure 2.47: (a) Experimental setup, (b) concept of critical contact length and approximate influenced zone, and (c) the quick release mechanism (Sharma 2019). 75

Figure 2.48: (a) Applied static rocking moment vs. footing rotation curves in snap-back stage, (b) moment-rotation in snap-back stage at different vertical loads, and (c) comparison of calculated and measured moment capacities for all tests in present study (Sharma 2019). 76

Figure 2.49: Observed relationship between footing rotation to mobilize moment capacity (g) and A/A_c (Sharma 2019). 76

Figure 2.50: Observations regarding the displacement behavior of full-scale rocking footings (a) soil-footing interface exhibited rounding during snap-back tests performed by Sharma (2019), and (b) comparison of the normalized residual settlement and the cumulative footing rotation. The envelopes of anticipated normalized residual settlement adapted from Deng et al. (2012; sand using centrifuge modeling), Hakhamaneshi (2014; clay using centrifuge modeling) and Sharma (2019; clay using full-scale modeling). 77

Figure 2.51: Conceptual moment vs. rotation curves for (a) relatively rigid interface (large L/L_c) resulting in minimal residual rotations and minimal energy dissipation, and (b) poor soil (low L/L_c) resulting in larger residual rotations and high energy dissipation. 78

Figure 2.52: Experimental prototype used by Faccioli et al. (1998). (Dimensions are in m) (Faccioli et al. 1998). 79

Figure 2.53: Overturning moment and horizontal forces vs. rocking for soils with different densities. 80

Figure 2.54: Comparison of vertical displacement of the rocking footings overlying loose and dense sand conditions for different phases of the tests: (a) Phase I, (b) Phase II, and (c) Phase III (Faccioli et al. 1998). 81

Figure 2.55: Effect of embedment on the cyclic loading behavior of the H-shaped footings with 35% missing area ratio. The results for h/L = 0.71. The left side results are for embedded and right side are for surface footings. 82

Figure 2.56: Deformation response of surface and embedded rocking footings. 83

Figure 2.57: Critical embedment, similar footing at three different initial embedment (Hakhamaneshi 2014). 84

Figure 2.58: Details of experiments by Sharma (2019): (a) Schematic of the setup for surface soil-footing-structure system, (b) Typical histories of deck drift ratio (Sharma 2019). 85

Figure 2.59: Relationship between moment, settlement and rotation for different embedded depth (Sharma 2019). 86

Figure 2.60: Different scenarios associated with water presence in rocking footing systems (Allmond 2014). 87

Figure 2.61: Concrete pads that were placed into the soil by Deng and Kutter (2012) to reduce settlement caused by liquefaction and rocking. 89

Figure 2.62: Movement of air-water interfaces during hydraulic hysteresis below a shallow foundation. 90

Figure 3.1: ODOT inventory column type distribution. 105
Figure 3.2: ODOT inventory square column width distribution. 106
Figure 3.3: ODOT inventory square column clear height distribution. 107
Figure 3.4: ODOT inventory column longitudinal reinforcement distribution. 108
Figure 3.5: ODOT inventory column longitudinal reinforcement bar size distribution. 108
Figure 3.6: ODOT inventory column transverse reinforcement distribution. 109
Figure 3.7: ODOT inventory column transverse reinforcement bar size distribution. 109
Figure 3.8: ODOT inventory splice length distribution. 110
Figure 3.9: ODOT inventory splice length distribution in terms of bar diameter. 111
Figure 3.10: ODOT inventory square columns distribution per bent. 113
Figure 3.11: ODOT inventory square columns axial load distribution. 114
Figure 3.12: ODOT inventory square spread footing width distribution. 115
Figure 3.13: ODOT inventory foundation depth distribution for 60 in. x 60 in. spread footings. 115
Figure 3.14: ODOT inventory spread footing reinforcement distribution. 116
Figure 3.15: ODOT inventory spread footing reinforcement bar size distribution. 116
Figure 3.16: ODOT inventory square pile cap width distribution. 117
Figure 3.17: ODOT inventory depth distribution for 60 in. x 60 in. pile caps 117
Figure 3.18: ODOT inventory pile cap reinforcement distribution. 118
Figure 3.19: ODOT inventory pile cap reinforcement bar size distribution. 118
Figure 3.20: ODOT inventory footing embedment depth (in) distribution 119
Figure 4.1: Effect of varying surface flux condition on soil suction and saturation profiles underneath a rocking shallow foundation (from Khosravi et al. 2021) 122
Figure 4.2: Comparison of the concepts of rocking foundation and hinging column in bridge column/footing systems (from Allmond 2014). 126
Figure 4.3: Different scenarios of groundwater table depths to consider in the estimate of the moment capacity of rocking shallow foundations (from Khosravi et al. 2021). 131
Figure 4.4: Schematic illustrating the methodology proposed by Vanapalli et al. (1998) to obtain the air entry suction from the characteristics of the SWRC (from Khosravi et al. 2021). 132
Figure 4.5: Comparison between the air entry values estimated using the proposed empirical model (Eq. 24) and those obtained experimentally for different USCS soil types (from Khosravi et al. 2021) (Note: 1 psi = 6.89 kPa). 134
Figure 4.6: Normalized profiles of (a) matric suction; (b) effective saturation; and (c) suction stress for the three hypothetical soils of clay, silt, and sand under different surface flux boundary conditions (from Khosravi et al. 2021) (Note: 1 psi = 6.89 kPa). 136

Figure 4.7: Variations in soil suction for different soils of (a) clay; (b) silt; and (c) sand for different groundwater table depths (from Khosravi et al. 2021) (Note: 1 psi = 6.89 kPa). 136

Figure 4.8: Variations in (a) ψ_{ave}; (b) $S_{e,ave}$; (c) L_c; and (d) M_c with D_w for different flow rates and ϕ' for a shallow foundation with D_f=0.5 m in clay (from Khosravi et al. 2021) (Note: 1 m = 3.3 ft; 1 kN-m = 0.74 kip-ft).....138

Figure 4.9: Variations in (a) ψ_{ave}; (b) $S_{e,ave}$; (c) L_c; and (d) M_c with D_w for different flow rates and ϕ' for a shallow foundation with D_f=0.5 m in sand (from Khosravi et al. 2021) (Note: 1 m = 3.3 ft; 1 kN-m = 0.74 kip-ft).....139

Figure 4.10: Elevation view of the rocking foundation test setup: (a) with the location of the base of specimens and groundwater elevation for different tests used by Antonellis et al. (2015); and (b) with the quick release mechanism used by Sharma (2019; from Khosravi et al. 2021) (Note: 1 m = 3.3 ft).....140

Figure 4.11: Soil comprising the subgrade below full-scale tests: (a) grain-size distributions; and (b) SWRCs of Carroll Canyon sand (SP; Fern et al. 2014) and high plasticity silt (MH; Nam et al. 2010; from Khosravi et al. 2021) (Note: 1 mm = 0.04 in.; 1 kPa = 0.145 psi). 141

Figure 4.12:: Variations in the predicted (solid line) (a) ψ_{ave}; (b) $S_{e,ave}$; (c) L_c; and (d) M_c and comparison to experimental data (open markers, reported by Antonellis et al. 2015) with D_w (from Khosravi et al. 2021) (Note: 1 m = 3.3 ft; 1 kN-m = 0.74 kip-ft; 1 kPa = 0.145 psi). ...143

Figure 4.13: Variations in the predicted (solid line) (a) ψ_{ave}; (b) $S_{e,ave}$; (c) L_c; and (d) M_c and comparison to experimental data (open markers; reported by Sharma 2019) with D_w (from Khosravi et al. 2021) (Note: 1 m = 3.3 ft; 1 kN-m = 0.74 kip-ft; 1 kPa = 0.145 psi). 146

Figure 5.1: Column dimensions and reinforcing steel details of (a) the vintage specimen with fixed base, PHV; and (b) the reinforcing steel details of the footings (from Khosravi et al. 2023) (Note: 1 m = 3.2808 ft).....159

Figure 5.2: Column dimensions and reinforcing steel details of (a) the retrofitted specimen with TiAB ligaments and spiral with fixed base, PHRSL; and (b) the retrofitted specimen with TiAB spiral only with fixed base, PHRS (from Khosravi et al. 2023) (Note: 1 m = 3.2808 ft). 160

Figure 5.3: TiAB retrofit installation process: (a) installation of the TiAB ligaments and spiral in their designated locations; (b) placement of the polycarbonate formwork around the spirals and filling concrete into the framework; and (c) the final retrofitted specimen (from Khosravi et al. 2023).....161

Figure 5.4: Load protocol used in this study (from Khosravi et al. 2022). 163

Figure 5.5: Experimental setup used to test specimen RRSL (from Khosravi et al. 2023) (Note: 1 m = 3.2808 ft).....164

Figure 5.6: Column base moment versus drift responses for the (a) vintage specimen with fixed base, PHV; (b) retrofitted specimen with TiAB ligaments and spiral and fixed base, PHRSL; (c) retrofitted specimen with TiAB spiral only and fixed base, PHRS; and (d) retrofitted specimen with TiAB ligaments and spiral and flexible support, RRSL (from Khosravi et al. 2023).....166

Figure 5.7: Performance at the base of specimen RRSL: (a) settlement profile for the XPS soil simulant at the end of testing; (b) visual damage to the top layer of the soil simulant after removal of specimen; and (c) cracking patterns along the sides and base of the footing (from Khosravi et al. 2023). 168

Figure 5.8: Components of the models used to simulate the: (a) specimens with fixed base, and (b) specimens with flexible support (from Khosravi et al. 2023) (Note: 1 m = 3.2808 ft)..... 171

Figure 5.9: Comparison of the numerical simulation of the unconfined compression test of the XPS soil simulant to the experimental results of Sample 3 (the experimental data has been corrected for initial seating deformations) (Note: 1 m = 3.2808 ft.; 1 MPa = 145 psi). 175

Figure 5.10: Moment–curvature relationships for the test column sections: (a) vintage column; (b) retrofitted column with TiAB ligaments and spiral; (c) retrofitted column with TiAB spiral only; and ; and (d) beam used in Section 5.5. 178

Figure 5.11: Comparison of the base column moment–column drift relationships observed from the experiments to the results of numerical simulations for the (a) PHV; (b) PHRSL; (c) PHRS; and (d) RRSL specimens (from Khosravi et al. 2023). 179

Figure 5.12: Effect of soil subgrade cohesion on the response of unretrofitted vintage column–footing specimen, including the variation of the (a) base moment with column drift; and (b) maximum base moment with cohesion (from Khosravi et al. 2023). 183

Figure 5.13: Effect of the soil subgrade elastic modulus on the response of unretrofitted vintage column–footing specimen including the variation of the (a) base moment with column drift; and (b) column drift at column failure with elastic modulus (from Khosravi et al. 2023). 184

Figure 5.14: Effect of the strength and flexural stiffness of the column on the response of the column–footing specimen retrofitted with TiAB spiral only including the variation of (a) base moment with column drift for different column strength ratios; (b) column drift at failure with strength ratio; (c) base moment with column drift for different flexural stiffnesses; and (d) column drift at soil failure with flexural stiffness (from Khosravi et al. 2023). 186

Figure 5.15: Components of the numerical bent models: (a) two column-footing bent system with flexible support, and (b) two column-footing bent system with fixed bases (Note: 1 m = 3.2808 ft). 189

Figure 5.16: Specified lateral velocity used to simulate the lateral loading to the multi-column bent models (Note 1 m/s = 3.2808 ft./s). 191

Figure 5.17: Results of the simulations of two-column bent systems and comparisons with the experiments on single column systems for moment at the base of the column vs. column drift: (a) the left column of the hinging vintage bent model (PHV-B1 – LBM), (b) the left column of hinging retrofit bent model (PHRSL-B1 – LBM). 193

Figure 5.18: Results of the simulations of two-column bent systems in terms of column axial forces vs. column drift for: (a) the plastic hinge vintage bent model (PHV-B1), and the (b) plastic hinge retrofit bent model (PHRSL-B1). 194

Figure 5.19: Results of the simulations of two-column bent systems and comparison to the experiments on single column systems in terms of the moment at the base of the column vs. column drift for (a) the left column of the hinging vintage bent model (PHV-B1 – LBM), (b)

the right column of the hinging vintage bent model (PHV-B1 – RBM), (c) the left column of hinging retrofit bent model (PHRSL-B1 – LBM), and (d) the right column of hinging retrofit bent model (PHRSL-B1 – RBM). 196

Figure 5.20: Results of the simulations of Two-Column Bent Systems in terms of the axial force at the top of the column vs. column drift for (a) the Rocking Vintage Bent Model (RV-B1), (b) Rocking Retrofit Bent Model with spiral and ligament (RRSL-B1), and (c) Rocking Retrofit Bent Model with spiral only (RRS-B1)..... 197

Figure 6.1: Typical vintage footing details (all dimensions are inches): (a) Plan view, (b) Elevation view. 209

Figure 6.2: Vintage column details (all dimensions are feet and inches): (a) Plan view, (b) Elevation view. (1 ft = 12 in.; 1 in. = 25.4 mm) 210

Figure 6.3: TiAB ligament details (all dimensions are feet and inches). 211

Figure 6.4: Complete specimen design with TiAB spiral details (all dimensions are feet and inches): (a) Plan view, (b) Elevation view. 212

Figure 6.5: Stages of construction for vintage spread footings: (a) Specimen geometry and formwork prior to casting, (b) Spread footing after concrete casting. 214

Figure 6.6: Stages of construction for the vintage column: (a) Column cage attached to the footing, (b) Tied down formwork with pump valve, and (c) Completed vintage column on the spread footing. 215

Figure 6.7: Specimen with a ligament installation (all dimensions are feet and inches): (a) Plan view, (b) Elevation view. 217

Figure 6.8: Construction sequence of TiAB ligament installation: (a) Drilled holes and plastic sheathing, (b) Complete installation of staggered ligaments. 218

Figure 6.9: Specimen 1 and 2 TiAB spiral construction sequence: (a) Spiral installation, (b) Formwork for infill..... 219

Figure 6.10: TiAB spiral installation: (a) threaded rod covers, (b) shell casting formwork used for installation on Specimen 3 which was failed prior to installation of the TiABs. 220

Figure 6.11: Soil simulant layout (all dimensions are feet and inches): (a) N-S elevation view and pieces used, (b) E-W Elevation view, (c) Plan view. 224

Figure 6.12: Approximate stress distribution assumption to determine soil simulant layout (all dimensions are feet, inches, degrees). 226

Figure 6.13: Spring design for horizontal reaction frame: (a) Angle dimensions, (b) Spring stiffness and bulk dimensions (all dimensions are feet and inches). 226

Figure 6.14: SSI test setup (all dimensions are feet and in): (a) Specimen loading dimensions, (b) horizontal brace frame. 227

Figure 6.15: Test 1 (Specimen 1): Complete Retrofit with Soil Simulant Embedment and Subgrade. Standard SSI test setup. 228

Figure 6.16: Test 2 (Specimen 2): Complete restrofit with no embedment and a soil simulant subgrade. 229

Figure 6.17: Test 3 & 4 (Specimen 3): Vintage column with soil simulant embedment, subgrade, and axial load at 150 kips and 100 kips. 230

Figure 6.18: Test 5, 6, & 7 (Specimen 3): Vintage column failure, vintage ligament retrofit, and vintage complete retrofit. All three tests used a damaged soil simulant subgrade but steel springs to represent embedment within soil. 231

Figure 6.19: Test 8 (Specimen 2): Complete retrofit with tied down footing test set up. 232

Figure 6.20: Observed damage to Specimen 1 during Test 1: (a) First cracks observed in the center of the footing on the west face, (b) Cracking of the retrofit shell indicating mobilization of the retrofit, (c) Cracking of the column above the retrofit, and (d) observed damage on the west face of the footing of Specimen 1 after testing. 237

Figure 6.21: Crushing of the footing into the soil simulant at drifts of: (a) 40.6 mm (1.6 in.), (b) 50.8 mm (2 in.), and (c) 102 mm (4 in.). 239

Figure 6.22: Soil simulant damage by layer. Layers are counted from closest to the floor up: (a) Layer 4, directly underneath the footing, (b) Layer 3, (c) Layer 2, and (d) Layer 1 on the floor. 240

Figure 6.23: Cracking distribution on the face of the vintage column. 241

Figure 6.24: Crack progression at 445 kN (100 kips) axial load: (a) Cracks on the east face, and (b) cracks on the south face. 242

Figure 6.25: Footing and column damage prior to spalling of the concrete around the lap-splice: (a) SE corner of the column, and (b) SW corner of the column. 244

Figure 6.26: Spalling of concrete from the column over the lap-splice length: (a) Initial spalling on the SW corner, and (b) Column damage after testing. 245

Figure 6.27: TiAB ligament strain profile. 247

Figure 6.28: Elastic buckling of the TiAB ligaments during axial load application. 247

Figure 6.29: Force-displacement responses of specimen with TiAB ligament retrofit only compared to residual response of unretrofitted column after failure. 248

Figure 6.30: Test 7: (a) Footing damage on the face of the footing after Test 7, and (b) condition of the soil simulant after Test 3 – Test 7. 249

Figure 6.31: Failure of footing on Specimen 2: (a) Cracks formed at 20.3 mm (0.8 in.), and (b) footing failure after testing. 250

Figure 6.32: Illustration of geometric factors influencing the additional drift (Shrestha 2019). 252

Figure 6.33: Overall force-displacement response of Test 1, Specimen 1. 253

Figure 6.34: Overall force-displacement response of Test 2, Specimen 2. 254

Figure 6.35: Overall force-displacement response of Test 3, Specimen 3. 254

Figure 6.36: Overall force-displacement response of Test 4, Specimen 3. 255

Figure 6.37: Overall force-displacement response of Test 5, Specimen 3. 255

Figure 6.38: Overall force-displacement response of Test 6, Specimen 3. 256

Figure 6.39: Overall force-displacement response for Test 7, Specimen 3. 256
Figure 6.40: Overall force-displacement response for Test 8, Specimen 2 (pre-failure). 257
Figure 6.41: Overall force-displacement response for Test 8, Specimen 2 (post-footing failure)...257
Figure 6.42: P-M interaction diagrams considering as-built specimen material properties.....258
Figure 6.43: Components of measured overall horizontal displacement in column at lateral loading point. 259
Figure 6.44: Component contributions to measured displacement in T2-S2. 261
Figure 6.45: Component contributions to measured displacement in T5-S3. 261
Figure 6.46: P-Delta effect on T5-S3, vintage column failure. 263
Figure 6.47: P-Delta effects on vintage column failure with fixed base by Shrestha (2019). 263
Figure 6.48: Footing bar strains T1-S1. 264
Figure 6.49: Starter Bar Strains T5-S3. 265
Figure 6.50: Column bar Strains T5-S3. 265
Figure 6.51: Column Tie Strains T5-S3. 266
Figure 6.52: Footing Bar Strains T8-S2 Post Failure. 266
Figure 6.53: Starter Bar Strains T8-S2 Post Failure. 267
Figure 6.54: Comparison of unretrofitted vintage columns with SSI (T5-S3) and without SSI. 268
Figure 6.55: Comparison of a complete TiAB retrofit with SSI (T1-S1) and without SSI. 269
Figure 6.56: Comparison of SSI response change with embedment. 270
Figure 6.57: Influence of axial load. 271
Figure 6.58: Soil simulant profile after testing. 272
Figure 6.59: Tangent stiffness degradation of specimens on new soil simulant. 273
Figure 6.60: Tangent stiffness of specimens on previously damaged soil simulant. 274
Figure 6.61: Secant stiffness of specimens on new soil simulant. 274
Figure 6.62: Secant stiffness of specimens on previously damaged soil simulant. 275
Figure 6.63: Strain rate of axial loading on new soil simulant. 276
Figure 6.64: Stress-strain relationship of axial loading on new soil simulant. 276
Figure 6.65: Average engineering stress-strain relationship for subsequent axial loading of previously damaged soil simulant. 277
Figure 6.66: Settlement with continued rocking on the soil simulant. 278
Figure 6.67: Soil simulant model. 280
Figure 6.68: Comparison of the soil simulant model with experimental response from Test 2 of Specimen 2. 283

Figure 6.69: Comparison of soil model, including face and base, with experimental results.....286
Figure 6.70: Soil simulant model comparison using a previously damaged soil simulant under the footing and steel springs at the face of the footing.....287
Figure 6.71: Comparison of a failed column with a complete retrofit repair and pristine vintage column with a complete retrofit. 288
Figure 6.72: Observed cracking patterns in the footing: (a) illustration of footing damage in specimen R-S-R-LTi-90-Spread (Shrestha 2019), and (b) illustration of footing damage in T1-S1.....289
Figure 6.73: Plan View of the STM to carry column axial load into the subgrade reaction through the footing due to rocking. 290
Figure 6.74: Elevation of the STM at Section A-A with end nodes rotated 45 degrees for convenience. 291
Figure 6.75: Forces acting on nodes.....291
Figure 6.76: Expected moment-column compression strain interaction as the neutral axis varies. 292
Figure 6.77: Location of resultant and length of plastically deformed soil from soil simulant model at 2 % drift. 293
Figure 7.1: Plan view of the column-footing specimen test site at the GEFRS indicating nominal dimensions of relevant experimental components. 309
Figure 7.2: Cross-section profile (Section A-A') representative of the GEFRS with the variation of q_t and V_s with depth and soil descriptions. The depths and locations of the west and east footings are outlined using dashed lines. 310
Figure 7.3: Depth-dependent water content and Atterberg Limits of the Upper Willamette Silt layer (Li et al. 2017). 311
Figure 7.4: Correlation of *LI* to undrained shear strength rati. 313
Figure 7.5: Correlations of shear wave velocity to undrained shear strength. 314
Figure 7.6: Depth-varying profiles of ϕ', OCR, and s_u for SCPT-1 and SCPT-3.....317
Figure 7.7: Elevation view of a typical column-footing specimen (Parson 2022).....320
Figure 7.8: Typical vintage footing details in plan (i.) and elevation (ii.) view (Parson 2022). 322
Figure 7.9: Typical vintage column details in plan (i.) and elevation (ii.) view (Parson 2022).....323
Figure 7.10: TiAB ligament details (Parson 2022). 324
Figure 7.11: Complete specimen design with TiAB spiral detail. 325
Figure 7.12: Footing retrofit plan view for Test 9 – S1. 326
Figure 7.13: Footing retrofit elevation view for Test 9 – S1.....327
Figure 7.14: Footing retrofit, plan view for Test 10 – S3. 328
Figure 7.15: Footing retrofit, elevation view for Test 10 – S3.....328

Figure 7.16: Typical Near Surface Mounted (NSM) reinforcing steel bar details used to strengthen the footing. 329
Figure 7.17: Stages of construction for a typical footing, both prior to (i.) and after (ii.) casting (Parson 2022). 330
Figure 7.18: Stages of construction for a typical column specimen, i.) Column cage attached to the cast footing, ii.) Tied-down formwork for concrete pour, iii.) Completed vintage column on cast footing (Parson 2022).....331
Figure 7.19: Typical ligament retrofit design (Parson 2022). 332
Figure 7.20: Construction sequence of TiAB ligament installation, i.) Drilled holes prior to ligament installation, ii.) Completed installation for a typical specimen (Parson 2022). 332
Figure 7.21: Construction sequence of TiAB spiral installation, i.) Spiral installation, ii.) Formwork for infill (Parson 2022). 333
Figure 7.22: Field specimen site, with Specimen 5 (west Footing) shown closer to the picture location and Specimen 4 (east footing) closer to the Structural Laboratory. 334
Figure 7.23: Excavations for the footings of Specimens 4 (i) and 5 (ii). 335
Figure 7.24: Structural reinforcement (i) and formwork (ii) for Specimen 4. 335
Figure 7.25: Vertical load setup with connection to the strong floor, Test 10 – S3.....336
Figure 7.26: Rocking deformation string potentiometer setup for Test 10 – S3, north face.....337
Figure 7.27: Load cell and quick release assembly for snap-back testing. 338
Figure 7.28: South-north elevation of Specimen 5 with TGPs and cross-hole rods. 340
Figure 7.29: Shear wave arrivals resulting from: (a) vertical hammer strikes on the tapper cross-hole rod, and (b) horizontal hammer strikes on the post-construction cross-hole rod. 340
Figure 7.30: Calibration curve for the silica flour based on laboratory tests. 341
Figure 7.31: Process for correlating volumetric water content of silica flour to native soil based on SWRC results. 342
Figure 7.32: Volumetric water content of the subsurface beneath the east and west column-footing specimens at two depths: 1.50 m (59 in.) and 1.76 m (69 in.). 343
Figure 7.33: Volumetric water content of the subsurface beneath the west column-footing specimens at a depth of 1.50 m (59 in.) compared with the shear wave velocity determination from both cross-hole (green) and tapper rod (red) tests. 344
Figure 7.34: Typical test setup use in the structural laboratory. 345
Figure 7.35: Specimen 1 anchored to the strong floor for Test 9 – S1. 346
Figure 7.36: Boom lift positioned for snap-back tests on west footing (Specimen 5). 347
Figure 7.37: Experimental setup for snap-back tests with critical nominal dimensions. 347
Figure 7.38: Schematic representation of forces and displacement experienced by test specimen. 351
Figure 7.39: Column shear-top drift hysteresis of Test 9 - S1. 355

Figure 7.40: Cracking observed on the north face of Specimen 1 at a top drift of 61 mm (2.4 in.), traced in green. 356
Figure 7.41: Cracking observed on the north face of Specimen 1 at a top drift of 81.3 mm (3.2 in.), traced in blue. 356
Figure 7.42: Cracking observed on the south face of Specimen 1 at a top drift of 81.3 mm (3.2 in.), 101.6 mm (4.0 in.) and 111.8 mm (4.4 in.) outlined in blue, red and green, respectively. 357
Figure 7.43: Punching shear cracks observed on the north face of Specimen 1 during the pull (south) portion of the cycle at a top drift of 182.9 mm (7.2 in.). 357
Figure 7.44: Post-testing cracks observed on the east side of the footing, Specimen 1. 358
Figure 7.45: Post-testing cracks observed on the west face of column, Specimen 1, after the removal of the TiAB spiral and retrofit shell. 360
Figure 7.46: Overall force-displacement comparison of Test 9 - S1, with R-S-R-L Ti-90 from Shrestha (2019). 360
Figure 7.47: Backbone curve for Test 9 – S1 and R-S-R-L Ti-90 (Shrestha 2019). 361
Figure 7.48: Column shear-top drift hysteresis of Test 10 – S3. 362
Figure 7.49: Column shear-top drift hysteresis of Test 10 – S3 compared with Test 7 by Parson (2022). 363
Figure 7.50: Footing uplift during north (push) and south (pull) cycles, Test 10 – S3. 363
Figure 7.51: Cracking observed on the west face of Specimen 3 at a top drift of 30.5 mm (1.2 in), traced in red. 364
Figure 7.52: Cracking observed on the east face of Specimen 3 at a top drift of 40.6 mm (1.6 in.), traced in green. 365
Figure 7.53: Cracking observed on the north face of Specimen 3 at a top drift of 71.1 mm (2.8 in.), traced in black. 366
Figure 7.54: Cracking observed on the west face of Specimen 3 at a top drift of 91.4 mm (3.6 in.), traced in red. 367
Figure 7.55: Relative motion of the retrofit shell with relation to the column, Tests 9 – S1 and Test 10 – S3. 368
Figure 7.56: Comparison of Test 10 - S3 with Test 9 - S1. 370
Figure 7.57: Comparison of backbone curve from Test 10 - S3 with Test 9 - S1. 370
Figure 7.58: Strain-top drift hysteresis for footing bars in Specimen 1 during Test 9. 371
Figure 7.59: Strain-top drift hysteresis for starter bars in Specimen 1 during Test 9. Note: strains larger than the yield strain are not considered reliable. 372
Figure 7.60: Strain-top drift hysteresis for column bars in Specimen 1 during Test 9. 373
Figure 7.61: Strain-top drift hysteresis for column ties in Specimen 1 during Test 9. 374
Figure 7.62: Strain-top drift hysteresis for TiAB ligaments in Specimen 1 during Test 9. 375

Figure 7.63: Strain-top drift hysteresis for the TiAB spiral in Specimen 1 during Test 9. 376
Figure 7.64: Strain-top drift hysteresis for footing bars in Specimen 3 during Test 10.....377
Figure 7.65: Strain-top drift hysteresis for column bars in Test 9 – S1 and Test 10 – S3. 378
Figure 7.66: Strain-top drift hysteresis for column ties in Test 10 – S3. 378
Figure 7.67: Strain-top drift hysteresis for TiAB ligaments in Test 10 – S3. 379
Figure 7.68: Strain-top drift hysteresis for the TiAB spiral in Test 10 – S3. 380
Figure 7.69: Typical snap-back test setup with applied lateral load just prior to the instantaneous release (i.e., snap-back). Photo taken during test performed on May 22nd, 2023. 382
Figure 7.70: Static and dynamic lateral displacement response of Specimen 5 during the November 29th snap-back test (F = 19.9 kN or 4.48 kips): (a) Lateral load time history (b) lateral column drift at the location of force application, and (b) vertical rocking displacements of the top of the footing 0.737 m (29 in.) from the center of the specimen. 384
Figure 7.71: Static and dynamic lateral displacement response of Specimen 5 during the December 2nd snap-back test (F = 19.1 kN or 4.34 kips): (a) Lateral load time history (b) lateral column drift at the location of force application, and (b) vertical rocking displacements of the top of the footing 0.737 m (29 in.) from the center of the specimen. 386
Figure 7.72: Static and dynamic lateral displacement response of Specimen 5 during the December 5th snap-back test (F = 28.1 kN or 6.34 kips): (a) Lateral load time history (b) lateral column drift at the location of force application, and (b) vertical rocking displacements of the top of the footing 0.737 m (29 in.) from the center of the specimen. 388
Figure 7.73: Comparison of the static and dynamic lateral displacement response of Specimen 5 during the December 2nd (F = 19.1 kN or 4.34 kip) and the December 5th snap-back test (F = 28.1 kN or 6.34 kips): (a) Lateral column drift at the location of force application, (b) vertical rocking displacements of the top of the footing on the east side, and (c) vertical rocking displacements of the top of the footing on the east side located 0.737 m (29 in.) from the center of the specimen. Note: Blue is from December 2nd and red is from December 5th. 390
Figure 7.74: Comparison of the static and dynamic lateral displacement response of Specimen 5 during the May 22nd (F = 28.9 kN or 6.50 kip) and the December 5th snap-back test (F = 28.1 kN or 6.34 kips): (a) Lateral column drift at the location of force application, (b) vertical rocking displacements of the top of the footing on the east side, and (c) vertical rocking displacements of the top of the footing on the east side located 0.737 m (29 in.) from the center of the specimen. Note: Red is from December 5th and light blue is from May 22nd. 392
Figure 7.75: Lateral load time history for May 22nd snap-back test on Specimen 5 (F = 38.6 kN or 8.67 kips). 393
Figure 7.76: Comparison of the static and dynamic lateral displacement response of Specimen 5 during the May 22nd (F = 28.9 kN or 6.50 kip, F = 38.6 kN or 8.67 kip) snap-back tests: (a) Lateral column drift at the location of force application, (b) vertical rocking displacements of the top of the footing on the east side, and (c) vertical rocking displacements of the top of the footing on the east side located 0.737 m (29 in.) from the center of the specimen. Note: Green is second test from May 22nd and blue is first test from May 22nd. 394

Figure 7.77: Comparison of the column drift time histories from: (a) the December 2nd, F = 19.3 kN (4.34 kip), (b) the December 5th. F = 28.1 kN (6.32 kip), (c) the May 22nd, F = 28.9 kN (6.50 kip), and (d) the May 22nd, F = 38.6 kN (8.67 kip) snap-back tests performed on Specimen 5. 395

Figure 7.78: Process for the determination of the positive-cycle ω_d, δ, and ζ from the column drift time recorded during the May 22nd snap-back test, F = 38.6 kN (8.67 kip). 397

Figure 7.79: Dynamic excitation of the column at the point of load application recorded during the December 5th (F = 28.1 kN 6.32 kip) snap-back test: (a) acceleration time history, and (b) the corresponding velocity time history. Note: The non-zero final velocity of the specimen can be attributed to imperfect baseline corrections. 399

Figure 7.80: Comparison of the column drift, east and west vertical footing displacement histories and east-west accelerations recorded during the December 5th (F = 28.1 kN or 6.32 kip) snap-back test. 400

Figure 7.81: Strain histories for starter bars during the December 5th, F = 28.1 kN (6.32 kip) snap-back test performed on Specimen 5. 402

Figure 7.82: Strain histories for starter bars during the December 5th, F = 28.1 kN (6.32 kip) snap-back test performed on Specimen 5. 402

Figure 7.83: Strain histories for column bars during the December 5th snap-back, F = 28.1 kN (6.32 kip). 404

Figure 7.84: Strain history comparison of column and starter bars at Location 2 during the December 5th snap-back, F = 28.1 kN (6.32 kip). 404

Figure 7.85: Strain histories for column ties during the December 5th snap-back, F = 28.1 kN (6.32 kip). 405

Figure 7.86: Comparison of the strain histories for column bars SW.2. and SE.3. during the May 22nd snap-back tests (F = 28.9 kN or 6.50 kip, F = 38.6 kN or 8.67 kip). 406

Figure 7.87: Comparison of the strain histories for starter bar SE.3. during the May 22nd snap-back tests (F = 28.9 kN or 6.50 kip, F = 38.6 kN or 8.67 kip). 407

Figure 7.88: Comparison of the strain histories for footing bars F.L.C.E. and F.T.E. during the: (a) 28.9 kN (6.50 kip) and (b) 38.6 kN (8.67 kip) snap-back tests on May 22nd. 408

Figure 7.89: Comparison of the strain time histories for starter bar SB.SE.2. during the 28.1 kN (6.32 kip) and 28.9 kN (6.50 kip) snap-back tests performed on December 5th and May 22nd, respectively. 409

Figure 7.90: Comparison of the strain time histories for two select column bars during the 28.1 kN (6.32 kip) and 28.9 kN (6.50 kip) snap-back tests performed on December 5th and May 22nd, respectively. 409

Figure 7.91: Fluctuation in mean shear wave velocity in relation to the “First” snap-back (F = 28.9 kN or 6.50 kip) and “Second” snap-back (F = 38.6 kN or 8.67 kip) performed on May 22nd. Note: shear wave velocities determined through the analysis of TGP z-direction histories when the cross-hole rod was subjected to twenty vertical strikes with a hammer. 411

Figure 7.92: Response of the bearing soils to the December 5th snap-back performed on Specimen 5 (F = 28.1 kN or 4.32 kip): (a) particle velocity, and (b) displacement time histories recorded by TGPs. 413

Figure 7.93: (a) particle velocity and (b) displacement time histories calculated from the voltage time histories recorded by TGPs during the May 22nd snap-back performed on Specimen 5 (F = 38.6 kN or 8.76 kip). 414

Figure 7.94: Average 1D shear strain history recorded by the south and north TGPs during the May 22nd snap-back (F = 38.6 kN or 8.67 kip). 415

Figure 7.95: Shear modulus reduction curve associated with the Vucetic and Dobry (1991) G/G_{max} curve (PI = 15) overlain with the shear strain, γ, and corresponding Shear Modulus, G, from the May 22nd (F = 38.6 kN or 8.67 kip) snap-back test. 417

Figure 7.96: SWRC test results for Upper Willamette Silt. 420

Figure 7.97: Nonlinear mobilized bearing resistance models for Upper Willamette Silt at GEFRS considering: (a) partially-saturated (S = 98%) conditions representative of the dry season, and (b) fully-saturated, undrained conditions representative of the wet season. 422

Figure 7.98: Nonlinear mobilized bearing resistance models normalized by the effective footing width for Upper Willamette Silt at GEFRS considering: (a) partially-saturated (S = 98%) conditions representative of the dry season, and (b) fully-saturated, undrained conditions representative of the wet season. The effective footing width, B', was equal to 1.72 m (5.6 ft.) and the maximum normalized displacement was equal to 0.10 for all five tests. 422

Figure 7.99: Schematic for nonlinear soil-structure interaction spring model representative of the static lateral pushover portion of a snap-back test prior to the instantaneous release of applied force. 423

Figure 7.100: Schematic for the determination of interface displacements in SSI spring model. ... 425

Figure 7.101: Soil-Structure Interaction model results for the May 22nd (F = 38.6 kN or 8.67 kip) snap-back, assuming partially saturated (S = 98%) conditions. The blue markers represent the full global rigid rotation of the specimen based on the recorded maximum top drift, whereas the red markers represent a combination of global rocking and column flexure. 430

Figure 7.102: Soil-Structure Interaction model results for May 22nd snap-back (F = 38.6 kN or 8.67 kip), assuming undrained conditions (S = 100%). The blue markers represent the full global rigid rotation of the specimen based on the recorded maximum top drift, whereas the red markers represent a combination of global rocking and column flexure. 430

Figure 7.103: Comparison of applied moment-drift responses at varying applied axial loads (P = 0, 50, and 100 kN) for wet season conditions at GEFRS. 431

Figure 7.104: Comparison of applied moment-drift responses at varying degrees of saturation (S = 90%, 95%, and 98%) assuming partially saturated conditions with no applied axial load (i.e., only self-weight). 432

Figure 7.105: Comparison of applied moment-drift responses at varying applied axial loads (P = 0, 50, and 100 kN) assuming partially saturated conditions. 433

Figure 7.106: Shear stress-strain hysteretic response of a soil modeled with consideration to the extended Masing rules (Kramer 1996). 434

Figure 7.107: Typical strain history from UCS tests on soil simulant foam performed by Shrestha (2019). 435

Figure 7.108: Pressure-normalized displacement (i.e., force/area-displacement/footing width) histories for the axial loading portion of full-scale, quasi-static, cyclic lateral loading tests on soil simulant foam performed by Parson (2022). 436

Figure 7.109: Compressive stress-strain histories for UCS testing on cylindrical soil simulant specimens at strain rates of: (a) 5%/sec, (b) 0.5%/sec, (c) 0.1%/sec, and (d) 0.05%/sec. 437

Figure 7.110: Compressive stress-strain histories at small strains for UCS testing on cylindrical soil simulant specimens at strain rates of: (a) 5%/sec, (b) 0.5%/sec, (c) 0.1%/sec, and (d) 0.05%/sec. 438

Figure 7.111: Correlation of strain rate from UCS tests (current study and Shrestha 2019) and axial load (Parson 2022) tests to the modulus of elasticity, E, of the soil simulant foam. The correlation presented was created using only the UCS test data from the current study and Parson (2022). 440

Figure 7.112: Correlation of strain rate from UCS tests (current study and Shrestha 2019) and axial load (Parson 2022) tests to the ultimate compressive strength, σ_{ult}, of the soil simulant foam. The correlation presented was created using only the UCS test data from the current study. . 440

Figure 7.113: Soil simulant cylindrical specimens after UCS testing. 441

Figure 7.114: Upper and lower bound estimates of the strain rate, $\boldsymbol{\varepsilon}$, at the edge of the footing during the 14th rocking cycle of Test 2 – S2 (data from Parson 2022). 442

Figure 7.115: Linear curve fit (m = 157 psi/η) of pressure-normalized displacement response during axial loading portion of Test 2 – S2 (Parson 2022) with the corresponding shifted normalized displacement-pressure history. 445

Figure 7.116: Mobilized force at all springs during the first nine cycles of Test 2 – S2 (Parson 2022). Each cycle has the mobilized response from the positive (solid lines) and negative (dashed lines) drifts, symmetrical about the centroid of the column-footing specimen. 447

Figure 7.117: Comparison of the elastic, perfectly plastic hysteretic SSI model output (considering strain rate-dependent parameters) with the backbone curve of Test 2 – S2 (Parson 2022). 448

Figure 7.118: Comparison of the simulated drift-lateral load backbone curves representative of the fully-saturated (undrained) conditions at the GEFRS with additional axial loads of 0 kN (0 kip), 25 kN (5.6 kip), 50 kN (11.2 kip), 75 kN (16.8 kip), and 100 kN (22.4 kip) applied to the specimen. 450

Figure 7.119: Comparison of the simulated drift-lateral load backbone curves representative of the fully-saturated (undrained) conditions at the GEFRS considering s_u = 63 kPa or 1,316 psf (average), 76 kPa or 1,580 psf (increase of 20%), and 50 kPa or 1,040 psf (decrease of 20%) with no additional axial load applied to the specimen. 451

Figure 7.120: Comparison of drift-lateral load backbone curves representative of the various partially saturated conditions at the GEFRS without any additional axial load applied to the

specimen. Degrees of saturation of 90%, 95%, and 98% corresponded to bearing capacities of 1,363 kPa (198 psi), 1,312 kPa (190 psi), and 1,281 kPa (186 psi), respectively. 452

Figure 7.121: Comparison of the simulated drift-lateral load backbone curves representative of the partially-saturated conditions at the GEFRS considering ϕ' = 30.4º (average), 33.4º (increase of 10%), and 27.4º (decrease of 10%) with no additional axial load applied to the specimen..... 453

Figure 7.122: Comparison of the simulated drift-lateral load backbone curves representative of the partially-saturated (S = 98%) conditions at the GEFRS with additional axial loads of 0 kN (0 kip), 100 kN (22.4 kip), 200 kN (45.0 kip), 300 kN (67.4 kip), and 400 kN (89.9 kip) applied to the specimen. 454

Figure 7.123: (a) CPT profile of test site with shear strengths from USC tests, and (b) site stratigraphy and lab test results (from Sharma 2019)..... 455

Figure 7.124: Typical top drift history for a reversed cyclic lateral load test (after Sharma 2019). 455

Figure 7.125: Setup of surface soil-footing-structure system: (a) drawing, and (b) photo of test (from Sharma 2019). 457

Figure 7.126: Relationship between applied moment and footing rotation for various tests conducted by Sharma (2019), with Test TS11shown in (b) (from Sharma 2019). 457

Figure 7.127: Comparison of the lateral load-drift backbone curves produced by the hysteretic SSI model provided the average (k_1 = 0.013, k_2 = 0.701), upper bound (k_1 = 0.003, k_2 = 0.540), and lower bound (k_1 = 0.003, k_2 = 0.960) hyperbolic parameter pairs (M_{STC} = 0.55, q_{ult} = 498 kPa or 10.4 ksf) with the load-drift backbone curve observed during Test TS11 (Sharma 2019).. 459

Figure 7.128: Comparison of the lateral load-drift backbone curve produced by the hysteretic SSI model provided the average (k_1 = 0.013, k_2 = 0.701) hyperbolic parameter pairs (M_{STC} = 0.55) and a reduced q_{ult} = 368 kPa (7.7 ksf) with the load-drift backbone curve observed during Test TS11 (Sharma 2019). 459

Figure 7.129: Comparison of the lateral load-drift backbone curve produced by the hysteretic SSI model provided the lower bound (k_1 = 0.03, k_2 = 0.540) hyperbolic parameter pairs (M_{STC} = 0.55) and a reduced q_{ult} = 368 kPa (7.7 ksf) with the load-drift backbone curve observed during Test TS11 (Sharma 2019). 460

Figure 7.130: Relationship between applied moment and footing rotation for Test LS11 (Sharma 2019)..... 461

Figure 7.131: Comparison of the lateral load-drift backbone curves produced by the hysteretic SSI model provided the average (k_1 = 0.013, k_2 = 0.701), upper bound (k_1 = 0.003, k_2 = 0.540), and lower bound (k_1 = 0.003, k_2 = 0.960) hyperbolic parameter pairs (M_{STC} = 0.55, q_{ult} = 498 kPa or 10.4 ksf) with the load-drift backbone curve observed during Test LS11 (Sharma 2019).. 462

Figure 7.132: Comparison of the lateral load-drift backbone curve produced by the hysteretic SSI model provided the upper bound (k_1 = 0.003, k_2 = 0.960) hyperbolic parameter pairs (M_{STC} = 0.55) and a reduced q_{ult} = 368 kPa (7.7 ksf) with the load-drift backbone curve observed during Test LS11 (Sharma 2019). 462

Figure 7.133: Comparison of simulated hypothetical quasi-static cyclic lateral loading backbone curves assuming an average (k_1 = 0.013, k_2 = 0.701), upper bound (k_1 = 0.003, k_2 = 0.960),

and lower bound (k_1 = 0.030, k_2 = 0.540) pair of hyperbolic parameters. The bearing capacity was assumed to be 1,281 kPa (26.8 kPa). 463
Figure A6.1.1: Shrestha (2019) Compression Test Result, Foam Cylinder 1. ....A6.1-4
Figure A6.1.2: Shrestha (2019) Compression Test Result, Foam Cylinder 2. ....A6.1-4
Figure A6.1.3: Shrestha (2019) Compression Test Result, Foam Cylinder 3. ....A6.1-5
Figure A6.1.4: FOAMULAR® 1000 material properties as reported by manufacturer. A6.1-6
Figure A6.1.5: Possible experimental setup envisioned to be deployed in the structural laboratory on full-scale column-footing specimens with the springs indicated in the red boxes. A6.1-7
Figure A6.1.7: Numerical simulations considered for calculating spring stiffness for large scale experiments A6.1-9
Figure A6.1.8: Lateral forces measured along the footing walls for: (a) an embedded footing in soil with no overburden pressure, (b) embedded footing in soil with 2' overburden soil on top equivalent to a 12 kPa (250 psf) surcharge, (c) embedded footing in soil with a 2' foam on top and 12 kPa (250 psf) normal force applied to the top of the foam, and (d) embedded footing in soil with no overburden soil but 12 kPa (250 psf) normal force applied to the top of the foam. A6.1-10
Figure A6.2.1: Location of footing strain gauges. A6.2-3
Figure A6.2.2: Starter bar strain gauge locations. A6.2-4
Figure A6.2.3: Column bar strain gauge locations. A6.2-5
Figure A6.2.4: Column tie strain gauge locations on the east face. A6.2-6
Figure A6.2.5: Column tie strain gauge locations on the north face. A6.2-7
Figure A6.2.6: Column tie strain locations on the south face. A6.2-8
Figure A6.2.7: TiAB ligament strain gauge locations. A6.2-9
Figure A6.2.8: TiAB spiral strain gauge locations. A6.2-10
Figure A6.2.9: String potentiometer locations on the top of the footing. A6.2-11
Figure A6.2.10: String potentiometers on the bottom of the footing. A6.2-11
Figure A6.2.11: String Potentiometer locations on the east and west of the footing. A6.2-11
Figure A6.2.12: String potentiometer locations on the north and south face of the column. A6.2-12
Figure A6.2.13: String Potentiometer locations on the west face. A6.2-13
Figure A6.3.1.1: Elevation View of Specimen 1 used in Test 1. ....A6.3-2
Figure A6.3.1.2: Plan View of Specimen 1 used in Test 1. ....A6.3-3
Figure A6.3.1.3: Overall Force Displacement Response – Test 1. ....A6.3-4
Figure A6.3.1.4: Component Contributions to Force Displacement – Test 1. ....A6.3-4
Figure A6.3.1.5: Overall Force Displacement Backbone Curve – Test 1. ....A6.3-5
Figure A6.3.1.6: P-Delta Effects Backbone Curve – Test 1. ....A6.3-5

Figure A6.3.1.7: P-Delta Effects – Test 1. ....A6.3-6
Figure A6.3.1.8: Settlement – Test 1. ....A6.3-6
Figure A6.3.1.9: Evolution Secant Stiffness – Test 1. ....A6.3-7
Figure A6.3.1.10: Evolution of Tangent Stiffness – Test 1. ....A6.3-7
Figure A6.3.1.11: Footing Bar Strains – Test 1. ....A6.3-8
Figure A6.3.1.12: Starter Bar Strains – Test 1. ....A6.3-8
Figure A6.3.1.13: Column Bar Strains – Test 1. ....A6.3-9
Figure A6.3.1.14: Column Tie Strains – Test 1. ....A6.3-9
Figure A6.3.1.15: TiAB Ligament Strains – Test 1. ....A6.3-10
Figure A6.3.1.16: TiAB Spiral Strains – Test 1. ....A6.3-10
Figure A6.3.1.17: Soil Simulant Profile After Testing – Test 1. ....A6.3-11
Figure A6.3.1.18: Soil Simulant Model Comparison – Test 1. ....A6.3-11
Figure A6.3.2.1 - Elevation View of Specimen 2 used in Test 2. ....A6.3-12
Figure A6.3.2.2: Plan View of Specimen 2 used in Test 2. ....A6.3-13
Figure A6.3.2.3: Overall Force Displacement Response – Test 2. ....A6.3-13
Figure A6.3.2.4: Component Contributions to Force Displacement – Test 2. ....A6.3-14
Figure A6.3.2.5: Overall Force Displacement Backbone Curve – Test 2. ....A6.3-14
Figure A6.3.2.6: P-Delta Effects Backbone Curve – Test 2. ....A6.3-15
Figure A6.3.2.7: P-Delta Effects – Test 2. ....A6.3-15
Figure A6.3.2.8: Settlement – Test 2. ....A6.3-16
Figure A6.3.2.9: Evolution of Secant Stiffness – Test 2. ....A6.3-16
Figure A6.3.2.10: Evolution of Tangent Stiffness – Test 2. ....A6.3-17
Figure A6.3.2.11: Footing Bar Strains -Test 2. ....A6.3-17
Figure A6.3.2.12: Starter Bar Strains – Test 2. ....A6.3-18
Figure A6.3.2.13: Column Bar Strains – Test 2. ....A6.3-18
Figure A6.3.2.14: Column Tie Strain – Test 2. ....A6.3-19
Figure A6.3.2.15: TiAB Ligament Strain – Test 2. ....A6.3-19
Figure A6.3.2.16: TiAB Spiral Strain – Test 2. ....A6.3-20
Figure A6.3.2.17: Soil Simulant Profile After Testing – Test 2. ....A6.3-20
Figure A6.3.2.18: Soil Simulant Model Comparison -Test 2. ....A6.3-21
Figure A6.3.3.1: Elevation View of Specimen 3 used in Test 3. ....A6.3-22
Figure A6.3.3.2: Plan View of Specimen 3 used in Test 3. ....A6.3-23

Figure A6.3.3.3: Overall Force Displacement Response – Test 3. ....A6.3-23
Figure A6.3.3.4: Component Contributions to Force Displacement – Test 3.....A6.3-24
Figure A6.3.3.5: Overall Force Displacement Backbone Curve – Test 3.....A6.3-24
Figure A6.3.3.6: P-Delta Effects Backbone Curve – Test 3. ....A6.3-25
Figure A6.3.3.7: P-Delta Effects – Test 3. ....A6.3-25
Figure A6.3.3.8: Settlement – Test 3. ....A6.3-26
Figure A6.3.3.9: Evolution of Secant Stiffness – Test 3.....A6.3-26
Figure A6.3.3.10: Evolution of Tangent Stiffness – Test 3. ....A6.3-27
Figure A6.3.3.11: Footing Bar Strains – Test 3. ....A6.3-27
Figure A6.3.3.12: Starter Bar Strains – Test 3. ....A6.3-28
Figure A6.3.3.13: Column Bar Strains – Test 3.....A6.3-28
Figure A6.3.3.14: Column Tie Strains – Test 3. ....A6.3-29
Figure A6.3.3.15: Soil Simulant Model Comparison – Test 3.....A6.3-29
Figure A6.3.4.1 - Elevation View of Specimen 3 used in Test 4.....A6.3-30
Figure A6.3.4.2 - Plan View of Specimen 3 used in Test 4. ....A6.3-31
Figure A6.3.4.3: Overall Force Displacement Response -Test 4.....A6.3-31
Figure A6.3.4.4: Component Contributions to Force Displacement – Test 4.....A6.3-32
Figure A6.3.4.5: Overall Force Displacement Backbone Curve – Test 4.....A6.3-32
Figure A6.3.4.6: P-Delta Effects Backbone Curve – Test 4. ....A6.3-33
Figure A6.3.4.7: P-Delta Effects – Test 4. ....A6.3-33
Figure A6.3.4.8: Settlement – Test 4. ....A6.3-34
Figure A6.3.4.9: Evolution of Secant Stiffness – Test 4.....A6.3-34
Figure A6.3.4.10: Evolution of Tangent Stiffness – Test 4. ....A6.3-35
Figure A6.3.4.11: Footing Bar Strains – Test 4. ....A6.3-35
Figure A6.3.4.12: Starter Bar Strains – Test 4. ....A6.3-36
Figure A6.3.4.13: Column Bar Strains – Test 4.....A6.3-36
Figure A6.3.4.14: Column Tie Strains – Test 4. ....A6.3-37
Figure A6.3.4.14: Soil Simulant Model – Test 4. ....A6.3-37
Figure A6.3.5.1 - Elevation View of Specimen 3 used in Test 5.....A6.3-38
Figure A6.3.5.2 - Plan View of Specimen 3 used in Test 5. ....A6.3-39
Figure A6.3.5.3: Overall Force Displacement Response – Test 5. ....A6.3-39
Figure A6.3.5.4: Component Contributions to Force Displacement – Test 5.....A6.3-40

Figure A6.3.5.5: Overall Force Displacement Backbone Curve – Test 5. ..... A6.3-40
Figure A6.3.5.6: P-Delta Effects Backbone Curve – Test 5. ..... A6.3-41
Figure A6.3.5.7: P-Delta Effects – Test 5. ..... A6.3-41
Figure A6.3.5.8: Settlement – Test 5. ..... A6.3-42
Figure A6.3.5.9: Evolution of Secant Stiffness – Test 5. ..... A6.3-42
Figure A6.3.5.10: Evolution of Tangent Stiffness – Test 5. ..... A6.3-43
Figure A6.3.5.11: Footing Bar Strains – Test 5. ..... A6.3-43
Figure A6.3.5.12: Starter Bar Strains – Test 5. ..... A6.3-44
Figure A6.3.5.13: Column Bar Strains – Test 5. ..... A6.3-44
Figure A6.3.5.14: Column Tie Strains – Test 5. ..... A6.3-45
Figure A6.3.5.15: Soil Simulant Model: Test 5. ..... A6.3-45
Figure A6.3.6.1 - Elevation View of Specimen 3 used in Test 6. ..... A6.3-46
Figure A6.3.6.2 - Plan View of Specimen 3 used in Test 6. ..... A6.3-47
Figure A6.3.6.3: Overall Force Displacement Response – Test 6. ..... A6.3-48
Figure A6.3.6.4: Component Contributions to Force Displacement – Test 6. ..... A6.3-48
Figure A6.3.6.5: Overall Force Displacement Backbone Curve – Test 6. ..... A6.3-49
Figure A6.3.6.6: P-Delta Effects Backbone Curve – Test 6. ..... A6.3-49
Figure A6.3.6.7: P-Delta Effects – Test 6. ..... A6.3-50
Figure A6.3.6.8: Settlement – Test 6. ..... A6.3-50
Figure A6.3.6.9: Evolution of Secant Stiffness – Test 6. ..... A6.3-51
Figure A6.3.6.10: Evolution of Tangent Stiffness – Test 6. ..... A6.3-51
Figure A6.3.6.11: Footing Bar Strains – Test 6. ..... A6.3-52
Figure A6.3.6.12: Starter Bar Strains – Test 6. ..... A6.3-52
Figure A6.3.6.13: Column Bar Strains – Test 6. ..... A6.3-53
Figure A6.3.6.14: Column Tie Strains – Test 6. ..... A6.3-53
Figure A6.3.6.15: TiAB Ligament Strains – Test 6. ..... A6.3-54
Figure A6.3.6.16: TiAB Ligament Strains Close Up – Test 6. ..... A6.3-54
Figure A6.3.6.17: Soil Simulant Profile After Test 6. ..... A6.3-55
Figure A6.3.6.18: Soil Simulant Model Comparison – Test 6. ..... A6.3-55
Figure A6.3.7.1: Elevation View of Specimen 3 used in Test 7. ..... A6.3-56
Figure A6.3.7.2: Plan View of Specimen 3 used in Test 7. ..... A6.3-57
Figure A6.3.7.3: Overall Force Displacement Response – Test 7. ..... A6.3-58

Figure A6.3.7.4: Component Contributions to Force Displacement -Test 7. .....A6.3-58
Figure A6.3.7.5: Overall Force Displacement Backbone Curve – Test 7. .....A6.3-59
Figure A6.3.7.6: P-Delta Effects Backbone Curve – Test 7. .....A6.3-59
Figure A6.3.7.7: P-Delta Effects – Test 7. .....A6.3-60
Figure A6.3.7.8: Settlement – Test 7. .....A6.3-60
Figure A6.3.7.9: Evolution of Secant Stiffness – Test 7. .....A6.3-61
Figure A6.3.7.10: Evolution of Tangent Stiffness – Test 7. .....A6.3-61
Figure A6.3.7.11: Footing Bar Strains – Test 7. .....A6.3-62
Figure A6.3.7.12: Column Bar Strains – Test 7. .....A6.3-62
Figure A6.3.7.13: Column Tie Strains – Test 7. .....A6.3-63
Figure A6.3.7.14: TiAB Ligament Strains – Test 7. .....A6.3-63
Figure A6.3.7.15: TiAB Spiral Strains – Test 7. .....A6.3-64
Figure A6.3.7.16: Soil Simulant Model Comparison – Test 7. .....A6.3-64
Figure A6.3.8.1: Elevation View of Specimen 2 used in Test 8. .....A6.3-65
Figure A6.3.8.2: Plan View of Specimen 2 used in Test 8. .....A6.3-66
Figure A6.3.8.3: Overall Force Displacement Response Pre-failure – Test 8. .....A6.3-67
Figure A6.3.8.4: Overall Force Displacement Response Post-failure – Test 8. .....A6.3-67
Figure A6.3.8.5: Overall Force Displacement Backbone Curve Pre-failure – Test 8. .....A6.3-68
Figure A6.3.8.6: Overall Force Displacement Backbone Curve Post-failure – Test 8. .....A6.3-68
Figure A6.3.8.7: P-Delta Effects Backbone Curve Pre-failure – Test 8. .....A6.3-69
Figure A6.3.8.8: P-Delta Effects Backbone Curve Post-failure – Test 8. .....A6.3-69
Figure A6.3.8.9: P-Delta Effects Pre-failure – Test 8. .....A6.3-70
Figure A6.3.8.10: P-Delta Effects Post-failure – Test 8. .....A6.3-70
Figure A6.3.8.11: Evolution of Secant Stiffness Pre-failure – Test 8. .....A6.3-71
Figure A6.3.8.12: Evolution of Secant Stiffness Post-Failure – Test 8. .....A6.3-71
Figure A6.3.8.13: Evolution of Tangent Stiffness Pre-failure – Test 8. .....A6.3-72
Figure A6.3.8.14: Evolution of Tangent Stiffness Post-Failure – Test 8. .....A6.3-72
Figure A6.3.8.15: Footing Bar Strains Pre-failure – Test 8. .....A6.3-73
Figure A6.3.8.16: Footing Bar Strains Post-Failure – Test 8. .....A6.3-73
Figure A6.3.8.17: Starter Bar Strains Pre-failure – Test 8. .....A6.3-74
Figure A6.3.8.18: Starter Bar Strains Post-failure – Test 8. .....A6.3-74
Figure A6.3.8.19: Column Bar Strain Pre-failure – Test 8. .....A6.3-75

Figure A6.3.8.20: Column Bar Strain Post-failure – Test 8. ..... A6.3-75
Figure A6.3.8.21: Column Tie Strains Pre-failure – Test 8. ..... A6.3-76
Figure A6.3.8.22: Column Tie Strains Post-failure – Test 8. ..... A6.3-76
Figure A6.3.8.23: TiAB Ligament Strains Pre-failure – Test 8. ..... A6.3-77
Figure A6.3.8.24: TiAB Ligament Strains Post-failure – Test 8. ..... A6.3-77
Figure A6.3.8.25: TiAB Spiral Strains Pre-failure – Test 8. ..... A6.3-78
Figure A6.3.8.26: TiAB Spiral Strains Post-failure – Test 8. ..... A6.3-78
Figure A6.3.9.1: Comparison of Complete Retrofit SSI. A6.3-79
Figure A6.3.9.2 – Comparison of Vintage Column SSI. A6.3-79
Figure A6.3.9.3: Subsequent Settlement Comparison. A6.3-80
Figure A6.3.9.4: Effect of Axial Load. A6.3-80
Figure A6.3.9.5: Effect of Embedment. A6.3-81
Figure A6.3.9.6: Tangent Stiffness Virgin Soil Simulant. A6.3-81
Figure A6.3.9.7: Secant Stiffness Virgin Soil Simulant. A6.3-82
Figure A6.3.9.8: Tangent Stiffness of Failed Soil Simulant. A6.3-82
Figure A6.3.9.9: Secant Stiffness of Failed Soil Simulant. A6.3-83
Figure A6.3.9.10: Strain Rate on Virgin Soil Simulant. A6.3-83
Figure A6.3.9.11: Bulk Engineering Stress-Strain Relationship on Virgin Soil. A6.3-84
Figure A6.3.9.12: Bulk Average Engineering Stress-Strain Relationship. A6.3-84
Figure A6.3.9.13: P-M Interaction Diagrams with As-Built Vintage Column Details. A6.3-85
Figure A6.3.9.14: Expected moment strain as neutral axis varies. A6.3-85
Figure A7.1.1.1: Overall force-displacement response, Test 9 – S1. ..... A7.1-1
Figure A7.1.1.2: Load-drift comparison, Test 9 – S1 and R-S-R-L Ti 90 (Shrestha 2019). A7.1-2
Figure A7.1.1.3: Backbone Curves, Test 9 – S1 and R-S-R-L Ti 90 (Shrestha 2019). A7.1-2
Figure A7.1.1.4: Footing bar strain-drift histories, Test 9 – S1. ..... A7.1-3
Figure A7.1.1.5: Starter bar strain-drift histories, Test 9 – S1. ..... A7.1-3
Figure A7.1.1.6: Column bar strain-drift histories, Test 9 – S1. ..... A7.1-4
Figure A7.1.1.7: Column tie strain-drift histories, Test 9 – S1. ..... A7.1-4
Figure A7.1.1.8: TiAB spiral strain-drift histories, Test 9 – S1. ..... A7.1-5
Figure A7.1.1.9: TiAB ligament strain-drift histories, Test 9 – S1. ..... A7.1-6
Figure A7.1.2.2: Overall force-displacement response comparisons: Test 7 – S3. ..... A7.1-8
Figure A7.1.2.4: Backbone curve comparisons: Test 9 – S1 and Test 10 – S3. ..... A7.1-9

Figure A7.1.2.5: Footing bar strain-drift histories, Test 10 – S3. ....A7.1-9
Figure A7.1.2.6: Column bar strain histories, Test 10 – S3. ....A7.1-10
Figure A7.1.2.7: Column tie strain histories, Test 10 – S3. ....A7.1-10
Figure A7.1.2.8: TiAB spiral strain histories, Test 10 – S3. ....A7.1-11
Figure A7.1.2.9: TiAB ligament strain histories, Test 10 – S3. ....A7.1-12
Figure A7.1.2.10: Vertical displacement of footing, Test 10 – S3. ....A7.1-13
Figure A7.1.3.1: Overall rocking displacement. A7.1-14
Figure A7.1.3.2: Footing bar strain histories. A7.1-15
Figure A7.1.3.3: Starter bar strain histories. A7.1-15
Figure A7.1.3.4: Column bar strain histories. A7.1-16
Figure A7.1.4.1: Overall rocking response. A7.1-17
Figure A7.1.4.2: Footing bar strain histories. A7.1-18
Figure A7.1.4.3: Starter bar strain histories. A7.1-18
Figure A7.1.4.4: Column bar strain histories. A7.1-19
Figure A7.1.4.5: Column tie strain histories. A7.1-19
Figure A7.1.5.1: Overall rocking displacements. A7.1-20
Figure A7.1.5.2: Footing bar strain histories. A7.1-21
Figure A7.1.5.4: Column bar strain histories. A7.1-22
Figure A7.1.5.5: Column tie strain histories. A7.1-22
Figure A7.1.6.1: Overall rocking displacements. A7.1-23
Figure A7.1.6.2: Footing bar strain histories. A7.1-24
Figure A7.1.6.3: Starter bar strain histories. A7.1-24
Figure A7.1.6.4: Column bar strain histories. A7.1-25
Figure A7.1.6.5: Column tie strain histories. A7.1-25
Figure A7.1.7.1: Overall rocking displacements. A7.1-26
Figure A7.1.7.2: Footing bar strain histories. A7.1-27
Figure A7.1.7.3: Starter bar strain histories. A7.1-27
Figure A7.1.7.4: Column bar strain histories. A7.1-28
Figure A7.1.7.5: Column tie strain histories. A7.1-28
Figure A7.2.1: Strain-time histories observed during rocking at the edge of the footing for Test 2 – S2 for all fifteen unique cycles, where N = the cycle number. A7.2-1

EXECUTIVE SUMMARY

This report provides comprehensive documentation of the research conducted in SPR 830. The focus of the research was on the performance and evaluation of a new type of seismic retrofitting technique for bridge column-footing substructure components considering the influence of soil-structure interactions (SSI). The seismic retrofitting technique used titanium alloy bars (TiABs) to provide both confinement of the concrete column and a supplemental flexural tension load path. The supplemental tension load path enables the column to sustain lateral resistance even after failure of the poorly detailed reinforcing steel lap splices found in many older bridge substructures just above the footing. The TiABs provide unique features that make them suitable for such an application as they exhibit high-strength, high-ductility, and are impervious to corrosion. Following construction, the column can be visually inspected after a seismic event to assess damage. Prior research by Shrestha (2019) demonstrated the effectiveness of the system in laboratory conditions where the footing was restrained from rotation, but only limited work focused on the subgrade's role on performance when the footing may be able to rock during lateral loading. SPR 830 focused on the role of the soil-structure interactions to help inform retrofit designs and decision-making to make the best use of limited resources available for seismic strengthening of ODOT's bridge population.

The report is divided into sections that detail the background knowledge, gaps in understanding, laboratory and field experimental tests, data collection and interpretation, methods used to calibrate analytical models, analytical methods used to correlate experimental results and investigate the influence of the salient parameters, development of assessment methods for evaluation of footings under rocking conditions, and considerations for including SSI into seismic retrofitting practices. Sections 1 to 3 provide background information that informs the other sections. Sections 4 to 8 serve as stand-alone records of the research done in each domain. The highlights of each section are summarized below.

Section 1: Provides an introduction to the problem and highlights the structural issues found in many older existing reinforced concrete substructures that were designed without consideration of seismic effects. The need for inclusion of SSI effects to provide clear design guidance for the evaluation of retrofit/replacement alternatives is described, especially with limited resources available for seismic strengthening.

Section 2: A literature review is provided that describes the evolution of ODOT's seismic design standards, distribution of ages and materials for the bridge population in Oregon, the key structural features that lead to poor seismic performance or collapse including: short and poorly located lap-splices, lack or transverse reinforcement and confinement, axial loads, and loading direction. Different available retrofit strategies are discussed, and limitations are described. The background on TiAB retrofitting is reported with a focus on column retrofitting. The pertinent elements of SSI are reported for column-footing assemblies and the limited prior work on TiAB retrofitted column-footing specimens in the laboratory. A detailed review of rocking foundation behavior is provided including the salient contributing factors. A summary at the end identifies gaps in knowledge for including SSI effects in seismic retrofit decision-making and designing.

Section 3: A detailed review of the ODOT bridge inventory on I-5, US-97 and OR-58 is reported. These highways serve as important transportation, evacuation, response corridors. Structural plans were reviewed to establish the typical construction details that best represent pre-1970 bridge column design to enable development of test specimens that are reasonable and representative of the bridge population. The column shape, materials, geometrical dimensions, column/footing service level axial loads, foundation types, depth of embedment, and reinforcing details are reported statistically.

Section 4: A new practical approach for estimating the moment capacity of rocking shallow foundations on partially saturated soil is developed. The method accounts for the effect of seasonal and/or long-term climate change to the degree of soil saturation, soils with different surface flux boundary conditions, and groundwater level depths. The methodology extends an existing approach by implementing suction stress-based effective stresses and a representation of the soil-water retention curve. The methodology was demonstrated over a range of hypothetical conditions and for existing shaking table and snap-back tests. It was observed that the moment capacity is more sensitive to clayey soils compared to sandy soils. Increases in surface flux boundary conditions due to infiltration in general produced larger moment capacity, increases in ground water depth generally increased moment capacity, seasonal effects on the soil properties affect moment capacity. The framework shows that the *in-situ* moment capacity for rocking bridge foundations will vary seasonally.

Section 5: Finite element models were developed and calibrated based on experimental results from four (4) previous laboratory tests. The following specimens were used in the calibration process: 1) column-footing specimen was unretrofitted with a rotationally fixed footing, 2) TiAB retrofitted column (spiral and ligament) with rotationally fixed footing, TiAB retrofitted column (spiral only) with rotationally fixed footing, 4) TiAB retrofitted column (spiral and ligament) with footing rocking on soil simulant. The specimens were modeled and the predicted responses from three-dimensional nonlinear finite-difference models compared well with the experimentally measured responses of the test specimens. Parametric studies were used to investigate the interactions of soil strength and stiffness with the column retrofit strength and stiffness. Results of the experiments and numerical simulations showed that the moment capacity of the unretrofitted vintage columns could not achieve the yield moment and the response exhibits rapid strength degradation and no ductility due to failure of the lap splice located in the column above the footing. SSI (rocking) would not have prevented failure of the unretrofitted specimen. Retrofitting of the column is necessary to mobilize the rocking response for the soil simulant considered. SSI reduced the moment demands on the retrofitted column. Therefore, the amount of TiAB required for a column retrofit could be reduced without negatively affecting the overall response of the system. Numerical simulations showed that rocking is induced when the soil subgrade becomes weaker and the rocking moment capacity becomes smaller relative to the column moment capacity, regardless of the column retrofit (either retrofitted or unretrofitted). The simulations demonstrated that for a given rocking moment capacity, differences in soil stiffness do not change the mode of behavior in terms of whether it rocks or not. However, reduced soil stiffness increases the drift at which the moment capacity is reached. There exists a threshold flexural strength at which the column-footing system behavior transitions from plastic hinging in the column to rocking of the column-footing system. This threshold can be used to optimize the selection and design of the retrofit. Numerical studies were then extended to multi-column bent systems to better understand system interactions and to inform

experimental studies. Equivalent-static pushover analyses with three-dimensional (3D), nonlinear, finite difference models were used to investigate the seismic response of multi-column bent bridge substructures. The numerical models simulated conventional bridge column-footing systems, including soil, foundations, columns, and bents. These models were based on geometric and reinforcement details observed in actual bridges constructed prior to the 1970s, before the implementation of modern seismic design provisions in the early 1990s. The results demonstrated that vintage column systems are susceptible to failure under lateral loading. Axial loads in the columns vary during lateral loading and can increase demands in the footing during rocking. Unretrofitted vintage columns exhibited significant strength degradation and loss of stiffness, emphasizing the importance of retrofitting measures to improve their performance under lateral loads. Systems with TiAB retrofitted columns exhibited substantial improvements in strength and stiffness, enabling them to delay strength reduction until much larger lateral drifts. Rocking of the foundation alone may not protect for vintage columns, but it may be possible to take advantage of rocking behavior to reduce the degree of retrofitting required to achieve desired seismic performance. Consideration of SSI enhances the understanding and optimization of retrofitting strategies to more effectively and economically achieve seismically resilient bridge substructures.

Section 6: Results from eight (8) experimental tests of three (3) full-scale square RC column-footing specimens constructed with vintage reinforcing details are reported. All specimens were subjected to column axial load and tested under fully reversed-cyclic lateral displacements. Most specimens were tested with simulated soil across the footing surfaces. TiAB retrofitted specimens all exhibited rocking without significant damage to the column. One specimen was a failed column that was retrofitted with TiAB ligaments and spirals, and it performed as well as a pristine retrofitted column when placed on simulated soil that allowed foundation rocking to occur. Based on the experimental results, an analytical model was developed to capture the effects of the soil simulant used under and at the vertical faces of the footing. The soil-footing-column model was used to further develop a design/analysis model for the footing using a three-dimensional strut and tie method (STM). The STM can capture demands in the transverse footing direction that cannot be identified using traditional sectional methods. The findings clearly show that interactions between the column-footing-soil need to be accounted for properly to be able to assess the demands in the soil, footing, and column, to optimize design of the retrofit, and to achieve overall seismic performance of vintage reinforced concrete bridge substructures.

Section 7: Laboratory test results of full-scale square RC column-footing specimens constructed with vintage reinforcing details that were seismically retrofitted with TiABs are reported. The footings were retrofitted and were restrained from rocking and enable the retrofitted column section to fail under reversed cyclically applied lateral displacements. A test of a TiAB retrofitted column that had been previously failed showed that it performed as well as if it was originally undamaged and demonstrates that the approach can be used after an earthquake to restore damaged columns to service. Snap-back tests were performed for a footing-column specimen constructed in native soil at the OSU Geotechnical Engineering Field Research Site. Rocking behavior was achieved for the tests with higher initial load. The tests were conducted at different times in the year having varying soil conditions. Damped free vibration responses demonstrated that the bearing soils loaded in the "dry" season produced stiffer responses as compared to that observed in the "wet" season. Nonlinear SSI spring models were developed to simulate snap-back, quasi-static, cyclic lateral loading tests of embedded footings that were calibrated using site-specific parameters. The SSI

model was used to parametrically investigate the sensitivity of variables which govern the response of a column-footing specimen bearing on soil when subjected to dynamic loading.

Section 8: A brief overall summary of the report is presented that ties the research components together, and specific recommendations to ODOT are provided.

Finally, a stand-alone guide for the analysis of spread footings under rocking conditions was developed based on the AASHTO-LRFD specifications. The analysis includes both conventional sectional methods for flexure and one-way shear as well as the strut-and-tie method. The steps for determining the STM components including nodal zones, tension ties, and compression struts is provided. Once the components are sized based on the specific materials and footing geometry their capacity can be evaluated to determine the limiting strength of the rocking footing. Based on typical conditions found in vintage spread footings, the relatively small amount of reinforcing steel placed in the transverse direction to rocking may limit footing capacity.

1.0 INTRODUCTION

1.1 OVERVIEW

Older bridges were designed principally for gravity loading with little consideration of seismic or lateral loading. They have historically been vulnerable to seismic effects, with numerous examples of damage occurring to both superstructure and substructure elements of the bridge, and, in some cases, complete collapse. The 1971 San Fernando earthquake was the watershed event that resulted in changes of philosophies and rationale for seismic design of bridges. Bridges that were designed and constructed under post-1971 design philosophies have generally performed well in recent earthquakes. However, past earthquakes (*e.g.*, the 1987 Whittier Narrows, the 1989 Loma Prieta, and the 1994 Northridge earthquakes) and research on substandard bridges have shown clear patterns of deficiencies in pre-1971 bridges. The 1989 Loma Prieta and the 1994 Northridge earthquakes are examples where several bridges collapsed due to specific structural design and detailing deficiencies. With a majority of state-owned bridges designed and built between 1950 and 1980, hundreds of older bridges in the Oregon bridge inventory are supported on seismically deficient reinforced concrete substructures that consist of the supporting columns and foundations. Accordingly, the state of Oregon would face a considerable post-earthquake challenge if a major event occurred in the state.

Typical structural deficiencies in pre-1971 bridges have included: (1) lap splices located at column bases, (2) low confinement and shear reinforcement in lap-splice regions and column/footing hinge regions, (3) insufficient footing plan area to resist soil pressures caused by earthquake forces, and (4) a lack of top steel in footings (Priestley, 1996; Xiao et al. 1996; Saiidi et al. 2001; Krish et al. 2018; Shrestha 2019). These four features result in a non-ductile response of reinforced concrete columns that can lead to bridge collapse during strong ground shaking. To correct these deficiencies and improve the seismic performance of existing RC bridges, different retrofitting strategies were developed including composite material jacketing, steel jacketing, and wire prestressing. Specifically, a novel retrofit method was developed for RC columns with vintage reinforcing details targeting their inherent deficiencies. The retrofit was applied to square RC columns and combines titanium alloy bars (TiABs) with conventional concrete. TiABs exhibit high ductility and limited strain hardening, provide corrosion resistance and ease of fabrication. In the retrofit method, continuous TiAB spirals are used to provide lateral confinement in the lap-splice region and supplemental longitudinal TiABs are added to provide a redundant flexural load path to resist seismic induced moment. The TiABs are installed using conventional construction industry practices and thus provide an effective and economical retrofit solution. The specimens with TiAB retrofits produced seismic performance that was as good as or even better than modern designs (Shrestha 2019). This was evident in the form of strength and ductility enhancement and increased hysteretic energy dissipation. The experimental and analytical results and studies were used to develop design recommendations for TiAB seismic retrofits of square RC columns by Shrestha (2019).

While the proposed retrofit strategy resulted in relatively stable hysteretic responses up to moderate ductility levels for the bridge column footings, the bridge foundations in the study by

Shrestha (2019) were modelled as fixed base with no soil–structure interaction (a typical structural assumption). Such assumptions for foundations in testing may lead to large demand on the columns, pier cap, and the joints, making the seismic retrofit of bridge elements unnecessarily costly (Saiidi et al. 2001). As part of the same study (Shrestha 2019), the influence of SSI and soil's nonlinear response on the seismic behavior of bridge columns was evaluated using a soil simulant, results of which indicated a reduction in the moment gradient along the column height and the demands in the column at the footing elevation. This has practical and important ramifications for retrofit designs for the entire substructure, including both footings and columns. SSI can be both beneficial and deleterious across different criteria, and improvements in understanding the effects of SSI are needed to ensure desired seismic performance of retrofitted substructures. Mitigation of collapse risk of the Oregon bridge inventory requires investments to efficiently improve their seismic resilience. To make best use of limited resources, retrofit design guidance that can properly account for the potential benefit or detriment of SSI of bridge-column footings must be developed to support design guidance within the ODOT Bridge Design and Geotechnical Design Manuals (BDM and GDM). Such design guidance must include a clear decision matrix and corresponding analytical and design protocol, which in turn must be based on experimental evidence developed from the evaluation of full-scale specimens. In addition, directed retrofit approaches need to be advanced and structural models need to be developed for spread footings to permit estimation of force and moment capacity and demands to enable system seismic performance and eliminate needless and costly foundation retrofits. Although some test data based on previous research efforts exist, further SSI tests that include real soils under seasonally extreme conditions are necessary to help inform the design guidance that is required for the evaluation of appropriate retrofit/replacement options.

1.2 OBJECTIVES OF THIS RESEARCH

The objectives of this research are to improve the experimental basis for assessing bridge column-footing performance with and without retrofits subject to SSI and to provide clear design guidance for the evaluation of retrofit/replacement alternatives, with full consideration of the moment capacity at the top of the columns as well as the evolution of the force flow within the spread footing. The proposed experiments will be coupled with numerical modeling to extend the experimental work, inform design guidance, and show the effect of various foundation soil conditions. Although the focus of this work is on spread footings, the outcomes may be applicable to retrofits of timber pile-supported substructures, if the pile caps can be retrofitted similar to spread footings under the assumption that deteriorated timber piles make the pile cap act like a spread footing under an extreme seismic event. The development and implementation of these guidelines in the BDM and GDM will allow for improved, less conservative design recommendations and the potential for improved cost savings as ODOT improves the seismic resilience of its transportation network. This research addresses seismically deficient bridges in the Oregon bridge inventory and the need for developing sufficient design strategies for cost-effective retrofits to their substructures and improved decision support tools. Limited resources require that methodologies that can take advantage of soil-structure interaction, where warranted, be used to extend the life of existing bridges, and that tools be developed to quickly assess whether retrofit of bridge substructures is preferable over replacement given the existing structural details, substructure type, and soil conditions. Incorporation of soil-structure interaction may also show that retrofit or replacement of the substructure is not necessary. Given

the number of bridges for which retrofit/replacement is considered desirable, the impact to both budget and project delivery could be significant, with significant potential implications for improving the seismic resilience of the state transportation network. This report provides an overview of the key research findings that are relevant to the proposed study.

1.3 ORGANIZATION OF THIS REPORT

This report is organized into seven main sections of content, a summary section, and a comprehensive set of appendices which concisely document the materials and test results, and includes the following:

- Section 2 presents a review of the literature relevant to structural retrofitting strategies for improving seismic resilience of bridge substructures and the mechanisms associated with rocking foundations.

- Section 3 presents a concise review of the ODOT Bridge Inventory with readily interpretable histograms of important variables characterizing ODOTS bridge substructures.

- Section 4 presents a new formulation for the moment capacity of shallow foundations for soils with seasonally varying saturation conditions.

- Section 5 presents the first in a series of three-dimensional numerical simulations aimed to study the effects of structural and bearing soil characteristics on the moment capacity of vintage and TiAB-retrofitted single column-footing substructures considering fixed base and rocking foundations. The numerical investigation of column-footing substructures is then extended to evaluate a two column-footing bent configuration to understand how vintage and TiAB-retrofitted bridge substructures operate as a system considering fixed base and rocking foundations.

- Section 6 presents the first part of an investigation on the full-scale performance of TiAB-retrofitted reinforced concrete columns including soil-structure interaction conducted using vintage and retrofitted column-footing specimens tested in the structural laboratory. The section presents the first effort to model the soil-structure-interaction of rocking foundations to serve as the basis for a strut-and-tie design methodology to increase the moment capacity of vintage substructures and enable the rocking mode of energy dissipation. The developed design guideline accompanies this report in a separate document.

- Section 7 presents the second part of the investigation on the full-scale performance of TiAB-retrofitted reinforced concrete columns, focusing on the performance of retrofitted, failed vintage column-footing specimens to identify the restored moment capacity following a seismic event. Section 7 also presents the results of snap-back tests of vintage, embedded, column-footing specimens constructed in the outdoor geotechnical field site, which provide the damped free-vibration response of the specimens to a released static lateral load. Section 7 concludes with the development

and implementation of improved soil-structure-interaction models which can capture the salient aspects of nonlinear bearing soil support.

- Section 8 presents a concise summary of the research and the specific recommendations stemming from this study. Areas for further research investigation are also suggested.

- The references cited in each section of this report are provided at the conclusion of each section for ease of access.

- Appendices conclude this report to provide the experimental details (e.g., characteristics of the materials used, sensor designations and location) and graphical representations of the experimental results.

2.0 LITERATURE REVIEW

2.1 DEVELOPMENT OF ODOT SEISMIC DESIGN STANDARDS

The recorded history of Oregon is accurately documented for a period of about 150 years which is a very short period of time in geologic terms. Records show that very few earthquakes with magnitudes, M_w, over 6.0 have occurred in the state, even though many smaller earthquakes occur each year (Figure 2.1). Accordingly, the state of Oregon has been considered as a region of relatively low seismicity and earthquake occurrence for a long time, particularly for the pre-1971 era. Based on historical records, seismic loading in the design of bridges was typically not considered for bridges in Oregon prior to 1958, whereas from 1958 to 1974, a seismic force equal to only 2 to 6% of the structure weight (i.e., 0.02*g* to 0.06*g*) was considered (Nako et al. 2009).

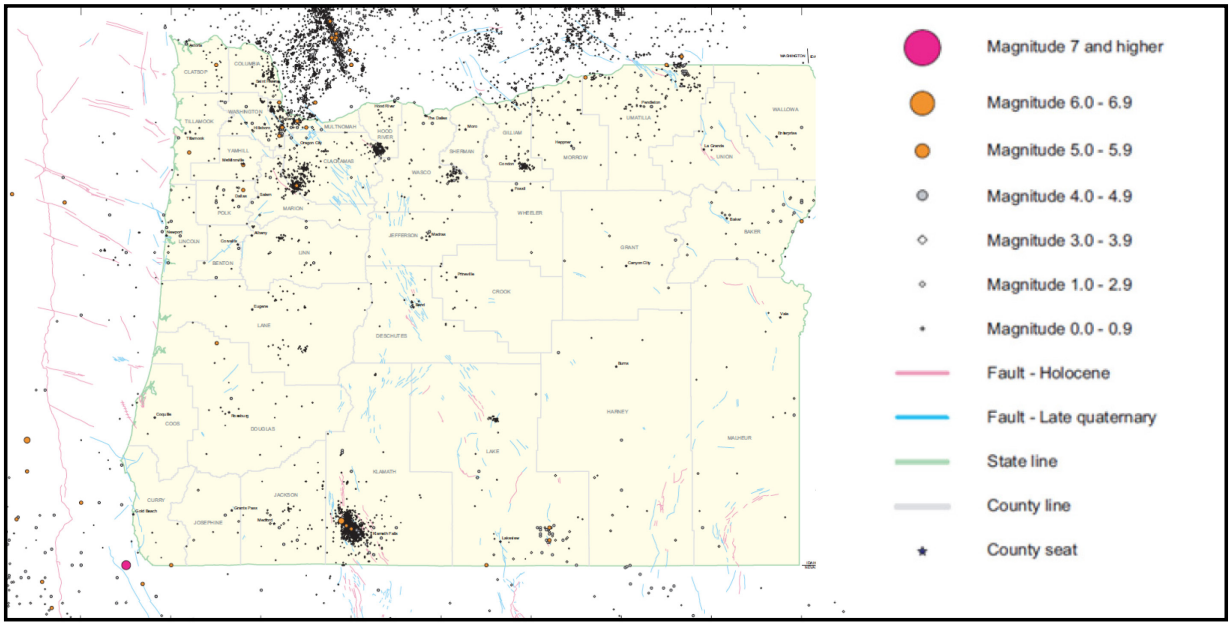

Figure 2.1 Distribution of over 14000 earthquakes in the state of Oregon over the years of 1841 to 2002 (Nako et al. 2009).

In 1971, the San Fernando earthquake marked a major turning point in the seismic design of bridges and a new set of design criteria for bridges in the US began to take shape. In 1975 the American Association of State Highway and Transportation Officials (AASHTO) adopted Interim Specifications which were based largely on the 1973 design criteria developed by the California Department of Transportation (Caltrans; Nako et al. 2009, and 2014). These code provisions were used by ODOT from 1975 to 1990. They resulted in a seismic design force equal to 8 to 12% of the structure weight and the introduction of ductile reinforcing details.

In 1989, the Loma Prieta earthquake in northern California prompted ODOT to take a close look at the overall seismic hazard in Oregon and the effects of this hazard on bridge design. During this time, several earthquake hazard studies (Wong et al. 1990; Flueck et al. 1997; Peterson and

Frankel 2000; Petersen et al. 2002), paleoseismic research (Adam 1990; Atwater and Hemphill-Haley. 1997; Kelsey et al. 2002; Goldfinger et al., 2003), and other geologic work (Ando and Balazs 1979; Mitchell et al. 1994; Clague 1997) began to be conducted that resulted in support for the theory that major seismic events had occurred along the Oregon coast regularly in the past that were not previously accounted for in the standard seismic hazard maps in use at that time. Active crustal faults were also discovered in many areas of the state. Geologic evidence also supported the likelihood of large subduction zone earthquakes, with magnitudes, M_w, greater than 8.0, occurring in the future somewhere along the Oregon coast (Atwater and Hemphill-Haley. 1997; Yeats 1998). These newly discovered sources indicated a much higher level of seismic risk to ODOT bridges than previously accounted for in many parts of the state.

Figure 2.2 shows the boundary of the Cascade Subduction Zone Plate and the fault map of Oregon (Nako et al. 2009). The west coast of Oregon is located at a convergent plate boundary where the western margin of the North American tectonic plate and the Juan de Fuca plate meet. This plate-to-plate boundary is called the Cascade Subduction Zone (CSZ). Each year, the North American and the Juan de Fuca plates converge at a rate of about 1 to 2 inches per year (Yeats 1998; Goldfinger et al. 2003; Nako et al. 2009). This relative plate movement results in the Juan de Fuca plate sinking below the North American plate along the Cascadia Subduction Zone (CSZ) and beneath northern California, Oregon, Washington, and British Columbia. The North American plate deforms as it accommodates strain along its boundaries with the Pacific and Juan de Fuca plates. While earthquakes along this zone occur infrequently, release of strain energy during rupture can produce major earthquakes. In addition, western Oregon is underlain by a large and complex system of faults that can produce crustal earthquakes. These smaller faults produce lower magnitude events, but the ground shaking and damage from these events can be great to structures located nearby owing to their closer proximity to populated areas. As an example, the damage resulting from three notable crustal earthquakes - including the 1993 Scotts Mills (M_w = 5.6) and the two 1993 Klamath Falls quakes (M_w = 5.9 and 6.0) - was estimated to cost about $40 million and included two fatalities.

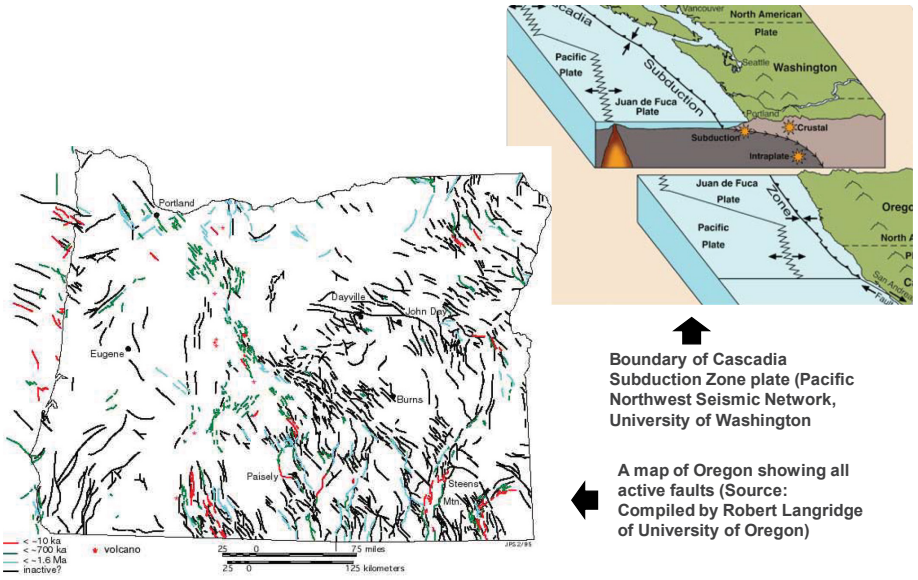

Figure 2.2: A map of Oregon showing all active faults (Source: Compiled by Robert Langridge of University of Oregon) and the location of Cascade Subduction Zone.

Based on this information, Nako et al. (2014) considered three sources of earthquakes affecting Oregon bridges:

- *Shallow crustal earthquakes*: These earthquakes with origins located at depths shallower than 12 miles are generated within the different seismotectonic provinces in the overlying North American Plate. The last occurrence in Oregon was the Scott Mills earthquake on March 25, 1993, with a magnitude of M_w = 5.9.

- *Deep intraplate earthquakes*: The origin of these earthquakes is expected to come from depths ranging from 25 to 45 miles. They are believed to occur from internal stresses associated with the bending and arching of the Juan de Fuca plate as it is subducted beneath the North American plate (Planning for Natural Hazards: Oregon Technical Resource Guide). An example of this type is the Nisqually earthquake which occurred on February 28, 2001, with a magnitude of M_w = 6.8.

- *Subduction zone megathrust earthquakes*: very large earthquakes originating at the boundary between the North American and Juan de Fuca plates. Their latest occurrence was on January 26, 1700, with an estimated magnitude of M_w = 9.0.

These primary earthquake sources are summarized in Table 2.1.

Table 2.1: Oregon Seismic Activity (Nako et al. 2014).

Source	Magnitude	Frequency	Latest Occurrence
Crustal	$M < 5.5$	Every 15-20 years	Annually
	$M \geq 5.5$	Unknown	1993: Scotts Mills & Klamath Falls
CSZ	$M \geq 8.0$	Every 350-500 years	Jan., 1700
Intraplate	M = 4.0-7.0	Every 30-50 years	Feb., 2009: M4.1, Grants Pass, OR

2.2 ODOT BRIDGE DESIGN PHILOSOPHY

Reinforced concrete bridges are among the primary choices for bridge construction in Oregon and throughout the nation. The nature of concrete and range in geometries, cost-effectiveness, durability, and precasting and prestressing, all serve to make it an efficient choice for highway construction. As a result, concrete bridges today form the backbone of Oregon's transportation network. Based on statistics provided by Nako et al. (2009), in an area including all highway routes lying inside or west of the I-5 corridor, highway routes in the Portland area, the entire length of US-101 and a part of I-84 Columbia River Highway, 1,041 of 1,900 bridges are concrete (conventional or prestressed) with two- or more spans (Figure 2.3). Bridge substructures, including the supporting columns or piers in these bridges, fall into two basic categories: square section columns, and round columns. There is no specific "standard" for construction of these columns and piers, creating a temporal guide as to which column is usually associated with what period. In general, however, columns with square section seem to precede columns with round sections, mostly due to improvements in construction technology rather than any particular design decision.

Modern reinforced concrete bridges in Oregon, specifically those constructed after 1995, have been designed to meet the minimum national bridge design standards established by AASHTO. Principles and concepts implemented in such standards are performance-based earthquake engineering (PBEE) and capacity design principles which allow the structures to sustain much greater deformations prior to collapse than their predecessors (Paulay and Priestley 1992; Priestley et al. 1996). These designs are typically based on the concept of concentrating inelastic deformation in plastic hinges at the ends of columns as the primary means of dissipating energy associated with seismic forces. The main advantage of plastic hinging is that the force capacity limit of the hinge limits the force magnitudes in other portions of the structure. During large earthquakes, if the bridge performs as intended, damage will localize in the plastic hinge region in the column, and the rest of the structure remains intact. Bridges constructed between 1980 and 1995 are mostly designed based on levels of ground shaking with much better design detailing and therefore are considered to have a moderate potential for damage or collapse (Xiao et al. 1996; Nako et al. 2009, 2014).

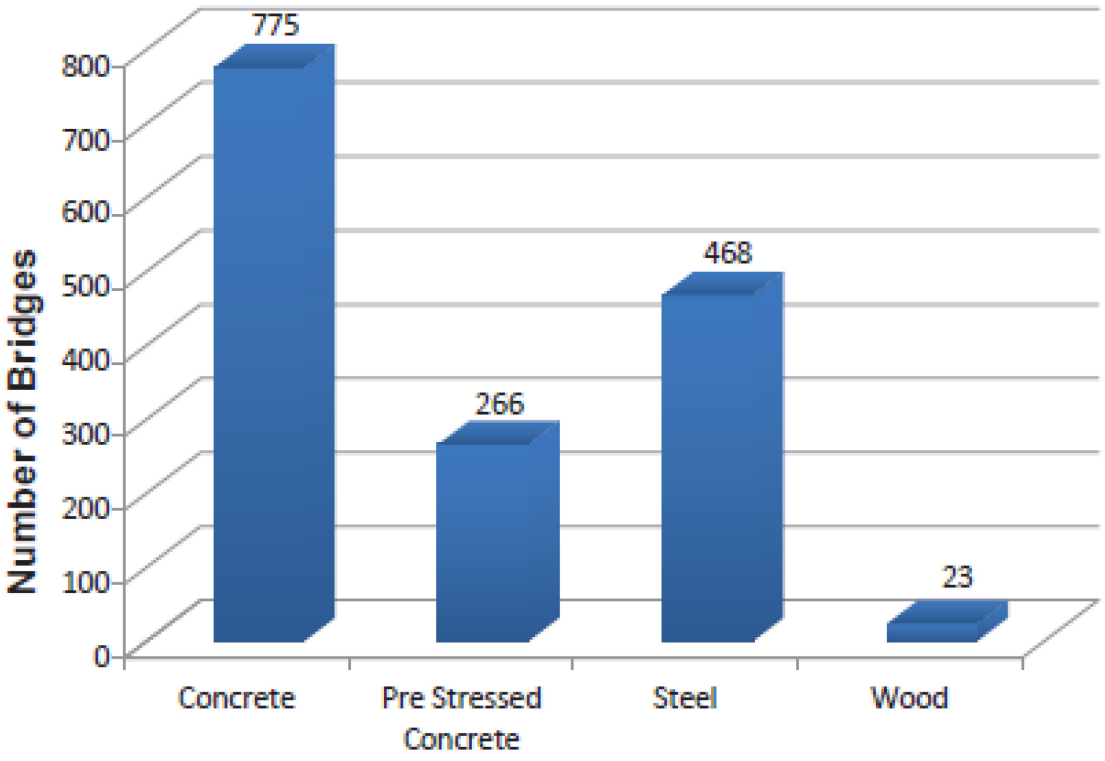

Figure 2.3: Distribution of predominant types of materials used for bridge construction in Oregon (Nako et al. 2014).

Reinforced concrete columns designed prior to 1970, particularly those located in the western portion of the state (west of the Cascade Range) or in the Klamath Falls area used older code provisions, in which design largely considered gravity loads with little consideration of lateral seismic loads (Nako et al. 2009 and 2014; Shrestha 2019). The most common deficiencies encountered in columns designed with pre-1970s provisions are: 1) short lap splices of longitudinal bars in plastic hinge regions, 2) low shear strength related to the lack of flexural ductility in the bridge columns, and 3) insufficient confinement of the column core. With their insufficient reinforcement details and low concrete grade, they are capable of withstanding only limited lateral seismic loads, and therefore are susceptible to severe seismic damage.

2.3 FAILURE MECHANISMS AND SEISMIC RETROFITTING OF BRIDGE COLUMNS

The vulnerability of highway segments of the state highway system in Oregon was analyzed to select appropriate earthquake scenarios for retrofit purposes by Nako et al. (2009 and 2014). The study region considered all highway routes lying inside or west of the I-5 corridor, highway routes in the Portland area, the entire length of US-101 and a part of I-84 Columbia River Highway. Figure 2.4 summarizes the year of construction completion of the bridges in the study area along with the collapse potential of the bridges relative to the year they have been constructed. Of the 1,900 bridges in the area, only 340 (18%) of the bridges were constructed after 1980, with the remainder constructed prior to 1980. With a majority of state-owned bridges

designed and built between 1950 and 1980, the State of Oregon would be subject to a significantly impaired transportation network after a major earthquake.

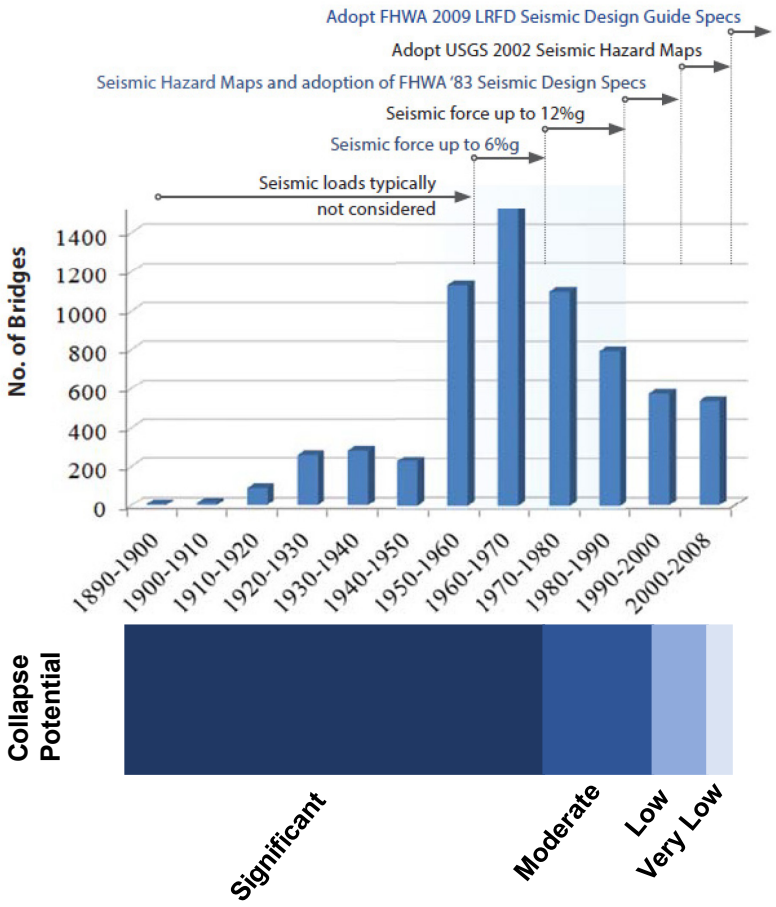

Figure 2.4: Distribution of year of construction completion and bridge collapse potential relative to the year of construction (Nako et al. 2014).

In recent years, the impact and cost of earthquake-induced damage on reinforced concrete bridges have raised serious questions as to what extent the current and old seismic design philosophies can satisfy the needs of society in terms of safety and service. Research efforts have been directed to different paths including the development of technologies that: (1) improve structural performance of these bridges during earthquake and minimize structural damage (*e.g.* Xiao et al. 1996; Zhang et al. 2000; Bournas et al. 2009; Cai et al. 2014; Krish et al. 2018; Shrestha 2019), (2) encompass self-centering characteristics considering both structural elements and supporting soil (Guerrini and Restrepo 2011; and Guerrini et al. 2015), and (3) reduce construction time and traffic impacts (Ralls et al. 2005; Palermo and Mashal 2012). The most ideal solution to address the seismically deficient bridges is their replacement with structures that are designed to current seismic design codes and standards. However, the significant number of bridge structures requiring replacement and the cost and time associated with the re-construction make retrofit options more appealing in many cases. Also, many of these structurally deficient or functionally obsolete bridges exist in densely populated urban areas or serve as key links in local

and national transportation networks. Their closure, therefore, may have severe impacts on traffic, environment, society, and economy.

2.3.1 Contributing Parameters to Column Failure

Earthquake-related catastrophic failure of bridges has commonly been attributed to the failure of one or more short and stubby reinforced concrete columns. Shear damage sustained by these columns is often responsible for the collapse of the entire structure. The deficiencies in the seismic shear resistance are believed to be related to the lack of flexural ductility in the bridge columns. Different sources are responsible for the lack of ductility such as: (1) inadequate lap splice length and details in the plastic hinge zone, and (2) lack of adequate confinement caused by insufficient transverse reinforcement in the hinging region. Also, the type and magnitude of axial loads, and the type of lateral loads have been also proven to play a key role in the deformation behavior of columns (Shrestha 2019). These deficiencies are described in detail herein.

2.3.1.1 *Lap-Splice Behavior*

In reinforced concrete bridges, the most critical region prone to bond failure is at the base of bridge piers or columns. Typically, vintage reinforced concrete bridge columns have the longitudinal reinforcing steel spliced with starter bars for ease of construction at the base of the column, above the foundation. Presence of splices at the region of highest flexural demand in columns (i.e. above the footing level) could be acceptable in case of buildings as long as the "strong column-weak beam" design philosophy is adopted (Paulay 1982). However, the base of bridge piers or columns supporting the superstructure are deliberately designed to develop plastic hinges during a major earthquake and bridge structures exhibit less redundancy than buildings. Several studies have attributed poor performance of these bridge columns to short lap-splice lengths and inadequate transverse reinforcing steel (e.g., Cairns and Arthur 1979; Lukose et al. 1982; Girard and Bastien 2002; Melek and Wallace 2004; El Gawady et al. 2010). Thus, researchers (e.g., Lynn et al. 1996; Paulay, 1982; Chai et al. 1994) argue that lap-splices in these regions should be avoided or at least be properly detailed with proper confinement and adequate development length to ensure lateral load capacity and ductility.

The results of previous work indicate that the performance of reinforced concrete columns with lap-spliced bars is affected by different parameters such as splice length, loading direction, longitudinal reinforcement ratio, bar size, yield strength of longitudinal reinforcing steel, spacing between vertical bars, lateral confinement, and applied axial load (Priestley et al.1996). Also, parameters such as thickness of concrete cover, distance between spliced bars, strength of the concrete have some effect on the seismic response of bridges, though their effects are less significant compared to other parameters (Paulay 1982).

Melek and Wallace (2004) studied the effect of lap-splice length on the behavior of concrete columns during cyclic loading. Particularly, the behavior of the columns with insufficient lap-splices under different axial loads, shear demands, and loading history were investigated. In this regard, six full-scale reinforced concrete cantilevered columns

with deficient lap-splices ($20d_b$ with d_b equal to the diameter of bar) were first loaded axially and then tested laterally under reversed cyclic loading. Results indicated that inadequate lap-splice lengths may cause lateral strength degradation. In cases with insufficient lap-splice length, columns experienced a larger body rotation, mainly due to the slippage of the longitudinal bars after bond deterioration. In this study, characterization of the column rigid body rotation due to slip over the splice length was found to be necessary to calibrate moment versus slip-rotation springs in modeling splice behavior. Also, from the results of this study, it was concluded that ACI 318-02 (ACI Committee 318, 2004) underestimated the bond stresses in the lap-spliced bars, which if used in design could lead to column failures in shear. The effect of axial load magnitude applied to the column during testing on normalized moment versus lateral drift behavior was found to be negligible. However, peak lateral load capacity was higher at higher axial load and the rate of lateral strength degradation increased slightly with increasing shear magnitude (Figure 2.5).

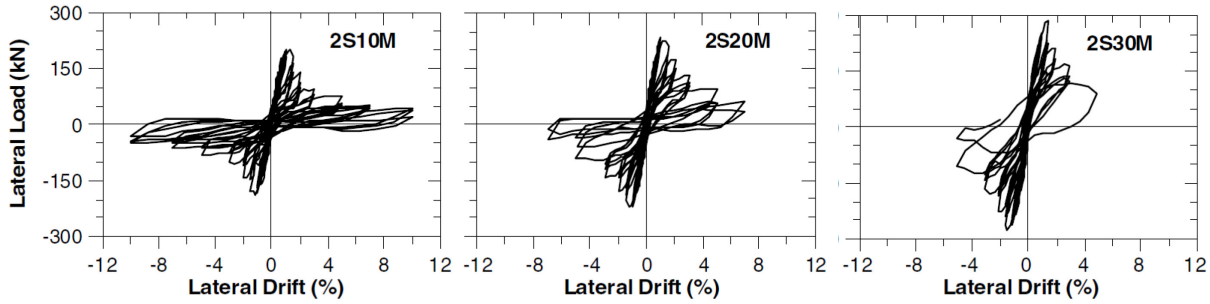

Figure 2.5: Base Moment - Rotation along splice length responses for columns under axial load levels of (a) 0.1, (b) 0.2, and (c) 0.3 $A_g f'_c$ (A_g: gross area and f'_c: concrete compressive design strength at 28 days) (Melek and Wallace 2004).

The direction and magnitude of lateral load have been also reported to be an important parameter in the response of bridge columns and the performance of spliced bars in the region of plastic hinge. Results of research by Lukose et al. (1982) on columns under repeated monotonic and reversed cyclic loading revealed that reversed cyclic loading is more detrimental to the performance of spliced bars than monotonic loading. This behavior is attributed to the increasing number of crossing concrete cracks and damage penetration during cyclic loading. Also, higher bond stresses were noticed in tension lap-splices compared to compression lap-splices followed by greater relative bar-slip under tension, as compared to compression. Bar-slip in compression was more pronounced once the cover concrete was lost due to longitudinal splitting of the concrete over the spliced reinforcing bars. In either case, they emphasized the importance of well-distributed and adequate transverse reinforcing steel along the splice, and extension beyond the high moment splice end to control bond deterioration thereby increasing strength and ductility of the splice region. Based on their results (Lukose et al. 1982), lap-splice lengths of 20 to 30 times the diameter of bar (d_b) were adopted in vintage bridge columns as compression lap-splices and are characteristic of columns with large diameter reinforcing bars. Later studies, however, revealed that lap-splices of this length may not be adequate to transfer the full tensile force of the longitudinal reinforcing steel to the

starter bars of the foundation in both rectangular and circular columns, resulting in rapid degradation of flexural strength (Chai et al. 1994; Xiao and Ma 1997; Breña and Schlick 2007; Harajli 2008; Chai et al. 2008).

Harries et al. (2006) investigated the effect of confinement on the performance of spliced bars during cyclic loading. In this study, carbon-fiber-reinforced polymer (CFRP) composite jackets were used to retrofit square reinforced concrete columns with inadequately detailed lap-splices and to provide external confinement to the column. With the external confinement provided by CFRP composite jacking, the lap-splice capacity of the columns increased so they were able to develop the nominal flexural capacity of columns with continuous longitudinal reinforcing steel bars. Also, the initiation of slip and thus splitting of concrete along the splice was delayed by limiting the transverse strains. After slippage, however, the confinement was observed to have negligible effect on the residual splice capacity and the column ductility capacity. From their results, Harries et al. (2006) suggested: 1) use of alternate load path or alternate measure (in addition to confinement) to control the slip in spliced bars once there is significant slip in the lap-spliced bars, and the inefficiency of using reinforcing plating for confinement on square and rectangular columns; and 2) proper detailing of the lap-spliced bars in potential plastic hinge regions including proper confinement and provision of alternate load path after splice failure.

Valluvan et al. (1993) noted the contribution of confinement in increasing splice strength when done properly without any intrusion to the existing column. In their research, confinement was used to improve the splice behavior in the critical region of the plastic hinge. Valluvan et al. (1993) used three different mechanisms to increase confinement: (1) steel angles and straps along the splice region, (2) external steel reinforcing bars ties, and (3) additional internal ties in the splice region. Different grouting conditions were also explored when using supplemental confinement. The results of this work indicated that external confinement of the splice region was effective in increasing the splice strength when steel elements and ties were added along with the grout. From these different confinement mechanisms, welding the splice bars provided the best continuity in the load path, provided additional ties are installed internally around the outer spliced bars. Welding the spliced bars in some cases had detrimental effects. If not controlled, welding can severely change the chemical properties of the reinforcing bars, causing brittle failure of the bars during loading. In addition, chipping through the cover concrete for welding of spliced bars resulted in stress concentrations in the core concrete, resulting in the formation of undesired micro-cracks.

2.3.1.2 Confinement and Ductility

The available ductility in RC columns is directly related to the longitudinal and transverse reinforcing steel details, especially in the critical plastic hinge regions (Daudey and Filiatrault, 2000). Inadequate confinement of RC columns tends to limit the ultimate curvature corresponding to the compressive strain in the range of 0.005 and may lead to bond failure between reinforcing steel bars and concrete in a brittle splitting mode and relatively low ductility (Chai et al. 1994; Harajli 2009). Under inelastic cyclic loading, as in the case of a strong seismic shaking, degradation of concrete results in the decrease of

shear capacity in the plastic hinge region. Therefore, RC columns need to be detailed for sufficient ductility through effective confinement of these critical regions to sustain the likely inelastic displacements without significant degradation of strength.

One of the first studies to understand the effect of confinement on the response of reinforced concrete was Saatcioglu and Ozcebe (1989). In this study, fourteen full-scale square RC column specimens confined by different configurations of transverse reinforcing steel bars were tested. The specimens used identical transverse reinforcing steel bars placed at various spacings. The results indicated that the specimens with spacing of 2 in. (51 mm) improved the column behavior most effectively. Also, it was observed that a proper arrangement of transverse steel could be more feasible than reducing the tie spacing to achieve the same level of confinement. The increase in shear capacity associated with increased transverse steel, over and above the shear capacity corresponding to the peak shear force, had little effect on improved response.

Ozcebe and Saatcioglu (1987) investigated the effect of the confinement details on the behavior of concrete columns by performing cyclic loading tests on four full-scale columns under constant axial load. The specimens were identical in terms of column cross- and longitudinal reinforcing steel detailing. The first and second specimens were confined with square hoops with 135˚ hooks with the second one having hoops spaced at two-thirds the spacing of the first one. The third and fourth specimens had additional cross-ties spaced at the same spacing as that of the first specimen. The cross-ties in the third specimen had 135˚ hooks whereas the fourth had 135˚ and 90˚ hooks. The performance of the columns with cross-ties were superior to the ones with only square ties. Although the specimen with closely spaced square ties performed better than the one with wide spacing, the performance enhancement was not as significant as the ones with the cross-ties. Hence, the authors suggested that the proper selection of confinement configuration is more efficient in improving confinement than increasing the transverse reinforcement ratio, which fails to engage the unsupported longitudinal reinforcing steel bars. They also compared the performance with the analytical prediction using the Kent and Park model (Kent and Park 1971) and the Sheikh and Uzumeri model (Sheikh and Uzumeri 1982). Results indicated that the analytical prediction underestimated column performance when the unconfined concrete model was used and strain hardening in the steel reinforcement was not considered.

Mander et al. (1988) developed a theoretical stress-strain model for concrete columns confined by different transverse reinforcing steel bars configurations. Results of the theoretical model were then compared with the results of experiments performed by Mander et al. (1984) on columns 19.7 in (500 mm) diameter and 59.1 in (1500 mm) height. Assumptions associated with the theoretical model is presented in Figure 2.6. Different types of transverse reinforcing steel bars were used for confinement including spirals, ties, and circular hoops.

Results indicated the greater efficiency of circular transverse reinforcement for concrete column confinement when compared to rectangular ties. Also, compression strength of the confined concrete was observed to be directly related to the effective lateral confining stress, f_l', that could be developed at yield of the transverse reinforcing steel. The

theoretical expression for lateral confining pressure, f_l, suggested that f_l, is inversely proportional to the longitudinal spacing of the ties or spiral. From the results of this study and further work, Watson et al. (1994) developed design charts using previously derived stress-strain relationships for confined concrete. These design charts allow for the determination of the quantity of transverse reinforcing steel required to achieve specified curvature-ductility factors in the potential plastic-hinge regions of reinforced concrete columns.

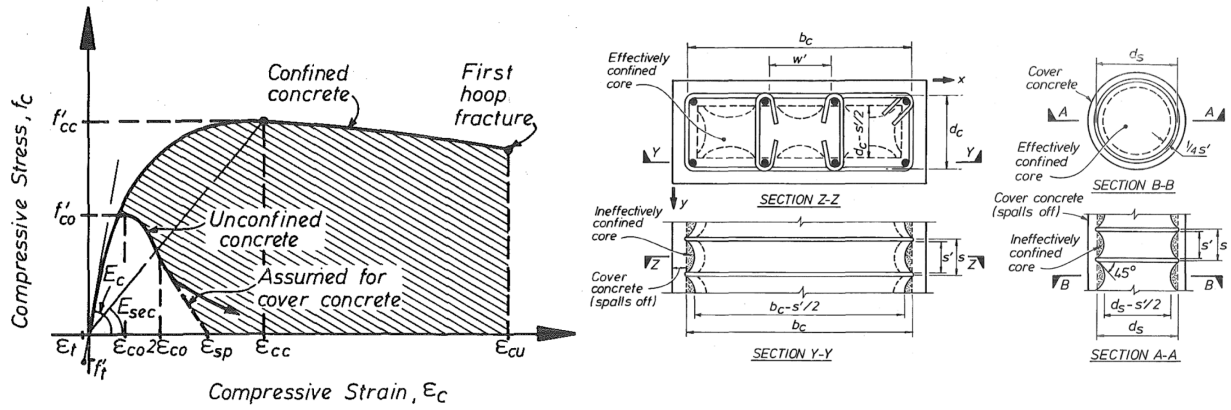

Figure 2.6: Details of the model proposed by Mander et al. (1988): (a) Stress-strain model proposed for monotonic loading of confined and unconfined concrete, (b) Effectively confined core for circular hoop reinforcement, (c) Effectively confined core for rectangular hoop reinforcement.

Razvi and Shaikh (2018) tested nine 1/3 scale square reinforced concrete columns to study the confinement contribution of ferro-mesh jacketing. Their test specimens consisted of three groups: (1) three specimens with stirrups as confinement (Type I), (2) three specimens with stirrups as well as ferro-mesh jacketing for confinement (Type II), and (3) three specimens having only ferro-mesh jacketing for confinement (Type III). All the specimens were subjected to concentric compressive load and their behavior in terms of axial load carrying capacity, energy dissipation, lateral displacement and ductility were studied. They observed that the specimens with just the stirrups or just the ferro-mesh jacketing had similar axial load carrying capacities. The specimens that combined stirrups and ferro-mesh jackets performed better than the other two types and showed 20% increase in the axial load carrying capacity (Figure 2.7). The specimens with ferro-mesh jacketing alone showed higher energy dissipation as compared to the conventional design.

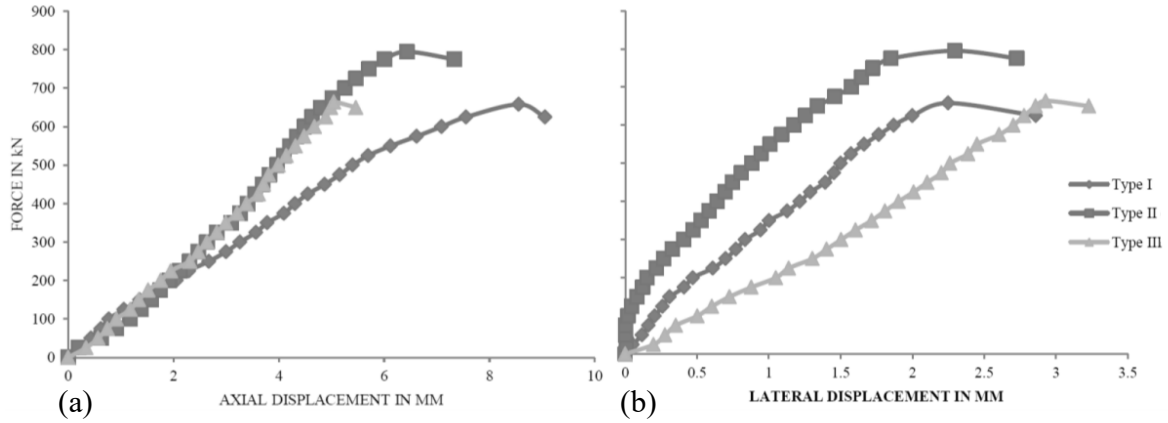

Figure 2.7: Load variation with respect to column's (a) axial and (b) lateral displacements Razvi and Shaikh (2018).

2.3.1.3 Effect of Axial Load Magnitude and Direction

Axial loads can be both detrimental and beneficial depending on the magnitude of axial load and the drift level. While the column axial load can have adverse effects in terms of crushing force and additional overturning moments due to P-Delta effects, it can also help increase the shear strength by arch action forming an inclined compression strut, thereby resisting the applied shear force directly through its horizontal component (Priestley et al. 1995). Many researchers investigated the effect of variation in axial loads magnitude and direction on the hysteretic lateral behavior of reinforced concrete columns. For example, the study by Saatcioglu and Ozcebe (1989) described previously considered bidirectional loading in the hysteretic behavior of reinforced concrete columns. The columns were tested under both tensile and compressive axial loads. The observed hysteretic responses indicated that the yield moment is affected by the level of concurrent axial load. The specimens exhibited an inelastic response with a delay in strength degradation beyond the initial yield when accompanied by axial tension; however, when accompanied by axial compression, the specimens produced a higher yield strength but earlier strength degradation. In addition, the behavior under increasing axial compression was similar to that of the specimens tested under constant axial compression.

2.3.1.4 Effect of Lateral Load Direction

Columns with rectangular and square cross sections in bridge structures are often subjected to biaxial bending owing to the bi-directional shaking associated with earthquake loading (Saatcioglu and Ozcebe 1989, Zahn et al., 1989). As part of their experiments, Saatcioglu and Ozcebe (1989) compared the response of columns subjected to different lateral loading directions. They noticed that the response of the columns loaded parallel to the principal axis in terms of strength, stiffness and ductility was similar to those loaded parallel to the section diagonal. However, when the columns were subjected to simultaneously varying bidirectional load reversals, the post-yield response was characterized by severe strength and stiffness degradation as compared to unidirectional load response.

Zahn et al. (1989) conducted lateral cyclic tests on axially loaded 400 mm (15.7 in.) square reinforced concrete columns with code-specified transverse reinforcing steel. Lateral loads were applied diagonally. The choice of the direction of lateral load application was to allow bending about the diagonal rather than the axis parallel to the face of the column. Results indicated that for the same quantity of confining steel and axial load, there was no significant difference between the flexural strength and ductility for bending about a section diagonal and for bending about a principal axis. A similar study was performed by Wang et al. (2018) where a series of ten full-scale rectangular reinforced concrete columns were performed to understand the effect of lateral loading direction on concrete column performance during a seismic event. The lateral load was applied to the columns in an angle varying from 0˚ (strong axis) to 90˚ (weak axis). Results were then discussed in different terms including lateral load capacity, ductility, stiffness, and energy dissipation capacity of the columns. Results indicated that the lateral drift, shear resistance, and energy dissipation capacities generally decrease with the increase in lateral loading direction angle (highest in strong axis and lower as the angle increased). The worst performance was for the columns loaded laterally at an angle of 60˚. The failure of columns generally varied from the brittle shear failure mode to the ductile flexural failure mode for the variation of lateral loading direction from strong to weak direction. In this study, carbon fiber reinforced polymer (CFRP) retrofitting was used to improve the performance of the columns during loading. Results indicated that CFRP retrofit enhanced the seismic performance of the columns. Their efficiency in improving the column performance, however, decreased as the lateral loading direction angle increased. CFRP retrofitting also altered the failure mode of the column to ductile behavior regardless of lateral loading direction.

2.3.2 Retrofit Strategies

Current design guides aim to either retrofit existing structures (ACI Committee 341, 2007; FEMA, 1997) to improve their seismic performance and prevent the possible collapse of a bridge (life safety), or to repair those that have undergone damage (ACI Committee 546, 2014; U.S. Army Corps of Engineers, 1995; Nako et al. 2009). The design philosophy for earthquake retrofit is similar to that of a new bridge. Where reasonable, retrofits are designed such that the bridge will be serviceable for a moderate earthquake and provide collapse prevention (life safety) in a large earthquake. Figure 2.8 shows various retrofit concepts for different substructure components of a bridge which include cap, columns, footings, and piling (Caltrans 1995; Nako et al. 2009). As presented in this figure:

- Retrofit of older foundations is performed by either increasing the size of footings or installing additional deep foundation elements adjacent to the existing pile caps and connecting the previous and extended pile caps together. In some cases, use of reinforcement overlay along with longer starter bars in columns are recommended. Since there is often limited room to work under existing bridges, foundation retrofit is both difficult and costly.

- For reinforced concrete columns, jacketing is probably one of the most widely accepted methods for retrofitting. The increase in shear strength and confinement, and improved lap-splice performance without significantly increasing the column

diameter makes jacketing an attractive option in comparison to other retrofitting techniques. The most popular retrofit solutions in practice are composite material jacketing, steel jacketing, and wire prestressing. Figure 2.9 presents approaches suggested by previous researchers to mitigate the different deficiencies in substructure capacity. These retrofit approaches include: (1) full-height jacketing which is typically used when concerns exist about the shear strength of the column; (2) jacketing applied only in the potential plastic hinge regions to provide external confinement and lap-splice improvement in the plastic hinge zones; and (3) FRP layered jacketing (Alvarez and Brena 2017).

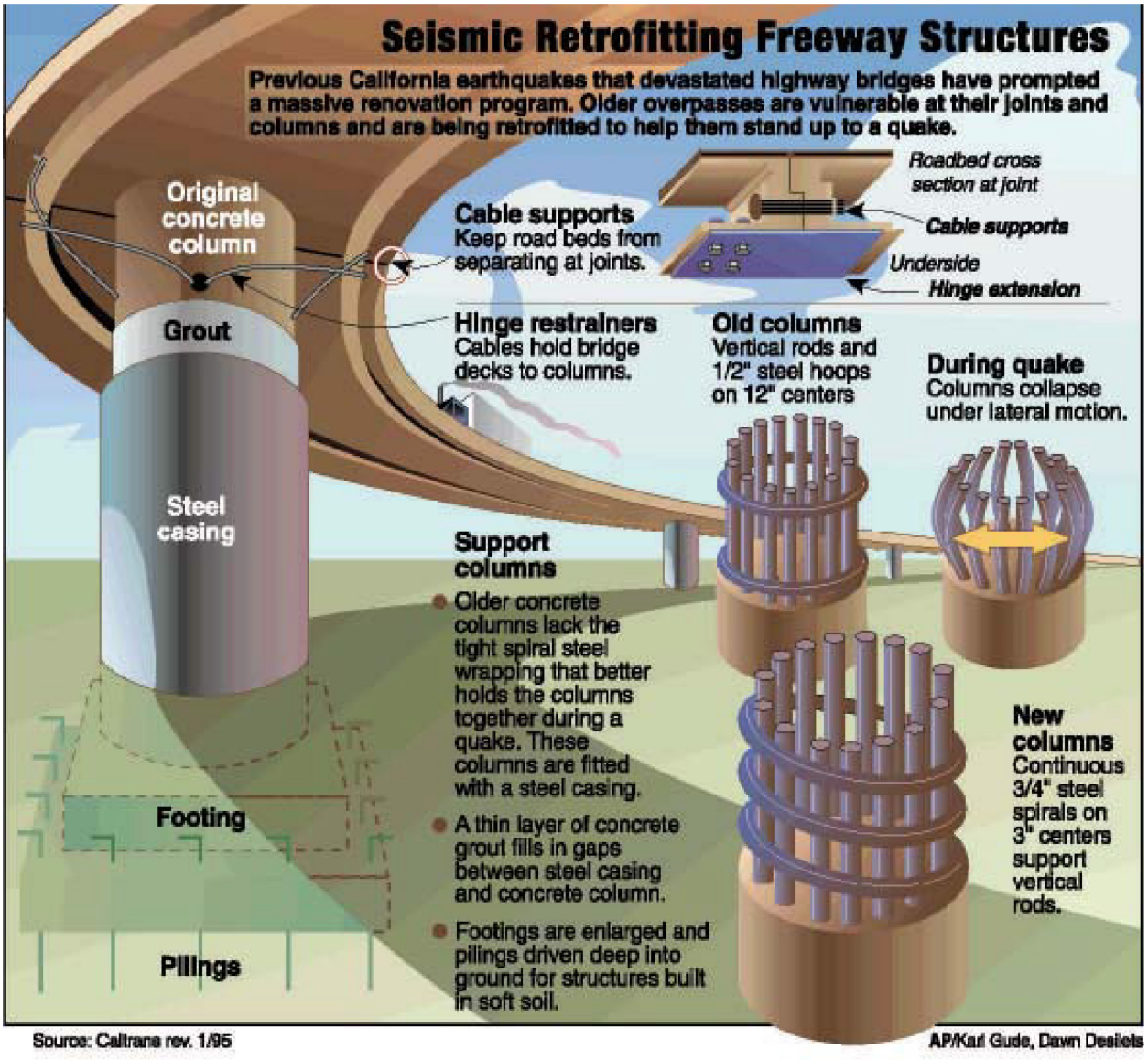

Figure 2.8 : Seismic Retrofit Concepts (Nako et al. 2009).

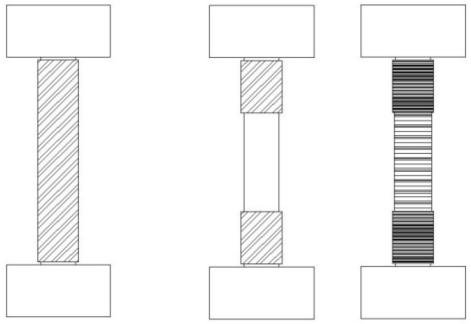

Figure 2.9: Typical jacket configurations (a) full-height (continuous) jacket, (b) jacketing applied only in the potential plastic hinge regions, and (c) layered jacketing (Alvarez and Brena 2017).

2.3.2.1 *Composite Material Jacketing*

Experimental studies demonstrating the performance of fiber-reinforced polymer (FRP) jackets as a means to improve the confinement of concrete have driven the increased use of advanced composite materials in the field of concrete construction (Figure 2.10). The application of FRP jackets has generally focused on seismic upgrades and/or rehabilitation, where confinement of concrete is the key to improving practically all performance aspects of reinforced concrete (RC) members (e.g., flexural deformability, shear strength, lap-splice strength). Early efforts to study and use this technology started more than 20 years ago. A study by Xiao and Ma (1997) on the behavior of reinforced concrete circular columns with poor lap-splice details retrofitted using prefabricated composite jacketing showed significant enhancement in flexural capacity and ductility of the columns after repair. Similar observations were reported by researchers such as Mirmiran et al. (1998), Haroun and Elsanadedy (2005), and Goksu et al. (2014).

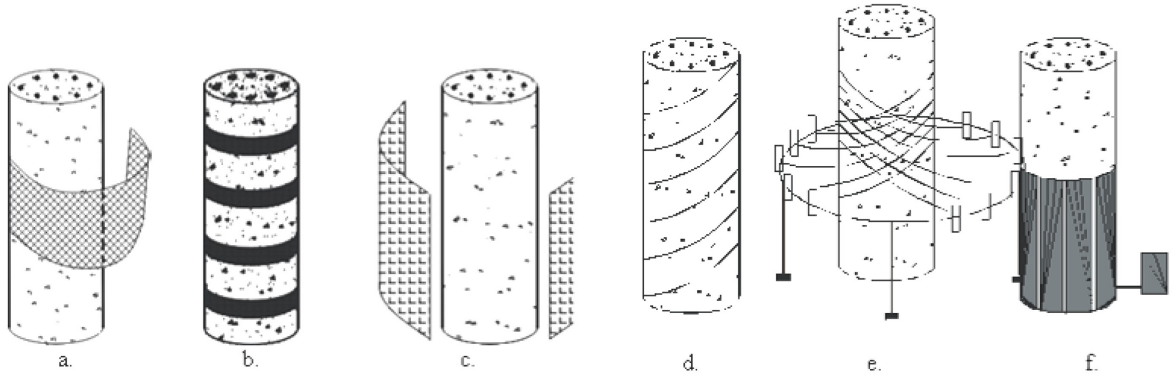

Figure 2.10: Methods of FRP strengthening for RC columns: (a) wrapping of fabric, (b) partially wrapping with strips, (c) prefabricated jackets, (d) spiral rings, (e) automated winding, (f) resin infusion (Taranu et al. 2008).

Results of these studies also revealed that when jacketing with composite materials, a circular profile is better than square profile in providing effective confinement. Haroun and Elsanadedy (2005) performed a series of lateral cyclic loading tests on ½ scale reinforced concrete bridge columns with insufficient lap-splice length to study the effect of fiber-reinforced plastic jackets on ductility of circular and rectangular columns. The circular columns were 24 in. (609 mm) in diameter and the square columns were 24 in. x 24 in. (609 mm x 609 mm) and 135 in. (3429 mm) tall. The circular columns had 20 #6 (#19M) longitudinal bars with #2 (#6M) circular hoops at 5 in. (127 mm) on center and the square ones had 28 #6 (#19M) longitudinal bars with #2 (#6M) square ties at 5 in. (127 mm) on center. In addition, a 2 in. (50.8 mm) circular radius was provided at the corners of the square columns. As expected, the circular columns retrofitted with FRP jacketing exhibited better cyclic performance. The effectiveness of jacketing, however, depended on the jacket strain. The columns retrofitted with FRP jackets designed for a larger jacket strain experienced partial slippage of the lap splice during loading and had lower lateral capacity. All retrofitted square columns, on the other hand, failed to meet their target ductility demand. Only one of the square columns that was retrofitted by adding pre-mold mortar blocks to provide a quasi-circular section with continuous confinement showed improved performance over the square jackets (Figure 2.11).

In a study by Galal et al. (2005), the response of columns retrofitted with CFRP was compared with the response of those retrofitted with glass fiber reinforced polymer (GFRP). Overall, seven 2/3-scale square reinforced concrete short columns with two different quantities of transverse reinforcement were under reversed cyclic lateral and constant axial load. In this study, one control specimen with higher transverse reinforcement was used and the remaining specimens were either retrofitted with CFRP or GFRP over the entire height with and without anchors. Results indicated that anchored CFRP sheets were more effective in increasing both shear and energy dissipation capacity in short, square RC columns than anchored GFRP. Both anchoring of the FRP jackets and increasing the number of FRP layers improved the confinement of the concrete as demonstrated by the decrease in strains in the transverse reinforcement and fiber materials. Use of anchored CFRP also resulted in a change in failure mechanism from brittle shear failure, observed in the control specimens, to ductile behavior with plastic hinging at the top and bottom of the retrofitted columns.

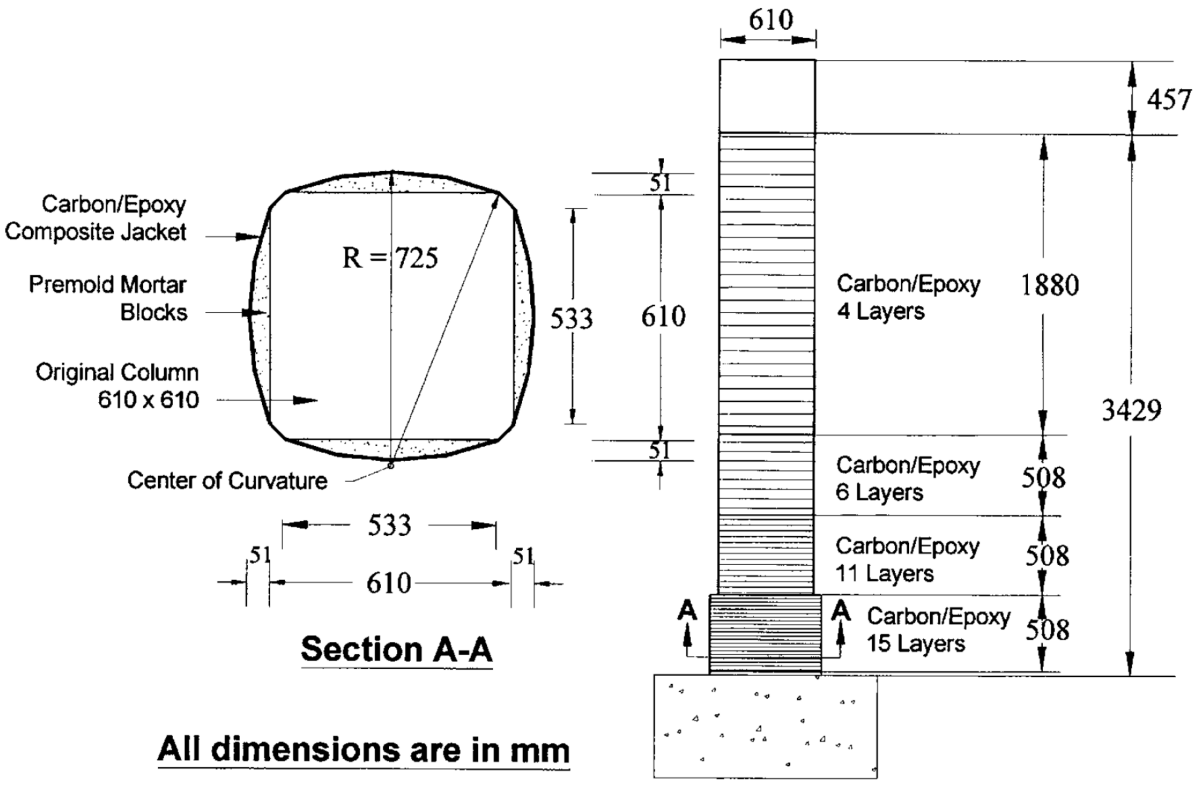

Figure 2.11: Jacket configuration for the sample with pre-mold mortar block (Haroun and Elsanadedy 2005).

Ozcan et al. (2008) investigated the effectiveness of CFRP to retrofit non-ductile square reinforced concrete columns with low strength concrete and continuous plain reinforcing bars. They also investigated the effect of axial load during the retrofit execution. Five reinforced concrete columns under reversed cyclic lateral loading were tested. One of the specimens was a control specimen, two of the specimens were retrofitted with 1-ply CFRP and the other two with 2-ply CFRP. The axial load on one specimen of each retrofitted group was maintained constant from the time of retrofitting till the end of test, whereas the remaining specimens were axially loaded only during testing. It was observed that the CFRP retrofit improved the column ductility significantly with negligible lateral load carrying capacity enhancement. Increasing the number of CFRP layers improved the column drift capacity irrespective of the presence of axial load during strengthening. However, the enhancement was not proportional to the number of added layers. The effect of having the axial load during FRP wrapping on the ultimate drift ratios was also observed to be negligible. The authors suggested additional studies were needed with higher loads to generalize the observation. It is important to note that all the specimens had continuous longitudinal bars whose behavior and failure mechanism can be different from specimens with lap-spliced bars.

A similar study was performed by Goksu et al. (2014) in which eight reinforced concrete rectangular columns were tested to study the behavior of non-ductile columns retrofitted with carbon fiber reinforced polymer (CFRP). Their specimens were 7.9 in. x 11.8 in.

(200 mm x 300 mm) with 4 – 0.55 in. (14 mm) diameter plain bars; four of the specimens used continuous reinforcements whereas the other four used lap-splices with a length of $40d_b$. For all specimens, transverse reinforcement was provided at 7.9 in. (200 mm) on center. Their results indicated that CFRP jackets were effective in increasing the ductility of the columns with continuous longitudinal reinforcement but not as much for the case of columns with inadequate lap-splices. The increase in ductility for the columns with continuous longitudinal bars was attributed to the prevention of buckling of the bars through effective confinement, whereas the columns with lap-splices exhibited bond slip failure and resulted in a significant loss of strength. These results indicate that along with effective confinement, an alternate load path is required after the lap-splice fails, which was not provided by CFRP jackets alone (Figure 2.12).

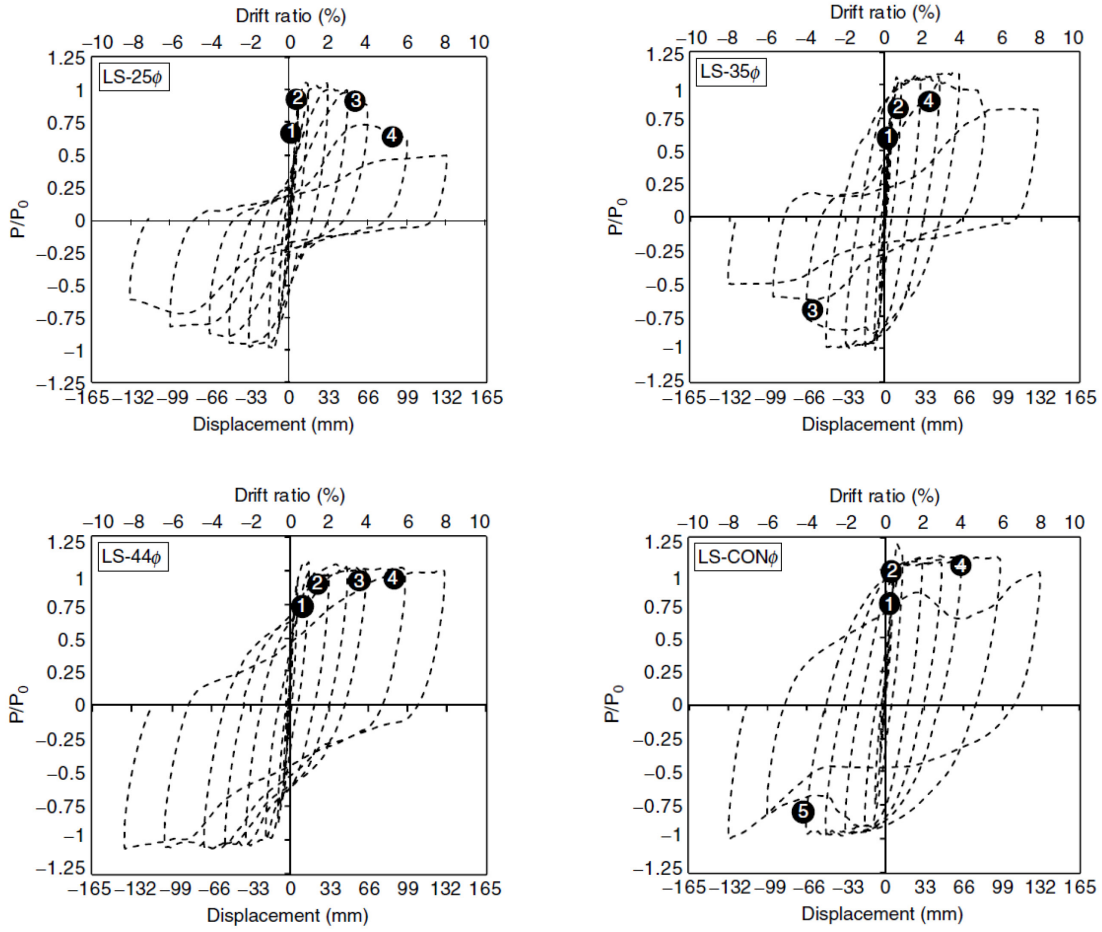

Figure 2.12: Lateral load-displacement relationships for the specimens with different lap-splice lengths (LS) of (ϕ: bar diameter): (a) 25ϕ, (b) 35ϕ, (c) 45ϕ, (d) continuous (1: Flexural crack, 2: Yielding of longitudinal bars, 3: Crack at the upper end of lap splices, 4: Spalling of concrete cover, and 5: Buckling of longitudinal bars) (Goksu et al. 2014).

2.3.2.2 *Steel Jacketing*

Use of steel jackets to improve the confinement of reinforced concrete columns is an effective method to improve the seismic performance of bridge columns. As compared with conventional hoops or spirals, steel jackets provide two advantages: 1) they provide a large amount of transverse steel and hence significant confinement, and 2) they prevent spalling of the shell concrete. Spalling of the shell concrete may be considered as the main reason for deterioration of bond and buckling of longitudinal bars of columns and is not sufficiently prevented by conventional hoops. Because of these advantages, the use of steel jackets has increased for the retrofitting and strengthening of existing reinforced concrete columns.

Chai et al. (2008) investigated the use of steel jacketing to retrofit circular columns with insufficient flexural strength and ductility. They tested six 0.4-scale circular column footings that included as-built and retrofitted columns and compared their behavior under lateral load with analytical predictions. The columns were all 24 in. (610 mm) diameter and 12 ft (3.657 m) tall and reinforced with 2.53% longitudinal reinforcement (26-#6 Gr. 40 deformed bars) and circular hoops (#2 Gr. 40 plain bars) placed at 5 in. (127 mm) spacing on center. Two columns were constructed to meet a 1960's era footing design, using only straight reinforcement (two orthogonal layers of 24 #6 bars each) in the bottom region of the footing (Figure 2.13). Footings with strong reinforcement detailing was used in the remaining four columns. For reinforcement, 3/16 inch (4.76 mm) thick A36 hot-rolled steel was used as the steel jacket. A gap of 0.25 inch (6.35 mm) was provided between the column and jacket. In five columns, a fully grouted steel jacketing was provided by fully pressure-injecting the gap with water/cement grout. One of the columns was partially retrofitted by placing a thin sheet of Styrofoam (0.25 in thick) between the column and the grout infill. This way, a controlled dilation of concrete cover at large lateral displacement was allowed, limiting improvement in the column's flexural capacity. The columns were subjected to lateral loading reversals while maintaining a vertical load of 400 kips (1779 kN, or $0.18f_c'A_g$) throughout the test. The damage to the control specimen was repaired after initial testing and loaded again.

The results indicated that the lap length of 20 times the longitudinal bar diameter was insufficient to develop yield stress of the longitudinal bar and rapid strength degradation due to bond failure was observed (Figure 2.13b). Fully grouted, steel jacketing was effective in increasing the lateral strength and ductility. The lateral stiffness increased about 10 to 20% for the case of a fully grouted, steel jacket in comparison to the as-built columns. The response of the column with partial retrofit was similar to the column without the steel jacket. Results indicated that the theoretical capacity of the column was not achieved. Similarly, the column with the partial retrofit experienced bond failure at initial stages of loading. However, the degradation of strength was more gradual. The results also highlighted the importance of ensuring enough footing strength before retrofitting the columns with steel jacketing, specifically for the column with fully grouted, steel jacket, as grouting can create inelastic strain penetration into the footing which can cause brittle footing shear failures. The steel jacketing was found to be challenging in areas with space constraints. Rectangular steel jackets were favored in areas with space constraints, but they suffered from out-of-plane bulging. Due to bulging,

adequate confinement to the concrete core was not maintained throughout the test, reducing the column's flexural capacity.

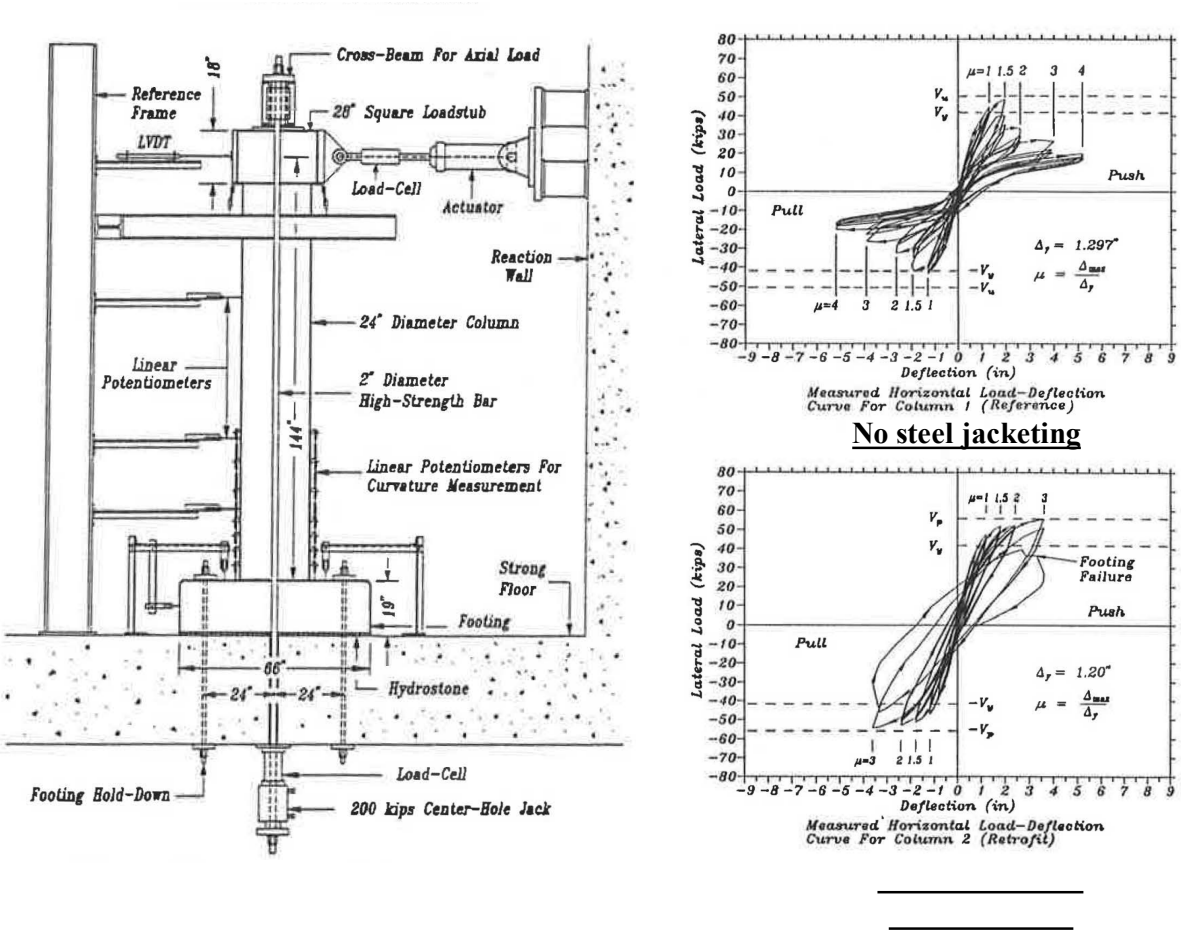

Figure 2.13: Details of experiments by Chai et al. (2008): (a) Experimental test setup, and (b) hysteretic response of columns with starter bar and weak footing.

El Gawady et al. (2010) tested eight 0.4-scale rectangular reinforced concrete columns with aspect ratios of 1.5 and 2.0 and with deficient lap-splice details to study the contribution of different retrofit jacketing techniques to improve their cyclic response. The column aspect ratio or shear span-to-depth ratio is defined as a/d, where a can be taken as equal to half the column clear height for columns loaded in contraflexure and d is the distance from extreme compression fiber to centroid of longitudinal tension reinforcement. The columns tested were constructed with a lap-splice length of $35d_b$, vertical reinforcement ratio of 1.2%, and were tested under a constant axial load equal to 7% of the column axial capacity (i.e. $0.07f_c'A_g$). The axial load was applied using a hydraulic jack mounted on a low-friction trolley and the horizontal force component was neglected. The test results revealed that the control specimens having $35d_b$ lap-splice length without any retrofit performed relatively better than previously-reported tests on columns with lap-splices shorter than 35 d_b. Retrofitting the columns using CFRP wraps

increased the displacement ductility about 10% to 14% and the failure mechanism consisted of low-cycle fatigue rupture of the longitudinal bars, with the exception of one of the control specimens, where lap-splice bond failure was observed in addition to low-cycle fatigue rupture of the longitudinal bars. The specimen retrofitted with steel jacketing performed worse than the control specimens, which was attributed to the crushing of the concrete in the gap provided between the jacket and footing that eventually led to buckling of the longitudinal bars within the gap. The retrofit did not change the initial stiffness of the specimens. However, the retrofitted specimens exhibited a more stable hysteretic response (Figure 2.14) and reduced pinching. The axial strains in the rectangular CFRP jackets were also significantly higher than those developing within specimens implementing the oval-shaped jacket. The authors indicated that the seismic performance of full-scale specimens might be different from, and in some cases worse than, the 0.4 scaled specimens that were considered in this study. Caution was suggested when applying the test conclusions to all existing rectangular bridge columns.

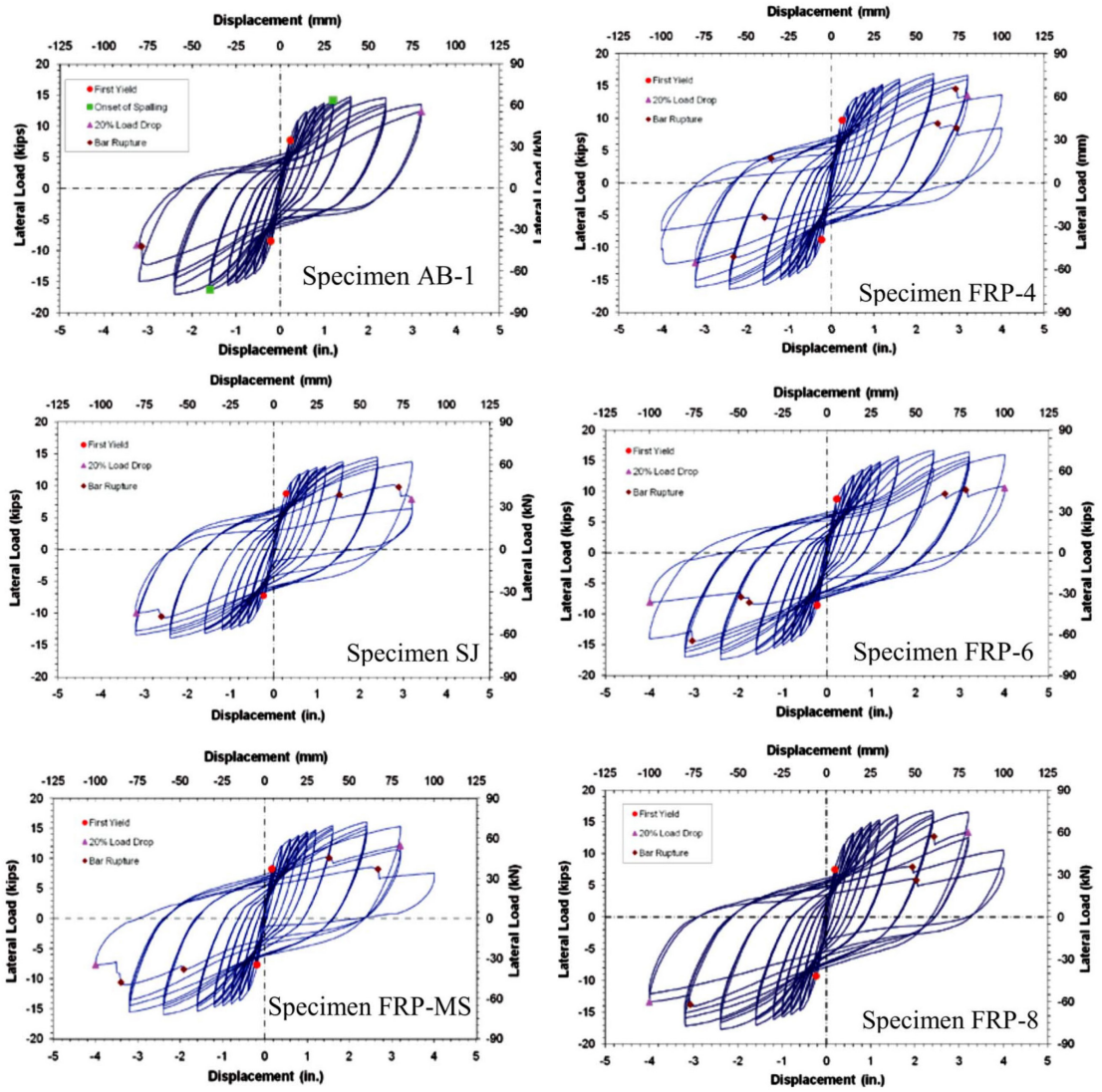

Figure 2.14: Hysteretic curves of the test specimens (AB-1: no retrofit; SJ: Oval shaped steel jacketing; FRP-MS: Oval shaped CFRP with 2 layers; FRP-4: CFRP with 4 layers; FRP-6: CFRP with 6 layers; FRP-8: CFRP with 8 layers;) (El Gawady et al. 2010).

2.3.2.3 *Wire Prestressing*

During the application of a repetitive lateral load, such as that occurring during earthquakes, short and stubby columns may attract shear stresses greater than the diagonal tension capacity of concrete, resulting in concentrated damage. In a reinforced concrete column, the excess shear can be resisted using sufficient transverse reinforcement. In addition to resisting the increased shear stresses, transverse reinforcement provides two other functions to the system: (1) restraining longitudinal reinforcement against buckling, and (2) confining concrete in the core for improved stiffness. The increase in lateral confinement results in an improvement in the bond between steel and concrete and provides enhanced performance of the spliced

longitudinal reinforcement in the plastic hinge region. Also, by proper confinement of the core concrete, the ductility capacity of the column is enhanced. Although passive confinement of concrete provided by external steel or FRP jacketing is the most common method used to improve the ductility capacity of columns (Budek et al. 2001; Federal Highway Administration 1995), work by Saatcioglu and Yalcin (2003), Andrawes et al. (2010) and Zong-Cai et al. (2014) have shown that active confinement using external pressure on the concrete column can enhance the strength and stiffness of concrete columns more effectively than passive systems.

In the design of concrete columns, shearing resistance is provided by the concrete and steel in the column. The concrete shear resistance includes contributions from uncracked and cracked concrete, where the latter is activated by aggregate interlock. These components of shear resistance are usually assessed using the 45° truss analogy employed in the ACI design code (ACI 318 2002). If the shear stress applied to the columns exceeds the shear resistance of the concrete, diagonal tension cracks form; further, if transverse reinforcement is insufficient, significant yielding occurs, diminishing the ability of concrete to carry shear across a crack. This leads to diagonal-tension failure of the column. The deterioration of concrete becomes faster under seismic-induced inelastic shear force reversals, which tend to produce wider cracks that cross over one another. Therefore, the shear carried by concrete may not be relied on for seismic resistance (ACI 318 2002), leaving the transverse steel reinforcement as the only element of resistance. Prestressing overcomes the tendency of diagonal cracks to form and widen, improving concrete shearing resistance. This improvement is directly proportional to the amount of prestressing that must be overcome before the concrete can develop diagonal-tension cracks.

There have been a number of studies that have explored the feasibility of active confinement for seismic retrofit of concrete columns. The seismic response and compressive strength of square cross section RC columns retrofitted with prestressed CFRP, AFRP, and metal strips was investigated by Gamble et al. (1995) and Saatcioglu and Yalcin (2003). The results of these two studies showed that a significant increase in the strength and ductility of specimens was possible due to active confinement. Specifically, prestressed high-strength steel strips were observed to greatly reduce the propagation of cracks, improving their ductility and deformation capacity. In a study by Saatcioglu and Yalcin (2003), the effectiveness of external lateral prestressing as a seismic retrofit strategy was investigated for shear deficient concrete columns. The retrofit technique involved external prestressing of circular, square, and rectangular columns with individual hoops that consisted of prestressing tendons and specially designed anchors (Figure 2.15). In the case of circular columns, the hoops were placed directly on the concrete surface, providing uniform lateral pressure generated by hoop tension. Additional hardware was used for square columns in the form of steel spreader frames and raiser discs, to enable the development of perpendicular force components on all faces, bringing lateral pressure to near uniform distribution. Column tests were conducted to verify the parameters involved in the technology. The results indicated improvement in lateral drift capacity from 1% in shear-critical columns to up to 5% in retrofitted columns.

Although prestressing with metal strips and wire strands can enhance the performance of RC columns by suppressing shear failure, installation of strand requires proper anchorage fixed onto the surface of existing concrete members. Also, tension for prestressing needs to be applied using a feed-through tensile jack. These tasks present a complex construction process for wire prestressing, and the operations can be detrimental to the columns (Zong-Cai et al. 2014).

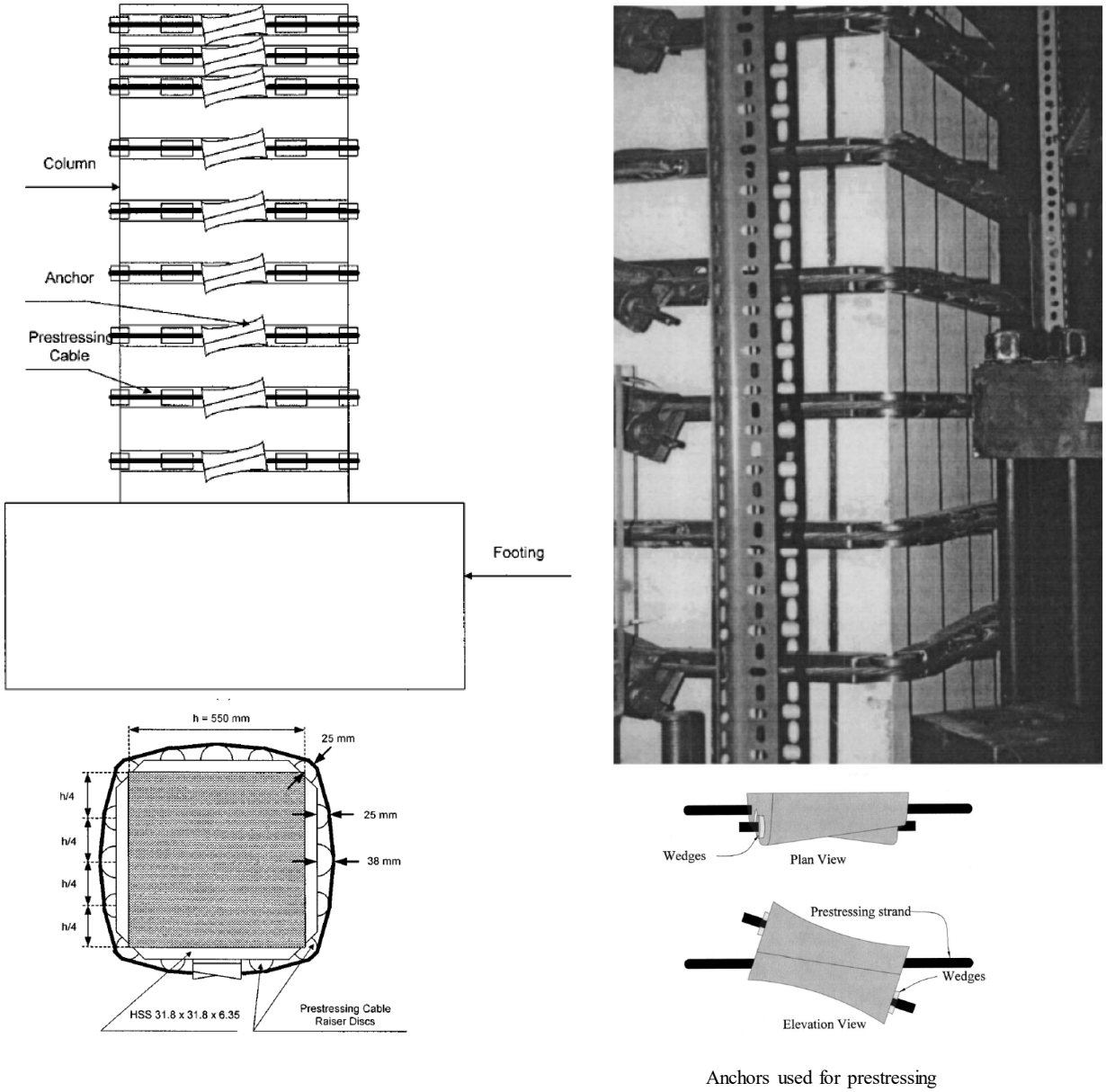

Figure 2.15 : An example of external prestressing square RC columns (Saatcioglu and Yalcin 2003).

Overall, most of the retrofitting techniques focus on lateral confinement only; whereas a column retrofitted to increase shear capacity also requires enhanced flexural ductility,

which they often lack. There are few studies that explored the provision of flexural load paths through the use of near-surface-mounted (NSM) bars. Bournas and Triantafillou (2009) studied three different types of NSM reinforcing materials (carbon, CFRP, and glass, GFRP, fiber-reinforced polymers versus stainless steel) with different configurations of NSM materials and bonding agents for flexural strengthening of RC square columns. The retrofitting scheme consisted of the combination of epoxy-bonded NSM bars with local confining jackets of textile-reinforced mortars (TRM). All bare column specimens were 250 mm x 250 mm (9.84 in. x 9.84 in.) in cross-section with cantilever column height of 63 in. (1.6 m) and reinforced with four 0.55 in. (14 mm) diameter smooth bars (except for one specimen, which had 0.47 in. [12 mm] smooth bars) along with 0.32 in. (8 mm) diameter smooth stirrups, closed with 90˚ hooks at both ends at a spacing of 7.87 in. (200 mm) on center. The columns were subjected to lateral loading cycles while maintaining constant axial load of $0.2f_c'A_g$ applied to the columns throughout the tests. Stainless steel and FRP NSM bonded bar with epoxy resin were determined to be the most effective approaches to enhance the flexural resistance and displacement ductility. Local TRM jacketing helped control buckling of the NSM reinforcement to some extent. The failure modes ranged from fracture and debonding of NSM FRP strips to buckling, fracture, and extraction of NSM stainless steel bars. Failures could be attributed to inadequate confinement since the jackets were applied to square columns. Moreover, the method was deemed challenging to implement in practice due to the necessary surface preparation and NSM grooving required during construction.

2.4 TITANIUM ALLOY BARS (TIABS) RETROFIT APPROACH

Many seismic retrofitting techniques available at present have been successful in effectively retrofitting circular reinforced concrete (RC) columns. However, application of similar retrofit techniques to square RC columns has not always led to comparable results. The main challenge lies in providing effective confinement of square columns. Effective confinement, considered possible when a uniform hoop stress can be provided, is best developed in circular sections. When applying jacketing to square columns, the edges of the section are often chamfered prior to application in order to improve the uniformity of hoop stress, which requires significant effort and cost as part of the retrofitting operation. Unfortunately, this approach appears to be ineffective in providing confinement to regions of concrete away from the chamfered corners, which remain essentially unconfined (Figure 2.16). Attempts to use FRP as circular jackets have been reported, but the method requires sophisticated installation techniques, and effective anchorage requires the use of proprietary anchors (Mirmiran et al. 1998; Galal et al. 2005). The FRP materials and bonding agents are also known to be limited by several environmental constraints (ACI 440.2R-17, ACI Committee 440, 2017). Furthermore, most common FRP materials are brittle, and thus cannot significantly contribute to ductility except through the increased confinement provided to the RC columns.

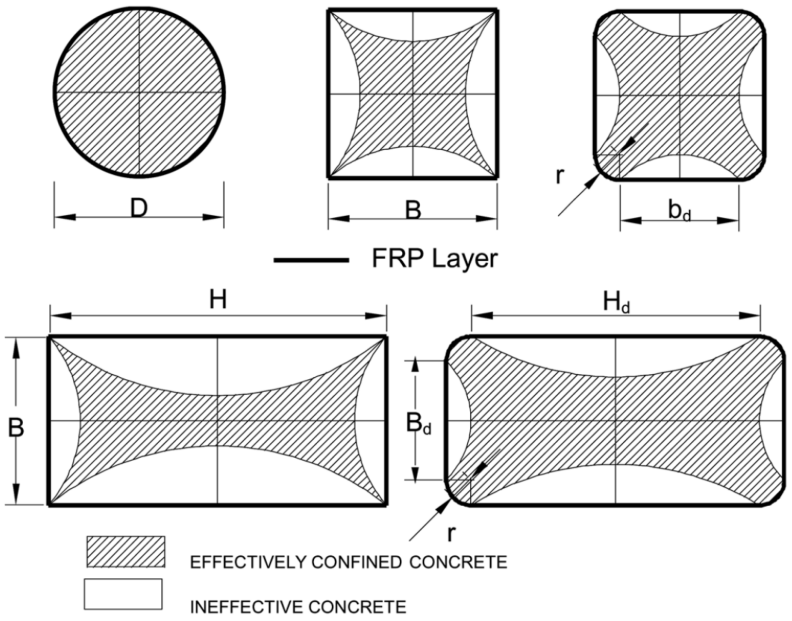

Figure 2.16: Effective confinement area in concrete columns with different cross sections (Campione et al. 2004).

Other retrofitting techniques like steel jacketing and column jacketing suffer from the disadvantage of being too stiff and adding to the seismic weight of the system that tend to increase the seismic demand (Bournas and Triantafillou 2009). It is also difficult to ensure proper compaction of the grout used in these techniques which may create weak pockets in the retrofit shell. Moreover, construction and post-earthquake inspection is difficult to perform on columns retrofitted with these techniques. Most of the contemporary retrofitting techniques focus on the provision of lateral confinement only and there has been limited study for flexural strengthening of columns with lap-spliced bars.

Recently, Shrestha (2019) described details of an economical and effective retrofit alternative using Titanium alloys bars (TiABs). Titanium alloys have been popular for their remarkable corrosion resistance characteristics, light weight, flexibility, and temperature insensitivity which makes them suitable for civil construction (Takahashi et al. 1994, Shrestha 2019). Use of titanium alloy bars have been reported to provide characteristics such as high tensile strength, ductility, environmental durability, high shear strength, resistance to mechanical damage, high maximum service temperature, and thermal compatibility. Also, they are stronger than carbon steels, nonmagnetic and nontoxic, and do not easily ionize or pollute the environment, all characteristics that make TiABs ideal materials for construction underwater or in marine environments. TiABs have been recently used for rehabilitation of cracked and deformed girders of Mosier Bridge over Oregon's main east-west highway, I-84, using the NSM technique. The rehabilitation process was fast (completed in a couple of weeks), cheaper than any other alternative (less than 3% of the estimated cost for bridge replacement and 30% lower than rehabilitation costs using alternative materials) and provided satisfactory improvement to the bridge performance in terms of strength and deformability (Higgins et al. 2017). These desirable features indicated that the TiAB retrofit method is a viable retrofit alternative, providing the

basis for experimental and analytical studies of the TiAB retrofit application to square RC bridge columns (Barker 2014; Amneus 2014; Knudtsen 2016; Vavra 2016; Higgins et al. 2017; Shrestha 2019).

This retrofitting technique included the use of: (1) TiAB ligaments to provide a simple and effective method for flexural strengthening of columns with lap-splices, and (2) TiAB spirals to ensure continuous confinement through hoop action. The anchorage of the ligaments and spirals were achieved by drilling and epoxying the titanium bars into the columns and footings. In this technique, no surface preparation was required other than the provision of anchorage holes. The retrofit was installed with conventional construction practice with no specialized labor. The use of polycarbonate formwork allows inspection of concrete compaction. No cover is required for TiAB spirals, and the retrofit shell allows post-earthquake visual inspection, an added advantage over other retrofit techniques.

2.4.1 Column-Footing Specimens

The frequency of certain geometric and reinforcement details in the ODOT bridge database (Shrestha 2019) was used as the basis for the design of the specimens used in the testing program. All column specimens were 24 in. × 24 in. (609 mm × 609 mm) square columns with 4 – #10 (#32M) Gr. 60 longitudinal reinforcing steel bars (i.e. $\rho_l = 0.88\%$), equivalent to the most common vintage detail of 4 – #11 (#36M) Gr. 40 longitudinal reinforcement bars (i.e. $\rho_l = 1.0\%$) and #3 (#10M) Gr. 40 square hoops with 90˚ hooks at 12 in. (305 mm) on center (i.e. $\rho_v = 0.09\%$) with 1.5 in. (38 mm) concrete cover. The reinforcing bars had an average yielding (f_y), ultimate (f_u) stresses and the ultimate elongation of 65 ksi (448 MPa), 95 ksi (655 MPa) and 32.4%, respectively.

The cross section of the control column-footing specimen is shown in Figure 2.17. The longitudinal reinforcement bars at the base of the column were spliced to the footing starter bars with a lap-splice length of 36 in. (914 mm: approximately $28d_b$). The first group of specimens consisted of five “tall columns” with 13 ft. (3,962 mm) overall column height and the second group consisted of nine “short column” specimens with 9 ft. (2,743 mm) overall column height. An extra foot (0.3 m) of height was provided for attachment of the lateral load assembly. The column formwork and reinforcing steel details are illustrated in Figure 2.17. Twelve of the columns were constructed with a heavily reinforced 6 ft x 6 ft (1828 mm x 1828 mm) and 2 ft (609 mm) deep footing with details shown in Figure 2.17. The footings of these specimens were over-designed to isolate the behavior and ensure the failure occurred in the column rather than the foundation and are not representative of the actual support conditions for the prototype structure. The remaining two footings were constructed to represent as-built foundations consisting of spread footings and timber pile caps with a single grid of reinforcing steel.

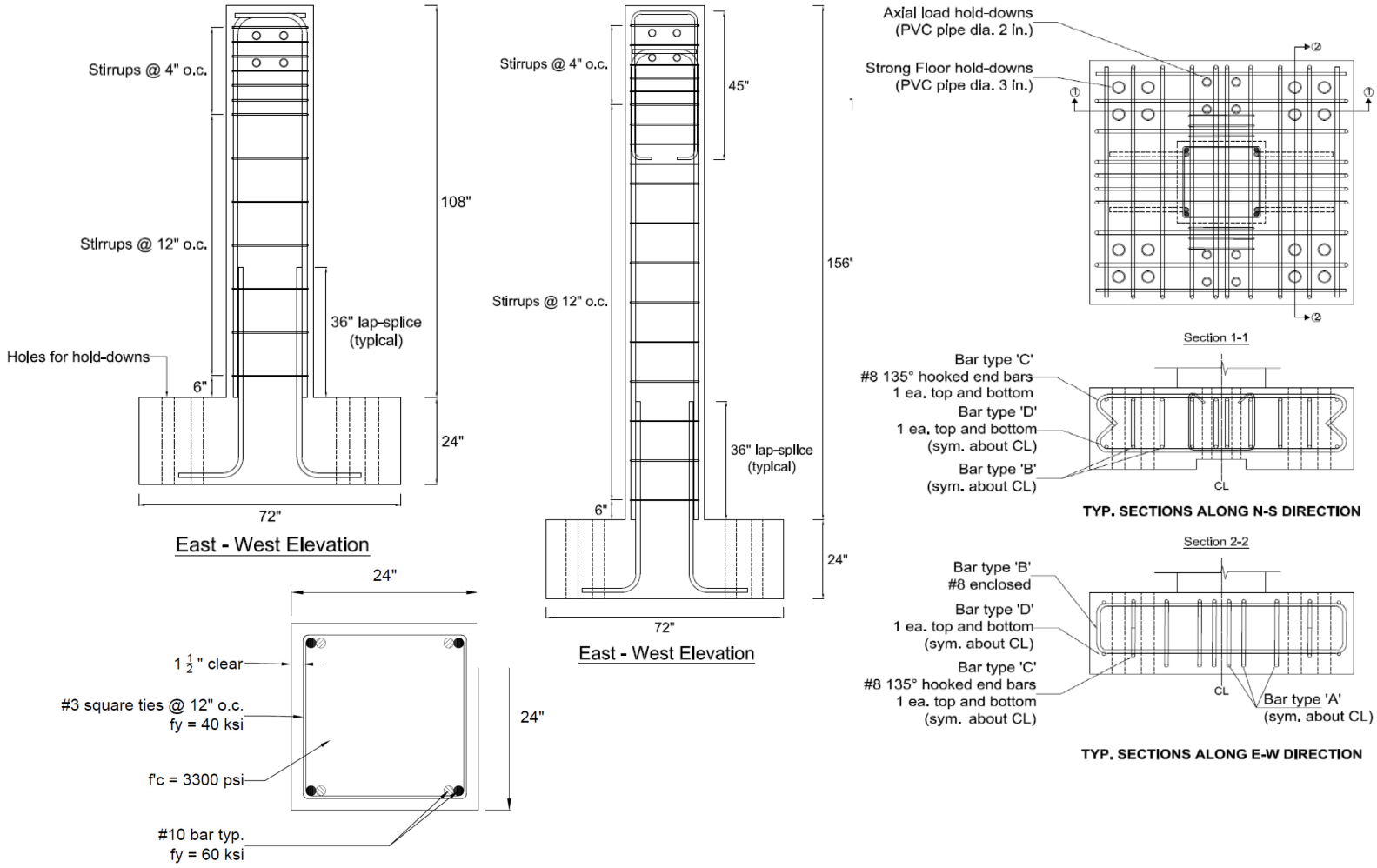

Figure 2.17: The column formwork and reinforcing steel details (Shrestha 2019).

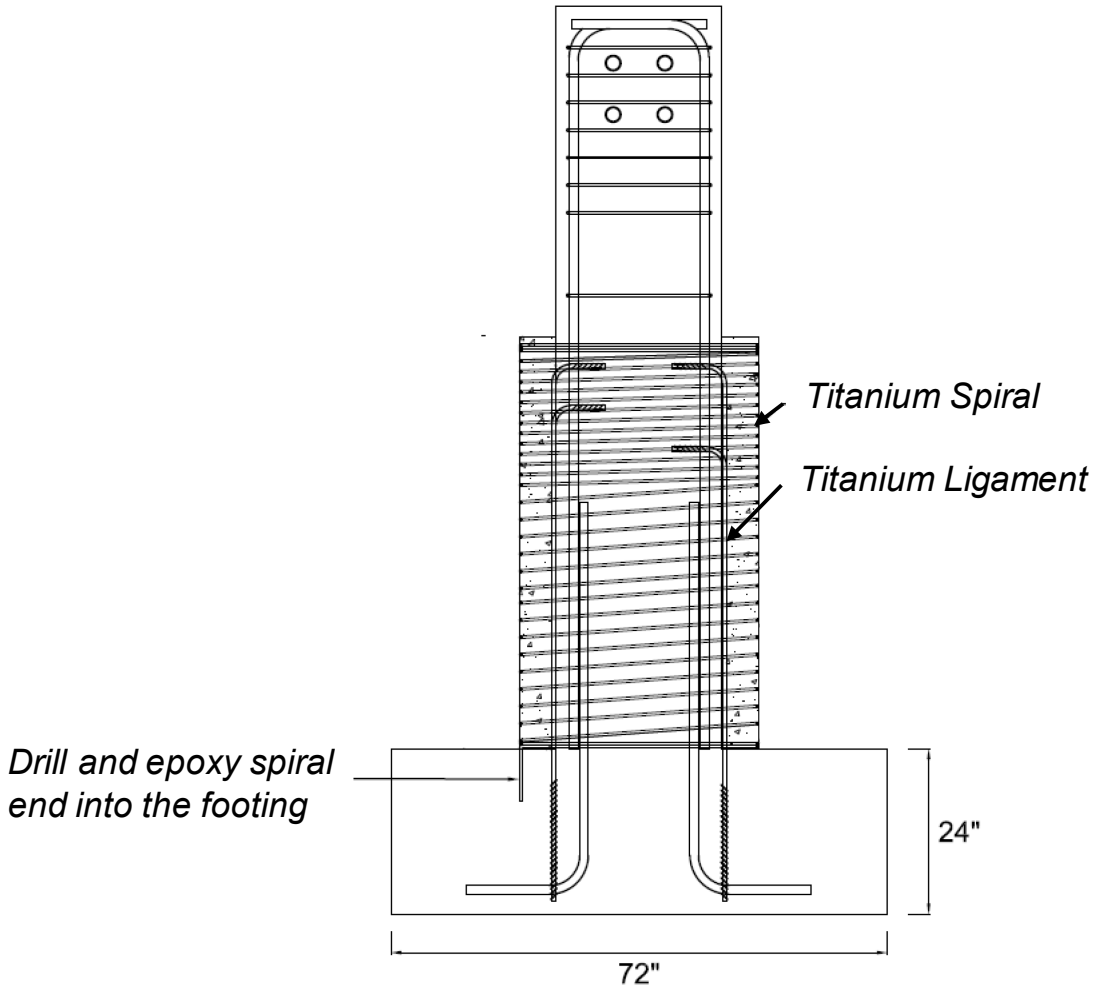

Figure 2.18: Retrofit details including the TiAB spiral and ligament (Shrestha 2019).

2.4.2 Retrofit Details

The retrofit design consisted of external TiAB ligaments uniformly distributed on all column faces with a hooked end anchored into the column face on one end and straight end anchored to the footing on the other with an epoxy-based adhesive. The other portions of the ligament lengths were unbonded from the column. Confinement was provided through a continuous tightly wrapped TiAB spiral with concrete infill between the spiral and debonded column faces. No cover concrete is used over the TiAB spiral. Figure 2.18 shows retrofit details including the spiral and ligament. In addition to TiAB ligaments, stainless-steel ligaments were also explored for the retrofit ligaments to evaluate the role of ligament material type on the retrofit efficiency of the structure.

2.4.2.1 TiAB Ligaments

The objective for introducing ligaments as a retrofit technique was to provide a supplemental load path when lap-splices remain functional and then to serve as an alternative load path following degradation and loss of lap-splice function under large

amplitude cyclic loading. The nominal yield stress of the TiAB ligaments was 130 ksi (896 MPa) and was used in the design of the specimens. The average length of the ligaments implemented was determined using AASHTO LRFD Bridge Design Specifications (2017) for tension lap-splice length for column longitudinal bars. TiAB ligaments consisted of 5/8 in. (16 mm) diameter bars with a 10 in. (250 mm) long 90° hook, whereas the lower 15 in. (380 mm) or 20 in. (500 mm) end, depending on the specimen, of each bar was fabricated with surface deformations to promote bonding as illustrated in Figure 2.19. The pin diameter for the 90º hook was 3 ¾ in. (95 mm). The hooked end of the bar was anchored into the column face and the straight portion was anchored into the footing. The textured anchored ends of the hook were implemented using a proprietary deformation pattern and technique to promote epoxy bonding (Figure 2.19). Three different lengths of vertical TiABs were used in each column to stagger the terminations with a 6 in. (150 mm) spacing and thereby reduce stress concentrations at a single section.

During loading, it was observed that conical concrete cracks formed around the TiAB ligaments at the footing surface, resulting in the buckling of some of TiAB ligaments in tall specimens. In order to prevent these cracks, only 15 in. (380 mm) of the straight end was deformed in short specimens to promote debonding along the top 5 in. (125 mm) of the embedded length. These deformed straight ends were placed into hammer-drilled holes to a depth of 22 in. (559 mm). The actual embedment length of the ligaments into the footing was 20 in. (508 mm). The 2 in. (51 mm) extra depth was provided to allow necessary bending of the ligaments to insert the hooks into the column.

2.4.2.2 Stainless-Steel Ligaments

For the stainless-steel ligaments, Grade 75 #6 (#19M) stainless-steel bars were used. The bars had yield and ultimate stresses of 95 (655) and 136 ksi (938 MPa), and an ultimate elongation of 32.4%. For comparison purposes, length and configurations similar to the TiAB ligaments were used for the stainless-steel ligaments.

2.4.2.3 TiAB Spiral

The pitch of the TiAB spirals was calculated using the guidelines from Priestley et al. (1996) based on the confinement model for circular reinforced column sections by Mander et al. (1988). The effective lateral pressure (f_l) of 320 psi (2.2 MPa; approximately $0.1f_c'$) was used in the design. The TiAB spiral was chosen to meet the AASHTO LRFD Bridge Design Specifications (2017) and requires the use of 3/8 in. (9.5 mm) aggregate size to construct the shell for the given longitudinal reinforcement. Based on AASHTO LRFD Bridge Design Specifications (2017), following details are recommended for spiral transverse reinforcement (Shrestha 2019):

- • Minimum spiral diameter: 0.375 in. (3/8 in.)
- • Maximum center to center spacing of the spirals: smaller of "$6.0d_b$" or "6.0 in."

- • Minimum clear spacing between the spirals: greater of “1.33 times the maximum size of aggregate” or “1.0 in.”

Based on these specifications, a 3/8 in. (9.5 mm) diameter, smooth TiAB spiral was chosen at 2.5 in. (63.5 mm) pitch. Based on Shrestha (2019), such design details ensured elastic performance of the spirals during testing. The top spiral was anchored into the column and the bottom spiral was anchored into the footing for most specimens. In some cases, the top and bottom spirals were anchored into the column sides to investigate the effect of spiral anchorage on the response of the column. The TiAB spiral anchorage depth was 8 in. (200 mm). The ends of the TiAB spirals were heated with an oxyacetylene torch and field-bent to produce a 90° hook as presented in Figure 2.19.

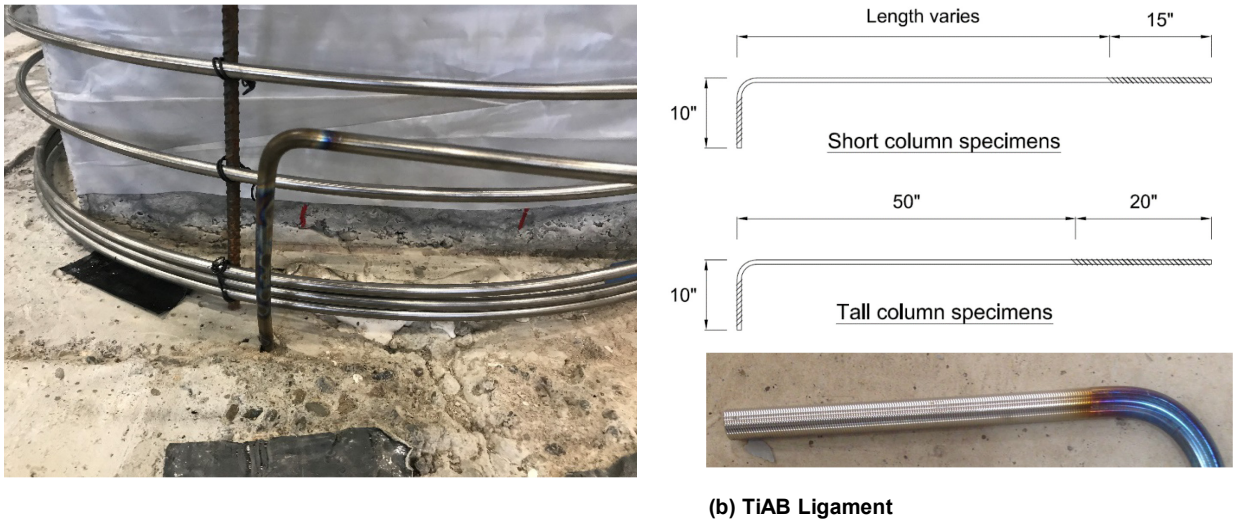

(b) TiAB Ligament

Figure 2.19: Anchorage details of TiAB components: (a) Straightened end of spiral TiAB and 90º anchorage hook, (b) TiAB ligament dimensions and details (Shrestha 2019).

The material properties and dead lay production method of the TiAB spirals allowed the spiral to easily open and be wound around the column without permanent deformation, and results in natural contact with the corners of the square column. The spiral was easily wrapped around the column by a single person without exertion given the lightweight nature of titanium (density equal to 281 lb/ft^3 or 4.5 g/cm^3). No other concrete preparation was required other than drilling four (4) holes in the column face and four (4) holes in the footing to anchor the ends of the vertical TiAB ligaments, and two (2) holes to anchor the TiAB spiral. Different retrofit heights were considered for the specimens depending on the column height.

2.4.2.4 Concrete and Epoxy Material Properties

Locally available concrete ready mix containing ¾ in. (9.5 mm) (for the column and footing specimens) and 3/8 in. (4.75 mm) (for the retrofit shell) minus aggregate was used in the construction of the specimens. Results of compressive strength tests performed in accordance with ASTM C39M/ C39M-05 and ASTM C617-98 indicated compressive strength of around 3,500 psi (22.7 MPa) for the columns and 4000 psi (28

MPa) for the retrofit shell. Tensile splitting tests results indicated average tensile strength values of 300, 235, and 420 psi for the column, footing, and shell concrete mix used for the study.

The epoxy used for TiAB ligament anchorage to the concrete substrate was Hilti HIT-RE 500 V3 Epoxy Adhesive. The epoxy manufacturer reports a bond strength of 1,560 psi (10.8 MPa) and 1,690 psi (11.7 MPa) for a 2- and 14-day cure period, and a tensile strength of 7,150 psi (49.3 MPa) at 7 days. The results of pull-out tests on a #5 TiAB bar indicated an average bond strength of approximately 1.4 ksi (9.6 MPa) over the embedded length of 15 in. (380 mm). This is comparable to an average bond strength of approximately 1.6 ksi (11.0 MPa) provided by a #6 stainless steel bar developed over an embedded length of 12 in. (305 mm).

2.4.3 Experimental Verification through Large-Scale Testing

Shrestha (2019) reported on the results of a suite of fourteen quasi-static cyclic loading tests on full-scale RC column-footing specimens to study the cyclic performance of the proposed titanium alloy bar (TiAB) retrofit. The experimental program consisted of design, construction, and reverse cyclic lateral loading of column specimens under constant axial load in the laboratory. The main test variables were the column height, lateral loading direction, height of the retrofit shell, presence or absence of vertical ligaments, hook angle of vertical ligaments, type of materials used for vertical ligaments, and the foundation details and restraints.

2.4.3.1 Specimens design and construction

The frequency of certain geometric and reinforcement details in the ODOT bridge database was used as the basis for the design of the specimens used in the testing program. All column specimens were 24 in. x 24 in. (609 mm x 609 mm) square columns with 4 – #10 (#32M) Gr. 60 longitudinal reinforcing steel bars (i.e. $\rho_l = 0.88\%$), equivalent to the most common vintage detail of 4 – #11 (#36M) Gr. 40 longitudinal reinforcement bars (i.e. $\rho_l = 1.0\%$) and #3 (#10M) Gr. 40 square hoops with 90˚ hooks at 12 in. (305 mm) on center (i.e. $\rho_v = 0.09\%$) with 1.5 in. (38 mm) concrete cover. The cross section of the control specimen is shown in Figure 2.20. The longitudinal reinforcement bars at the base of the column were spliced to the footing starter bars with a lap-splice length of 36 in. (914 mm: approximately $28d_b$). The first group of specimens consisted of five “tall columns” with 13 ft. (3,962 mm) overall column height and the second group consisted of nine “short column” specimens with 9 ft. (2,743 mm) overall column height. An extra foot (0.3 m) of height was provided for attachment of the lateral load assembly. The column formwork and reinforcing steel details are illustrated in Figure 2.17. Twelve of the columns were constructed with heavily reinforced 6 ft x 6 ft (1828 mm x 1828 mm) and 2 ft (609 mm) deep footing block with details shown in Figure 2.17. The footings of these specimens were over-designed to isolate the behavior and ensure the failure occurred in the column rather than the foundation. Thus, they are not representative of the actual support conditions for the prototype structure. The remaining two footings were constructed to represent as-built foundations consisting of spread footings and timber pile caps with a single grid of reinforcing steel.

2.4.3.2 Retrofit Installation

All column specimens were constructed in two stages: the footings with starter reinforcing bars were constructed first, and then the column was constructed after the footing concrete had cured. The concrete mixture for the footings and columns were designed to provide material proportions and mechanical properties that are consistent with vintage RC bridge components. The concrete mix contained 3/8 inch (9.5 mm) minus aggregate and had a 28-day design compressive strength of 3 ksi (21 MPa), compared to the test strengths of 3.5 ksi (22.7 MPa) as described in Section 2.4.2.4. The control specimen was tested after the 28th day of column construction, while the remaining specimens were prepared for retrofit.



Figure 2.20: TiAB retrofit processing (Shrestha 2019).

Holes were hammer drilled at the pre-determined locations for TiAB ligaments and spirals. To get the bend of the vertical TiABs to rest against the column, rounding out of the bottom side of the drilled holes was required prior to anchorage. The holes were carefully cleaned by brushing and vacuuming. The column was then wrapped in plastic sheathing to de-bond the concrete shell from the column faces as seen in Figure 2.20. After placing and bonding the ligaments with epoxy, one end of the TiAB spiral was bonded to the column face at the top of the retrofit height. The spirals were then wrapped around the columns and drawn tight around the corners at the designated pitch and the other end was bonded to the footing. Polycarbonate formwork was then placed directly around the spirals with no cover. The polycarbonate sheet was held together using ratchet straps as shown in Figure 2.20. Concrete was then filled into the formwork to the height of the shell. For retrofit shell, concrete with 3/8 in. (9.5 mm) minus aggregate and nominal compressive strength of 4 ksi (27.6 MPa) was used. The polycarbonate form

allows visual inspection of the fill to ensure the shell is properly placed and consolidated. The final retrofitted specimen is shown in Figure 2.20.

2.4.3.3 Instrumentation and Testing Setup

Various instruments were used to observe the force, displacement, and strain developing in the specimens. The applied loads included lateral and gravity forces and were measured with load cells mounted to hydraulic cylinders. String potentiometers were used to measure the column deflection at the point of lateral load application, flexural and shear deformation of the column, and rigid body motion of the footing. Although restrained laterally, the footing was permitted to displace vertically, and these displacements were measured using four string potentiometers at the mid-height of the footing on the NW, NE, SW, and SE corners. Strain gauges were installed on the steel reinforcement and TiAB and stainless-steel ligaments. A data acquisition system was used to collect data.

The test setup consisted of a servo-hydraulic controlled horizontal actuator with a capacity of 110 kips (489 kN) mounted on a strong wall to supply the necessary lateral reaction. Figure 2.21 shows a schematic of the loading frame used in the experiments (Shrestha 2019). The location of the lateral load application was 96 in. (2438 mm) and 144 in. (3658 mm) above the finished top surface of the footing for the short and tall columns, respectively. For the tests with diagonally loaded specimens, a steel loading assembly was constructed of mild carbon steel plates and angles to load the specimen at a corner.

Testing was performed under constant axial load, equal to 8% (for short columns) and 10% (for tall columns) of the nominal axial compressive capacity of the column, or 150 kips (667 kN) in “short columns” and 200 kips (890 kN) in “tall columns.” Under the applied axial load, the specimens were subjected to displacement-controlled reversed cyclic loading and the response of column and footing was monitored using the aforementioned instruments.

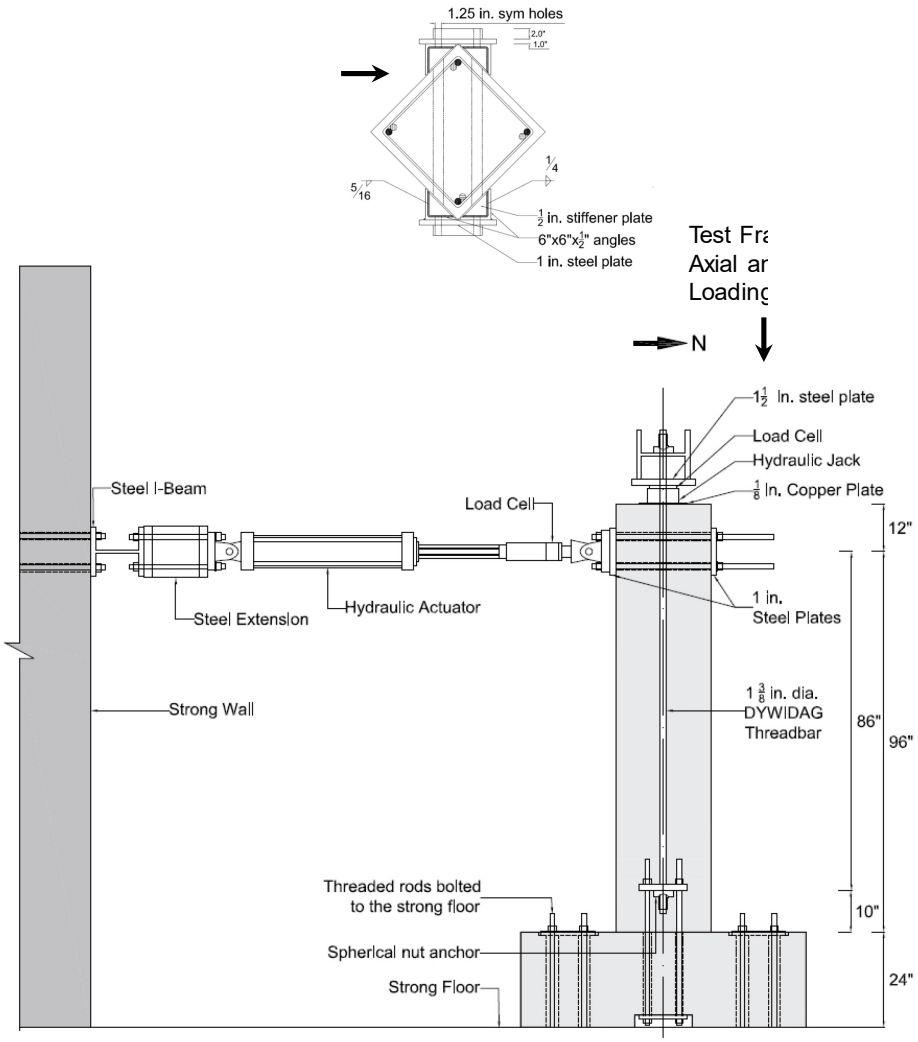

Figure 2.21: Typical setup with lateral and axial loading for lateral seismic tests on "short" column (Shrestha 2019).

2.4.3.4 Results

Shrestha (2019) performed 14 full-scale quasi-static cyclic load tests on reinforced concrete square columns and the effects of different parameters including loading direction, retrofit details, column height, and footing rocking were discussed. The response of each specimen was presented and compared in terms of their global structural behavior, force-deformation response, strength degradation, displacement ductility, energy dissipation, equivalent viscous damping, and stiffness degradation. In addition, the strain response of transverse and longitudinal reinforcing steel bars and elements of the retrofit system, average curvature, and shear deformation response of test specimens were also presented. A brief summary of the test results is presented, focusing on the response of shear-critical short columns. Further details on this testing program can be found in Shrestha (2019).

Effect of Loading Direction

Two (2) control specimens were initially tested as representatives of as-constructed bridge columns. Both specimens had the same reinforcing details and footing dimensions (Figure 2.17). However, one specimen was loaded perpendicular to the face of the column whereas the other was loaded at an oblique, 45° angle to investigate the effect of lateral loading direction relative to the column's principal axes. The columns were expected to exhibit inadequate shear capacity to resist inelastic force reversals at large magnitudes of displacement corresponding to deterioration of the cracked concrete. The results of these tests are presented in Figure 2.22.

The short, square and diamond control columns behaved in a similar manner irrespective of the loading direction. The square and diamond control specimens exhibited a peak force of approximately 37 kips (165 kN) and 36 kips (160 kN), respectively, and the drift ratio at failure was 0.87% for square and 1.25% for diamond column. Both columns exhibited significant strength and stiffness degradation after the initiation of shear failure. Failure in both cases happened prior to achieving the nominal moment capacity of the column.

Results also indicated a brittle behavior with no notable displacement ductility for both columns. The failure mechanism was characterized by a bond failure between the longitudinal bars of the column and the starter bars of the foundation. In the specimen with a square column, the failure mode was indicated by vertical cracking and progressive splitting at column corners over the lap-splice region and spalling of the concrete at the base of the column. Because of the orientation of the lateral load application in the case of the specimen with the diamond column, crossing diagonal shear cracks were not clearly formed in any faces, although some 45° cracks extended from one face to the other face of the column on the east and west faces.

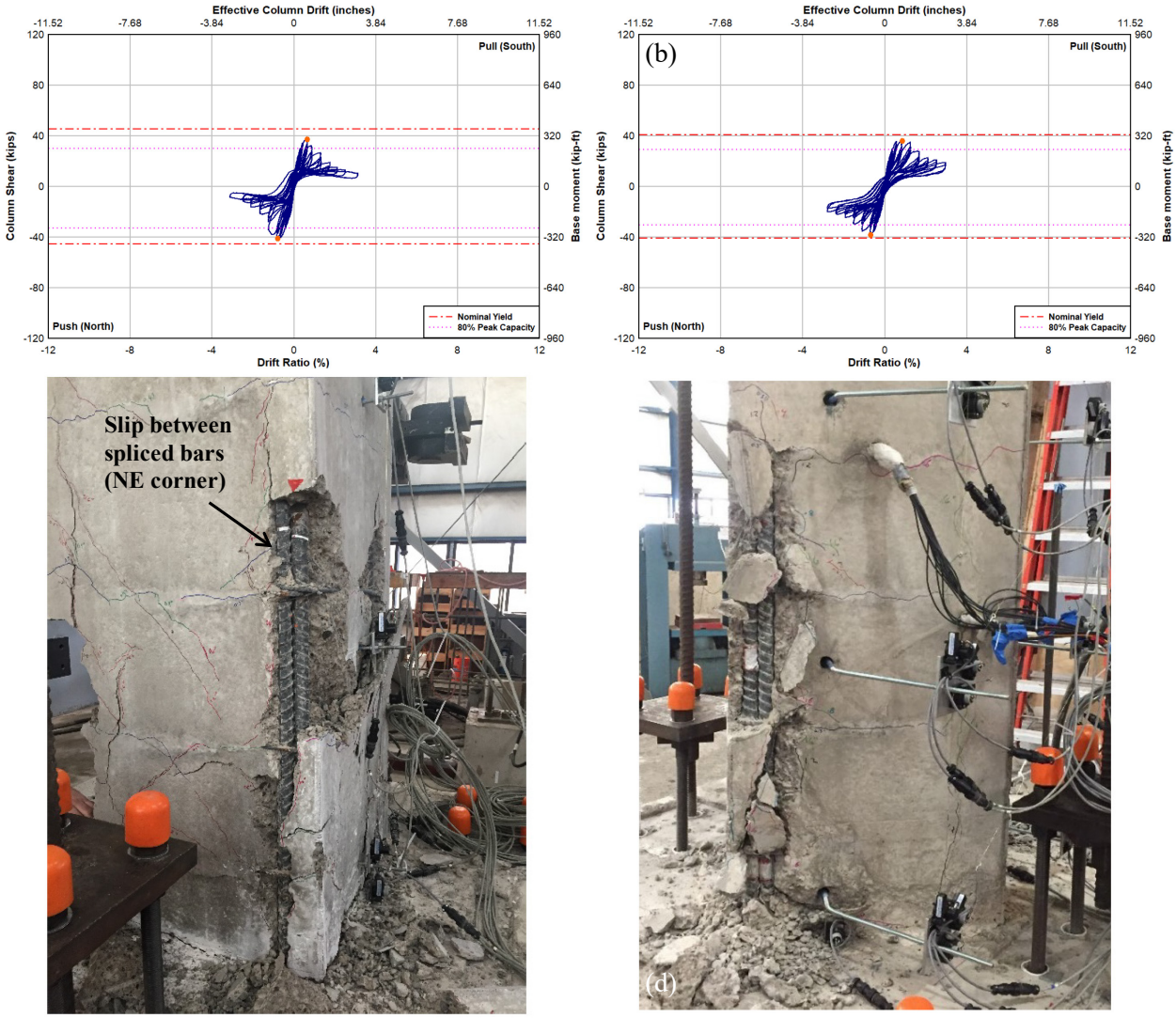

Figure 2.22: The equivalent lateral load, expressed as column shear, versus drift response for the control columns (representatives of as-constructed bridge columns): (a) loading perpendicular to column face, and (b) loading 45° to column face (Shrestha 2019).

Effect of Retrofit Details

The retrofit system investigated by Shrestha (2019) uses two (2) components to improve the performance of columns during cyclic loading: (a) titanium alloy bar (TiAB) ligaments for flexural strengthening; and (b) TiAB spirals for lateral confinement. Different sets of experiments were performed on columns with square cross sections to understand the effect of each of these retrofit components on the response of columns. The tests are categorized into three different groups herein: (1) tests comparing the response of control vs retrofitted columns, (2) tests assessing the role of ligaments, (3) tests comparing the effect of the ligament hook angle, and (4) tests comparing the effect of ligament material on the response of laterally loaded columns.

Effect of Retrofitting

A specimen with square column retrofitted with both TiAB spiral and 90° hooked ligaments was laterally loaded under the condition of constant axial load of 150 kips (667 kN). The results of this test were then compared with results of experiment on the short square column (Figure 2.22). As presented in Figure 2.23, the capacity of the specimen increased by a factor of 2.5 to 92 kips (409 kN) as a result of the retrofit. It exhibited a displacement ductility of about 11 for push- and 15 for pull-cycles. The retrofit method was not able to completely prevent the lap-splice failure. However, it was able to delay it successfully, so the specimen could maintain its strength to drift of about 4.0% which was a significant improvement when compared to the control specimens. The specimen experienced loss of strength in both pull- and push-cycles. The loss of strength happened in a greater rate in the push-cycles with the column shear dropping from 90 kips to almost 25 kips. This can be noted in the bottom left quadrant of the load-deflection hysteresis.

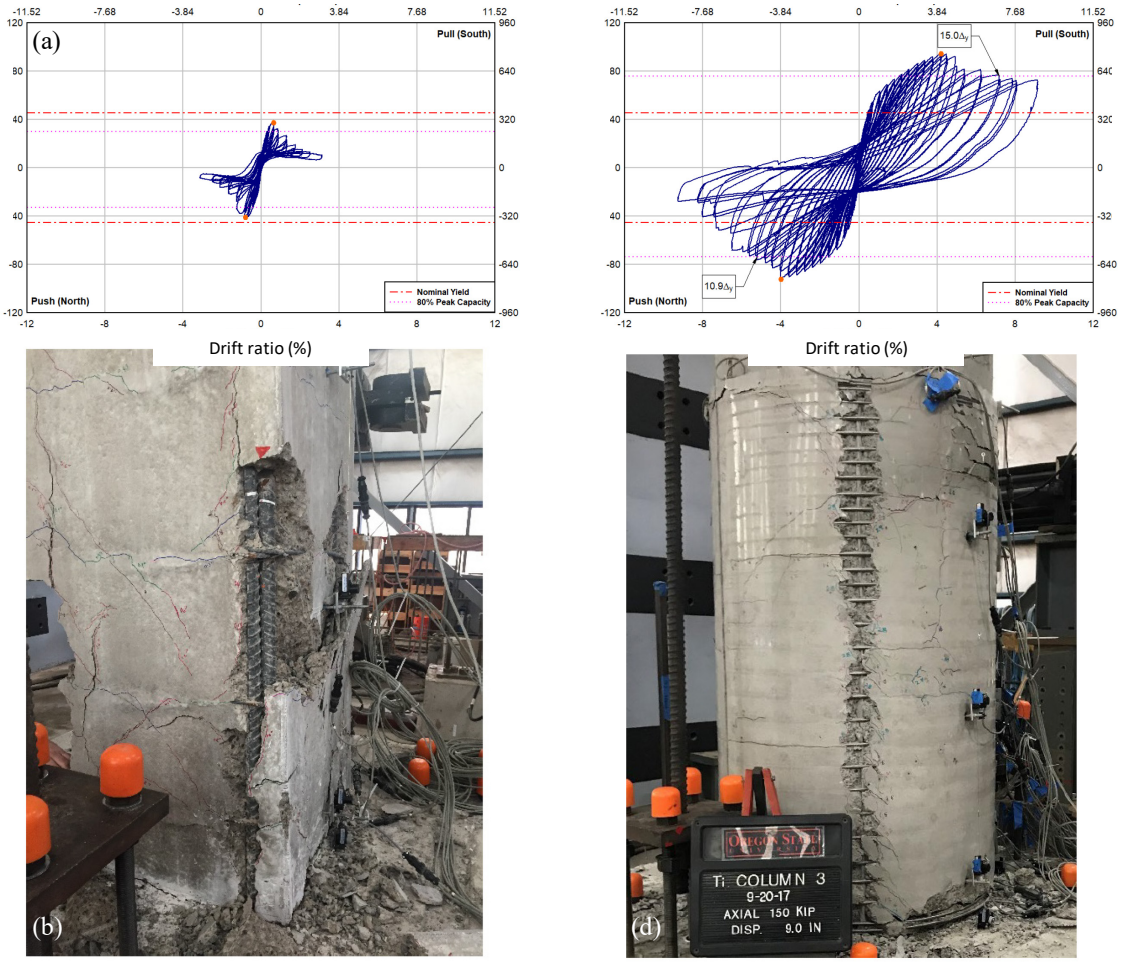

Figure 2.23: The equivalent lateral load, expressed as column shear, versus drift response for the control columns (representatives of as-constructed bridge columns) (a) control short square column, and (b) retrofitted short square column with 90° hooked ligament (Shrestha 2019).

Effect of Ligament Hook Angle

A square column specimen was retrofitted with a TiAB spiral and 135° hooked ligaments to study the influence of hook angle on hook extraction from the column in response to observations that specimens with 90° hooks exhibited extraction during lateral loading. The footing/column dimensions and other retrofit details for this specimen were similar to the control specimens with square column. The rationale behind this experiment was that the anchored hook, when placed in a 90° angle, would align with a potential plane weakened by horizontal flexural cracks which could otherwise be prevented if the hook would be oriented at a different angle. The results of this experiment are presented in Figure 2.24. Although diagonal cracks crossing several spirals on the east and west face of the retrofit shell were noted, the 135° hook was successful in suppressing hook extraction as indicated by reduced cracking and dilation of concrete around the hook regions. The TiAB ligaments with 135° hooks exhibited the least amount of hook withdrawal. In this experiment, the column experienced some sliding along the bottom plane of the column-footing interface after the second cycle of 4.0 in. (102 mm or 4.0 %) drift. Due to this sliding, the ligaments on the north and south sides exhibited buckling. The shear load versus drift response for the column was fairly symmetric prior to the initiation of shear failure at approximately 89 kips (396 kN) and 92 kips (409 kN) shear loads for the push- and pull-cycles, respectively. Failure in the pull-cycle occurred at a lower drift (4.3%) than the push cycle (6.3%). The displacement ductility also ranged from 9 for the pull-cycles to as high as 13 for the push-cycles.

Role of TiAB Ligament

Shrestha (2019) also performed another experiment on a specimen retrofitted with the TiAB spiral to understand the participation of the ligament in resisting flexure at the foundation level. Figure 2.25 compares the results of this experiment (Figure 2.25a and Figure 2.25b) with those from experiments on retrofitted columns with both TiAB spiral and ligament (Figure 2.25c and Figure 2.25d). The results of the experiments are presented in terms of load-drift level and cracking patterns.

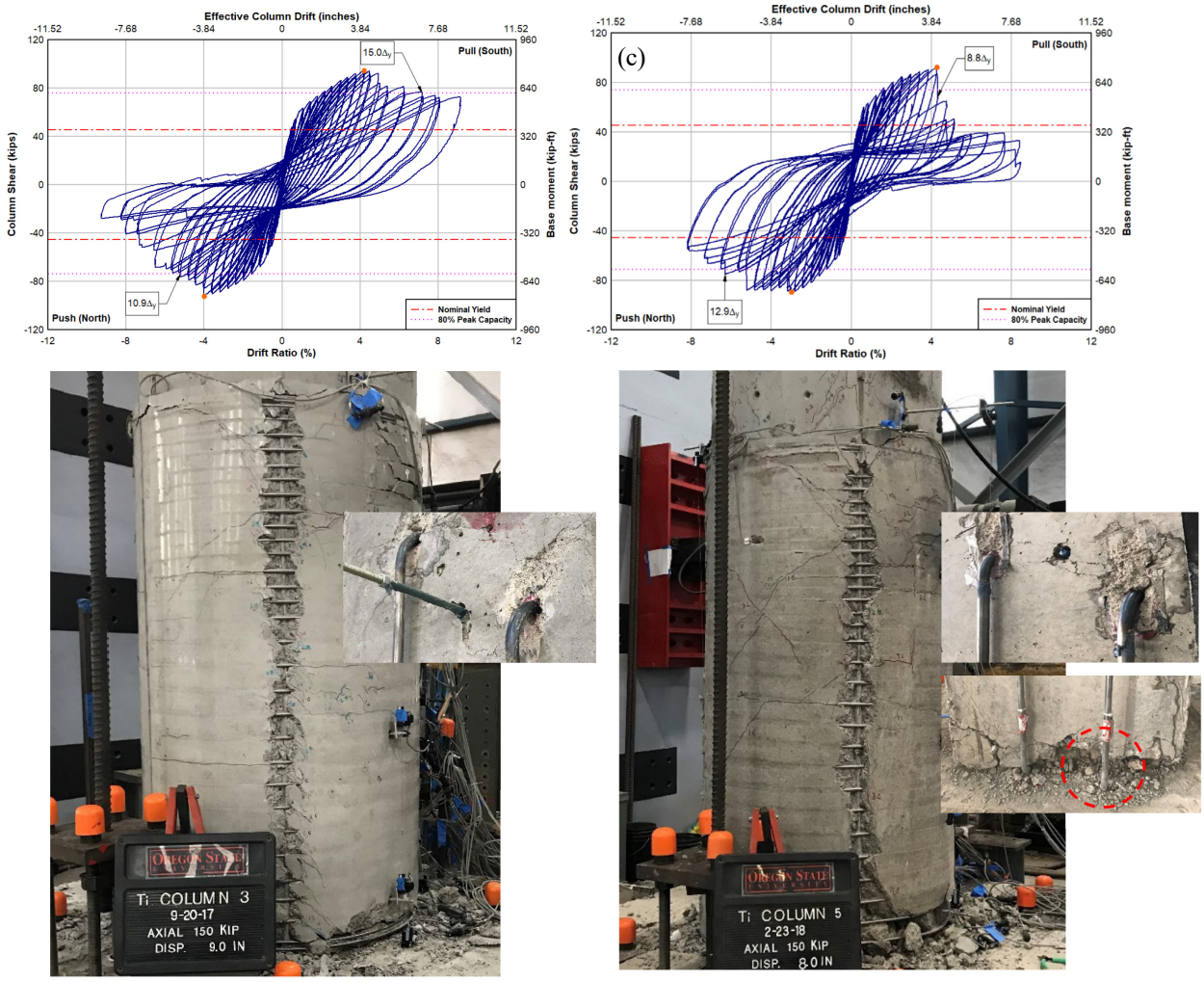

Figure 2.24: The equivalent lateral load, expressed as column shear, versus drift response for the control columns (representatives of as-constructed bridge columns) (a) retrofitted short square column with 90° hooked ligament, and (b) retrofitted short square column with 135° hooked ligament (Shrestha 2019).

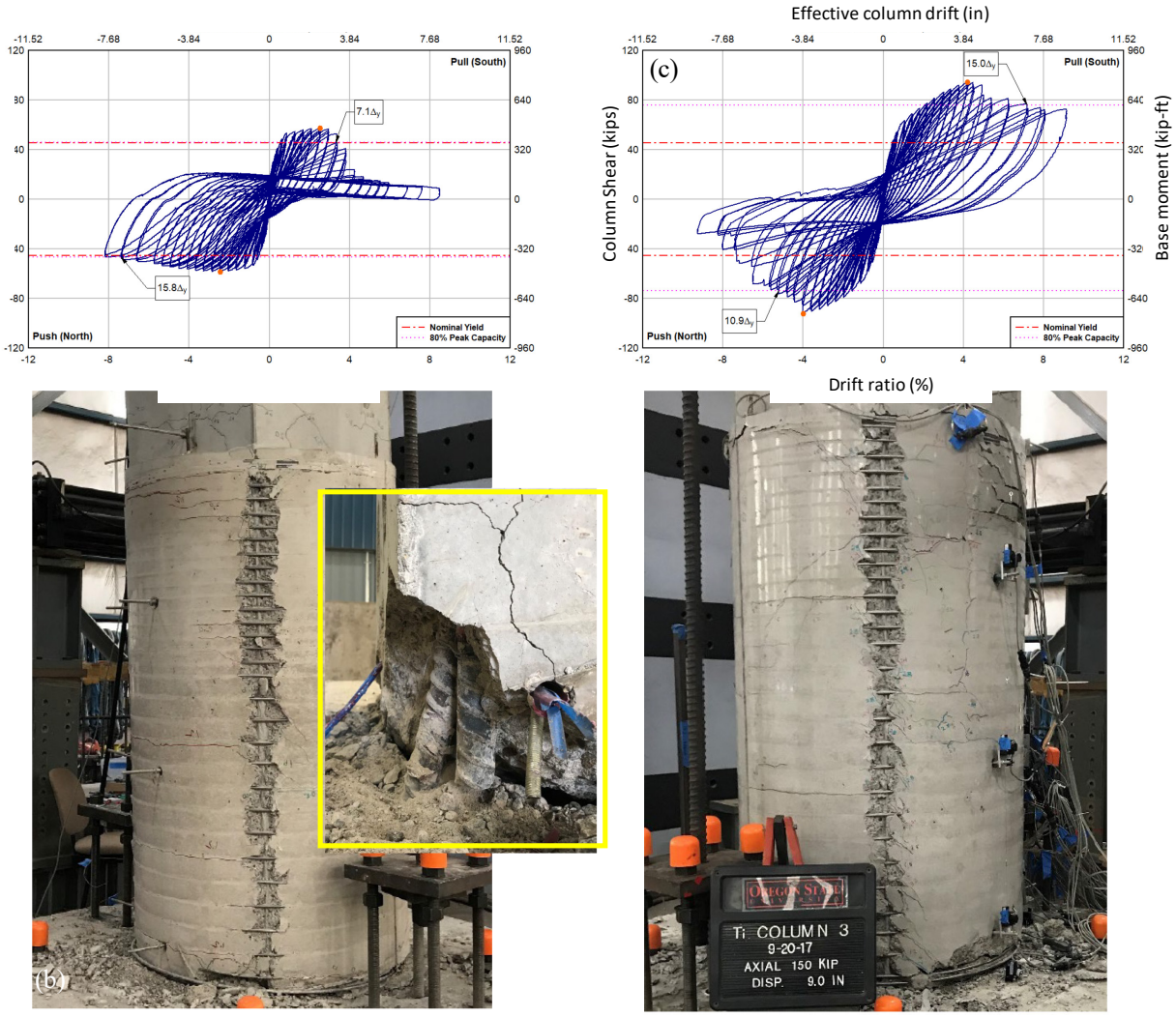

Figure 2.25: The equivalent lateral load, expressed as column shear, versus drift response for the control columns (a) retrofitted short square column with no ligament, and (b) standard retrofitted short square column (Shrestha 2019).

In comparison with the specimen without ligaments, the standard TiAB retrofitted specimens exhibited better energy dissipation with wider hysteresis loops and higher equivalent viscous damping. The column specimens without TiAB ligaments exhibited sliding at the column-footing interface towards the strong wall, resulting in an unsymmetrical load-drift response for the push- and pull-cycles. This was due to higher shear demands in the short columns for the same flexural capacity and insufficient dowel action or interface friction to resist the sliding. With the TiAB ligaments, the column exhibited some self-centering capacity (less residual drift at zero lateral load). This was evident from the force-deformation response of the columns retrofitted with just TiAB spirals (Figure 2.25a) and with both TiAB ligaments and spirals (Figure 2.25b). Although both columns were able to develop similar displacement ductility capacity, residual drifts were much lower for columns retrofitted with TiAB ligaments. The capacity of the column without ligaments was 58.3 kips (259 kN) and 57.3 kips (255 kN) at

approximately 2.5% drift for push- and pull-cycles, respectively. The capacity dropped to 80% at about 3.3% drift (pull), whereas for push, the column maintained its capacity to 7.4% drift with a stable hysteretic response due to the sliding of the column. This was attributed to the constant engagement of the flexural steel which helped to maintain the capacity. It was observed that the anchorage of the TiAB hoop allowed for the continued engagement of one side of the flexural steel, even with spalling cover concrete on the opposite side. As a result, the pull capacity dropped to 9 kips while the push capacity maintained 46 kips.

The progression of distress for the two specimens are shown in Figure 2.25(b, d). The behavior of the column without ligaments can range from the degrading pull cycle behavior to the stable push cycle behavior. The column retrofitted with both TiAB ligaments and spiral clearly shows the importance of the ligaments to produce a stable and symmetrical hysteretic response with self-centering behavior. During the application of loading cycles, the retrofitted specimen without ligaments initially experienced a series of cracks including shrinkage (at 0.2% lateral drift), splitting (at 0.8% lateral drift along the retrofit shell and at 1.6% along the lap-splice starting at the end of the spliced starter bar end), and horizontal (at 1.2% lateral drift). At 2.0% lateral drift, diagonal cracks appeared on the column above the retrofit shell, splitting cracks widened, and as a result, the shell concrete along the corners of the column started to crush. Increased drifts resulted in the complete spalling of the bottom concrete cover and widening of diagonal cracks. Progressive concrete crushing occurred along the bottom of the column and exposing the spirals at a drift of 3.6 in. (91 mm or 3.6%). Upon further inspection of the column following removal of the confinement shell, it was clear that the concrete at the bottom of the column was pulverized, and the starter bars had bent along the same plane that the column slid upon. Some hairline flexural cracks could also be seen on the north and south faces. Splice failure was evident from the cracks along the splice length of the columns in all four corners.

Effect of TiAB Ligament Material

The effect of ligament material on column-footing response was investigated by the comparison of columns retrofitted with the TiAB spiral and stainless-steel ligaments under loading conditions similar to those described previously. The results of this experiment, along with data from the test on the control column is presented in Figure 2.26, which shows that the use of a stainless-steel ligament increased the capacity of the column by a factor of approximately 2.7 compared to that of the control specimen. The overall shear load versus drift response of the column was fairly symmetric up to the point of shear failure with the specimen reaching a capacity of 108 kips (482 kN) at 3.12% drift for the push-cycle and 106 kips (472 kN) at 3.31% drift for the pull-cycle. The capacity dropped by more than 50% in the push-cycle at 4.4 in. (112 mm or approximately 4.4%) drift which marked the failure of the specimen. The specimen attained displacement ductility of about 8 and 9 for push- and pull-cycles, slightly lower than the specimens retrofitted with TiAB ligaments. Use of stainless-steel ligaments and the corresponding over-strength of this material resulted in higher shear and moment in the column leading to failure above the retrofit shell. This resulted in reduced seismic performance and an unintended failure mechanism that differed significantly from the

specimens with TiAB ligaments. The well-defined TiABs material properties allow for confident estimation of the maximum strength which can ensure force protection of other structural details.

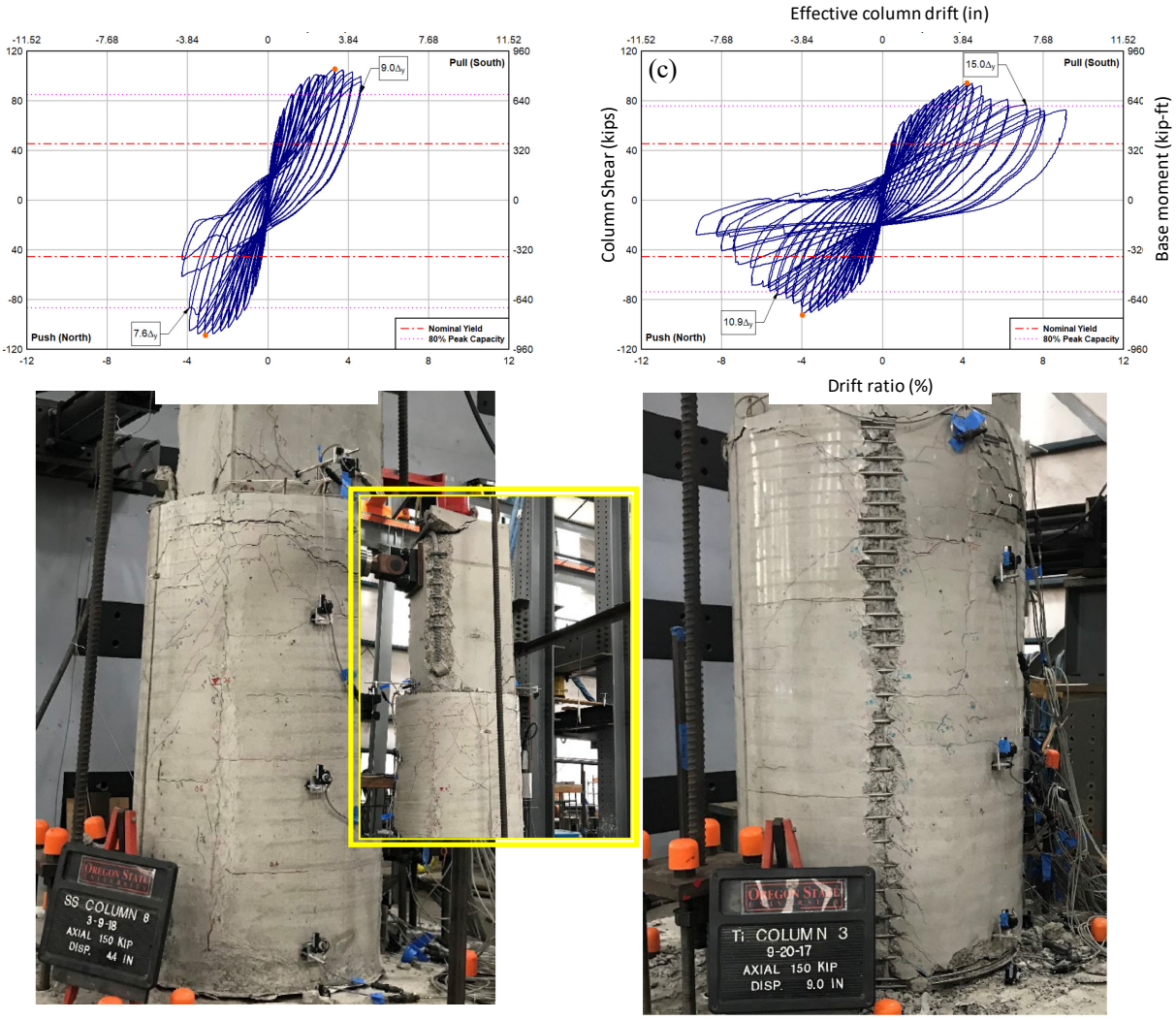

Figure 2.26: The equivalent lateral load, expressed as column shear, versus drift response for the control columns (a) retrofitted short square column with stainless steel ligament, and (b) control short square column (Shrestha 2019).

For the specimen with stainless steel ligaments, cracking started with splitting along the retrofit shell at 0.6% lateral drift and then continued with diagonal and horizontal cracks right above the shell from the locations where the SS ligaments were anchored to the column. Some flexural cracks opened noticeably along the centerline of the footing that seemed to start from the column to run along the footing faces. At lateral drifts above 3.3%, significant damage was observed on the south face of the column with formation of new - and widening of existing - cracks for subsequent cycles. Cracking continued until the face of the column on the south side spalled off at a 4.4% lateral draft. As stated earlier, a plastic hinge formed just above the top of the retrofit shell, resulting in column

rotations about the top of the retrofit shell and with negligible motions below. Underneath the retrofit shell, the column exhibited negligible damage and the ligaments were still intact. The damage above the shell was more dramatic with wide cracks connecting the hooked region of all ligaments, leading to the creation of a weak failure plane corresponding to the tallest ligaments about which the column rotated.

Shrestha (2019) provided design and construction recommendations for the seismic retrofitting of square reinforced concrete bridge columns with vintage column details using the aforementioned experiments as the basis. Columns with bars spliced with footing starter bars originating just above the footing with insufficient lap-splice length and inadequate transverse reinforcement represent the conditions to be mitigated with this retrofit alternative. The retrofit details of an example bridge column, corresponding to a symmetric 4-span bridge constructed in 1952, are presented in Figure 2.27. The bridge examined is a typical highway overcrossing of the type that were built in Oregon prior to the adoption of seismic design provisions and is classified as ‘standard’.

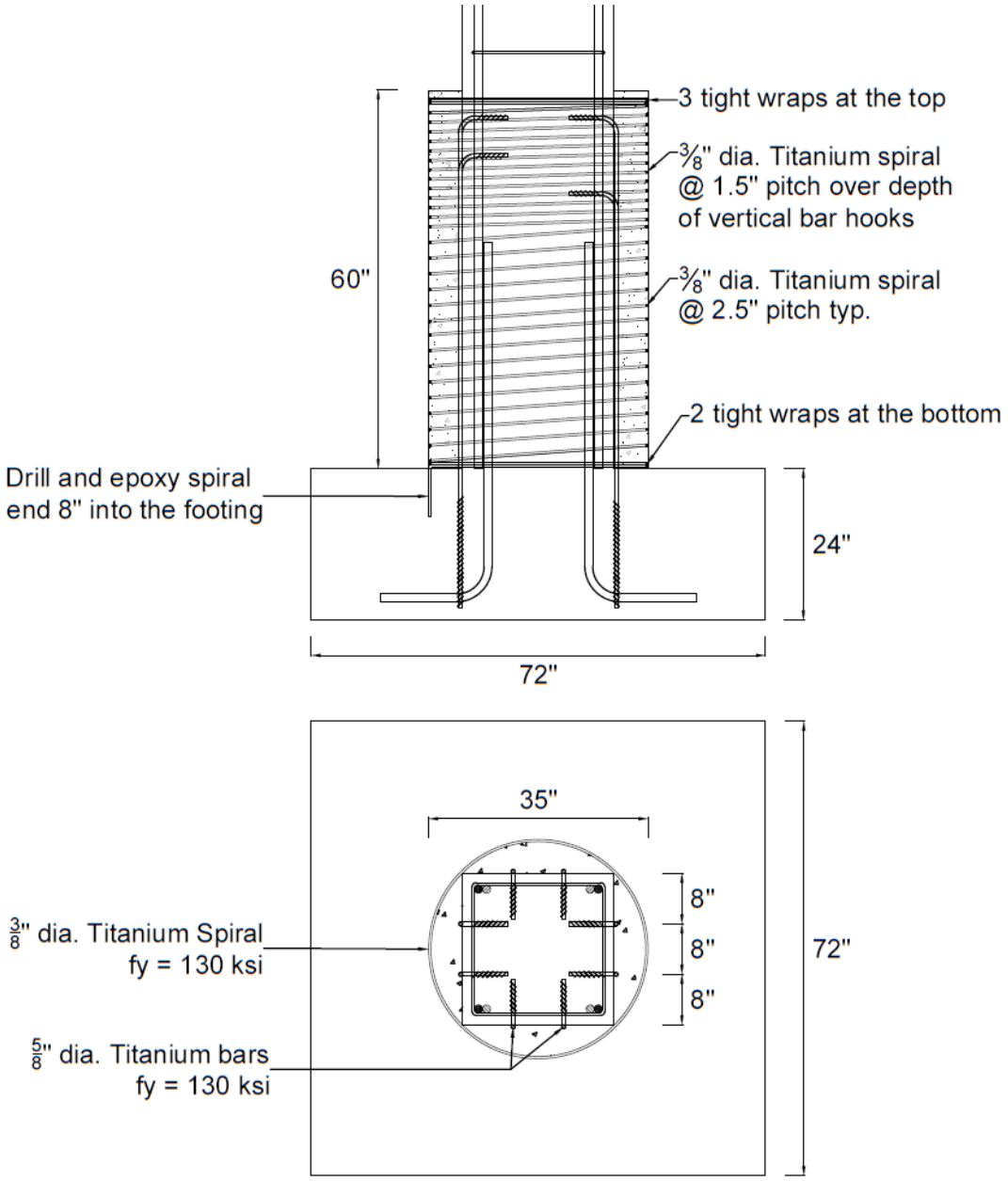

Figure 2.27: Column retrofit design of the example bridge (Shrestha 2019).

2.5 CONCEPT OF ROCKING FOUNDATION AND ITS EFFECT ON SEISMIC ASSESSMENT OF RETROFITTED BRIDGE COLUMN FOOTING SYSTEM

While techniques for retrofitting columns are now well developed, many other problems exist in older bridge structures that need to be addressed. Specifically, bridge footings from the 1950s to the early 1970s were typically designed using an elastic analysis with consideration of very low lateral seismic input compared to recent design provisions (Figure 2.28). Such a design approach

resulted in footing reinforcement that consisted of a single two-dimensional mat of reinforcement at the bottom of the footings without top or shear reinforcement.

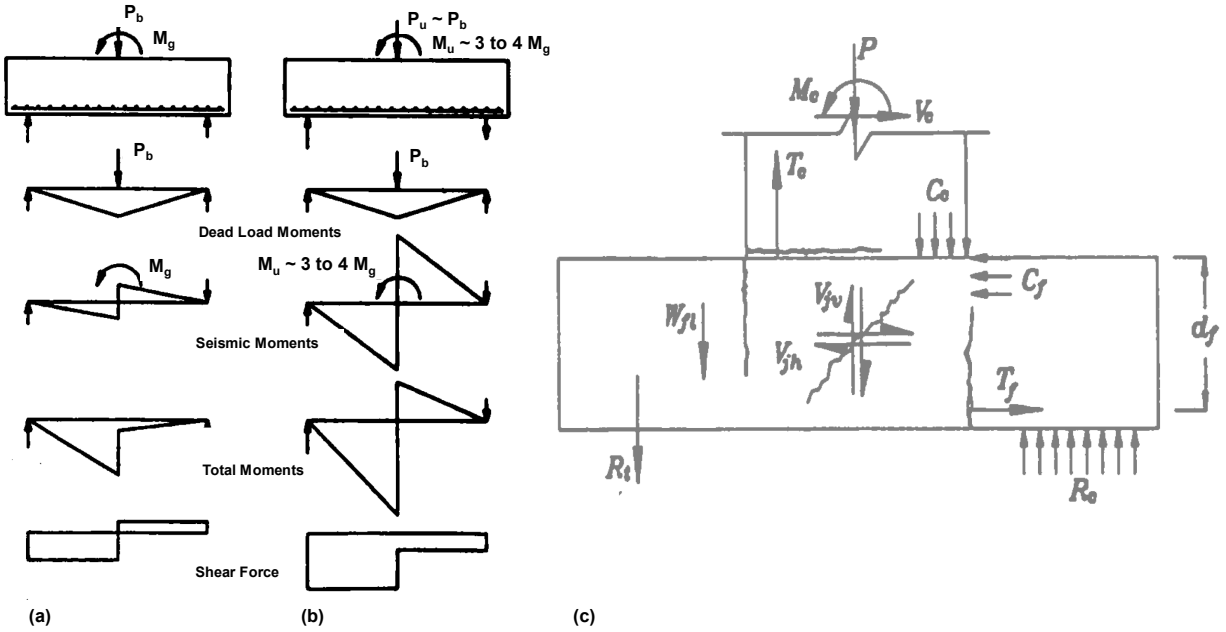

Figure 2.28: (a) Footing moments and shears corresponding to elastic design forces; (b) Shear force in column/footing joint under seismic actions; and (c) actual earthquake inputs (with gray lines; Xiao et al. 1996).

The actual seismic force acting on the footing corresponding to the formation of a plastic hinge in the column can be three to four times larger than the elastic design magnitude. Consequently, the following inherent potential problems are likely to exist in many older bridge foundations (Xiao et al. 1996; Shrestha 2019):

1. Inadequate tension capacity in footing and pile/cap connections. This may result in footing uplift and local failure of supporting soil in regions near the footing edge. Results of recent research shows that this uplift or rocking behavior can be beneficial, as forces entering the structure may be significantly lower under this condition than if the columns were to yield in flexure (Xiao et al. 1996).

2. Footings with only a bottom reinforcement mat and designed based on a low level of earthquake shaking exhibit inadequate flexural and shear strength. Accordingly, footing failure may be expected due to excessive moment and shear induced by currently anticipated seismic loading.

3. Similar to beam/column joints in frame structures, the column/footing connection may be subjected to large shear stresses, a point that has not been recognized until recently. Column hoops or spirals were typically not extended into the footing, providing no reliable shear-resisting mechanism. In addition, column longitudinal reinforcement anchorage with 90° hooks bent outwards results in additional tension

stress in the connection. Deficiency in the column/footing connection is the most difficult to repair and/or retrofit.

4. The use of jacketing in column retrofitting may result in enhancement of column flexural strength, consequently increasing demand to the footing, and increasing potential for premature footing failure.

Some researchers such as Xiao et al. (1996) and McLean and Marsh (1999) conducted comprehensive column footing research programs to address the problems associated with bridge footings and developed retrofits for improving their seismic performance. Xiao et al. (1996) performed a series of cyclic tests on 1/3-scale column footing models (one as-built and three with retrofitted footings) to investigate the seismic performance of existing footings and to evaluate the effectiveness of various retrofit measures. The specimen in the as-built column/footing system exhibited low shear capacity with ductile behavior during loading. Although retrofitted columns are expected to develop an excellent hysteretic response, some of the retrofitted column/footing connections exhibited shear distress and severe damage. Consequently, the retrofitted column could not realize its full deformation potential during seismic loading. From the results of these tests, Xiao et al. (1996) proposed an improved retrofit design using long dowels for the column/footing system.

Retrofitting strategies for footings are based on traditional concepts and verified by the significantly improved hysteretic behavior and energy dissipation obtained from full- and model-scale column/footing systems. Since there is often limited access for work under existing bridges, their implementation is both difficult and costly. Recently, researchers have proposed the concept of “rocking foundations” for bridge column-footings. A rocking foundation takes advantage of soil failure to protect the bridge during seismic loading. In this way, the foundation may act as a fuse, to an extent isolating the bridge system from serious earthquake damage. This usually involves under-designing the geotechnical capacity of the foundations (i.e., using foundations with smaller dimensions or leaving the as-built foundations in-place for the case of retrofitted column/footing systems), thereby transferring the plastic hinge to the soil. In this approach, depending on the factor of safety against bearing failure, the mode of foundation failure is either uplift (cases with larger factors of safety) or localized soil failure (cases with smaller factors of safety), and settlement (Anastasopoulos et al. 2012; Hakhamaneshi 2014). Permitting these mechanisms to occur results in a reduction in the ductility demand and the amount of ground shaking that can be transmitted to the columns and superstructure.

Considering the current seismic design approach for bridge columns which allows for formation of plastic hinges at the column base, the question is whether the soil underneath the footing or the column should be allowed to fail during seismic loading. The concept of a rocking foundation is simple and highly compatible with the current state of practice. The rocking footing concept might offer the simplest solution for existing bridges that require seismic retrofit to achieve seismic performance or for deck widening purposes. This would focus the retrofit on the superstructure, taking no action on the existing foundations, allowing them to rock and uplift. Thus, the earthquake forces that must be resisted by the columns can be dramatically reduced and, in many cases, the column/footing retrofit can be reduced or eliminated.

In recent years, some researchers have investigated the effect of rocking on performance of bridges for retrofitting purposes (Kawashima and Nagai 2006; Hung et al. 2011; Liu et al. 2013; Shrestha 2019). For example, Kawashima and Nagai (2006) analytically investigated the effect of rocking of under-designed shallow bridge foundations to reduce the seismic load. Deliberate rocking of the footing reduced the seismic shear force of the footing significantly. However, rocking led to detrimental footing and bridge displacements. A similar study carried out by Liu et al. (2013) demonstrated compatible yielding between soil-foundation and superstructure components of a building by highlighting the rocking response of the foundations. Hung et al. (2011) tested three circular reinforced concrete columns with spread footings to study the effect of rocking behavior for columns with: (1) lap-spliced longitudinal reinforcement and inefficient transverse confinement (two specimens), and (2) a steel jacket representing columns with sufficient ductility (one specimen). One of the as-built columns was tested with its foundation constrained to the strong floor to serve as a benchmark column and the rest were rested on a neoprene pad that allowed footing rocking. The specimens were tested under pseudo-dynamic loading and cyclic loading under constant axial load of $0.15f_c'A_g$. The comparison of results for specimens with restrained and rocking spread footing supported the implementation of the isolation effect produced by rocking, which reduced the ductility demand on the columns. However, the reduction in the local ductility demand can only be achieved as long as the system has sufficient ductility to ensure that the isolation effect of the rocking mechanism occurs (Hung et al. 2011).

Shrestha (2019) performed an experimental study on two full-scale retrofitted RC columns, one with realistic footing details and one with fixed base with no soil-foundation-structure interaction to compare the performance of retrofitted columns under rocking. The effect of a soil subgrade was simulated using FOAMULAR® 1000 Extruded Polystyrene (XPS) Rigid Foam Insulation to evaluate the specimen constructed with realistic reinforcement details. Two layers of 3 in. (75 mm) thick foam placed on the strong floor prior to placement of the test specimen; thereafter, application of the axial load engaged the footing-XPS-strong floor system. Lateral loading applied thereafter could thus be dissipated using the rocking mode, the results of which are presented in Figure 2.29. The column and footing remained elastic throughout the test when allowed to rock upon the XPS soil simulant. The foam exhibited permanent deformation with a convex curve profile as shown in Figure 2.29(c). Minor hairline cracks were observed in the footing after the test, which were connected and ran through the middle of each face of the footing, roughly dividing the footing into four quadrants as shown in Figure 2.29(d). Although a little separation of the retrofit shell from the footing top was noticed during testing, no new cracks were observed in the shell or the column above the shell. Based on the results of this research, the authors claimed that the reduction in the local ductility demand can be achieved as long as the system has sufficient ductility to ensure that the isolation effect of the rocking mechanism can be achieved. Therefore, without the retrofit, the column would likely have failed under the applied lateral load. Results of this work highlighted the benefits of the rocking mode of energy dissipation and soil-structure interaction for seismic retrofit of bridge columns. The concept of footing rocking and soil-structure interaction are addressed below.

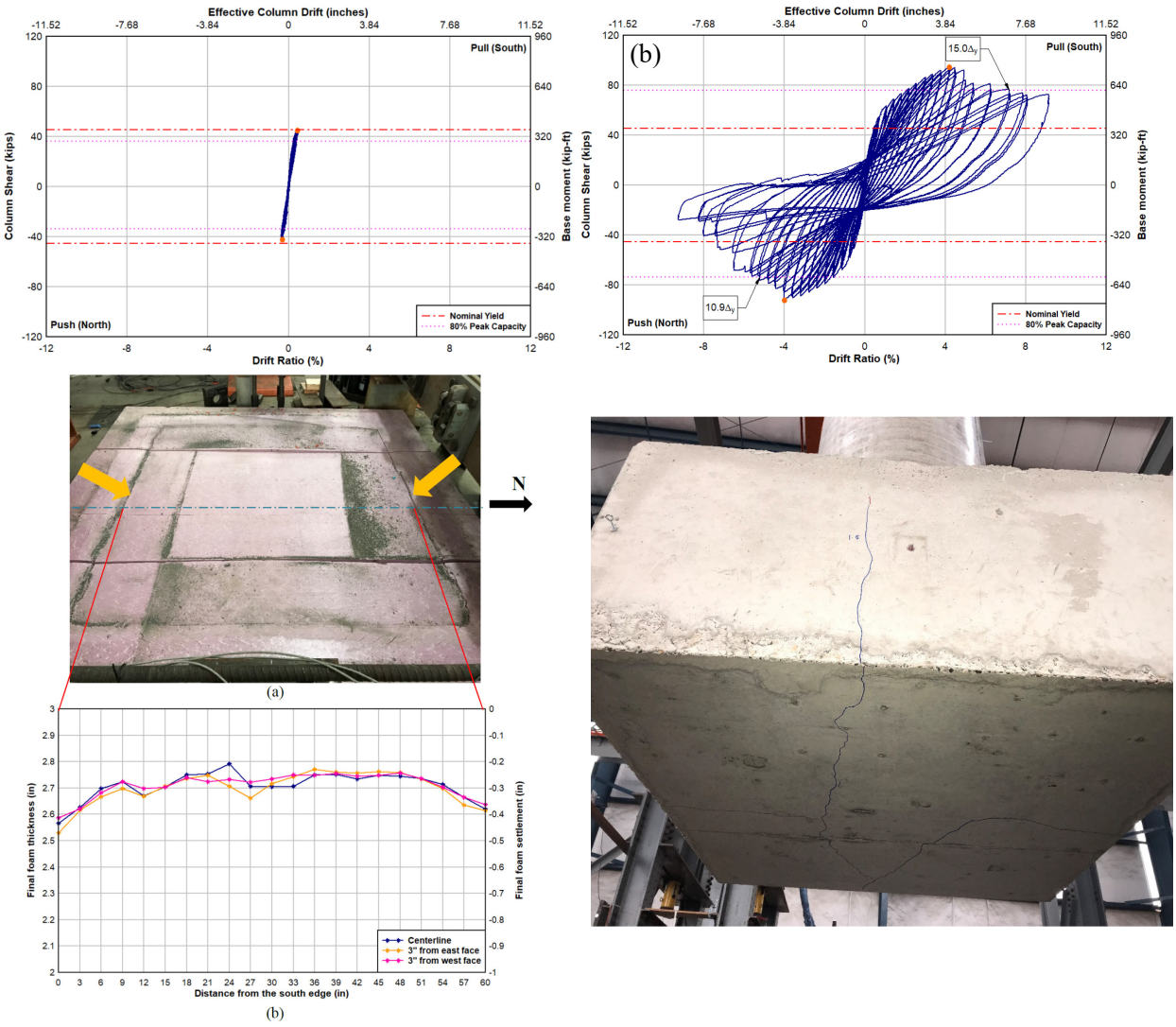

Figure 2.29: The equivalent lateral load, expressed as column shear, versus drift response for (a) the retrofitted short square column with 90° hooked ligament on foam, and (b) fixed-base retrofitted short square column with 90° hooked ligament , (c) foam profile at the end of testing, (d) visual damage to top layer of XPS foam after removal of specimen (Shrestha 2019).

2.6 SOIL STRUCTURE INTERACTION: ROCKING FOUNDATIONS

2.6.1 Overview

The interaction between a foundation and soil and the contribution of footing displacements in the form of sliding or settlement to the overall structural response in a seismic event is generally described as soil-structure interaction (SSI). Given that all civil infrastructure is subject to SSI, understanding its role in the seismic response of structures can lead to significant design advantages or reduction in risk. Proper evaluation of SSI effects on seismic behavior of soil–

foundation system requires knowledge of dynamic soil properties, seismic response of soil, and the interaction of soil with the foundation. In addition, the RC substructure and superstructure properties including non-linear characteristics and behavior of the materials, cross sections, and interactions under combined axial, shear, and flexural loads are required.

Studies that include the effects of both SSI and inelastic bridge substructures are limited. Structures in previous studies are traditionally modelled with either a fixed base with no soil–structure interaction or with the supporting soil treated as a homogeneous medium and assuming a linear elastic behavior of the pier column and the superstructure elements (Shrestha 2019). Although results of such studies provide engineers and researchers with valuable information about the overall response of the bridge column/footing system, they do not reflect realistic foundation scenarios observed in the field. Accordingly, such results may obscure the role of structural non-linearity on seismic demand of the structure. For example, the results of research by Ciampoli and Pinto (1995) and Chaudhary et al. (2001) indicated an insignificant effect of SSI on ductility demand of bridge column footing systems, whereas work by Mylonakis and Gazetas (2000), Gazetas and Mylonakis (2001), and Fraino et al. (2012) reported the detrimental effect of SSI on the behavior of bridge columns, especially in cases with foundations supported on soft soils.

Following observations and recommendations of such studies, modern seismic codes recognize highly inelastic responses of materials in a bridge column footing system under strong seismic events (e.g., a design earthquake motion). However, the effect of SSI and nonlinear footing response in these codes is not considered due to the fear of toppling collapse possibly resulting from foundation uplift or soil yield. Instead, inelastic flexural deformations imposed by gravity and seismic loads are considered as concentrated only over a finite hinge length of above-ground structural members (e.g. beams and columns). In bridges, the plastic hinge consists of a portion of the column above the footing where substantial yielding occurs before the rest of the column is damaged during an earthquake (Figure 2.30). With good reinforcement details, ductility demand and energy dissipation of the system can be imposed in the hinge at the base of the column rather than other parts of the bridge. Allowing a plastic hinge to form without additional material degradation or structural instability limits the load applied to the bridge (Cheng and Mander 1997). Also, it allows the bridge to experience greater deflection during seismic loading. If the hinge areas are properly detailed and confined, they can provide the bridge with a function similar to a fuse in an electrical circuit, preventing possible collapse.

The determination of the magnitude and location of plastic deformations as well as the hinge length plays an important role in characterizing the performance of bridge columns during earthquakes. Although it is possible that some ductility will be provided by beam hinges in bridge systems, it is generally bridge columns that must have inelastic rotational capacity. In this case, the base shear coefficient (C_y) of the column, defined as the ratio of the lateral force to the weight of the superstructure required to mobilize the bending moment capacity of the column, may be obtained as follows:

$$\boldsymbol{C_y = \frac{M_{c_col}}{PH_{cg}}} \qquad \textbf{(2-1)}$$

where M_{c_col} is the column's bending moment capacity, H_{cg} is the height from the center of gravity of the bridge to the base of the footing, a_y is the acceleration of motion in the y direction, P is the axial load, and g is the operating gravitational constant. M_{c_col} can be determined using Eq. (2.2):

$$\boldsymbol{M_{c_col} = \frac{a_y}{g} P H_{cg}} \tag{2.2}$$

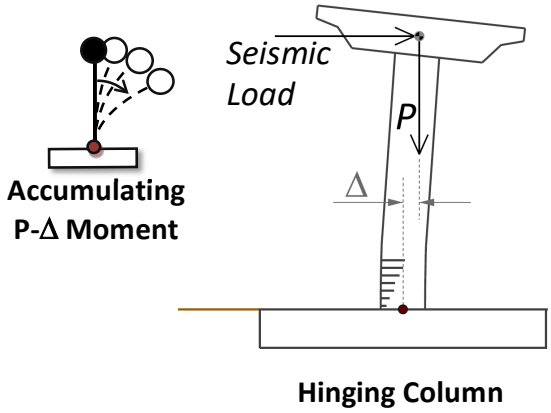

Figure 2.30: A schematic describing the concept of plastic hinge in bridge columns (Allmond 2014).

This conservative treatment of the foundation, which is designed to retain elastic behavior, conflicts with some findings of recent studies, indicating that:

1. Nonlinear foundation response is probable for seismic events of moderate intensity or larger. Foundations designed using the concept of plastic hinging are sometimes very heavy compared to the superstructure. In cases with stiff soil, the moment capacity of the footing may be extremely high as compared to the yield moment capacity of the column. As a result, even moderate excitation may result in formation of the plastic hinge at the base of the column resulting in brittle failure. An example of such cases is presented in Figure 2.31, showing the failure of the one-story reinforced concrete building that occurred due to moderate excitation in 1999 (Gazetas 2019; Sharma 2019).

2. Strong ground motions and earthquakes may result in soil failure and permanent deformations. Kawashima and Nagai (2006) and Apostolou et al. (2007) indicated that the uplift of spread footings occurred in earthquakes such as the 1964 Good Friday (Alaska), 1971 San Fernando, 1999 Kocaeli, and 1999 Athens earthquakes. In general, the authors argue that when spread footings supported on the soil only through gravity loading are subjected to strong ground motion, foundation rocking is inevitable. While neglecting the effect of foundation rocking could be conservative in seismic design, thereby overestimating the seismic forces applied to the structures,

the possible impacts due to rocking such as large lateral displacements of the overall structure and permanent settlement in soils can lead to catastrophic consequences.

3. Rocking may be favorable for the overall system performance. Due to the cyclic and kinematic nature of seismic shaking, soil failure or foundation uplift caused by the combined moment-shear-vertical loading does not necessarily lead to structure collapse (Anastasopoulos et al. 2012; Gajan et al. 2005; Hakhamaneshi 2014; and Kutter et al. 2016). There have been numerous structures resting on shallow foundations and subjected to seismic events such as 1952 Arvin-Tehachapi (Housner 1956), 1960 Chili (Housner 1963), 1977 Tongan (Campbell 1977), 1989 Loma Prieta (Elghazouli 2009), 1993 Hokkaido Nansei-Oki and 1995 Kobe (NEHRP 2004), 1999 Kocaeli (Gazetas et al. 2003), and 2011 Christchurch (Storie et al. 2014) earthquakes that have avoided severe damage by rocking on their shallow foundations.



Figure 2.31: Columns and foundations of a one-story building that collapsed during the moderate 1999 Athens earthquake (Gazetas 2019; Sharma 2019).

Based on Gajan and Kutter (2008), Anastasopoulos et al. (2011), and Hakhamaneshi (2014), when a structural system is subjected to a set of vertical (*P*; applied at the center of gravity of the bridge) and horizontal (*H)*; applied at a height, H_{cg}, above the base of the footing) loads, three components of external load effects, vertical, V, lateral, *H*, and moment, M, act at the base center point, O, of the footing (Figure 2.32). Under such loading, system nonlinearity manifests through alternating uplift of the foundation (geometric nonlinearity), sliding at the soil-foundation interface (interface inelasticity), and bearing failure in the supporting soil (soil inelasticity) at the footing edges. In the case of slender structures such as high-rise building and long-span bridges, rocking motion prevails and geometric nonlinearity dominates. Earlier studies on rocking structures have indicated the beneficial role of foundation uplift and subsequent soil–foundation plastic yielding on improved bridge performance (Housner 1963; Meek 1978; Priestley et al. 1978; Huckelbridge and Clough 1978; Psycharis and Jennings 1983; Chopra and Yim 1985). Through rocking, seismic ductility demands on bridge columns are reduced and significant amounts of seismic energy are dissipated at the foundation level rather than from the hinging

columns (Gajan and Kutter 2008; Allmond 2014). The rocking mechanism further improves the re-centering potential in the bridge system due to *P*-Δ effects, particularly those resting on dense or very stiff soil. In the traditional hinging column mechanism, *P*-Δ effects produce a detrimental negative stiffness effect at the plastic hinge in the column and result in residual deformation of the structure. Through rocking, however, allowing the mobilization of the system capacity at the soil-foundation interface implies the development of a plastic hinge in the soil. Oscillation of the hinge point from one edge of the footing to another results in a "re-centering" moment that brings the structure back toward a vertical position (Figure 2.32).

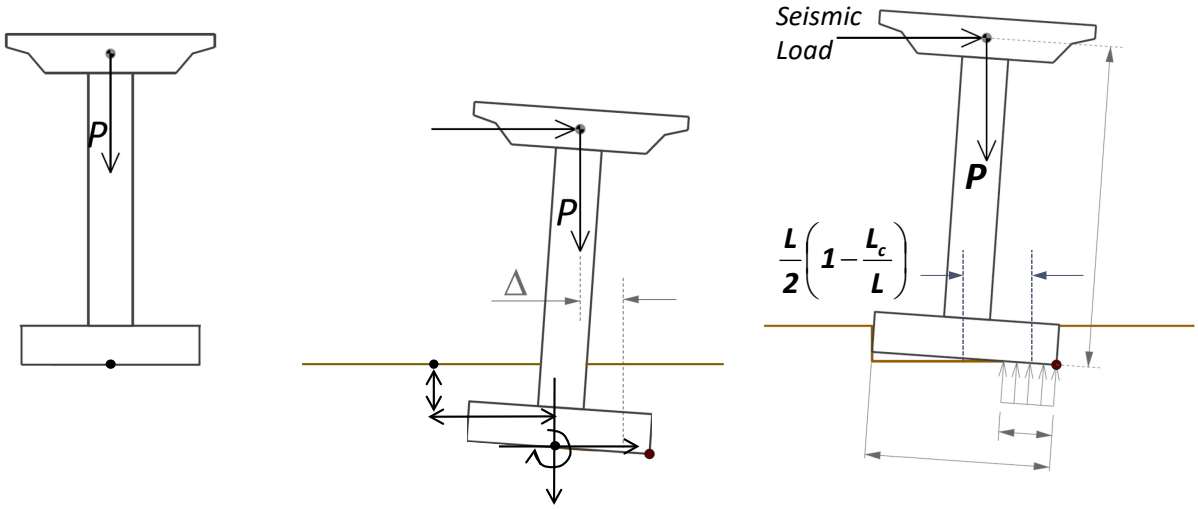

Figure 2.32: Forces and displacements at footing–soil interface during combined loading (Hakhamaneshi 2014; Allmond 2014).

The concept of foundation rocking has been proposed by several researchers as an effective method of seismic isolation (Housner 1963; Beck and Skinner 1973; Huckelbridge and Ferencz 1981; Priestley et al. 1996; Mergos and Kawashima 2005; Chen et al. 2006; Sakellaraki and Kawashima 2006; Gajan and Kutter 2008; Kutter et al. 2011; Anastasopoulos et al. 2010; Deng et al. 2012; Hakhamaneshi 2014; Allmond et al. 2015) and has been applied in the design and construction of some of modern bridges, such as the Rio–Antirrio bridge in Greece and the Vasco de Gama bridge in Portugal (Pecker 2003). Rocking foundations must exhibit low moment capacities, which are achieved by reducing the footing dimensions. Neglecting the potential for large displacements, Gajan and Kutter (2008) proposed that the moment capacity of a shallow rocking foundations can be obtained as:

$$M_{c_foot} = P\Delta = \frac{PL}{2}\left[1 - \frac{A_c}{A}\right] \quad \textbf{(2-3)}$$

where *P* is the vertical load carried, Δ is the rocking re-centering distance, *L* is the width of the footing in the direction of rocking, *A* is the area of the footing, and A_c is the critical contact area

of the footing. The moment capacity of the footing reduces with decreasing footing width. If a proper width is considered for the footing, M_{c_foot} can be smaller than M_{c_col} and the rocking mode can control. Such rocking systems are termed a weak footing/strong column system where plastic hinging of the column is prevented (Allmond 2014). In traditional plastic hinging columns, the moment capacity of the footing is larger than the moment capacity of the column, which results in mobilization of the superstructure displacements about the column base hinge and consequently creating a strong footing/weak column hinging system (Figure 2.33).

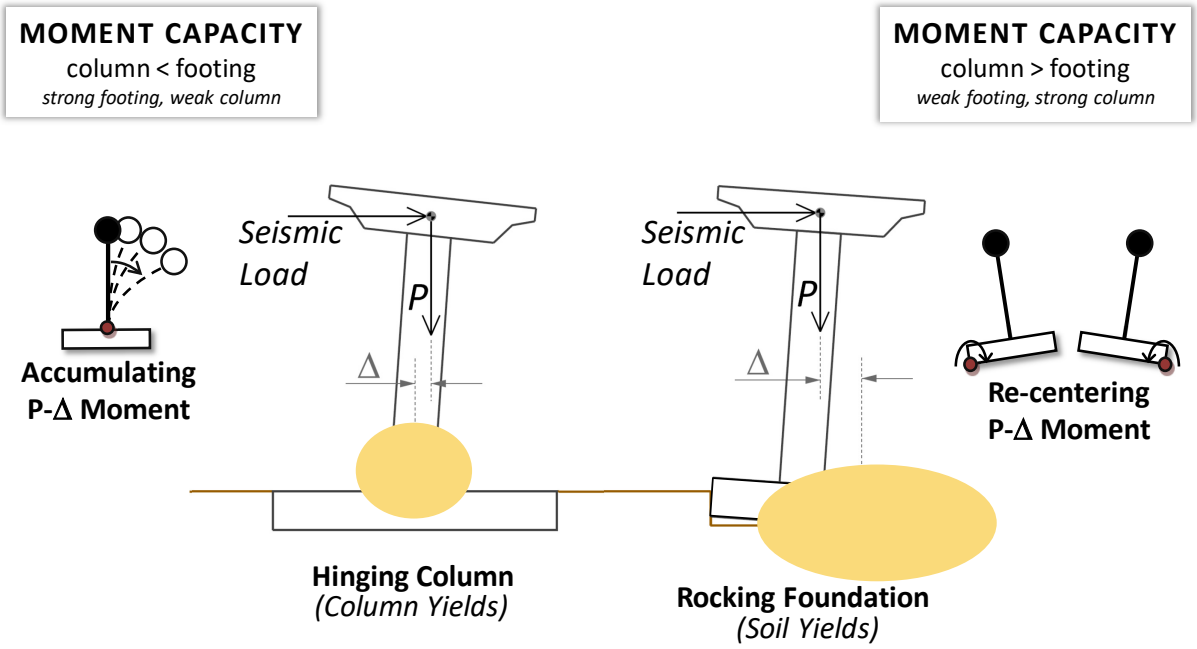

Figure 2.33: Comparison of the concepts of rocking foundation and hinging column in bridge column/footing systems (Allmond 2014).

2.6.2 Estimation of critical contact length (L_c)

The response of a rocking footing subject to cyclic loading consists of alternating contact between the base of the footing with the subgrade and uplift and gapping under the unloaded portion of the footing. This results in the formation of a curved surface at the soil-footing interface (Rosebrook 2002; Gajan et al. 2005). As the magnitude of rotation increases, the contact area between the footing and underlying soil becomes smaller and shifts to the edge of the footing due to the overturning moment. As the contact area decreases, the bearing pressure along the contact area increases to satisfy vertical equilibrium. Under sufficient footing rotation, the bearing pressure along the available contact area becomes equal to the ultimate bearing resistance and no further reduction in contact area is possible. This minimum contact area is equal to the critical contact area (A_c) as previously defined. For rectangular footings, with loading in the long (L) direction, the ratio A_c/A can be equated to a length ratio, L_c/L, where L_c is referred to as critical contact length and is directly related to the critical contact area: $L_c = A_c/B$. When the structure is unloaded, depending on the magnitude of axial load and the structure's seismic-induced rotation, gravity may cause gap closure and thus provides a natural self-centering mechanism. The result of footing rocking is a curved soil-foundation interface with local bearing

failure in proximity to the edges of the footing (Allmond 2014; Hakhamaneshi 2014; Sharma 2019). The critical length of a rocking foundation can be computed based on consideration of the bearing capacity (q_b) of the footing under vertical loading as:

$$\boldsymbol{L_c = P/(q_b B)} \tag{2-4}$$

where the bearing capacity of a shallow foundation is given by:

$$\boldsymbol{q_b = (s_c d_c) c' N_c + (s_q d_q) q'_0 N_q + 0.5 (s_\gamma d_\gamma) \gamma B N_\gamma} \tag{2-5}$$

where B is the smallest plan dimension of the footing, q_0 is the soil surcharge, γ is the unit weight of the soil, N_c, N_q and N_γ are cohesion, surcharge, and unit-weight bearing capacity factors, d_c, d_q, and d_γ are the cohesion, surcharge, and unit-weight embedment factors, respectively, and s_c, s_q, and s_γ are the cohesion, surcharge, and unit-weight shape factors, respectively.

For a rocking footing, depending on the footing dimension and the characteristics of the supporting soil, L_c might become smaller than the width of the footing. Considering this, Equation (2.5) should be rewritten as:

$$\boldsymbol{q_{b_L_c} = (s_c d_c) c' N_c + (s_q d_q) q_0 N_q + 0.5 (s_\gamma d_\gamma) \gamma L_c N_\gamma \qquad L_c < B} \tag{2-6}$$

$$\boldsymbol{q_{b_L_c} = (s_c d_c) c' N_c + (s_q d_q) q_0 N_q + 0.5 (s_\gamma d_\gamma) \gamma B N_\gamma \qquad L_c > B} \tag{2-7}$$

with corresponding embedment and shape factors. When the rocking capacity is fully mobilized, the applied vertical load and bearing capacity are related as:

$$\boldsymbol{q_{b_L_c} B L_c = P} \tag{2-8}$$

Thus, iteration of Equations 2.6, 2.7 and 2.8 may be required to determine L_c.

2.6.3 Rocking Effects on Overall Performance of Bridge Column/ Footing Systems

A pioneering study by Housner (1963) investigated the dynamic response of a rocking block subjected to different excitations and the beneficial self-centering mechanism identified following observations of the damage to some large, elevated water tanks and survival of many others during the 1960 Chili earthquake. Researchers have since incorporated this concept into different structures such as rigid shear-walls and bridges founded on shallow footings. Different approaches have been used in these studies to understand the rocking mechanism and its effect on the overall performance of structures including numerical models (Anastasopoulos et al. 2010

and 2011; Deng et al. 2014; Gavras et al. 2015; Agalianos et al. 2017), centrifuge tests (Gajan and Kutter 2008; Deng et al. 2012; Anastasopoulos et al. 2012; Hakhamaneshi 2014; Allmond 2014), large- and lab-scale tests (Drosos et al. 2012; Antonellis et al. 2015), and in-situ tests (Phipps et al. 2012; Sharma 2019). Different parametric evaluations have been performed that include a wide range of properties for the soil–foundation system and pier columns in order to generalize the SSI effect of rocking bridge foundations. Parameters relevant to bridge structures include the substructure typology, soil type and stiffness, groundwater elevation, foundation embedment, and seasonal weather changes. These studies have pointed to both theoretically plausible and practically significant observations for application to the design of bridges, depending on the governing foundation soils. The following discussion is organized by first the bridge topologies, and then the governing soil conditions as follows: (1) competent soil conditions, (2) saturated or submerged soil conditions, and (3) unsaturated soil conditions.

2.6.3.1 Bridge Typologies

RC bridges in the State of Oregon can be classified into different categories based on the following criteria (Kramer 2004): 1) type of column 2) number of spans, 3) span continuity (continuous or simply supported spans), and 4) type of bent to girder connection (integral, bearings, or combination). Bents are substructure elements, consisting of a transverse girder supported by columns that supports the longitudinal girders. RC bridges can be further categorized based on column geometry (square vs. round). Examples of different substructure systems are shown in Figure 2.34.



Figure 2.34: Two variants of square columns and transverse members, with a bent with cantilevers on the left and integral bent on the right (Isaac Constant Bridge #697, Central Point, Oregon; Kramer 2004).

In addition to the two basic column types, there are two other forms of bridge piers or substructure elements: panel piers and monolithic piers. Panel piers were mostly used for instream work and consist of circular columns with a wall as an interior connector.

Monolithic piers are simple flat panels which are available in various types as presented in Figure 2.35 derived from various overpasses on Interstate 5 in Washington State. Bridges are constructed with single- and multi-spans, depending on the length of the crossing. Single-span bridges are normally constructed with continuous decks which are either fixed or with bearing connections on the sides. Multi-span bridges, on the other hand, have continuous or simply supported decks with bearings and fixed column-to-deck connections.

Over the past four decades, the behavior of structural bridge elements like columns, beam-column joints, and crossbeams under seismic loading has been thoroughly examined. Initial studies of the response of bridges were simplified by modeling the structure using a single degree of freedom system (SDOF) to represent a bridge column and two spans with seat-type abutments. This approach has been deemed acceptable for some long multi-span bridges (Deng et al. 2012), however it may lead to large errors in moment capacity calculations if the contribution of the deck and of the abutment are not taken into account (Malhotra 2007; Deng et al. 2012; Anastasopoulos et al. 2015).



Figure 2.35: Examples of various monolithic concrete bridge piers along Interstate-5 (Kramer 2004).

Deng et al. (2012) investigated the seismic response of multi-column-bent bridges designed with rocking foundations considering two idealized deformation mechanisms: (1) a rocking foundation with the column monolithically fixed to the deck, and (2) a rocking foundation with the column pinned to the deck. In the first case, they noticed that if rocking occurs, plastic hinges can form at the column-deck joint because of the large bending moment demand at these sections (Figure 2.36a). In this case, the stiffness of a bridge deck is expected to have significant effect on the overall response of the bridge. The portion of total vertical load taken by the footings may be affected by the vertical stiffness and the deck rotation and uplift may be considerably affected by the torsional stiffness of the long axis of the bridge deck. This is particularly concerning if the deck is integrated into diaphragm-type abutments. Also, inertial forces from the bridge may push the abutment into the backfill, resulting in passive earth pressures that are generally 10 to 30 times greater (or more) than the existing earth pressure. For abutment walls which

have been designed for just active earth pressures, severe damage to the abutment may occur under the seismic passive pressures (Malhotra 2007).

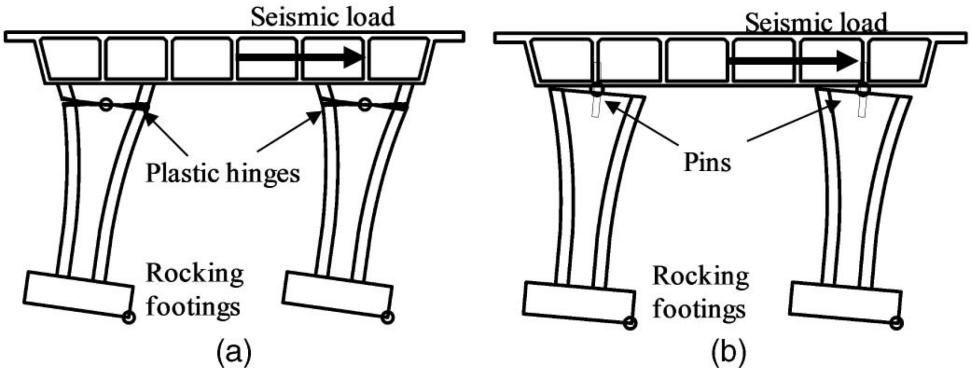

Figure 2.36: Idealized failure mechanisms: (a) rocking foundation and column yielding at the top; (b)rocking foundation and pinned column (Deng et al. 2012).

For pinned column-bridge connections, only the shear load is transferred to the column and therefore the development of plastic hinges is prevented (Figure 2.36b). In this case, abutments on the bridge systems may also have significant and direct effect on the vertical load applied to the column. For the bridge system with seat-type abutments, no shear is expected to transfer at the abutment-deck bearing connection and the entire horizontal shear load attributed to the superstructure response is absorbed by the columns and footings. However, with abutments, only a fraction of the vertical load from the superstructure would be applied to the footings (Figure 2.37). The reduction in vertical load affects the moment capacity and base shear coefficient. The load distribution between abutments and footings depends on different factors including the mass distribution of the bridge components, settlement of the footings relative to the abutments, and the stiffness of the deck. Deng et al. (2012) defined a factor, x, as the portion of the superstructure weight taken by the footings and reformulated the base shear coefficient, C_r, as follows:

$$\boldsymbol{C_r = \frac{L_f}{2H_c}\left(1 - \frac{A_c}{A}\right)(x + 2r_m)} \qquad \textbf{(2-9)}$$

where $r_m = (m_o+m_f)/m_d$, m_d, m_o, and m_f are masses of deck, overburden soil, and footing, respectively, L_f, is the footing length in the shaking direction, A_c is the critical contact area, A is the footing base area, H_c is the height of the column plus the footing thickness, g is the gravitational constant.

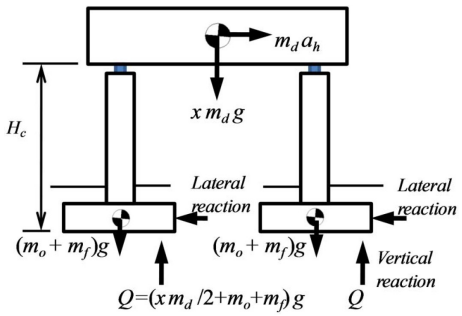

Figure 2.37: Free-body diagram for a two-column bent system with abutments on the side of the bridge (Deng et al. 2012).

Deng et al. (2012) also performed a series of centrifuge model tests to investigate the effect of the deck and abutment on the seismic performance of bridges. Three tests were performed in this series, including one SDOF rocking system (SF), one SDOF hinging column system (LF), and a multi-degree of freedom (MDOF) four column-four bents system (4CSF). Figure 2.38(a) and Figure 2.38(b) show the experimental configuration evaluated by Deng et al. (2012). The results of these experiments are presented in Figure 2.38(c) in terms of the peak and cumulative permanent drift angles. In terms of peak and cumulative permanent drift angles, results indicated little difference in performance under small seismic excitation. However, under strong ground motion, the rocking foundation and multi-span models exhibited a similar response. The LF model, however, produced a plastic hinge in the column resulting in system failure.

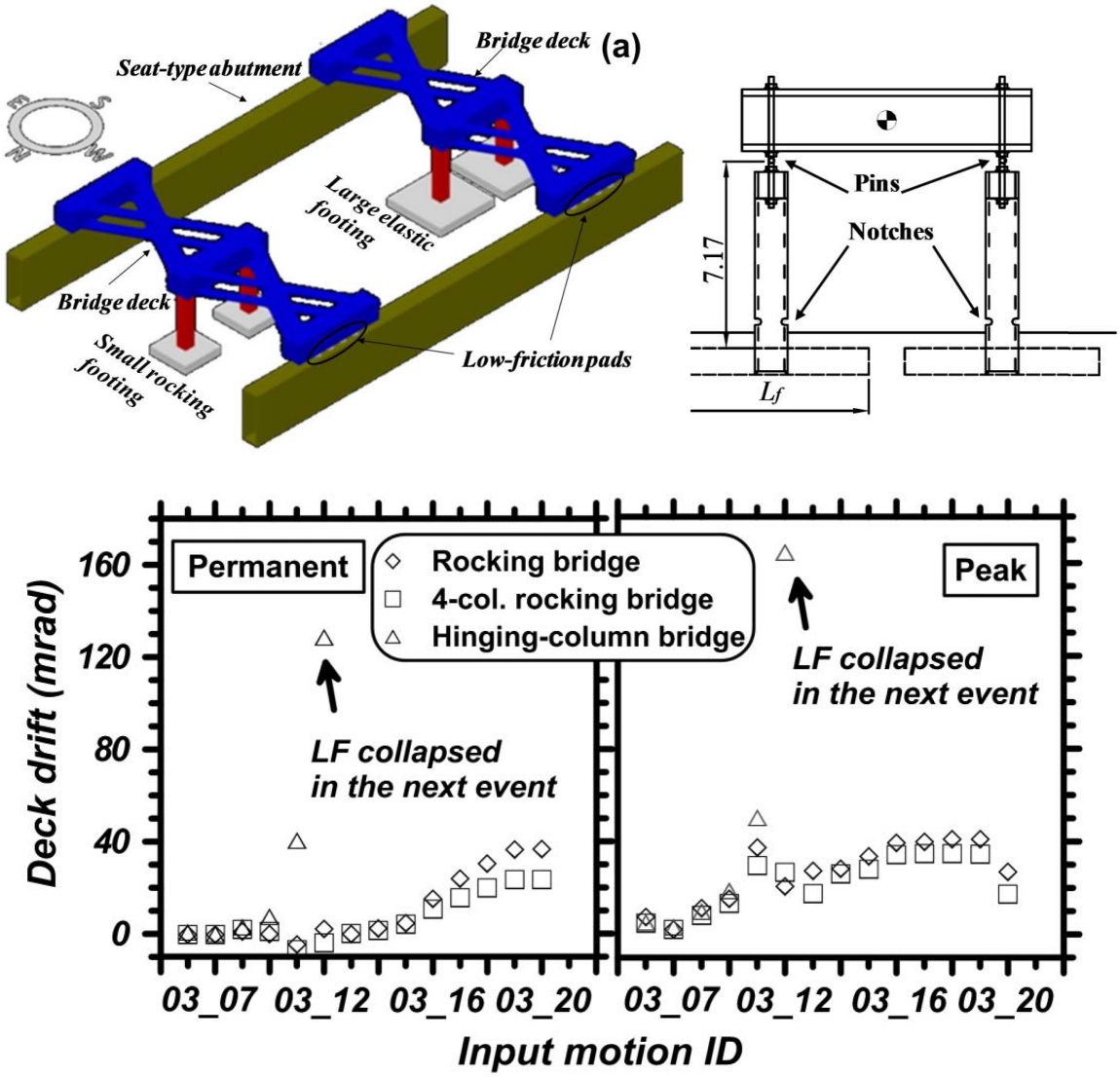

Figure 2.38: Experimental setup used by Deng et al. (2012): (a) 3D view; (b) an elevation view of the bridge model in transverse direction (note: L_f = 5.04 m for rocking bridge and L_f = 7.56 m for hinging-column bridge); (c) deck drift angles of models: (left) permanent; (right) peak.

Anastasopoulos et al. (2015) used three simplified systems to illustrate the effect of structural components such as bridge decks and abutments on the seismic behavior of rocking foundations, as presented in Figure 2.39. The first system (System A) ignores the contribution of the deck and uses an equivalent SDOF system having the stiffness, height, moment–curvature response, and a concentrated mass m_p for a single bridge pier. In the second simplified system (System B), the shear stiffness of the abutment bearings was also considered by adding a lateral spring ($K_{s,t}$) and a lateral dashpot ($C_{s,t}$) at the top of the SDOF system. The third and more complete simplified model (System C) was similar to System B but added the true bending stiffness of the deck. For this purpose, the fixity at the top of the SDOF system was replaced with a rotational spring ($K_{r,t}$) and a rotational

dashpot ($C_{r,t}$) as presented in Figure 2.39(c). The stiffness and damping (associated with the dashpot) are defined in Figure 2.39. Analytical models representing the physical models were then compared with a detailed 3D FE model of the bridge with all its deck, column, footing, and abutment components as described in Figure 2.39. The comparison was performed in terms of both static pushover and dynamic loading. For the case with static loading, monotonic pushover loading was applied to the model. For the latter case, dynamic time history analyses were performed with 29 seismic records used as seismic excitation.

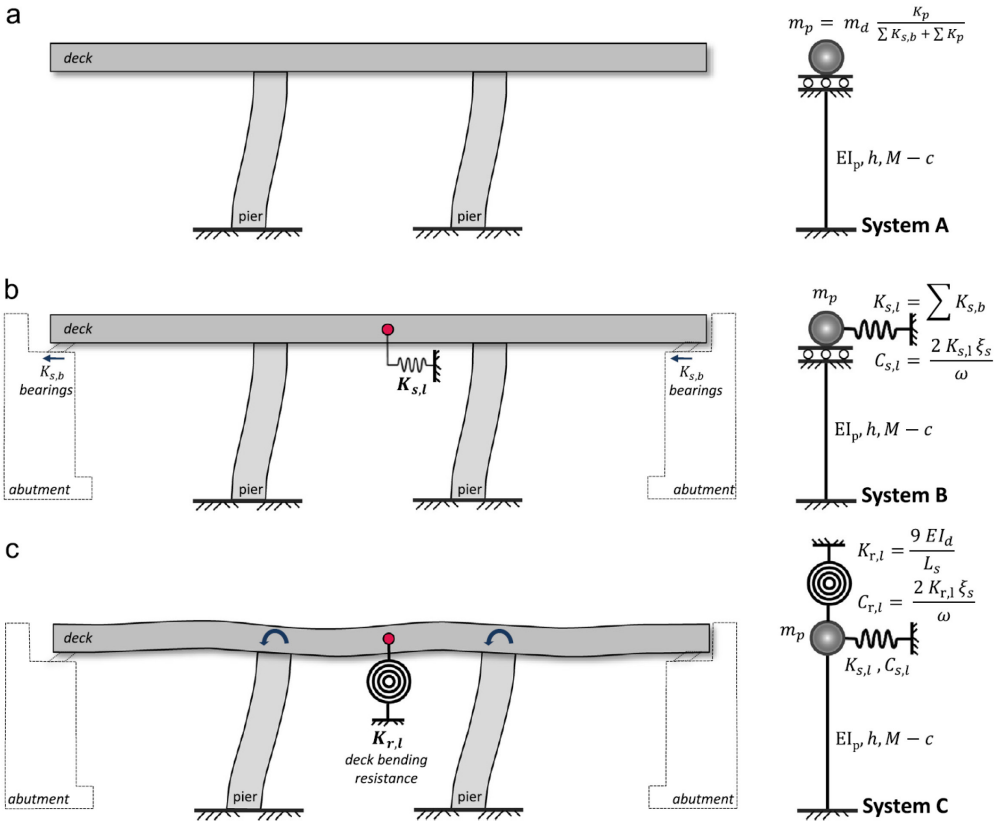

Figure 2.39: Simplified models assuming fixed-base conditions, for the longitudinal direction: (a) System A, considering a single pier; (b) System B, taking account of the contribution of the lateral stiffness of the abutment bearings; and (c) System C, also accounting for the rotational restraint provided by the torsional resistance of the deck acting in series with the transverse moment resistance provided by the system of bearings.

The results of the study by Anastasopoulos et al. (2015) are presented in Figure 2.40. System A ignores the contribution of the lateral and rotational restraint associated with the deck and abutment bearings and its results are unrealistically conservative. Prior to yield ($\delta < 1.6$ in or 0.04 m), System A exhibited a slightly stiffer behavior as compared to the comparable 3D numerical model. For larger displacements, greater error between the two analyses was observed (e.g., the pushover capacity of System A exhibited about 85% of the capacity computed using the detailed 3D model), although the simplified analytical

model for System A generally captured the ultimate and post-peak softening response. In terms of the ratio of ductility demand, μ_d, to ductility capacity, μ_c, μ_d/μ_c, the performance of System A was in acceptable range (Figure 2.40b). Only in one of the examined seismic excitations, System A predicted total collapse of the bridge, in contrast to the results obtained with the detailed 3D model. When considering the abutment bearings in calculations (System B), the prediction of the simplified model improved, and the pushover capacity predicted by the simplified model was only 3% lower than the capacity obtained from the 3D model. In terms of μ_d/μ_c, there was no erroneous prediction of collapse. Evidently, the contribution of the deck and the abutment bearings cannot be neglected and should be taken into calculations (Anastasopoulos et al. 2015). When considering the effect of the true bending stiffness of the deck (System C), the static pushover response of System C produced the best performance relative to the 3D numerical model for all imposed displacements, especially prior to yield ($\delta < 1.6$ in or 0.04 m) (Figure 2.40c). From the results of the study, Anastasopoulos et al. (2015) concluded that the assumption of full rotational fixity is a good approximation as long as the system has reached its full ductility.

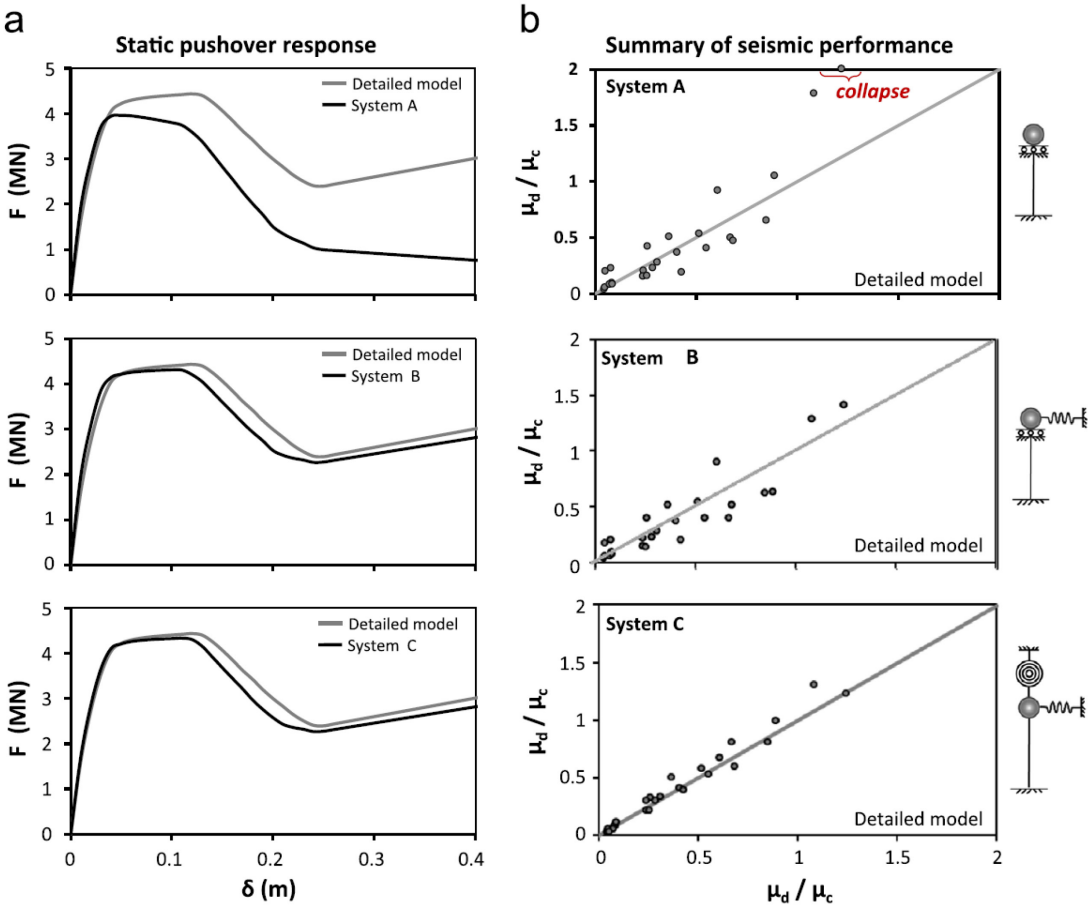

Figure 2.40: Response of bridge columns with different typologies (Anastasopoulos et al. 2015).

Reinhardt et al. (2003) performed an experimental study to evaluate the effect of footing flexibility and rocking behavior on the dynamic response of a two-column bridge pier with an innovative structural frame and flexible footings. The tests were conducted on quarter-scale bents with two square columns supported on isolated spread footings using shaking table under different earthquake records. The Sylmar record of the 1994 Northridge earthquake was simulated on the shake table. Three scaled bridge bents were tested: (1) one with substandard footings resting on flexible supports (B2SA); (2) one with a retrofitted footing resting on flexible supports (B2SR; increased footing dimensions and improved reinforcement details); and (3) one with the footing fixed to the shake table (B2SF). In the two experiments with flexible footings, elastomeric bearing pads were used to represent the stiffness of spread footings supported on compacted cohesionless soil with medium density. The tests with flexible footings were performed in elastic range. Testing the fix-base footing, however, continued under increasing amplitudes of simulated earthquakes until it failed. Figure 2.41 shows the details of the experiments performed by Reinhardt et al. (2003).

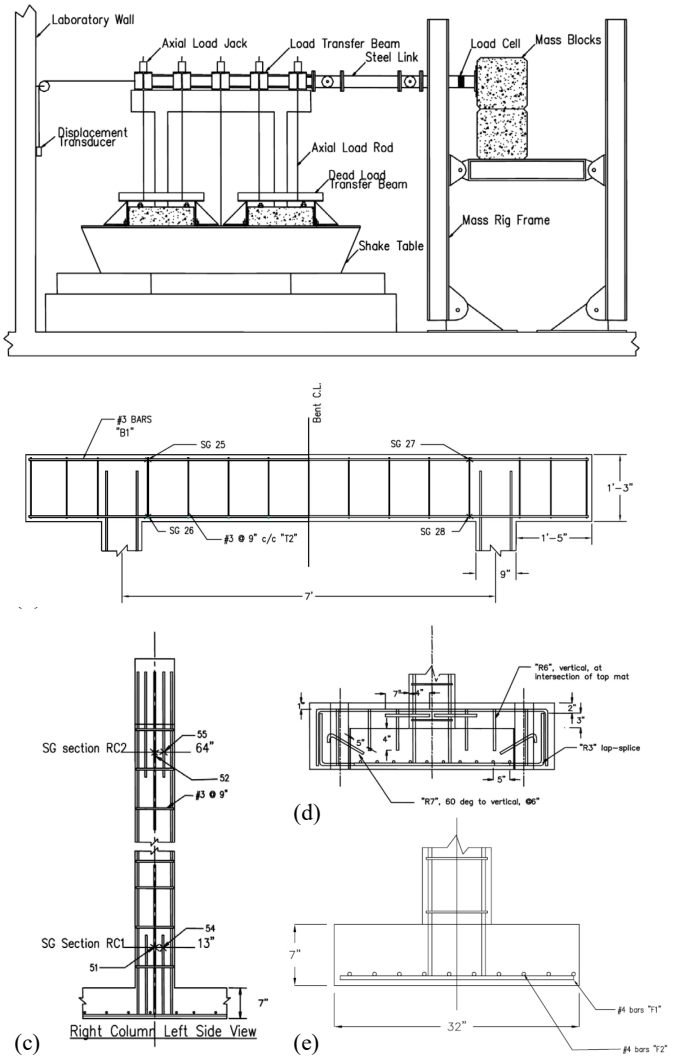

Figure 2.41: Experimental Details by Reinhardt et al. (2003): (a) Overall Test setup, (b) steel details for beam, (c) steel details of the as-built column, (c) elevation view of the retrofitted footings, and (d) plan view of the as-built footing.

Figure 2.42 shows the lateral force histories and envelopes for different bent systems in terms of bent displacement. As presented in Figure 2.42, the absolute maximum values of displacement and lateral force experienced by B2SF specimen were 4.3 in. (109 mm) and 31.0 kips (138 kN), respectively. The accumulated hysteresis curves for the specimens with flexible footing exhibited a relatively elastic behavior during the tests. Also, considerable reduction in the lateral forces, particularly at or near the base of the columns, was observed because of the footing flexibility. The reduction in column load demand due to footing flexibility potentially implies a reduction in retrofit detailing requirements for substandard columns such as those with lap splices, inadequate confinement, or insufficient shear reinforcement, which could lead to substantial savings in the cost of column retrofit. The result of experiments by Reinhardt et al. (2003) also showed a decrease in the shear force of the joints and beams due to footing flexibility.

However, the amount of reduction in shear force was not sufficiently large to justify a waiver of seismic retrofit requirements for these structural elements.

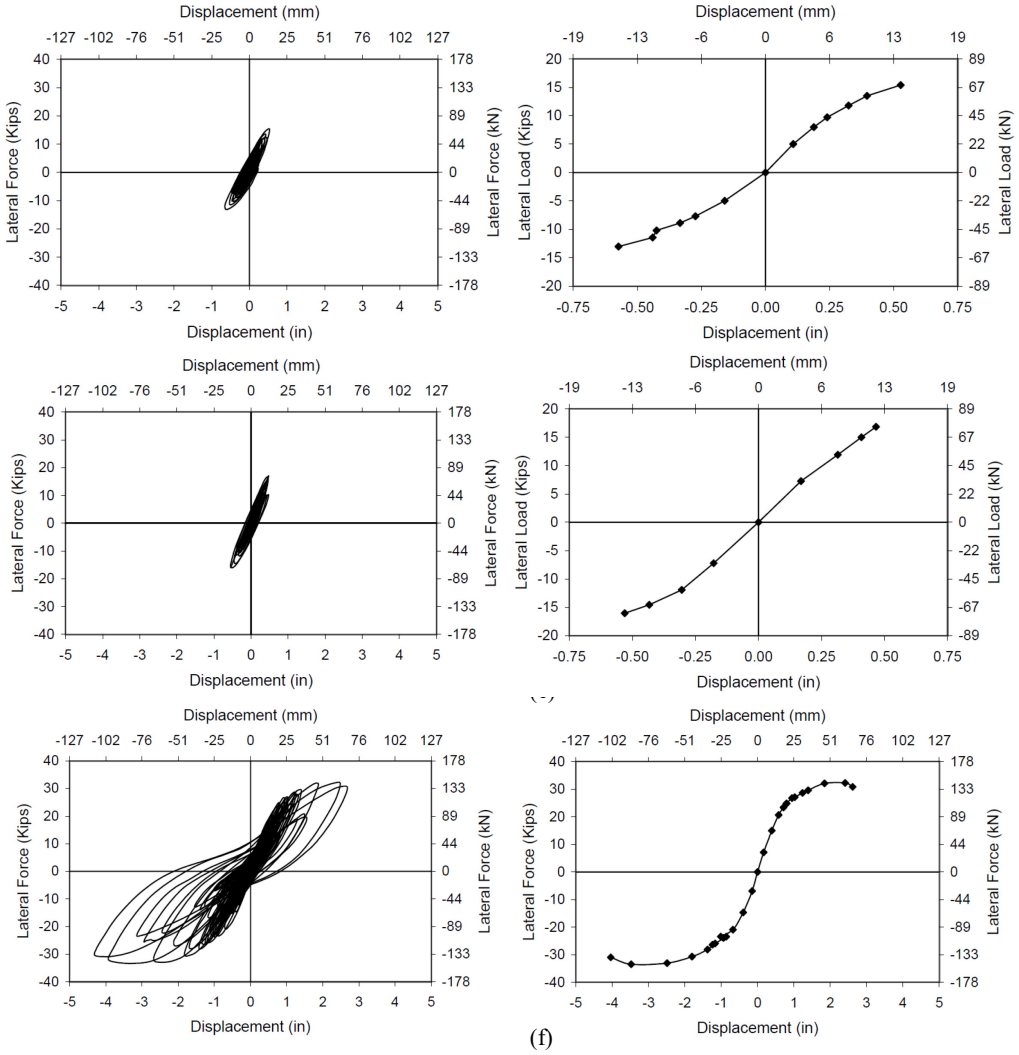

Figure 2.42: Accumulated Force-Displacement Hysteresis Curve for (a) B2SA, (b) B2SR, (c) B2SF, Envelope of Accumulated Force-Displacement Hysteresis Curve for (d) B2SA, (e) B2SR, and (f) B2SF (Reinhardt et al. 2003).

Results by Reinhardt et al. (2003) also indicated a lower stiffness for the footing with flexibility. This reduced stiffness may lead to higher lateral yield and ultimate displacements for the systems. Accordingly, the apparent displacement ductility capacity of the structure is expected to decrease. The amount of reduction in the system's displacement demand, however, changed depending on the stiffness of the footing itself. Figure 2.43 shows the horizontal displacements and rotations of the specimens with flexible footings reported by Reinhardt et al. (2003). As observed in this figure, the absolute maximum horizontal displacement for the specimen with retrofitted footing (B2SR) was 0.11 in. (2.7 mm). For the as-built column footing system (B2SA), the horizontal displacement was higher due to a lower footing stiffness. Also, B2SA

experienced a smaller rotation (less rocking) during loading. These changes in the system's displacement ductility capacity need to be considered when deciding about the displacement capacity of bents on flexible footings (Reinhardt et al. 2003).

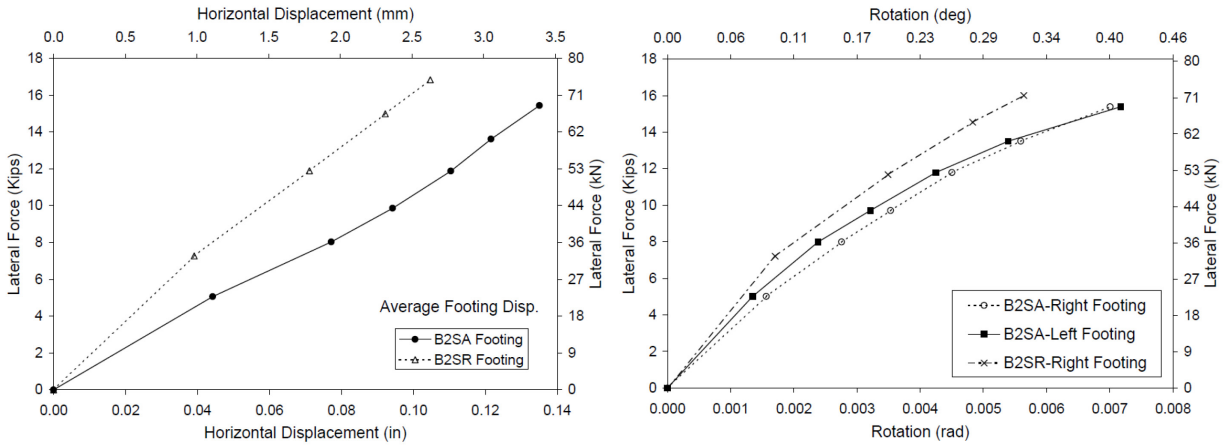

Figure 2.43: Comparison of measured (a) average footing horizontal displacement and (b) rotations vs Lateral Force for the B2SA and B2SR specimens (Reinhardt et al. 2003).

2.6.3.2 Rocking Response in Competent Soil Conditions

Rocking foundations in competent soil have been tested and validated by many researchers, and much work has been done toward implementation of these systems in practice (Gajan and Kutter 2008; Deng et al. 2012; Anastasopoulos et al. 2012; Hakhamaneshi 2014; Allmond 2014; Kutter et al. 2016). Application of rocking foundations within competent soils can produce minimal residual rotations of substructures with significant energy dissipation. It has been shown experimentally that rocking foundations on competent soils can reduce seismic ductility demand on bridge columns and improve overall bridge performance (Gajan et al. 2005; Algie et al. 2010). Figure 2.44 compares the behavior of a rocking foundation system with that of a hinging column system in terms of moment-rotation hysteresis. The results presented in these figures are from a series of seismic centrifuge tests on model column/footing systems performed by Deng et al. (2012). No degradation in the moment capacity of the rocking footing was observed after two full cycles and the moment-rotation curves exhibited large hysteresis that correspond to energy dissipation through the footing. In a bridge with a hinging column system, the footing largely remained quasi-elastic with very small hysteretic loops and corresponding low energy dissipation. Instead, the energy in this case largely dissipated through the column which exhibited greater rotation. The results of Deng et al. (2012) indicated that in a bridge with a hinging column system, the column accounts for 88% of the total energy dissipation.

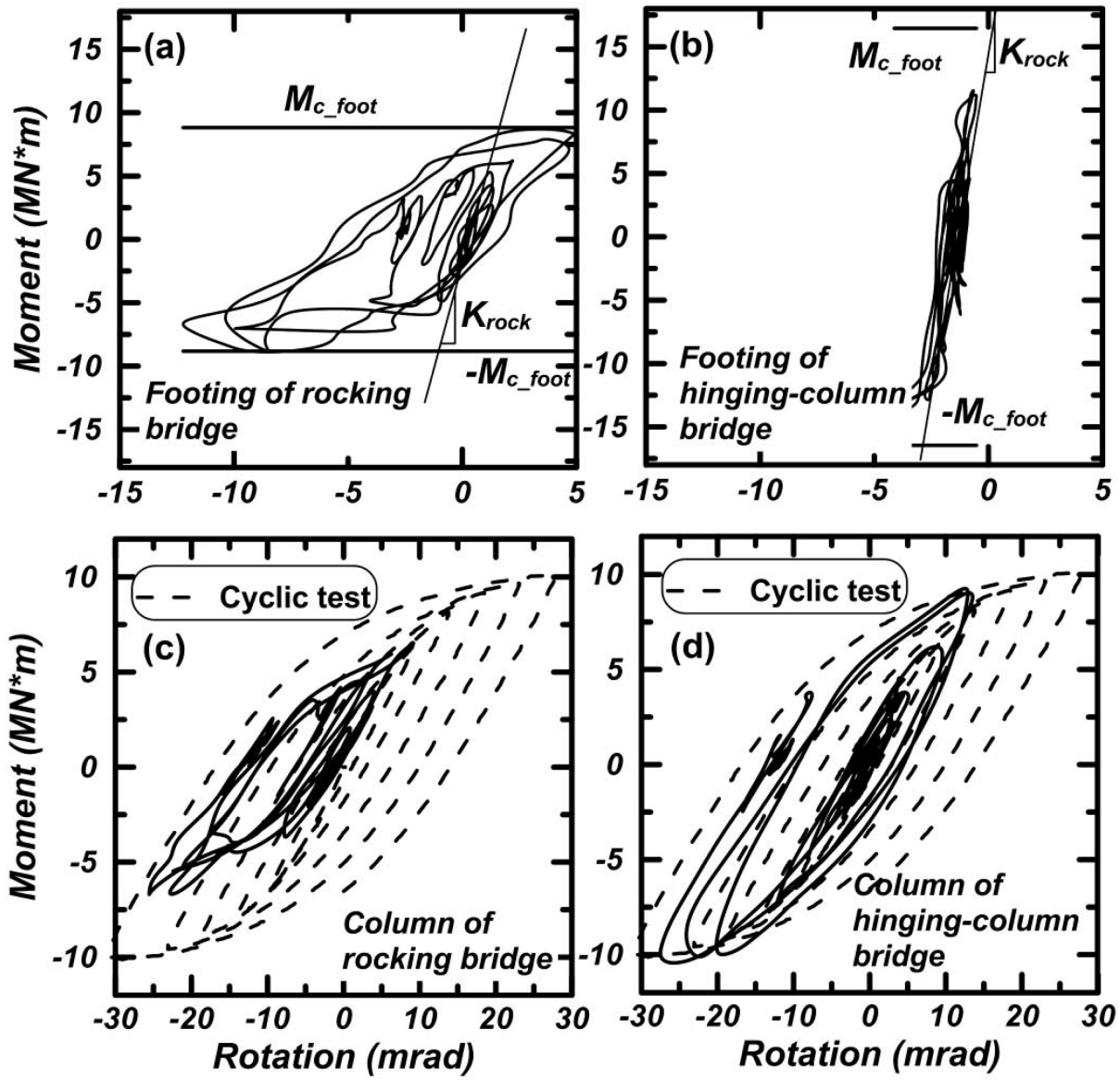

Figure 2.44: Comparison of the performance of footing/columns systems designed based on different concepts of foundation rocking bridge and plastic hinging (a) Moment-rotation behavior of footing of rocking bridge (b) performance of column of hinging column bridge (c) performance of footing of hinging column bridge (Deng et al. 2012).

Effect of Soil Type

Previous experimental and numerical research has shown that rocking foundations on competent soils can reduce the seismic ductility demand on bridge columns and improve bridge performance through significant energy dissipation at the foundation level (Gajan et al 2005, Deng et al. 2012). Early studies have been predominantly focused on the performance of model foundations in sandy soils (Gajan and Kutter; Hakhamaneshi 2014; Allmond 2014). From the cyclic moment−rotation behavior of foundations on sand, three main characteristics have been observed: (1) no degradation in moment capacity (though degradation in stiffness is observed during cyclic loading), (2) hysteretic behavior that is indicative of sufficient energy dissipation, and (3) a re-centering capability with relatively low residual drift. As rocking proceeds, the soil beneath the foundation was observed to become rounded at the edges due to the oscillating nature of the applied load. The rounded interface reduced the contact area between the footing and the foundation and produced localized bearing failure at the edges and consequently resulted in permanent settlement of the foundation during rocking. In some cases, footings embedded in sand and subjected to rocking exhibited residual uplift of the foundation; this has been attributed to sand falling into the gap during uplift, which is then compacted upon the subsequent contact of the footing with the subgrade. The displacement response of rocking footings largely depends on the footing shape and the density of supporting soil. For footings with small ratio of width to critical contact length (b/L_c) on or embedded in loose sand, a greater magnitude of normalized residual uplift may be observed during rocking.

While research has shown the beneficial energy dissipation potential of rocking foundations in sand, the number of studies in plastic soils (e.g., clayey silt, silty clay and clay) has been limited (Algie 2011; Deng et al. 2012; Phipps 2013; Hakhamaneshi 2014; Sharma 2019). Gajan et al. (2005) performed a series of centrifuge tests on shear wall footing models embedded in sand and clay to compare their nonlinear load-displacement characteristics during cyclic and earthquake loading. Figure 2.45 shows the model container and experimental setup employed by Gajan et al. (2005) for different vertical push, slow cyclic lateral push, and dynamic loading tests. The tests were performed at 20-g centrifuge acceleration in a rigid container. Four series of tests were conducted on dry sand (D_r = 60 and 80%) and one test series was on saturated clay (with undrained shear strength, c_u = 100 kPa).

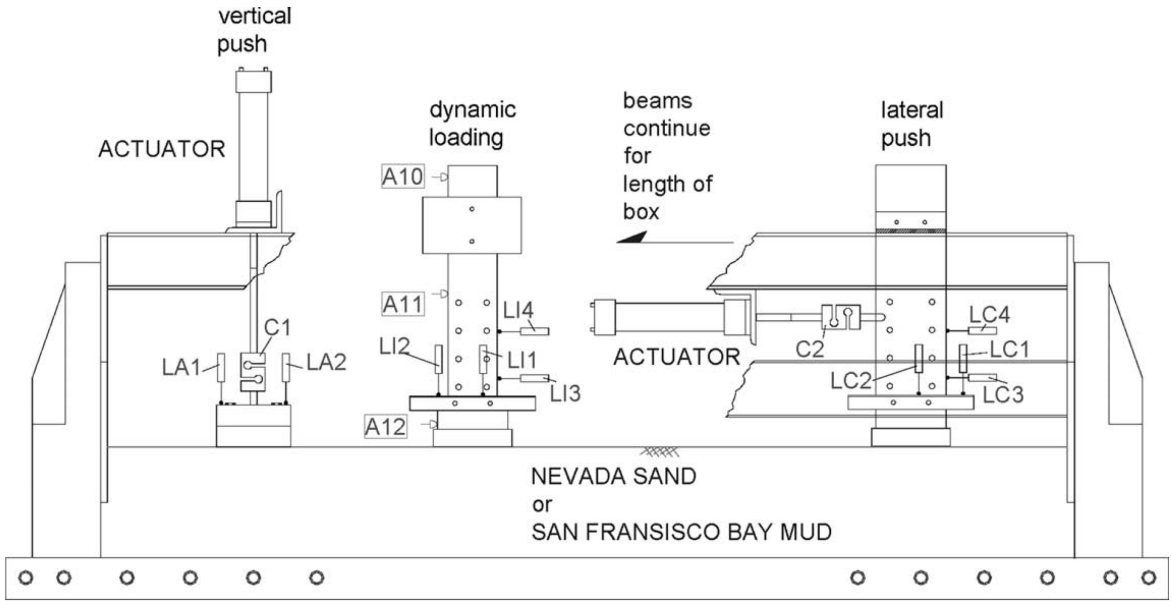

Figure 2.45: Model container and experimental setup with instrumentation for vertical push, slow cyclic lateral push and dynamic loading tests (Gajan et al. 2005).

The results of the research by Gajan et al. (2005) are presented in Figure 2.46 in terms of the moment–rotation, horizontal force–sliding, settlement–rotation, and settlement–sliding relationships at the center of the footing. Similar for the case of sandy bearing soils, the moment-rotation curve for footings on the clayey subgrade exhibited hysteresis during cyclic or earthquake loading, indicating that a considerable amount of energy is dissipated at the footing-soil interface. Results also indicated no moment capacity degradation with the number of cycles and the moment capacity remained constant during loading. However, the excellent energy dissipation mechanism in the plastic soil was paired with a large amount of permanent footing settlement. However, as the footing settled, the increased depth of embedment increased the overburden stress and vertical stiffness, resulting in a reduction in the rate of settlement. Results also indicated the absence of sliding during rocking until the shear capacity at the soil-foundation interface was reached. Thereafter, lateral translation of the footing proceeded to accumulate in the direction of the first loading cycle. Permanent displacements of this type may result in increased strain within the substructure and/or the supported superstructure depending on the details of the connections.

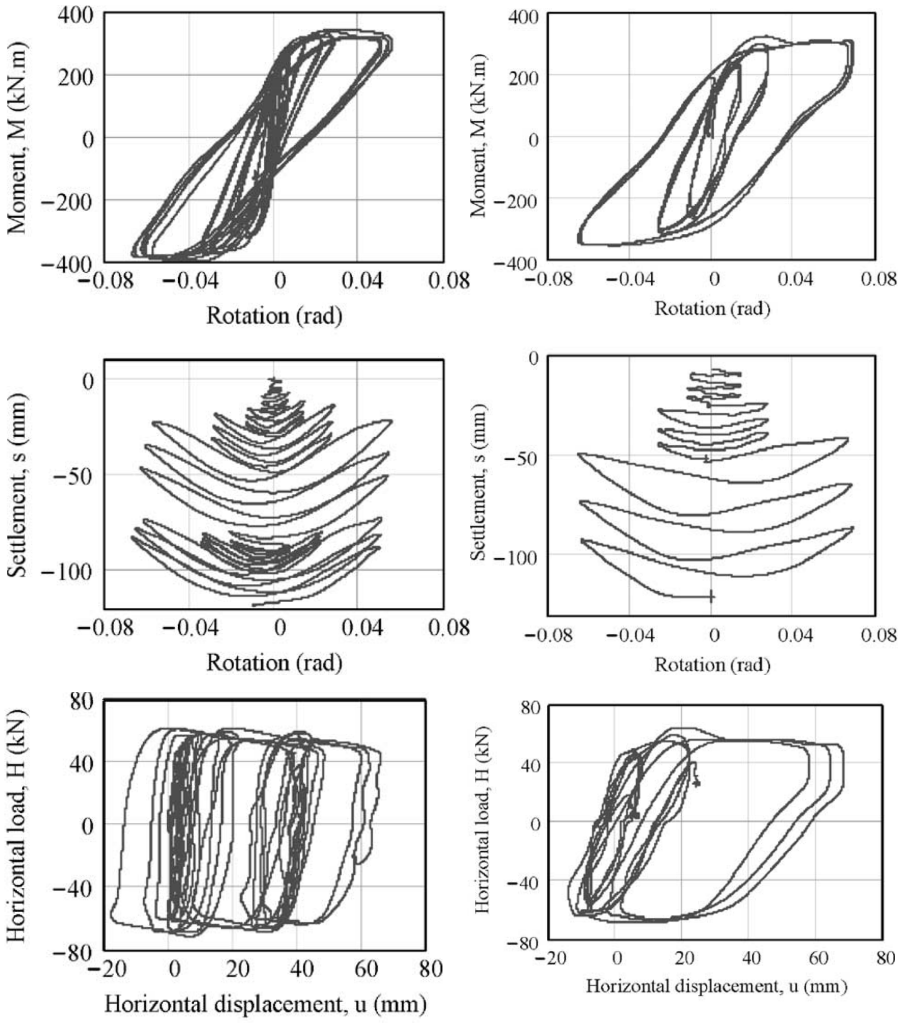

(a) Sand

Figure 2.46: Slow cyclic lateral push tests (a) sand, and (b) clay (Gajan et al. 2005).

In a study by Sharma (2019), a series of snap-back tests were performed to characterize the rocking behavior and energy dissipation of footings embedded in stiff, over-consolidated clay. The rocking foundation system developed by Sharma (2019) was an idealized single degree of freedom system which was supported by an isolated footing (Figure 2.47). The footing was 1.5 m long, 1.0 m wide and 0.3 m thick. The column of the system was a square steel tube with 0.2 m by 0.2 m outer dimension and 12.7 mm wall thickness. The rigidity (EI) of the column was 6.44 MN-m^2. The first yield moment of the column (113 kN m) was designed to be greater than M_{c_foot} to enable the rocking mode of energy dissipation. The snap-back tests were conducted by pulling the deck at an angle of 45° with respect to the footing axis, using chains attached to a quick release mechanism (Figure 2.47), followed by release of the pulling force. RC slabs on the column were used as the superstructure weight. The number of RC slabs varied depending on the vertical safety factor, FS_v, considered for testing. Sharma (2019) used four different FS_vs of FS_v=18.4-19.8 (FL01), FS_v=10.3-11 (FL02), FS_v=7.1-7.6 (FL03),

FS_v=5.5-5.8 (FL04). Various trials conducted for each FS_v, each with a different amplitude of initial drift, were conducted.

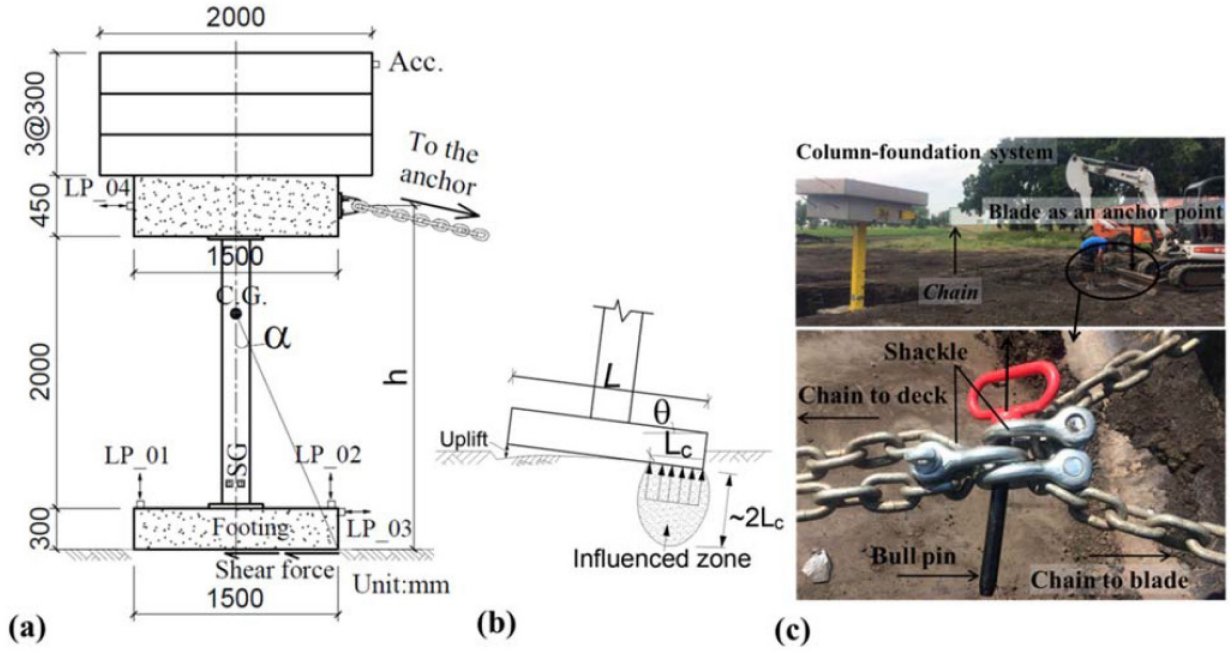

Figure 2.47: (a) Experimental setup, (b) concept of critical contact length and approximate influenced zone, and (c) the quick release mechanism (Sharma 2019).

Similar to previous studies in sandy subgrades, the results of this study indicated that the moment-rotation curves exhibited considerable nonlinearity, with the rotational stiffness degrading from one trial to the next during the early snap-backs tests (Figure 2.48a). However, the moment capacity, M_{c_foot}, remained constant with the number of trials or rotation amplitude. This has also been observed for rocking foundations in sandy subgrades (Gajan et al. 2005). The moment capacity formulation presented for rocking footings in sand (Equation 2.3) adapted for use with plastic soils was found to be applicable for the snap-back tests reported by Sharma (2019; Figure 2.48c).

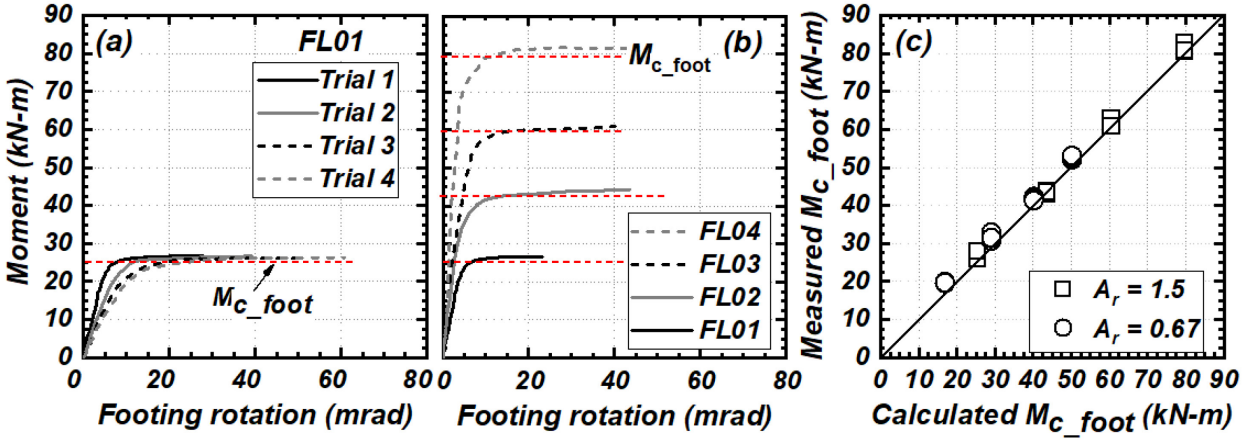

Figure 2.48: (a) Applied static rocking moment vs. footing rotation curves in snap-back stage, (b) moment-rotation in snap-back stage at different vertical loads, and (c) comparison of calculated and measured moment capacities for all tests in present study (Sharma 2019).

Sharma (2019) observed no significant difference between the rotation angle, ς, for footings tested in stiff clay at his test site and that of previous tests in sand. Furthermore, the magnitude of footing rotation necessary to mobilize the moment capacity appeared to be insensitive to the area ratio A/A_c, consistent with previous results. A rotation angle, ς, of 0.012 radians corresponding to the footing moment capacity recommended by Deng et al. (2014) and Hakhamaneshi (2014) appeared sufficiently reasonable given the scatter in Figure 2.49.

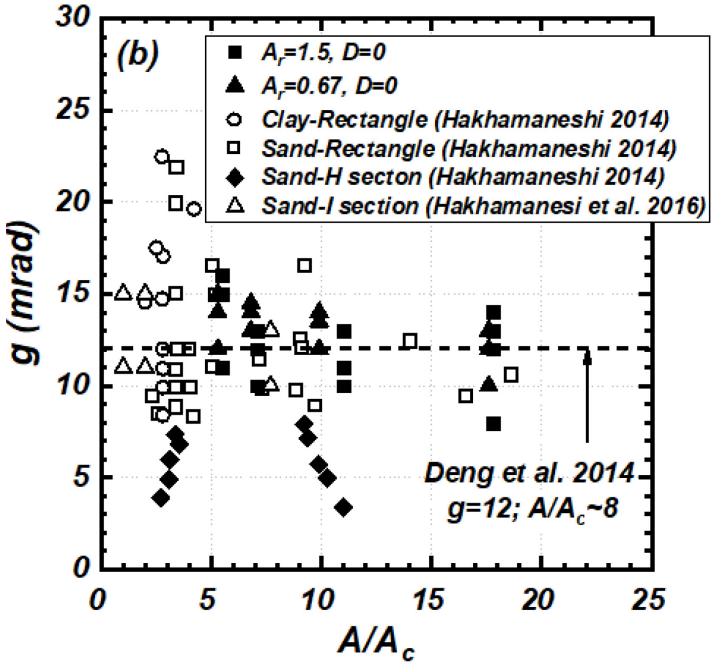

Figure 2.49: Observed relationship between footing rotation to mobilize moment capacity (g) and A/A_c (Sharma 2019).

The soil-foundation interface for footings investigated in Sharma (2019) exhibited rounding along the loading direction as observed following completion of each rocking test. Similar to the previous studies of rocking foundations in sand, the progressive development of the rounded subgrade in the stiff clay subgrade results from localized bearing failure at the edge of the footing and gradual settlement.

Figure 2.50 presents the normalized residual settlement of the foundation, defined as the ratio of settlement, w, to the footing length, L, as a function of the cumulative amplitude of rotation for test data reported by Sharma (2019) and Hakhamaneshi (2014) in clayey subgrades and sandy subgrades by Deng et al. (2012). The residual settlements were much less for the plastic soils than for those on sand. As a result, the boundaries for sand set previously by Deng et al. (2012) appear conservative for footing applications on clay subgrades. Furthermore, for $A/A_c > 8$, the footing settlement was consistently less than $0.01L$, independent of the footing rotation magnitude.

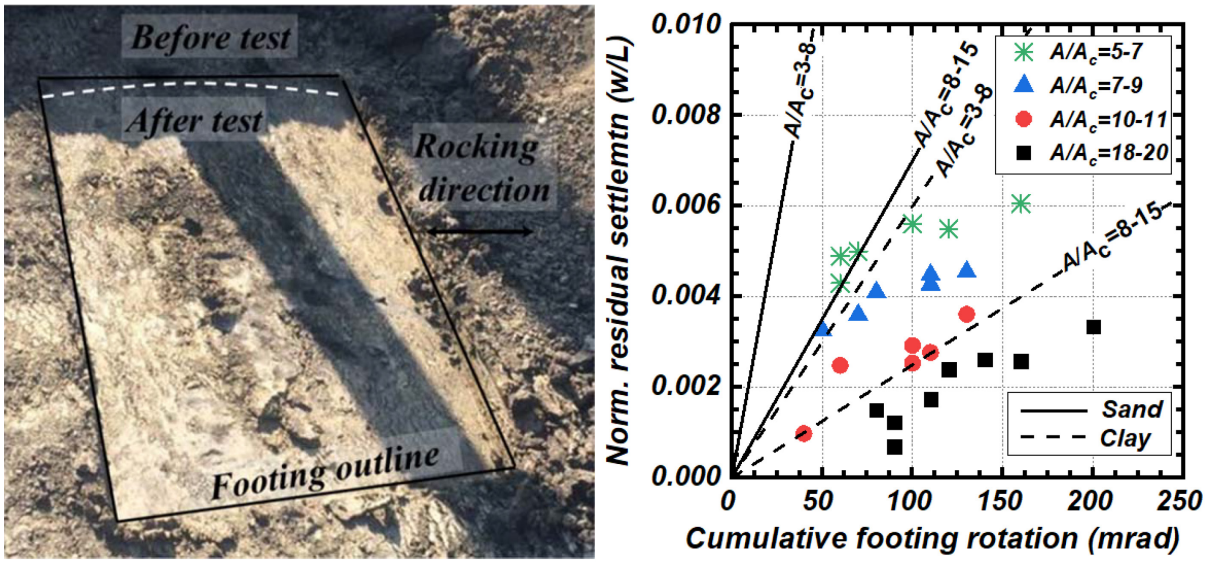

Figure 2.50: Observations regarding the displacement behavior of full-scale rocking footings (a) soil-footing interface exhibited rounding during snap-back tests performed by Sharma (2019), and (b) comparison of the normalized residual settlement and the cumulative footing rotation. The envelopes of anticipated normalized residual settlement adapted from Deng et al. (2012; sand using centrifuge modeling), Hakhamaneshi (2014; clay using centrifuge modeling) and Sharma (2019; clay using full-scale modeling).

Effect of Soil Density

In granular materials, a denser specimen is expected to have a larger mean effective stress during shear. The increase in mean effective stress results from the greater *in-situ* horizontal effective stress, and larger dilatancy and particle rotation frustration that characterizes the behavior of denser granular assemblies (e.g. Santamarina 2001; Santamarina and Cho 2004). Due to the higher mean effective stress, the normalized moment capacity is expected to be larger for footings resting on denser material.

Additionally, the moment-rotation hysteresis may exhibit less energy dissipation (Figure 2.51). Faccioli et al. (1998), Negro et al. (2000), and Anastasopoulos et al. (2011) investigated the effect of soil density and initial void ratio on the behavior of rocking foundations.

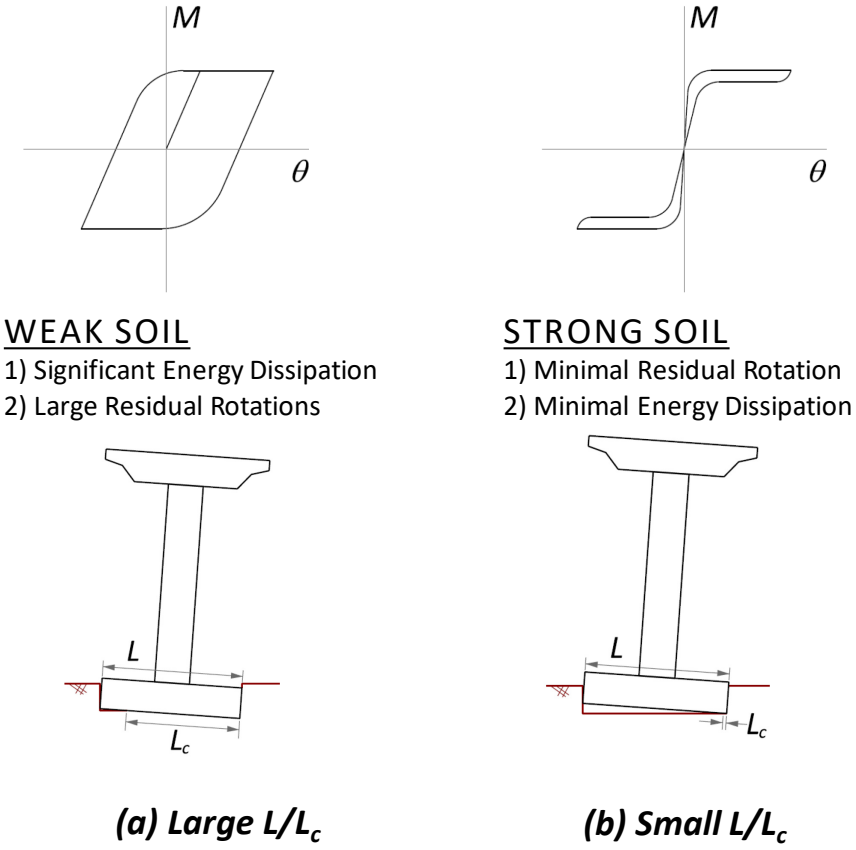

Figure 2.51: Conceptual moment vs. rotation curves for (a) relatively rigid interface (large L/L_c) resulting in minimal residual rotations and minimal energy dissipation, and (b) poor soil (low L/L_c) resulting in larger residual rotations and high energy dissipation.

Faccioli et al. (1998) performed two large, 1*g*, cyclic loading experiments to investigate the effect of soil density on the nonlinear interaction between shallow foundations of building structures and the supporting soil. Two relative densities of the footing subgrade were evaluated: a loose sand with $D_r = 45\%$ and very dense sand with $D_r = 85\%$. Figure 2.52 shows the details of the experimental setup used by Faccioli et al. (1998). The experimental prototype consisted of a concrete tank with rigid boundaries, filled with coarse-to-medium Ticino sand, and a 1 m by 1 m (in plan) concrete shallow foundation embedded by 1 m in the sand. The caisson was 4.60 m long, 4.60 m wide, and 4 m tall. Vertical loads of 100 and 300 kN were transmitted by an air cushion system to the column footing systems for the specimens of loose and dense sands, respectively. A hydraulic actuator, acting 0.9 m above the foundation level, was used to impose the prescribed time-varying horizontal force and/or displacement to the foundation. The vertical force was kept constant throughout the test and the horizontal cyclic loading was

applied in three phases: Phase I consisting of single cycles of small force-controlled amplitude, Phase II with the application of an earthquake-like time history of horizontal forces, and Phase III with sine-shaped displacement cycles of increasing amplitude imposed to the top of the structure.

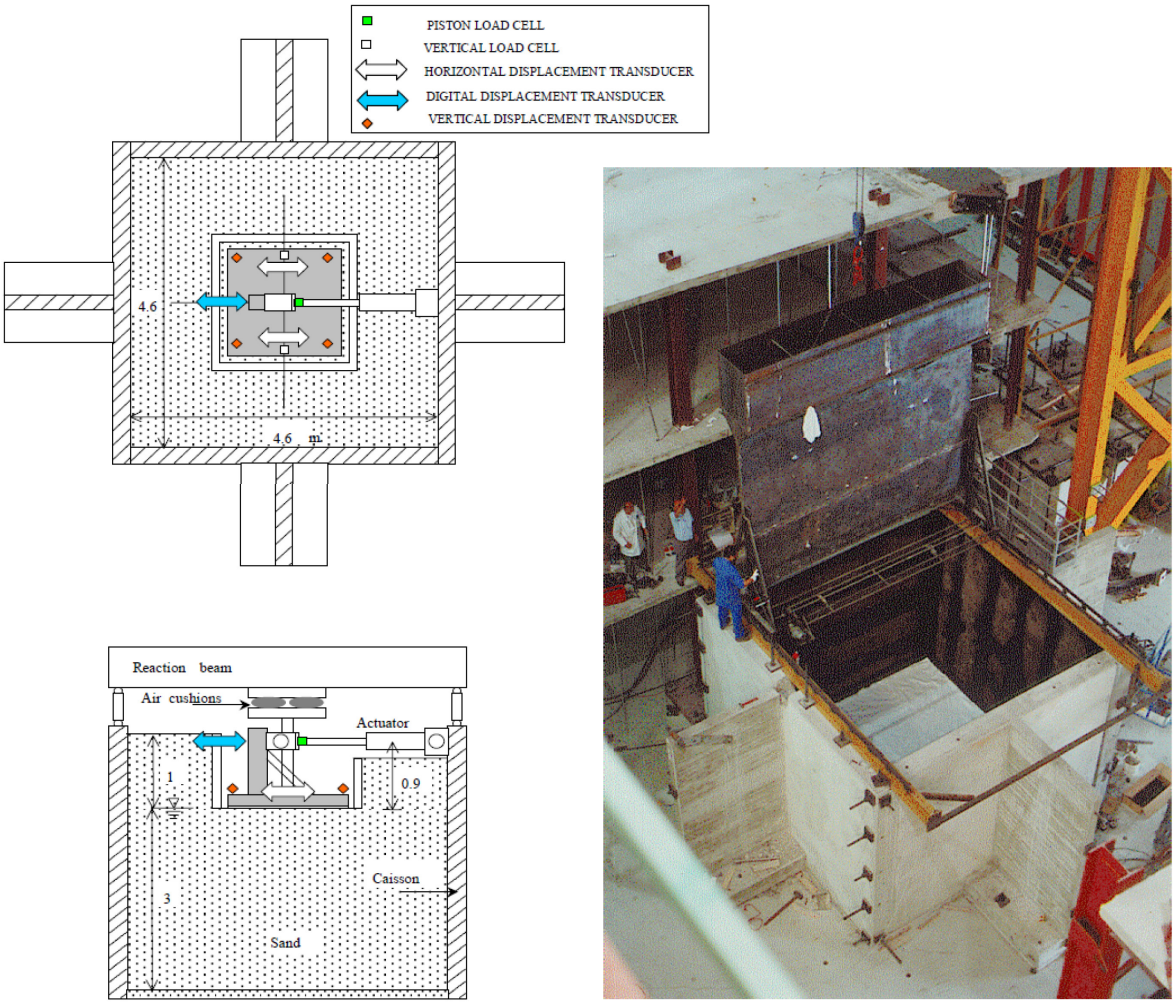

Figure 2.52: Experimental prototype used by Faccioli et al. (1998). (Dimensions are in m) (Faccioli et al. 1998).

The response of the system for the two conditions for Phase III is presented in Figure 2.53 terms of moment vs rotation and horizontal force vs displacement. Regardless of the initial soil density, the moment vs. rotation behavior of the footing showed a stiff response for the initial, small rotations. The moment-rotation relationship transitioned to nonlinear as the cumulative rotation increased, and the rotational stiffness degraded as the soil beneath the footing became rounded and local bearing failure initiated along the intermittent soil-footing interface. The degradation in rotational stiffness was observed to vary with the initial density of the soil. Owing to the larger bearing capacity, the moment capacity for the footing placed on dense sand (D_r=85%) was larger than that of loose sand (D_r=45%) and the moment-rotation hysteresis indicated that less energy was

dissipated. The hysteretic curve for the dense sand was S-shaped, indicative of footing uplift. In comparison, the foundation on loose sand experienced substantial permanent settlement. In this case, moment capacity degradation occurred at larger rotations and the moment-rotation curves exhibited larger hysteresis loops that clearly demonstrated larger energy dissipation during rocking. The asymmetry observed in the horizontal force-displacement hysteresis for the footing on the loose sand indicated the development of sliding, which apparently was prevented for the footing resting on dense sand.

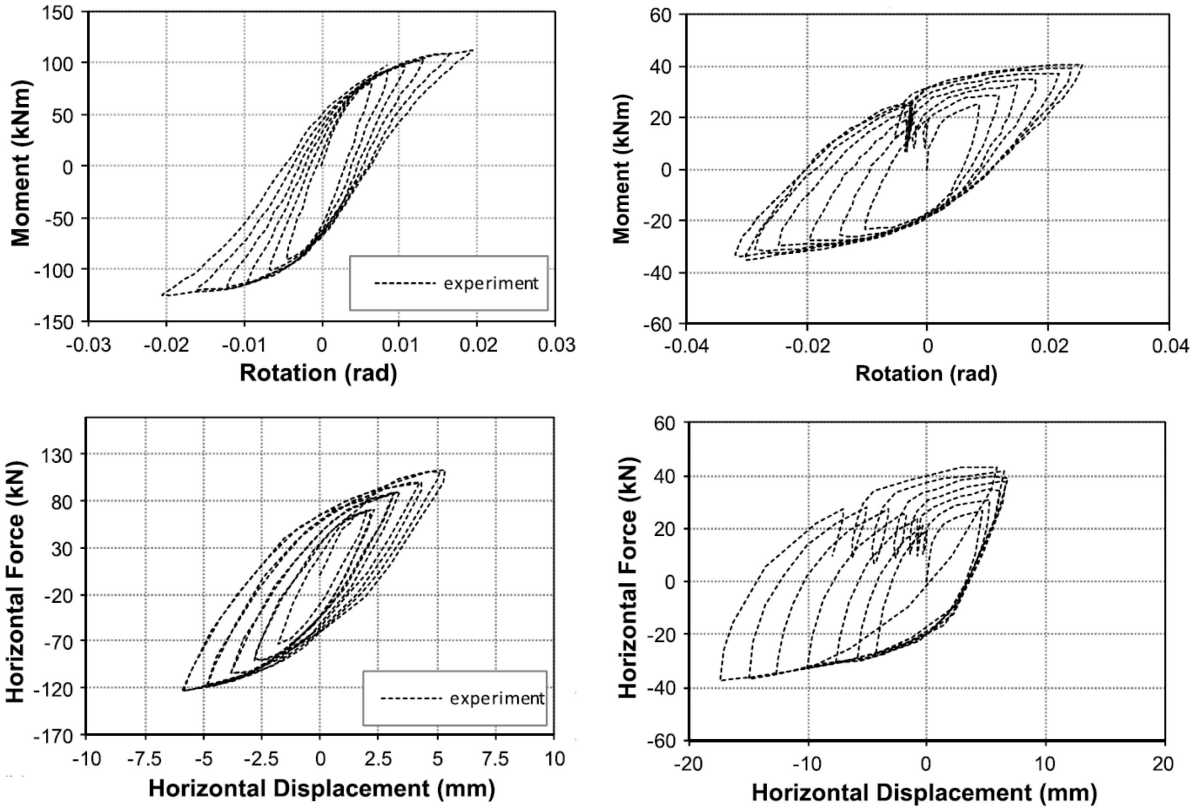

Figure 2.53: Overturning moment and horizontal forces vs. rocking for soils with different densities.

Faccioli et al. (1998) also reported a development of significant permanent settlements and rotations. Figure 2.54 presents vertical displacement time history of the two footings during different stages of loading. In both cases, results indicated large permanent settlements even during moderate seismic excitations. This is particularly relevant for the footing on the loose sand. The footing on the dense sand initially experienced an uplift after the first cycles of loading, and then started to settle with further loading. The foundation on the loose sand, on the other hand, sank continuously in the sand with no sign of uplift behavior. The footing rotation and the amount of energy being dissipated through foundation rocking was also noted to be larger for the low-density sand model.

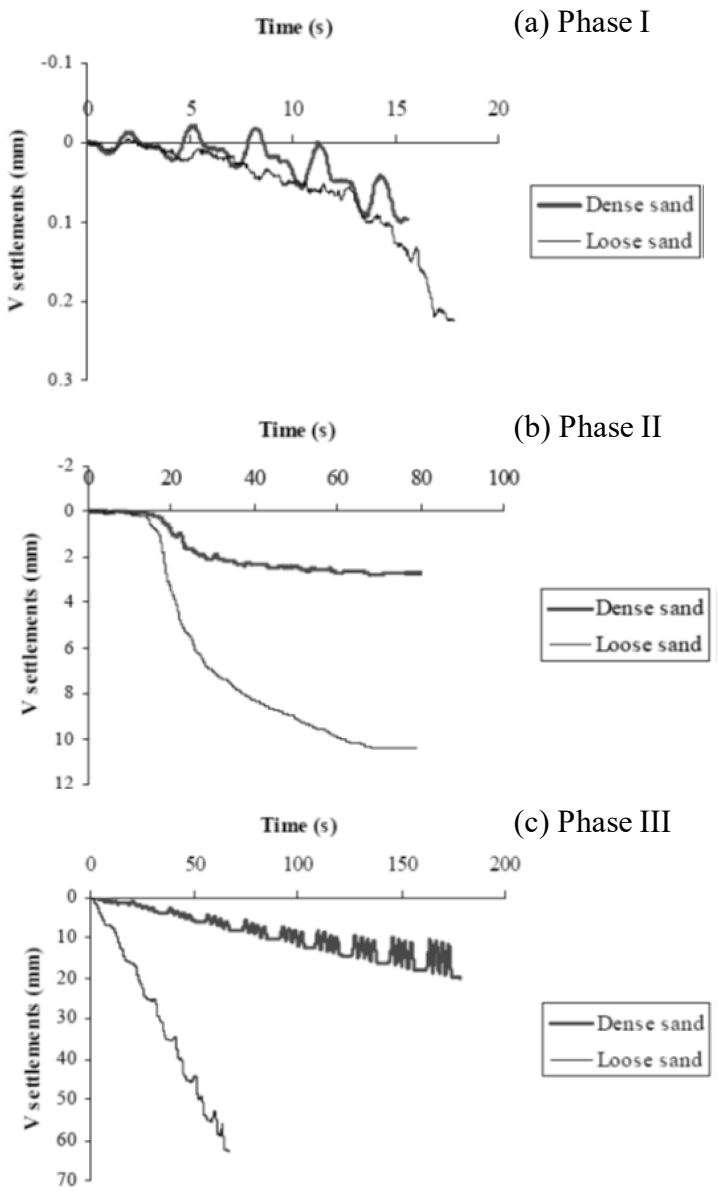

Figure 2.54: Comparison of vertical displacement of the rocking footings overlying loose and dense sand conditions for different phases of the tests: (a) Phase I, (b) Phase II, and (c) Phase III (Faccioli et al. 1998).

Effect of Embedment

The effect of embedment on the cyclic response of foundations was studied by various researchers. These studies suggested that embedment increases the stiffness of the foundation system and reduces the displacement amplitude during shaking (Lysmer and Kuhlemeyer 1969; Novak 1970; Chae 1971; Novak and Beredugo 1972; Gupta 1972; Novak 1974; Novak et al 1978; Gazetas 1983; Lin and Jennings 1984; Gazetas and Stokoe 1991; Inukai and Imazawa 1992). As the footing embedment increases, the soil surrounding the foundation provides additional confinement to the foundation, increasing

its bearing capacity and therefore the corresponding moment capacity. It has been further noted that the distribution of the contact stresses under, and passive earth pressures acting on the sides, of the foundation are affected by the amount of embedment. Due to these changes, a stiffer rotation and displacement response is expected in the foundations with higher embedment depths.

Hakhamaneshi (2014) performed a series of lateral slow cyclic centrifuge tests on model foundations using a 1-m radius centrifuge to evaluate the effect of foundation shape and embedment on rocking performance. Three different soil-foundation-superstructure models were tested at a centrifugal acceleration of 35*g*. The model foundations in this study were placed on sandy soils with relative density of 80%. Figure 2.55 presents a comparison of embedded and surface footings, indicating that permanent uplift occurred for the embedded footing, as compared to settlement for the surface-supported footing. The observed uplift was attributed to sand falling into the gap during uplift as the footing rocked in the opposite direction. The amount of footing uplift varied depending on the depth of embedment, shape of footing, and moment to shear stress (M/VL) ratio. For example, as M/VL increased, the magnitude of the gap between the subgrade and footing decreased, serving to suppress the residual heave or uplift of the footing. However, the increased M/VL also appeared to promote sliding as a consequence of the suppressed uplift. Due to the foundation sliding some particles were pushed out from the edge of the footing, which in cases caused some settlement during rocking. The combination of these events resulted in smaller uplift during rocking. Sand falling into the gap during uplift appeared to reduce the re-centering capability of the footing; this behavior is likely to be different than footings resting on plastic soils, which exhibit an apparent cohesion and should not as readily flow into the gap.

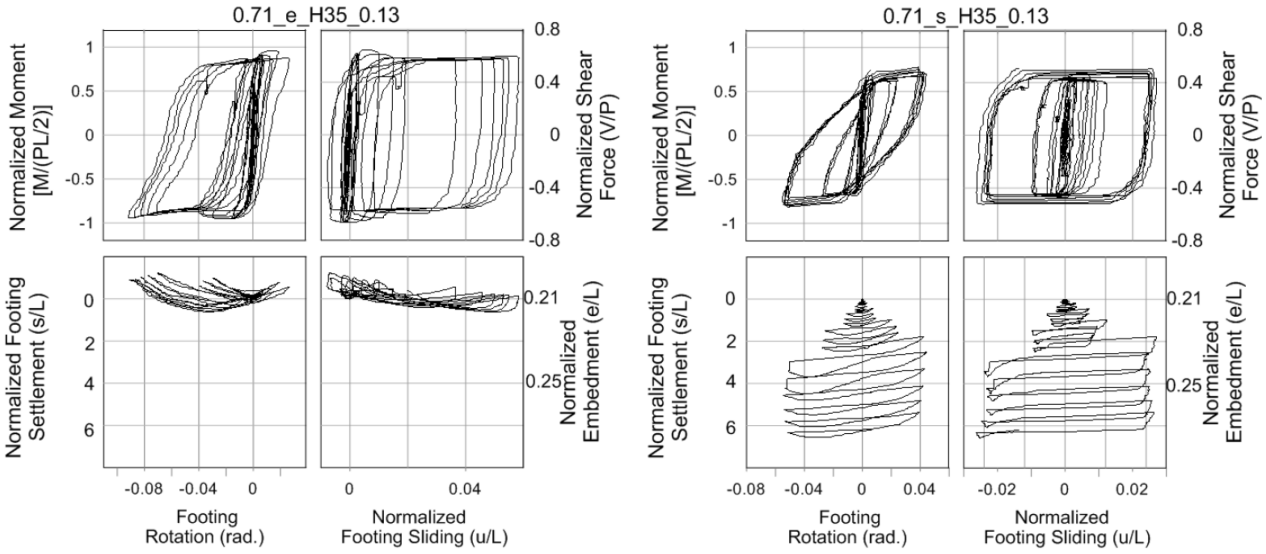

Figure 2.55: Effect of embedment on the cyclic loading behavior of the H-shaped footings with 35% missing area ratio. The results for h/L = 0.71. The left side results are for embedded and right side are for surface footings.

Rocking of surface-supported footings (or in cases when sand particles were prevented from entering the gap upon uplift) with similar A_c/A appeared to exhibit relatively larger magnitudes of settlement. The settlement was mainly due to: (1) localized bearing failure at the footing edges, and (2) soil being pushed away from the sides of the footing due to sliding (Figure 2.56). The sliding mechanism appeared to produce a relatively large amount of energy dissipation. Furthermore, the surface-supported foundations, especially those with larger A_c/A ratio, appeared to exhibit better re-centering capability compared to the embedded footings.

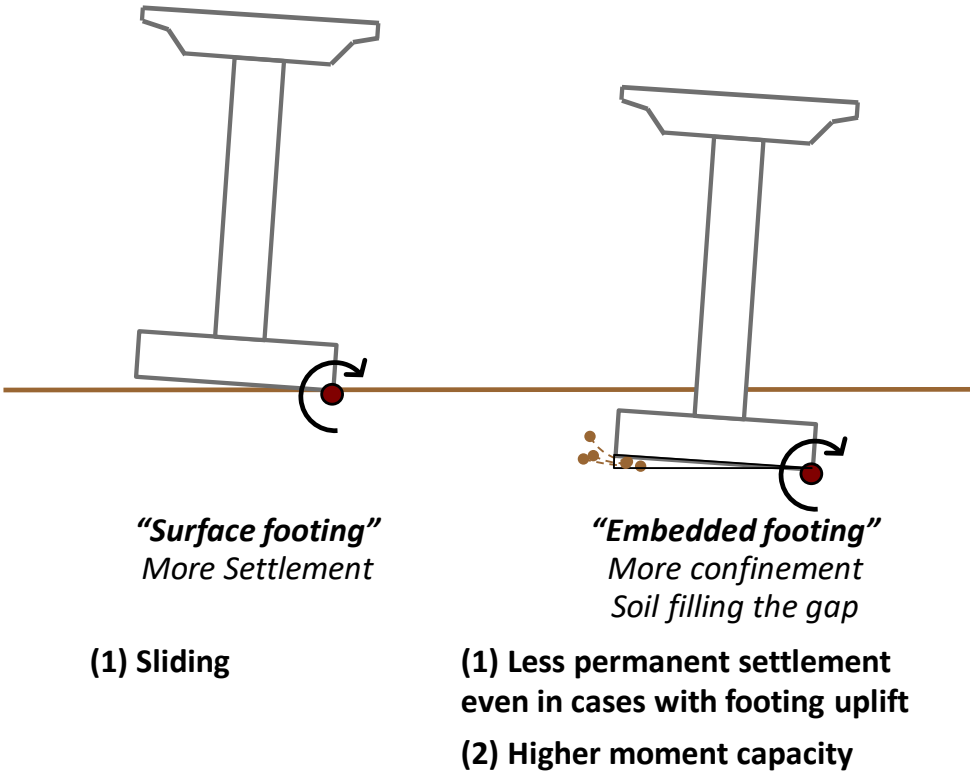

Figure 2.56: Deformation response of surface and embedded rocking footings.

Results of experiments by Hakhamaneshi (2014) demonstrate that similar foundation-superstructure systems reach the same final embedment regardless of the initial embedment (Figure 2.57). At this final embedment, the amount of soil flowing into the gap formed during rocking equals the settlement caused by local bearing failure or sliding, creating a balanced rocking system. Hakhamaneshi (2014) recommended the use of this critical embedment as a potential approach to minimize permanent settlement caused by rocking in design.

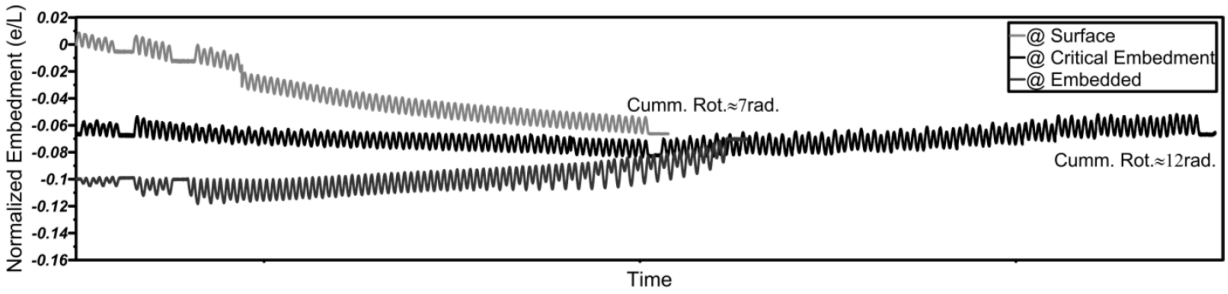

Figure 2.57: Critical embedment, similar footing at three different initial embedment (Hakhamaneshi 2014).

Sharma (2019) performed a series of static cyclic loading tests on large, model footings placed on clay to investigate the effect of embedment on the rocking behavior of footing in clayey materials. The rocking foundation system developed by Sharma (2019) is presented in Figure 2.58. As described earlier, the rocking footing developed by Sharma was an ideal single degree of freedom system consisting of a footing of 1.5 m by 1.0 m and a square, steel column 0.2 m by 0.2 m (outer dimension) and 12.7 mm wall thickness. Various RC slabs were used to provide the axial loads to the column and a reaction frame and hydraulic jack was used to provide cyclic lateral loads. The cyclic lateral load was applied to the column at the height of 2.5 m above the footing level and consisted of 4 to 5 packets, each containing 3 to 4 cycles of the same displacement amplitude (Figure 2.58b). Two different embedment depths of 0.0 (footing on the ground surface) and 0.5 m were considered for experiments.

The rocking moment vs. rotation loops in clay exhibited a “pinched”, highly nonlinear, S-shaped hysteresis with a large, enclosed area, indicating a significant amount of energy dissipation due to the soil-footing interaction. The embedded footing exhibited higher initial rocking stiffness and moment capacity, M_{c_foot}, than the footing that rested on the ground surface. Also, the hysteresis loops for the specimen with the surface footing were less pinched and not S-shaped. The unloading stiffness was also nearly linear for the unembedded footing. Similar to sand, the footing embedded in clay exhibited uplift due to soil in-filling or dilatancy, whereas the surface footing experienced settlement rather than uplift (Figure 2.59).

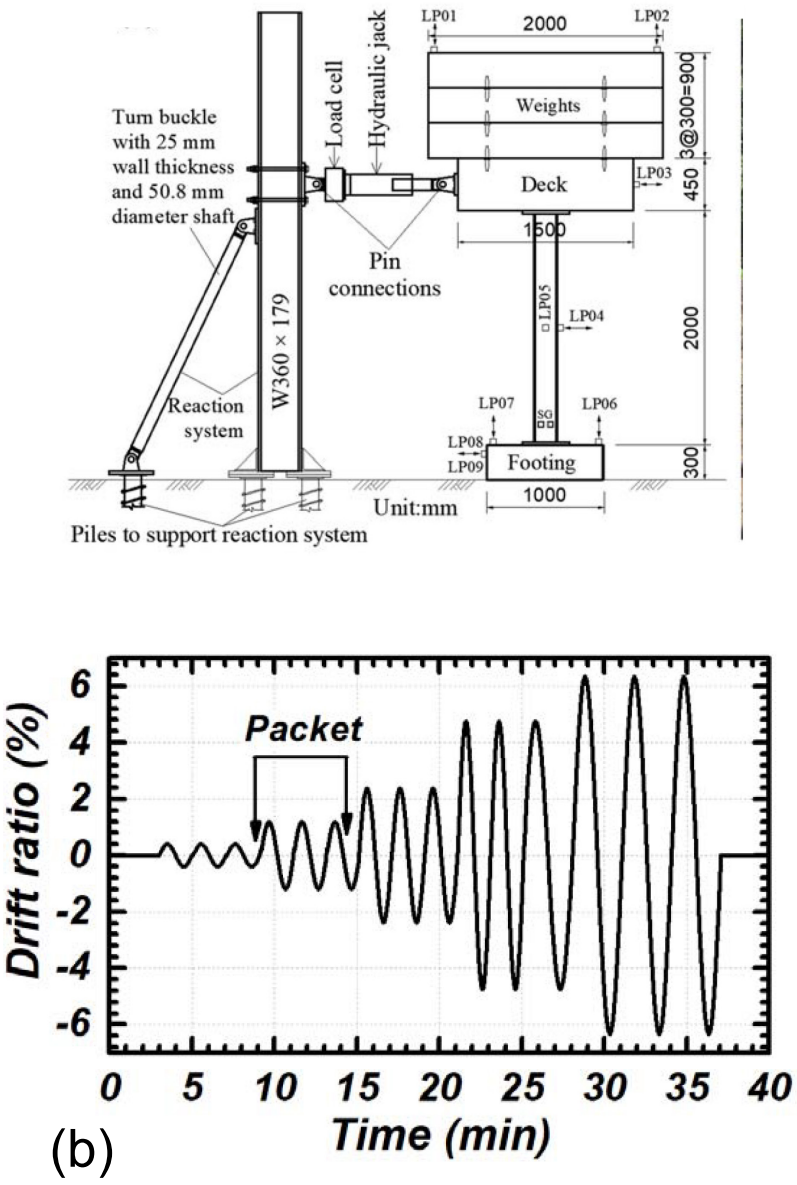

Figure 2.58: Details of experiments by Sharma (2019): (a) Schematic of the setup for surface soil-footing-structure system, (b) Typical histories of deck drift ratio (Sharma 2019).

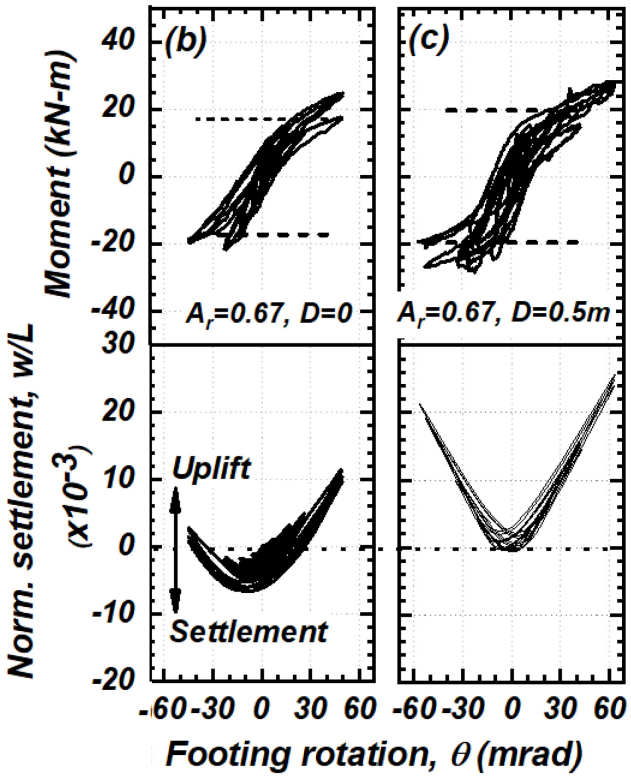

Figure 2.59: Relationship between moment, settlement, and rotation for different embedded depth (Sharma 2019).

2.6.3.3 *Submerged or Saturated Soil Condition*

Based on experimental observations on competent, dry soils and the results of numerical models, the seismic performance of bridges supported on shallow foundations can be significantly improved by the rocking mode of energy dissipation. However, the presence of water may introduce new mechanisms and scenarios that may affect the dissipation of energy and structural response. Depending on soil permeability and initial density, two potential scenarios may occur during rocking in saturated soils: localized erosion in more permeable soils, and suction around the footing for soils with lower permeability (Allmond 2014; Allmond and Kutter 2014). If either of these mechanisms occurs, there may be a significant effect on the resulting seismic SSI. Additionally, the presence of a loose layer of soil increases concern and potential for liquefaction (Allmond 2014; Allmond and Kutter 2014). Allmond (2014) performed a comprehensive numerical and centrifuge testing program to understand the response of a rocking system in the presence of water. The following sections summarizes the various scenarios investigated and corresponding changes in rocking response.

Suction

When a footing is allowed to rock or vibrate in saturated soils, depending on the rate of drainage (a function of soil permeability and rate of loading), two potential scenarios may occur: (1) a “breakaway” condition which is mostly the case in more permeable soils,

such as gravels and coarse sands; and (2) a "no-breakaway" condition which happens mostly in less permeable soil. In permeable soil, as the footing rocks up, water can flow into the opened gap. The consequences of water flow are the movement of particles into the gap, localized erosion on the footing edge, and significant uplift. Under the "no-breakaway" condition, a large drop in pore pressure, or suction, may force granular materials to move with the uplifting foundation at the side or directly under the footing (Figure 2.60). If this no-gap condition is created, uplift locally around the footing will occur, resulting in an increase in the moment capacity. An over-strengthened moment capacity may result in large residual rotation and loss of re-centering. It may also increase ductility demands on the column.

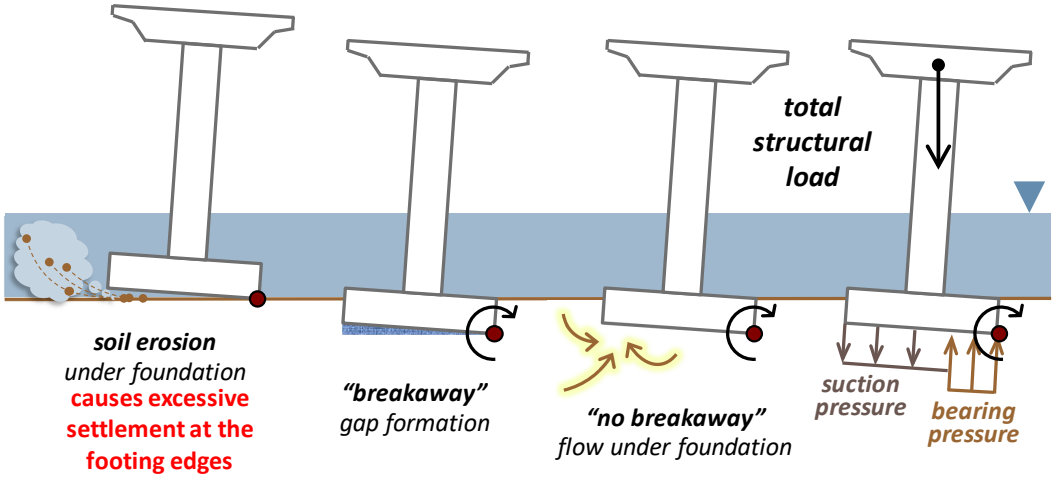

Figure 2.60: Different scenarios associated with water presence in rocking footing systems (Allmond 2014).

Erosion

Water flow under and around the footing can result in the potential for soil erosion and particle movement near the footing edges. Water flow can manifest in two ways: the flow of water and soil into the gap upon uplift, or the flowing out when the footing closes the gap under bearing. This hysteretic interaction can result in a cyclic fluid shear stress at the footing edges to result in erosion, undesired settlement, and rounding of the subgrade. The potential for erosion depends on such factors as the fluid velocity profile created at the footing edge, footing rotation amplitude, frequency of loading, fluid viscosity, particle size, and permeability, which can be characterized by the Reynolds Number and Shields Number, both nondimensional ratios of which that are typically used in river and sediment transport mechanics (Allmond 2014; Allmond and Kutter 2014).

Excess pore water pressure generation and Liquefaction

Saturated, loose to medium dense sands subjected to cyclic loading may generate excess pore pressures in response to the tendency for contraction under shear to result in liquefaction. Soil liquefaction and its detrimental effects such as excessive settlement, sliding, void redistribution, and bearing failure have caused catastrophic damage to structures during the past earthquake events. Over the years, an extensive amount of

research has been performed on different aspects of liquefaction including the susceptibility, triggering, response, and mitigation of liquefaction for a multitude of scenarios (e.g., Idriss and Boulanger 2008). A series of experiments and numerical simulations of the response of footings on saturated, liquefiable soil have been conducted by various researchers (e.g., Whitman and Lambe 1988; Liu and Dobry 1997; Bouckovalas et al. 1991; Dashti 2009; Allmond 2014; Allmond and Kutter 2014). Based on the results of these studies, pore pressure generation and dissipation under footings depends on the relative density, liquefiable layer thickness, drainage, static shear stresses, structure geometry (e.g., foundation width, structure height to width ratio, structure weight), and characteristics of the ground motion (intensity, duration, and frequency content). These factors contribute to different mechanisms of settlement during shaking, including localized volumetric strain due to partial drainage, sedimentation after liquefaction, consolidation due to excess pore pressure dissipation, volumetric expansion due to decreases in effective stresses, and deviatoric effects such as partial bearing failure due to strength loss, SSI-induced building ratcheting-induced settlements (Dashti 2009; Allmond 2014). Rocking foundations contribute to these settlement mechanisms, which may in some cases result in excessive settlement and tilting.

Allmond and Kutter (2014) investigated the response of rocking foundations embedded in liquefiable fine and coarse sands through a series of centrifuge tests. The results of their study indicated that considerable residual uplift and tilt occurred in fine sands due to the reduction in pore pressure under the embedded footing. Heavier-loaded footings produced greater residual sliding, and the result of the combined uplifting and sliding behavior was the flow of soil under the footing, reducing the re-centering mechanism and overturning resistance. Different approaches were implemented to improve the performance of footings resting on liquefiable soils and reduce settlement associated with liquefaction and rocking. Allmond (2014) indicated that the use of coarse materials as the soil subgrade can reduce the effects of suction and control erosion. The footing in this case was observed to have the moment capacity, energy dissipation and re-centering mechanisms of rocking foundations in competent soil. In a study by Deng and Kutter (2012), the implementation of concrete pads into the ground was proposed to minimize rocking-induced footing settlements on saturated layers of liquefiable soils (Figure 2.61).

The results of a series of centrifuge tests on a reduced-scale SDOF structure with four concrete pads that were placed into the ground soil at four edge locations demonstrated the effectiveness of this strategy in reducing settlement. This approach, however, over-strengthened the footing, influencing the energy dissipation during rocking and the footing's moment capacity (Hakhamaneshi 2011). Furthermore, such countermeasure may not be cost-effective for new construction and are not appropriate for existing column-footings.

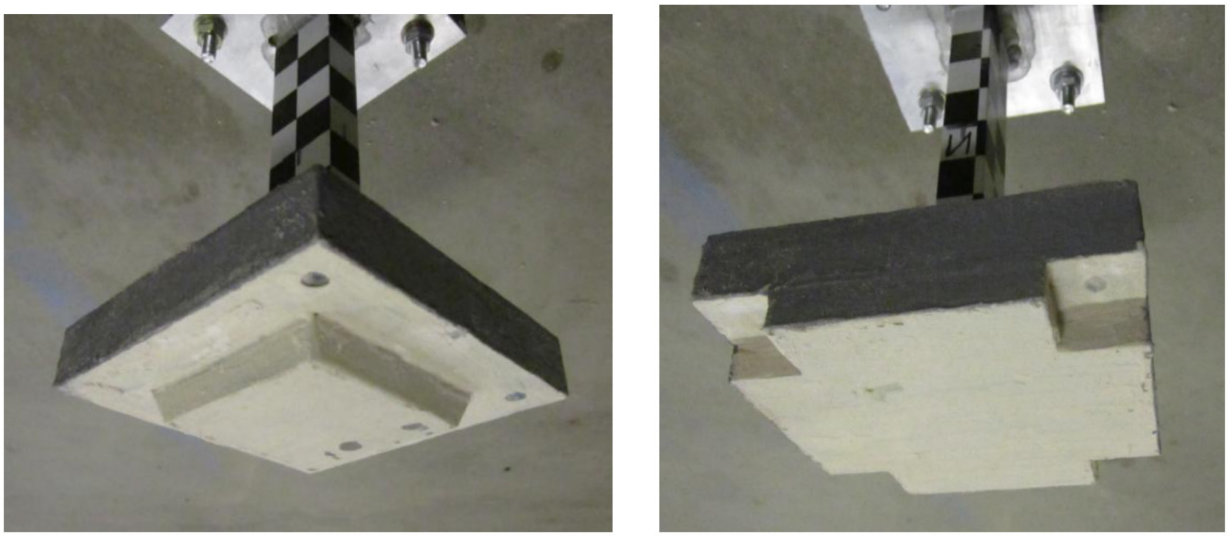

Figure 2.61: Concrete pads that were placed into the soil by Deng and Kutter (2012) to reduce settlement caused by liquefaction and rocking.

2.6.3.4 Unsaturated Soil Conditions

Most of the advances in the understanding of rocking foundations in the past 30 years have focused on the response in competent or saturated soils. In competent soils, rocking has been proven to improve the performance of bridges by reducing ductility demand on bridge columns and dissipating energy at the foundation level. Saturated soils, on the other hand, have the potential to liquefy during propagation of seismic waves, leading to significant deformations. These deformations along with those associated with rocking may result in significant settlement or tilting of the structure during and following shaking. Different approaches have been developed to analyze the nonlinearity of soil and rocking systems during shaking (Gajan and Kutter 2008; Deng and Kutter 2012; Kutter et al. 2016). Conversely, almost no work has been done on the response of rocking foundations in unsaturated soils or soils subjected to seasonal fluctuations in moisture content and strength. Many near-surface geotechnical systems, including bound and unbound pavements, machine foundations, foundations for wind turbines and retaining walls are routinely subjected to dynamic, seasonal loading due to precipitation and evaporation, commonly residing in the partially saturated or unsaturated condition. The seasonal wetting and drying of unsaturated soils in these systems imply that the small- and large-strain stiffness of the soils may change during operation, complicating the prediction of performance in static and seismic loading.

Figure 2.62 shows variations in soil saturation during different seasonal conditions. Considering the groundwater table elevation at some depth below a foundation, the degree of saturation in the soil would vary nonlinearly through the soil above, and potentially below, the groundwater table, depending on the permeability of the soil. In some cases, the degree of saturation, S_r, defined as the ratio of water volume to void volume, will likely be 100% near the groundwater table due to phenomena such as capillary rise or absorbed water. Under the condition of hydraulic equilibrium with no

upward or downward flow, the curve describing variations in the degree of saturation with depth (also interpreted as suction head) is called the soil water retention curve, SWRC. When the soil is subjected to an upward or downward movement of water as a result of events such as evaporation or precipitation, it will experience a drying/wetting process through which air will start to flow into or out of the voids between the particles. The presence of air and water as fluids filling the interparticle voids results in the formation of menisci of air-water at the soil-water interface. The magnitude or frequency of the air-water menisci vary with S_r and is expected to be higher in soils with lower S_r. The surface tension associated with air-water menisci have a direct effect on inter-particle connections for a given suction head and may result in varying soil strength and stiffness (Khalili and Khabbaz 1998; Sivakumar 1993; Khalili et al. 2004; Lu and Likos 2006; Gallipoli et al. 2003; Lu et al. 2010; Khosravi and McCartney 2012). The response of a rocking footing on soils with seasonally varying S_r would deviate from what has been observed in dry or fully saturated soils, yet no prior studies have been conducted, indicating that further research is warranted.

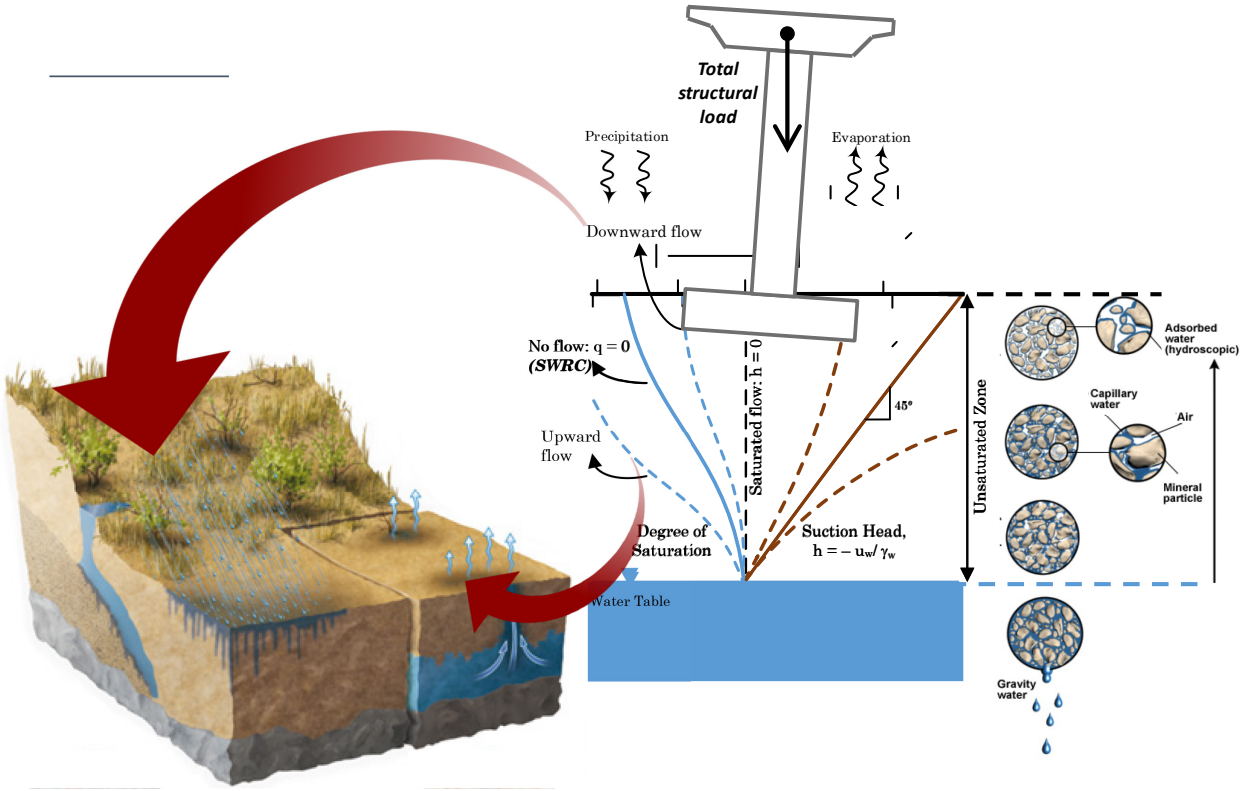

Figure 2.62: Movement of air-water interfaces during hydraulic hysteresis below a shallow foundation.

2.7 SUMMARY

The need for cost-effective seismic retrofits to older bridge substructures has been well-recognized following observation of poor performance following earthquakes, experimental findings from large- and full-scale structural specimens, and numerical investigations. In Oregon, the inadequacies of pre-1971 bridge substructure designs represent a particularly pressing need

for seismic remediation. Vintage column-footing systems were not designed for seismic loads. The design inadequacies of these substructures include short lap splices at the base of column-footing, low confinement of the concrete core, very light transverse reinforcement over the lap-splice region, potentially insufficient footing plan dimensions, and a lack of reinforcing steel at the top of the footing. The lack of transverse reinforcement in the columns results in unreliable shear-resistance. Design and detailing deficiencies can result in significant damage of the substructure and inadequate ductility. Various techniques have been proposed to improve the seismic performance of bridge substructures including increasing the footing size, typically in conjunction with underpinning, use of long dowels, and reinforcement overlays. Despite their mechanical effectiveness, these mitigation techniques are difficult to implement due to foundation embedment and site constraints such as limited access and overhead clearance.

Extensive research on the structural response of column-footing scenarios have provided the theoretical and experimental background for seismic assessment and retrofit. In particular, application of titanium alloy bar (TiAB) ligaments combined with continuous TiAB spirals to existing bridge columns has been shown to improve ductility without substantially increasing stiffness or strength. The continuous TiAB spiral provides additional confinement over the lap-splice region and core. The supplemental longitudinal TiABs, anchored into the column face and footing, provide a redundant flexural load path to resist seismic induced moment and provide dowel-action resistance to sliding of the column relative to the footing. Previous research has demonstrated that TiAB-retrofitted columns develop excellent hysteretic responses during cyclic loading; however, the experimental basis for this retrofit is generally limited to restrained column/footing specimens that do not consider soil-structure interaction (SSI) and its effect on the overall response of the structure. In reality, such rigid boundary conditions do not exist, and the increased substructure stiffness may impart forces to and on the bridge foundations that are not reflective of in situ conditions. These additional forces may cause damage to other parts of the bridge substructure, particularly to vintage column-footing and column cap-beams due to the lack of reinforcing steel in these connections.

Foundation rocking presents an alternative method for improving the seismic performance of retrofitted column-footing systems. Based on the results of rocking tests on “as built” and retrofitted column footing in competent soils, if rocking behavior dominates the response of the system, the column and footing remain elastic during shaking and damage is minimized. A rocking footing provides the system with an alternative hinging mechanism where a plastic hinge forms in supporting soil at its contact with the loaded edge of the footing. With rocking, the foundation is expected to exhibit improved performance in terms of the re-centering characteristics, energy dissipation, ductility, and retention of strength compared to a yielding reinforced concrete column. The rocking behavior of footings depends on factors such as bridge typology, soil type and density, foundation embedment depth, and the presence of water. The results of centrifuge tests and numerical models indicated that for bridge systems with two-column bents and pin connections at the column-deck connections, rocking foundations improve the seismic performance of the bridge in terms of reducing deck drift and permanent drift. Soil type was observed to have negligible effect on the hysteresis response of rocking footings, provided the soil was sufficiently dense (granular soils) or stiff (plastic soils). However, the displacement of a rocking footing, in terms of settlement or sliding, may exhibit differences depending on soil type. For example, foundations embedded in loose sand may exhibit a net uplift displacement rather than settlement after seismic loading. The effect of the sand flowing

into the gap between the subgrade and footing upon an uplift cycle may reduce the re-centering capability of the footing; on the other hand, this effect may enhance energy dissipation. In surface footings, regardless of the type of soil, the footing experiences settlement due to rocking. However, lateral loading may result in footing sliding, resulting in an asymmetric hysteretic response. The presence of water and the degree of saturation near the footing may also have detrimental effects on the rocking response of footing. For example, in saturated or submerged soils, the act of rocking may result in water flow from or into the gap underneath the uplifted portion of the foundation, resulting in possible soil erosion, pumping, and tilting of the structure. In the case with a saturated layer of loose sand underneath the footing, liquefaction caused by shaking may result in excessive footing settlement, resulting in catastrophic damage to different structural components. As the degree of saturation decreases, the capillary forces and surface tension at the air-water-soil particle interface increase the soil strength and improves its deformation response. Accordingly, a rocking footing is expected to perform better during shaking under these seasonal conditions.

In summary, new provisions associated with shallow rocking foundations have been developed as a result of the previously conducted research. However, there remains no rational design approach for retrofitted column-footing systems for bridges that consider the combined effects of the nonlinearity of structural components and soil. Design questions remain to be answered, such as (1) does column strengthening due to retrofitting cause unintended damage to footings with vintage reinforcing details? (2) will resulting seismic settlements and sliding occur within an allowable magnitude? (3) should rocking and soil failure underneath the footing be allowed during loading? Limited resources require that methodologies that can take advantage of soil-structure interaction, where warranted, be used to extend the life of existing bridges, and that tools be developed to quickly assess whether retrofit of bridge substructures is preferable over replacement given the existing structural details, substructure type, and soil conditions. Incorporation of soil-structure interaction may also show that retrofit or replacement of the substructure is not necessary. Given the number of bridges for which retrofit/replacement is considered desirable, the impact to both budget and project delivery could be significant, with significant potential implications for improving the seismic resilience of the transportation network.

Development of new methodologies and holistic retrofit design approaches for bridges in the State of Oregon requires the performance of a novel and thorough experimental program that: (1) considers those SSI aspects that are lacking or have not been sufficiently addressed in previous research; and (2) ensures that the reinforcement details of those bridge column-footings in ODOTs inventory that are in most need of being addressed are prioritized. Such experimental program requires to first focus on large-scale retrofitted and vintage specimens coupled with a suitable soil simulant under controlled laboratory conditions to capture the effect of some relevant parameters on the footing moments and the horizontal face reactions. Some of these parameters are foundation embedment depth, passive lateral resistance and overburden pressure of soil resting at the top of the footing, and axial loading representative of the “system” response of a multi-column bridge bent. Short, shear-sensitive column-footing conditions need to be considered for such testing program, as they may attract shear stresses greater than the diagonal tension capacity of concrete during earthquakes. Then, vintage and retrofitted specimens with “short” columns need to be built and tested while bearing on the stiff clayey silt deposits (representative of much of the surficial deposits in Oregon, specifically the Willamette Valley).

These tests allow to focus on the footing-soil response of vintage footings (since the column response is well understood at this stage). Because clayey silt deposits are highly sensitive to seasonal variations in moisture, footing tests need to evaluate wet and dry conditions to establish the bounds of the range in SSI. Following review of the experimental and numerical data, appropriate design guidelines can be developed to capture the salient aspects of SSI on seismic performance of vintage and retrofitted column-footings.

2.8 REFERENCES

AASHTO. (2017). AASHTO LRFD Bridge Design Specifications (8th ed.). American Association of State Highway and Transportation Officials. ACI Committee 440. (2017). ACI 440.2R-17: Guide for the Design and Construction of Externally Bonded FRP Systems for Strengthening Concrete Structures. ACI 440.2R-17. Detroit, MI.

Agalianos, A., Psychari, A., Vassiliou, M.F., Stojadinovic, B. and Anastasopoulos, I. (2017). Comparative Assessment of Two Rocking Isolation Techniques for a Motorway Overpass Bridge. Frontiers in built environment, 3, p.47.

Algie, T. B., Pender, M. J., Orense, R. P., Wotherspoon, L. M. (2010). "Dynamic Field Testing of Shallow Foundations Subject to Rocking." Proceedings of the 2010 New Zealand Society for Earthquake Engineering Conference, Wellington, New Zealand, March 2010.

Algie, T. B. (2011). Nonlinear Rotational Behaviour of Shallow Foundations on Cohesive soil. PhD Dissertation, University of Auckland, New Zealand.

Allmond, J. D. (2014). Shallow Rocking Foundations in Liquefiable and Saturated Soil Conditions. PhD Dissertation, University of California, Davis.

Allmond, J. D. and Kutter, B. L. (2014). Fluid Effects on Rocking Foundations in Difficult Soil. Proc. Tenth US National Conference on Earthquake Engineering Frontiers of Earthquake Engineering. July.

Allmond, J., Kutter, B. L., Bray, J. and Hayden, C., (2015). New database for foundation and ground performance in liquefaction experiments. Earthquake Spectra, 31(4), pp.2485-2509.

American Concrete Institute Committee 318, "Building Code Requirements for Structural Concrete (ACI 318-02)," American Concrete Institute, Farmington Hills, Michigan, 2002, Section 10.11.1.

Amneus, D. (2014). Methods for Strengthening Flexural Steel Details in Reinforced Concrete Bridge Girders using a Near-Surface Mounted Retrofitting Technique. M.Sc. Thesis, Oregon State University, Corvallis, OR.

Anastasopoulos, I., Gazetas, G., Loli, M., Apostolou, M., Gerolymos, N. (2010). "Soil Failure Can Be Used for Seismic Protection of Structures." Bulletin of Earthquake Engineering, 8, 309-326.

Anastasopoulos, I., Gelagoti, F., Kourkoulis, R., and Gazetas, G. (2011) "Simplified Constitutive Model for Simulation of Cyclic Response of Shallow Foundations: Validation against Laboratory Tests" Journal of Geotechnical and Geoenvironmental Engineering ASCE 137(12), 1154–1168.

Anastasopoulos, I., Kourkoulis, R., Gelagoti, F. and Papadopoulos, E. (2012). Rocking Response of SDOF Systems on Shallow Improved Sand: An Experimental Study. Soil Dynamics and Earthquake Engineering, 40, pp.15-33.

Ando, M., and Balazs, E. I. (1979). Geodetic Evidence for A Seismic Subduction of the Juan de Fuca Plate. Journal of Geophysical Research: Solid Earth, 84(B6), 3023-3028.

Andrawes, B., Shin, M. and Wierschem, N., (2010). Active Confinement of Reinforced Concrete Bridge Columns using Shape Memory Alloys. Journal of Bridge Engineering, 15(1), pp.81-89.

Antonellis, G., Gavras, A. G., Panagiotou, M., Kutter, B. L., Guerrini, G., Sander, A. C., and Fox, P. J. (2015). Shake Table Test of Large-Scale Bridge Columns Supported on Rocking Shallow Foundations. Journal of Geotechnical and Geoenvironmental Engineering, ASCE, 141(5): 04015009.

Apostolou, M., Gazetas, G., and Garini, E. (2007). Seismic Response of Slender Rigid Structures with Foundation Uplifting," Soil Dynamics and Earthquake Engineering 27(7), 642–654.

Barker, L. (2014). Flexural Anchorage Performance and Strengthening on Negative Moment Regions Using Near-Surface Mounted Retrofitting in Reinforced Concrete Bridge Girders, M.Sc. Thesis, Oregon State University, Corvallis, OR.

Beck, J. and Skinner, R. I. (1974.) The Seismic Response of a Reinforced Concrete Bridge Pier Designed to Step. Earthquake Engineering and Structural Dynamics 2(4), 637–655.

Bournas, D. A., and Triantafillou, T. C. (2009). Flexural Strengthening of Reinforced Concrete Columns with Near-Surface-Mounted FRP or Stainless Steel. ACI Structural Journal, 106(4), 495–505. https://doi.org/10.14359/56615

Breña, S., and Schlick, B. (2007). Hysteretic Behavior of Bridge Columns with FRP-Jacketed Lap Splices Designed for Moderate Ductility Enhancement. Journal of Composites for Construction, 11(December), 565–574.

Budek, A. M., Lee, C. O., and Priestley, M. J. N. (2001). Seismic Design of Circular Bridge Columns with Unstressed Prestressing Strand for Transverse Reinforcement.'' Research Rep. No. SSRP-2001/16, Dept. of Structural Engineering, Univ. of California at San Diego, San Diego. Federal Highway Administration 1995.

Cairns, J., and Arthur, P. D. (1979). Strength of Lapped Splices in Reinforced Concrete Columns. ACI Journal Proceedings, 76(2). https://doi.org/10.14359/6947

Campione, G., Miraglia, N. and Papia, M. (2004). Strength and Strain Enhancements of Concrete Columns Confined with FRP Sheets. Structural Engineering and Mechanics, 18(6), pp.769-790.

Campbell, K. W. (1977). The Use of Seismotectonics in the Bayesian Estimation of Seismic Risk, Report UCLA-ENG-7744, School of Engineering and Applied Science, University of California, Los Angeles, CA

Chai, Y. H., Priestley, M. J. N., and Seible, F. (1994). Analytical Model for Steel-Jacketed RC Circular Bridge Columns. ASCE Journal of Structural Engineering, 120(8), 2358–2376.

Chai, Y. H., Priestley, M. J. N., and Seible, F. (2008). Seismic Retrofit of Rectangular Bridge Columns by Steel Jacketing. In Third Bridge Engineering Conference: Papers Presented at the Third Bridge Engineering Conference, March 10-13, 1991, Denver, Colorado (pp. 95–103).

Chaudhary, M.T.A., Abé, M. and Fujino, Y. (2001). Performance Evaluation of Base-isolated Yama-agé Bridge with High Damping Rubber Bearings using Recorded Seismic Data. Engineering Structures, 23(8), pp.902-910.

Chen, Y.H., Liao, W.H., Lee, C.L. and Wang, Y. P. (2006). Seismic Isolation of Viaduct Piers by Means of a Rocking Mechanism. Earthquake Engineering and Structural Dynamics, 35(6), pp.713-736.

Cheng, C. T. and Mander, J. B. (1997). Seismic Design of Bridge Columns based on Control and Repairability of Damage.

Chopra, A. K., and Yim, C. (1985). Simplified earthquake analysis of structures with foundation uplift. Journal of Structural Engineering, ASCE, 111 (4): 906-930.

Ciampoli, M. and Pinto, P. E., (1995). Effects of Soil-Structure Interaction on Inelastic Seismic Response of Bridge Piers. Journal of structural engineering, 121(5), pp.806-814.

Clague, J. J. (1997). Evidence for Large Earthquakes at the Cascadia Subduction Zone. Reviews of Geophysics, v. 35, p. 439-60.

Deng, L., Kutter, B. L., and Kunnath, S. K. (2012). Centrifuge Modeling of Bridge Systems Designed for Rocking Foundations. Journal of Geotechnical and Geoenvironmental Engineering, ASCE, 138(3): 335–344.

Deng, L., Kutter, B.L, and Kunnath, S. (2014). Seismic Design of Rocking Shallow Foundations: A Displacement-Based Methodology.” Journal of Bridge Engineering, ASCE.

Drosos, V., Georgarakos, T., Loli, M., Anastasopoulos, I., Zarzouras, O., and Gazetas, G. (2012). Soil-Foundation-Structure Interaction with Mobilization of Bearing Capacity: An Experimental Study on Sand. Journal of Geotechnical Geoenvironmental Engineering, ASCE, 138(11): 1369-1386.

ElGawady, M., Endeshaw, M., McLean, D., and Sack, R. (2010). Retrofitting of Rectangular Columns with Deficient Lap Splices. Journal of Composites for Construction, 14(1), 22–35.

Elghazouli, A. Y. (2009). Seismic Design of Buildings to Eurocode 8, Spon Press.

Faccioli, E., Vanini, M. and Paolucci, R. (1999). TRISEE: 3D Site Effects and Soil-Foundation Interaction in Earthquake and Vibration Risk Evaluation. European commission. Directorate-General 12. Science, Research and Development.

Fraino, M., Ventura, C. E., Liam Finn, W.D. and Taiebat, M. (2012). September. Seismic Soil-Structure Interaction Effects in Instrumented Bridges. In Proceedings of the 15th World Conference on Earthquake Engineering (pp. 1-10). Portuguese Association for Earthquake Engineering.

Flück, P., Hyndman, R.D. and Wang, K., (1997). Three-Dimensional Dislocation Model for Great Earthquakes of the Cascadia Subduction Zone. Journal of Geophysical Research: Solid Earth, 102(B9), pp.20539-20550.

Gabriele, G., Restrepo, J. I., Vervelidis, A., and Massari, M. (2015). Self-Centering Precast Concrete Dual-Steel-Shell Columns for Accelerated Bridge Construction: Seismic Performance, Analysis, and Design. Report No. PEER 2015 13.

Gajan, S., Kutter, B. L., Phalen, J. D., Hutchinson, T. C., Martin, G. R. (2005). "Centrifuge Modeling of Load-Deformation Behavior of Rocking Shallow Foundations." Soil Dynamics and Earthquake Engineering, 25, 773–783.

Gajan, S. and Kutter, B. (2008). Capacity, Settlement, and Energy Dissipation of Shallow Footings Subjected to Rocking," Journal of Geotechnical and Geoenvironmental Engineering ASCE 135(3), 407–420.

Galal, K., Arafa, A., and Ghobarah, A. (2005). Retrofit of RC Square Short Columns. Engineering Structures, 27(5), 801–813.

Gallipoli, D., Wheeler, S.J. and Karstunen, M., (2003). Modelling the Variation of Degree of Saturation in a Deformable Unsaturated Soil. Géotechnique, 53(1), pp.105-112.

Gamble, W. L., Hawkins, N. M., and Kaspar, I. I. (1996). Seismic Retrofitting Experience and Experiments in Illinois. Proc. 5th National Workshop on Bridge Research in Progress, National Center for Earthquake Engineering Research (NCEER), State Univ. of New York at Buffalo, Buffalo, N.Y., 245–250.

Gavras, A. G., Antonellis, G., Panagiotou, M., and Kutter, B. L. (2015). Analytical and Experimental Development of Bridges with Foundations Allowed to Uplift Part II: Analytical Studies" Technical report, State of California, Department of Transportation.

Gazetas, G., and Mylonakis, G. (2001). "Soil–Structure Interaction Effects on Elastic and Inelastic Structures." In Fourth International Conference on Recent Advances in Geotechnical Earthquake Engineering and Soil Dynamics. Symposium in Honor of Professor WD Liam Finn, 1–13. Paper No. SOAP 2, San Diego, California, University of Missouri-Rolla.

Gazetas, G., Apostolou, M. and Anastasopoulos, J. (2003). Seismic Uplifting of Foundations on Soft Soils, with Examples from Adapazari (Izmit 1999 Earthquake). Proc. of BGA International Conference on Foundations: Innovations, observations, design and practice, Dundee. 37-49.

Gazetas, G. (2019). Benefits of Unconventional Seismic Foundation Design. BGS 59th Rankine Lecturer, https://www.youtube.com/watch?reload=9&v=pOXzqjTo34o&feature=youtu.be.

Girard, C., and Bastien, J. (2002). Finite-Element Bond-Slip Model for Concrete Columns under Cyclic Loads. ASCE Journal of Structural Engineering, 128(12), 1502–1510.

Goksu, C., Yilmaz, H., Chowdhury, S. R., Orakcal, K., and Ilki, A. (2014). The Effect of Lap Splice Length on the Cyclic Lateral load Behavior of RC Members with Low-Strength Concrete and Plain Bars. Advances in Structural Engineering, 17(5), 639–658.

Goldfinger, C., C. H. Nelson, and J. E. Johnson. (2003). Holocene Earthquake Records from the Cascadia Subduction Zone and Northern San Andreas Fault based on Precise Dating of Offshore Turbidites. Annual Reviews of Earth and Planetary Sciences, v. 31, p. 555-77

Guerrini, G. and Restrepo, J.I. (2011). Advanced Precast Concrete Dual-Shell Steel Columns. Proc. of the 8th International Conference on Urban Earthquake Engineering (Vol. 1, pp. 1125-1129).

Hakhamaneshi, M. (2014). Rocking Foundations for Building Systems-Effect of Footing Shape, Soil Environment, Embedment and Normalized Moment-to-Shear Ratio. PhD Dissertation, University of California, Davis, CA, USA.

Harajli, M. H. (2008). Seismic Behavior of RC Columns with Bond-Critical Regions: Criteria for Bond Strengthening Using External FRP Jackets. Journal of Composites for Construction, 12(1), 69–79.

Harajli, M. H. (2009). Bond Stress-Slip Model for Steel Bars in Unconfined or Steel, FRC, or FRP Confined Concrete under Cyclic Loading. ASCE Journal of Structural Engineering, 135(5), 509–518.

Haroun, M. A., and Elsanadedy, H. M. (2005). Fiber-Reinforced Plastic Jackets for Ductility Enhancement of Reinforced Concrete Bridge Columns with Poor Lap-Splice Detailing. ASCE Journal of Bridge Engineering, 10(6), 749–757.

Harries, K. A., Ricles, J. R., Pessiki, S., and Sause, R. (2006). Seismic Retrofit of Lap Splices in Non-ductile Columns Using CFRP Jackets. ACI Structural Journal, 103(6), 874–884. https://doi.org/10.14359/18242

Higgins, C. C., Knudtsen, J., Amneus, D., and Barker, L. (2017). Shear and Flexural Strengthening of Reinforced Concrete Beams with Titanium Alloy Bars. Proceedings of the 2nd World Congress on Civil, Structural, and Environmental Engineering (CSEE'17), 1–8.

Housner, G. W. (1956). Limit Design of Structures to Resist Earthquakes. Proc. of World Conference on Earthquake Engineering, Earthquake Engineering, Research Institute, University of California, Berkeley.

Housner, G. W. (1963) The Behavior of Inverted Pendulum Structures during Earthquakes. Bulletin of the Seismological Society of America 53(2), 404–417.

Huckelbridge, A. A. and Clough, R. W. (1978). Seismic Response of Uplifting Building Frame. Journal of the Structural Division, 104(8), pp.1211-1229.

Huckelbridge, A. A. and Ferencz, R. M. (1981). Overturning Effects on Stiffened Building Frames," Earthquake Engineering and Structural Dynamics 9(1), 69–83.

Hung, H., Liu, K., Ho, T., and Chang, K. (2011). An Experimental Study on the Rocking Response of Bridge Piers with Spread Footing Foundations," Earthquake Engineering and Structural Dynamics 40(7), 749–769.

Ozcebe, G., and Saatcioglu, M. (1987). Confinement of Concrete Columns for Seismic Loading. ACI Structural Journal. https://doi.org/10.14359/1660

Kawashima, K. and Nagai, T. (2006). Effectiveness of Rocking Seismic Isolation on Bridges. Proc. 4th International Conference on Earthquake Engineering (pp. 12-13). National Center for Research on Earthquake Engineering of Taiwan.

Kawashima, K. and Nagai, T. (2006). Effectiveness of rocking seismic isolation on bridges. In 4th International Conference on Earthquake Engineering, National Center for Research on Earthquake Engineering of Taiwan (pp. 12-13).

Kent, D. C., and Park, R. (1971). Flexural Members with Confined Concrete. ASCE Journal of Structural Division, 97(7), 1969–1990.

Khalili, N. and Khabbaz, M.H. (1998). A Unique Relationship for χ for the Determination of the Shear Strength of Unsaturated soils. Geotechnique, 48(5), pp.681-687.

Khalili, N., Geiser, F. and Blight, G. E. (2004). Effective Stress in Unsaturated Soils: Review with New Evidence. International Journal of Geomechanics, 4(2), pp.115-126.

Khosravi, A. and McCartney, J. S. (2012). Impact of Hydraulic Hysteresis on the Small-Strain Shear Modulus of Low Plasticity Soils. Journal of Geotechnical and Geoenvironmental Engineering, 138(11), pp.1326-1333.

Knudtsen, J. (2016). Shear Strengthening Reinforced Concrete Bridge Girders Using Near-Surface Mounted Titanium Alloy Bars. M.Sc. Thesis, Oregon State University, Corvallis, OR.

Kutter, B.L., Moore, M., Hakhamaneshi, M. and Champion, C. (2016). Rationale for Shallow Foundation Yocking Provisions in ASCE 41-13. Earthquake Spectra, 32(2), pp.1097-1119.

Kutter, B. L., Hutchinson, T. C, Aschheim, M., Kunnath, S., Liu, W., and Hakhamaneshi, M. (2011). Design of Soil and Structure Compatible Yielding to Improve System Performance. 2011 NSF Engineering Research and Innovation Conference, Atlanta, GA, Jan 4-7.

Kramer, M. H. (2004). Slab, Beam, and Girder Bridges in Oregon. Technical report, State of Oregon, Department of Transportation.

Krish, Z.F., Kowalsky, M.J., Nau, J.M. and Seracino, R., (2018). Repair of Reinforced Concrete Bridge Columns via Plastic Hinge Relocation, Volume 1: Repair Using Conventional Materials (No. Report No. 4000 (142)).

Liu, W., Hutchinson, T. C., Kutter, B. L., Hakhamaneshi, M., Aschheim, M. A. and Kunnath, S. K. (2013). Demonstration of Compatible Yielding between Soil-Foundation and Superstructure Components. Journal of Structural Engineering, 139(8), pp.1408-1420.

Lu, N. and Likos, W. J. (2006). Suction Stress Characteristic Curve for Unsaturated Soil. Journal of Geotechnical and Geoenvironmental Engineering, 132(2), pp.131-142.

Lu, N., Godt, J. W., and Wu, D. T. (2010). A Closed-Form Equation for Effective Stress in Unsaturated Soil. Water Resources Research, 46(5).

Lukose, K., Gergely, P., and White, R. N. (1982). Behavior of Reinforced Concrete Lapped Splices for Inelastic Cyclic Loading. Journal of American Concrete Institute, 79(5), 355–365.

Lynn, A. C., Moehle, J. P., Mahin, S. A., and Holmes, W. T. (1996). Seismic Evaluation of Existing Reinforced Concrete Building Columns. Earthquake Spectra, 12(4), 715–739.

Malhotra, S. (2007). Foundation Considerations for Seismic Retrofit of Bridges. Proc. Ninth Canadian Conference on Earthquake Engineering, June, Ottawa, Ontario, Canada.

Mander, J. B., Priestley, M. J. N., and Park, R. (1988). Observed Stress-Strain Behavior of Confined Concrete. ASCE Journal of Structural Engineering, 114(8), 1827–1849.

McLean, D. I. and Marsh, M. L. (1999). Seismic Retrofitting of Bridge Foundations. Structural Journal, 96(2), pp.174-182.

Meek, J. W. (1978). Dynamic Response of Tipping Core Buildings.” Earthquake Engineering and Structural Dynamics. Volume 6: 437-454.

Melek, M., and Wallace, J. W. (2004). Performance of Columns with Short Lap Splices. In 13th World Conference on Earthquake Engineering Vancouver, B.C., Canada August 1-6, 2004

Mergos, P. E. and Kawashima, K. (2005). Rocking Isolation of a Typical Bridge Pier on Spread Foundation. Journal of Earthquake Engineering, 9(sup2), pp.395-414.

Mitchell, C. E., Vincent, P., Weldon, R. J., and Richards, M. A. (1994). Present-Day Vertical Deformation of the Cascadia Margin, Pacific Northwest, United States. Journal of Geophysical Research, v. 99, p. 12, 257-12, 277

Mylonakis, G. and Gazetas, G. (2000). Seismic Soil-Structure Interaction: Beneficial or Detrimental?. Journal of Earthquake Engineering, 4(3), pp.277-301.

Nako, A., Shike, C., Six, J., Johnson, B., Dusicka, P., and Selamawit, M. (2009). Seismic Vulnerability of Oregon State Highway Bridges: Mitigation Strategies to Reduce Major Mobility Risks. Salem, OR: Oregon Department of Transportation, Bridge Engineering Section.

Nako, A., Shike, C., Six, J., Johnson, B., Dusicka, P., and Selamawit, M. (2014). Oregon Highways Seismic Plus Report. Salem, OR: Oregon Department of Transportation, Bridge and Geo-Environmental Sections.

National Earthquake Hazards Reduction Program (NEHRP) (2004). Recommended Seismic Design Criteria for New Steel Moment-frame Buildings, FEMA-273, Federal Emergency Management Agency, Washington, DC, USA.

Negro, P., Paolucci, R., Pedretti, S., and Faccioli, E. (2000). Large-Scale Soil–Structure Interaction Experiments on Sand under Cyclic Load. Proc. of the 12th World Conference on Earthquake Engineering, Auckland, New Zealand.

Palermo, A. and Mashal, M. (2012). Accelerated Bridge Construction (ABC) and seismic damage resistant technology. Bulletin of the New Zealand Society for Earthquake Engineering, 45(3), pp.123-134.

Paulay, T. (1982). Lapped Splices in Earthquake-Resisting Columns. Journal of American Concrete Institute, 79(6), 458–469.

Paulay T., and Priestley M. J. N. (1992). Seismic Design of Reinforced Concrete and Masonry Buildings. John Wiley and Sons, New York,

Pecker, A. (2003). “Aseismic foundation design process, lessons learned from two major projects: the Vasco de Gama and the Rion Antirion bridges,” in ACI Int. Conf. Seismic Bridge Design and Retrofit (La Jolla: University of California at San Diego).

Peterson, M. D. and Frankel, A. D. (2000), Deep Intraslab Earthquakes and How They Contribute to Seismic Hazard in the Pacific Northwestern U.S., Intraslab Earthquakes Workshop Abstracts, September 18–21, 2000, Victoria, B. C., To be published as U.S. Geological Survey Open-File Rept.

Petersen, M. D., Cramer, C. H., and Frankel, A. D. (2002). Simulations of Seismic Hazard for the Pacific Northwest of the United States from Earthquakes Associated with the Cascadia Subduction Zone. In Earthquake Processes: Physical Modelling, Numerical Simulation and Data Analysis Part I (pp. 2147-2168). Birkhäuser, Basel.

Phipps, J. N., Ashlock J.C., and Sritharan, S. (2012). Experimental Results of Foundation Rocking on a Natural Clay Deposit. Proc. of the 15th World Conference on Earthquake Engineering, Lisbon, Portugal.

Phipps, J. N. (2013). Experimental and Numerical Investigation of Dynamic Rocking Foundation Behavior, M.Sc. Thesis, Iowa State University, USA.

Priestley, M. J. N., Evison, R. J. and Carr, A. J. (1978). Seismic Response of Structures Free to Rock on their Foundations. Bulletin of the New Zealand National Society for Earthquake Engineering, 11(3), pp.141-150.

Priestley, M. J. N., Verma, R., and Xiao, Y. (1995). Seismic Shear Strength of Reinforced Concrete Columns. ASCE Journal of Structural Engineering, 120(8), 2310–2329.

Priestley, M. J. N., Seible, F., and Calvi, G. M. (1996). Seismic Design and Retrofit of Bridges, John Wiley and Sons, New York, NY.

Psycharis, I. N. and Jennings, P. C. (1983). Rocking of slender rigid bodies allowed to uplift. Earthquake Engineering and Structural Dynamics, 11(1), pp.57-76.

Ralls, M.L., Tang, B., Bhide, S., Brecto, B., Calvert, E., Capers, H., Dorgan, D., Matsumoto, E., Napier, C., Nickas, W., Russell, H. (2005). "Prefabricated Bridge Elements and Systems in Japan and Europe". Federal Highway Administration, FHWA-PL-05-003, March. United States.

Razvi, S. W. N., and Shaikh, M. G. (2018). Effect of Confinement on Behavior of Short Concrete Column. Procedia Manufacturing, 20(01), 563–570.

Reinhardt, E., Saiidi, M., and Siddharthan, R. (2003) Seismic Performance of a CFRP/Concrete Bridge Bent on Flexible Footings. Technical Report CCEER-03-4, Civil Engineering Department, University of Nevada, Reno, NV, August 2003.

Rosebrook K. R. (2001). Moment Loading on Shallow Foundations: Centrifuge Test Data Archives. M.Sc. Thesis. University of California at Davis, School of Engineering.

Saatcioglu, M., and Ozcebe, G. (1989). Response of Reinforced Concrete Columns to Simulated Seismic Loading. ACI Structural Journal, 86(1), 3–12.

Saatcioglu, M. and Yalcin, C., (2003). External Prestressing Concrete Columns for Improved Seismic Shear Resistance. Journal of Structural Engineering, 129(8), pp.1057-1070.

Sakellaraki, D.I.M.I.T.R.A. and Kawashima, K. (2006). Effectiveness of Seismic Rocking Isolation of Bridges based on Shake Table Test. Proc. First European Conf. on Earthquake Engineering and Seismology.

Sharma, K. (2019). Field Investigation and Performance-Based Seismic Design of Rocking Shallow Foundations in Cohesive Soil. PhD Dissertation, University of Alberta, Edmonton, Alberta, CA.

Shrestha, S. (2019). Seismic Retrofit of Square Reinforced Concrete Bridge Columns using Titanium Alloy Bars. PhD Dissertation, Oregon State University, Corvallis, OR.

Sivakumar, V. (1993). A Critical State Framework for Unsaturated Soil, PhD Dissertation, University of Sheffield).

Storie, L., Pender, M., Clifton, G., and Wotherspoon, L. (2014). Soil Foundation-Structure Interaction for Buildings on Shallow Foundations in the Christchurch Earthquake. Proc. of 10th NCEE, Anchorage, Alaska.

Sheikh, S. A., and Uzumeri, S. M. (1982). Analytical Model for Concrete Confinement in Tied Columns. ASCE Journal of Structural Division, 108(12), 2703–2722.

Taranu, N., Gabriel, O., Dorina, I., Ioana, E., Vlad, M., and Catalin, B. (2008). Fibre Reinforced Polymer Composites as Internal and External Reinforcements for Building Elements. Buletinul Institutului Politehnic din lasi. Sectia Constructii, Arhitectura, 54(1), p.7.

Valluvan, R., Kreger, M. E., and Jirsa, J. O. (1993). Strengthening of Column Splices for Seismic Retrofit on Non-ductile Reinforced Concrete Frames. ACI Structural Journal, 90(4), 432–433.

Vavra, E. (2016). Application of Titanium Alloy Bars for Strengthening Reinforced Concrete Bridge Girders in Flexure. M.Sc. Thesis, Oregon State University, Corvallis, OR.

Wang, D., Wang, Z., Yu, T., and Li, H. (2018). Seismic Performance of CFRP-Retrofitted Large-Scale Rectangular RC Columns Under Lateral Loading in Different Directions. Composite Structures, 192(3), 475–488.

Watson, S., Zahn, F. A., and Park, R. (1994). Confining Reinforcement for Concrete Columns. ASCE Journal of Structural Engineering, 120(6), 1798–1824.

Wong, I. G., Silva, W. J., and Madin, I. P. (1990). Preliminary Assessment of Potential Strong Earthquake Ground Shaking in the Portland, Oregon, Metropolitan Area. Oregon Geology, 52(6), 131-134. Flueck et al. 1997.

Xiao, Y., Priestley, M.N. and Seible, F. (1996). Seismic Assessment and Retrofit of Bridge Column Footings. Structural Journal, 93(1), pp.79-94.

Xiao, Y., and Ma, R. (1997). Seismic Retrofit of RC Circular Columns Using Prefabricated Composite Jacketing. ASCE Journal of Structural Engineering, 123(10), 1357–1364.

Yeats, R. (1998). Living with Earthquakes in the Pacific Northwest. Oregon Press

Zahn, F. A., Park, R., and Priestley, M. J. N. (1989). Strength and Ductility of Square Reinforced Concrete Column Sections Subjected to Biaxial Bending. ACI Structural Journal.

Zhang, G., Unjoh, S., Hoshikuma, J. I. and Sakai, J. (2000). Seismic Retrofit Techniques for Reinforced Concrete Bridge Columns with Combination of FRP Sheet and Steel Jacketing.

Zong-Cai, D., Daud, J.R. and Hui, L. (2014). Seismic Behavior of Short Concrete Columns with Prestressing Steel Wires. Advances in Materials Science and Engineering, 2014.

3.0 REVIEW OF THE ODOT BRIDGE INVENTORY

A study of the detailed structural drawings of the bridges along I-5, US-97 and OR-58 in the state of Oregon from the ODOT bridge database was performed by Shrestha (2019) to establish with the typical construction details that would reflect the pre-1970 bridge column design. This report summarizes and expands upon the database review by Shrestha (2019). On I-5 Oregon alone, 223 bridges were built prior to 1970s (i.e. before the adoption of modern seismic design provisions in the early 1990s), out of this population 69 bridges are supported on poorly detailed reinforced concrete (RC) square columns (most of them solely supported on square columns and some in combination with RC circular and rectangular columns). The number of these RC square columns was approximately 600 (Figure 3.1).

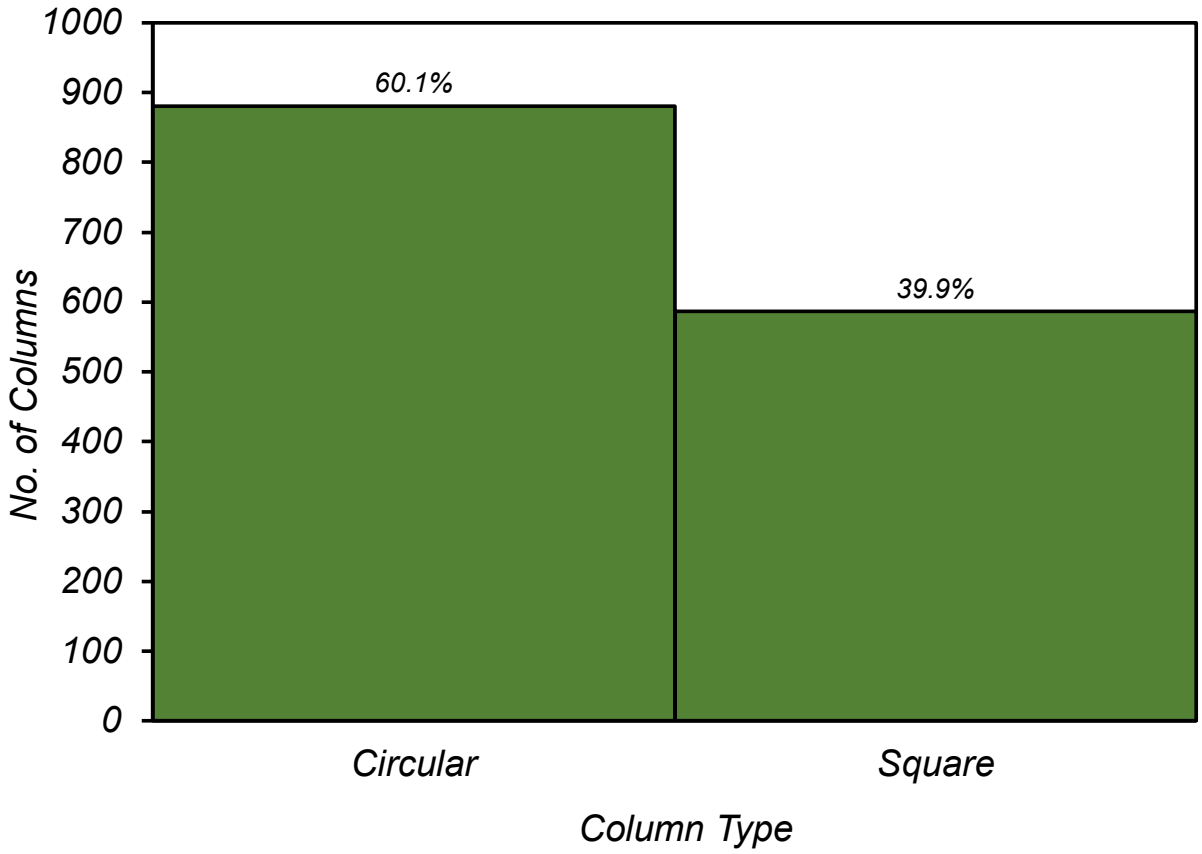

Figure 3.1: ODOT inventory column type distribution.

The RC square columns were then sorted and characterized in terms of their geometries (column dimension and clear height from footing top to the base of bent beam), material properties (concrete and reinforcing steel grade), longitudinal and transverse reinforcement details (reinforcing steel quantity, bar size, and bar type), details of bar splice at the column base (lap-splice length in terms of diameter of bar), axial load supported by each column (tributary weight from the super structure), foundation details (size, depth, and reinforcing steel details), and

foundation embedment depth. These characteristic details are summarized in the following sub-sections.

3.1 COLUMN DIMENSIONS

The most common column size is 24 in. x 24 in. (610 mm x 610 mm) square having a frequency of 55%, the second being 20 in. x 20 in. (508 mm x 508 mm) square with 25% frequency. The distribution of column section dimensions was grouped together using a bin size of 2 in. (50.8 mm) and is shown in Figure 3.2: ODOT inventory square column width distribution.

The column clear heights were measured from the bottom of the cap beam to the ground level or the top of footing in each column. The column heights were found to vary even in the same bridge depending on the gradient of the soil profile. The columns were thus treated individually to summarize the distribution of their clear height. Using a 3 ft (0.91 m) bin size, the mean clear height of the columns measured from the foundation top to the bottom of bent caps was 16 ft (4.88 m) with the mode being in the range of 15 ft (4.58 m) to 18 ft (5.49 m), as seen in Figure 3.3.

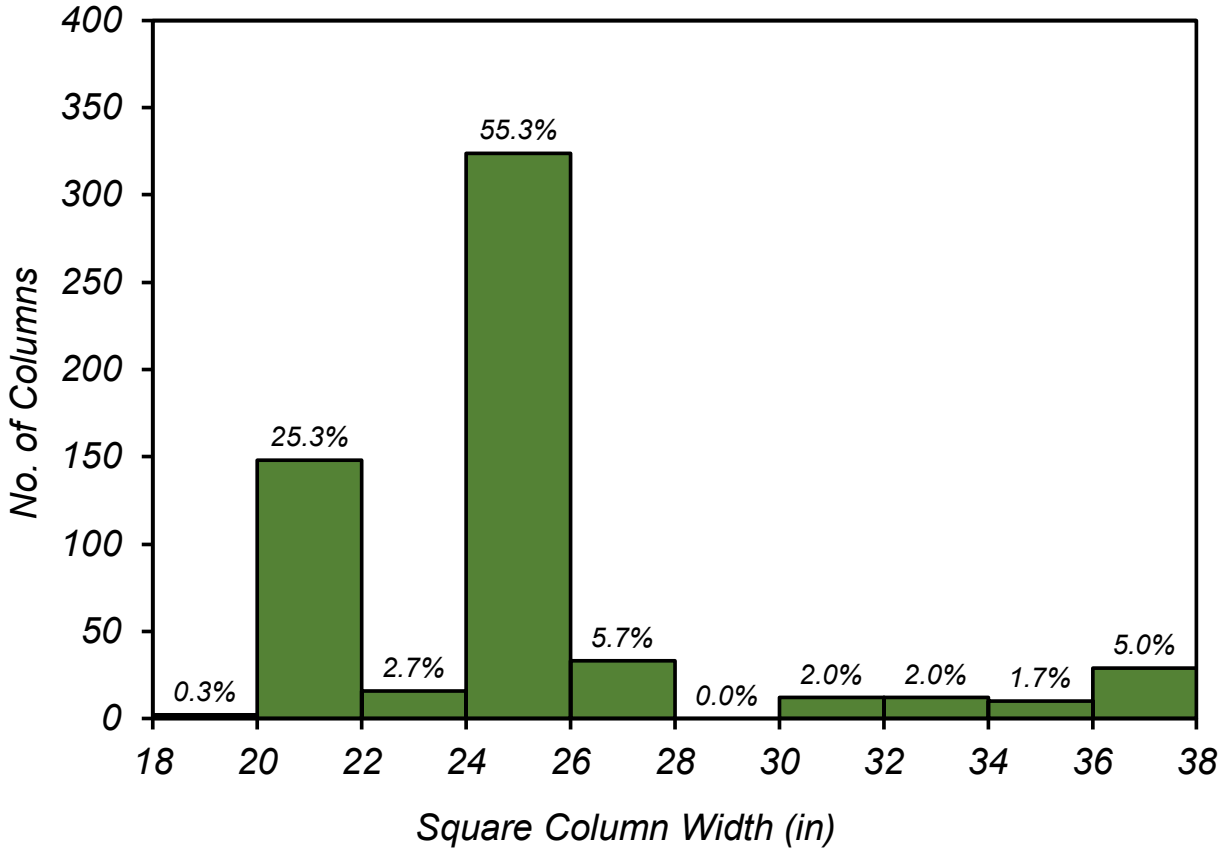

Figure 3.2: ODOT inventory square column width distribution.

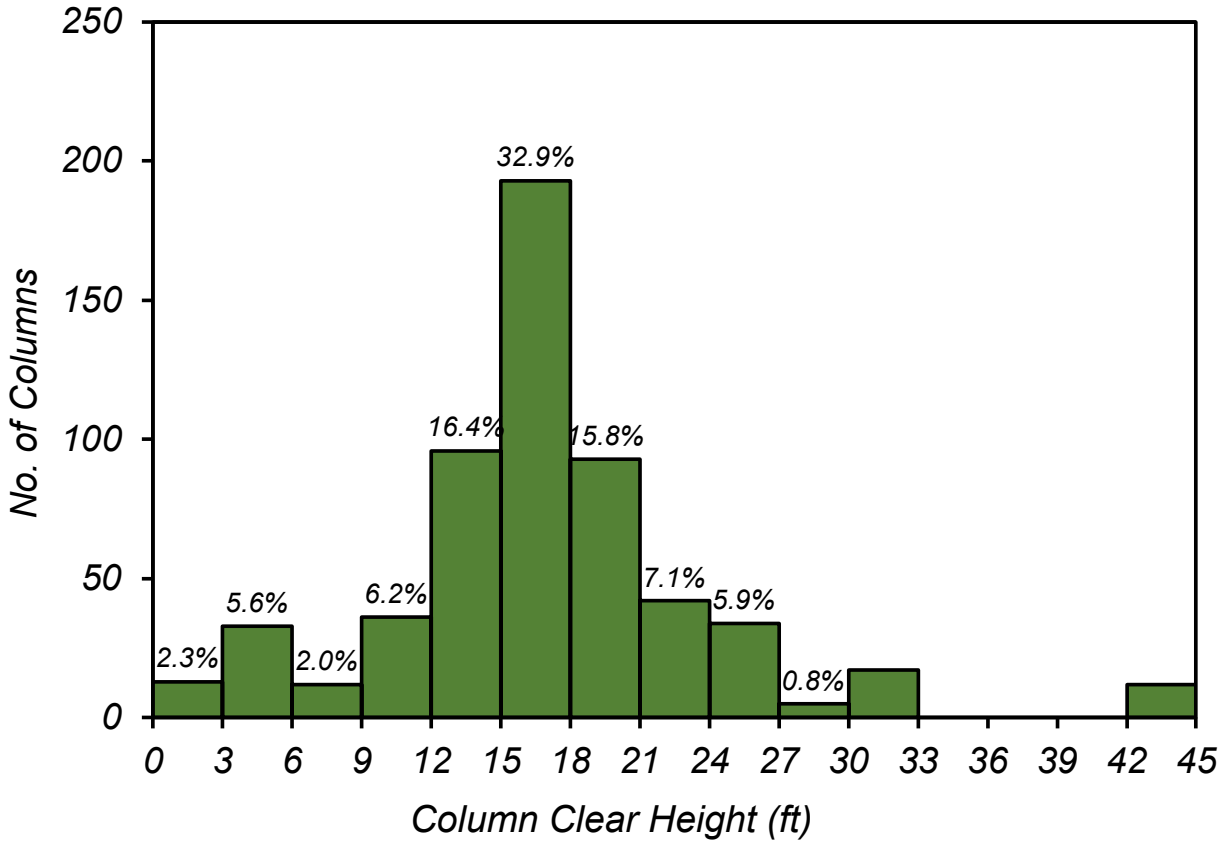

Figure 3.3: ODOT inventory square column clear height distribution.

3.2 REINFORCEMENT DETAILS

The majority of square columns were reinforced with only four longitudinal bars laid out in each corner and tied with square ties having 90˚ hook details. The most common longitudinal reinforcement was 1% of the gross area of column with the most common rebar size used being intermediate grade (Grade 40 equivalent) #11 (#36M) deformed bars. Some columns had square longitudinal rebar. The most common transverse reinforcement arrangement was intermediate grade (Grade 40 equivalent) #3 (#10M) square ties provided at 12 in. (305 mm) on center starting 6 in. (152 mm) from the top of footing. The mean transverse reinforcement ratio was found to be 0.09% of the column shear area. Distributions of the observed reinforcing details are shown in Figure 3.4 to Figure 3.7. It is noted the transverse reinforcement data are skewed and the median value is approximately 0.07%.

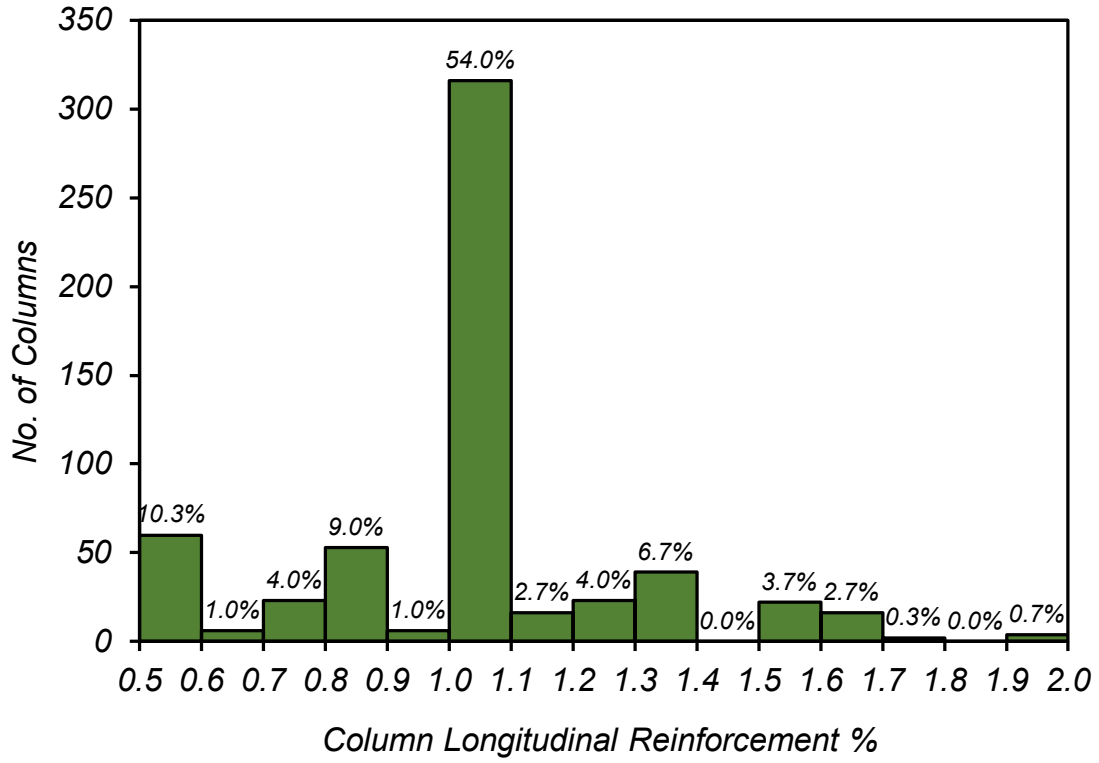

Figure 3.4: ODOT inventory column longitudinal reinforcement distribution.

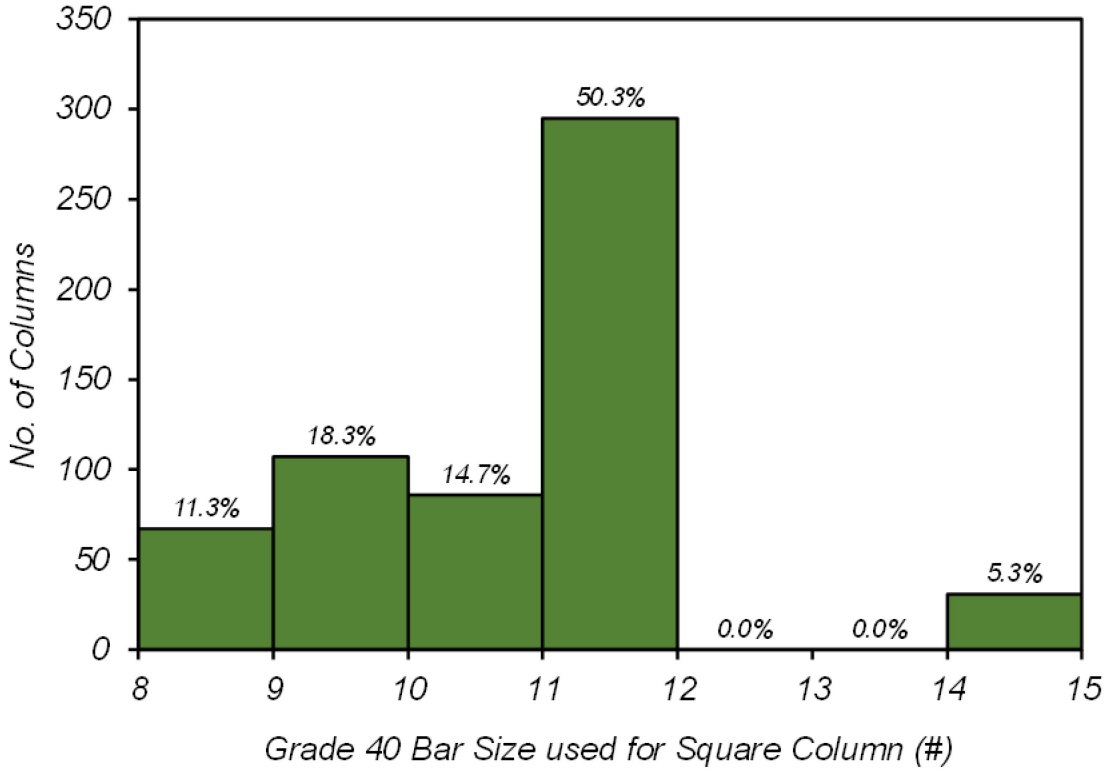

Figure 3.5: ODOT inventory column longitudinal reinforcement bar size distribution.

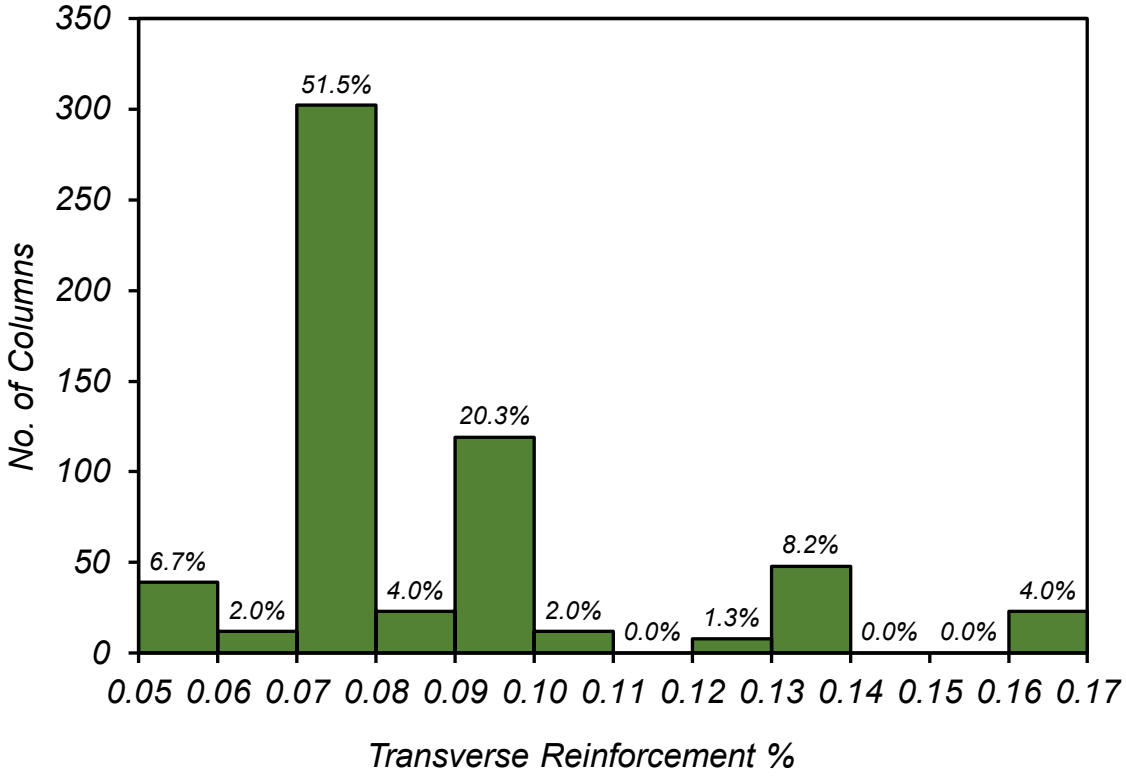

Figure 3.6: ODOT inventory column transverse reinforcement distribution.

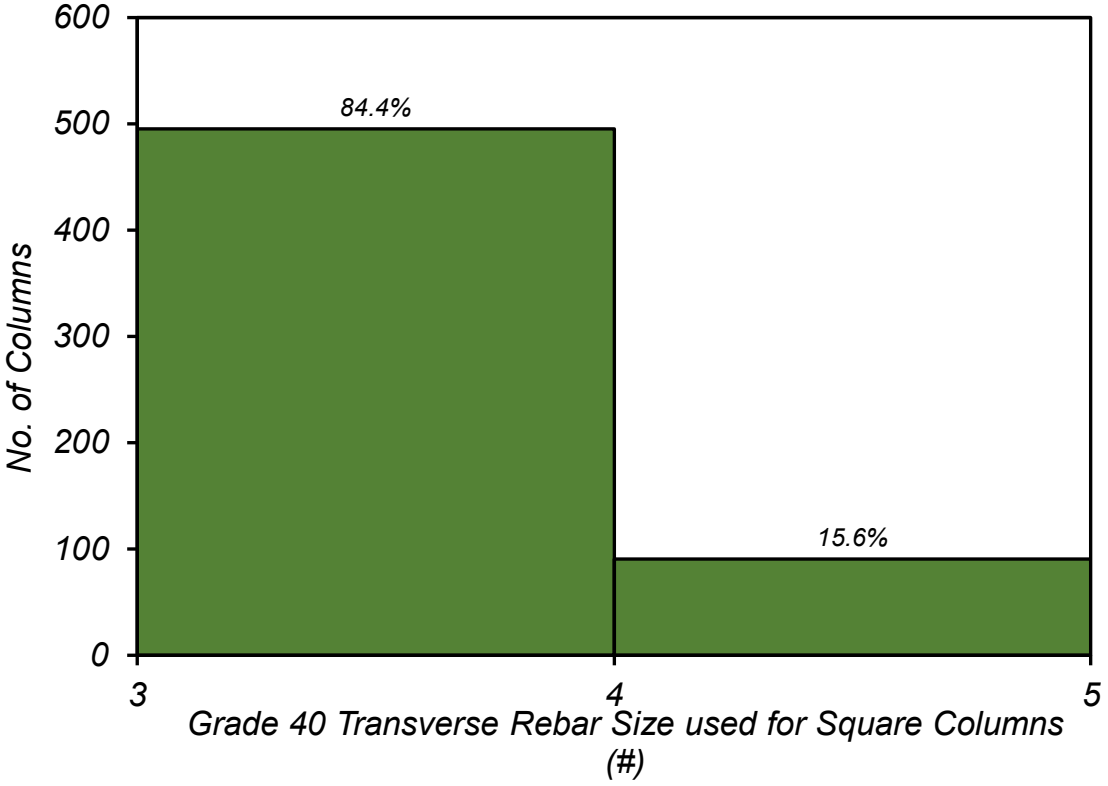

Figure 3.7: ODOT inventory column transverse reinforcement bar size distribution.

3.3 LONGITUDINAL SPLICE DETAIL

The column longitudinal bars were lap-spliced to the starter bars from the footing right above the footing (i.e., the base of the columns). The length of the starter bars measured from the top of the foundation (i.e. splice length) ranged from 24 in. (609 mm) to 60 in. (1524 mm) with no clear distribution pattern. The average lap-splice length was found to be 38.2 in. (970 mm; Figure 3.7). To observe the distribution of splice length in terms of the diameter of starter bars (d_b) (which is the same as that of vertical reinforcement in columns), histograms were generated for splice length in terms of d_b. Average value was found to be 28.9 times d_b with the modal value ranging from $24d_b$ to $27d_b$. Since the most common reinforcement bar type was Grade 40 #11 bars, the distribution of splice length in terms of #11 bar diameter was presented. The average splice length for #11 bars was found to be $29d_b$ with the modal value ranging from $33d_b$ to $36d_b$. Histograms of the longitudinal splice details observed from the database are shown in Figure 3.8 and Figure 3.9.

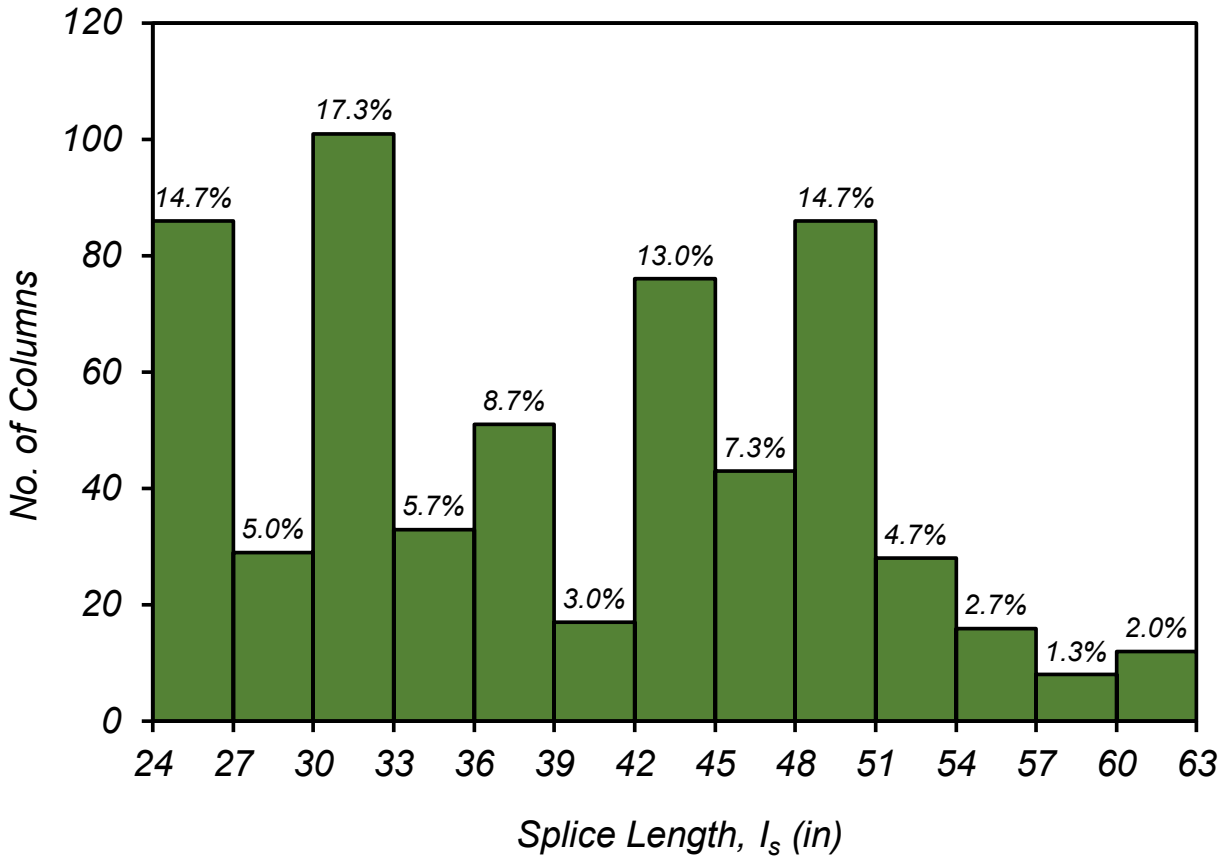

Figure 3.8: ODOT inventory splice length distribution.

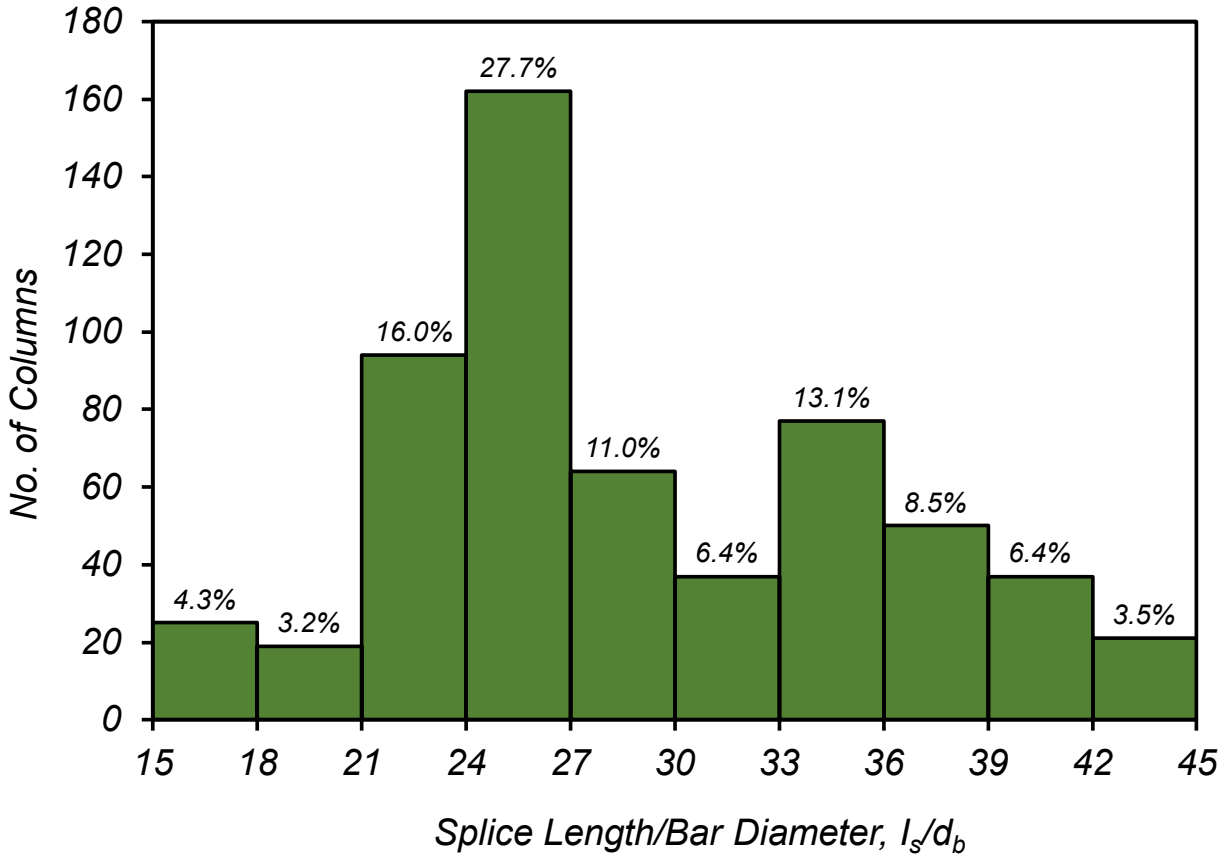

Figure 3.9: ODOT inventory splice length distribution in terms of bar diameter.

3.4 AXIAL LOAD

The number of square columns observed in a single bent across the bridge inventory is shown in Figure 3.10 and shows that most have either 2 or 4 columns per bent. Service-level axial loads in the columns produced by the weight of components (DC) and the weight of the wearing surface (DW) was calculated by distributing tributary weight of the superstructure to the bent columns and taking the load from the column with the largest load. A sample calculation of axial load based on structural drawings of a 1950's era reinforced concrete deck girder bridge located in Springfield, Oregon is shown below.

Table 3.1 Sample calculation of axial load for a column in a 1950s bridge located in Springfield, Oregon. The values used in this calculation are based on the structural drawings for the bridge.

Bridge Parameters			
Grade of Concrete	=	3,300	psi
Grade of Steel	=	40	ksi
Unit Weight of Concrete	=	150	psf
Unit Weight of Asphalt	=	145	pcf
Thickness of deck	=	6	in
Number of girders	=	5	
		ft	**in**
Deck width	=	30	0
Span (L1)	=	55	0
Span (L2)	=	55	0
Average Span (L)	=	55	0
Deck Load Calculation			
Thickness of deck	=	0.5	ft
Width of deck	=	30	ft
Length of deck	=	55	ft
Total weight of deck	=	123750	lb
	=	**124**	**kip**
Curb Load Calculation			
Height of curb	=	0.75	ft
Width of curb	=	1.5	ft
Length of curb	=	55	ft
Weight of one curb	=	9281	lb
Total weight of two (2) curbs	=	**19**	**kip**
Rail Load Calculation			
Height of rail	=	2	ft
Width of rail	=	0.67	ft
Length of rail	=	55	ft
Weight of one rail	=	11000	lb
Total weight of rail	=	**22**	**kip**
Girder Load Calculation			
Total depth of girder	=	5.39	ft
Depth excluding deck	=	4.89	ft
Width of girder	=	1.42	ft
Length of girder	=	55	ft
Weight of one girder	=	57271	lb
Total weight of 4 girders	=	**229**	**kip**
Asphalt Load Calculation			
Thickness of wearing	=	0.17	ft
Width of wearing	=	30	ft
Length of wearing	=	55	ft
Total weight of wearing	=	39875	lb
	=	**40**	**kip**
Total dead load per bent	=	433	kip
Number of columns per	=	2	
Axial load per column	=	**217**	**kip**

The average service-level axial load per column was calculated to be approximately 120 kips with the modal value ranging from 50 to 100 kips (222 to 444 kN). This was equivalent to an average axial stress of $0.055f_c'$ with the modal range $0.04f_c'$ to $0.05f_c'$. The distribution is shown in Figure 3.11.

Lostra (2016) used $0.1f_c'A_g$ as the constant axial load. For this research, $0.08f_c'A_g$ was applied as the axial load which is equivalent to 150 kips.

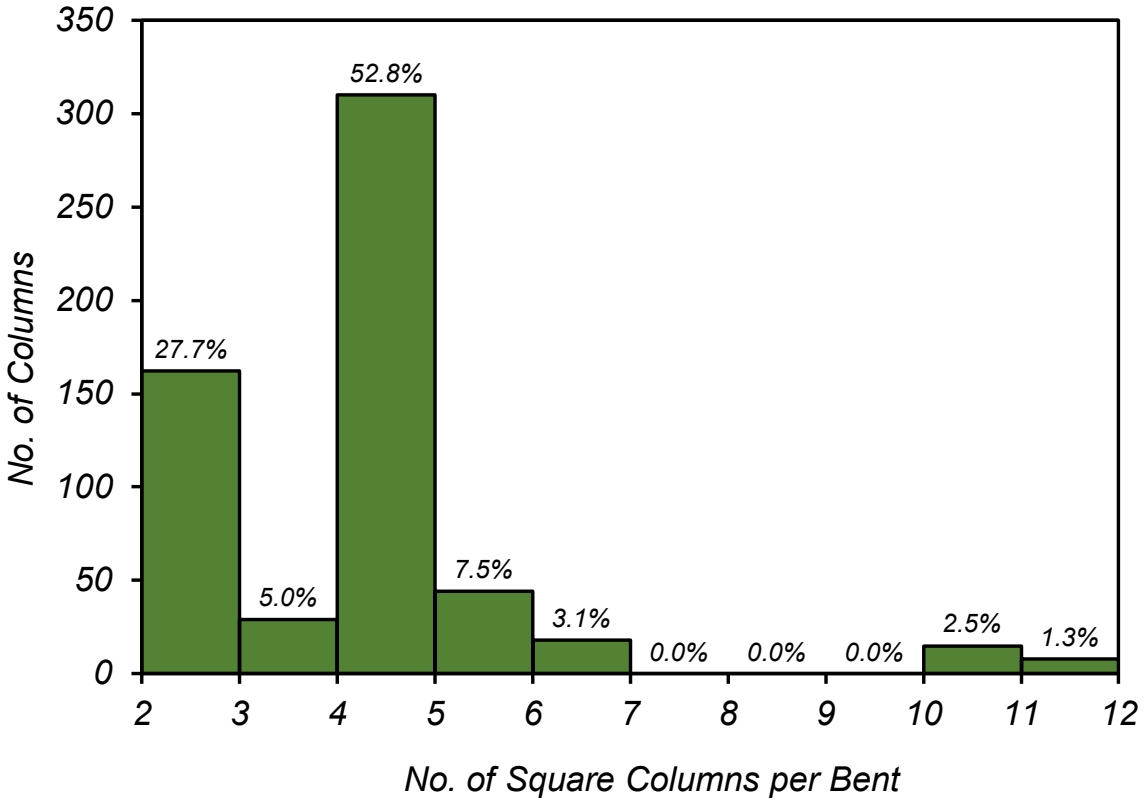

Figure 3.10: ODOT inventory square columns distribution per bent.

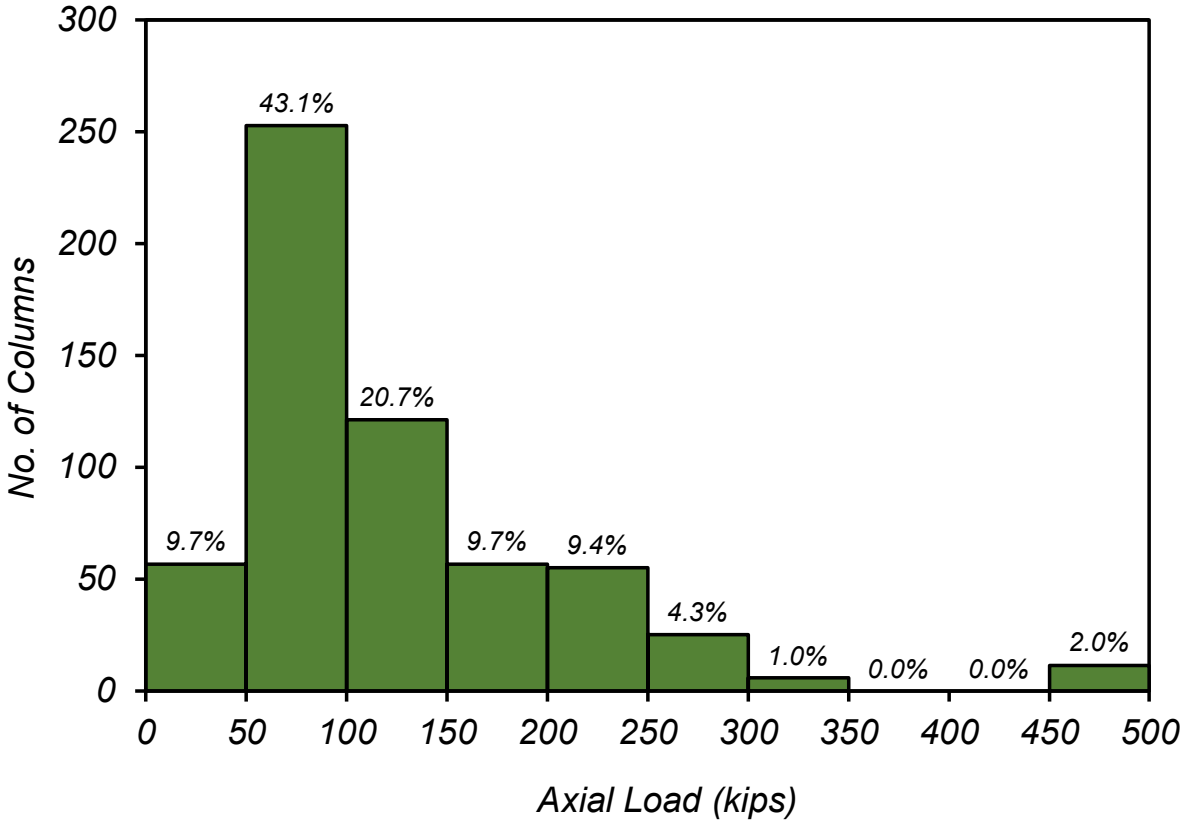

Figure 3.11: ODOT inventory square columns axial load distribution.

3.5 FOUNDATION DETAILS

Histograms of the relevant spread footing details are shown in Figure 3.12 to Figure 3.15. Histograms of the relevant pile supported foundation details are shown in Figures Figure 3.16 to Figure 3.19. The majority of square columns (79%) were found to be resting on RC spread footing and the rest (21%) on pile foundations. Of the pile foundations, 78% were built with 10 in. (254 mm) diameter timber piles (96% of the timber piles were found to be treated and the rest were untreated). Only 22% of the pile foundations were built with 10BP42 Steel Piles (AISC Steel Construction Manual, 1956). The piles were capped with a RC pile cap with 6 in. (152 mm) embedment on the timber pile into the pile cap without any supplemental connection. Both spread footings and pile caps are reinforced with a single mesh of reinforcement at the bottom with 3 in. (76 mm) of clear cover.

The most common size for both spread footings and the timber pile caps was 60 in. x 60 in. (1524 mm x 1524 mm) and the most common foundation depth for 60 in. x 60 in. (1524 mm x 1524 mm) spread footings and timber pile caps was 24 in. (609 mm). The most common timber pile size was 10 in. (254 mm) diameter. Both spread footings and pile caps were reinforced with a single mesh of reinforcement at the bottom with 3 in. (76 mm) of clear cover. The most common reinforcement used was Gr. 40 #5 (#16M) with average reinforcement of 0.21% in spread footings and 0.13% in timber pile caps.

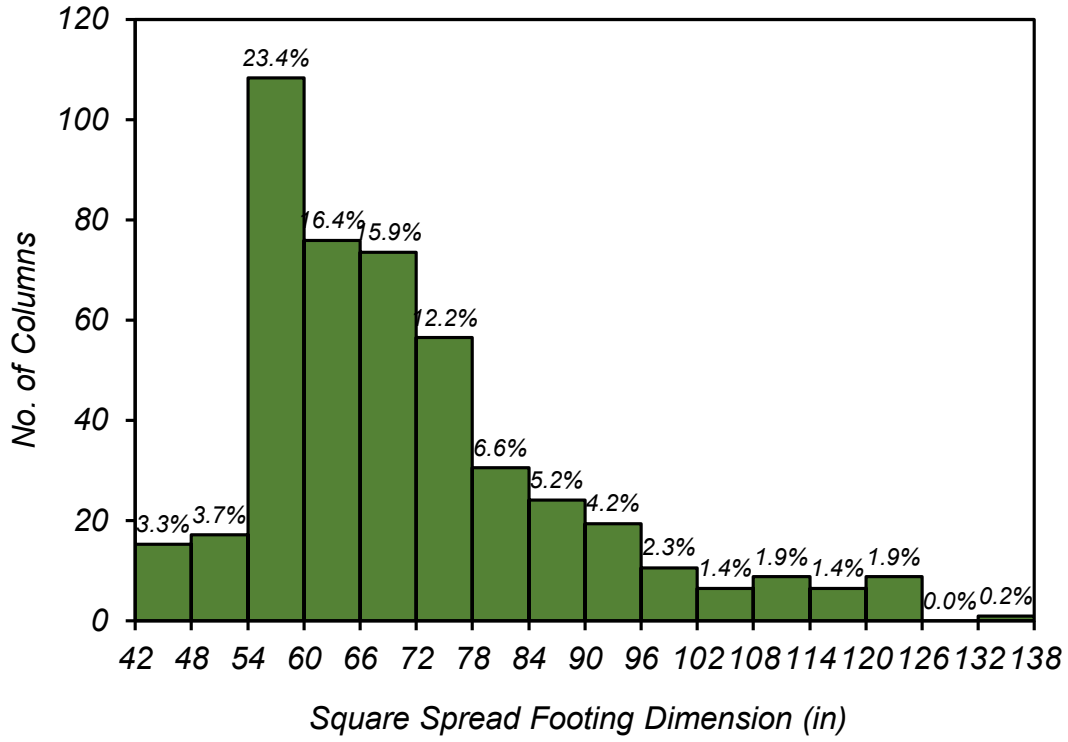

Figure 3.12: ODOT inventory square spread footing width distribution.

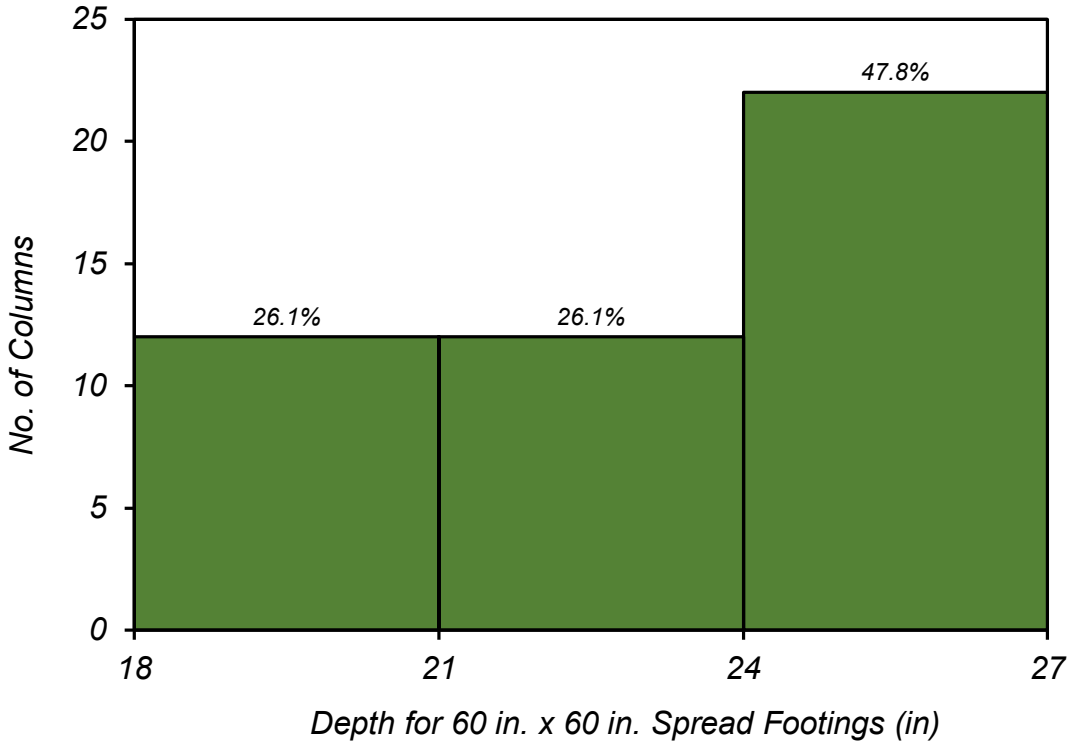

Figure 3.13: ODOT inventory foundation depth distribution for 60 in. x 60 in. spread footings.

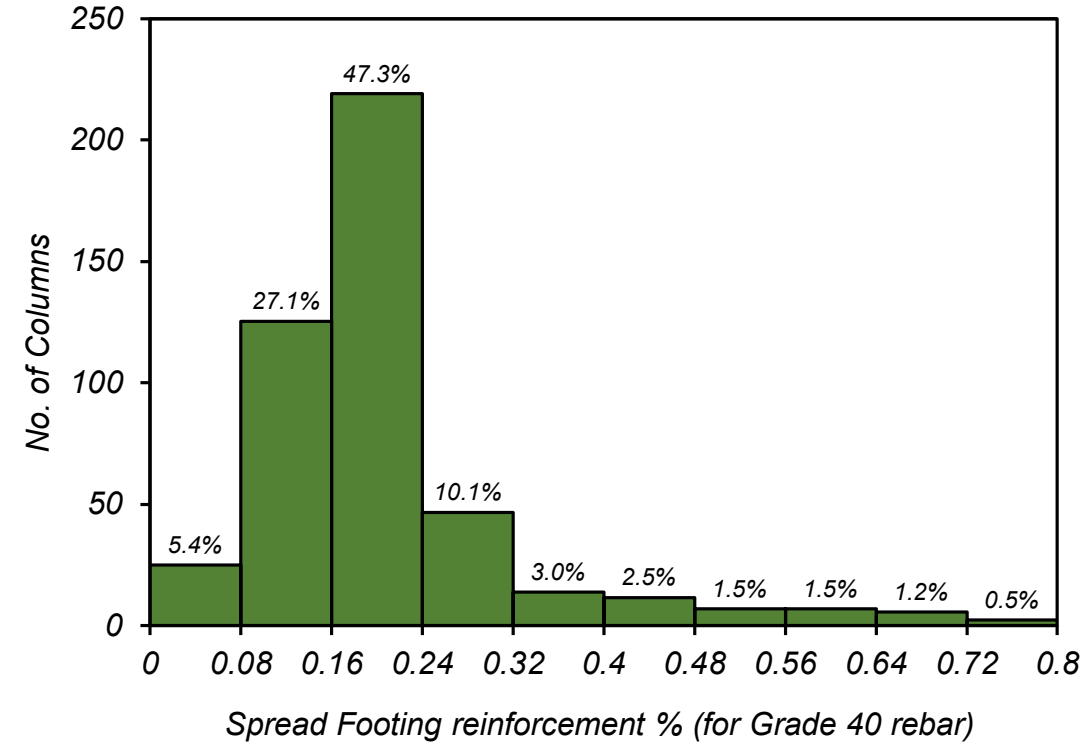

Figure 3.14: ODOT inventory spread footing reinforcement distribution.

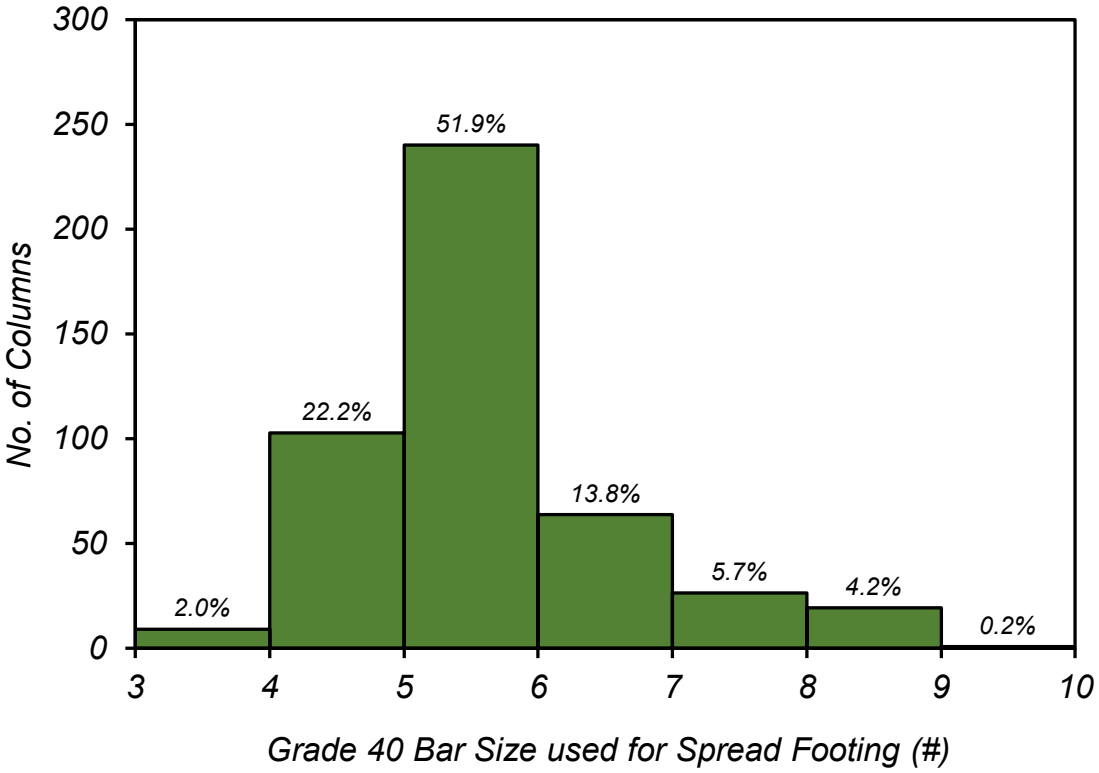

Figure 3.15: ODOT inventory spread footing reinforcement bar size distribution.

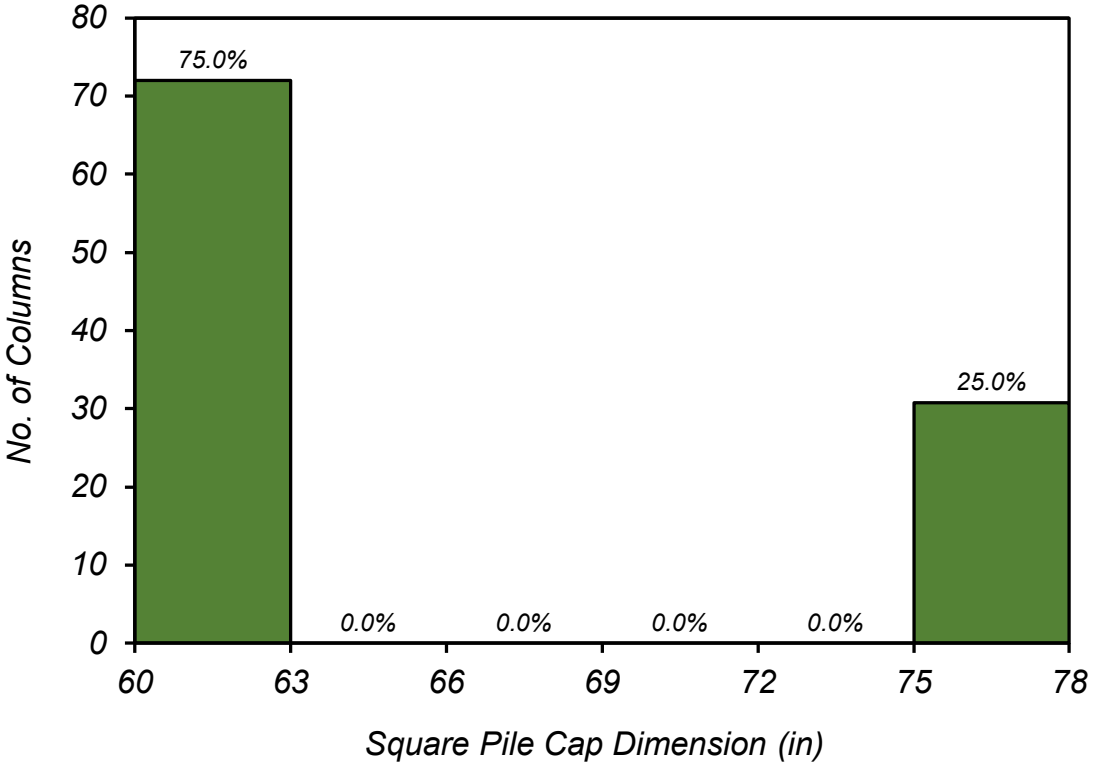

Figure 3.16: ODOT inventory square pile cap width distribution.

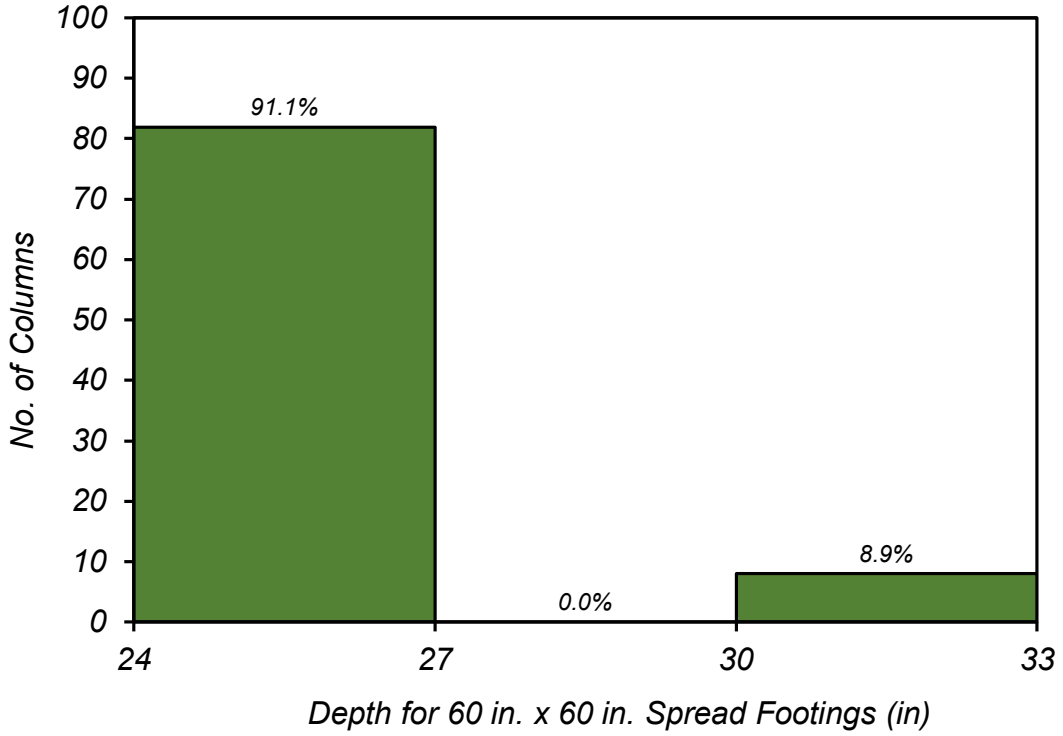

Figure 3.17: ODOT inventory depth distribution for 60 in. x 60 in. pile caps.

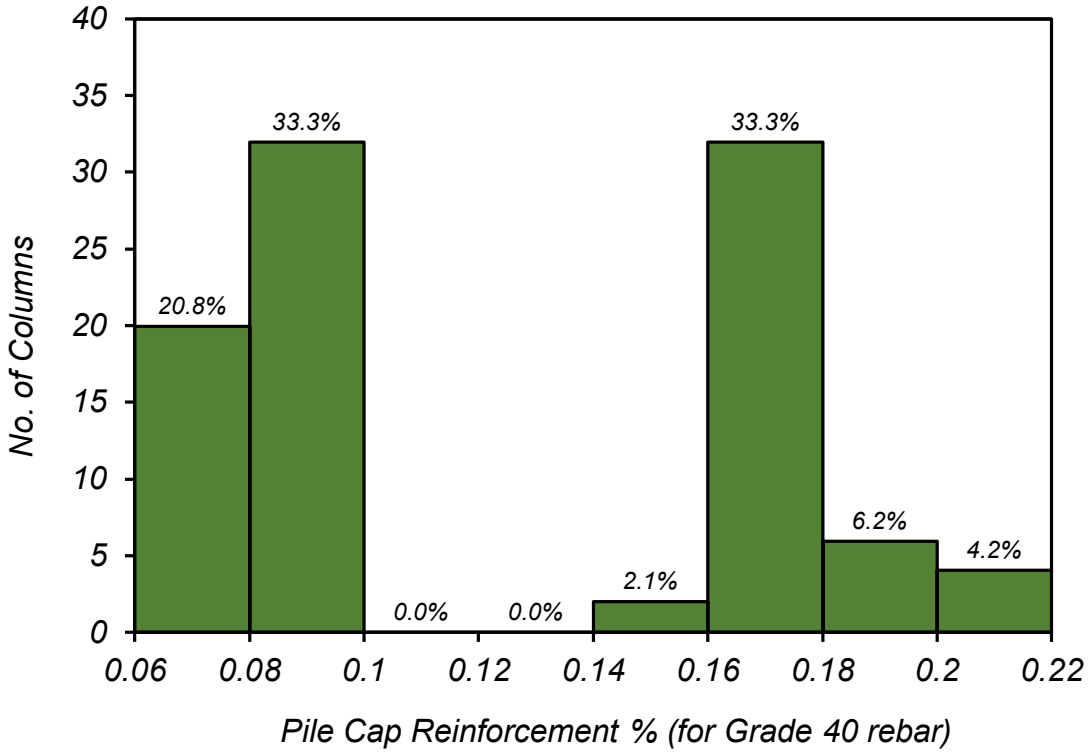

Figure 3.18: ODOT inventory pile cap reinforcement distribution.

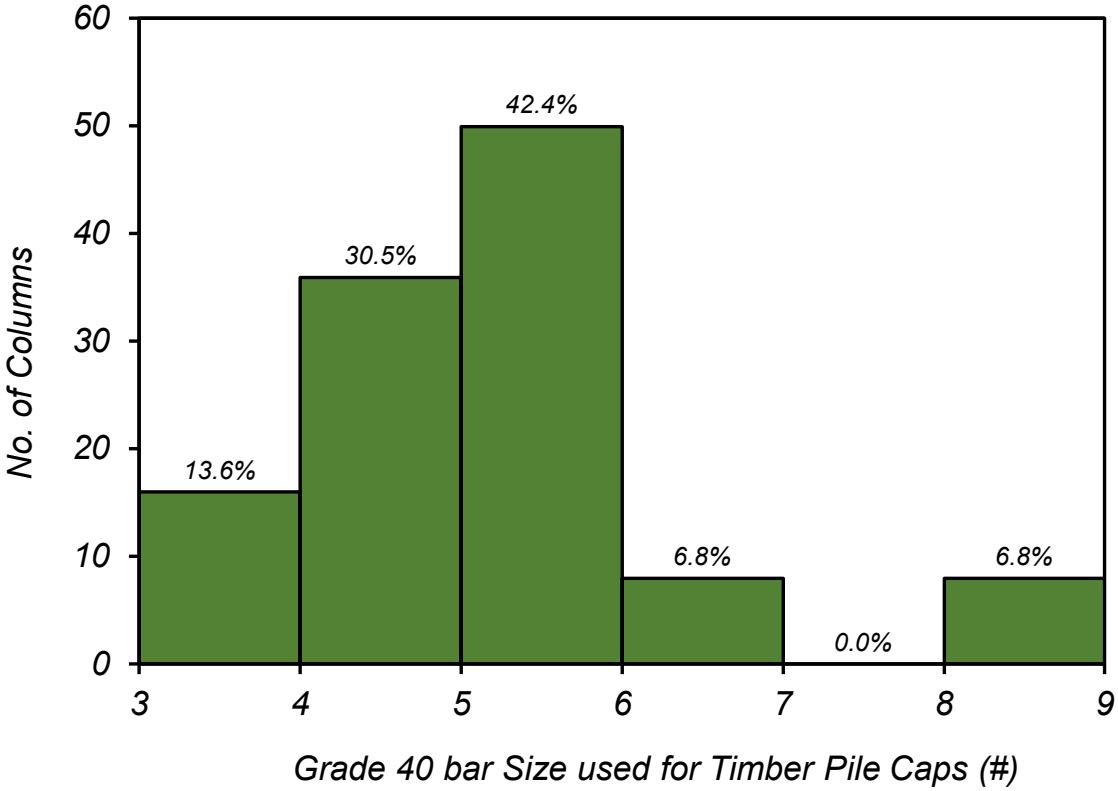

Figure 3.19: ODOT inventory pile cap reinforcement bar size distribution.

3.6 Foundation Embedment Depth

Figure 3.20 displays the histogram of the embedment depths (depth from the ground surface to the bottom of the footing) of 190 foundations from the bridge inventory of the state of Oregon. For each bridge, only one footing embedment depth was measured and used for the embedment depth distribution presented in Figure 3.20. The histogram is a right-skewed distribution with 70% of the embedment depths lower than 100 inches. The footing embedment depths range from 30 to 240 inches with a mean embedment depth of about 100 inches. The data shows that almost all the footings are embedded more than 18 inches which is the average soil frost depth in the state of Oregon (ASCE 32). As shown in this figure, embedment depths between 60 and 80 inches are quite frequent. There were few bridges with footings embedded at depths greater than 240 inches.

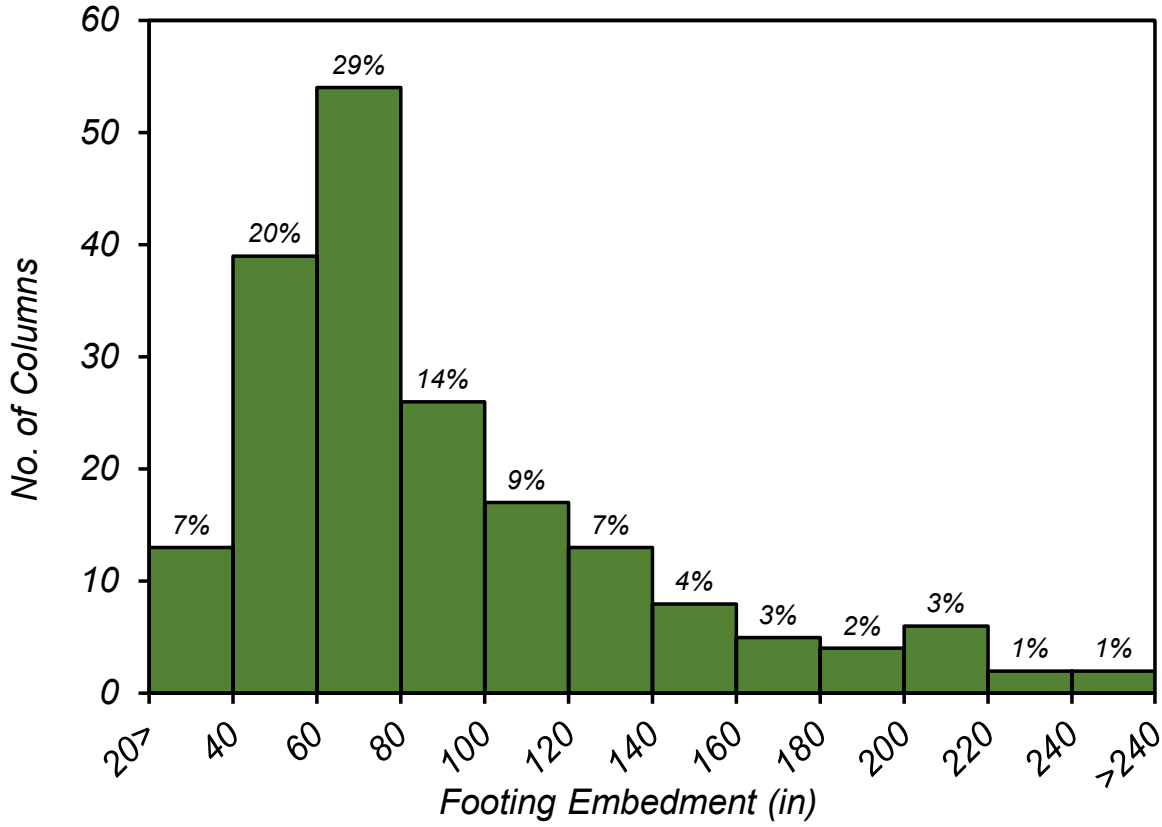

Figure 3.20: ODOT inventory footing embedment depth (in) distribution.

3.7 REFERENCES

ASCE 32-01 (2001). Design and Construction of Frost-Protected Shallow Foundations. American Society of Civil Engineers, Reston, VA

Shrestha, S. (2019). Seismic Retrofit of Square Reinforced Concrete Bridge Columns using Titanium Alloy Bars. PhD Dissertation, Oregon State University, Corvallis, OR.

4.0 NEW FORMULATION FOR ESTIMATING THE MOMENT CAPACITY OF ROCKING SHALLOW FOUNDATIONS RESTING ON PARTIALLY SATURATED SOIL

4.1 INTRODUCTION

The concept of rocking foundations within the class of analyses known as soil-structure interaction (SSI) has been proposed by several researchers as an effective method of seismic isolation (Housner 1963; Beck and Skinner 1974; Huckelbridge and Ferencz 1981; Priestley et al. 1996; Mergos and Kawashima 2005; Chen et al. 2006; Sakellaraki and Kawashima 2006; Gajan and Kutter 2008; Kutter et al. 2011; Anastasopoulos et al. 2010; Deng et al. 2012; Hakhamaneshi 2014; Allmond et al. 2015) and has been applied in the design and construction of some of modern bridges, such as the Rio–Antirrio bridge in Greece and the Vasco de Gama bridge in Portugal (Pecker 2003) or for retrofitting purposes (Kawashima and Nagai 2006; Hung et al. 2011; Liu et al. 2013; Shrestha 2019). Most of the advances in the understanding of rocking foundations in the past 30 years have focused on the response in competent or fully saturated soils. Rocking has proven to improve the performance of bridges by reducing ductility demand on bridge substructures and dissipating energy when foundations bear onto competent soils (Reinhardt et al. 2003; Anastasopoulos et al. 2015). Loose, saturated soils, on the other hand, have the potential to liquefy during propagation of seismic waves, leading to significant deformations (Gajan and Kutter 2008; Deng et al. 2012; Kutter et al. 2016; Allmond 2014; Allmond et al. 2015). Such ground motion-induced deformations may couple with those associated with soil-foundation interaction and rocking to result in significant settlement or tilting of the supported structure during and following shaking. These effects are poorly captured when modeling soil with linear-elastic elements (e.g., Güllü and Özel 2020). Various approaches have been developed to analyze the nonlinearity of soil and rocking systems during shaking (Gajan and Kutter 2008; Deng et al. 2012; Kutter et al. 2016). Conversely, little work has been done on the response of rocking shallow bridge foundations in soils subjected to seasonal fluctuations in moisture content and strength.

Taking into account their relatively long service life, bridges represent one of the most sensitive elements within the transportation infrastructure network to climate-change and are routinely subjected to dynamic, seasonal effects due to precipitation and evaporation. The seasonal wetting and drying of unsaturated soils in these systems imply that the small- and large-strain stiffness of the soils may change during operation (Khosravi and McCartney 2012; Khosravi et al. 2018; Khosravi et al. 2020), complicating the prediction of performance for static and seismic loading. Figure 4.1 shows variations in soil saturation during different seasonal conditions. Under varying climate conditions, the soil underneath the foundation will experience cycles of drying and wetting (due to evaporation, infiltration, and/or groundwater level fluctuations) and changing profiles of the degree of saturation, S_r, defined as the ratio of water volume to void volume, in the soil above the groundwater table (Figure 4.1). The degree of saturation has a direct effect on the magnitude and frequency of air-water menisci and surface tension between the particles, and is expected to be higher in soils with lower S_r. The surface tension associated with air-water menisci has a direct effect on inter-particle connections for a given suction, ψ, (defined as the negative pore water pressure above the groundwater table) and its variation with S_r may result in

varying soil strength and stiffness (Khalili and Khabbaz 1998; Sivakumar 1993; Khalili et al. 2004; Lu and Likos 2006; Gallipoli et al. 2003; Lu et al. 2010; Khosravi and McCartney 2012; Khosravi et al. 2020). The response of a rocking foundation on soils with seasonally varying S_r deviates from what has been observed in dry or fully saturated soils, yet no prior studies have been conducted to investigate this effect on rocking moment capacity. This may be of particular importance for implementation to bridges with rocking shallow bridge foundations within the performance-based earthquake engineering (PBEE) framework (Moehle and Deierlein 2004), where the consideration of seasonal effects could raise or lower the overall hazard.

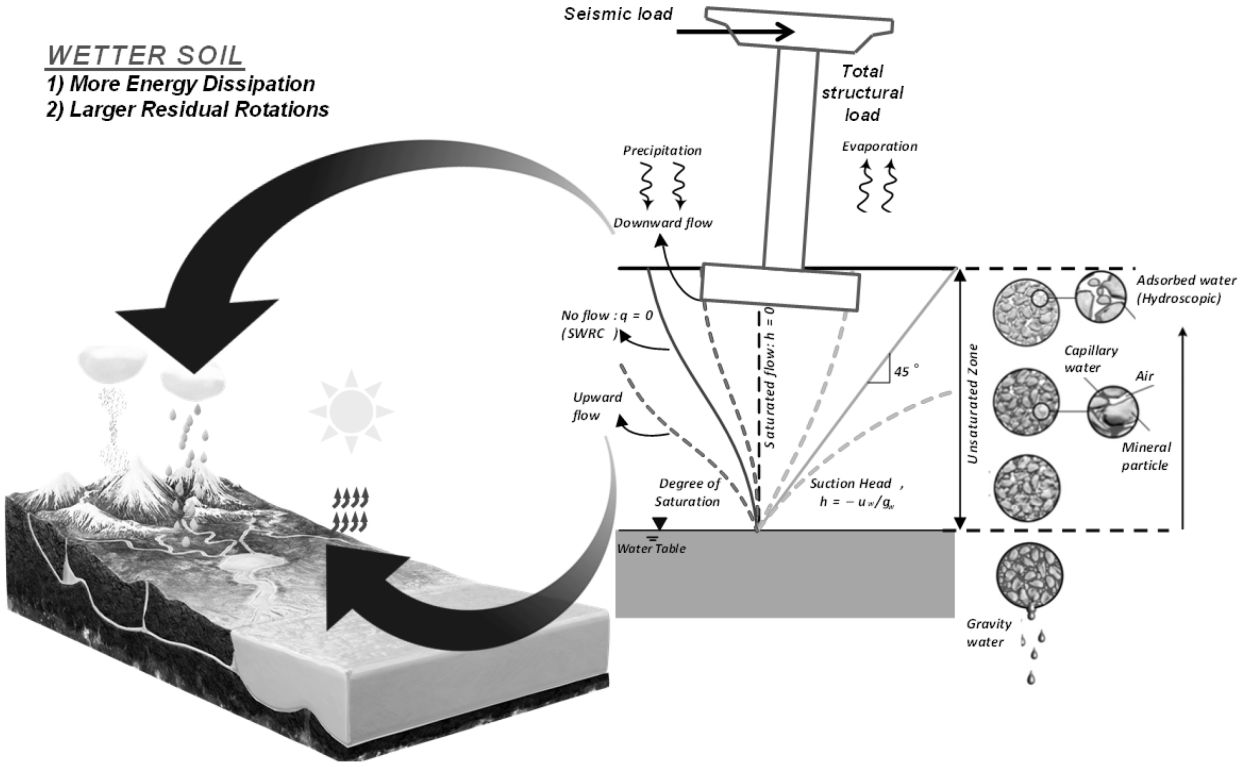

Figure 4.1: Effect of varying surface flux condition on soil suction and saturation profiles underneath a rocking shallow foundation (from Khosravi et al. 2021).

This section presents a procedure to account for the role of varying climate conditions and unsaturated state variables (i.e., S_r and suction) in estimating the moment capacity of rocking shallow bridge foundations resting on variably saturated soils subjected to steady flow. The proposed procedure leverages the equation originally employed for competent soils to estimate the moment capacity of rocking shallow bridge foundations. Then, recent advances in the definition of the effective stress state in unsaturated soils and hysteretic SWRCs are implemented to capture the effects of S_r and unsaturated stress states on moment capacity. The closed-form suction stress model proposed by Lu et al. (2010) is used to define the effective stress state of soils with varying saturation and matric suction conditions. Since S_r and ψ vary nonlinearly with depth above the groundwater table (Lu and Likos 2006), the numerical integration of differential elements is used to calculate the average S_r and ψ within the wedge of failure below the edges of the rocking foundation that accounts for the depth to the groundwater table and surface fluxes. An analytical solution is developed for the air entry suction using the methodology described by

Vanapalli et al. (1998) and the van Genuchten (1980) SWRC model. A parametric study is performed to determine the effects of surface flux conditions, soil type, and groundwater table depth on the moment capacity of rocking shallow bridge foundations and demonstrates the strong influence of flow conditions and groundwater table depth on the moment capacity of plastic soils. The proposed method for estimating the moment capacity of rocking shallow bridge foundations in soils subjected to varying climate conditions is validated through comparison against the results of full-scale shaking table and snap-back tests reported in literature. This procedure may enable a broad advance of bridge design principles including refinement of load and resistance factor design as embodied in the American Association of State Highway and Transportation Officials (AASHTO) load and resistance factor design (LRFD) specifications. This refinement is particularly important for regions where seasonal weather or long-term climate changes are expected to significantly influence soil response characteristics.

4.2 UNIFIED METHODOLOGY FOR THE MOMENT CAPACITY OF ROCKING SHALLOW BRIDGE FOUNDATIONS UNDER VARYING SATURATION CONDITIONS

4.2.1 Concept of Foundation Rocking in Competent Soil Conditions

Differing from traditional bridges and bridge foundation systems, in which inelastic flexural deformations imposed by gravity and seismic loads are designed to concentrate over a finite hinge length of the above-ground structural elements (e.g. bents), a rocking foundation takes advantage of soil failure to protect the bridge during seismic loading (Figure 4.2). Rather than allowing plastic hinges to form in the substructure, this design philosophy allows the foundation act as a fuse, to dissipate energy during an earthquake. This usually involves under-designing the geotechnical capacity of the foundations, for example, using foundations with smaller dimensions or leaving the as-built foundations in-place for the case of retrofitted column/footing systems, thereby transferring the plastic hinge to the soil. In this approach, depending on the factor of safety against bearing failure, the mode of foundation failure is either uplift (cases with larger factors of safety) or localized soil failure (cases with smaller factors of safety) and settlement (Anastasopoulos et al. 2012; Hakhamaneshi 2014). Permitting these mechanisms to occur results in reduced ductility demand and intensity of ground shaking that is transmitted to the superstructure.

The response of a rocking foundation subject to cyclic loading consists of alternating contact between the base of the footing and subgrade, and separation and gapping under the unloaded portion of the footing. This results in the formation of a curved surface at the soil-footing interface (Rosebrook 2002; Gajan et al. 2005) that serves to recenter the column following loading. As the magnitude of rotation increases, the contact area between the foundation and underlying soil becomes smaller and shifts to the toe of the footing due to the overturning moment. As the contact area decreases, the bearing pressure along the contact area increases to satisfy vertical equilibrium. Under sufficient footing rotation, the bearing pressure along the available contact area becomes equal to the ultimate bearing resistance, q_{ult}, and no further reduction in contact area is possible. This minimum contact area is referred to as the critical contact area (A_c). For rectangular footings, with loading in the long (L) direction, the ratio A_c/A can be equated to a length ratio, L_c/L, where L_c is referred to as critical contact length and is

directly related to the critical contact area: $L_c = A_c/B$, where B = width of the footing (i.e., the smallest plan dimension of the footing). When the structure is unloaded, depending on the magnitude of axial load and the seismic-induced rotation of the structure, gravity may cause gap closure and thus provides a natural self-centering mechanism. The critical length of a rocking foundation can be computed based on consideration of q_{ult} under static vertical loading:

$$\boldsymbol{L_c = P/(q_{ult}B)}$$

(4-1)

where P is the vertical load transmitted to the foundation. Under fully saturated or dry conditions, the bearing capacity of an embedded shallow foundation under vertical loading is given by (Terzaghi 1943):

$$\boldsymbol{q_{ult} = s_c d_c c' N_c + s_q d_q q'_0 N_q + 0.5 s_\gamma d_\gamma \gamma B N_\gamma}$$

(4-2)

where q'_0 is the soil surcharge, γ is the unit weight of the soil. N_c, N_q and N_g are cohesion, surcharge, and weight and width bearing capacity factors d_c, d_q, and d_γ are the Vesic (1973) cohesion, surcharge, and weight embedment factors, respectively, and s_c, s_q, and s_γ are the cohesion, surcharge, and weight shape factors, respectively, given by (Vesic 1973):

$$\boldsymbol{s_c = 1 + (N_q/N_c)(B'/L')}$$

(4-3)

$$\boldsymbol{s_q = 1 + B'/L' \tan\phi'}$$

(4-4)

$$\boldsymbol{s_\gamma = 1 - 0.4(B'/L')}$$

(4-5)

where B' and L' are effective foundation dimensions, which are reduced to represent that portion of the foundation plan area that is in contact with soil during rocking. For cases with $L_c < B$, $B' = L_c$ and $L' = B$, while in cases with $L_c > B$, B' and L' are equal to B and L_c, respectively (Gajan and Kutter 2008). For a rocking foundation, depending on the foundation dimensions and the characteristics of the supporting soil, L_c might become smaller than B. Thus, Eq. 4.2 is rewritten as:

$$\boldsymbol{q_{ult,L_c} = s_c d_c c' N_c + s_q d_q q_0 N_q + 0.5 s_\gamma d_\gamma \gamma L_c N_\gamma \qquad L_c < B}$$

(4-6)

$$q_{ult,L_c} = s_c d_c c' N_c + s_q d_q q_0 N_q + 0.5 s_\gamma d_\gamma \gamma B N_\gamma \qquad L_c > B$$

(4-7)

When the rocking capacity becomes fully mobilized, the applied bearing pressure and capacity are related:

$$q_{ult,L_c} B L_c = P$$

(4-8)

and thus, iteration of Eqs. 4.6, 4.7 and 4.8 may be required to determine L_c. When the critical length of the rocking foundation is determined, and neglecting the potential for large displacements at this stage of the evaluation, the moment capacity, M_c, of a rocking shallow foundation can be obtained by (Gajan and Kutter 2008):

$$M_c = P\Delta = \frac{PL}{2}\left[1 - \frac{A_c}{A}\right]$$

(4-9)

where Δ is the rocking re-centering distance, defined as the horizontal distance between the location of the applied vertical load, P, and the center of the soil-foundation contact area under the foundation (Figure 4.2).

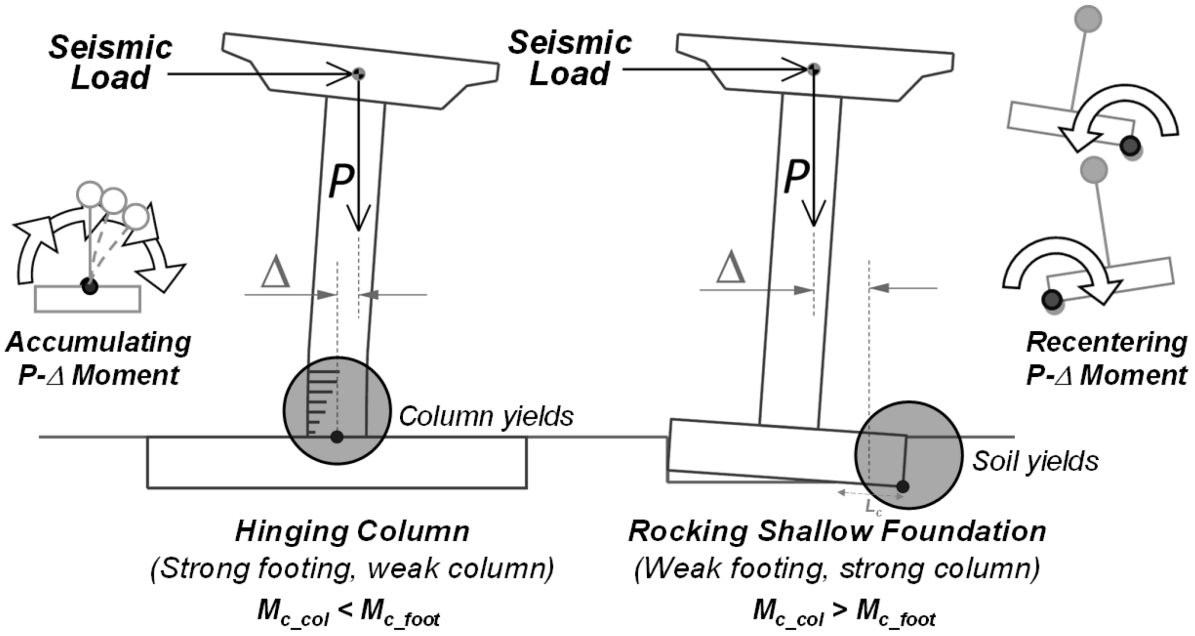

Figure 4.2: Comparison of the concepts of rocking foundation and hinging column in bridge column/footing systems (from Allmond 2014).

4.2.2 Moment Capacity of Rocking Shallow Foundations under Varying Saturation Conditions

Eq. (4.9) provides satisfactory estimation of the moment capacity of competent soils (Gajan and Kutter 2008). However, the effect of parameters associated with unsaturated conditions such as matric suction or degree of saturation is not considered. In an unsaturated condition, an appropriate description of the soil state requires consideration of the thermodynamic properties of the pore water in terms of soil suction and state variables such as degree of saturation and inter-particle forces arising from matric suction (Lu and Likos 2006; Khosravi and McCartney 2012). Changes in the degree of saturation and matric suction directly affect the strength and stiffness of soils (e.g., Oloo et al. 1997; Costa et al. 2003; Khosravi et al. 2012; Oh and Vanapalli 2011; Vanapalli and Mohamed 2013) and the corresponding q_{ult} (Wuttke et al. 2013; Vahedifard and Robinson 2016), and therefore M_c of foundations resting on soils under varying saturation conditions are expected to be different from that in saturated or competent soils.

Various approaches have been proposed to capture the effect of unsaturated state parameters on q_{ult}, such as formulations developed using a single stress-state variable (Bishop 1959) or independent stress state variables, (*e.g.,* ψ and net confining stress, p_n; Fredlund and Morgenstern 1977; Oloo et al. 1997; Oh and Vanapalli 2011; Vanapalli and Mohamed 2013). Vahedifard and Robinson (2016) incorporated the suction stress-based effective stress approach proposed by Lu and Likos (2006) into Terzaghi's (1943) bearing capacity equation through the total cohesion concept and proposed:

$$q_{ult,unsat} = s_c d_c c_{app} N_c + s_q d_q q_0 N_q + 0.5 s_\gamma d_\gamma \gamma N_\gamma \quad for \;\; L_c < B$$

(4-10)

where c_{app} is the apparent cohesion (Vahedifard and Robinson 2016):

$$c_{app} = c' + \psi_{AE}(1 - S_{e,ave})\tan\phi' + (yS_e)_{ave}\tan\phi'$$

(4-11)

and where y_{AE} is the air-entry matric suction and $S_{e,ave}$ represents the average effective degree of saturation within the zone of influence below the shallow foundation, given by:

$$S_e = \frac{S_r - S_{r,res}}{1 - S_{r,res}}$$

(4-12)

and where S_e is used to scale the current degree of saturation S_r by the degree of saturation at residual state condition, $S_{r,res}$. The residual state condition occurs when the water phase is discontinuous and isolated with thin films of water surrounding the soil particles (Vanapalli et al. 1998). In Eq. 4.11, c' = the effective cohesion of the soil under saturated or dry conditions, the second term describes changes in cohesion due to changes in matric suction and effective saturation up to the air-entry suction, and the third term describes the contribution of ψ and S_e on the cohesion beyond the air-entry suction. Lu and Likos (2006) referred to the product of ψ and S_r in the third term in Eq. 4.11 as the suction stress, p_s, and defined it as a macroscopic stress that collectively incorporates the effects of capillarity, soil, and pore fluid-specific forces such as van der Waals forces, electrical double-layer repulsion forces, and net attraction forces arising from chemical cementation at the grain contacts.

Under a hydrostatic condition, the effective saturation can be expressed in terms of the matric suction using the van Genuchten (1980) model:

$$S_e = \left\{\frac{1}{1 + (\alpha\psi)^n}\right\}^{\left(1-\frac{1}{n}\right)}$$

(4-13)

where a and n are the fitting parameters of the model determined using ordinary least squares (OLS). For cases where soil suction is relatively independent of time, it may be simply defined as $\psi = \gamma_w \times z$, where γ_w = unit weight of water, and z = the height above the groundwater table. Under varying saturation conditions, however, soil suction tends to fluctuate as a function of time-dependent factors, such as relative humidity, temperature, evaporation, and precipitation. Events resulting in water infiltration and downward flow lead to a decrease in matric suction,

while evaporation results in upward flow and increases soil suction (Lu and Likos 2004, McCartney and Khosravi 2013, Vahedifard and Robinson 2016). Lu and Likos (2004) proposed a one-dimensional analytical solution of ψ profiles under steady-state vertical infiltration or evaporation:

$$\psi = -\frac{1}{\alpha} ln \left[\left(1 + \frac{q_w}{k_s} \right) e^{-\gamma_w \alpha z} - \frac{q_w}{k_s} \right] \quad \textbf{(4-14)}$$

where k_s = hydraulic conductivity of saturated soil and q_w = water flow rate at the ground surface. In order to mathematically ensure that ψ obtained from Eq. 4.14 is zero or positive, the bracketed term must be greater than 0 and less than or equal to 1. Substitution of Eq. 4.14 into Eq. 4.13 facilitates calculation of S_e profiles under varying climate conditions with steady-state vertical infiltration or evaporation rates (Vahedifard and Robinson 2016):

$$S_e = \left\{ \frac{1}{1 + \left\{ -ln \left[\left(1 + \frac{q}{k_s} \right) e^{-\gamma_w \alpha z} - \frac{q}{k_s} \right] \right\}^n} \right\}^{\left(1 - \frac{1}{n}\right)} \quad \textbf{(4-15)}$$

A unified equation for the bearing capacity of soils under varying saturation conditions can be obtained through substitution of Eqs. 4.14 and 15 into Eq. 4.11, and then into Eq. 4.10. This form of bearing capacity (i.e., Eq. 4.10) can be used to iteratively evaluate L_c for the design of rocking foundations resting on soils with varying saturation conditions to produce a refined estimate of M_c. The resulting L_c can then be used along with Eq. 4.9 to compute M_c for different surface flux boundary conditions and groundwater table depths. Such an approach requires the calibration of the methodology prior to use, as described subsequently.

4.3 APPLICATION TO UNSATURATED MOMENT CAPACITY

The contribution of matric suction and changes in saturation due to variations in the depth of the water table, D_w, and various surface flux boundary conditions in the moment capacity are considered through the evaluation of three factors: (1) the assessment of the apparent cohesion (Eq. 11) to accommodate changes in soil suction and S_r, (2) modification of q_0 when the water table lies above the base of the foundation, and (3) the adjustment of the soil unit weight when the water table is within the zone of shear below the foundation. The depth of the failure mechanism comprising the zone of shear, D_s, for use in determining the quantities necessary for application of Eq. 4.10 may be readily estimated using bearing capacity theory (Figure 4.3). Differing from classical bearing capacity theory, where the zone of shear extends to $D_s = 0.5B'\tan(\phi'+45/2)$, the failure zone of a rocking foundation occurs at the edges of the foundation. In rocking foundations, D_s may change depending on the magnitude of L_c. For $L_c > B$, $D_s = 0.5B'\tan(\phi'+45/2)$, while for cases with $L_c < B$, $D_s = 0.5 \times L'_c \tan(\phi'+45/2)$, where ϕ' = effective

friction angle of the soil. Given that many plastic soil profiles exhibit depth-varying strength profiles with near-surface overconsolidation, the capacity of footings during rocking may be significantly larger than under a general bearing capacity failure.

Three different cases are considered to appropriately capture the variations in shear strength and corresponding M_c due to changes in D_w and various saturation conditions (Figure 4.3):

Case 1: The groundwater table depth, D_{w1}, is located above the base of the foundation ($D_w < D_f$). In this case, soil underneath the foundation can be assumed to be fully saturated and consequently the matric suction in the bearing capacity formulations is zero. However, the overburden pressure, q_0, requires modification (Terzaghi 1943):

$$\boldsymbol{q_0 = D_f \widetilde{\gamma}} \tag{4-16}$$

where:

$$\boldsymbol{\widetilde{\gamma} = (\gamma_{sat} - \gamma_w) + \frac{D_w}{D_f}\gamma_w} \tag{4-17}$$

where γ_{sat} = saturated unit weight of soil.

Case 2: The groundwater table is located within the zone of soil failure, i.e. $D_f < D_w < D_s$. In this case, γ should be modified to account for the presence of water in the failure zone as follows:

$$\boldsymbol{\widetilde{\gamma} = (\gamma_{sat} - \gamma_w) + \left(\frac{D_w - D_f}{D_s}\right)\gamma_w} \tag{4-18}$$

Moreover, terms related to the soil suction and effective saturation are calculated by considering the profiles of matric suction, effective saturation, and suction stress from the base of the foundation to D_w. Based on Lu and Likos (2006), McCartney and Khosravi (2013), and Vahedifard and Robinson (2016), the profiles of these variables are nonlinear for fine- and coarse-grained soils under different boundary conditions such as the flux boundary conditions or D_w. Considering the nonlinearity of these variables, numerical integration of differential elements over the relevant geometrical extents given by the depth of the failure mechanism is required to calculate the average values of ψ, S_e, and p_s within the influence zone below the foundation for the calculation of q_{ult}. This study proposes the implementation of the horizontal coordinates of the centroid of profiles of ψ and S_e within the triangular failure wedge as representative or average values of ψ and S_e, and are calculated using:

$$\psi_{ave} = \frac{\int_{\psi_l}^{\psi_u} \psi z(\psi) d\psi}{\int_{\psi_l}^{\psi_u} z(\psi) d\psi}$$

(4-19a)

$$S_{e,ave} = \frac{\int_{S_{e,l}}^{S_{e,u}} S_e z(S_e) dS_e}{\int_{S_{e,l}}^{S_{e,u}} z(S_e) dS_e}$$

(4-19b)

In Eqs. 4.19a and 4.19b, ψ_u and ψ_l characterize the upper and lower limits of the matric suction for integration, which for Case 2 are the matric suction at the depths of the foundation level and ground water table ($\psi_l = 0$), respectively. $S_{e,u}$ and $S_{e,l}$ characterize the upper and lower limits of effective saturation for integration, which for Case 2, are the effective saturations at D_f and D_w (i.e., $S_{e,l} = 1$), respectively.

Case 3: The groundwater table is located below the failure zone, i.e. $D_w > D_s$. In this case, no modification is needed for q_0 or γ and the average values of matric suction and effective saturation can be calculated using Eqs. 4.19a and 4.19b, respectively. The upper and lower limits of integration of matric suction, y_u and y_l, are those calculated at D_f and D_s, respectively. Similarly, the upper and lower limits of integration for effective saturation, $S_{e,u}$ and $S_{e,l}$, are the effective saturations calculated at D_f and D_s, respectively.

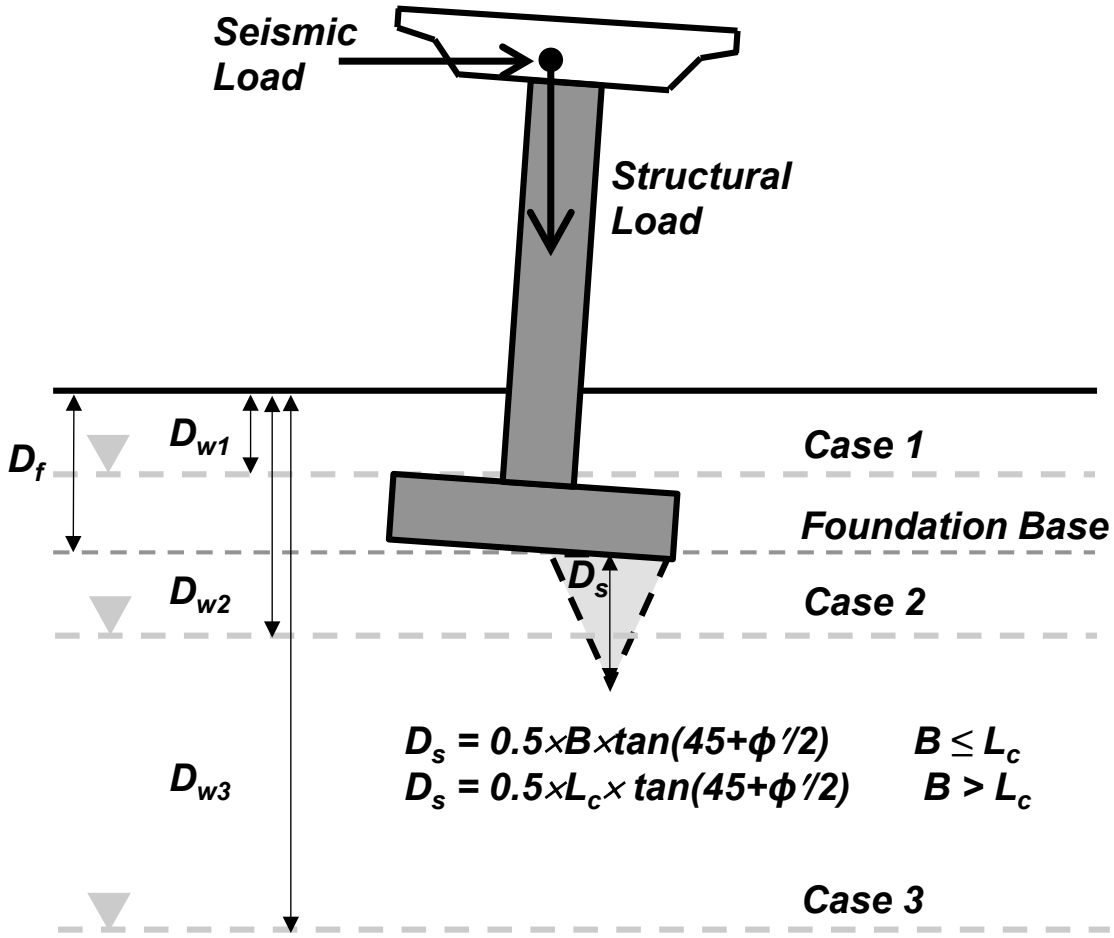

Figure 4.3: Different scenarios of groundwater table depths to consider in the estimate of the moment capacity of rocking shallow foundations (from Khosravi et al. 2021).

The air entry suction represents a critical parameter for the determination of M_c under varying saturation conditions. The air entry suction (ψ_{AE}) is defined as the matric suction from which air starts to enter the soil and is usually selected using ocular inspection of the SWRC (Vanapalli et al. 1998). Under hydrostatic conditions, the SWRC can be described in terms of ψ and S_e using the van Genuchten (1980) SWRC model (Eq. 4.13). Since the SWRC is usually presented in a semi-logarithmic scale in the horizontal axis, Eq. 4.13 can be rewritten in the form of:

$$S_e = \left\{\frac{1}{1 + (\alpha\, exp(s))^n}\right\}^{\left(1-\frac{1}{n}\right)} \quad \textbf{(4-20)}$$

where:

$$\psi = exp(s) \quad \textbf{(4-21)}$$

Based on Vanapalli et al. (1998), ψ_{AE} can be defined as the point of intersection of two lines, one tangent to the SWRC at the inflection point (Line 1; Figure 4.4) and a horizontal line passing through $S_e = 1$ (Line 2; Figure 4.4).

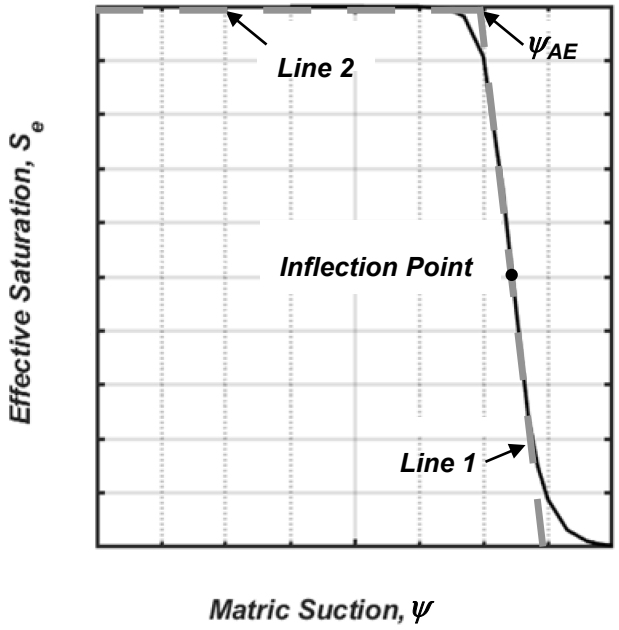

Figure 4.4: Schematic illustrating the methodology proposed by Vanapalli et al. (1998) to obtain the air entry suction from the characteristics of the SWRC (from Khosravi et al. 2021).

The line passing through the inflection point can be defined as:

$$S_e - S_{e,inf} = m \ln\left(\frac{\psi}{\psi_{inf}}\right) \tag{4-22}$$

where $m = dS_e(s_{inf})/ds$ is the first derivative of Eq. 4.20 and $S_{e,inf}$ and ψ_{inf} are the effective saturation and matric suction at the inflection point, respectively. The slope of the SWRC is greatest at the inflection point and consequently the second derivative of Eq. 4.20 is zero at this point. Thus, the values of effective saturation and matric suction at the inflection point are equal to:

$$S_{e,inf} = \frac{1}{\left(\frac{2n-1}{n-1}\right)^{1-\frac{1}{n}}} \tag{4-23a}$$

$$\psi_{inf} = exp(s_{inf}) = \frac{1}{\alpha}\sqrt[n]{\frac{n}{n-1}}$$

(4-23b)

An analytical expression for ψ_{AE} can be obtained using the coordinate of the inflection point thus determined through the fitted van Genuchten SWRC parameters, *a* and *n*, as follows:

$$\psi_{AE} = \left(\frac{1}{\alpha}\sqrt[n]{\frac{n}{n-1}}\right) exp\left(\frac{\frac{2n-1}{n-1}\left[\left(\frac{2n-1}{n-1}\right)^{1-\frac{1}{n}} - 1\right]}{(1-n)\sqrt[n]{\frac{n}{n-1}}}\right)$$

(4-24)

The values of ψ_{AE} reported in the technical literature (Brooks and Corey 1964; Leong and Rahardjo 1997; and Vanapalli et al. 1998) were compared against values computed using Eq. 4.25 (Figure 4.5) and demonstrated a coefficient of determination, R^2 = 0.99 and indicates the validity of the proposed predictive relationship of Eq. 4.24.

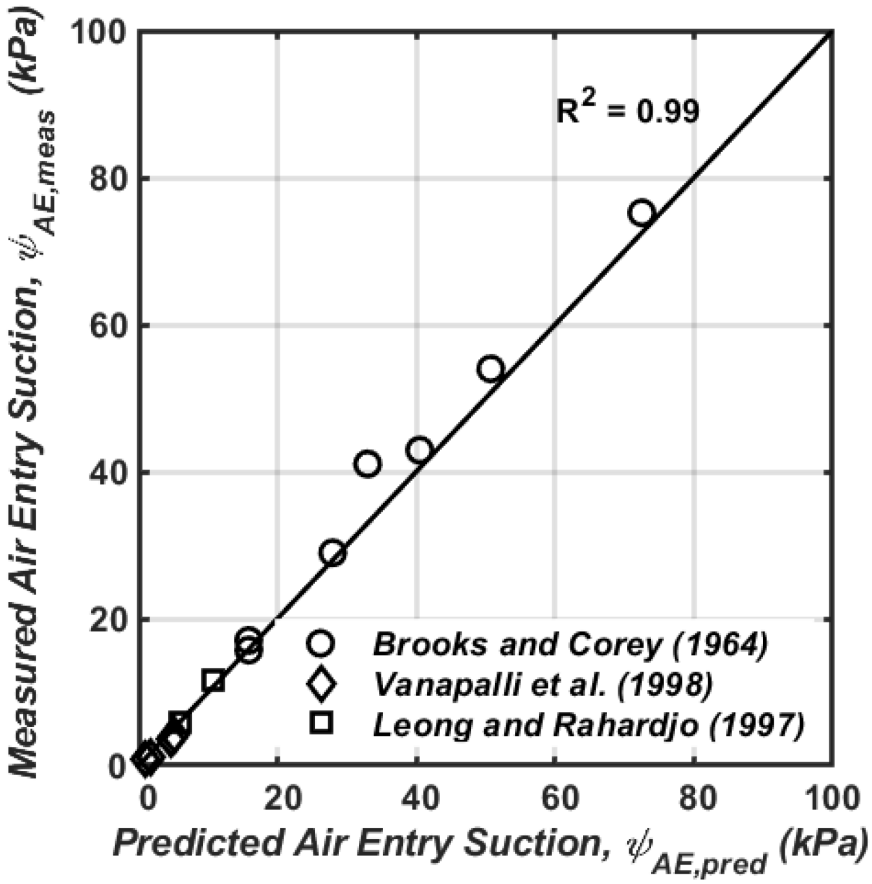

Figure 4.5: Comparison between the air entry values estimated using the proposed empirical model (Eq. 24) and those obtained experimentally for different USCS soil types (from Khosravi et al. 2021) (Note: 1 psi = 6.89 kPa).

4.4 PARAMETRIC ANALYSIS: EFFECT OF VARYING SATURATION CONDITIONS ON MOMENT CAPACITY

A set of parametric studies was performed to investigate the variation in M_c for hypothetical fine- and coarse-grained soils under various S_r and surface flux boundary conditions. The results are presented for three (3) different hypothetical characteristic soil types: clay, silt, and sand, with variations in the depth of the groundwater table, i.e., $0 \leq D_w \leq 10$ m (33 ft), beneath the foundation. Input parameters for the hypothetical soils are shown in Table 4.1. Three (3) surface flow rates, q_w, of -3.15×10^{-8} (infiltration), 0 (hydrostatic), and 1.15×10^{-8} m/s (evaporation) were considered for analyses, corresponding to -1.03×10^{-7} and 3.77×10^{-8} feet/second, respectively. These rates of flow were selected on the basis of typical flow rates reported by Lu and Likos (2004, 2006) and Vahedifard and Robinson (2016).

4.4.1 Profiles of Soil Suction, Effective Saturation, and Suction Stress under Various Surface Flux Boundary Conditions

Figure 4.6 presents the depth-normalized profiles of matric suction (Figure 4.6a), effective saturation (Figure 4.6b), and suction stress (Figure 4.6c) for the three (3) hypothetical soils under different surface flux boundary conditions. The suction stress profiles in Figure 4.6(c) were obtained by multiplying Eqs. 4.14 and 4.15. Under hydrostatic conditions with no surface flux ($q_w = 0$), the gradient of ψ is 1 and the effective saturation profile is the same as the soil water retention curve of the soil for the particular range of z. Such an equilibrium situation may occur in winter and early spring in the free-field with a constant, shallow water table (i.e., a 1D condition). Under steady-state conditions, the profiles of ψ (Figure 4.6a) begin to deviate from the hydrostatic curve as the height above the water table increases, most notably for clay and silt, where significant changes in ψ are observed with water flux into and out of the soil. For sand, the profiles of ψ remain essentially constant with variation concentrated near the ground surface under steady flow conditions (e.g., $z > 0.65D_w$). The influence of surface flux boundary conditions on the profiles of effective saturation (Figure 4.6b) and suction stress (Figure 4.6c) for clay and silt is significant, with the greatest effect corresponding to the infiltration case. In sand, the influence of steady flow conditions on profiles of S_e and p_s is negligible.

Table 4.1: Parameters used in the parametric study for different soil types.

Parameter	Symbol	Clay	Silt	Sand
Unit weight, pcf (kN/m^3)	γ	115 (18)	115 (18)	115 (18)
SWRC Parameters, unitless (van Genuchten's 1980)	n_w	1.5	2.5	4
	α_w	0.005	0.01	0.08
Saturated hydraulic conductivity, feet/second (m/s)	k_s	1.64×10^{-7} (5×10^{-8})	3.28×10^{-7} (1×10^{-7})	9.84×10^{-5} (3×10^{-5})
Cohesion, psi (kPa)	c'	2.9 (20)	1.45 (10)	0

Figure 4.7 shows the depth-normalized profiles of ψ for the hypothetical clay (Figure 4.7a), silt (Figure 7b), and sand (Figure 4.7c) for selected groundwater table depths. These curves indicate that the rate of change in ψ and evaporation/infiltration is significantly affected by D_w. When D_w is near the surface (e.g., 1 m), ψ is low, and the q_w resulting from evaporation/infiltration does not affect the profiles of ψ significantly. Lowering D_w can reduce the rate of capillary rise and accordingly, q_w can result in greater change in ψ.

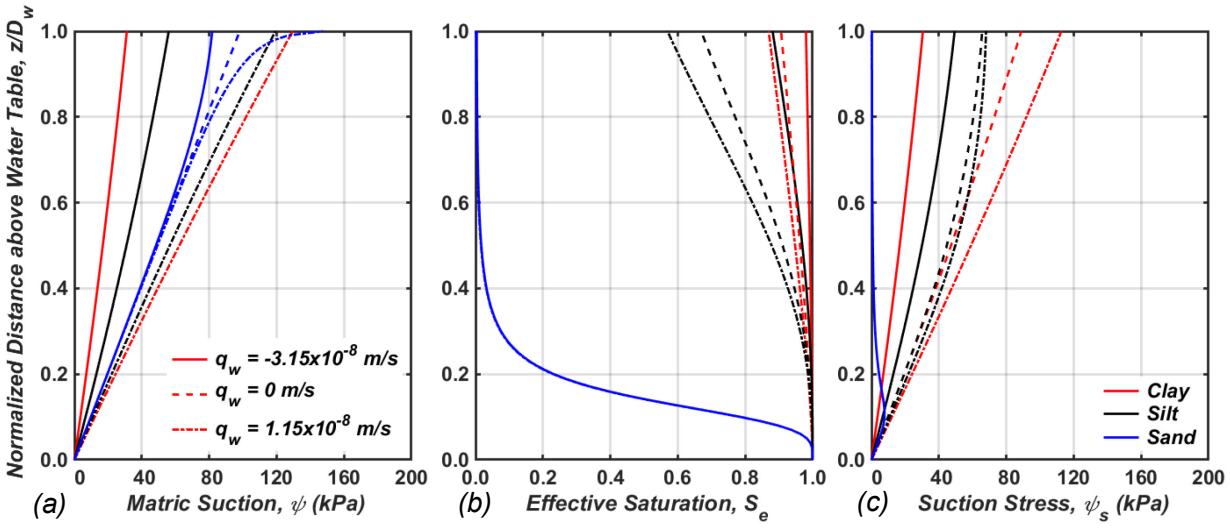

Figure 4.6: Normalized profiles of (a) matric suction; (b) effective saturation; and (c) suction stress for the three hypothetical soils of clay, silt, and sand under different surface flux boundary conditions (from Khosravi et al. 2021) (Note: 1 psi = 6.89 kPa).

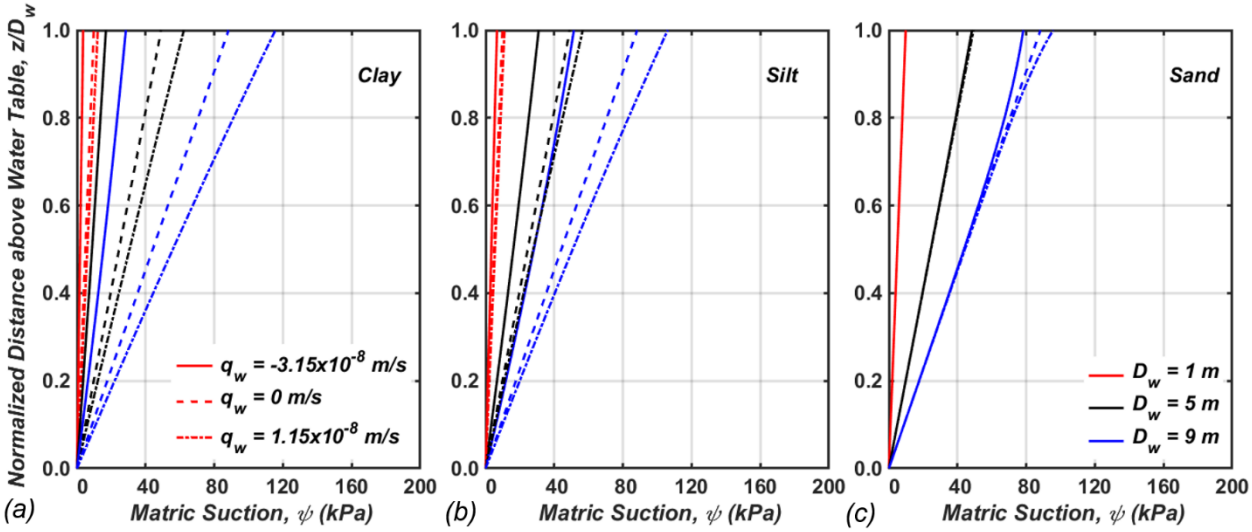

Figure 4.7: Variations in soil suction for different soils of (a) clay; (b) silt; and (c) sand for different groundwater table depths (from Khosravi et al. 2021) (Note: 1 psi = 6.89 kPa).

4.4.2 Effect of Soil Types, Groundwater Table Depth, and Flow Rates on the Moment Capacity

An investigation into the effect of soil type, D_w, and q_w on L_c and M_c of the rocking shallow bridge foundations follows. Owing to their correspondence to small and large sensitivity, the investigation focuses on two hypothetical, but representative, sand and clay deposits, respectively. The depth of the groundwater table is assumed to vary from $0 \leq D_w \leq 33$ft (10 m), under the footing. Figure 4.8 illustrate variations in ψ (Figure 4.8a), S_e (Figure 4.8b), L_c (Figure

4.8c), and M_c (Figure 4.8d) with D_w for shallow foundations embedded 20 in. (0.5 m) into clay. Figure 4.9 presents the same analyses for shallow foundations embedded 20 in. (0.5 m) into sand.

Figure 4.8 and Figure 4.9 indicate that the effect of varying saturation conditions is more pronounced in clay than in sand. In clay with an embedment depth of 20 in. (0.5 m; Figure 4.8), the trends for the average values of ψ and S_e are similar to the profiles presented in Figure 4.6 and Figure 4.7. For the surface flux boundary conditions and the D_w considered, ψ increases linearly as D_w increases. However, a greater variation in the rate of ψ with D_w occurs when $D_w > D_s$ (e.g. inside the triangular soil wedge). Changes in q_w result in significant changes in the profiles of ψ, particularly under the infiltration condition with a decrease in ψ of almost 70%. The variation of ψ considered here results in a moderate change in $S_{e,ave}$, as observed in Figure 4.8b. $S_{e,ave}$ varies by approximately 11, 8, and 2% as D_w drops from 3.3 to 33 ft (1 to 10 m) for the evaporation, hydrostatic, and infiltration conditions, respectively. ϕ' has small effect on the profiles of ψ_{ave} and $S_{e,ave}$. Higher ψ and lower S_e values complement higher values of p_s, leading to a larger $q_{ult,unsat}$ and consequently a lower L_c for the rocking foundation (Figure 4.8c). Specifically, the 11% drop in $S_{e,ave}$ under the evaporation condition contributes to a decrease of more than 25% in L_c. As a result, an increase of 20% in M_c is anticipated for the rocking shallow foundation. As presented in Figure 4.8d, M_c increases as D_w increases. However, the rate of increase in M_c decreases as D_w becomes closer to D_s. Also, the results show that q_w of -1.03 × 10^{-7} feet/sec (-3.15 × 10^{-8} m/s) results in the greatest effect on M_c in the variably saturated clay. The effect of q_w on M_c is not as pronounced for smaller values of D_w. As also reported in previous studies (Gajan and Kutter 2008; Hakhamaneshi 2014), ϕ' has significant effect on M_c. However, as ϕ' increases, the effect of ψ and S_e on M_c decreases. For the case of a shallow foundation on clay with $\phi' = 10°$, M_c varies by approximately 20% as D_w increases from 0 to 33 ft (0 to 10 m; Figure 4.8d), while for $\phi' = 15$ and 20°, the increase in M_c is 15 and 8%, respectively.

In sand (Figure 4.9), the average values of matric suction increases and effective saturation sharply decreases with an increase in D_w. However, q_w exhibits a small effect on the average suction, particularly for $D_w < 20$ ft. (6 m). For $D_w > 20$ ft. (6 m), the increase in soil suction with D_w for the infiltration condition begins to diminish, whereas the increase in soil suction is greater for the evaporation condition. Similar to the case of a shallow foundation on clay, a higher ψ and lower S_e lead to lower L_c for the rocking foundation in sand (Figure 4.9c). However, changes in L_c in sand is much smaller than that in clay. Figure 4.9 shows that the decrease in $S_{e,ave}$ from 100% to 0% (expected under an evaporation condition) results in a change in L_c of less than 2 in. (0.05 m; Figure 4.9c). As a result, a slight increase in M_c (less than 2%) is anticipated for the rocking shallow foundation. At a D_w equal to D_s, M_c reaches its maximum value and then stabilizes with further increase in D_w (Figure 9d). As shown in Figure 4.9d, the effect of D_w and q_w on M_c in sand is largely negligible, in stark contrast to the comparable effect of q_w on M_c in clay. Thus, little to no difference in M_c is observed for different surface flux boundary conditions (i.e., polarity of q_w). Similar to clay, increases in the friction angle of sand results in an increase in M_c, and exhibits sensitivity to D_w for small D_w only.

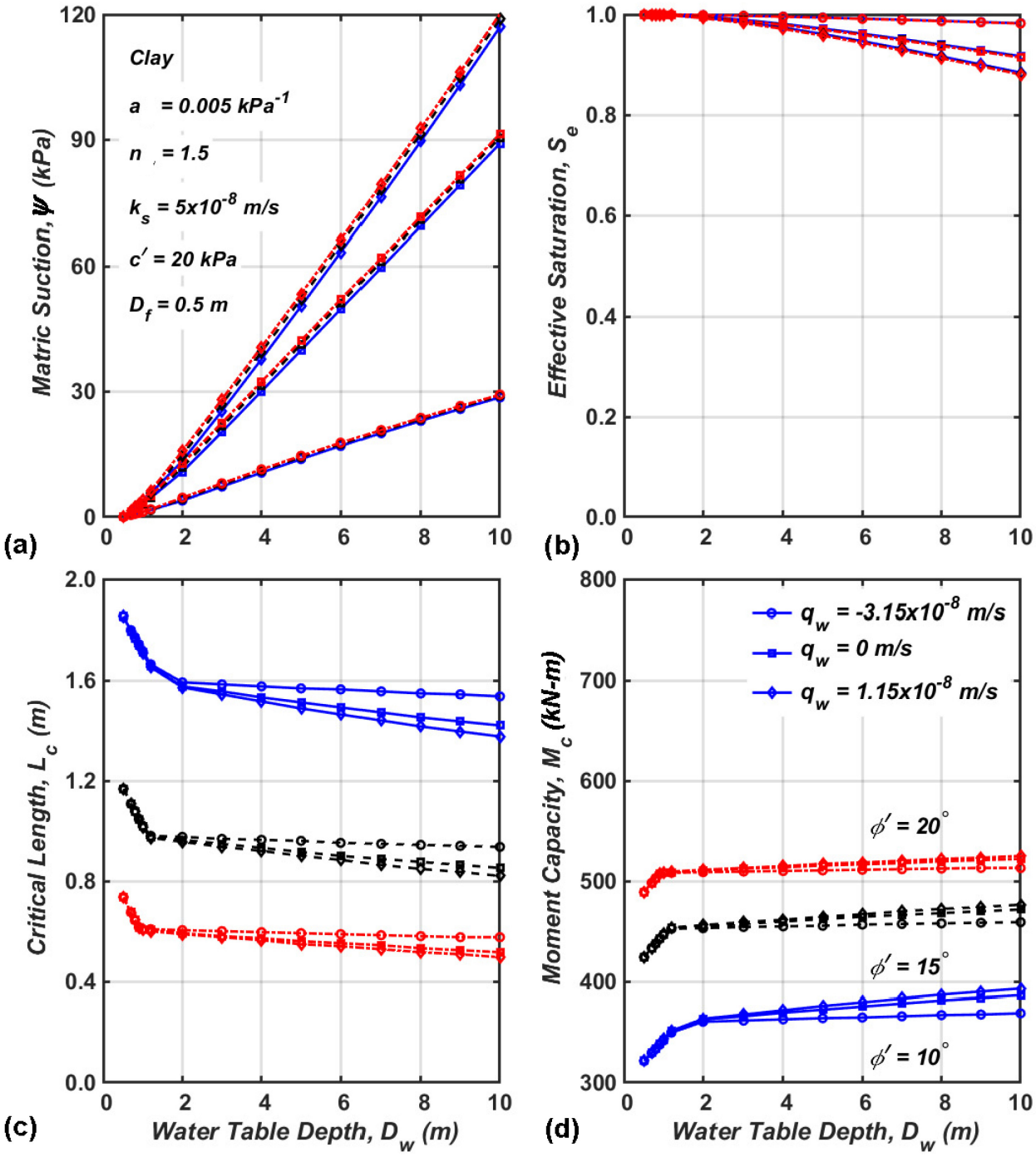

Figure 4.8: Variations in (a) ψ_{ave}; (b) $S_{e,ave}$; (c) L_c; and (d) M_c with D_w for different flow rates and ϕ' for a shallow foundation with D_f=0.5 m in clay (from Khosravi et al. 2021) (Note: 1 m = 3.3 ft; 1 kN-m = 0.74 kip-ft).

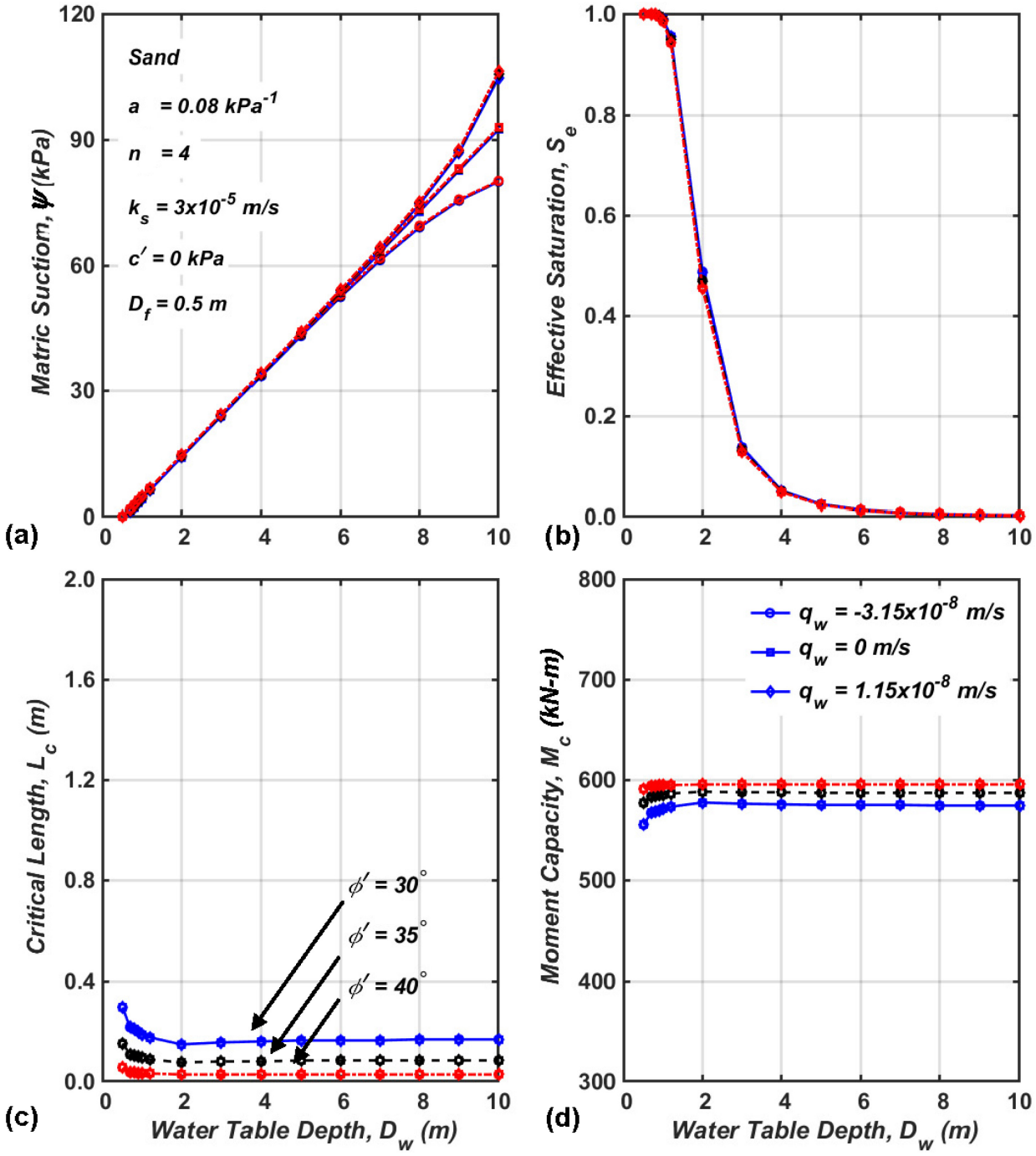

Figure 4.9: Variations in (a) ψ_{ave}; (b) $S_{e,ave}$; (c) L_c; and (d) M_c with D_w for different flow rates and ϕ' for a shallow foundation with D_f=0.5 m in sand (from Khosravi et al. 2021) (Note: 1 m = 3.3 ft; 1 kN-m = 0.74 kip-ft).

4.5 VALIDATION AGAINST FULL-SCALE EXPERIMENTS

The proposed method for estimating the moment capacity of rocking shallow foundations in variably saturated soils is validated by comparison against two sets of experimental results from

full-scale shaking table tests and snap-back tests after Antonellis et al. (2015; Figure 4.10a) and Sharma (2019; Figure 4.10b), respectively. Antonellis et al. (2015) performed shaking table tests on two bridge columns supported on shallow foundations resting on top of clean, well-compacted sand, and subjected to unidirectional seismic excitation. The experimental prototype consisted of a concrete tank with rigid boundaries, a 5 ft. by 5 ft. (1.52 m by 1.52 m) concrete shallow foundation, 20 in. (0.51 m) thick, embedded 26 in. (0.66 m) into the sand, and circular columns 4.43 ft (1.35 m) tall with 18 in. (0.46 m) diameter carrying 56 kip (250 kN) axial load. The soil used for this test was dense (relative density, D_r = 90%), Carroll Canyon type II ASTM C33 washed concrete sand with a constant volume friction angle of 33° and minimum and maximum dry unit weights of 91.6 and 112.6 pcf (14.4 and 17.7 kN/m^3), respectively. The material was classified as uniformly graded, medium sand.

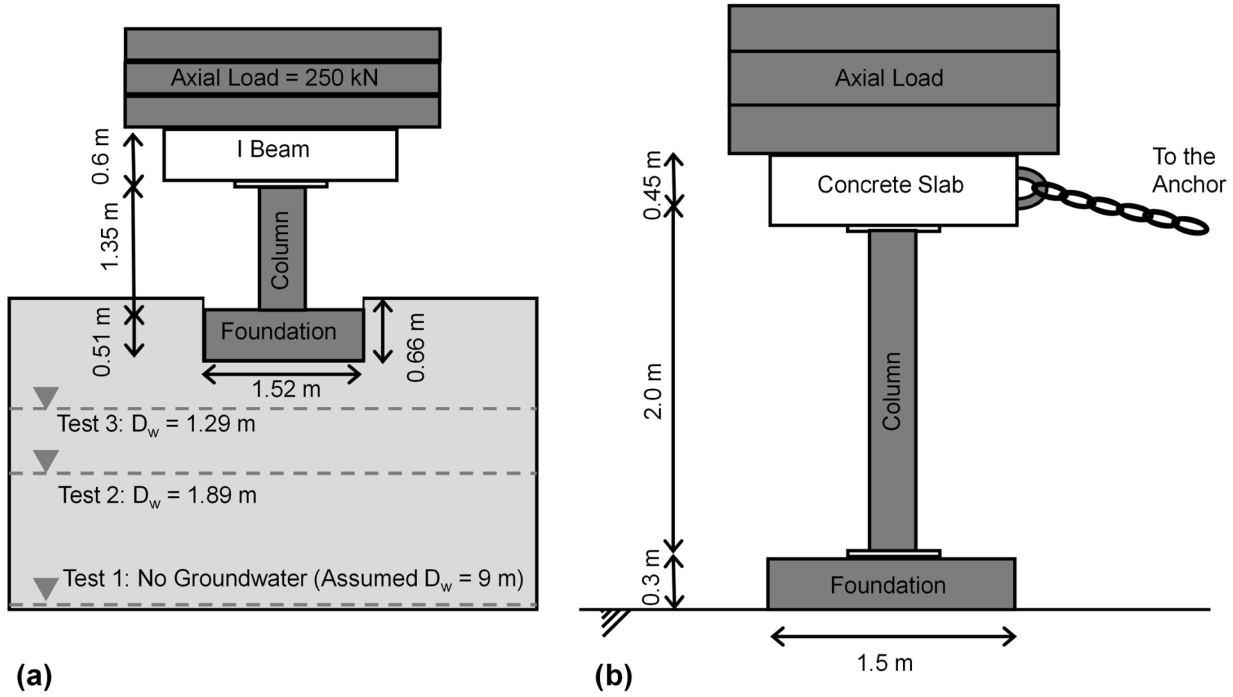

Figure 4.10: Elevation view of the rocking foundation test setup: (a) with the location of the base of specimens and groundwater elevation for different tests used by Antonellis et al. (2015); and (b) with the quick release mechanism used by Sharma (2019; from Khosravi et al. 2021) (Note: 1 m = 3.3 ft).

Although no information on the hydraulic properties of the sand were reported (e.g., hydraulic conductivity, SWRC), the necessary parameters may be readily estimated from the literature. The SWRC for Carroll Canyon sand (Figure 4.11), a uniformly graded sand with zero fines, coefficient of uniformity, C_u, coefficient of curvature, C_c, and median grain diameter, D_{50} equal to 3.3, 0.9, and 0.6, and similar grain size distribution as the sand (C_u = 5.3, C_c = 0.9, D_{50} = 0.74 mm) used in the shake table tests was used as the representative SWRC. Fern et al. (2014) reported the SWRC for Carroll Canyon sand for D_r = 0, 33, and 65%. The SWRC at D_r = 90% corresponding to that used in the shake table tests was established by extrapolation of the SWRC in consideration of the typical trends reported in the literature (Figure 4.11b).

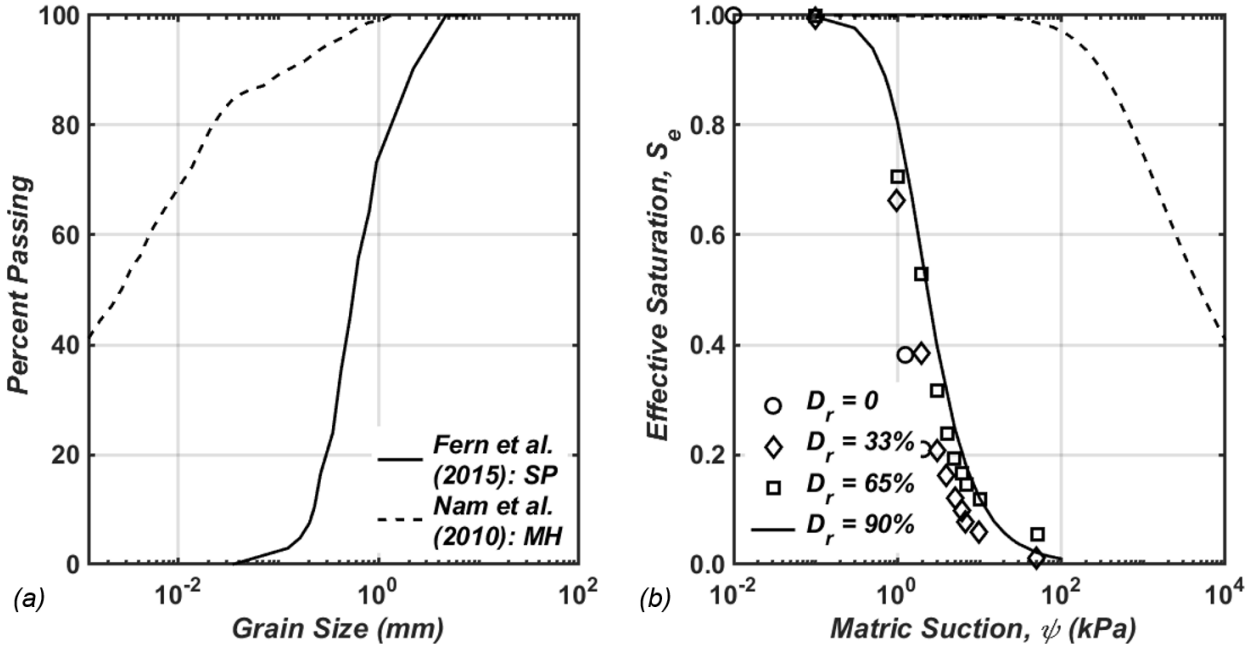

Figure 4.11: Soil comprising the subgrade below full-scale tests: (a) grain-size distributions; and (b) SWRCs of Carroll Canyon sand (SP; Fern et al. 2014) and high plasticity silt (MH; Nam et al. 2010; from Khosravi et al. 2021) (Note: 1 mm = 0.04 in.; 1 kPa = 0.145 psi).

Three (3) series of tests were performed by Antonellis et al. (2015), each with different groundwater table elevations and backfill conditions. Test 1 consisted of no groundwater and a well-compacted backfill sand with *in-situ* moisture content, w_c, of 5% above the foundation elevation. The analysis using the proposed methodology set D_w = 29.5 ft (9 m) for this case which resulted in S_r = 0.25, similar to the *in-situ* S_r assuming a specific gravity, G_s, of 2.7, reported by Fern et al. (2014). Test 2 considered a groundwater level of D_w = 6.2 ft. (1.89 m) and a nearly dry ($w_c \approx 2\%$), loose backfill sand above the base of the foundation. Test 3 consisted of a groundwater level of D_w = 4.23 ft. (1.29 m). To prevent sand from falling into the gap that formed between the soil and the foundation during rocking, a layer of weak concrete was placed around the perimeter of the foundation for Test 3. The use of this weak concrete skirt prevented the sand from flowing under the foundation but also introduced a modest increase in the moment capacity of the rocking foundation (Antonellis et al. 2015); owing to this modification, Test 3 was not used for the validation conducted herein.

A comparison of M_c derived from the proposed analytical methodology and the experimental results for the Tests 1 and 2 with different D_w is presented in Figure 4.12. Figure 4.12 presents the relationships between ψ_{ave} (Figure 4.12a), $S_{e,ave}$ (Figure 4.12b), and L_c (Figure 4.12c) with D_w from the proposed analytical approach. To properly capture the effect of footing embedment on M_c, the moment capacity of embedded shallow foundations was computed using (Antonellis et al. 2015):

$$M_c = \frac{PL}{2}\left[1 - \frac{A_c}{A}\right] + P_p\frac{D_f}{3} + kP_p\frac{B}{2} \quad \textbf{(4-25)}$$

where P_p is the passive earth force, and k is concrete-soil friction coefficient, which was assumed to be two-thirds of the constant volume friction angle. As observed in Figure 4.12, the response of soil to changes in D_w is similar to the response of hypothetical sand presented in Figure 4.9 in the hydrostatic condition ($q_w = 0$). The average matric suction increases linearly with increases in D_w, resulting in soil drainage and a decrease in the average effective saturation. Due to these changes in soil's matric suction and effective saturation, the critical length reduces slightly for $D_w < D_s$, which results in a slight increase in M_c. As observed in Figure 4.12, the model provides good estimates of the experimentally derived M_c data over a broad range in D_w.

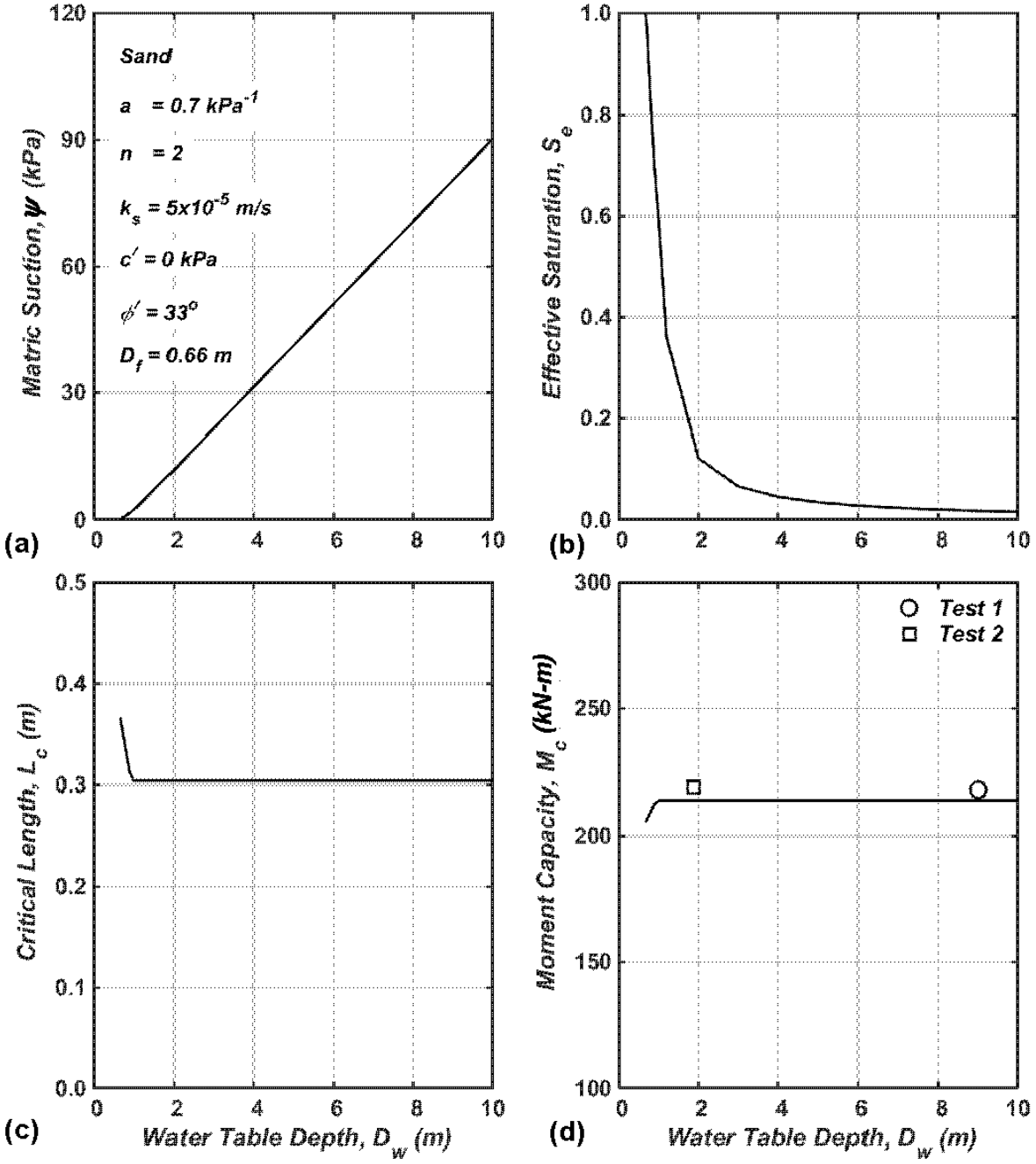

Figure 4.12:: Variations in the predicted (solid line) (a) ψ_{ave}; (b) $S_{e,ave}$; (c) L_c; and (d) M_c and comparison to experimental data (open markers, reported by Antonellis et al. 2015) with D_w (from Khosravi et al. 2021) (Note: 1 m = 3.3 ft; 1 kN-m = 0.74 kip-ft; 1 kPa = 0.145 psi).

Sharma (2019) performed a series of snap-back tests to characterize the rocking behavior and energy dissipation of footings overlying stiff, overconsolidated clay. The rocking foundation system was idealized as a single degree of freedom system supported by an isolated footing (Figure 4.10b) 5 ft. (1.5 m) long, 3.3 ft. (1.0 m) wide, and 12 in. (0.3 m) thick. The column consisted of a square steel tube with an 8 in. by 8 in. (0.2 m by 0.2 m) outer dimension and 0.5

in. (12.7 mm) wall thickness. The flexural rigidity, EI, of the column was 6.44 MN-m^2. The first yield moment of the column (83.6 kip-ft or 113 kN-m) was designed to be greater than M_c to enable the rocking mode of energy dissipation. The snap-back tests were conducted by pulling the deck at an angle of 45° with respect to the footing axis, using chains attached to a quick release mechanism (Figure 4.10b), followed by release of the pulling force. The superstructure weight was simulated using a number of R/C slabs that varied depending on the vertical axial load considered for testing, including 8.1, 19.5, 28, and 36.6 kips (36, 64, 92, and 120 kN). Various trials conducted for each load, each with a different amplitude of initial drift, were conducted. Two series of tests were performed by Sharma (2019), with Test 1 performed with the lateral load applied along the length of the foundation and Test 2 performed with the lateral load applied along the width of the foundation. The foundation was placed on the surface (D_f = 0).

The soil subgrade consisted of a soft to medium stiff, fine-grained clay of 2.3 ft. (0.7 m) thickness overlying a thick layer of stiff to very stiff silty clay to clayey silt. Based on Unified Soil Classification System, USCS, the soil at the site is classified as silt of high plasticity, MH. The *in-situ* S_r ranged from 86 to 91%, with liquid limit, *LL*, and plastic index, *PI* of about 75 and 40 (Figure 4.11a), respectively. The undrained shear strength, s_u, estimated from unconfined compressive strength (UCS) and correlations to the cone penetration tests varied from 50 to 85 kPa. In this study, the lower value of s_u = 1,000 psf (50 kPa) was considered as the s_u in bearing and moment capacity calculations due to the embedment depth and local measurements. No information on the hydraulic conductivity and SWRC of the soil was reported; therefore, the SWRC for a high plasticity silt with average *LL* = 54, *PI* = 21, and fines content, *FC* = 83 to 98% reported by Nam et al. (2010) was used as the representative SWRC (Figure 4.11b).

Figure 4.13 presents the comparison of M_c derived from the proposed analytical methodology and the experimental results for Tests 1 and 2 with different D_w. Figures 4.13a and 4.13b present the variations of ψ_{ave} and $S_{e,ave}$ with D_w, respectively, whereas Figure 4.13c demonstrates the variation of L_c with D_w derived from the proposed analytical approach. Based on the S_r and SWRC in the analysis, a depth of 25 m was assumed for the groundwater table. To properly capture the undrained response of a rocking footing on fine-grained, high plasticity soils, the bearing capacity was calculated using:

$$\boldsymbol{q_{ult,unsat} = 5.14 s_c d_c s_{u,unsat}} \tag{4-26}$$

where $s_{u,unsat}$ is the undrained shear strength of unsaturated fine-grained soils. To predict $s_{u,unsat}$, an equation proposed by Oh and Vanapalli (2018) was used, where s_u is related to matric suction as follows:

$$\boldsymbol{s_{u,unsat} = s_{u,sat}\left[1 + \left(\frac{\psi}{\mu}\right)\left(\frac{P_a}{101.4}\right)(S_r)^2\right]} \tag{2-47}$$

where $s_{u,sat}$ is the undrained shear strength of soil in the fully saturated condition, P_a is atmospheric pressure, and μ is a model parameter that is estimated using (Oh and Vanapalli 2018):

$$\boldsymbol{\mu = 10} \qquad \boldsymbol{8 \leq PI \leq 15.5} \tag{4-28a}$$

$$\boldsymbol{\mu = 1.77\, exp(0.0937\, PI)} \qquad \boldsymbol{15.5 < PI \leq 60} \tag{4-28b}$$

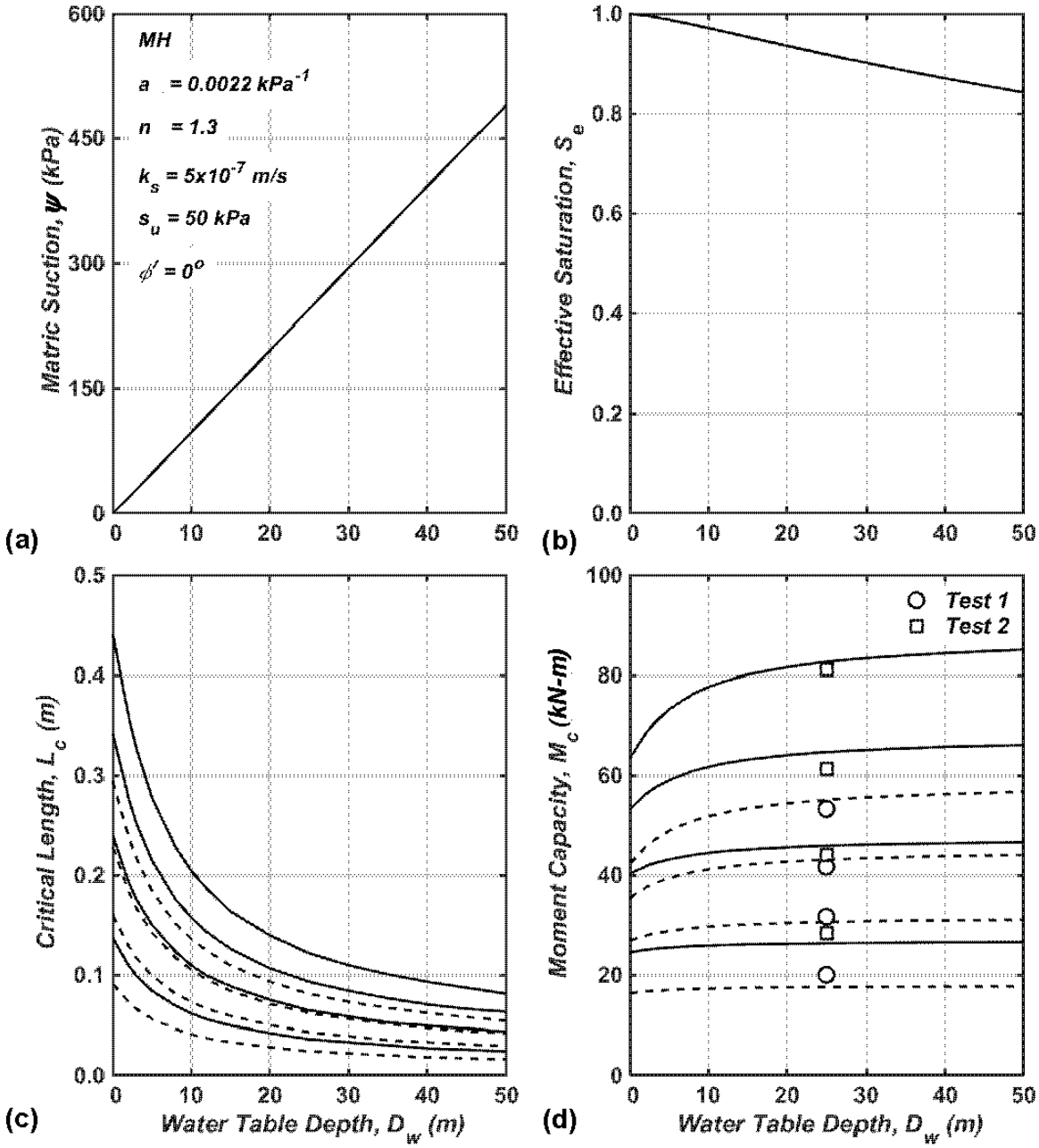

Figure 4.13: Variations in the predicted (solid line) (a) ψ_{ave}; (b) $S_{e,ave}$; (c) L_c; and (d) M_c and comparison to experimental data (open markers; reported by Sharma 2019) with D_w (from Khosravi et al. 2021) (Note: 1 m = 3.3 ft; 1 kN-m = 0.74 kip-ft; 1 kPa = 0.145 psi).

Figure 4.13 shows that the hydraulic response to changes in D_w is similar to that of the hypothetical clay presented in Figure 4.8 in the hydrostatic condition ($q_w = 0$). The average matric suction increases linearly with increases in D_w, resulting in the decrease of average S_e. These changes in ψ and S_e result in a dramatic decrease in L_c, which results in a considerable increase in M_c. As observed in Figure 4.13, the model captures the moment capacity reported by

Sharma (2019) for the vertical loading considered. Further comparison of the proposed methodology against additional experimental data, as it becomes available, is warranted.

4.6 DISCUSSION AND IMPLICATIONS FOR PRACTICE

New design provisions associated with shallow rocking foundations have been developed as a result of the previously conducted research (Kutter et al. 2016). While the new provisions encourage the use of rocking foundations in practice, they are mostly limited to cases associated with rocking in competent soils. Procedures to account for the effect of seasonally varying S_r or select state variables that properly represent conditions in the field under different seasonal weather conditions are not yet established. Under varying climate conditions, variation in saturation profiles result in the variation in suction, strength, and the deformation response of foundation soils at differing depths. Therefore, a bridge with a rocking shallow foundation is expected to have a different response during shaking under such varying conditions.

Presently, it is generally assumed that a hydraulic equilibrium condition with stationary groundwater table and no significant rate of precipitation or evaporation exists when computing the bearing and moment capacity using classical approaches. The groundwater table is mainly accounted for by choosing a suitable magnitude of soil unit weight (*e.g.,* the buoyant, saturated, or weighted average). The hydraulic equilibrium assumption, while being reasonable in arid regions, may overestimate bearing capacity in many cases, leading to erroneous evaluation of the ability of foundations to resist rocking rotations. In less arid regions, seasonal weather changes or fluctuations in the groundwater table depth will tend to be larger and hydraulic equilibrium conditions can occur rapidly. In these conditions, neglecting the hydro-mechanical processes caused by seasonal weather changes may affect the accuracy of the corresponding moment capacity.

The present study suggests that the moment capacity of bridge foundations can be better estimated if measurements of groundwater levels and their seasonal fluctuation, and the variation in the degree of saturation with depth, were conducted at bridges slated for retrofit or replacement. Such measurements could be used to establish regional trends for broader application (e.g., along a particular highway corridor) and establish the trends in the intensity of precipitation, evaporation, temperature fluctuations, and other measurements relevant for the identification of the rate of infiltration and evaporation. Transportation agencies may leverage the expertise of associated government agencies tasked with establishing such environmental measurements and associated forecasts to assist in bridge program planning and decision-making.

4.7 CONCLUSION

The present study proposes a design method for moment capacity of rocking shallow bridge foundations that accounts for the effect of seasonal and/or long-term climate change to the degree of soil saturation, S_r. s. The analytical method facilitates estimates of moment capacity of rocking shallow bridge foundations in soils with different surface flux boundary conditions, q_w, and groundwater level depths. The proposed methodology extends an existing approach by implementing suction stress-based effective stresses and a representation of the soil-water retention curve. With only two van Genuchten's SWRC parameters, a and n, the new analytical

approach can provide a practical framework to analyze the moment capacity for rocking shallow bridge foundations resting on various soils with different saturation.

The effect of surface flux boundary condition and groundwater table depth on the moment capacity was examined using the proposed methodology for hypothetical clays, silts, and sands, under infiltration ($q_w < 0$), hydrostatic ($q_w = 0$), and evaporation ($q_w > 0$) conditions, and provides the basis for the following conclusions:

1. Moment capacity is highly sensitive for clayey soils under variably saturated and various flux boundary conditions, with an increase of up to 20% for foundations embedded just 0.5 m into clay with $\phi' = 10°$. In contrast, the moment capacity of footings embedded within sandy soils are not particularly sensitive to these variable hydraulic conditions.

2. Changes in q_w result in slight to significant changes in the profiles of ψ and $S_{e,ave}$ for sands and clays, respectively, particularly under the infiltration condition. The increase in q_w due to infiltration resulted in lower ψ and higher S_e in the soil. Due to these changes in soil conditions, a rocking shallow bridge foundation will require a smaller L_c and consequently produce a larger moment capacity, M_c. The effect of q_w on M_c was not as pronounced for smaller groundwater table depths, D_w.

3. In clayey soils, increases in D_w resulted in significant increases in M_c regardless of the surface flux boundary conditions. However, the rate of increase in M_c decreases as D_w approaches the depth to the base of the shallow bearing failure mechanism, D_s.

4. The effective friction angle, ϕ', has small effect on the profiles of ψ_{ave} and $S_{e,ave}$. However, due to its effect on the depth of the shear zone underneath the soil-footing contact area, D_s, the effects associated with seasonal weather changes (changes in D_w or q_w) on M_c were different for soils with different ϕ'.

The proposed methodology for computing the moment capacity in unsaturated soils was applied to the results of large-scale shaking table and snap-back tests and suitably predicted the observed moment capacity. The proposed analytical framework can serve to establish the moment capacity of shallow foundations in varying saturation conditions – a common scenario for such bridge foundations. As significant changes in S_r may occur during the life of a bridge foundation, measurement of the *in-situ* saturation and groundwater fluctuations could be of significant benefit. Such data allow for more accurate quantification of rocking shallow bridge foundation moment capacity. Future additional comparison to the results of large-scale rocking tests is necessary to further validate the proposed analytical methodology over a wider range of conditions (e.g., different groundwater level depths and surface flux boundary conditions.

4.8 REFERENCES

Allmond, J. D. (2014). Shallow Rocking Foundations in Liquefiable and Saturated Soil Conditions. PhD Dissertation, University of California, Davis.

Allmond, J., Kutter, B. L., Bray, J. and Hayden, C., (2015). "New database for foundation and ground performance in liquefaction experiments. Earthquake Spectra, 31(4), pp.2485-2509.

Anastasopoulos, I., Gazetas, G., Loli, M., Apostolou, M., Gerolymos, N. (2010). Soil Failure Can Be Used for Seismic Protection of Structures. Bulletin of Earthquake Engineering, 8, 309-326.

Anastasopoulos, I., Kourkoulis, R., Gelagoti, F. and Papadopoulos, E. (2012). Rocking Response of SDOF Systems on Shallow Improved Sand: An Experimental Study. Soil Dynamics and Earthquake Engineering, 40, pp.15-33.

Anastasopoulos, I., Sakellariadis, L., & Agalianos, A. (2015). Seismic Analysis of Motorway Bridges Accounting for Key Structural Components and Nonlinear Soil–Structure Interaction. Soil Dynamics and Earthquake Engineering, 78, 127-141.

Antonellis, G., Gavras, A. G., Panagiotou, M., Kutter, B. L., Guerrini, G., Sander, A. C., and Fox, P. J. (2015). Shake Table Test of Large-Scale Bridge Columns Supported on Rocking Shallow Foundations. Journal of Geotechnical and Geoenvironmental Engineering, 141(5), 04015009.

Beck, J. and Skinner, R. I. (1974.) The Seismic Response of a Reinforced Concrete Bridge Pier Designed to Step. Earthquake Engineering and Structural Dynamics 2(4), 637–655.

Bishop, A. W. (1959). The Principle of Effective Stress. Tek. Ukeblad, 106(39), 859–863.

Brooks, R. H. and Corey, A. T. (1964). Hydraulic Properties of Porous Media. Hydrology papers (Colorado State University); no. 3.

Chen, Y.H., Liao, W.H., Lee, C.L. and Wang, Y. P. (2006). Seismic Isolation of Viaduct Piers by Means of a Rocking Mechanism. Earthquake Engineering and Structural Dynamics, 35(6), pp.713-736.

Costa, Y. D., Cintra, J. C., and Zornberg, J. C. (2003). Influence of Matric Suction on the Results of Plate Load Tests Performed on a Lateritic Soil Deposit. Geotech. Test. J., 2(2), 219–226.

Deng, L., Kutter, B. L., and Kunnath, S. K. (2012). Centrifuge Modeling of Bridge Systems Designed for Rocking Foundations. Journal of Geotechnical and Geoenvironmental Engineering, ASCE, 138(3): 335–344.

Fern, J., Soga, K., and Robert, D. J. (2014). Shear Strength and Dilatancy of Partially Saturated Sand in Direct Shear Tests. In Proc., TC105 ISSMGE Int. Symp. on Geomechanics from Micro to Macro (pp. 1391-1396).

Fredlund, D. G. and Morgenstern, N. R. (1977). Stress State Variables for Unsaturated Soils. Journal of Geotechnical and Geoenvironmental Engineering, 103(ASCE 12919).

Gajan, S., Kutter, B. L., Phalen, J. D., Hutchinson, T. C., Martin, G. R. (2005). "Centrifuge Modeling of Load-Deformation Behavior of Rocking Shallow Foundations." Soil Dynamics and Earthquake Engineering, 25, 773–783.

Gajan, S. and Kutter, B. (2008). Capacity, Settlement, and Energy Dissipation of Shallow Footings Subjected to Rocking. Journal of Geotechnical and Geoenvironmental Engineering ASCE 135(3), 407–420.

Gallipoli, D., Wheeler, S.J. and Karstunen, M., (2003). Modelling the Variation of Degree of Saturation in a Deformable Unsaturated Soil. Géotechnique, 53(1), pp.105-112.

Güllü, H., Özel, F. (2020). Microtremor Measurements and 3D Dynamic Soil-Structure Interaction Analysis for a Historical Masonry Arch Bridge under the Effects of Near- and Far-Fault Earthquakes. Environ Earth Sci 79, 338.

Hakhamaneshi, M. (2014). Rocking Foundations for Building Systems-Effect of Footing Shape, Soil Environment, Embedment and Normalized Moment-to-Shear Ratio. PhD Dissertation, University of California, Davis, CA, USA.

Housner, G. W. (1963). The Behavior of Inverted Pendulum Structures during Earthquakes. Bulletin of the Seismological Society of America 53(2), 404–417.

Huckelbridge, A. A. and Ferencz, R. M. (1981). Overturning Effects on Stiffened Building Frames. Earthquake Engineering and Structural Dynamics 9(1), 69–83.

Hung, H., Liu, K., Ho, T., and Chang, K. (2011). An Experimental Study on the Rocking Response of Bridge Piers with Spread Footing Foundations," Earthquake Engineering and Structural Dynamics 40(7), 749–769.

Kawashima, K. and Nagai, T. (2006). Effectiveness of rocking seismic isolation on bridges. In 4th International Conference on Earthquake Engineering, National Center for Research on Earthquake Engineering of Taiwan (pp. 12-13).

Khalili, N. and Khabbaz, M.H. (1998). A Unique Relationship for χ for the Determination of the Shear Strength of Unsaturated soils. Geotechnique, 48(5), pp.681-687.

Khalili, N., Geiser, F. and Blight, G. E. (2004). Effective Stress in Unsaturated Soils: Review with New Evidence. International Journal of Geomechanics, 4(2), pp.115-126.

Khosravi, A., Alsherif, N., Lynch, C., and McCartney, J. (2012). Multistage Triaxial Testing to Estimate Effective Stress Relationships for Unsaturated Compacted Soils. Geotechnical testing journal, 35(1), 128-134.

Khosravi, A. and McCartney, J. S. (2012). Impact of Hydraulic Hysteresis on the Small-Strain Shear Modulus of Low Plasticity Soils. Journal of Geotechnical and Geoenvironmental Engineering, 138(11), pp.1326-1333.

Khosravi, A., Shahbazan, P., and Pak, A. (2018). Impact of Hydraulic Hysteresis on the Small Strain Shear Modulus of Unsaturated Sand. Soils and Foundations, 58(2), 344-354.

Khosravi, A., Hashemi, A., Ghadirianniari, S., & Khosravi, M. (2020). Variation of Small-Strain Shear Modulus of Unsaturated Silt under Successive Cycles of Drying and Wetting. Journal of Geotechnical and Geoenvironmental Engineering, 146(7), 04020050.

Khosravi, A., Stuedlein, A. W., & Higgins, C. (2021). New formulation for estimating the moment capacity of rocking shallow foundations resting on partially saturated soil. Journal of Bridge Engineering, 26(11), 04021084.

Kutter, B. L., Hutchinson, T. C, Aschheim, M., Kunnath, S., Liu, W., and Hakhamaneshi, M. (2011). Design of Soil and Structure Compatible Yielding to Improve System Performance. 2011 NSF Engineering Research and Innovation Conference, Atlanta, GA, Jan 4-7.

Kutter, B.L., Moore, M., Hakhamaneshi, M. and Champion, C. (2016). Rationale for Shallow Foundation Yocking Provisions in ASCE 41-13. Earthquake Spectra, 32(2), pp.1097-1119.

Leong, E. C., and Rahardjo, H. (1997). Permeability Functions for Unsaturated Soils. Journal of Geotechnical and Geoenvironmental Engineering, 123(12), 1118-1126.

Liu, W., Hutchinson, T. C., Kutter, B. L., Hakhamaneshi, M., Aschheim, M. A. and Kunnath, S. K. (2013). Demonstration of Compatible Yielding between Soil-Foundation and Superstructure Components. Journal of Structural Engineering, 139(8), pp.1408-1420.

Lu, N., and Likos, W. J. (2004). Unsaturated Soil Mechanics, Wiley, New York.

Lu, N. and Likos, W. J. (2006). Suction Stress Characteristic Curve for Unsaturated Soil. Journal of Geotechnical and Geoenvironmental Engineering, 132(2), pp.131-142.

Lu, N., Godt, J. W., and Wu, D. T. (2010). A Closed-Form Equation for Effective Stress in Unsaturated Soil. Water Resources Research, 46(5).

McCartney, J. S. and Khosravi, A. (2013). Field-Monitoring System for Suction and Temperature Profiles under Pavements. Journal of performance of constructed facilities, 27(6), 818-825.

Mergos, P. E. and Kawashima, K. (2005). Rocking Isolation of a Typical Bridge Pier on Spread Foundation. Journal of Earthquake Engineering, 9(sup2), pp.395-414.

Moehle, J. and Deierlein, G. G. (2004). A framework methodology for performance-based earthquake engineering. In 13th world conference on earthquake engineering, August 2004 (Vol. 679).

Nam, S., Gutierrez, M., Diplas, P., Petrie, J., Wayllace, A., Lu, N., and Muñoz, J. J. (2010). Comparison of testing techniques and models for establishing the SWCC of riverbank soils. Engineering Geology, 110(1-2), 1-10.

Oh, W. T., and Vanapalli, S. K. (2011). Modelling the Applied Vertical Stress and Settlement Relationship of Shallow Foundations in Saturated and Unsaturated Sands. Can. Geotech. J., 48(3), 425–438.

Oh, W. T. and Vanapalli, S. (2018). Undrained Shear Strength of Unsaturated Soils under Zero or Low Confining Pressures in the Vadose Zone. Vadose Zone Journal, 17(1), 1-13.

Oloo, S. Y., Fredlund, D. G., and Gan, J. K. M. (1997). Bearing Capacity of Unpaved Roads. Can. Geotech. J., 34(3), 398–407.

Pecker, A. (2003). A seismic Foundation Design Process, Lessons Learned from Two Major Projects: the Vasco de Gama and the Rion Antirion Bridges. in ACI Int. Conf. Seismic Bridge Design and Retrofit (La Jolla: University of California at San Diego).

Priestley, M. J. N., Seible, F., and Calvi, G. M. (1996). Seismic Design and Retrofit of Bridges, John Wiley and Sons, New York, NY.

Reinhardt, E., Saiidi, M., and Siddharthan, R. (2003) Seismic Performance of a CFRP/Concrete Bridge Bent on Flexible Footings. Technical Report CCEER-03-4, Civil Engineering Department, University of Nevada, Reno, NV, August 2003.

Rosebrook, K. R. (2002). Moment Loading on Shallow Foundations: Centrifuge test data archives." MS thesis, University of California, Davis, CA, USA.

Sakellaraki, D.I.M.I.T.R.A. and Kawashima, K. (2006). Effectiveness of Seismic Rocking Isolation of Bridges based on Shake Table Test. Proc. First European Conf. on Earthquake Engineering and Seismology.

Sharma, K. (2019). Field Investigation and Performance-Based Seismic Design of Rocking Shallow Foundations in Cohesive Soil. PhD Dissertation, University of Alberta, Edmonton, AB, Canada.

Shrestha, S. (2019). Seismic Retrofit of Square Reinforced Concrete Bridge Columns using Titanium Alloy Bars. PhD Dissertation, Oregon State University, Corvallis, OR.

Sivakumar, V. (1993). A Critical State Framework for Unsaturated Soil, PhD Dissertation, University of Sheffield).

Terzaghi, K. (1943). Theoretical Soil Mechanics, Wiley, New York.

Vahedifard, F., and Robinson, J. D. (2016). Unified Method for Estimating the Ultimate Bearing Capacity of Shallow Foundations in Variably Saturated Soils under Steady Flow. Journal of Geotechnical and Geoenvironmental Engineering, 142(4), 04015095.

van Genuchten, M. Th. (1980). A Closed-Form Equation Predicting the Hydraulic Conductivity of Unsaturated Soils. Soil Sci. Soc. Am., 44(5), 892–898.

Vanapalli, S. K., and Mohamed, F. M. O. (2013). Bearing Capacity and Settlement of Footings in Unsaturated Sands. Can. Geotech. J., 5(1), 595–604.

Vanapalli, S. K., Sillers, W. S., and Fredlund, M. D. (1998). The Meaning and Relevance of Residual State to Unsaturated Soils. *51st Canadian Geotechnical Conference*, (pp. 4-7).

Vesic, A. S. (1973). Analysis of Ultimate Loads of Shallow Foundations. Journal of Soil Mechanics and Foundations Div, 99 (sm1).

Wuttke, F., Kafle, B., Lins, Y., and Schanz, T. (2013). "Macro-element for Statically Loaded Shallow Strip Foundation Resting on Unsaturated Soil." Int. J. Geomech., 0.1061/(ASCE)GM.1943-5622.0000254, 557–564.

5.0 TITANIUM SEISMIC SUBSTRUCTURE RETROFIT TO ENABLE ROCKING OF BRIDGE FOUNDATIONS CONSIDERING SOIL-STRUCTURE INTERACTION: EXPERIMENTS AND NUMERICAL SIMULATIONS

5.1 INTRODUCTION

The need for cost-effective seismic retrofits to older bridge substructures has been recognized based on observed poor performance in past earthquakes, experimental findings from large- and full-scale experiments, and numerical investigations (Cairns and Arthur 1979; Girard and Bastien 2002; Melek and Wallace 2004; El Gawady et al. 2010). The inadequacies of reinforcement detailing associated with pre-1971 bridge substructures represent a particularly pressing need for seismic remediation, as many of these systems were not designed for seismic effects. Design inadequacies of substructures include short lap splices in the column base above the footing, low confinement of the concrete core, very light transverse reinforcement over the lap-splice region, potentially insufficient footing plan dimensions, and a lack of reinforcing steel at the top of the footing. The lack of transverse reinforcement in the columns results in unreliable shear-resistance, early buckling of longitudinal reinforcing, and loss of core concrete during seismic loading. Design and detailing deficiencies can result in significant damage of the substructure, large residual drift, inadequate ductility, and/or collapse.

Various retrofitting techniques have been proposed to correct these deficiencies and to improve the seismic performance of bridge substructures. Accepted retrofit solutions include composite material jacketing (Xiao and Ma, 1997; Mirmiran et al., 1998; Haroun and Elsanadedy, 2005; and Goksu et al., 2014), steel jacketing (Chai et al., 2008; El Gawady et al., 2010), and wire prestressing (Gamble et al., 1996; Saatcioglu and Yalcin, 2003, Zong-Cai et al. 2014). The increase in shear strength and confinement, improved lap-splice performance, and small increase in column diameter makes jacketing an attractive option in comparison to other retrofitting techniques. The application of jacketing to square RC columns has not produced comparable performance improvements relative to circular columns. The main challenge associated with such techniques lies in providing effective confinement to square columns (Campione et al. 2004). When applying jackets to square columns, the corners of the section are typically chamfered to improve the uniformity of hoop stress, which requires significant effort and cost. Even then, this approach does not substantially improve confinement in regions distant from the chamfered corners, remaining essentially unconfined (Campione et al. 2004). Also, most of the contemporary retrofitting techniques focus on the provision of lateral confinement only, and there has been limited study on the flexural enhancement of columns with lap-spliced bars. Providing flexural load paths with near-surface-mounted (NSM) bars combined with local confining jackets of textile-reinforced mortars has led to enhanced flexural resistance and displacement ductility of square RC columns (Bournas and Triantafillou, 2009). The surface preparation and NSM grooving required for construction makes this retrofit alternative challenging to implement in practice.

This section describes the use of an economical and effective seismic retrofit alternative for RC footing-column systems containing vintage reinforcing steel details. The retrofit approach

mitigates the inherent deficiencies of such substructures and changes their mode of energy dissipation from plastic hinging of the columns to rocking of the foundations. The retrofit is demonstrated on square RC columns and combines titanium alloy bars (TiABs) with conventional concrete to provide improved confinement and secondary flexural resistance. TiABs exhibit well-defined yield stress, high ductility, moderate stiffness, and limited strain hardening. They are resistant to corrosion, and their light weight and flexibility make them easy to handle and install (Takahashi et al. 1994, Shrestha 2019). Khadka et al. (2020) and Acharya et al. (2022) reported results from a comprehensive mechanical testing program including tension, hardness, Charpy V-notch, and galling tests to characterize mechanical properties of Grade 5 TiABs of the type used in this study. The experimental tensile strengths ranged from 140 ksi (960) to 160 ksi (1,100 MPa). TiAB samples exhibited modulus of elasticity that was 50% smaller, a modulus of resilience that was 27% greater, and ductility that was 50% greater, than that of the similar high-strength steel. While Brinell hardness tests indicated that TiABs were about 5.5% softer, Charpy V-notch tests indicated toughness that were 100% greater, than that measured for the steel.

TiABs were first used to rehabilitate the Mosier Bridge over I-84 in Oregon, using the NSM technique. The rehabilitation process was completed in two weeks, cheaper than other alternatives (e.g., the cost was less than 3% of the estimated cost for bridge replacement, and 30% cheaper than rehabilitation using alternative materials), and provided satisfactory improvement to the bridge performance in terms of strength and deformability (Higgins et al. 2017). These desirable features indicated that the TiAB retrofit method is a viable retrofit alternative, providing the basis for experimental and analytical studies of the TiAB retrofit application to other applications (Barker 2014; Amneus 2014; Knudtsen 2016; Vavra 2016; Higgins et al. 2017; Shrestha 2019).

A set of quasi-static reversed cyclic loading tests were performed on full-scale RC column-footing specimens to study the cyclic performance of the proposed TiAB retrofit. The specimens were designed and constructed to have vintage column proportions and reinforcing details that are widely recognized as being seismically deficient and representative of bridges built prior to the introduction of seismic design provisions (Shrestha 2019). To investigate the influence of soil structure interaction (SSI) on the seismic behavior of retrofitted bridge substructures, two different foundation support conditions were investigated: fixed base with no soil–structure interaction and flexible support under the footing provided by a nonlinear soil simulant. The experimental results were used to calibrate three-dimensional (3D), nonlinear numerical models that capture the responses of vintage and retrofitted column-footing systems. The numerical models were then used to investigate the seismic performance of vintage and retrofitted column-footing specimens and assess factors such as soil and structure characteristics that affect the performance of the system during lateral loading.

5.2 DETAILS OF THE EXPERIMENTAL FULL-SCALE SPECIMENS

5.2.1 Experimental Specimens and Vintage Structural Detailing

Quasi-static, cyclic loading tests were performed on four (4) full-scale specimens in the laboratory to study the seismic performance of different vintage and retrofitted column-footing systems with and without a soil simulant to capture the effects of SSI. Each specimen consisted

of a single column with footing. Three (3) experiments were performed on specimens with fixed foundation support. The fixed foundation support forces damage into the column, typically observed as plastic hinging at the column base. The fixed foundation specimens consisted of one (1) vintage and two (2) TiAB retrofitted specimens, designated PHV, PHRS, and PHRSL, respectively. The two (2) different retrofitted specimens were used to evaluate the effectiveness of alternative retrofit measures. A fourth experiment was performed on a TiAB retrofitted specimen bearing on a soil simulant to consider the effect of foundation rocking and SSI on the system response, designated RRSL. These experiments represent a portion of a larger study conducted to evaluate the innovative retrofitting technique for RC bridge systems using TiABs, described by Barker (2014), Amneus (2014), Knudtsen (2016), Lostra (2016), Vavra (2016), Higgins et al. (2017), and Shrestha (2019).

To develop a representative structural archetype for the experimental program, bridge drawings from the Oregon Department of Transportation (ODOT) Bridge Database were reviewed (Shrestha 2019). The frequency of occurrence of certain substructure geometric, material, and reinforcement details were summarized. The most common features were used as the basis for the design of the specimens. All the specimens were constructed with 24 in. × 24 in. (0.61 m × 0.61 m) square columns with four (4) #10 (#32M) Gr. 60 longitudinal reinforcing steel bars (i.e. $\rho_l = 0.88\%$). The specimen flexural reinforcement is equivalent in strength to the most common vintage reinforcement detail, which consisted of four (4) #11 (#36M) Gr. 40 longitudinal reinforcement bars (i.e. $\rho_l = 1.0\%$). The transverse column ties were #3 (#10M) Gr. 40 ties with 90˚ hooks spaced at 12 in. (0.305 m) on center (i.e. $\rho_v = 0.09\%$) with 1.5 in. (0.04 m) concrete cover. The average nominal yield stress, f_y, of the bars was 65 ksi (448 MPa), with an average ultimate stress, f_u = 95 ksi (655 MPa), and an ultimate elongation of 32.4%. Table 5.1 compares the characteristics of the materials used to construct the representative column-footing specimens; slight differences in the reinforcing steel strength and dimensions were required because large diameter bars are no longer available in Gr. 40. Thus, smaller diameter longitudinal bars were used to target the vintage bar strength. This results in lower dowel action at the column-footing interface.

The cross sections of vintage and retrofitted specimens with fixed foundation are shown in Figures 5.1 and 5.2. For the vintage system with fixed foundation (Figure 5.1a), the longitudinal reinforcing bars at the base of the column were spliced to the footing starter bars with a contact lap-splice length of 36 in. (0.914 m, or approximately 28 times the diameter of the bar, d_b). The column height of the tested specimens was 9 ft. (2.743 m); the height of the specimens represents half that of a typical bridge column, whereby the flexural point of inflection is located at mid-height and thereby corresponds to the laboratory horizontal loading point to produce a realistic shear-span. The columns were constructed with a heavily reinforced 6 ft × 6 ft (1.83 m × 1.83 m) and 2 ft (0.61 m) thick footing with details shown in Figure 5.1b. The footings were over-designed to isolate the behavior of the column and ensure that failure would not occur in the footing. These heavily reinforced footings are not representative of the actual details contained in the bridge inventory database.

5.2.2 Titanium Alloy Bar Retrofit Details

Two (2) of the retrofitted specimens (Specimens PHRSL and PHRS; Fig. 5.2) used TiAB reinforcing. Both specimens used TiAB spirals to ensure continuous confinement through hoop

action in the lower portion of the column. Specimen PHRSL (Fig. 5.2a) also used TiAB ligaments to provide a supplemental flexural load path that bridges over the deficient reinforcing steel lap-splice and can delay splice failure and carry flexural tension upon anchorage loss of the reinforcing steel in the splice.

Table 5.1: Comparison of different characteristics of the materials for the test specimens and the column-footing system representative of the bridge inventory.

	Column Type	Test Specimen		Bridge Inventory	
		SI	Eng	SI	Eng
Column Dimension	length	0.61 m	24 in	0.61 m	24 in
	width	0.61 m	24 in	0.61 m	24 in
Ties	Bar Size	10M	#3	10M	#3
	Spacing	0.3 m	12 in	0.3 m	12 in
	Grade	-	40	-	40
	$f_{y,\text{steel}}$	276 MPa	40 ksi	276 MPa	40 ksi
	Concrete Cover	0.04 m	1.5 in	0.04 m	1.5 in
Longitudinal Bars	Bar Size	32M	#10	36M	#11
	Grade	-	60	-	40
	$f_{y,\text{steel}}$	448 MPa	65 ksi	276 MPa	40 ksi
	$f_{u,\text{steel}}$	655 MPa	95 ksi	-	-
	Ultimate Elongation, %	32.4		-	

The nominal yield stress of the TiAB ligaments was 130 ksi (896 MPa), and the average length of the ligaments implemented was determined using AASHTO LRFD Bridge Design Specifications (2017) for tension lap-splice length for longitudinal column bars. TiAB ligaments consisted of smooth 5/8 in. (16 mm) diameter bars with a 10 in. (250 mm) long 90° hook on one end. Surface deformations are located only over the hook tail and the lower 15 in. (380 mm) end of each bar. The surface deformations facilitate anchorage of the bars into concrete using structural epoxy as illustrated in Figure 5.1b. The pin diameter for the 90º hook was 95 mm (3 ¾ in.). The hooked end of the TiAB ligament was anchored into the column face and the straight portion was anchored into the footing. Three different lengths of vertical TiABs were used in each column to stagger the terminations with a 6 in. (150 mm) spacing and thereby reduce stress concentrations at a single section.

The pitch of the TiAB spirals was calculated using the guidelines from Priestley et al. (1996) based on the confinement model for circular reinforced column sections by Mander et al. (1988). The effective lateral pressure (f_l) of 320 psi (2.2 MPa), approximately $0.1f_c'$, was used in the design. The TiAB spiral was chosen to meet the AASHTO LRFD Bridge Design Specifications

(2017) and requires the use of 3/8 in. (9.5 mm) aggregate to construct the shell for the given longitudinal reinforcement. Based on AASHTO LRFD Bridge Design Specifications (2017), a 3/8 in. (9.5 mm) diameter, smooth TiAB spiral was chosen at 2.5 in. (63.5 mm) pitch. Such design details ensured elastic performance of the spirals during loading. The top spiral was anchored 8 in. (200 mm) into the column and the bottom spiral was anchored into the footing. The ends of the TiAB spirals were heated with an oxyacetylene torch and field-bent to produce a 90° hook. The material properties and dead lay production method of the TiAB spirals allowed the spiral to easily open and manually wind around the column without permanent deformation or exertion, and results in natural contact with the 90° formed corners of the square column. No surface preparation is required for the concrete surface of the column.

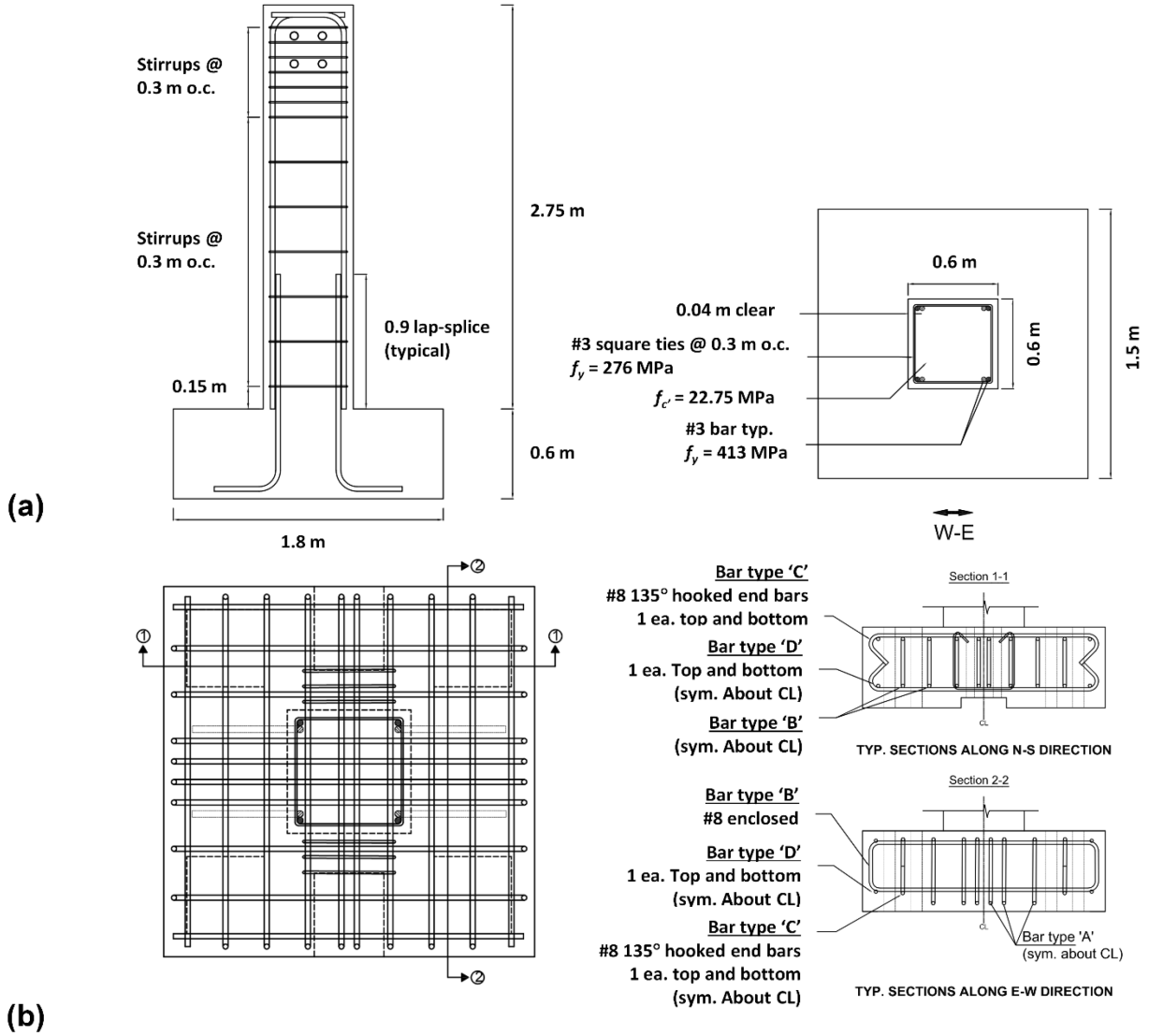

Figure 5.1: Column dimensions and reinforcing steel details of (a) the vintage specimen with fixed base, PHV; and (b) the reinforcing steel details of the footings (from Khosravi et al. 2023) (Note: 1 m = 3.2808 ft).

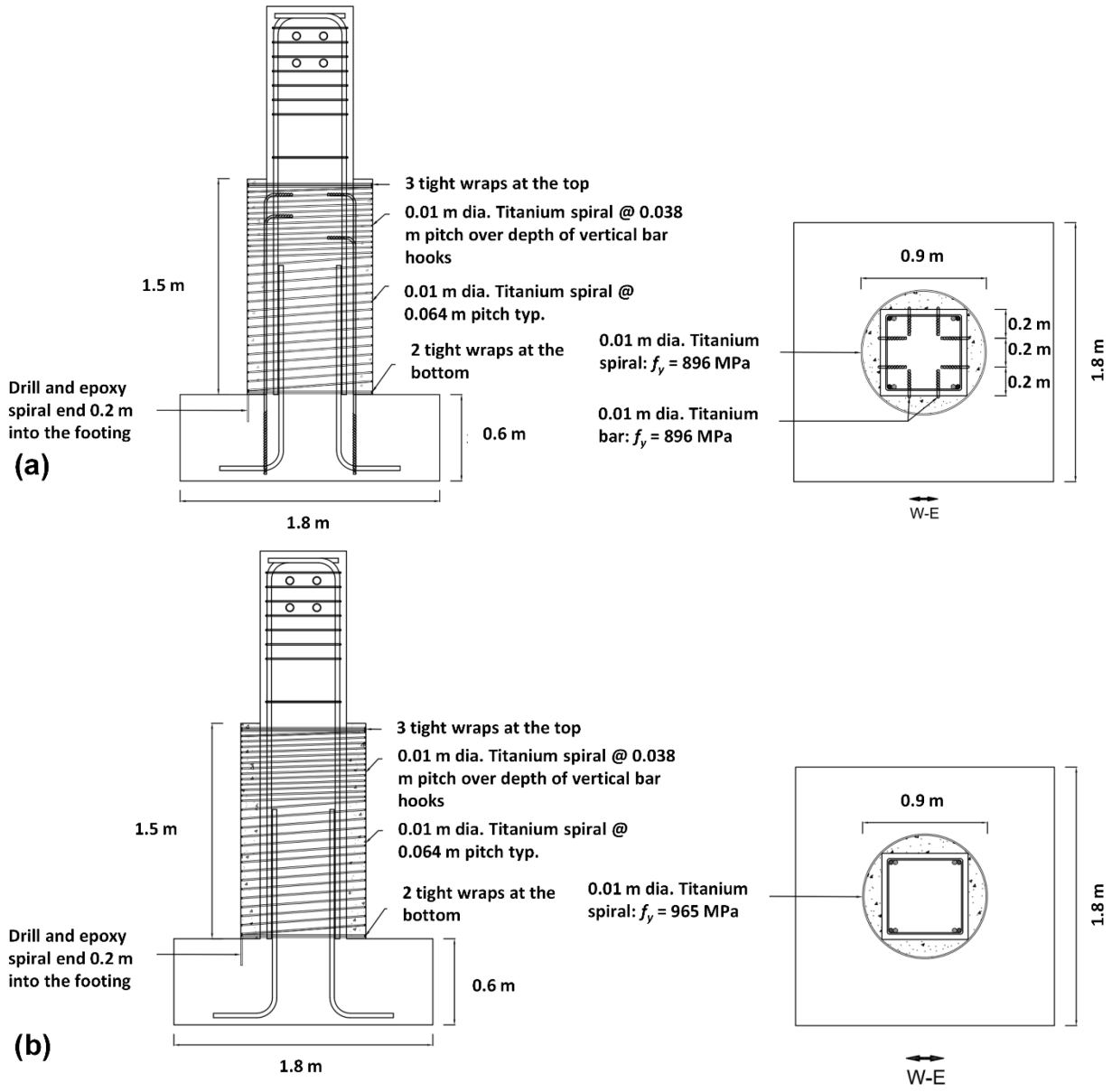

Figure 5.2: Column dimensions and reinforcing steel details of (a) the retrofitted specimen with TiAB ligaments and spiral with fixed base, PHRSL; and (b) the retrofitted specimen with TiAB spiral only with fixed base, PHRS (from Khosravi et al. 2023) (Note: 1 m = 3.2808 ft).

5.2.3 Concrete and Epoxy Material Properties

Locally available concrete ready mix containing ¾ in. (9.5 mm) aggregate was used for the column and footing specimens, and 3/8 in. (4.75 mm) minus aggregate was used for the retrofit shell. The results of compressive strength tests performed in accordance with ASTM C39M/C39M-05 (ASTM 2005) and ASTM C617-98 (ASTM 1998) indicated design compressive strength of around 3,500 psi (22.7 MPa) for the columns and footing and 4000 psi (28 MPa) for the retrofit shell. Tensile splitting tests results indicated average tensile strength

values of 300 (2), 235 (1.6), and 420 psi (2.9 MPa) for the column, footing, and shell concrete mix respectively used for the study.

The epoxy used for TiAB ligament anchorage to the concrete substrate was Hilti HIT-RE 500 V3 Epoxy Adhesive. The epoxy manufacturer reports a bond strength of 1,560 psi (10.8 MPa) and 1,690 psi (11.7 MPa) for a 2- and 14-day cure period, and a tensile strength of 7,150 psi (49.3 MPa) at 7 days. The results of pull-out tests on a #5 TiAB bar indicated an average bond strength of approximately 1.4 ksi (9.6 MPa) over the effective embedded length of 15 in. (380 mm).

5.2.4 Specimen Construction and Retrofit Installation

All column specimens were constructed in two stages: the footings with starter reinforcing bars were constructed first, and then the column was constructed after the footing concrete had cured. The TiAB retrofit installation process is presented in Figure 5.3. For the retrofit installation, holes for TiAB ligaments and spirals were hammer-drilled at the pre-determined locations. To get the bend of the vertical TiABs to rest against the column face, rounding out of the bottom side of the drilled holes was required prior to anchorage. The holes were carefully cleaned by brushing and vacuuming. The column was wrapped in plastic sheathing to debond the concrete shell from the column faces as shown in Figure 5.3a. Debonding was considered in this study to minimize changing the stiffness of the retrofitted system. The intent of the shell was to provide confinement without changing the effective moment of inertia of the cross-section that could otherwise attract load in an indeterminate bridge substructure system. With debonding, the retrofit shell can slide up and down relative to the column minimizing crushing at the toe region of the shell.

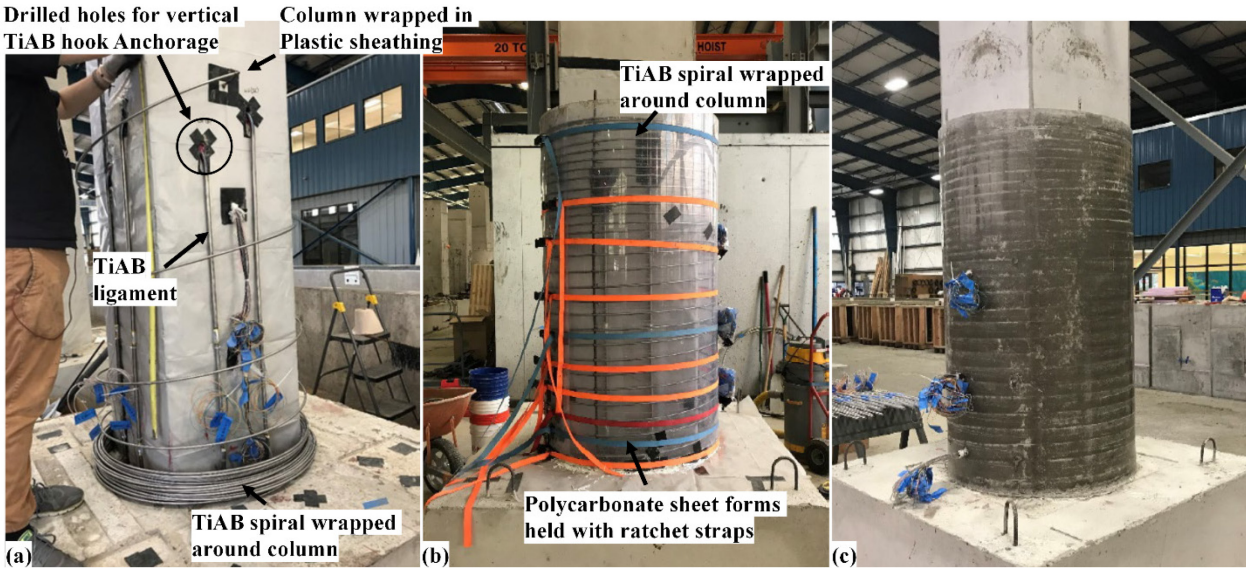

Figure 5.3: TiAB retrofit installation process: (a) installation of the TiAB ligaments and spiral in their designated locations; (b) placement of the polycarbonate formwork around the spirals and filling concrete into the framework; and (c) the final retrofitted specimen (from Khosravi et al. 2023).

After placing and bonding the ligaments with epoxy, one end of the TiAB spiral was anchored to the column face at location of the longest TiAB ligament. The spirals were then wrapped around the columns and drawn tightly at the corners of the column and tied at the designated pitch, whereas the other end of the spiral was anchored to the footing (Figure 5.3b). Polycarbonate formwork was then placed directly around the spirals with no cover. It is important to note that TiABs are impervious to corrosion in such structural applications and thus concrete cover is not required for environmental durability. The polycarbonate sheet was held together using ratchet straps as shown in Figure 5.3b. Concrete was then filled into the formwork to the height of the shell. The polycarbonate form allows visual inspection of the fill to ensure that the shell is properly placed and consolidated. The final retrofitted specimen is shown in Figure 5.3c.

5.2.5 Soil Simulant to Enable Soil-Structure Interaction

The rocking retrofitted specimen was constructed with column dimensions and reinforcement and retrofit details similar to specimen PHRSL (Figure 5.1b). However, the footing was constructed with smaller plan dimensions of 5 × 5 ft (1.5 × 1.5 m) that better represent actual footing dimensions observed in the bridge database for the selected column (Figure 5.1). The effect of the yielding soil subgrade was simulated using FOAMULAR® 1000 Extruded Polystyrene (XPS) Rigid Foam Insulation. Details on the strength and stiffness of the soil simulant are provided below. Two layers of foam 3 in. (75 mm) thick and 4 layers of 0.5 in. (12 mm) thick concrete boards as a load distribution slab (LDS) were placed on the strong floor, prior to the placement of the test specimen; thereafter, application of the axial load engaged the footing-LDS-XPS-strong floor system. Lateral loading applied to the column could thus be dissipated using the rocking mode. Horizontal sliding of the footing was resisted by a steel frame that reacted on the front and back faces of the footing at 2/3 of the footing thickness from the base.

5.3 FULL-SCALE LOADING TESTS OF VINTAGE AND RETROFITTED SPECIMENS

5.3.1 Instrumentation and Loading Protocol

Instruments were used to observe the forces, deformations, and strains developing in the specimens, including load cells mounted to hydraulic actuators, displacement sensors, and bonded foil resistance strain gauges installed on the steel reinforcement and TiABs. A commercially available data acquisition system was used to collect data at a sampling rate of 5 Hz. Testing was performed under constant axial load, equal to 8% of the nominal axial compressive capacity of the column, or 150 kips (667 kN). Under the applied axial load, the specimens were subjected to displacement-controlled reversed cyclic loading and the response of column. The loading history was derived according to the ACI 374.2R-13 (ACI Committee 374, 2013) protocol, and is presented in Figure 5.4.

5.3.2 Experimental Test Setup

Figure 5.5 presents the loading frame used in the experiment on the rocking retrofitted specimen (i.e., Specimen RRSL). The test setup consisted of a servo-hydraulic controlled horizontal actuator with a capacity of 110 kips (489 kN) mounted on a strong wall to supply the necessary

lateral force. A hydraulic jack was positioned on a 1/8 in. (3.2 mm) thick copper plate placed on top of the column surface finished with Hydrostone. The copper plate was intended to allow uniform pressure distribution to the column by accommodating surface imperfections. The column was compressed by tensioning Dywidag bars located on the east and west side of the column. The Dywidag bars were anchored to a steel spreader beam at the top and connected to steel plates attached to the specimen footing. The Dywidag bars were anchored with special spherical bearings to permit rotation of the bars during lateral deformation. For the three (3) rigid footing specimens, the footings were through-bolted to the strong floor at all four (4) corners. Tensioning of the anchor bolts prevented rotation and sliding of the footing relative to the strong floor.

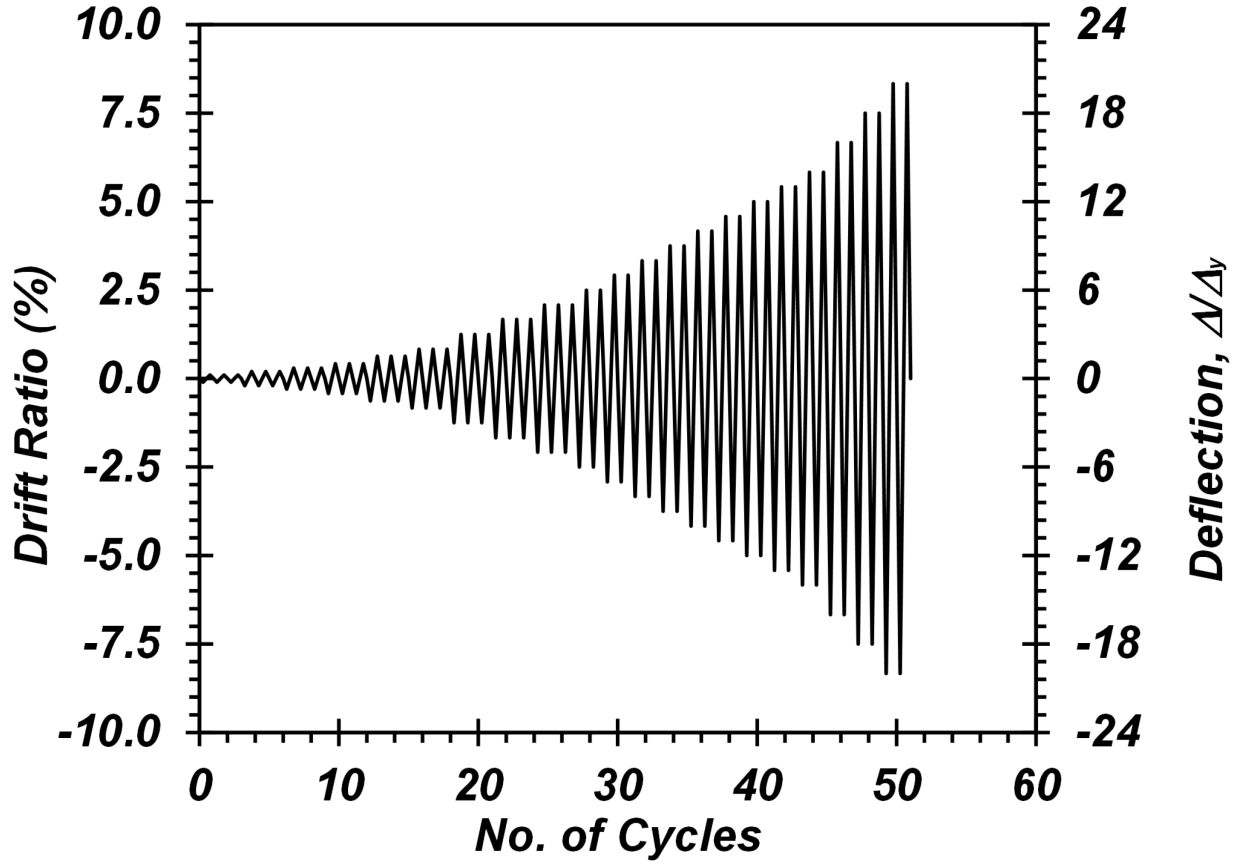

Figure 5.4: Load protocol used in this study (from Khosravi et al. 2022).

The specimen with the flexible support (Specimen RRSL) was squeezed onto the strong floor by the applied column axial load. Horizontal sliding of specimen during loading was prevented by placing a steel framework around the footings (Figure 5.5). The contact points on the concrete footing had roller bearings to allow the footing to move up or down, but restricted horizontal translation. The horizontal reactions on the north and south faces of the footing were located 203 mm (8 in.) from the top of the footing. Another hydraulic jack with load cell was used to ensure contact between the restraining system and the footing so that no gaps occurred.

At the beginning of the test, the axial load was applied slowly to the top of the specimen until the desired magnitude (667 kN) was achieved. The axial load was then maintained constant. Fluctuations in axial load when the column was pushed and pulled through higher drifts were monitored and actively controlled by releasing or adding jack pressure as needed.

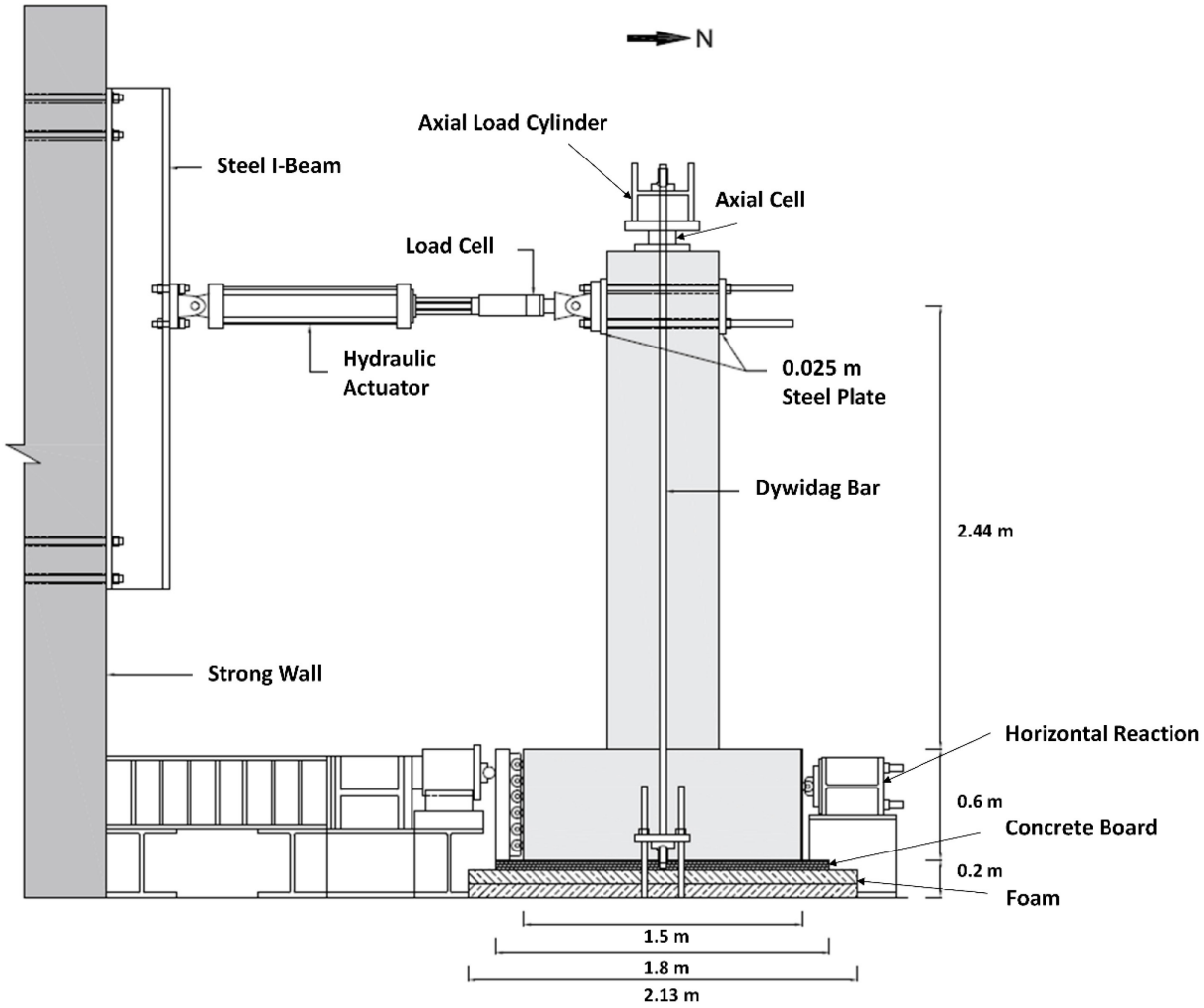

Figure 5.5: Experimental setup used to test specimen RRSL (from Khosravi et al. 2023) (Note: 1 m = 3.2808 ft).

5.3.3 Experimental Response of the Single Column-Footing Specimens

Figure 5.6 presents the moment at the base of the column against the column drift for the vintage and retrofitted specimens with fixed base and flexible support. These moment-drift responses have been corrected for P-Delta effects as described by Shrestha (2019). Specimen PHV (Figure 5.6a) exhibited a maximum moment of approximately 301 kip-ft (409 kN-m) at a column drift of 0.4 in (0.01 m) which was below the computed yield displacement for the specimen. At this drift level, the column failed due to lap-splice bond failure and relative slip between the bars in the lap splice was observed. This resulted in significant strength and stiffness degradation (Figure 5.6a). The moment resistance decreased significantly with continuing loading cycles, reducing from its

maximum to approximately 140 kip-ft (190 kN-m) at a drift of 1.18 in. (0.03 m). This can be noted in the push cycles in the bottom left quadrant of the load-deflection hysteresis. As failure occurred prior to achieving the nominal moment capacity of the column, the specimen exhibited no ductility.

Figure 5.6b shows that the TiAB retrofit implemented with specimen PHRSL exhibited a 2.5-fold increase in moment capacity, or 733 kip-ft (995 kN-m). It produced a displacement ductility of approximately 11 and 15 for the push and pull-cycles, respectively, exhibiting a loss of strength of 10% relative to the maximum. The retrofitting method did not prevent lap-splice failure; however, it delayed the onset of this behavior, so the specimen achieved a higher moment capacity of 738 kip-ft (1,000 kN-m) at a larger column drift of about 4.3 in (0.11 m), a substantial improvement compared to the unretrofitted vintage specimen. The load capacity dropped in the push cycle at a drift of 4.4 in. (112 mm), whereas it maintained its capacity on the pull cycle.

An experiment was performed on Specimen PHRS, retrofitted with the TiAB spiral alone (no TiAB ligaments), to understand the participation of the ligament in resisting flexure at the foundation level (Figure 5.1c). Figure 5.6c shows the base moment-column drift curve; comparison of the two retrofitted specimens shows that the standard TiAB retrofitted specimen (PHRSL) exhibited larger energy dissipation with wider hysteresis loops and produced higher equivalent viscous damping. The retrofitted specimen without TiAB ligaments (PHRS) exhibited unsymmetrical moment-drift response for the push- and pull-cycles, which is an indication of sliding of the column relative to the footing at the column-footing interface. The reduced dowel action in specimen PHRS contributed to the observed sliding. The TiAB ligaments also provide some self-centering capacity (less residual drift at zero lateral load). This was evident from comparing the force-deformation response of specimen PHRS (Figure 5.6c) with specimen PHRSL (Figure 5.6b). Although both specimens were able to develop similar displacement ductility capacity, residual drifts were much lower for specimen PHRSL. The maximum moment capacity of specimen PHRS was 442 kips-ft (600 kN-m) and 435 kips-ft (591 kN-m) at approximately 2.5% drift for push- and pull-cycles, respectively. The capacity dropped to 80% at about 3.3% drift (pull), whereas for push-cycles, the column maintained capacity to 7.4% drift with a stable hysteretic response. This behavior was attributed to sliding of the column which was wedged against the well-anchored TiAB confinement spiral during push cycles due to the anchorage location at the top of the footing. This maintained the geometry of the column allowing the confining effect to maintain force transfer through the lap splice thereby sustaining the resistance. It was observed on pull-cycles that column sliding allowed the spiral to open (i.e., oval) which allowed damage to the concrete shell and interior column concrete in the splice region and thereby reduced the ability to provide flexural tension resistance. As a result, the pull capacity dropped to 88 kip-ft (120 kN-m) while the push capacity was maintained at 353 kip-ft (480 kN-ft).

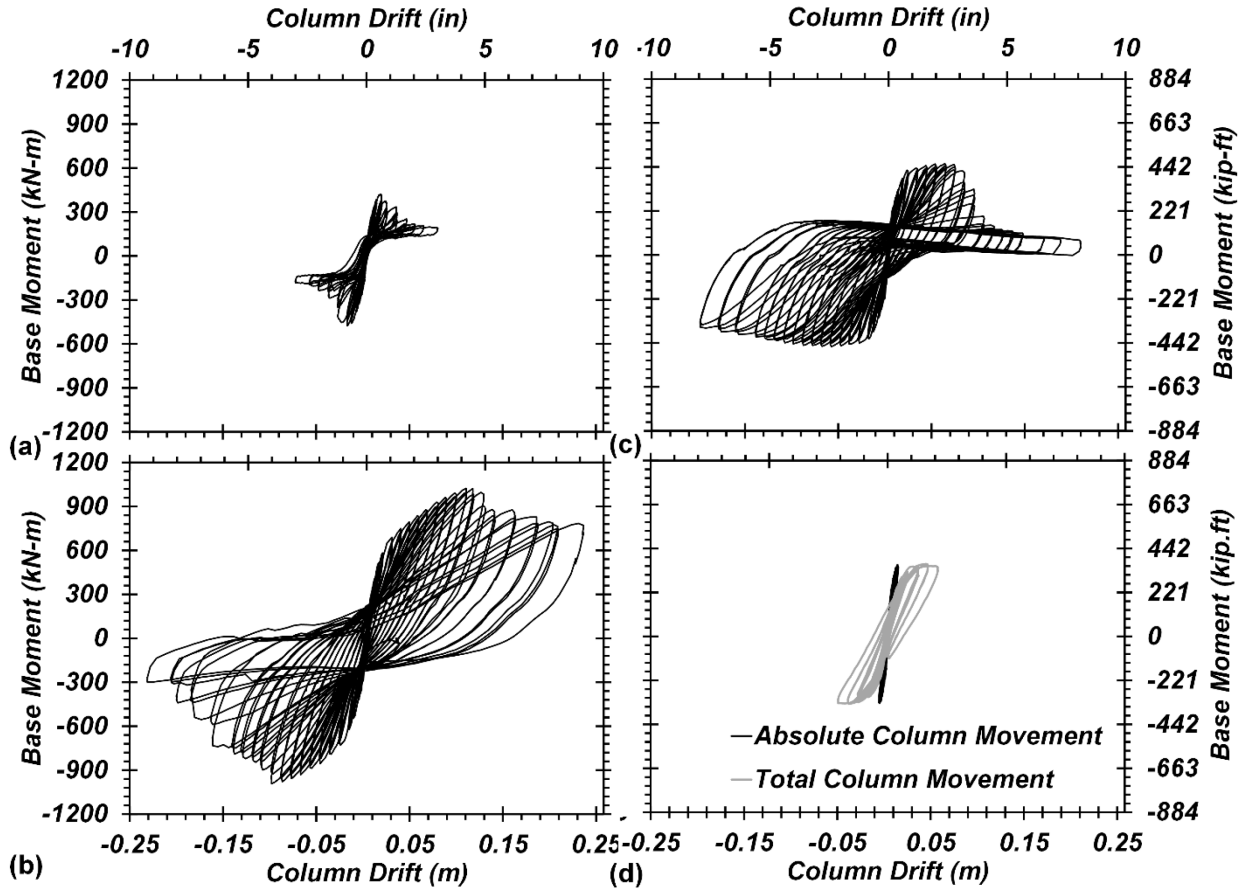

Figure 5.6: Column base moment versus drift responses for the (a) vintage specimen with fixed base, PHV; (b) retrofitted specimen with TiAB ligaments and spiral and fixed base, PHRSL; (c) retrofitted specimen with TiAB spiral only and fixed base, PHRS; and (d) retrofitted specimen with TiAB ligaments and spiral and flexible support, RRSL (from Khosravi et al. 2023).

Figure 5.6d shows the strikingly different moment-column drift response for the RRSL specimen. The overall cyclic response of the rocking specimen was symmetric and exhibited a peak moment of 350 kip-ft (473 kN-m) at 0.4 in. (0.01 m) column drift and 331 kip-ft (450 kN-m) at 0.31 in. (0.008 m) column drift for the push- and pull-cycles, respectively. The test was terminated due to stroke limitations of the experimental setup. In general, response degradation of the column footing system was not observed due to the transfer of the failure mechanism to yielding of the soil simulant. Specimen RRSL remained essentially elastic with very small hysteretic loops and corresponding low energy dissipation. In this case, as indicated by Deng et al. (2012), significant energy dissipation is expected to occur in the foundation subgrade, resulting in permanent deformation induced within the soil simulant at the toe and heel of the footing. Figure 5.7 shows the settlement profile of the soil simulant along with cracking patterns of the footing base after the test. The soil simulant exhibited permanent deformation with a rounded deformation profile similar to observations reported by Gajan and Kutter (2008), Hakhamaneshi et al. (2012), and Sharma (2019) for soil, with a maximum permanent vertical deformation of 0.2 in. (5 mm), as shown in Figures 5.7a and 5.7b. Foundation rocking in this

case also resulted in formation of minor cracks in the footing, which were connected and ran through the middle of each face of the footing, roughly dividing the footing into four quadrants as shown in Figure 5.6c. In a bridge substructure with a hinging column system, energy is largely dissipated through the column whereas the footing remains quasi-elastic throughout the event. The results of Deng et al. (2012) indicated that in this case, the column accounts for 88% of the total energy dissipation. Comparison of Figures 5.6a and 5.6d indicates that without the TiAB retrofit, the vintage specimen would likely have failed in a nonductile manner due to loss of the reinforcing steel lap splices rather than due to excessive drift.

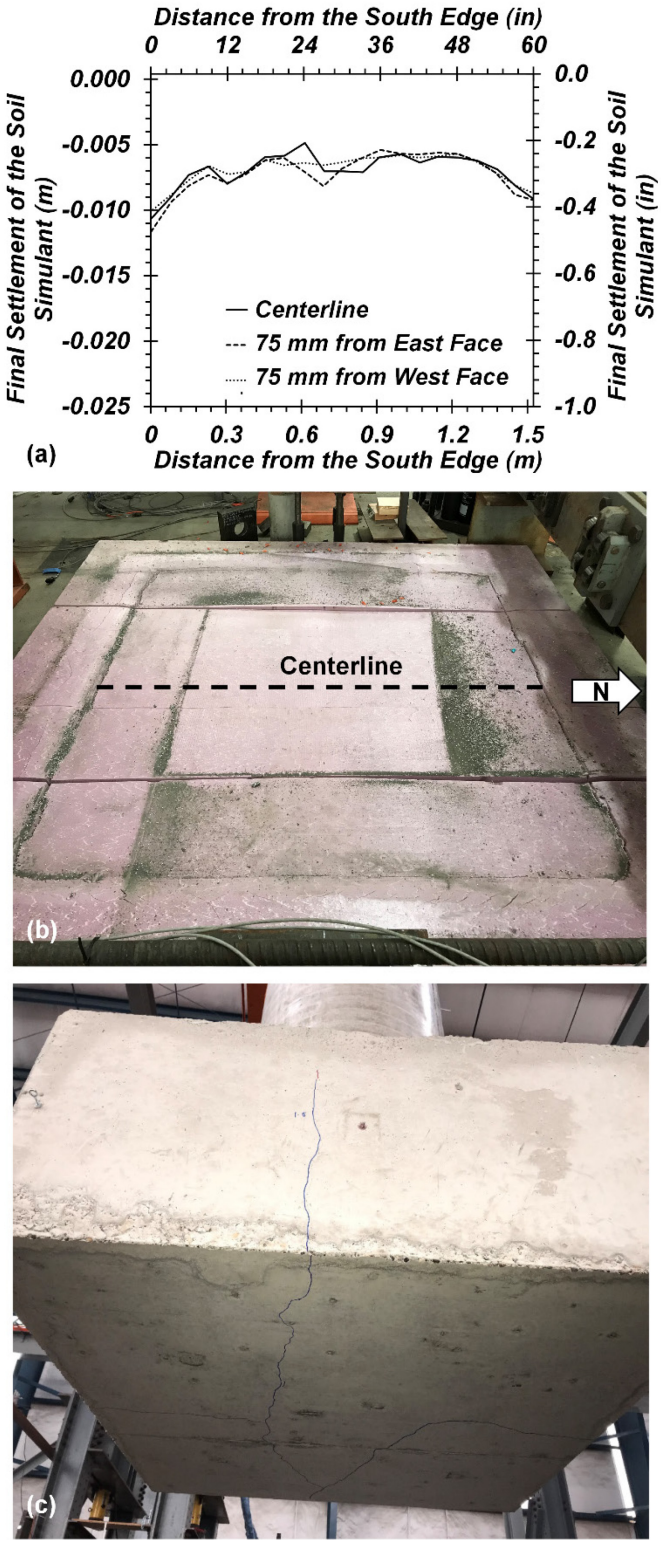

Figure 5.7: Performance at the base of specimen RRSL: (a) settlement profile for the XPS soil simulant at the end of testing; (b) visual damage to the top layer of the soil simulant after removal of specimen; and (c) cracking patterns along the sides and base of the footing (from Khosravi et al. 2023).

5.4 3D NUMERICAL STUDY OF FIXED AND ROCKING FOUNDATIONS FOR SINGLE- AND TWO-COLUMN BRIDGE SUBSTRUCTURES

The experiments highlighted the differences in response for fixed and rocking foundations for retrofitted bridge columns. Rocking changes the source of the energy dissipation and produces soil-structure interaction. A reduction in the ductility demand can be achieved as long as the system has sufficient ductility to ensure that the isolation effect of the rocking mechanism can be achieved. The column-footing specimens that were evaluated experimentally would fail under the applied lateral load in the absence of the retrofit, whereas the retrofitted specimens (with or without ligaments) could be expected to rock, depending on the subgrade strength and stiffness, which would reduce the structural demand associated with lateral loading. However, the experiments considered a limited number of scenarios, and variations in the strength and stiffness of the retrofit and foundation subgrade are anticipated to influence the column-footing responses. Accordingly, additional scenarios of retrofitted column-footing systems calibrated to the experimental results were subjected to numerical equivalent-static pushover tests simulated using three-dimensional (3D), nonlinear simulations using FLAC3D (Itasca 2012) software. The primary goal of these analyses is to understand how variations in the governing design variables affect the rocking behavior and to seek optimal retrofit configurations given the moment demands and foundation subgrade strength and stiffness.

5.4.1 Model Components and Boundary Conditions

Figures 5.8a and 5.8b present the numerical meshes and components comprising the fixed base and rocking column-footing systems, respectively. Four models of the single column-footing system with different structural details and base boundary conditions were selected based on the experimentally evaluated conditions. Fixed base numerical models were used for the vintage (PHV) and TiAB retrofitted (PHRS and PHRSL) single column-footing specimens, whereas the soil simulant was numerically modeled for the rocking base TiAB retrofitted single column-footing system (RRSL). Table 5.2 summarizes the characteristics of each simulation conducted in this study.

The dimensions used for the column, foundation, concrete load distribution slab, and soil simulant in the numerical study were identical to those in the corresponding experimental specimens (Figures 5.1, 5.2, and 5.3). A concrete base with dimensions 98 in. × 98 in. × 6 in. (2.5 m × 2.5 m × 0.15 m) underneath the XPS soil simulant was included to capture the stiffness of the laboratory strong floor. Isotropic, linear-elastic beam elements that can exhibit axial tensile and compressive failure modes and the bending failure mode through specification of a limiting plastic moment were used to model the columns. Two segments were considered for each column: (1) a cantilevered segment extending 12 in. (0.3 m) above the column-footing connection following recommendations for modeling lap splices by Megalooikonomou et al. (2017) that the plastic hinge length be equal to half of the effective depth (modeled using two-beam elements), and (2) the remaining 84 in. (2.15 m) height of the column, modeled using 20 elements. Since the beam elements did not have the same plan area as the actual columns, stresses at the point of the column-footing connection are different from those in the experiments. To realistically model the column-footing connection, the beam element was

connected to the footing using shell elements which shared the same plan area of the columns. This modeling approach facilitates an accurate transfer of stresses to the footing. Although the models for the vintage and retrofitted systems were identical, the limiting plastic moments were specified in accordance with the experimentally observed characteristics to properly capture flexural responses, described below.

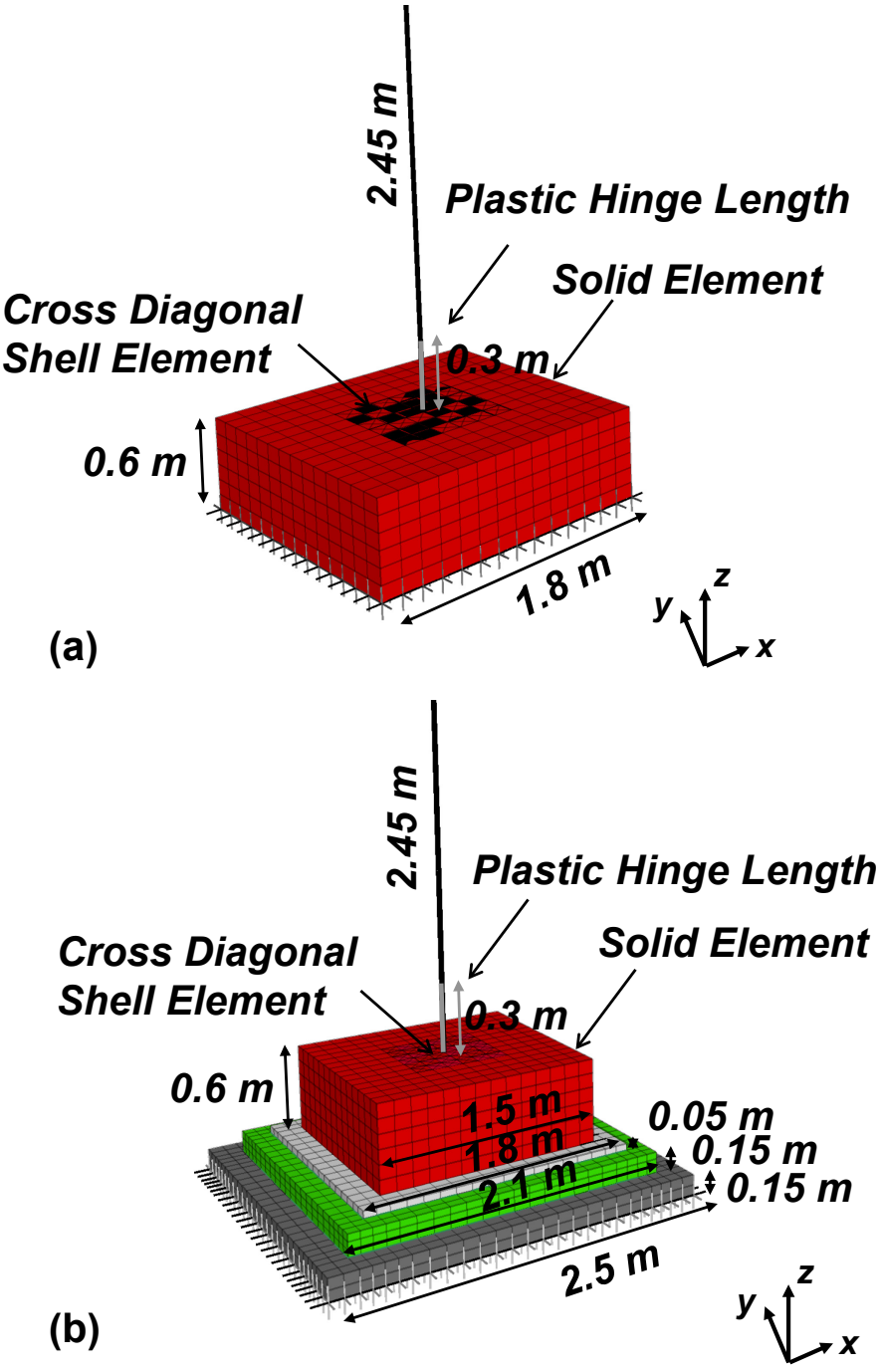

Figure 5.8: Components of the models used to simulate the: (a) specimens with fixed base, and (b) specimens with flexible support (from Khosravi et al. 2023) (Note: 1 m = 3.2808 ft).

Table 5.2: Characteristics of each of the simulations conducted for model validation.

Elements of System	Type of System	Fixed Based System						Rocking System	
		Vintage Specimen, PHV		Retrofitted Specimen with Spiral and Ligament, PHRSL		Retrofitted Specimen with Spiral Only, PHRS		Retrofitted Specimen with Spiral and Ligament, RRSL	
		SI	Eng	SI	Eng	SI	Eng	SI	Eng
Column	Length	0.6 m	24 in	0.6 m	24 in	0.6 m	24 in	0.6 m	24 in
	Width	0.6 m	24	0.6 m	24 in	0.6 m	24 in	0.6 m	24
	Height	4.9 m	192	4.9 m	192 in	4.9 m	192 in	4.9 m	192
	Type	Beam Element							
	Model	Elastic with plastic hinge to capture the non-linear response							
	Hinge Length	0.3 m	12 in	30 m	12 in	30 m	12 in	30 m	12 in
Footing	Length	1.8 m	72 in	1.8	72 in	1.8 m	72 in	1.5 m	60 in
	Width	1.8 m	72 in	1.8	72 in	1.8 m	72 in	1.5 m	60 in
	Height	0.6 m	24 in	0.6 m	24 in	0.6 m	24 in	0.6 m	24 in
	Type	Solid Element							
Concrete Base	Length	-	-	-	-	-	-	2.5 m	98 in
	Width	-	-	-	-	-	-	2.5 m	98 in
	Height	-	-	-	-	-	-	0.15 m	6 in
	Type	-	-	-	-	-	-	Solid Element	
Load Distributio n Plate	Length	-	-	-	-	-	-	2.1 m	84 in
	Width	-	-	-	-	-	-	2.1 m	84 in
	Height	-	-	-	-	-	-	0.15 m	6 in
	Type	-	-	-	-	-	-	Solid Element	
Foam	Length	-	-	-	-	-	-	1.8 m	72 in
	Width	-	-	-	-	-	-	1.8 m	72 in
	Height	-	-	-	-	-	-	0.15 m	6 in
	Type	-	-	-	-	-	-	Solid Element	

The foundation, the concrete load distribution slab, and the XPS soil simulant were modeled with quadratic solid elements (solid green elements; Figure 5.8b). Reinforced concrete was modeled

as linear elastic with a Young's modulus, E, and Poisson's ratio, ν, of 3,278 ksi (22.6 GPa) and 0.17, respectively. The elastic-perfectly plastic Mohr–Coulomb model was used to simulate the response of the soil simulant for the rocking systems as described below. The Hoek-Brown-Pac model (Brown and Hoek, 1980; Hoek et al. 2002) intended for rock materials was used to capture the response of the unreinforced load distribution slab during loading. The Hoek-Brown-Pac model allows specification of compressive and tensile strengths, equal to 4,000 psi (27.5 MPa) and 600 psi (4.13 MPa), respectively, with a corresponding E and ν of 4,200 ksi (29 MPa) and 0.17, respectively. The interfaces between the footing, LDS, XPS, and the strong floor were modeled using linear elastic-perfectly plastic spring–sliders, with interface shear strength defined by the Mohr–Coulomb failure criterion. Each interface element is characterized with strength and stiffness properties that control the normal and shear behavior of the interface including the normal and shear stiffnesses (k_n and k_s), tensile and shear bond strengths (σ_t and S_s), shear coupling spring cohesion (c) and friction angle (ϕ'), and dilation angle (ψ'). The stiffness properties, k_s and k_n, of the interface are specified using the following expression (Itasca 2000):

$$\boldsymbol{k = max\left(\frac{K + \frac{4}{3}G}{\Delta z_{min}}\right)} \quad \textbf{(5-1)}$$

in order to prevent penetration of elements across the interface and numerical instability, where K and G are the bulk and shear modulus of the stiffest adjoining material, respectively; and Δz_{min} is the smallest dimension of an adjoining zone in the normal direction.

The boundary conditions were specified based on the system being simulated. The nodes at the bottom of the footing were restrained in six degrees of freedom for the fixed base systems (PHV, PHRSL, and PHRS). In the rocking system (RRSL), the footing was allowed to rotate in response to loading (i.e., around the y-axis as the column moves along the x-axis). The nodes at the bottom of the strong floor elements were restrained in six degrees of freedom and all other nodes were unrestrained. Since the experimental rocking specimen (RRSL) was restrained against sliding, nodes located on the bottom side of the footing and perpendicular to the loading direction were fixed in the longitudinal (loading, or "x") direction to prevent translation during loading. Pseudo-static pushover tests were simulated using a gradually increasing, horizontal velocity applied to the top of the column while maintaining an axial load of 150 kips (667 kN), similar to the experiments which ensured numerical stability.

5.4.2 Calibration of Constitutive Models

5.4.2.1 Calibration of the Soil Simulant Material Model

Three (3) replicate uniaxial unconfined compression tests were performed on samples taken from the XPS soil simulant used in the experiments. These uniaxial compression tests were used to calibrate the Mohr-Coulomb constitutive model for the soil simulant. Two (2) 3 in. (75 mm) thick XPS cylindrical specimens of 4 in. (100 mm) diameter were stacked to form 6 in. (150 mm) tall test specimens. The specimens were placed in a

uniaxial testing device and compressed at a strain rate of 10%/min. The Young's Modulus, compressive strength, and compressive strains are reported in Table 5.3.

The elastic-perfectly plastic Mohr–Coulomb model was used to simulate the nonlinear response of the numerical XPS material, the basal nodes of which were fixed in all directions. A constant nodal velocity of 2.79×10^{-6} ft./step (8.5×10^{-7} m/step) was applied at the top of the numerical specimen to simulate uniaxial loading. The density, $\rho = 3.1$ pcf (50 kg/m^3) and friction angle, $\phi' = 0$, cohesion (c'; one-half of the compressive strength) was specified, and the shear modulus (G) and Poisson's ratio (ν) were varied to capture the observed experimental stiffness.

Figure 5.9 presents the experimental and simulated compressive stress-axial displacement responses (Sample 3; Table 5.3), indicating good agreement when using $c' = 58$ psi (400 kPa), $E = 5.8$ ksi (40 MPa), and $\upsilon = 0.2$. Negussey (2007) summarized the sample-size effects which govern the deformation response of foam specimens: 24 in (0.6 m) cube specimens and full-height foam embankments exhibited a Young's modulus two to three times larger than that of a small sample at the same density. Furthermore, foam materials exhibit strain-rate effects that are manifested by a stiffer response during faster rates of loading, similar to the well-known strain-rate effects that govern plastic soils (e.g., Vucetic and Tabata 2003). Thus, the actual Young's modulus specified in the numerical simulation must be larger than that measured in uniaxial compression tests due to sample-size and strain-rate effects. Based on the observations summarized by Negussey (2007), the elastic modulus of the XPS soil simulant in the column-footing models, E, was set equal to 11.6 ksi (80 MPa) to capture sample size- and strain rate-effects.

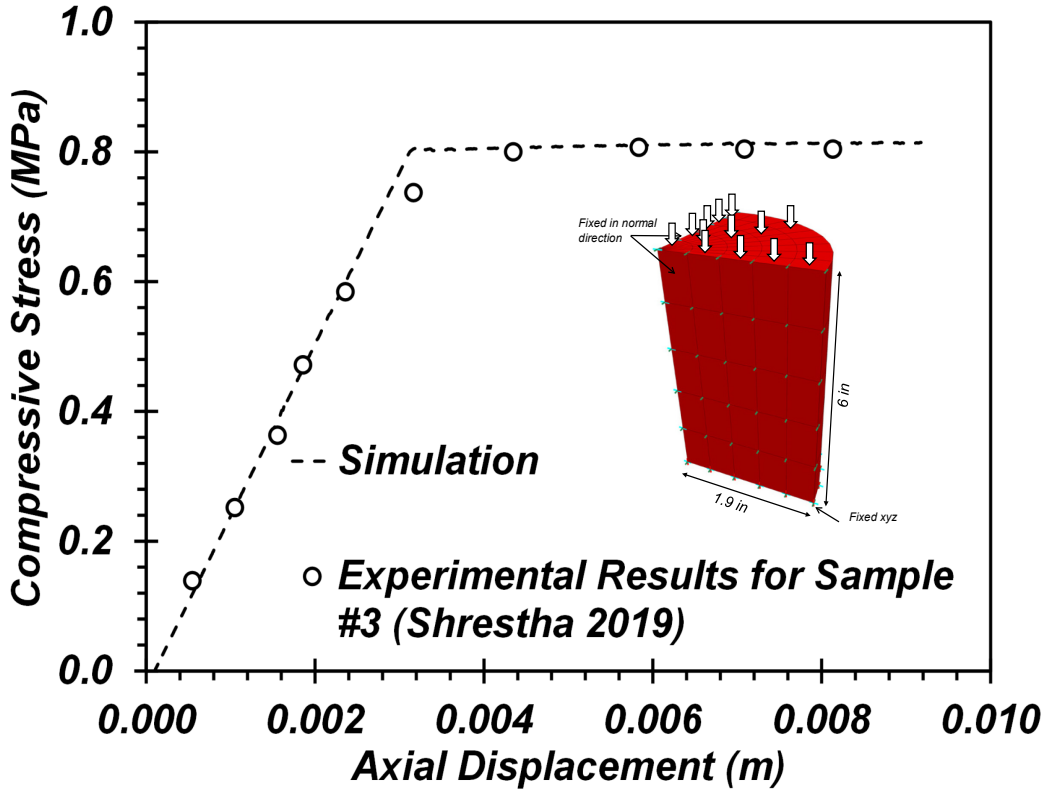

Figure 5.9: Comparison of the numerical simulation of the unconfined compression test of the XPS soil simulant to the experimental results of Sample 3 (the experimental data has been corrected for initial seating deformations) (Note: 1 m = 3.2808 ft.; 1 MPa = 145 psi).

Table 5.3: Summary of compression test results on the FOAMULAR® 1000 XPS foam (Shrestha 2019).

Specimen #	1		2		3		Average	
	SI	Eng	SI	Eng	SI	Eng	SI	Eng
Young's Modulus, MPa (psi)	30.3	4393	37.5	5442	39.5	5736	35.8	5190
Compressive Strength, kPa (psi)	738	107	807	117	793	115	780	113
Compressive Strain (%)	3.58		3.26		3.14		3.33	

5.4.2.2 Flexural Responses of the Simulated Columns

The beam elements comprising the columns were calibrated with flexural rigidities, *EI*, and the experimentally observed, plastic-moment capacities. Section analyses of the vintage (PHV) and retrofitted (PHRS and PHRSL) columns were conducted using the finite difference platform LPILE (Ensoft 2019), and the resulting column-specific moment-curvature, M-ϕ, relationships obtained were approximated within FLAC3D. Table 5.4 summarizes the parameters that were used in the section analysis for the cases considered. The as-built dimensions of the vintage column were used in the LPILE section analyses; however, the TiAB ligaments and spirals and corresponding concrete cover could not be modeled directly. The effect of the retrofit elements on the M-ϕ response of the retrofitted column section was captured through the use of a higher f_y for the longitudinal and transverse bars and a reduced transverse steel spacing (i.e., 100 mm or 4 in. rather than 300 mm or 12 in.) to account for the increased confinement provided by the TiAB spiral (Table 5.4). Figures 5.10a, 5.10b, and 5.10c compare the M-ϕ relationships obtained using LPILE to that specified in the numerical simulations for the vintage, retrofitted columns with TiAB spiral and ligaments, and retrofitted columns with TiAB spiral, and indicate the increased flexural rigidity associated with the TiAB retrofit (Figures 5.10b and 5.10c). The linear-elastic portion of the specified M-ϕ relationships was captured by setting the concrete E_c = 3,275 ksi (22.5 GPa; corresponding to f'_c of 3,300 psi or 22.75 MPa) and was paired with moments of inertia of 7,208 in^4 (0.003 m^4), 9,610 in^4 (0.004 m^4), and 9,610 in^4 (0.004 m^4) for the vintage column (PHV), column retrofitted with TiAB spiral and ligament (PHRSL), and column retrofitted with only the TiAB spiral (PHRS), respectively. To properly capture the post-failure response of the columns, the plastic moment experimentally observed from the full-scale specimens PHV, PHRSL, and PHRS (Figure 5.6) were prescribed for the plastic hinge at the column-footing connection. Also, when calibrating the model for the retrofitted specimens (PHRSL, PHRS, RRSL), the retrofit was assumed to be extended to the top of the column. Therefore, similar structural properties were considered for the whole column. This is a reasonable assumption as the retrofitted section of the column dominates the behavior of the column.

Table 5.4: Model parameters used to simulate the moment-curvature responses of the test column sections in LPILE.

	Type	Vintage Specimen, PHV		Retrofitted Specimens with Spiral and Ligament, PHRSL and RRSL		Retrofitted Specimen with Spiral, PHRS	
		SI	**Eng**	**SI**	**Eng**	**SI**	**Eng**
Concrete	f'_c	22.7 MPa	3300 psi	22.7 MPa	3300 psi	22.7 MPa	3300 psi
	E	22.5 GPa	3275 psi	22.6 GPa	3274 psi	22.6 GPa	3274 psi
	ν	0.15		0.15		0.15	
Stirrup Bars	Bar	10M	#3	10M	#3	10M	#3
	Spacing	0.3 m	12 in	0.1 m	4 in	0.1 m	4 in
	$f_{y,steel}$	276 MPa	40 ksi	586 MPa	85 ksi	586 MPa	85 ksi
	E	200 GPa	29000 ksi	200 GPa	29000 ksi	200 GPa	29000 ksi
Longitudinal Bars	Bar	32M	#10	32M	#10	32M	#10
	$f_{y,steel}$	448 MPa	65 ksi	689 MPa	100 ksi	448 MPa	65 ksi
	$f_{u,steel}$	634 MPa	95 ksi	931 MPa	135 ksi	634 MPa	95 ksi
	ε_y	0.006		0.004		0.006	
	ε_u	0.02		0.01		0.02	
	E	200 GPa	29000 ksi	200 GPa	29 ksi	200 GPa	29000 ksi

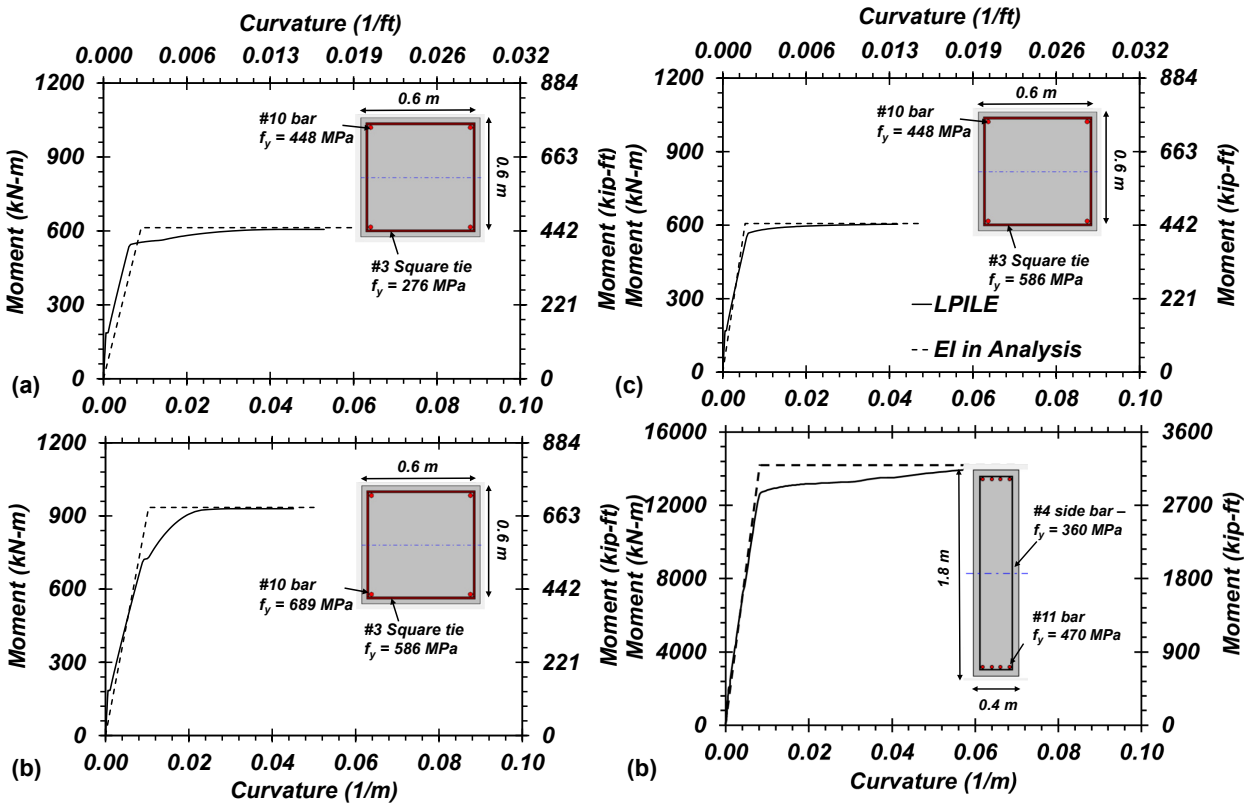

Figure 5.10: Moment–curvature relationships for the test column sections: (a) vintage column; (b) retrofitted column with TiAB ligaments and spiral; (c) retrofitted column with TiAB spiral only; and ; and (d) beam used in Section 5.5.

5.4.3 Pushover Response of the Single-Column-Footing Systems

Figure 5.11 compares the observed and simulated moment-column drift backbone curves resulting from the monotonic pushover simulations at the base of the column (top of footing). Good agreement between the experimental and simulated responses is observed. For example, a moment capacity of 310 kip-ft (430 kN-m) obtained experimentally may be compared to that of 310 kip-ft (429 kN-m) resulting from the FLAC3D simulation for the fixed base vintage column-footing system (PHV). Moment degradation was experimentally observed upon the initiation of splitting of concrete along the splice length relative slip between adjacent reinforcing bars and occurred at a column drift of about 0.06 in. (0.015 m). The moment envelope at the end of the simulation degraded to a value of 88 kip-ft (100 kN-m; Figure 5.11a).

The simulated PHRSL system achieved a moment capacity nearly twice as large as that of the nominal moment capacity of a similar column with continuous longitudinal reinforcing steel bars, and similar to the PHRSL specimen. The moment capacity continued to gradually increase after reaching 443 kip-ft (600 kN-m) at a column drift of 0.79 in (0.02 m) due to the presence of TiAB ligaments that provide increased moment capacity to a column drift of 3.9 in. (0.1 m). Thereafter, a 20% decrease in the column base moment resistance was observed at larger drifts (Figure 5.11b). Comparison of the

numerical simulation and experiments also indicated good prediction of the post-peak response for the PHRSL specimen as shown in Figure 5.11b.

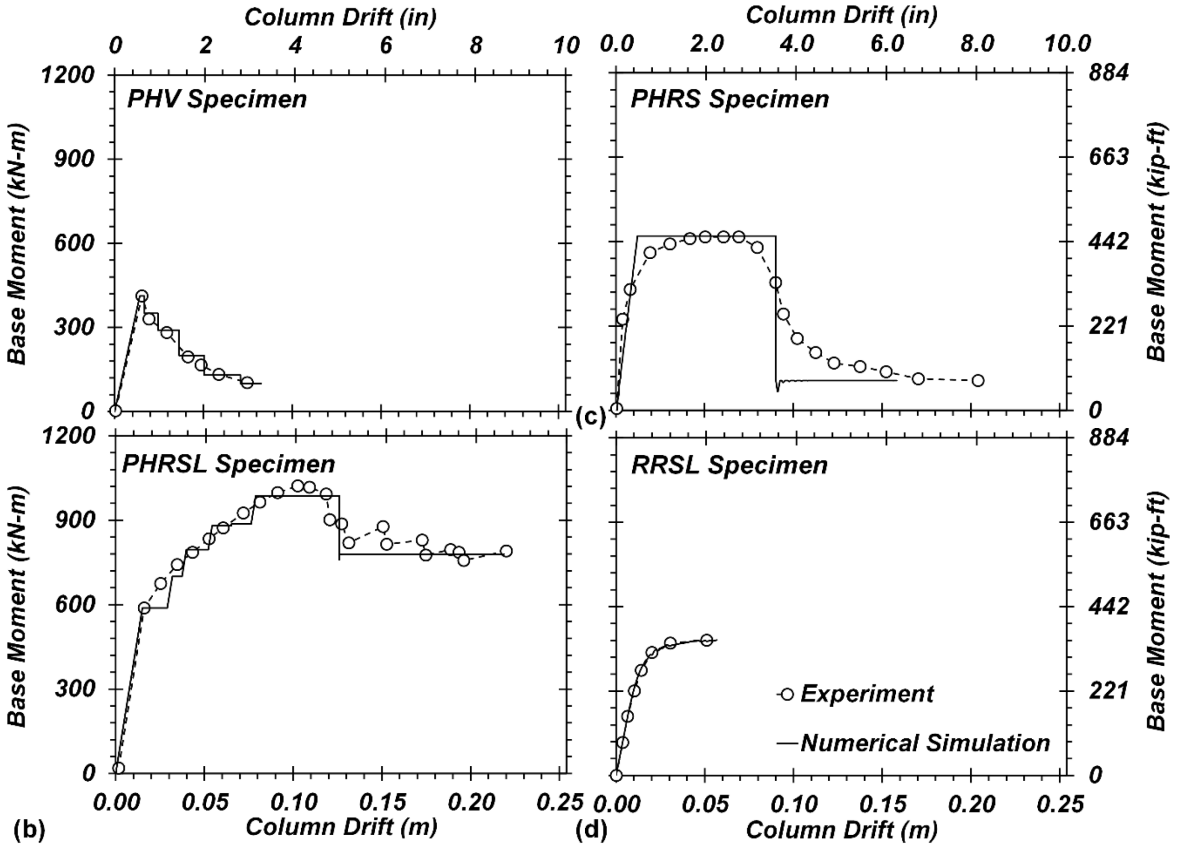

Figure 5.11: Comparison of the base column moment−column drift relationships observed from the experiments to the results of numerical simulations for the (a) PHV; (b) PHRSL; (c) PHRS; and (d) RRSL specimens (from Khosravi et al. 2023).

For the PHRS specimen (Figure 5.11c), the external confinement provided by the TiAB jacketing produced an increase in the lap-splice capacity that enabled it to develop the nominal moment capacity of the column section as though it had continuous longitudinal reinforcing steel bars instead of a splice (Shrestha 2019). Failure of the column was delayed relative to the unretrofitted specimen. At column drifts larger than 3.54 in. (0.09 m) on the pull cycles, the confinement provided by the retrofit was reduced due to the spiral opening as the column exhibited sliding relative to the top of the footing described previously and this is represented in the base moment becoming similar to the unretrofitted vintage column-footing specimen.

The simulated pushover response of Specimen RRSL, rocking system with TiAB spiral and ligament, is compared to the experimental backbone response in Figure 5.11d. The simulated retrofitted rocking system shows an initial nonlinear increase in column base moment due to foundation rocking, which progressively deforms the soil beneath the footing into a rounded profile. This evolution of the supporting soil surface reduces the

footing-subgrade contact length and results in initial nonlinearity and reduced stiffness of the moment-drift response of the column. The simulated pushover behavior is consistent with the measured response, exhibiting a maximum base moment of 352 kip-ft (477 kN-m) that is mobilized at a column drift of 0.79 in. (0.02 m) and shows no degradation in the column base moment.

5.4.4 Parametric Study of Soil and Structural Characteristics on Rocking Responses

A parametric study was conducted to understand the role of foundation soil and structural strength and stiffness on the hinging and rocking behavior of the column-footing systems using the calibrated models. Two different types of analysis were conducted: (1) pushover analyses on rocking vintage column-footing systems to investigate the effect of soil properties, and (2) analyses performed on TiAB spiral-only retrofitted specimens, to identify transitions in hinging/rocking responses. The four parameters identified for study include the strength (i.e., cohesion) and elastic modulus of the foundation soils, and the flexural stiffness and strength of the retrofitted column (Table 5.5). Simulations were conducted by incrementally increasing or decreasing the investigated parameter while holding all other previously defined parameters constant. The upper and lower bound of each of the investigated parameters were selected so as to identify transitions in system response (i.e., rocking vs. plastic hinging) and represent realistic soil and structural strengths and stiffnesses.

5.4.4.1 Effect of Foundation Strength and Stiffness on the Pushover Response of Vintage Column Systems

The performance of a vintage column-footing system was investigated by varying the soil strength from 1,000 to 8,360 psf (50 to 400 kPa) and Young's modulus from 1.45 ksi to 11.6 ksi (10 to 80 MPa) in separate analyses. The effect of cohesion on the response of the unretrofitted vintage column footing specimen is described considering base moment vs. column drift (Figure 5.12a) and maximum base moment vs. cohesion (Figure 5.12b). For the rocking vintage system with c' = 8,360 psf (400 kPa) and E = 11.6 ksi (80 MPa; VR-C400), an initial nonlinear increase in the column base moment is observed due to foundation rocking. The maximum base moment of the column reaches 310 kip-ft (430 kN-m) at a column drift of 1 in. (0.025 m), considered as the failure drift, after which considerable strength degradation is observed in the column due to column failure. As the foundation soil strength decreased, the moment-column drift curves exhibited reduced flexural stiffness and became nonlinear at lower moments (Figure 5.12a). Lower soil strengths lead to local bearing failure in soil at the footing edges that result in a smaller rocking moment capacity compared to the plastic moment capacity of the column at the footing. Figure 5.12b shows that as the soil strength increases to approximately 4,175 psf (200 kPa), the soil strength is sufficient to induce plastic hinging in the column. Soil subgrades with cohesion greater than 4,175 psf (200 kPa) result in the reduction in column failure drift amplitudes. The reduction in failure drift is due to reduced rigid body soil deformations with concentrated hinging in the column.

Table 5.5: Case numbers and model parameters varied in the parametric study.

Case #	System	Soil Simulant		Column		
		Elastic modulus, *E* in ksi (MPa)	**Cohesion, *C* in psf (kPa)**	**Flexural Rigidity, *EI* in kip-ft.^{2} (MN-m^2)**	**Flexural Strength, M_B in kip-ft. (kN-m)**	**Rocking Moment Capacity, M_c, in kip-ft. (kN-m)**
VR-C400	Unretrofitted Specimen	11.6 (80)	8,360 (400)	0.163 (67.5)	310 (420)	350 (475)
VR-C350			7,300 (350)			
VR-C300			6,000 (300)			
VR-C250			5,220 (250)			
VR-C200			4,175 (200)			
VR-C150			3,100 (150)			
VR-C100			2,100 (100)			
VR-C50			1,000 (50)			
VR-E80	Unretrofitted Specimen	11.6 (80)	8,360 (400)	0.163 (67.5)	310 (420)	350 (475)
VR-E40		5.8 (40)				
VR-E20		2.9 (20)				
VR-E10		1.45 (10)				
VR-E5		0.73 (5)				
RRS-M1.00	Retrofitted Specimen with Spiral Only	11.6 (80)	8,360 (400)	0.272 (113)	460 (620)	350 (475)
RRS-M0.85					390 (527)	
RRS-M0.80					367 (496)	
RRS-M0.75					344 (465)	

Case #	System	Soil Simulant		Column		
		Elastic modulus, *E* in ksi (MPa)	**Cohesion, *C* in psf (kPa)**	**Flexural Rigidity, *EI* in kip-ft.^{2} (MN-m^2)**	**Flexural Strength, M_B in kip-ft. (kN-m)**	**Rocking Moment Capacity, M_c, in kip-ft. (kN-m)**
RRS-M0.70					321 (434)	
RRS-M0.60					275 (372)	
RRS-I.005	Retrofitted Specimen with Spiral Only	11.6 (80)	8,360 (400)	0.272 (113)	460 (620)	350 (475)
RRS-I.004				0.218 (90)		
RRS-I.003				0.163 (67.5)		
RRS-I.002				0.109 (45.0)		

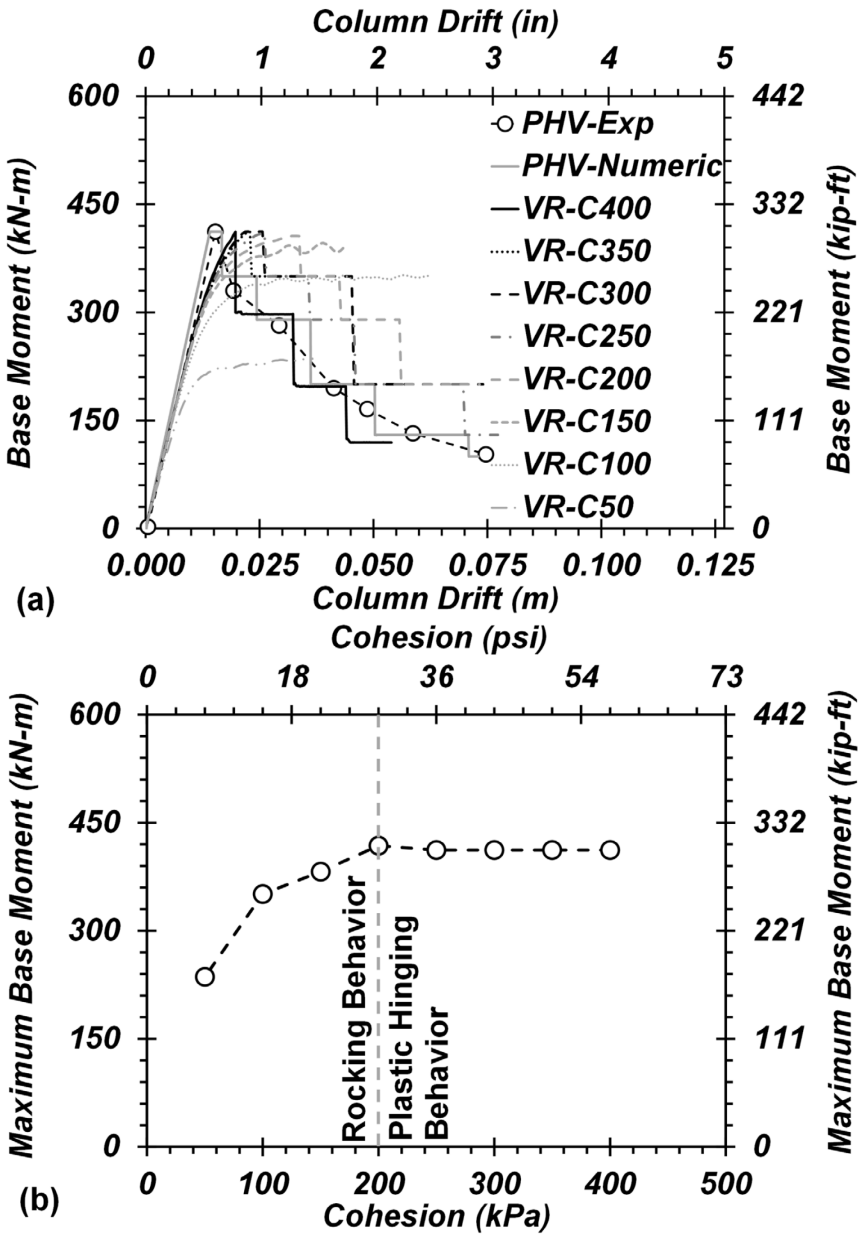

Figure 5.12: Effect of soil subgrade cohesion on the response of unretrofitted vintage column–footing specimen, including the variation of the (a) base moment with column drift; and (b) maximum base moment with cohesion (from Khosravi et al. 2023).

Figures 5.13a and 5.13b show the effect of the foundation soil elastic modulus on the response of unretrofitted vintage column-footing specimens in terms of the base moment vs. column drift and column drift at failure vs. elastic modulus, respectively. The reduction in soil stiffness produces early onset of nonlinear response and decreases the global flexural stiffness of the column-footing system (Figure 5.13a), similar to the effect of reduced soil strength. It also results in larger total drift deformations and thus greater P-Δ effects in the column which would increase demands when the column begins to hinge at the base. These analyses show that the system cannot transition to a rocking

mode when the rocking capacity (Khosravi et al. 2021) of the footing remains larger than the plastic moment capacity of the column (Table 5.5, Figure 5.12). These results also show that to determine which action controls the behavior of a spread footing, the site-specific soil and structural characteristics need to be assessed.

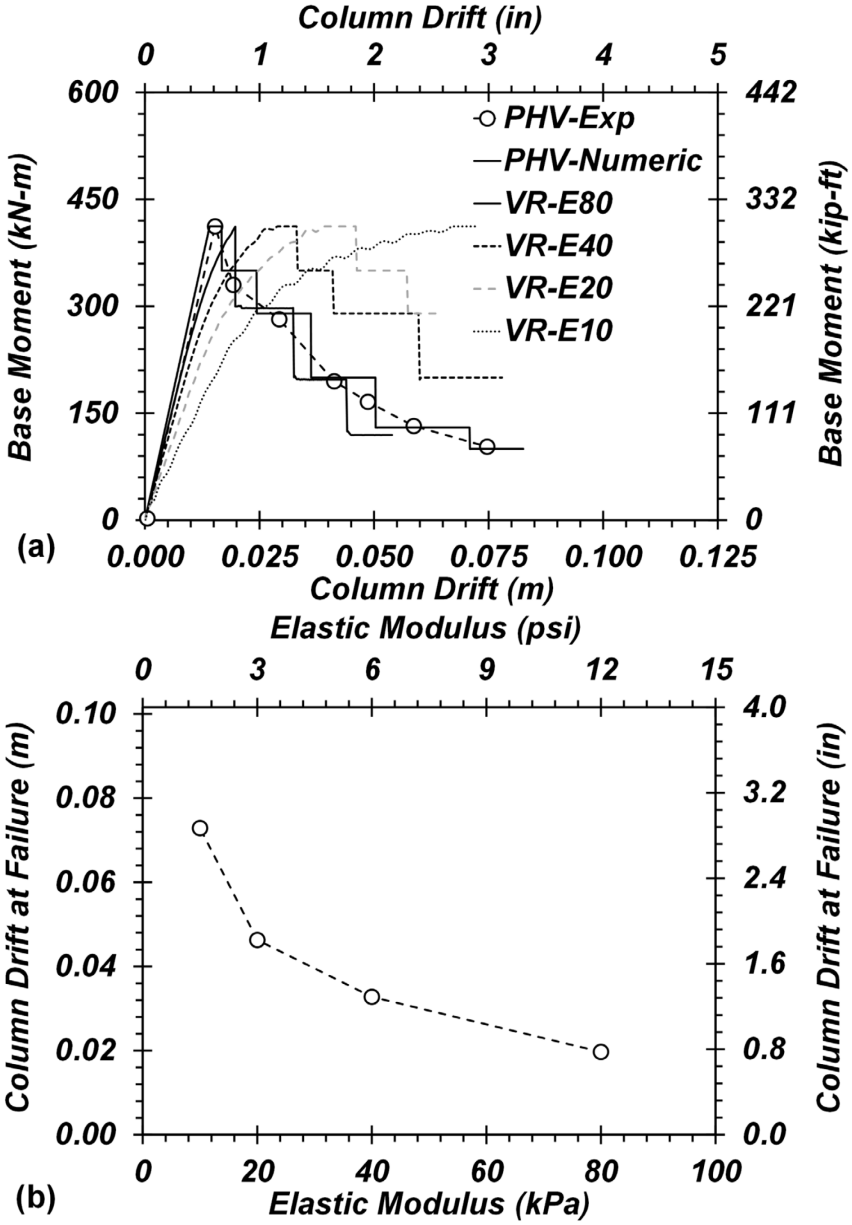

Figure 5.13: Effect of the soil subgrade elastic modulus on the response of unretrofitted vintage column–footing specimen including the variation of the (a) base moment with column drift; and (b) column drift at column failure with elastic modulus (from Khosravi et al. 2023).

5.4.4.2 Effect of Structural Strength and Flexural Rigidity on Pushover Response of Bridge Column Footing Systems

The experimental tests on column-footing specimens demonstrated that significant enhancement in flexural capacity and ductility is obtained following retrofit with TiAB jacketing in the absence of a TiAB ligament (Figure 5.11c). While providing significant confinement, the retrofit also prevented spalling of the original concrete cover, which maintains bond stresses across the flexural reinforcing splice and restricts buckling of the longitudinal column bars (Shrestha 2019). The confinement provided by the TiAB spiral alone may be sufficient to achieve the level of column strength to enable activation of foundation rocking that would subsequently reduce overall ductility demand of the system. To test this hypothesis, simulations were performed using the column-footing system with the characteristics of the PHRS specimen, but on simulated soil. A parametric study was performed to investigate the retrofitted column stiffness and strength requirements to ensure the rocking mechanism can be activated, enabling isolation of the system. The flexural strength and stiffness of the retrofit was varied, and the corresponding pushover responses were determined.

Table 5.5 summarizes the plastic moment capacity of each of the TiAB spiral-retrofitted column simulations. The simulated moment capacity can be normalized with respect to the moment capacity of the experimentally measured PHRS specimen (600 kN-m or 442 kip-ft) and reported as a strength ratio, *RS*. The corresponding strength ratios ranged from 0.6 to 1.0. Figure 5.14a shows that as flexural strength the retrofitted column increases above the rocking moment capacity, the foundation soil controls the response. As presented in Figure 5.14b, the threshold maximum base moment at which the response of the system changes from plastic hinge to rocking for these conditions correspond to 333 kip-ft. (450 kN-m) with a $RS = 0.74$. This threshold indicates that the TiAB spiral alone is capable of providing sufficient strength and ductility to enable foundation rocking to occur for the simulated conditions. Results of these analyses indicate that by utilizing soil-structure interaction, column retrofit designs can be made more efficient and cost-effective while maintaining desirable performance for both the superstructure and substructure (Figure 5.14b).

Considering the influence of the column flexural stiffness, reducing *EI* from 0.272 kip-ft^2 (113 MN-m^2 for the case of $I = 0.58$ ft.^{4} or 0.005 m^4) to 0.109 kip-ft^2(45 MN-m^2; for the case of $I = 0.232$ ft.^{4} or 0.002 m^4) resulted in an increase in drift for a given moment magnitude, as expected (Figure 5.14c). The retrofit moment capacity was selected to be sufficiently high so that rocking could eventually manifest. As the column stiffness increased, the drift observed at the onset of rocking reduced (Figure 5.14c). Figure 5.14d indicates that the column drift at the onset of rocking is not particularly sensitive to the variation in *EI*. Since the Mohr-Coulomb model (with an elastic-perfectly plastic behavior) was used to simulate the behavior of the soil simulant in FLAC3D, the column drift at the onset of rocking over the range of *EI* where failure occurs in the soil was defined as the point of maximum curvature in the moment-drift relationship (Herdrich 2015).

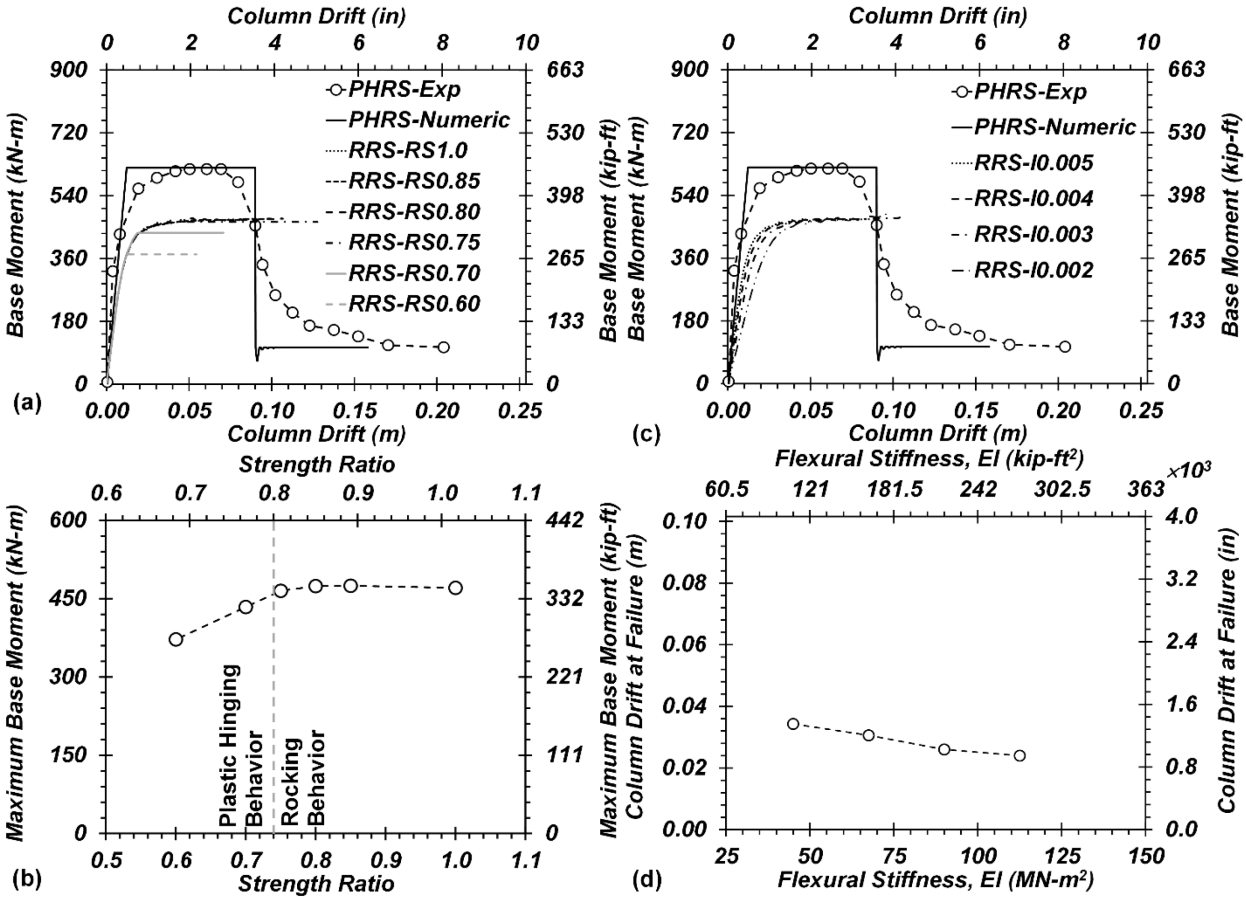

Figure 5.14: Effect of the strength and flexural stiffness of the column on the response of the column–footing specimen retrofitted with TiAB spiral only including the variation of (a) base moment with column drift for different column strength ratios; (b) column drift at failure with strength ratio; (c) base moment with column drift for different flexural stiffnesses; and (d) column drift at soil failure with flexural stiffness (from Khosravi et al. 2023).

5.5 NUMERICAL SIMULATION OF BRIDGE BENT SYSTEMS

Several recent studies have investigated the seismic response of multi-column-bent bridges designed with rocking foundations (Reinhardt et al. 2003; Malhotra 2007; Deng et al. 2012; Anastasopoulos et al. 2015). Reinhardt et al. (2003) performed an experimental study to evaluate the effect of rocking behavior on the dynamic response of a two-column bridge bent with an innovative structural frame. The tests were conducted on quarter-scale bents with two square columns supported on isolated spread footings using a shaking table under different earthquake records. The results of these experiments indicated considerable reduction in the lateral forces due to the foundation rocking, particularly at or near the base of the columns. The shear force of the joints and beams was also decreased due to footing flexibility. Anastasopoulos et al. (2015) reported the effect of bridge deck stiffness on the overall rocking response of the bridge bent systems. Whereas the portion of the total vertical load taken by the footings was affected by the vertical stiffness, deck rotation and uplift controlled by the torsional stiffness of the long axis of

the bridge deck. This is particularly concerning if the deck is integrated into diaphragm-type abutments.

This portion of the numerical study uses equivalent-static pushover analyses with a three-dimensional (3D), nonlinear, finite difference model to investigate the seismic response of multi-column bent bridge substructures. The data for these models were obtained from the Oregon Department of Transportation (ODOT) bridge database (Section 3), specifically focusing on bridges along I-5, US-97, and OR-58 in Oregon (Shrestha, 2019; Khosravi et al., 2022). The column footing systems in the numerical models were designed to replicate the dimensions of the conventional systems for columns and bents. The study considered both retrofitted and vintage (as-built) bridge column footing systems to evaluate their seismic performance. The application of this modeling approach yields valuable insights into the behavior of multi-column bent systems, both with and without seismic retrofit measures, as described herein.

5.5.1 OVERVIEW OF THE 3D NUMERICAL STUDY OF MULTI-COLUMN BRIDGE SUBSTRUCTURES

Figure 5.15 present the numerical meshes and components comprising the rocking and fixed base multi-column bent systems simulated using FLAC3D. Five models of two-column bent systems with different structural details and base boundary conditions were selected for investigation based on the conditions evaluated in Section 5.4 and by Khosravi et al. (2022). The numerical models developed included fixed base two-column bent system models using the vintage unretrofitted column-footing system (PHV-B1) and TiAB retrofitted models: one with spiral only (PHRS-B1) and one with both spiral and ligaments (PHRSL-B1). Three models with a flexible base were developed to investigate rocking two-column bent systems, including the vintage column-footing substructure (RV-B1) and TiAB retrofitted substructures: one with spiral only (RRS-B1) and one with both spiral and ligaments (RRSL-B1). Table 5.6 summarize the characteristics of each numerical model assessed in this study.

Isotropic, linear-elastic beam elements capable of exhibiting axial tensile and compressive failure modes, as well as the flexural (bending) failure mode with a specified limiting plastic moment, were used to model the columns. Each column was divided into two segments: (1) a cantilevered segment extending12 in. (0.3 m) above the column-footing connection, following the recommendations by Megalooikonomou et al. (2017) that the plastic hinge length should be equal to half of the effective depth (modeled using two beam elements), and (2) the remaining height of the column, which was 84 in. (2.15 m) modeled using 20 elements. Since the beam elements did not have the same plan area as the actual columns, the stresses at the column-footing connection point differed from those in the experiments. To accurately model the column-footing connection, shell elements were used to connect the beam element to the footing, ensuring that the shell elements shared the same plan area as the columns. This modeling approach effectively enabled transfer of stresses to the footing. Although the models for the vintage and retrofitted systems were identical, the limiting plastic moments were specified according to the experimentally observed characteristics to appropriately capture the flexural responses, described in detail below. The beams were also modeled using isotropic, linear-elastic beam elements with characteristics presented in Table 5.6. The beams for the bent systems were 24 ft. (7.3 m) long.

Table 5.6: Characteristics of the two-column bent system models.

Test #	Terms	PHV_B1	PHRSL_B1	RV_B1	RRSL_B1	RRS_B1
System		**Vintage**	**Retrofitted**	**Vintage**	**Retrofitted**	**Retrofitted with Spiral**
Base Condition		**Fixed**	**Fixed**	**Flexible**	**Flexible**	**Flexible**
Reinforcement Details	**Ligament**		**X**		**X**	
	Spiral		**X**		**X**	**X**
Foam	Elastic Modulus ksi (MPa)			11.6 (80)	11.6 (80)	11.6 (80)
	Cohesion, psf (kPa)			8,360 (400)	8,360 (400)	8,360 (400)
Column	Number	2	2	2	2	2
	Height, ft. (m)	16.1 (4.9)	16.1 (4.9)	16.1 (4.9)	16.1 (4.9)	16.1 (4.9)
Beam	Number	1	1	1	1	1
	Length, ft. (m)	24 (7.3)	24 (7.3)	24 (7.3)	24 (7.3)	24 (7.3)
Footing	Height, ft. (m)	2 (0.6)	2 (0.6)	2 (0.6)	2 (0.6)	2 (0.6)
	Length, ft. (m)	6 (1.8)	6 (1.8)	6 (1.8)	6 (1.8)	6 (1.8)
Vertical load kip (kN)	Column 1	150 (667)	150 (667)	150 (667)	150 (667)	150 (667)
	Column 2	150 (667)	150 (667)	150 (667)	150 (667)	150 (667)

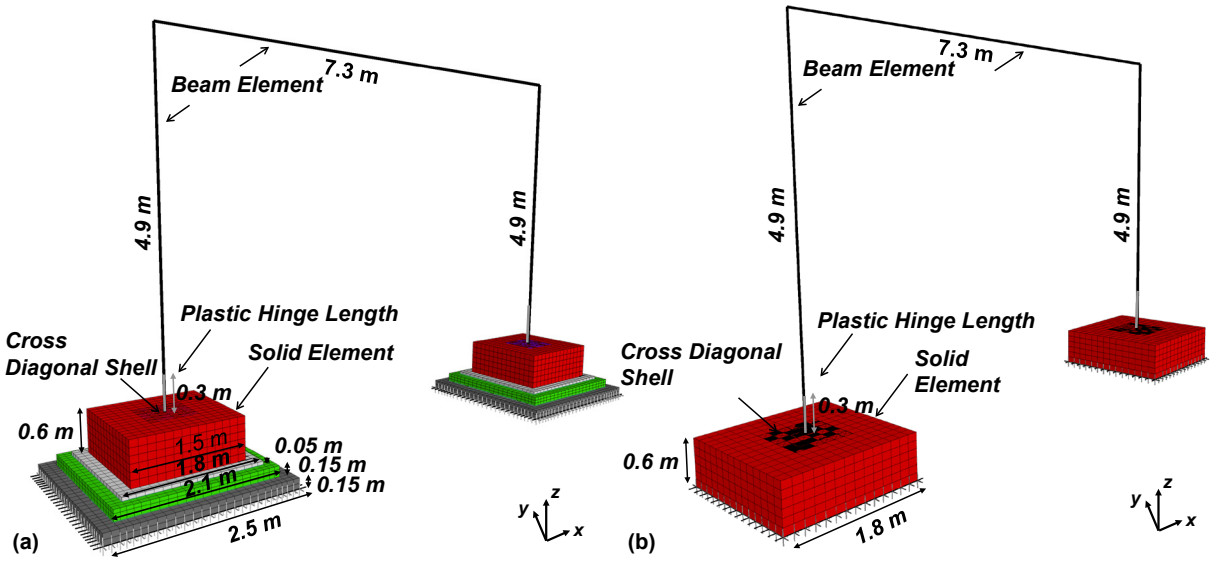

Figure 5.15: Components of the numerical bent models: (a) two column-footing bent system with flexible support, and (b) two column-footing bent system with fixed bases (Note: 1 m = 3.2808 ft).

The foundation, concrete load distribution slab, and XPS soil simulant were represented in the numerical model using quadratic solid elements, as depicted in Figure 5.15. The reinforced concrete was assumed to behave linear elastically, with Young's modulus, E, equal to 3,278 ksi (22.6 GPa) and Poisson's ratio, v, of 0.17. The response of the soil simulant in the rocking systems was captured using the elastic-perfectly plastic Mohr-Coulomb model. For capturing the behavior of the unreinforced load distribution slab during loading, the Hoek-Brown-Pac model (Hoek and Brown 1980; Hoek et al. 2002) was used. This constitutive model provides a framework to describe the stress at failure in intact rock and rock masses. The generalized Hoek-Brown failure criterion (Hoek and Brown 1982) is an empirical relationship that characterizes the expected behavior of the unreinforced load distribution slab and is expressed by:

$$\boldsymbol{\sigma_1 = \sigma_3 + \sigma_{ci}\left(m_b \frac{\sigma_3}{\sigma_{ci}} + s\right)^a} \qquad \textbf{(6-1)}$$

where σ_1 and σ_3 are the major and minor principal effective stresses, σ_{ci} is the uniaxial compressive strength of the material, m_b, s, and a are material constants that can be related to the Geological Strength Index and rock integrity (Hoek et al. 2002). The Hoek-Brown-Pac model utilized in this study allows for the specification of compressive and tensile strengths, which were set to 4,000 psi (27.5 MPa) and 600 psi (4.13 MPa), respectively. The corresponding values of E and v assigned to the load distribution slab was 4,200 psi (29 MPa) and 0.17, respectively. All aspects of modeling and calibration of constitutive models for the materials and interface behavior between disparate materials follow those described in Section 5.4.

The boundary conditions deployed in the simulations were set based on the specific system under investigation. In the fixed base bent systems, the nodes at the bottom of the footing were restrained in all six degrees of freedom to prevent displacements and rotations in any direction. In the rocking systems, however, the footing was allowed to rotate around the y-axis in response to loading, while the column moved along the x-axis (Figure 5.15). The nodes at the bottom of the strong floor elements were restrained in all six degrees of freedom, similar to the fixed base systems. The remaining nodes in the model were left unrestrained. To maintain consistency with the experimental rocking specimen (RRSL), which was restrained against sliding, the bottommost side nodes located along the footing and perpendicular to the loading direction were fixed in the longitudinal (x) direction. This prevented translation of the bent model during loading, to better simulate the experimental conditions.

Pseudo-static pushover tests were conducted by gradually increasing the horizontal velocity applied to the top of the column while maintaining a constant axial load of 150 kips (667 kN). To ensure numerical stability, the column was displaced using a gradually-increasing horizontal velocity with an incremental velocity that varied as shown in Figure 5.16a to produce the resulting displacement time history at the loading point shown in Figure 5.16b. The use of such a numerical loading protocol is helpful in time-domain simulations that solve the equations of motion since the rapid application of nominally pseudo-static displacements or loads can result in poorly damped oscillation of the unbalanced forces that need to be resolved during model convergence. Note that the “step” defining the incremental velocity and displacement time history in Figure 5.16 is the numerical equivalent of time.

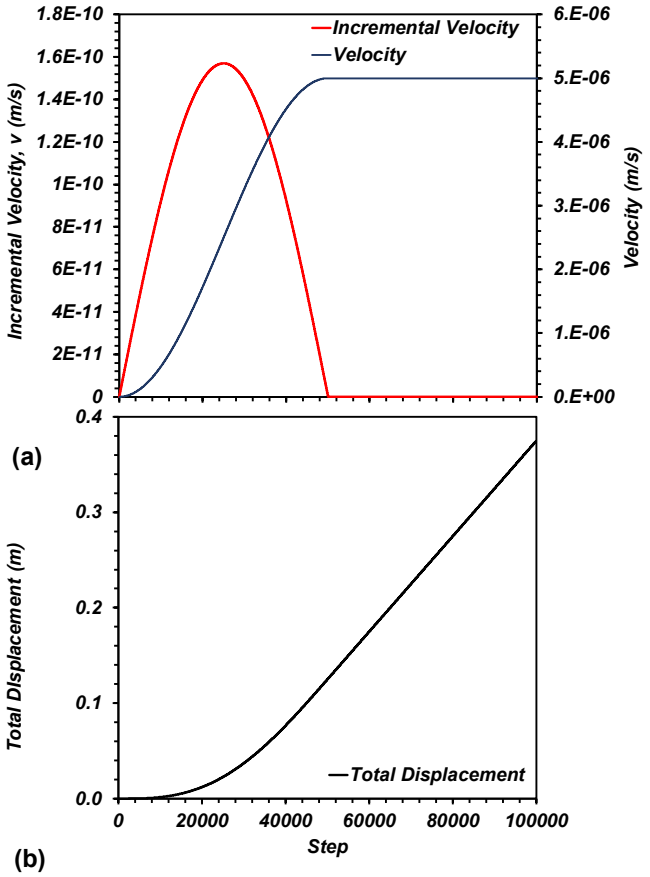

Figure 5.16: Specified lateral velocity used to simulate the lateral loading to the multi-column bent models (Note 1 m/s = 3.2808 ft./s).

The beam elements comprising the columns were set with specified flexural rigidities, *EI*, and the experimentally observed plastic moment capacities. Section analyses of the vintage (PHV) and retrofitted (PHRS and PHRSL) columns were conducted using the finite difference platform LPILE (Ensoft 2019), and the resulting column-specific moment-curvature, M-ϕ, relationships obtained were approximated within FLAC3D, similar to the process described in Section 5.4. The effect of confinement on the concrete in the columns is incorporated into section analyses following the approach of Mander et al. (1988). Table 5.7 summarizes the parameters that were used in the section analysis for the cases considered.

The as-built dimensions of the vintage column were used in the LPILE section analyses; however, the TiAB ligaments and spirals and corresponding concrete cover could not be modeled directly. The effect of the retrofit elements on the M-ϕ response of the retrofitted column section was captured through the use of a higher f_y for the longitudinal and transverse bars and a reduced transverse steel spacing (i.e., 4 in. or 100 mm rather than 12 in. or 300 mm) to account for the increased confinement provided by the TiAB spiral (Table 5.7). Figures 5.10a to 5.10d compare the M-ϕ relationships obtained using LPILE to that specified in the numerical

simulations for the vintage, retrofitted columns with TiAB spiral and ligaments, and retrofitted columns with TiAB spiral.

Table 5.7: Model parameters used to simulate the moment-curvature responses of the test column sections in LPILE.

	Type	Vintage Column		Retrofitted Column		Beam	
		SI	Eng	SI	Eng	SI	Eng
Concrete	f'_c	22.7 MPa	3300 psi	22.7 MPa	3300 psi	22.7 MPa	3300 psi
	E	22.5 GPa	3275 psi	22.6 GPa	3274 psi	22.6 GPa	3274 psi
	ν	0.15		0.15		0.15	
Stirrup Bars	Bar Size	3		3		4	
	Spacing	0.3 m	12 in	0.1 m	4 in	0.3 m	12 in
	$f_{y,steel}$	276 MPa	40 psi	586 MPa	85 psi	358 MPa	52 psi
	E	200 GPa	29 ksi	200 GPa	29 ksi	200 psi	29 ksi
Longitudinal Bars	Bar Size	10		10		11	
	$f_{y,steel}$	469 MPa	68 psi	689 MPa	100 psi	469 MPa	68 psi
	$f_{u,steel}$	634 MPa	75 psi	931 MPa	135 psi	634 MPa	92 psi
	ε_y	0.006		0.004		0.0125	
	ε_u	0.02		0.01		0.09	
	E	200 GPa	29 ksi	200 GPa	29 ksi	200 GPa	29 ksi

5.5.2 3D Numerical Study of Multi-Column Bridge Bents

5.5.2.1 Pushover Response of the Plastic Hinging Two-Column Bent Systems

The responses of the plastic hinging vintage (PHV-B1) and retrofitted (PHRSL-B1) two-column bent systems subjected to a lateral pushover displacement at the top of the left column are presented and compared in Figures 5.17 and 5.18. Results are presented in terms of the base moment capacity (Figure 5.17) and axial force at the top of the columns (Figure 5.18) against the column drift at the mid-height of the column. The figure also shows the experimental base moment measurements of the PHV and PHR systems (data points) for reference. The responses of the left and right columns are similar in the PHV-B1 and PHRSL-B1 simulations due to the resistance model not including the influence of axial force on moment capacity. The rigid footing model also ignores the soil-structure interactions. In the PHV-B1 simulation, the system exhibits a peak base moment of approximately 310 kip-ft. (420 kN-m) and a column drift at failure of 0.6 in. (15 mm), producing a nearly identical response as the single column system against which the model was validated. Brittle behavior is observed for the system with vintage column

after the initiation of column failure with significant degradation in strength and stiffness. These findings strongly suggest that under lateral loading, the moment capacity of the vintage columns could be reached and even surpassed, underscoring the necessity for a comprehensive retrofit of the columns. For the PHV-B1 system, the moment capacity of the columns increases to 730 kip-ft. (990 kN-m) as a result of the column retrofit. However, similar to the results of the experiments and numerical simulations on the rocking single column system, column TiAB retrofitting does not completely prevent column failure, but rather delays it to substantially larger column drifts.

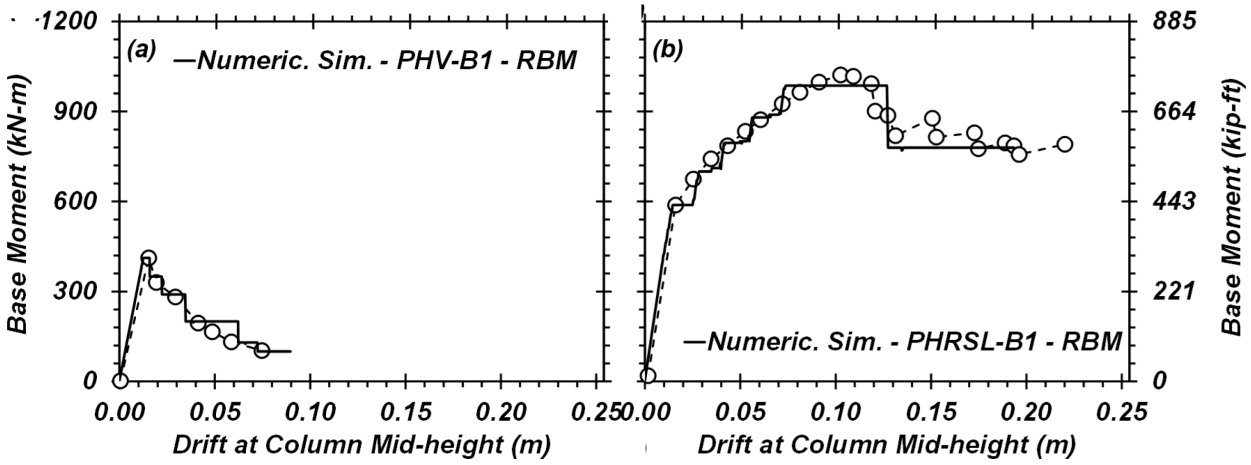

Figure 5.17: Results of the simulations of two-column bent systems and comparisons with the experiments on single column systems for moment at the base of the column vs. column drift: (a) the left column of the hinging vintage bent model (PHV-B1 – LBM), (b) the left column of hinging retrofit bent model (PHRSL-B1 – LBM).

Figures 5.18a and b show variations in the axial force of the left and right columns for the PHV-B1 and PHRSL-B1 systems, respectively. Due to the stiffness of the beam and its deflection during loading, the portion of the total vertical load taken by the right and left columns are different. The left columns in both the vintage (PHV-B1 – L. Col) and retrofitted (PHRSL-B1 – L. Col) systems are subjected to tension during lateral loading and experience a net decrease in the axial force as column drift increases until a minimum axial load of about 124 kip (550 kN) is reached. In the right columns of the vintage (PHV-B1 – R. Col) and retrofitted (PHRSL-B1 – R. Col) systems, the axial force increases as the column drift increases, reaching a maximum of about 180 kip (800 kN). The column drift associated with the minimum and maximum axial forces in the vintage system occurs at column failure. For the retrofitted system, however, the minimum and maximum axial forces occur when hardening initiates.

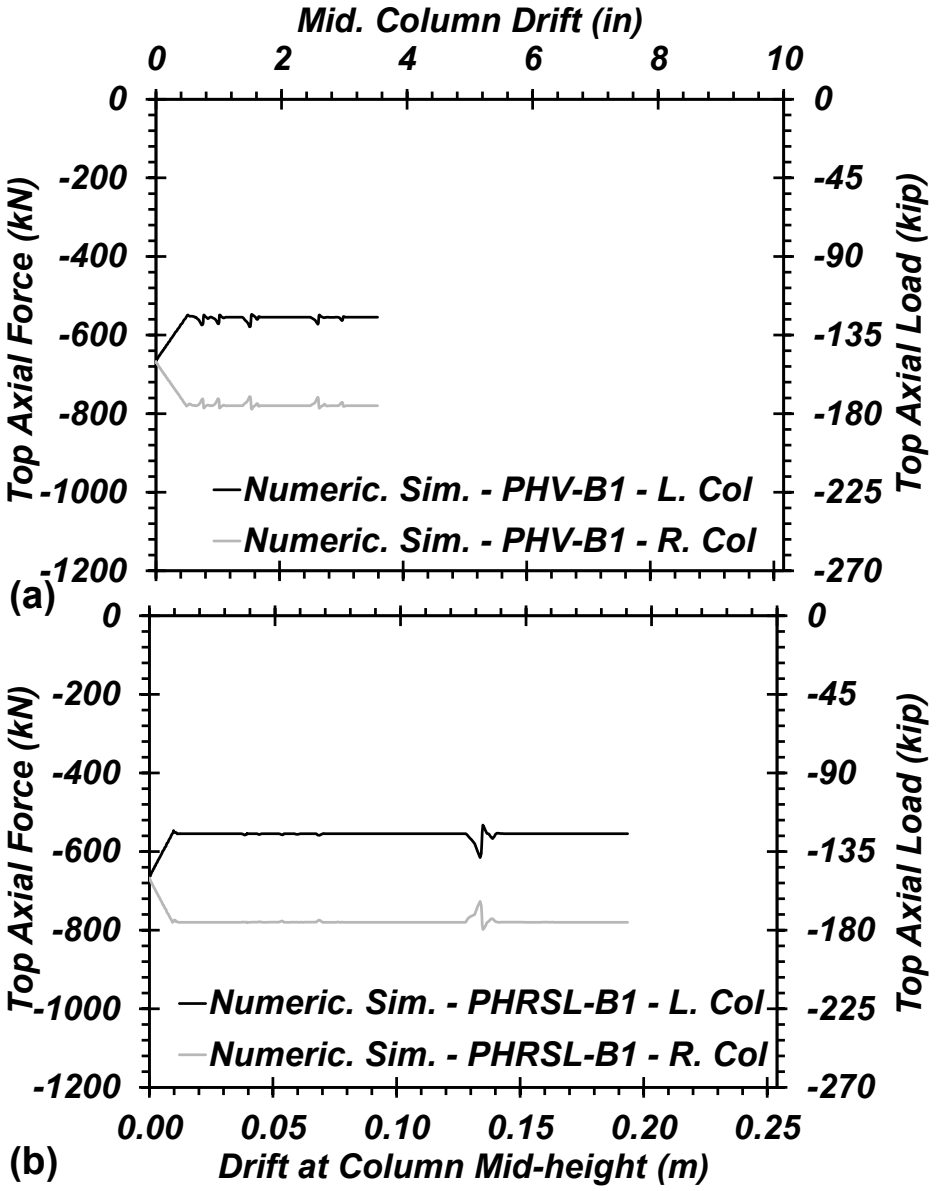

Figure 5.18: Results of the simulations of two-column bent systems in terms of column axial forces vs. column drift for: (a) the plastic hinge vintage bent model (PHV-B1), and the (b) plastic hinge retrofit bent model (PHRSL-B1).

5.5.2.2 Pushover Response of the Rocking Two-Column Bent Systems

The behavior of a rocking two-column bent system can be characterized by the column base moment and axial force at the top of the column vs. drift at the mid. height of column relationships (Figures 5.19 and 5.20). The moment-drift curves of the left and right columns in the rocking vintage (RV-B1) bent system are presented in Figures 5.19a and 5.19b, respectively. It is apparent from the results that there is considerable nonlinearity in the moment-column drift curves of the columns due to foundation rocking. Results also indicate that the moment capacity of the columns can be reached

and exceeded under lateral load in the RV-B1 system. However, column failure initiates first at the bottom of the right column. This difference in behavior is a consequence of the axial force increasing in the right column during lateral loading (Figure 5.20a). In contrast, the left column experiences a reduction in the axial force with increasing column drift. After the failure of the right column, the right footing ceases to rock whereas the left footing continues to rock. After failure, the columns experience degradation in the base moment of the columns as observed in Figure 5.19a to result in a gradually and irregularly reducing axial force (Figure 5.20a).

Similar to the RV-B1 system, the RRSL-B1 system displayed a nonlinear moment-drift behavior attributed to rocking, as depicted in Figures 5.19c and 5.19d. The measured responses confirmed that the system was loaded to its moment capacities, which differed among the two column-footing substructures. Notably, the moment capacity of the right column (Figure 6.14d) exceeded that of the left column in Figure 5.19c, with a value of 580 kN-m for the right column compared to 310 kip-ft. (420 kN-m) for the left column. This disparity in moment-drift behavior between the left and right columns can be attributed to the differing axial force-drift behaviors during lateral loading, as illustrated in Figure 5.20b. While the axial force in the left column decreased during rocking, the right column experienced an increase of approximately 20%, reaching a maximum value of 180 kip (800 kN) at a column drift of 0.6 in. (16 mm). The rocking moment capacity of the left and right columns was achieved at drift levels of approximately 1.6 in. (0.04 m) and 2.17 in. (55 mm), respectively. Consequently, due to the increasing axial force in the right column, it is anticipated that the right footing would exhibit less rocking motion compared to the left footing during loading.

Figures 5.19e and 5.19f show the moment-drift curves of the left and right columns of the two-column bent system with columns retrofitted with only TiAB spirals (RRS-B1). The moment-drift response of the RRS-B1 system resembles that of the RRSL-B1 system. Similar to the RRSL-B1, the columns did not fail in plastic hinging but were loaded to their moment capacities. The right column demonstrated a higher moment capacity due to the increased axial load (Figure 5.20c) experienced during rocking. This indicates that, depending on the soil conditions, a retrofit of the column using only the TiAB spirals may be sufficient to achieve desired substructure response.

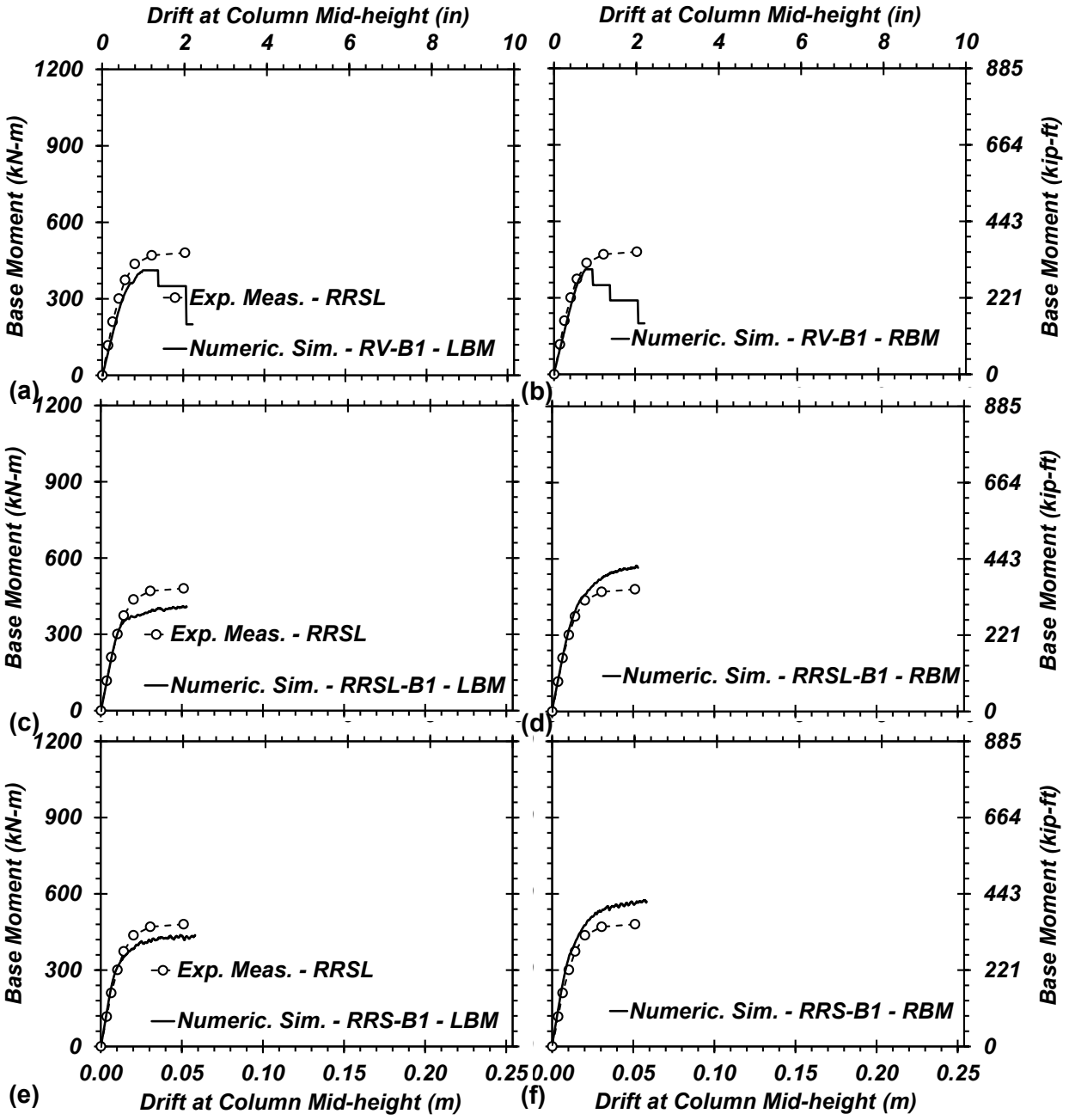

Figure 5.19: Results of the simulations of two-column bent systems and comparison to the experiments on single column systems in terms of the moment at the base of the column vs. column drift for (a) the left column of the hinging vintage bent model (PHV-B1 – LBM), (b) the right column of the hinging vintage bent model (PHV-B1 – RBM), (c) the left column of hinging retrofit bent model (PHRSL-B1 – LBM), and (d) the right column of hinging retrofit bent model (PHRSL-B1 – RBM).

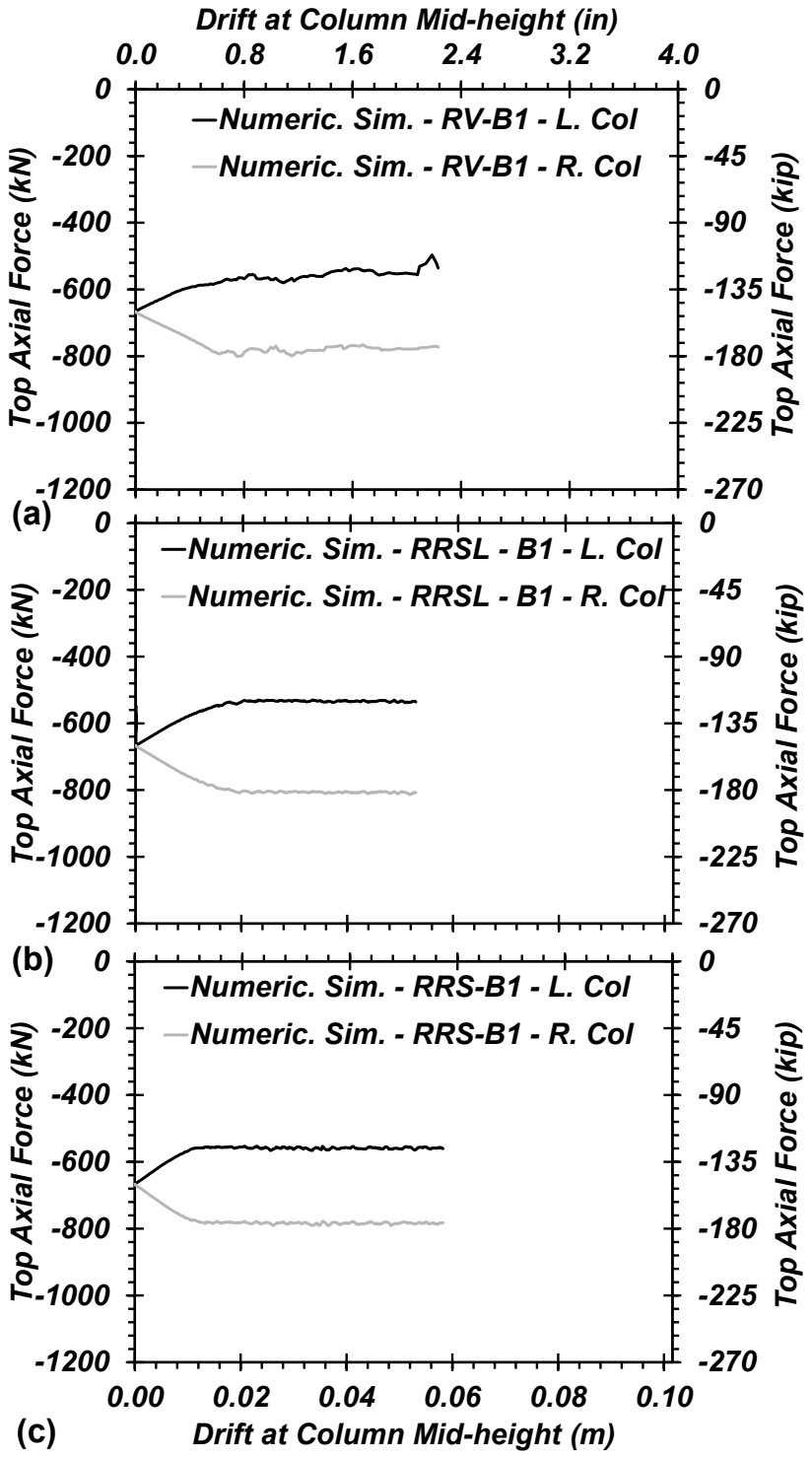

Figure 5.20: Results of the simulations of Two-Column Bent Systems in terms of the axial force at the top of the column vs. column drift for (a) the Rocking Vintage Bent Model (RV-B1), (b) Rocking Retrofit Bent Model with spiral and ligament (RRSL-B1), and (c) Rocking Retrofit Bent Model with spiral only (RRS-B1).

5.6 DISCUSSION AND IMPLICATIONS FOR PRACTICE

Older bridges were designed principally for gravity loading with little consideration of seismic or lateral loading. They have historically been vulnerable to seismic effects, with numerous examples of damage occurring to both superstructure and substructure elements of the bridge, and, in some cases, complete collapse. Typical structural deficiencies in pre-1971 bridges have included: (1) lap splices located at column bases, (2) low confinement and shear reinforcement in lap-splice regions and column/footing hinge regions, (3) insufficient footing plan area to resist soil pressures caused by earthquake forces, and (4) a lack of top steel in footings (Priestley et al. 1996; Xiao et al. 1996; Saiidi et al. 2001; Krish et al. 2018; Shrestha 2019). These four features result in a non-ductile response of RC columns that can lead to collapse during strong ground shaking. This study proposes a novel retrofit method for RC columns with deficient reinforcing details. The retrofit was applied to square RC columns and combined titanium alloy bars (TiABs) with conventional concrete. The proposed retrofitting technique addresses the following needs:

- While effective for retrofitting circular reinforced concrete (RC) columns, currently available retrofit techniques are not as effective for square RC columns. The main challenge lies in providing effective confinement of square columns. In this technique, TiAB spirals ensure continuous confinement through hoop action, providing effective confinement for the column.

- Retrofitting techniques like steel jacketing and column jacketing suffer from the disadvantage of being too stiff and adding to the seismic weight of the system that tend to increase the seismic demand (Bournas and Triantafillou 2009). In this technique, by debonding the retrofit shell, any stiffness increase in the retrofitted region can be prevented. Also, it facilitates construction and post-earthquake inspection which is usually difficult to perform on columns retrofitted with alternative jacketing/wrapping retrofit techniques.

- Most of the contemporary retrofitting techniques focus on the provision of lateral confinement only. There has been limited study on providing an alternative flexural load path after the lap-spliced reinforcing steel bars fail. TiAB ligaments in this technique provide a simple and effective flexural tension component after failure of the steel lap-splices.

- Also, this retrofit option is considered an economic option due to the ease of construction, efficiency of retrofit materials used, limited surface preparation, and inherent corrosion resistance of TiAB bars, which makes it viable to use for such exposure and limited to no need for future maintenance.

The use of TiABs advances development retrofit design approaches for bridges. However, there still remains no rational design approach for retrofitted column-footing systems for bridges that consider the combined effects of the nonlinearity of structural components and soil. Without consideration of the SSI, design questions remain to be answered, such as (1) does column strengthening due to retrofitting cause unintended damage to similarly poorly detailed footings? (2) will resulting seismic settlements and sliding in the soil occur within an allowable

magnitude? (3) should rocking and soil failure underneath the footing be allowed and/or facilitated during loading? Results of this study indicate a reduction in the moment gradient along the column height and the demands in the column at the footing elevation and suggest that SSI can be both beneficial and deleterious across different criteria, and improvements in understanding the effects of SSI are needed to ensure desired seismic performance of retrofitted substructures. Also, limited resources require that methodologies that can take advantage of soil-structure interaction, where warranted, be used to extend the life of existing bridges, and that tools be developed to quickly assess whether retrofit of bridge substructures is preferable over replacement given the existing structural details, substructure type, and soil conditions. Incorporation of soil-structure interaction may also show that retrofit or replacement of the substructure is not necessary. Given the number of bridges for which retrofit/replacement is considered desirable, the impact on both budget and project delivery could be significant, with significant potential implications for improving the seismic resilience of the transportation network.

5.7 CONCLUSIONS

An effective retrofit that uses vertical bars and a continuous spiral made of titanium alloy bars (TiABs) was developed for seismically deficient square reinforced concrete columns. The TiAB spiral ensured continuous confinement of the underlying square column within the region of the flexural reinforcing lap splice located above the footing. The TiAB vertical bars provided a redundant flexural load path to resist seismically induced moment and provide additional dowel reinforcement at the column-footing interface to enhance interface shear strength. The performance of the retrofitting technique was demonstrated by pseudo-static reversed-cyclic tests on large-scale single column bridge substructures. In these tests, the effect of soil-structure interaction and support flexibility on the strength and deformability of retrofitted columns were also investigated. The measured response of the test specimens compared well with the predictions of three-dimensional nonlinear finite-difference models calibrated with properties obtained from experimental tests and section analyses. Parametric studies were undertaken to investigate the interactions of soil strength and stiffness with the column retrofit strength and stiffness. Results of the experiments and numerical simulations provides the basis for the following conclusions:

1. The moment capacity of the unretrofitted vintage columns could not achieve the yield moment and the response exhibits rapid strength degradation and no ductility due to failure of the lap splice located in the column above the footing.

2. The proposed TiAB retrofit details modestly increased the column strength and greatly increased the deformation capacity of the columns, and reduced damage in the columns at all drift levels. The columns maintained full axial load capacity at the end of the tests.

3. Introducing flexibility from a simulated soil subgrade and consideration of soil-structure interaction (SSI) would not have prevented failure of the unretrofitted specimen. Retrofitting of the column is necessary to mobilize the rocking response within the soil simulant considered.

4. SSI reduced the moment demands on the retrofitted column. Therefore, the amount of TiAB required for the column retrofit could be reduced without negatively affecting the overall response of the system. Numerical simulations showed that rocking is induced when the soil subgrade becomes weaker and the rocking moment capacity becomes smaller relative to the column moment capacity, regardless of the application of column retrofit (either retrofitted or unretrofitted).

5. The simulations demonstrated that for a given rocking moment capacity, differences in soil stiffness do not change the mode of behavior in terms of whether it rocks or not. However, reduced soil stiffness increases the drift at which the moment capacity is reached.

6. There exists a threshold flexural strength at which the column-footing system behavior transitions from plastic hinging in the column to rocking of the column-footing system, which can be used to optimize the selection and design of the retrofit.

7. Multi-column bent substructures exhibit axial load redistribution which leads to differential rocking responses of the footings and corresponding column moment capacities.

8. Depending on the soil conditions, a retrofit of the column using only the TiAB spirals may be sufficient to achieve desired substructure response for rocking systems.

These results showed that to determine which action controls the behavior of a spread footing, assessment of the site-specific soil and structural characteristics is necessary. Furthermore, the experimental program and numerical simulations were conducted using a quasi-static loading protocol; the effect of the transient loading associated with earthquake ground motions on the retrofit and rocking performance remains to be evaluated in future research.

5.8 REFERENCES

Acharya, M., Khadka, R., and Mashal, M. (2022). Preliminary Bond Testing and Splicing of Titanium Alloy Bars. Transportation Research Record, 03611981211067785.

ACI Committee 374. (2013). ACI 374.2R-13: Guide for Testing Reinforced Concrete Structural Elements under Slowly Applied Simulated Seismic Loads. Detroit, MI.

Amneus, D. (2014). Methods for Strengthening Flexural Steel Details in Reinforced Concrete Bridge Girders using a Near-Surface Mounted Retrofitting Technique (master's thesis). Oregon State University, Corvallis, OR.

Anastasopoulos, I., Kourkoulis, R., Gelagoti, F. and Papadopoulos, E. (2012). Rocking Response of SDOF Systems on Shallow Improved Sand: An Experimental Study. *Soil Dynamics and Earthquake Engineering*, 40, pp.15-33.

ASTM C617-98 (1998). Standard Practice for Capping Cylindrical Concrete Specimens. USA.

ASTM C39/C39M-05 (2005). Standard Test Method for Compressive Strength of Cylindrical Concrete Specimens.

Barker, L. (2014). Flexural Anchorage Performance and Strengthening on Negative Moment Regions Using Near-Surface Mounted Retrofitting in Reinforced Concrete Bridge Girders (master's thesis). Oregon State University, Corvallis, OR.

Bournas, D. A., and Triantafillou, T. C. (2009). Flexural Strengthening of Reinforced Concrete Columns with Near-Surface-Mounted FRP or Stainless Steel. ACI Structural Journal, 106(4), 495–505. https://doi.org/10.14359/56615

Brown, E. T., and Hoek, E. (1980). Underground excavations in rock. CRC Press.

Campione, G., Miraglia, N. and Papia, M. (2004). Strength and Strain Enhancements of Concrete Columns Confined with FRP Sheets. Structural Engineering and Mechanics, 18(6), pp.769-790.

Cairns, J., and Arthur, P. D. (1979). Strength of Lapped Splices in Reinforced Concrete Columns. ACI Journal Proceedings, 76(2). https://doi.org/10.14359/6947

Chai, Y. H., Priestley, M. J. N., and Seible, F. (2008). Seismic Retrofit of Rectangular Bridge Columns by Steel Jacketing. In Third Bridge Engineering Conference: Papers Presented at the Third Bridge Engineering Conference, March 10-13, 1991, Denver, Colorado (pp. 95– 103).

Deng, L., Kutter, B. L., and Kunnath, S. K. (2012). Centrifuge Modeling of Bridge Systems Designed for Rocking Foundations. Journal of Geotechnical and Geoenvironmental Engineering, ASCE, 138(3): 335–344.

El Gawady, M., Endeshaw, M., McLean, D., and Sack, R. (2010). Retrofitting of Rectangular Columns with Deficient Lap Splices. Journal of Composites for Construction, 14(1), 22–35. https://doi.org/10.1061/(asce)cc.1943-5614.0000047

Ensoft. (2019). LPILE v2019 User's Manual: A Program for the Analyses of Deep Foundations under Lateral Loading. Ensoft, Austin, TX.

Gajan, S., Kutter, B. L., Phalen, J. D., Hutchinson, T. C., Martin, G. R. (2005). "Centrifuge Modeling of Load-Deformation Behavior of Rocking Shallow Foundations." Soil Dynamics and Earthquake Engineering, 25, 773–783.

Gajan, S. and Kutter, B. (2008). Capacity, Settlement, and Energy Dissipation of Shallow Footings Subjected to Rocking," Journal of Geotechnical and Geoenvironmental Engineering ASCE 135(3), 407–420.

Gamble, W. L., Hawkins, N. M., and Kaspar, I. I. (1996). Seismic retrofitting experience and experiments in Illinois. Proc., 5th National Workshop on Bridge Research in Progress, National Center for Earthquake Engineering Research (NCEER), State Univ. of New York at Buffalo, Buffalo, NY, 245–250.

Girard, C., and Bastien, J. (2002). Finite-Element Bond-Slip Model for Concrete Columns under Cyclic Loads. ASCE Journal of Structural Engineering, 128(12), 1502–1510. https://doi.org/10.1061/(ASCE)0733-9445(2002)128:12(1502)

Goksu, C., Yilmaz, H., Chowdhury, S. R., Orakcal, K., & Ilki, A. (2014). The Effect of Lap Splice Length on the Cyclic Lateral load Behavior of RC Members with Low-Strength Concrete and Plain Bars. Advances in Structural Engineering, 17(5), 639–658. https://doi.org/10.1260/1369-4332.17.5.639

Haroun, M. A., and Elsanadedy, H. M. (2005). Fiber-Reinforced Plastic Jackets for Ductility Enhancement of Reinforced Concrete Bridge Columns with Poor Lap-Splice Detailing. Journal of Bridge Engineering, 10(6), 749–757. https://doi.org/10.1061/(ASCE)1084-0702(2005)10:6(749)

Higgins, C. C., Knudtsen, J., Amneus, D., and Barker, L. (2017). Shear and Flexural Strengthening of Reinforced Concrete Beams with Titanium Alloy Bars. Proceedings of the 2nd World Congress on Civil, Structural, and Environmental Engineering (CSEE'17), 1–8.

Hoek, E., Carranza-Torres, C., and Corkum, B. (2002). Hoek-Brown Failure Criterion-2002 Edition. Proceedings of NARMS-Tac, 1(1), 267-273.

Itasca. (2000). FLAC (Fast Lagrangian Analysis of Continua) User's Manuals. Minneapolis: Itasca Consulting Group, Inc.

Khadka, R., Mashal, M., & Cantrell, J. (2020). Experimental Investigation on Mechanical Properties of Titanium Alloy Bars: Comparison with High-Strength Steel. Special Publication, 341, 160-187.

Khosravi, A., Shrestha, S., Stuedlein, A. W., & Higgins, C. (2023). Titanium Seismic Substructure Retrofit to Enable Rocking of Bridge Foundations Considering Soil–Structure Interaction: Experiments and Numerical Simulations. Journal of Bridge Engineering, 28(2), 04022143.

Knudtsen, J. (2016). Shear Strengthening Reinforced Concrete Bridge Girders Using Near-Surface Mounted Titanium Alloy Bars (master's thesis). Oregon State University, Corvallis, OR.

Krish, Z. F., Kowalsky, M. J., Nau, J. M. and Seracino, R., (2018). Repair of Reinforced Concrete Bridge Columns via Plastic Hinge Relocation, Volume 1: Repair Using Conventional Materials (No. Report No. 4000 (142)).

Lostra (2016). Seismic Performance of Square Reinforced Concrete Columns Retrofitted with Titanium Alloy Bars (master's thesis). Oregon State University, Corvallis, OR.

Malhotra, S. (2007). Foundation Considerations for Seismic Retrofit of Bridges. Proc. Ninth Canadian Conference on Earthquake Engineering, June, Ottawa, Ontario, Canada.

Megalooikonomou, K., Pantazopoulou, S., & Tastani, S. (2017). Plastic Hinge Length Definition in Column-Definition through Consideration of Yield Penetration Effects. In 16th World Conference on Earthquake (16WCEE), Santiago, Chile.

Melek, M., and Wallace, J. W. (2004). Performance of Columns with Short Lap Splices. In 13th World Conference on Earthquake Engineering Vancouver, B.C., Canada August 1-6, 2004, Paper No. 1034 (pp. 1–15). https://doi.org/10.1002/eqe.4290180114

Mirmiran, A., Shahway, M., Samaan, M., Echary, H. El, Mastrapa, J. C., and Pico, O. (1998). Effect of Column Parameters on FRP-Confined Concrete. *Journal of Composites for Construction*, 2 (November), 175–185.

Negussey, D. (2007). Design Parameters for EPS Geofoam. *Soils and Foundations*, 47(1), 161-170.

Priestley, M. J. N., Evison, R. J. and Carr, A. J. (1978). Seismic Response of Structures Free to Rock on their Foundations. Bulletin of the New Zealand National Society for Earthquake Engineering, 11(3), pp.141-150.

Priestley, M. J. N., Seible, F., and Calvi, G. M. (1996). Seismic Design and Retrofit of Bridges, John Wiley and Sons, New York, NY.

Reinhardt, E., Saiidi, M., and Siddharthan, R. (2003) Seismic Performance of a CFRP/Concrete Bridge Bent on Flexible Footings. Technical Report CCEER-03-4, Civil Engineering Department, University of Nevada, Reno, NV, August 2003.

Saatcioglu, M. and Yalcin, C., (2003). External Prestressing Concrete Columns for Improved Seismic Shear Resistance. ASCE Journal of Structural Engineering, 129(8), pp.1057-1070.

Saiidi, M. S., Sanders, D., & Acharya, S. (2001). Seismic retrofit of spread footings supporting bridge columns with short dowels. Construction and building Materials, 15(4), 177-185.

Shrestha, S. (2019). Seismic Retrofit of Square Reinforced Concrete Bridge Columns using Titanium Alloy Bars. PhD Dissertation, Oregon State University, Corvallis, OR.

Takahashi, Y., Muto, I., Hitoshi, S., Tadokoro, Y., & Tagomori, N. (1994). Application of Titanium to Construction and Civil Engineering. Nippon Steel Technical Report. Nippon Steel Corp, 1994. 9-15. https://doi.org/UDC669.295.7:624/627

Vavra, E. (2016). Application of Titanium Alloy Bars for Strengthening Reinforced Concrete Bridge Girders in Flexure (master's thesis). Oregon State University, Corvallis, OR.

Vucetic, M., and Tabata, K. (2003). Influence of Soil Type on the Effect of Strain Rate on Small-Strain Cyclic Shear Modulus. Soils and Foundations, 43(5): 161-173. doi:10.3208/sandf.43.5_161.

Xiao, Y., Priestley, M.N. and Seible, F. (1996). Seismic Assessment and Retrofit of Bridge Column Footings. Structural Journal, 93(1), pp.79-94.

Xiao, Y., and Ma, R. (1997). Seismic Retrofit of RC Circular Columns Using Prefabricated Composite Jacketing. ASCE Journal of Structural Engineering, 123(10), 1357–1364.

6.0 FULL-SCALE PERFORMANCE OF RETROFITTED REINFORCED CONCRETE COLUMNS INCLUDING SOIL-STRUCTURE INTERACTION: PART I

6.1 INTRODUCTION

Failure mechanisms that typically develop in substructures of pre-1971 reinforced concrete bridges during earthquakes arise from common detailing deficiencies originating at design. These structural deficiencies include inadequate lap-splice detailing, insufficient confinement and ductility in the plastic hinge regions, low grade concrete, insufficient footing area, and inadequate shear and flexural strength to resist soil pressures caused by seismic activity (Priestly 1996; Xiao et al. 1996; Saiidi et al. 2001; Krish et al. 2018; Shrestha 2019). To mitigate existing deficiencies, retrofitting has been used and there are several successful seismic retrofitting strategies that effectively increase the seismic performance of RC columns during an earthquake. The retrofit strategies for RC columns are categorized as passive or active confinement.

Passive confinement is characterized by jacketing a column using steel or a fiber-reinforced polymer (FRP). This is the most common type of method used to provide confinement and shear strength, especially in areas with poor lap splice performance. Jacketing also offers a minimal increase in the overall column dimensions. Carbon fiber reinforced polymers (CFRP) or glass fiber reinforced polymer (GFRP), for short square RC columns, have been found to not only increase their shear strength but also energy dissipation capacity (Mirmiran et al. 1998; Haroun and Elsanadedy 2005; Galal et al. 2005). Additionally, steel jacketing provides confinement of the RC column along the height of the jacket and prevents spalling that leads to the deterioration of the bond of longitudinal bars.

Active confinement provides another approach for retrofitting RC columns. The primary method for accomplishing this is by applying external transverse prestress using metal hoops. Tension in the metal hoops provides transverse confining pressure that increases the shear resistance in the concrete. This technique is effective in improving ductility and limits the development of diagonal tension cracks (Saatcioglu & Yalcin 2003).

While these strategies represent effective methods for providing confinement and shear and flexural resistance during a seismic event, each technique exhibits deficiencies. FRP techniques require a complicated installation method and proprietary anchors to achieve effective anchorage; furthermore, the bonding agents are limited by environmental factors and FRP materials are often unable to provide adequate ductility without confinement (Mirmiran et al. 1998; Galal et al. 2005; ACI 440.2R-17, ACI Committee 440 2017). Steel jacketing adds to the effective seismic weight of the system and can produce inelastic strain penetration into footings as well as brittle shear failures from grouting. Additionally, retrofitting a square or rectangular RC columns with a rectangular jacket prevents adequate confinement over the flat surfaces of the retrofitted area due to bulging (Chai et al. 2008; Bournas & Triantafillou 2009). Lastly, wire prestressing requires a complex construction process that includes fixing anchors into existing members (Zong-Cai et al. 2014). These deficiencies led to the development of a novel titanium retrofit technique for square RC columns that combines titanium alloy bars (TiABs) and

conventional concrete to satisfy the requirements of a passive confinement strategy. By implementing supplemental TiAB ligaments, a redundant flexural load path is provided for the lapped footing and column bars. A TiAB spiral installed over the lap splice region and over the anchor points of the supplemental TiAB ligaments provides lateral confinement by casting an unbonded concrete shell between the TiAB spiral and the column. The novel retrofit using the TiAB produced seismic performance that was equivalent or greater than modern seismic designs (Shrestha 2019). The ease of installation and performance makes the TiAB retrofit technique ideal for square RC columns in high seismic regions. The proposed retrofit not only successfully improves strength, ductility, and energy dissipation, but is corrosion resistant, easy to fabricate and install, and visually inspectable. However, the previous study by Shrestha (2019) had limited considerations for soil-structure-interaction (SSI) and exhibited sustainably high performance on only half of the loading cycle due to rigid body translation of the column across the top of the footing due to lack of dowel action of the reinforcing steel.

The research compiled in this section accomplishes three objectives: (1) investigation of soil-structure interaction (SSI) effects on square RC columns with a new TiAB retrofit, (2) characterization of column behavior with a TiAB retrofit after prior failure of the column without retrofit, and (3) development of footing analysis methods using strut and tie methods that include SSI. Critically, 3D numerical simulations of the type described in Sections 5 and 6 were used to design the simulated soil spring system used to conduct the SSI experiments, as reported in Appendix A6.1.

To fulfill the requirements of the first objective, seven (7) quasi-static cyclic tests were carried out using full-scale square RC columns on a soil simulant. Two (2) specimens were retrofitted with both TiAB ligaments and two (2) TiAB spirals, and one (1) specimen was a vintage column with no retrofit. One (1) retrofitted specimen was tested on the soil simulant considering an embedment depth of 0.61 m (2 ft.) and a 0.203 m (8 in.) thick subgrade. The second retrofit was tested without embedment. The third specimen consisted of a vintage column with no retrofit. This column was tested first with both a soil simulant embedment and subgrade under an axial load of 667 kN (150 kips), and then again with axial load of 445 kN (100 kips). The embedment was then stiffened, by removing the soil simulant and replacing it with steel springs, to eventually fail the vintage column without retrofit. The last two (2) tests consisted of a TiAB ligament retrofit applied to the previously failed column tested under the same soil conditions used during the vintage column failure.

To characterize the behavior of a column retrofitted after failure, five (5) of the previously described seven (7) tests were conducted on a vintage column. After the retrofit using only TiAB ligaments was completed, the specimen was tested in the elastic range to see how the response changed due to addition of only the TiAB ligaments at deflections sufficiently large for comparison with the results from column failure tests but without producing further damage to the specimen. The TiAB spiral was then installed, and the shell was cast, before the final test on soil simulant for the rehabilitated column was completed.

Characterizing vintage footing behavior included recording visual damage during the seven (7) experimental tests on the soil simulant and one (1) test in which the top of the footing was restrained using supplemental steel beams anchored into the strong floor. For this test, a hole was cored through the center of the foundation face 165 mm (6.5 in.) down from the top of the

footing and a 34.9 mm (1-3/8 in.) diameter Dywidag bar was placed through the footing and mechanically tensioned. The Dywidag bar was intended to provide a resistance to tension stresses at the top of the footing as there is no reinforcing steel mat at the top of the vintage footings. The test was intended to fail the column; however, the lack of reinforcing at the top of the footing resulted in failure of the footing. Lastly, a strut and tie model was developed using the AASHTO-LRFD framework to allow analysis and design of spread footings under rocking conditions that include SSI.

6.2 EXPERIMENTAL PROGRAM

An experimental program was developed to characterize the effects of SSI on square RC columns, constructed using vintage details with a new TiAB retrofit strategy. The program included an improvement on the original TiAB retrofit design developed by Shrestha (2019), by installing a second spiral over the plastic hinge length. Additionally, it included construction of three (3) full-scale square RC column specimens and eight (8) different tests on these specimens. Test variables included axial load magnitude, with and without retrofit, soil simulant, embedment, and stiffness of provided by the simulated soil at the vertical faces of the footing.

Specimen design and construction were based on bridge columns along the critical transportation pathways: I-5, US-97, and OR-58. The overall geometries, reinforcing details, retrofit details, and construction process are described below, followed by instrumentation, test setup, vertical loading, and lateral displacement protocol. Material properties can be found in Appendix A6.1.

6.2.1 Specimen Design

Specimens were designed based on the ODOT bridge inventory review completed by Shrestha (2019). The review explains that 75% of columns were square and 32.9 % were between 4.57 m (15 ft.) and 5.49 m (18 ft.). Furthermore, longitudinal reinforcement for the columns was most commonly 1% of the gross cross-sectional area, typically 4-#36M (#11) Intermediate Grade (Grade 40) bars. Transverse reinforcement most commonly provided were #10M (#3) square ties, equivalent to Grade 40, at 305 mm (12 in.) on-center with 38.1 mm (1.5 in.) clear cover. The average lap-splice for the typical longitudinal reinforcement was $29d_b$, where d_b is the diameter of the longitudinal bar.

Spread footings were used as the foundation for 79% of the columns. Footings were most commonly 1.52 m (5 ft.) square and reinforced with a steel mesh of #16M (#5) Grade 40 at the bottom of the footings with 76.2 mm (3 in.) clear cover.

The concrete mix-design used in the experimental program was provided by a local ready-mix supplier. The 28-day design compressive strength was 28 MPa (4 ksi) and the maximum aggregate size was 4.75 mm (3/8 in.). Three (3) specimens were constructed from the design and eight (8) tests were conducted on the three (3) specimens. Specimens 1 and 2 were retrofitted with TiAB ligaments and TiAB spirals, and Specimen 3 was first failed as an unretrofitted vintage column and then retrofitted in phases to achieve the second objective. Table 6.1 outlines test numbers and descriptions and matches them with the corresponding specimen. Tests after column failure with subsequent stages of retrofit, T6 and T7, were intended to mimic conditions

during an aftershock following a seismic event in which a damaged or failed column-footing would rest on adjacent soil that was also damaged during the initial earthquake.

Table 6.1: Test specimen designation and test description.

Test ID	Specimen ID	Test Description
1	S.1	Complete Retrofit w/ Foam Embedment & Subgrade
2	S.2	Complete Retrofit w/ No Embedment & Foam Subgrade
3	S.3	Vintage w/ Foam Embedment, Subgrade, 150 kip axial
4	S.3	Vintage w/ Foam Embedment, Subgrade, 100 kip axial
5	S.3	Vintage Failure w/ Foam Subgrade and Steel Embedment
6	S.3	Vintage TiAB Ligaments w/ Foam Subgrade & Steel Embedment
7	S.3	Vintage Complete Retrofit w/ Foam Subgrade & Steel Embedment
8	S.2	Complete Retrofit w/ Tied Down Footing

6.2.1.1 Footing Details

Spread footing dimensions used in the experimental program were 1.52 m (5 ft.) square and 0.609 m (2 ft.) deep following the results of the bridge inventory review. A single mesh of reinforcement was used with 76.2 mm (3 in.) clear cover; however, Grade 40 reinforcing bars were not available. Therefore, an equivalent mesh of #13M (#4) Grade 60 bars was used. 18-#13M (#4) bars spaced 171 mm (6.75 in.) on center, and 4-#32M (#10) starter bars with a 559mm (22 in.) tail in accordance with ACI 318-02. Figure 6.1 illustrates the footing design for all specimens.

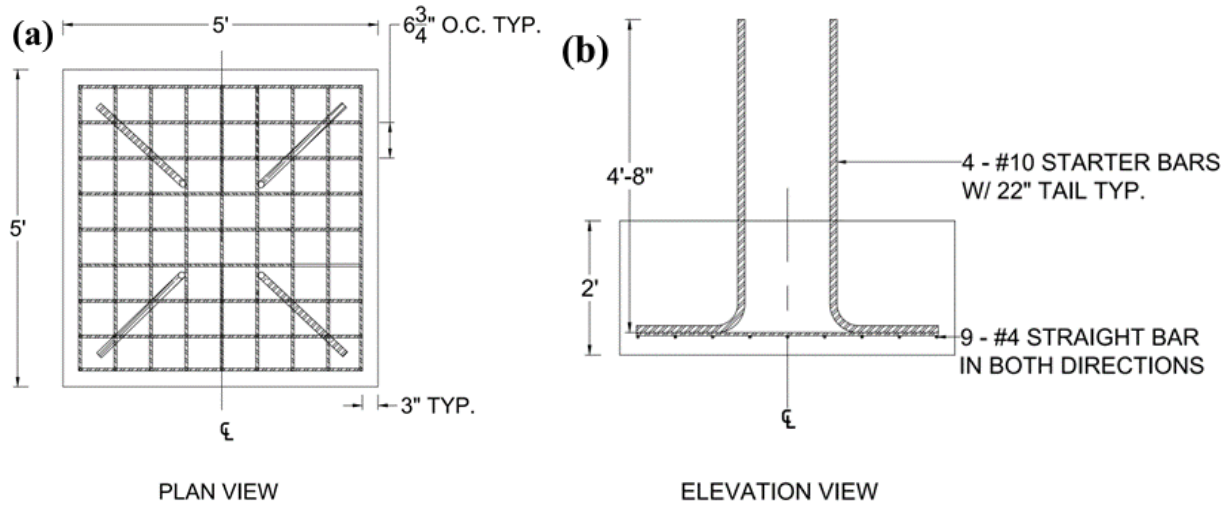

Figure 6.1: Typical vintage footing details (all dimensions are inches): (a) Plan view, (b) Elevation view.

6.2.1.2 Column Details

The overall height of the columns was 2.74 m. (9 ft.) above the top of the footing. The location of the lateral load was 2.438 m (8 ft.) above the top of the footing. The specimen represents the lower half of an actual bridge column whereby the point of inflection is assumed to occur at mid-height. The column cross section was 609 mm (24 in.) square. Equivalent longitudinal reinforcement of 4-# 32M (#10) Grade 60 was used due to unavailability of #36M (#11) Grade 40. Transverse reinforcement included #10M (#3) Grade 40 square ties with 90˚ hooks spaced 305 mm (12 in.) on center starting at 152 mm (6 in.) from the top of the footing and clear cover measures 38 mm (1.5 in.) over the length of the column. The longitudinal reinforcing bars measured 2.62 m (8 ft.-7in.) and 2.67 m (8 ft. – 9 in.) to avoid clash of the hooks. To secure the point of loading #13M (#4) Grade 60 square ties with 90˚ hooks 122 mm (4 in.) on-center were used as reinforcement, and four 60.3 mm (2-3/8 in.) holes were blocked out. Lap-splice length chosen was $30d_b$ to achieve a comparable length to the average lap-splice of vintage columns. Figure 6.2 depicts column details for all specimens.

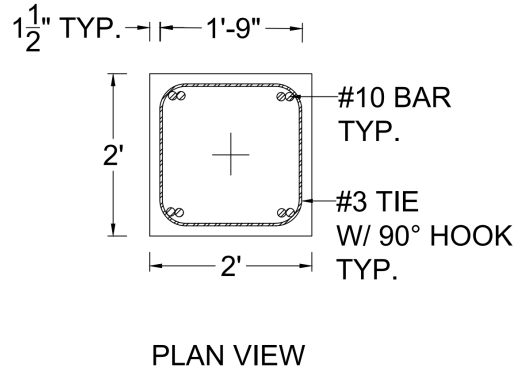

PLAN VIEW

(a)

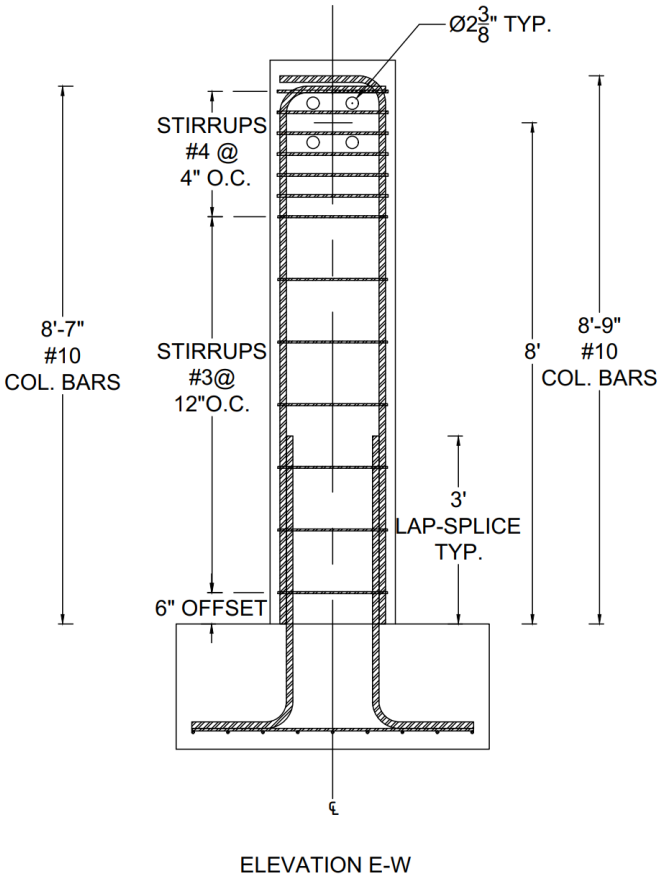

ELEVATION E-W

(b)

Figure 6.2: Vintage column details (all dimensions are feet and inches): (a) Plan view, (b) Elevation view. (1 ft = 12 in.; 1 in. = 25.4 mm)

6.2.2 Retrofit Design

The retrofit design included two (2) main TiAB components: ligaments and spirals. There were two (2) ligaments placed on each face of the column. These were anchored into the column face and the footing. The rest of the ligament lengths were unbonded. Confinement was provided by applying a TiAB spiral over the length of the ligaments. Clear polycarbonate sheets were used as formwork over the spiral and infilled with concrete for form a reinforced shell over the square column. The formwork was in direct contact with the TiAB spiral. The retrofit shell was cast with a nominal 889 mm (35 in.) diameter around the column, and 1.52 m (5 ft.) tall to prevent the extraction of the ligaments from the column face. A second spiral was installed over the plastic hinge length to improve the ductility of the retrofit designed by Shrestha (2019). No concrete cover was provided over the TiAB spiral due to the inherent corrosion-resistant properties of the TiABs.

6.2.2.1 TiAB Ligament

TiAB ligaments varied in length to prevent an abrupt change in stress that would occur if all were terminated at a single elevation. Three different lengths were used 1.93 m (6 ft.-4 in.), 1.78 m (5ft.-10in.), and 1.63 m (5ft.-4in.). Shrestha (2019) determined the average ligament length by calculating the tension lap-splice length recommended for column longitudinal bars by AASHTO LRFD Bridge Design Specification (2017). The TiAB ligaments were fabricated with 254 mm (10 in.) 90˚ hook with a proprietary deformation pattern machined 191 mm (7.5 in.) along the length of the hook tail. At the opposite end, the bars were smooth and had the proprietary deformation along the lowest 381 mm (15 in.) of the length. The deformations allow the TiABs to be anchored into the concrete using structural epoxy. TiAB ligaments had a nominal diameter of 15.9 mm (5/8 in.). The details of the TiAB ligaments are illustrated in Figure 6.3.

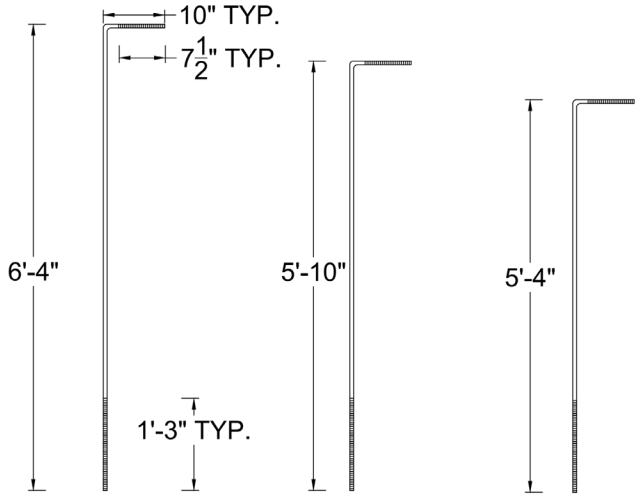

Figure 6.3: TiAB ligament details (all dimensions are feet and inches).

6.2.2.2 TiAB Spiral

TiAB spirals are shipped from the manufacturer as a 9.52 mm (3/8 in.) diameter coil. There are no special instructions for fabrication. All cutting and bending of the TiAB spiral are completed during construction using conventional construction practices, and there are no proprietary deformations added to any part of the spiral. However, Shrestha (2019) used the following AASHTO LRFD design specifications (2017) recommendations for spirals as transverse reinforcement in the selection of size and spacing of the TiAB spirals.

- Minimum spiral diameter of 9.52 mm (3/8 in.)
- Maximum center to center spacing of spirals should be the smaller of $6.0d_b$ or 152 mm (6 in.)
- Minimum clear spacing between the spirals should be the greater of 1.33 max aggregate size or 25.4 mm (1 in.)

Based on a sensitivity analysis, guidelines from Priestly et al. (1996) and Mander et al. (1988), and the recommendations from AASHTO LRFD, Shrestha (2019) chose a 9.52 mm (3/8 in) diameter for the TiAB spiral with a 63.5 mm (2.5 in.) pitch over the majority of the height allowing at least 2.2 MPa (0.32 ksi) lateral pressure and uniform confinement to develop. To allow space for installation of a second spiral, the pitch was extended to 127 mm (5 in.) over the plastic hinge length of the column so that the total pitch was 63.5 mm (2.5 in.). A tighter pitch of 38.1 mm (1.5 in.) was used over the length of ligament hooks and extended 152 mm (6 in.) below the lowest TiAB hook installed. A completed specimen design is shown in Figure 6.4.

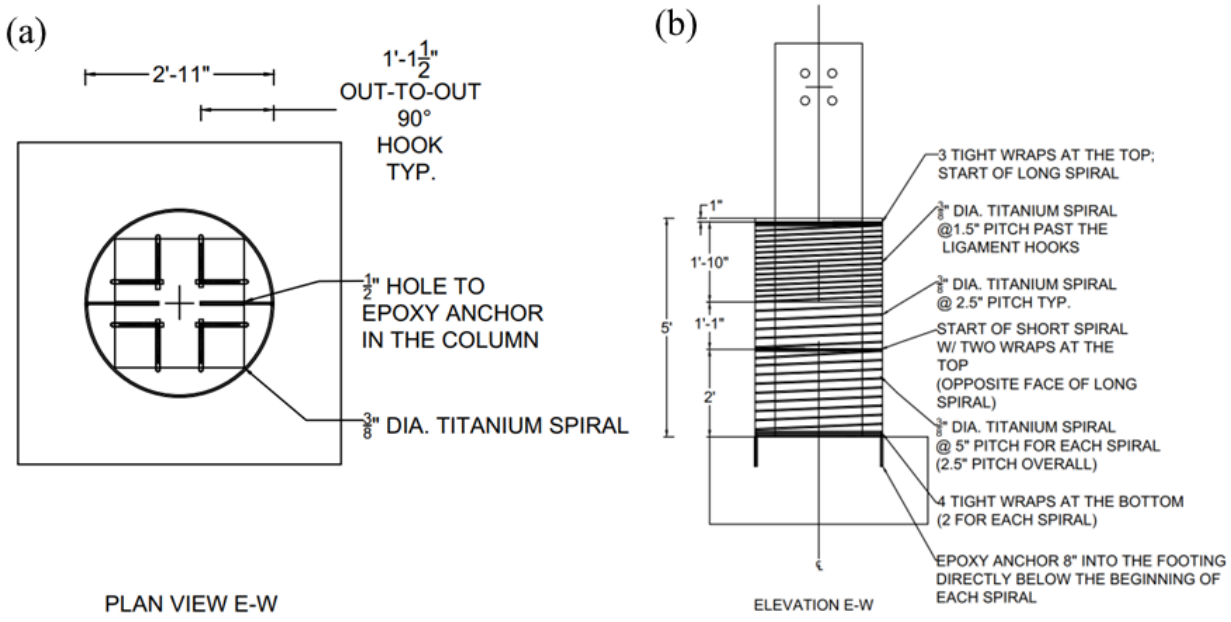

Figure 6.4: Complete specimen design with TiAB spiral details (all dimensions are feet and inches): (a) Plan view, (b) Elevation view.

6.2.3 Specimen Construction

Specimen construction was completed in the Structural Engineering Laboratory at Oregon State University. The following section describes the sequential construction process in detail.

6.2.3.1 Footing Construction

The footings were constructed of a mesh grid of 18-#13M (#4) Grade 60 reinforcing steel with 7.62cm. (3 in.) of cover from the bottom and faces of the footing, 4-#32M (#10) starter bars, and the ready-mix concrete previously described in the specimen design. Reinforcing steel was laid out in a grid with bars at 171.5 mm. (6-3/4 in.) on-center and tied together using conventional tie wire. The bars in the north-south (N-S) direction were on the bottom to correspond with the lateral loading direction. Concrete dobies were 7.62 mm (3 in.) and were tied to the reinforcing mesh to maintain cover. Starter bars used in the connection to the column had a 0.914 m. (3 ft.) lap-splice length above the top of the footing and had a standard 90˚ hook with a length of 559 mm. (22 in.). The starter bars were oriented 45˚ toward the corner of the formwork to accommodate the footing geometry, and a plywood jig was cut and tied to the bars to maintain the geometry of the starter bars during concrete placement. After placing the concrete, lifting hooks were inserted into the footing to facilitate moving specimens around the laboratory and the surface coincident with the column was raked to roughen the cold joint. Footing construction stages can be viewed in Fig 6.5.



(a) **(b)**

Figure 6.5: Stages of construction for vintage spread footings: (a) Specimen geometry and formwork prior to casting, (b) Spread footing after concrete casting.

6.2.3.2 Column Construction

The columns were constructed (Figure 6.6) using 4-#32M (#10) bars, 2.616 m. (8ft-7in.) and 2.667 m. (8ft-9in.) in length. The 50.8 mm. (2 in.) offset allowed the geometry of the column to be maintained for the standard 55.9 cm. (22 in.) hook length and the 3.81 cm. (1-1/2 in.) cover for the column. The longitudinal reinforcing steel was laid on its side using stands. Transverse



(a) **(b)** **(c)**

Figure 6.6: Stages of construction for the vintage column: (a) Column cage attached to the footing, (b) Tied down formwork with pump valve, and (c) Completed vintage column on the spread footing.

reinforcement locations were marked and then tied to the longitudinal bars to complete the cage. A crane was used to lift the cage into place over the footing. After the formwork was assembled holes were blocked out for actuator attachment. The formwork was then anchored to the footing to prevent movement during casting. Concrete was then pumped from the bottom by a local concrete pumping company. Columns were cast at 2.74 m. (9 ft.) tall to accommodate the loading setup. Figure 6.6 provides several images showing different stages of column construction.

6.2.3.3 TiAB Installation & Shell Construction

Ligaments were installed by first drilling 559 mm (22 in.) deep holes, 19 mm (3/4 in.), into the footing at 102 mm (4 in.) from the center of the column, and directly against the column face. The actual embedment depth into the footing was 508 mm (20 in.). The 50.8 mm (2 in.) extension of the hole allows TiAB ligaments to sit flush against the column by first placing the bar all the way down into the hole and then bending it back to align with the anchor hole in the column face. Furthermore, the top 127 mm (5 in.) of the embedment depth were left undeformed to increase the anchorage strength and enlarge the potential cone of concrete developed during pullout. Because ligament heights were staggered, 238 mm (9-3/8 in.) anchor holes were drilled into the column at either 1.11m (3ft. – 7-3/4 in.), 1.26 m (4 ft. – 1-3/4in.), or 1.42m (4ft. - 7-3/4in.) and holes were rounded out at the bottom to accommodate the radius of the ligament hooks. All holes were cleaned thoroughly using a vacuum and bottle brush and epoxy was injected into the holes so that when ligaments were installed the epoxy was flush with the surface of the specimen. Columns were then wrapped in plastic sheathing to prevent the shell from

bonding to the column, ensuring a clear characterization of the retrofit behavior without contamination from composite action. After TiAB ligament installation, a ratchet strap was used to hold the ligaments tight against the face of the column as the epoxy cured, and TiAB spiral installation began. Figures 6.7 and 6.8 show the ligament installation dimensions and process, respectively. Installation of the second spiral was as straightforward as that for a single long spiral and was completed using conventional placement practices.

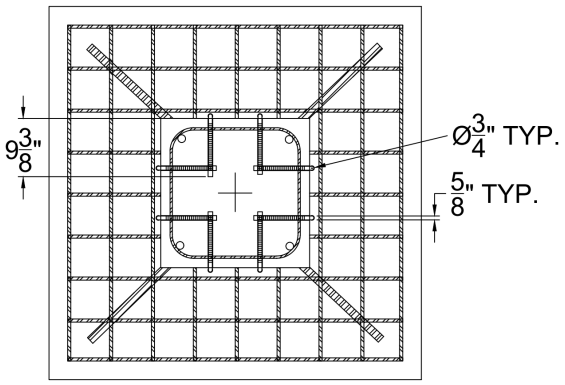

PLAN VIEW E-W

(a)

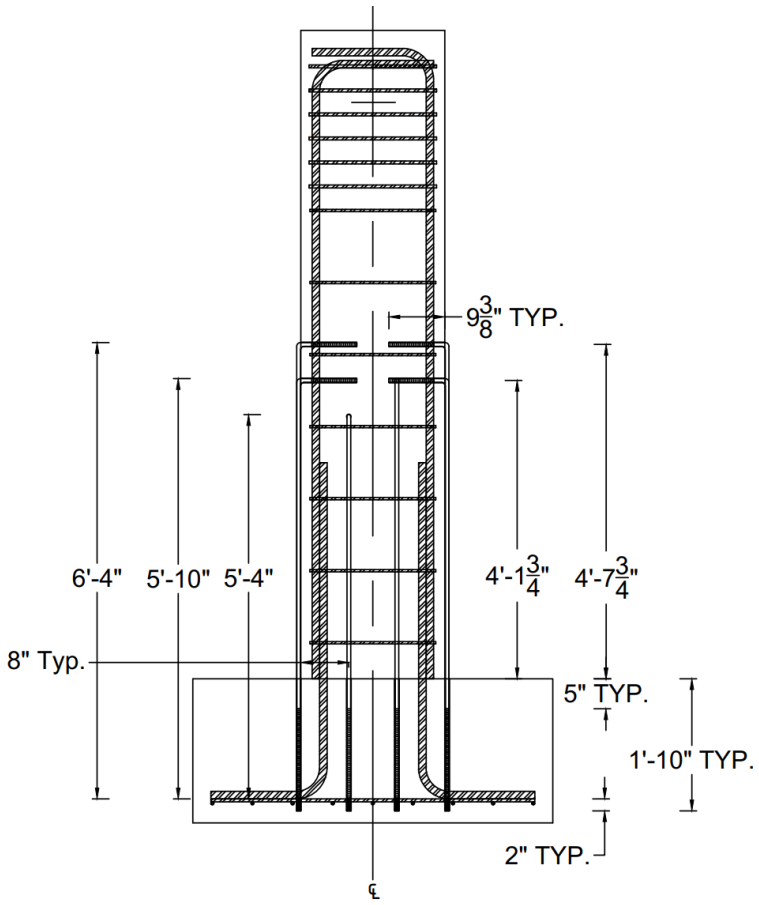

ELEVATION N-S

(b)

Figure 6.7: Specimen with a ligament installation (all dimensions are feet and inches): (a) Plan view, (b) Elevation view.



(a) (b)

Figure 6.8: Construction sequence of TiAB ligament installation: (a) Drilled holes and plastic sheathing, (b) Complete installation of staggered ligaments.

TiAB spirals required 90˚ hooks to be bent to anchor the TiAB spirals into the column and footing. An oxyacetylene torch was used to heat the bars to facilitate bending. Anchor depth into the concrete for the spirals were 203 mm (8 in.) following design guidance given by Shrestha (2019). While the length of the hooks for the footing could be bent to the 203 mm (8 in.) depth, hooks in the column needed to be 343 mm (13.5 in.) to account for the column geometry. 12.7 mm (1/2 in.) holes, 203 mm (8 in.) deep, in the column were drilled in the center of the column on opposite faces, except for the vintage column. Holes in the vintage column were drilled in adjacent faces due to the lack of material on the north and south face after failure. For a flat concrete surface at the top of the shell, the top spiral was anchored 25.4 mm (1 in.) below the height of the shell at 1.5 m (4 ft. – 11 in.). The second spiral was anchored into the column at the height of the plastic hinge length 0.61 m (2 ft.). Hooks were then anchored into the column with the same method used on the ligaments. Three (3) tight wraps were pulled around the column for the first spiral and two (2) were used for the second spiral to prevent pullout of the hooks. Spirals were tied with mild steel to maintain the spiral pitch. At the bottom of the column two (2) tight wraps for each spiral were used to prevent pullout of the hooks from the footing. Once the wraps were complete the holes were measured, drilled, cleaned, and hooks were bonded into the footing with structural epoxy. In the case of specimen 3, small PVC, pipe insulation foam, and duct tape were used to cover threaded rods installed for instrumentation required for testing the vintage column. Furthermore, because there was material missing from the bottom of the column a straight edge and a level were used

to maintain the diameter of the TiAB spiral around the bottom portion of the column. Spray foam was used to dam the bottom of the formwork to prevent concrete from flowing out of the bottom. Concrete infill was cast by wrapping a polycarbonate sheet around the TiAB spiral and held in place with ratchet straps. TiAB spiral installation for specimens 1 and 2 are shown in Figure 6.9, and Figure 6.10 shows TiAB spiral installation for specimen 3.



(a) **(b)**

Figure 6.9: Specimen 1 and 2 TiAB spiral construction sequence: (a) Spiral installation, (b) Formwork for infill.

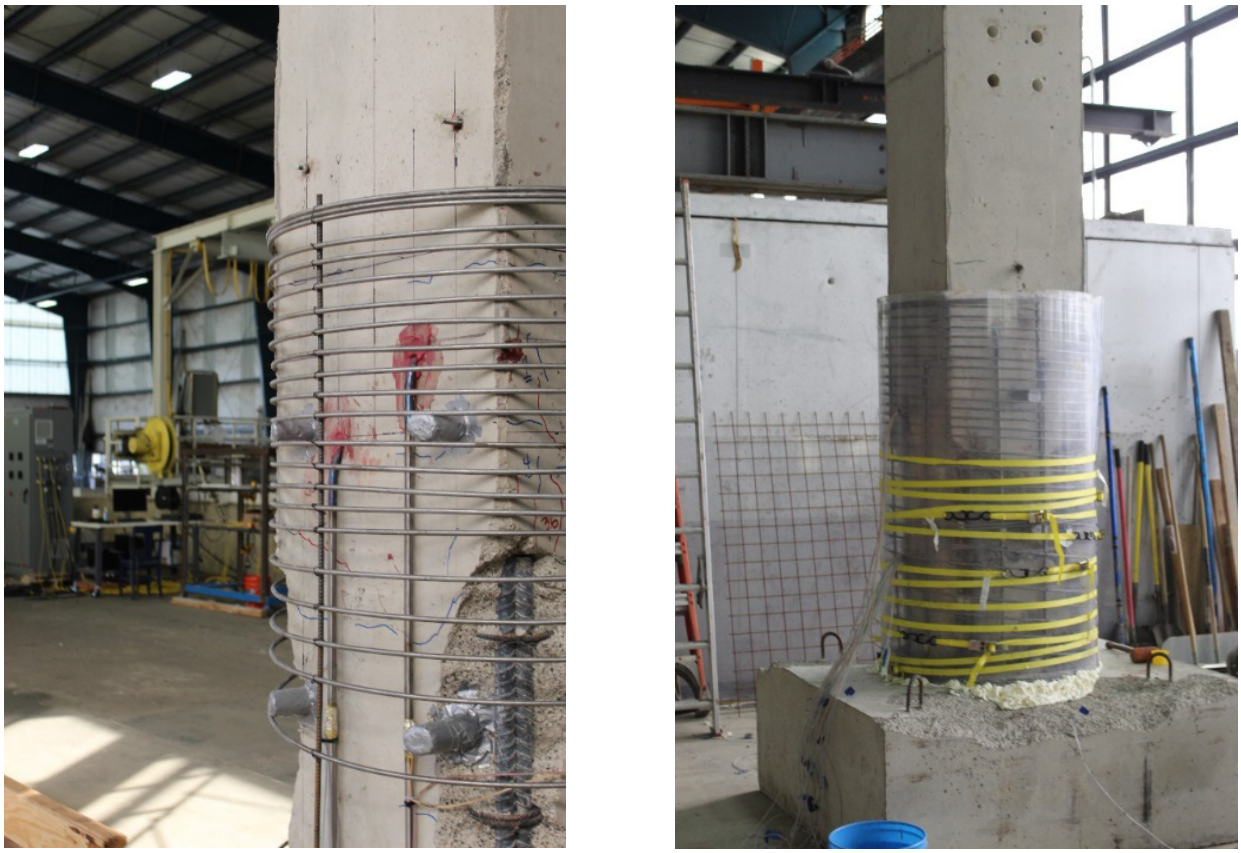

(a) **(b)**

Figure 6.10: TiAB spiral installation: (a) threaded rod covers, (b) shell casting formwork used for installation on Specimen 3 which was failed prior to installation of the TiABs.

6.2.4 Material Properties

The material properties of the reinforcing steel bars were tested at a commercial, materials-testing facility. The titanium mill certifications were used without additional testing, and the concrete compressive and tensile tests were completed for day of test strength and 28-day strength. The results of these tests are shown in Tables 6.2 to 6.6. A comprehensive description of material properties can be found in Appendix A6.2.

Table 6.2: Compressive strength of concrete at 28 days.

Specimen ID	Specimen Component	Compressive Strength, M PA (psi)	Standard Deviation	Coefficient of Variation
S.1	Footing	27.07 (3926)	238	6
S.1	Column	27.06 (3924)	181	4.6
S.1	Shell	35.07 (5086)	160	3.1
S.2	Footing	27.07 (3926)	238	6
S.2	Column	27.06 (3924)	181	4.6
S.2	Shell	35.07 (5086)	160	3.1
S.3	Footing	38.90 (5647)	161	2.9
S.3	Column	30.86 (4476)	141	3.1

Table 6.3: Compressive strength of concrete on the day of testing.

Specimen ID	Test ID	Test Date	S.C.	Compressive Strength, MPa (psi)	Standard Deviation (psi)	Coefficient of Variation
S.1	1	11/17/2021	Footing	39.70 (5757)	78	1.4
S.1	1	11/17/2021	Column	46.24 (6707)	216	3.2
S.1	1	11/17/2021	Shell	39.0 (5655)	132	2.3
S.3	3,4	12/17/2021	Footing	47.39 (6873)	179	2.6
S.3	3,4	12/17/2021	Column	36.59 (5307)	277	5.2
S.3	7	4/20/2022	Shell	24.35 (3532)	109	3.1
S.2	8	6/1/2022	Footing	39.84 (5778)	124	2.1

Table 6.4: Tensile strength of concrete on the day of testing.

Specimen ID	Test ID	Test Date	Specimen Component	Tensile Strength, MPa (psi)	Standard Deviation, MPa (psi)	Coefficient of Variation (%)
S.2	8	6/1/2022	Footing	2.68 (389)	0.456 (66.1)	17

Table 6.5: Results of tensile tests on reinforcing steel.

Bar Size	Bar Type	Tensile Strength, MPa (ksi)	Yield Strength, MPa (ksi)	Elongation in 4D (%)	Reduction of Area (%)	Original Gauge Diameter, mm (in.)
#10M, #3	Tie	583 (86)	386 (56)	27.78	-	-
#13M, #4	Footing	614 (89)	372 (54)	28	56	6.4 (0.252)
#32M, #10	Column / Starter	758 (110)	490 (71)	21	49	12.8 (0.503)

Table 6.6: Results of tensile tests on TiABs.

TiAB Bar Type	Tensile Strength, MPa (ksi)	Yield Strength, MPa (ksi)	Elongation 4D (%)	Reduction of Area (%)
Ligament	1126 (163.3)	1037 (150.4)	21	55
Spiral	1010 (146.5)	920 (133.4)	19	50

6.2.5 Instrumentation

The global and local responses of the specimens during tests were captured using strain gauges, string potentiometers, spring return linear position sensors (LPS), and load cells. Commercially available strain gauges, with a gauge resistance of 120±0.3 Ω, were bonded to the footing bars, starter bars, column bars, column ties, TiAB ligaments, and TiAB spirals to capture strains. Axial load was measured with a 1335 kN (300 kip) load cell attached to a steel beam and connected to a pin and clevis, using Dywidag bars. A 31.7 mm (1-1/4 in.) LPS was bonded in the center of the column above the shell to measure shell movement relative to the column. A load cell attached to the lateral load hydraulic actuator was used to directly measure the applied column shear.

Four (4) different lengths of string potentiometer were used; 50.8 mm (2 in.), 119 mm (4.7 in.), 254 mm (10 in.), and 1016 mm (40 in.). The global behaviors captured by these sensors were rigid body translation, rigid body rotation, column bending, and total column displacement. Measuring the rigid body rotation was accomplished by anchoring eight (8) eye bolts into the footings, four (4) at the corners 76.2 mm (3 in.) each face, and four (4) in the center of the footings 76.2 mm (3 in.) from the face. String potentiometers were suspended from an instrumentation frame located above the specimen. Redundant sensors were added to the bottom of the footing by drilling a 15.9 mm (5/8 in.) diameter hole, 25.4 mm (1 in.) deep and adhering a stud using epoxy into the footings. Using a hole saw, 102 mm (4 in.) holes were drilled through the soil simulant subgrade and string potentiometers were placed on the strong floor. A magnet

was then tied to the end to connect to the studs embedded in the footings. All string potentiometers used to measure rigid body rotation were 254 mm (10 in.) range except for two (2) in the center of the footing on the east and west faces, that were 119 mm (4.7 in.) range.

Rigid body translation was measured using two (2) 119 mm (4.7 in.) range string potentiometers attached to the instrumentation frame 305 mm (12 in.) from the top of the footing on the east and west faces. These were attached to eye bolts anchored in the geometric center of the footing on the east and west face.

Total column displacement was measured by attaching a 1016 mm (40 in.) range string potentiometer to fixed frame opposite the top of the column to measure the overall lateral motion of the specimen at the point of loading. Using this and the previously mentioned string potentiometers the column bending could be derived.

Local responses including curvature, strain penetration, and shear strain of the column core were captured using string potentiometers. To capture these, threaded rods were bonded into the core of the column. This was achieved by drilling oversized holes through the cover and shell concrete and smaller holes into the core of the column. The threaded rod was then bonded into the column core. The purpose was to prevent contamination of the measurement from movement produced by the cover concrete and shell. String potentiometers were mounted to aluminum plates and bolted to the threaded rods. Strain penetration was captured by placing two 50.8 mm (2 in.) range string potentiometers on the footing, at the center of the column on the north and south sides. The strings were attached to the lowest threaded rod embedded in the column. Three (3) 254 mm (10 in.) range string potentiometers were mounted in the center of the column along its height to capture column curvature. Shear strain was measured using three (3) panels consisting of two horizontal, two diagonal, and two vertical string potentiometers bolted to threaded rod along the height of the column on the west face at 102 mm (4 in.) from the north and south faces. The top horizontal for the lowest panel acted as the bottom horizontal for the second lowest panel, this was also the case between the second and third panels. All string potentiometers in the panels had a measurement range of 119 mm (4.7 in.), except the verticals which had a range of 254 mm (10 in.). Appendix A6.2 contains sensor naming conventions and sensor placement diagrams.

6.2.6 Test Setup

Two (2) different setups were used to conduct the 8 tests. The first setup was designed to allow for rocking of the footing to occur, and the second setup was designed to restrain the footing and ensure column failure. Both setups required use of the laboratory strong wall and strong floor. The following section describes the test setup details and functions of the components.

6.2.6.1 Soil Simulant Layout

FOAMULAR® 1000 Extruded Polystyrene (XPS) was used as the soil simulant. The material properties can be found in Appendix A6.1. The soil simulant started as 50.8 mm (2 in.) thick sections that measured 0.61 m x 2.44 m (2 ft. x 8ft.). Sections were then cut to into several sections to provide the subgrade under the footing of the specimens and to provide the passive pressures on the north and south vertical faces of the footing. Holes

were drilled into the soil simulant to accommodate the string potentiometers used to measure footing rotation as described previously. Figure 6.11 illustrates the soil simulant layout and the pieces cut to construct the soil simulant around the footing.

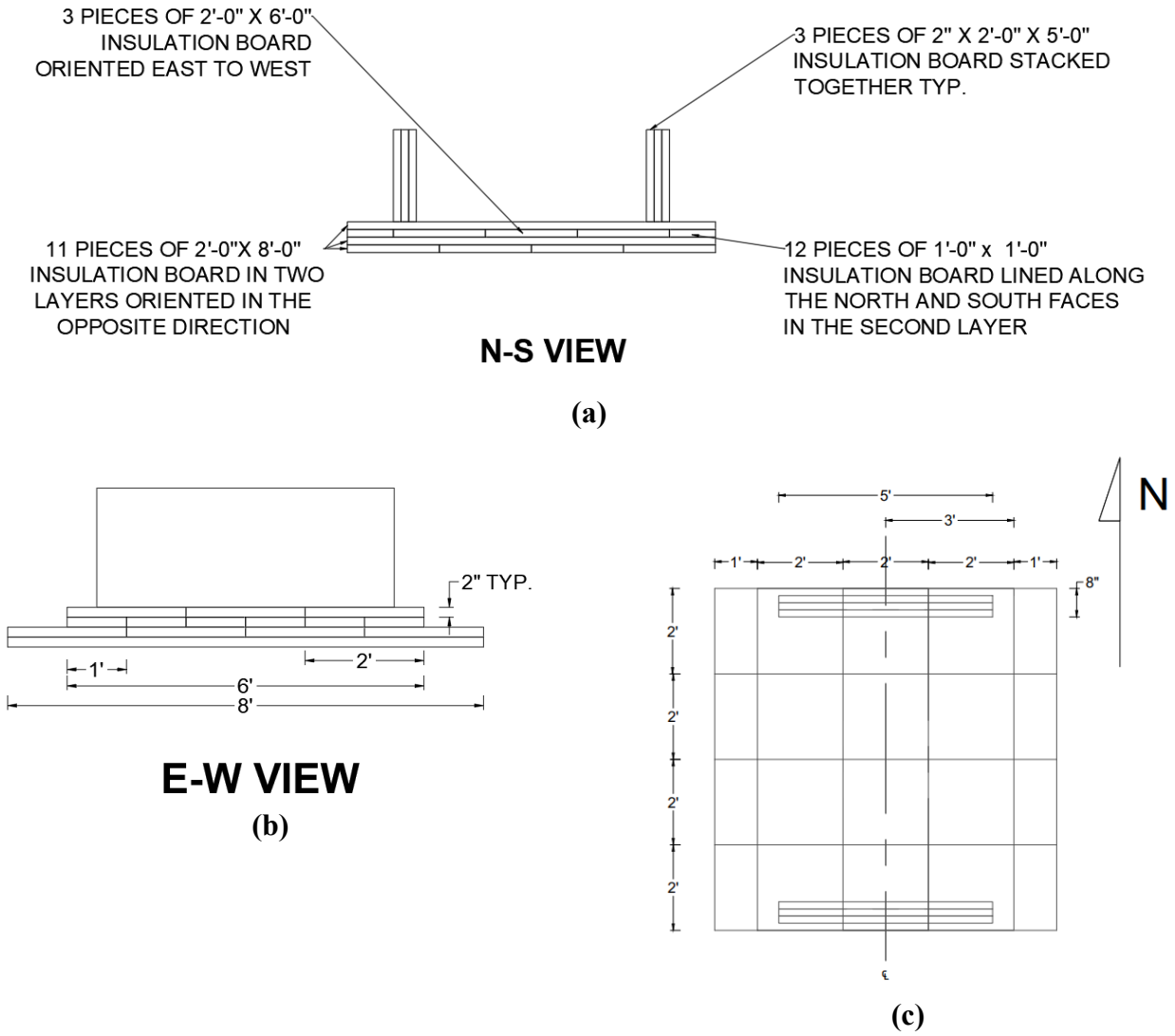

Figure 6.11: Soil simulant layout (all dimensions are feet and inches): (a) N-S elevation view and pieces used, (b) E-W Elevation view, (c) Plan view.

6.2.6.2 Soil-Structure Interaction Setup

Investigation of the soil-structure interaction (SSI) required a reaction frame to be built in the horizontal plane around the footing. This frame functioned to hold the soil simulant against the north and south vertical faces of the footing and to react the passive pressure generated as the footing rocked and pushed the simulant against it. Specimens were placed on a 203 mm (8 in.) subgrade of soil simulant, assuming a 2:1, vertical to horizontal, stress distribution (Figure 6.12) as defined by Budhu (2011), made up of four (4) layers of soil simulant. The lateral resistance was provided by three (3) layers of soil simulant to a total thickness of 152 mm (6 in.). It required two (2) sets of steel springs to be built to provide support for the soil simulant. The spring stiffnesses were designed based on the expected load at depth, using three (3) different lengths of steel angle; 63.5 mm (2-1/2 in.), 82.5 mm (3-1/4 in.), and 85.7 mm (3-3/8 in.). Angles were welded on to a backing plate by only one (1) leg to provide the required horizontal stiffness variation with depth, and six (6) steel plates measuring 102 mm (4 in.) were welded onto the apex of the angles to provide a uniform loading surface against the soil simulant. The top four (4) rows of springs had a stiffness of 20.15 kN/mm (115 kip/in.), the fifth row of springs' stiffness was 30.13 kN/mm (172 kip/in.), and the bottom row springs had a stiffness of 41.17 kN/mm (235 kip/in.). These stiffnesses were generated from numerical simulations completed using uniaxial compression test data in the analysis program FLAC3D from the previous study. Figure 6.13 illustrates the springs built and used in the test setup. On the north face of the footing a large reaction beam was used to support the springs and the reaction frame was anchored to the strong wall using four (4) Dywidag bars.

Tests were performed using a servo-hydraulic control system that was used to impose predetermined horizontal displacements to the column at a location 3.25 m (128 in.) above the surface of the strong floor using a hydraulic actuator with a 914 mm (36 in.) stroke. Tests were first initiated by applying a 667 kN (150 kip) axial load to the column top. The column load was resisted by a spreader beam that anchored to the strong floor at 1.22 m (4 ft) on both the east west sides of the specimen. A clevis and pin connection was used to prevent bending of the axial load anchor rods. A separate servo-hydraulic control system was used for the axial load. The axial load was controlled using load control to hold the force constant even as the column undergoes lateral drift. Attached to the beam was a 1335 kN (300 kip) load cell that measured the applied axial load. Figure 6.14 illustrates the test set up; however, minor changes to the test setup were made to accomplish particular test objectives. Figures 6.15 to 6.18 display the minor differences in each test setup.

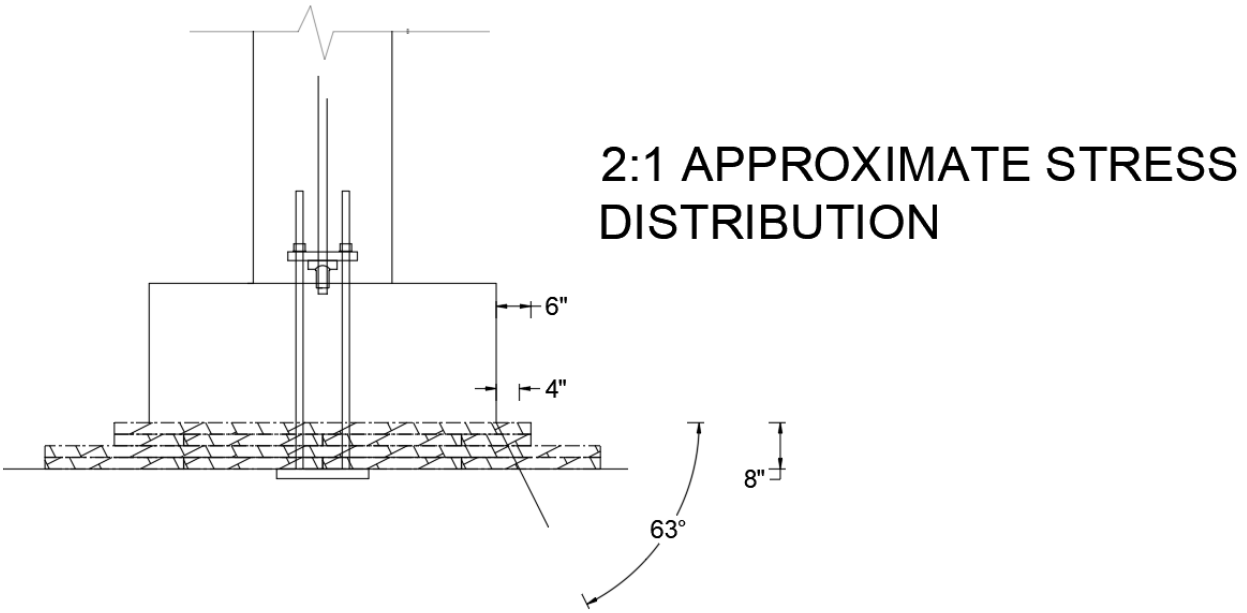

Figure 6.12: Approximate stress distribution assumption to determine soil simulant layout (all dimensions are feet, inches, degrees).

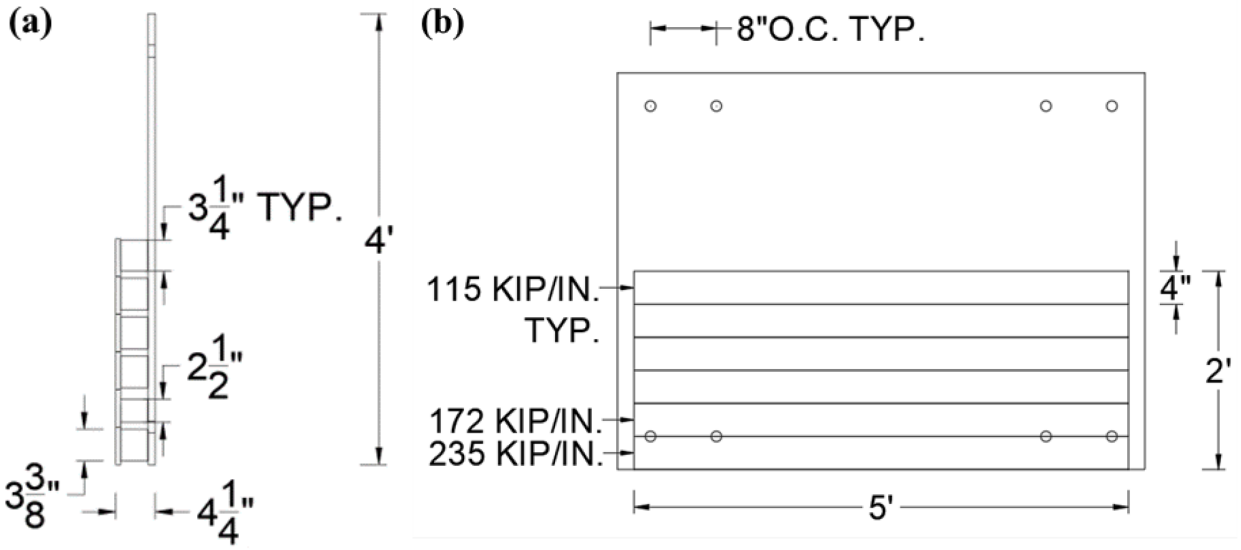

Figure 6.13: Spring design for horizontal reaction frame: (a) Angle dimensions, (b) Spring stiffness and bulk dimensions (all dimensions are feet and inches).

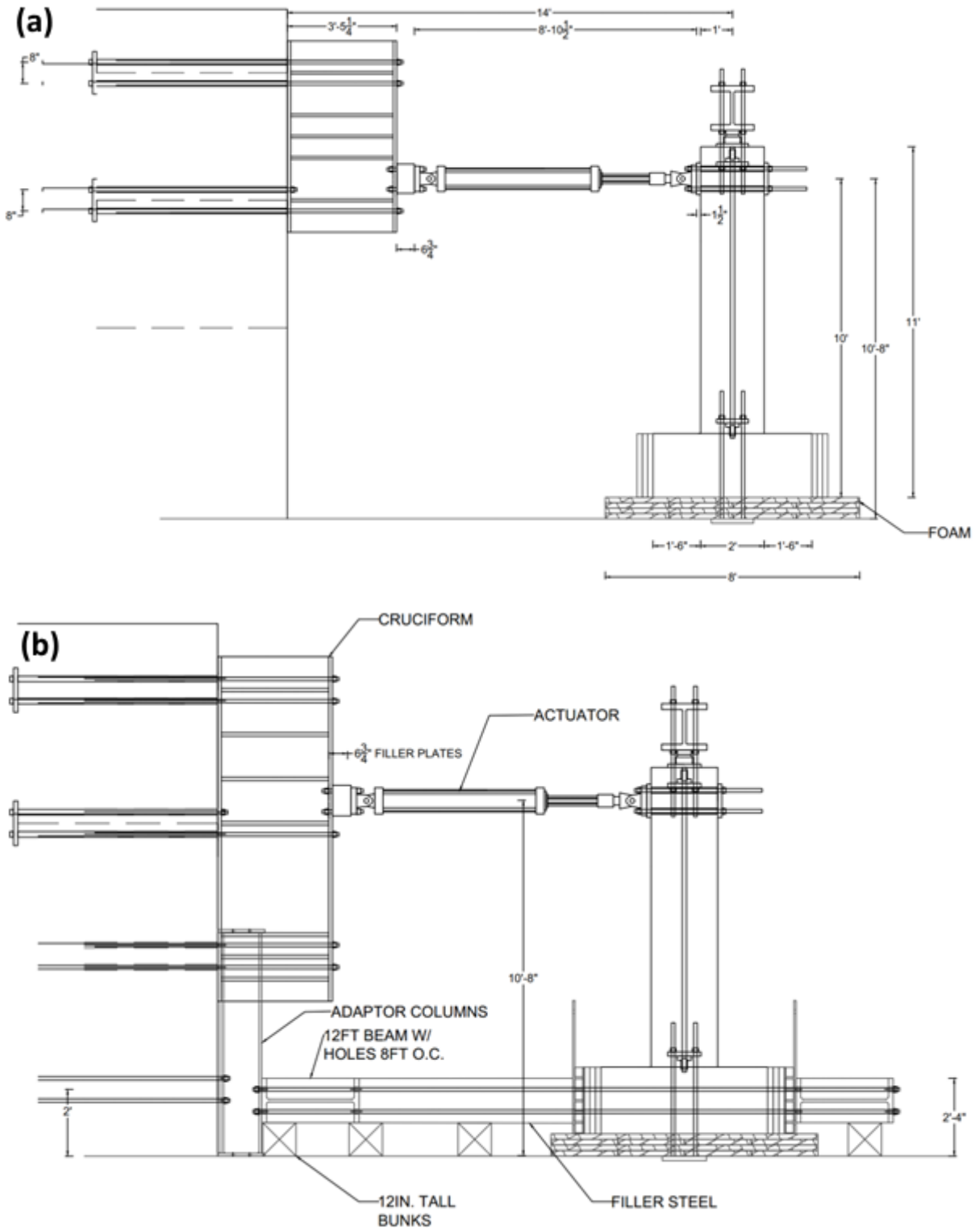

Figure 6.14: SSI test setup (all dimensions are feet and in): (a) Specimen loading dimensions, (b) horizontal brace frame.



Figure 6.15: Test 1 (Specimen 1): Complete Retrofit with Soil Simulant Embedment and Subgrade. Standard SSI test setup.



Figure 6.16: Test 2 (Specimen 2): Complete restrofit with no embedment and a soil simulant subgrade.



Figure 6.17: Test 3 & 4 (Specimen 3): Vintage column with soil simulant embedment, subgrade, and axial load at 150 kips and 100 kips.



Figure 6.18: Test 5, 6, & 7 (Specimen 3): Vintage column failure, vintage ligament retrofit, and vintage complete retrofit. All three tests used a damaged soil simulant subgrade but steel springs to represent embedment within soil.

6.2.6.3 Experimental Setup for Failure Test of Retrofitted Column

To test the columns to failure required that the footing be restrained to force deformations and thus demands into the column. Because footing sizes are representative of vintage designs, they were too small to attach directly to the strong floor. An alternative vertical reaction system was devised with large beams to tie down the footing and restrict rotation and restrain rigid body motions. Furthermore, a reinforced concrete slab was cast and placed under the footing so that the horizontal actuator elevation could remain the same for all tests. Figure 6.19 displays the test setup used for specimen failure.



Figure 6.19: Test 8 (Specimen 2): Complete retrofit with tied down footing test set up.

6.2.7 Loading Protocol

Specimens were subjected to both applied axial load and lateral displacement. Column axial load was derived from the work by Shrestha (2019) based on review of the ODOT bridge inventory. The most common column axial load observed in the bridge database was approximately 8% of the concrete compressive strength acting on the gross area of the column ($0.08f'_cA_g$). For the 24 in. square column the magnitude of the axial load was 677 kN (150 kip). This was used for all tests except for Test 4, in which the axial load was reduced to 448 kN (100 kips) to observe the influence of the axial load on response of the specimen. The lateral displacement protocol imposed on the specimens was derived by Shrestha (2019) in accordance with ACI 364.2R-13 based on the calculated yield displacement from moment-curvature analysis of the column. Table 6.7 shows the lateral displacement protocol imposed on the specimens for Tests 1 to 8.

Table 6.7: Lateral displacement loading protocol (Shreshtha 2019).

Displacement Cycle (in)	Displacement Cycle (% drift)	Loading Rate (in/sec)
0.10	0.10	0.005
0.19	0.20	0.01
0.29	0.30	0.02
0.40	0.42	0.03
0.80	0.83	0.04
1.20	1.25	0.04
1.60	1.67	0.08
2.00	2.08	0.08
2.40	2.50	0.1
2.80	2.92	0.1
3.20	3.33	0.12
3.60	3.75	0.12
4.00	4.17	0.12
4.40	4.58	0.12
4.80	5.00	0.12
5.20	5.42	0.12
5.60	5.83	0.12
6.00	6.25	0.12
6.80	7.08	0.12
7.60	7.92	0.12
8.00	8.33	0.12
9.60	10.00	0.12

6.3 EXPERIMENTAL OBSERVATIONS AND ANALYSIS

The results of each reverse cyclic test on the full-scale square RC column-footing-soil specimens are presented in this section. Observations during tests are discussed to inform the analysis of results and are presented in terms of observed global structural behavior, force-displacement response, the evolution of stiffness degradation, strain magnitude and distribution, soil-structure interactions, post-failure retrofit analysis, and vintage footing behavior. Using the experimentally measured response, an analytical model of the synthetic soil was developed to predict the soil simulant pressures acting on the bottom and sign faces of the footing, and a strut and tie model was used to describe the performance of a footing containing as-built vintage details having only a single mat of reinforcing steel located at the bottom of the footing. A full archive of all experimentally measured data for each test is contained in Appendix A6.3.

6.3.1 Observed Global Structural Behavior

All tests were completed in accordance with the predetermined loading protocols described previously. Observations were made during each test and formation and propagation of concrete cracking, or other visible distress were noted and photographed during each step of the displacement history. The column portion of the specimens remained elastic in seven (7) of the tests, even as the overall response was nonlinear. Non-linear behavior was due to inelastic deformations observed in the soil-simulant. In one case, Test 8-Specimen 2, failure of the footing contributed to nonlinear response of the system. Test 5 was the only test in which the performance and failure were controlled by the column (unretrofitted column) as laps splice failure of the flexural steel was observed in the column above the footing. This was for the case of steel springs as the embedment soil which generated higher pressures across the vertical footing face compared to the soil simulant foam. Test 1 and Test 8 were the only tests in which damage to the footing was observed. The following sections describe the overall soil-structure responses of the tested specimens based on the observations and data collected. Tests 1-3 were tested on new soil simulant each time, and Tests 4-7 were tested on soil simulant that had failed previously to mimic aftershock conditions. The strain rate for the axial loading on the soil simulant was 252 με/sec for the first test, and 49.6 με/sec for subsequent tests; soil stiffness is discussed in Section 6.3.4. Note that the horizontal reaction frame was more flexible during push cycles (north displacement of column) and relatively stiffer during pull cycles (south displacement of column). This resulted in larger forces for the same actuator displacement amplitudes on the pull side of each cycle.

6.3.1.1 Test 1-Specimen 1: Complete Retrofit with New Soil Simulant Subgrade and Soil Simulant Embedment

This test was conducted over two (2) days and data from both days were combined to provide a continuous record. On the first test day, the imposed lateral displacements were half those of the predetermined loading protocol until a drift of 1.67%. To draw the horizontal reaction frame into contact with the soil simulant, the connecting Dywidag rods were tightened. After applying the 667 kN (150 kip) axial load, the footing settlement was measured at approximately 2.54 mm (0.1 in.). During lateral loading, vertical cracks in the center of the footing on the west face were observed at a drift of 30.5 mm (1.2 in.). Offsets of vertical cracks at the corners of the retrofit, indicating

mobilization of the retrofit, were observed at a drift of 71.1 mm (2.8 in.). Footing cracking continued on the corners of the west face and minor horizontal cracks appeared on the NW corner of the column above the retrofit. At a drift of 81.3 mm (3.2 in.), additional flexural cracks formed in the footing, and the total lateral force acting on the vertical face of the footing were measured and observed to remain in the range of 182 kN (41 kips) on the push cycle. At a drift of 122 mm (4.8 in.), the second layer of foam on each face began to fail, and punching began to occur in the first layer of the foam subgrade. The center footing bar at the bottom of the footing mat in the direction of loading achieve yield stress at a drift of 132 mm (5.2 in.). The lateral pressure increased to 5.52 MPa (800 psi) at 203 mm (8 in.), and 6.21 MPa (900 psi) at 244 mm (9.6 in.). The lateral force increased to 200 kN (45 kips) and remained stable as the specimen underwent inelastic deformations. Upon the force reaching and maintaining 200 kN (45 kips), no other damage was observed in the specimen. After testing was complete and the specimen was removed from the test setup vertical cracks near the center of the footing were also observed and the cracks coalesced under the footing. Figure 6.20 displays the progression damage in Specimen 1 during Test 1.

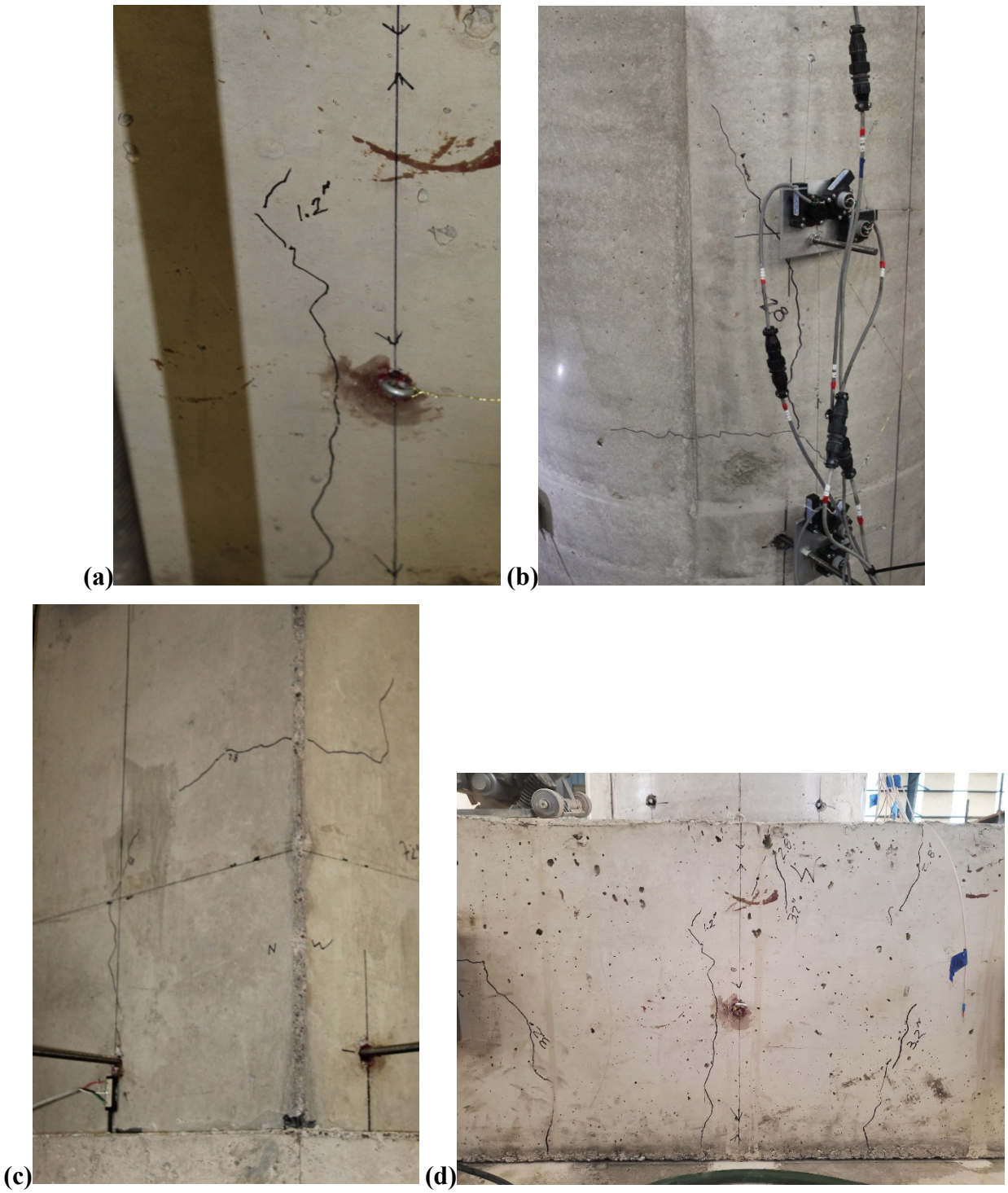

Figure 6.20: Observed damage to Specimen 1 during Test 1: (a) First cracks observed in the center of the footing on the west face, (b) Cracking of the retrofit shell indicating mobilization of the retrofit, (c) Cracking of the column above the retrofit, and (d) observed damage on the west face of the footing of Specimen 1 after testing.

6.3.1.2 Test 2-Specimen 2: Complete Retrofit with New Soil Simulant Subgrade and No Embedment

Prior to testing, shrinkage cracks were observed and marked to distinguish them from cracks that might emerge during testing. The axial load was then applied, and an initial settlement distortion of 2.92 mm (0.115 in.) was recorded. During lateral loading, the specimen initially behaved elastically followed by inelastic behavior initiating a drift of 20.3 mm (0.8 in.). At a drift of 40.6 mm (1.6 in.) in the north direction, the footing on the south side lifted approximately 4.76 mm (3/16 in.) up from the soil simulant and 11.1 mm (7/16 in.) into the soil simulant on the north side. At 2% drift, the overall load-deformation response began to flatten out and the footing punched into the soil simulant 12.7 mm (1/2 in.). The soil simulant began curling up and moving with the footing, and at 71.1 mm (2.8 in.) of drift, the footing punched into the soil simulant 19 mm (3/4 in.). The footing punched into the soil simulant approximately 25.4 mm (1 in.) at a displacement of 102 mm (4 in.), which was the last drift cycle imposed during the test. While there was minor concrete cracking near the toe of the footing, there was no other observable damage to the footing, column, or retrofit. The bottom of the footing had no observable damage. The cracks on the side of the footing did not appear to propagate to the bottom surface of the footing. Figure 6.21 displays the progression of punching into the soil simulant and Figure 6.22 shows the soil simulant damage by layer.

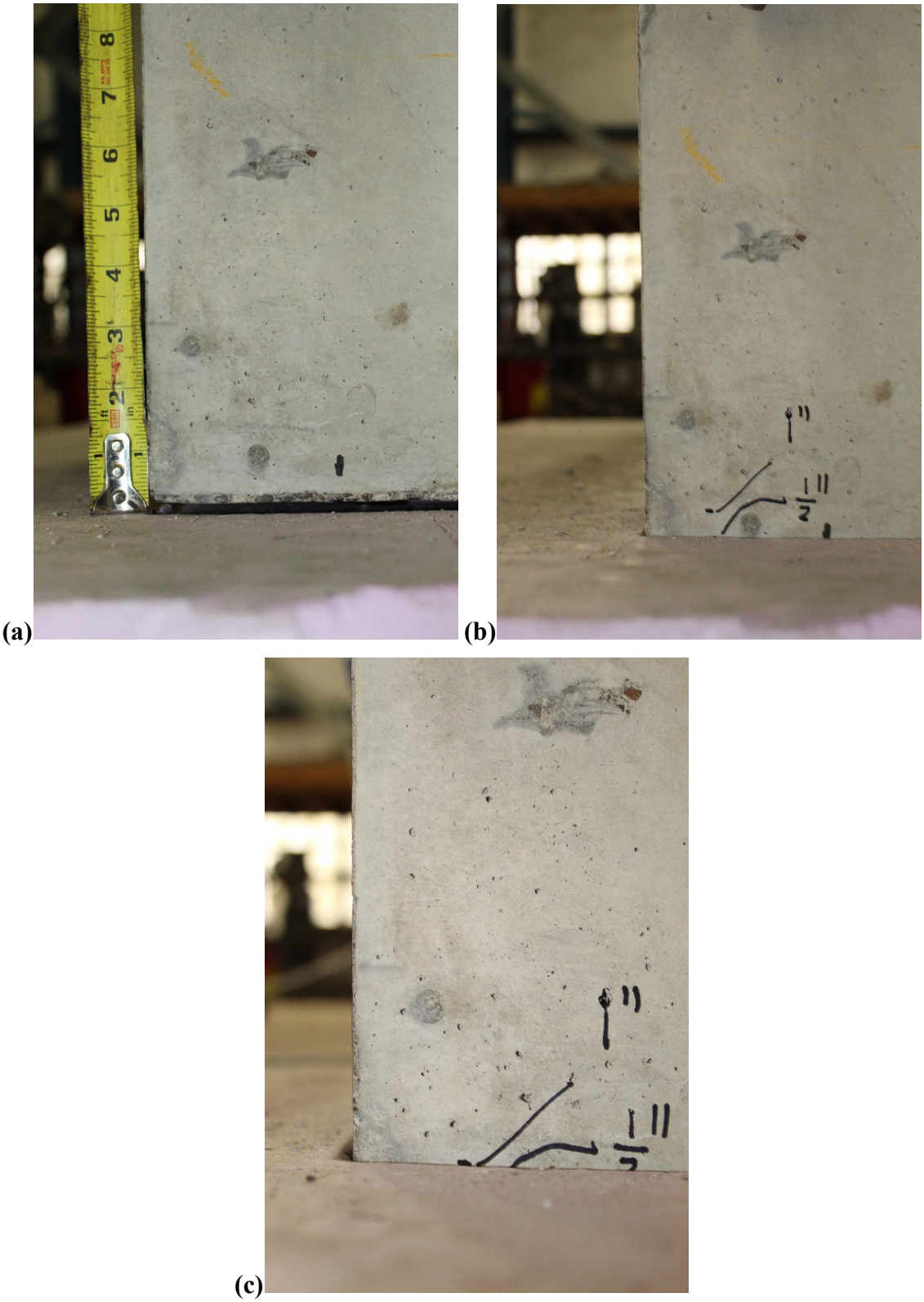

Figure 6.21: Crushing of the footing into the soil simulant at drifts of: (a) 40.6 mm (1.6 in.), (b) 50.8 mm (2 in.), and (c) 102 mm (4 in.).

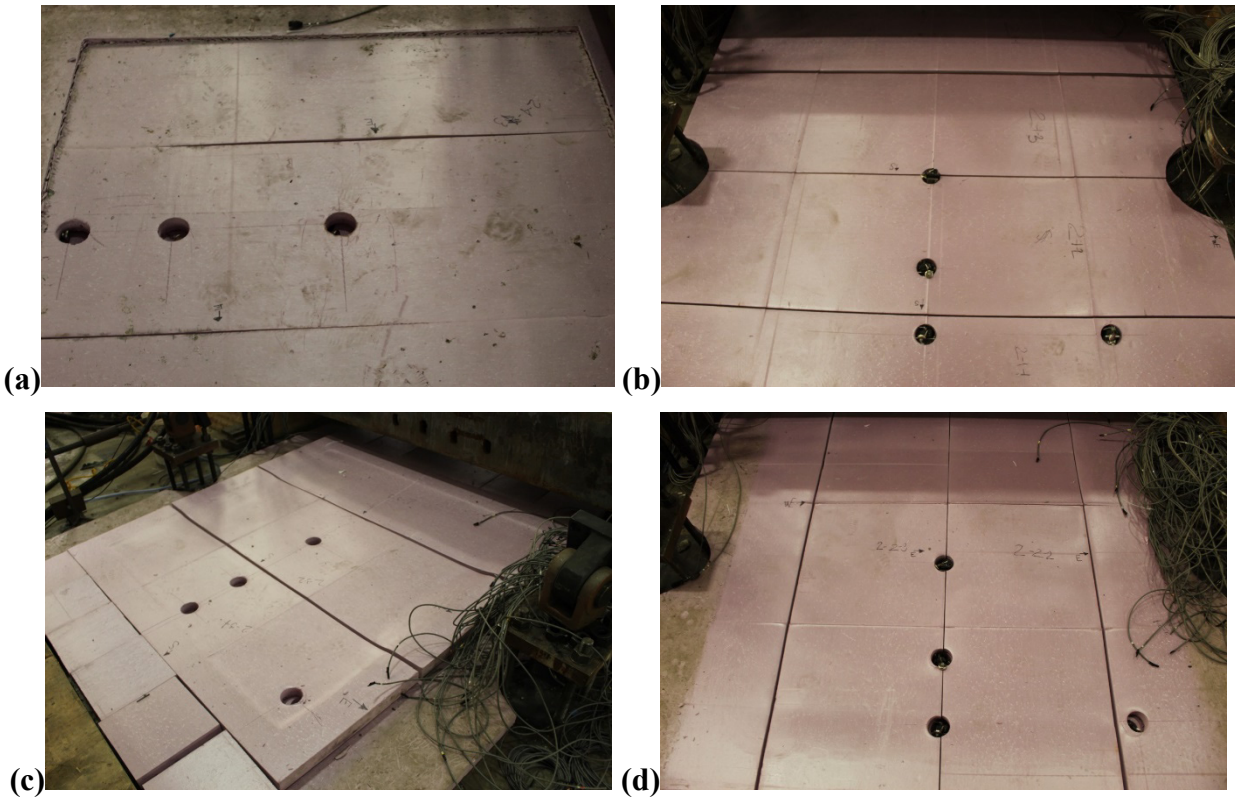

Figure 6.22: Soil simulant damage by layer. Layers are counted from closest to the floor up: (a) Layer 4, directly underneath the footing, (b) Layer 3, (c) Layer 2, and (d) Layer 1 on the floor.

6.3.1.3 Test 3-Specimen 3: Vintage Column with New Soil Simulant Subgrade, Soil Simulant Embedment, 150-kip Axial Load

The specified axial load was first applied, and an average initial settlement distortion of 2.79 mm (0.11 in.) was recorded. Lateral displacements were imposed, and no damage occurred until a drift of 50.8 mm (2 in.). Visual rocking of the footing was observed at a drift of 20.3 mm (0.8 in.). Flexural cracking on the column along the lap-splice length on the second cycle of 50.8 mm (2 in.) displacement. At 61 mm (2.4 in.) of displacement vertical cracking along the bars continued to propagate, cracks began to form at the bottom of the column, and permanent deformations in the soil occurred. Horizontal cracks along the faces of the column also occurred at 61 mm (2.4 in.). Vertical cracks emerged of the lap-splice in the SW corner at 91.4 mm (3.6 in.) of displacement. The expected moment capacity, at 667 kN (150 kips) axial load, based on actual material properties is 579.5 kN-m (427 kip-ft); however, the soil began to fail first. At 102 mm (4 in.) of displacement, cracks on the NW corner were a little wide near the bottom of the column. The column was tested to 152 mm (6 in.) of displacement and column failure did not occur. The soil simulant continued to plastically deform at subsequent displacements and the crack patterns observed at the end of the test on the face of the column are shown in Figure 6.23. The specimen axial load was unloaded by 1/3 and then the specimen was retested as detailed in the next section.

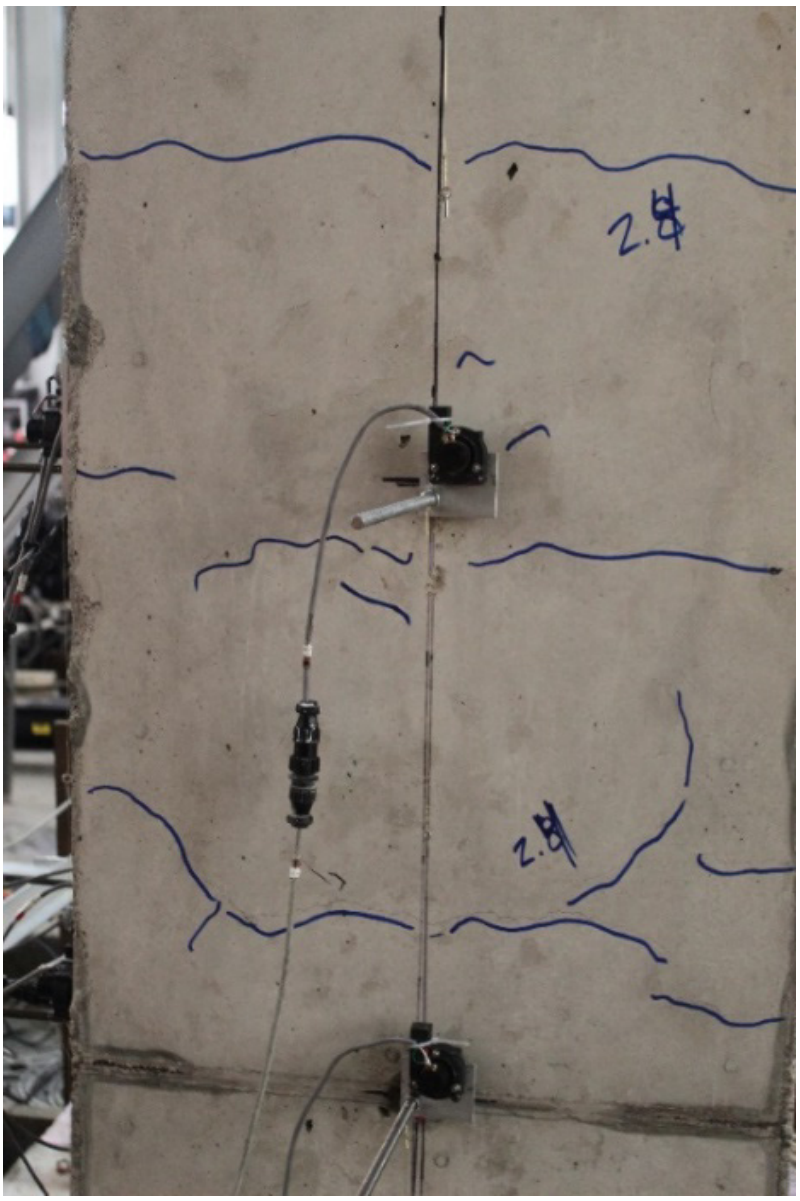

Figure 6.23: Cracking distribution on the face of the vintage column.

6.3.1.4 Test 4-Specimen 3: Vintage Column with Damaged Soil Simulant Subgrade, Soil Simulant Embedment, 100-kip Axial Load

This test was a repeat of the prior test of Specimen 3 but with the reduced column axial load. The column was moved back to zero drift and 222 kN (50 kips) was removed from the axial load to a lower value of 445 kN (100 kips). This was done to lower the column moment capacity in an attempt to produce failure of the column. Based on the actual column properties, the moment capacity with a 445 kN (100 kips) axial load was 526.6 kN-m (388 kip-ft). A 445 kN (100 kips) axial load is at the lower end of likely service levels in this size bridge column. Lateral displacements were applied using only one cycle at each interval until the column began to pick up load when the drift displacement

was 91.4 mm (3.6 in.). This was due to nonparticipation of the soil simulant in lower displacements from prior permanent deformations under the footing and at the vertical faces of the footing. Vertical cracks began to appear at this displacement on the face of the column over the lap-splice length at a drift of 152 mm (6 in.) and 173 mm (6.8 in.; Figure 6.24). The furthest displacement imposed on the specimen was 193 mm (7.6 in.), but the lateral forces did not increase substantially as the soil simulant plastically deformed under and at the faces of the footing. The specimen was unloaded and changes to the soil simulant were made as detailed in the next section.

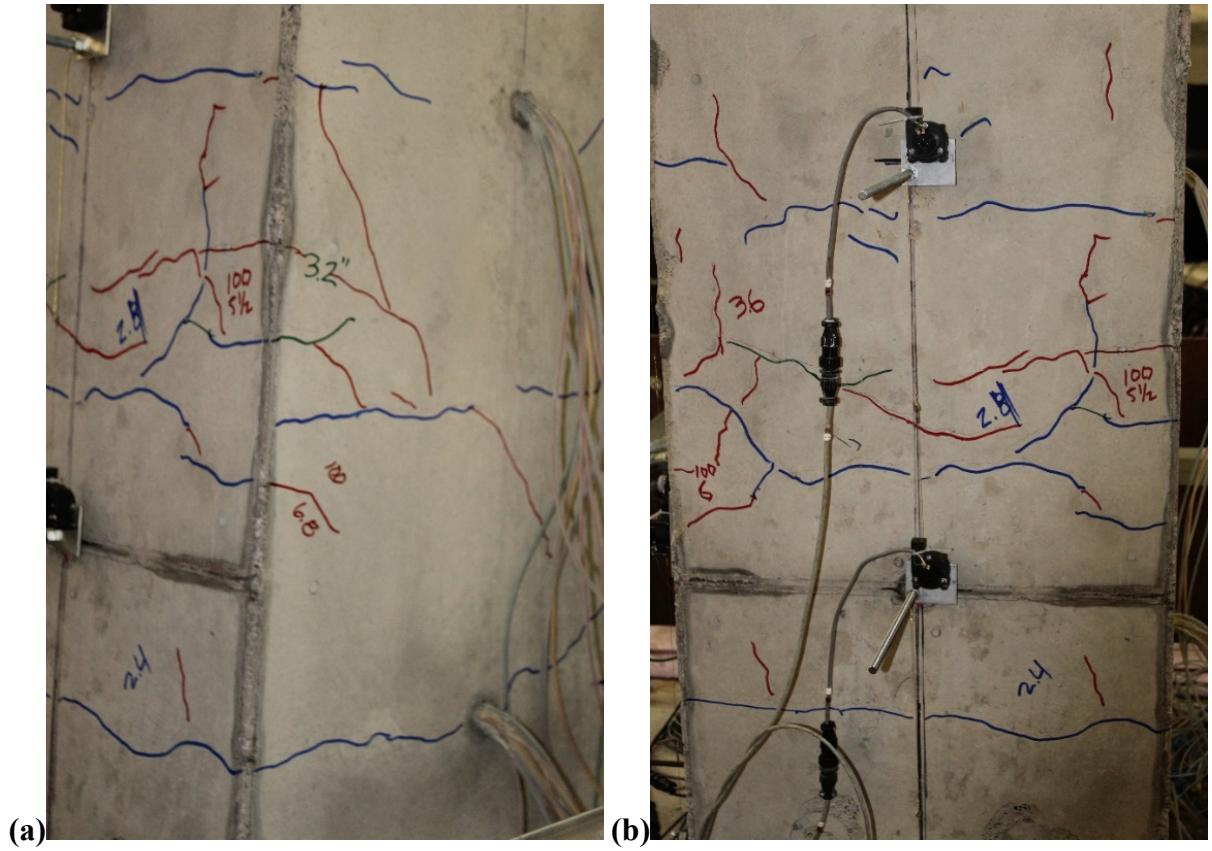

(a) **(b)**

Figure 6.24: Crack progression at 445 kN (100 kips) axial load: (a) Cracks on the east face, and (b) cracks on the south face.

6.3.1.5 Test 5-Specimen 3: Vintage Column Failure with Damaged Soil Simulant Subgrade and Steel Embedment

This test was a repeat of the prior test of Specimen 3 but with column axial load increased back to 667kN (150 kip) and with removal of the soil simulant foam at the footing vertical faces leaving only the steel springs to provide the lateral resistance across the footing faces. After the 667kN (150 kips) of axial compression was applied, the lateral drift protocol was imposed. The top of the footing began spalling at a drift 40.6 mm (1.6 in) along the top of the north and south face. The starter bar on the NE corner yielded in the push cycle at approximately 76.2 mm (3 in.). At 81.3 mm (3.2 in.) the top SE corner of the footing broke off contaminating subsequent displacement measurements

of the footing. At a drift of 102 mm (4 in.), a large concrete wedge on the top of the footing on the south face broke off, and the starter bar on the north side yielded. The top of the footing continued to exhibit progressive damage on both faces as the test continued. At a drift of 107 mm (4.2 in.), the column bar on the SE corner yielded. Local bearing on the steel soil springs caused damage to the face of the footing from the broken concrete that fell in between the steel springs and the footing at 122 mm (4.8 in.). Vertical cracks also occurred at this displacement along the lap-splice on the south face of the column, and further yielding occurred in the starter bars on the north side. Flexural cracks were observed at a drift of 132 mm (5.2 in.) on the south face of the column. Progressively larger strains occurred in the NE starter bar, while the SE starter bar did not yield. The column tie closest to the end of the lap-splice length, at 762 mm (30 in.) exhibited yield. Failure of the lap splice on the south face of the column occurred at a drift of 152 mm (6 in.). The test continued to a drift of 173 mm (6.8 in.) when the lap splice failed on the north face of the column. Settlement of the soil at the end of the test was approximately 31.7 mm (1-1/4 in.). Column and footing damage can be seen in Figure 6.25 and Figure 6.26.

(a)



(b)

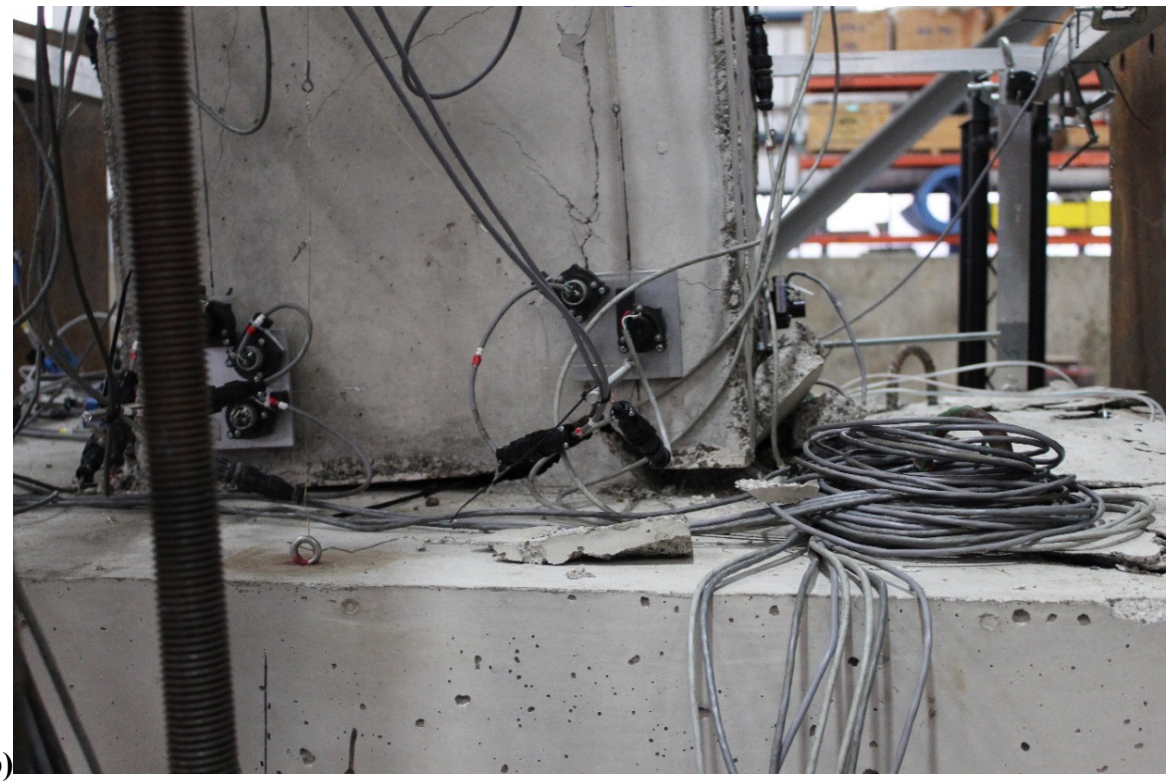

Figure 6.25: Footing and column damage prior to spalling of the concrete around the lap-splice: (a) SE corner of the column, and (b) SW corner of the column.

(a)



(b)

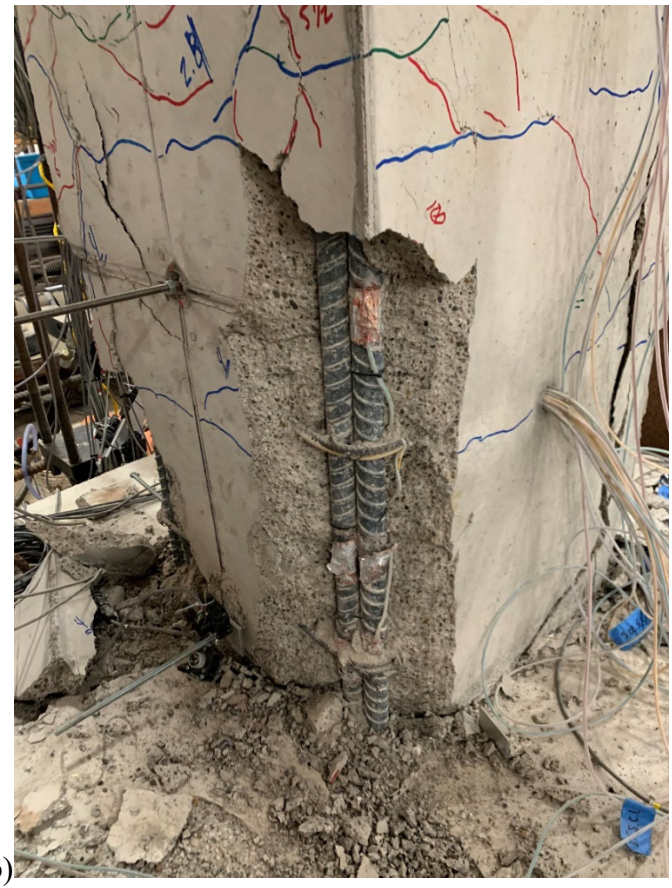

Figure 6.26: Spalling of concrete from the column over the lap-splice length: (a) Initial spalling on the SW corner, and (b) Column damage after testing.

6.3.1.6 Test 6-Specimen 3: Failed Vintage Column with Ligament Retrofit, Damaged Soil Simulant Subgrade, and Steel Embedment

The test was conducted after the TiAB ligaments were installed to observe how the behavior changes when only ligaments are in place prior to placement of the spiral shell. This test and Test 7 represent the substructure of a bridge that has experienced a damaging seismic event, and the retrofit has been installed to allow the column to remain in service even while subjected to aftershocks. Thus, the subgrade was damaged, but the column remains in service following the retrofit. Because the retrofit was installed without axial load in the laboratory, this test is more representative of the case where the bridge is shored during retrofit installation. The test was kept well within the elastic range to avoid yielding the ligaments. Because the ligaments were installed before the axial load was applied, they exhibited elastic buckling of approximately 500 με as seen in Figures 6.27 and 6.28. The column axial precompression of produced stiffened initial response since the compressive strain must be overcome before flexural tension in eventually produced by application of the lateral load. The force-displacement plot was compared to the post-failure response of the column in Test 5, and stiffening response was observed after the lateral force resulted in overcoming the column axial pre-compression. This shows the TiAB ligaments provide flexural tension to enable the column to carry additional overturning moment as also seen in Figure 6.33. The difference in the capacity on the push and pull cycles, as seen in Figure 6.27 and 6.29, is a result of the difference between when the axial pre-compression was overcome, and the elastic losses due to the different horizontal reaction from stiffnesses in the test setup. Figure 6.29 shows the difference between the response of the column after failure and the column response after only the TiAB ligaments were installed. This demonstrates that the ligaments provide flexural tension, enabling the column to carry additional overturning moment. For clarity, the sensor naming conventions are reported in Appendix A6.2 as stated previously.

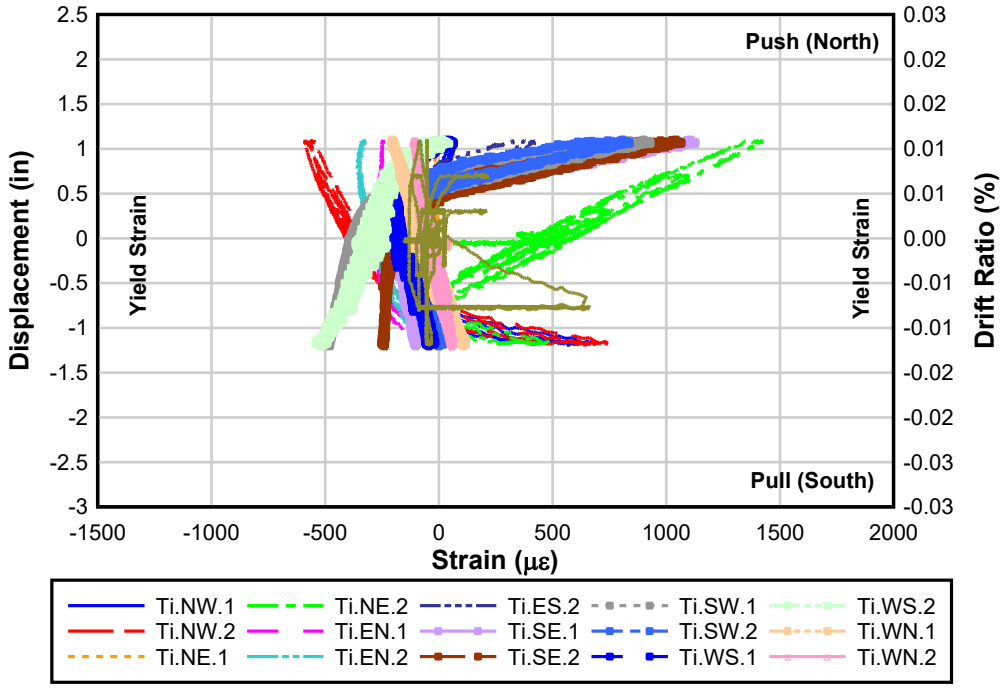

Figure 6.27: TiAB ligament strain profile.

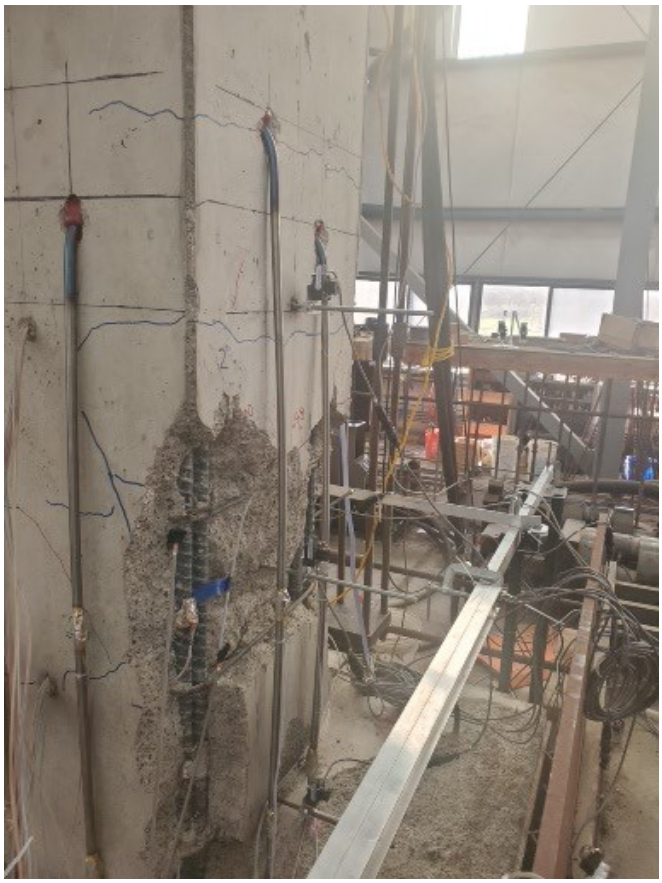

Figure 6.28: Elastic buckling of the TiAB ligaments during axial load application.

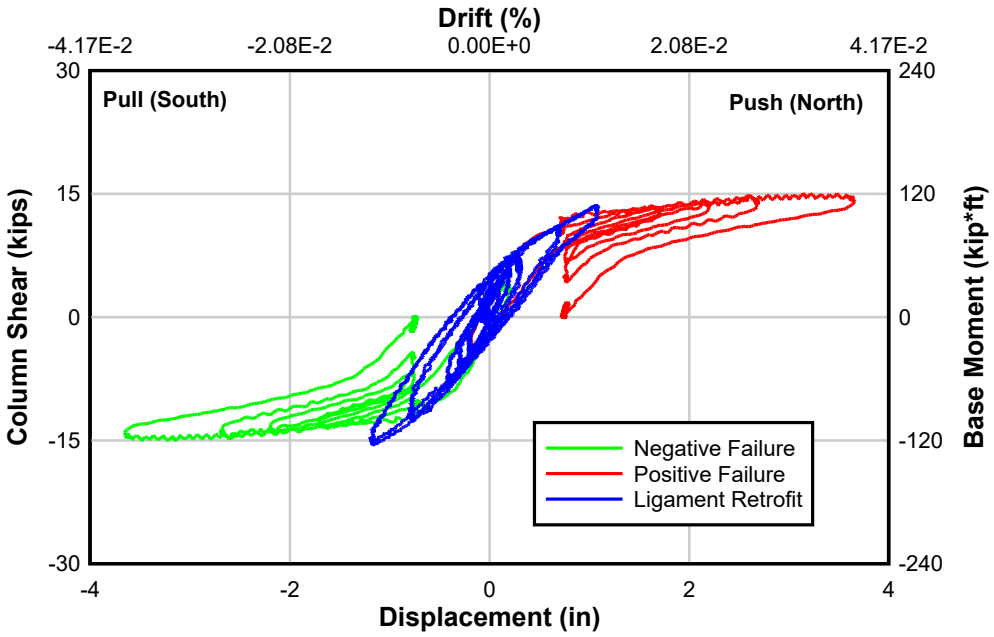

Figure 6.29: Force-displacement responses of specimen with TiAB ligament retrofit only compared to residual response of unretrofitted column after failure.

6.3.1.7 Test 7-Specimen 3: Failed Vintage Column with Complete Retrofit, Damaged Soil Simulant Subgrade, and Steel Embedment

After the failed vintage column (Specimen 3) was fully retrofitted, it was tested again on the same soil simulant that was previously damaged during Tests 3-6. The axial load was applied, and the specimen subjected the lateral displacement protocol. The specimen exhibited softening at a drift of 71.1 mm (2.8 in.) and at 81.3 mm (3.2 in.) on pull cycles. The footing began to exhibit spalling on the south face. On the second cycle of the 91.4 mm (3.6 in.) displacement amplitude, the string potentiometer on the NE corner became contaminated because the footing spalled further. The soil simulant steel springs plastically deformed at 122 mm (4.8 in.) and a single new crack on the NE corner of the footing formed. The footing continued to spall on the north and south face. The sensor used to capture horizontal sliding of the footing on the east face was contaminated by the spalling concrete at a drift of 173 mm (6.8 in.). All of the visual distress occurred in the footing or the steel springs, and the springs were pushed into the soil simulant as the damaged concrete on the footing came into contact with the steel springs at a drift of 173 mm (6.8 in.) through the rest of the test. Strains in the starter bars could not be measured because the strain gauges were damaged in the previous tests; however, the TiAB ligaments exhibited a maximum tensile strain in the range of 1400 με. Footing and soil simulant damage is shown in Figure 6.30.

(a)  (b) 

Figure 6.30: Test 7: (a) Footing damage on the face of the footing after Test 7, and (b) condition of the soil simulant after Test 3 – Test 7.

6.3.1.8 Test 8-Specimen 2: Completely Retrofitted Column without Simulated Soil and Tied Down Footing

The last test in this series was the first attempt to fail a retrofitted column. Because the vintage designed footing had no reinforcing steel in the top, a 44.4 mm (1-3/4 in.) diameter hole, 165 mm (6-1/2 in.) from the top of the footing was cored through the center of the footing. A 41.3 mm (1-5/8 in.) diameter Dywidag bar was placed through the hole and tightened against two (2) 190 mm (7-1/2 in.) square anchor plates to provide passive confinement at the top of the footing. To maintain the geometry of the test setup, a 203 mm (8 in.) thick reinforced concrete slab was constructed that took the place of the soil simulant, and two W12x136 beams were used to anchor the footing to the strong floor to prevent footing rotation and translation. Prior to testing, shrinkage cracks were marked to distinguish them from any subsequent load-induced cracks. The axial load was applied, and the lateral displacement protocol imposed on the specimen. The SE starter bar was observed to yield at a drift of16.5 mm (0.65 in.) on the push side; however, a significant drop in the resisting force was observed at a drift of 20.3 mm (0.8 in.) of displacement. At this displacement cracks were observed in the footing, and the footing began to separate into four (4) quadrants. Due to the enlargement of the footing, the string potentiometers measuring sliding and rotation were contaminated. Therefore, the responses were considered separately pre- and post-footing damage. At 30.5 mm (1.2 in.) of drift on the push cycle, both north transverse footing bars yielded, as did the north side of the column tie located 762 mm (30 in.) above the top of the footing. Cracks then propagated into four (4) quadrants at 40.6 mm (1.6 in.) of drift, and horizontal cracks opened across the lower portion of the footing at the north face. The test was terminated as the footing continued to lose strength at a peak drift of 61 mm (2.4 in.). At this displacement, horizontal cracks on both the north and south faces of the footing were very wide. The anchor rods used to tie down the footing were observed to be bent out of the vertical plane because the footing spread approximately 12.7 mm (1/2 in.) on the north face and slightly less on the south face. This spreading of the footing is attributed to the axial load pushing the column into the footing after the footing cracked and the lack of distributed reinforcing steel at the top of the footing to restrain the cracks. Figure 6.31 shows the footing failure progression.

(a)



(b)

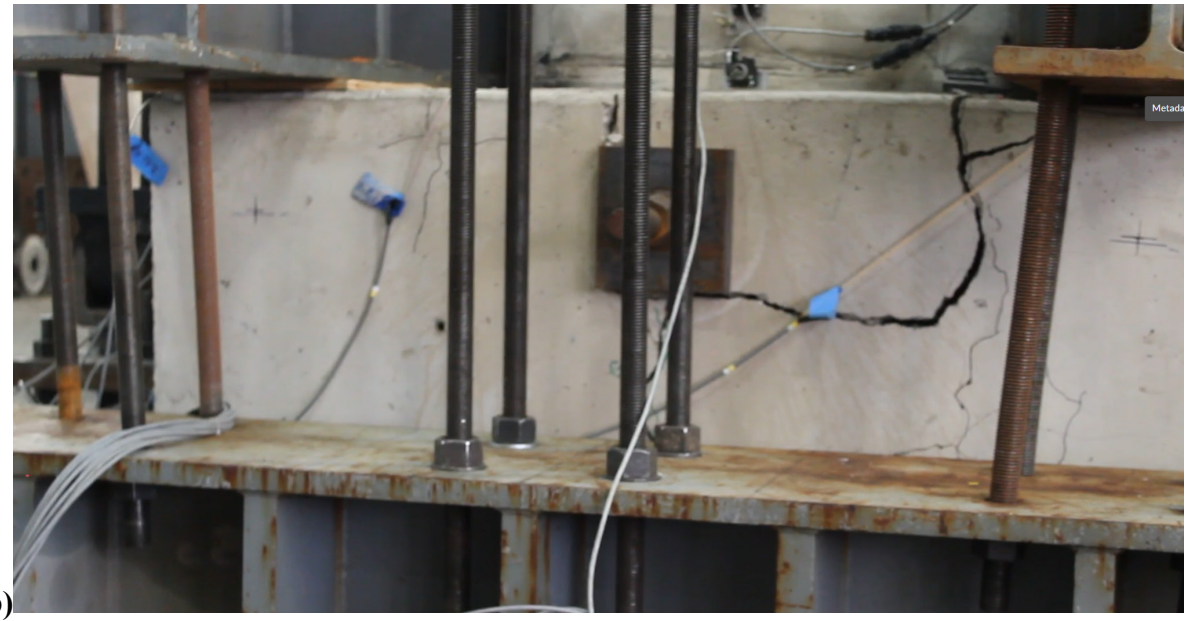

Figure 6.31: Failure of footing on Specimen 2: (a) Cracks formed at 20.3 mm (0.8 in.), and (b) footing failure after testing.

6.3.2 Force Displacement Responses

The displacement response was recorded using a string potentiometer located on the column at the lateral loading point, and the applied load was recorded from the load cell attached to the lateral load actuator. These sensor data were used to characterize the overall specimen force-displacement response. The column moment from the applied lateral force was computed for the column at the top of the footing. Responses are reported in terms of column shear and drift ratio. The drift ratio is calculated by dividing the column lateral displacement by the distance from this location to the top of the footing. Inherent in the experimental setup is a restoring force that comes from the horizontal component of the axial load as the specimen undergoes lateral displacement. The internal column shear was computed as the equivalent lateral load at the base of the column after removing the horizontal component of the axial load as detailed in the subsequent section.

6.3.2.1 Data Processing for Column Shear Force

The horizontal restoring force due to axial load setup was removed from the applied lateral load to compute the internal column shears during post-processing of the test data. The correction is a function of the drift magnitude, axial force, and geometry. Shrestha (2019) illustrated the components of the axial load and the applied load as shown in Figure 6.32. In Figure 6.32, Δ_T is the drift at the top of the column, $\Delta_{Measured}$ is the measured displacement, Δ' is the additional drift, H' is the distance from the top of the column to the point of rotation, and H_L is the height of loading measured from the column footing interface to the point of loading. The point of rotation for the axial load remains same throughout all tests because it is fixed at the pins anchored into the strong floor. The horizontal and vertical components of the axial load were determined for any given drift by utilizing equations 6.1 to 6.5:

$$\tan(\beta) = \Delta_{Measured} / H' \quad \textbf{(6-1)}$$

$$\text{atan}(\beta) = \beta \quad \textbf{(6-2)}$$

$$P_H = P \sin(\beta) \quad \textbf{(6-3)}$$

$$P_V = P \cos(\beta) \quad \textbf{(6-4)}$$

$$\Delta_T = \Delta_{Measured} + \sin(\beta) \quad \textbf{(6-5)}$$

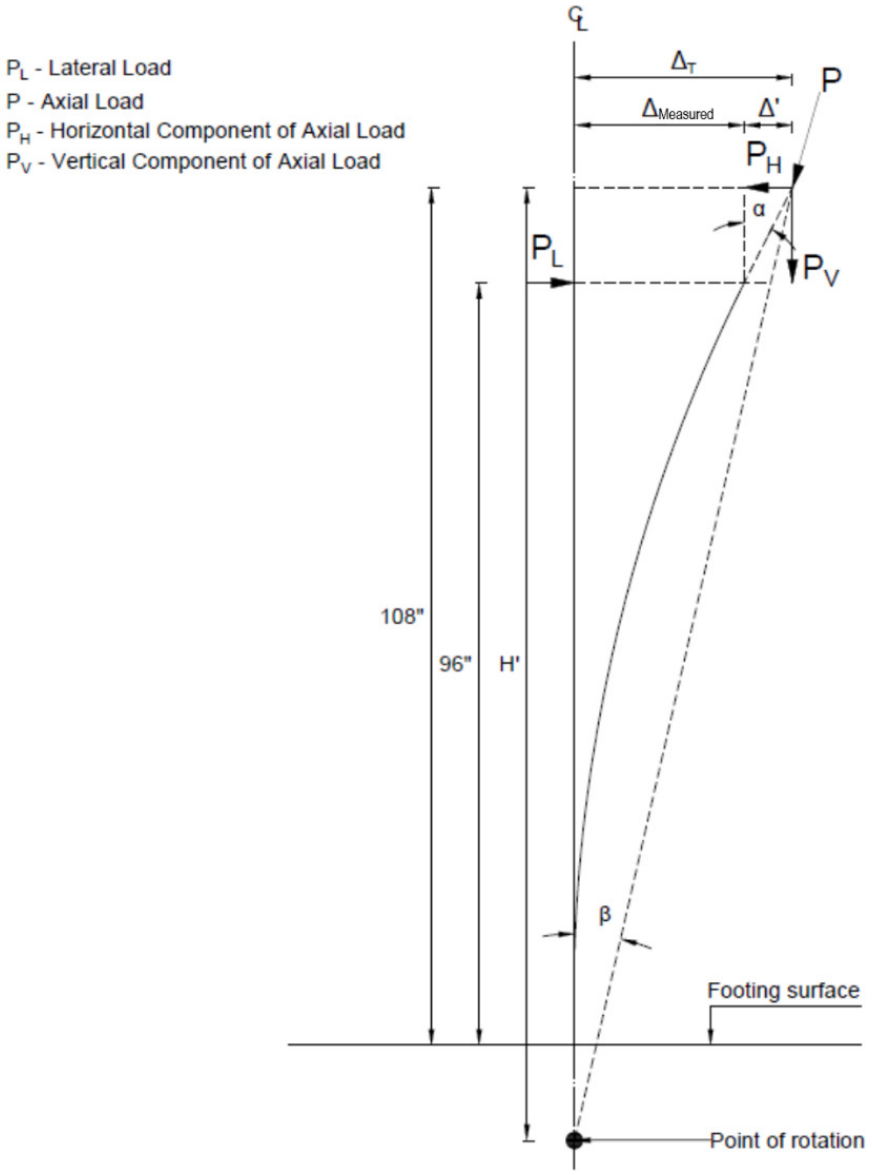

Figure 6.32: Illustration of geometric factors influencing the additional drift (Shrestha 2019).

In the present set of tests, axial load was applied 0.305 m (1 ft.) above the point of lateral loading. Because this is located higher up the column, additional horizontal deflection occurs at this point that is dependent on angle α, the angle change at the point of loading due to the column deformation, and angle β, the angle of the applied axial load. Because angle α is small over the 0.305 m (1 ft.) length, it is considered negligible. However, angle β was measured from the point of rotation of the axial load setup. This was measured by taking the average height of the pin joints on the strong floor, 3026 mm (119.125 in.) from the top of the column. The moment on the column was summed at the column footing interface, including effects from P-Delta as seen in equation 6.6:

$$M_{base} = P_L H_L + P_V \Delta_T - P_H H'$$

(6-6)

The equivalent lateral load, or column shear, was computed using equation 6.7:

$$V = M_{base}/H_L$$

(6-7)

Using the post-processed experimental data, the overall force-displacement responses for each test were determined and are shown in Figures 6.33 to 6.41. Horizontal dotted reference lines in these figures represents 80% of the measured peak capacity during the tests, commonly taken as the threshold for determining ductility. The expected yield moment was plotted as horizontal dashed lines and represents the required shear to produce flexural yielding in the column. The expected yield moment was determined using as-built dimensions and measured mechanical properties of concrete strength and steel yield strength for the materials used to construct the specimens. Test 6 had an expected yield moment that also included the TiAB ligament contribution assuming these to be fully bonded to the column without longitudinal steel reinforcing bars. Axial load-moment interactions were used to determine the expected yield moment as shown in Figure 6.42. A summary of notable force-drift performance metrics is tabulated in Table 6.8.

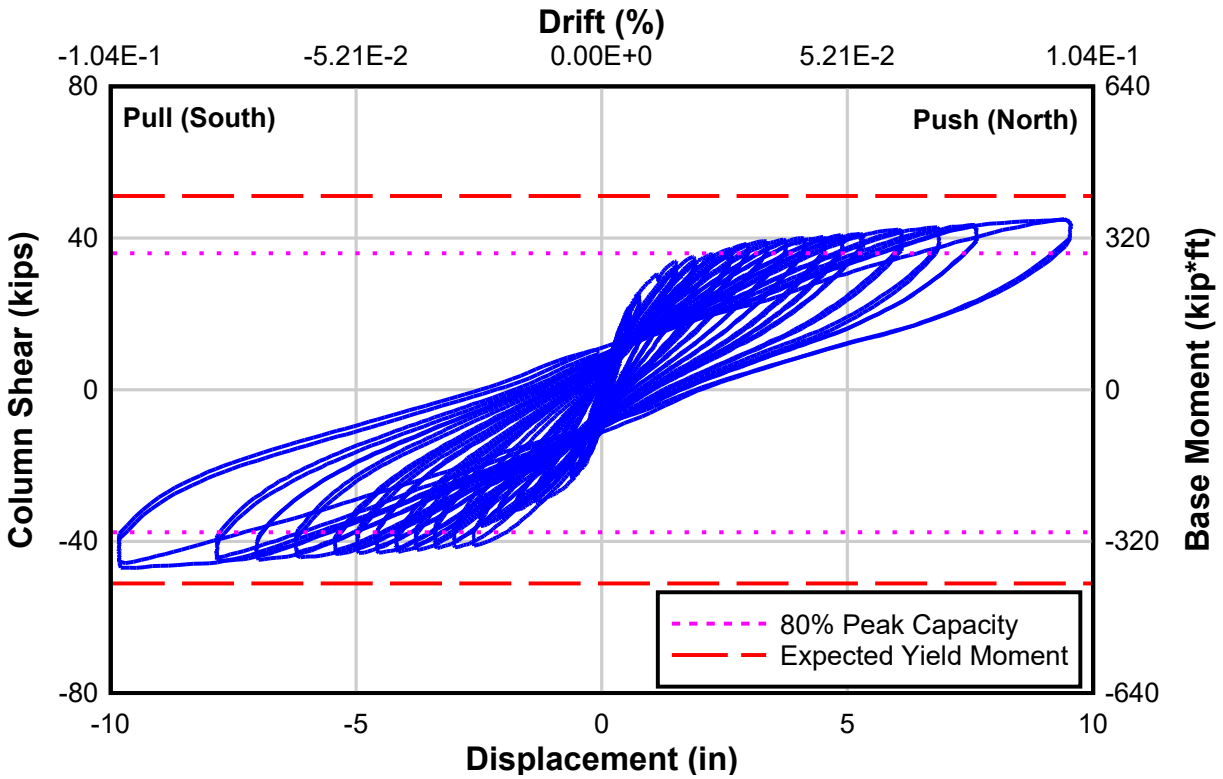

Figure 6.33: Overall force-displacement response of Test 1, Specimen 1.

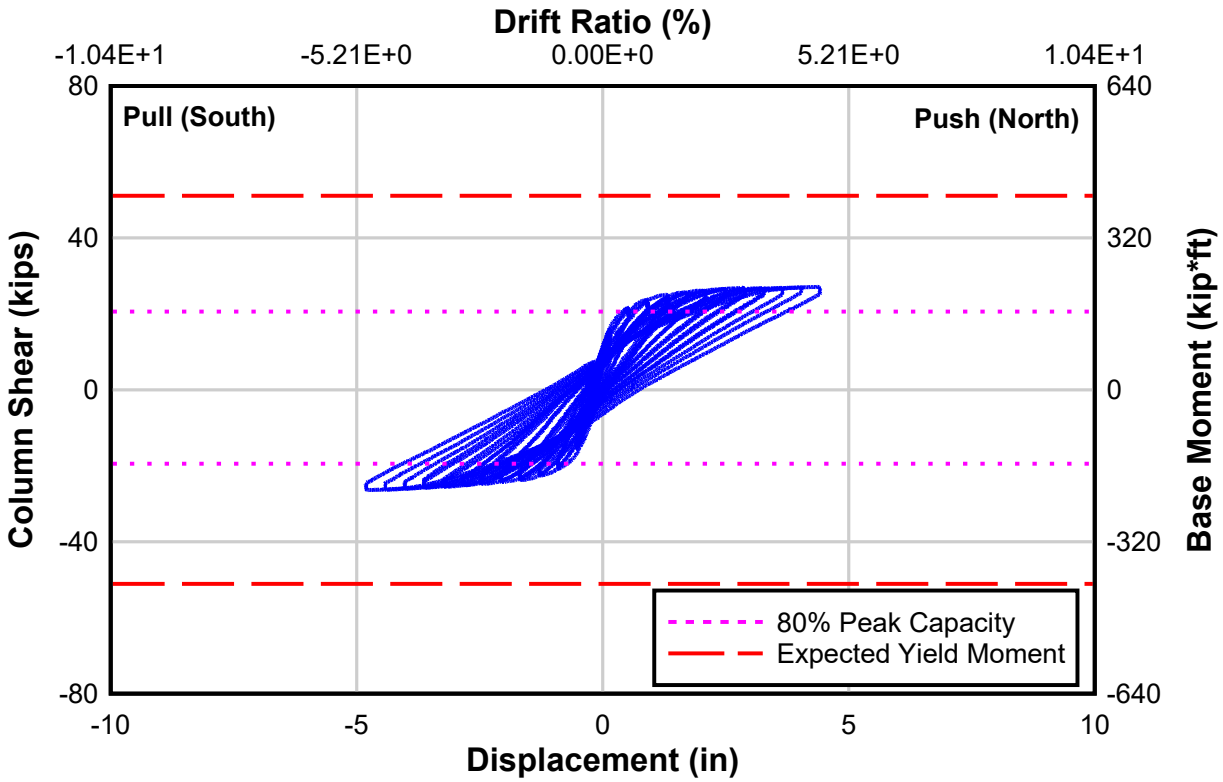

Figure 6.34: Overall force-displacement response of Test 2, Specimen 2.

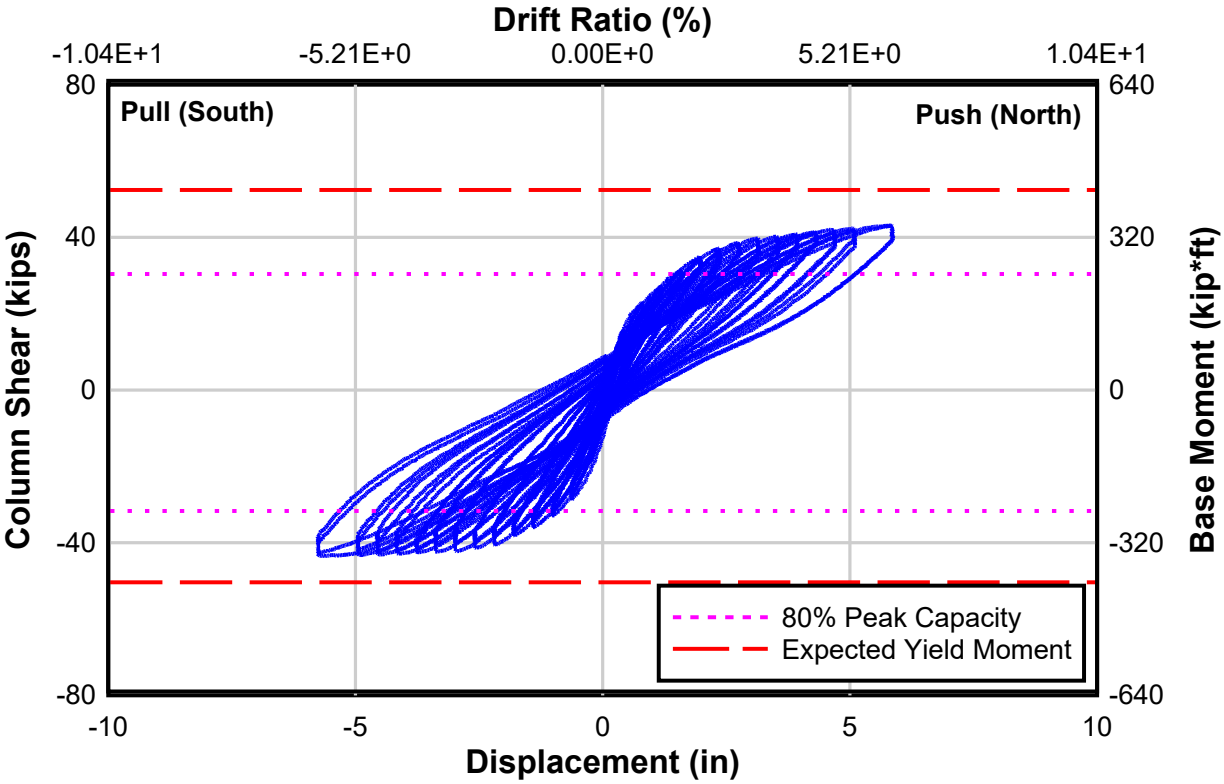

Figure 6.35: Overall force-displacement response of Test 3, Specimen 3.

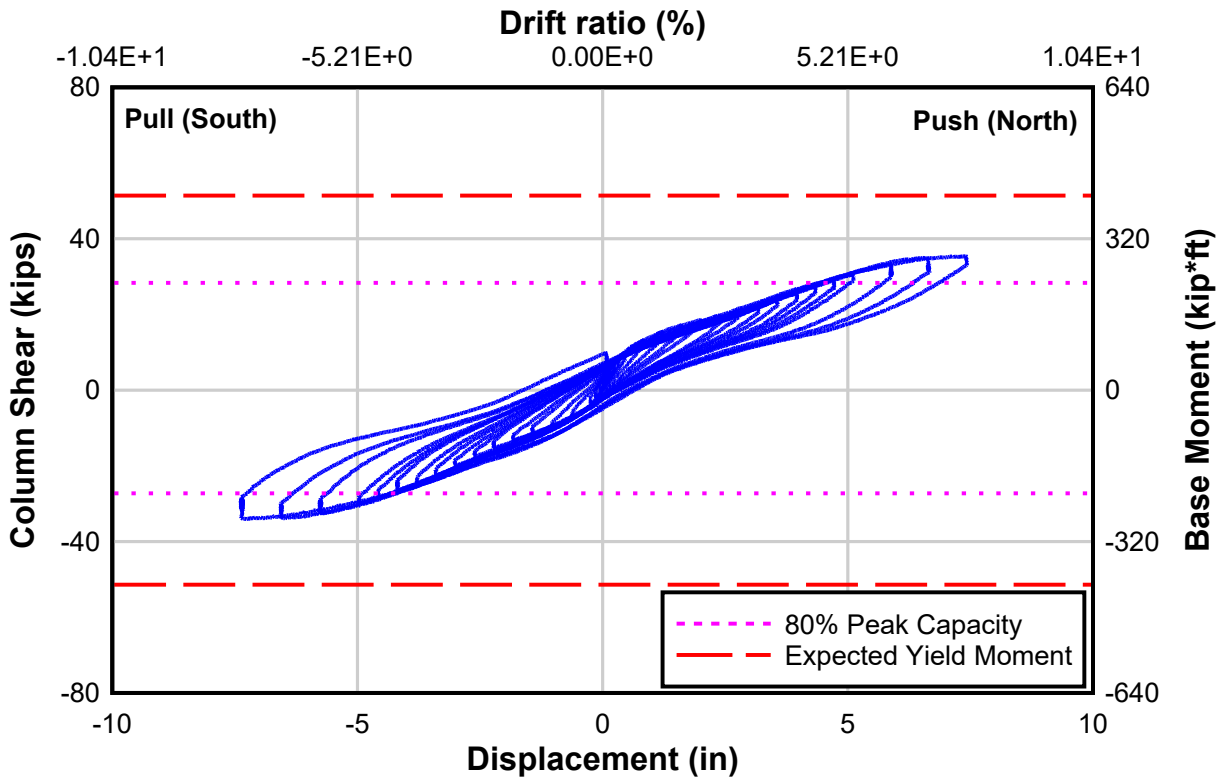

Figure 6.36: Overall force-displacement response of Test 4, Specimen 3.

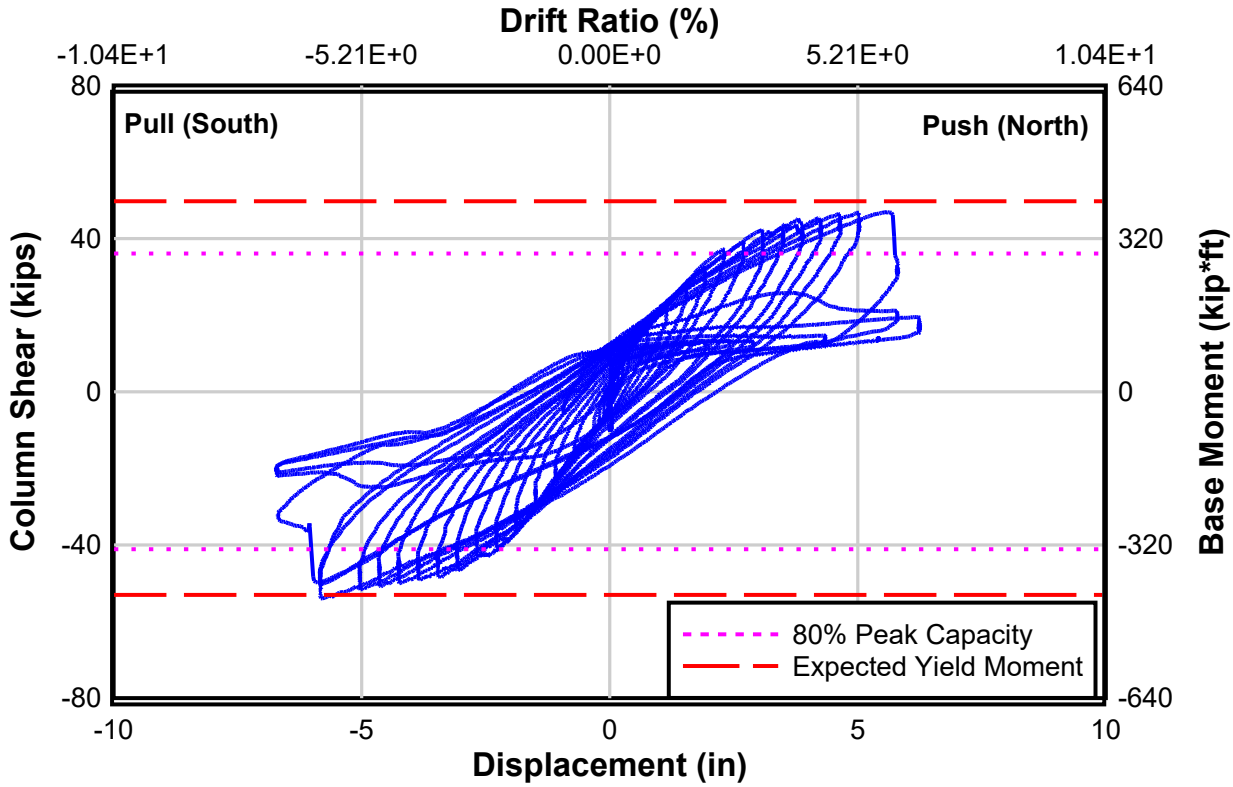

Figure 6.37: Overall force-displacement response of Test 5, Specimen 3.

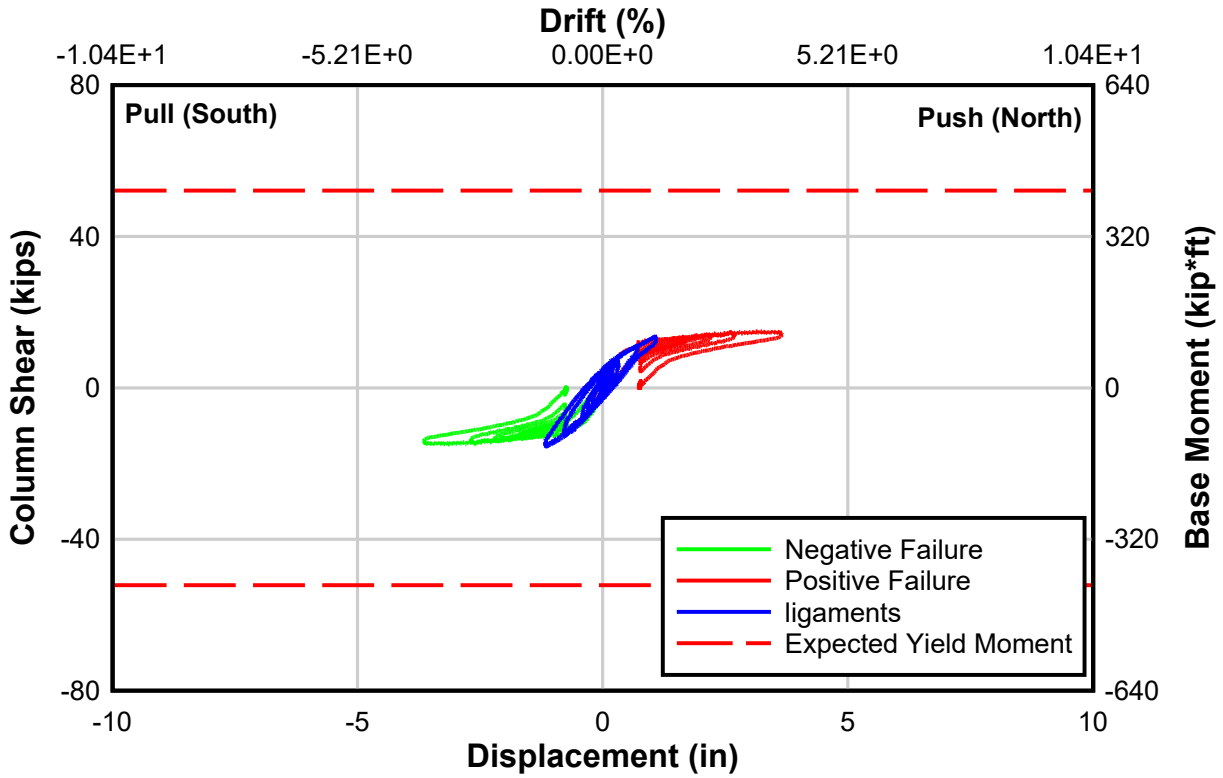

Figure 6.38: Overall force-displacement response of Test 6, Specimen 3.

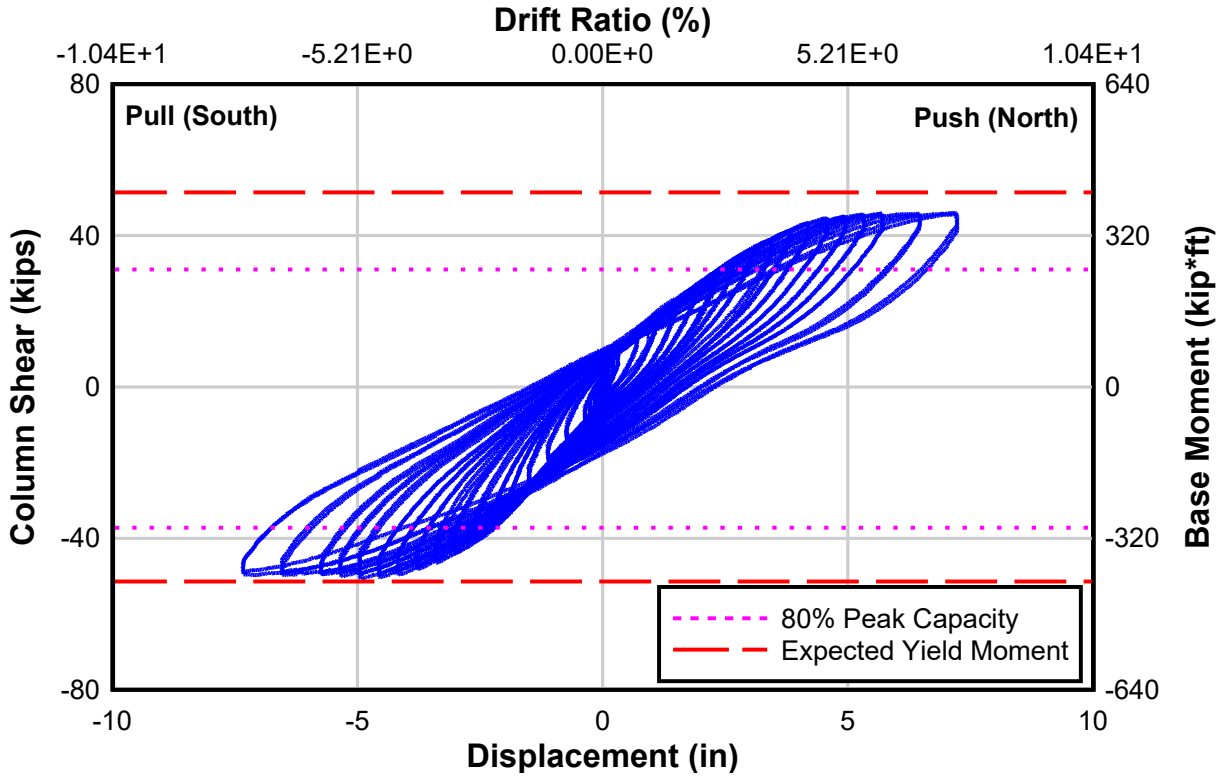

Figure 6.39: Overall force-displacement response for Test 7, Specimen 3.

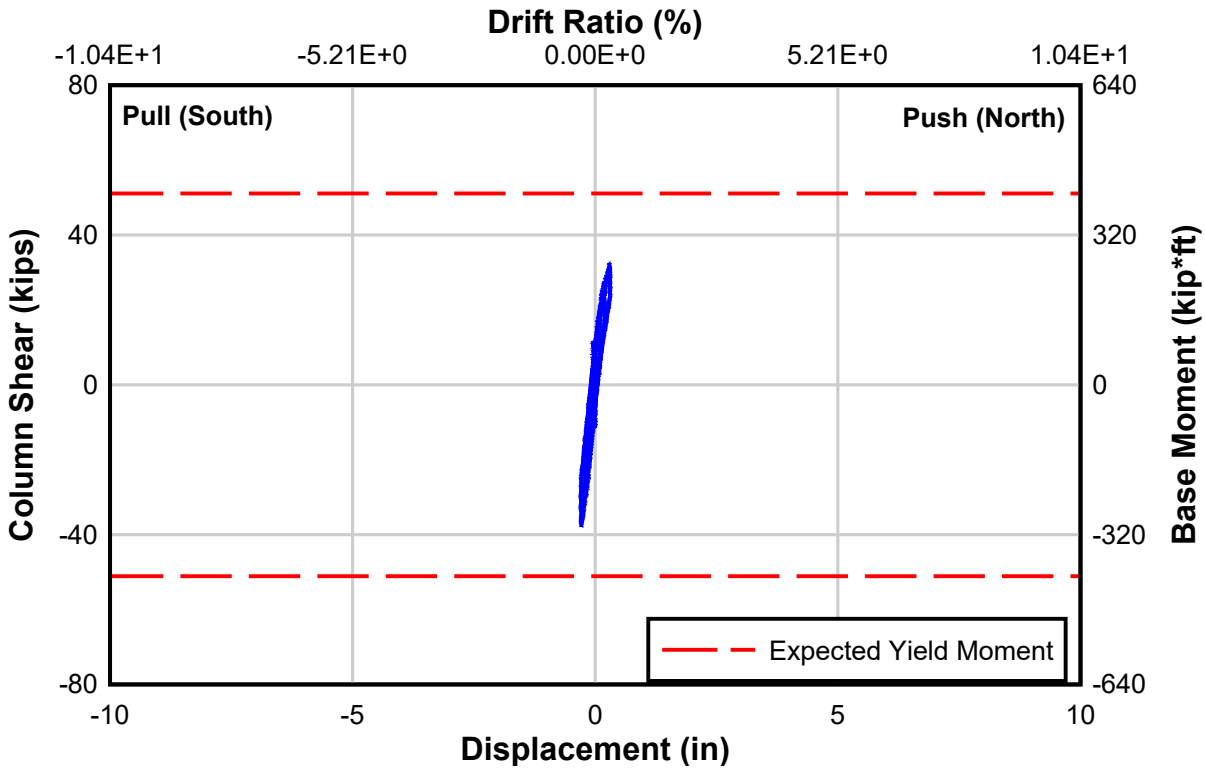

Figure 6.40: Overall force-displacement response for Test 8, Specimen 2 (pre-failure).

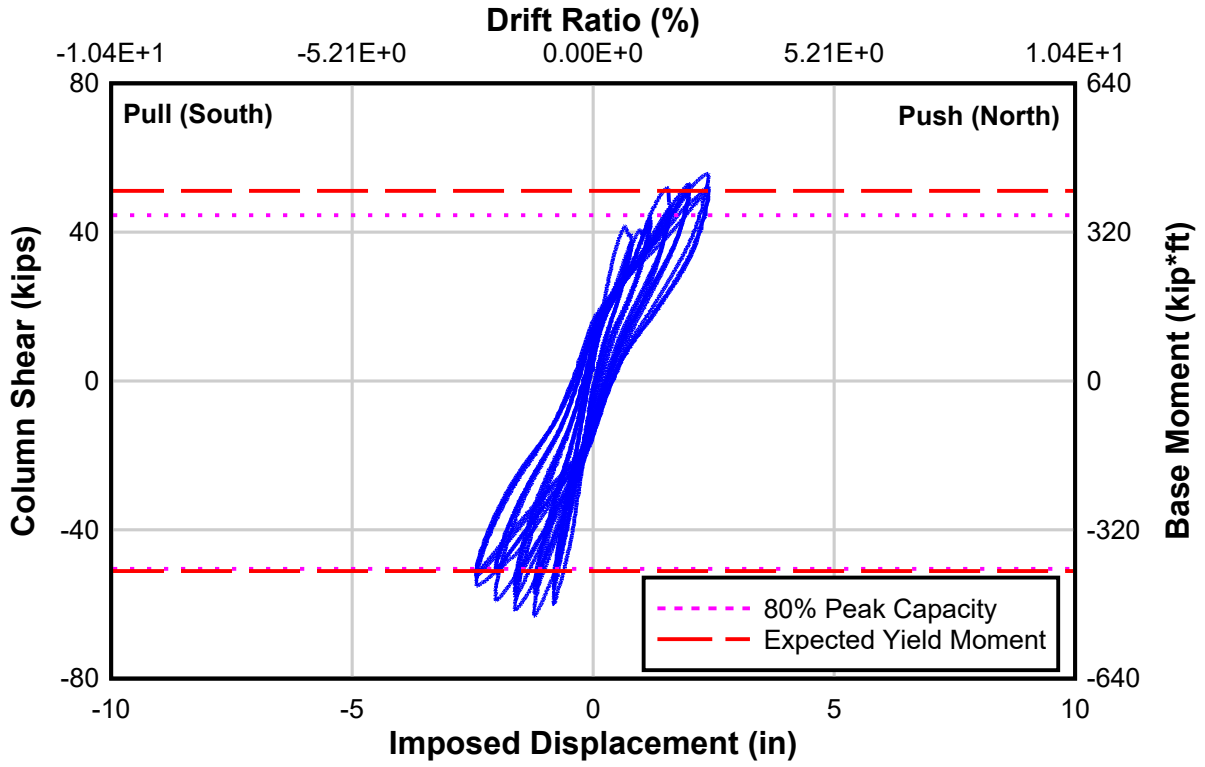

Figure 6.41: Overall force-displacement response for Test 8, Specimen 2 (post-footing failure).

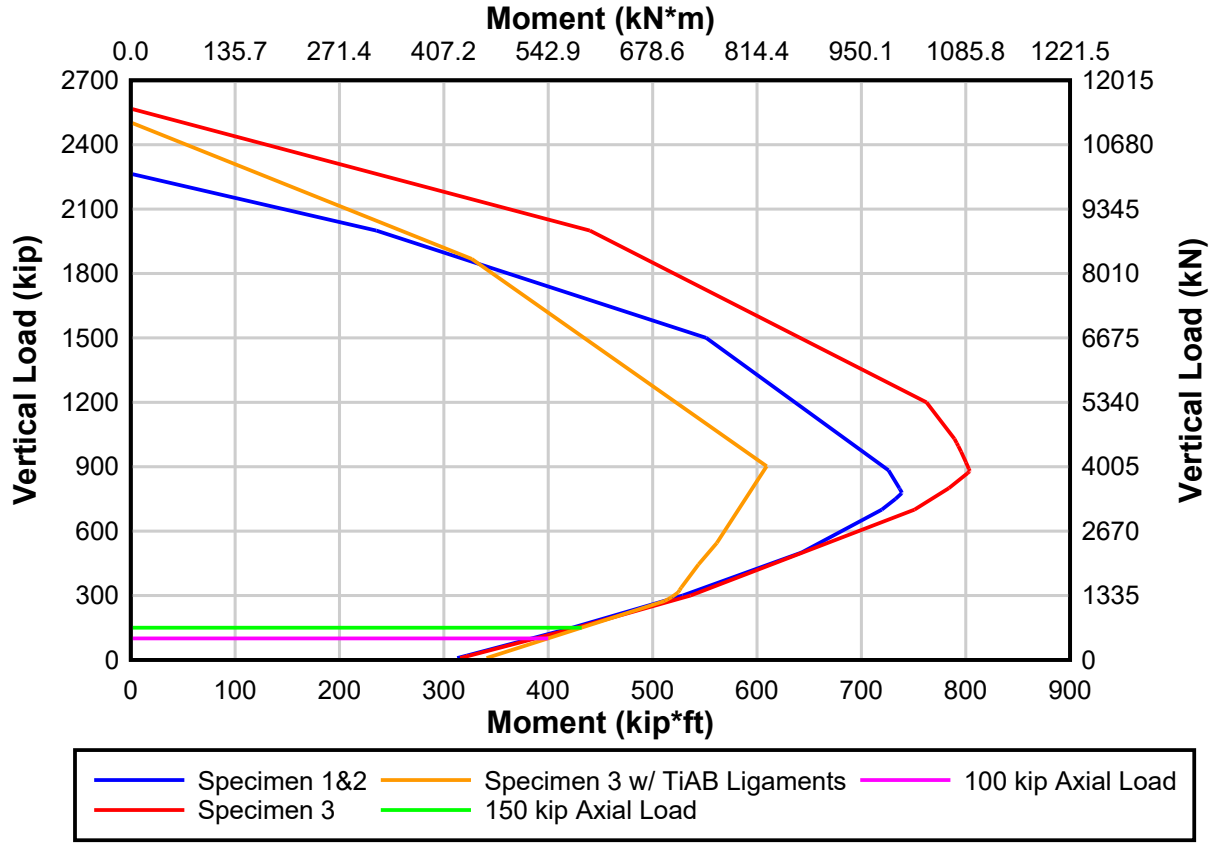

Figure 6.42: P-M interaction diagrams considering as-built specimen material properties.

Table 6.8: Summary of notable force-drift performance metrics.

Test Number – Specimen	Peak Capacity, kN (kip)		Drift Ratio (%) At Peak		Drift Ratio (%) At Failure	
	Push (+)	Pull (-)	Push (+)	Pull (-)	Push (+)	Pull (-)
T1-S1	199 (44.8)	209 (46.9)	9.9	10	2.2	2.4
T2-S2	121 (27.1)	112 (25.2)	4.5	5	0.79	0.8
T3-S3	188 (42.2)	197 (44.3)	6	6	2.2	2.3
T4-S3	158 (35.4)	151 (34)	7.7	7.6	5.2	5.3
T5-S3	212 (47.7)	235 (52.9)	5.9	6	-	-
T6-S3*	44.5 (10)	48.9 (11)	0.52	0.625	-	-
T7-S3	205 (46)	224 (50.3)	7.5	5.2	4.7	5.2
T8-S2	248 (55.7)	281 (63.1)	2.4	1.3	0.73	0.84

** T6-S3: Test was not conducted to failure. Values reported are recorded load and displacement when pre-compression is overcome.*

6.3.2.2 Components of Overall Force-Displacement

Because a flexible foundation was used to investigate soil-structure interaction (SSI), the contributions to overall lateral displacement come from several different components. Therefore, to obtain the effective column drift relative to the top of the footing, other contributing deformation components must be removed from the measured overall column displacement. These components include rigid body translation and rigid body rotation as illustrated by Shrestha (2019) in Figure 6.43.

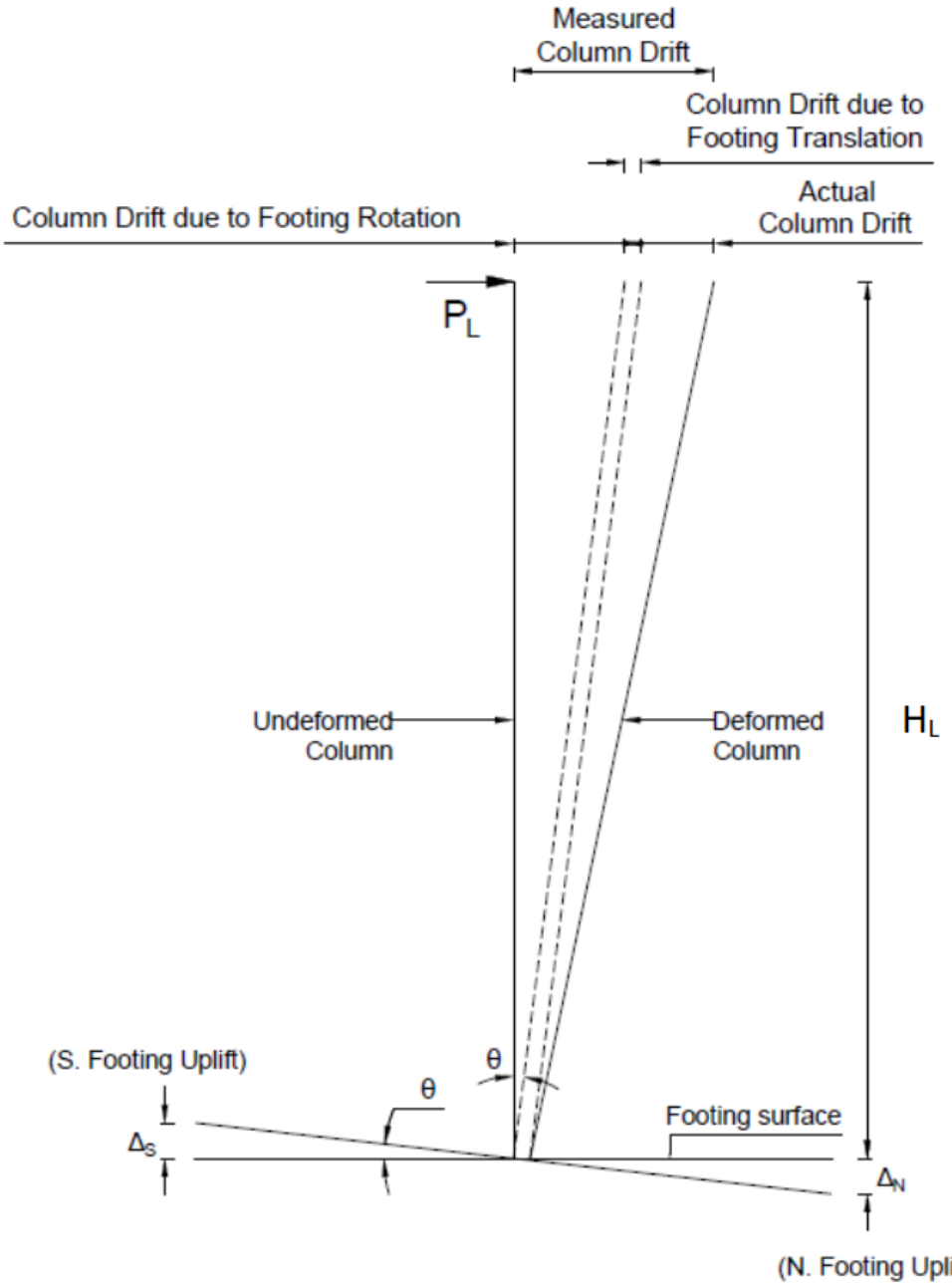

Figure 6.43: Components of measured overall horizontal displacement in column at lateral loading point.

The rigid body horizontal translation, $\Delta_{slide,}$ in the direction of loading was measured using a string potentiometer on the west and east faces of the footing at the geometric center and was computed in Equation 6.8 where *SP* is the string potentiometer reading on the face.

$$\Delta_{slide} = (SP_{west} + SP_{east})/2 \quad \textbf{(6-8)}$$

The rigid body rotation was measured using three (3) sensors on the top of the footing surface 76.2 mm (3 in.) from the north and south face with two (2) sensors located at the corners and one (1) in the center as seen in Appendix A6.2, Figure A6.2.9. Rigid body rotation was calculated in Equations 6.9-6.12:

$$\Delta_{rN} = (SP_{NW} + SP_{N} + SP_{NE})/3 \quad \textbf{(6-9)}$$

$$\Delta_{rS} = (SP_{SW} + SP_{S} + SP_{SE})/3 \quad \textbf{(6-10)}$$

$$\tan(\theta) = (\Delta_{rN} - \Delta_{rS})/54 \quad \textbf{(6-11)}$$

$$\Delta_{rotation} = H_L \tan(\theta) \quad \textbf{(6-12)}$$

Where Δ_{rN} and Δ_{rS} are the average measured displacements on the north and south side of the footing respectively, $\tan(\theta)$ is the difference in the measured displacements divided by the distance between sensors with units of inches, and H_L is the height of the column measured from the column footing interface to the point of loading. Effective column drift was determined by subtracting rigid body translation and rigid body rotation. These values were calculated in Equation 6.13:

$$\Delta_{eff} = \Delta_{measured} - \Delta_{slide} - \Delta_{rotation} \quad \textbf{(6-13)}$$

Figure 6.44 illustrates that the column deformation provides only a small contribution to the overall column deformation, and Figure 6.45 shows the contribution from the column which occurred during the vintage column failure. Component contributions to the measured displacements for all tests can be found in Appendix A7.3.

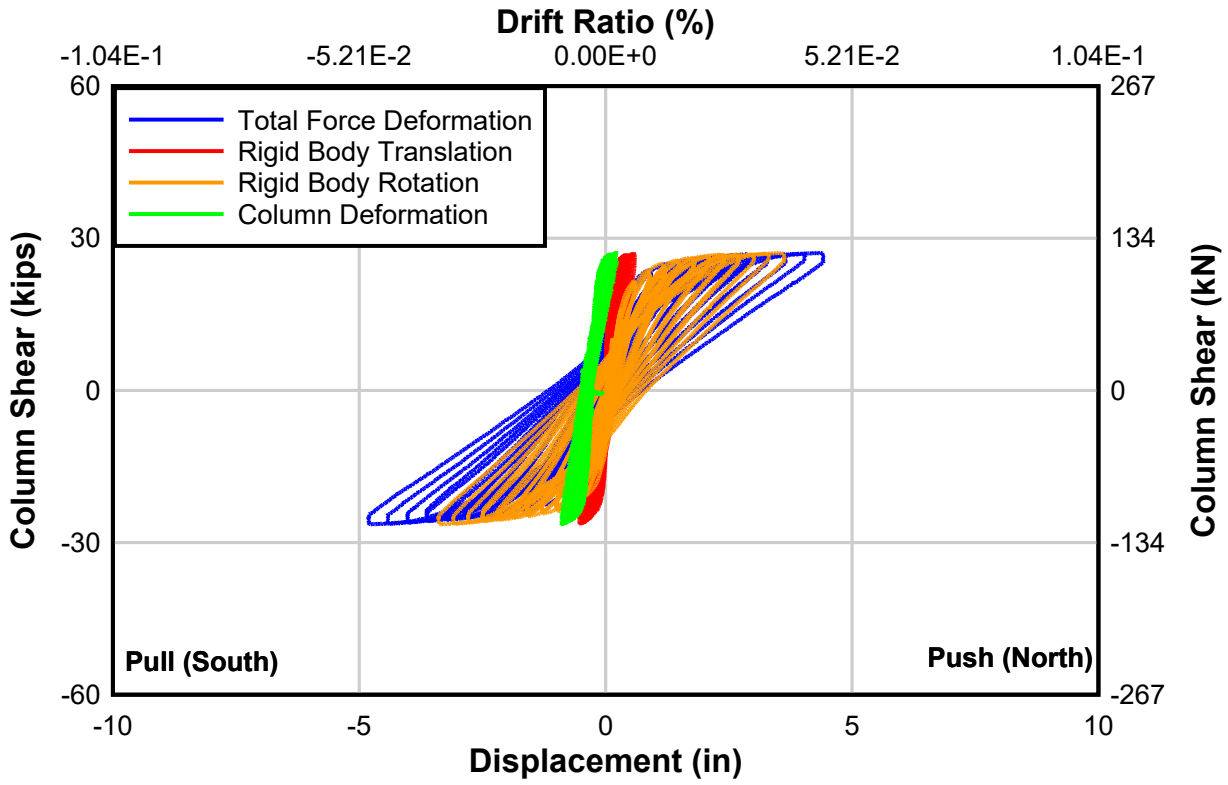

Figure 6.44: Component contributions to measured displacement in T2-S2.

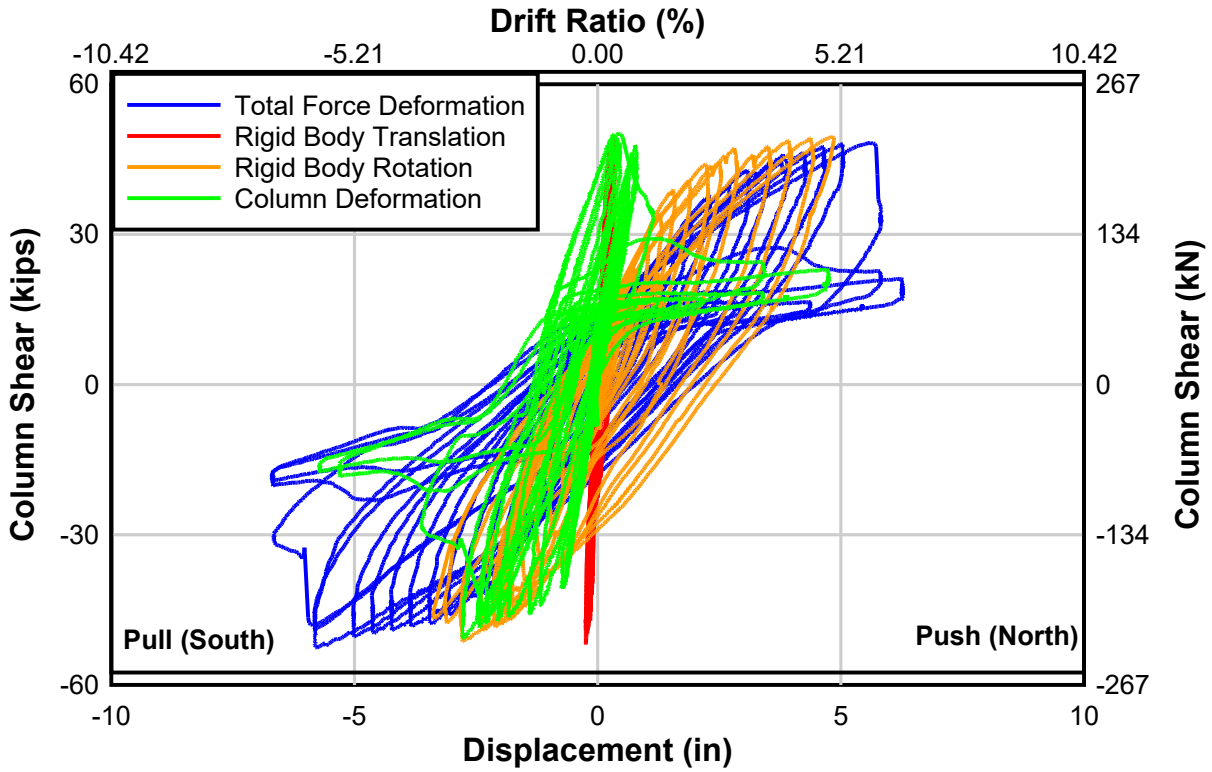

Figure 6.45: Component contributions to measured displacement in T5-S3.

6.3.2.3 P-Delta Effects

Axial load applied at the top of the column creates a second-order moment due to the drift imposed by the lateral loading. While the horizontal component of the axial load is a restoring force that must be removed from the lateral loads to determine the internal moment in the column, the vertical component acting at a distance creates an additional overturning moment. This produces a softening response due to the negative stiffness associated with the vertical component that is linearly dependent on the lateral drift magnitude. To better understand the force-displacement response the degrading effects of P-Delta behavior were isolated using the geometric relationships established in Section 6.3.2.1. Equations 6.14 – 6.15 were used to remove P-Delta effects from the force-displacement response. Because P-Delta creates a softening response the difference in the moment must be added to the experimental response to obtain the response of the column without P-Delta.

$$\mathbf{M_{base\text{-}[remove\ P\text{-}D]} = P_L H_L - P_H H'} \tag{6-14}$$

$$\mathbf{M_{w/o\ [P\text{-}D]} = M_{base} + (M_{base} - M_{base\ [remove\ P\text{-}D]})} \tag{6-15}$$

where M_{base} is the moment at the base of the column calculated using equation 6.6. P-Delta has a more significant effect on the column response at higher drift levels when the soil simulant is acting inelastically. When removed, much of the post-peak degradation can be attributed to the P-Delta effect as reported by Shrestha (2019), and this can be seen in Figure 6.47. However, Shrestha (2019) used a fixed foundation. For a flexible foundation, a minor positive post-failure slope increases to a much larger positive post-failure slope due to the soil simulant eventually stiffening at large plastic deformations. This is evident in Figure 6.46, where the vintage column failure occurs with a flexible subgrade. P-Delta effects on the force-displacement response for all tests can be viewed in Appendix A6.3.

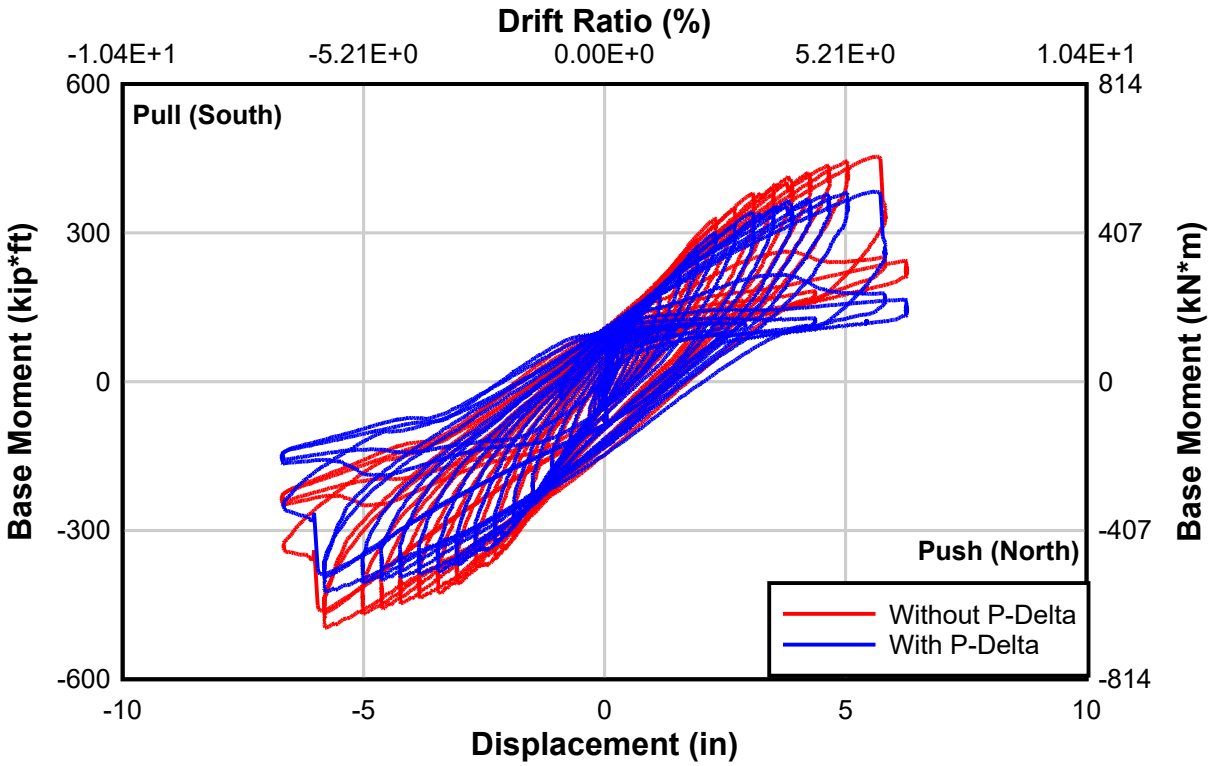

Figure 6.46: P-Delta effect on T5-S3, vintage column failure.

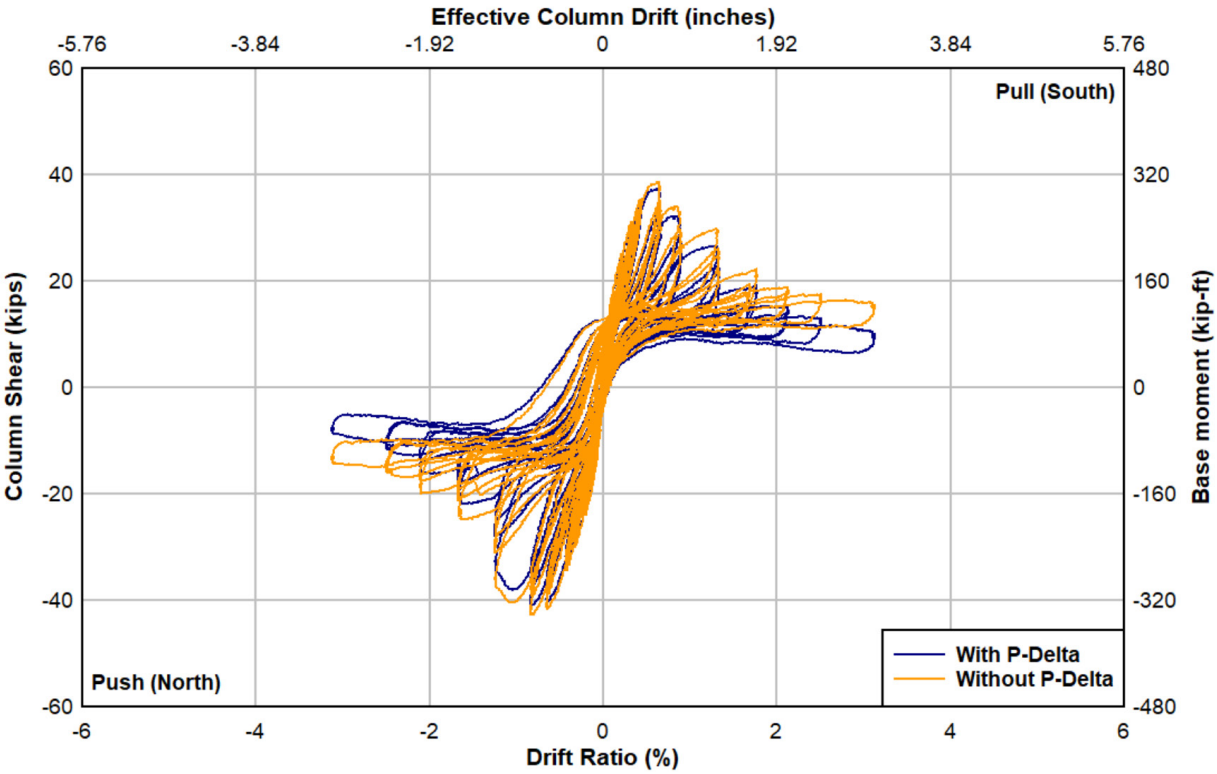

Figure 6.47: P-Delta effects on vintage column failure with fixed base by Shrestha (2019).

6.3.3 Reinforcing Steel and TiAB Strains

Strain data from instrumented reinforcing steel and TiABs showed that yielding occurred in only three (3) of the tests; Test 1 of Specimen 1, Test 2 of Specimen 2, and Test 3 of Specimen 3. Yielding more often occurred in the pull cycle due to the higher stiffness of the horizontal reaction frame setup in this direction. This behavior did not appear to occur in the column bars on the pull cycle in Specimen 3 during Test 5 and is attributed to slipping of the spliced bars which occurred earlier on the south side than on the north side. Figure 6.48 shows that the only bar that exhibited yielding in Test 1 of Specimen 1, was the center bar in the direction of loading at the bottom of the footing bar mesh. During Test 5, the starter bars yielded before the column bar and column tie as seen in Figures 6.49 – 6.51. Lastly, Figure 6.52 and Figure 6.53 show that in Test 8 of Specimen 2 the NE starter bar yielded at the column footing interface and two (2) reinforcing steel bars in the footing mesh reached yield strain. Strain gauges on the TiABs were used during characterization testing for the post-failure retrofit process as seen in Figure 6.27 in Section 6.3.1.6. All other strain data can be viewed in Appendix A6.3.

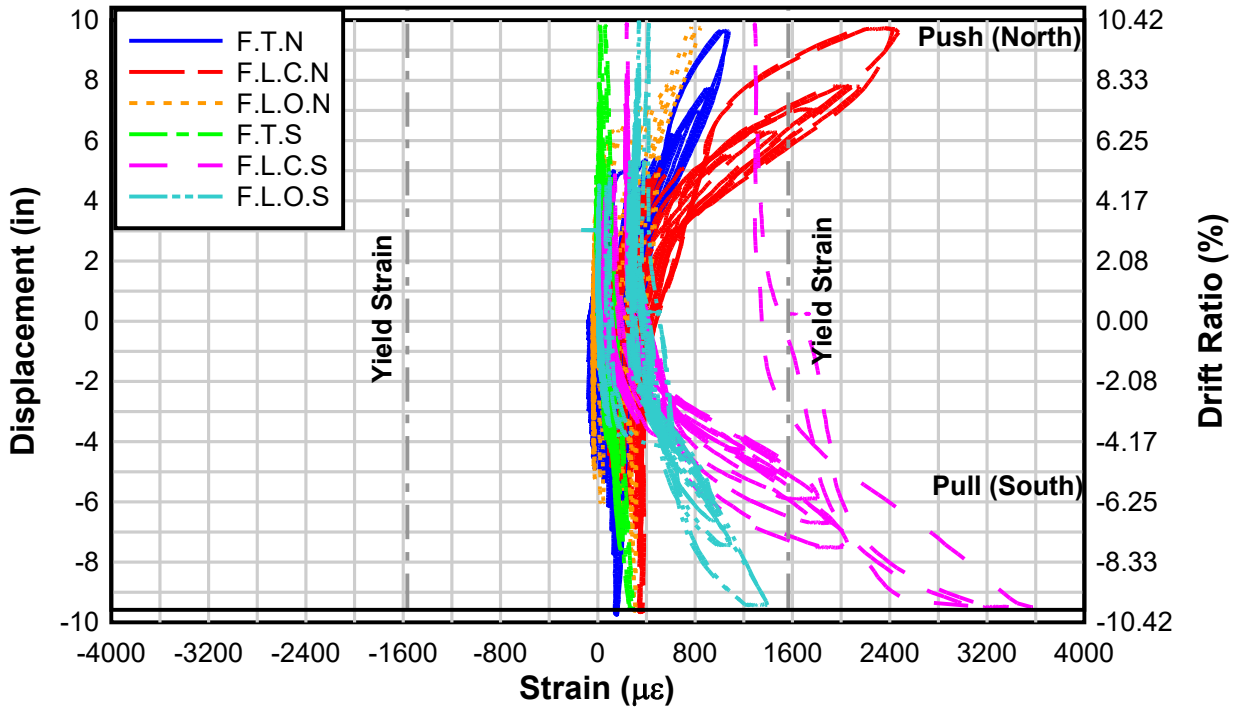

Figure 6.48: Footing bar strains T1-S1.

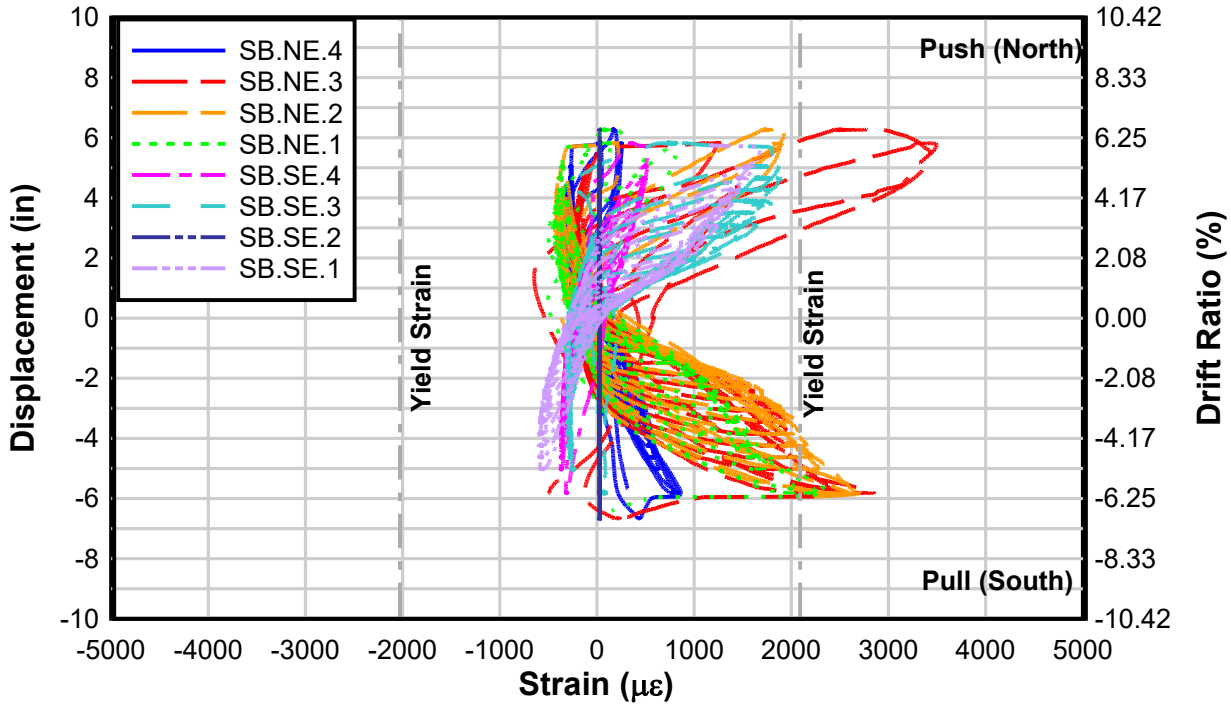

Figure 6.49: Starter Bar Strains T5-S3.

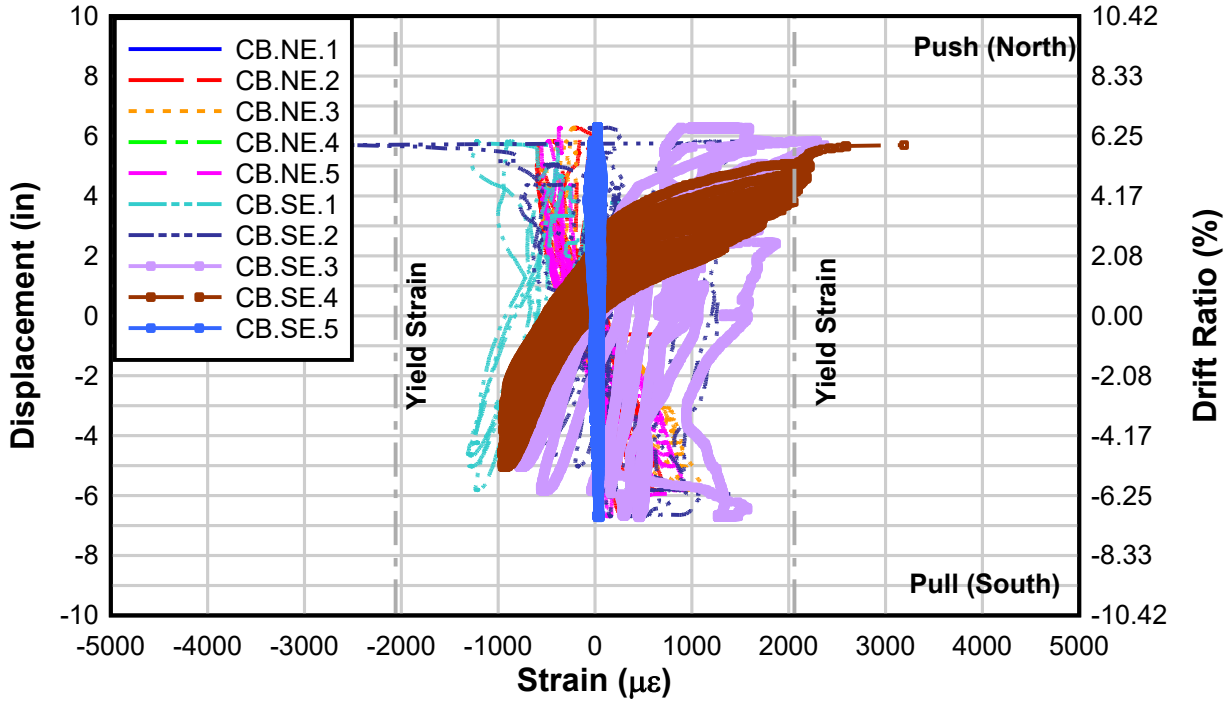

Figure 6.50: Column bar Strains T5-S3.

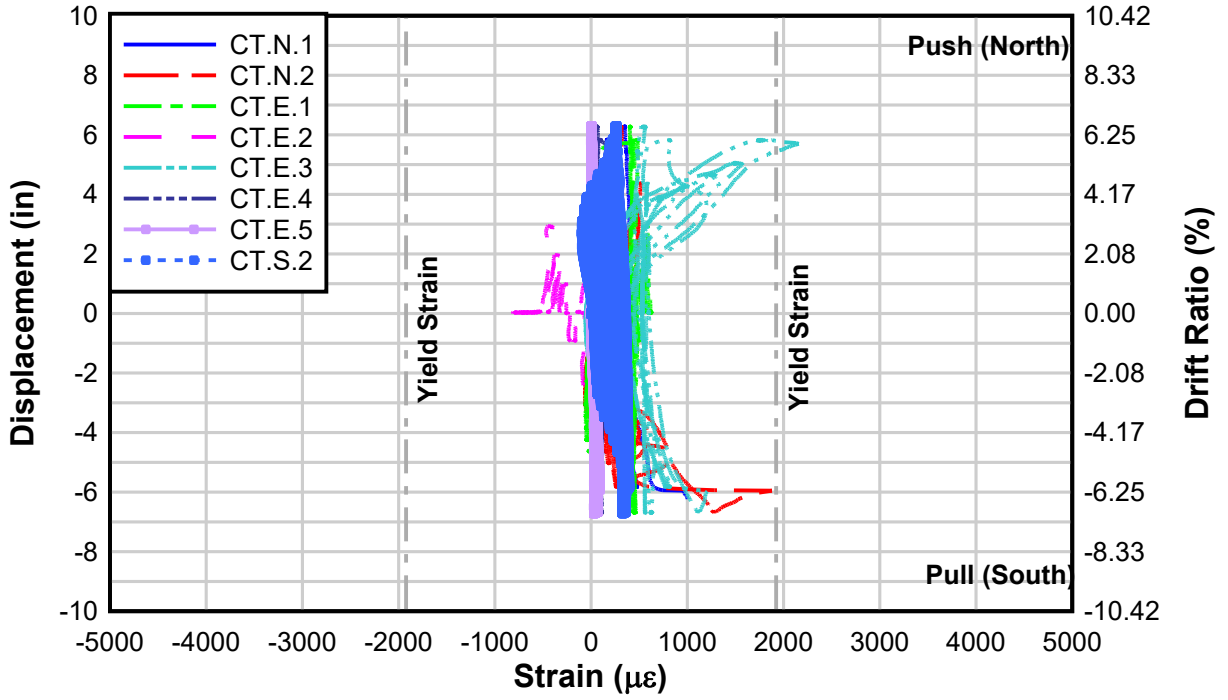

Figure 6.51: Column Tie Strains T5-S3.

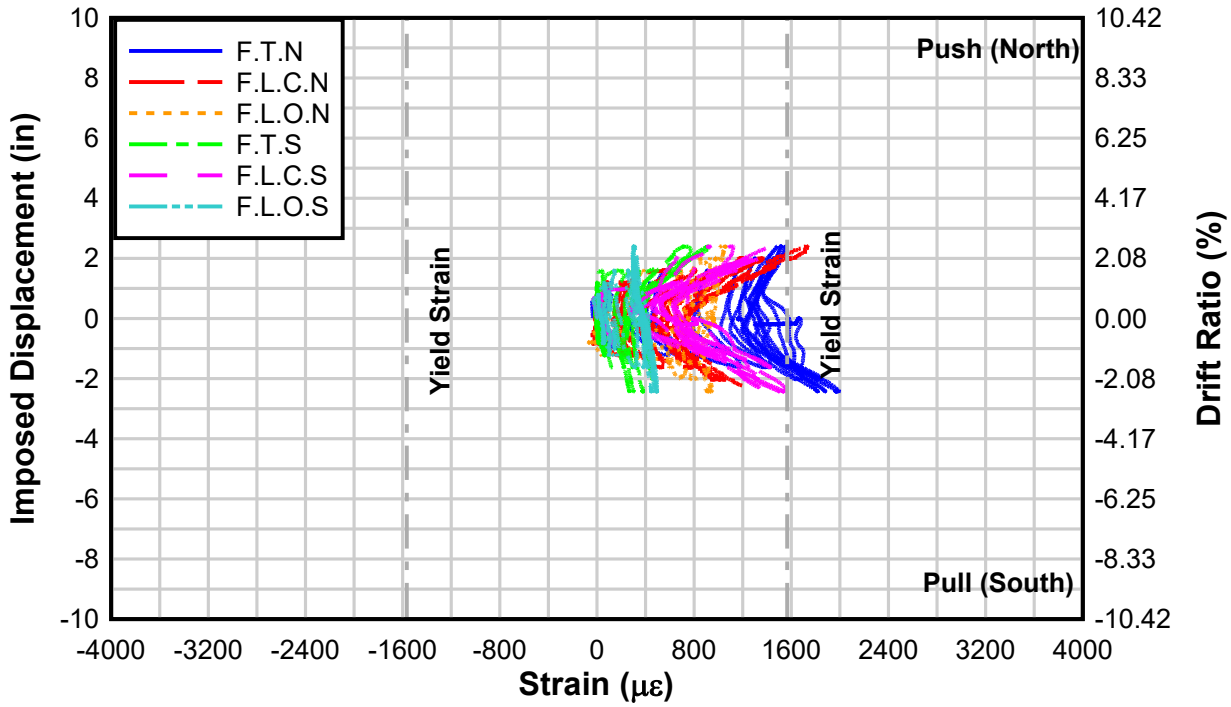

Figure 6.52: Footing Bar Strains T8-S2 Post Failure.

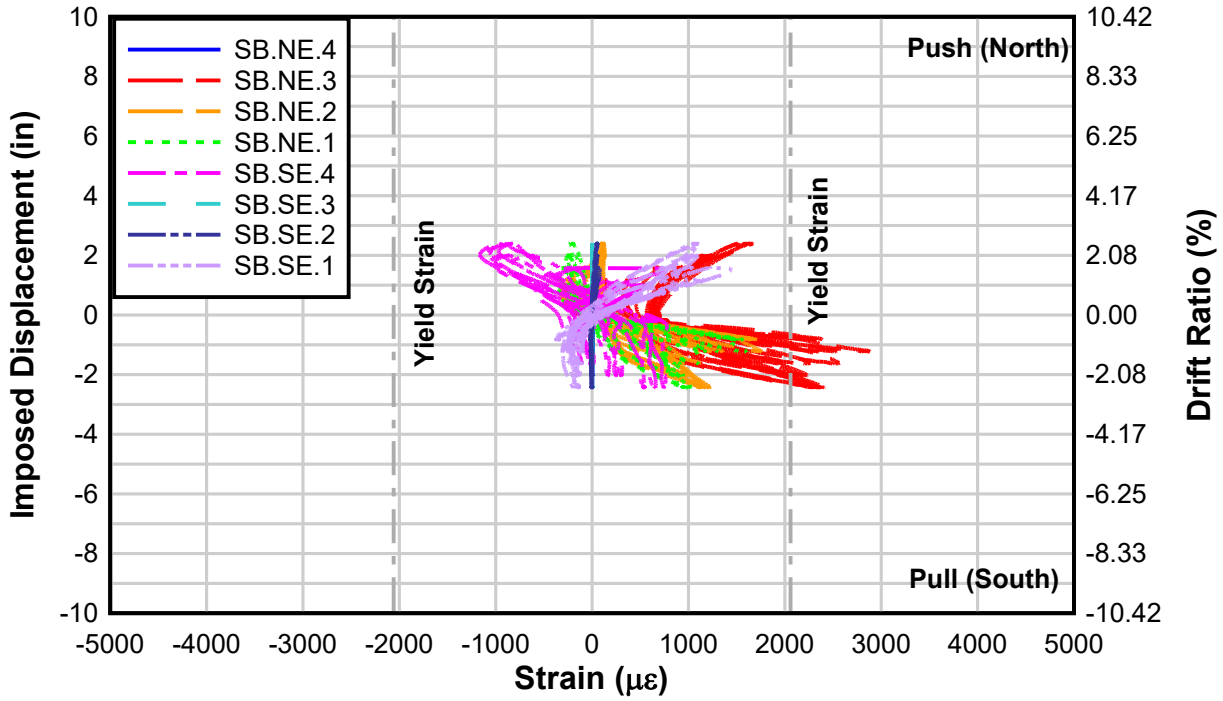

Figure 6.53: Starter Bar Strains T8-S2 Post Failure.

6.3.4 Soil-Structure Interaction

The use of soil simulant allowed for the inclusion of the subgrade flexibility including the occurrence of foundation rocking behavior into the lateral response of the column-footing system. This facilitates a more realistic representation of an in-situ column-footing but with laboratory-controlled conditions. Response of the substructure under different soil characteristics including rocking, embedment, stiffness, settlement, and footing size can be reasonably captured with the soil simulant used in this study. The following section discusses the effects of soil-structure interaction (SSI) on the column-footing response.

6.3.4.1 Effect of Rocking on TiAB Retrofitted Bridge Columns

Effects of rocking foundation behavior were determined by comparing both the results of Test 1 with the results of specimen R-S-R-LTi-90 tested by Shrestha (2019) and the results of Test 5 with the results of specimen C-S-R tested by Shrestha (2019). Figure 6.54 displays the difference SSI made in the response of the vintage column. Test 5 was tested with a soil simulant subgrade and steel spring embedment soil, while C-S-R was tested with the footing fixed to the strong floor. There is a clear difference due to activation of rocking behavior of the column foundation. The rigid body motion seen in Test 5 exhibited a higher peak response of 235 kN (52.9 kips) at a drift of 6% before failure compared to the C-S-R with a peak shear of 182 kN (40.9 kips), at a drift of only 0.81% before failure. Furthermore, Test 5 was conducted after progressive damage in the column occurred during Tests 2 and 3 as described in Sections 6.3.1.3 and 6.3.1.4. It is also clear that the SSI produced a softer lateral load – deformation response which would influence the natural period of the structure and thus the response to ground accelerations.

SSI also produced larger energy dissipation which would act to dampen dynamic response.

SSI can reduce the column force demands and thereby ductility demands of columns. Figure 6.55 compares the results of Test 1 and the results of specimen R-S-R-LTi-90 tested by Shrestha (2019), both unretrofitted columns, but one on simulated soil and the other fixed to the laboratory floor. Test 1 displayed a much lower column shear due to the soil acting as a fuse to limit the demands compared to specimen R-S-R-LTi-90. The simulated soil had a more stable response from the inelastic material response of the soil simulant subgrade and passive pressure provided by a soil simulant embedment and the thresholds were sufficiently low as to prevent column failure. This demonstrates that SSI can be of significance when making retrofit decisions as component demands may be reduced compared to idealized fixity assumptions.

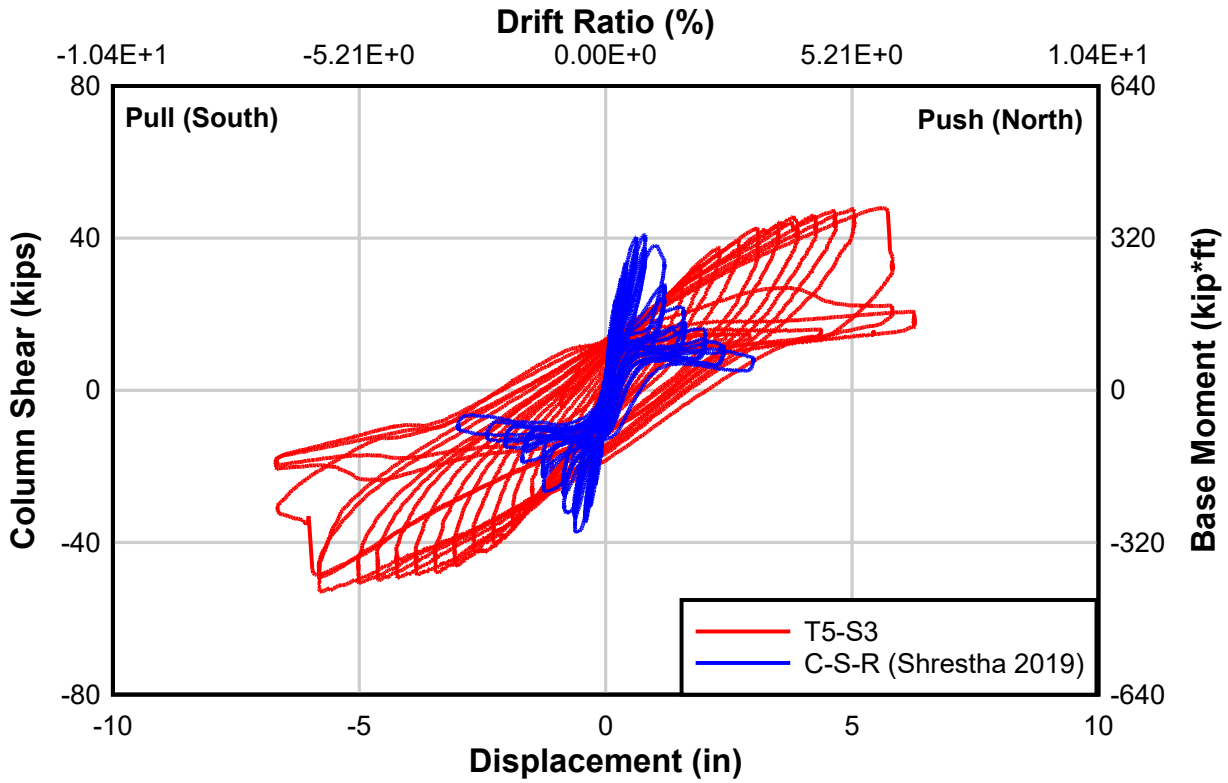

Figure 6.54: Comparison of unretrofitted vintage columns with SSI (T5-S3) and without SSI.

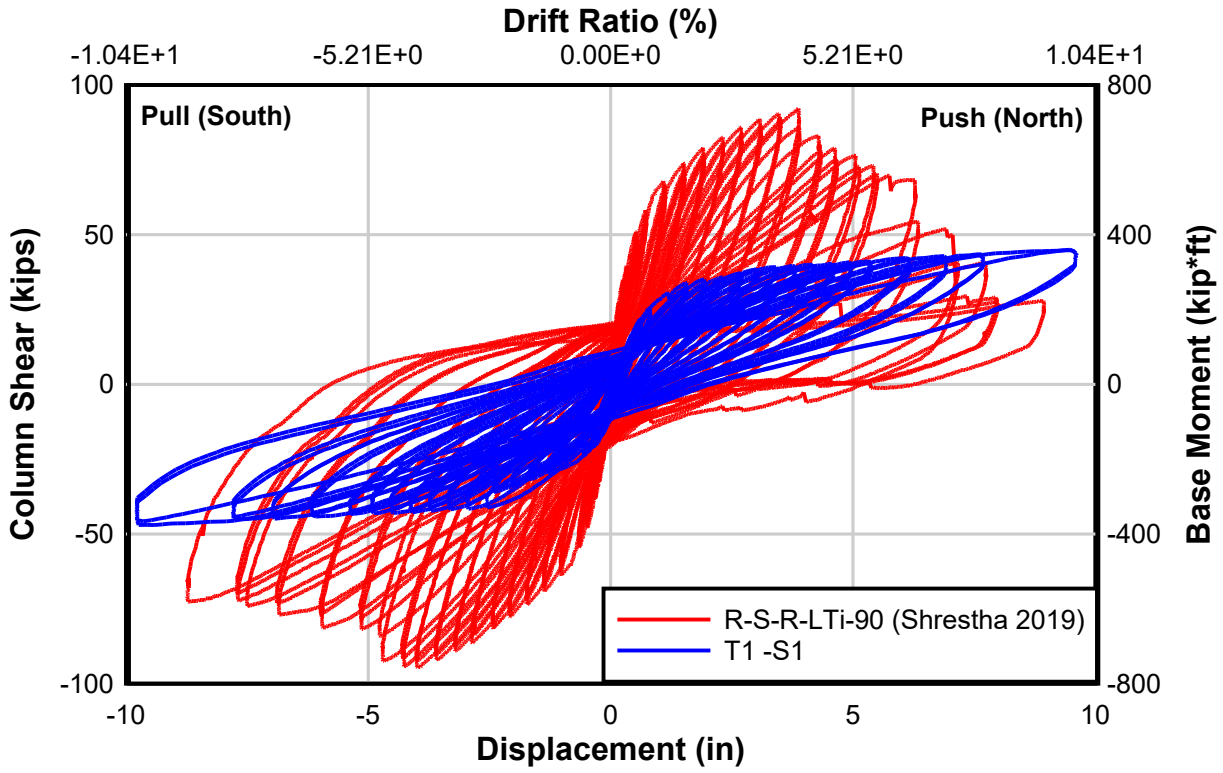

Figure 6.55: Comparison of a complete TiAB retrofit with SSI (T1-S1) and without SSI.

6.3.4.2 Effect of Embedment Depth

Another factor in characterizing SSI response is the effect of embedment depth. Figure 6.56 compares the response from Test 1 of Specimen 1 and Test 2 of Specimen 2. In Test 1, a 0.61 m (2 ft.) embedment depth was provided using the soil simulant in series with the steel springs, and no embedment was provided in Test 2. Both specimens had the same as-built properties; therefore, the change in response is principally due to differences in embedment. Test 1 had a column shear of 179 kN (40.3 kips) at a drift of 4.7%, and Test 2 had a column shear of 118 kN (26.6 kips) at a drift of 4.6% on the push cycle. On the pull cycle, Test 1 had a column shear of 191 kN (43 kips) at a drift of 5.2%, and Test 2 had a column shear of 118 kN (26.6 kips) at a drift of 5% on the pull cycle. Without embedment, the difference in stiffness between the push and pull cycles was removed; therefore, when comparing the differences in embedment, the average was taken as the difference between the two (2) half cycles. The average contribution to column shear from difference in embedment was 67 kN (15.1 kips). Furthermore, the post-yield slope is visibly larger in Test 1 compared to Test 2. Assuming a linear trend over the yield and post-yield slopes we see that the post-yield slope in Test 1 is approximately 3% of the yield slope, and 1.26% for Test 2. Therefore, most of the stiffness occurs due to embedment, and bearing pressures alone are enough to counter the negative slope effects from P-Delta due to the stiffening of the soil simulant at larger plastic deformations. Based on these results, the rocking behavior of the foundation is more likely to occur at reduced embedment.

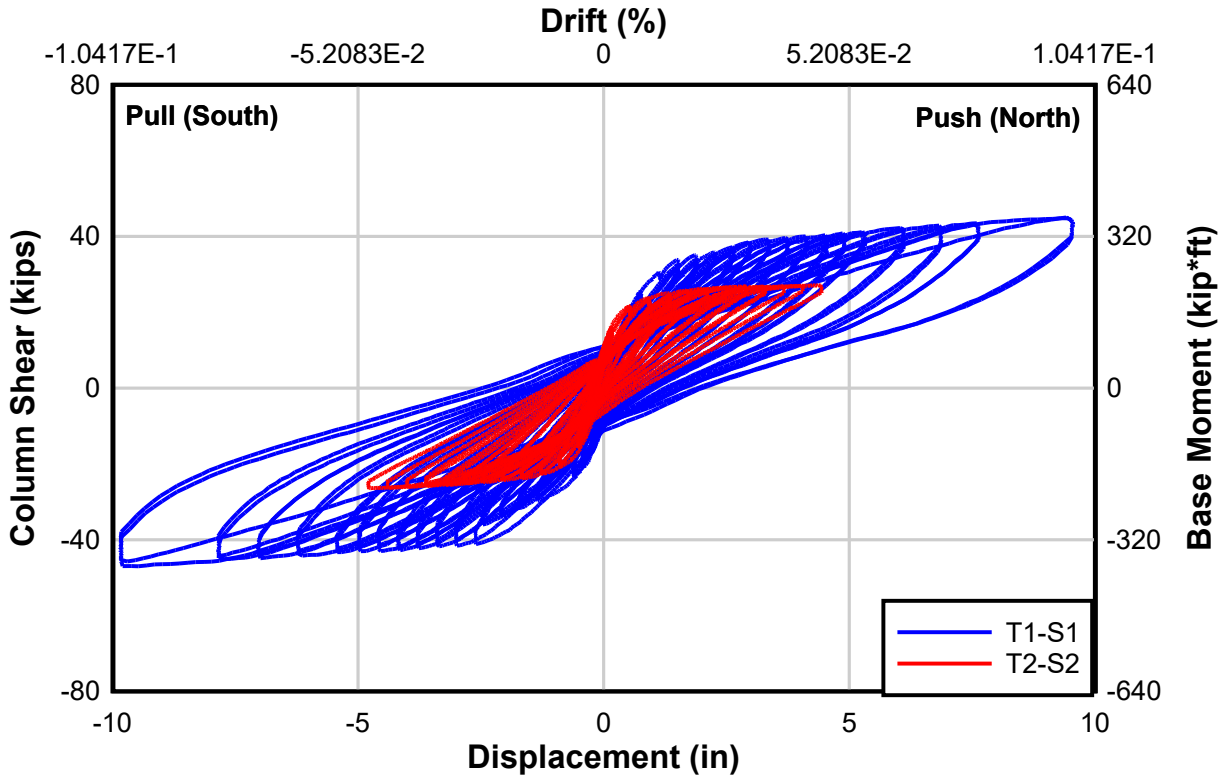

Figure 6.56: Comparison of SSI response change with embedment.

6.3.4.3 Effect of Axial Loads

Test 3 was conducted with a 667 kN (150 kips) axial load. After completing the test, the axial load was lowered to 445 kN (100 kips) in an effort to decrease the yield moment of the column. Previous soil failure in Test 3 caused no participation from the embedment soil simulant (vertical faces of the footing). Furthermore, the soil simulant subgrade had already exhibited plastic deformations, which resulted in a softer response through the previous drift cycles. Participation from the embedment soil simulant starts to occur at a 6.1% drift on the push cycle, and 6% drift on the pull cycle in Test 4. On the push cycle, the column shear in Test 3 at 6.1% drift is 191 kN (43 kips), and the column shear in Test 4 is 147 kN (33.1 kips). On the pull cycle, the column shear in Test 3 at 6% drift is 196 kN (44 kips), and the column shear in Test 4 is 144 kN (32.3 kips) as seen in Figure 6.57. Even though the embedment soil simulant had failed during the previous test, the responses are comparable due to the recovery of the soil simulant. During both tests, at 6.1% and 6% drift, the face of the footing was in contact with the embedment soil simulant. A reduction in axial load reduced the column shear in the specimen at similar drift magnitudes.

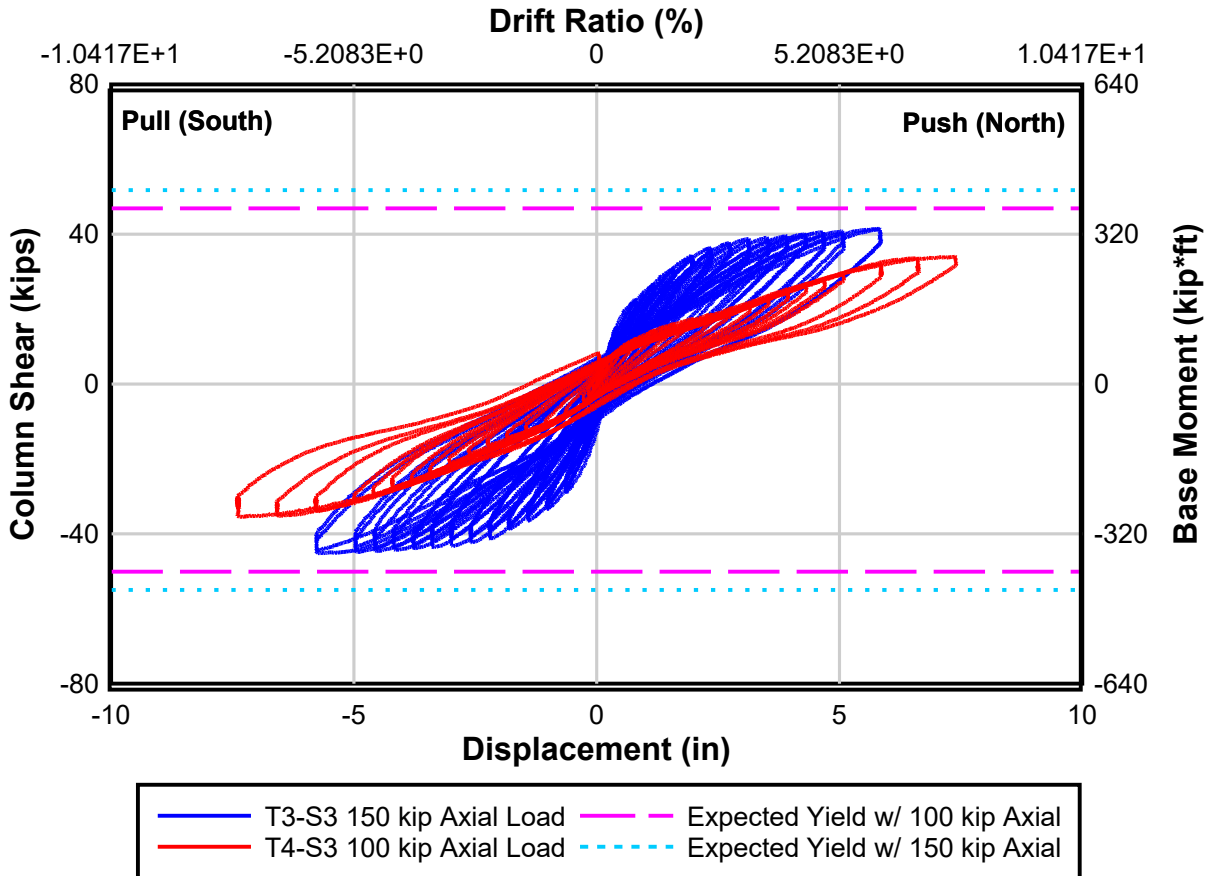

Figure 6.57: Influence of axial load.

6.3.4.4 Effect of Soil Stiffness

Soil stiffness and strength are contributing factors for characterizing SSI. The soil simulant subgrade was highly compressed and exhibited permanent deformation at larger excursions. These plastic deformations also result in increased the soil simulant stiffness as the loading continues. During lateral loading, the soil simulant is loaded non-uniformly due to the rocking behavior of the foundation, and as a result, there is an arch-like profile under the footing and as the column returns to the original position, a smaller area of soil simulant becomes loaded during subsequent cycles and in some cases subsequent tests on the same soil. Figure 6.58 illustrates the arch-like profile after Test 1. For Test 1, the soil simulant depth was recorded at 76.2 mm (3 in). increments along the length of the footing footprint. This record was taken after the specimen was removed. For other tests, punching and damage occurred to the soil simulant during subsequent tests and thus the soil profiles recorded were more variable but are reported in Appendix A6.3. Based on test results there are four (4) important contributing factors to the evolution of the stiffness of the soil simulant; elastic loading stiffness, strength upon nonlinear stress-strain response, large strain stiffening, and the strain rate.

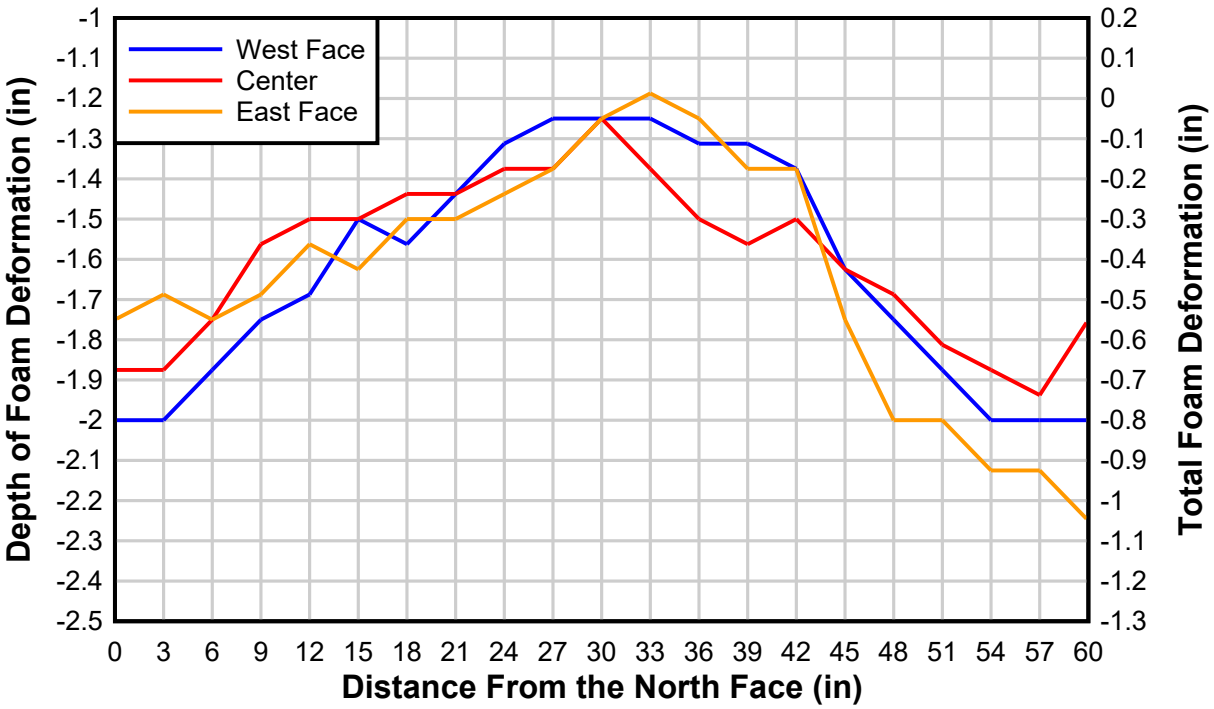

Figure 6.58: Soil simulant profile after testing.

Evolution of Stiffness Degradation

The evolution of the overall stiffness degradation was developed for each test in terms of both the tangent stiffness and the secant stiffness. To obtain the tangent stiffness, the backbone curve of the overall force-displacement hysteresis was differentiated with respect to the displacement. The secant stiffness was determined from the slope of a line radiating from the origin to points on backbone curve. Both the tangent stiffnesses and

secant stiffness variations were grouped for comparison based on whether new soil simulant was used in the test or the soil simulant that had already been damaged in a prior test. Figure 6.59 – Figure 6.62 compare the evolution of the stiffness degradation for each test. By observation, stiffness degraded for new soil simulant at a faster rate due to creation of at first localized plastic strains in the extreme edges of the footing that progressively take place over larger regions. Subsequent tests of previously damaged soil simulant produced smaller changes because large portions of the simulant were already plasticized.

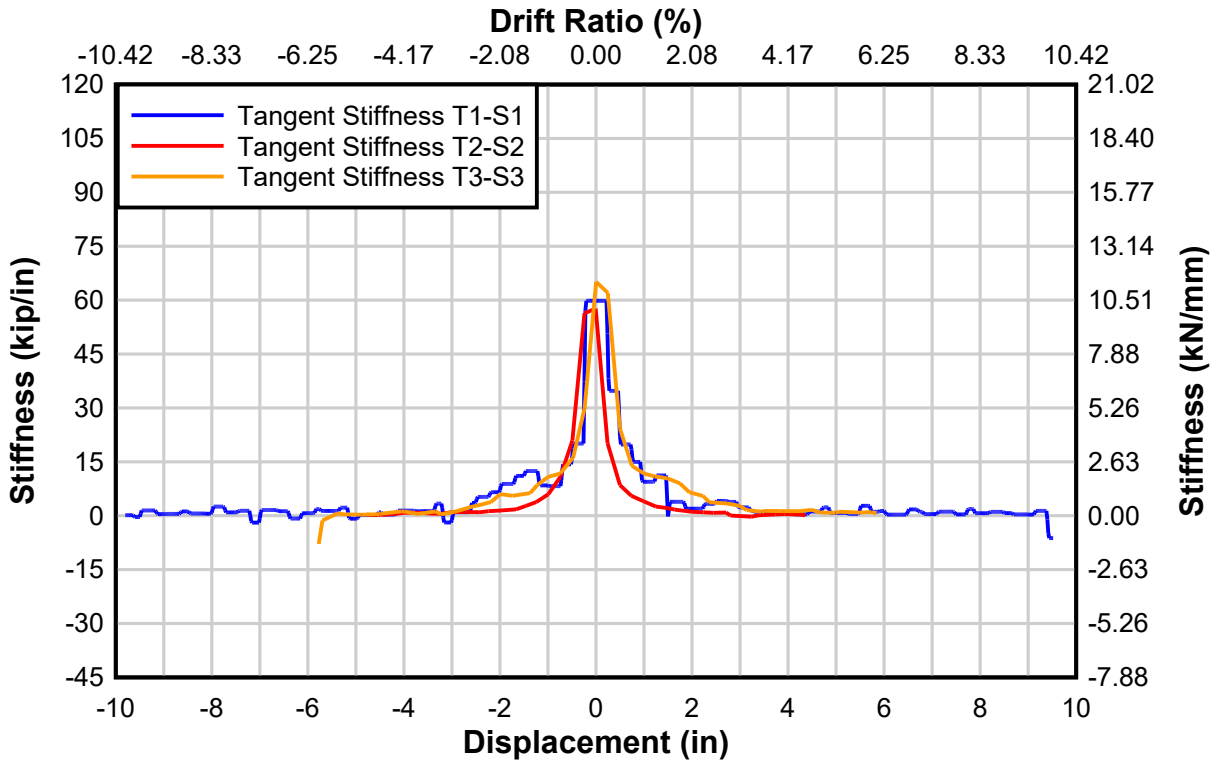

Figure 6.59: Tangent stiffness degradation of specimens on new soil simulant.

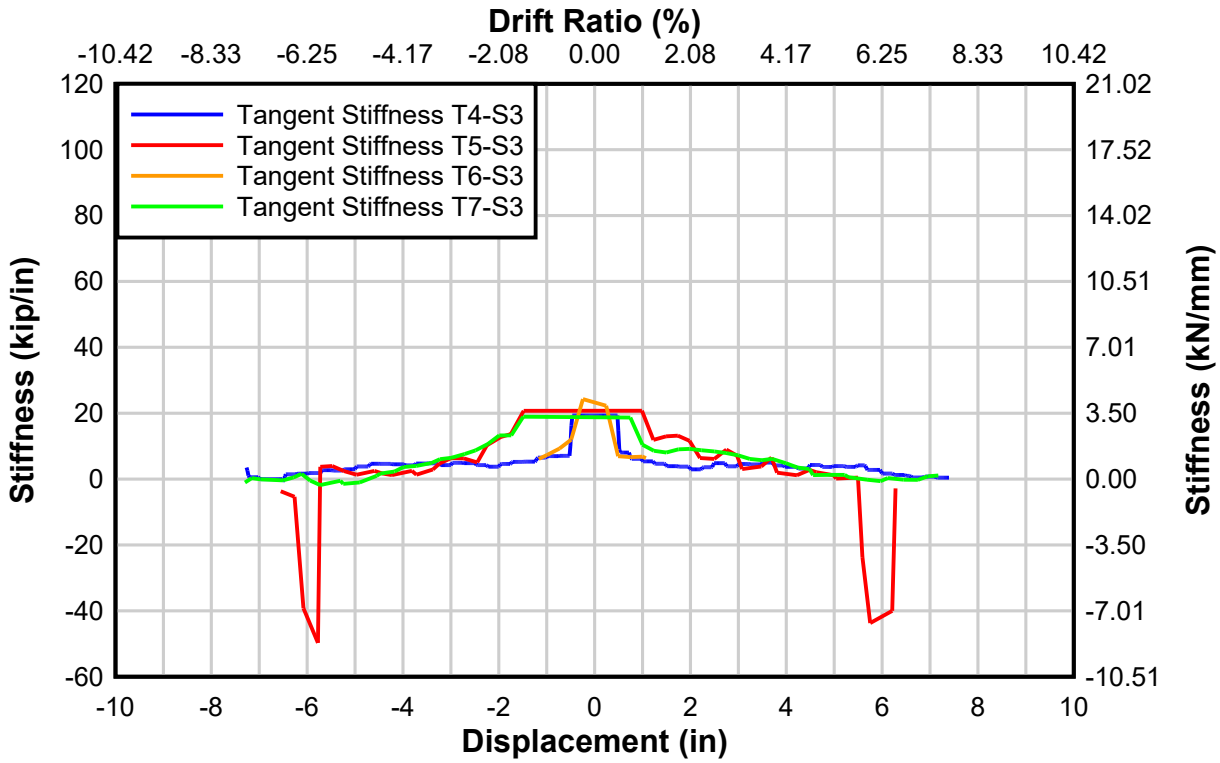

Figure 6.60: Tangent stiffness of specimens on previously damaged soil simulant.

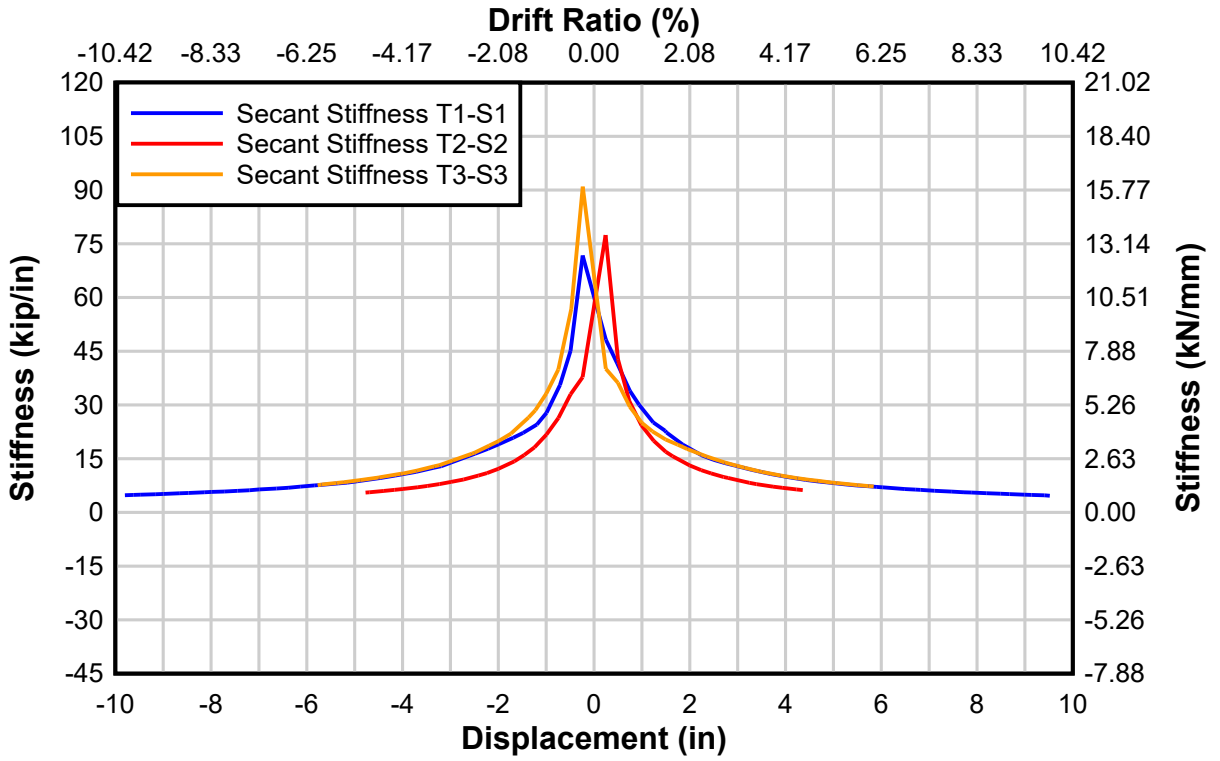

Figure 6.61: Secant stiffness of specimens on new soil simulant.

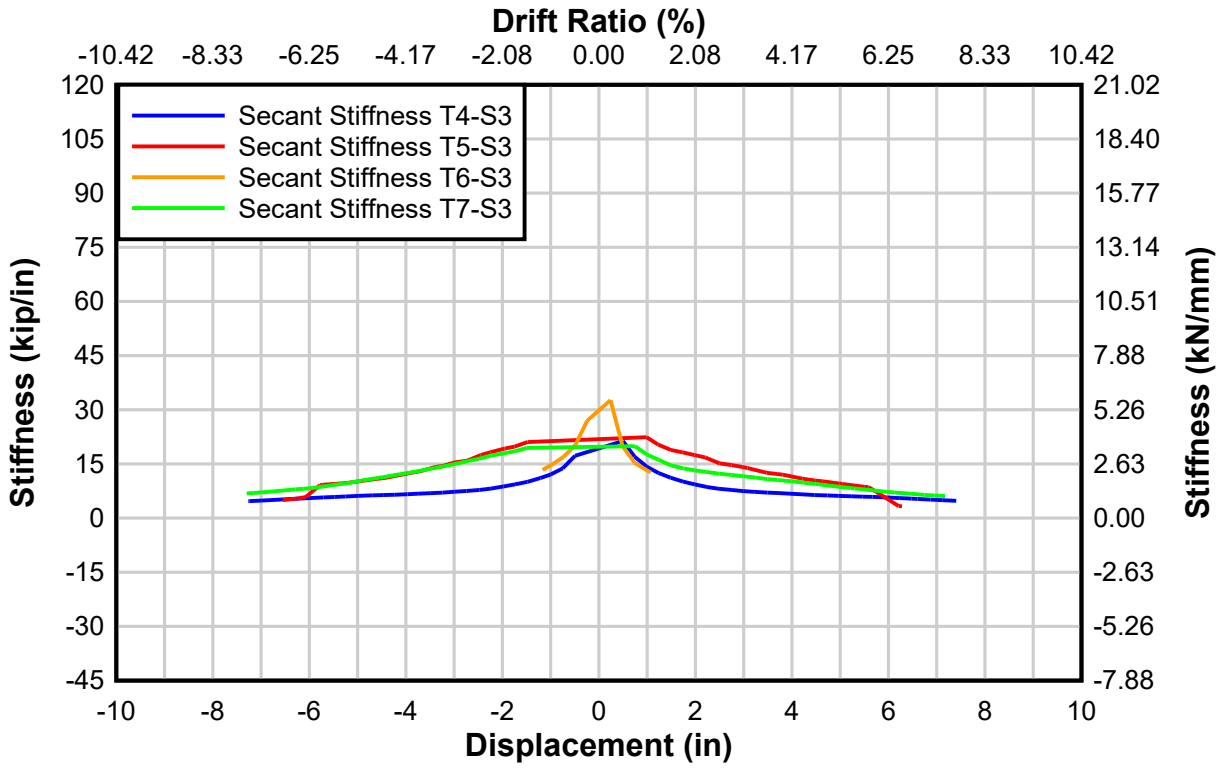

Figure 6.62: Secant stiffness of specimens on previously damaged soil simulant.

Strain Rate

Because the chosen soil simulant is a polymer, it has viscoelastic material properties. Thus, the stress can be sensitive to the strain rate (or rate of loading). Strain for the soil simulant under the footing was taken as an average of three (3) sensors along the center of the footing on the east-west axis and divided by the original thickness of the subgrade. The stress was calculated by dividing the applied axial load in time by the original area of the subgrade in contact with the footing. After failure of the subgrade occurred the area in contact was unknown; therefore, all stress-strain relationships are averages of the engineering stress and engineering strain. As seen in Figure 6.63 and Figure 6.64, a slower strain rate results in a lower stiffness subgrade. While the first test was loaded at a strain rate of 252 με/sec and all subsequent tests on new soil simulant were loaded at a strain rate of 49.6 με/sec. Creep of the soil simulant can be observed in Fig. 6.64 whereby stain increases as the axial stress is held constant. A progressively softer stress-strain response was observed when loading previously damaged soil simulant subgrades due to the changing loaded area and reloading branch from plastically deformed soil simulant. Figure 6.65 shows the average engineering stress-strain relationship for previously failed soil simulant.

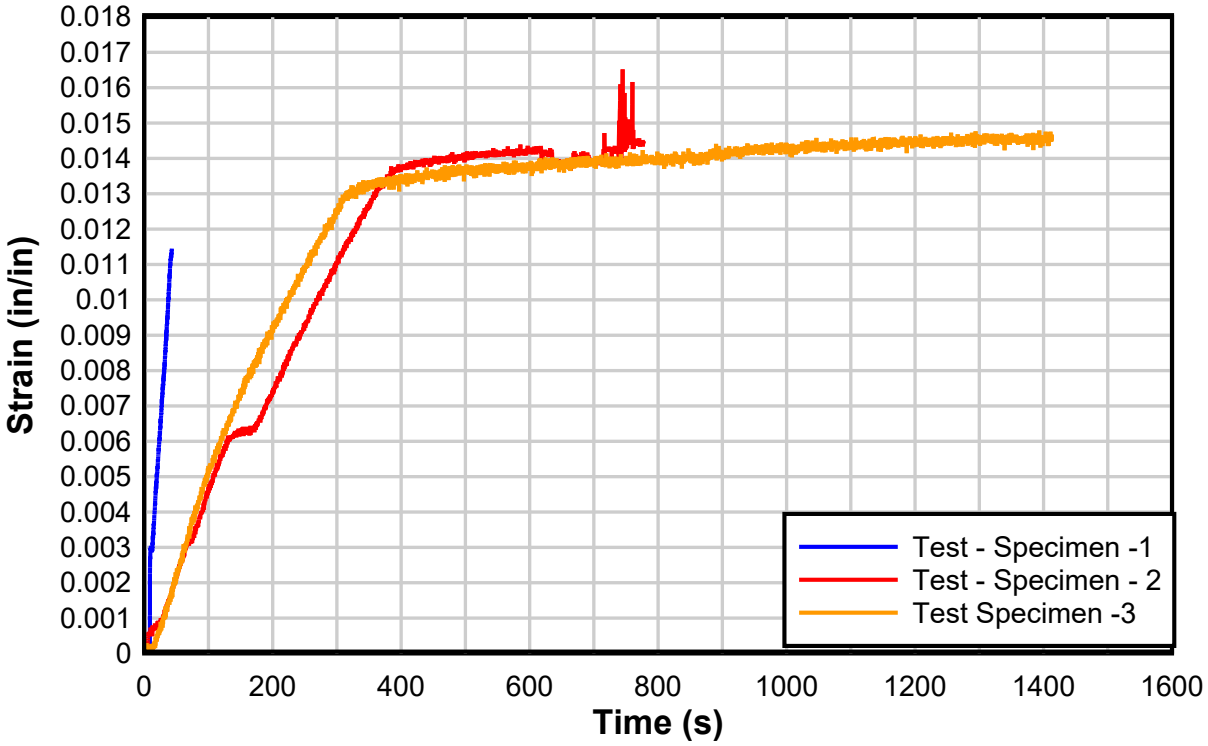

Figure 6.63: Strain rate of axial loading on new soil simulant.

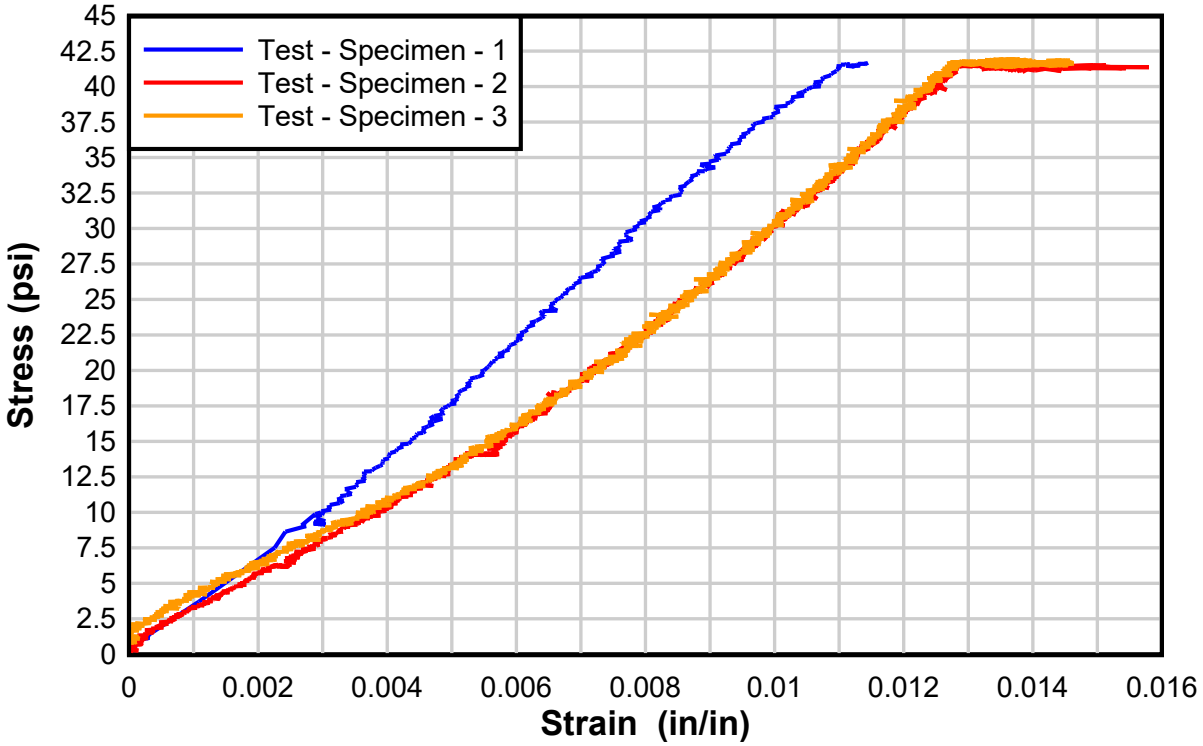

Figure 6.64: Stress-strain relationship of axial loading on new soil simulant.

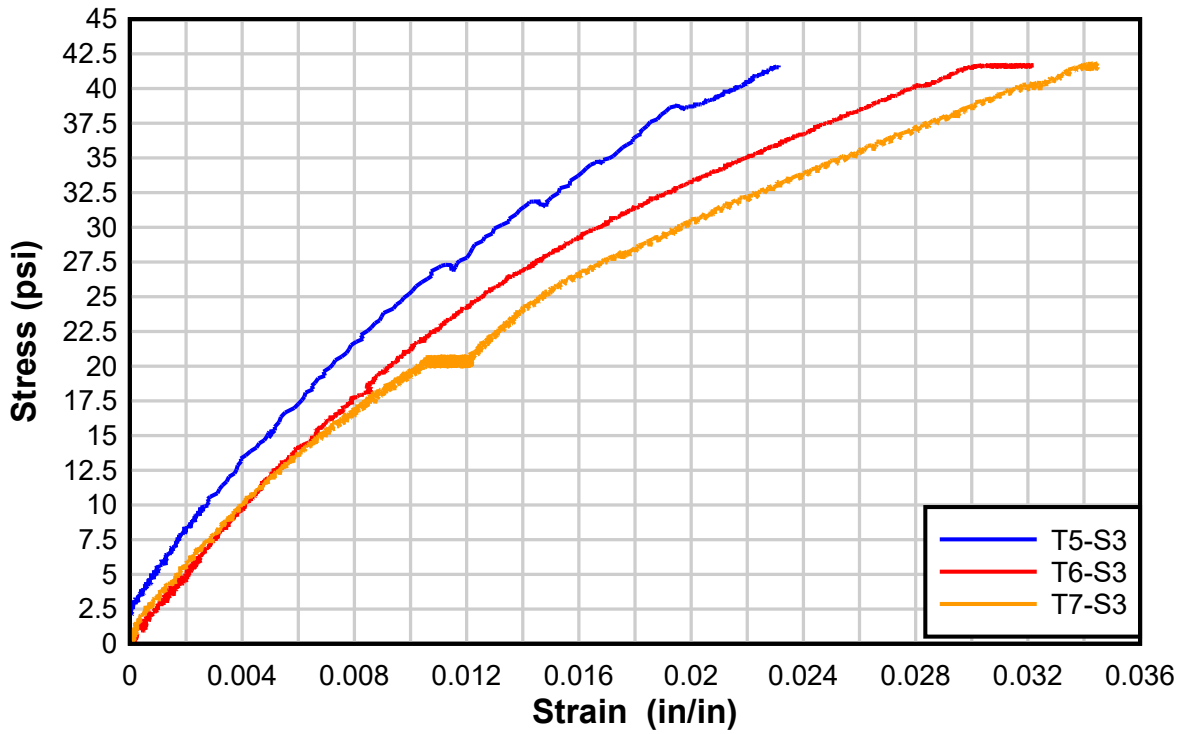

Figure 6.65: Average engineering stress-strain relationship for subsequent axial loading of previously damaged soil simulant.

6.3.4.5 Footing Settlement due to Rocking

Settlement due to rocking for each test was taken as the average of the three (3) sensors along the north and south face of the footing and plotted in relation to the drift ratio to compare the variation in settlement during testing, and on previously failed soil simulant. In Figure 6.66 settlement due to rocking, initial settlement distortions, and recovery of the soil simulant are shown. Settlement distortions were recorded for tests with soil simulant and can be found in Appendix A6.3.

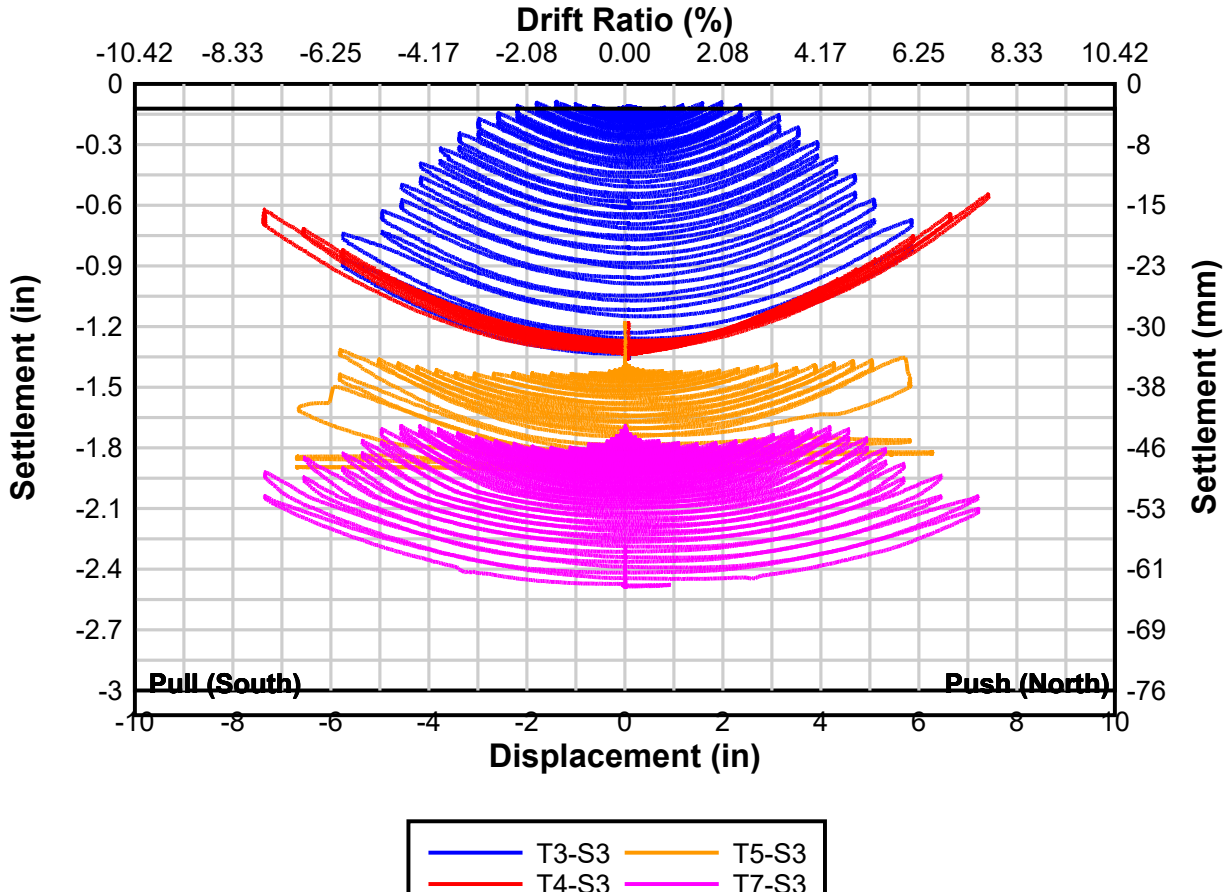

Figure 6.66: Settlement with continued rocking on the soil simulant.

6.3.5 Soil Simulant Model

The experimentally observed SSI responses were used to develop an analytical model of the soil simulant assuming rigid body motion of the footing. The soil simulant was modeled as nonlinear contact springs along the base of the footing and nonlinear contact springs in series with the steel springs. The footing base and face were discretized into 102 mm (4 in.) strips as seen in Figure 6.67, with a length of 1524 mm (60 in.). The model was developed using the average effective elastic modulus of 21.96 MPa (3185 psi) from the axial loading on new soil simulant over the gross area of the footing. The soil simulant model was considered elasto-plastic, with the yield strain, 0.0355 in/in, and yield stress, 779 kPa (113 psi) based on the uniaxial tests completed by Shrestha (2019). The base model was developed separately from the face model to facilitate

flexibility in modeling, and compatibility in the rotation of the footing, and the point about which moments were summed was used to resolve the deformations for a particular rotation in both directions. The soil thickness used was 203 mm (8 in.). An axial load of 667 kN (150 kips) was applied, and initial stress, strain, and settlement were computed using equations 6.14 – 6.16, respectively:

$$\sigma_{initial} = P/A_{footing} \quad \textbf{(6-14)}$$

$$\varepsilon_{initial} = \sigma_{initail}/E_{soil\ simulant} \quad \textbf{(6-15)}$$

$$\Delta_{intial\ settlement} = \varepsilon_{intial} \times h \quad \textbf{(6-16)}$$

where P is the axial load, $A_{footing}$ is the area of the base of the footing, and h is the original thickness of the soil simulant. By convention, the down direction is negative for the base model and away from the springs in the face model.

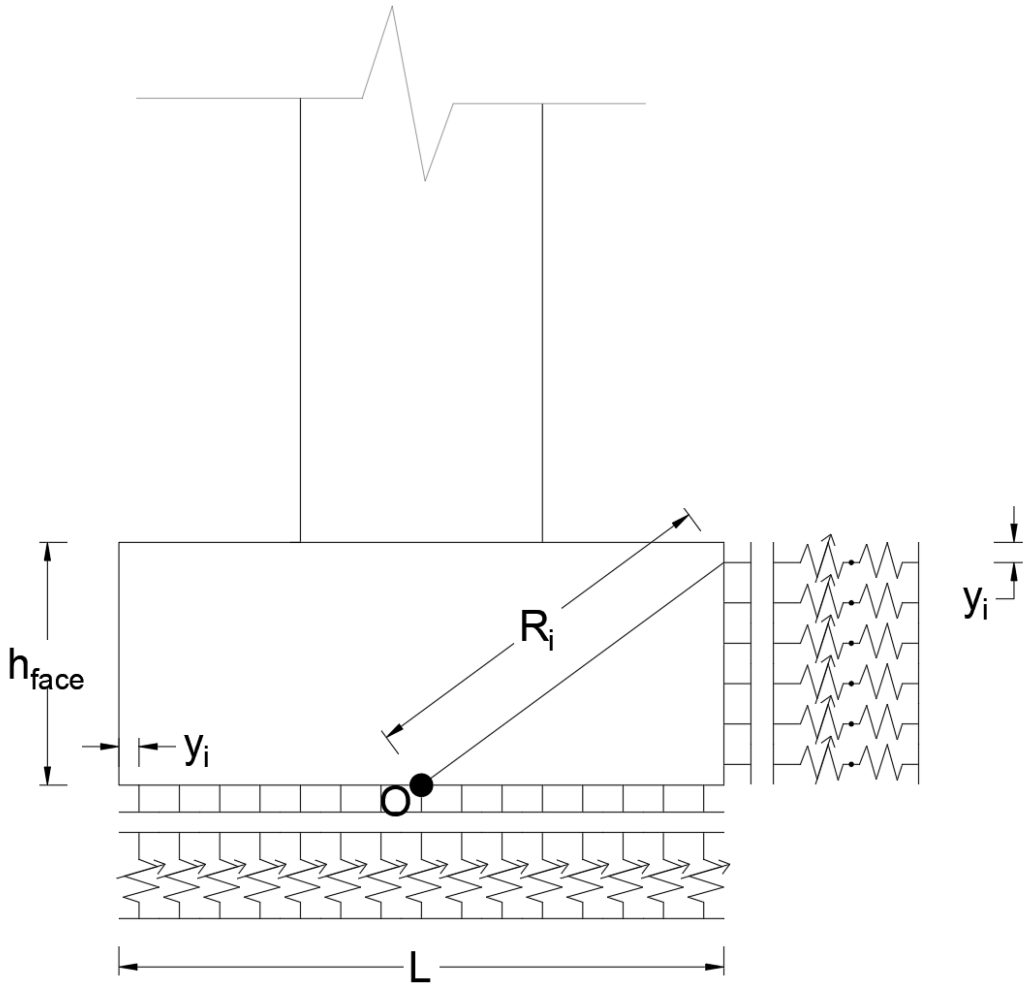

Figure 6.67: Soil simulant model.

6.3.5.1 Model for Contribution from Bottom of Footing

The contribution of the soil simulant at the bottom of the footing to force-displacement response was developed by first imposing a rotation to the footing about the origin labeled as O in Figure 6.67. Given this rotation, the average settlement is computed to achieve equilibrium and the displacement at the top of the column. Average settlement and the displacement at the top of the column were determined using Equations 6.17-6.19, respectively. In 6.17 to 6.19, $\theta_{rotation}$ is the rotation in radians, Δ_1 and Δ_2 are the vertical displacements at each edge of the footing, L is the length of the footing and the distance between the footing corners, and H_L is the distance from the bottom of the footing to the top of the column.

$$\theta_{rotation} = (\Delta_1 - \Delta_2)/L \quad \textbf{(6-17)}$$

$$\Delta_{settlement} = (\Delta_1 + \Delta_2)/2 \quad \textbf{(6-18)}$$

$$\Delta_{top} = \theta_{rotation} \text{ x } H_L$$

(6-19)

A vertical contribution was necessary to obtain equilibrium as the footing tips up on the toe due to the rotation. Total deformation at the ith spring was found using equation 6.20, and strain in the ith spring was found using Equation 6.21.

$$\Delta_{Total,i} = \Delta_1 - (\theta_{rotation} \text{ x } y_i) + \Delta_{vert} + \Delta_{settlement}$$

(6-20)

$$\varepsilon_i = \Delta_{Total} / \text{ h}$$

(6-21)

where Δ_1 is the imposed displacement at the bottom of the footing, y_i is the distance from the toe, and Δ_{vert} is the vertical addition to obtain equilibrium. If the strain in the ith spring is positive, the stress is set to zero because the spring is not in contact. If the strain in the ith spring is more negative than the yield strain, then the stress is set to the yield stress, otherwise stress in the ith spring is calculated using Equation 6.22

$$\sigma_i = \varepsilon_i \text{ x } E_{soil}$$

(6-22)

The force in each spring is then calculated using Equation 6.23.

$$p_i = \sigma_i \text{ x } w_i \text{ x } l_i$$

(6-23)

where w_i is the width of the ith spring, and l_i is the length of the ith spring. The location of each spring was measured from the center of the footing, at the origin O, to the yth depth. This was also the moment arm length used to calculate the moment contribution from each spring. Equations 6.24 and 6.25 were used to calculate the moment arm and moment contribution from each slice.

$$L_y = (L/2) - y_i$$

(6-24)

$$M_y = p_i \text{ x } L_y$$

(6-25)

where L_y is the length of the moment arm from the center of the footing at point O, and M_y is the moment from the yth slice. The total force, total moment, moment arm of the resultant reaction, and the force at the top of the column required to resist the footing induced moment were calculated using Equations 6.26 – 6.29.

$$\mathbf{P_{footing} = \Sigma\, p_i} \tag{6-26}$$

$$\mathbf{M = \Sigma M_y} \tag{6-27}$$

$$\mathbf{L_M = M/P_{footing}} \tag{6-28}$$

$$\mathbf{H = M/H_L} \tag{6-29}$$

The initial assumption is that the point of rotation of the footing does not change from point O (Figure 6.67). However, because this point changes in reality, a vertical motion is needed to achieve equilibrium. The vertical addition was iterated to find equilibrium between the applied axial load, the reaction at the base of the footing, and the lateral load at the top of the column. According to the model, as the moment becomes constant, the soil simulant resultant force is located 0.457 m (1.5 ft.) from point O (Figure 6.67). The force-displacement response backbone curve from the model was compared to the force-displacement backbone curve from Test 2 of Specimen 2 as seen in Figure 6.68. The response in the model was assumed to be symmetric. The pull side was closer to the experimental response than the push side because of the stiffer side of the test setup.

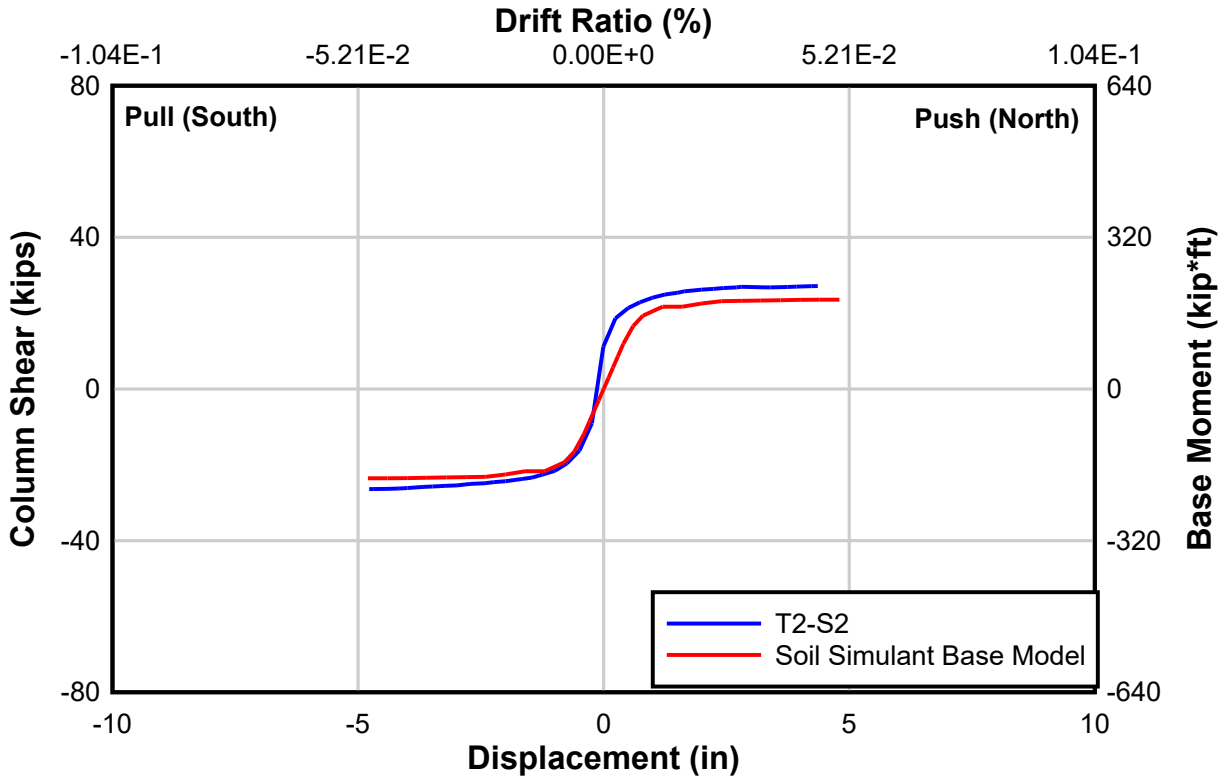

Figure 6.68: Comparison of the soil simulant model with experimental response from Test 2 of Specimen 2.

6.3.5.2 Model for Contribution from Footing Face

The contribution from the soil simulant along the face of the footing was treated separately in the model using the same size nonlinear contact springs as the footing base along the 610 mm (24 in.) depth. The back face pressures and horizontal shear at the bottom of the footing are neglected in this analysis as the column shear is assumed to be resisted by the soil acting on the front footing face. The rotation from the footing base model was used to maintain compatibility when combining the footing base and face model contributions. The initial radius from the origin, O, to the center of each spring, where the intended reaction of each spring was assumed to be, was taken as Equation 6.30, and an initial angle in radians was determined using Equation 6.31:

$$R = ((L/2)^2 + (h_{face} - y_i)^2)^{1/2} \quad \textbf{(6-30)}$$

$$\theta = \arccos(L/R) \quad \textbf{(6-31)}$$

where $L/2$ is the length from the center of the footing, at point O, to the toe, h_{face} is the height of the footing on the face, and y_i is the depth of the ith spring. An adjustment angle

is then calculated as the difference between the original angle theta and the angle of imposed rotation, and a new horizontal deformation was calculated using Equations 6.32, 6.33, and 6.34:

$$\theta_{adj.} = \theta - \theta_{rotation} \quad \textbf{(6-32)}$$

$$R_{adj.} = R \times \cos(\theta_{adj.}) \quad \textbf{(6-33)}$$

$$\Delta_i = L' - L \quad \textbf{(6-34)}$$

The change in horizontal distance, Δ_i, is calculated as the difference between the new horizontal distance, L', and the original horizontal distance, L, as seen in equation 6.34. This difference is the displacement of the footing at y_i for any given rotation. Soil simulant strain can then be found using equation 6.35. Because the model uses contact springs and the footing rotates into the springs at the face at larger displacements the toe of the footing moves away from the springs; therefore, if the strain is negative the footing is not in contact with the springs. Stress in the soil simulant springs depends on the strain amplitude. If the strain is negative then the stress is set to zero, if the strain is greater than the yield strain then the stress is set to the yield stress, otherwise it is calculated using Equations 6.36.

$$\varepsilon_{soil} = \Delta_i / w_{soil} \quad \textbf{(6-35)}$$

$$\sigma_{soil} = \varepsilon_{soil} \times E_{soil} \quad \textbf{(6-36)}$$

The force in each soil simulant spring could then be derived using Equation 6.37. This was then be used to inform the displacement of the steel springs by Equation 6.38, based on the stiffness of the steel springs discussed in Section 6.2.6.2.

$$p_i = \sigma_i \times A_{soil} \quad \textbf{(6-37)}$$

$$\Delta_{steel} = p_i / K_{steel} \quad \textbf{(6-38)}$$

where A_{soil} is the area of the ith spring series, and K_{steel} is the stiffness of the steel at the yth depth. This process is iteratively solved from equations 6.34 to 6.38 for each spring along the height of the footing by updating the foam displacement based on the calculated steel displacement in the previous iteration. The moment contribution from the yth depth was found using equation 6.39; moments are summed about the center of the footing at point O, as seen in equation 6.40, and the force resultant is determined using equation 6.41.

$$\mathbf{M_y = p_i*(h_{face}-y_i)} \tag{6-39}$$

$$\mathbf{M_{face} = \Sigma M_y} \tag{6-40}$$

$$\mathbf{H' = M_{face}/(H_L-h_{face}/2)} \tag{6-41}$$

The forces acting on the face and the bottom of the footing were summed to combine their effects and produce a force-displacement backbone curve for the given displacements of the imposed lateral displacement protocol from Section 6.2.6. Figure 6.69 is a comparison of the model backbone curve to the backbone curve from Test 1 of Specimen 1 with new soil simulant.

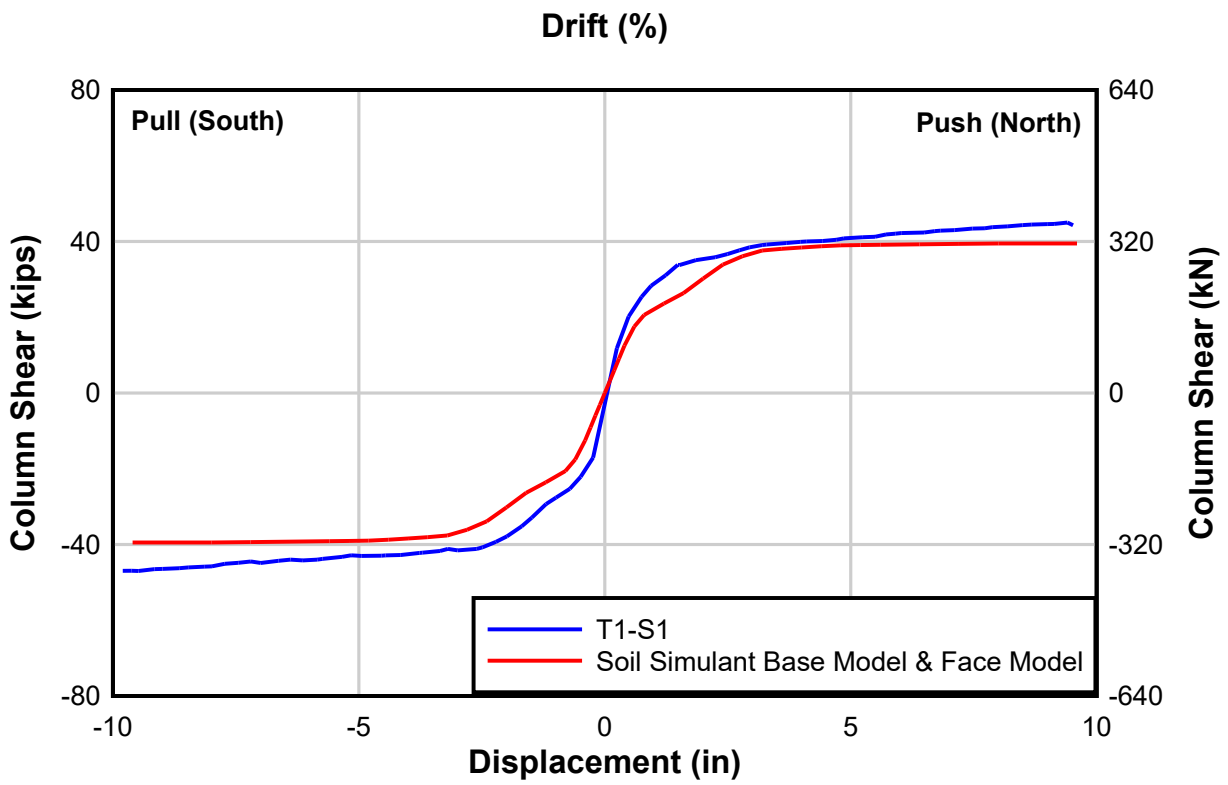

Figure 6.69: Comparison of soil model, including face and base, with experimental results.

Because failure of the vintage column did not occur with the soil simulant, the soil simulant was removed and only the steel springs were used as an embedment soil for the footing face; furthermore, the soil simulant subgrade had already plastically deformed. Figure 6.70 illustrates the comparison of a backbone force-displacement response, with new soil simulant and steel embedment soil, with Test 5 of Specimen 3 backbone force-displacement response. Comparison plots were made for all tests assuming ideal springs and new soil simulant and can be found in Appendix A6.3. It is important to note that in Test 5 progressive damage to the face of the footing reduced the reaction area of the springs, and the soil spring model does not have limits set for column failure or steel spring nonlinearity.

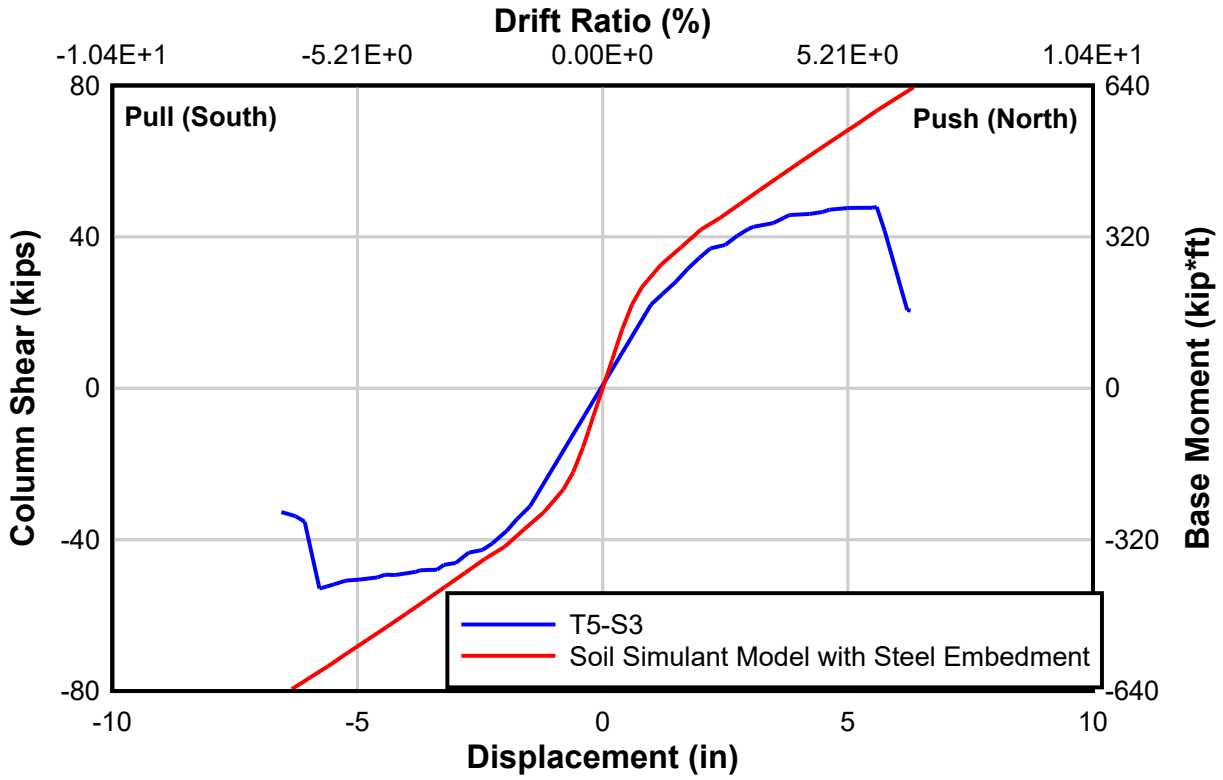

Figure 6.70: Soil simulant model comparison using a previously damaged soil simulant under the footing and steel springs at the face of the footing.

6.3.6 Post-Failure TiAB Retrofit

To better understand the performance of the TiAB retrofit two (2) tests were completed after the SSI investigation of the vintage column that produced failure of the unretrofitted column. Firstly, the column was left in place, latent spalled concrete was removed. Then TiAB ligaments were installed, and the specimen tested with small laterally imposed displacements. Then the retrofit was completed by installing the two (2) TiAB spirals and casting the concrete shell. To mimic realistic conditions of column performance after failure and installation of the retrofit, the soil simulant that failed in previous tests 3-5 was kept under the specimen. The final conditions that resulted in the vintage column failure were repeated by placing only the steel spring soil embedment on the north and south footing faces. The intent of these tests was to investigate retrofit performance that might occur during aftershocks, or subsequent earthquakes.

As previously stated, the column failed during Test 5 after failure of the lap-splice. Eventual loss of flexural tension capacity in the column occurred due to damage in the lap-splice region resulting in bond-slip of the column bars and starter bars. The response of the specimen in the failed condition at small excursions were captured for comparison with the incrementally retrofitted column.

The influence of the TiAB ligaments alone were shown previously in Figure 6.33 that shows that ligaments do not significantly increase the expected yield moment for a service axial load of 667 kN (150 kips). Their intent is not to provide strength, but an alternate flexural load path after

failure of the reinforcing steel lap splice. This can also be seen in the overall force-displacement response for Test 6 (Figure 6.38) when comparing the capacity of the column after failure and the response of the column with only ligaments. Ligament installation occurred without the axial load applied. These results may be more directly compared to a case in which the damaged bridge is actively shored to remove axial load from the column during installation of the retrofit.

Lastly, the retrofit was completed as described in Section 6.2.3. Without retrofitting, or repair of the footing, the Specimen 3 was tested again in Test 7 and the results were compared with Test 1of Specimen 1 as seen in Figure 6.71. The completely retrofitted failed column was able to sustain a higher load than the pristine vintage column with a complete retrofit. This is most likely due to the steel spring soil simulant at the footing face for Test 7. The retrofitted failed column performed as well as the retrofitted pristine column which can be attributed to casting of new concrete in the shell that also serves to restore the previously failed lap splice. The shell thus provided two (2) benefits; it prevented pull-out and elastic buckling of the TiAB ligaments on the compression face of the column and it restored the bond between the lap-spliced column reinforcing steel bars.

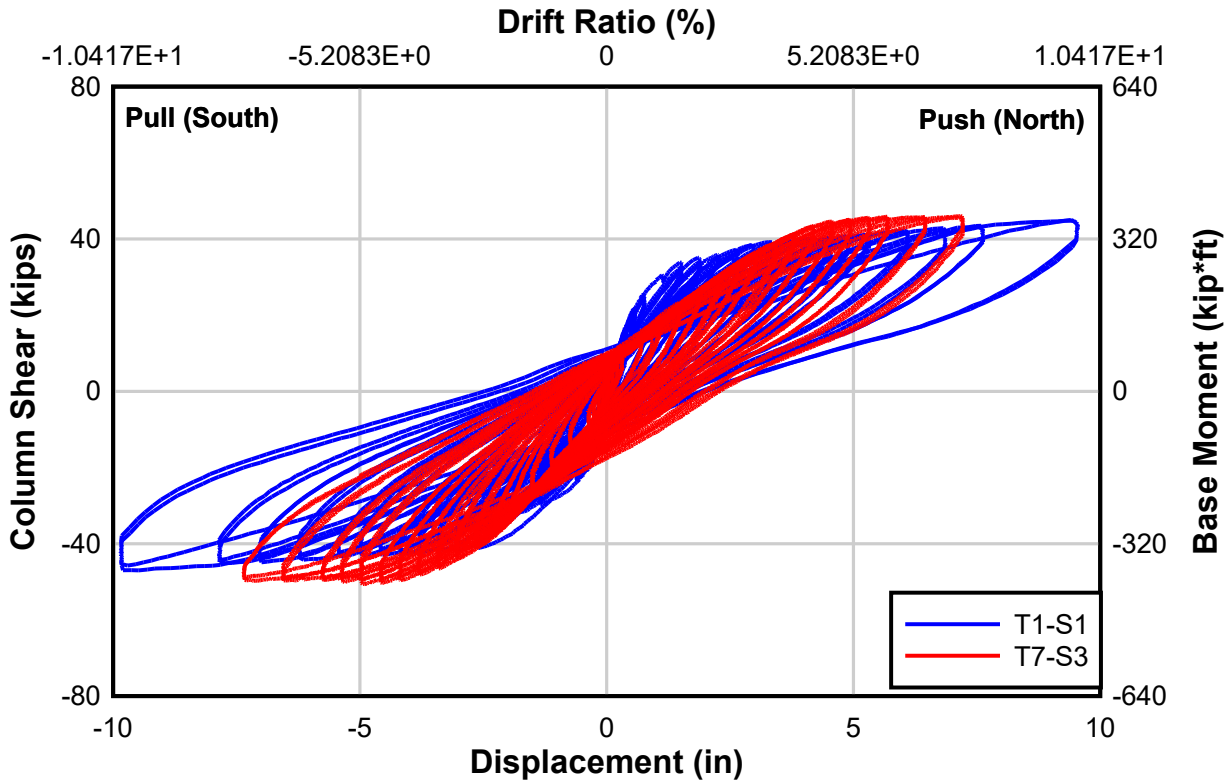

Figure 6.71: Comparison of a failed column with a complete retrofit repair and pristine vintage column with a complete retrofit.

6.3.7 Vintage Footing Performance

After testing, the specimens were removed from the soil simulant and the base of each footing was inspected for damage. Observed damage was noted and recorded in specimens that exhibited cracking along the base. Shrestha (2019) observed a crack pattern in center of the footing in both

directions. The footing of Specimen 1 after Test 1 exhibited a similar pattern. Figure 6.72 illustrates the crack patterns in each footing.

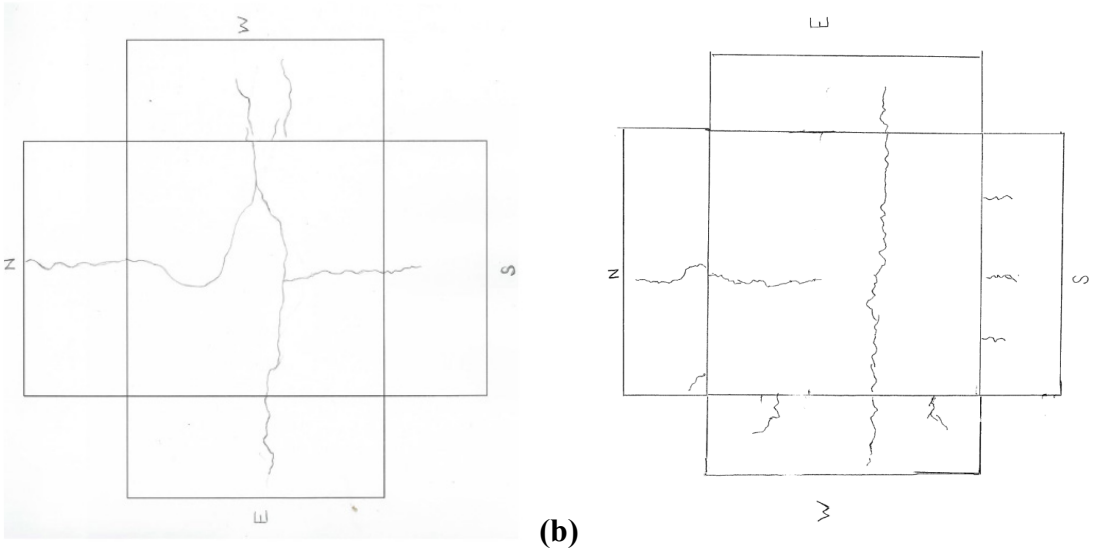

(a) **(b)**

Figure 6.72: Observed cracking patterns in the footing: (a) illustration of footing damage in specimen R-S-R-LTi-90-Spread (Shrestha 2019), and (b) illustration of footing damage in T1-S1.

In the direction of bending imposed on the column and footing for the present study, cracking between the east and west faces across the bottom of the footing would be anticipated based on one-way bending. However, the cause of cracking between the north and south faces is less obvious but can be anticipated when considering a truss model for the force transfer mechanism through the footing between the column and soil. The cracking moment can be found using Equations 6.42-6.44, with Equation 6.43 from AASHTO-LRFD 5.4.2.6 for the modulus of rupture of concrete:

$$S = 1/6 \times b \times h^2 \quad \textbf{(6-42)}$$

$$f_r = 0.24 \times f'c^{0.5} \quad \textbf{(6-43)}$$

$$M_{cr} = S \times f_r \quad \textbf{(6-44)}$$

where *S* is the section modulus of the footing, b is the width of the footing, h is the thickness of the footing, f'_c is the compressive strength of the concrete (ksi), and M_{cr} is the cracking moment. The cracking moment of the footing is nominally 244 kip-ft. As the soil force resultant location

under the footing increases at higher rotations, the moment in the footing eventually becomes large enough to induce flexural cracking in the cracking due to one-way bending.

The horizontal force acting on the vertical face of the footing is ignored as no damage was observed in the footings when the soil simulant was used. It was only observed when the steel springs were placed directly against the face of the footing and allowed to become nonlinear. In practice, soil failure will occur and thereby limit the pressures exerted on the face of the footing.

Capturing the cracking in the orthogonal direction of lateral loading requires development of a phenomenological model that represents the load path the axial load takes through the footing. To accomplish this task, a Strut-and-Tie Model (STM) was developed using Chapter 23 of ACI 318-19. A separate technical design guide is provided for the STM using AASHTO-LRFD provisions. A direct strut STM was developed to represent the force flow through the footing and is illustrated in Figures 6.73 to 6.75. At 2% lateral drift the soil simulant begins to yield; therefore, this displacement was chosen as the representative case for the STM. The nodal surfaces were first determined and then the nodes were turned 45˚ for mathematical and visual convenience. The width of the top node in the plan view was chosen as half of the width of the column.

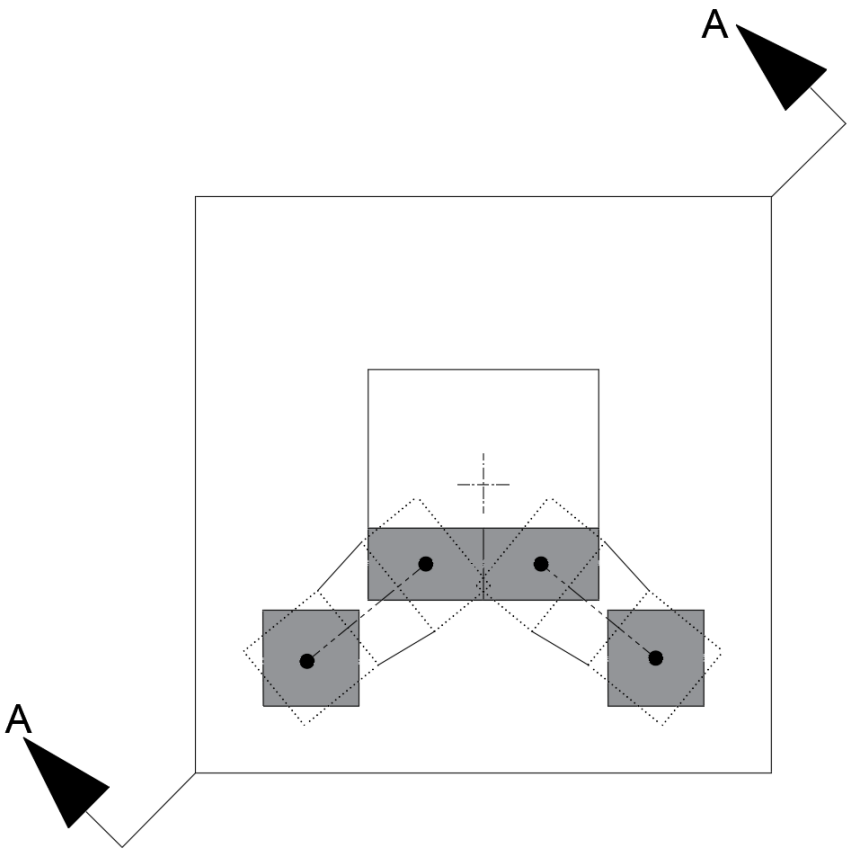

Figure 6.73: Plan View of the STM to carry column axial load into the subgrade reaction through the footing due to rocking.

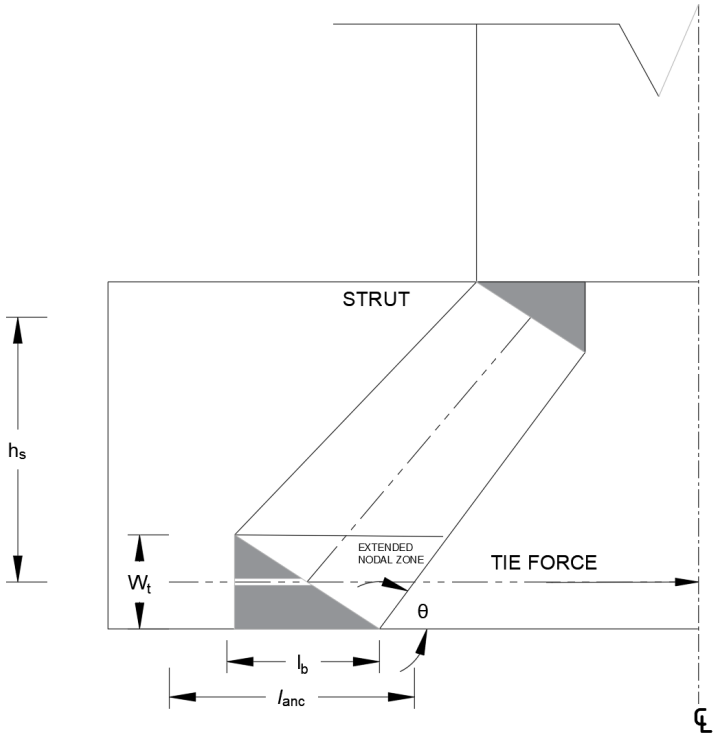

Figure 6.74: Elevation of the STM at Section A-A with end nodes rotated 45 degrees for convenience.

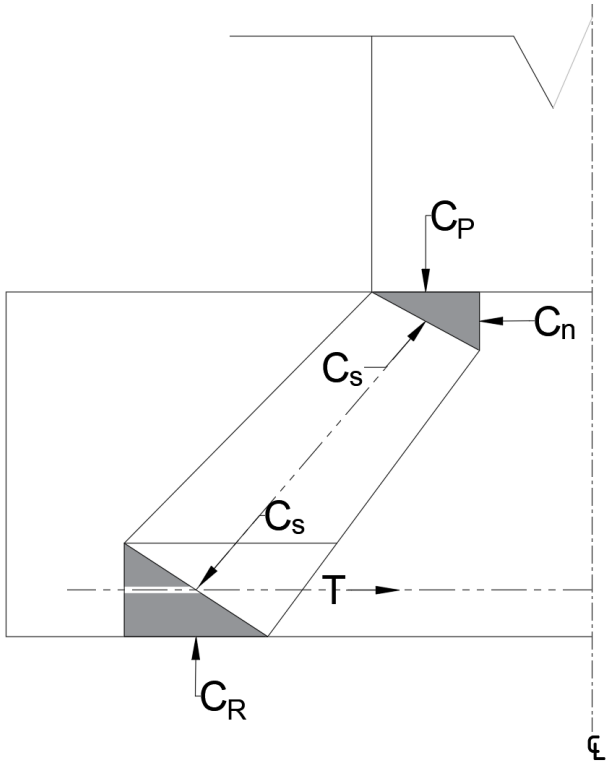

Figure 6.75: Forces acting on nodes.

Considering axial load-moment interactions for the column and the actual material properties used in the specimens the neutral axis location can be found as illustrated in Fig. 6.76. For the present case, the neutral axis location for 667 kN (150 kip) axial load in the column is located 190 mm (7.5 in.) from the compression face of the column. This served as the length of the upper node. Because there is no distinguished bearing area under the footing as the specimen undergoes rocking behavior, the bearing area on the bottom of the footing was determined using the soil model described previously in Section 6.3.5 and the resulting stress profile is illustrated in Fig. 6.77

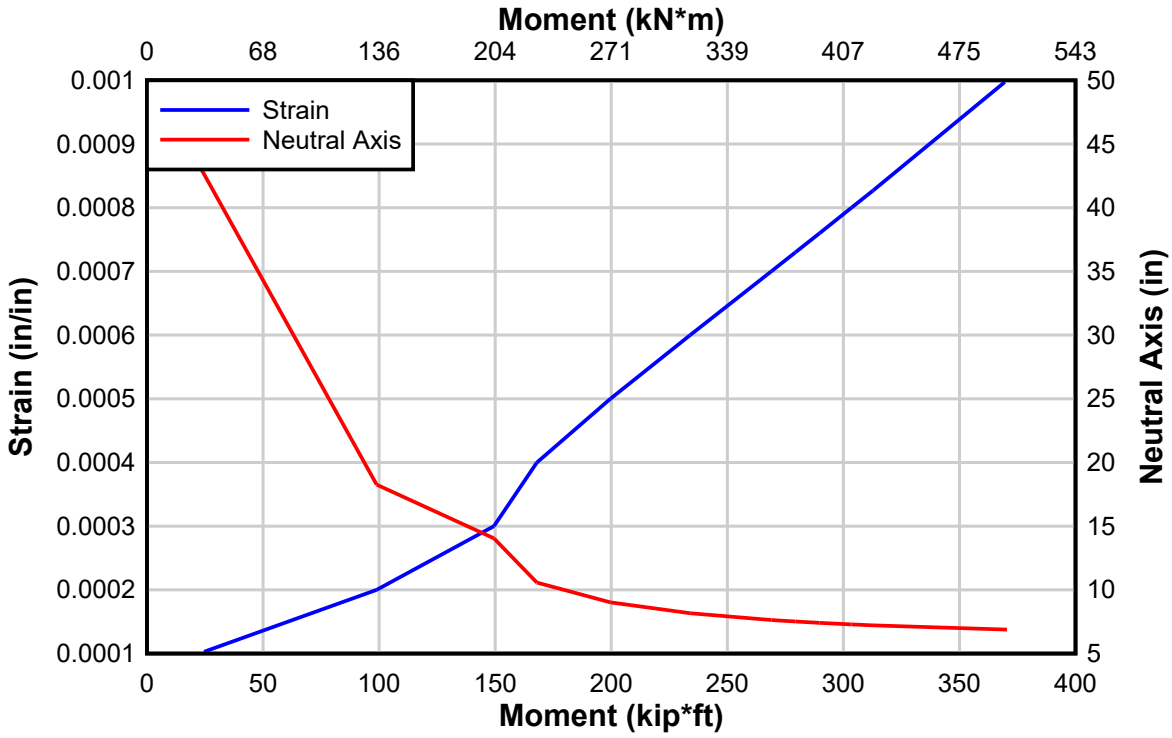

Figure 6.76: Expected moment-column compression strain interaction as the neutral axis varies.

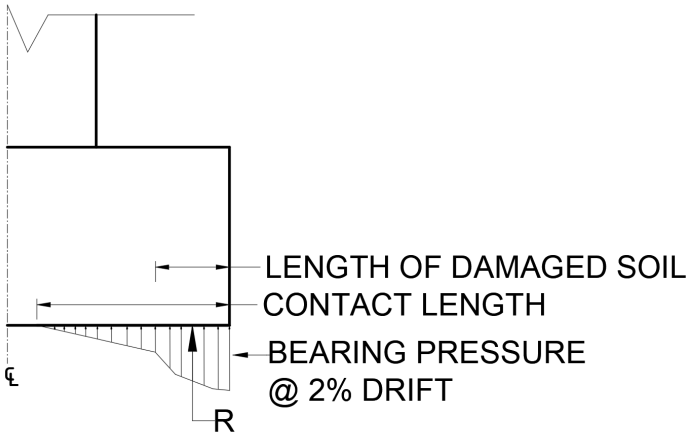

Figure 6.77: Location of resultant and length of plastically deformed soil from soil simulant model at 2 % drift.

The bearing area for the bottom node in the footing was selected based on the length of soil simulant under the footing that achieved yield. Thus, a bottom node measuring 254 mm (10 in.) square was used, as seen in Figure 6.73. Furthermore, the bottom node was placed at the location of the soil force resultant. The dimension, W_t, of the bottom node was then chosen as 165 mm (6.5 in.) using ACI 318-19 R.23.8.1.a. The planes of the top and bottom nodal faces that intersect with the strut were assumed to be parallel and the remaining dimensions of the upper node were determined, making the W_t of the upper node as 124 mm (4 – 7/8 in.). The line of action of the strut was determined to be where the axial force, C_p, and the reaction force, C_R, intersect at the diagonal face of each node. The tie, T, was located in a plane centered 82.5 mm (3-1/4 in.) from the bottom surface of the footing, and has a line of action intersecting C_R and C_s. An extended nodal zone was used to maximize available development length. The development length of the footing reinforcing steel was determined to be 305 mm (12 in.) in accordance with ACI 318- 19 section 25.4.2.1. The angle between the strut and tie was then determined, based on the geometry of the model, to be 54˚. The width of the strut W_s at the face of each node as determined using equation given in ACI 318-19 Fig. R23.2.6.b seen below as Equation 6.45.

$$W_s = W_t \, x \cos\theta + l_b \sin\theta \qquad \textbf{(6-45)}$$

The smaller area of the face of each node in which the forces converged was then calculated using equation 6.46 as described in ACI 318-19 R23.4. The effective compressive strength of the compressive elements was also determined using ACI 318-19 23.4.3, written as Equation 6.46. β_c and β_s were determined equal to 1.0 and 0.7 respectively, from ACI318-19 Table 23.4.3.

$$\mathbf{A_{cs} = W_s \; x \; 12in.} \qquad \textbf{(6-46)}$$

$$f_{ce} = 0.85\beta_c\beta_s f'_c$$

(6-47)

Tie strength is derived from the reinforcing bars that are oriented in both directions at the bottom of the footing. The strength of the tie oriented in the 45˚ orientation used for the model was broken down based on the vector components. In the direction of loading, N-S direction, all of the steel participates based on the footing surface in bearing. This was observed in the experimental data where even bars under the column exhibited yield. In addition, four (4) bars were assumed to be acting E-W direction based on the length of footing in bearing in this direction. The strength of the strut was calculated as 1103 N (247.8 kips), and the tie strength was calculated to be 192 N (43.2 kips). The strengths were determined in accordance with ACI 318-19 23.4.1 and 23.7.2 using equations 6.48 and 6.49.

$$F_{ns} = f_{ce} \text{ x } A_{cs}$$

(6-48)

$$F_{nt} = A_{ts} \text{ x } f_y$$

(6-49)

where A_{ts} is taken as the participating area of steel reinforcement, and f_y is the yield strength of the steel reinforcement. The strength of the node was then determined to be 690 N (155 kips), in accordance with ACI318-19 23.9, using equations 6.50 and 6.51. β_n was computed as 0.8 from ACI318-19 Table 23.9.2, and A_{nz} was taken as the area of the smallest face on the upper node as a conservative estimate.

$$F_{nn} = f_{ce} \text{ x } A_{nz}$$

(6-50)

$$f_{ce} = 0.85\beta_c\,\beta_n f'_c$$

(6-51)

The component strengths were then compared to the forces acting in each element. The applied axial force of 667 kN (150 kips) was divided into each of the two (2) column nodes. This means there was 334 kN (75 kips) acting vertically into the top node, equal and opposite to the reaction force in the bottom of the footing. Based on the geometry of the STM, the force acting in the strut was 412 kN (92.7 kips) and the force in the tie was 243 kN (54.5 kips). Based on the results of the analysis it was determined that the limiting components in the STM are the upper node and the tension tie. The STM can then be updated for different footing rotations and the corresponding changes in soil pressure distributions to compute strengths. Bearing failure of the soil would be the limiting condition and act to limit the forces.

6.4 CONCLUSIONS

Many bridges remain in service in the United States and worldwide that were constructed without consideration of modern seismic design standards and practices. These bridges are expected to exhibit poor performance under seismic loading. The cause of poor performance is often due to inadequate RC substructures, especially the supporting columns and foundations that have seismically deficient details. The most common deficiencies include insufficient lap-splice length, lap-splices located within the plastic hinge region, and insufficient confinement of the concrete core due to a lack of transverse reinforcement. These deficiencies contribute to non-ductile behavior during earthquakes that can lead to collapse and significant impairment of the transportation system. The most financially and environmentally sustainable approach for improving the robustness of seismically deficient substructures is to retrofit them. There are many techniques available to retrofit deficient RC columns; however, each technique has inherent drawbacks. This led to the more recent development of a novel retrofit approach that makes use of TiABs. Due to durable and high-strength material properties, ease of installation, and resulting high seismic performance TiABs are a viable option for seismic retrofitting deficient RC bridge columns.

While the flexural capacity and ductility of deficient RC columns retrofitted with TiAB have been established, sufficient data on the impact of soil-structure interactions on seismic retrofit design decisions are not available. In general, there is limited data on soil-structure interactions including nonlinear soil response for full-scale RC substructures.

This research reports on eight (8) experimental tests of three (3) full-scale square RC column-footing specimens constructed with vintage reinforcing details. The specimen proportions, materials, and details were based on an ODOT bridge inventory review of critical transportation corridors consisting of I-5, US-97, and OR-58. All footings were 1.52 m (5 ft.) square spread footings that measure 0.61 m (2 ft.) in depth and all columns were 0.61 m square and were 2.44 m (8 ft.) tall. All specimens were subjected to column axial load and then tested under fully reversed-cyclic lateral displacements. The experimental results were described in terms of overall force-displacement response, the contribution of the different components to the overall force-displacement response, P-Delta effects, strain distributions, and the effects of SSI.

Based on the experimental findings, an analytical model was developed to capture the effects of the soil simulant used under and at the vertical faces of the footing. Nonlinear contact springs were developed with the elastic stiffness based on the effective bulk properties of the measured specimen responses during application of the axial load and a constitutive model based on previous uniaxial testing. The soil-footing model was used to further develop a design/analysis model for the footing using STM.

Based on the experimental results and analytical findings in this section, the following conclusions are presented:

1. Installation of a second spiral only requires a single person and is not more difficult to place than a single spiral. The second spiral prevented the previously observed column sliding translation at the column-footing interface.

2. Axial soil simulant stiffness was dependent on strain rate. During lateral loading, the soil simulant is subjected to varying strain rates over the surface of contact with the footing which influences the stress distribution.

3. The vintage columns retrofitted before failure did not exhibit notable damage when lateral displacement was applied, even to very large drift levels for the conditions investigated. Instead, rocking of the foundation occurred with large inelastic deformations in the soil simulant that limited forces produced in the column and footing.

4. Embedment provided approximately 1/3 of the lateral capacity during a rocking footing condition. The contributions from deeper embedment and stiffer/stronger soils would be expected to further increase this effect. If the soil strength is sufficient, it can lead to higher column demands which could lead to failure of unretrofitted columns.

5. Bearing capacity was sufficiently large to counter P-Delta effects during rocking but should not be relied on in the design of bridge substructure.

6. Reduced axial load on a column specimen increased the tensile demand in the flexural steel of the column resulting in more flexural damage along the lap-splice length. Even with the increased demands, the soil simulant enabled foundation rocking, which limited the overall demand, and the column did not fail even at very large drift.

7. Flexural cracking over the lap-splice length was observed at large drifts during rocking, but the lap splices did not fail when the soil simulant was used at the faces of the footing.

8. When stiffer soil simulant was placed at the faces of the footing (steel soil springs), sufficient resistance was produced by the foundation to increase the demand in the column and eventually the unretrofitted vintage column failed. The specimen exhibited non-ductile behavior due to failure of the lap splices.

9. TiAB ligaments provide an alternative flexural tension load path to replace that provided by the reinforcing steel after the lap splice fails.

10. If the TiAB ligaments are used without the concrete shell, they can buckle elastically when the column moment places them into compression.

11. TiABs begin to act more strongly in tension after the column axial load precompression is overcome.

12. A failed column that was retrofitted with TiAB ligaments and spirals performed as well as a pristine retrofitted column when placed on simulated soil that allowed foundation rocking to occur.

13. Lack of reinforcement in the top of the footing produced a non-ductile response of the footing when it was restrained from rocking by anchoring the top surface. Significant retrofitting of the footing may be required if a retrofit approach seeks to prevent foundation rocking as tensile stresses are produced in the top surface of the footing and typically there is no upper reinforcing steel located in that region.

14. The soil simulant used in this study exhibited viscoelastic material properties and provided properties that allowed reasonable laboratory simulation of column-footing-soil response including settlement, plastic soil deformations due to rocking, stiffening of the soil, and rocking footing behavior.

15. A model was developed that could capture the nonlinearly distributed pressures acting on the bottom and vertical face of the footing. The model reasonably predicted the experimentally observed overall response.

16. A 3D strut-and-tie model was developed based on the experimental observations and soil-spring contact model that permits estimation of the capacity of reinforced concrete footings during rocking and explains the cracking observed in the footing.

17. The findings of this study demonstrate that interactions between the column-footing-soil need to be properly accounted for to ensure the desired seismic performance when considering and implementing seismic retrofit strategies on bridge substructures.

6.5 REFERENCES

AASHTO. (2017). *AASHTO LRFD Bridge Design Specifications* (8th ed.). American Association of State Highway and Transportation Officials

ACI Committee 318. (2014). *Building code requirements for structural concrete (ACI 318-14): an ACI standard: commentary on building code requirements for structural concrete (ACI 318R-14), an ACI report*. Farmington Hills, MI: American Concrete Institute.

ACI Committee 440. (2017). *ACI 440.2R-17: Guide for the Design and Construction of Externally Bonded FRP Systems for Strengthening Concrete Structures*. *ACI 440.2R-17*. Detroit, MI.

Allmond, J. D. (2014). Shallow Rocking Foundations in Liquefiable and Saturated Soil Conditions. PhD Dissertation, University of California, Davis.

Allmond, J., Kutter, B. L., Bray, J. and Hayden, C., (2015). New database for foundation and ground performance in liquefaction experiments. *Earthquake Spectra, 31(4),* pp.2485-2509.

Anastasopoulos, I., Gazetas, G., Loli, M., Apostolou, M., Gerolymos, N. (2010). "Soil Failure Can Be Used for Seismic Protection of Structures." *Bulletin of Earthquake Engineering, 8*, 309-326

Anastasopoulos, I., Gelagoti, F., Kourkoulis, R., and Gazetas, G. (2011) "Simplified Constitutive Model for Simulation of Cyclic Response of Shallow Foundations: Validation against Laboratory Tests" *Journal of Geotechnical and Geoenvironmental Engineering ASCE 137(12),* 1154–1168.

Anastasopoulos, I., Kourkoulis, R., Gelagoti, F. and Papadopoulos, E. (2012). Rocking Response of SDOF Systems on Shallow Improved Sand: An Experimental Study. *Soil Dynamics and*
Earthquake Engineering, 40, pp.15-33.

Andrawes, B., Shin, M. and Wierschem, N., (2010). Active Confinement of Reinforced Concrete Bridge Columns using Shape Memory Alloys. *Journal of Bridge Engineering, 15(1),* pp.81-89.

Apostolou, M., Gazetas, G., and Garini, E. (2007). Seismic Response of Slender Rigid Structures with Foundation Uplifting," *Soil Dynamics and Earthquake Engineering 27(7),* 642–654.

Barker, L. (2014). Flexural Anchorage Performance and Strengthening on Negative Moment Regions Using Near-Surface Mounted Retrofitting in Reinforced Concrete Bridge Girders (master's thesis). Oregon State University, Corvallis, OR.

Beck, J. and Skinner, R. I. (1974.) The Seismic Response of a Reinforced Concrete Bridge Pier Designed to Step. *Earthquake Engineering and Structural Dynamics 2(4),* 637–655.

Breña, S., and Schlick, B. (2007). Hysteretic Behavior of Bridge Columns with FRP-Jacketed Lap Splices Designed for Moderate Ductility Enhancement. *Journal of Composites for Construction,* 11(December), 565–574

Bournas, D. A., T. C. Triantafillou, K. Zygouris, and F. Stavropoulos. (2009). "Textile-Reinforced Mortar versus FRP Jacketing in Seismic Retrofitting of RC Columns with Continuous or Lap-Spliced Deformed Bars." *Journal of Composites for Construction* 13, no. 5: 360–71.

Cairns, J., & Arthur, P. D. (1979). Strength of Lapped Splices in Reinforced Concrete Columns. *ACI Journal Proceedings*, *76*(2). https://doi.org/10.14359/6947

Campbell, K. W. (1977). The Use of Seismotectonics in the Bayesian Estimation of Seismic Risk, Report UCLA-ENG-7744, School of Engineering and Applied Science, University of California, Los Angeles, CA

Chai, Y. H., Priestley, M. J. N., and Seible, F. (1994). Analytical Model for Steel-Jacketed RC Circular Bridge Columns. *ASCE Journal of Structural Engineering, 120(8),* 2358–2376

Chai, Y. H., Priestley, M. J. N., and Seible, F. (2008). Seismic Retrofit of Rectangular Bridge Columns by Steel Jacketing. In Third Bridge Engineering Conference: Papers Presented at the Third Bridge Engineering Conference, March 10-13, 1991, Denver, Colorado (pp. 95–103)

Chaudhary, M.T.A., Abé, M. and Fujino, Y. (2001). Performance Evaluation of Base-isolated Yama-agé Bridge with High Damping Rubber Bearings using Recorded Seismic Data. *Engineering Structures, 23(8),* pp.902-910.

Chen, Y.H., Liao, W.H., Lee, C.L. and Wang, Y. P. (2006). Seismic Isolation of Viaduct Piers by Means of a Rocking Mechanism. *Earthquake Engineering and Structural Dynamics, 35(6),* pp.713-736.

Cheng, C. T. and Mander, J. B. (1997). Seismic Design of Bridge Columns based on Control and Repairability of Damage.

Ciampoli, M. and Pinto, P. E., (1995). Effects of Soil-Structure Interaction on Inelastic Seismic Response of Bridge Piers. *Journal of structural engineering, 121(5),* pp.806-814.

Daudey, X., & Filiatrault, A. (2000). Seismic Evaluation and Retrofit with Steel Jackets of Reinforced Concrete Bridge Piers Detailed with Lap-Splices. *Canadian Journal of Civil Engineering*, *27*(1), 1–16.

Deng, L., Kutter, B. L., and Kunnath, S. K. (2012). Centrifuge Modeling of Bridge Systems Designed for Rocking Foundations. *Journal of Geotechnical and Geo-environmental Engineering, ASCE, 138(3)*: 335–344.

ElGawady, M., Endeshaw, M., McLean, D., & Sack, R. (2010). Retrofitting of Rectangular Columns with Deficient Lap Splices. *Journal of Composites for Construction*, *14*(1), 22–35. https://doi.org/10.1061/(asce)cc.1943-5614.0000047

Elghazouli, A. Y. (2009). *Seismic Design of Buildings to Eurocode 8,* Spon Press

Faccioli, E., Vanini, M. and Paolucci, R. (1999). TRISEE: 3D Site Effects and Soil-Foundation Interaction in Earthquake and Vibration Risk Evaluation. European Commission. Directorate General 12. Science, Research and Development.

Fraino, M., Ventura, C. E., Liam Finn, W.D. and Taiebat, M. (2012). September. Seismic Soil Structure Interaction Effects in Instrumented Bridges. In Proceedings of the 15th World Conference on Earthquake Engineering (pp. 1-10). Portuguese Association for Earthquake Engineering.

Gajan, S., Kutter, B. L., Phalen, J. D., Hutchinson, T. C., Martin, G. R. (2005). "Centrifuge Modeling of Load-Deformation Behavior of Rocking Shallow Foundations." *Soil Dynamics and Earthquake Engineering, 25,* 773–783.

Gajan, S. and Kutter, B. (2008). Capacity, Settlement, and Energy Dissipation of Shallow Footings Subjected to Rocking," *Journal of Geotechnical and Geoenvironmental Engineering ASCE 135(3)*, 407–420.

Galal, K., A. Arafa, and A. Ghobarah. (2005). "Retrofit of RC Square Short Columns." *Engineering Structures* 27, no. 5 (April): 801–13.

Gamble, W. L., Hawkins, N. M., and Kaspar, I. I. (1996). Seismic Retrofitting Experience and Experiments in Illinois. Proc. 5th National Workshop on Bridge Research in Progress, National Center for Earthquake Engineering Research (NCEER), State Univ. of New York at Buffalo, Buffalo, N.Y., 245–250.

Gazetas, G. (2019). Benefits of Unconventional Seismic Foundation Design. BGS 59th Rankine Lecturer, https://www.youtube.com/watch?reload=9&v=pOXzqjTo34o&feature=youtu.be.

Gazetas, G., Apostolou, M. and Anastasopoulos, J. (2003). Seismic Uplifting of Foundations on Soft Soils, with Examples from Adapazari (Izmit 1999 Earthquake). Proc. of BGA International Conference on Foundations: Innovations, observations, design and practice, Dundee. 37-49.

Gazetas, G., and Mylonakis, G. (2001). "Soil–Structure Interaction Effects on Elastic and Inelastic Structures." In Fourth International Conference on Recent Advances in Geotechnical Earthquake Engineering and Soil Dynamics. Symposium in Honor of Professor WD Liam Finn, 1–13. Paper No. SOAP 2, San Diego, California, University of Missouri-Rolla.

Gazetas, George, and Kenneth H. Stokoe. 1991. “Free Vibration of Embedded Foundations: Theory versus Experiment.” *Journal of Geotechnical Engineering* 117 (9): 1382–1401. https://doi.org/10.1061/(ASCE)0733-9410(1991)117:9(1382).

Girard, C., & Bastien, J. (2002). Finite-Element Bond-Slip Model for Concrete Columns under Cyclic Loads. *ASCE Journal of Structural Engineering*, *128*(12), 1502–1510. https://doi.org/10.1061/(ASCE)0733-9445(2002)128:12(1502)

Goksu, C., Yilmaz, H., Chowdhury, S. R., Orakcal, K., & Ilki, A. (2014). The Effect of Lap Splice Length on the Cyclic Lateral load Behavior of RC Members with Low-Strength Concrete and Plain Bars. *Advances in Structural Engineering*, *17*(5), 639–658. https://doi.org/10.1260/1369-4332.17.5.639

Gupta, B. N. 1972. “Effect of Foundation Embedment on the Dynamic Behaviour of the Foundation-Soil System.” *Géotechnique* 22 (1): 129–37. https://doi.org/10.1680/geot.1972.22.1.129.

Hakhamaneshi, M. (2014). Rocking Foundations for Building Systems-Effect of Footing Shape, Soil Environment, Embedment and Normalized Moment-to-Shear Ratio. PhD Dissertation, University of California, Davis, CA, USA.

Harajli, M. H. (2008). Seismic Behavior of RC Columns with Bond-Critical Regions: Criteria for Bond Strengthening Using External FRP Jackets. *Journal of Composites for Construction, 12(1)*, 69–79.

Harajli, M. H. (2009). Bond Stress-Slip Model for Steel Bars in Unconfined or Steel, FRC, or FRP Confined Concrete under Cyclic Loading. *ASCE Journal of Structural Engineering*, *135*(5), 509–518.

Haroun, Medhat A., and Hussein M. Elsanadedy. (2005). “Fiber-Reinforced Plastic Jackets for Ductility Enhancement of Reinforced Concrete Bridge Columns with Poor Lap-Splice Detailing.” *Journal of Bridge Engineering 10,* no. 6 (November): 749–57.

Harries, K. A., Ricles, J. R., Pessiki, S., & Sause, R. (2006). Seismic Retrofit of Lap Splices in Non-ductile Columns Using CFRP Jackets. *ACI Structural Journal*, *103*(6), 874–884. https://doi.org/10.14359/18242

Higgins, C. C., Knudtsen, J., Amneus, D., & Barker, L. (2017). Shear and Flexural Strengthening of Reinforced Concrete Beams with Titanium Alloy Bars. *Proceedings of the 2nd World Congress on Civil, Structural, and Environmental Engineering (CSEE’17)*, 1–8. https://doi.org/10.11159/icsenm17.141

Housner, G. W. (1956). Limit Design of Structures to Resist Earthquakes. Proc. of World Conference on Earthquake Engineering, Earthquake Engineering, Research Institute, University of California, Berkeley.

Housner, G. W. (1963) The Behavior of Inverted Pendulum Structures during Earthquakes. *Bulletin of the Seismological Society of America 53(2),* 404–417.

Huckelbridge, A. A. and Ferencz, R. M. (1981). Overturning Effects on Stiffened Building Frames," *Earthquake Engineering and Structural Dynamics 9(1),* 69–83.

Hung, H., Liu, K., Ho, T., and Chang, K. (2011). An Experimental Study on the Rocking Response of Bridge Piers with Spread Footing Foundations," *Earthquake Engineering and Structural Dynamics,* 40(7), 749–769.

Inukai, Tomoyuki, Tamio Imazawa, Kaoni Kusakabe, and M. Yamaoto. "Dynamic behavior of embedded structure on hard rock site." *Proceedings*, pp. 1695-1700. 1992.

Kawashima, K. and Nagai, T. (2006). Effectiveness of rocking seismic isolation on bridges. In 4th International Conference on Earthquake Engineering, National Center for Research on Earthquake Engineering of Taiwan (pp. 12-13).

Kent, D. C., & Park, R. (1971). Flexural Members with Confined Concrete. *ASCE Journal of Structural Division*, *97(7),* 1969–1990.

Krish, Z.F., Kowalsky, M.J., Nau, J.M. and Seracino, R., (2018). Repair of Reinforced Concrete Bridge Columns via Plastic Hinge Relocation, Volume 1: Repair Using Conventional Materials (No. Report No. 4000 (142)).

Knudtsen, J. (2016). Shear Strengthening Reinforced Concrete Bridge Girders Using Near Surface Mounted Titanium Alloy Bars (master's thesis). Oregon State University, Corvallis, OR

Kutter, B. L., Hutchinson, T. C, Aschheim, M., Kunnath, S., Liu, W., and Hakhamaneshi, M. (2011). Design of Soil and Structure Compatible Yielding to Improve System Performance. 2011 NSF Engineering Research and Innovation Conference, Atlanta, GA, Jan 4-7.

Kutter, B.L., Moore, M., Hakhamaneshi, M. and Champion, C. (2016). Rationale for Shallow Foundation Yocking Provisions in ASCE 41-13. *Earthquake Spectra, 32(2),* pp.1097-1119.

Lin, Albert N., and Paul C. Jennings. 1984. "Effect of Embedment on Foundation - Soil IMPEDANCES." *Journal of Engineering Mechanics* 110 (7): 1060–75. https://doi.org/10.1061/(ASCE)0733-9399(1984)110:7(1060).

Lukose, K., Gergely, P., & White, R. N. (1982). Behavior of Reinforced Concrete Lapped Splices for Inelastic Cyclic Loading. *Journal of American Concrete Institute*, *79*(5), 355–365.

Lynn, A. C., Moehle, J. P., Mahin, S. A., and Holmes, W. T. (1996). Seismic Evaluation of Existing Reinforced Concrete Building Columns. *Earthquake Spectra, 12(4),* 715–739.

Lysmer, J., & Kuhlemeyer, R. L. (1969). Finite Dynamic Model for Infinite Media. *Journal of the* Engineering Mechanics Division, 95(4), 859–877. https://doi.org/10.1061/JMCEA3.0001144

Mander, J. B., Priestley, M. J. N., & Park, R. (1988). Observed Stress-Strain Behavior of Confined Concrete. *ASCE Journal of Structural Engineering*, *114*(8), 1827–1849.

Mander, J. B., Priestley, M. J. N., & Park, R. (1988). Theoretical Stress-Strain Model for Confined Concrete. *ASCE Journal of Structural Engineering*, *114*(8), 1804–1826.

McLean, D. I. and Marsh, M. L. (1999). "Seismic Retrofitting of Bridge Foundations". *Structural Journal*, 96(2), pp.174-182.

Mergos, P. E. and Kawashima, K. (2005). Rocking Isolation of a Typical Bridge Pier on Spread Foundation. Journal of Earthquake Engineering, 9(sup2), pp.395-414.

Melek, M., & Wallace, J. W. (2004). Performance of Columns with Short Lap Splices. In *13th World Conference on Earthquake Engineering Vancouver, B.C., Canada August 1-6, 2004* Paper No. 1034 (pp. 1–15). https://doi.org/10.1002/eqe.4290180114

Mirmiran, A., Shahway, M., Samaan, M., Echary, H. El, Mastrapa, J. C., & Pico, O. (1998). Effect of Column Parameters on FRP-Confined Concrete. *Journal of Composites for Construction*, *2*(November), 175–185.

Mylonakis, G. and Gazetas, G. (2000). Seismic Soil-Structure Interaction: Beneficial or Detrimental?. *Journal of Earthquake Engineering, 4(3)*, pp.277-301.

National Earthquake Hazards Reduction Program (NEHRP) (2004). Recommended Seismic Design Criteria for New Steel Moment-frame Buildings, FEMA-273, Federal Emergency Management Agency, Washington, DC, USA.

Negro, P., Paolucci, R., Pedretti, S., and Faccioli, E. (2000). Large-Scale Soil–Structure Interaction Experiments on Sand under Cyclic Load. Proc. of the 12th World Conference on Earthquake Engineering, Auckland, New Zealand.

Novak, Milos. 1970. "Prediction of Footing Vibrations." *Journal of the Soil Mechanics and* Foundations Division 96 (3): 837–61. https://doi.org/10.1061/JSFEAQ.0001422.

Novak, Milos. 1974. "Effect of Soil on Structural Response to Wind and Earthquake." *Earthquake* Engineering & Structural Dynamics 3 (1): 79–96. https://doi.org/10.1002/eqe.4290030107.

Novak, Milos, and Youpele O. Beredugo. 1972. "Vertical Vibration of Embedded Footings." *Journal of the Soil Mechanics and Foundations Division* 98 (12): 1291–1310. https://doi.org/10.1061/JSFEAQ.0001815.

Ozcan, O., Binici, B., & Ozcebe, G. (2008). Improving Seismic Performance of Deficient Reinforced Concrete Columns Using Carbon Fiber-Reinforced Polymers. *Engineering Structures*, *30(6),* 1632–1646. https://doi.org/10.1016/j.engstruct.2007.10.013

Ozcebe, G., & Saatcioglu, M. (1987). Confinement of Concrete Columns for Seismic Loading. *ACI Structural Journal*. https://doi.org/10.14359/1660

Paulay, T. (1982). Lapped Splices in Earthquake-Resisting Columns. *Journal of American Concrete Institute, 79(6),* 458–469.

Pecker, A. (2003). "Aseismic foundation design process, lessons learned from two major projects: the Vasco de Gama and the Rion Antirion bridges," in ACI Int. Conf. Seismic Bridge Design and Retrofit (La Jolla: University of California at San Diego).

Priestley, M. J. N., Verma, R., and Xiao, Y. (1995). Seismic Shear Strength of Reinforced Concrete Columns. *ASCE Journal of Structural Engineering*, 120(8), 2310–2329

Priestley, M. J. N., Seible, F., and Calvi, G. M. (1996). Seismic Design and Retrofit of Bridges, John Wiley and Sons, New York, NY.

Razvi, S. W. N., & Shaikh, M. G. (2018). Effect of Confinement on Behavior of Short Concrete Column. Procedia Manufacturing, 20(01), 563–570. https://doi.org/10.1016/j.promfg.2018.02.084

Rosebrook K. R. (2001). Moment Loading on Shallow Foundations: Centrifuge Test Data Archives. M.Sc. Thesis. University of California at Davis, School of Engineering.

Saatcioglu, M., & Ozcebe, G. (1989). Response of Reinforced Concrete Columns to Simulated Seismic Loading. *ACI Structural Journal*, *86(1),* 3–12.

Saatcioglu, M. and Yalcin, C., (2003). External Prestressing Concrete Columns for Improved Seismic Shear Resistance. *Journal of Structural Engineering, 129(8)*, pp.1057-1070.

Saiidi, M., David Sanders, and Suresh Acharya. (2001). "Seismic Retrofit of Spread Footings Supporting Bridge Columns with Short Dowels." *Construction and Building Materials 15, no. 4* (June): 177–85.

Sakellaraki, D.I.M.I.T.R.A. and Kawashima, K. (2006). Effectiveness of Seismic Rocking Isolation of Bridges based on Shake Table Test. Proc. First European Conf. on Earthquake Engineering and Seismology.

Santamarina, J. Carlos. 2001. "Soil Behavior at the Microscale: Particle Forces." *In Soil Behavior and Soft Ground Construction*, 25–56. Cambridge, Massachusetts, United States: American Society of Civil Engineers. https://doi.org/10.1061/40659(2003)2.

Santamarina, J. C., & Cho, G. C. (2004). "Soil behaviour: The role of particle shape". Proc. Skempton Conference, London.

Sharma, K. (2019). Field Investigation and Performance-Based Seismic Design of Rocking Shallow Foundations in Cohesive Soil. PhD Dissertation, University of Alberta, Edmonton,
Alberta, CA.

Sheikh, S. A., & Uzumeri, S. M. (1982). Analytical Model for Concrete Confinement in Tied Columns. *ASCE Journal of Structural Division*, *108(12),* 2703–2722.

Shrestha, S. (2019). Seismic Retrofit of Square Reinforced Concrete Bridge Columns using Titanium Alloy Bars. PhD Dissertation, Oregon State University, Corvallis, OR.

Storie, L., Pender, M., Clifton, G., and Wotherspoon, L. (2014). Soil Foundation-Structure Interaction for Buildings on Shallow Foundations in the Christchurch Earthquake. Proc. of 10th NCEE, Anchorage, Alaska.

Takahashi, Y., Muto, I., Hitoshi, S., Tadokoro, Y., & Tagomori, N. (1994). Application of Titanium to Construction and Civil Engineering. https://doi.org/UDC669.295.7:624/627

Valluvan, R., Kreger, M. E., & Jirsa, J. O. (1993). Strengthening of Column Splices for Seismic Retrofit on Non-ductile Reinforced Concrete Frames. *ACI Structural Journal*, *90(4),* 432–433.

Wang, D., Wang, Z., Yu, T., & Li, H. (2018). Seismic Performance of CFRP-Retrofitted Large-Scale Rectangular RC Columns Under Lateral Loading in Different Directions. *Composite Structures*, *192*(3), 475–488. https://doi.org/10.1016/j.compstruct.2018.03.029

Watson, S., Zahn, F. A., & Park, R. (1994). Confining Reinforcement for Concrete Columns. *ASCE Journal of Structural Engineering*, *120(6),* 1798–1824.

Xiao, Y., and Ma, R. (1997). Seismic Retrofit of RC Circular Columns Using Prefabricated Composite Jacketing. *ASCE Journal of Structural Engineering, 123(10)*, 1357–1364.

Xiao, Y., Priestley, M.N. and Seible, F. (1996). Seismic Assessment and Retrofit of Bridge Column Footings. *Structural Journal, 93(1)*, pp.79-94.

Zahn, F. A., Park, R., & Priestley, M. J. N. (1989). Strength and Ductility of Square Reinforced Concrete Column Sections Subjected to Biaxial Bending. *ACI Structural Journal,* Vol. 86, No. 2, pp. 123-131.

Zong-Cai, D., Daud, J.R. and Hui, L. (2014). Seismic Behavior of Short Concrete Columns with Prestressing Steel Wires. *Advances in Materials Science and Engineering,* Vol. 2014, Article ID 180193, 10 pages, 2014. https://doi.org/10.1155/2014/180193

7.0 FULL-SCALE PERFORMANCE OF RETROFITTED REINFORCED CONCRETE COLUMNS INCLUDING SOIL-STRUCTURE INTERACTION: PART II

7.1 INTRODUCTION

This report section introduces the experimental program and nonlinear SSI analytical framework that was developed to better understand the soil-structure interactions of footing-column substructures that can rock when subjected to the lateral loading that may be associated with a seismic event. The experimental program and structural content within this section builds on the work by Parson (2022) described in Section 6, with efforts to further understand the performance of column-footing specimens loaded to its structural capacity. These elements are presented in Sections 7.2 and 7.3. The geotechnical component of this study is also initiated in Section 7.2, and continued in Section 7.4 and 7.5, to provide a soil-structure-interaction (SSI) perspective for these critical substructures when subjected to snap-back and quasi-static, cyclic lateral loading.

Section 7.3 presents the experimental findings from quasi-static cyclic lateral load tests on vintage and retrofitted reinforced concrete column-footing specimens. The performances of two specimens are presented based on visual observation and instrument measurements which include strain gauges on steel reinforcing bars and TiABs, string potentiometers, load cells, and other sensors that varied dependent on the test performed as was detailed in Section 7.2.3. Section 7.2.5 describes the standard loading protocol implemented during tests conducted for this thesis. The complete datasets for the specimens described in this section are provided within Appendix A7.1.

Section 7.4 presents the results from snap-back tests conducted without an applied axial load on a vintage reinforced concrete column-footing specimen at the GEFRS. The performance of the specimen is presented based on instrument measurements which include strain gauges attached to the embedded reinforcing steel, string potentiometers, load cells, accelerometers, tensiometers, and triaxial geophone packages (TGPs). Section 7.2.5 describes the loading protocol implemented during the snap-back tests conducted and described herein; the complete datasets for each snap-back test described in this section are provided within Appendix A7.1. The results from the snap-back tests are used to inform the nonlinear soil-structure interaction models described subsequently in Section 7.4.

Section 7.5 presents nonlinear soil-structure interaction (SSI) models created to represent snap-back and quasi-static cyclic lateral loading structural laboratory and geotechnical field tests on column-footing substructures along with a sensitivity analysis to investigate the role of variables contributing to rocking performance. Sensitivity analyses include investigations into the seasonally dependent saturation-conditions which may impact the geotechnical response to such loading scenarios as discussed in Section 7.2. The results from the introductory force-displacement models provided a basis for the development of force-displacement models that consider strain history for reversed cyclic loading on soil presented herein. The hysteretic SSI models attempt to simulate the force-displacement backbone curves observed during full-scale cyclic lateral load tests performed as part of the current study and previously reported, full-scale

snap-back tests. This section concludes with a summary of work conducted and specific conclusions in Section 7.6.

7.2 EXPERIMENTAL PROGRAM

7.2.1 Subsurface Characterization of the Geotechnical Test Site

Two column-footing specimens were constructed within the Geotechnical Engineering Field Research Site (GEFRS) at Oregon State University. The subsurface characteristics at the GEFRS has been extensively studied and summarized by Dickenson et al. (2006). The report presents the results from explorations, including standard penetration tests (SPTs), cone penetration tests (CPTs), dilatometer penetration tests (DMTs), and geophysical data. Laboratory tests presented in the report included one-dimensional oedometer consolidation tests, unconfined compression tests, and undrained triaxial tests conducted on material sampled from the site. Laboratory test data include the index properties of materials retrieved from borings, such as the plasticity index (*PI*) and liquidity index (*LI*). Dickenson et al. (2006) also present site-specific correlations to various soil properties. The correlations were unique to the subsurface conditions present at Oregon State University and included only data from the GEFRS and similar site explorations on campus.

Additional seismic cone penetration tests (SCPTs) and a traditional CPT with pore pressure measurements at the locations corresponding to the outdoor field column-footing specimens were conducted by Li et al. (2017) as part of their study on the response of drilled shafts to axial and lateral loading. SCPT-1 was pushed through the center of the east footing footprint, referred to herein as Specimen 4. The exploration was performed on April 6th, 2015. Similarly, SCPT-3 was pushed through the center of the west footing footprint, referred to herein as Specimen 5, on January 22nd, 2016. On June 15th, 2016, CPT-4 was pushed at the location centered between the two specimens. Figure 7.1 presents a plan view of the portion of the GEFRS relevant to this study, with the locations of Specimens 4 and 5 and the CPTs performed as part of Li et al. (2017) depicted.

In Oregon, the climate fluctuates between two main seasonal conditions, including the “dry” season from May to October, and the “wet” season from November to April. A seasonally dependent comparison of the interactions between the column-footing specimens and the subsurface will be described in Section 7.5. Soil strength depends on the seasonal moisture content of the soil, and the expected response to loading (e.g., bearing capacity) differs by nearly a factor of three.

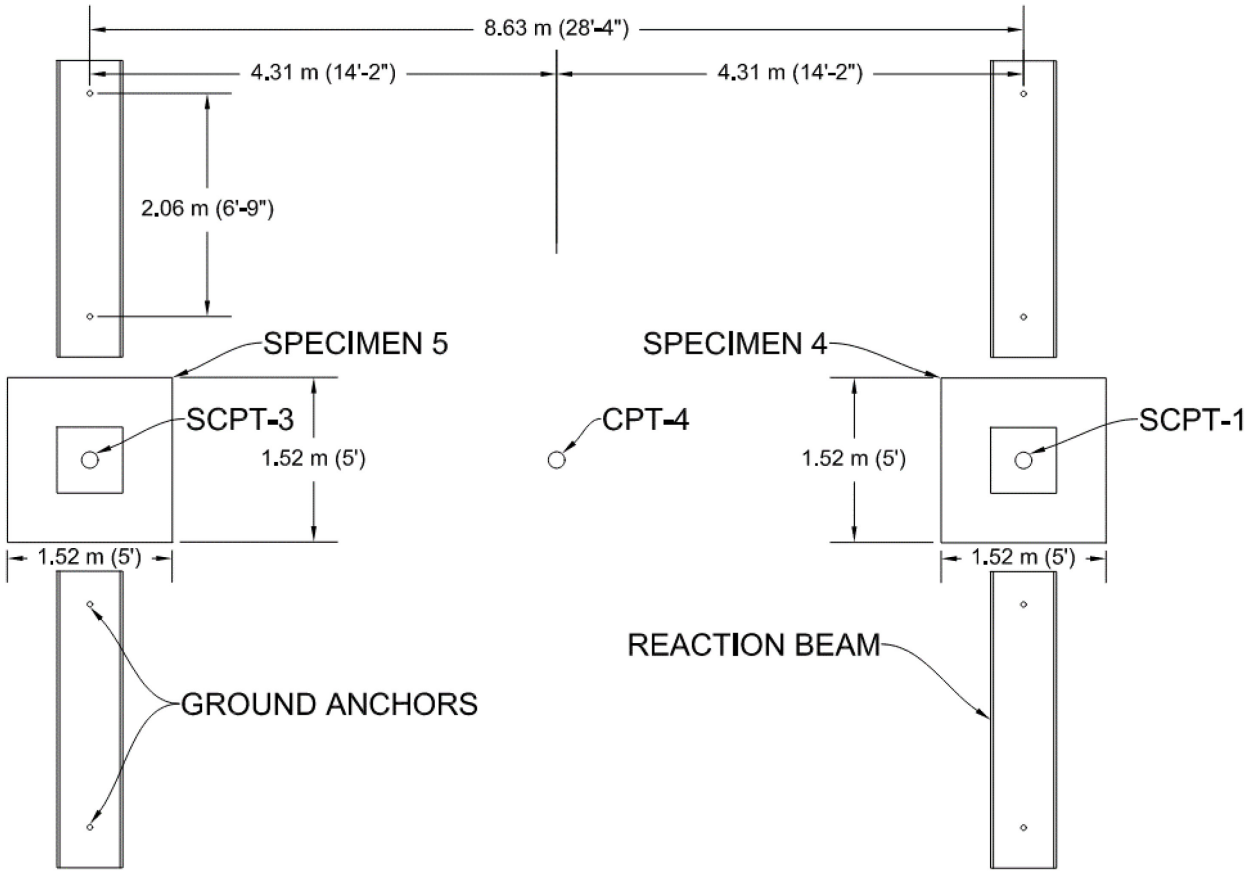

Figure 7.1: Plan view of the column-footing specimen test site at the GEFRS indicating nominal dimensions of relevant experimental components.

Both SCPT-1 and SCPT-3 were deemed representative of the wet season conditions, as both explorations were performed during the typical rainy season at the GEFRS. CPT-4 was pushed in June, representative of the transitional season where the soil is expected to have neither the softest (wet season) or most stiff (dry season) response to loading. Consideration of the data presented in Dickenson et al. (2006) and the SCPTs performed at the site facilitated the determination of the properties for the weaker, wet season. Khosravi et al. (2021) provide a basis for the determination of soil properties in the dry, partially saturated condition. The soil strength in the partially saturated condition depends on the magnitude of matric suction, as determined using the analysis of soil-water retention curves (SWRCs). A detailed description of strength estimates is presented below. Properties of the subsurface material at the two extreme cases (i.e., the wet and dry seasons with potentially fully- and partially saturated soil conditions) are used to bound the interpretation of the SSI response of the test specimens and corresponding parametric analyses described in Section 7.5.

In addition to the subsurface explorations conducted, the GEFRS has also been the location of numerous large-scale field tests. Footing loading tests (Newton, 1975; Martin, 2018) relevant to the current study are used to calibrate parameters associated with a nonlinear bearing resistance model for the hyperbolic model proposed by Huffman et al. (2015). The model parameters

derived from these field tests are used in the parametric SSI study performed in the current study (Section 7.5).

7.2.1.1 Subsurface Conditions at the Column-Footing Test Site

Dickenson (2006) summarizes the geology at the GEFRS and the laboratory data available at the time. The GEFRS is located to the west of the Hinsdale Wave Laboratory and has a ground surface elevation equal to about 73.1 m (240 ft.) above sea level. The site previously hosted a loose gravel and sand deposit estimated to be 18 to 61 m (60 to 200 ft.) thick, which was subsequently eroded. Thereafter, a fine-grained Willamette Silt deposit was deposited during the Missoula Floods. The previous gravel and sand deposits resulted in large overconsolidation ratios (OCRs) for deeper soil deposits, such as the blue-gray clay deposit located at depths greater than 6 m (20 ft.), exceeding the depths of interest for the current study. The results from the test site-specific cone penetration tests (SCPT-1, SCPT-3, and CPT-4) reported by Li et al. (2017) indicate a two-layer stratigraphy in the depths of interest (Figure 7.2).

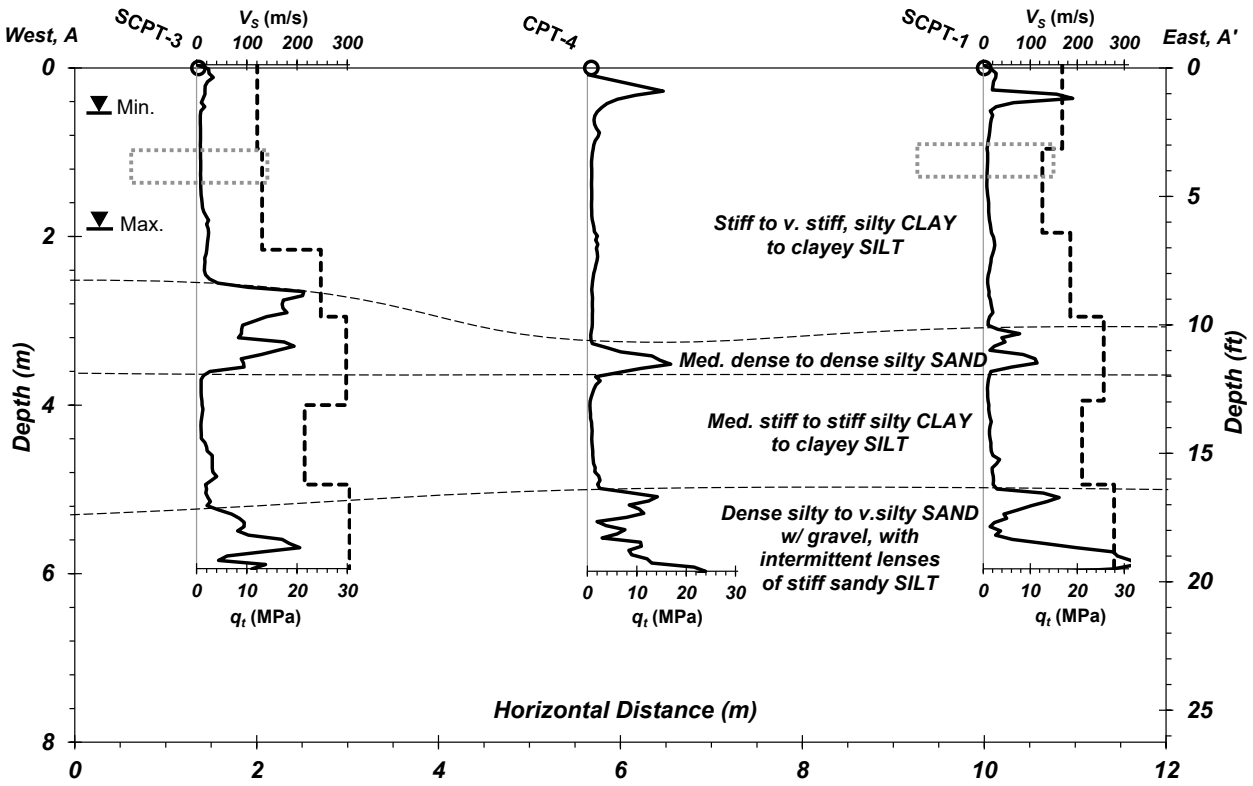

Figure 7.2: Cross-section profile (Section A-A') representative of the GEFRS with the variation of q_t and V_s with depth and soil descriptions. The depths and locations of the west and east footings are outlined using dashed lines.

Figure 7.2 shows that the uppermost layer extends to a depth of 2.55 m (8.4 ft.) at the location of the west footing (Specimen 5) and 3.1 m (10.2 ft.) at the location of the east footing (Specimen 4). This layer is comprised of stiff to very stiff silty clay to clayey silt, collectively classified as Upper Willamette Silt. From a depth of 1.39 m (4.56 ft.) to 2.91

m (9.56 ft.), representing the range in depth extending from the base of the footing to one times the footing width below the base, the average cone tip resistance, q_t, soil behavior index, I_c, and shear wave velocity, V_s, were 4.8 MPa (50.1 tsf), 2.40, and 154 m/s (505 ft/s), respectively, at the time of exploration.

Figure 7.3 presents the depth-dependent water contents and Atterberg Limits for the Upper Willamette Silt at the column-footing test site location (after Li et al. 2017). At the time of sampling, the water content increased with depth from a minimum of 15.6% at a depth of 0.3 m (1 ft.) to a maximum of 44.8% at a depth of 2.7 m (9 ft.); the similarity between the natural water content and the plastic limit is indicative of its stiff and overconsolidated nature. Plastic indices ranged from a minimum of 1 at a depth of 0.3 m (1 ft.) to a maximum of 36 at a depth of 2.0 m (6.5 ft.).

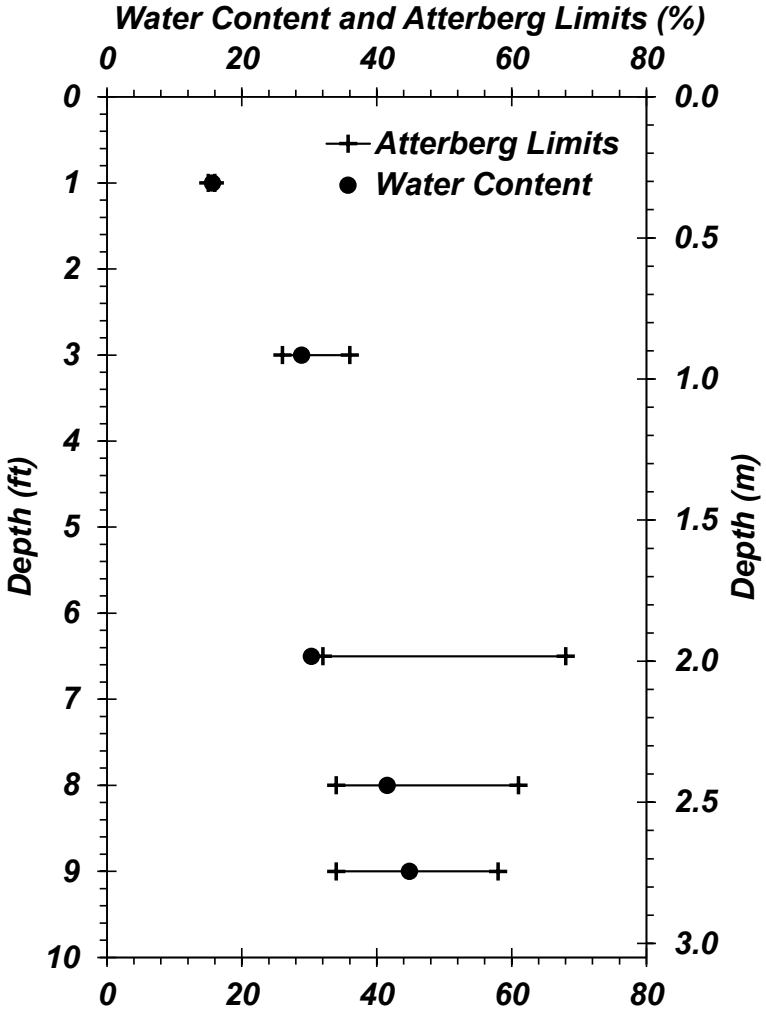

Figure 7.3: Depth-dependent water content and Atterberg Limits of the Upper Willamette Silt layer (Li et al. 2017).

A thin lens of medium dense to dense silty sand underlays the Upper Willamette Silt, ranging in depths of 2.55 to 3.6 m and 3.1 to 3.6 m for the west and east footings, respectively, associated with notable increases in q_t, V_s, and sleeve friction, f_s, relative to the Upper Willamette Silt layer. Table 7.1 summarizes the average values for q_t, f_s, I_c, and V_s at the center of the east and west specimens.

Table 7.1: Summary of average SCPT results for locations of Specimen 4 and 5.

SCPT-1 – Specimen 4 (east footing)						
Soil Layer	**USCS**	**Depth (m)**	**q_t (MPa)**	**f_s (MPa)**	**I_c**	**V_s (m/s)**
Upper Willamette Silt	ML and MH	0 to 3.1	2.04	0.07	2.59	173
Silty Sand	SP-SM	3.1 to 3.6	6.02	0.14	2.24	256

SCPT-3 – Specimen 5 (west Footing)						
Soil Layer	**USCS**	**Depth (m)**	**q_t (MPa)**	**f_s (MPa)**	**I_c**	**V_s (m/s)**
Upper Willamette Silt	ML and MH	0 to 2.55	1.44	0.07	2.60	126
Silty Sand	SP-SM	2.55 to 3.6	13.36	0.28	1.84	272

Groundwater levels at the site fluctuate with the seasonal conditions. In the wet season, the groundwater table had been identified at a minimum depth of 0.6 m (2 ft.) below the ground surface. In the dry season, the water table elevation has been observed to fall to a maximum depth of 2.1 m (7 ft.) below the ground surface (Martin 2018). For the current study, the volumetric water content has been monitored by tensiometers beneath both Specimens 4 and 5.

7.2.1.2 Site-Specific Correlations to Soil Properties

A relationship between the liquidity index, *LI*, and the ratio of undrained shear strength to vertical effective stress, s_u/σ'_{vo}, is presented in Dickenson et al. (2006) and is applied to the test site-specific data as shown in Figure 7.4. Two additional *LI* to s_u/σ'_{vo} relationships are included in the correlation based on the data presented in Martin (2018). Since the site-specific dataset is limited to five data points, the trend shown in Figure 7.4 is uncertain. From the limited data available, it is evident that an increase in *LI* corresponds to a decrease in the undrained shear strength as expected owing to its relationship with the overconsolidation ratio (Vardanega and Haigh 2014).

A correlation of s_u to V_s is also reported by Dickenson et al. (2006). The dataset includes consolidated undrained (CU) triaxial strength test data from numerous sites on the Oregon State University campus as well as four CU triaxial strength tests on samples

retrieved from the GEFRS. Figure 7.5 is adapted from Dickenson et al. (2006) and illustrates significant scatter in the in the s_u - V_s correlation; however, the relationship appears stronger for specimens which exhibit relatively lower undrained shear strengths. Generally, an increase in shear wave velocity corresponds to an increase in undrained shear strength. Two correlations are shown in Figure 7.5; one which has been fit to all of the available data using an exponential trend, and one that has been fit to data specific to the GEFRS only using a linear trend.

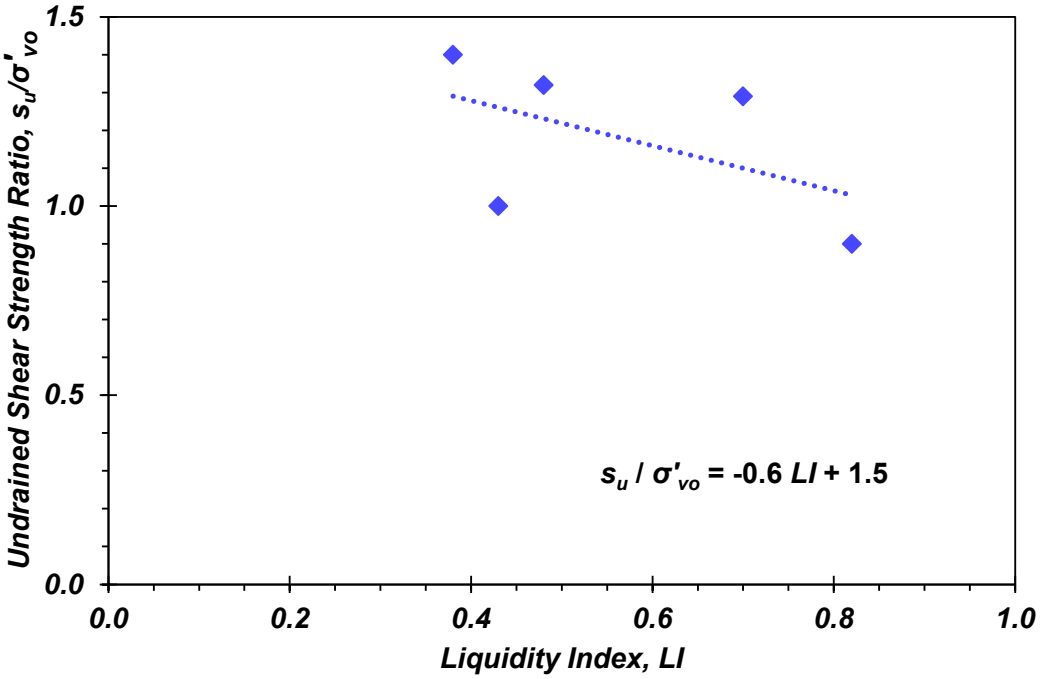

Figure 7.4: Correlation of *LI* to undrained shear strength ratio (Dickenson et al. 2006; Martin, 2018).

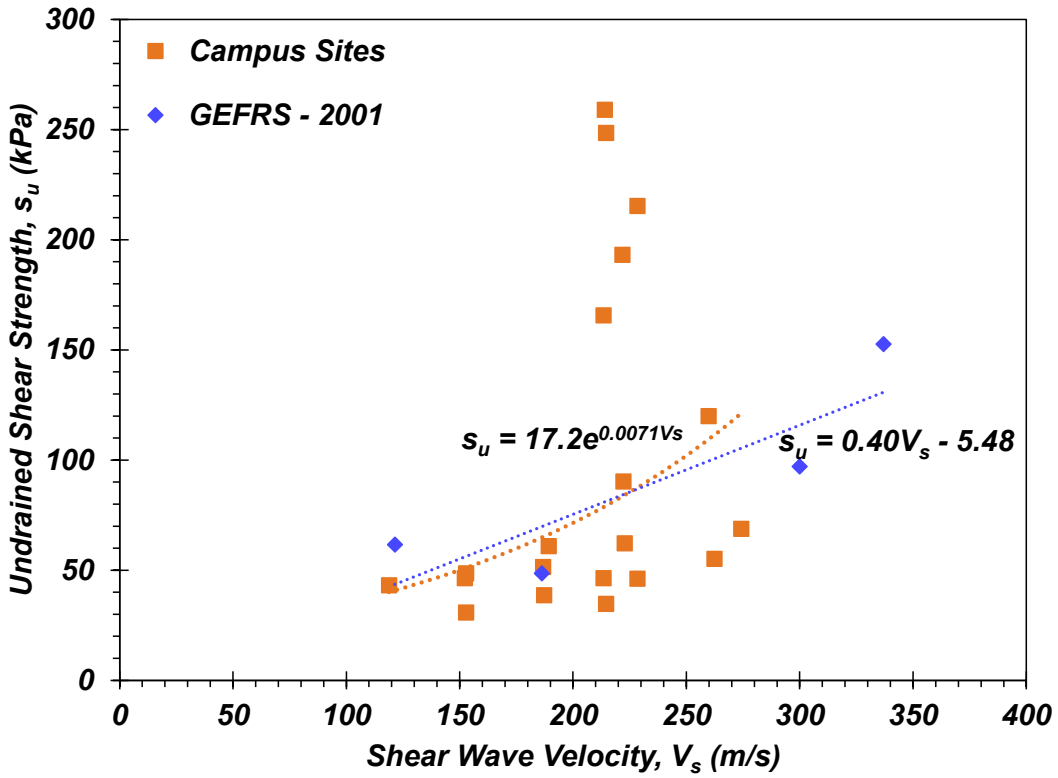

Figure 7.5: Correlations of shear wave velocity to undrained shear strength, adapted from Dickenson et al. (2006).

7.2.1.3 Estimates of Soil Strength Properties at the Test Site

Estimates of the depth-varying undrained shear strength at the test site were prepared using the correlations presented in Figures 7.4 and 7.5. Table 7.2 summarizes the estimates of s_u made using the reported water contents and Atterberg Limits from Li et al. (2017), which range from 6 kPa at a depth of 0.3 m (1.0 ft.) to 47 kPa at a depth of 2.0 m (6.5 ft.). The V_s determined using SCPT data facilitated estimates of undrained shear strength, which range from 49 kPa at a depth of 2.0 m (6.5 ft.) to 85 kPa at a depth of 2.7 m (9.0 ft).

Table 7.2: Comparison of initial estimates of s_u based on correlations to *LI* and V_s.

Sample	Depth, m (ft.)	Estimation of s_u, kPa (psf)			
		LI - Based	Average V_s - Based	SCPT-1	SCPT-3
1	0.3 (1.0)	6 (125)	40 (835)	-	92 (1,921)
2	0.9 (3.0)	21 (439)	51 (1,065)	58 (1,211)	52 (1,086)
3	2.0 (6.5)	47 (1,546)	50 (1,044)	96 (2,005)	132 (2,757)
4	2.4 (8.0)	46 (1,337)	49 (1,023)	72 (1,504)	84 (1,754)
5	2.7 (9.0)	46 (1,337)	39 (815)	59 (1,232)	-

Dickenson et al. (2006) presented the results from unconsolidated undrained (UU) triaxial compression tests, isotropic consolidated undrained (ICU) triaxial compression tests, and unconfined compression (UC) tests. Results from the UU and ICU triaxial tests indicate that the undrained shear strength for the Upper Willamette Silt appears depth-dependent, whereas the in-situ degree of saturation remains relatively constant and corresponding to nearly fully- and fully saturated conditions. Table 7.3 summarizes the results from ICU tests conducted on four specimens prepared from samples retrieved from boreholes advanced at the GEFRS.

Table 7.3: Summary of ICU triaxial strength tests on specimens of Upper Willamette Silt retrieved from the GEFRS (after Dickenson et al. 2006).

Test Designation	Depth, m (ft)	Undrained Shear Strength, s_u kPa (psf)	Degree if Saturation, S (%)
101	2.4 (8.0)	42 (877)	100.0
7C	2.3 to 2.7 (7.5 to 9.0)	55 (1,149)	99.8
8C	3.8 to 4.4 (12.5 to 14.5)	69 (1,441)	98.2
-	2.6 (8.5)	43 (898)	97.9

Two site-specific SCPT in-situ explorations were conducted at the locations of Specimens 4 and 5 prior to their construction. SCPT-1 and SCPT-3 provide the basis for the most up-to-date correlation of in-situ test results to engineering properties, which are used in the analyses presented in this study. The undrained shear strength of fine-grind materials can be estimated using:

$$s_u = \frac{q_t - \sigma'_v}{N_k} \quad \textbf{(7-1)}$$

where the empirical cone factor, N_k, is often back-calculated from other available in-situ or laboratory test data. A typical value of N_k for overconsolidated soils is 17, as summarized in Robertson and Campanella (1986). Dickenson (2006) proposed a cone factor equal to 24 for Willamette Silt; however, significant variability was noted in the correlation, raising concerns regarding the validity of the representative N_k. The use of low N_k values correspond to an over-estimate of s_u. For the current study, a N_k value equal to 18 was used for undrained shear strength estimations based on the data presented in Martin (2018).

Figure 7.6 shows the variation of selected soil parameters within the depths of particular interest for bearing capacity, which range from the base of the footing to a depth equal to

the footing width, B, below the base. The friction angle of the fine-grained Upper Willamette Silt was estimated using (Ouyang and Mayne, 2017):

$$\boldsymbol{\phi' = 29.5 B_q^{0.121}(0.256 + 0.336 B_q + \log(Q))}$$

(7-2)

where B_q is the normalized pore-water pressure parameter, defined as:

$$\boldsymbol{B_q = \frac{\Delta u_2}{q_t - \sigma_{vo}}}$$

(7-3)

and the normalized cone tip resistance, Q, defined as:

$$\boldsymbol{Q = \frac{q_t - \sigma_{vo}}{\sigma_{vo}'}}$$

(7-4)

Ouyang and Mayne (2017) recommend implementing Equation 4.2 only when $0.1 < B_q < 1.0$, but the low total vertical stress and relatively high cone tip resistances of the stiff Upper Willamette Silt at the column-footing test site results in B_q values smaller than 0.1 through the entirety of the depth of interest. As a result, this correlation of ϕ' is used with caution in the subsequent analyses. For granular materials, ϕ' is estimated by (Kulhawy and Mayne, 1990):

$$\boldsymbol{\phi' = 17.6 + 11.0 * \log\left(\frac{q_c/p_a}{(\sigma_{vo}/p_a)^{0.5}}\right)}$$

(7-5)

where q_c is the corrected cone tip resistance and p_a is atmospheric pressure. The overconsolidation ratio was estimated by (Mayne 2007):

$$\boldsymbol{OCR = 0.33 * \left(\frac{q_t - \sigma_v}{\sigma'_v}\right)}$$

(7-6)

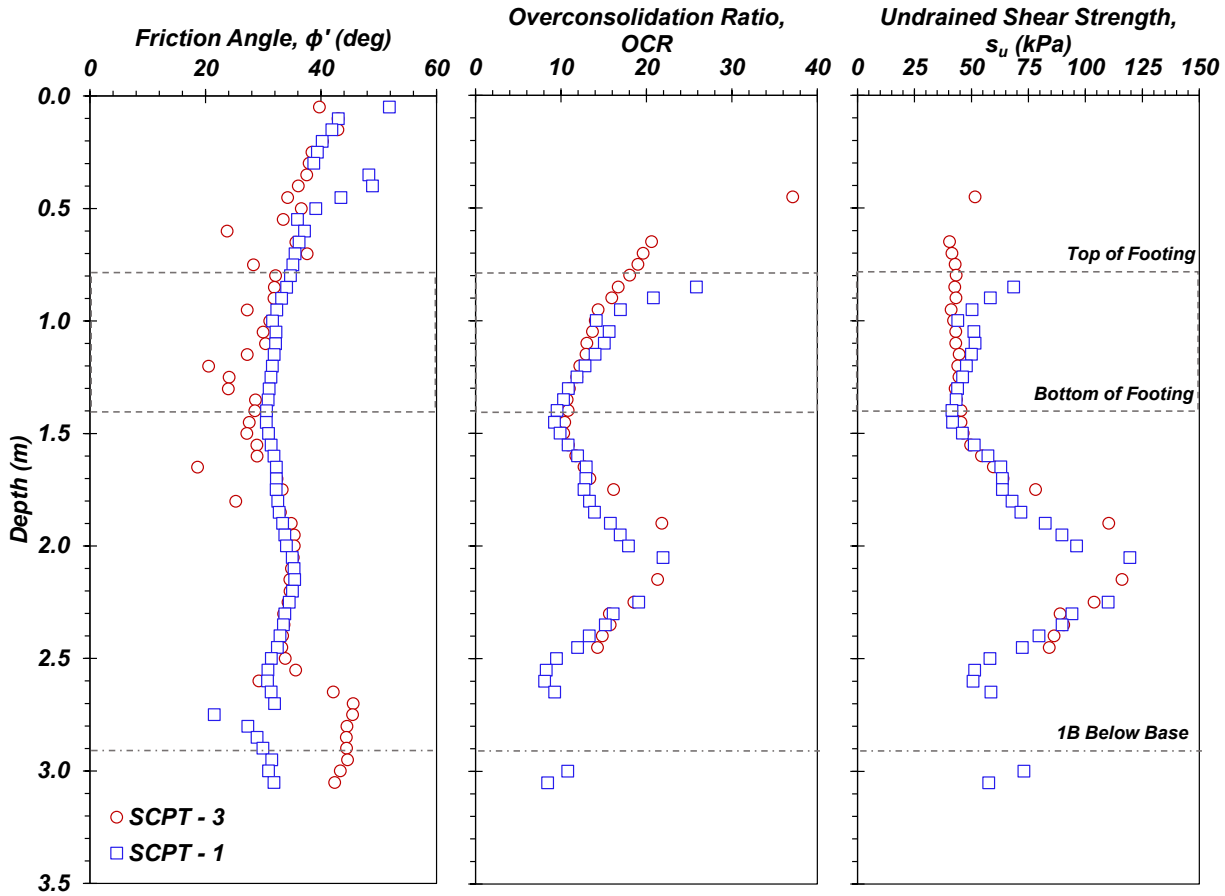

Figure 7.6: Depth-varying profiles of ϕ', OCR, and s_u for SCPT-1 and SCPT-3.

In the zone of interest (1.39 m to 2.91 m), the friction angles determined from SCPT-1 remained relatively constant, whereas an increase in ϕ' was evident below a depth of 2.55 m for SCPT-3. This increase in the effective friction angle resulted from the high cone tip resistances encountered as the cone was pushed through the dense silty sand layer present below the west footing. Values of OCR were high for both the SCPT-1 and SCPT-3 profiles due to the relatively low effective stress and the high cone tip resistances in the Upper Willamette Silt. The estimates of undrained shear strength peaked at 110 kPa (2297 psf) for both SCPT-1 and SCPT-3 at a depth of about 2.1 m (6.9 ft.).

SCPT-3 was pushed at the site of the west footing, designated as Specimen 5. This specimen was subjected to snap-back tests (discussed in Sections 7.2.4.2 and 7.4) and is further studied using a parametric study in Section 7.5. For the wet season, the most critical aspect for SSI modeling was the determination of a representative undrained shear strength for the subsurface. As shown in Figure 7.6 and Tables 7.2 and 7.3, the undrained shear strength was both depth-dependent and spatially dependent. It also exhibits variability spatially across the entire GEFRS based on data reported by Dickenson et al. (2006). Table 7.4 presents estimates of the undrained shear strength determined using correlations from the SCPT data and compared with the previously reported estimates. Undrained shear strength values within the dense silty sand layer encountered by SCPT-3

from a depth of 2.55 to 3.6 m were omitted from Table 7.4. The SCPT-1 and SCPT-3 results indicated estimates of s_u comparable to the initial estimations based on index properties and shear wave velocities. Table 7.5 provides a summarization of the effective friction angle for use in estimating strengths for the dry season in consideration of matric suction. The results from the SCPT correlations compare well to the ICU strength test data presented by Dickenson et al. (2006).

Table 7.4: Summary and comparison of s_u estimations from various correlations.

Sample	Depth (ft)	Estimates of s_u, kPa (psf)			
		***LI* - Based**	**Average V_s - Based**	**SCPT-1**	**SCPT-3**
1	1.0	6 (125)	55 (1,149)	-	92 (1,921)
2	3.0	21 (439)	55 (1,149)	58 (1,211)	52 (1,086)
3	6.5	47 (982)	51 (1,065)	96 (2,005)	132 (2,757)
4	8.0	46 (961)	58 (1,211)	72 (1,504)	84 (1,754)
5	9.0	46 (961)	75 (1,566)	59 (1,232)	-

Table 7.5: Summary and comparison of ϕ' estimates from ICU tests and SCPT results.

Depth, m (ft)	*Dickenson et al. (2006)*			*SCPT-1*	*SCPT-3*
	Test Designation	**Test**	**ϕ' (deg)**	**ϕ' (deg)**	**ϕ' (deg)**
2.3 to 2.7 (7.5 to 9.0)	7C	ICU	38.7	32.1	29.3
3.8 to 4.4 (12.5 to 14.5)	8C	ICU	35.0	31.1	30.4
2.6 (8.5)	-	ICU	32.2	30.7	29.3

7.2.2 Column-Footing Specimens

Shrestha (2019) documented an inventory review of bridges under the jurisdiction of the Oregon Department of Transportation (ODOT) along key transportation corridors in the state that would be susceptible to strong ground shaking from a Cascadia seismic event. As described in Parson (2022), the column-footing specimens constructed for this work represented typical substructures from the inventory review. The specimens tested as part of the current study had 1.52 m (5.0 ft.) square footings that were 0.61 m (2.0 ft.) in thickness, with 0.61 m square columns extruding 2.74 m (9 ft.) vertically from the top of the footing. An illustration of the elevation view of a typical test specimen is provided in Figure 7.7.

As described in Parson (2022), the concrete mix-design required a maximum aggregate size of 4.75 mm (0.75 in.) and had a 28-day compressive strength of 28 MPa (4 ksi). This relatively low strength concrete was chosen to best represent the concrete used at the time of construction for

the bridge foundation systems that were built over 50 years prior. The material properties used in the specimens are presented in Appendix A7.1.1.

Five (5) column-footing specimens were constructed as part of the joint effort with Parson (2022) to observe the behavior of substructures when subjected to cyclic lateral loading. Specimens 1, 2, and 3 were constructed to be tested in the Large-Scale Structural Laboratory at Oregon State University. Specimens 4 and 5 were tested at the Oregon State University Geotechnical Engineering Field Research Site (GEFRS). Tests conducted on Specimens 1, 3, 4, and 5 were performed as part of the current study. Table 7.6 summarizes the tests performed as part of this thesis and those performed by Parson (2022) on the same/similar specimens as part of the same study. Tests 1 through 8 were performed and described by Parson (2022), whereas Tests 9 and 10 were conducted as part of the current study. A given specimen is designated by "Test X – SY", where "X" is equal to the chronological test number and "Y" corresponds to the specimen number (e.g., Test 9 – S3 corresponds to the ninth test different performed chronologically on the same column-footing structure identified as Specimen 3).

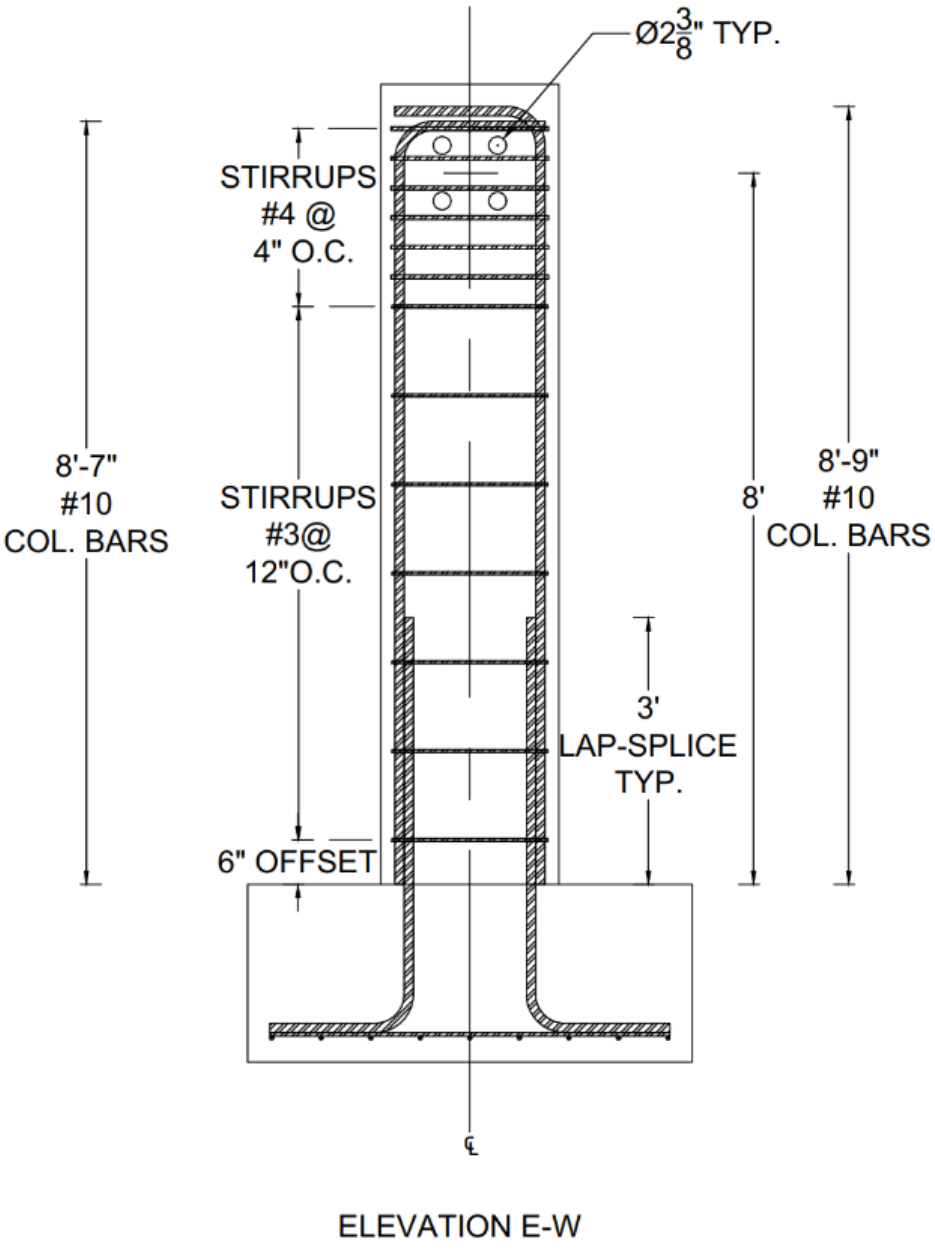

Figure 7.7: Elevation view of a typical column-footing specimen (Parson 2022).

Table 7.6: Specimen Designations and Descriptions.

Designation	Description	Tested By
Test 1 - S1	Complete Retrofit with Soil Simulant Subgrade and Embedment	Parson (2022)
Test 2 - S2	Complete Retrofit with Soil Simulant Subgrade and No Embedment	Parson (2022)
Test 3 - S3	Vintage Column with New Subgrade, Embedment, and Axial Load	Parson (2022)
Test 4 - S3	Vintage Column with Damaged Subgrade, Embedment, and Reduced Axial Load	Parson (2022)
Test 5 - S3	Vintage Column Failure with Damaged Subgrade and Steel Embedment	Parson (2022)
Test 6 - S3	Failed Vintage Column with Ligament Retrofit, Damaged Subgrade, and Steel Embedment	Parson (2022)
Test 7 - S3	Failed Vintage Column with Complete Retrofit, Damaged Subgrade, and Steel Embedment	Parson (2022)
Test 8 - S2	Complete Retrofit with Tied Down Footing and No Soil Simulant	Parson (2022)
Test 9 - S1	Vintage Column with Ligament and Spiral Retrofit, Restrained Footing with Retrofit	Current Study
Test 10 - S3	Vintage, Failed Column with Ligament and Spiral Retrofit, Restrained Footing with Additional Retrofit	Current Study
S.5 – west footing	Unloaded Snap-Back at Field Site	Current Study
S.4 – east footing	Future Work	Current Study

7.2.2.1 Specimen Design

As described in Parson (2022), an orthogonal reinforcement layer was installed at the bottom of each footing, with a 76 mm (3 in.) clear cover between the reinforcement and the base. The reinforcement mesh was constructed of #4 (#13M) Grade 40 bars spaced 171 mm (6.75 in.) center to center. In accordance with standard design practices at the time of construction, four (4) #10 (#32M) starter bars with 559 mm (22 in.) tails were placed diagonally to each respective corner of the footing, as shown in Figure 7.8.

The column-footing specimens were 3.35 m (11 ft.) in total height, with the elevation of the applied lateral load 2.44 m (8 ft.) above the top of the footing. The column contained four (4) #10 (#32M) Grade 60 bars as longitudinal reinforcement and #3 (#10M) Grade 40 square ties spaced vertically at 305 mm (12 in.) as transverse reinforcement. The first

row of ties was placed 152 mm (6 in.) above the top of the footing. At a height of 1.98 m (6.5 ft.) above the footing, the tie spacing was reduced to 122 mm (4 in.) while the yield strength was increased to 60 ksi (Grade 60) to prevent localized column failure near the lateral load application point. A lap-splice length equal to 0.91 m (3 ft.) was implemented to replicate the $30d_B$ (i.e., 30 times the bar diameter) requirement set for the construction of vintage columns. The dimensions and details of a typical specimen are shown in Figure 7.9.

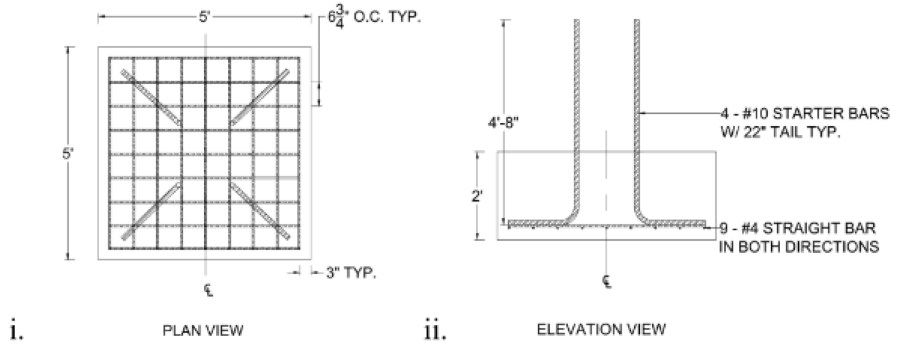

Figure 7.8: Typical vintage footing details in plan (i.) and elevation (ii.) view (Parson 2022).

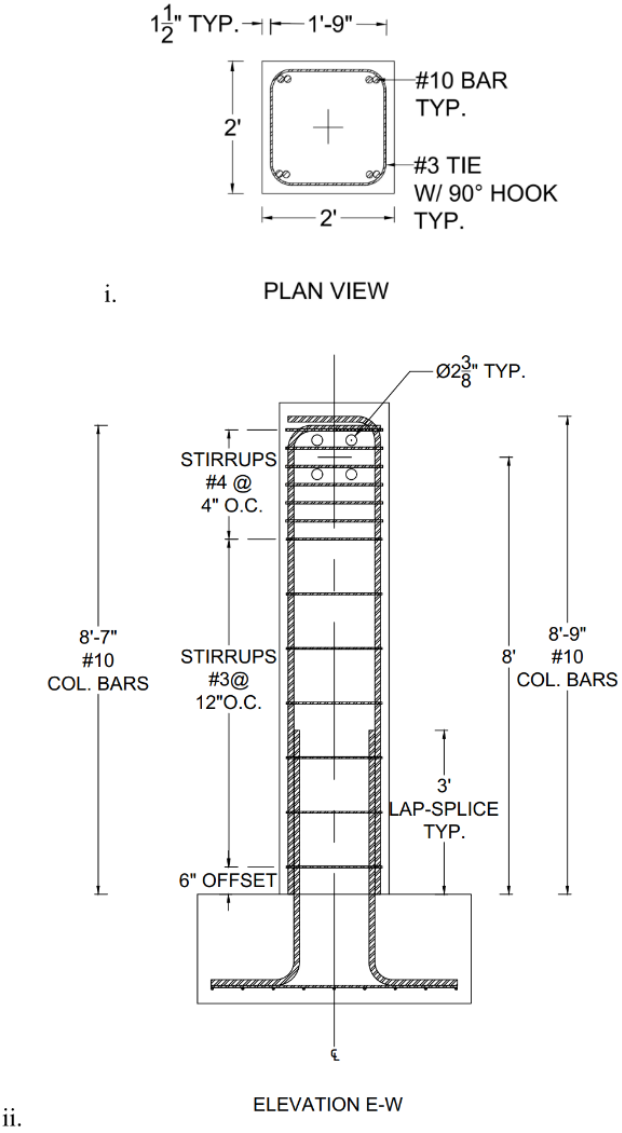

Figure 7.9: Typical vintage column details in plan (i.) and elevation (ii.) view (Parson 2022).

7.2.2.2 Retrofit Design

Titanium alloy bar (TiAB) ligaments and spirals were used for the retrofit design of all specimens. As described in Parson (2022), the ligaments were embedded into the vintage column at three (3) varying elevations to avoid an abrupt change of stress at a single elevation. Aside from the portion at the 90-degree hook embedded into the column, the ligaments were unbonded to the column until they were embedded into the footing. The spiral provided confinement to the column and TiAB ligaments. The mechanical properties for the TiAB materials are presented in Appendix A7.1.3.

Three (3) ligament lengths were implemented for the retrofit: 1.93 m (6.25 ft.), 1.78 m (5.88 ft.), and 1.63 m (5.25 ft.). Shrestha (2019) specified these lengths based on the average ligament length; a quantity determined through the computation of the tension

lap-splice length required by the AASHTO LRFD Bridge Design Specification (2017) for the #10 (#32M) embedded reinforcing steel column bars. As shown in Figure 7.10, the 90-degree hooks had 254 mm (10 in.) tails embedded 203 mm (8.0 in.) into the column. Additionally, proprietary deformations (i.e., grooves) were machined along the last 191 mm (7.5 in.) of the tail to be embedded into the column and the last 381 mm (15 in.) of the portion to be embedded into the footing. These deformations allow the TiAB ligaments to be bonded to the concrete column and footing with structural epoxy.

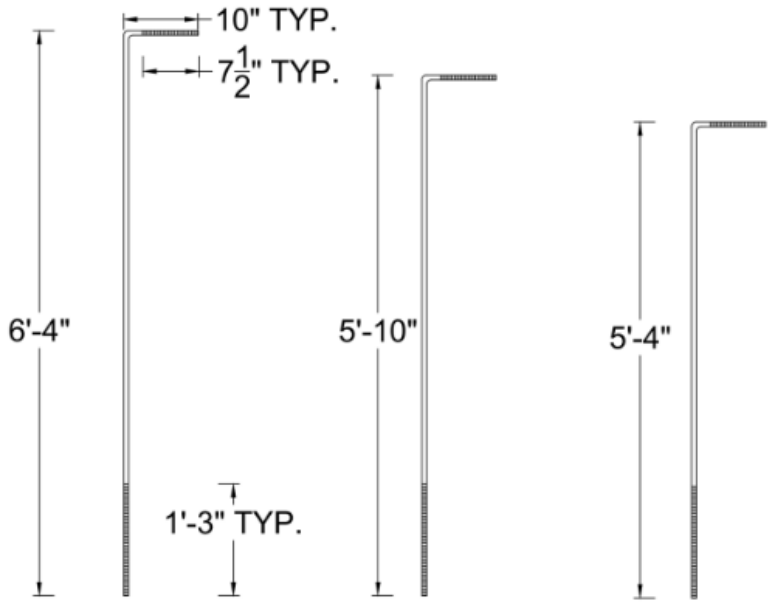

Figure 7.10: TiAB ligament details (Parson 2022).

Providing confinement to the ligaments and vintage column were TiAB spirals made with a 9.5 mm (0.75 in.) diameter TiAB. Unlike the ligaments, no proprietary deformations were added to the portion of the spiral that was embedded into either the column or footing. The 2017 AASHTO LRFD Design Specifications prescribe the following design practices regarding the reinforcing spiral: a minimum spiral diameter of 9.5 mm (0.375 in.), a max c/c spacing equal to the smaller of $6d_B$ and 152 mm (6.0 in.), and a minimum clear spacing between spiral layers equal to the greater of 1.33 times the maximum aggregate size or 25 mm (1.0 in). The design for the retrofit spiral was first performed by Shrestha (2019), with an alteration in the design near the column-footing interface recommended based on the test observations. The recommendation was followed for Specimens 1 through 3 to include two (2) TiAB spirals over the lower 0.61 m (24 in.) of the column, with each embedded into opposite sides of the footing. Figure 7.11 illustrates the typical TiAB retrofit detail for test specimens.

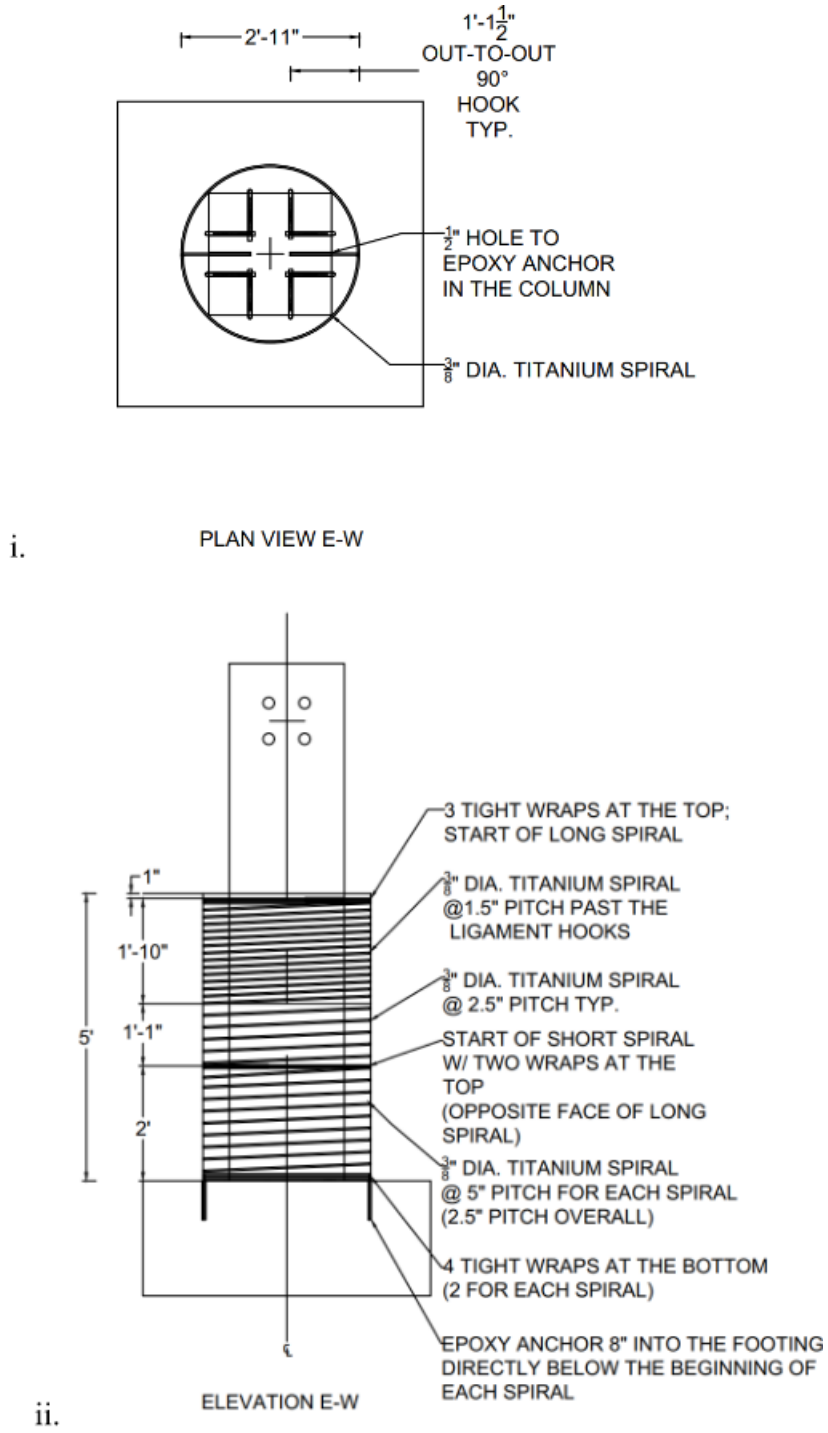

Figure 7.11: Complete specimen design with TiAB spiral details in plan (i.) and elevation (ii.) view (Parson 2022).

As a continuation of the research performed by Parson (2022), Test 9 – S1 and Test 10 – S3 were conducted to observe the structural behavior of a column-controlled response, where strength degradation was to primarily result from lap-splice failure of the flexural tension steel reinforcement within the column above the footing. The purpose of this was

to examine both the local and global structural responses of the specimen when subjected to cyclic loading substantial in magnitude to cause damage and strength degradation. Ideally, the associated deformations of the column at large imposed top drift ratios would result in eventual loss of the embedded steel flexural reinforcement due to lap-splice failure, allowing the TiAB ligaments to be the primary elements resisting flexural tension.

To increase the resistance of the as-built vintage footings to cyclic loading, two (2) near-surface-mounted (NSM) bars were installed into the top of the footing of Specimen 1. These bars were #6 (#19M) stainless steel, Grade 80, and extended 305 mm (12 in.) into the footing via 90-degree hooks. The bars were installed on the east and west sides of the footing, providing passive reinforcement at the top of the footing. Additionally, post-tensioned Dywidag bars were installed on all sides of the footing to increase the compressive strength of the concrete. The Dywidag bars were 38 mm (1.625 in.) diameter, Grade 150, and rested on 12.7 mm (0.5 in.) thick, 178 mm (7 in.) square bearing plates. Each bar was post-tensioned to 623 kN (140 kips) using a specially fabricated, steel bridge and a hollow core ram with a stressing nut. The footing retrofit implemented for Test 9 – S1 is illustrated in Figures 7.12 and 7.13.

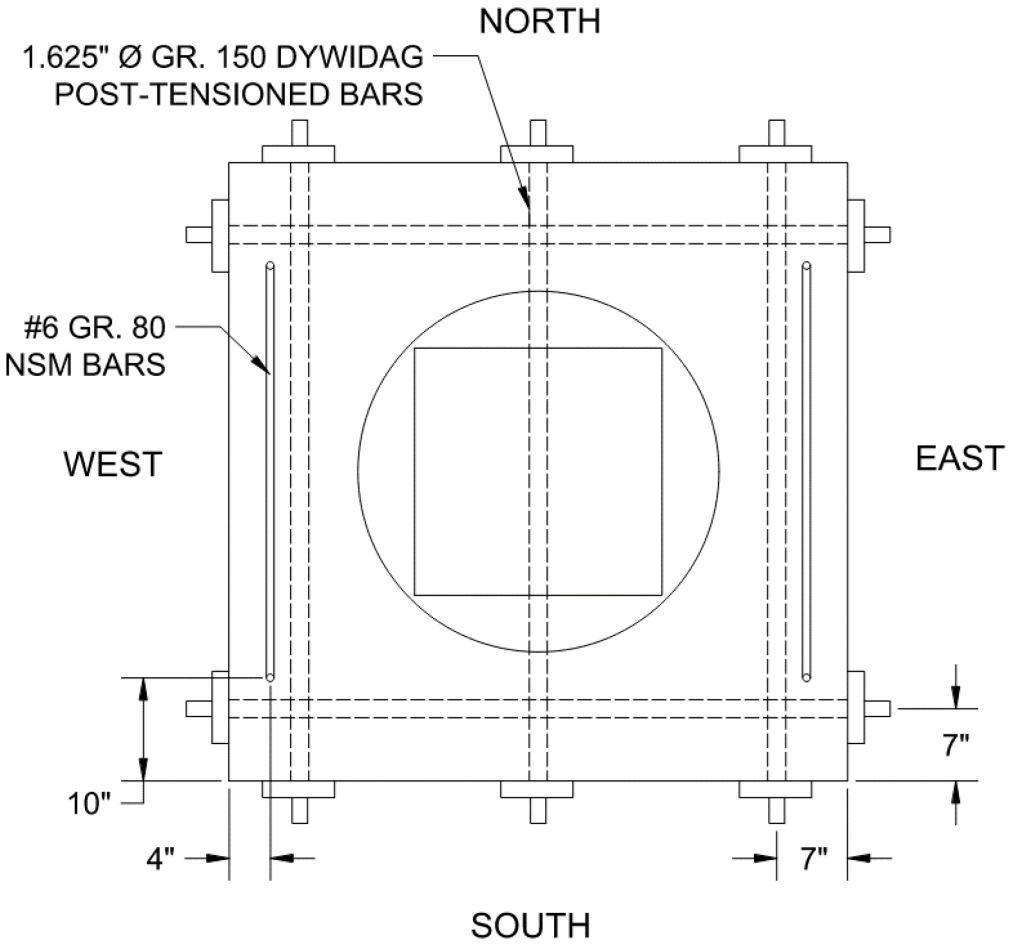

Figure 7.12: Footing retrofit plan view for Test 9 – S1.

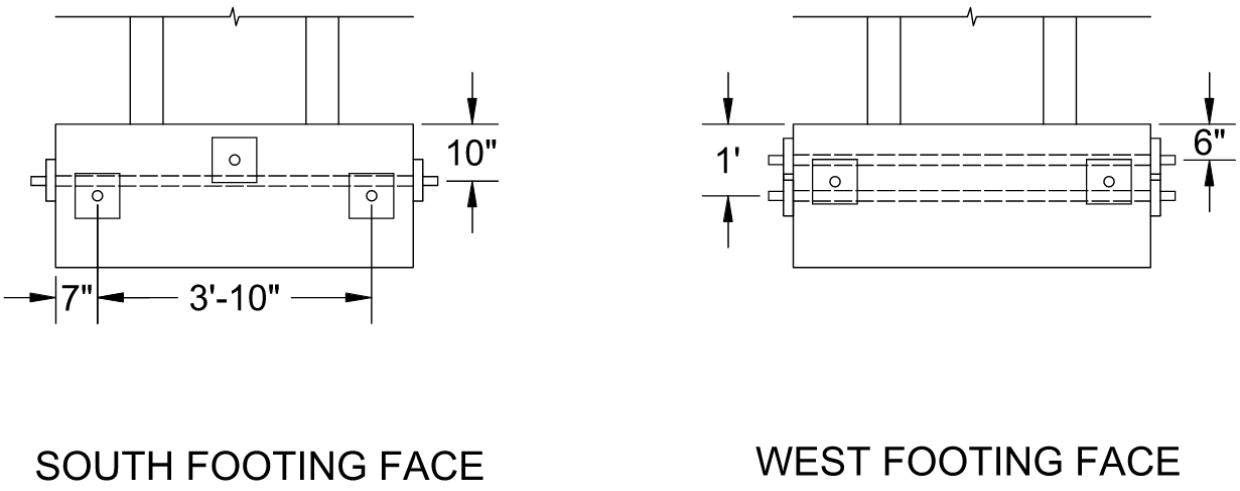

Figure 7.13: Footing retrofit elevation view for Test 9 – S1.

Based on the experimental response of Test 9 – S1, the footing retrofit was increased for Test 10 – S3 to increase resistance to the imposed cyclic loading. Similar to Test 9 – S1, NSM bars were installed on the east and west sides of the footing, with an increase in embedment depth from 305 mm (12 in.) for Test 9 – S1 to 381 mm (15 in.) for Test 10 – S3. Additional NSM bars were installed on the north and south sides of the footing, embedded 381 mm (15 in.) into the footing. Additional measures included the installation of four (4) 508 mm (20 in.), Grade 80 #5 (#16M) vertical reinforcement bars into the footing on both the north and south sides, with the bars spaced at 203 mm (8 in.) c/c and installed symmetrically about the axis parallel to the direction of loading. Five (5) 38 mm (1.625 in.) Dywidag bars were installed and post-tensioned to the same standard as Test 9 – S1. The footing retrofit implemented for Test 10 – S3 is illustrated in Figures 7.14 and 7.15. Typical NSM bar details are presented in Figure 7.16.

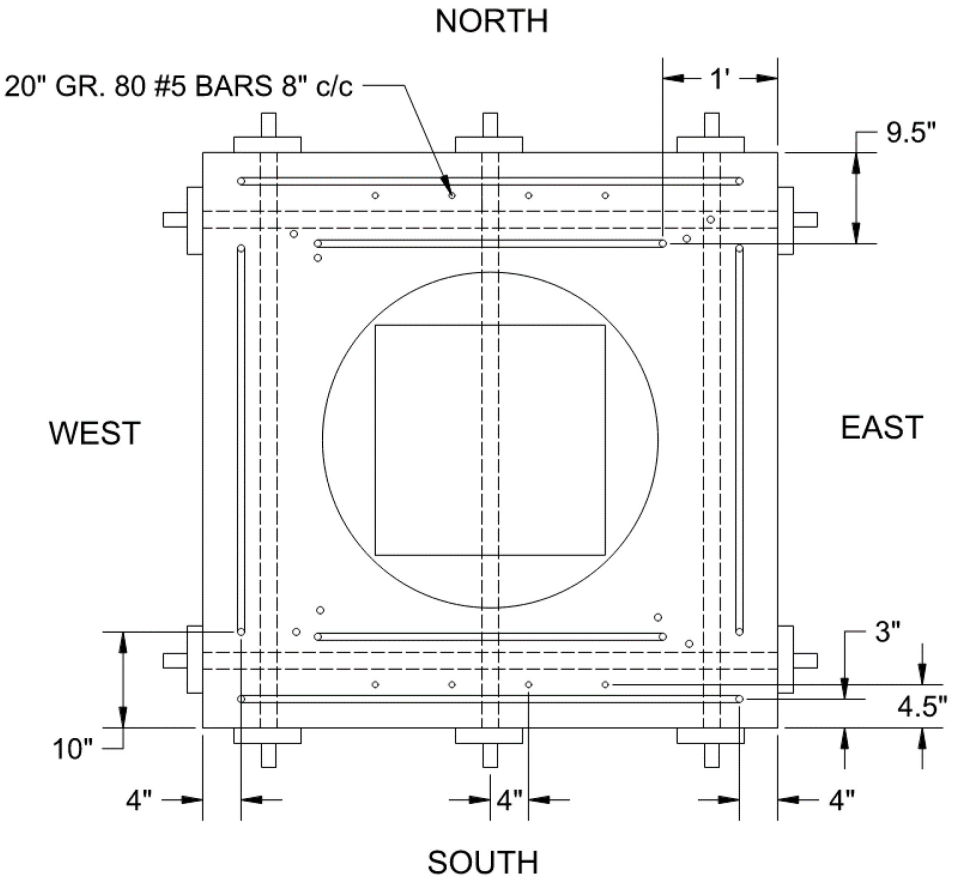

Figure 7.14: Footing retrofit, plan view for Test 10 – S3.

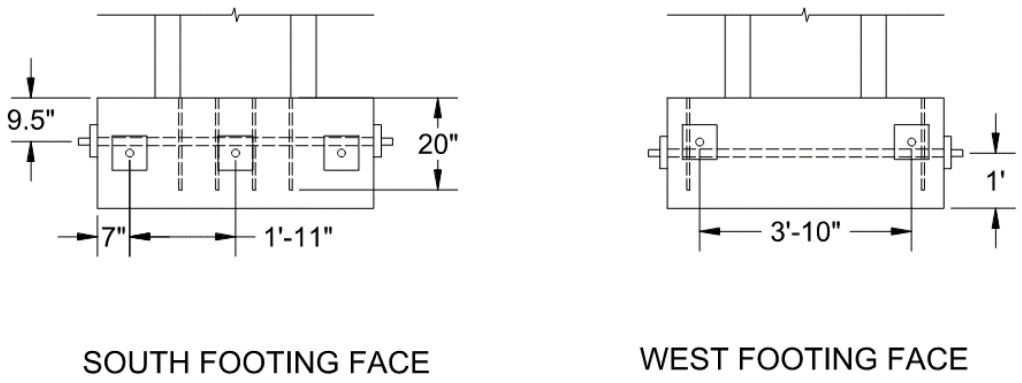

Figure 7.15: Footing retrofit, elevation view for Test 10 – S3.

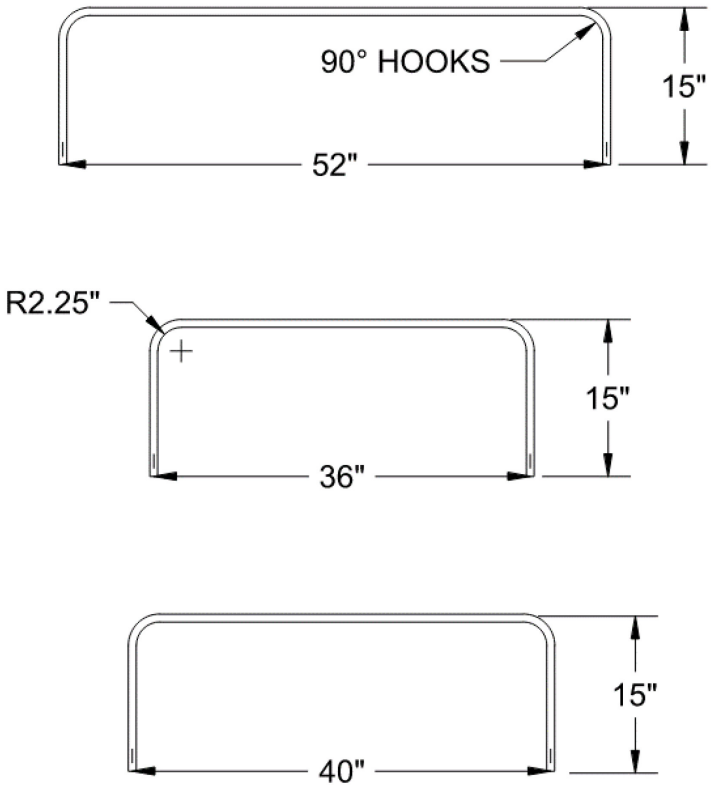

Figure 7.16: Typical Near Surface Mounted (NSM) reinforcing steel bar details used to strengthen the footing.

7.2.2.3 Specimen Construction

Specimen construction was completed in the Large-Scale Structural Engineering Laboratory at Oregon State University and overseen by Parson (2022). The detailed sequential construction process is described in Parson (2022), with a summarization of critical aspects provided herein.

Footings were constructed of a mesh grid of #4 (#13M) Grade 60 reinforcing steel spaced 172 mm (6.75 in.) c/c, #10 (#32M) starter bars, and the ready-mix concrete described in Section 7.2.2. A 7.6 cm (3 in.) clear cover was provided in between the mesh reinforcement and the bottom and faces of the footing. After the concrete was placed, lifting inserts were installed into the footings to facilitate movement of specimens to the testing site. Figure 7.17 shows the stages of construction of a footing, both before and after concrete casting.

i. 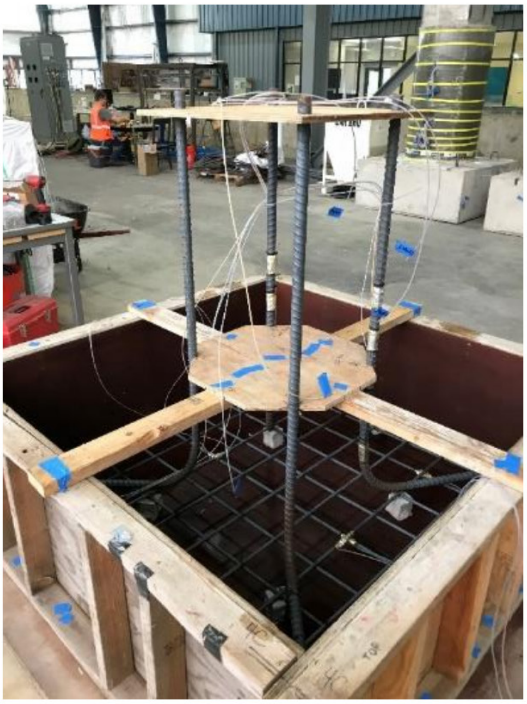 ii. 

Figure 7.17: Stages of construction for a typical footing, both prior to (i.) and after (ii.) casting (Parson 2022).

The columns were constructed using #10 (#32M) column bars, either 2.62 m (8.6 ft.) or 2.67 m (8.8 ft.) in length, and #3 or #4 (#10M or #13M) transverse stirrups tied to the longitudinal reinforcement at the elevations described in Section 7.2.2.1. The 50.8 mm (2 in.) variation in length of the column bars facilitated the presence of a 90-degree hook at the top of each bar, as shown in Figure 7.18, which depicts the stages of construction for the typical column of a specimen. After the formwork had been placed, four (4) PVC pipes were installed on the north and south faces of the column at the elevation at which the lateral loading was to be applied to allow connection of the actuator to the specimen.

TiAB ligaments were installed after column construction was completed and the concrete cured past 28 days to represent the retrofit of an actual column-footing substructure. As described in Section 7.2.2.2, the ligaments were to sit flush against the column face, be staggered in the elevation at which they were terminated, and to be embedded 239 mm (9.4 in.) and 508 mm (20 in.) into the column and footing, respectively. Holes were drilled into the specimen where the retrofit was to be embedded and were subsequently cleaned out to facilitate the epoxy-TiAB-concrete bond. Prior to the installation of the ligaments, plastic sheathing was wrapped around Specimens 1 and 2 to de-bond the concrete shell from the column and prevent composite action. For Specimen 3, this plastic sheathing was omitted, which allowed for the column and shell to act compositely to resist cyclic lateral loading. Figure 7.19 shows the ligament retrofit design for a typical column-footing specimen. Figure 7.20 shows the sequence of construction for a typical specimen.

i.



ii.



iii.

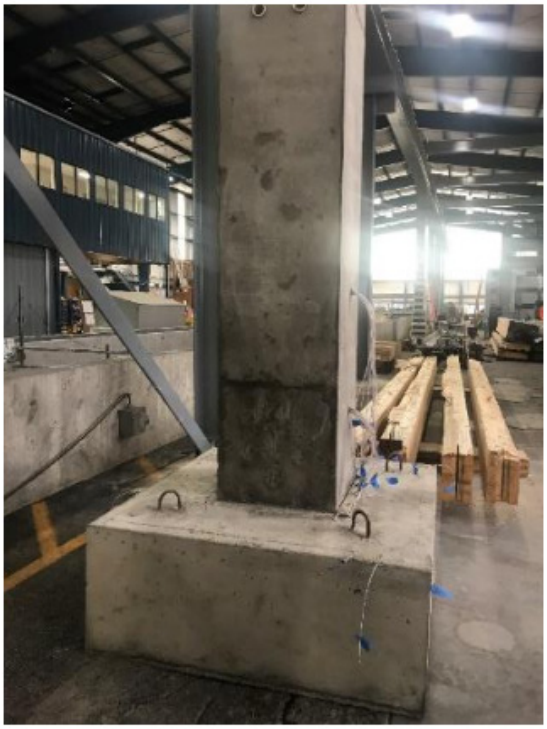

Figure 7.18: Stages of construction for a typical column specimen, i.) Column cage attached to the cast footing, ii.) Tied-down formwork for concrete pour, iii.) Completed vintage column on cast footing (Parson 2022).

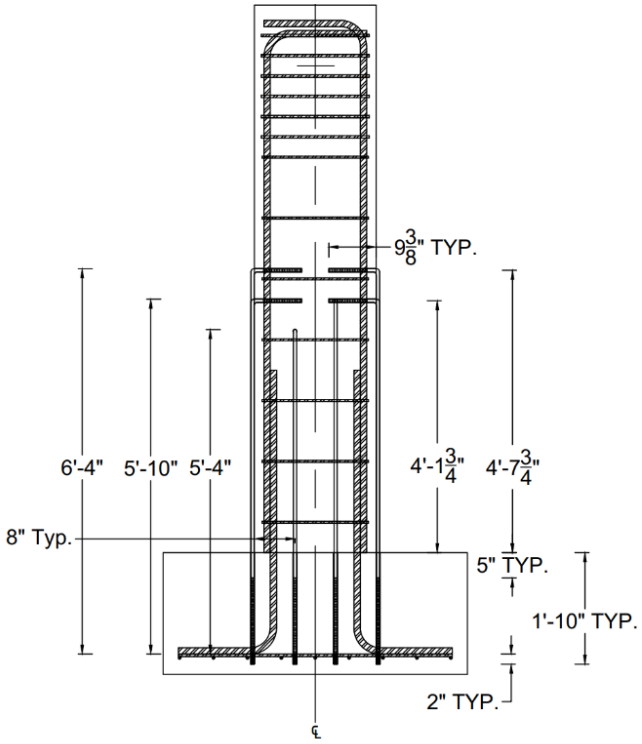

Figure 7.19: Typical ligament retrofit design (Parson 2022).

i. ii.

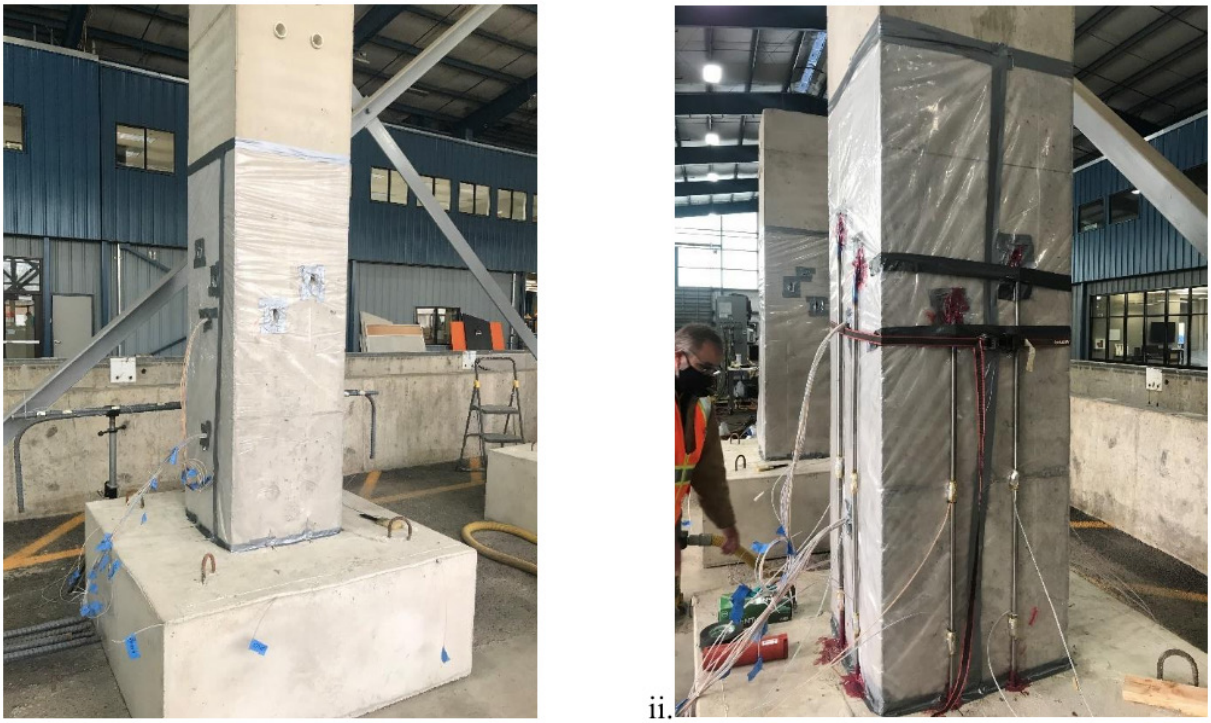

Figure 7.20: Construction sequence of TiAB ligament installation, i.) Drilled holes prior to ligament installation, ii.) Completed installation for a typical specimen (Parson 2022).

TiAB spirals required 203 mm (8.0 in.) embedment into the footing, per guidance provided in Shrestha (2019). An oxyacetylene torch was used to heat the bar and facilitate bending to form 90-degree hooks that were embedded into the footing. The retrofit consisted of two (2) TIAB spirals; a long spiral initiating at an elevation 1.524 m (5.0 ft.) above the top of the footing, and a short spiral starting 0.61 m (2.0 ft.) above the top of the footing. The spirals were embedded into the footing on opposite sides, as described in Section 7.2.2.2. Similar to the ligament installation, the holes drilled for spiral embedment were cleaned prior to the application of the epoxy to facilitate the TiAB-epoxy-concrete bond. The spiral retrofit was installed on Specimens 1 and 2 following the specimen construction, while Specimen 3 was not retrofitted until after the conclusion of Test 7, as described in Parson (2022). Figure 7.21 shows the construction sequence of the spiral for Specimens 1 and 2.

i.  ii. 

Figure 7.21: Construction sequence of TiAB spiral installation, i.) Spiral installation, ii.) Formwork for infill (Parson 2022).

7.2.2.4 Field Specimens

Two column-footing specimens were tested at the geotechnical field site described in Section 7.2.1. Specimens 4 and 5 were constructed using the same methods as Specimens 1, 2, and 3, which were tested in the structural laboratory. To best represent the standard vintage substructure design used in critical transportation corridors in Oregon, the west and east footing were embedded 1.4 m (55 in.) and 1.3 m (51 in.) beneath the ground surface, respectively. Figure 7.22 shows the orientation of the specimens at the geotechnical field site.



Figure 7.22: Field specimen site, with Specimen 5 (west Footing) shown closer to the picture location and Specimen 4 (east footing) closer to the Structural Laboratory.

In addition to the specimens at the field site, Figure 7.22 shows two W27x258 steel beams laying horizontally on the ground surface. Two 0.76 m (2.5 ft.) continuous flight auger piles extending to a depth of 16.8 m (55 ft.) and reinforced with a #18 (#57M) steel, threaded bar, were anchored through the webs of the beams to allow the specimens to be connected to a lateral loading system.

The field site preparation work initiated in October of 2021 with the excavations for the footings. Figure 7.23 depicts the excavations for Specimens 4 and 5. The depth of the excavated material was 1.3 m (51 in.) and 1.4 m (55 in.) beneath the ground surface for Specimens 4 and 5, respectively. The footings were cast neat using the soil as a form and with reinforcing details identical to those used in the structural laboratory experiments. Formwork for the column of each specimen was then constructed and the column reinforcements installed. Concrete was poured for the column on November 21st, 2021. The specifications for the concrete and the sequential construction processes were identical to those of Specimens 1, 2, and 3 constructed in the structural laboratory. Figure 7.24 depicts the steel reinforcements for the column of Specimen 4 and the formwork for the concrete placement at the GEFRS.



Figure 7.23: Excavations for the footings of Specimens 4 (i) and 5 (ii).

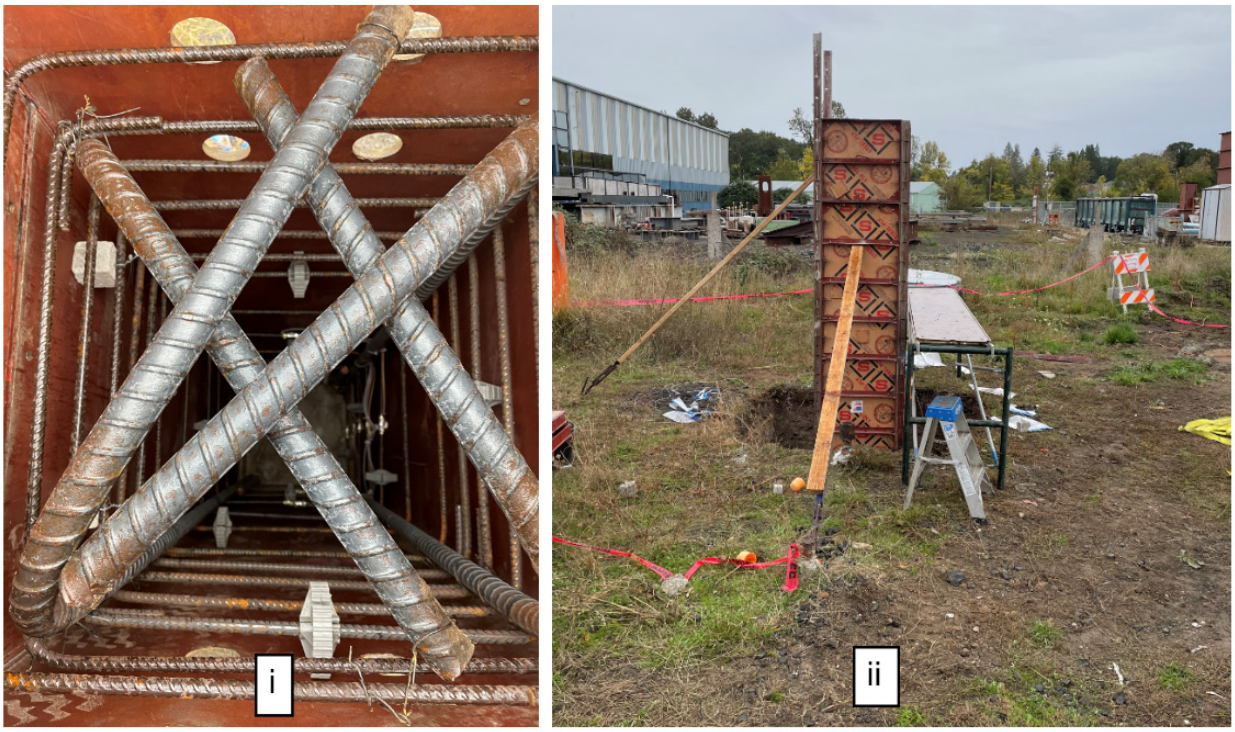

Figure 7.24: Structural reinforcement (i) and formwork (ii) for Specimen 4.

7.2.3 Instrumentation

As described by Parson (2022), various instruments were installed to measure the global and local responses of the specimen during cyclic loading. These instruments included strain gauges, string potentiometers, spring return linear position sensors (LPS), and load cells. To capture the strains within the structural reinforcement, strain gauges with a gauge resistance of 120±0.3 ohms (Ω) were bonded to the column ties and the footing, starter, and column bars. Additional strain gauges were fixed to the TiAB spirals and ligaments used for the column retrofit of Specimens 1 and 3.

7.2.3.1 Structural Laboratory Specimens

For structural laboratory tests, an axial load was applied to simulate the gravity load acting on a typical substructure. The applied axial force was measured by a 1,335 kN (300 kip) capacity load cell. The load cell was placed at the top of the column and a hydraulic jack was used to apply force to the column and load cell through a reaction beam connected to the strong floor through the use of Dywidag bars and a pin and clevis connection. This setup is illustrated in Figure 7.25, taken during Test 10 – S3.



Figure 7.25: Vertical load setup with connection to the strong floor, Test 10 – S3.

A 25.4 mm (1.0 in.) LPS was bonded to the south face of the column at the center and directly above the retrofit shell. This sensor measured relative movement between the shell and column face during testing. A load cell was also attached to the lateral load actuator to measure the lateral force applied to the column during testing. Various string potentiometers were used to measure displacements during testing. The most critical string potentiometer was connected to the column at the height of the applied load, which recorded top drift of the specimen during testing. For quasi-static cyclic loading, this instrument had a maximum displacement of 1.01 m (40 in.).

Eye hooks were drilled and bonded into the north and south sides of the footing. String potentiometers were connected to the eye hooks to measure the vertical motions of the footing (i.e., rocking). These sensors were attached to a fixed reference frame attached to the strong floor. An example of the setup for testing is provided in Figure 7.26.

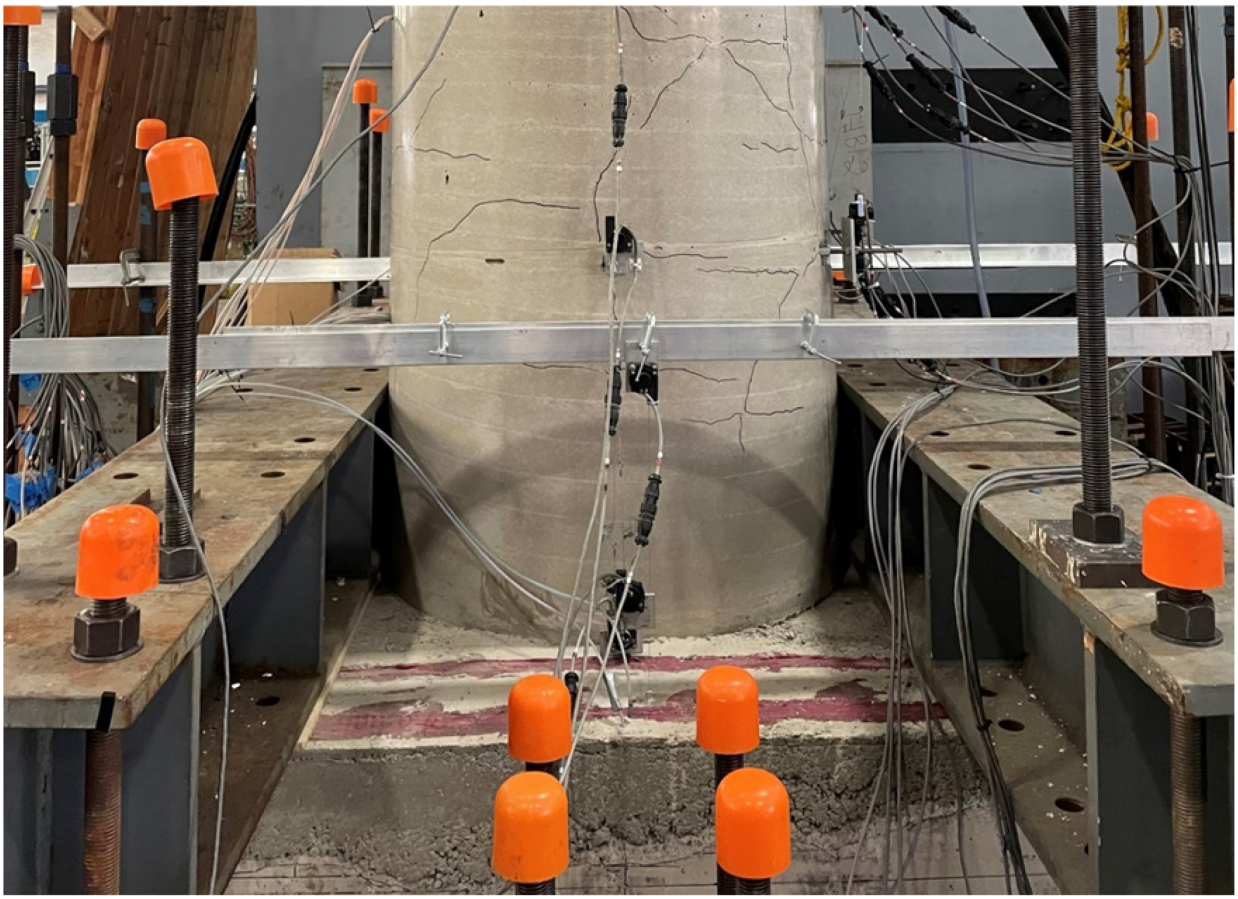

Figure 7.26: Rocking deformation string potentiometer setup for Test 10 – S3, north face.

To measure sliding of the specimen relative to the strong floor during testing, an eye hook was anchored in the south face of the footing. A string potentiometer was placed on the strong wall to the south of the test setup and connected to the eye hook on the footing face. Additional string potentiometers were placed in accordance with the procedures outlined in Parson (2022): sensors on the west face of the shell measured displacements

required to measure shear deformations, whereas those on the north and south faces measured displacements to enable estimations of column curvature.

7.2.3.2 Field Site Specimens

Specimens subjected to snap-back tests at the GEFRS site were instrumented with accelerometers attached to the column at the elevation at which the load was applied to record vertical and horizontal accelerations. String potentiometers with a displacement range of 50.8 mm (2.0 in.) were used to record the top drift and footing uplift during snap-back tests and provided greater signal-to-noise ratio for the small lateral motions which were induced during snap-back tests. A Sea Catch Toggle brand quick release with a 14.8 kN (3.3 kip) capacity was used for the snap-back tests on the specimens for which no axial column load was applied. A load cell attached to the quick release was used to record the pre-snap loading. Figure 7.27 shows the load cell attached in-line with the quick-release assembly, which included clevis clamps and eye bolts, prior to tensioning the assembly. Similar to the specimens tested in the structural laboratory, the steel reinforcements within the field specimens were instrumented with strain gauges. The instrumented reinforcements included footing bars, starter bars, column bars, and column ties. Due to the environmental exposure of the specimens for over a year, many strain gauges failed to function at the time of snap-back testing.

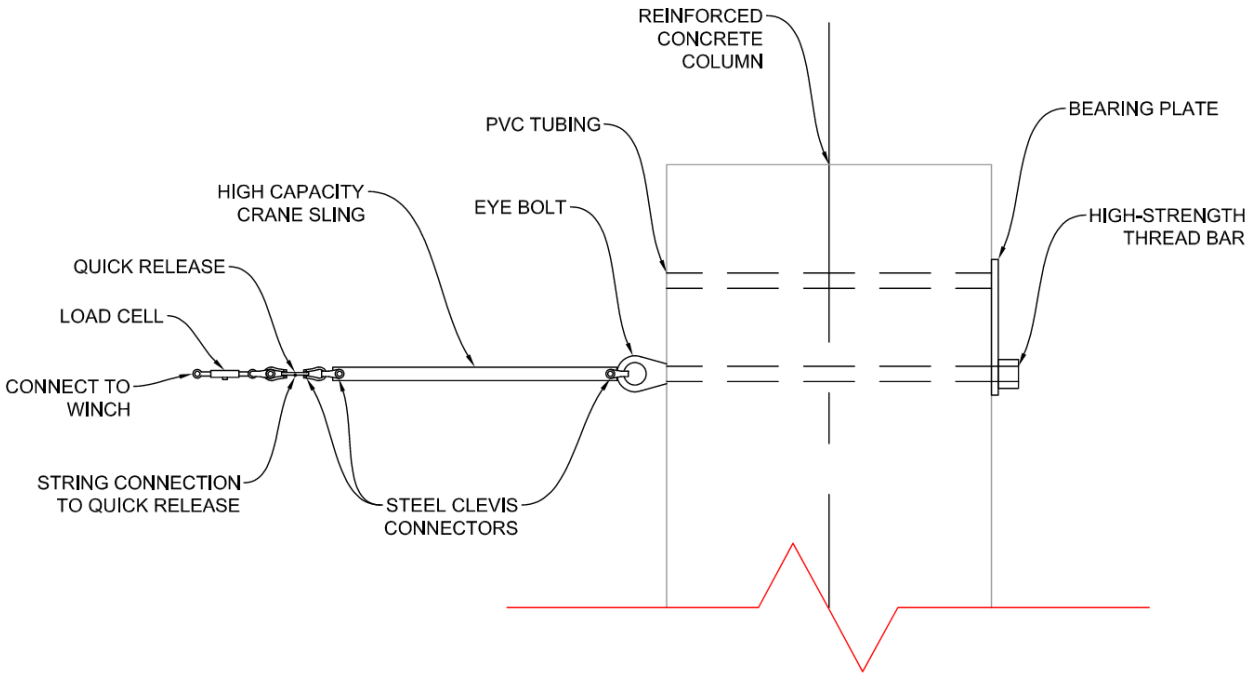

Figure 7.27: Load cell and quick release assembly for snap-back testing.

Two (2) 28-Hz triaxial geophone packages (TGPs) were installed beneath the west footing and were used for cross-hole geophysical testing and record the body waves that propagated from the base of the footing during each snap-back test. The TGPs selected

were Geospace Technologies Model GS-14-L9 with a natural frequency of 28 Hz and an open circuit damping of 31%. The coil resistance and open circuit sensitivity was 1,500 Ω and 23.62 V/m/s, respectively. Calibration of the geophones was described in Jana et al. (2021), as each TGP was independently calibrated to develop a sensitivity curve, which relates the voltage to the particle velocity for a given excitation frequency. The triaxial geophone packages recorded waves in three orthogonal directions of interest: the z-direction (up and down), the y-direction (east and west), and the x-direction (north and south). The z-geophones facilitated the determination of shear wave velocity, a value that was continuously monitored throughout the study. A cross-hole rod was hammered into place to the south of Specimen 5, adjacent to the north face of the footing. The rod was installed 89 cm (35 in.) directly to the south and in-line with the north and south TGPs to a similar depth as the TGPs. To create a shear wave that propagated through the subsurface, the cross-hole rod was struck by a rock hammer in the east-west direction. The distance of the rod in relation to the TGPs combined with its rough installation resulted in significant variability in the arrival times of waves.

An additional steel “tapper” cross-hole rod was installed at the time of specimen construction, adjacent to the east face of the footing and 40.6 cm (16 in.) directly to the north of the closest TGP. The rod terminated at an equivalent depth to that of the TGPs. Vertical strikes on this tapper with a traditional nail hammer created vertically propagating shear waves, which facilitated the determination of the shear wave velocity of the subsurface with little variability. Figure 7.28 shows the orientation of the TGPs in relation to the cross-hole rods and Specimen 5. Figure 7.29 provides a comparison of the propagated waves from strikes on the cross-hole and tapper rods.

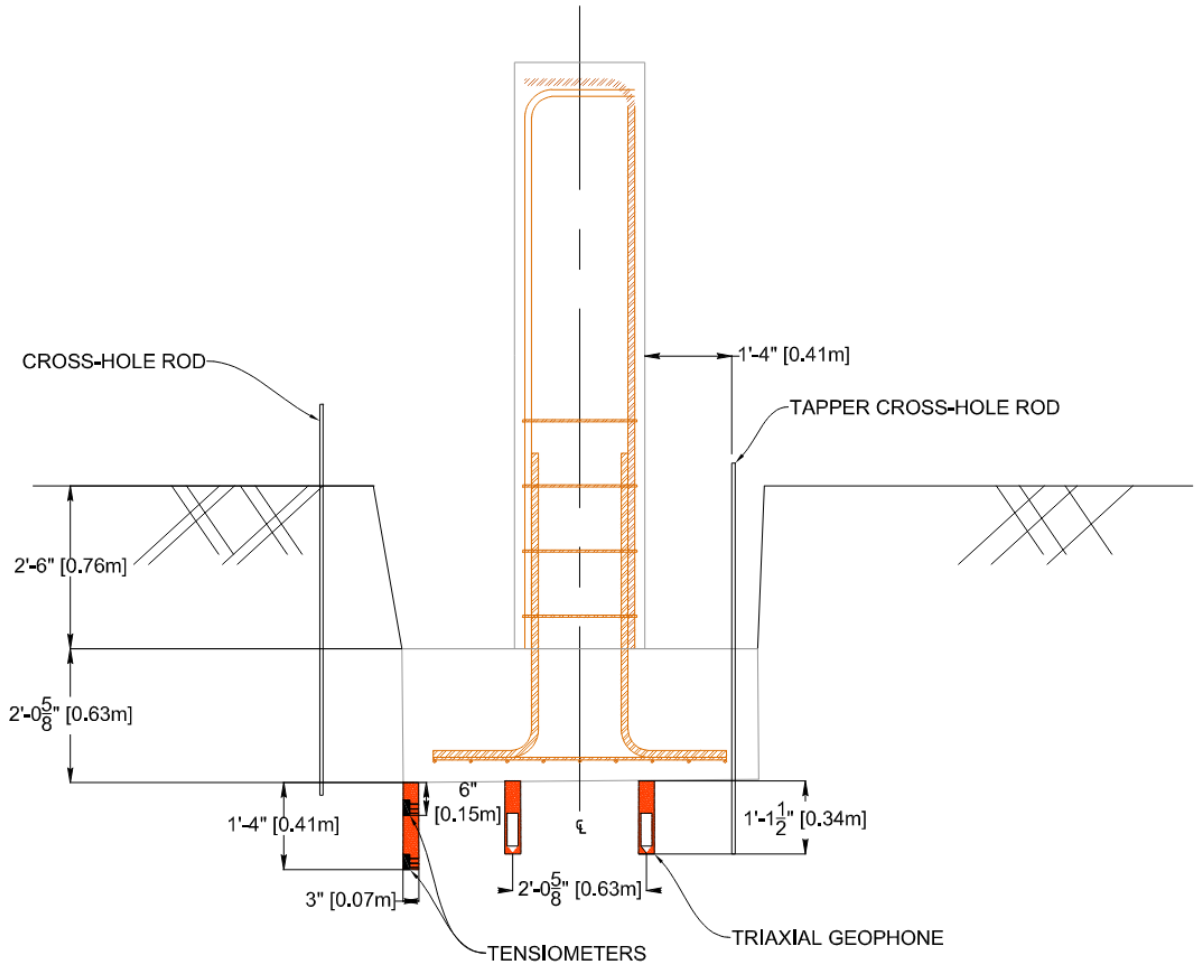

Figure 7.28: South-north elevation of Specimen 5 with TGPs and cross-hole rods.

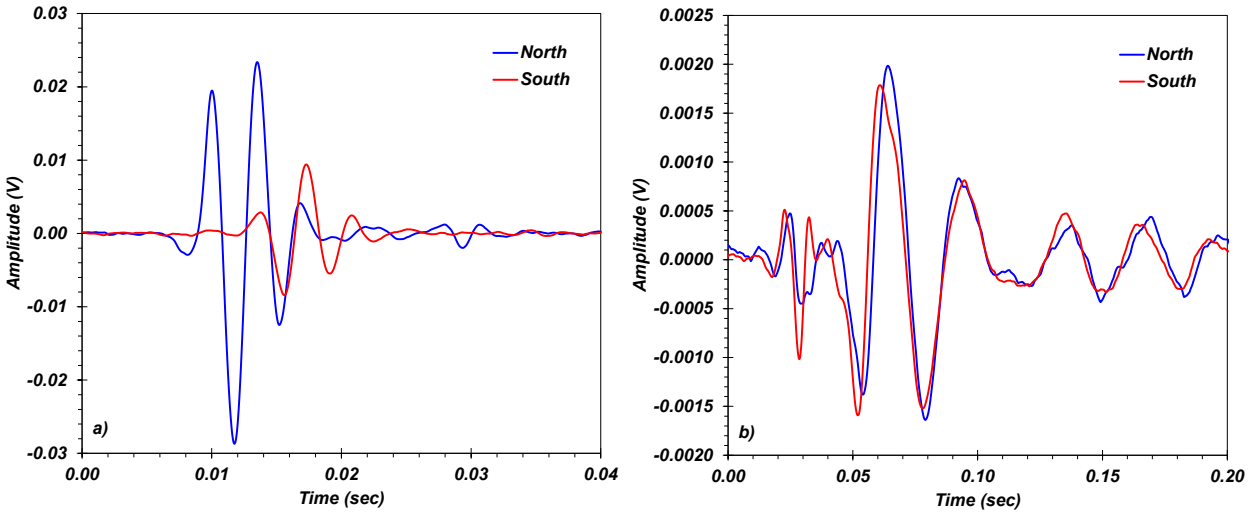

Figure 7.29: Shear wave arrivals resulting from: (a) vertical hammer strikes on the tapper cross-hole rod, and (b) horizontal hammer strikes on the post-construction cross-hole rod.

Two TEROS 12 tensiometers were installed in the material underlying each specimen, with the first embedded 0.15 m (6 in.) and the other 0.41 m (16 in.) beneath the base of the footing, as shown in Figure 7.28. Each sensor was hooked up to a data logger to evaluate fluctuations in volumetric water content, temperature, and matric suction at the south edge of the footing. For installation, a hole was augured to a depth of 0.61 m (2 ft.) below the excavation for the footing. The tensiometers were subsequently placed in the augured hole at the elevations noted. Owing to the challenge of backfilling the borehole with the native material extracted during auguring without introducing extensive sample disturbance, silica flour was backfilled into the hole to act as a substitute for the native material (McCartney and Khosravi 2013). Silica flour provides a desirable backfill material owing to its high hydraulic conductivity. Measurements of the moisture content of the native materials is performed by assuming that the water content in the silica flour will equilibrate with the surrounding native soils after a suitable period; then, the SWRC for the silica flour and native materials allows the matric suction in the native material to be determined. The volumetric water content measured by the silica flour measured by the tensiometers required that the instruments be calibrated following the procedure described by McCartney and Khosravi (2013), with the representative calibration curve shown in Figure 7.30.

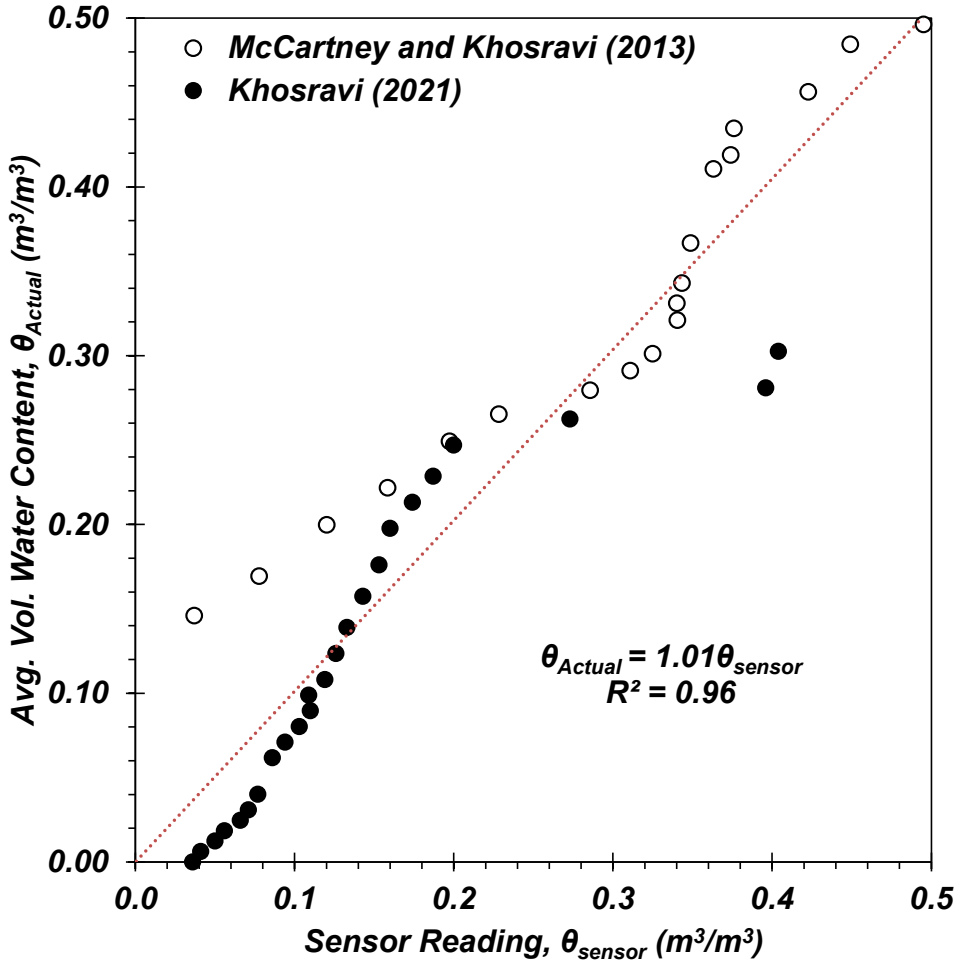

Figure 7.30: Calibration curve for the silica flour based on laboratory tests.

After the first sensor was lowered into the borehole, the silica flour was subsequently placed and tamped into place to an elevation slightly above the top of the tensiometer. A layer of granular bentonite was placed at this elevation which provided a hydraulic seal in between the two tensiometers to limit the influence that each sensor has on the other. This process was repeated for the upper sensor, providing two (2) silica flour zones representative of two (2) depths within the subsurface. The surface layer was then filled with granular bentonite, providing an additional hydraulic seal around the cables connecting to the data logger. For the test site, the data logger was located in an enclosed field trailer. The logger recorded volumetric water content, matric suction, and soil temperature at 12-hour intervals over the course of the study.

The SWRC results are subsequently used to correlate the volumetric water content of the silica flour to that of the surrounding material. Although the water content of the silica flour and in-situ soil is unequal, the matric suction at the interface of the materials is constant. By using the SWRC of the silica flour in combination with the SWRC of the native material, the respective water contents at any constant matric suction were determined, as shown in Figure 7.31. The fluctuation of volumetric water content with time is presented in Figure 7.32.

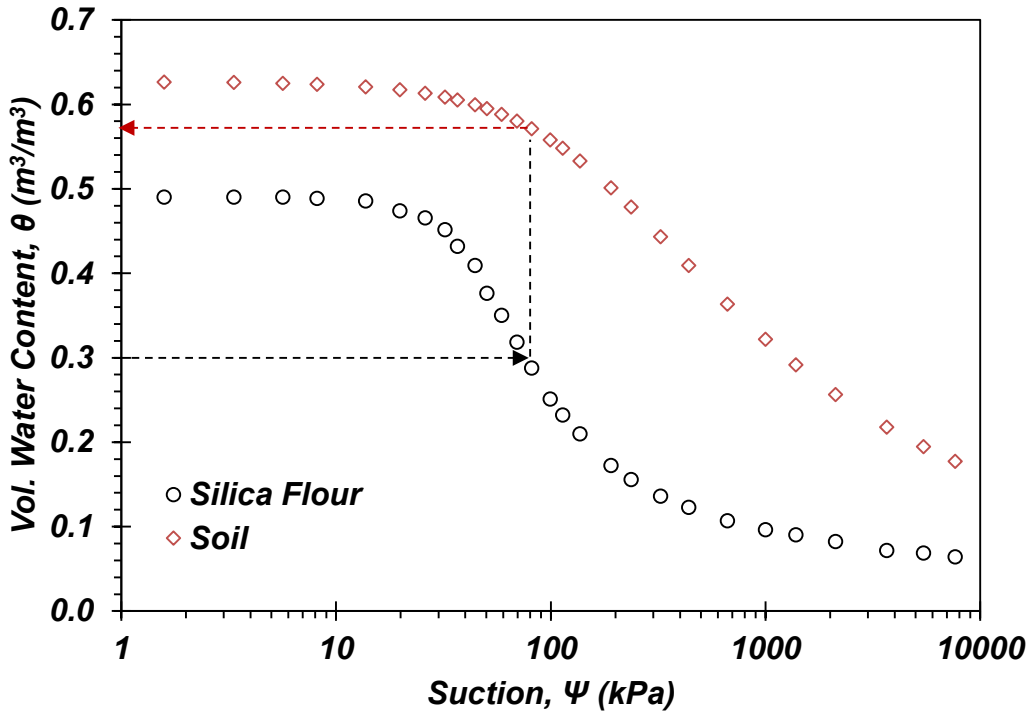

Figure 7.31: Process for correlating volumetric water content of silica flour to native soil based on SWRC results.

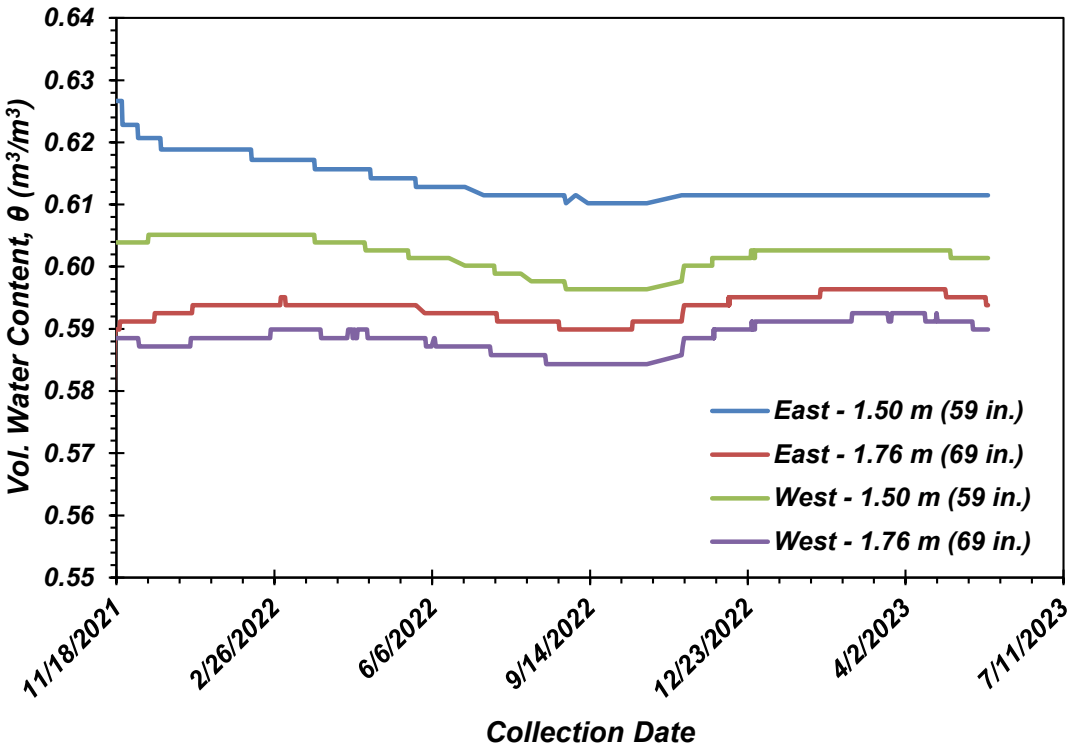

Figure 7.32: Volumetric water content of the subsurface beneath the east and west column-footing specimens at two depths: 1.50 m (59 in.) and 1.76 m (69 in.).

A comparison of the continuously monitored volumetric water content and shear wave velocity is presented in Figure 7.33. Results from the shallowest tensiometer installed directly beneath the west footing was used for the comparison, as this was the location closest to the TGPs. Generally, an increase in the volumetric water content of the subsurface was accompanied by a decrease in the V_s determined through tests using the cross-hole rod. As previously discussed, the shear wave velocities determined through the use of the cross-hole rod had high variability when compared to the determinations from tests using the tapper rod. The results from tests on the tapper rod indicated no evident trend between volumetric water content and shear wave velocity. With the range in volumetric water content being so minimal (59.6% to 60.3% for the timeframe of the current study), it is likely that the footing acts as a barrier for water to exit the material, resulting in the minimal seasonal changes in shear wave velocity evident from tests on the tapper rod.

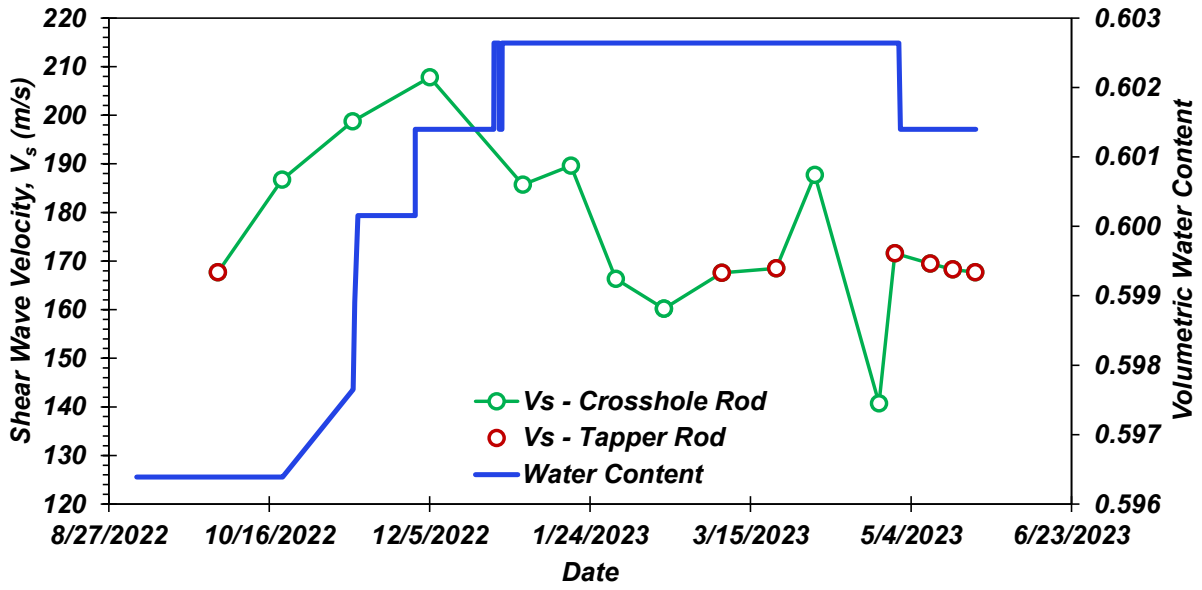

Figure 7.33: Volumetric water content of the subsurface beneath the west column-footing specimens at a depth of 1.50 m (59 in.) compared with the shear wave velocity determination from both cross-hole (green) and tapper rod (red) tests.

7.2.4 Test Setup

Two (2) test setups were utilized as part of the current study: the quasi-static cyclic lateral load tests performed in the structural laboratory, and the snap-back tests performed at the Oregon State University GEFRS. Tests in the structural laboratory required the use of the strong wall and strong floor, whereas snap-back field tests used reaction systems that varied dependent on the test performed.

7.2.4.1 Structural Laboratory Specimens

As described in Parson (2022), the structural laboratory setup included the use of the strong wall, strong floor, cruciform reaction beam, and vertical load reaction system. The actuator was connected to a pin and clevis on the strong wall at the same elevation at which the load was applied to the column. A 511 kN (115 kip) capacity actuator was used to apply the lateral load to the specimens. The actuator was servo-hydraulically controlled using an MTS TestStar system. The axial load was applied to the column top with a vertical actuator that was also servo-hydraulically controlled to provide constant load. A reaction system for this vertical actuator consisted of a large hot-rolled steel column section (W14x283) that was connected to the strong floor using high-strength threaded rods attached to a pin and clevis. The pin and clevis prevented bending of the threaded rods as the column underwent horizontal movement due to the application of lateral loads. This system ensured that the axial load was always applied normal to the top face of the column. Below the specimen a 0.15 m (6 in.) thick, 1.83 m (6 ft.) square reinforced concrete slab was placed to maintain the original geometry of the lateral loading setup from earlier tests performed on soil simulant (e.g., Parson 2022 Tests 1

through 7). Prior to the specimen being placed on the slab, USG-11 Hydro-stone, a high-strength cementitious plaster, was placed on the slab to ensure a uniform contact surface between the footing and the concrete base slab. Since Specimens 1 and 3 had been previously tested, the Hydro-stone additionally served to limit the effects from any prior localized deformations at the base of the footing (e.g., rounding, chipping of corners). Figure 7.34 illustrates the typical setup for the structural laboratory tests.

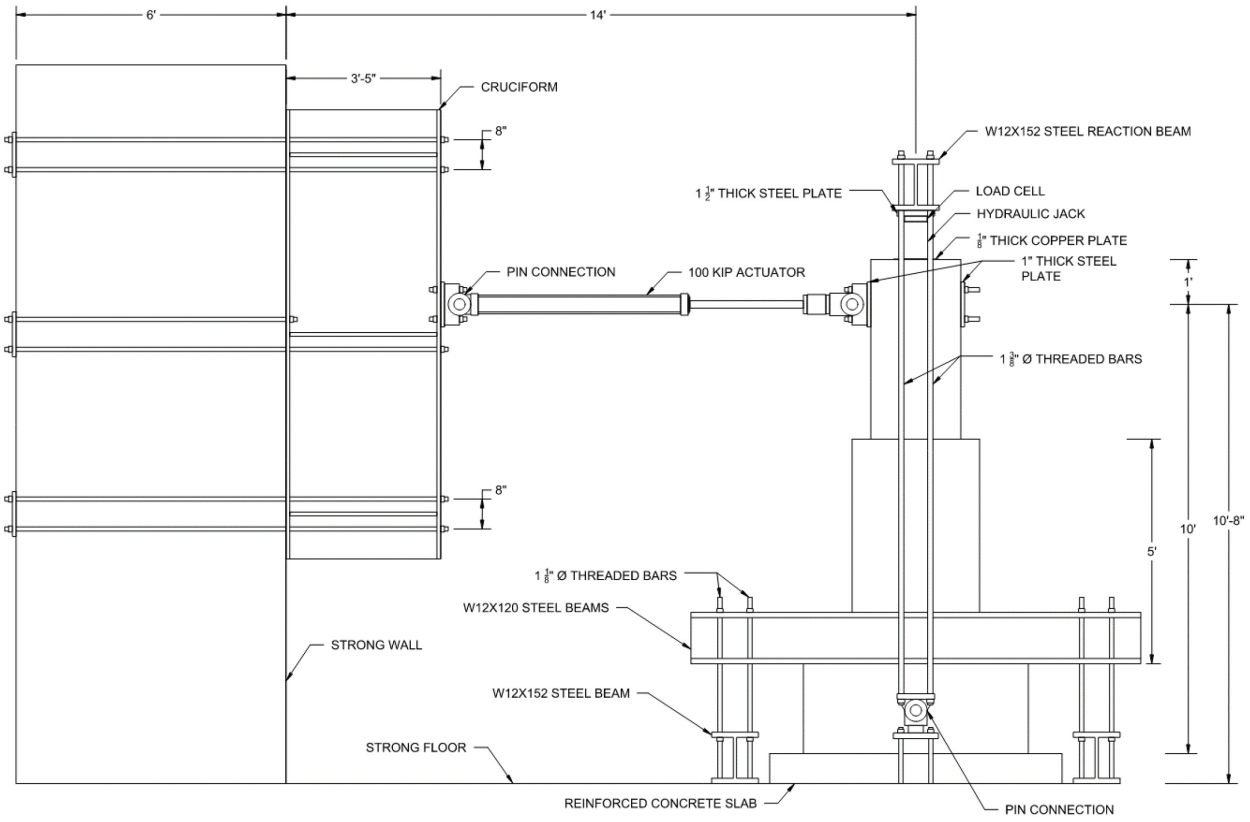

Figure 7.34: Typical test setup use in the structural laboratory.

A system of steel beams was used to restrain the footing and prevent rocking during the imposed cyclic load to the top of the column. This system consisted of two (2) W12x152 steel beams held down using high-strength, threaded rods embedded 1.4 m (55 in.) into the strong floor. With the specimen in position, two (2) W12x120 steel beams were placed on top of the east and west sides of the footing. The W12x120 beams were connected to the W12x152 beams with additional high-strength, threaded rods. Fiber board was placed between the top of the footing and the W12x120 beams to enable a more uniform bearing across the imperfect concrete finished surface. A photograph of the test setup for Test 9 - S1 is provided as Figure 7.35.



Figure 7.35: Specimen 1 anchored to the strong floor for Test 9 – S1.

7.2.4.2 Field Site Specimens

The experimental setup used to test the field specimens was designed to apply a desired lateral force to the column and subsequently release the load instantaneously to perform snap-back tests on specimens without an additionally applied axial load. The quick release, described in Section 7.2.3.2, was attached to a steel chain and winch, allowing for the application of a desired lateral force and then a subsequent instantaneous release of the load. As previously discussed, a load cell was attached to the quick release through the use of clevis clamps and eye bolts. Acting as an anchor for the winch was a boom lift, which was maneuvered so the load could be applied normal to the column face. The data acquisition system used in the structural laboratory was relocated to the field trailer and located just to the south of the field site. This experimental setup is shown in Figures 7.36 and 7.37 from the November unloaded snap-back tests.



Figure 7.36: Boom lift positioned for snap-back tests on west footing (Specimen 5).

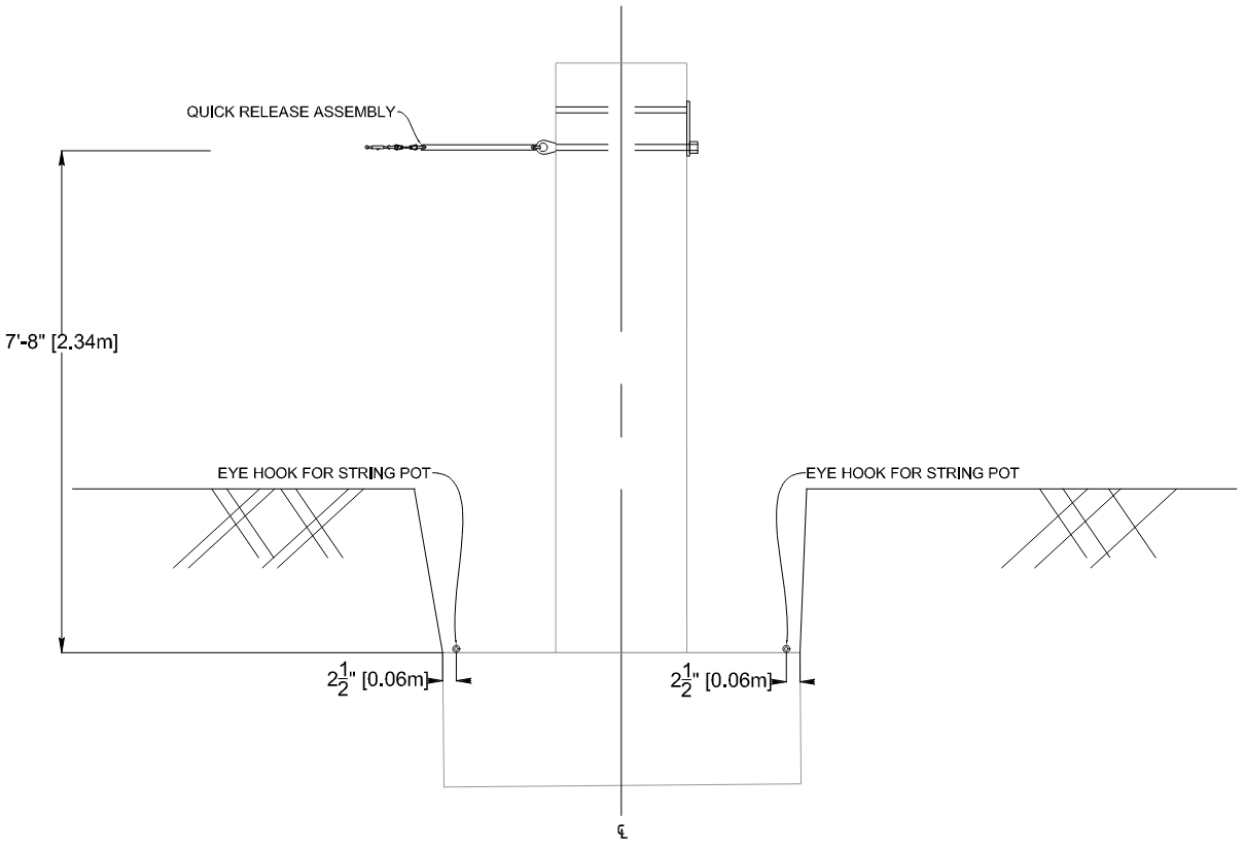

Figure 7.37: Experimental setup for snap-back tests with critical nominal dimensions.

7.2.5 Loading Protocol

The loading protocol utilized in this work was dependent on the test conducted. Structural laboratory specimens were subjected to a loading protocol that imposes incrementally larger lateral displacements with repetitions to the specimens as was used and reported by both

Shrestha (2019) and Parson (2022). New loading protocols were developed for the snap-back field tests, limited by the capacity of the quick release.

7.2.5.1 Structural Laboratory Specimens

As described in Parson (2022), the 667 kN (150 kip) column axial load applied for tests performed in the structural laboratory was derived by Shrestha (2019) based on review of the ODOT bridge inventory for bridges used in transportation corridors that were designed/constructed prior to the implementation of seismic design standards. This axial load represents a typical service-level gravity load on a single column-footing substructure for relevant bridges in the inventory. For a given displacement cycle, a desired lateral displacement at the load point was input and the resulting lateral force was measured by the load cell attached to the horizontal actuator. The displacement protocol was derived by Shrestha (2019) in accordance with ACI 314.2R-13 based on the calculated yield displacement from a moment-curvature analysis of the column, as described by Parson (2022). For smaller displacements, three (3) cycles of push and pull were performed at each displacement. This repetition in loading was performed to observe possible strength degradation on a per-cycle basis. At relatively small displacements, it was unlikely that any major damage in the specimen would be present; however, after a top drift of 60 mm (2.4 in.), the number of cycles was reduced to two (2), as damage begins to accumulate. Table 7.7 depicts this loading protocol, along with the associated number of cycles at each displacement amplitude.

The 14.8 kN (3.3 kip) capacity quick release shown in Figure 7.26 controlled the loading protocol for snap-back tests. Initial calculations of the seasonally dependent, lateral force required to induce lift off indicated that the capacity of the quick release was insufficient to achieve rocking behavior. The snap-back tests were performed with applied lateral forces that increased by 4.5 kN (1.0 kip) incrementally to a maximum of 13.3 kN (3.0 kips). Tests were repeated at the maximum force during the spring season to determine the season-dependent response of the subsurface to the snap-back tests.

Table 7.7: Lateral Displacement Protocol (Modified from Shrestha 2019).

Loading Protocol			
Displacement cycle	**Displacement cycle**	**Number of cycles**	**Loading rate**
cm (in)	**(% drift)**		**mm/sec (in/sec)**
0.25 (0.10)	0.10	3	0.127 (0.005)
0.51 (0.20)	0.20	3	0.25 (0.01)
0.76 (0.30)	0.30	3	0.51 (0.02)
1.01 (0.40)	0.42	3	0.51 (0.02)
1.52 (0.60)	0.63	3	0.76 (0.03)
2.03 (0.80)	0.83	3	0.76 (0.03)
3.05 (1.20)	1.25	3	1.02 (0.04)
4.06 (1.60)	1.67	3	1.02 (0.04)
5.08 (2.00)	2.08	3	1.27 (0.05)
6.10 (2.40)	2.50	2	1.27 (0.05)
7.11 (2.80)	2.92	2	1.27 (0.05)
8.13 (3.20)	3.33	2	1.27 (0.05)
9.14 (3.60)	3.75	2	1.52 (0.06)
10.16 (4.00)	4.17	2	2.03 (0.08)
11.18 (4.40)	4.58	2	2.03 (0.08)
12.19 (4.80)	5.00	2	2.54 (0.10)
13.21 (5.20)	5.42	2	2.54 (0.10)
14.22 (5.60)	5.83	2	3.05 (0.12)
16.26 (6.40)	6.67	2	3.05 (0.12)
18.29 (7.20)	7.50	2	3.56 (0.14)
20.32 (8.00)	8.33	2	3.56 (0.14)
22.86 (9.00)	9.38	1	3.56 (0.14)

7.2.5.2 Field Site Specimens

The 14.8 kN (3.3 kip) capacity quick release shown in Figure 4.26 controlled the loading protocol for snap-back tests. Initial calculations of the seasonally dependent lateral force

required to induce lift off indicated that the capacity of the quick release was insufficient to achieve rocking behavior. The snap-back tests were performed with applied lateral forces that increased by 4.5 kN (1.0 kip) incrementally to a maximum of 13.3 kN (3.0 kips). Tests were repeated at the maximum force during the spring season to determine the season-dependent response of the subsurface to the snap-back tests.

7.2.6 Summary of Section 7.2

The subsurface characteristics of the GEFRS have been summarized in Dickenson (2006) through numerous in-situ explorations and laboratory tests on soil samples retrieved from the site. In recent years, additional SCPT in-situ explorations at the site of the current study have been performed. This sub-section provided an up-to-date synopsis of the geologic history, soil properties with consideration to seasonal-dependence, and initial estimations for the strength parameters for the material in both the seasonally wet and dry conditions. The results presented within this section will be referenced extensively in the full-scale field test results and parametric analyses presented in Sections 7.3 and 7.4, respectively.

Column-footing Specimens 1, 3, 4, and 5 were tested as part of the current study. The specimen designs and construction processes were summarized in this section, including the sequential construction steps for vintage columns and footings, structural details, and the TiAB retrofit design and implementation. Vintage column-footing substructure specimens were constructed to best represent typical vintage column-footing substructures supporting transportation corridors in Oregon, and the TiAB retrofit represented a plausible field-constructible scheme to ensure ductile and predictable seismic performance. Specimens were instrumented to measure the response to either quasi-static cyclic lateral loading or snap-back tests at the OSU Structural Laboratory or GEFRS, respectively.

7.3 EXPERIMENTAL OBSERVATIONS, RESULTS, AND ANALYSES

7.3.1 Shear Force-Displacement Responses

The application of axial load to the column specimens simulated the tributary dead load attributed to a column in a typical bridge bent system of the era considered in the research program. The experimental tests imposed vertical load to the specimen with a servo-hydraulically controlled hydraulic actuator attached to a gravity-load reaction system. As lateral drift was applied to the column, the gravity load setup produced both vertical and horizontal forces on the column. Due to the experimental arrangement, the column shear imposed during the cyclic tests was not equal to the force measured by the lateral actuator load cell. The horizontal component of the axial load reduces the internal column shear. In the discussion to follow, the shear force-displacement responses are shown in terms of internal column shear, base moment (i.e., internal column shear multiplied by the moment arm, or height of the column and the vertical component of the gravity load from *P-Δ* effects), top of column drift, and drift ratio (i.e., the ratio of top drift and the distance from the top of the footing to the location at which drift is measured).

7.3.2 Correction of Column Shear Force for *P-Δ* Effects

Two components of axial load affect the internal force and moments within the footing-column specimen: one is a counteracting force from the horizontal component of the gravity load simulator and the other is the *P-Δ* effect from the vertical component that adds to the internal column moment. Both effects are small at small top drifts, but they become more substantial at the higher drifts imposed during cyclic testing.

Shrestha (2019) and Parson (2022) outline the procedure for determining internal column shear using the measured actuator load. At any point throughout the test where the drift at the point of load application is nonzero, there is a horizontal component of the axial load that counteracts the actuator load. This horizontal component acts at the point at which the axial load is applied, 2.7 m (9 ft.) above the top of the footing, as depicted in Figure 7.38.

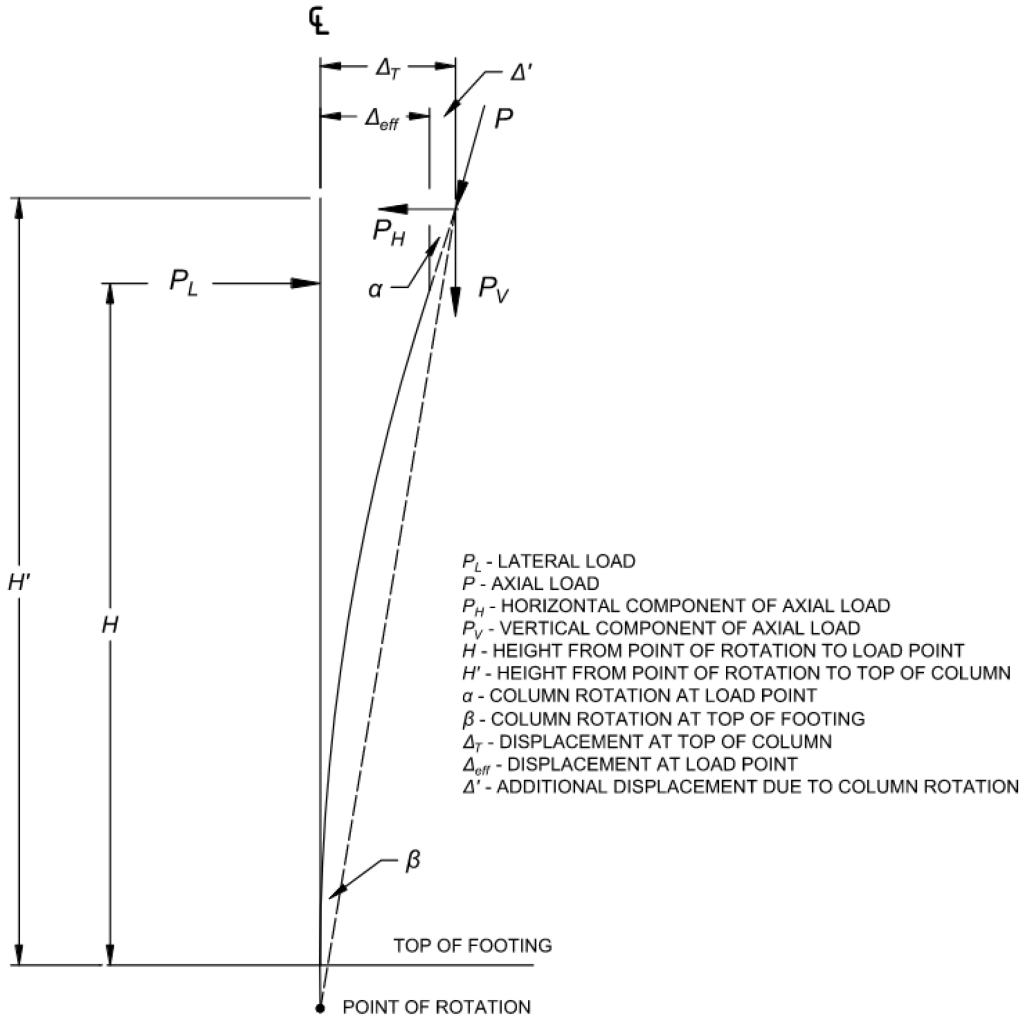

Figure 7.38: Schematic representation of forces and displacement experienced by test specimen.

Figure 7.38 shows that an additional moment, $P_V\Delta_T$, develops at the location of axial load application relative to the lateral load, which results in the *P-Δ* effect. This effect must be removed to calculate the moment in the column at the top of the footing, *M*. The top drift, Δ_{eff}, was measured using a string potentiometer attached at the height of load application. The height from the point of rotation to the lateral load application point, *H*, was equal to 2.4 m (8 ft.). The total height from the point of rotation to the vertical load application point, *H'*, was equal to 2.7 m (9 ft.) assuming the footing itself is prevented from rotation (e.g., Test 9 – S3 and Test 10 – S1). The column rotation at the load point, *α*, was derived using the virtual work method (Shrestha 2019).

$$\boldsymbol{\alpha = \frac{3\Delta_{eff}}{2H}} \tag{7-7}$$

The additional drift at the column load point due to the column rotation at the lateral load point, *Δ'*, using small angle theory is therefore calculated as:

$$\Delta' = \boldsymbol{\alpha(H' - H)} \tag{7-8}$$

The angle of incidence for the axial load, *β*, is computed from the geometry of the deformed column as:

$$\boldsymbol{\beta = \frac{\Delta_{eff} + \Delta'}{H_{az}}} \tag{7-9}$$

Where H_{ax} is the vertical distance from the center of rotation to the top of the column where the axial load is applied. The vector components of the axial load are determined from the angle that the axial load application makes to the center of rotation, *β*, as:

$$\boldsymbol{P_V = Pcos\beta\ ; P_H = Psin\beta} \tag{7-10}$$

The moment in the column at the top of the footing is determined by adding and subtracting the moment contributions from the vector components of the *P-Δ* effect with that of the applied lateral force as:

$$\boldsymbol{M = P_L H + P_V \Delta_T - P_H H'} \tag{7-11}$$

The column shear within the specimen, *V*, can be determined at any top drift as the summation of the applied lateral force and horizontal component of the axial load as:

$$\boldsymbol{V = P_L - P_H} \tag{7-12}$$

7.3.3 Observed Global Structural Behavior

As described in Section 7.2, the reinforced concrete column-footing specimens were constructed to best represent vintage substructures commonly in service in highway systems across the State of Oregon. Two specimens tested in prior work by Parson (2022) were loaded until failure as a part of this study to quantify the structural capacity in terms of the moment-drift performance of the retrofitted bridge column-footing specimens.

7.3.3.1 Overview

Table 7.8 summarizes the tests performed as part of this thesis and those performed by Parson (2022) on the same specimens as part of the same study. Tests 1 through 8 were performed and described by Parson (2022), whereas Tests 9 and 10 were conducted as part of the current study. A given specimen is designated by "Test X – SY", where "X" is equal to the chronological test number and "Y" corresponds to the specimen number (e.g., Test 9 – S3 corresponds to the ninth test performed chronologically on a column-footing substructure identified as Specimen 3). Prior to beginning Tests 9 and 10, cracks resulting from the previous tests were visually indentified and marked on the specimen with a black marker to differentiate cracks arising from the subsequent tests (described herein) from those generated previously. A typical test initiated with the concentric application of 667 kN (150 kips) of axial load to the specimen. The axial load magnitude was held constant during the entirety of the test. Once the axial load was applied, the specimen was subjected to the quasi-static cyclic displacement-based lateral loading protocol specified in Section 4.6. The displacement of the specimen was measured at the elevation where the load was applied, subsequently referred to as top drift. At various top drifts, lateral loading was paused once the cycle was complete to allow for the identification of cracks, spalling and other visual distress which developed on the column and footing of the specimen.

Table 7.8: Specimen Designations and Descriptions.

Designation	Description	Reference
Test 1 - S1	Complete Retrofit with Soil Simulant Subgrade and Embedment	Parson (2022)
Test 2 - S2	Complete Retrofit with Soil Simulant Subgrade and No Embedment	Parson (2022)
Test 3 - S3	Vintage Column with New Subgrade, Embedment, and Axial Load	Parson (2022)
Test 4 - S3	Vintage Column with Damaged Subgrade, Embedment, and Reduced Axial Load	Parson (2022)
Test 5 - S3	Vintage Column Failure with Damaged Subgrade and Steel Embedment	Parson (2022)
Test 6 - S3	Failed Vintage Column with Ligament Retrofit, Damaged Subgrade, and Steel Embedment	Parson (2022)
Test 7 - S3	Failed Vintage Column with Complete Retrofit, Damaged Subgrade, and Steel Embedment	Parson (2022)
Test 8 - S2	Complete Retrofit with Tied Down Footing and No Soil Simulant	Parson (2022)
Test 9 - S1	Vintage Column and Retrofitted, Restrained Footing with Ligament and Spiral Retrofit	Current Study
Test 10 - S3	Vintage Column with Ligament and Spiral Retrofit and Restrained Footing with Additional Retrofit	Current Study

7.3.3.2 Test 9 – S1: Vintage Column and Retrofitted, Restrained Footing with Ligament and Spiral Retrofit

The previous test on Specimen 1 (Test 1 – S1) included cyclic loading to a maximum top drift of 254 mm (10 in.). A maximum lateral force of 200 kN (45 kips) was applied to the fully-retrofitted specimen. The test resulted in numerous flexural cracks forming in the footing, retrofit shell, and column. These cracks were indentified prior to the start of Test 9.

As depicted in Figure 7.39, Test 9 – S1 demonstated a nonlinear force-displacement response after a top drift of 10.1 mm (0.4 in.) was reached. No damage was observed on the footing for this magnitude of drift; however, small cracks were noted on the column faces at a drift of 15.2 mm (0.6 in.), indicating that the observed nonlinear response was associated with initial minor damage to the column. Cracking in the footing first became apparent at a top drift of 81.3 mm (3.2 in.), with cracks becoming more prevalent at a drift of 111.8 mm (4.4 in.). The cracks occurred on the north and south faces of the footing, with cracks emanating from the anchor plate of the center-most post-tensioned footing bar (see Figure 7.43 for condition at failure). After achieving the top drift of 81.3 mm (3.2 in.), the previously existing cracks in the column no longer propagated, as the footing appeared to control the response. Shear strength degradation of the specimen initiated at a top drift of 91.4 mm (3.6 in.), as the maximum column shear reduced with increased column drift. Additionally, the observed column shear decreased on a per-cycle

basis, further exemplifying the shear strength degradation of the specimen during cyclic loading. The test was terminated once Specimen 1 failed at a top drift of 183 mm (7.2 in.), with failure defined as sufficient strength degradation of the specimen. Photographs depicting the progressive damage observed on Specimen 1 from Test 9 are presented in Figures 7.40 through 7.43.

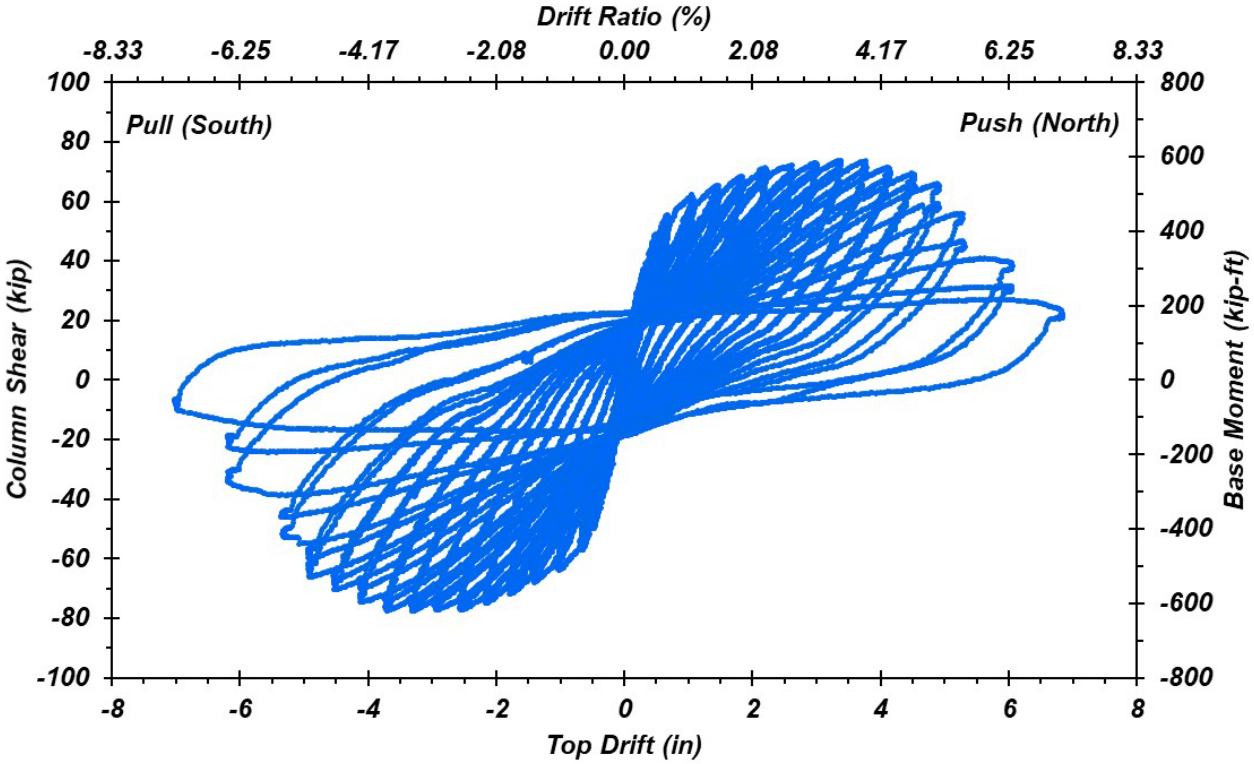

Figure 7.39: Column shear-top drift hysteresis of Test 9 - S1.

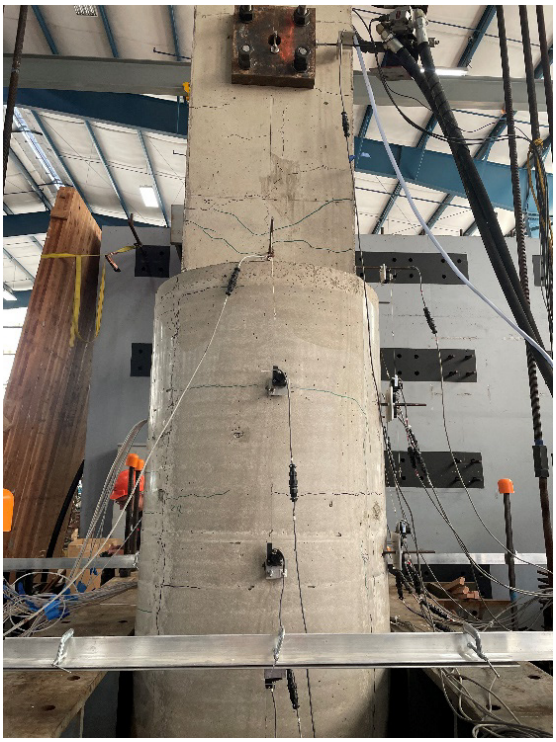

Figure 7.40: Cracking observed on the north face of Specimen 1 at a top drift of 61 mm (2.4 in.), traced in green.



Figure 7.41: Cracking observed on the north face of Specimen 1 at a top drift of 81.3 mm (3.2 in.), traced in blue.



Figure 7.42: Cracking observed on the south face of Specimen 1 at a top drift of 81.3 mm (3.2 in.), 101.6 mm (4.0 in.) and 111.8 mm (4.4 in.) outlined in blue, red and green, respectively.

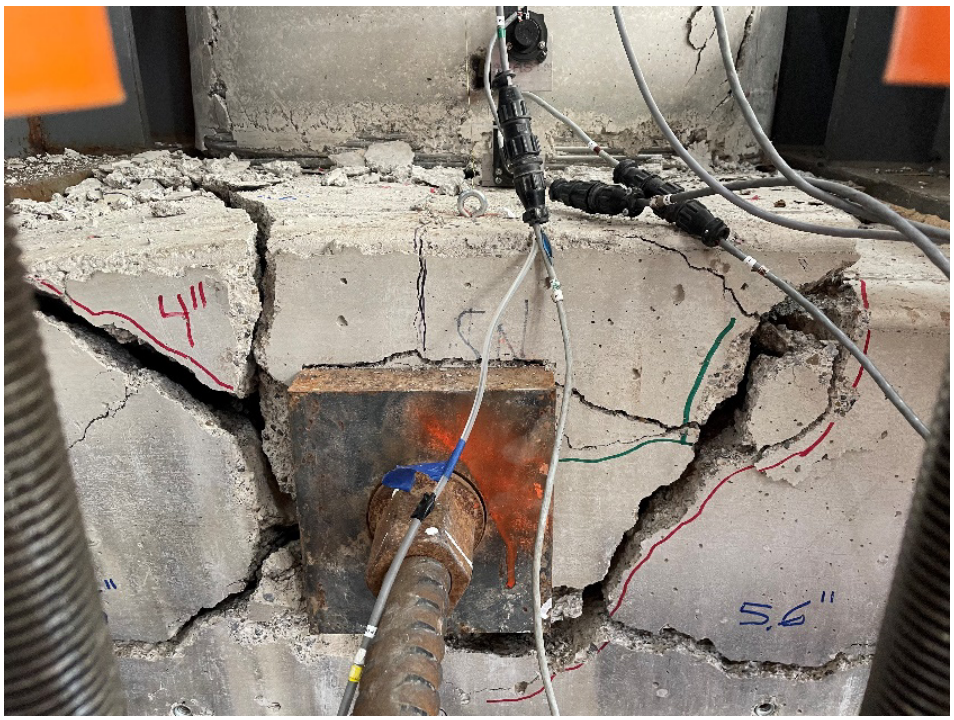

Figure 7.43: Punching shear cracks observed on the north face of Specimen 1 during the pull (south) portion of the cycle at a top drift of 182.9 mm (7.2 in.).

After the steel beams which provided restraint of the footing through anchorage to the strong floor had been removed, a full visual inspection of the footing was performed. As depicted in Figure 7.44, cracks on the top of the footing spanned from the outermost post-tensioned steel bar to the near-surface mounted (NSM) bars. These cracks propagated towards the center of the footing, but did not extend beyond the NSM bars, indicating that the footing retrofit succeeded in restraining cracks and delating footing damage.



Figure 7.44: Post-testing cracks observed on the east side of the footing, Specimen 1.

After dismantling the test specimen, the retrofit shell and TiAB spiral were removed on the west face of the specimen. This was done to observe the column condition and the TiAB ligaments within the retrofitted region. As depicted in Figure 7.45, the TiABs prevented propagation of cracks in the column and footing and showed no signs of damage. Additionally, cracks in the portion of the column that were covered by the retrofit shell were limited compared to those observed above the retrofitted portion. These observations clearly demonstrate that damage to the column was mitigated by the shell retrofit. As a result, the subsequent test was conducted using the same column reinforcement; however, additional post-tensioning and steel reinforcement bars, both vertical anchors and NSM were added to the footing to sufficiently strengthen the footing so as to force failure in the column.



Figure 7.45: Post-testing cracks observed on the west face of column, Specimen 1, after the removal of the TiAB spiral and retrofit shell.

Figure 7.46 compares the shear force-lateral displacement response of Test 9 – S1 with Test R-S-R-L Ti-90 from Shrestha (2019), performed on a similar specimen with the only alteration in the column retrofit being the location at which the TiAB spiral was embedded into the footing and the footing restraint to the strong floor. Specimen 1 exhibited stiffer behavior than the specimen tested by Shrestha (2019), with a more linear shear force-lateral displacement response for top drifts smaller than 10.1 mm (0.4 in.). Test 9 resulted in a maximum column shear of 326 kN (73.3 kips) on the push and 347 kN (78.1 kips) on the pull portions of the quasi-static cyclic loading. The maximum column shear occurred at a top drift of 91.4 mm (3.6 in.). For comparison, Specimen R-S-R-L Ti-90 (Shrestha 2019) resulted in a maximum column shear of 417 kN (93.7 kips) and 406 kN (91.2 kips) during the push and pull cycles, respectively. The maximum column shear occurred at a top drift of 121.9 mm (4.8 in.) on the push cycle, compared to 101.6 mm (4.0 in.) on the pull cycle. Degradation was observed at a smaller drift during Test 9 (91.4 mm compared to 101.6 mm), while also demonstrating a greater degradation per load increment after the maximum column shear was achieved.

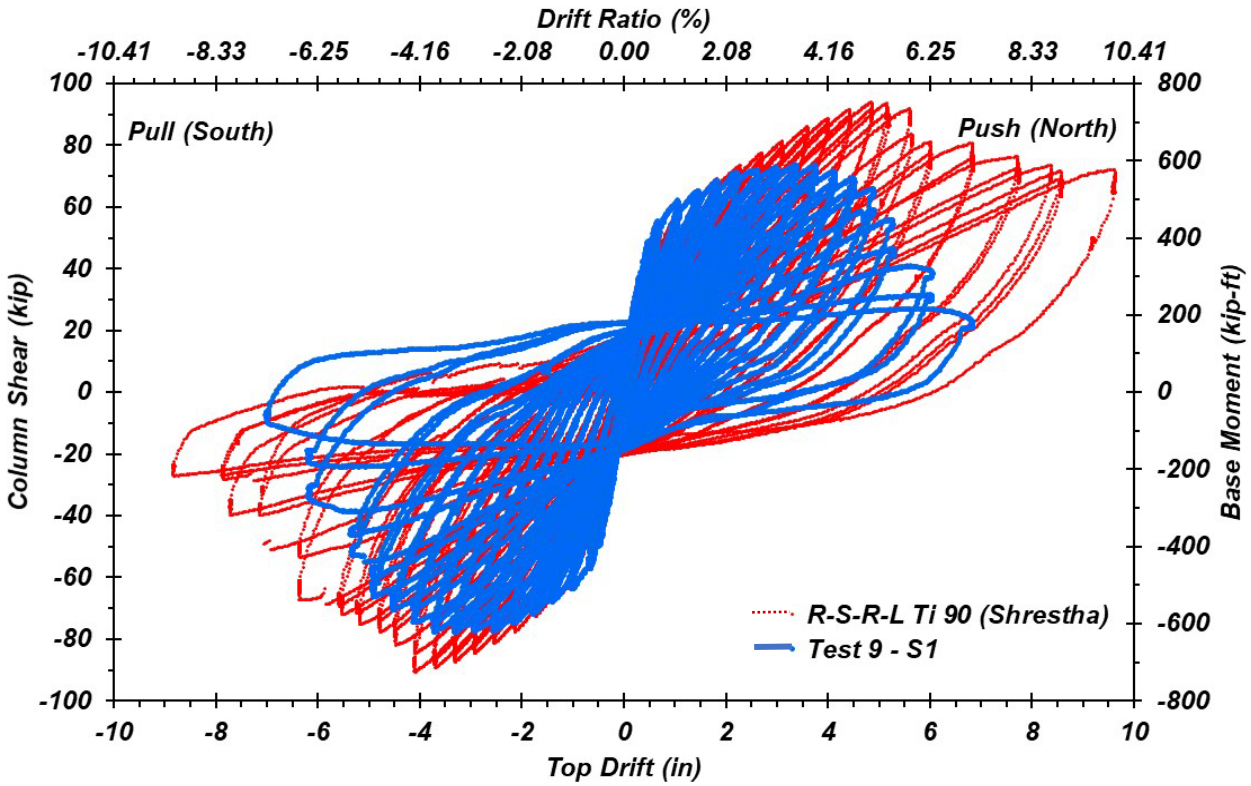

Figure 7.46: Overall force-displacement comparison of Test 9 - S1, with R-S-R-L Ti-90 from Shrestha (2019).

The difference in observed strength between the two specimens is associated with details of the TiAB spiral reinforcement. For Specimen R-S-R-L Ti-90 from Shrestha (2019), the

spiral reinforcement was anchored into the north face of the footing. Because of this, the spiral uncoiled (i.e., pulled) out of the footing, during the pull cycle. This led to a smaller column shear on the pull compared to the push cycles for Specimen R-S-R-L Ti-90 at a given drift ratio. In the push direction, the column pushed into the spiral anchored into the footing base which confined the column and increased the strength in this direction. The result was an asymmetrical cyclic response for Specimen R-S-R-L Ti-90. For Test 9 – S1, two (2) TiAB spirals were used over the lower 0.61 m (24 in.) of the specimen and anchored into the footing on opposing column faces. This prevented the spiral from opening up and the resulting loss of confinement. The two (2) spirals resulted in a more symmetrical load-displacement response (Figure 7.46). The backbone curve for Test 9 in Figure 7.47 depicts the maximum column shear at each drift ratio and ignores the effect of degradation for a given load cycle.

The backbone curve observed by Shrestha for similar specimens appears to indicate better performance at larger drifts. This is true because Shrestha's specimens have no footing damage and all the response is associated with the column and TiAB retrofit. The loss in performance at large drifts for the present Test 9 – S1 is due to footing damage and loss of strength.

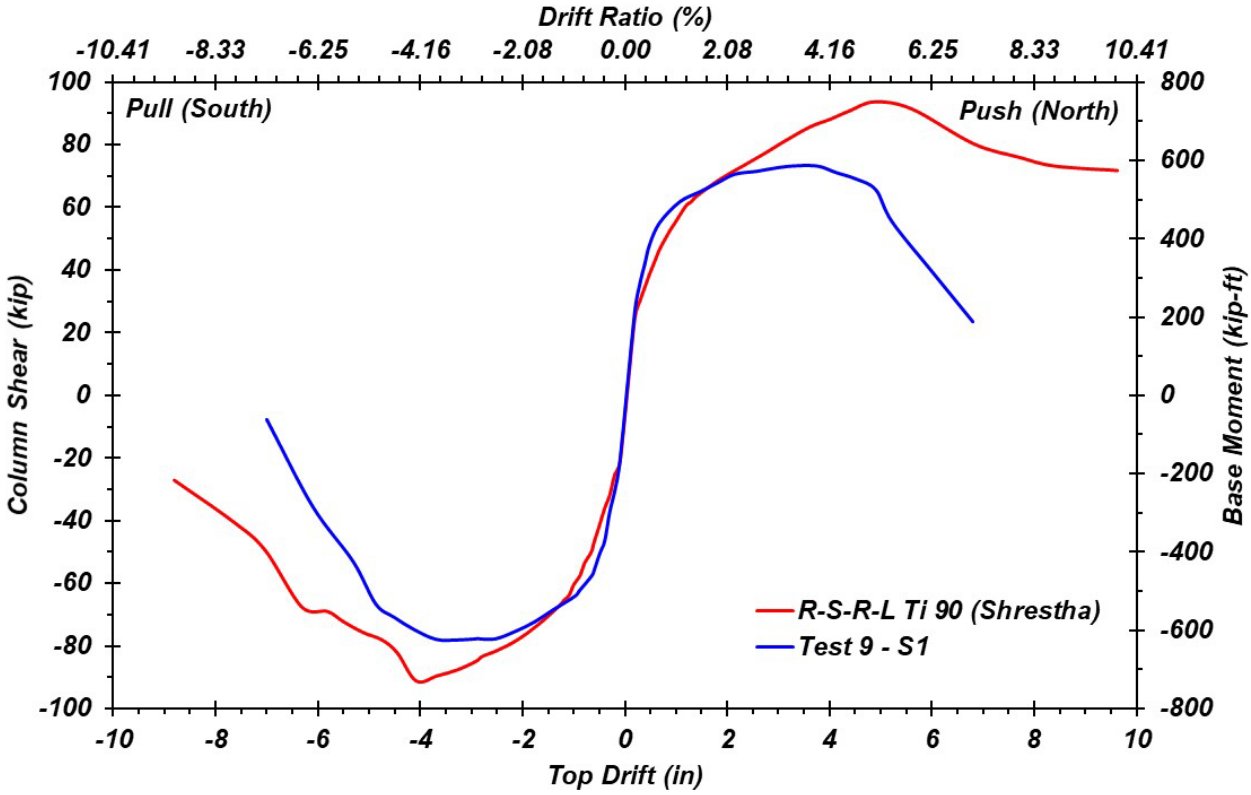

Figure 7.47: Backbone curve for Test 9 – S1 and R-S-R-L Ti-90 (Shrestha 2019).

7.3.3.3 Test 10 – S3: Vintage Column with Ligament and Spiral Retrofit and Restrained Footing with Additional Retrofit

Specimen 3 had been tested by Parson (2022) five times (Tests 3 through 7) prior to the start of the current study. The specimen was not retrofitted for these five tests, which caused widespread cracking and spalling of the vintage column (Parson 2022). Test 7 was terminated once failure in the specimen occurred (Parson 2022). For the present study, the column was subjected to the full TiAB column and footing retrofit as described in Section 4.3.2. Similar to Test 9 – S1, cracks on the specimen from the previous tests were identified prior to the start of Test 10 – S3.

As depicted in Figure 7.48, Test 10 – S3 demonstrated a nonlinear force-displacement response after a top drift of 10.1 mm (0.4 in.) was reached. No damage was observed on the column, shell, or footing at this drift magnitude. The test was terminated after a top drift of 224 mm (8.8 in.) was reached. Figure 7.49 compares the results from Test 10 to the previous test of Specimen 3 by Parson (2022). The footing uplift-top drift hysteresis is presented in Figure 7.50. The asymmetrical behavior of the footing during cyclic loading is associated with the northern side of Specimen 3 displacing up and down during pull and push cycles, respectively, whereas the southern side only displaced during push cycles. This behavior resulted from a combination of two factors: A north/south side discrepancy in the forces induced to the 28.5 mm (1-1/8") diameter post-tensioned bars confining the footing, and the slight rounding of the footing from previous tests that was not counteracted by the hydro-stone plaster underlying Specimen 3.

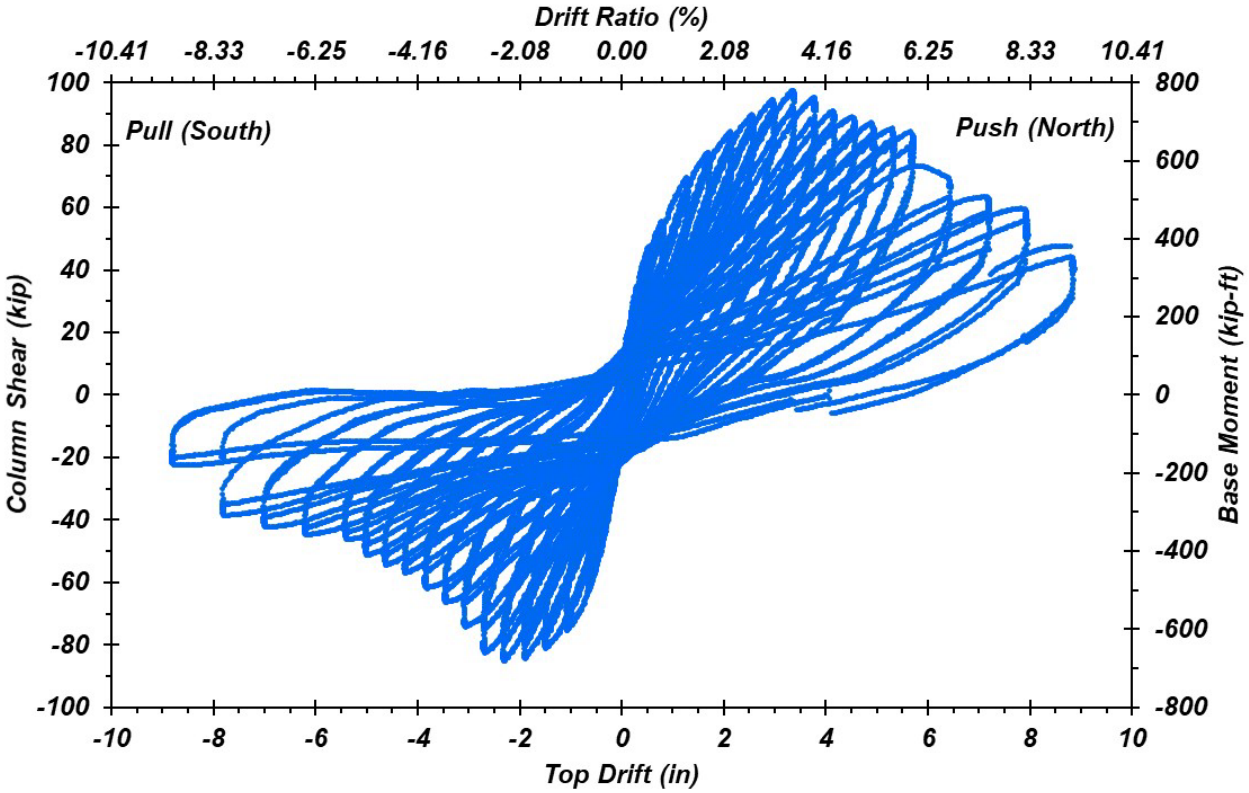

Figure 7.48: Column shear-top drift hysteresis of Test 10 – S3.

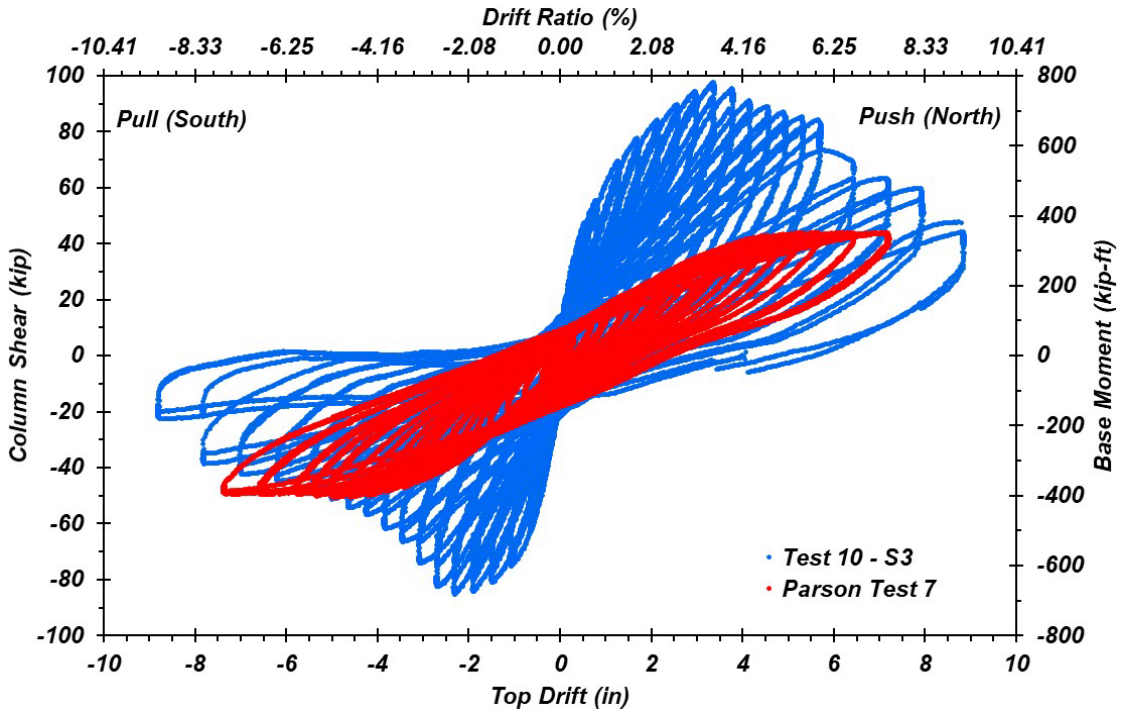

Figure 7.49: Column shear-top drift hysteresis of Test 10 – S3 compared with Test 7 by Parson (2022).

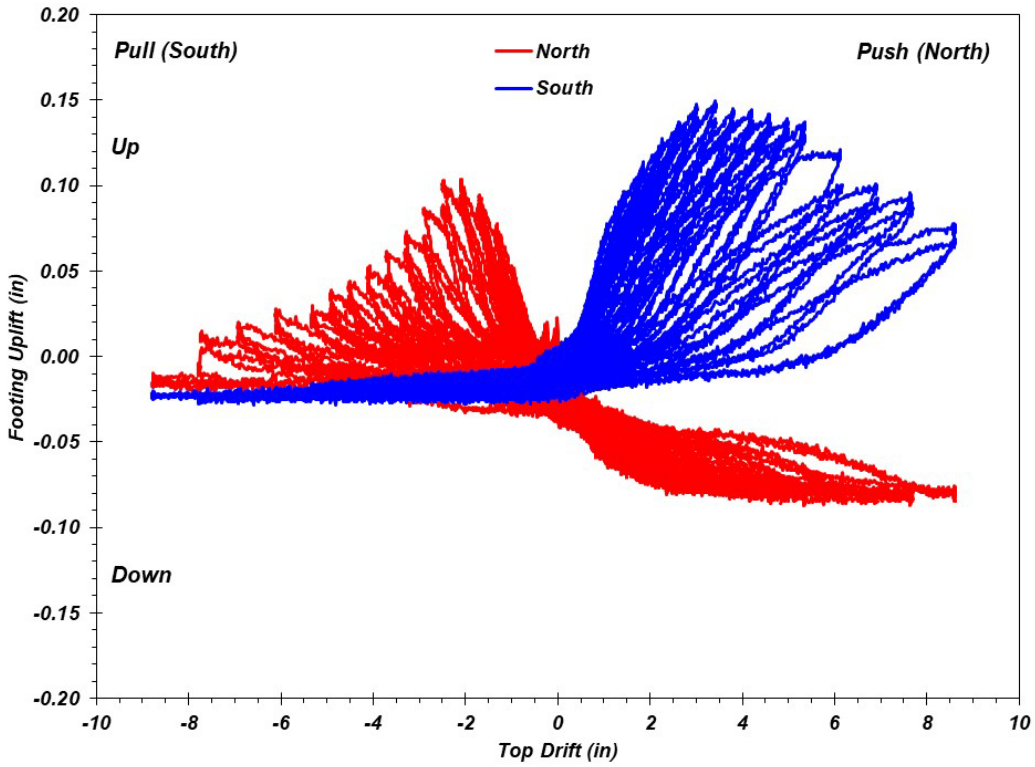

Figure 7.50: Footing uplift during north (push) and south (pull) cycles, Test 10 – S3.

Test 10 was paused to identify new cracks following completion of loading cycles with top drifts of 30.5 mm (1.2 in.), 40.6 mm (1.6 in.), 71.1 mm (2.8 in.), and 91.4 mm (3.6 in.). The progression of damage is depicted in Figures 5.51 through 5.54. Diagonal cracks were observed on the northern side of the east, west, and north faces of the column following a top drift of 30.5 mm (1.2 in.). On the west face, diagonal cracks were only noted on the northern (push) side of the column. The diagonal crack propagation on the west face further exemplified the aforementioned, asymmetrical footing uplift response, as Specimen 3 deformed in a relatively rigid manner (i.e., rocked) on the push cycle. Significant spalling of the retrofit shell was first evident during cycles at a top drift of 61 mm (2.4 in.), primarily on the southern side of the specimen. Additionally, the gap formed between the specimen footing and shell became progressively more apparent as the imposed top drift increased in magnitude.



Figure 7.51: Cracking observed on the west face of Specimen 3 at a top drift of 30.5 mm (1.2 in), traced in red.



Figure 7.52: Cracking observed on the east face of Specimen 3 at a top drift of 40.6 mm (1.6 in.), traced in green.



Figure 7.53: Cracking observed on the north face of Specimen 3 at a top drift of 71.1 mm (2.8 in.), traced in black.



Figure 7.54: Cracking observed on the west face of Specimen 3 at a top drift of 91.4 mm (3.6 in.), traced in red.

No measures to eliminate the bonding between the column and retrofit shell were taken for Specimen 3, in contrast to the construction of Specimen 1 for Test 9. In order to establish the characteristics of the bond between the retrofit shell and column concrete, a linear position sensor (LPS) was placed on the column face above the shell to enable observation of potential relative movements. Figure 7.55 compares the relative movements between Test 9 – S1 and Test 10 – S3, which indicates negligible relative movement between the bonded shell and column for Test 10. Thus, it appears that Specimen 3 resisted column shear as a composite member with the column and shell acting monolithically, based on the lack of movement.

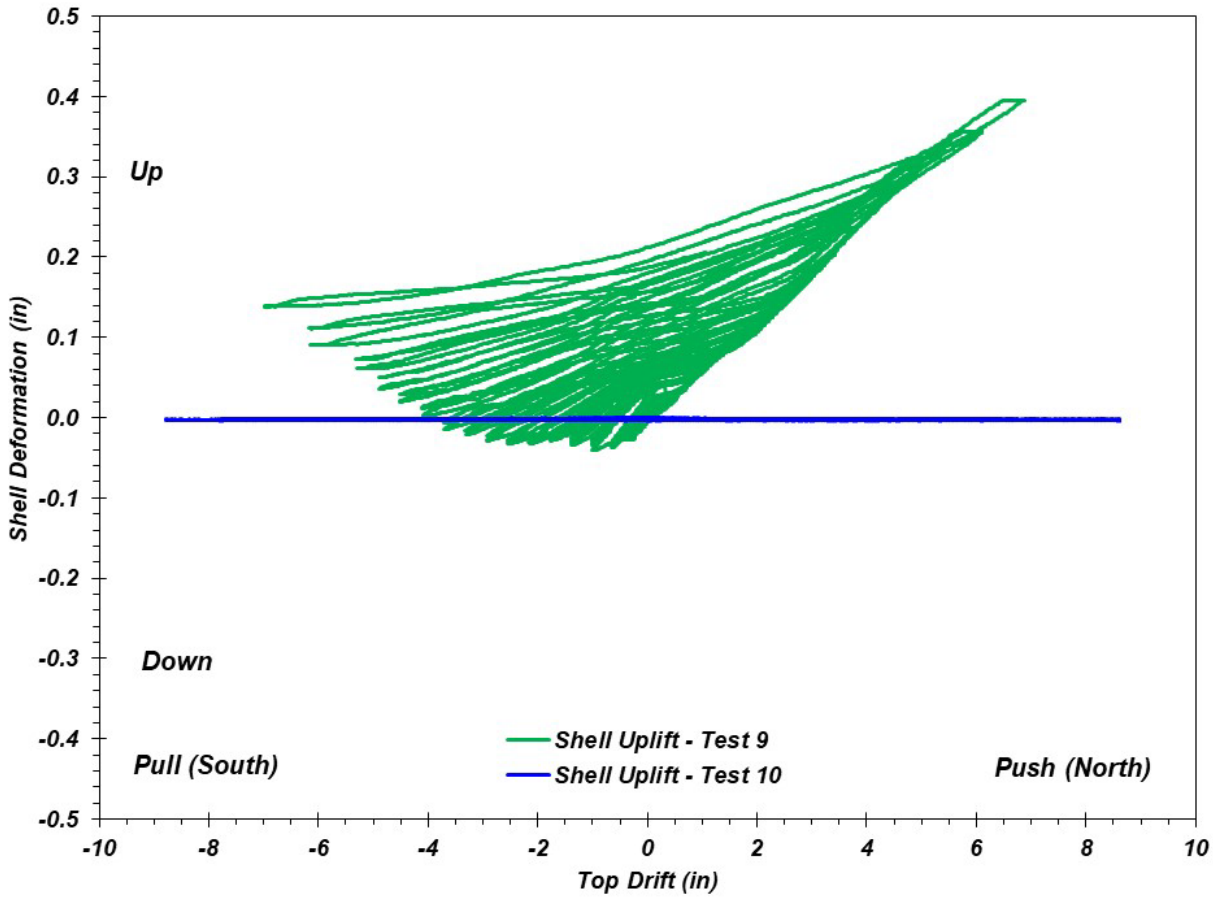

Figure 7.55: Relative motion of the retrofit shell with relation to the column, Tests 9 – S1 and Test 10 – S3.

At the top drift of 50.8 mm (2.0 in.) on the pull cycle, the column shear-top drift hysteresis curve presented in Figure 7.48 exhibited shear strength degradation corresponding to a column shear of 380 kN (85.5 kips). The degradation resulted from bond failure of the reinforcing steel in the column. As the imposed top drift of Specimen 3 was progressively increased, the maximum column shear per pull cycle continued to decrease. At a top drift of 81.3 mm (3.2 in.) and a corresponding column shear of 432 kN (97.2 kips), the push cycle of the column shear-top drift hysteresis exhibited degradation associated with the aforementioned failure of the embedded steel reinforcement. As

depicted in Figure 7.48, Specimen 3 exhibited strength degradation at a smaller top drift on the pull cycle. This is attributed to variation in the bonding of the embedded reinforcing steel during the retrofit, nonuniform cross sectional damage to the column section, and nonuniform support conditions under the footing.

An audible "pop" was heard on the pull cycle at a drift of 81.3 mm (3.2 in.) as the steel reinforcement pulled out during cyclic loading displaced back into its original position. Abrupt changes in column shear at a constant drift, particularly demonstrated on unloading (i.e., to zero drift), were caused by the rapid displacement of reinforcing members. For Specimen 3, the peak column shear was reached by the combined resistance of the embedded-reinforcing steel and TiAB reinforcements; however, after a top drift of 50.8 mm (2.0 in.) was reached, the peak shear continuously decreased with increasing drift. This behavior is associated with the failure of the original flexural steel reinforcement (e.g., column and starter bars). After these elements lost capacity, the TiAB ligaments served as the primary resisting element against imposed flexural tension.

At a top drift of 101.6 mm (4.0 in.) on pull cycles, constant column shear was maintained as displacement increased due to the resistance of the TiAB retrofit. The specimen continued to exhibit constant column shear resistance with increasing displacements until a top drift of 203.2 mm (8.0 in.) was imposed, associated with 222 kN (50 kips) of column shear. This performance demonstrates the effectiveness of the TiAB retrofit to sustain significant quasi-static cyclic lateral demands, as a hypothetical structure supported by a column-footing substructure would be damaged at this top drift. Eventually, some TiAB ligaments failed after an induced drift of 203.2 mm (8.0 in.), by bar pullout or rupture. The failure of these elements resulted in a further reduction in peak column shear for Specimen 3, as depicted in Figure 7.48.

The asymmetric cyclic column shear-top drift response of Specimen 3 at large drifts was caused by the vintage steel reinforcement failing at a drift of 142.2 mm (5.6 in.) on push cycles. Test 10 – S3 demonstrated two types of responses, both representative of retrofitted substructures: a combined vintage and retrofit-controlled flexural response with a high resistance to cyclic loads on push cycles, and a lower retrofit-controlled resistance on pull cycles.

Figures 7.56 and 7.57 provide comparisons of the two tests of structural lab specimens conducted as part of this research (Test 9 – S1 and Test 10 - S3). As previously mentioned, a goal of Test 10 – S3 was to observe behavior with only the TiAB ligaments acting as flexural reinforcement, with minimal contribution from the vintage steel reinforcement at high drifts. Cracks in the footing developed during Test 9 –S1 prior to the failure of the column reinforcement, which caused degradation primarily associated with damage to the footing. Through the implementation of additional NSM bars and additional vertical steel anchors in the footing of Specimen 3, Test 10 was sufficient to enable column failure rather than footing failure.

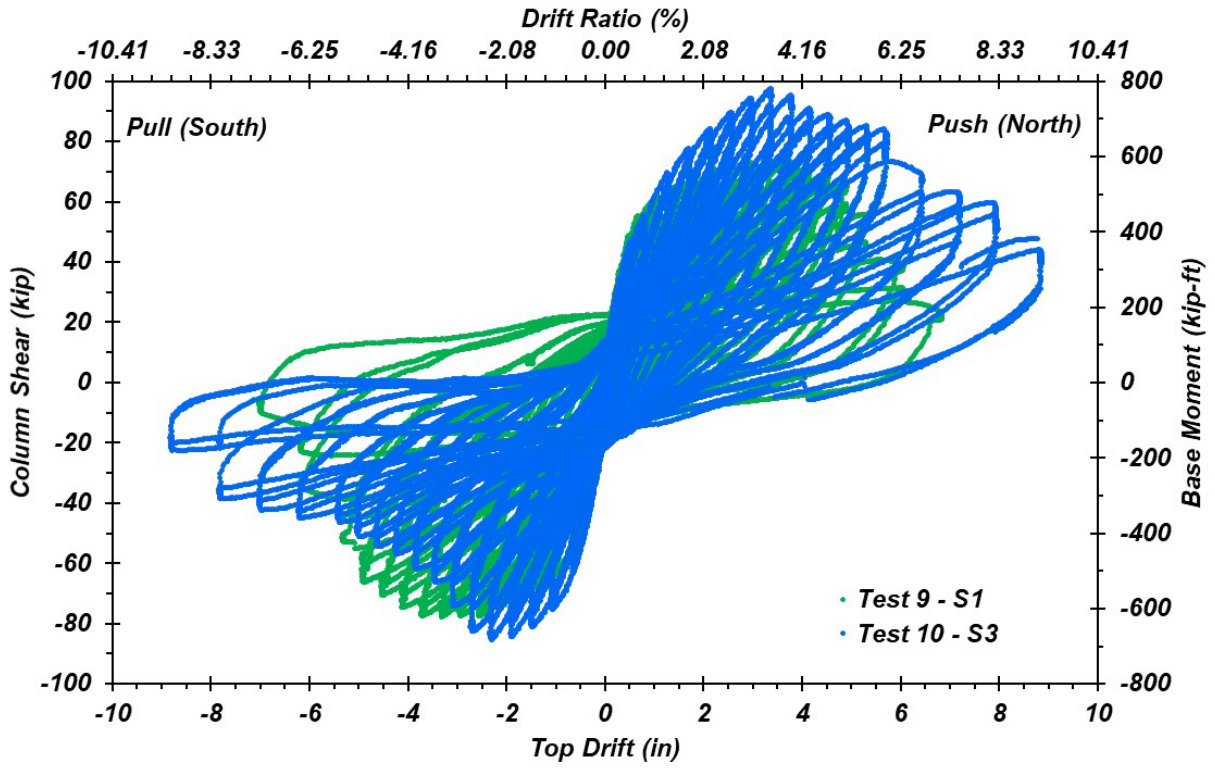

Figure 7.56: Comparison of Test 10 - S3 with Test 9 - S1.

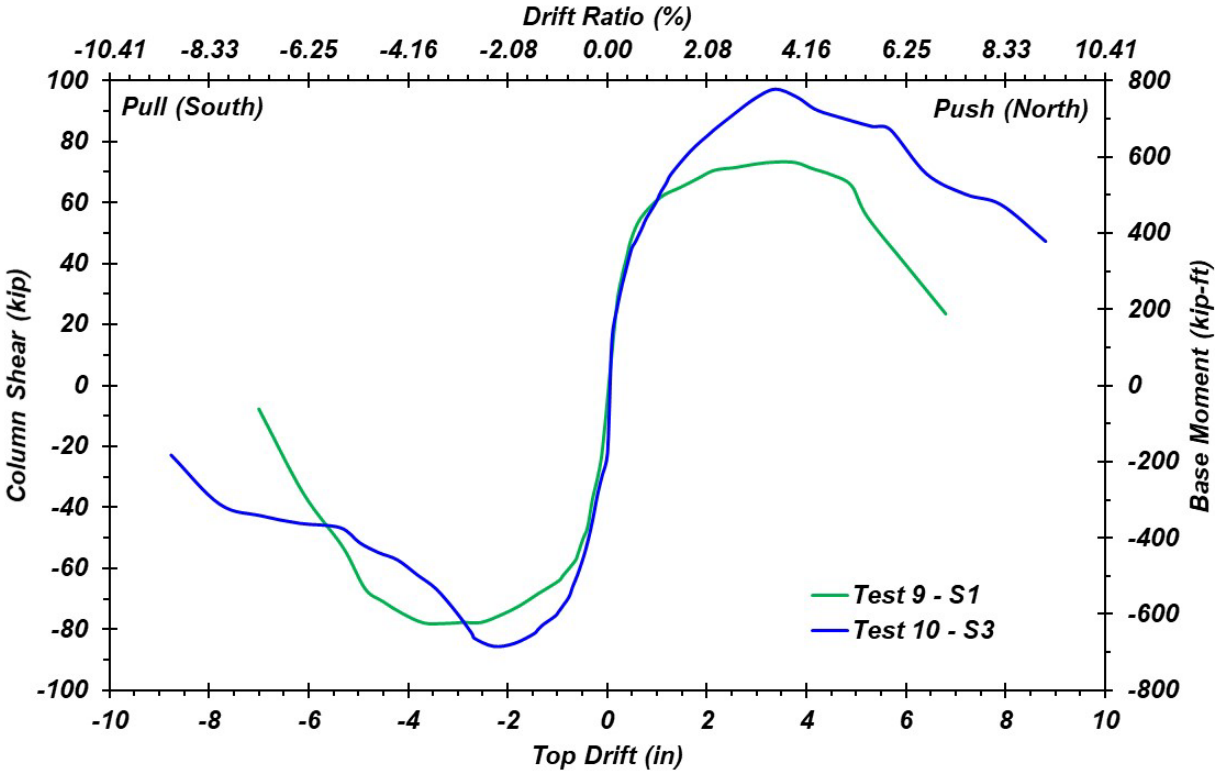

Figure 7.57: Comparison of backbone curve from Test 10 - S3 with Test 9 - S1.

7.3.4 Reinforcing Steel and Titanium Alloy Bar Strains

Strain gauges applied to the steel and TiAB reinforcements were used to assess the flexural behavior and identify potential yielding of the elements. Unfortunately, the repeated tests of a given specimen led to the increased risk of damage to any given strain gauge, with loss of gauge reliability noted for the bars within Specimens 1 and 3 (i.e., Tests 9 and 10). For example, all of the strain gauges fixed to the column reinforcing bars, except one, and all gauges fixed to the starter bars, had ceased to function in Specimen 3, Test 10. The number of functional strain gauges on footing bars was insufficient to obtain a robust understanding of the footing response to the cyclic loading of both specimens. For all tests, the strain gauges reached a limit of range of roughly +/- 9500 micro-strain (με) and responses after this limit were disregarded. Other suspect strain measurements were removed prior to their analysis, such that only the results deemed representative are presented herein.

7.3.4.1 Test 9 – S1: Vintage Column and Retrofitted, Restrained Footing with Ligament and Spiral Retrofit

Test 9, conducted on Specimen 1, was loaded cyclically until failure of the footing or column was reached. Failure, deemed as the point of severe shear strength degradation combined with concerns regarding test safety, was reached at a top drift of 183 mm (7.2 in.), as evident in the load-top drift hysteresis presented in Figure 7.39. Strength degradation began after a top drift of 101.6 mm (4.0 in.) was induced, which led to the onset of cracks throughout the footing. Figure 7.58 illustrates the strain recorded by the functioning strain gauges on the footing bars during the test. Although the footing cracked severely during the test (Figures 7.41 and 7.42), the strains in the footing bars did not approach the yield stress of the reinforcements due to the reduction in strength and positioning in regions away from the footing cracks.

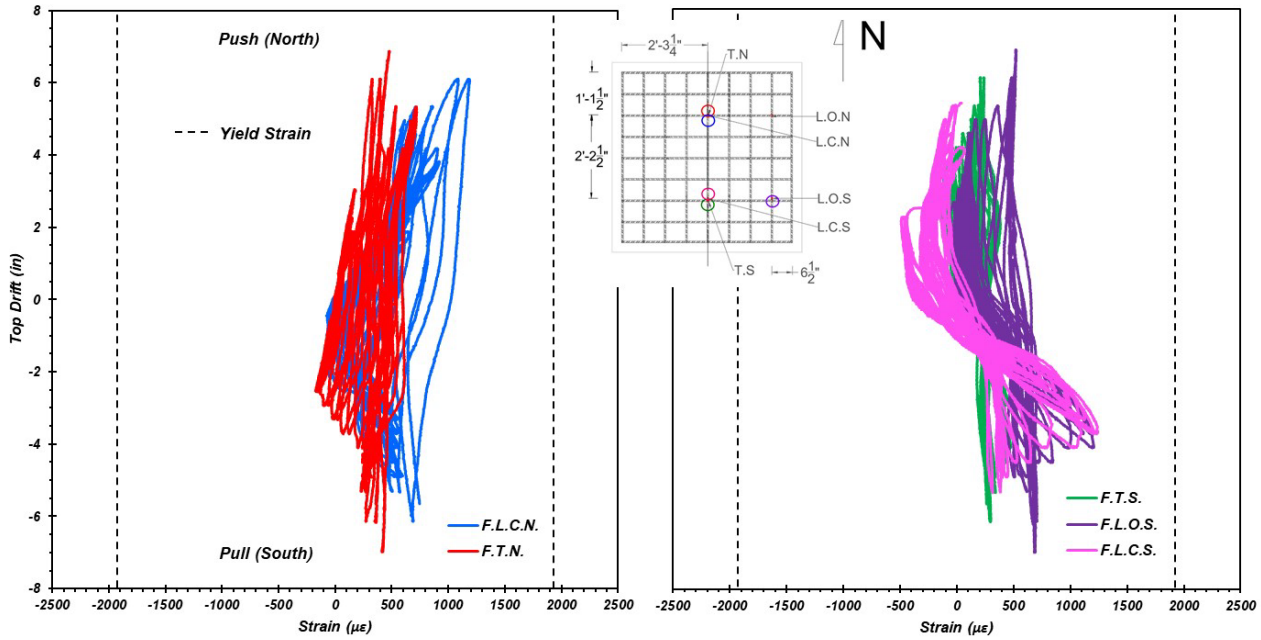

Figure 7.58: Strain-top drift hysteresis for footing bars in Specimen 1 during Test 9.

Figure 7.59 shows that all eight (8) strain gauges on the reinforcing steel starter bars achieved yield prior to reaching the top drift of 50.8 mm (2.0 in.). These bars were expected to yield relatively quickly during the test as they span the footing and column, where moment was to be resisted. Since the footing was restricted from rocking, the starter bars exhibited strain histories associated with the cycles of tension and compression due to the column bending moment induced during quasi-static cyclic lateral loading.

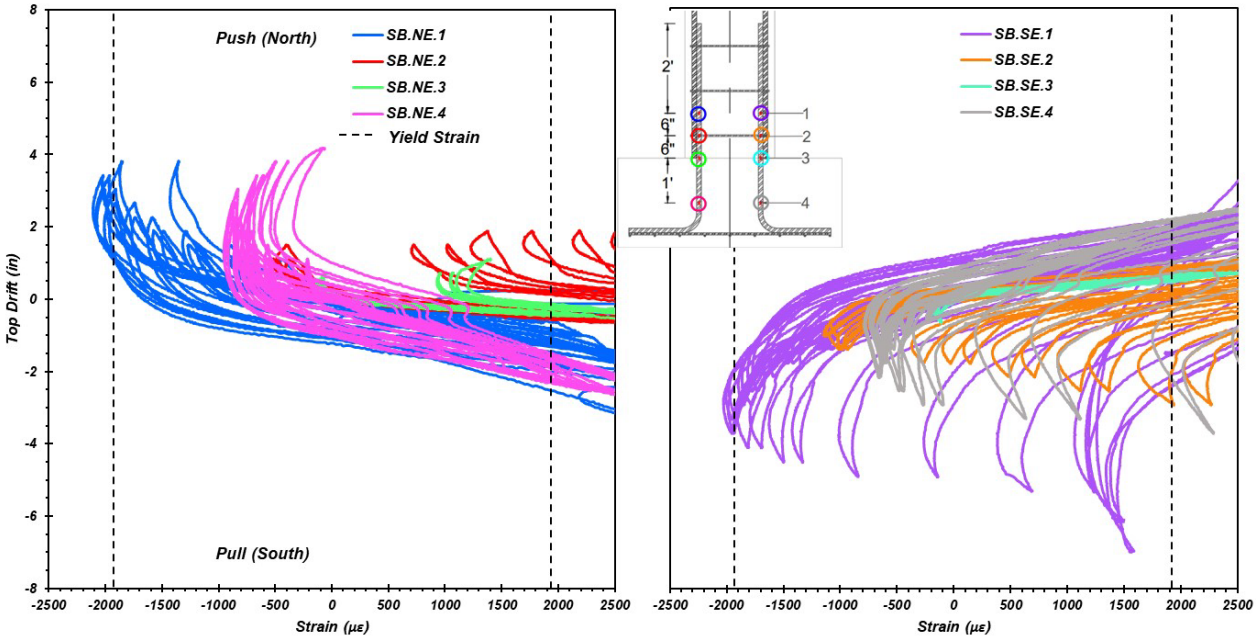

Figure 7.59: Strain-top drift hysteresis for starter bars in Specimen 1 during Test 9. Note: strains larger than the yield strain are not considered reliable.

Whereas all of the starter bars yielded during Test 9, only those strain gauges fixed to the column bars that were located 0.61 m (24 in.) or more above the top of the footing reached yield, as shown in Figure 7.60. These show a clear development of the stress along the length of the bars starting from the top of the footing due to the monolithic placement of the retrofit shell concrete that "rebonds" the bars to the column. Column bars on the north side of the column were observed to yield on the pull (south) cycles, whereas those on the south yielded on the push (north) cycles when each are engaged in flexural tensile stress from bending. Yielding first occurred at drift levels of 51 mm (2 in.) and 25 mm (1.0 in.) on the north and south sides of the column, respectively. The reduction in strain after achieving a maximum indicates a loss of bond. This was observed at a top drift of 96 mm (3.8 in.) on both the north and south sides of the column.

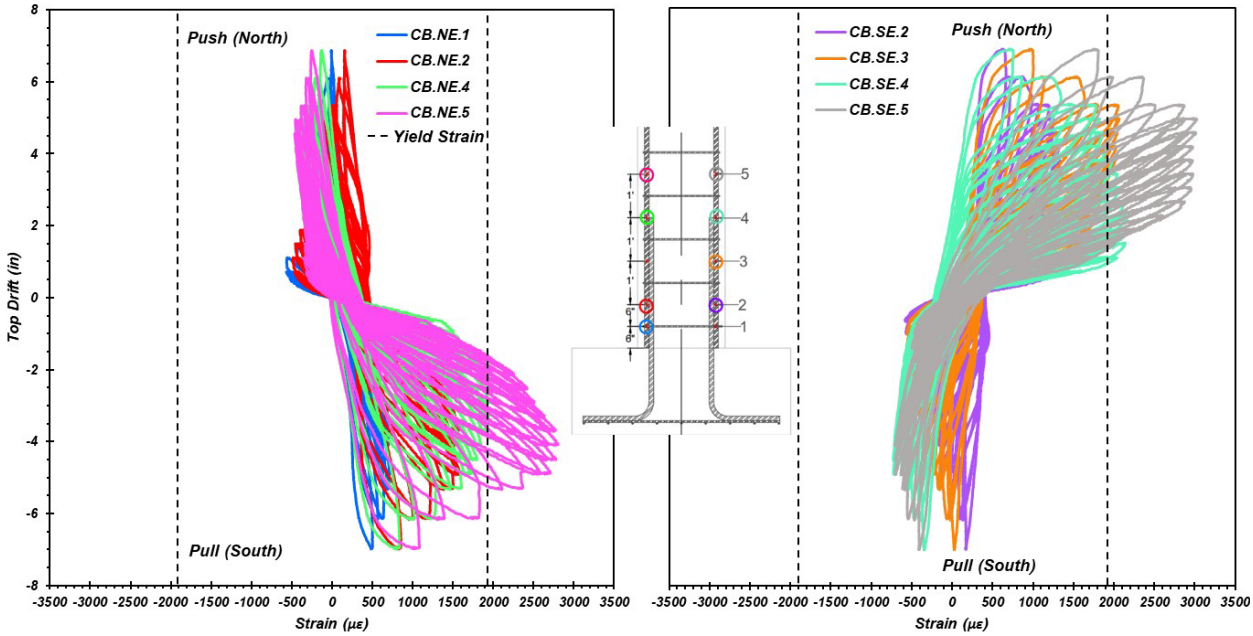

Figure 7.60: Strain-top drift hysteresis for column bars in Specimen 1 during Test 9.

Figure 7.61 presents the strain-top drift hysteresis observed in the column's reinforcing steel ties and shows that the ties achieved yield. All column ties yielded except that located 0.46 m (18 in.) above the footing, corresponding to the second tie location. The fifth column tie (located at a distance of 1.22 m or 4 ft. above the footing) yielded first due to the lack of the TiAB spiral retrofit surrounding this location on the column. The spiral effectively restrained the other ties and prevented yielding until a top drift of 61 mm (2.4 in.) was achieved. The increase in tie strain corresponds with the loss of bond of the column flexural bars and may indicate dilation and splitting of the core concrete. The near-symmetrical response about the zero-drift axis shown in Figure 7.61 stems from the location of the strain gauges, which were attached to the east face of the column (perpendicular to the loading direction) and roughly at the vertical neutral axis.

Due to the progressive damage accumulated and the loss of strength in the footing, only three of the instrumented TiAB ligaments achieved yield during Test 9, as shown in the strain-top drift hysteresis presented in Figure 7.62. The ligaments that yielded acted as the principal flexural tension components to resist column bending. Cycles that produce compression in the ligament show that the TiAB doesn't produce large compression strains because the bars are smooth and unbonded and the concrete section is able to provide the flexural compression force with relatively low strain levels, especially as it is confined within the TiAB spiral. The goal in this test, however, was to examine the behavior of these elements within the column until failure of the column was reached. As a result of the footing damage, the test was terminated prior to column failure. The footing was substantially retrofitted for Test 10 – S3 through further reinforcement of the footing, as described in Section 7.2.2.2 to preclude footing failure. Figure 7.63 depicts the strain-top drift hysteresis of the retrofit spiral within Specimen 1 and demonstrates how that the TiAB spiral is not subjected to large strains as it remains elastic. The design of

the spiral is based on geometrically providing overlapping zones of confinement to the core at each bar, rather than a force-based design. Some additional refinement and economy could be achieved through future work to make more efficient use of the yield strength of the TiAB spiral. Appendix A7.1 presents additional reinforcement strain figures for Test 9 – S1.

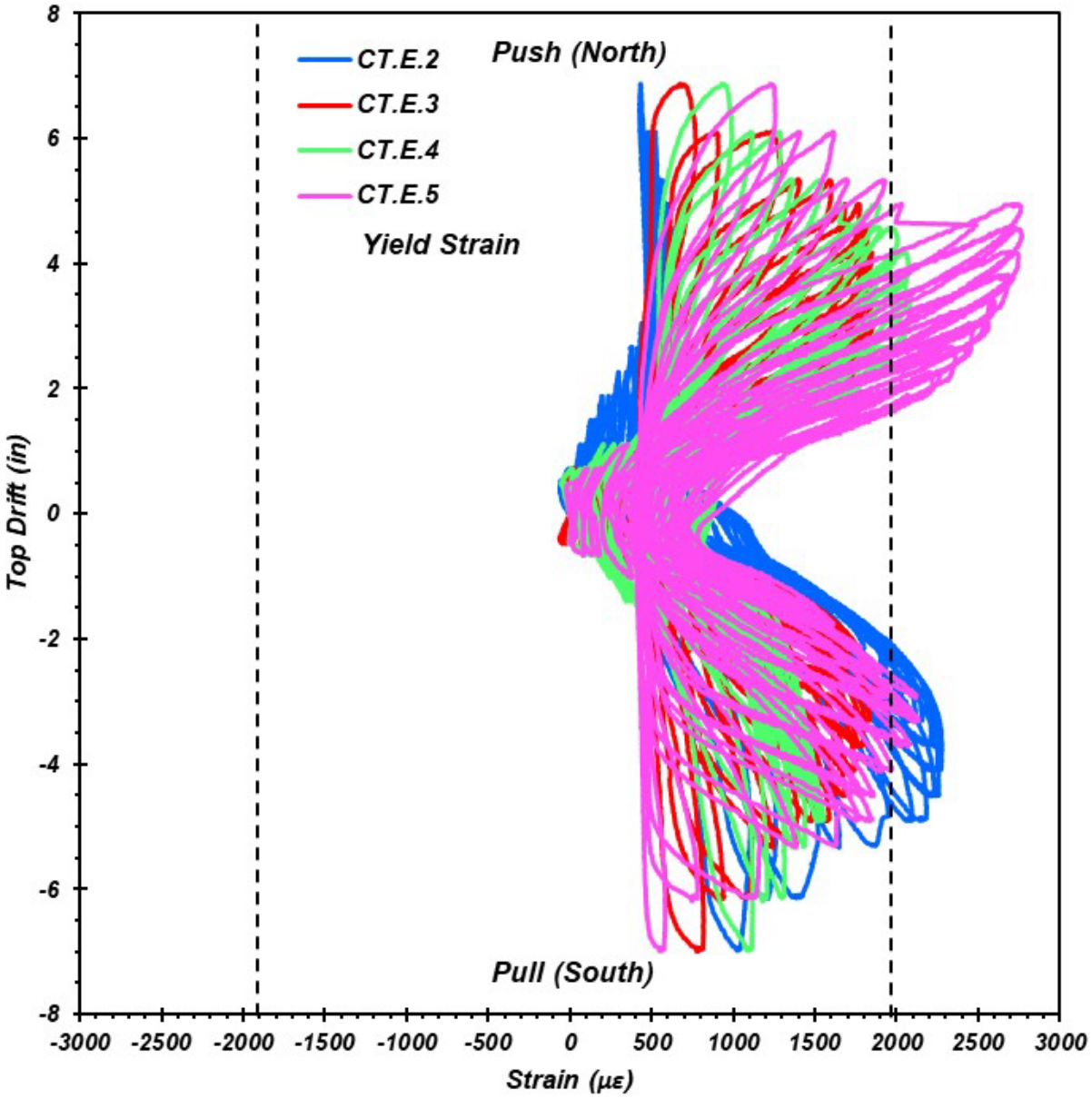

Figure 7.61: Strain-top drift hysteresis for column ties in Specimen 1 during Test 9.

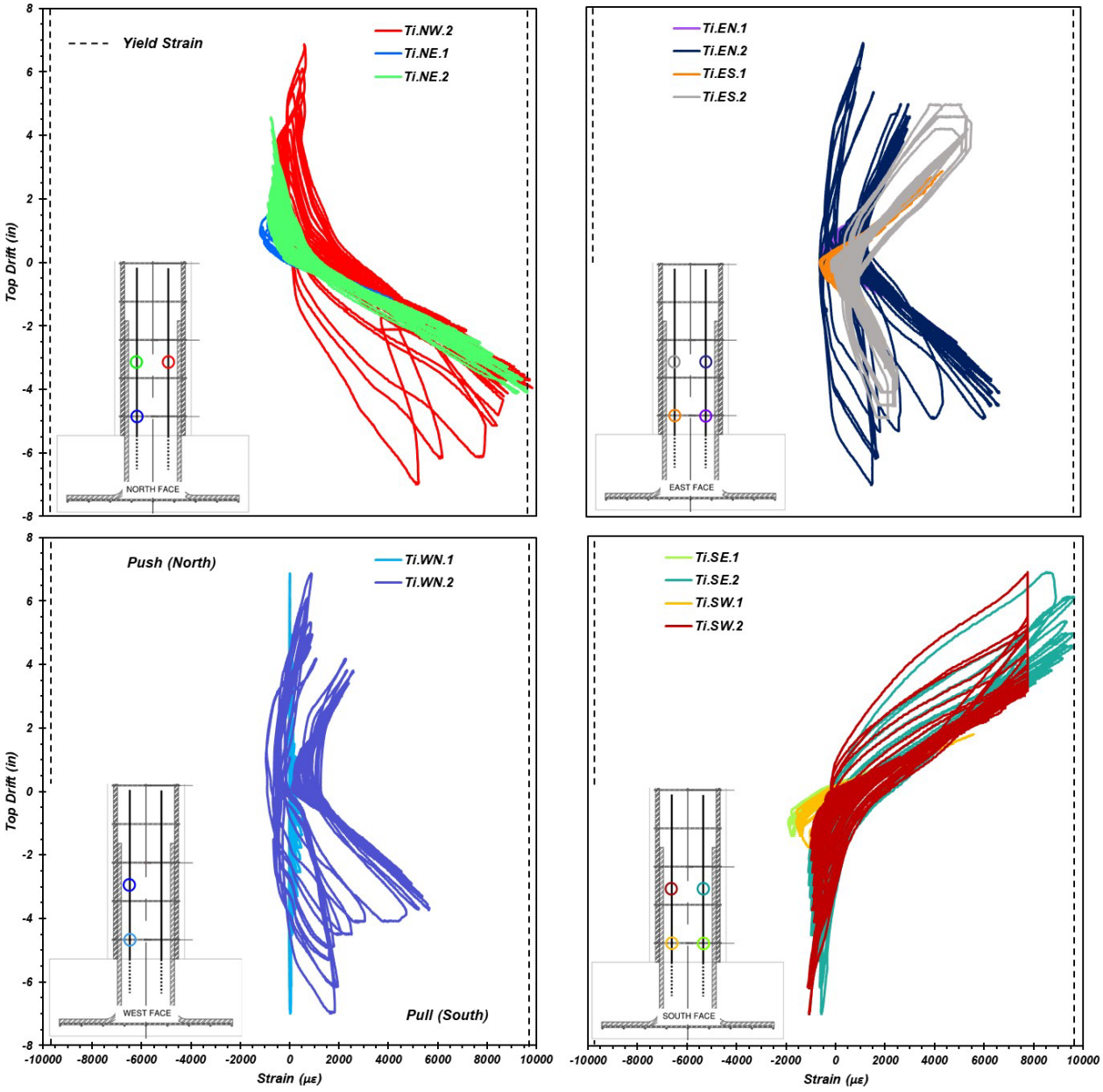

Figure 7.62: Strain-top drift hysteresis for TiAB ligaments in Specimen 1 during Test 9.

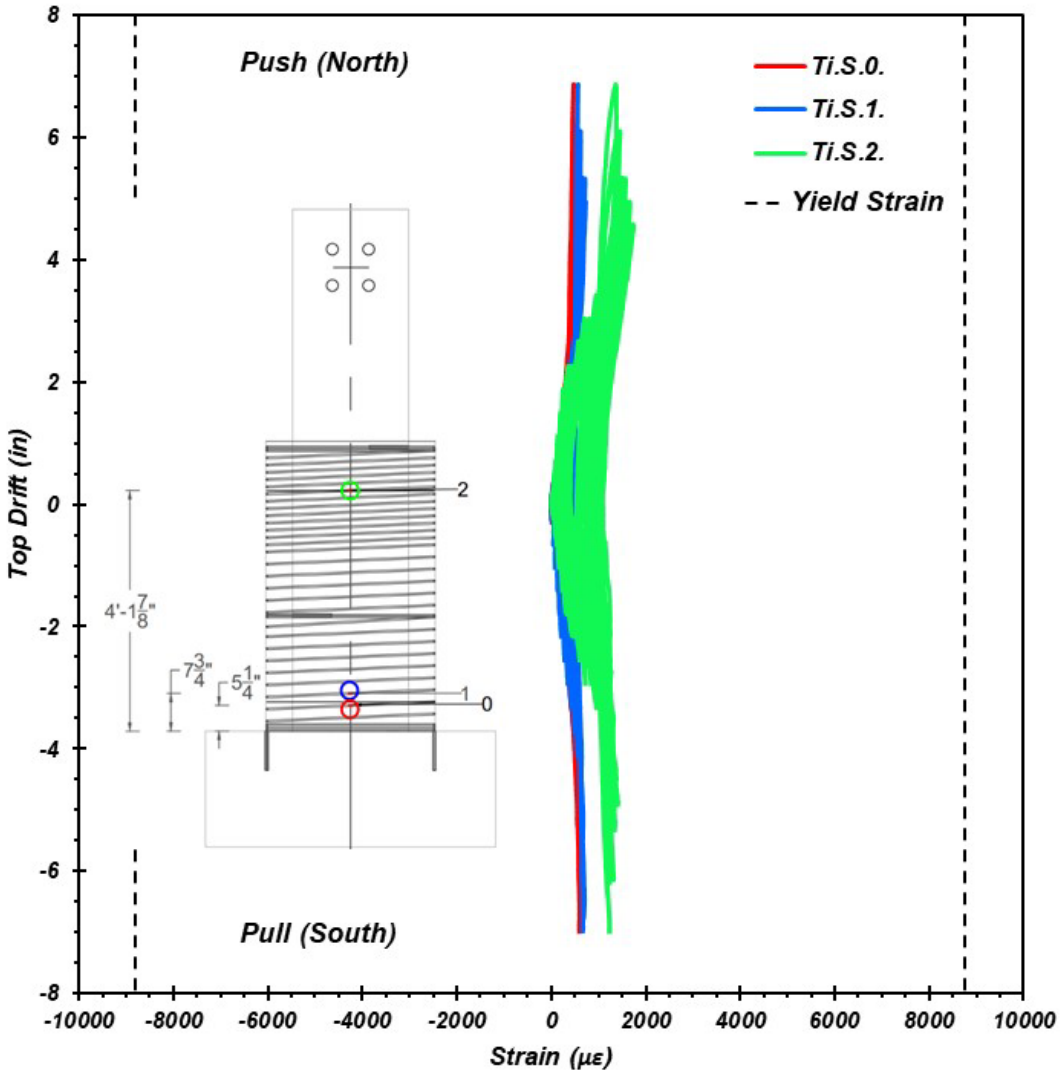

Figure 7.63: Strain-top drift hysteresis for the TiAB spiral in Specimen 1 during Test 9.

7.3.4.2 Test 10 – S3: Vintage Column with Ligament and Spiral Retrofit and Restrained Footing with Additional Retrofit

Similar to Test 9 on Specimen 1, Test 10 on Specimen 3 was loaded cyclically until failure of the specimen. To ensure that Test 10 – S3 was controlled by column failure, additional steel was added to the footing retrofit, as described in Section 4.3.2. Strength degradation was initially observed after reaching a top drift of 61 mm (2.4 in.), and the test was terminated after a top drift of 224 mm (8.8 in.) was imposed. Due to the failure of the column in the prior test, none of the starter bar strain gauges were functional.

The strain-top drift hysteresis presented in Figure 7.64 shows that the strain gauge fixed to the longitudinal footing bar (i.e., reinforcement parallel to the direction of loading) began to fail after a top drift of 91.4 mm (3.6 in.). On the southern side of the footing, two functioning strain gauges indicate that strains in the footing reinforcements

approached 25% of yield. During Test 9 – S1, footing bars reached roughly 70% of their yield. Thus, Specimen 3 exhibited an increase in the cyclic resistance of the footing during Test 10 due to the additional steel added to the footing retrofit.

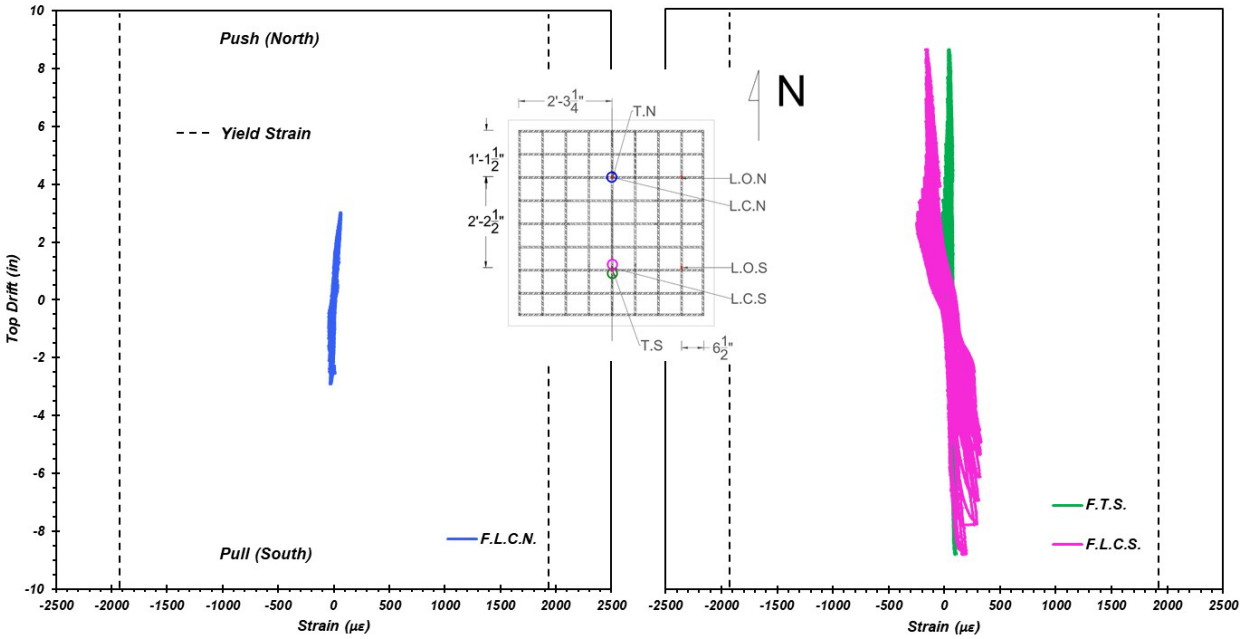

Figure 7.64: Strain-top drift hysteresis for footing bars in Specimen 3 during Test 10.

Figure 7.65 presents the strain-top drift hysteresis of a column bar located on the northeast corner at an elevation 1.2 m (4 ft.) above the top of the footing during Test 9 – S1 and Test 10 – S3. The strain accumulated in the column bar during Test 10 – S3 reached 60% of yield, whereas the column bar achieved yield during Test 9 – S1. After a top drift of 50.8 mm (2.0 in.) was reached, the strain of the column bar for Test 10 – S3 began to decrease with increasing drift, indicating the loss of bond. The same behavior was observed for Test 9 – S1 after a top drift of 101.6 mm (4.0 in.). The hysteresis from Figure 7.65 exemplifies how the loss of bond between the column bars and concrete results in a reduction of the flexural tension force contribution made by the steel. As a result, the TiAB ligament strain must increase to achieve equilibrium, albeit with a resulting lower moment resistance. Similarly, Figure 7.66 shows that the retrofit reduces the column tie strains within the shell, while strains above the spiral are larger in comparison.

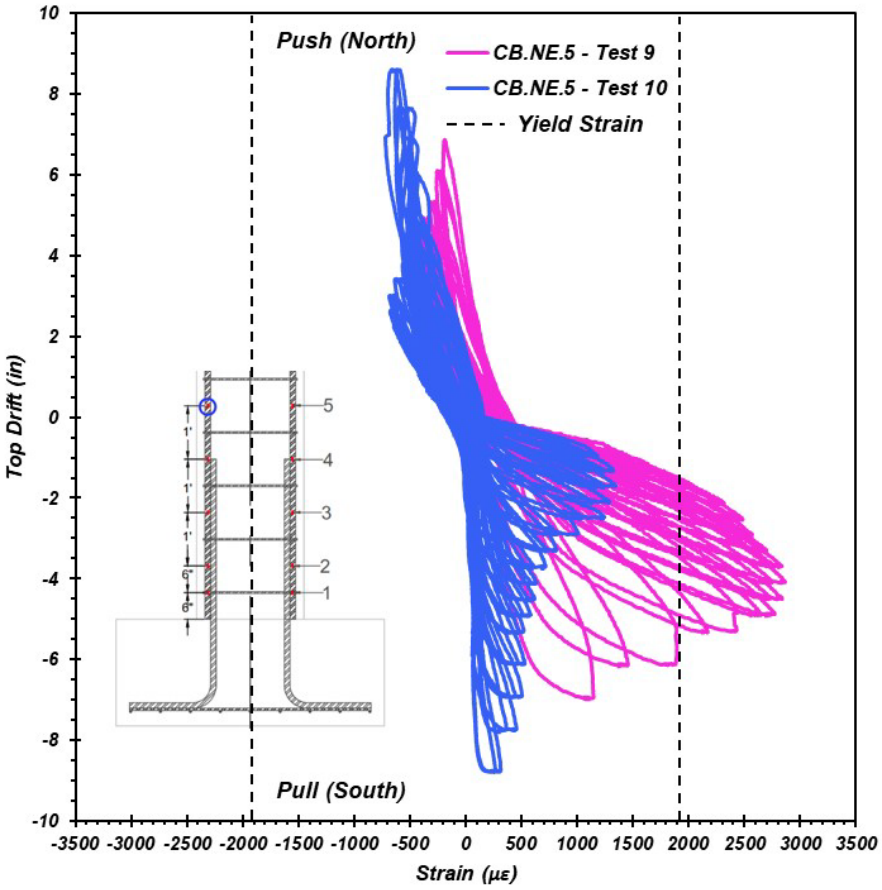

Figure 7.65: Strain-top drift hysteresis for column bars in Test 9 – S1 and Test 10 – S3.

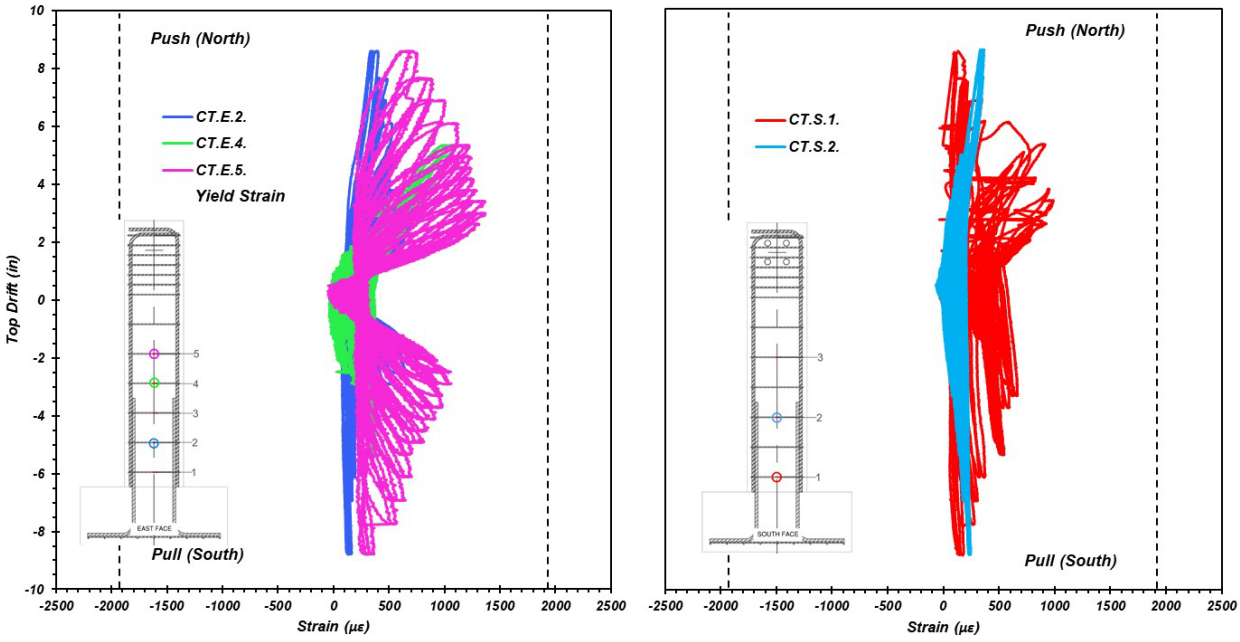

Figure 7.66: Strain-top drift hysteresis for column ties in Test 10 – S3.

Test 10 – S3 was terminated at an imposed top drift of 224 mm (8.8 in.) after failure of the column was evident, as depicted in the hysteresis presented in Figure 7.48. The TiAB ligaments acted as the primary flexural tension resistance to the applied cyclic loads for top drifts greater than 101.6 mm (4.0 in.), as the vintage reinforcing steel (i.e., starter and column bars) exhibited bond failure with progressively reduced contributions. Strain-top drift hysteresis of the TiAB ligaments for Test 10 – S3 are presented in Figure 7.67. Nine of the ligament bars reached yield during Test 10, whereas only three reached yield during Test 9. This observation is associated with the steel column bars delaying loss of bond for Test 9 and the increased footing strength achieved for Test 10 – S3, which allowed column failure to control the behavior. Strains within the spiral were again minimal in comparison to their respective yield stress, as depicted in the strain-top drift hysteresis illustrated in Figure 7.68. Appendix A7.1 presents additional reinforcement strain figures for Test 10 – S3

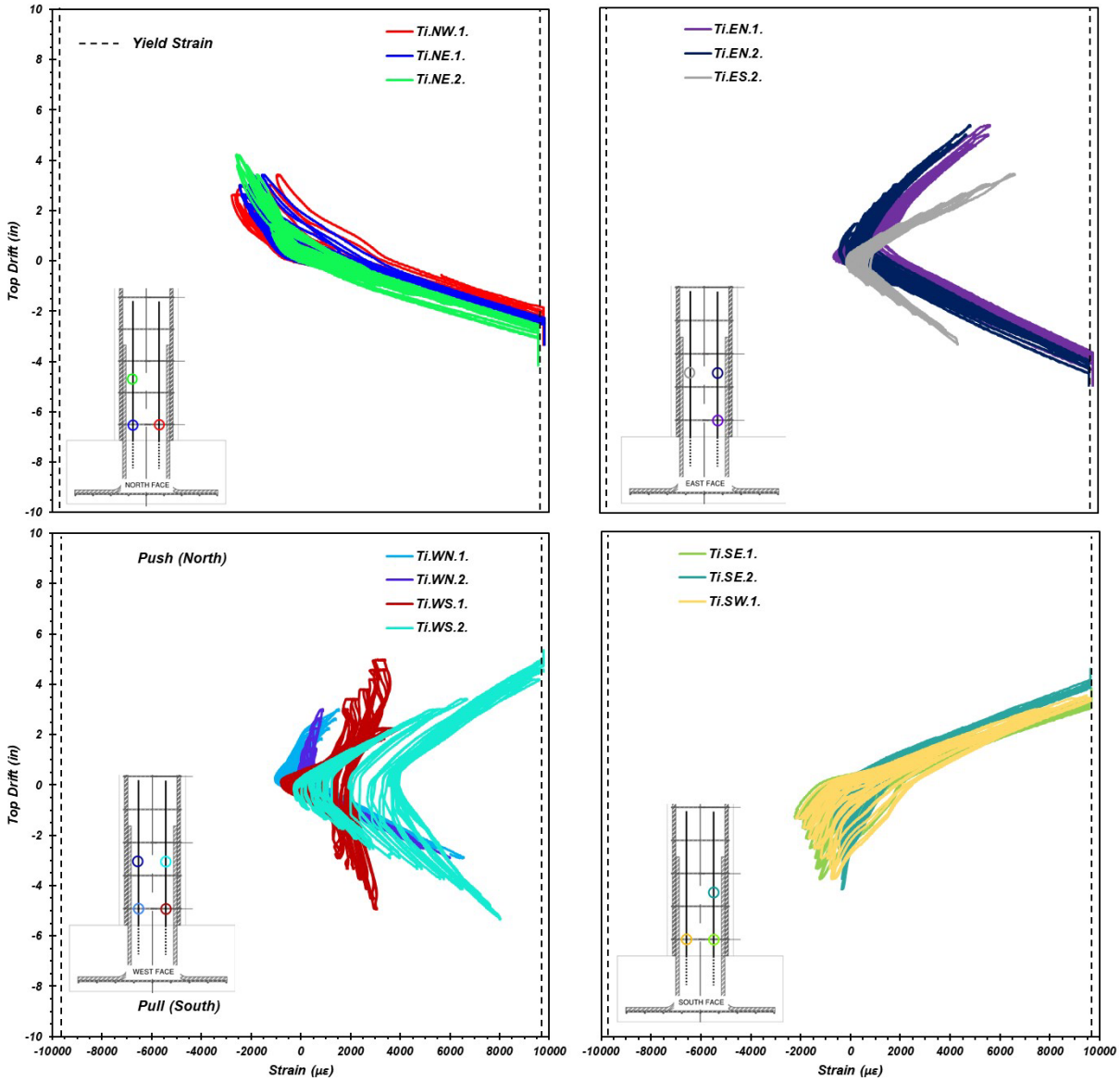

Figure 7.67: Strain-top drift hysteresis for TiAB ligaments in Test 10 – S3.

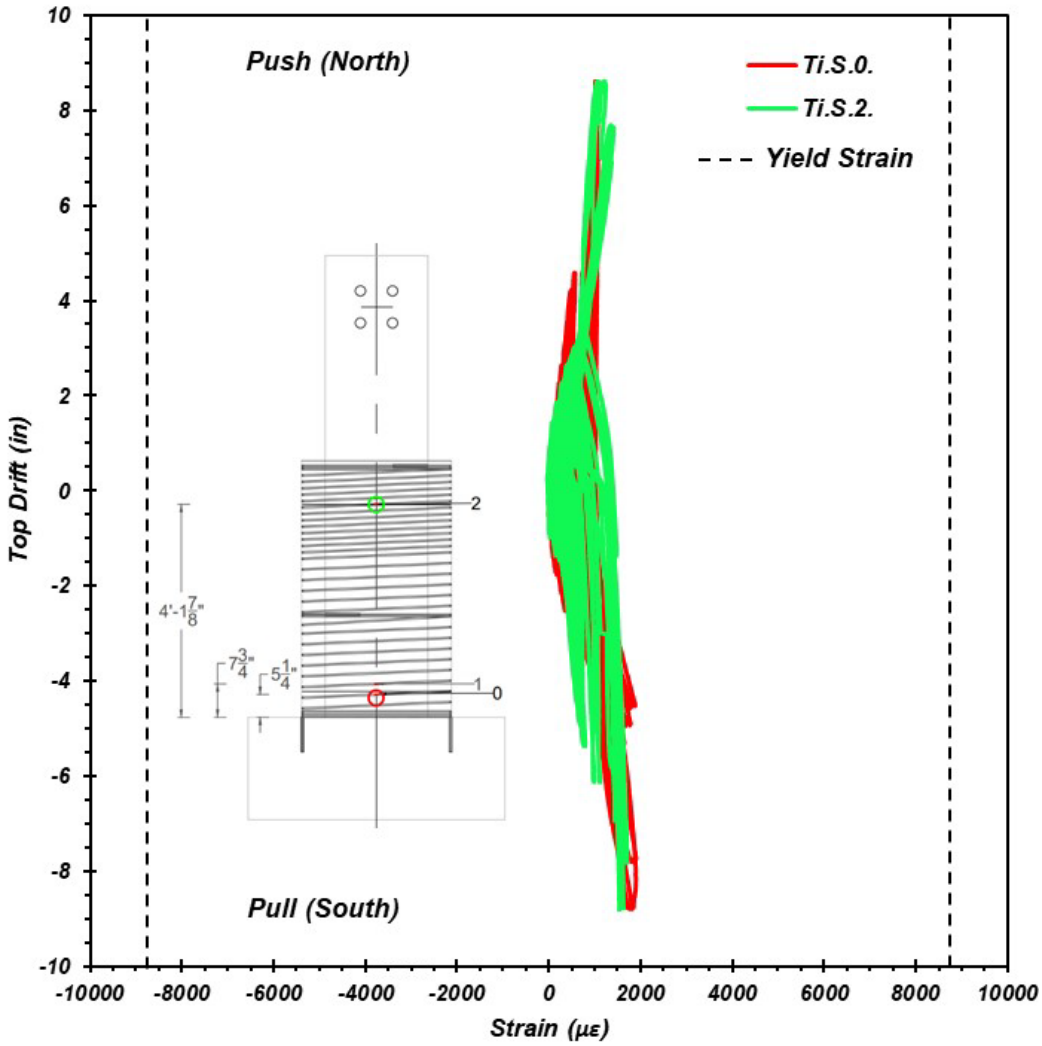

Figure 7.68: Strain-top drift hysteresis for the TiAB spiral in Test 10 – S3.

7.3.5 Summary of Section 7.3

Tests 9 and 10 performed on Specimens 1 and 3 in the Oregon State University structural laboratory concluded the work initiated in Parson (2022) that studied the behavior of column-footing substructures when subjected to quasi-static cyclic lateral loading protocols. The tests performed as part of this study resulted in failure of the specimens: Specimen 1 failed within the footing, whereas Specimen 3 failed in the column above the column-footing interface. This section reported the performance of the substructure specimens through the data analysis of instrumental measures of response (e.g., strain gauges, displacement sensors, and load cells) and physical observations collected during tests.

The effect of applying a TiAB retrofit (ligaments and spiral) to a previously tested but not-failed column that was completely failed during a previous test was first explored in Test 9 – S1. The footing was retrofitted with additional footing NSM steel reinforcement and post-tensioning. It was determined through Test 9 that these measures were insufficient to force a column-footing

connection controlled behavioral response, as severe strength degradation first occurred in the footing of Specimen 1 during the cyclic loading. The strength degradation of the footing allowed for the column to rock freely with the induced top displacements, with the column-footing connection remaining in-tact for the entirety of the test. To further examine the response of the structural members within the column, it was determined that Specimen 3 required additional reinforcement within the footing prior to the initiation of Test 10.

Specimen 3 was further retrofitted with additional NSM and vertical reinforcement bars to increase the resistance of the footing to quasi-static cyclic lateral loading. This previously failed specimen (Test 8, Parson 2022) was subjected to the same lateral loading protocols as Specimen 1 during Test 9. Test 10 resulted in negligible observable damage in the footing, achieving the desired column-footing connection-controlled response. Specimen 3 exhibited an asymmetrical response, with vintage failure occurring earlier during the test on the southern side of the specimen. The effectiveness of the TiAB retrofit was demonstrated by the constant strength of Specimen 3 when subjected to increasing values of top drift, as the high-strength TiAB elements assisted in the overall resistance.

Table 7.9 summarizes the results from tests performed as part of this thesis and those performed by Parson (2022) on the same specimens as part of the same study. Test 9 – S1 and Test 10 – S3 imposed maxium column shears that far exceeded previous tests on the specimens (Test 1 and Tests 3 through 7 for Specimens 1 and 3, respectively). Due to the confinement of the footing to the strong floor, both Tests 9 and 10 achieved maximum column shear values at smaller drift ratios, compared to previous tests.

Table 7.9: Summary of results from structural tests on column-footing specimens.

Designation	Maximum Column Shear, kN (kip)		Drift Ratio (%) at Peak		Drift Ratio (%) at Failure	
Test # - S#)	Push (+)	Pull (-)	Push (+)	Pull (-)	Push (+)	Pull (-)
Test 1 - S1	199 (44.8)	209 (46.9)	9.9	10.0	2.2	2.4
Test 2 - S2	121 (27.1)	112 (25.2)	4.5	5.0	0.8	0.8
Test 3 - S3	188 (42.2)	197 (44.3)	6.0	6.0	2.2	2.3
Test 4 – S3	158 (35.4)	151 (34.0)	7.7	7.6	5.2	5.3
Test 5 - S3	212 (47.7)	235 (52.9)	5.9	6.0	-	-
Test 6 - S3	45 (10.0)	49 (11.0)	0.5	0.6	-	-
Test 7 - S3	205 (46.0)	224 (50.3)	7.5	5.2	4.7	5.2
Test 8 - S2	248 (55.7)	281 (63.1)	2.4	1.3	0.7	0.8
Test 9 - S1	326 (73.3)	347 (78.1)	3.2	3.6	7.0	7.0
Test 10 - S3	432 (97.2)	380 (85.5)	3.2	2.0	9.4	9.0

7.4 EXPERIMENTAL OBSERVATIONS AND ANALYSIS OF FIELD SNAP-BACK TESTS

7.4.1 Overall Force-Deformation Response of Column-Footing Specimen to Snap-Back Tests

Five snap-back tests were performed on the west column-footing specimen located at the GEFRS. The tests were conducted with the specimen bearing on native Upper Willamette Silt over a number of seasonal conditions. Table 7.10 summarizes the snap-back tests performed, including the test dates, the specimen tested, the applied lateral force, *F*, prior to release, and the axial load. Snap-back tests were performed on the west Specimen 5 (only) on November 29th, December 2nd, and December 5th of 2022 and May 22nd of 2023. For all cases, no additional axial load was applied to the column top and thus only self-weight of Specimen 5 contributes to the initial pressure applied to the bearing soils. An example of a typical snap-back test prior to the release of the applied lateral load is shown in Figure 7.69. The force-displacement measurements described herein include the imposed lateral (tension) force used to displace the column-footing specimen towards the west, with the resultant located 2.946 m (9.67 ft.) above the base of the footing and the corresponding static and dynamic static lateral displacements. String potentiometers located 0.737 m (29 in.) from the center of the column-footing specimen were used to measure vertical displacements of the footing during the initial imposed static displacement and the subsequent dynamic displacements following release.



Figure 7.69: Typical snap-back test setup with applied lateral load just prior to the instantaneous release (i.e., snap-back). Photo taken during test performed on May 22nd, 2023.

Table 7.10: Summary of Snap-Back Tests Conducted

Test Date	Specimen I.D.	Maximum Applied Lateral Force, *F*	Applied Axial Load
11/29/2022	5 - west	4.48 kip (19.9 kN)	0 kip
12/2/2022	5 - west	4.34 kip (19.1 kN)	0 kip
12/5/2022	5 - west	6.32 kip (28.1 kN)	0 kip
5/22/2023	5 - west	6.50 kip (28.9 kN)	0 kip
5/22/2023	5 - west	8.67 kip (38.6 kN)	0 kip

7.4.1.1 November 29th, 2022, Snap-Back Test

The November 29th snap-back test (F = 19.9 kN or 4.48 kip) served as an initial trial to identify improvements in the experimental procedures used for subsequent tests. For example, string potentiometers used to measure column drift at the lateral load point and vertical footing displacements were of similar sensitivity and range to those used in the structural laboratory and which experienced much larger displacements. The first set of string potentiometers allowed the measurement of displacements up to 101.6 cm (40 in.) and 12.7 cm (5 in.) for the column drift and vertical footing displacements, respectively, and as such lacked the sensitivity to precisely measure the smaller displacements observed during the November 29th test. Figure 7.70 presents the rocking behavior of the column-footing specimen in terms of the column lateral drift and vertical footing displacements resulting from the release of the 19.9 kN (4.48 kip) lateral load which are of just slightly larger in magnitude than the noise threshold from the instrument. 7.70a presents the lateral load time history measured using a 25-kip capacity load cell attached in-line with the quick release as described in Section 7.2.3.2. The applied lateral load just prior to release was equal to 19.9 kN (4.48 kips) corresponding to the column drift of approximately 0.02 in (0.5 mm). It is possible that some footing uplift occurred in response to the applied static lateral load, but Figure 7.70 shows that the resolution of the dynamic vertical displacements was insufficient to distinguish rocking displacements of the footing as a result of the instrument noise.

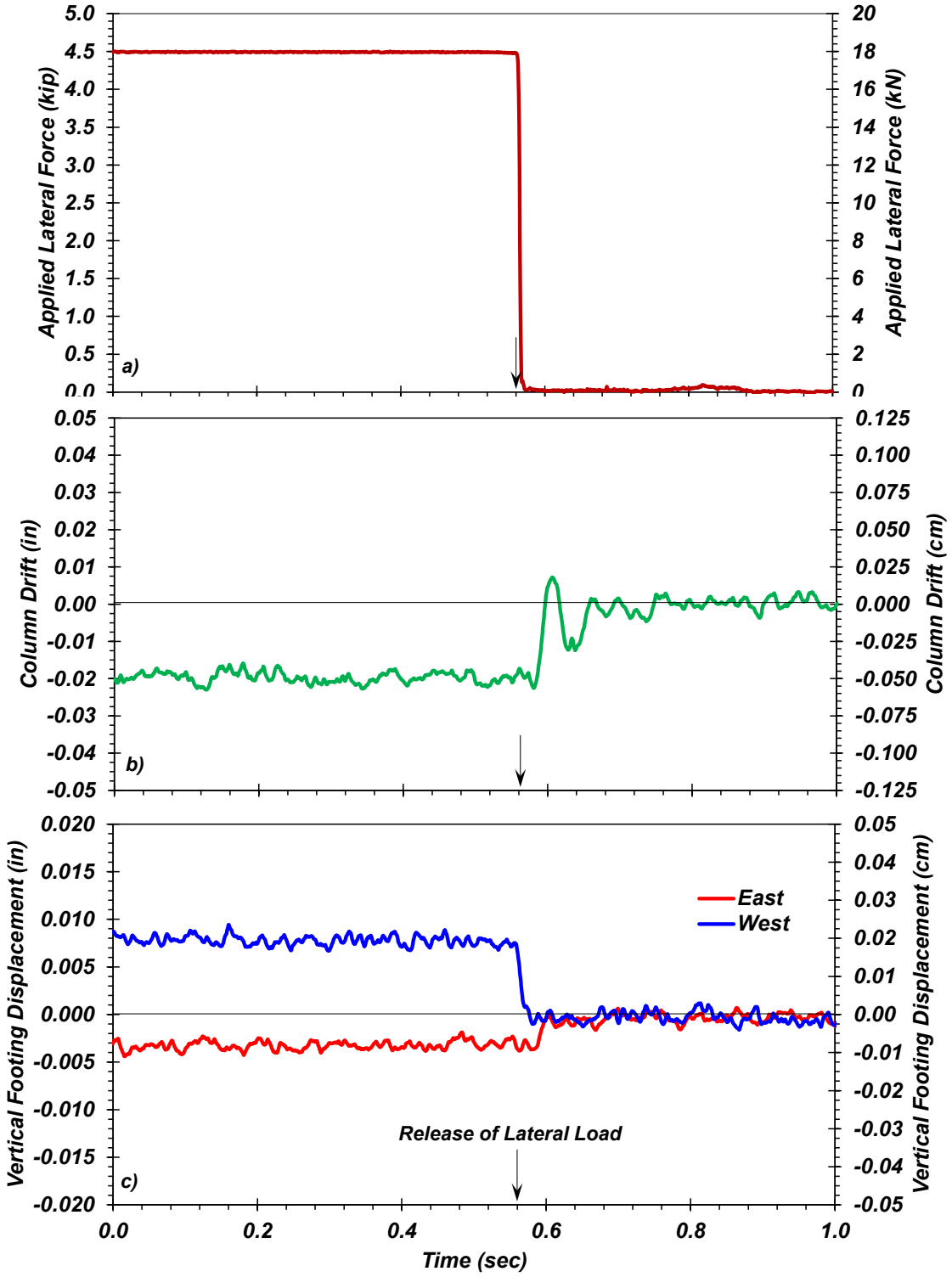

Figure 7.70: Static and dynamic lateral displacement response of Specimen 5 during the November 29th snap-back test (F = 19.9 kN or 4.48 kips): (a) Lateral load time history (b) lateral column drift at the location of force application, and (b) vertical rocking displacements of the top of the footing 0.737 m (29 in.) from the center of the specimen.

7.4.1.2 December 2nd, 2022, Snap-Back Test

The December 2nd snap-back test (Table 7.10) was performed after adjustments were made to the instrumentation setup, which included the use of smaller range string potentiometers increase the signal to noise ratio for capturing specimen displacements during the test. The test was performed in the afternoon of December 2nd, 2022, a few days after the first snap-back test with a similar maximum applied lateral load as that conducted on 29 November (i.e., 19.1 kN or 4.34 kips; Table 7.10).

The December 2nd snap-back test resulted in an imposed column drift equal to 1.2 mm (0.047 in.) just prior to the instantaneous release of the 19.1 kN (4.34 kip) lateral load, which took 0.0047 seconds to fully release. The minor oscillations observed after the release of load (Figure 4.3a) are associated with the load cell recording tension while suspended (Figure 7.71) by safety mechanism (i.e., ropes tied to ensure the load cell would not impact the ground). Figures 7.71b and 71c presents the rocking displacement time histories developed in response to the static load release which show that no rocking displacements could be detected at the top of the footing. Rather, the applied lateral load appeared to slightly and rigidly rotate the footing to engage in sufficient passive restraint and friction to prevent rocking of the footing under the imposed small lateral load; as such, the dynamic response of the column-footing specimen resulted entirely from flexure of the column. At the lateral load point, the column had a residual displacement of 0.6 mm (0.024 in.) to the west after the vibration of the column had concluded.

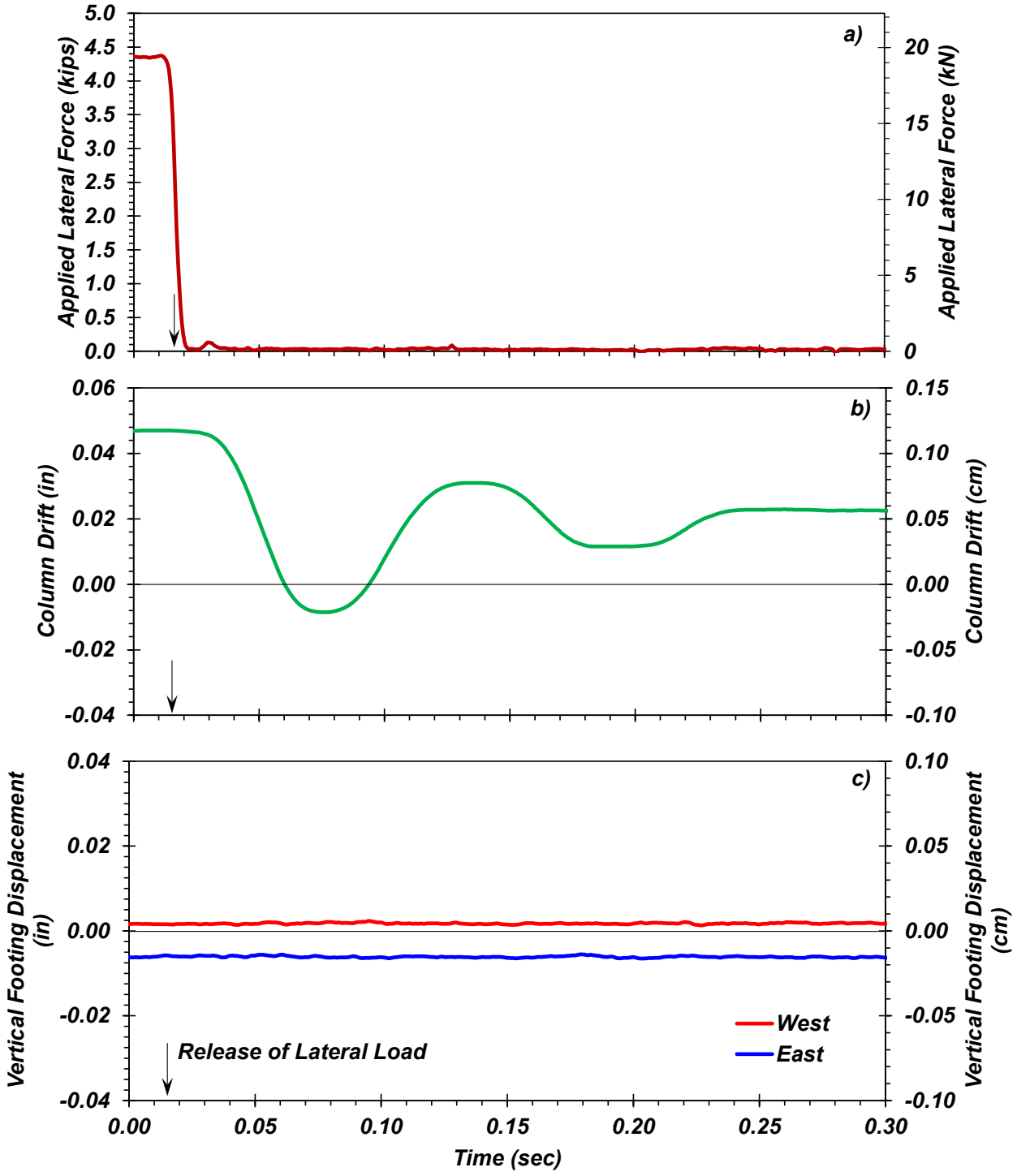

Figure 7.71: Static and dynamic lateral displacement response of Specimen 5 during the December 2nd snap-back test (F = 19.1 kN or 4.34 kips): (a) Lateral load time history (b) lateral column drift at the location of force application, and (b) vertical rocking displacements of the top of the footing 0.737 m (29 in.) from the center of the specimen.

7.4.1.3 December 5th, 2022, Snap-Back Test

The December 5th snap-back test resulted in an imposed column drift equal to 2.08 mm (0.082 in.) just prior to the release of the 28.1 kN (6.32 kip) lateral load, which took 0.0086 seconds to fully release. The applied lateral load history is presented in 7.72a, whereas 7.72b and 6.4c present the rocking displacement time histories developed in response to the static load release. The top drift oscillated for 2.25 cycles and resulted in a permanent drift offset of 0.6 mm (0.024 in.) to the west from the initial position. The vertical footing displacement histories indicated that rocking displacements were detected only on the east side of the footing (opposite to the direction of the applied lateral load) as it oscillated for 1.25 cycles. The final displacements of the east and west sides of the footing equal to 0.3 mm (0.011 in.) and 0.4 mm (0.017 in.), respectively. The applied lateral load rigidly rotated the footing to engage some passive restraint and friction to prevent global rocking of the footing under the imposed lateral load; as such, the dynamic response of the column-footing specimen resulted from a combination of flexure of the column and slight rocking deformations, whereas the dynamic response of Specimen 5 during December 2nd (F = 19.1 kN or 4.34 kips) only resulted from column flexure.

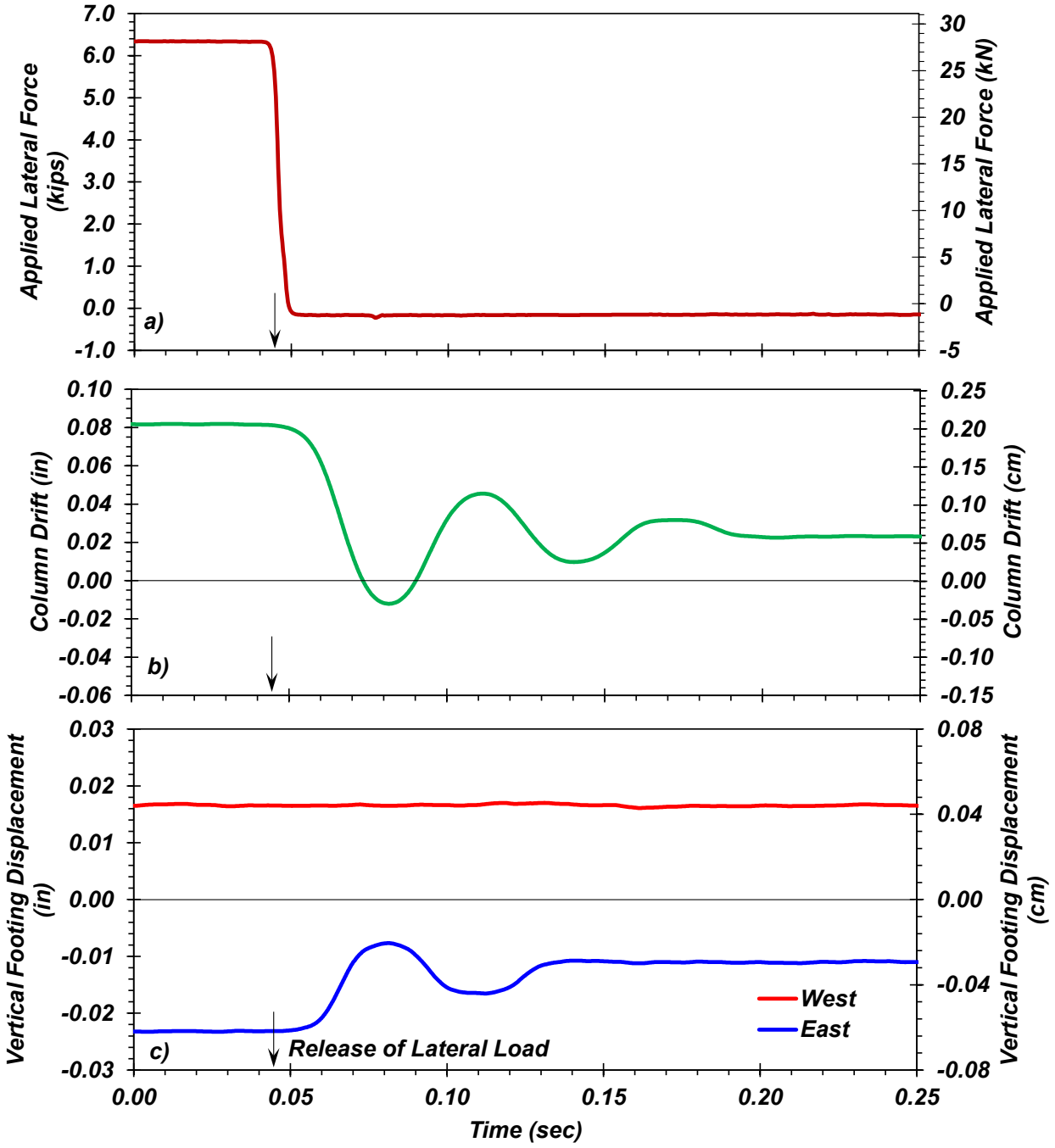

Figure 7.72: Static and dynamic lateral displacement response of Specimen 5 during the December 5th snap-back test (F = 28.1 kN or 6.34 kips): (a) Lateral load time history (b) lateral column drift at the location of force application, and (b) vertical rocking displacements of the top of the footing 0.737 m (29 in.) from the center of the specimen.

A comparison of the top drift histories from the December 2nd (F = 19.1 kN or 4.34 kip) and December 5th (F = 28.1 kN or 6.32 kip) is shown in Figure 7.73. While the December 2nd test imposed less dynamic displacement when compared to the December 5th test, the permanent top drift displacements observed after the snap-back tests were nearly equal. However, the permanent vertical footing displacements were greater for the December 5th test compared to the December 2nd. The differences in the permanent footing deformations are most likely associated with the change in the point of rotation about the base of the footing for the December 5th test compared to that on December 2nd. The permanent footing displacements for the December 5th snap-back test were nearly symmetrical about the zero-displacement axis, whereas the east and west footing displacements for the December 2nd snap-back differed by a magnitude of three. While the recorded displacements were small, the difference contributed to the final "at-rest" column drifts being nearly identical due to differing points of rotation, as the varying vertical displacements of the footing acted to re-center the column at its previous permanent location oriented (or leaning) to the west.

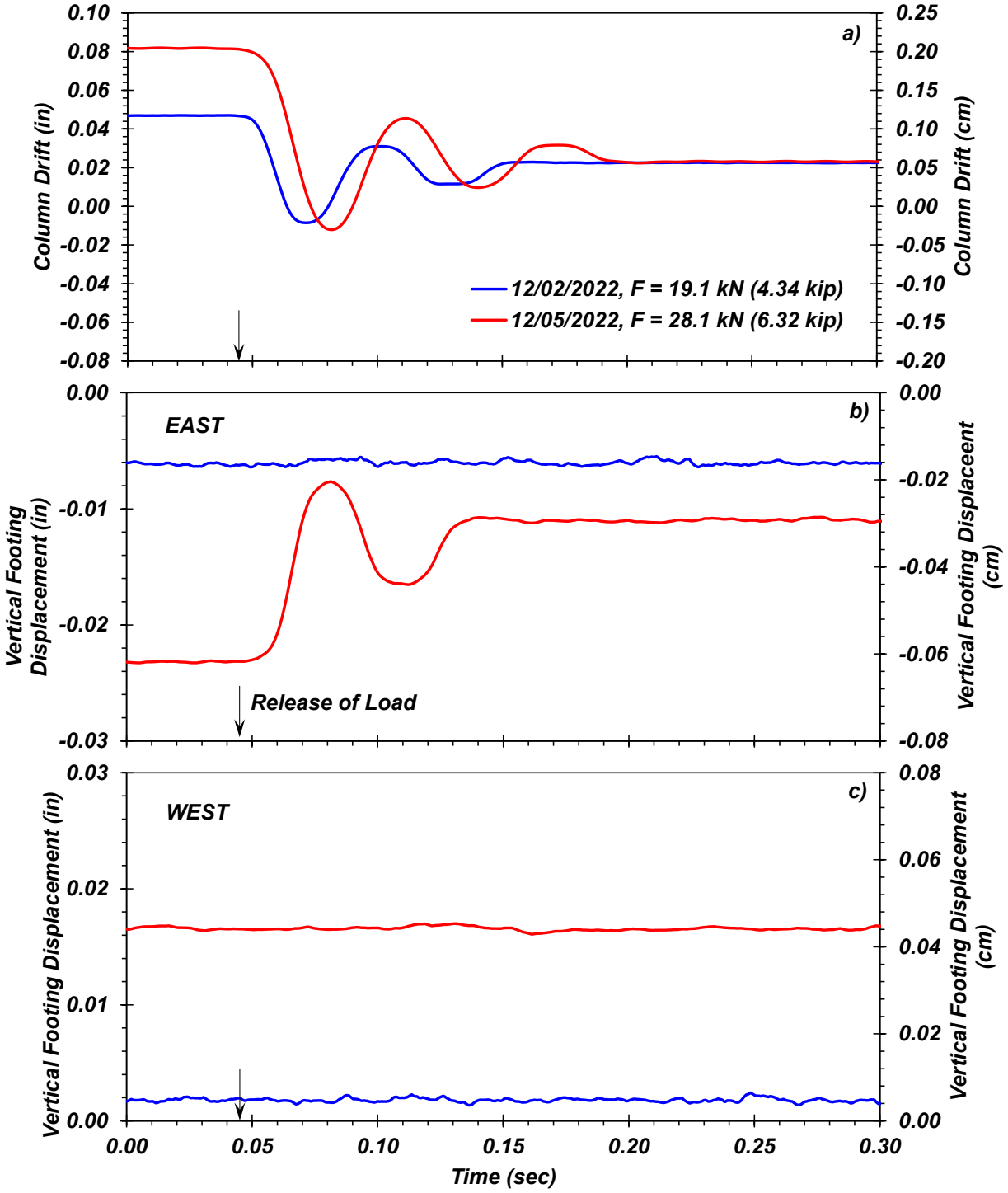

Figure 7.73: Comparison of the static and dynamic lateral displacement response of Specimen 5 during the December 2nd (F = 19.1 kN or 4.34 kip) and the December 5th snap-back test (F = 28.1 kN or 6.34 kips): (a) Lateral column drift at the location of force application, (b) vertical rocking displacements of the top of the footing on the east side, and (c) vertical rocking displacements of the top of the footing on the east side located 0.737 m (29 in.) from the center of the specimen. Note: Blue is from December 2nd and red is from December 5th.

7.4.1.4 May 22nd Snap-Back Tests

The lateral load applied during the December 5th snap-back test (F = 28.1 kN or 6.32 kip) was reproduced on May 22nd, 2023, to assess the influence of seasonal near-surface moisture changes on the response of the specimen. Although the weather pattern had been relatively warm and dry leading up to the May 22nd test date, the volumetric water content of the foundation soils upon which the footing was bearing was nearly identical to the water content recorded during the December 5th test (Figure 7.32). It appears that the footing potentially shielded the bearing soils from development of significant matric suctions associated with evapotranspiration processes. The lateral load at the time of release was 28.9 kN (6.50 kip) which took 0.0034 seconds to fully release, similar to the magnitude of the lateral applied to the column-footing specimen on December 5th.

The column drift at the time of the instantaneous release was equal to 2.67 mm (0.0105 in.). The column rocked for 2.5 cycles before resting at a permanent displacement 1.0 mm (0.04 in.) to the west of the initial position. The top of the footing displaced to a maximum of 0.57 mm (0.022 in.) upwards on the east side of the column and 0.38 mm (0.015 in.) downwards on the west side of the column. Rocking behavior was observed from the displacement histories recorded on both the east and west sides of the footing surface, with the rocking displacements observed to be more significant on the west side compared to the east. The permanent displacements after the snap-back test were 0.5 mm (0.02 in.) up and 0.15 mm (0.005 in.) down for the east and west sides of the footing (Figure 7.76), respectively. The displacement time histories from the December 5th and May 22nd snap-back tests indicate minor differences, apparently stemming from potential differences in the bearing surface provided by the foundation soils (stemming from repeated rocking events; Sharma 2019) and potentially differing soil conditions as a result of seasonal conditions. Whereas the volumetric water content in the soil immediately below the footing was more or less identical for both tests, the water content of the soil at the vertical footing interfaces may be subject to greater environmental dynamics but was not monitored.

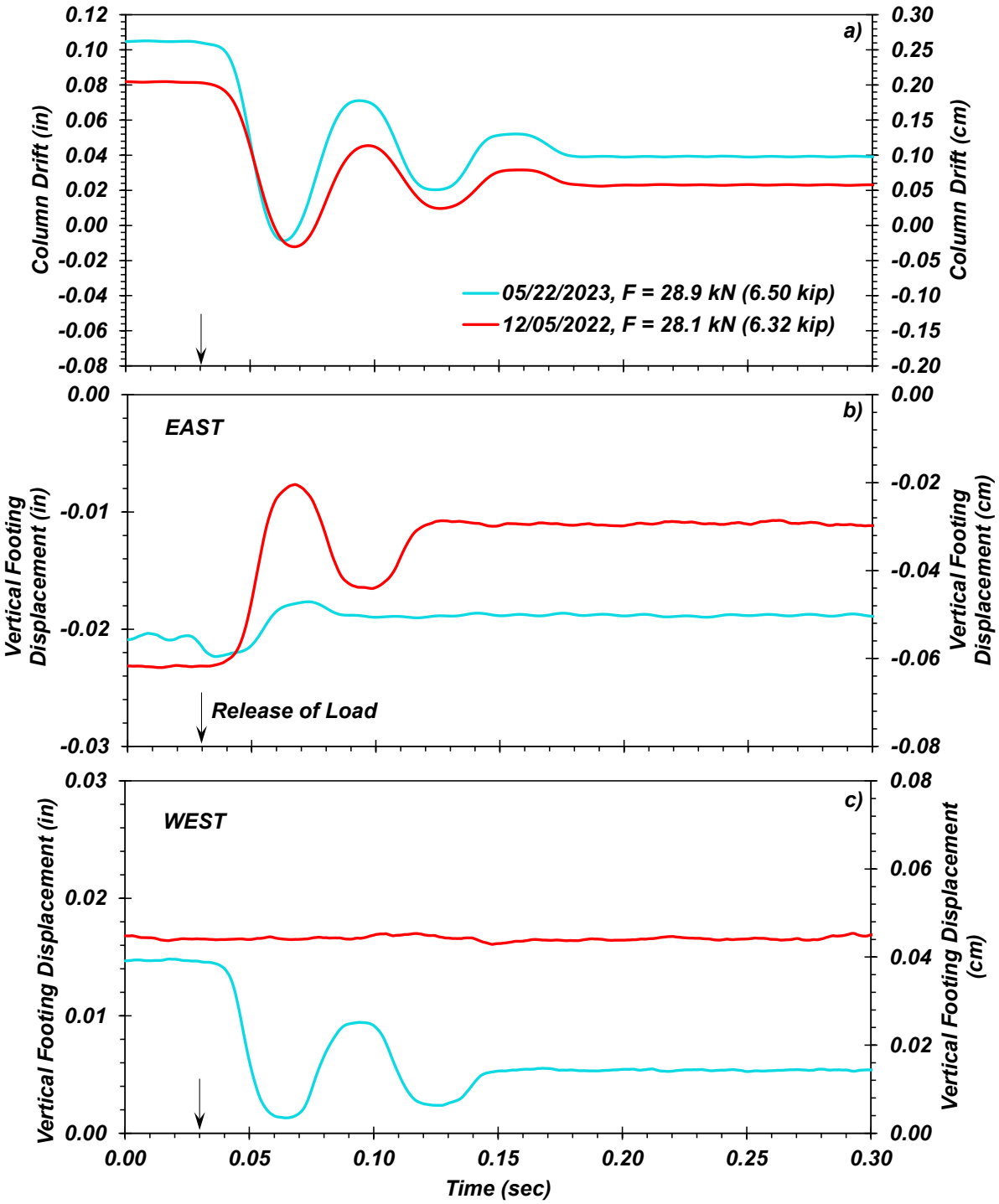

Figure 7.74: Comparison of the static and dynamic lateral displacement response of Specimen 5 during the May 22nd (F = 28.9 kN or 6.50 kip) and the December 5th snap-back test (F = 28.1 kN or 6.34 kips): (a) Lateral column drift at the location of force application, (b) vertical rocking displacements of the top of the footing on the east side, and (c) vertical rocking displacements of the top of the footing on the east side located 0.737 m (29 in.) from the center of the specimen. Note: Red is from December 5th and light blue is from May 22nd.

An additional snap-back test was performed on May 22nd roughly 15 minutes after the first snap-back test using a larger lateral load (38.6 kN or 8.67 kip). The column drift imposed prior to the instantaneous release was equal to 5.33 mm (0.21 in.), with the maximum static pre-release vertical footing top displacements equal to 0.84 mm (0.033 in.) upwards and 0.83 mm (3.3 in.) downwards on the east and west sides of the column, respectively. Figure 7.75 presents the lateral load time history which indicated that it took 0.0047 seconds for the applied load to fully release. As previously discussed, the rapid fluctuations in the lateral load time history post-release can be associated to the quick-release setup suspended from the safety system. The column oscillated for a maximum of 3.25 cycles, whereas the east and west sides of the footing oscillated for 0.75 and 2.25 cycles, respectively. The displacement histories from the 38.6 kN (8.67 kip) test are compared with the displacement histories from the 28.9 (6.50 kip) test performed earlier on the same day in Figure 7.76, which indicated that the 38.6 kN (8.67 kip) test imposed greater initial column drifts and vertical footing displacements pre-release, induced a greater amount of rocking cycles with respect to both the footing and column, and imposed greater permanent displacements with respect to column drift and vertical footing displacements on the west side.

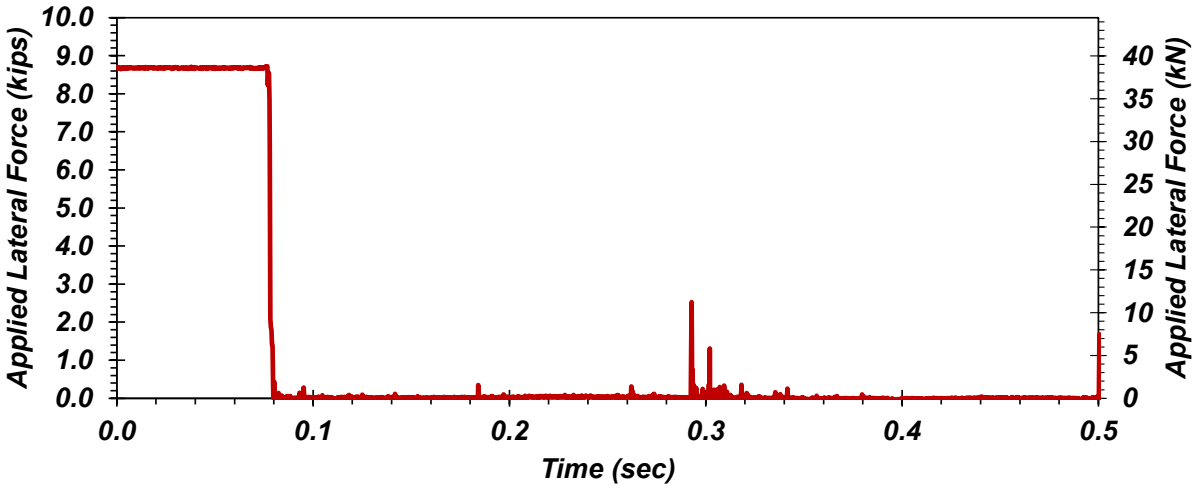

Figure 7.75: Lateral load time history for May 22nd snap-back test on Specimen 5 (F = 38.6 kN or 8.67 kips).

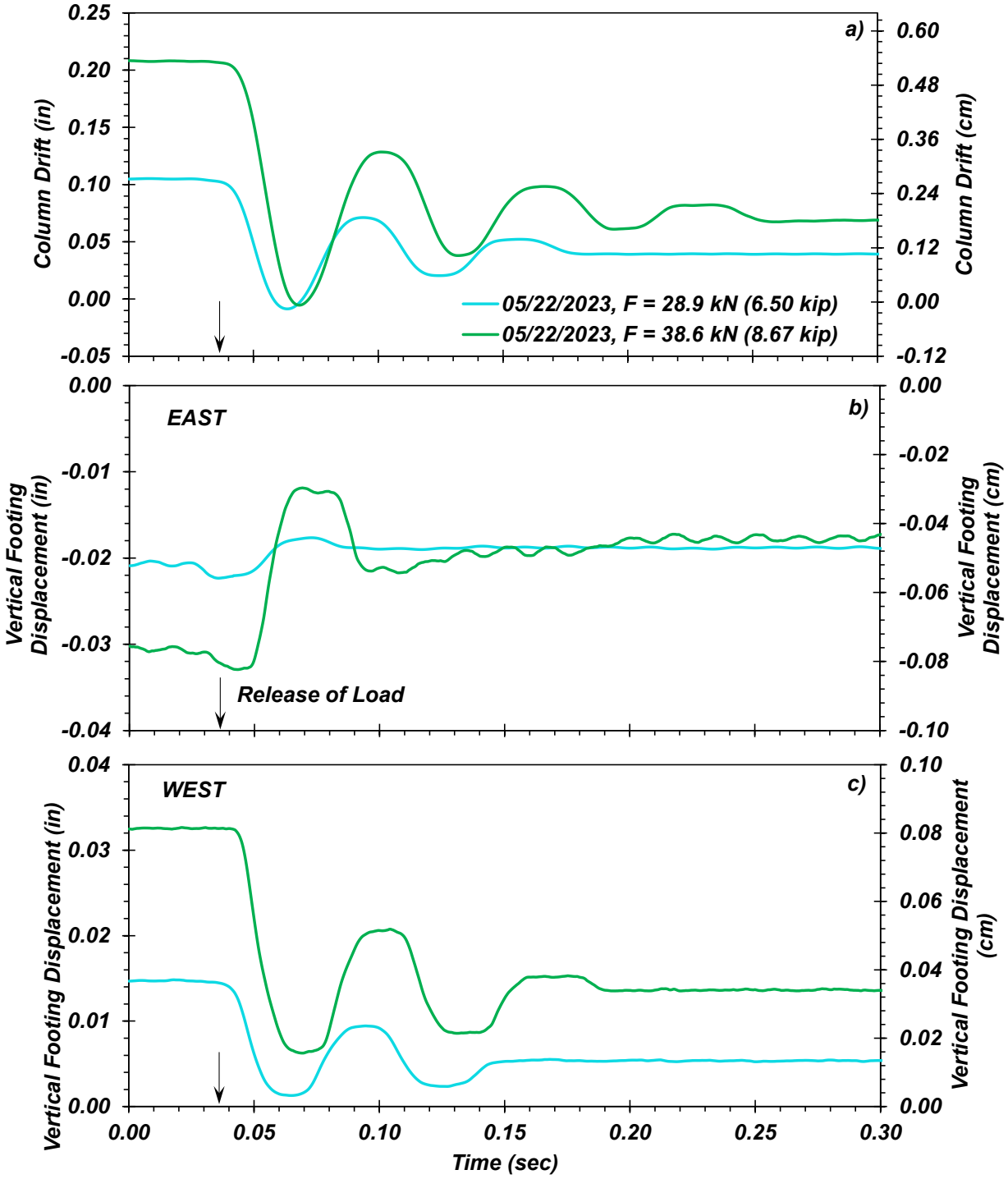

Figure 7.76: Comparison of the static and dynamic lateral displacement response of Specimen 5 during the May 22nd (F = 28.9 kN or 6.50 kip, F = 38.6 kN or 8.67 kip) snap-back tests: (a) Lateral column drift at the location of force application, (b) vertical rocking displacements of the top of the footing on the east side, and (c) vertical rocking displacements of the top of the footing on the east side located 0.737 m (29 in.) from the center of the specimen. Note: Green is second test from May 22nd and blue is first test from May 22nd.

7.4.1.5 Summary of Displacements Recorded During Snap-Back Tests

The snap-back tests conducted at the GEFRS using the higher sensitivity displacement sensors allowed for comparison of column and footing displacements for varying seasonal conditions and different magnitude applied lateral loads prior to release. Figure 7.77 shows the comparison of the recorded column drift for the December 2nd, December 5th, and both May 22nd snap-back tests. The recorded column drift time histories indicated that tests performed with an applied lateral force less than or equal to 19.1 kN (4.34 kips) induced 1.75 rocking cycles. Tests performed with greater applied lateral loads indicated that a lateral load of both 28.1 kN (6.34 kip) and 28.9 kN (6.50 kip) induced 2.25 rocking cycles, whereas the test with an applied lateral force of 38.6 kN (8.67 kip) was sufficient to induce 3.25 rocking cycles. The tests demonstrated two types of dynamic response: global rocking of the specimen, where the footing rocks and the column vibrates, and column vibration alone, where the footing does not rock but the column exhibits free vibration after release.

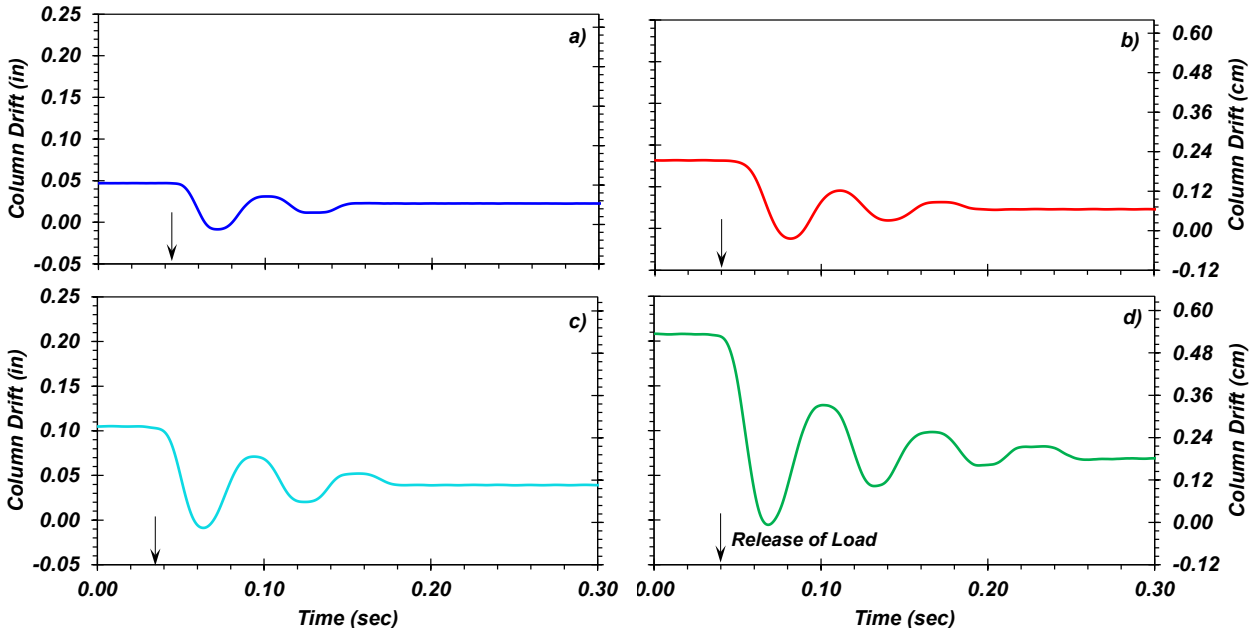

Figure 7.77: Comparison of the column drift time histories from: (a) the December 2nd, F = 19.3 kN (4.34 kip), (b) the December 5th. F = 28.1 kN (6.32 kip), (c) the May 22nd, F = 28.9 kN (6.50 kip), and (d) the May 22nd, F = 38.6 kN (8.67 kip) snap-back tests performed on Specimen 5.

The damped frequency, ω_d, was determined for each test by calculating the period of the positive or negative top drift cycle (Figure 7.78). The damping ratio, ζ, corresponding to the damped, free-vibration, snap-back response of the column-footing specimen was computed using the logarithmic decrement, δ, ascertained using the amplitudes of the column drift response for two successive peak cycles, Δ_n and Δ_{n+1}, (Figure 7.78) using:

$$\boldsymbol{\delta = \ln\left(\frac{\Delta_n}{\Delta_{n+1}}\right)}$$

(7-13)

which facilitates the calculation of ζ, given by (Kramer 1996):

$$\boldsymbol{\zeta = \frac{\delta}{\sqrt{4\pi^2 + \delta^2}}}$$

(7-14)

Hysteretic damping is dynamic parameter that allows for the dissipation of seismic energy, and therefore is a critical aspect of column-footing substructure design (Sharma 2019). Column-footing structures with high damping ratios will oscillate for relatively few cycles (i.e., energy is rapidly dissipated) prior to achieving the permanent "at-rest" position. The rapid dissipation of energy increases the seismic resistance of a column-footing substructure.

A summary of the damped free vibrations from each of the four well-instrumented snap-back tests is presented in Table 7.11. It is evident that an increase in the applied lateral load prior to the instantaneous snapped release corresponds to a decrease in the damped frequency, the logarithmic decrement, and the damping ratio, for both the positive and negative (east and west) top drift displacements. The decrease in ζ with increasing magnitudes of the applied lateral load is representative of an elastic response to loading, with further justification for the elastic response of the column is demonstrated by the strain gauge time histories of the vintage steel reinforcement (Section 7.4.2). The decrease in ζ corresponds to a globally stiffer response of the specimen subjected to snap-back tests. The stiffer responses with increasing applied lateral loads are most likely caused by the increase in the amount of soil engaged in both bearing and passive resistance, and thus causes a decrease in the damping ratio.

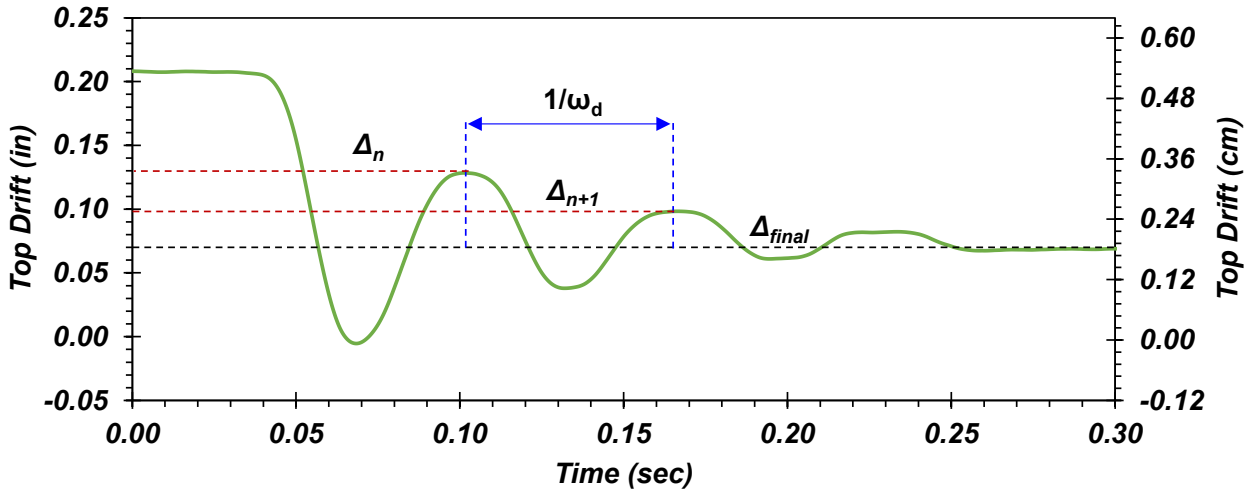

Figure 7.78: Process for the determination of the positive-cycle ω_d, δ, and ζ from the column drift time recorded during the May 22nd snap-back test, F = 38.6 kN (8.67 kip).

Table 7.11: Summary of the damped free vibration coefficients and parameters determined through the analyses of snap-back top drift histories. Note: An insufficient number of cycles was recorded during the 19.1 kN (4.34 kip) test to determine the damped parameters for positive cycles. They are therefore omitted.

Test Designation	Lateral Force, kN (kip)	Polarity	Damped Frequency, ω_d (s^{-1})	Logarithmic Decrement, δ	Damping Ratio, ζ
December 2nd, 2022	19.1 (4.34)	Positive	-	-	-
		Negative	18.14	1.046	0.164
December 5th, 2022	28.1 (6.32)	Positive	16.44	0.943	0.148
		Negative	17.09	0.978	0.154
May 22nd, 2023	28.9 (6.50)	Positive	15.96	0.905	0.143
		Negative	16.44	0.932	0.147
May 22nd, 2023	38.6 (8.67)	Positive	15.26	0.701	0.111
		Negative	15.76	0.721	0.114

Comparison of the dynamic properties of the December 5th (F = 28.1 kN or 6.32 kip) and May 22nd (F = 28.9 kN or 6.50 kips) tests allow assessment of the seasonal-dependency of the column-footing responses under snap-back test conditions. The December 5th test was performed with an applied lateral load 47.1% greater relative the "base" test (December 2nd, F = 19.1 kN or 4.34 kips), whereas the May 22nd test was performed at a lateral load 51.3% greater than the base test. The % increase in the applied lateral load corresponded to an 8.3% and 13.2% decrease in the damping ratio for the December 5th

and May 22nd tests, respectively. The "dry season" conditions (considered to be represented by May 22nd, F = 28.9 kN or 6.50 kip) corresponded to a greater relative decrease in the damping ratio relative to the base test compared to the "wet season" conditions (considered to be represented by December 5th, F = 28.1 kN or 6.32 kip), as presented in Table 7.12. The greater relative reduction in the damping ratio for the dry season test was indicative of a stiffer response, most likely due to the increase in the strength of the soil at the vertical footing interfaces due to environmental dynamic (i.e., effects of partial saturation).

Table 7.12: Comparison of the relative change in the damped free vibration parameters for the December 5th (F = 28.1 kN or 6.32 kips) and the May 22nd (F = 28.9 kN or 6.50 kips) snap-back tests.

Test Designation	Applied Lateral Load, F, kN (kip)	% Increase in F Relative to 12/2/2022 Test	Average % Decrease in Damping Ratio, ζ	Ratio of % Decrease in ζ to % Increase in F
December 2nd, 2022	19.1 (4.34)	-	-	-
December 5th, 2022	28.1 (6.32)	47.1	8.3	0.176
May 22nd, 2023 (1)	28.9 (6.50)	51.3	13.2	0.257
May 22nd, 2023 (2)	38.6 (8.67)	102.1	40.8	0.400

Two accelerometers were fixed to Specimen 5 at the elevation at which the lateral load was applied: one that recorded accelerations in the east-west and one that recorded accelerations in the vertical direction. The instruments were attached to the east face of the column opposite the direction of the lateral load application. The signal was filtered with a lowpass filter having a cutoff frequency of 59 Hz and then baseline corrected to remove noise and artifacts. Figure 7.79a shows the acceleration time history recorded by the east-west direction accelerometer during the December 5th (F = 28.1 kN or 6.32 kip) snap-back test, indicating that the acceleration in the east-west direction reached a peak of 15.3 m/s^2 (1.56g). The signal recorded in the vertical direction was particularly small relative to the noise (0.49 m/s^2 or 0.05g) and is thus omitted herein. The corrected acceleration history was integrated to determine the velocity time history of the column at the point of load point and is presented in Figure 7.79b. Although the drift observed in the velocity indicates that typical baseline corrections were insufficient to fully correct the signal, the peak east-west velocity was observed to 0.16 m/s.

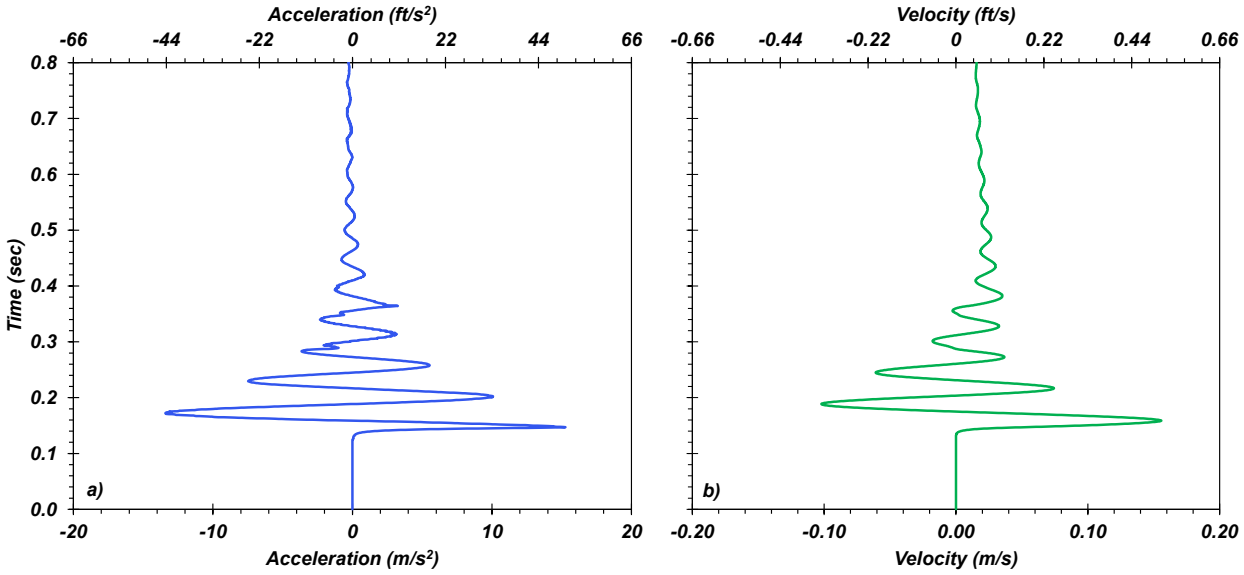

Figure 7.79: Dynamic excitation of the column at the point of load application recorded during the December 5th (F = 28.1 kN 6.32 kip) snap-back test: (a) acceleration time history, and (b) the corresponding velocity time history. Note: The non-zero final velocity of the specimen can be attributed to imperfect baseline corrections.

It is of interest to compare the damped natural frequency and damping determined from the acceleration time history to that calculated using the results of the string-potentiometer measurements of displacement. The process for computing of ω_d, δ, and ζ followed that described above using Eqns. 6.1 and 6.2. Acceleration half-cycles in the positive (east direction) and negative (west direction) accelerations were analyzed to determine the overall damped free vibration response of the column-footing specimen, as presented in Table 7.13. The second cycle was the most-damped cycle for both the positive and negative cycles, corresponding to the highest values of δ and ζ. This second cycle of rocking corresponds to the time at which the footing remained stagnant; the first rocking cycle induced cyclic deformations observed on the east side of the footing, whereas the footing came to rest after this first cycle had completed. This increase in δ and ζ and the corresponding decrease in ω_d was caused by the rocking deformation changing from the global footing-and-column behavior to the column-only damped free vibration. The column drift history and vertical footing displacement histories are presented concurrently with the accelerometer history in Figure 7.80.

Table 7.13: Summary of the damped free vibration coefficients and parameters determined through the analyses of the December 5th snap-back accelerometer history. Note: Acceleration is denoted by the variable, *u*.

December 5th Snap-Back, F = 28.1 kN (6.32 kip)							
Cycle	t_n (s)	u_n (m/s^2)	t_{n+1} (s)	u_{n+1} (m/s^2)	ω_d (s^{-1})	δ	ζ
Positive	0.147	15.187	0.203	10.032	18.06	0.41	0.0659
	0.203	10.032	0.258	5.508	17.89	0.60	0.0950
	0.258	5.508	0.314	3.189	18.06	0.55	0.0866
	Average				18.00	0.52	0.0825
Negative	0.173	13.453	0.230	7.506	17.64	0.58	0.0925
	0.230	7.506	0.283	3.651	18.67	0.72	0.1140
	0.283	3.651	0.340	2.296	17.64	0.46	0.0736
	Average				17.99	0.59	0.0933

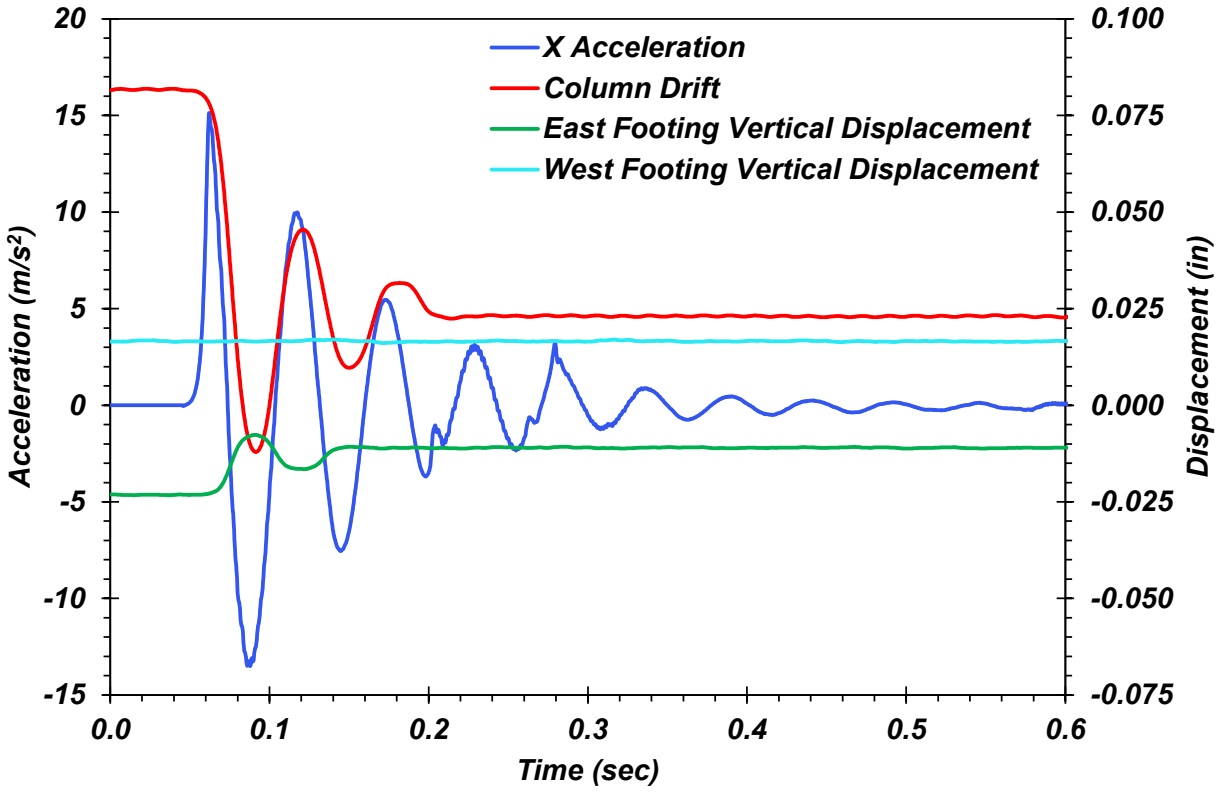

Figure 7.80: Comparison of the column drift, east and west vertical footing displacement histories and east-west accelerations recorded during the December 5th (F = 28.1 kN or 6.32 kip) snap-back test.

7.4.2 Reinforcing Steel Strains

Similar to the structural laboratory specimens for which Tests 1 through 10 were conducted and discussed in Section 7.3, strain gauges were bonded to the embedded reinforcing steel bars in the footing and column (e.g., footing bars, starter bars, column bars, and column ties) for the test specimen. The reinforcement strains were continuously recorded at a frequency of 3,846 Hz during the snap-back tests. Due to the time elapsed between construction of the field specimens and testing (i.e., approximately one year), sufficient environmental exposure of the strain gauges and wires resulted in a number of lost sensors. Only those functional strain gauges are reported herein. All of the strains recorded during snap-back tests were small relative to yield strains. Selected gauge locations which exhibited the largest responses are presented herein to facilitate the comparison of flexural responses between the tests conducted. Complete strain time histories are provided in Appendix A7.1.

7.4.2.1 Snap-Back Tests Performed in the Wet Season

The column-footing connection of a reinforced concrete substructure is the region commonly subjected to the highest flexural demand (Section 2). As a result, the lap splice, containing both starter bars from the footing and column bars are subjected to the highest magnitude of flexural tension and thus corresponding strain. Figure 7.81 presents the strains recorded by the functioning strain gauges fixed to the footing starter bars during the December 5th snap-back test, performed with the greatest lateral load applied of the three tests conducted during the wet season (F = 28.1 kN or 6.32 kip). The strains recorded in this region of highest flexural demand were small, with a maximum strain of 58 με (approximately 3% of nominal yield stress). The strain time histories exhibited an oscillating response, which appeared to dampen to the threshold of noise over the span of roughly 0.35 seconds, slightly after the quiescent period was reacquired at the top of the column at the point of load application (Figure 7.81). The column drift time history of Specimen 5 during the December 5th snap-back test (Figure 7.73b) indicated 2.25 cycles of motion before the response became fully damped, whereas the starter bar histories indicated up to six full cycles of east-west oscillations occurred in instrumented starter bar SB.SE.2 before the dynamic response became fully damped. These differences point to the internal oscillating response of the structural reinforcing elements being more sensitive to snap-back tests than what is evident from an overall displacement history (i.e., column flexure and rocking displacements). Figure 7.82 presents a comparison of the strain history of bar SB.SE.2. and the column drift time history recorded just after the instantaneous release of the applied lateral load. The responses share similar frequency and are just slightly out of phase with one another upon release of the static lateral load, however, the phase differences increased with time. The oscillations of the starter bar strain history continue for about 0.20 seconds after the column has reached the permanent plastic deformation of 0.6 mm (0.024 in.).

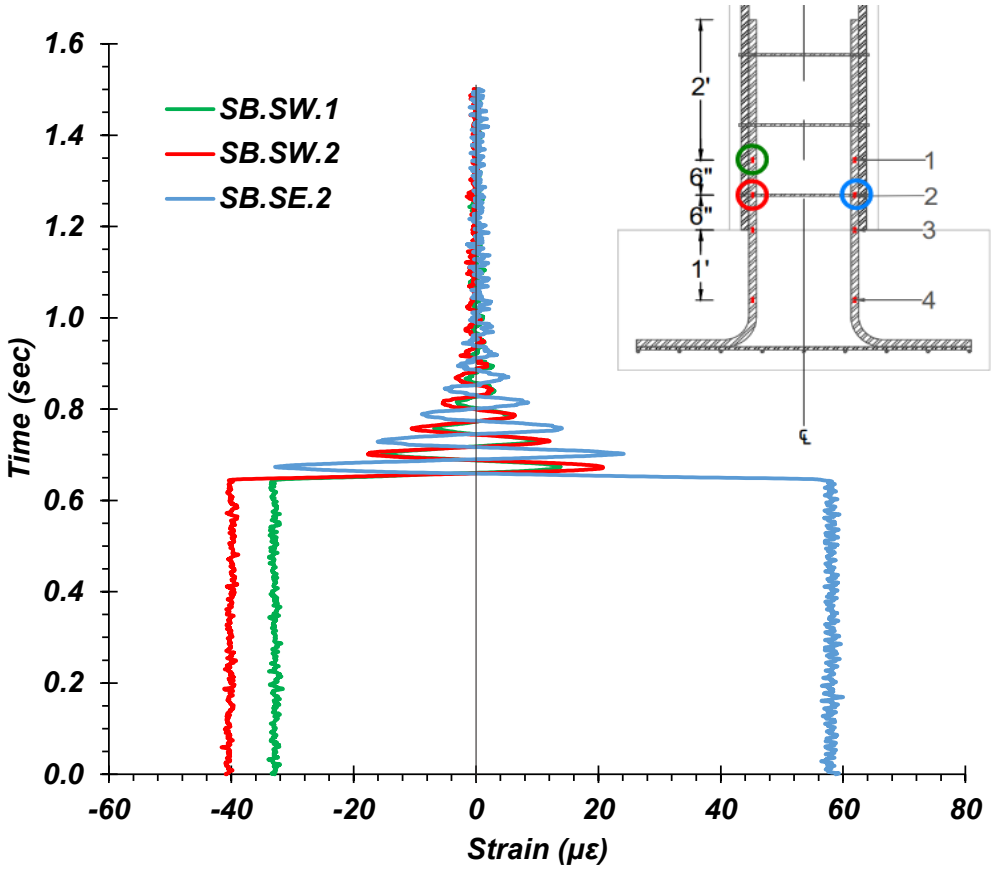

Figure 7.81: Strain histories for starter bars during the December 5th, *F* = 28.1 kN (6.32 kip) snap-back test performed on Specimen 5.

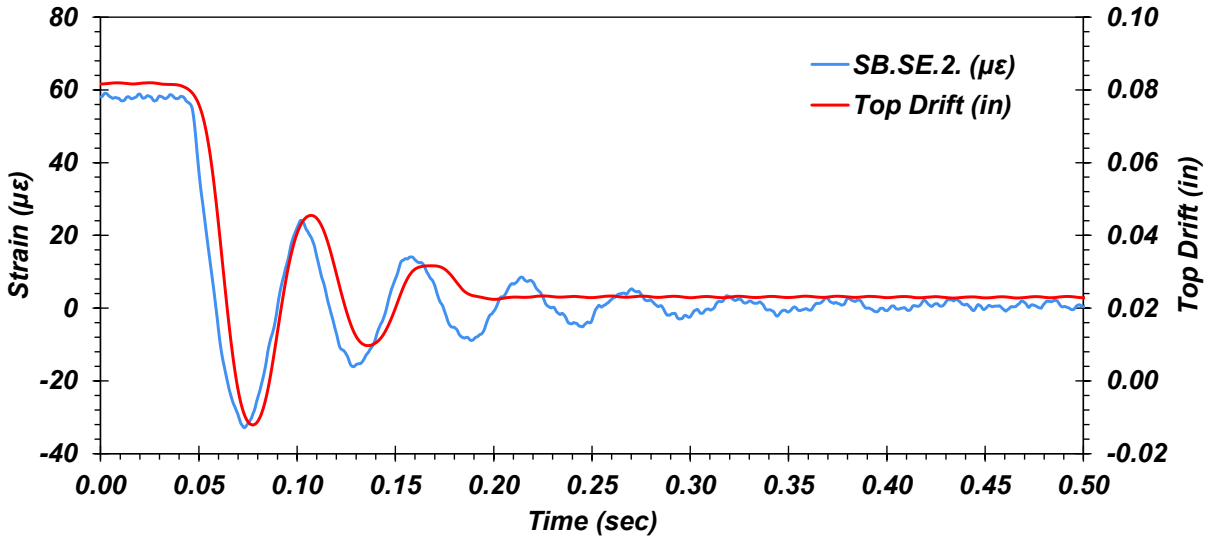

Figure 7.82: Strain histories for starter bars during the December 5th, *F* = 28.1 kN (6.32 kip) snap-back test performed on Specimen 5.

Strains within the column bars were likewise small relative to their yield strain; however, the magnitude of tensile strain during application of the static lateral load was 70% of that in the starter bar, demonstrating the transfer of stress that occurs over the splice. This transfer of strain from the starter bars to the column bars was also observed in the full-scale quasi-static cyclic lateral load tests performed at the OSU Structural Laboratory (Section 7.3). Figure 7.83 shows the column bar histories recorded by the strain gauges within Specimen 5 at three respective elevations on the column. The strain time histories indicated that the elevations at which the column bars were lap-spliced with the starter bars were relatively high (e.g., CB.SE.1. and CB.SE.2.) due to the substantial (but incomplete) strain transfer, whereas the strains were small at elevations where the column bars were not bonded to the starter bars (e.g., CB.SE.5). Figure 7.84 shows a comparison of the column and starter bar strain histories at the same elevation (Location 2) within the column, indicative of the stress transfer occurring between the starter bars and column bars.

Very small, but discernable strains were recorded in the column ties of Specimen 5 during all of the snap-back tests performed in the wet season (i.e., November and December), and although small relative to their yield, the response was more prevalent on the east and west sides of the column when compared to the south owing to the direction of loading applied (Figure 7.85). The strains on the east and west portions of the column demonstrated oscillating strain time histories distinguishable from the noise during the snap-back test on December 5th, whereas the dynamic response was significantly less noticeable perpendicular to loading.

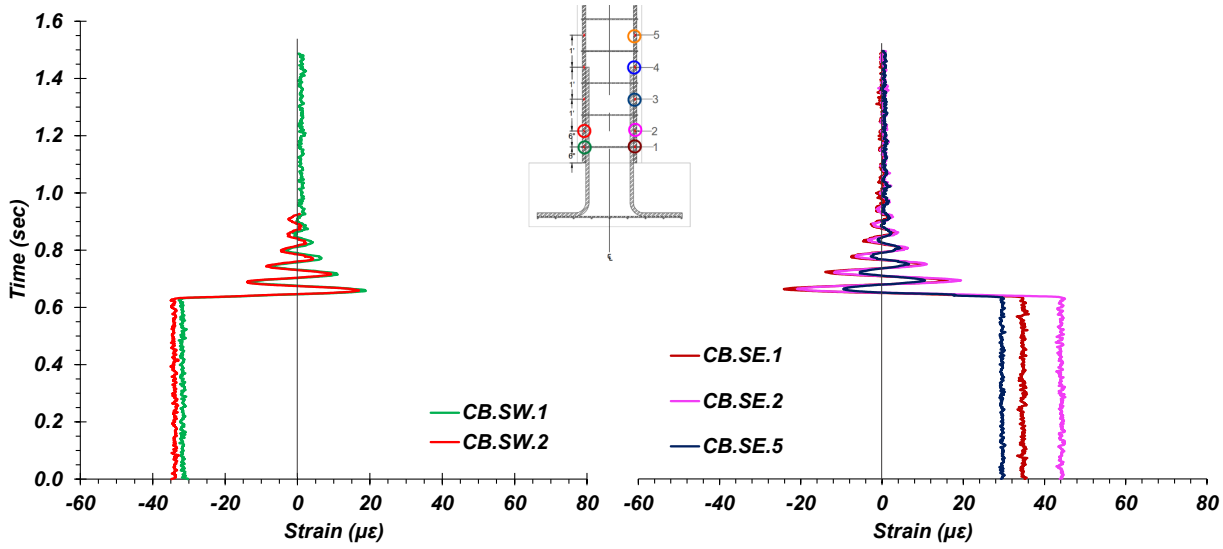

Figure 7.83: Strain histories for column bars during the December 5th snap-back, *F* = 28.1 kN (6.32 kip).

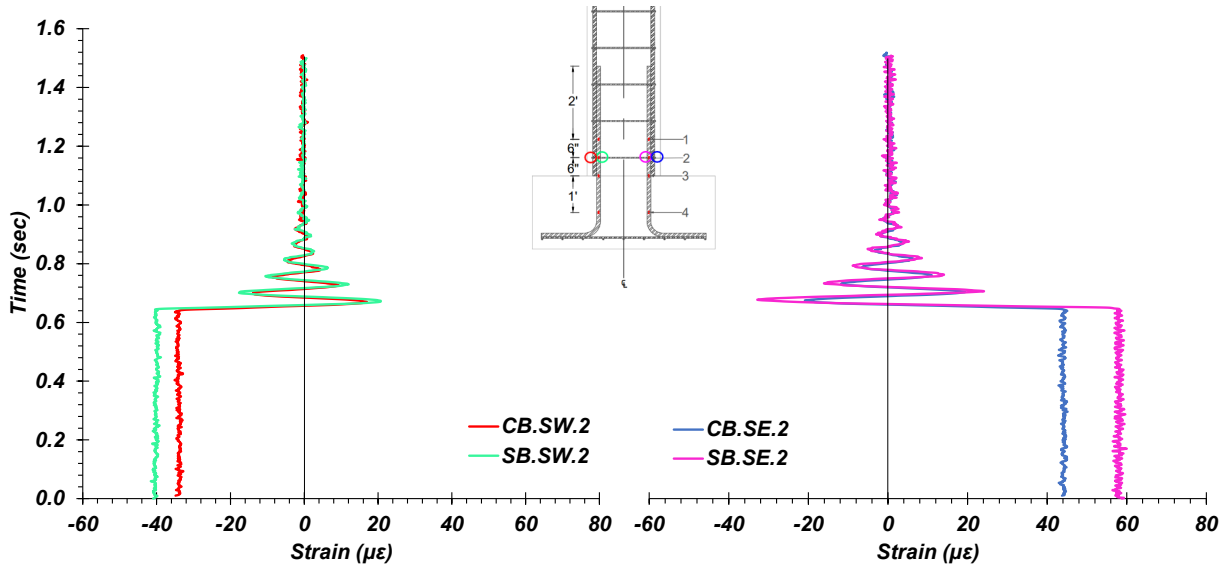

Figure 7.84: Strain history comparison of column and starter bars at Location 2 during the December 5th snap-back, *F* = 28.1 kN (6.32 kip).

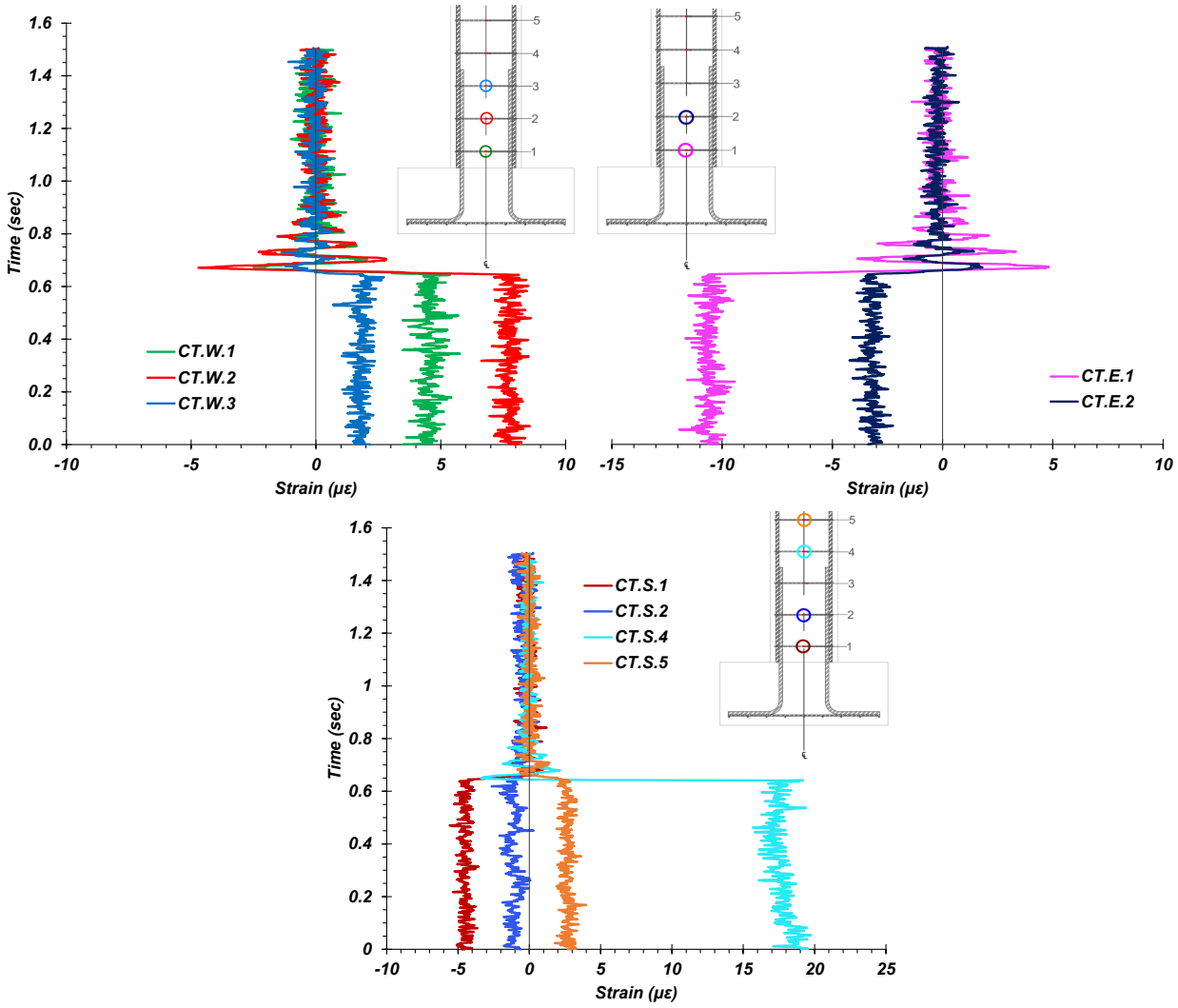

Figure 7.85: Strain histories for column ties during the December 5th snap-back, *F* = 28.1 kN (6.32 kip).

7.4.2.2 Snap-Back Tests Performed in the Dry Season

The subsequent set of snap-back tests were performed on May 22nd, 2023. As discussed in Section 7.3.1, two tests were performed: a 28.9 kN (6.50 kip) test aimed to reproduce the December 5th snap-back test loading, and a 38.6 kN (8.67 kip) test that was the largest magnitude of lateral load applied throughout all tests. Similar to the wet season snap-back tests, none of the strains recorded in the vintage reinforcement approached yield. A select subset of strain histories are presented herein, with the full set of strain histories presented in Appendix A7.1. It is evident that the increased lateral force applied to the second May 22nd snap-back (38.6 kN or 8.67 kip) produced strains larger than the previous snap-back tests and that the strain amplitude was in proportion to the applied load for most strain locations, consistent with an uncracked elastic response of the column. Comparisons of a column and a starter bar strain histories from both snap-back tests performed on May 22nd are presented in Figures 7.86 and 7.87, respectively. The

difference in the strain time histories of the column bars for the two snap-back tests was small, whereas a substantial difference was present in the starter bars. At the time of the snap-back release, the strain in SB.SE.3. during the 28.9 kN (6.50 kip) test was equal to 57 με, whereas the strain at the same location was 186 με during the 38.6 kN (8.67 kip) snap-back test. This three-fold increase in the starter bar was not directly proportional to the 33% increase in the applied lateral load prior to the snap, owing to the presence of a temperature, shrinkage, or flexural crack at the location of SB.SE.3. The applied lateral load of 8.67 kips (38.6 kN) was sufficient to decompress the column and open the cracks at the location of the strain gauge by overcoming the self-weight of the specimen, therefore leading to the significant increase in the tension recorded (Figure 7.87).

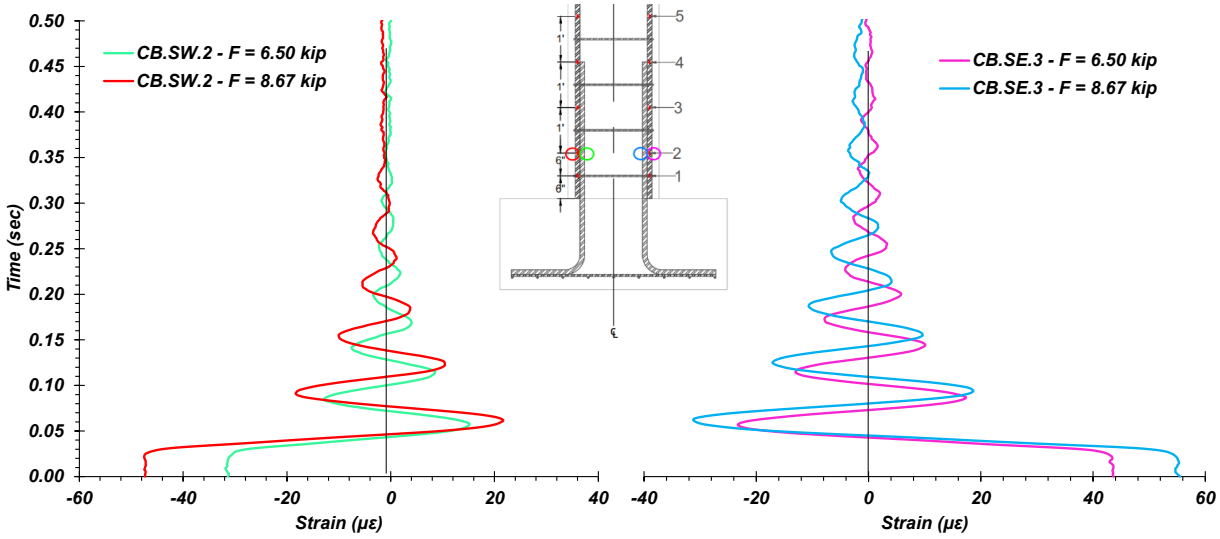

Figure 7.86: Comparison of the strain histories for column bars SW.2. and SE.3. during the May 22nd snap-back tests (*F* = 28.9 kN or 6.50 kip, *F* = 38.6 kN or 8.67 kip).

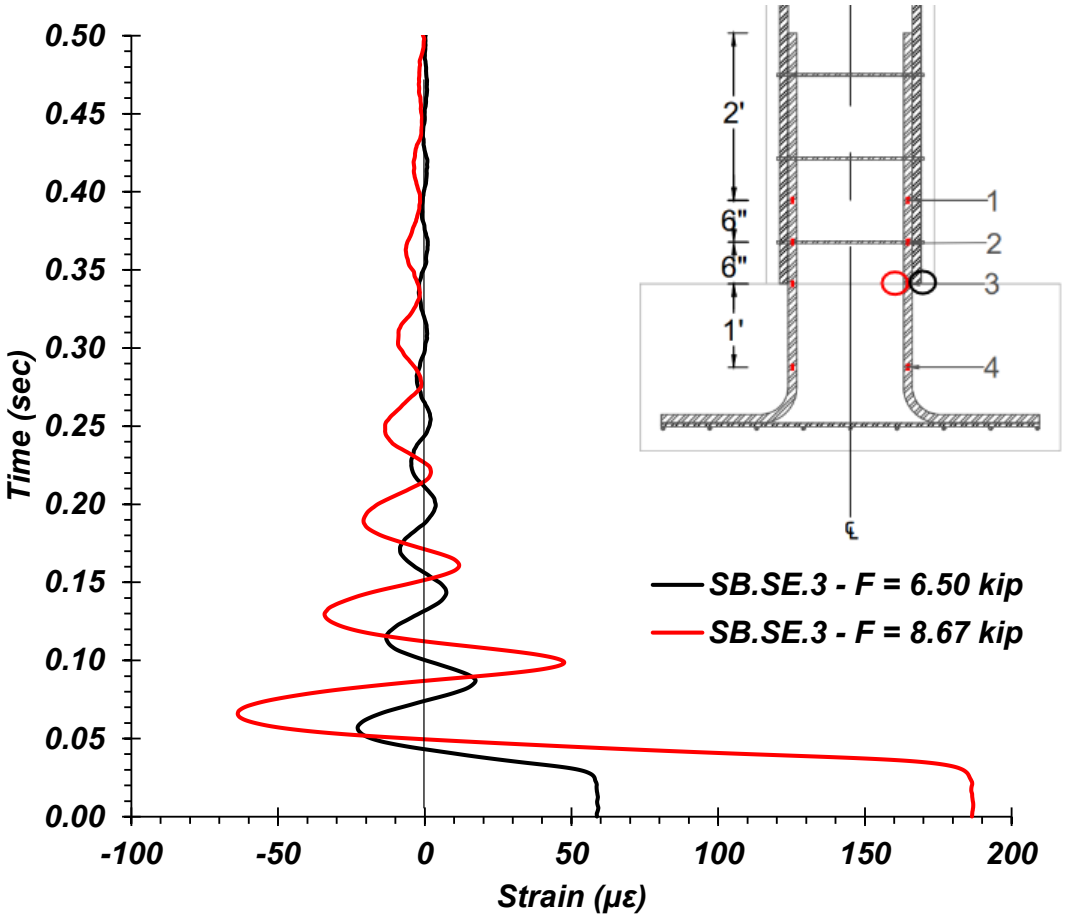

Figure 7.87: Comparison of the strain histories for starter bar SE.3. during the May 22nd snap-back tests (*F* = 28.9 kN or 6.50 kip, *F* = 38.6 kN or 8.67 kip).

Very small strains were recorded in the column ties and the footing bars similar to the tests performed during the wet season. The lift-off and subsequent rocking of the footing had minimal impact on the strain histories recorded in the longitudinal and transverse (i.e., bars spanning parallel and perpendicular to the direction of loading) footing reinforcement, as the footing bar strain time histories were nearly identical for the 28.9 kN (6.50 kip) and 38.6 kN (8.67 kip) tests performed on May 22nd (Figure 6.20). The transverse and longitudinal footing bars recorded strain time histories that were symmetrical about the zero-strain axis, indicative of the oscillating behavior of the column-footing specimen.

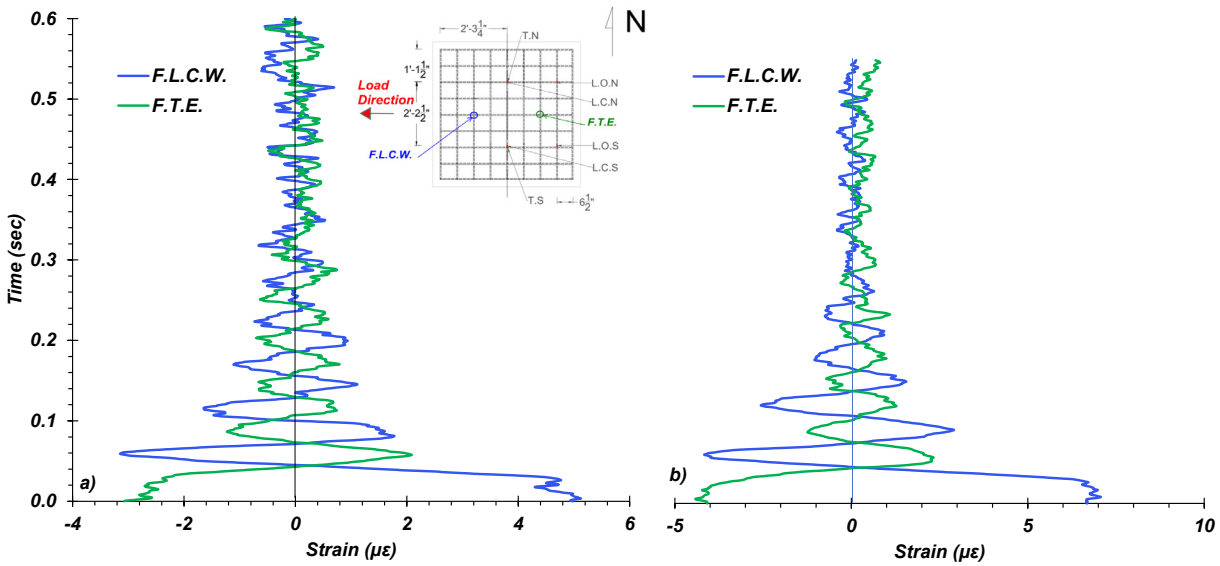

Figure 7.88: Comparison of the strain histories for footing bars F.L.C.E. and F.T.E. during the: (a) 28.9 kN (6.50 kip) and (b) 38.6 kN (8.67 kip) snap-back tests on May 22nd.

7.4.2.3 Summary of Reinforcing Steel Strain Responses

As described in Section 7.3.1, the changing seasonal conditions had minimal effect on the starter bar strain histories observed during snap-back tests. The recorded strain time histories of column, starter, and footing bars indicated almost identical strain magnitudes and oscillations in response to the snap-back tests on December 5th (F = 28.1 kN or 6.32 kip) and May 22nd (F = 28.9 kN or 6.50 kip). For example, strain time histories of the southeast starter bar at location 2 for both snap-back tests exhibited very similar responses (Figure 7.89). A comparison of the strain histories of two column bars, CB.SE.1. and CB.SW.2., also exhibited similar responses (Figure 7.90). The similarities between strain histories further exemplified that the structural response of the column and footing was not substantially affected by seasonal changes to the soil properties at the load and displacement thresholds imposed during the snap-back tests.

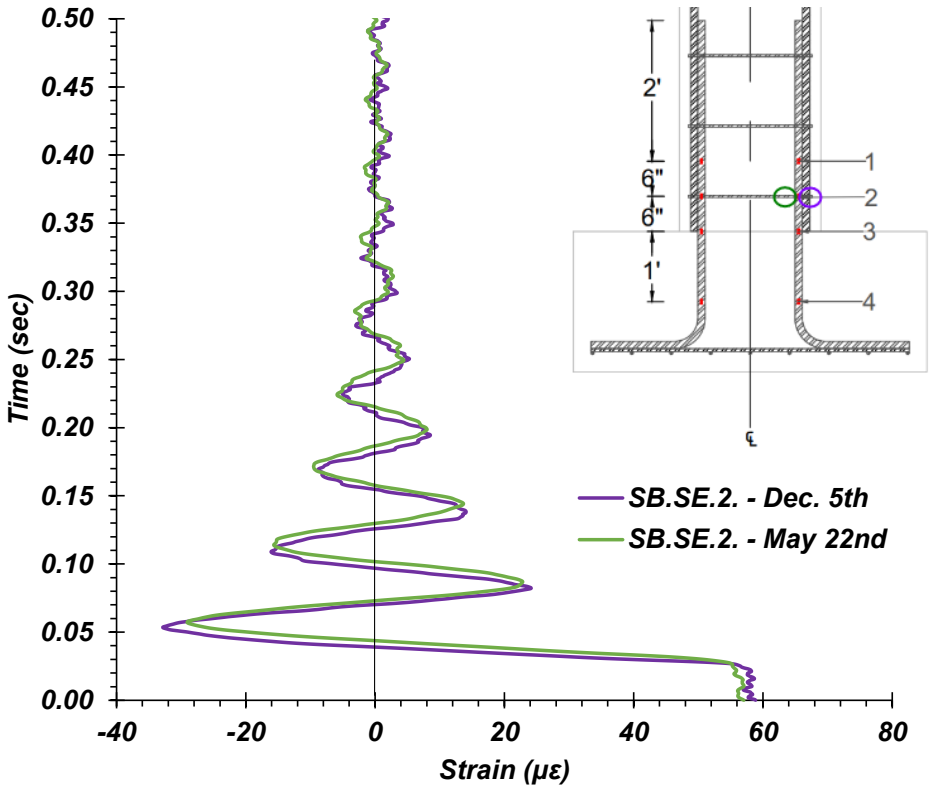

Figure 7.89: Comparison of the strain time histories for starter bar SB.SE.2. during the 28.1 kN (6.32 kip) and 28.9 kN (6.50 kip) snap-back tests performed on December 5th and May 22nd, respectively.

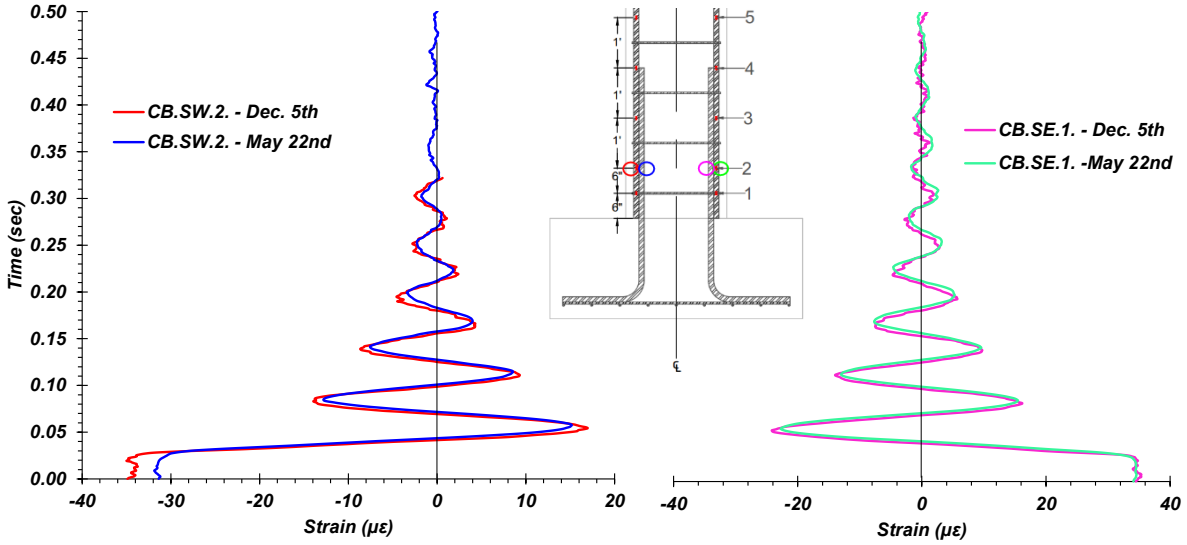

Figure 7.90: Comparison of the strain time histories for two select column bars during the 28.1 kN (6.32 kip) and 28.9 kN (6.50 kip) snap-back tests performed on December 5th and May 22nd, respectively.

7.4.3 Some Observations on the Response of Bearing Soils to Snap-Back Tests

The shear wave velocity of the subsurface was tested incrementally throughout the study, with additional testing frequencies on the dates on which snap-back tests were performed. The goal was to establish a reliable framework for future assessments of the bearing soils when the instrumented specimens will be subjected to planned quasi-static, cyclic lateral loading tests. Section 7.2 describes the installation of Triaxial Geophone Packages (TGPs) below the base of the footing to record the cross-hole body waves propagating from the cross-hole rod and the base of the footing during snap-back tests. These TGPs provide the basis for some observations of the response of the bearing soils throughout snap-back testing.

7.4.3.1 Changes in Shear Wave Velocity During Snap-Back Tests

Cross-hole testing was conducted at specific points in time relative to a given test: a morning baseline dataset was collected prior to the snap-back, a dataset was collected after the "pull" portion of the snap-back had concluded with the desired lateral load held constant (i.e., the bearing soils at the TGP locations were unloaded), a dataset collected immediately after the snap, and a final dataset collected at least an hour after the test had been performed. Since V_s is a direct function of the effective stress, the determination of V_s facilitates the assessments of potential (unmeasured) fluctuations in the vertical effective stress of the bearing soils directly beneath the footing throughout the snap-back test procedure.

An interpretation of the response of the bearing soils to rocking motions of the column-footing specimen is presented for the two snap-back tests performed on May 22nd (F = 28.9 kN or 6.50 kips, F = 38.6 kN or 8.67 kips). Seven V_s determinations were performed on May 22nd before, during, and after specific events associated with the snap-back test and with each determination consisting of 20 vertical hammer strikes (a "dataset") on the tapper cross-hole rod installed directly to the north of the TGPs (Figure 4.28). Figure 7.91 presents the mean V_s determined for each of the seven tests shown with the associated standard deviation, σ. The standard deviation was observed to be relatively constant for each event and equal to 1.55 m/s on average.

The pull portion of the first snap-back test (F = 28.9 kN or 6.50 kips) resulted in a slight decrease in V_s as a result of the unloading of the bearing soils at the location of the TGPs. Following a thirteen-minute resting period between the release of the static lateral load, an increase in the mean V_s was observed (166.4 m/s after the first snap-back and 169.5 m/s before the second snap-back). This slight increase in V_s may be indicative of the generation of negative excess pore pressures that could have migrated to the TGP region during the 13-minute interval.

After the pull portion of the 2nd snap-back test (F = 38.6 kN or 8.67 kip), the mean V_s increased slightly to 169.5 m/s, which was unexpected due to the unloading of the bearing soils. After the release of the static lateral load to V_s decreased to 164.8 m/s, which suggested the possibility that the transient snap-back bearing pressures may have been sufficient to induce a net contractive response within the bearing soil. If positive excess pore water pressures had been triggered immediately following the release of the

applied lateral load, a decrease in V_s would be expected. If such a contractive response had occurred, it would be expected that the shear wave velocity, and thus the effective stress, would gradually increase following the dissipation of excess pore water pressures. The mean V_s three hours after the snap-back (167.3 m/s) was comparable to the morning baseline (167.9 m/s). The possibility of excess pore pressure generation is further explored below.

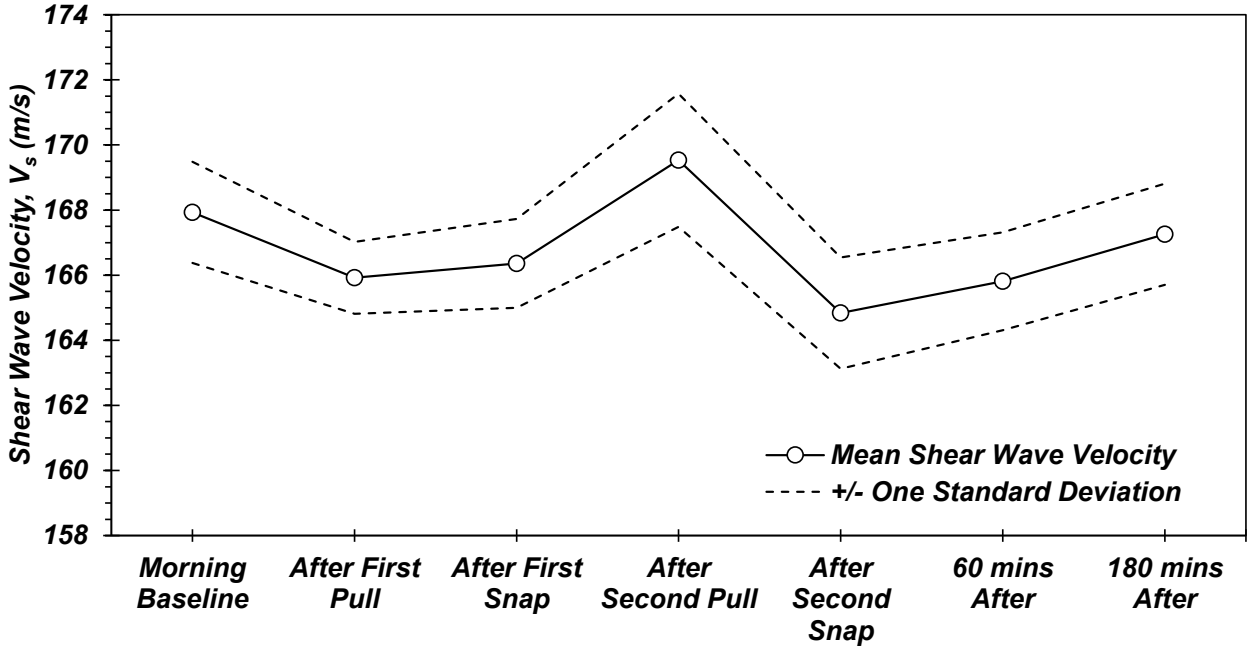

Figure 7.91: Fluctuation in mean shear wave velocity in relation to the "First" snap-back (F = 28.9 kN or 6.50 kip) and "Second" snap-back (F = 38.6 kN or 8.67 kip) performed on May 22nd. Note: shear wave velocities determined through the analysis of TGP z-direction histories when the cross-hole rod was subjected to twenty vertical strikes with a hammer.

7.4.3.2 Bearing Soil Response to Rocking

As discussed in Section 7.2, the TGPs were independently calibrated based on the procedure outlined in Jana et al. (2021). The implementation of the instrument-specific calibration factors allowed for the development of a relationship between the voltage recorded by the TGP to the particle velocity, *PV*. The particle velocities were integrated to obtain the displacement time histories, which can be compared to the vertical footing displacements measured using the string potentiometers. The *PV* time histories also facilitated the determination of the 1-dimensional (1D) shear strain, γ_{xz}, given by (Rathje et al. 2005):

$$\gamma_{xz} = -\frac{PV}{V_s} \tag{7-15}$$

The particle velocity time histories recorded by the *z*-direction north and south TGPs during the December 5th snap-back (F = 28.1 kN or 4.32 kips) are shown in Figure 7.92a, with the corresponding displacement histories provided in Figure 7.92b. The histories from the north and south TGPs are nearly identical, as expected due to the symmetrical placement about the east-west centerline of the footing (Figure 7.28). The north and south TGPs recorded absolute maximum *PV*s of 0.012 m/s and 0.011 m/s, respectively. Both histories indicated that roughly seven full cycles occurred prior to fully attenuating. The north TGP recorded a maximum (positive, upward) and minimum (negative, downward) displacement of 0.087 mm (0.003 in.) and 0.125 mm (0.005 in.), respectively. Similarly, the south TGP recorded maximum and minimum displacements of 0.076 mm (0.003 in.) and 0.109 mm (0.004 in.), respectively.

These displacements can be compared to the vertical, footing displacements measured at the top of the footing. The string-potentiometer located on the east side of the footing 0.737 m (29 in.) from the center of the column recorded a maximum imposed displacement of 0.59 mm (0.023 in.) upwards before the release of the static lateral load (F = 28.1 kN or 4.32 kip), with a final displacement after the snap-back test equal to 0.28 mm (0.011 in.) greater than the initial position (Figure 7.73). Owing to the uncertain distance between the bottom of the footing and the bearing soils due to the expected rounding of the bearing soils following prior snap-back tests, the reference displacement for comparison to the particle displacements in the bearing soils was taken as the final resting position of the top of the footing. The maximum rocking displacement downwards relative to the final position of the footing was 0.085 mm (0.003 in.), only slightly smaller than the 0.125 mm and 0.106 mm downward displacement calculated from the *PV* time history recorded by the north and south TGPs, respectively. The slight difference can be partially justified by the closer proximity of the geophones to the center of the footing (0.69m or 27 in.) compared to the string potentiometer (0.737 m or 29 in.). Thus, it can be surmised that the footing rocked rigidly and that the depth of the TGPs below the footing was insufficient to provide attenuation of the body waves generated during the dynamic soil-structure-interaction of the footing and the bearing soils.

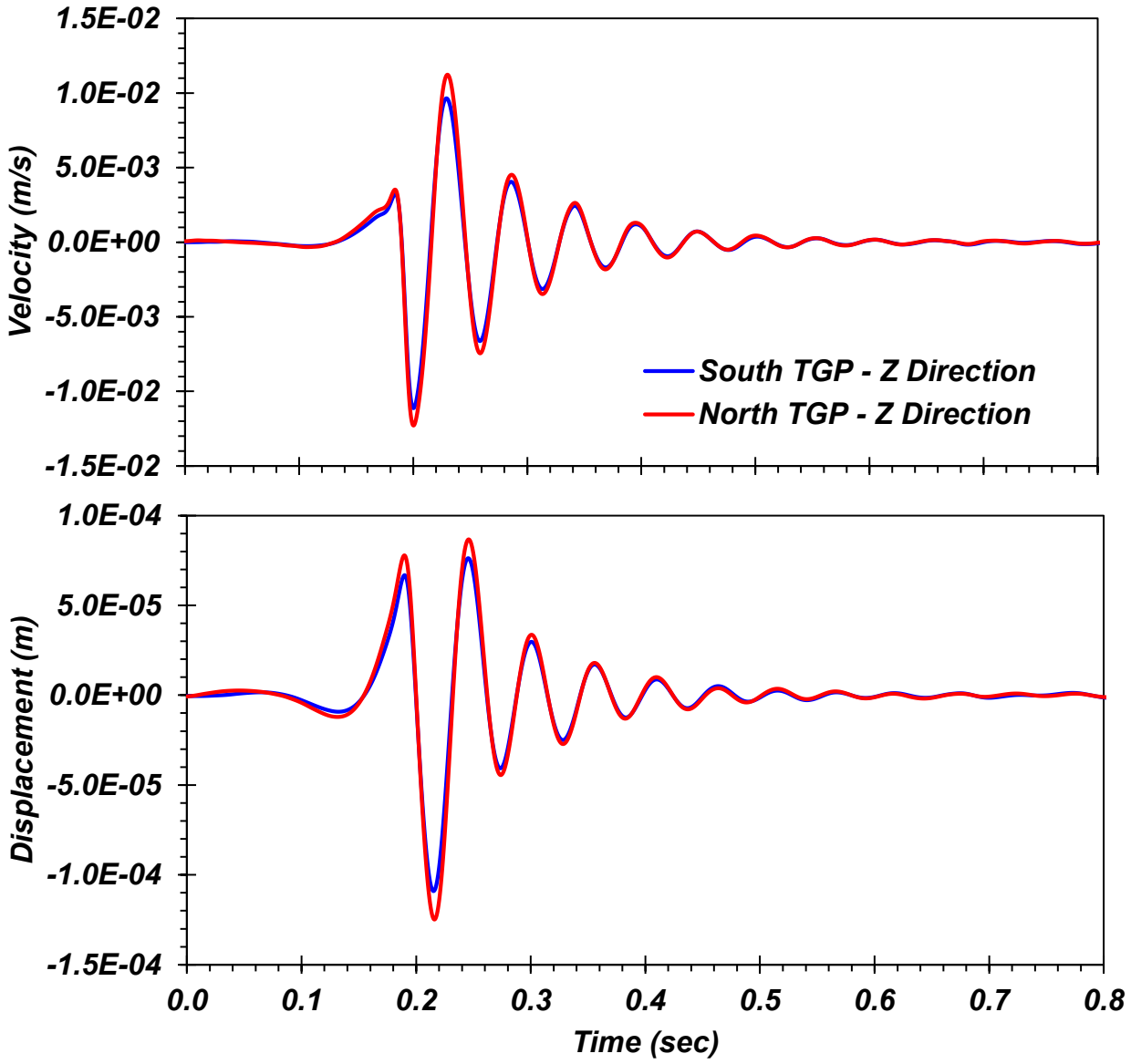

Figure 7.92: Response of the bearing soils to the December 5th snap-back performed on Specimen 5 (F = 28.1 kN or 4.32 kip): (a) particle velocity, and (b) displacement time histories recorded by TGPs.

The *PV* and displacement time histories calculated from the time histories recorded by the TGPs during the May 22nd (F = 38.6 kN or 8.67 kip) snap-back test are presented in Figure 7.93. Similar to the time PV and displacement histories recorded during the December 5th snap-back test (Figure 7.92), the responses recorded by the TGPs were nearly identical. The north and south TGPs recorded absolute maximum *PV*s of 0.013 m/s and 0.011 m/s, respectively. Both histories indicated that roughly seven full cycles occurred prior to becoming fully damped. The north TGP recorded a maximum (positive, upward) and minimum (negative, downward) displacement of 0.098 mm (0.004 in.) and 0.145 mm (0.006 in.), respectively. Similarly, the south TGP recorded maximum and

minimum displacements of 0.086 mm (0.003 in.) and 0.128 mm (0.005 in.), respectively. The string-potentiometer located on the top of the east side of the footing 0.737 m (29 in.) from the center of the column recorded a maximum static imposed displacement of 0.78 mm (0.03 in.) upwards before the release of the applied static lateral load (F = 38.6 kN or 8.67 kip), with a final displacement following the test equal to 0.35 mm (0.014 in.) downwards relative to the initial position (Figure 7.76). The maximum rocking displacement downwards relative to the final position of the footing was 0.044 mm (0.002 in.), which was small relative to the maximum displacement recorded by the TGPs (0.145 mm). It was hypothesized that this difference may be associated with further rounding of the bearing soil-footing interface from the prior snap-back tests conducted.

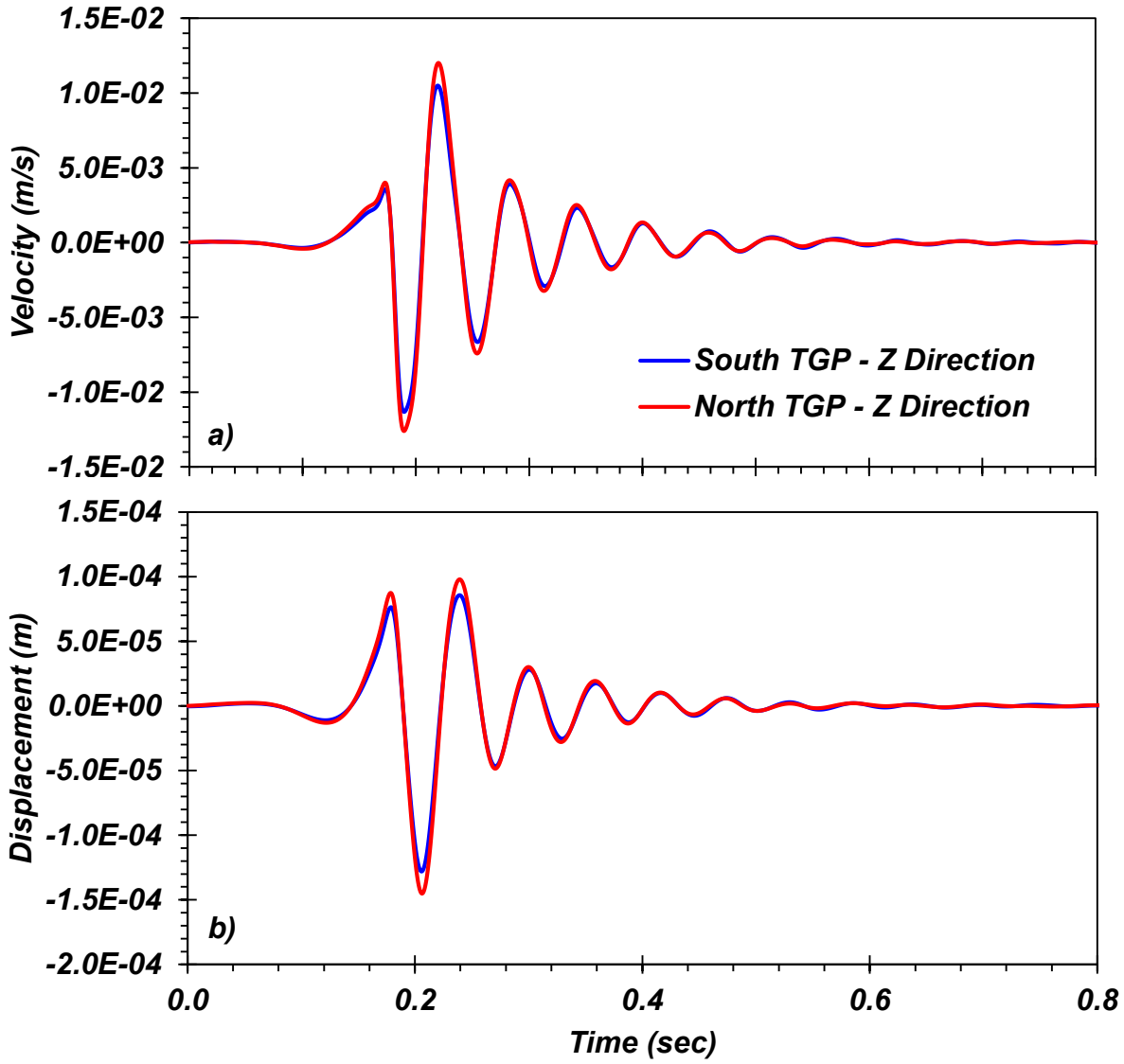

Figure 7.93: (a) particle velocity and (b) displacement time histories calculated from the voltage time histories recorded by TGPs during the May 22nd snap-back performed on Specimen 5 (F = 38.6 kN or 8.76 kip).

The particle velocity time histories facilitated the determination of the 1D strain time histories through the use of Eq. 6.3. The average 1D strains calculated from the south and north TGP records from the May 22nd (F = 38.6 kN or 8.67 kip) snap-back test are shown in Figure 7.94. The maximum positive and negative 1D shear strains were 0.0073% and 0.0068%, respectively.

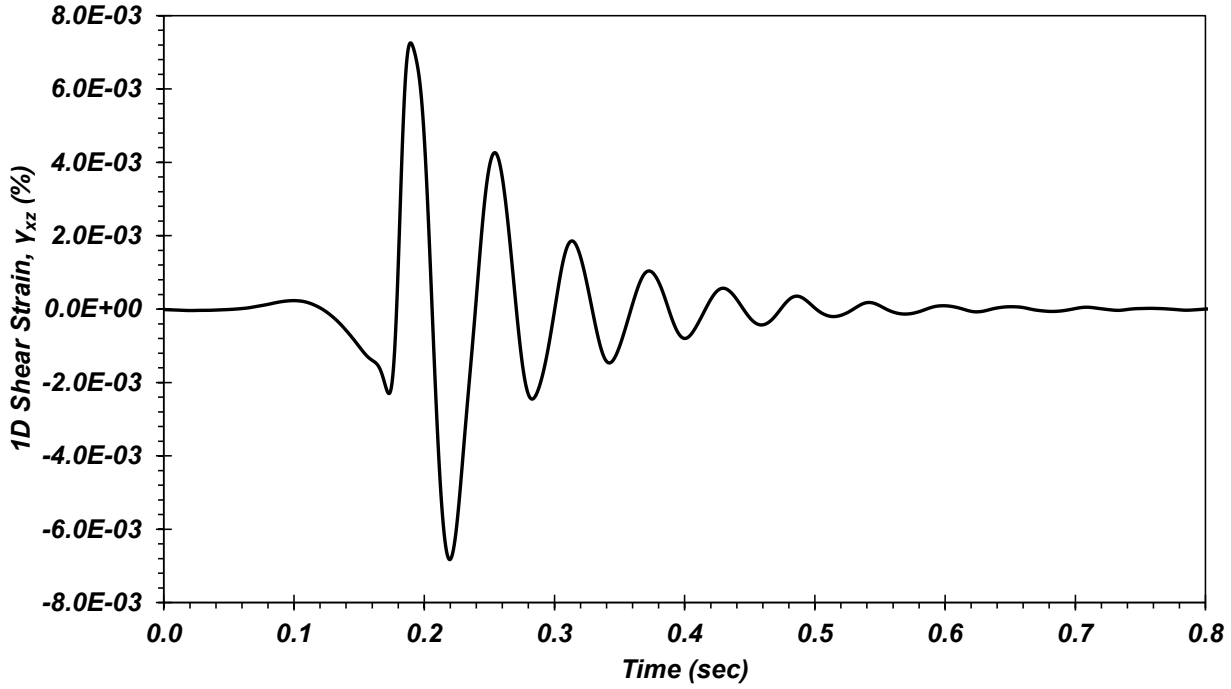

Figure 7.94: Average 1D shear strain history recorded by the south and north TGPs during the May 22nd snap-back (F = 38.6 kN or 8.67 kip).

The threshold shear strain to trigger excess pore pressure and associated nonlinear inelasticity of soil, γ_{tp}, is defined as the shear strain amplitude for which the residual excess pore pressure remains zero regardless of the number of loading cycles. Jana and Stuedlein (2021) reported a γ_{tp} of 0.012% for a medium stiff, plastic, lightly overconsolidated, alluvial clayey silt deposit, similar to the Upper Willamette Silt at the location of the snap-back test site. The 1D strains calculated during the snap-back test performed with the largest static lateral load were smaller than the assumed γ_{tp}, which indicated that the bearing soil was within the nonlinear elastic regime. It is likely that no excess pore pressures would have been generated during the 38.6 kN (8.67 kip) test. Because the 1D strains are measured at two discrete locations below the footing, it is impossible to make a firm conclusion regarding the development of excess pore pressures in response to the magnitude of the imposed lateral load for snap-back tests conducted.

The small-strain shear modulus, G, of the bearing soil is given by (Vucetic and Dobry 1991):

$$G_{max} = \rho * V_s^{\,2} \qquad \textbf{(7-16)}$$

where ρ is equal to the mass density of the soil, estimated to be 1,827 kg/m^3 at the depth of the geophones from the SCPT-3 data. The baseline V_s of 167.9 m/s corresponds to an initial G_{max} of 52.6 MPa. Vucetic and Dobry (1991) provide a *PI*-dependent relationship between the shear strain and the ratio of the secant shear modulus to the small-strain shear modulus, G/G_{max}. The 1D shear strain time history from the May 22nd, F = 38.6 kN or 8.67-kip snap-back test allowed for a relationship between shear strain and the number of cycles, N, to be developed (Table 7.14). The representative *PI* at the depth of the TGPs (1.73 m or 5.68 ft.) facilitated the development of an estimate of the backbone curve describing the variation of G with shear strain for the May 22nd snap-back test. Figure 7.95 presents the estimated variation in the shear modulus of the bearing soils at the location of the TGPs and indicates that ~50% of the loading cycles (i.e., N = 0.25, 0.75, …,3.25) resulted in nonlinear-elastic soil behavior with a maximum instantaneous reduction in G of approximately 13 %. Typically, excess pore pressures are generated following a reduction in G of 20 to 40%, depending on the soil type, lending additional evidence pointing to the likely lack of excess pore pressures generation associated with the magnitude of bearing pressures generated under the released static lateral load.

Table 7.14: Number of cycles and corresponding shear strain representative of the May 22nd snap-back (F = 38.6 kN or 8.67 kip).

Number of Cycles, N	1D Shear Strain, γ_{xz} (%)
0.25	0.00726
0.75	0.00683
1.25	0.00426
1.75	0.00245
2.25	0.00186
2.75	0.00147
3.25	0.00104
3.75	0.000799
4.25	0.000569
4.75	0.000431
5.25	0.000354
5.75	0.000203
6.25	0.000181
6.75	0.000134
7.25	0.0000919
7.75	0.0000738

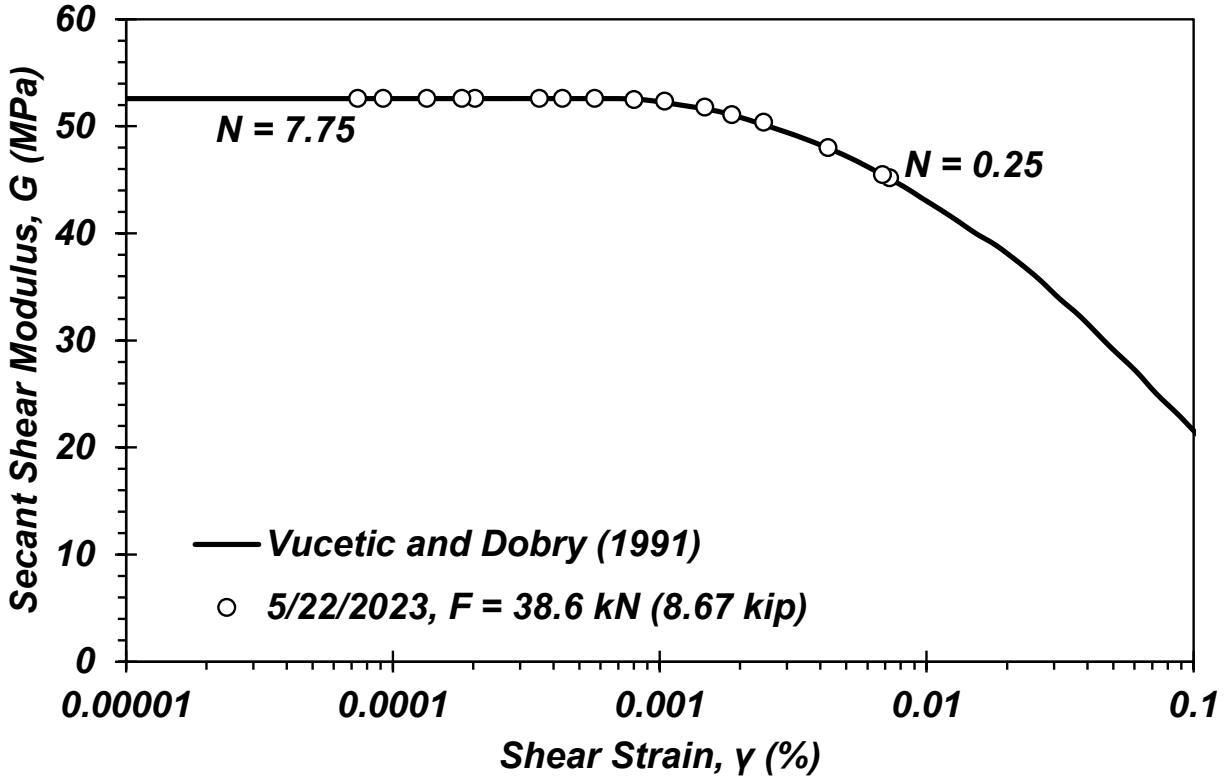

Figure 7.95: Shear modulus reduction curve associated with the Vucetic and Dobry (1991) G/G_{max} curve (PI = 15) overlain with the shear strain, γ, and corresponding Shear Modulus, G, from the May 22nd (F = 38.6 kN or 8.67 kip) snap-back test.

7.4.4 Summary of Section 7.4

The performance of a full-scale, embedded, vintage column-footing specimen at the GEFRS subjected to instantaneous-release snap-back tests has been observed and analyzed within this section. Specimen 5 (west footing) has been subjected to five snap-back tests: a 19.9 kN (4.48 kip) test on November 29th, 2022, a 19.1 kN (4.34 kip) test on December 2nd, 2022, a 28.1 kN (6.32 kip) test on December 5th, 2022, a 28.9 kN (6.50 kip) test on May 22nd, 2023, and a 38.6 kN (8.67 kip) test also performed on May 22nd, 2023. All snap-back tests performed as part of this thesis had no additional axial load applied to the specimen (only self-weight).

The November 29th test served as an initial trial run to note improvements to be implemented in the snap-back tests to follow. Instruments installed in and below the footing (e.g., strain gauges, string potentiometers, TGPs) facilitated the comparison of results to assess whether the rocking response of the specimen was affected by changing environmental conditions. The December 5th (F = 28.1 kN or 4.32 kip) and the first May 22nd test (F = 28.9 kN or 6.50 kip) were considered equal-load tests that were conducted during the wet and dry seasonal conditions, respectively. Comparisons of the rocking displacements from the snap-back tests indicated that the dry season (May 22nd, 2023) produced a stiffer response to the imposed loading, possibly owing to the increase in strength of the lateral resisting soils at the vertical footing interfaces. The comparisons of the strain histories indicated minimal differences between the December 5th and

May 22nd tests. The experimental results from the equal-load snap-back tests indicated that the strains imposed to the embedded reinforcement within the column and footing was dependent only on the magnitude of the applied lateral load prior to the instantaneous release and not the subsurface conditions.

The strain histories recorded during all snap-back tests indicated that oscillating behavior of the vintage reinforcement (i.e., dynamic tension-to-compression time histories) continued after observable (and recordable) displacement-rocking of the specimen had concluded. While the strains recorded in the vintage reinforcement were minimal, the strain time histories still facilitated comparisons between individual snap-back tests.

The shear wave velocity of the bearing soils was determined on a snap-back test day at specific points in time relative to a given test: a morning baseline dataset, a dataset was collected after the "pull" portion of the snap-back, a dataset collected immediately after the snap, and a final dataset collected at least an hour after the test had been performed. The change of V_s with time on the May 22nd test date (F = 28.9 kN or 6.50 kip, and F = 38.6 kN or 8.67 kip) suggested that excess pore pressures may have been generated following the snap-back tests.

The possibility of excess pore pressure generation during snap-back tests was further explored using the time histories recorded by the north and south TGPs. The respective time histories were corrected for TGP-specific calibrations (Section 7.2) and used to determine the particle velocity and displacement time histories. The displacement time history from the December 5th test (F = 28.9 kN or 4.32 kip) indicated a relatively comparable maximum downward displacement relative to the maximum recorded by the string potentiometer on the east side of the footing.

The average 1D strains calculated from the south and north TGP particle velocity time histories from the May 22nd (F = 38.6 kN or 8.67 kip) snap-back test resulted in maximum positive and negative 1D shear strains smaller than the threshold shear strain to trigger excess pore pressure and associated nonlinear inelasticity of soil, γ_{tp}, reported by Jana and Stuedlein (2021) for a similar material. Because the 1D strains are measured at two discrete locations below the footing, it is impossible to make a firm conclusion regarding the development of excess pore pressures in response to the magnitude of the imposed lateral load for snap-back tests conducted.

7.5 DEVELOPMENT OF A NONLINEAR SOIL-STRUCTURE-INTERACTION MODEL FOR ROCKING BRIDGE SUBSTRUCTURES AND PARAMETRIC STUDY

7.5.1 Development of Static-Force SSI Models Representative of Snap-Back Tests

The nonlinear bearing pressure-displacement response of shallow foundations bearing on plastic soils has been studied using the results of full-scale loading tests (Huffman et al. 2015). The nonlinear bearing pressure-displacement response can be represented using a hyperbolic bearing resistance model, given by Huffman et al. (2015):

$$q^* = \frac{q_{mob}}{q_{ref}} = \frac{\eta}{k_1 + k_2 * \eta}$$

(7-17)

where q^* = the reference capacity-normalized, displacement-dependent mobilized resistance, $\eta = \delta/B'$ is the displacement, δ, normalized by the equivalent footing diameter, B', defined as the diameter that produces the same area as that of a square footing (e.g., Mayne and Polous 1999), and k_1 and k_2 are fitted parameters determined for specific footing loading test data. The reference capacity, q_{ref}, has been used to reduce scatter in various reliability-based serviceability limit state models (Huffman et al. 2015, Akbas and Kulhawy 2009, Uzielli and Maybne 2011), and is defined in this study as (Huffman et al. 2015) the slope-tangent capacity, q_{STC} (Phoon and Kulhawy 2008), with a displacement offset equal to $0.03B'$. The mobilized resistance calculated for use in Eq. (7.18) is then calculated as a function of the bearing capacity as:

$$q_{mob} = q^* M_{STC} q_{ult,p}$$

(7-18)

where M_{STC} is a model scale factor equal to the mean ratio, $q_{STC}/q_{ult,p} = 0.643$, where the calculated ultimate bearing resistance (e.g., using the bearing capacity equation for shallow foundations), $q_{ult,p}$, based on the global dataset reported by Huffman et al. (2015). In this study, $q_{ult,p}$ may represent the bearing capacity of the footings in a fully- or partially saturated state depending on the seasonal moisture conditions, as described below. Five of the footing loading tests included within the Huffman et al. (2015) global dataset were tests specific to the GEFRS or the Upper Willamette Silt layer at other parts of the OSU campus, performed by Newton (1975) and Martin (2018). The hyperbolic model parameters, k_1 and k_2, and model factors M_{STC} derived from these loading test results are used as the basis for the SSI model presented herein; specifically, the M_{STC} for the five site-specific tests ranged from 0.45 to 0.66, with the representative magnitude of 0.55 used for analyses.

7.5.1.1 Seasonally Dependent, Subsurface Conditions

The bearing capacity for the field column-footing specimens subjected to snap-back tests was estimated based on the Terzaghi (1943) equation for embedded shallow foundations using Vesic (1973) and Meyerhof (1963) bearing capacity factors. The key parameter controlling bearing capacity in fully saturated plastic soils (corresponding to the wet season at GEFRS) is the representative undrained shear strength, s_u. As described in Section 7.2.2, estimates of s_u strength vary substantially based on the correlation used. A representative undrained shear strength of 63 kPa (1,320 psf) was used for the wet season analysis considering the correlated estimates and laboratory results for additional locations at GEFRS (Dickenson et al. 2006) shown in Table 7.4. The degree of saturation in the Upper Willamette Silt ranges from 98% to 100%, as shown in Table 7.3 based on laboratory test results reported by Dickenson et al. (2006).

The bearing capacity calculated during partially saturated conditions (i.e., the dry season) was determined using a form of the bearing capacity equation proposed by Lu and Likos

(2006). This formulation considers the effects of partial saturation on bearing capacity determined using a soil-water retention curve (SWRC) analysis with consideration to the air-entry matric suction, ψ_{AE}, and the effective saturation, S_e, obtained from the SWRC. Under partially saturated conditions, the SWRC can be described by Van-Genuchten (1980) fitting parameters, α and n. Samples extracted during the tensiometer installation were sent to Auburn University for SWRC testing. The results from the analyses are presented in Figure 7.96, with the sample-specific Van-Genuchten fitting parameters. The additional parameters, y and S_r, correspond to the volumetric water content at small values of suction (less than 1 kPa) and large magnitudes (greater than 10,000 kPa), respectively.

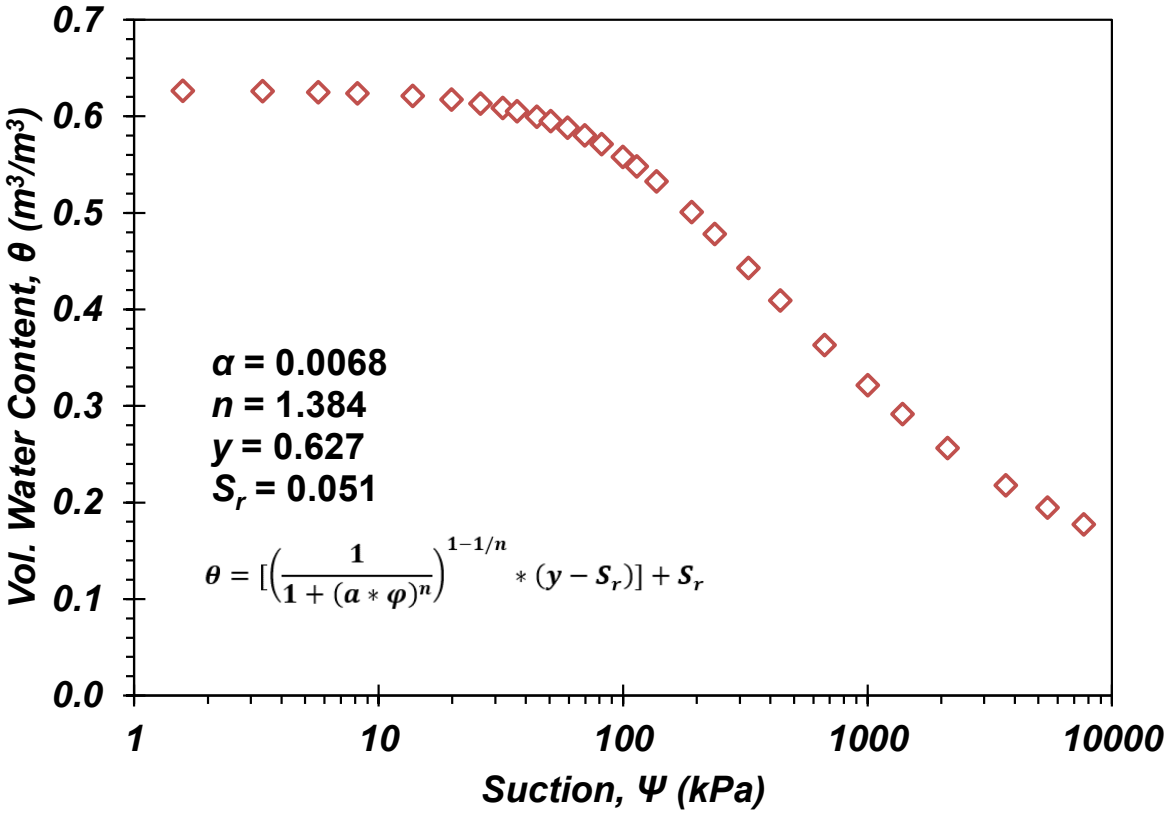

Figure 7.96: SWRC test results for Upper Willamette Silt.

The SWRC facilitated the determination of the parameters necessary to compute the apparent cohesion for use with the modified bearing capacity equation. The analytical expression for air entry matric suction is given by (Vanapalli et al. 1998):

$$\psi_{AE} = \frac{1}{\alpha}\sqrt[n]{\frac{n}{n-1}} * \exp\left(\frac{((2n-1)/(n-1)[\left(\frac{2n-1}{n-1}\right)^{1-\left(\frac{1}{n}\right)}-1]}{(1-n)\sqrt[n]{n/(n-1)}}\right) \quad \textbf{(7-19)}$$

and the effective saturation, S_e, is given by (Vanapalli et al. 1998):

$$S_e = \left(\frac{1}{1 + (\alpha\psi)^n}\right)^{1-\left(\frac{1}{n}\right)} \quad \textbf{(7-20)}$$

where the matric suction, ψ, was determined from the SWRC results to be 7.3 kPa (150 psf), simply defined as $\psi = \gamma_w$ x z, where γ_w = the unit weight of water (9.81 kN/m^3 or 62.4 pcf) and z = the height above the groundwater table (0.744 m or 2.44 ft.). The apparent cohesion, c_{app}, is determined by (Vahedifard and Robinson 2016):

$$c_{app} = (\psi_{AE}(1 - S_e)\tan(\phi') + \psi S_e \tan(\phi')) \quad \textbf{(7-21)}$$

A representative effective friction angle, ϕ', equal to 30.4 degrees was chosen based on available laboratory information (Dickenson et al. 2006) and SCPT correlations to ϕ' for fine-grained materials presented in Figure 4.6. The estimates of bearing capacity are presented in Table 7.15.

Table 7.15: Summary of seasonally dependent strength parameters and bearing capacities.

Season	Degree of Saturation, S (%)	Undrained Shear Strength, s_u, or Apparent Cohesion, c_{app}, kPa (psf)	Friction Angle, ϕ' (deg)	Bearing Capacity, q_{ult}, kPa (psf)
Wet	100	63 (1,316)	-	476 (9,941)
Dry	90	5.8 (121)	30.4	1,363 (28,467)
Dry	95	5.1 (107)	30.4	1,312 (27,402)
Dry	98	4.6 (96)	30.4	1,281 (26,754)

The seasonally dependent bearing capacities computed using the strength parameters in Table 7.15 and Eqs. (7.17) and (7.18) allowed specification of the backbone force-displacement curves to be specified for the base of the model of the column-footing specimens. The nonlinear bearing resistance-pressure backbone curves are presented in Figure 7.97 for the unique set of hyperbolic parameters corresponding to each of the five footings loaded in the Upper Willamette Silt deposit (i.e., Newton 1975, Martin 2018). The bearing pressure-displacement relationships normalized by the effective footing width are shown in Figure 7.98. Test 1 and Test 5 yield the greatest and smallest force-displacement responses, respectively. At a normalized displacement of 0.02, the range in possible normalized bearing pressures is 0.604 (Test 5) to 0.837 (Test 1; Figure 7.98), whereas the range in normalized bearing pressures decreased to 1.128 (Test 2) to 1.202 (Test 1) at a normalized displacement of 0.06. The relationship derived from the parameters representative of Test 3 were deemed the average response and are

subsequently used in the SSI models described herein. A summary of the hyperbolic parameters, model scale factor, and seasonally dependent bearing capacities used to create the pressure-displacement relationships is provided in Table 7.16.

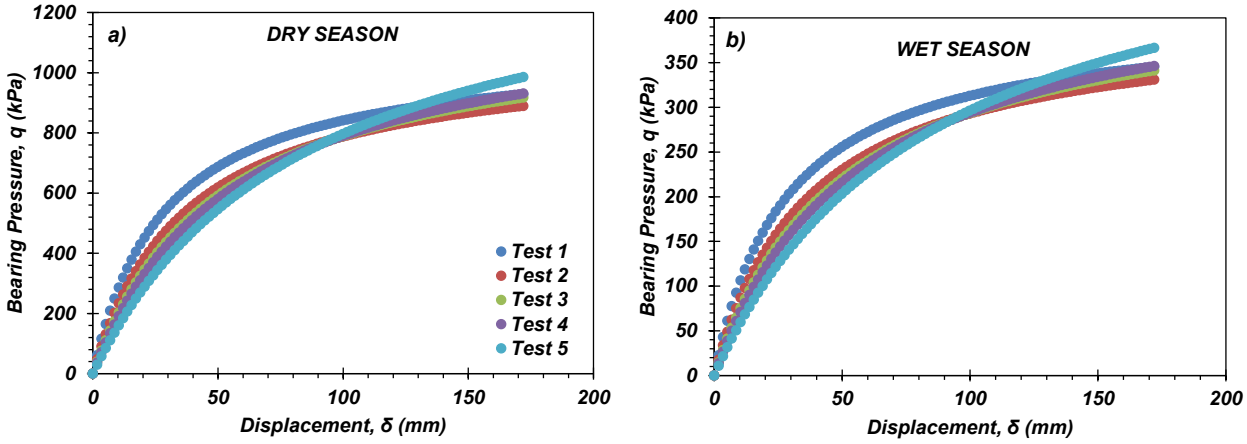

Figure 7.97: Nonlinear mobilized bearing resistance models for Upper Willamette Silt at GEFRS considering: (a) partially-saturated (S = 98%) conditions representative of the dry season, and (b) fully-saturated, undrained conditions representative of the wet season.

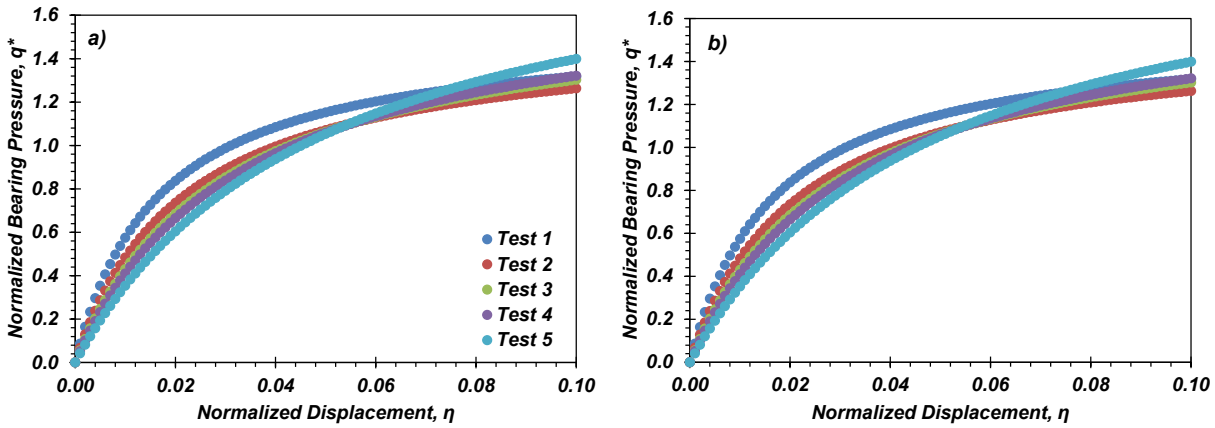

Figure 7.98: Nonlinear mobilized bearing resistance models normalized by the effective footing width for Upper Willamette Silt at GEFRS considering: (a) partially-saturated (S = 98%) conditions representative of the dry season, and (b) fully-saturated, undrained conditions representative of the wet season. The effective footing width, B', was equal to 1.72 m (5.6 ft.) and the maximum normalized displacement was equal to 0.10 for all five tests.

Table 7.16: Summary of inputs for nonlinear pressure-displacement relationships.

Test Designation	Dry Season Bearing Capacity (S = 98%), q_{ult}, kPa (psf)	Wet Season Bearing Capacity, q_{ult}, kPa (psf)	Hyperbolic Parameters		Model Scale Factor, M_{STC}
			k_1	k_2	
1	1,281 (26,750)	476 (9,940)	0.0109	0.650	0.55
2			0.0142	0.650	
3			0.0173	0.595	
4			0.0187	0.570	
5			0.0235	0.480	

7.5.1.2 Development of a Static-Force SSI Model for Snap-Back Tests

A series of nonlinear springs representative of the bearing soils as described above were used to simulate the nonlinear response of substructure footings in consideration of the SSI associated with the static lateral pushover portion of a snap-back test prior to the instantaneous release of applied force. Bearing soil springs were applied to the base of the model footing using a spacing of 1.52 cm (0.6 in.), to result in 100 springs for a 1.52 m wide square footing, which provided an appropriately discretized footing to satisfactorily capture the bearing response of similarly sized footings analyzed by Stuedlein et al. (2022). Forty springs were placed at 1.52 cm (0.6 in.) spacing on the vertical faces of the footing to capture the lateral passive earth pressure response (Figure 7.99). In order to supply compression only responses, the springs were developed to allow "gapping" for tensile forces; that is, no tension could be developed at the horizontal and vertical interfaces between the soil and the footing.

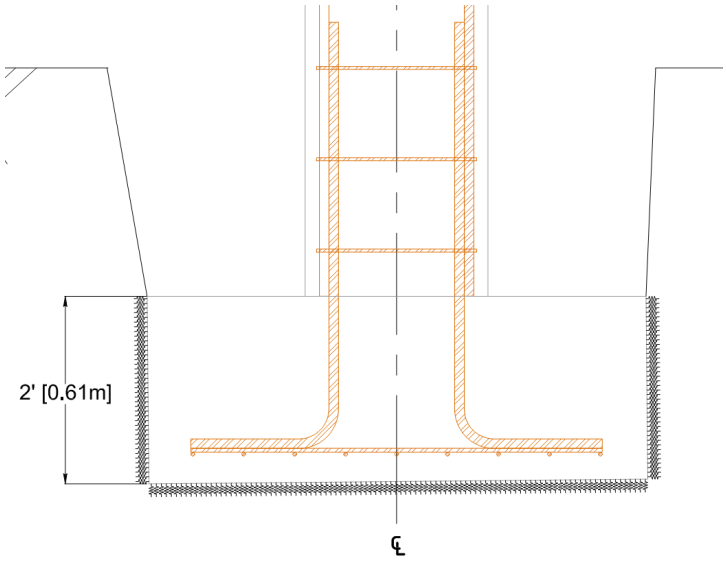

Figure 7.99: Schematic for nonlinear soil-structure interaction spring model representative of the static lateral pushover portion of a snap-back test prior to the instantaneous release of applied force.

Owing to the self-weight of the specimen equal to 57.4 kN (12.9 kips), the bearing springs were subjected to an initial uniform displacement at the base of the footing by the amount dictated by Eq. (7-18). Through the use of the hyperbolic parameters from Test 3, the initial settlements were determined equal to 0.8 mm (0.033 in.) and 2.3 mm (0.09 in.) for the S = 98% and undrained conditions (i.e., the dry and wet seasons), respectively.

Inputs to the models include the dimensions of the footing, the desired imposed drift at the column load point, the model scale factor, the hyperbolic model parameters, and the additional applied axial load. The corresponding vertical displacement at the edge of the footing is determined through trigonometric functions, assuming that the column-footing specimen globally displaces as a rigid member (i.e., no bending of the column due to an applied lateral force).

The imposed displacement at any spring is then computed through the assumption of a point of rotation. The results from the 38.6 kN (8.67 kip) snap-back test on May 22nd indicated that the east and west sides of the footing had exhibited nearly symmetrical displacements at the time of release (Figure 6.8), indicative that the point of rotation was at the center of the footing. The displacement-based mobilized resistance of each spring is then multiplied by the tributary area of the respective spring to resolve the bearing pressure into a resisting force. The resisting moment at any given column drift is then determined by multiplying the mobilized resisting force by the distance from the point of rotation (i.e., the center of the footing).

In addition to the mobilized resistance at the horizontal footing-soil interface, the contribution to the global resistance to the imposed deformation from the vertical interfaces at the footing faces must be considered in the analyses. Since the footing is assumed to displace as a rigid member, the displacement at the face of the footing is a function of the imposed displacement at the toe of the footing. Figure 7.100 provides a schematic representative of this relation with consideration to any point of rotation.

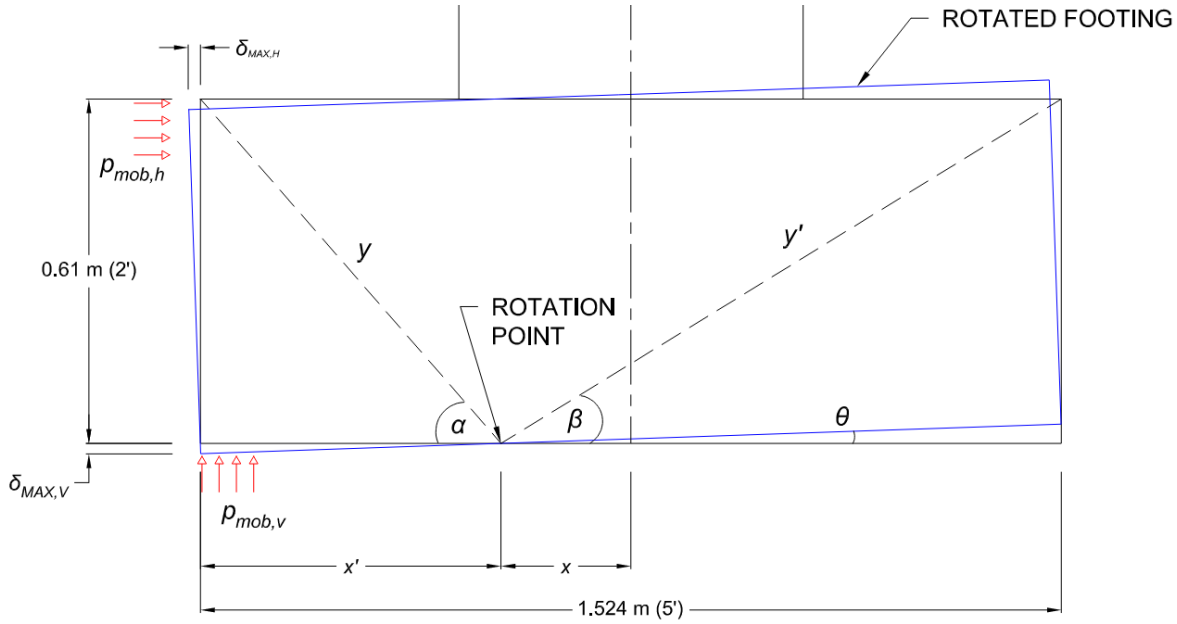

Figure 7.100: Schematic for the determination of interface displacements in SSI spring model.

The distance from the rotation point to the top corner of the footing, *y*, is determined by:

$$\boldsymbol{y = \sqrt{H^2 + x'^2}}$$

(7-22)

where *H* is the thickness of the footing equal to 0.61 m (2 ft.) and *x'* is the horizontal distance from the toe of the footing to the point of rotation. The angle between the base of the footing and the top corner about the rotation point, *α*, is therefore determined by:

$$\boldsymbol{\alpha = tan^{-1}(\frac{H}{x'})}$$

(7-23)

The angle between the imposed maximum displacement, *θ*, is then calculated by:

$$\boldsymbol{\theta = sin^{-1}(\frac{\delta_{max,v}}{x'})}$$

(7-24)

where $\delta_{max,v}$ is the maximum vertical displacement at the toe of the footing. The maximum horizontal displacement on the load application side, $\delta_{max,h}$, is subsequently calculated through trigonometry by:

$$\boldsymbol{\delta_{max,h} = y(\cos(\alpha - \theta) - \cos(\alpha))}$$

(7-25)

The horizontal displacement at the toe of the footing on the load application side is given by:

$$\boldsymbol{\delta_{toe,h} = \left(\cos(\theta) * \left(\frac{B}{2} - x\right)\right) - \left(\frac{B}{2} - x\right)}$$

(7-26)

where x is the horizontal distance from the center of the column-footing specimen to the rotation point. The resulting displacement at any spring located away from the edges of the footing was then linearly interpolated based on the displacement at the toe, similar to the process for the base of the footing. As described in Stuedlein et al. (2022), the horizontal, three-dimensional (3D) passive mobilized resistance, P_{mob}, is given by the following hyperbolic relationship presented by Duncan and Mokwa (2001):

$$\boldsymbol{P_{mob} = \frac{\delta_h}{\frac{1}{K_{max}} + R_f \frac{\delta_h}{P_{ult}}}}$$

(7-27)

where R_f is the failure ratio, given as 0.85 in Duncan and Mokwa (2001), and K_{max} is the initial stiffness of the force-displacement curve. Herein, it is assumed that the initial stiffness in vertical compression (i.e., bearing) is equal to the initial stiffness in lateral compression (passive earth pressure). Future studies may be able to assess the validity of this assumption. The initial stiffness of the hyperbolic curves from Test 3 presented in Figure 7.97 indicated K_{max} values equal to 24.6 and 66.1 kN/mm for the wet and dry seasons, respectively. The ultimate passive resistance, P_{ult}, is seasonally dependent. For the undrained, wet condition, the total 3D ultimate passive resistance is given by:

$$\boldsymbol{P_{ult,wet} = 2 s_u H^2}$$

(7-28)

For the partially saturated, dry condition, the 3D P_{ult} is pressure dependent and given by:

$$\boldsymbol{P_{ult,dry} = \left(P_p - P_a\right) + \frac{1}{3} K_o \gamma \left(\sqrt{K_p} - \sqrt{K_a}\right)\left(\frac{H}{N_{face}}\right)^3 \tan\left(\varphi'\right)}$$

(7-29)

where P_p and P_a are the passive and active lateral earth pressure (LEP) resultants, K_p, K_a, and K_o are the Rankine passive, active, and at-rest LEP coefficients, and N_{face} is the

number of springs on the face of the footing. The passive and active LEP resultants depend on the effective vertical stress acting over the tributary area of a given spring, which gives rise to the depth-dependency of the ultimate passive resistance.

Whereas the vertical face of the footing opposing the imposed lateral column load gives rise to passive earth pressure, the opposite face of the footing experiences active earth pressure in response to footing rotation. The active earth pressure developed in response to the imposed deformations was determined in a manner similar to the passive earth pressure. The distance from the rotation point to the top corner of the footing, *y'*, is determined by:

$$\boldsymbol{y' = \sqrt{H^2 + (B + x)^2}}$$

(7-30)

and the angle between the base of the footing and the top corner of the footing on the back face about the rotation point, β, is determined through trigonometry as:

$$\boldsymbol{\beta = tan^{-1}(\frac{H}{B + x})}$$

(7-31)

The horizontal displacement at any spring is subsequently calculated in a manner identical to that for the vertical footing face in the direction of loading, except in consideration of active earth pressures. Similar to the mobilized resistance at the base of the footing, the force from each spring is multiplied by the moment arm to the rotation point to determine the resulting moment.

7.5.1.3 Soil-Structure Interaction Model of Snap-Back Tests

Figure 7.101 presents the results of an SSI model representative of the "pull" for the May 22nd snap-back test (F = 38.6 kN or 8.37 kip) test on Specimen 5 using the partially saturated (S = 98%) bearing capacity, equal to 1,281 kPa (26.75 ksf). The resultant force, F, required to impose a column drift of 5.33 mm (0.21 in.) was calculated through the summation of forces about the rotation point, given by:

$$\boldsymbol{F = \frac{\Sigma M_{base} + \Sigma M_{front\ face} - \Sigma M_{back\ face} + (P * W_{spec}) * x}{H_F}}$$

(7-32)

where P is the applied axial load, W_{spec} is the self-weight of the specimen, and H_F is the vertical distance from the base of the footing to the point of lateral load application (2.95 m). The rotation point of the specimen was determined to be at the center line of the base of the footing based on the displacement time histories recorded during the May 22nd snap-back (Figure 6.8). Figure 7.100 presents the SSI model representative of the same

snap-back test assuming partially saturated conditions with the degree of saturation equal to 98%. Provided the recorded maximum column drift of 5.33 mm (0.021 in.), the corresponding vertical footing displacements calculated through rigid body rotation were 1.33 mm (0.005 in.) on both the east and west sides of the footing, whereas the displacement time recorded histories indicated slightly smaller maximum vertical footing displacements of 0.84 mm (0.003 in.) and 0.83 mm (0.003 in.) on the east and west sides of the footing, respectively. Thus, it appears at first that the error associated with the selected and/or assumed model parameters for the dry season conditions have appeared to over-predict the vertical footing displacements.

However, the SSI model does not account for column flexure which will have occurred during the pull portion of the snap-back test. The column drift caused by only flexure of the column, Δ_f, can be determined based on the typical displacement calculation for a cantilever beam, given by:

$$\Delta_f = \frac{\boldsymbol{PL^3}}{\boldsymbol{3EI}} \quad \textbf{(7-33)}$$

where P = the applied later load, L = the length of the cantilevered beam (i.e., column), E = Young's modulus, and I = moment of inertia. Based on the section analyses conducted for the typical vintage column constructed as part of this and the wider research study on TiAB retrofits (Khosravi et al. 2022), the flexural rigidity of the column, EI, equals 92.6 MN-m^2 and 130 MN-m^2 for the pre-cracking and cracked column section. The applied moment for the May 22nd snap-back test equaled 114 kN-m, corresponding to the pre-cracking flexural rigidity. Assuming that the footing was fixed rigidly, the anticipated column drift would equal 3.6 mm (0.14 in.). Therefore, the true column drift only associated with global rotation (i.e., no contribution from column flexure) would equal 1.8 mm (0.07 in.)

If the column-footing specimen only displaced as a rigid member (i.e., if no column flexure was observed), the initial bearing pressure induced by the self-weight of the specimen was equal to 24.7 kPa (516 psf), which corresponded to an initial settlement of 1.07 mm (0.004 in.). Prior to the application of the lateral load, the mobilized bearing pressure distribution was a uniform 24.7 kPa (516 psf), with no corresponding mobilized resistance on either the front or back vertical interfaces, owing to the absence of any initial lateral load. The inputted top drift caused the specimen to rotate such that a portion of the footing was no longer in contact with the bearing soil; thus, no bearing resistance was mobilized along this portion of the footing. The model for the May 22nd snap-back test (F = 38.6 kN or 8.67 kip) returned a length of uplift of 17.5 cm (6.9 in.) from the heel (i.e., opposite to the direction of the applied lateral load) for which no bearing resistance was generated. The distribution of the mobilized bearing resistance increased linearly from this location to the west edge of the footing to a maximum bearing resistance of 55 kPa (1,150 psf). The mobilized lateral resistance distributions on the vertical faces of the footing were highly nonlinear, with the west face (i.e., the face in the direction of the applied static lateral force) mobilizing a maximum passive resistance of 55 kPa (1,150

psf) and the east face mobilizing active resistance with a maximum of only about 8 kPa (167 psf). Despite the potential for error in the model input parameters described above, Figure 7.101 (blue markers) provides a quantitative perspective of the soil-structure interaction expected for rocking footings subjected to a lateral pushover force.

If the column flexure contribution to the column drift was removed, the input column drift would decrease to 1.8 mm (0.07 in.). The corresponding vertical footing displacements calculated through rigid body rotation were 0.47 mm (0.019 in.) on both the east and west sides of the footing, compared to the actual maximum vertical footing displacements of 0.84 mm (0.003 in.) and 0.83 mm (0.003 in.) on the east and west sides of the footing, respectively. The comparisons of the SSI model output with and without the consideration of column flexure evidently bound the actual vertical footing displacements recorded during the snap-back test. The mobilized resistances assuming that column flexure corresponds to a decrease in the global rocking displacements are presented in Figure 7.101 with red markers.

In order to assess the reasonableness of the assumed degree of saturation and corresponding bearing capacity computed for Specimen 5, the SSI model was also applied to simulate the wet season (i.e., undrained) response for the May 22nd snap-back test (Figure 7.102). The initial settlement imposed by the self-weight of the specimen determined using the model was calculated equal to 2.97 mm (0.012 in.), owing to the lower bearing capacity calculated for the wet season (476 kPa or 9.94 ksf) compared to the dry season (1,281 kPa or 26.75 ksf). The imposed column displacement of 5.33 mm (0.021 in.) did not sufficiently rotate the specimen such that lift-off of the footing occurred, owing to the greater initial settlement imposed during the wet season. The mobilized bearing resistance was distributed in a nearly linear fashion, with a minimum mobilized bearing resistance of 14 kPa (290 psf) on the east side of the footing to a maximum of 35 kPa (730 psf) on the west side. The mobilized lateral pressures at the east and west vertical footing interfaces were symmetrical, owing to the undrained condition where the active earth pressure coefficient is equivalent to the passive earth pressure coefficient. The maximum lateral resistance (56.4 kPa or 8.2 psi) was mobilized at both vertical footing interfaces, indicative of the low strength of the soil providing lateral resistance. Similar to Figure 7.101, The mobilized resistances assuming the specimen rotates as a rigid member with no column flexure are presented in Figure 7.102 with blue markers, whereas the mobilized resistances assuming that column flexure corresponds to a decrease in the global rocking displacements are presented in Figure 7.102 with red markers.

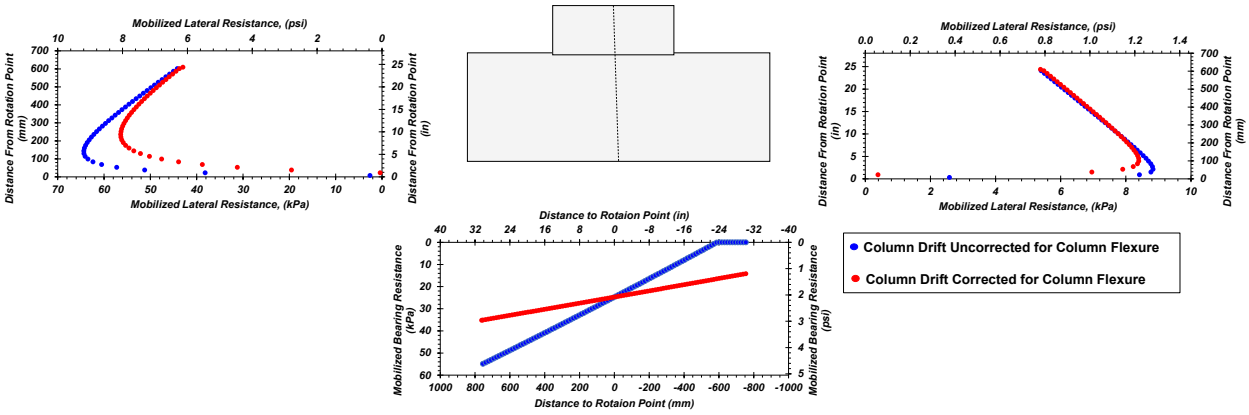

Figure 7.101: Soil-Structure Interaction model results for the May 22nd (F = 38.6 kN or 8.67 kip) snap-back, assuming partially saturated (S = 98%) conditions. The blue markers represent the full global rigid rotation of the specimen based on the recorded maximum top drift, whereas the red markers represent a combination of global rocking and column flexure.

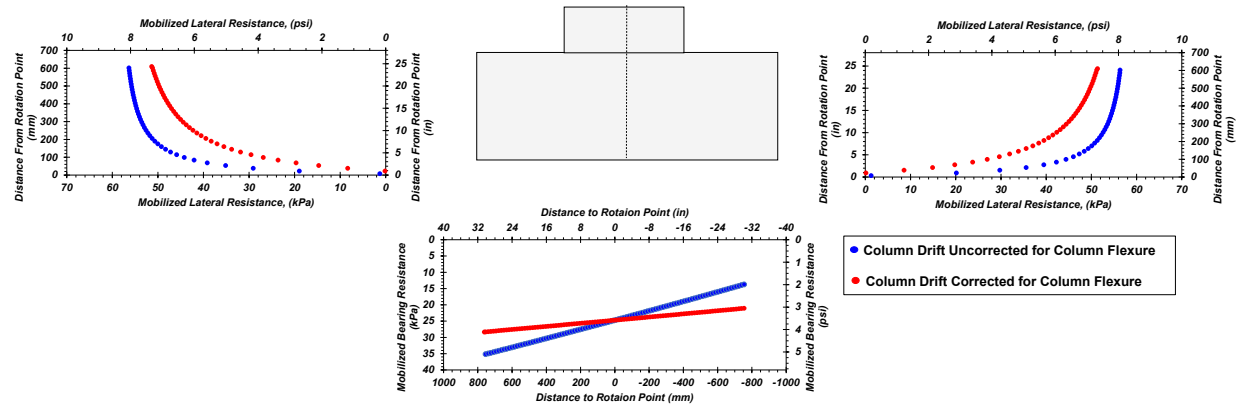

Figure 7.102: Soil-Structure Interaction model results for May 22nd snap-back (F = 38.6 kN or 8.67 kip), assuming undrained conditions (S = 100%). The blue markers represent the full global rigid rotation of the specimen based on the recorded maximum top drift, whereas the red markers represent a combination of global rocking and column flexure.

While only axially unloaded, snap-back, field tests were performed as part of the current study, the SSI model allowed for the input and simulation of the effects of any axial load, P. A comparison of the applied moment-drift responses at axial loads equal to 0, 50, and 100 kN (0, 11.2, and 22.5 kip) for the wet, undrained condition are presented in Figure 7.103. The overall moment-drift relationship is nonlinear for all column drifts regardless of the magnitude of axial load applied, owing to the nonlinear bearing resistance springs implemented. The moment-drift relationships were nearly identical for drifts smaller than 2 cm (0.8 in.), owing to the magnitude of initial settlement imposed for a given applied axial load. An increase in the applied axial load (e.g., P = 100 kN or 22.5 kip) corresponded to an increase in the mobilized bearing resistance; however, the

corresponding initial settlement also increased, forcing the drift required to induce footing lift-off to increase accordingly. Through the summation of moments about the point of rotation (i.e., the center of the footing along the base), the resultant of the mobilized lateral pressure on the east side of the footing (opposite the direction of load application) partially counteracted the resultant on the west side of the footing, thus reducing the required moment. For a specimen with a smaller applied axial load (P = 50 kN or 11.2 kip), lift off was achieved at smaller drifts, corresponding to the increase in the required moment to induce a top drift of 3.0 cm (1.18 in.) compared to the specimen with a larger applied axial load (P = 100 kN or 22.5 kip). The moment-drift relationships for the varying magnitudes of the applied axial load began to converge at high top drifts (exceeding 25 cm or 10 in.) as the ultimate bearing resistance was mobilized.

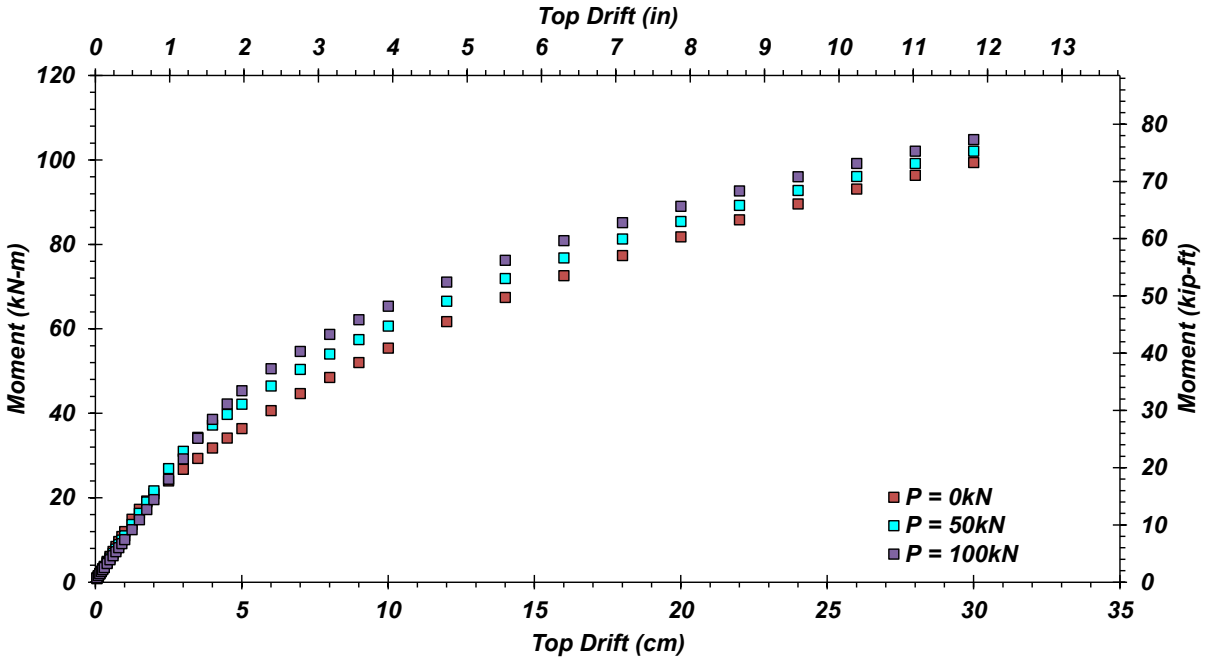

Figure 7.103: Comparison of applied moment-drift responses at varying applied axial loads (P = 0, 50, and 100 kN) for wet season conditions at GEFRS.

The applied moment-drift relationship for the snap-back specimen in the dry, partially saturated condition depends on the degree of saturation of the bearing soil. As shown in Table 7.15, an increase in S in the bearing soil corresponds to a decrease in apparent cohesion, c_{app}, and therefore a decrease in bearing capacity. Figure 7.104 shows the applied moment-drift relationships determined through the implementation of the SSI model at varying degrees of saturation (S = 90%, 95%, and 98%) with no additional applied axial load (i.e., only self-weight).

The moment-drift relationships for the partially saturated bearing soil demonstrated a nonlinear trend, similar to that of the undrained season; however, the increased bearing and lateral resistance of the subsurface owing to the effects of partial saturation required significantly greater applied moments to impose a given drift. The effects of the various

degrees of saturation on the moment-top drift relationships were minimal at small top drifts, with more prevalent differences developing at drifts exceeding 10 cm (3.9 in.). A decrease in the degree of saturation corresponded to an increase in the applied moment required to impose a given top drift, owing to the increase in bearing capacity due to the apparent cohesion.

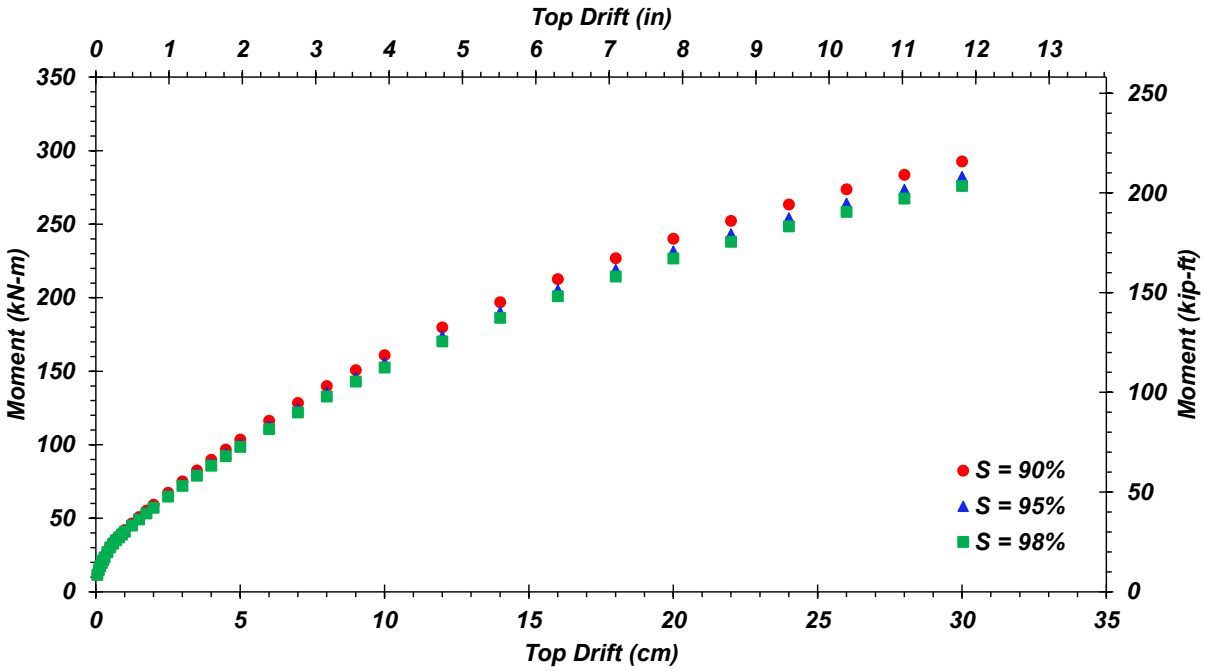

Figure 7.104: Comparison of applied moment-drift responses at varying degrees of saturation (*S* = 90%, 95%, and 98%) assuming partially saturated conditions with no applied axial load (i.e., only self-weight).

Figure 7.105 shows the applied moment-top drift relationship at various applied axial loads (P = 0, 50, and 100 kN) for the subsurface condition with S equal to 98%, a value representative of the dry season conditions based on laboratory results summarized by Dickenson et al. (2006). The response of a specimen with varying magnitudes of the applied axial load with spring parameters representative of partially saturated conditions was similar to that of the undrained season, with the aforementioned effects of the immediate settlement and bearing area evident (Figure 7.105).

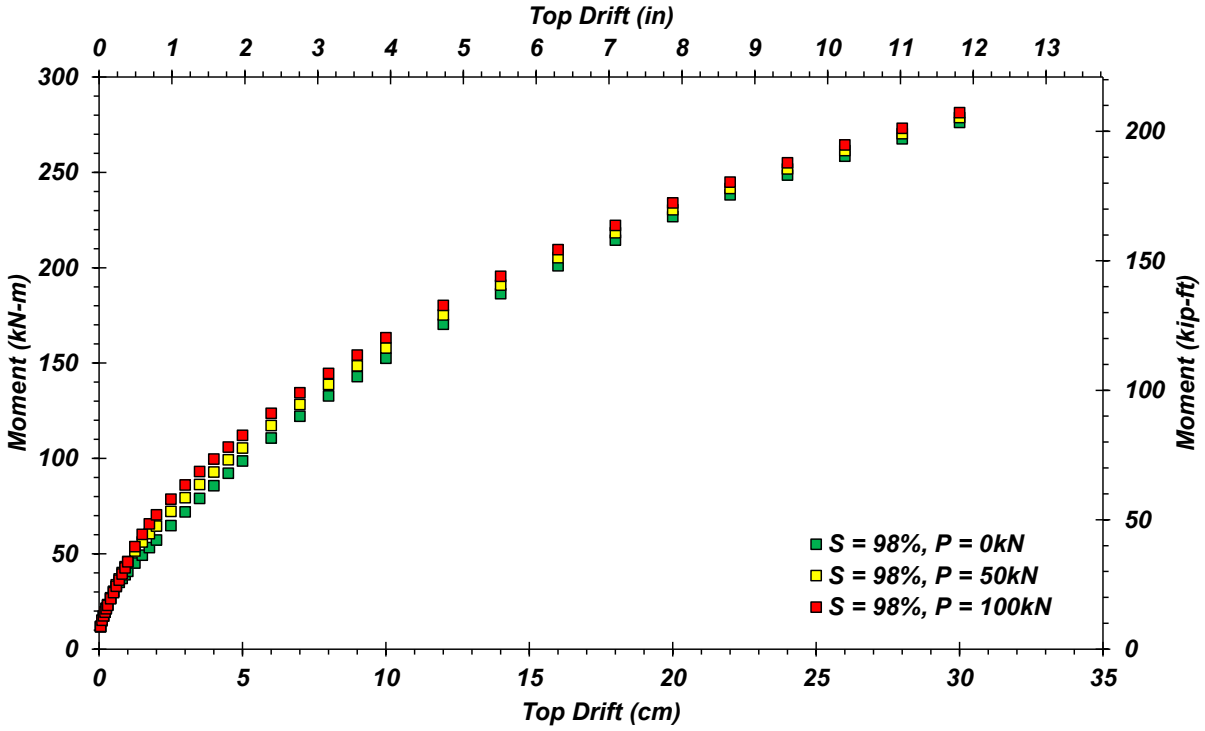

Figure 7.105: Comparison of applied moment-drift responses at varying applied axial loads (P = 0, 50, and 100 kN) assuming partially saturated conditions.

7.5.1.4 Development of Hysteretic Force-Displacement Models

Soil produces a nonlinear force-displacement response when subjected to significant deformations associated with the rocking of shallow foundations, as described in Section 2. While the simulation of the pull associated with the snap-back test described in Section 7.5.1.3 captured the initial nonlinear mobilized resistance to the imposed deformations, the model failed to capture the hysteretic force-displacement response as the soil springs are loaded, unloaded, and reloaded during the rocking response to snap-back testing. Accordingly, hysteretic rules to capture the loading/unloading/reloading response of the soil-footing interfaces must be established.

7.5.1.5 Basis for the Development of a Hysteretic SSI Model

The shear stress-shear strain (γ - τ) response of soil subjected to hysteresis initially follows a linear-elastic path or slope described by the maximum shear modulus, G_{max}, of the soil. This linear shear stress-strain relationship is typically only valid for small shear strains in soil (Section 7.4.3). Upon exceeding the material-dependent linear-elastic threshold shear strain, γ_{te}, the soil begins to exhibit a nonlinear shear stress-shear strain relationship. The nonlinearity of this relationship (i.e., the rate of curvature) increases with increasing shear strain amplitudes; however, the soil remains elastic until the threshold shear strain to trigger excess pore pressure, γ_{tp}, has been reached. The soil subsequently enters the nonlinear-inelastic regime and accumulated strains become

irreversible. Masing rules (Masing 1926) provide a nonlinear model that has been used to replicate the hysteretic behavior of soil. The shear strain-shear stress path initially follows G_{max} along what is termed a backbone curve until the first stress reversal, where the shear stress unloads along a path that is of the same shape as the initial backbone curve but is amplified (or expanded) by a factor of two. The starting point of the curve is shifted from the origin to the shear stress and strain at reversal. To best replicate the hysteretic behavior of a soil, the following two additional rules described by Kramer (1996) provide an extended set of Masing rules: (1) if an unload or reload curve exceeds the maximum past strain and intersects the backbone curve, the curve subsequently follows the backbone curve until the next reversal, and (2) if an unload or reload curve crosses an unload or reload curve from a previous cycle, the stress-strain curve follows that of the cycle intersected. Figure 7.106 presents a schematic demonstrating the hysteretic behavior captured using the extended Masing rules (Kramer 1996).

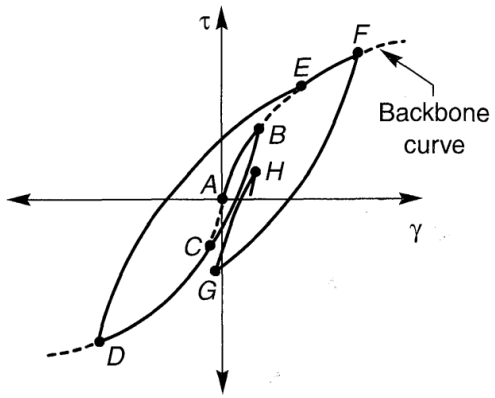

Figure 7.106: Shear stress-strain hysteretic response of a soil modeled with consideration to the extended Masing rules (Kramer 1996).

The implementation of the extended Masing rules for the bearing pressures acting along the vertical and horizontal planes of the soil-footing interfaces requires the specification of a backbone curve. Equations (7-17) and (7-18) provide the formulation for the backbone curves for bearing resistance. Prior to implementing these nonlinear relationships, the hysteretic formulation of the column-footing SSI model was validated against the results of the full-scale quasi-static cyclic lateral loading tests performed by Parson (2022) on a foam soil simulant. Test 2 – S2 (Table 7.6) was performed without embedment and on a soil simulant subgrade, creating an appropriate baseline test for the development of the advanced displacement history-dependent model without the complication of lateral resistance. First, the stress-strain-strength properties of the soil simulant material is presented; thereafter, the displacement history-dependent model for the bearing response of the column-footing specimen S2 is established and validated.

7.5.1.6 Response of Foam Soil Simulant to Compressive Loading

The soil simulant studied was an Extruded Polystyrene (XPS) Rigid Foam Insulation, which had been previously used as a subgrade for full-scale quasi-static cyclic lateral loading tests performed by Shrestha (2019) and Parson (2022). Shrestha (2019) described

the results of three unconfined compression strength (UCS) tests performed on 15.24 cm by 9.53 cm (6 in. by 3.75 in.) cylindrical soil simulant specimens. The three tests were performed at an average strain rate, $\dot{\varepsilon}$, equal to $1.2E^{-3}$ in./in./sec (0.12 %/sec). A typical strain history with three load/unload cycles performed by Shrestha (2019) is shown in Figure 7.107. Three load/unload cycles were performed as part of the study to examine potential stiffness and/or strength degradation of the soil simulant specimens with respect to unloading and reloading.

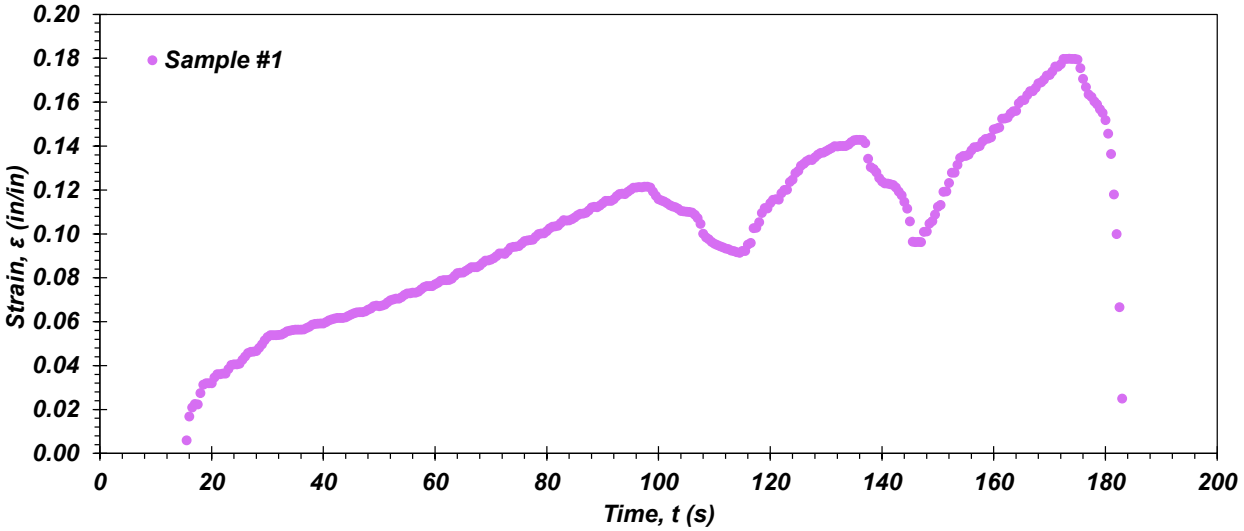

Figure 7.107: Typical strain history from UCS tests on soil simulant foam performed by Shrestha (2019).

The full-scale quasi-static, cyclic lateral loading tests of full-scale bridge column-footing specimens on soil simulant foam performed by Parson (2022) facilitated the determination of parameters required to calibrate the hysteretic response of the soil simulant. Full-scale tests were performed with an applied vertical axial load equal to 667 kN (150 kips). As the axial load was continuously increased, the settlement of the soil simulant subgrade was recorded with six string potentiometers fixed to the top of the footing. This facilitated the determination of an average strain rate and an elastic modulus for the portion of each full-scale test when the axial load was applied. The pressure-displacement results from six of the full-scale tests are presented in Figure 7.13, with Tests 1 through 3 performed on undamaged simulant and Tests 5 through 7 performed on damaged simulant. It is worth noting that no tests were taken to the compressive strength of the soil simulant, and that tests were held at the constant maximum load to observe the effects of creep.

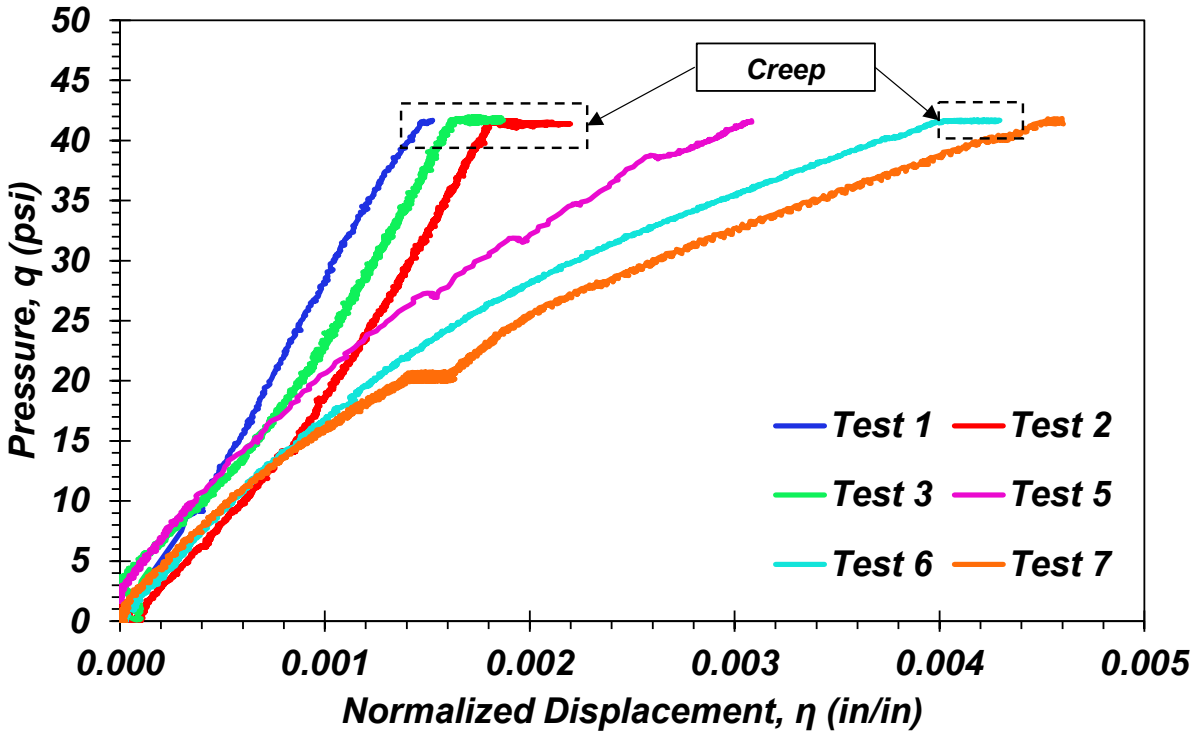

Figure 7.108: Pressure-normalized displacement (i.e., force/area-displacement/footing width) histories for the axial loading portion of full-scale, quasi-static, cyclic lateral loading tests on soil simulant foam performed by Parson (2022).

Additional UCS tests were conducted as part of the current study on cylindrical soil simulant foam specimens 20.3 cm in height by 9.5 cm in width (8 in. by 3.75 in.) to maintain a typical 2:1 height to width ratio; to accomplish this, four soil simulant foam "sub-specimens" 5.08 cm (2.0 in.) in thickness were stacked vertically with special care to ensure no eccentric stresses were developed due to an initial misalignment. Three unconfined compression tests were conducted to observe the effect of strain rate on the ultimate strength and stiffness of the specimens, considering the following strain rates: $5E^{-4}$ in./in./sec ($5E^{-2}$ %/sec), $1E^{-3}$ in./in./sec (0.1 %/sec), $5E^{-3}$ in./in./sec (0.5%/sec), and $5E^{-2}$ in./in./sec (5 %/sec). Three tests were conducted on the cylindrical specimens at each of the four strain rates.

The complete compressive stress-strain results from the twelve UCS tests are presented in Figure 7.109, with Figure 7.110 depicting the near linear-elastic portion of each compressive test. The initial seating behavior (i.e., curvature in the stress-strain relationship at small strains) was disregarded for the determination of the elastic modulus for all tests. The foam soil simulant exhibits a nearly linear-elastic, post-yield hardening and post-peak softening stress-strain response. The threshold between the linear-elastic and the plastic response was typically observed at a strain of about 0.025 in./in. The threshold strain at which the ultimate or peak strength was observed depended on the strain rate and the unique cylindrical stack of sub-specimens, indicating that variability from specimen to specimen contributed to the peak strength threshold strain. After correcting for the initial seating behavior (not shown), the stress-strain response of the

soil simulant could be simulated by assuming a linear-elastic (with slope equal to the modulus of elasticity, *E*), perfectly plastic regime (with strength equal to the unconfined compressive strength).

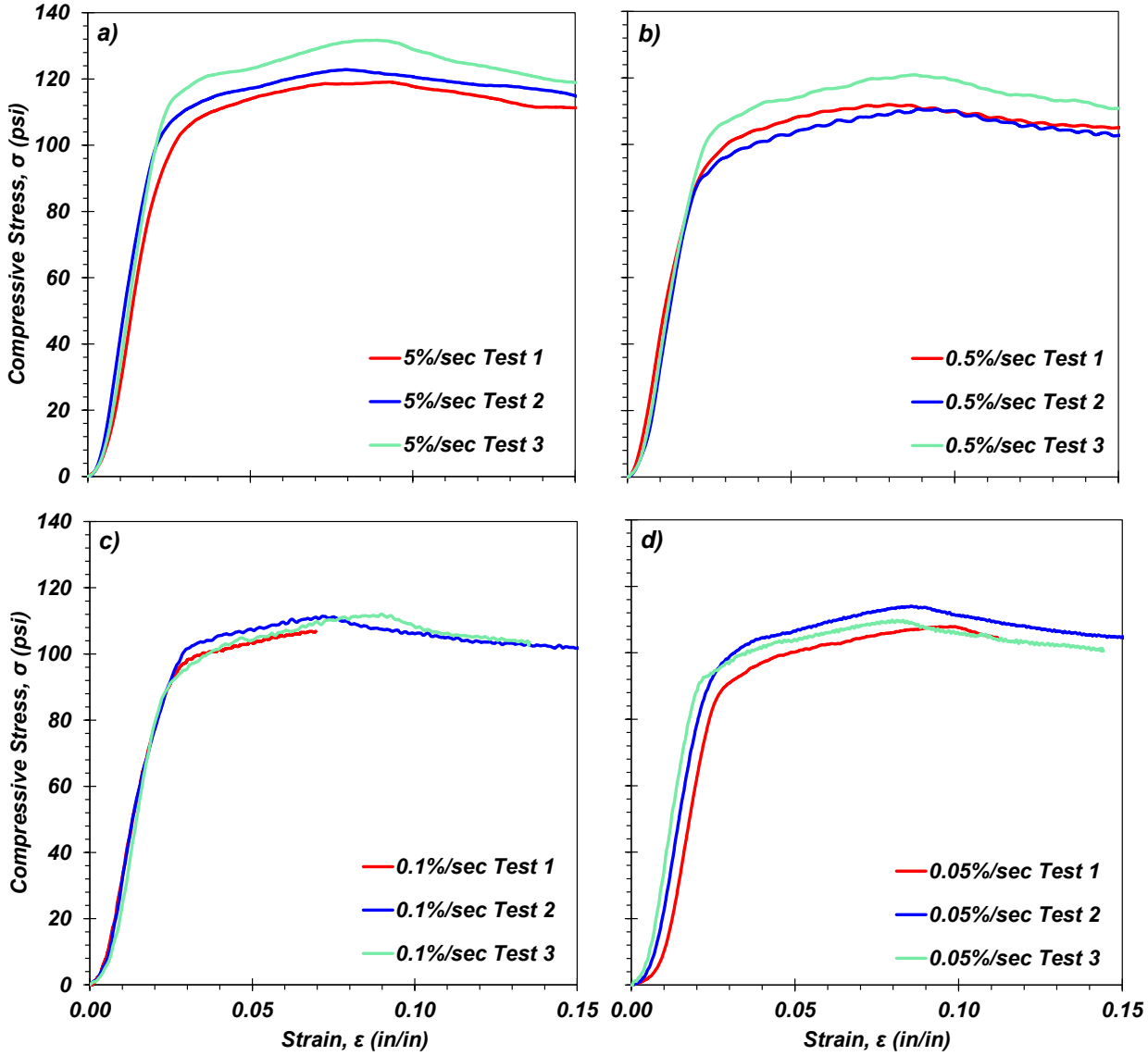

Figure 7.109: Compressive stress-strain histories for UCS testing on cylindrical soil simulant specimens at strain rates of: (a) 5%/sec, (b) 0.5%/sec, (c) 0.1%/sec, and (d) 0.05%/sec.

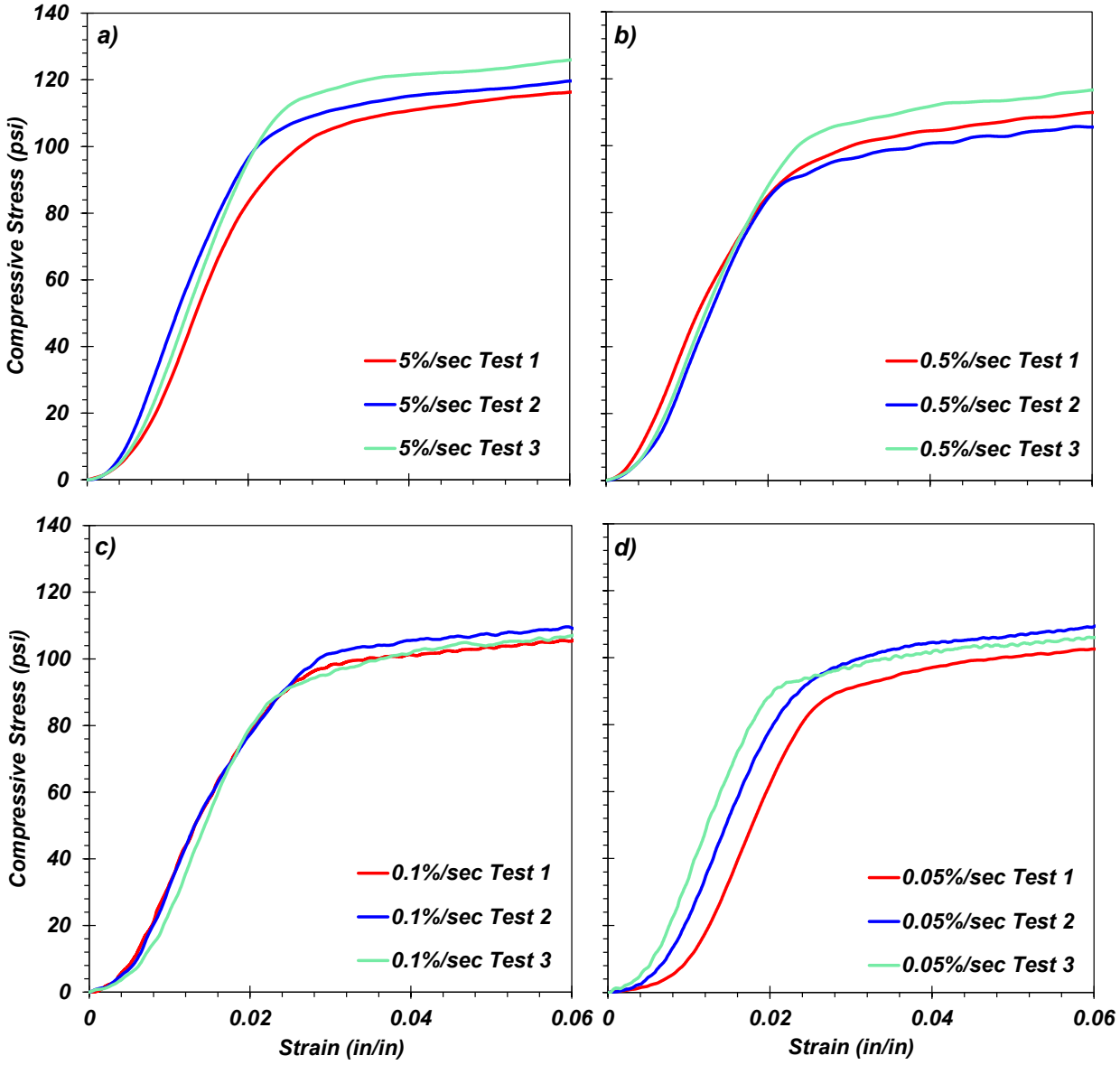

Figure 7.110: Compressive stress-strain histories at small strains for UCS testing on cylindrical soil simulant specimens at strain rates of: (a) 5%/sec, (b) 0.5%/sec, (c) 0.1%/sec, and (d) 0.05%/sec.

The compressive tests on the soil simulant foam facilitated the determination of the strain rate-dependent elastic modulus, E, and unconfined compressive strength, (σ_{ult}), for use in the displacement history-dependent model simulation of Test 2 – S2 (Parson 2022). The unconfined compressive strength was taken as the maximum stress recorded during the UCS tests. The compiled results are presented in Table 7.17.

Table 7.17: Summary of UCS and axial load tests on soil simulant foam with varied strain rates, $\dot{\varepsilon}$.

Study	Designation	Strain Rate, $\dot{\varepsilon}$ (%/sec)	Elastic Modulus, E MPa, (psi)	Ultimate Compressive Strength, σ_{ult}, kPa (psi)
Shrestha (2019)	Foam 1	$1.23E^{-01}$	30.7 (4,449)	793 (115)
	Foam 2	$1.07E^{-01}$	39.9 (5,789)	834 (121)
	Foam 3	$1.20E^{-01}$	40.8 (5,917)	848 (123)
Parson (2022)	Test 1 - S1 Day 1	$2.60E^{-03}$	28.9 (4,188)	-
	Test 2 - S2	$3.90E^{-03}$	27.6 (4,001)	-
	Test 3 - S3	$3.50E^{-03}$	27.9 (4,044)	-
Current Study	5%, Trial 1	$5.00E^{+00}$	43.8 (6,355)	820 (119)
	5%, Trial 2	$5.00E^{+00}$	46.4 (6,725)	848 (123)
	5%, Trial 3	$5.00E^{+00}$	46.5 (6,739)	903 (131)
	0.5% Trial 1	$5.00E^{-01}$	40.8 (5,913)	772 (112)
	0.5% Trial 2	$5.00E^{-01}$	41.7 (6,043)	765 (111)
	0.5% Trial 3	$5.00E^{-01}$	42.7 (6,195)	834 (121)
	0.1%, Trial 1	$1.06E^{-01}$	36.6 (5,308)	710 (103)
	0.1%, Trial 2	$1.05E^{-01}$	35.6 (5,157)	765 (111)
	0.1%, Trial 3	$1.03E^{-01}$	41.2 (5,981)	772 (112)
	0.05%, Trial 1	$5.13E^{-02}$	39.7 (5,751)	745 (108)
	0.05%, Trial 2	$5.20E^{-02}$	40.6 (5,884)	786 (114)
	0.05%, Trial 3	$5.15E^{-02}$	43.4 (6,301)	758 (110)

The compression tests performed on the soil simulant samples facilitated the determination of relationships between the strain rate and the parameters necessary to formulate the backbone curve for the strain history-dependent model (e.g., E and σ_{ult}). As summarized in Table 7.17, an increase in the strain rate generally corresponded to an increase in both E and σ_{ult}, indicating the soil simulant exhibits viscous behavior. The effect of strain-rate on E and σ_{ult} is presented concisely in Figures 7.111 and 7.112, respectively. It is worth noting that the soil simulant foam material exhibits variability in material properties from lot to lot; further deformations developed in the cylindrical specimens in an apparently random manner where a local weakness within any one sub-specimen cylinder yielded first to control the global deformation of the specimen. During UCS testing, failure planes developed in a random manner. Bulging developed in the

stacked sub-specimens when the plastic portion of the stress-strain curve was reached. Figure 7.113 presents the deformed shapes of the soil simulant UCS specimens.

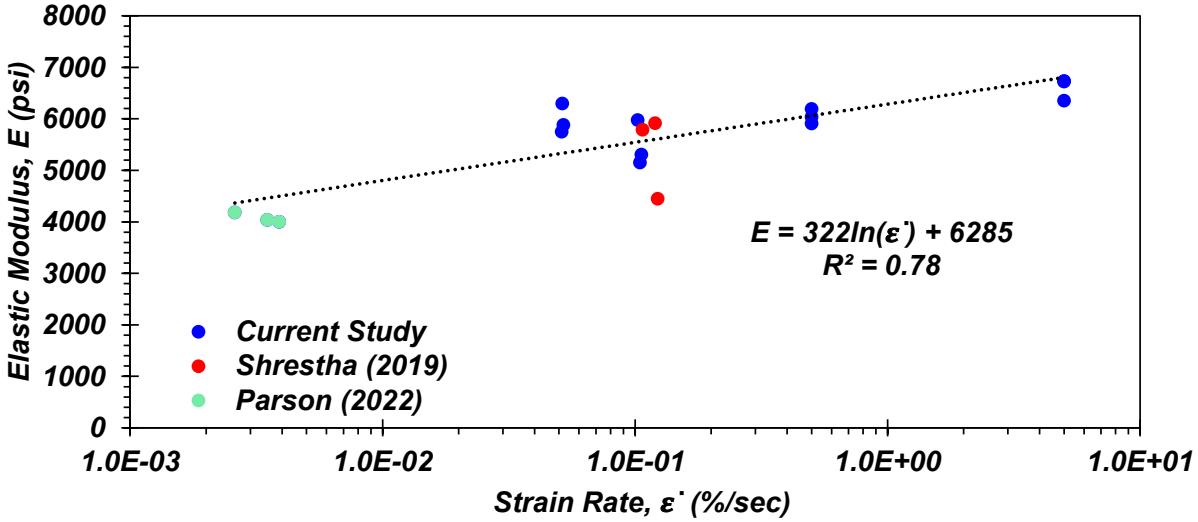

Figure 7.111: Correlation of strain rate from UCS tests (current study and Shrestha 2019) and axial load (Parson 2022) tests to the modulus of elasticity, *E*, of the soil simulant foam. The correlation presented was created using only the UCS test data from the current study and Parson (2022).

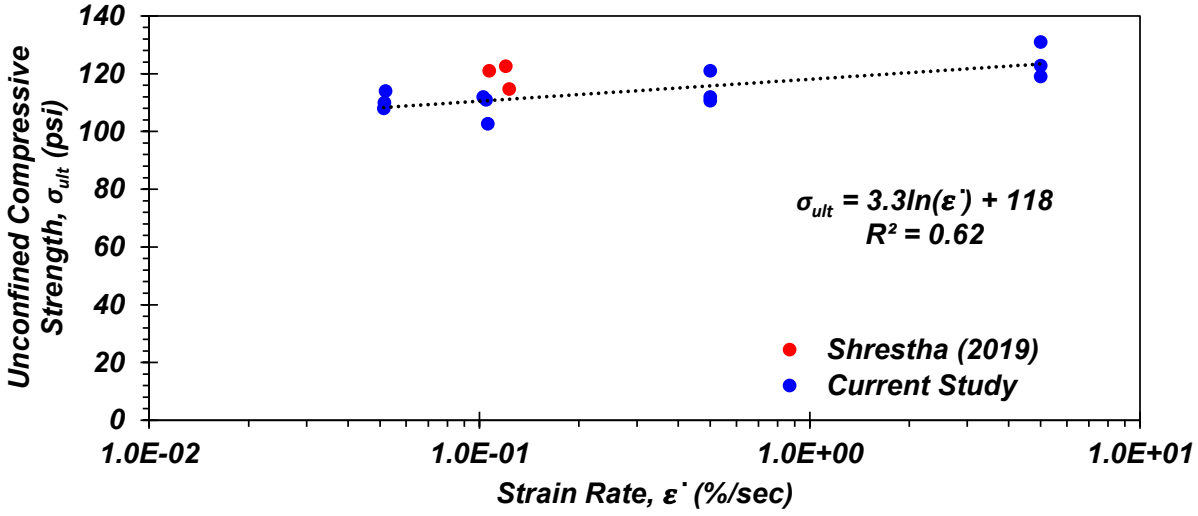

Figure 7.112: Correlation of strain rate from UCS tests (current study and Shrestha 2019) and axial load (Parson 2022) tests to the ultimate compressive strength, σ_{ult}, of the soil simulant foam. The correlation presented was created using only the UCS test data from the current study.



Figure 7.113: Soil simulant cylindrical specimens after UCS testing.

7.5.1.7 Soil Simulant Foam SSI Model

A hysteretic SSI model was developed to replicate the lateral load-drift backbone curve of cyclic lateral load tests on full-scale specimens. The springs implemented in the model consider displacement history and adhere to the Masing rules (Section 7.5.1.5) with respect to loading/unloading/reloading. The model uses a modulus of elasticity factor and strain-rate appropriate elastic moduli and compressive strengths for each loading cycle.

The full-scale column-footing specimen S2 subjected to the second round of quasi-static cyclic lateral load testing (i.e., Test 2 – S2; Table 7.6) was used to confirm the accuracy of the SSI model. It was determined through the aforementioned analyses of UCS test results that the stress-strain relationship of the soil simulant could be simply represented by a linear-elastic, perfectly plastic force-displacement response. In the SSI model, it was assumed that a linear mobilized resistance backbone curve would be initially followed until the ultimate strength was reached, where the path would remain perfectly plastic as the strain was increased.

Test 2 – S2 was performed in accordance with the standard loading protocol prescribed in Section 7.2 using cyclic reversals of positive and negative drift to an ultimate top drift equal to 12.1 cm (4.8 in.). The cyclic loading produced 15 cycles of uplift on the north and south sides of the footing, respectively. The strain rate for a given footing uplift cycle was determined through the analysis of vertical footing displacement recorded histories from Test 2 – S2 (Parson 2022), which allowed estimation of upper and lower bounds of the representative strain rate during rocking near the edge of the footing. Figure 7.114 shows the strain time history near the edge of the footing during the 14th loading cycle. The strain time histories for all loading cycles are presented in Appendix A7.2, with the upper and lower bound estimates for the strain rates during rocking computed for all 15 rocking cycles as summarized in Table 7.17. The loading cycles corresponding to smaller top drifts resulted in lower strain rates, with the highest strain rates associated with the

cycle with the largest top drift. The strain rates ranged from $3.20E^{-2}$ %/sec to $5.82E^{-1}$ %/sec. The parameters required for input into the hysteretic SSI model were estimated using the strain rate-elastic modulus and the strain rate-ultimate strength correlations presented in Figures 7.111 and 7.112, respectively, and are summarized in Table 7.18.

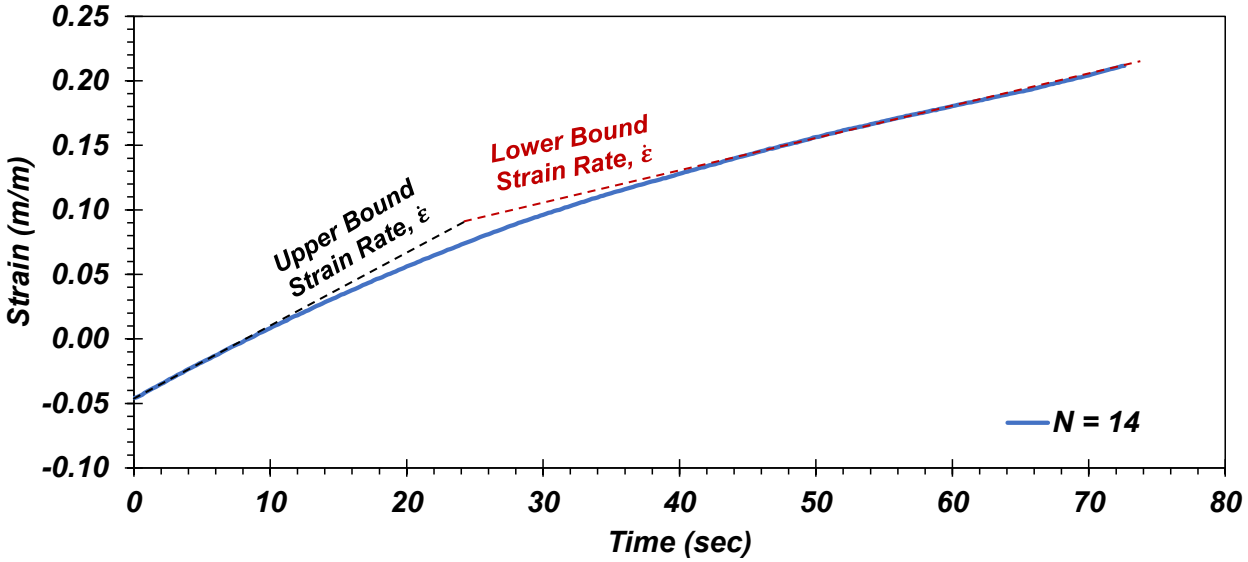

Figure 7.114: Upper and lower bound estimates of the strain rate, $\dot{\varepsilon}$, at the edge of the footing during the 14th rocking cycle of Test 2 – S2 (data from Parson 2022).

Table 7.18: Summary of strain rates at the edge of the footing during Test 2 – S2.

Parson (2022) Test 2		Strain Rate, $\dot{\varepsilon}$ (%/sec)	
Cycle	**Top Drift, cm (in)**	**Upper Bound**	**Lower Bound**
15	12.19 (4.80)	$5.82E^{-01}$	$2.56E^{-01}$
14	11.18 (4.40)	$5.93E^{-01}$	$2.49E^{-01}$
13	10.16 (4.00)	$5.80E^{-01}$	$2.30E^{-01}$
12	9.14 (3.60)	$5.38E^{-01}$	$2.29E^{-01}$
11	8.13 (3.20)	$5.50E^{-01}$	$2.21E^{-01}$
10	7.11 (2.80)	$5.40E^{-01}$	$2.24E^{-01}$
9	6.10 (2.40)	$4.52E^{-01}$	$1.84E^{-01}$
8	5.08 (2.00)	$4.40E^{-01}$	$1.80E^{-01}$
7	4.06 (1.60)	$3.60E^{-01}$	$1.56E^{-01}$
6	3.05 (1.20)	$3.32E^{-01}$	$1.38E^{-01}$
5	2.03 (0.80)	$1.40E^{-01}$	$7.00E^{-02}$
4	1.02 (0.40)	$1.54E^{-01}$	$7.20E^{-02}$
3	0.74 (0.29)	$1.06E^{-01}$	$5.60E^{-02}$
2	0.48 (0.19)	$5.00E^{-02}$	$3.20E^{-02}$
1	0.25 (0.10)	$5.00E^{-02}$	$3.20E^{-02}$

Table 7.19: Summary of upper and lower bound estimates of E and σ_{ult} at the edge of the footing during Test 2 – S2 based on strain-rate, $\dot{\varepsilon}$, correlations from the UCS test data.

Upper Bound			Lower Bound		
$\dot{\varepsilon}$ (%/sec)	E, MPa (psi)	σ_{ult}, kPa (psi)	ε (%/sec)	E, MPa (psi)	σ_{ult}, kPa (psi)
$5.82E^{-01}$	42.1 (6,111)	801 (116)	$2.56E^{-01}$	40.3 (5,846)	783 (114)
$5.93E^{-01}$	42.2 (6,117)	802 (116)	$2.49E^{-01}$	40.2 (5,837)	783 (113)
$5.80E^{-01}$	42.1 (6,110)	801 (116)	$2.30E^{-01}$	40.1 (5,812)	780 (113)
$5.38E^{-01}$	42.0 (6,085)	800 (116)	$2.29E^{-01}$	40.1 (5,810)	779 (113)
$5.50E^{-01}$	42.0 (6,092)	800 (116)	$2.21E^{-01}$	40.0 (5,799)	779 (113)
$5.40E^{-01}$	42.0 (6,087)	800 (116)	$2.24E^{-01}$	40.0 (5,803)	780 (113)
$4.52E^{-01}$	41.6 (6,029)	796 (115)	$1.84E^{-01}$	39.6 (5,740)	775 (112)
$4.40E^{-01}$	41.5 (6,021)	795 (115)	$1.80E^{-01}$	39.5 (5,733)	774 (112)
$3.60E^{-01}$	41.1 (5,956)	790 (115)	$1.56E^{-01}$	39.2 (5,687)	771 (112)
$3.32E^{-01}$	40.9 (5,930)	789 (114)	$1.38E^{-01}$	38.9 (5,647)	768 (111)
$1.40E^{-01}$	39.0 (5,652)	769 (112)	$7.00E^{-02}$	37.4 (5,429)	753 (109)
$1.54E^{-01}$	39.2 (5,683)	771 (112)	$7.20E^{-02}$	37.5 (5,438)	754 (109)
$1.06E^{-01}$	38.3 (5,562)	763 (112)	$5.60E^{-02}$	36.9 (5,357)	748 (108)
$5.00E^{-02}$	36.7 (5,320)	745 (108)	$3.20E^{-02}$	35.7 (5,177)	735 (107)
$5.00E^{-02}$	36.7 (5,320)	745 (108)	$3.20E^{-02}$	35.7 (5,177)	735 (107)

The estimated elastic modulus at the edge of the footing during the cyclic loading portion of Test 2 – S2 ranged from 35.7 MPa (5,177 psi) to 42.2 MPa (6,117 psi), whereas the estimated ultimate compressive strengths ranged from 735 kPa (107 psi) to 802 kPa (116 psi). Material parameters E and σ_{ult} were input into the SSI model. The column drift was corrected for column flexure based on the applied lateral load using (Eq. 7.33). The E and σ_{ult} were varied on a per-cycle basis to capture the strain-rate dependency of the soil simulant foam (Table 7.19).

The SSI model required the following inputs: (1) a well-documented, clear top drift-lateral load (or footing rotation-lateral load) hysteresis or backbone curve, (2) the calculated drift associated with flexure of the column, and (3) the modulus of elasticity factor, m. The slope of the pressure-normalized displacement response during the axial loading portions of full-scale tests (Figure 7.108, Figure 7.115) was represented by m. It was determined through comparison with the E values presented in Table 7.16 that the modulus of elasticity factor was roughly equivalent to $E/25$ (i.e., the conversion of δ/η to δ/ε). The m parameter was determined by correcting the pressure-normalized displacement responses for initial seating effects. An example of this analysis is

presented in Figure 7.115, where the results from Test 2 – S2 indicated a m value equal to 157 psi/normalized displacement (E = 3,900 psi).

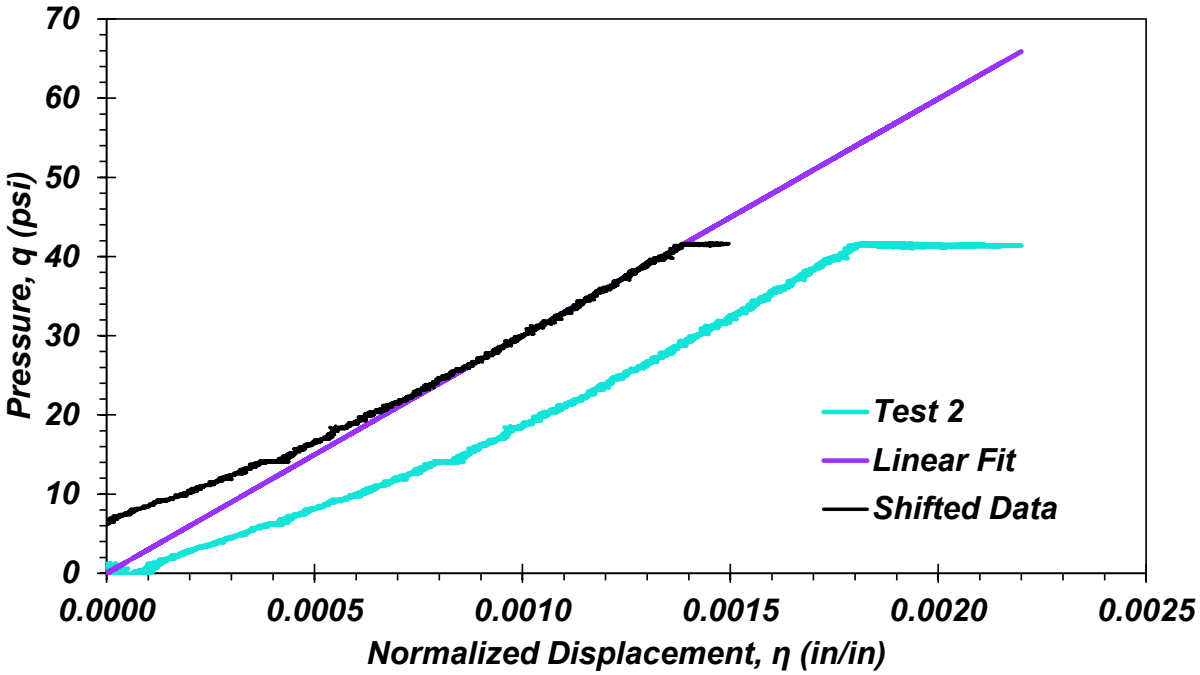

Figure 7.115: Linear curve fit (m = 157 psi/η) of pressure-normalized displacement response during axial loading portion of Test 2 – S2 (Parson 2022) with the corresponding shifted normalized displacement-pressure history.

The ultimate strength of the foam soil simulant was inputted into the model rather than a representative bearing capacity due to the limited depth of foam beneath the rocking foundation. An additional calculation within the model was simulated the vertical footing displacement time history determined using trigonometric functions with respect to the flexure-corrected effective column drift (Eq. 7-33). Test 2 – S2 resulted in a footing response that was near-perfect symmetric rocking behavior, which allowed for the linear interpolation of the imposed vertical footing displacement at any spring along the base of the footing within the model, identical to the method used in the static load SSI model. Similarly, the mobilized resistance due to the imposed initial settlement was determined in the same manner as the static load snap-back model, through the use of the linear-elastic perfectly plastic mobilized resistance model rather than the hyperbolic model implemented for true soil. For each rocking cycle, the mobilized resistance at each of the 100 springs was determined based on the imposed deformation using:

$$F = m \cdot \eta_i \cdot \sigma_{ult} \tag{7-34}$$

if the force-displacement curve was following the backbone curve (i.e., the spring had exceeded the maximum past displacement). In accordance with the extended Masing rules (Kramer 1996), if the force-displacement curve returned by the spring had yet to

intersect the backbone curve on an unload or reload cycle, the mobilized resistance was given by:

$$\boldsymbol{F = 2 \cdot m \cdot \eta_i \cdot \sigma_{ult}} \quad \textbf{(7-35)}$$

with the mobilized resistance, F, capped at the strain-rate dependent compressive strengths presented in Table 7.18.

The mobilized resistance is multiplied by the tributary area of each spring (i.e., B^2/N, where N is equal to the number of springs) to obtain the mobilized force. By multiplying this mobilized resistance (in terms of force) at the midpoint of each spring tributary area by the moment arm, given by the distance to the center of the footing (which corresponded to the point of rotation), the moment corresponding to each spring is calculated and summed to quantify the resistance mobilized by the soil simulant.

The mobilized force for all springs along the base of the footing is shown in Figure 7.116, which presents the simulated responses for each of the first nine rocking cycles of the Test 2 – S2 model simulation. The mobilized force consisted of three regimes: loading along the backbone curve, reloading or unloading where the slope of the force-displacement curve follows the backbone but was amplified by a factor of two, and the constant force at increasing displacement when the soil simulant reached the ultimate compressive strength (i.e., entered the perfectly plastic region). These regimes are reflected in Figure 7.116, with the springs first reaching the ultimate strength during Cycle 6 for both positive and negative drifts. During the first four cycles, the footing was always in contact with the soil simulant subgrade due to the initial settlement (0.29 cm or 0.11 in.) imposed during the axial load application. After Cycle 5, it is evident that the footing has lost contact with the subgrade as zero mobilized resistance was observed at the heel of the footing (i.e., the side of the footing opposite to the direction of the lateral load application). This effect became more substantial with increasing cycles, as the specimen was subjected to increasing magnitudes of drifts (and thus, rocking displacements).

The SSI model allows for the generation of the global backbone drift-lateral load hysteresis for comparison with the backbone curve from Test 2 – S2 (Parson 2022), as shown in Figure 7.117. The results of the Test2 – S2 simulation using the SSI model were obtained using the strain rate-dependent upper bounds for E and σ_{ult} (Table 7.18). The asymmetry demonstrated within the experimental backbone curve was associated to biases within the test setup that facilitated a stiffer, stronger response for positive imposed drifts (i.e., during the "push" cycle) compared to negative drifts ("pull" cycle). From the comparison it is evident that the implementation of strain-rate-dependent parameters (E and σ_{ult}) is critical to obtain a simulated response comparable to the experimental results.

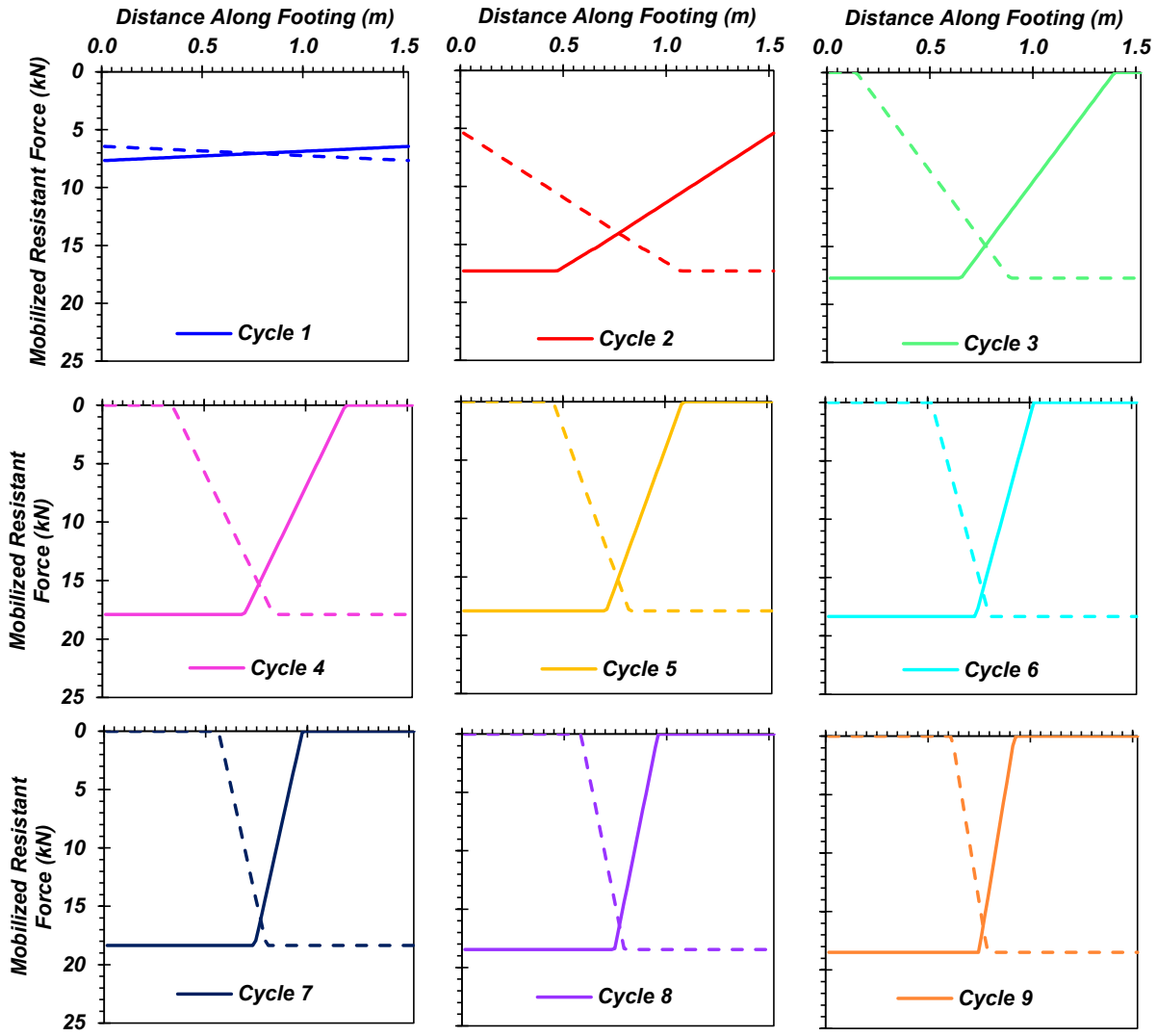

Figure 7.116: Mobilized force at all springs during the first nine cycles of Test 2 – S2 (Parson 2022). Each cycle has the mobilized response from the positive (solid lines) and negative (dashed lines) drifts, symmetrical about the centroid of the column-footing specimen.

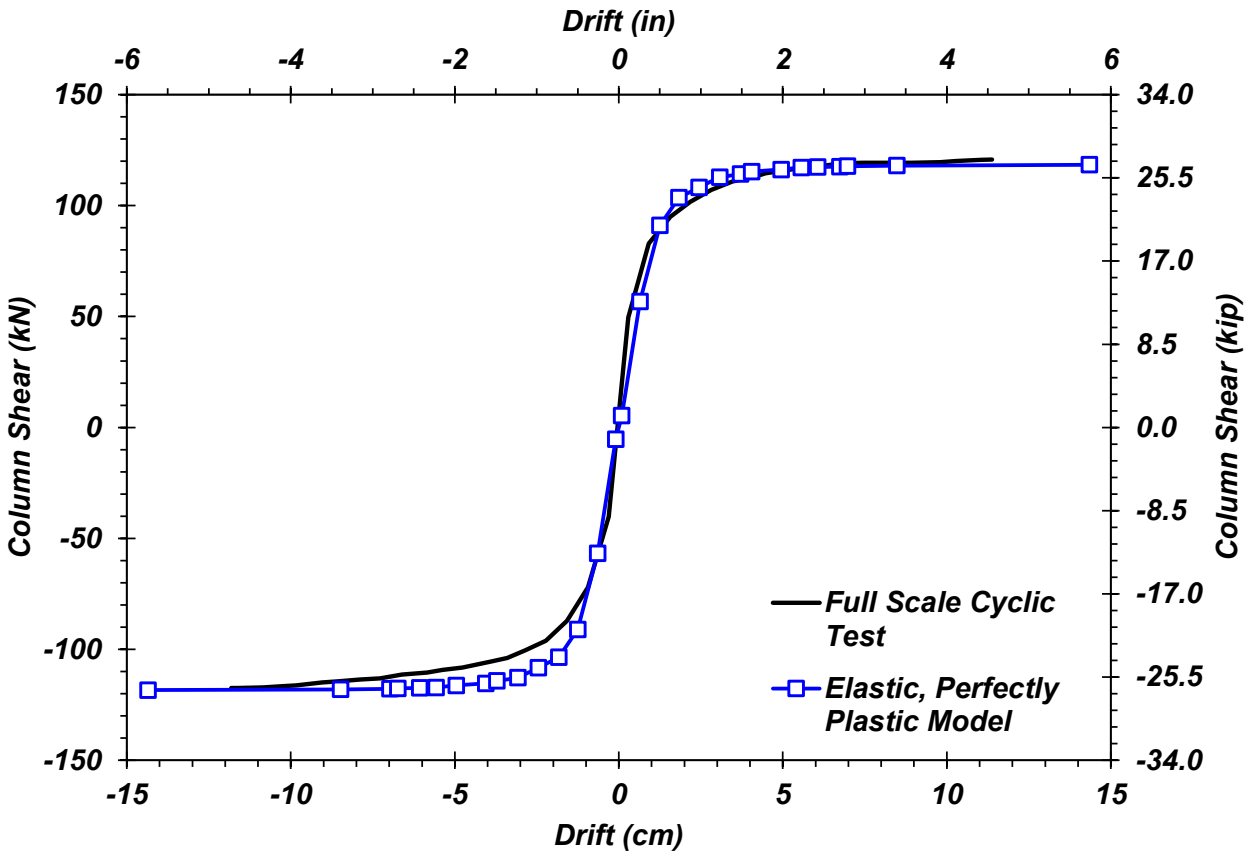

Figure 7.117: Comparison of the elastic, perfectly plastic hysteretic SSI model output (considering strain rate-dependent parameters) with the backbone curve of Test 2 – S2 (Parson 2022).

7.5.2 Hysteretic Soil-Structure Interaction Model and Results

7.5.2.1 Hysteretic Soil-Structure Interaction Model and Results

The hysteretic SSI model was further adjusted to simulate the nonlinear hyperbolic response of true soil to the quasi-static cyclic lateral loading of column-footing specimens at the GEFRS. The model used hyperbolic parameters representative of the Upper Willamette Silt (Huffman et al. 2015) to produce simulated backbone curves representative of varying seasonal conditions, degrees of saturation, and applied axial load. The hyperbolic model parameters from Test 3 (k_1 = 0.0173, k_2 = 0.595) were used in the analyses, as this test was deemed the average response of the five footing loading tests.

The response of the subsurface when subjected to cyclic lateral loading was dependent on the seasonal conditions (Section 7.5.1.1). An undrained bearing capacity analysis was used by the model to represent the wet season conditions, with a s_u equal to 63 kPa (1,316 psf) and a corresponding bearing capacity of 476 kPa (9.94 ksf). An M_{stc} of 0.55 was used as the scaling factor within the hyperbolic model in accordance with GEFRS test results presented by Huffman et al. (2015). The hyperbolic model parameters from Test 3 (k_1 =

0.0173, k_2 = 0.595) were used in the analyses, as this test was deemed the average response of the five footing loading tests.

The column drift history from Test 2 – S2 was the baseline displacement input for the analyses presented herein. Figure 7.117 shows drift-lateral load backbone curves produced by the model provided undrained conditions various magnitudes of an applied axial load (P = 0 kN or 0 kip, 25 kN or 5.6 kip, 50 kN or 11.2 kip, 75 kN or 16.8 kN, and 100 kN or 22.4 kip. The backbone curve simulating an unloaded test (P = 0 kN) initiates with relatively stiff lateral load-top drift response for the first two reversed cycles. As the magnitude of drift is incrementally increased, the required lateral load to impose the footing displacements observed during Test 2 – S2 continued to follow the nonlinear trend that has a decreasing slope with increasing drifts. With no additional applied axial load, the mobilized resistance of the bearing soil fell just shy of reaching bearing failure during the final cycle, as the mobilized pressure at the edge of the footing was equal to 442 kPa (9.2 ksf).

The initial stiffness of the simulated lateral load-drift curve remained relatively constant, regardless of the magnitude of the applied axial load (Figure 7.118). The increase in the applied axial load corresponds to an increase in the applied lateral load beginning at a drift equal to 2.5 cm (1.0 in.). The larger axial load resulted in a slightly larger nearly linear portion of the backbone curve, as the drift at which the backbone curves began to demonstrate a noticeable nonlinear response was higher for a greater axial load.

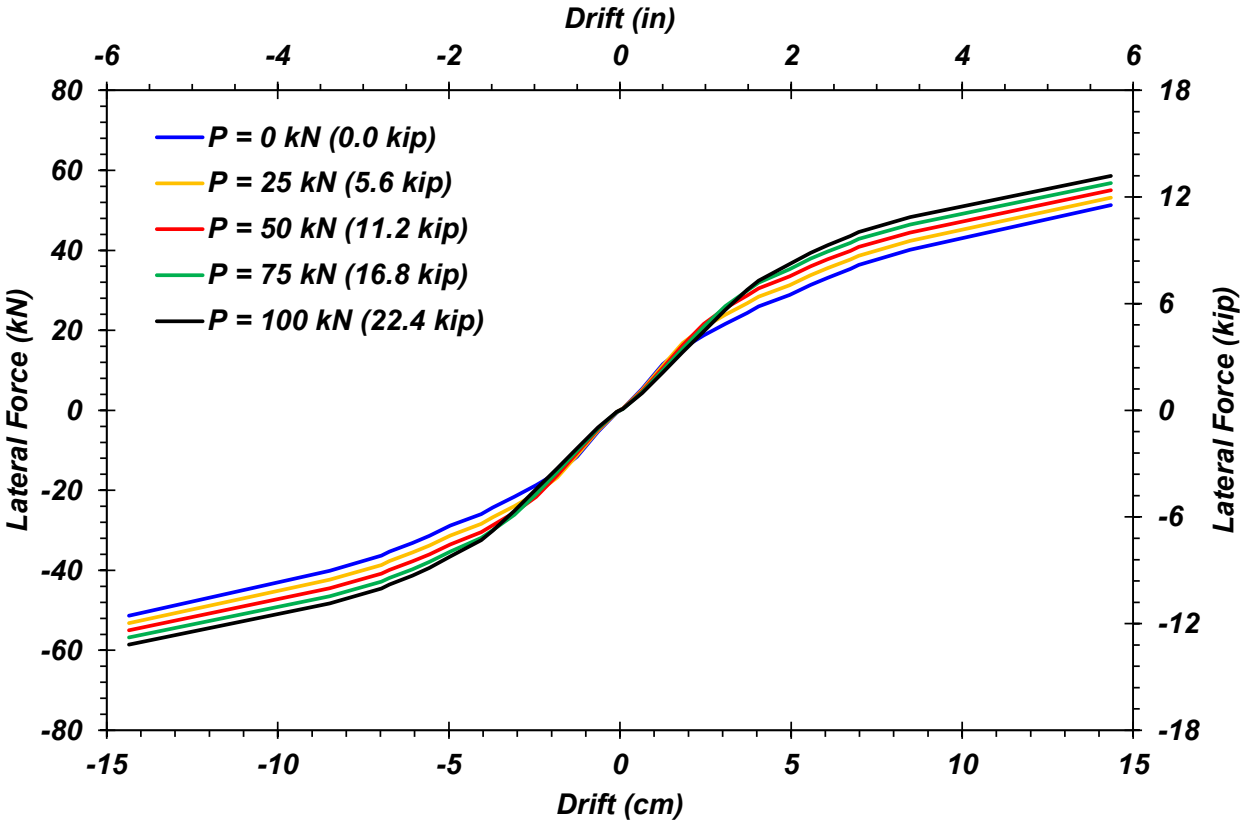

Figure 7.118: Comparison of the simulated drift-lateral load backbone curves representative of the fully-saturated (undrained) conditions at the GEFRS with additional axial loads of 0 kN (0 kip), 25 kN (5.6 kip), 50 kN (11.2 kip), 75 kN (16.8 kip), and 100 kN (22.4 kip) applied to the specimen.

A sensitivity analyses was performed to determine the effect of a 20% change in the representative undrained shear strength on the simulated response of a specimen to cyclic lateral loading, owing to the uncertainty regarding this parameter (Section 7.2). The response assuming the representative s_u of 63 kpa (1,316 psf) is compared to that of a bearing soil with an upper and lower bound of 76 kPa (1,580 psf) and 50 kPa (1,040 psf), respectively, in Figure 7.119. The undrained bearing capacity of the subsurface had a minimal effect on the lateral load required to impose the deformations representative of the first three cycles (i.e., up to a drift of 1.2 cm (0.5 in.). This observation corresponded to the negligible difference in the initial stiffness for each of the backbone curves. As the drift was gradually increased, the difference between the simulated responses was more apparent, as the s_u = 76 kPa (1,580 psf) condition required the highest lateral force, whereas the s_u = 50 kPa (1,040 psf) conditions required the smallest lateral force for column drifts representative of the final thirteen cycles.

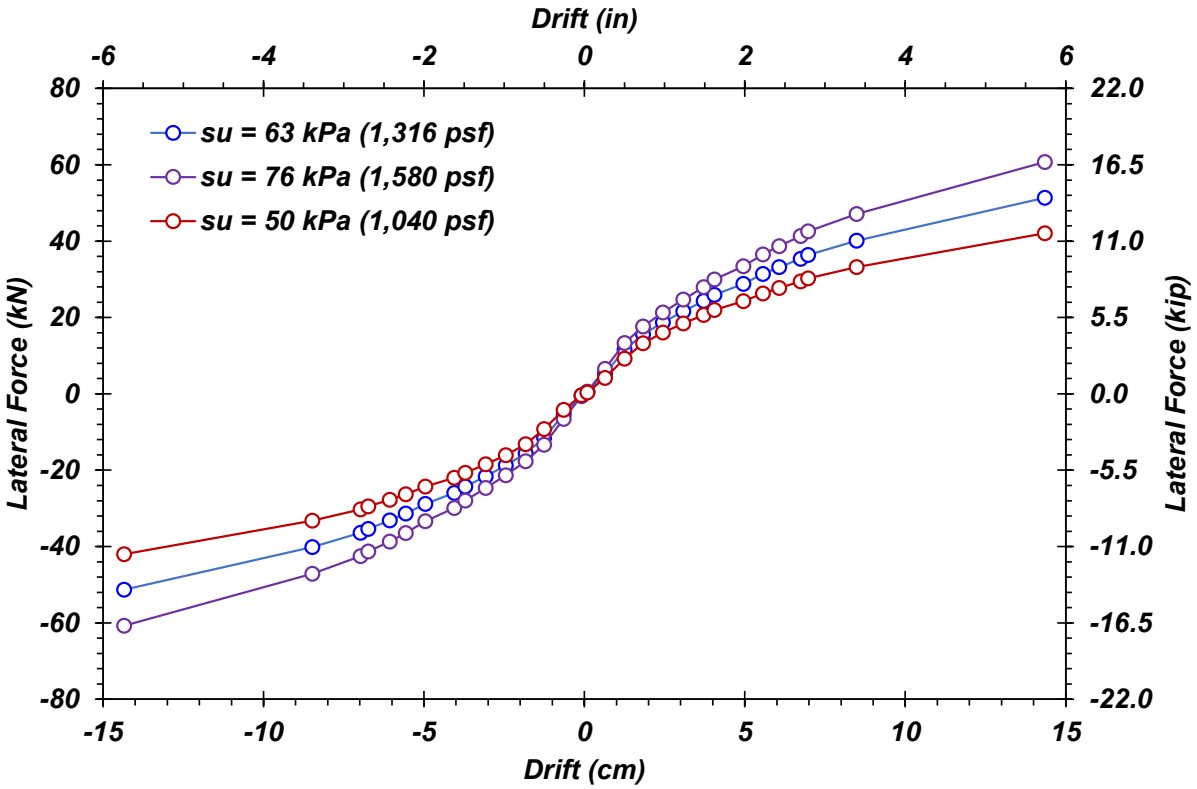

Figure 7.119: Comparison of the simulated drift-lateral load backbone curves representative of the fully-saturated (undrained) conditions at the GEFRS considering s_u = 63 kPa or 1,316 psf (average), 76 kPa or 1,580 psf (increase of 20%), and 50 kPa or 1,040 psf (decrease of 20%) with no additional axial load applied to the specimen.

During the dry season at the GEFRS, the upper most layer of Willamette Silt is nearly fully- or fully saturated at the depth of the base of the footing, according to relevant laboratory data (Dickenson et al. 2006). A representative friction angle of 30.4 degrees for the bearing soil was estimated from SCPT correlations for use in bearing capacity calculations (Section 7.2). The hysteretic SSI model simulated quasi-static, cyclic lateral loading tests on column-footing specimens bearing on soil which had varying degrees of saturation (S = 90%, 95%, and 98%). Similar to the model representative of the undrained conditions, the drift history recorded during Test 2 – S2 was used as an input to the model representative of the partially-saturated season, in addition to the saturation-dependent bearing capacity. The simulated drift-lateral load backbone curves for column footing specimens bearing on soils with various levels of partial saturation (Figure 7.120) demonstrated that changes in saturation had minimal effects on the simulated response of rocking specimens.

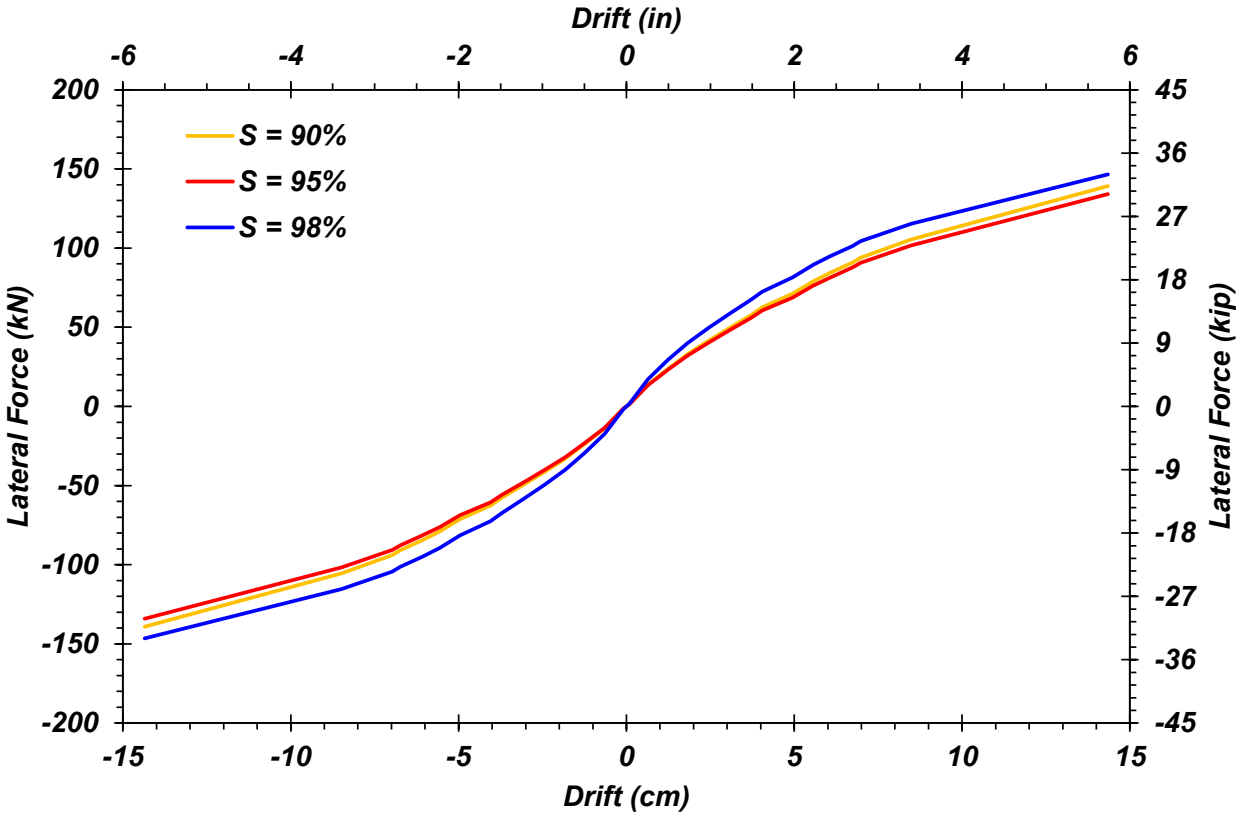

Figure 7.120: Comparison of drift-lateral load backbone curves representative of the various partially saturated conditions at the GEFRS without any additional axial load applied to the specimen. Degrees of saturation of 90%, 95%, and 98% corresponded to bearing capacities of 1,363 kPa (198 psi), 1,312 kPa (190 psi), and 1,281 kPa (186 psi), respectively.

The response of a simulated column-footing specimen subjected to a cyclic lateral loading test was substantially affected by the implementation of a 10% change in the effective friction angle, owing to the significant change in bearing capacity for relatively minor change in ϕ' (Figure 7.121, which considered S = 98%). The 10% increase in ϕ' corresponded to a 65 kN (14.6 kip) increase in the lateral load required to impose the column drift associated with the final, whereas a 10% decrease in ϕ' corresponded to a 41.5 kN (9.3 kip) decrease in the required lateral load. The increase in ϕ' also demonstrated a globally stiffer response, with a relatively high stiffness even at large column drifts exceeding 2.5 cm (1.0 in.).

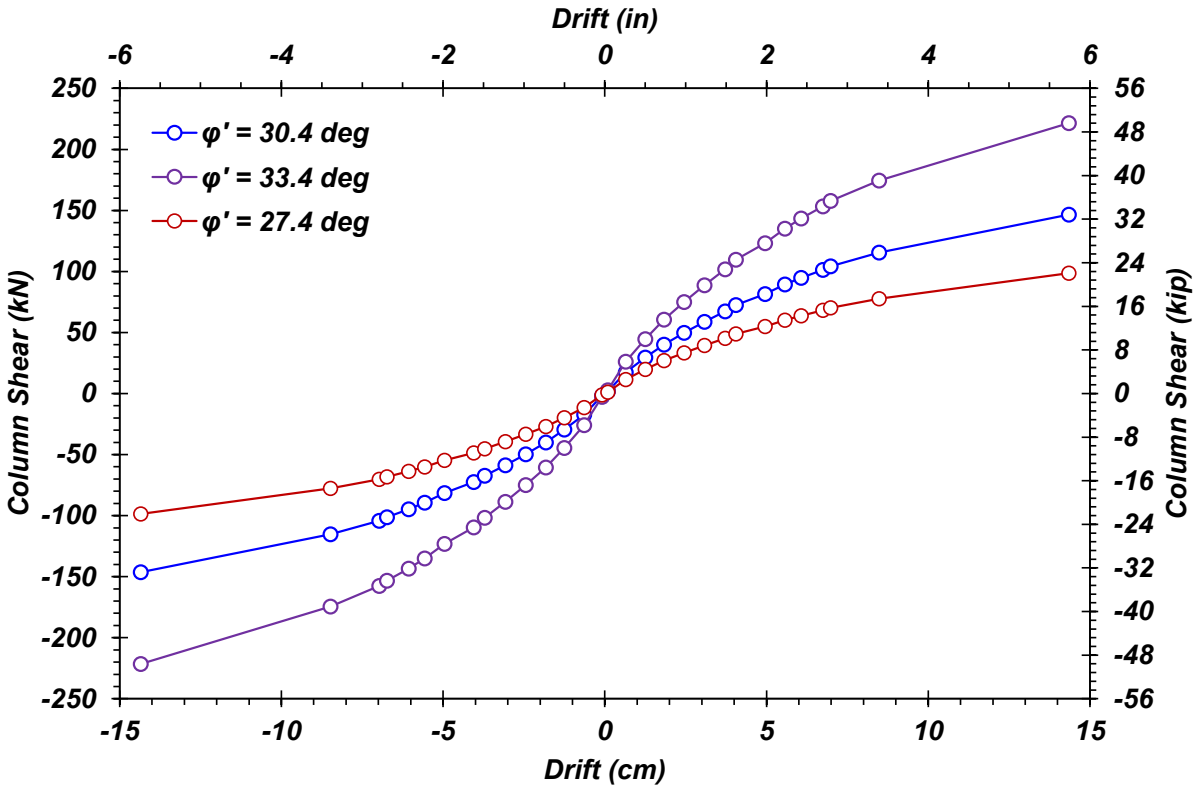

Figure 7.121: Comparison of the simulated drift-lateral load backbone curves representative of the partially-saturated conditions at the GEFRS considering ϕ' = 30.4º (average), 33.4º (increase of 10%), and 27.4º (decrease of 10%) with no additional axial load applied to the specimen.

Figure 7.122 shows a comparison of the backbone curves with varying magnitudes of axial load applied, provided a degree of saturation equal to 98% and a representative ϕ' of 30.4 degrees. The responses are similar to that of the undrained simulation, as the curves follow a similar initial stiffness regardless of the magnitude of the axial load applied. A larger axial load resulted in a larger nearly linear portion of the backbone curve, as the drift at which the backbone curves began to demonstrate a noticeable nonlinear response was higher for a greater axial load.

The model simulations of the seasonal-dependent subsurface response at the GEFRS facilitated the determination of critical parameters for the analyses to follow. The sensitivity analyses indicated that the undrained shear strength (undrained conditions), effective friction angle (partially saturated conditions), and the magnitude of the applied gravity load were the most critical parameters for the study. A less-critical parameter that still impacted the response to cyclic loading was the degree of saturation of the subsurface.

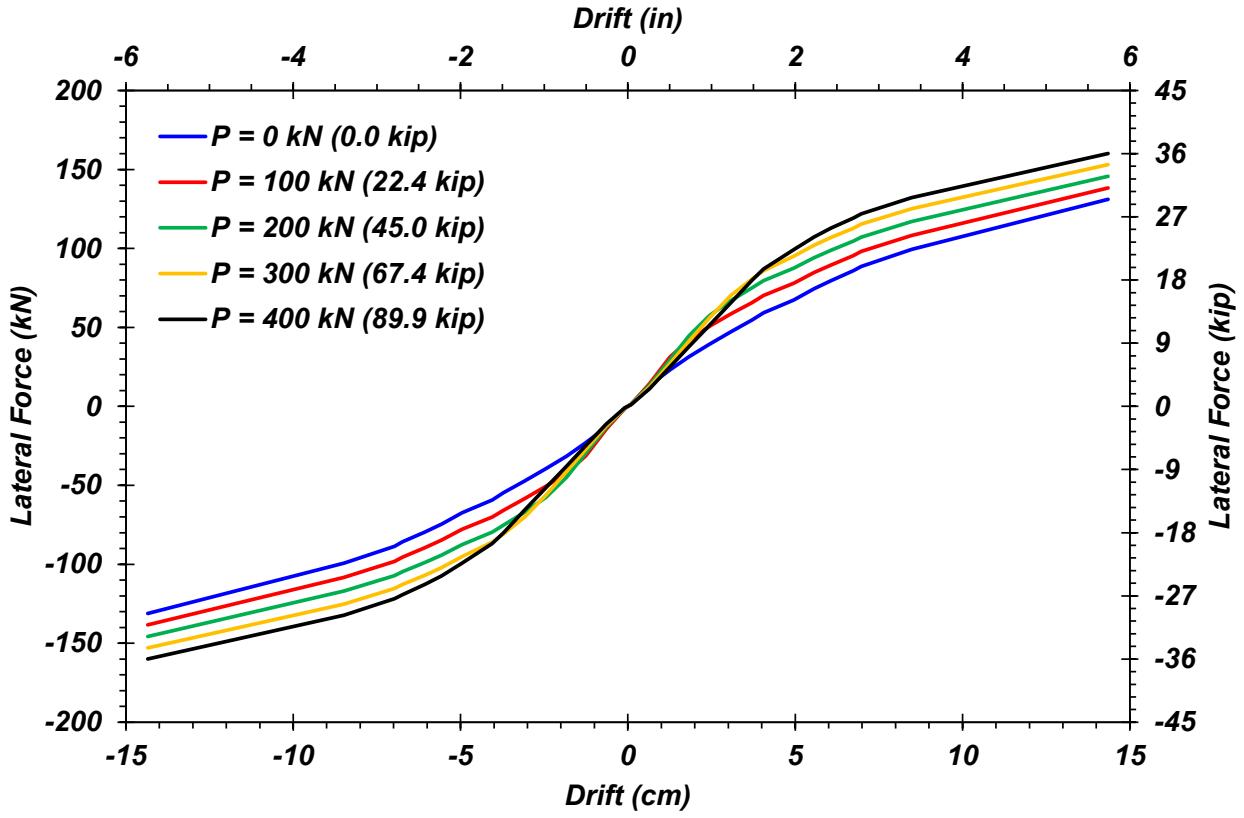

Figure 7.122: Comparison of the simulated drift-lateral load backbone curves representative of the partially-saturated (S = 98%) conditions at the GEFRS with additional axial loads of 0 kN (0 kip), 100 kN (22.4 kip), 200 kN (45.0 kip), 300 kN (67.4 kip), and 400 kN (89.9 kip) applied to the specimen.

7.5.2.2 Simulation of Full-Scale Cyclic Tests Performed by Sharma (2019)

Sharma (2019) performed a series of large-scale cyclic lateral loading tests on reinforced concrete footing specimens underlain by plastic soil. Extensive *in-situ* explorations and laboratory tests were performed to quantify the expected response of the subsurface to the rocking of foundations. The soil profile at the test site used by Sharma (2019) shares similar subsurface conditions with the OSU GEFRS (e.g., w, PL, LL, S), and thus provides an appropriate basis for evaluation of the SSI model developed herein. The range in undrained shear strength at the test site was 40 kPa (835 psf) to 80 kPa (1,671 psf) based on CPT correlations and UCS laboratory tests, with an initial, representative s_u of 75 kPa (1,566 psf) used in the study (Figure 7.123). Sharma (2019) reported a bearing capacity of 498 kPa as representative of the footings tested at this field site (introduced below), which does not appear to have been reduced for the resultant inclined load developed due to combined axial and lateral loading.

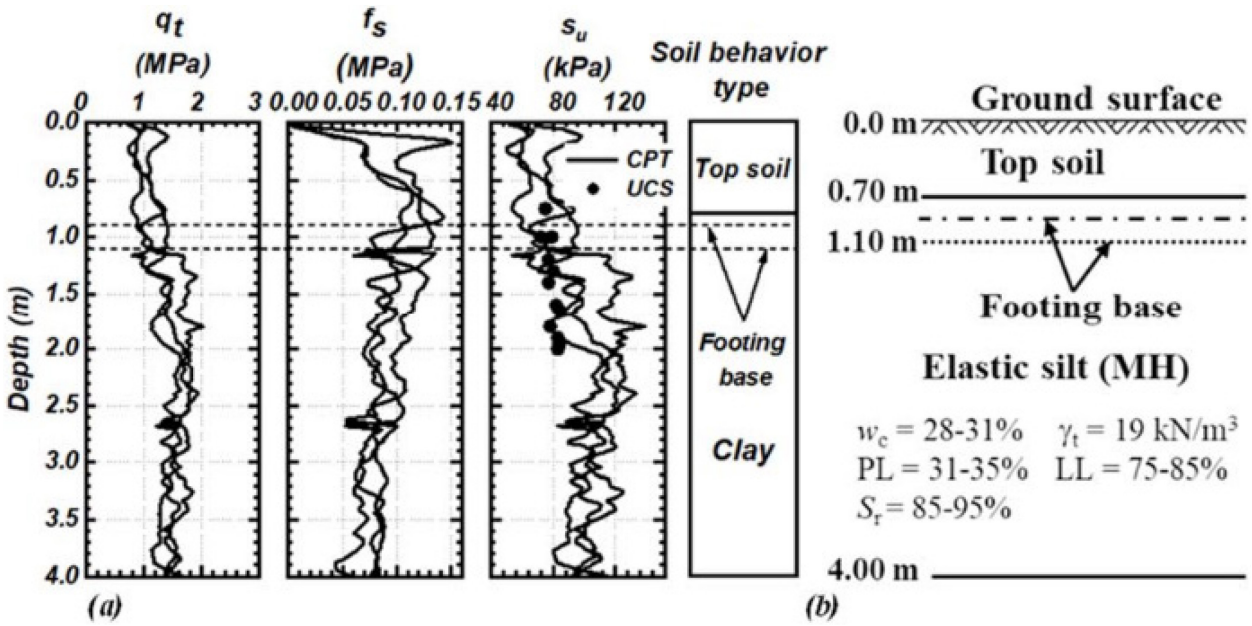

Figure 7.123: (a) CPT profile of test site with shear strengths from USC tests, and (b) site stratigraphy and lab test results (from Sharma 2019).

The specimens were subjected to cyclic loading and simulated using the hysteretic SSI model were 1.5 m by 1.0 m (4.9 ft. by 3.3 ft.) rectangular footings with a square steel tube column (0.2 m by 0.2 m in plan, 12.7 mm wall thickness) 2 m in length (6.6 ft.) extending from the center of the footing. The lateral load point was 2.53 m (8.3 ft.) above the base of the footing. The specimens were subjected to a series of quasi-static reversed lateral load cycles, controlled by a specified drift ratio (i.e., a displacement-controlled cyclic test) with a typical example provided in Figure 7.124.

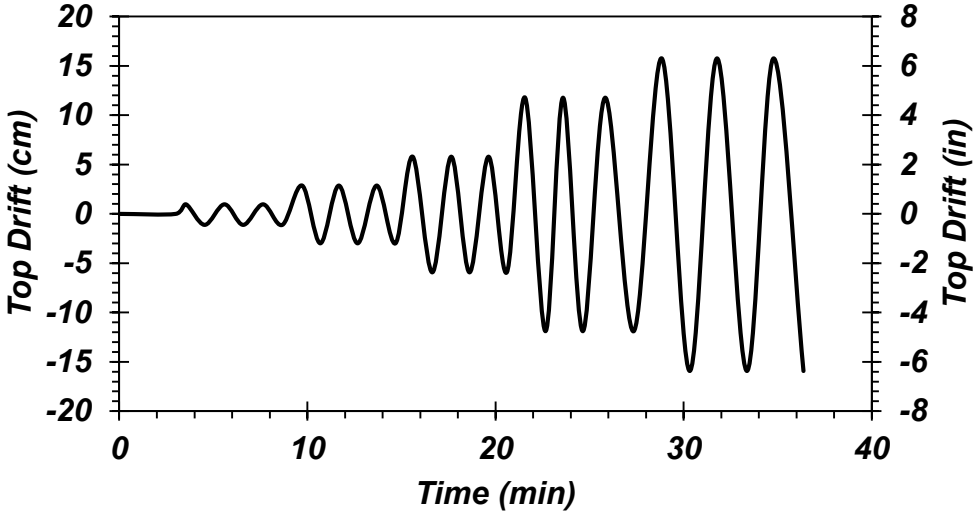

Figure 7.124: Typical top drift history for a reversed cyclic lateral load test (after Sharma 2019).

The hyperbolic spring-based hysteretic SSI model was used to simulate the quasi-static, cyclic lateral loading tests performed on rocking column-footing specimens reported by Sharma (2019). The parameters required to simulate the tests included the bearing capacity of the footing, the dimensions of the footing, and the lateral loading protocol. To compare the model output with the test results, a clear top drift-, footing rocking-, or footing rotation-lateral load hysteresis was mandatory. The hysteretic loading facilitated the determination of the other relationships based on trigonometric functions, as described in Section 7.5.1. Provided the required model inputs, the hyperbolic spring parameters were varied based on the ranges reported by Huffman et al. (2015) for the global footing database and the model output compared with the drift-lateral load backbone curve from the experimental tests.

The loading protocol consists of five "packets" (Figure 7.124), each with three cycles of identical displacement amplitude. The repetition of identical cycles has no impact on the SSI model output and are therefore neglected. To simulate a given test, the footing rotation shear force hysteresis was specified, with two data points representative of each loading "packet" (one for positive drift, one for negative drift). The footing rotation allowed for an estimate of the corresponding column drift to be calculated through trigonometry. The *EI* for the column was provided as 6.44 MN-m^2, and calculations of the imposed flexural deformations indicated that the additional drifts resulting from column bending were minimal due to the relatively low magnitudes of lateral force applied during the experimental program.

Two large-scale tests with no embedment were simulated as part of the current study: Test TS11 and Test LS11. Both tests were performed at the ground surface elevation (i.e., no embedment), with the combined self-weight and applied axial load equal to 58.5 kN (13.2 kip) and 64.1 kN (14.4 kip) for Test Ts11 and LS11, respectively, and were laterally loaded normal to the face of the footing (i.e., no oblique/diagonal loading). Test TS11 was performed at Station 2 and had an initial vertical factor of safety against bearing, FS_v, estimated to be 18.5. Specimen TS11 was loaded normal to the 1.5 m in length face of the footing, with the 1.0 m face running parallel to the direction of loading. The initial settlement from the self-weight of the specimen was determined to be 0.183 cm (0.07 in.). Figure 7.125 presents a schematic of the typical test setup and Figure 7.126b presents the footing rotation-applied moment (θ-M) results from Test TS11 (relationship shown within the red box).

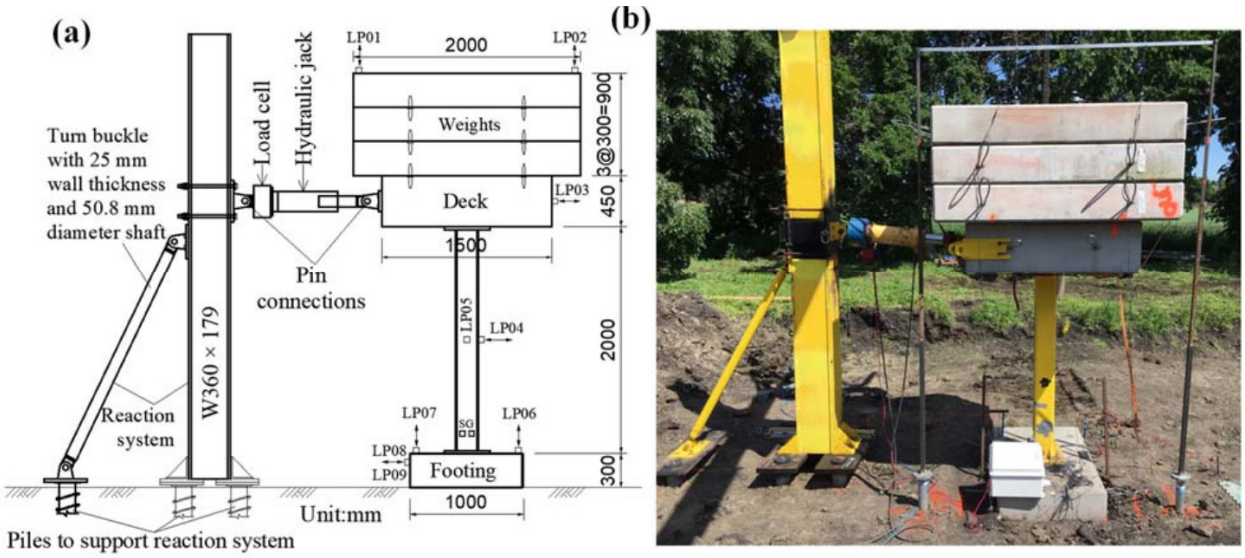

Figure 7.125: Setup of surface soil-footing-structure system: (a) drawing, and (b) photo of test (from Sharma 2019).

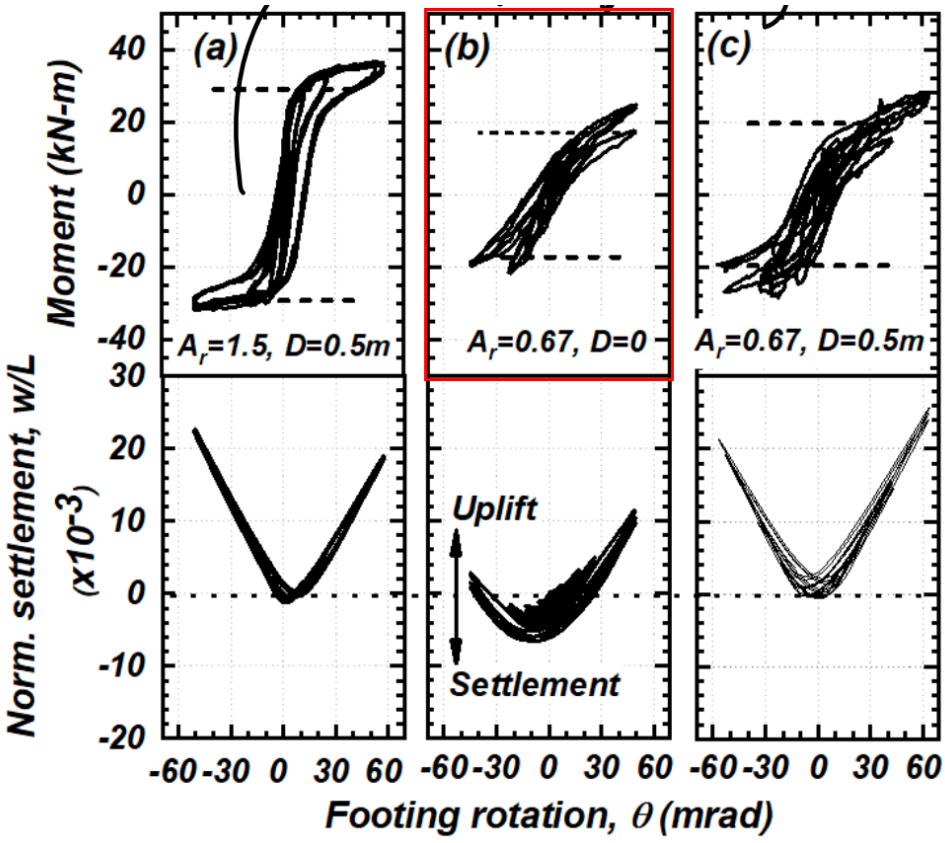

Figure 7.126: Relationship between applied moment and footing rotation for various tests conducted by Sharma (2019), with Test TS11shown in (b) (from Sharma 2019).

Three pairs of hyperbolic model parameters were used to simulate the quasi-static, cyclic column-drift-lateral load response of TS11 (Huffman et al. 2015): the global mean of k_1 = 0.013 and k_2 = 0.701, a pair representing the upper bound of the reported hyperbolic parameters (k_1 = 0.003, k_2 = 0.96), and the lower bound pair of parameters (k_1 = 0.003, k_2 = 0.96). The M_{stc} factor was held constant at the average value of 0.643 reported by Huffman et al. (2015). The representative bearing capacity was reported by Sharma (2019) as 498 kPa (10.4 ksf) based on laboratory test data and *in-situ* site investigations that indicated a representative s_u equal to 75 kPa or 1,566 psf (Figure 7.123). The CPT and laboratory results indicated a minimum s_u equal to 40 kPa (835 psf) which corresponded to a bearing capacity of 368 kPa (7.7 ksf) in proximity to the local zone of shearing under rocking loads below the footing. When considering the inclined loading due to the axial and lateral load acting on the footing and typical bearing capacity modification factors for inclined loading (Meyerhof 1963; Fang 1991) and the minimum s_u, the realistic minimum bearing capacity was calculated equal to 360 kPa (7.7 ksf).

A parametric evaluation of Test TS11 was conducted to identify ranges in simulated responses for comparison to the reported experimental lateral load-drift results and are presented in Figures 7.127 to 7.129. The variation of the hyperbolic model (bearing spring) parameters indicated that the lower bound and average pairs represented the shape of the experimental backbone curve the best, whereas the upper bound provided an over-estimate of the curvature of the hyperbolic response. All hyperbolic pairs over-estimated the experimental lateral loads required to impose the rotation history (Figure 7.127). The reduction in shear strength from 75 kPa to 40 kPa (1,566 psf to 835 psf) and including the effect of load inclination resulted in a simulated curve that also over-estimated the experimental results when using the average bearing spring hyperbolic model parameters (Figure 7.128). Owing to the soil deposit-specific nature of the hyperbolic model parameters and lack of site-specific footing axial loading test data for the conditions at the Sharma (2019) test site, a third simulation was conducted using the lower bound hyperbolic model parameters, the minimum s_u, and a bearing capacity reduced for load inclination (Figure 7.129). The results indicate that these combinations of parameters most appropriately capture the observed lateral load-column drift response for drifts of up to approximately 7 cm (2.75 in). These parametric investigations of the rocking response of TS11 and of footings in general indicate that forward predictions of the rocking behavior of bridge substructures are controlled by accurate estimates of undrained shear strengths in the local zone of soil directly below the footing, bearing capacity calculations which account for load inclination, and selection of appropriate hyperbolic parameters.

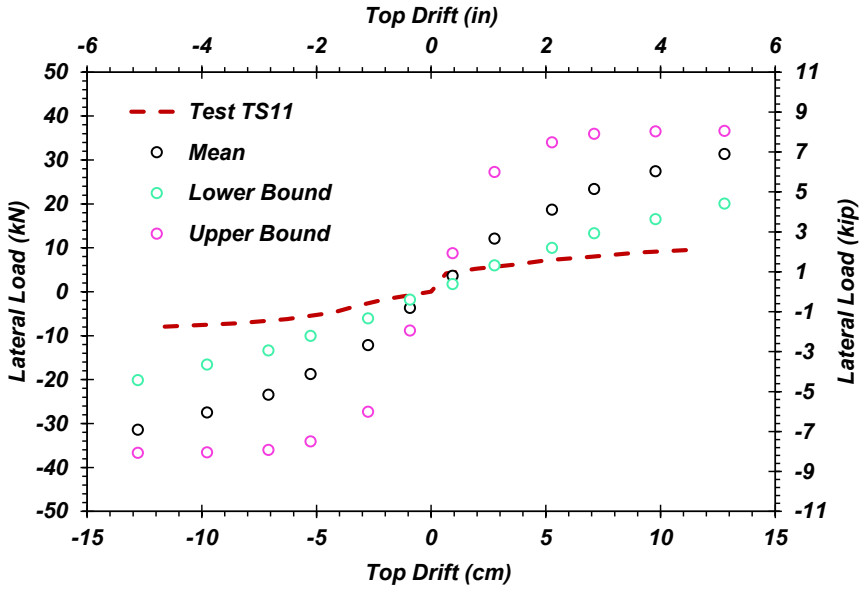

Figure 7.127: Comparison of the lateral load-drift backbone curves produced by the hysteretic SSI model provided the average (k_1 = 0.013, k_2 = 0.701), upper bound (k_1 = 0.003, k_2 = 0.540), and lower bound (k_1 = 0.003, k_2 = 0.960) hyperbolic parameter pairs (M_{STC} = 0.55, q_{ult} = 498 kPa or 10.4 ksf) with the load-drift backbone curve observed during Test TS11 (Sharma 2019).

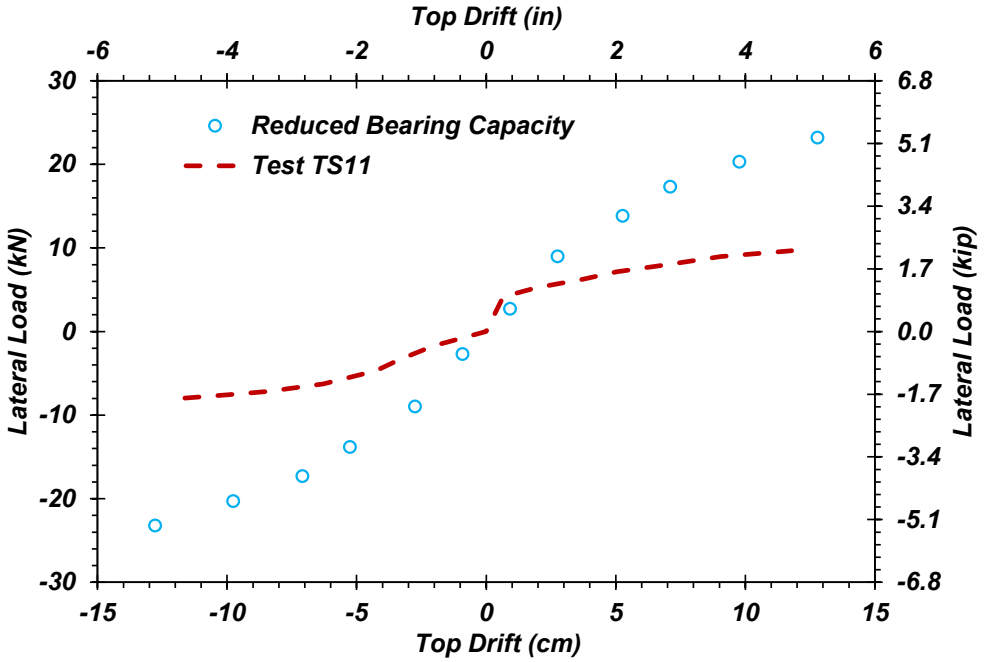

Figure 7.128: Comparison of the lateral load-drift backbone curve produced by the hysteretic SSI model provided the average (k_1 = 0.013, k_2 = 0.701) hyperbolic parameter pairs (M_{STC} = 0.55) and a reduced q_{ult} = 368 kPa (7.7 ksf) with the load-drift backbone curve observed during Test TS11 (Sharma 2019).

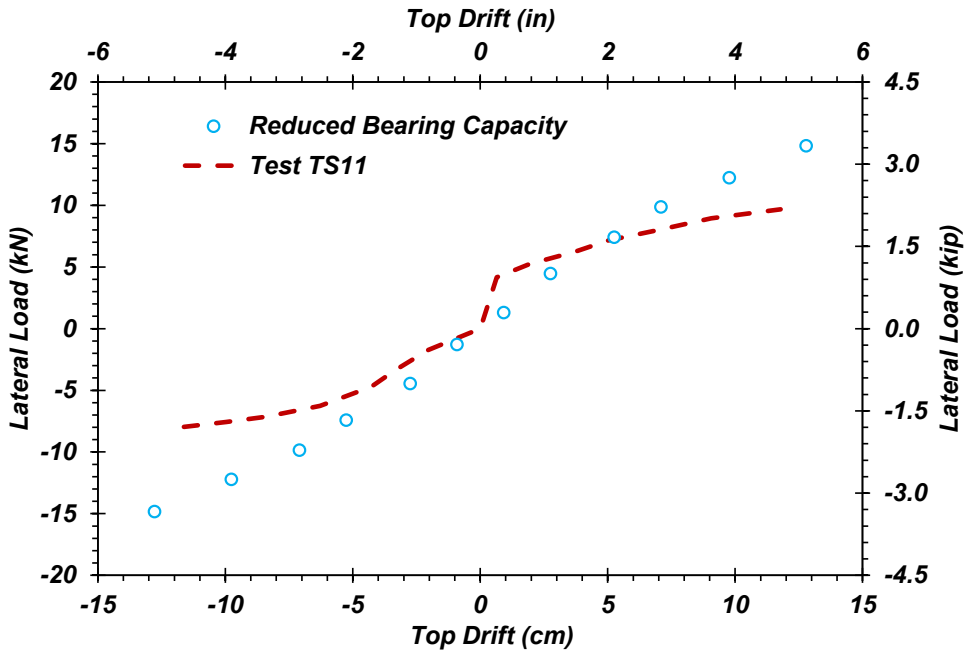

Figure 7.129: Comparison of the lateral load-drift backbone curve produced by the hysteretic SSI model provided the lower bound (k_1 = 0.03, k_2 = 0.540) hyperbolic parameter pairs (M_{STC} = 0.55) and a reduced q_{ult} = 368 kPa (7.7 ksf) with the load-drift backbone curve observed during Test TS11 (Sharma 2019).

The SSI model was also used to simulate Test LS11 performed by Sharma (2019). Test LS11 produced a footing rotation-column shear hysteresis substantially stiffer than the response observed TS11, with Sharma (2019) owing this behavior to changes in the direction of loading relative to the orientation of the footing. Specimen LS-11 was loaded normal to the 1.0 m in length face of the footing, with the 1.5 m face running parallel to the direction of loading. The initial FS_v and the initial settlement were equal to 19.7 (P = 64.1 kN or 14.4 kip) and 0.29 cm (0.11 in.), respectively. Figure 7.130a presents the footing rotation-applied moment (θ-M) results from Test TS11 (relationship shown within the red box).

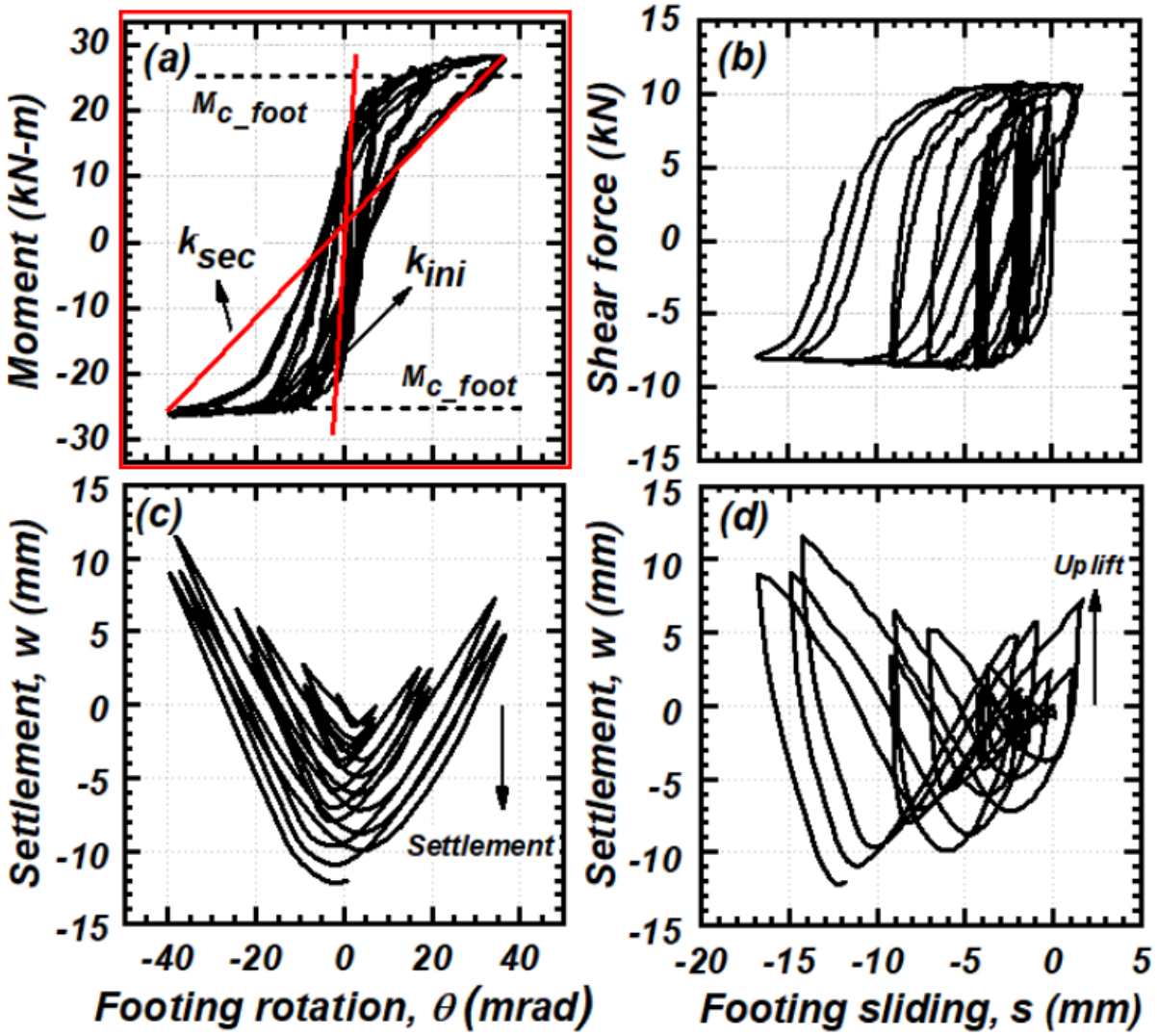

Figure 7.130: Relationship between applied moment and footing rotation for Test LS11 (Sharma 2019).

The initial portion of the backbone curve followed by the rapid change to a near-zero slope proved to be best simulated by the upper bound hyperbolic parameter pair (k_1 = 0.003, k_2 = 0.960), provided the representative s_u of 75 kPa (1,566 psf) with a corresponding bearing capacity of 498 kPa (10.4 ksf) reported by Sharma (2019), as shown in Figure 7.131. Similar to the simulation of Test TS11, all hyperbolic parameter pairs overestimated the lateral load-drift experimental response. The simulation was repeated using the reduced undrained shear strength and inclusion of load inclination reductions to bearing capacity which similarly overestimated the response using the average hyperbolic parameters (Figure 7.132), although the small-drift initial stiffness appeared well-captured.

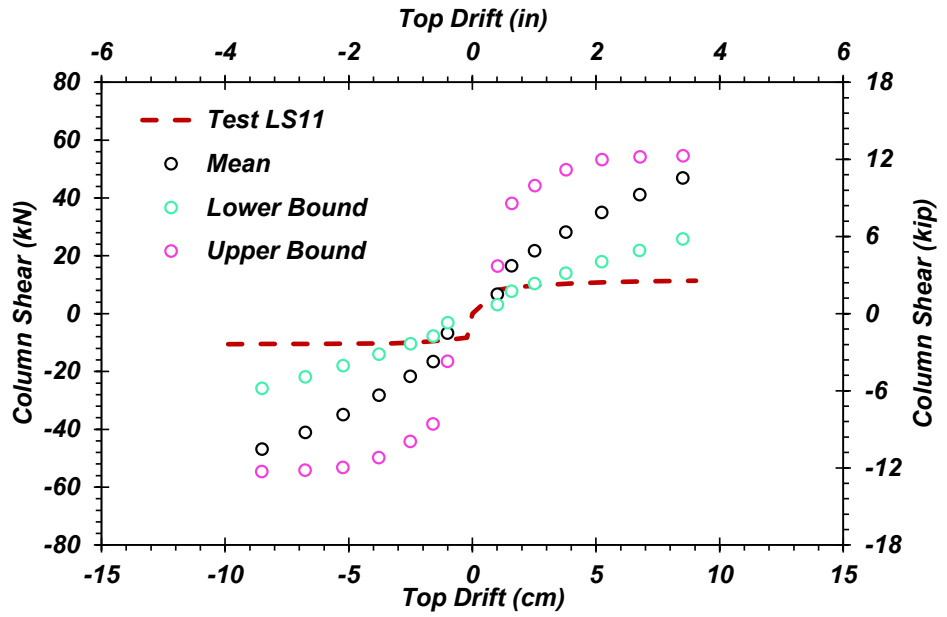

Figure 7.131: Comparison of the lateral load-drift backbone curves produced by the hysteretic SSI model provided the average (k_1 = 0.013, k_2 = 0.701), upper bound (k_1 = 0.003, k_2 = 0.540), and lower bound (k_1 = 0.003, k_2 = 0.960) hyperbolic parameter pairs (M_{STC} = 0.55, q_{ult} = 498 kPa or 10.4 ksf) with the load-drift backbone curve observed during Test LS11 (Sharma 2019).

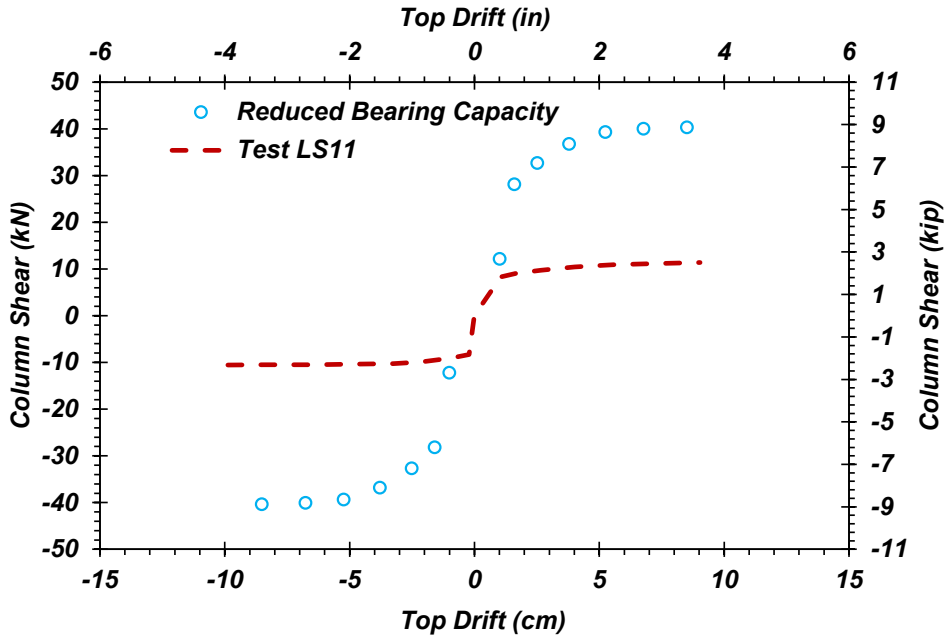

Figure 7.132: Comparison of the lateral load-drift backbone curve produced by the hysteretic SSI model provided the upper bound (k_1 = 0.003, k_2 = 0.960) hyperbolic parameter pairs (M_{STC} = 0.55) and a reduced q_{ult} = 368 kPa (7.7 ksf) with the load-drift backbone curve observed during Test LS11 (Sharma 2019).

The effect of varying the hyperbolic parameters is best analyzed through the simulation of a full-scale experimental test with clear displacement histories. Test 2 – S2, while performed on foam soil simulant rather than actual soil, produced a clear displacement history using a loading protocol prescribed by (Shrestha 2019) that has been proven effective for the evaluation of column-footing substructures. Figure 7.133 presents a comparison of the backbone curves simulated using the average (k_1 = 0.013, k_2 = 0.701), upper bound (k_1 = 0.003, k_2 = 0.960), and lower bound (k_1 = 0.030, k_2 = 0.540) hyperbolic parameter pairs (Huffman et al. 2015), provided the Test 2 – S2 drift history, no additional applied axial load, and assuming the partially-saturated season (S = 98%) bearing capacity representative of the field site at the GEFRS (1,281 kPa or 26.75 ksf) and the corresponding load inclination factors (Meyerhof 1963, Feng 1991). It is evident that the response of foundations subjected to rocking depends on the hyperbolic parameters chosen, as the difference in the simulated lateral force may be substantial depending on the parameters selected.

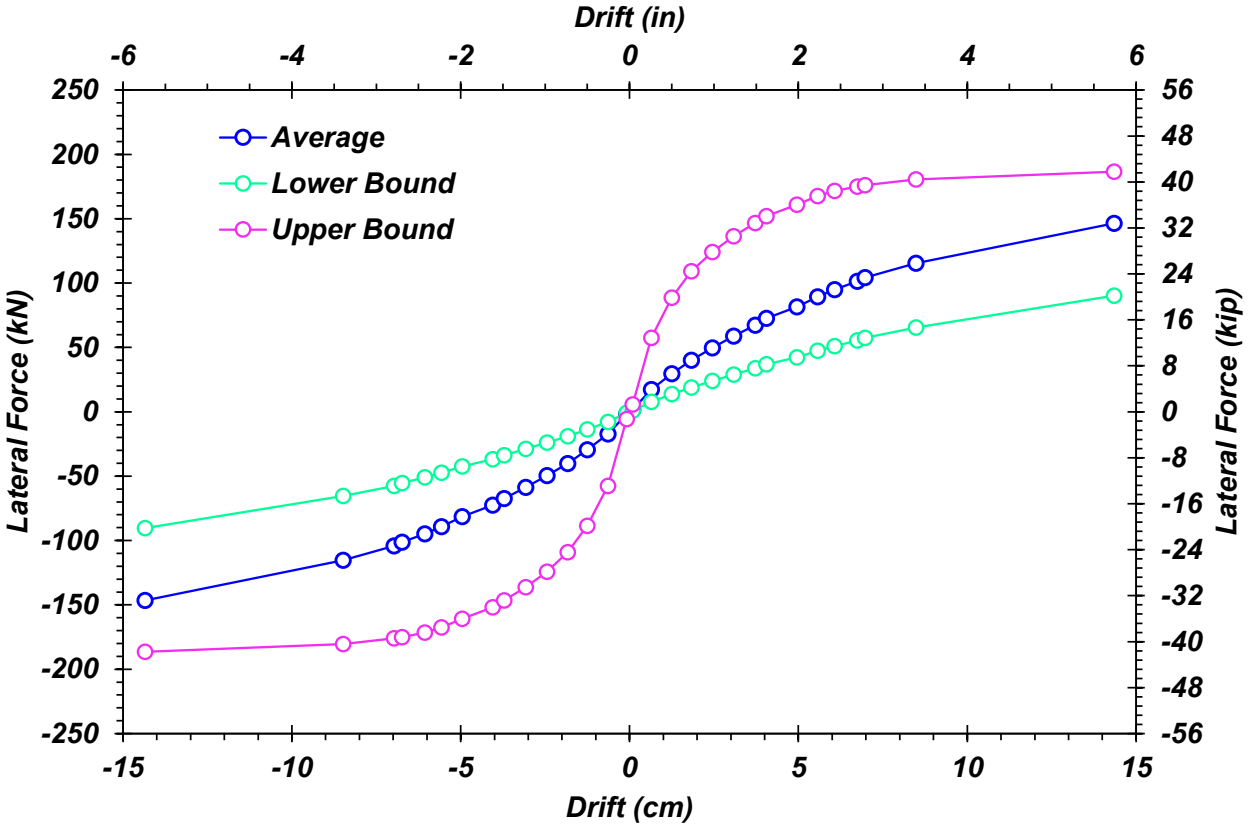

Figure 7.133: Comparison of simulated hypothetical quasi-static cyclic lateral loading backbone curves assuming an average (k_1 = 0.013, k_2 = 0.701), upper bound (k_1 = 0.003, k_2 = 0.960), and lower bound (k_1 = 0.030, k_2 = 0.540) pair of hyperbolic parameters. The bearing capacity was assumed to be 1,281 kPa (26.8 kPa).

7.5.3 Summary of Section 7.5

The development of a hysteretic SSI force-displacement model required the prior development of a nonlinear mobilized bearing resistance model and the nonlinear SSI spring model that replicated the initial "pull" portion of snap-back tests. The mobilized bearing resistance curves that further models built upon used hyperbolic mobilized resistance parameters provided by Huffman et al. (2015) based on full-scale footing loading tests at the GEFRS. The static load snap-back models, discussed in Section 7.5.1.3, simulated the full-scale snap-back test performed on May 22nd, 2023.

From the snap-back SSI models and with consideration to the extended Masing rules (Kramer 1996), a hysteretic SSI model was developed and used as the bases for a parametric study aimed to determine the most critical factors influencing the column drift-lateral load relationship of column-footing specimens subjected to quasi-static, cyclic lateral loading. Unconfined compression tests were performed on XPS soil simulant foam to better understand the strength and stiffness of the material, in addition to observing the strain rate-dependency of these properties to facilitate the simulation of Test 2 – S2 (Parson 2022). The UCS test program indicated an elastic, nearly perfectly plastic stress-strain response of the soil simulant. These properties were subsequently used to create the SSI model, which was validated with the drift-lateral load backbone curve from Test 2 – S2.

After the model had been verified against the full-scale tests on the soil simulant foam, the hysteretic SSI model was adapted to include real-soil hyperbolic properties and subjected to a parametric study. The study concluded that the column drift-lateral load backbone curve depends on the seasonal conditions (i.e., a weaker response considering an undrained analysis representative of the wet season and stiffer, stronger response considering a drained analysis representative of the dry season). Additionally, the applied axial load that the column-footing specimen was subjected to was a significant parameter that governed the response. The last critical parameter was the strength of the material (e.g., s_u for wet season, ϕ' for dry season). A far less critical parameter was the degree of saturation for the partially saturated condition representative of the dry, summer season.

The SSI model was then used to simulate two full-scale cyclic lateral loading tests performed by Sharma (2019) within a parametric study. The parametric evaluation of Tests TS11 and LS11 concluded that the range in simulated responses varied substantially based on the hyperbolic parameters chosen and the bearing capacity of the footing. The simulated load-drift responses developed through the use of the global mean hyperbolic parameters were compared with the upper and lower bounds (Huffman et al. 2015), where the shape of the Test TS11 load-drift experimental results best represented by the lower bound pair of parameters and Test LS11 best represented by the upper bound pair, albeit both simulated load-drift curves overestimated the experimental response. The bearing capacity used in each model was reduced to the realistic minimum based on the site-specific data resented by Sharma (2019) and also considered the reduction in bearing capacity due to the effects of load inclination. The combination of these parameters produced a simulated load-drift curve that most appropriately represented Test TS11, whereas the simulation still overestimated the experimental response observed from Test LS11. A controlled quasi-static cyclic lateral loading test at the GEFRS would be of great assistance in the assessment of accuracy of the SSI model.

7.6 SUMMARY AND CONCLUSIONS

7.6.1 Summary

The detrimental effects of seismic loading to structures since the 1971 San Fernando earthquake brought attention to structural deficiencies present in reinforced concrete column-footing substructures. Bridge substructures constructed in Oregon prior to this period likewise exhibit structural reinforcement detailing deficiencies, pointing to the need to develop cost-effective, rapidly employed retrofit strategies to restore the critical transportation network necessary to perform post-earthquake rescue and recovery operations. The majority of vintage bridge substructures in Oregon were designed to withstand only gravity loads, with little to no consideration of the dynamic loading associated with a seismic event. Recent studies (Higgins et al. 2017, Shrestha 2019, Parson 2022) have suggested a novel Titanium Alloy Bar (TiAB) ligament and spiral retrofit approach to improve the seismic performance of circular vintage column-footing specimens due to the high strength of the retrofit, the ease of constructability, and the additional confinement provided by the retrofit.

The structural portion of this thesis completed the work initiated by Parson (2022) through the conduct and analyses of two quasi-static, cyclic lateral loading tests performed on full-scale, previously failed, reinforced concrete column footing specimens passively confined to prevent rocking displacements. The experimental results were described in terms of the overall force-displacement response and strain histories recorded by instruments within, and fixed to, the specimen. The effects of soil-structure interaction (SSI) on the performance of column-footing specimens subjected to dynamic loading have only been recently studied by Parson (2022) through the use of a soil simulant and fabricated springs. This thesis advances the previous work through the performance and analysis of experimental snap-back tests on full-scale, embedded vintage column-footing specimens constructed at the Geotechnical Engineering Field Research Site (GEFRS). Further, this thesis presents development and calibration of nonlinear SSI models in order to simulate the snap-back and previously performed quasi-static, cyclic lateral loading tests on a soil simulant. Critically, the effects of strain rate on the strength and stiffness of the soil simulant on the global response of such specimens could now be assessed. The calibrated hysteretic SSI models also facilitated the simulation of previously conducted quasi-static, cyclic lateral loading tests on actual soil (Sharma 2019). The hysteric SSI models also allowed a parametric study to be conducted to explore the critical elements impacting the dynamic response of column-footing specimens bearing on soils that are influenced by changing environmental factors.

7.6.2 Conclusions

The following conclusions based on the experimental results and analytical findings stemming from this study include:

1. The experimental results from the quasi-static, cyclic lateral load test performed on a previously-failed and subsequently-retrofitted Specimen 1 (Test 1 – S9) indicated that an insufficient retrofit of the footing (i.e., near-surface-mounted and post-tensioned steel bars) led to a footing failure-controlled response as the footing was passively confined to the strong floor, thus restrained from rocking. Failure of the footing did

not allow the TiAB retrofit to reduce the seismic demand on the vintage specimen as designed, owing to the severe strength degradation observed within the footing (i.e., concrete cracking and splitting).

2. The experimental results from Test 10 – S3, performed on a previously-failed and subsequently-retrofitted column, had additional reinforcement installed within the footing and led to a column-footing connection-controlled response. Negligible damage was observed in the footing which allowed the TiAB retrofit to withstand the majority of the flexural demands imposed as the vintage steel reinforcement yielded at large drift ratios.

3. The experimental results from snap-back tests on embedded, full-scale, vintage column-footing specimens performed in the wet and dry seasons indicated the global rocking response of a substructure was dependent on the seasonal-conditions of the bearing and lateral resistance soils.

4. The experimental results from the snap-back tests indicated that the strains induced within the embedded steel reinforcements depended only on the magnitude of the applied lateral load prior to the instantaneous release.

5. Through analyses of the damped free vibration response of the specimen subjected to repeated snap-back testing, it was evident that the dry season resulted in a stiffer response of the subsurface compared to the wet season when subjected to rocking displacements due to the decrease in the damping ratio relative to the percent change in the applied lateral load (26%) calculated from the May 22nd snap-back (F = 28.9 kN or 6.50 kip) compared to the 18% relative reduction in the damping ratio calculated from the December 5th snap-back test (F = 28.1 kN or 6.32 kip). Similarly, an increase in the applied lateral load (May 22nd snap-back, F = 38.6 kN or 8.67 kip) corresponded to a stiffer response, as the relative reduction in the damping ratio increased to 40%.

6. Analysis of the bearing soil response to snap-back testing indicated that for the lateral loads applied (e.g., maximum of 38.6 kN or 8.67 kip), the bearing soils responded in a nonlinear-elastic manner and induced a maximum reduction in the soil shear modulus of 14%.

7. Nonlinear SSI models were developed to simulate the snap-back and quasi-static, cyclic lateral loading tests using a previously developed bearing pressure-displacement model by Huffman et al. (2015) developed for shallow foundations bearing on plastic soils which can be calibrated through specification of site-specific hyperbolic model parameters.

8. Simulations of the initial lateral load application of snap-back tests (i.e., the “pull” prior to release) indicated that applied moment-imposed drift relationships were not substantially impacted by a 100 kN (22.4 kip) increase in the axial load applied to the top of the column. Additionally, the seasonal changes in the expected bearing capacity (drained, “dry”, and undrained, “wet” conditions) of the footing were

evaluated, with the simulated responses for the dry season observed to be significantly stiffer than the wet season. The effects of varying degrees of saturation on the applied moment-imposed drift relationships were minimal.

9. The unconfined compression test program on Extrude Polystyrene (XPS) foam soil simulant used in the quasi-static, cyclic lateral loading tests indicated sensitivity of the strength and stiffness to strain rate-effects and facilitated specification of strain rate-compatible material properties and led to an accurate simulation of the full-scale quasi-static, cyclic lateral loading test conducted on a specimen situated on the soil simulant.

10. A parametric study conducted with the hysteretic SSI model indicated that the strength parameter (e.g., undrained shear strength for the wet season, effective friction angle for the dry season) was the most critical parameter when simulating hypothetical quasi-static, cyclic lateral loading tests at the GEFRS. Less critical parameters included the degree of partial saturation of the subsurface and the magnitude of the axial load applied to the top of the specimen.

11. The simulation of full-scale, quasi-static, cyclic lateral loading test performed on actual soil (Sharma 2019) resulted in overestimates of the lateral load-drift relationships, which exemplified the importance of accounting for load inclination on the computed/specified bearing capacity, obtaining site-specific hyperbolic parameters to capture the bearing response of foundation soils, and a laboratory test program to determine the appropriate shear strength parameters.

7.7 REFERENCES

AASHTO. (2017). AASHTO LRFD Bridge Design Specifications (8th ed.). American Association of State Highway and Transportation Officials. ACI Committee 440. (2017). ACI 440.2R-17: Guide for the Design and Construction of Externally Bonded FRP Systems for Strengthening Concrete Structures. ACI 440.2R-17. Detroit, MI.

Akbas, S. O., and Kulhawy, F. H. (2009). Axial Compression of Footings in Cohesionless Soils I: Load-Settlement Behavior. Journal of Geotechnical and Geoenvironmental Engineering, ASCE, 135(11), 1562-1574.

American Concrete Institute Committee 318, "Building Code Requirements for Structural Concrete (ACI 318-02)," American Concrete Institute, Farmington Hills, Michigan, 2002, Section 10.11.1.

Andrus, R. D., & Stokoe II, K. H. (2000). Liquefaction Resistance of Soils from Shear Wave Velocity, Journal of Geotechnical and Geoenvironmental Engineering, 126(1), 1015-1025.

Cairns, J., and Arthur, P. D. (1979). Strength of Lapped Splices in Reinforced Concrete Columns. ACI Journal Proceedings, 76(2). https://doi.org/10.14359/6947

Campione, G., Miraglia, N. and Papia, M. (2004). Strength and Strain Enhancements of Concrete Columns Confined with FRP Sheets. Structural Engineering and Mechanics, 18(6), pp.769-790.

Chai, Y. H., Priestley, M. J. N., and Seible, F. (1994). Analytical Model for Steel-Jacketed RC Circular Bridge Columns. ASCE Journal of Structural Engineering, 120(8), 2358–2376.

Dickenson, S. E., Haines, B. Z., McMullen, C.T. and Reznick, B. S. (2006). "Characterization of the Geotechnical Engineering Field Research Site at Oregon State University, 3rd Edition." Oregon State University Engineering, Corvallis, OR.

Duncan, J.M., and Mokwa, R.L. (2001). Passive Earth Pressure: Theories and Tests. Journal of Geotechnical and Geoenvironmental Engineering, 127(3), 248-257.

ElGawady, M., Endeshaw, M., McLean, D., and Sack, R. (2010). Retrofitting of Rectangular Columns with Deficient Lap Splices. Journal of Composites for Construction, 14(1), 22–35.

Fang, H. Y. (1991). "Foundation Engineering Handbook". 2nd edition, Springer Science and Business Media.

Girard, C., and Bastien, J. (2002). Finite-Element Bond-Slip Model for Concrete Columns under Cyclic Loads. ASCE Journal of Structural Engineering, 128(12), 1502–1510.

Higgins, C. C., Knudtsen, J., Amneus, D., and Barker, L. (2017). Shear and Flexural Strengthening of Reinforced Concrete Beams with Titanium Alloy Bars. Proceedings of

the 2nd World Congress on Civil, Structural, and Environmental Engineering (CSEE'17), 1–8.

Huffman, J. C., Strahler, A. W., and Stuedlein, A. W. (2015). "Reliability-based serviceability limit state design for immediate settlement of spread footings on clay." Soils Found., 55(4), 798–812.

Jana, A., & Stuedlein, A. W. (2021) Monotonic, Cyclic, and Post-cyclic Responses of an Alluvial Plastic Silt Deposit. Journal of Geotechnical and Geoenvironmental Engineering, 147(3), 04020174.

Jana, A., Donaldson, A. M., Stuedlein, A. W., Evans, T. M. (2021) Deep, In Situ Nonlinear Dynamic Testing of Soil with Controlled Blasting; Instrumentations, Calibration, and Application to a Plastic Silt Deposit. Geotechnical Testing Journal.

Khosravi, A. and McCartney, J. S. (2012). Impact of Hydraulic Hysteresis on the Small-Strain Shear Modulus of Low Plasticity Soils. Journal of Geotechnical and Geoenvironmental Engineering, 138(11), pp.1326-1333.

Khosravi, A., Stuedlein, A. W., and Higgins, C. (2021). New Formulation for Estimating the Moment Capacity of Rocking Shallow Foundations Resting on Partially Saturated Soil. Journal of Bridge Engineering, 26(11), 04021804.

Khosravi, A., Shrestha, S. Stuedlein, A. W., Higgins, C. (2022). Titanium Seismic Substructure Retrofit to Enable Rocking of Bridge Foundations Considering Soil–Structure Interaction: Experiments and Numerical Simulations. Journal of Bridge Engineering, 28(2).

Kramer, S. L. (1996). "Geotechnical Earthquake Engineering." Prentice-Hall, New Jersey.

Kulhawy, F. H., and Mayne, P.W. (1990). Manual on Estimating Soil Properties for Foundation Design. EL-6800, Research Project 1493-6, Electric Power Research Institute, Palo Alto, California. 308 pp.

Li, Q., Stuedlein, A. W., and Barbosa, A. R. (2017). Torsional Load Transfer of Drilled Shaft Foundations. Journal of Geotechnical and Geoenvironmental Engineering, 143(8).

Lu, N. and Likos, W. J. (2006). Suction Stress Characteristic Curve for Unsaturated Soil. Journal of Geotechnical and Geoenvironmental Engineering, 132(2), pp.131-142.

Lukose, K., Gergely, P., and White, R. N. (1982). Behavior of Reinforced Concrete Lapped Splices for Inelastic Cyclic Loading. Journal of American Concrete Institute, 79(5), 355–365.

Lynn, A. C., Moehle, J. P., Mahin, S. A., and Holmes, W. T. (1996). Seismic Evaluation of Existing Reinforced Concrete Building Columns. Earthquake Spectra, 12(4), 715–739.

Martin, J. P. (2018). A Full-Scale Experimental Investigation of the Bearing Performance of Aggregate Pier-Supported Shallow Foundations. M.S. Thesis, Oregon State University, Corvallis, OR.

Masing, G. (1926). "Eigenspnnungen und Verfestigung beim Messing." 2nd Int. Congress on Applied Mechanics, Orell Fussli Zurich, Switzerland.

Mayne, P. W. (2007). Cone Penetration Testing, A Synthesis of Highway Practice. National Cooperative Highway Research Program, Synthesis 368. Transportation Research Board, Washington, D.C. 126 pp.

McCartney, J.S., and Khosravi, A. (2013). Field-Monitoring System for Suction and Temperature Profiles under Pavements. Journal of Performance of Constructed Facilities, 27(6)

Melek, M., and Wallace, J. W. (2004). Performance of Columns with Short Lap Splices. In 13th World Conference on Earthquake Engineering Vancouver, B.C., Canada August 1-6, 2004.

Meyerhof, G. G. (1963). Some Recent Research on the Bearing Capacity of Foundations. Canadian Geotechnical Journal, 1(1), 16-26.

Nako, A., Shike, C., Six, J., Johnson, B., Dusicka, P., and Selamawit, M. (2009). Seismic Vulnerability of Oregon State Highway Bridges: Mitigation Strategies to Reduce Major Mobility Risks. Salem, OR: Oregon Department of Transportation, Bridge Engineering Section.

Nako, A., Shike, C., Six, J., Johnson, B., Dusicka, P., and Selamawit, M. (2014). Oregon Highways Seismic Plus Report. Salem, OR: Oregon Department of Transportation, Bridge and Geo-Environmental Sections.

Newton, V. C. (1975). Ultimae Bearing Capacity of Shallow Foundations on Plastic Silt. M.S. Thesis, Oregon State University, Corvallis, OR.

Ouyang, Z., and Mayne, P. W. (2017). Effective Friction Angle of Clays and Silts from Piezocone Penetration Tests. Canadian Geotechnical Journal, 55, 1230-1247.

Parson, L. (2022). Seismic Performance of Retrofitted Reinforced Concrete Columns Including Soil Structure Interaction, Master's Thesis, Oregon State University, Corvallis, OR.

Paulay, T. (1982). Lapped Splices in Earthquake-Resisting Columns. Journal of American Concrete Institute, 79(6), 458–469.

Phoon, K. K., and Kulhawy, F. H. (2008). Serviceability Limit State Reliability-Based Design. Reliability-Based Design in Geotechnical Engineering: Computations and Applications, Taylor and Francis, London, 344-384.

Rathje, E. M., Chang, W. H., and Stokoe II, K. H. (2005) Development of an In Situ Dynamic Liquefaction Test. Geotechnical Testing Journal, 28(1), 50-60.

Robertson, P.K., and Cabal, K.L. (2015). Guide to Cone Penetration Testing for Geotechnical Engineering, 6th Edition. Gregg Drilling and Testing, Inc., Signal Hill, California, 143 pp.

Sharma, K. (2019). Field Investigation and Performance-Based Seismic Design of Rocking Shallow Foundations in Cohesive Soil. PhD Dissertation, University of Alberta, Edmonton, Alberta, CA.

Shrestha, S. (2019). Seismic Retrofit of Square Reinforced Concrete Bridge Columns using Titanium Alloy Bars. PhD Dissertation, Oregon State University, Corvallis, OR.

Stuedlein, A. W., Huffman, J. C., Barbosa, A. R., Belejo, A. F. V. (2022). Probabilistic Structural System Response to Differential Settlement Resulting from Spatially Variable Soil. Journal of Geotechnical and Geoenvironmental Engineering, 148(2).

Terzaghi, K. 1943. "Theoretical soil mechanics". New York: Wiley.

Van Genuchten, M. T. 1980. "A closed-form equation for predicting the hydraulic conductivity of unsaturated soils." Soil Sci. Soc. Am. J. 44 (5): 892–898

Vanapalli, S. K., Sillers, W. S., Fredlund, M. D. (1998). The Meaning and Relevance of Residual State to Unsaturated Soils. In Proceedings, 51st Canadian Geotechnical Conference, 4-7. Canada: Canadian Geotechnical Society.

Vesic, A. S. 1973. "Analysis of ultimate loads of shallow foundations." J. Soil Mech. Found. Div. 99 (sm1): 45–73.

Vucetic, M., and Dobry, R. (1991). Effect of Soil Plasticity on Cyclic Response. Journal of Geotechnical Engineering, 117(1), 87-107.

Xiao, Y., Priestley, M.N. and Seible, F. (1996). Seismic Assessment and Retrofit of Bridge Column Footings. Structural Journal, 93(1), pp.79-94.

8.0 SUMMARY AND SUGGESTIONS FOR FUTURE RESEARCH

8.1 SUMMARY OF THIS REPORT

This report presents the results of a comprehensive study focused on the effects of soil-structure-interaction (SSI) associated with rocking bridge substructures considering vintage and titanium alloy bar (TiAB) retrofitted column-footing specimens. Section 2 provides a full literature review covering aspects ranging from available retrofitting strategies to strengthen existing vintage substructures which suffer from poor structural reinforcement detailing. Section 3 provides a review of the Oregon Department of Transportation Bridge Inventory, summarizing the findings in a suite of readily digestible histograms. Section 4 provides a novel framework facilitating estimation of the moment capacity of rocking shallow foundations resting on partially saturated soils, and includes parametric studies and comparison of moment capacities calculated using the formulation to that observed in previously-reported physical model tests. Section 5 presents the results of three-dimensional numerical simulations calibrated against full-scale tests on fixed and rocking foundations, used to present a parametric study of the effects of foundation soil conditions and structural retrofit characteristics on whether plastic hinging or soil bearing failure mechanisms will govern the global moment resistance of bridge substructures. Additionally, Section 5 investigates the effects of system performance of multi-column bent systems with and without the TiAB retrofit to identify the role of the TiAB retrofit in delaying the drift at failure in such systems. Section 6 presents the first part of a full-scale structural laboratory-based investigation on the role of the TiAB retrofit to produce rocking behavior in view of flexible bearing and lateral earth pressure support provided by a soil simulant and spring system devised based on the results of 3D numerical simulations of embedded column-footing bridge substructures. The basis for a strut-and-tie model to design TiAB-retrofitted structures was also presented and is accompanied by a design memorandum included in the transmission of this report. The second part of the full-scale laboratory investigation is presented in Section 7 which reports measures taken to retrofit selected column-footing specimens in order to determine the plastic hinging moment capacity of TiAB retrofitted substructures. Section 7 also presents the experiment results obtained from snap-back tests conducted at the Geotechnical Engineering Field Research Site (GEFRS) on embedded vintage column-footing specimens constructed in anticipation of future quasi-static, cyclic lateral loading tests. Finally, Section 7 presented the development of a nonlinear SSI model which was shown to capture salient aspects of the footing-structure interaction of rocking foundations for the soil simulant used along with demonstrating the effects of seasonal conditions affecting the strength and stiffness of the bearing soils. This report concludes with suggestions for future research to further elucidate the aspects governing the SSI of embedded bridge substructure systems, presented below.

8.2 SUMMARY OF RECOMMENDATIONS FOR IMPLEMENTATION OF THIS RESEARCH

1. Soil-structure interactions should be considered as part of a retrofit strategy. The local site conditions will strongly influence the design outcome. Best and worst-case soil strengths corresponding to seasonally dry and wet conditions (Section 4), respectively, should be used to bound the soil reaction to rocking foundations for use in the design. Selection of the TiAB details and/or other retrofits should be done to enable rocking behavior where possible and to force-protect other structural elements in the system (Section 6). It may be possible to minimize the extent of the retrofit (i.e. only use hoop confinement) to achieve the design objectives.

2. The forces and moments induced on the column footing should be considered in the rocking condition (Sections 5 – 7). There are soil-structure interactions that influence the soil pressures acting on the footing (underneath, and along faces). Strut and tie models, as described in this report (Section 6), were developed that can represent the force flow through the footing. These are provided in an accompanying standalone design guide that includes an Excel spreadsheet that simplifies computation of the soil pressures.

3. To economize the retrofit, intact soil samples should be retrieved near the bridge substructure for the purposes of establishing the soil water retention curve (SWRC) and determining the design undrained shear strength of the bearing soils for use in calculations.

4. Rocking foundations should only be implemented in competent bearing soils. Bearing soils which are not competent include those that exhibit high erodibility or susceptibility to liquefaction. Erodible soils can be considered saturated or near-saturated fine sands and non-plastic silts for the purposes of this recommendation. To establish if the bridge is located in competent bearing soils, the site-specific soil should be tested. Low plasticity soils potentially susceptible to liquefaction (i.e., exhibiting “sand-like” behavior based on their behavioral characteristics such as ultimate hysteretic behavior; Bray & Sancio 2006, Stuedlein et al. 2023) should be sampled in an intact state and tested cyclically to establish the potential for strength loss under cyclic loading.

5. Wherever and whenever possible, periodic groundwater table elevation data should be collected near bridge substructures being considered for retrofit, to understand seasonal fluctuations in the ground water table, and the corresponding influence on the soil properties.

8.3 SUGGESTIONS FOR FUTURE RESEARCH

Further work on the modes of failure and performance of the system should be undertaken. Further advancement of the research could include the following:

1. Conduct full-scale in-situ testing of vintage column-footing specimens in both soft and stiff soil conditions.

2. Perform full-scale tests on columns with TiAB retrofits in-situ.

3. Consider full-scale studies on the dynamic response of TiAB retrofitted columns during a shake table experiment.

4. Confirm the seasonally dependent response of column-footing specimens subjected to snap-back testing through the completion of additional full-scale snap-back tests further on into the dry season (e.g., August or September).

5. Confirm the snap-back applied moment-induced drift relationships simulated by the nonlinear SSI models through the completion of snap-back tests at applied lateral loads exceeding the bounds of this experimental program.

6. Confirm the effect of axial load with respect to the snap-back applied moment-drift relationships developed through SSI simulations by performing snap-back tests at GEFRS with the addition of various magnitudes of applied axial loads.

7. Perform full-scale, quasi-static, cyclic lateral loading tests on the vintage and to-be-retrofitted column-footing specimens at the GEFRS in the wet and dry seasons to explore the large-drift rocking responses in changing soil conditions.

8. Consider the effects of embedment (i.e., nonlinear lateral resistance) within the hysteretic SSI models to simulate the response of future full-scale cyclic tests conducted on embedded column-footing specimens.

8.4 REFERENCES

Bray, J. D., & Sancio, R. B. (2006). Assessment of the liquefaction susceptibility of fine-grained soils. *Journal of geotechnical and geoenvironmental engineering*, 132(9), 1165-1177.

Mayne, P. W., & Poulos, H. G. (1999). Approximate displacement influence factors for elastic shallow foundations. *Journal of geotechnical and geoenvironmental engineering*, 125(6), 453-460.

Stuedlein, A. W., Dadashiserej, A., Jana, A., & Evans, T. M. (2023). Liquefaction susceptibility and cyclic response of intact nonplastic and plastic silts. *Journal of Geotechnical and Geoenvironmental Engineering*, 149(1), 04022125.

APPENDIX A6.1: MATERIAL PROPERTIES

A6.1.1 Concrete

The concrete mix design for the columns, footings, and shell were all the same. The design contained 4.75 mm (3/8 in.) aggregate, slag, no air entrainment, and a 28-day design compressive strength of 28 MPa (4 ksi). Table A6.1.1 contains the 28 compressive tests of 102 x 203 mm (4 x 8 in.) cylinders in accordance with ASTM C39M/ C39M-05 and ASTM C617-98. After the shell was cast for specimen 3 it was tested a week after casting and before the 28 day period, and the results can be found in Table A6.1.2 and Table A6.1.3 with the day of test results for the other specimens.

Table A6.1.1 – 28 Day Concrete Compressive Strength.

Specimen ID	Specimen Component	Compressive Strength, MPa (psi)	Standard Deviation	Coefficient of Variation
S.1	Footing	27.07 (3926)	238	6
S.1	Column	27.06 (3924)	181	4.6
S.1	Shell	35.07 (5086)	160	3.1
S.2	Footing	27.07 (3926)	238	6
S.2	Column	27.06 (3924)	181	4.6
S.2	Shell	35.07 (5086)	160	3.1
S.3	Footing	38.90 (5647)	161	2.9
S.3	Column	30.86 (4476)	141	3.1

Day of test compressive were conducted according to ASTM C39M/ C39M-05 and ASTM C617-98 and the results can be found in Table A6.1.2. Tests were not conducted for specimen Tests 2, 5, and 6. While failure occurred in specimen Test 5 limited test cylinders prevented day of test compressive and tensile tests from being completed. No damage to the concrete was observed during test 2 and 6; therefore, no compressive or tensile were conducted on the day of specimen testing. Furthermore, specimen Tests 3, and 4 were conducted on the same day. Due to limited cylinder availability tensile tests were conserved for column failure and were only conducted for Test 8, and because only the footing exhibited damage it was the only component tested. Tensile tests were conducted on 152 x 305 mm (6 x 12 in.) cylinders in accordance with ASTM C496/ C496M-04 and results can be found in Table A6.1.3.

Table A6.1.2 – Day of Test Concrete Compressive Strength.

Specimen ID	Test ID	Test Date	S.C.	Compressive Strength, MPa (psi)	Standard Deviation	Coefficient of Variation
S.1	1	11/17/2021	Footing	39.70 (5757)	77.9	1.4
S.1	1	11/17/2021	Column	46.24 (6707)	216	3.2
S.1	1	11/17/2021	Shell	39.0 (5655)	132	2.3
S.3	3,4	12/17/2021	Footing	47.39 (6873)	179	2.6
S.3	3,4	12/17/2021	Column	36.59 (5307)	277	5.2
S.3	7	4/20/2022	Shell	24.35 (3532)	109	3.1
S.2	8	6/1/2022	Footing	39.84 (5778)	124	2.1

Table A6.1.3 – Day of Test Concrete Tensile Strength.

Specimen ID	Test ID	Test Date	S.C.	Compressive Strength, MPa (psi)	Standard Deviation	Coefficient of Variation
S.2	8	6/1/2022	Footing	2.68 (389)	66.1	17

A6.1.2 REINFORCING STEEL

A local rebar fabricator fabricated all of the reinforcing steel. Shrestha (2019) tested the #10M (#3) Grade 40 column ties using a 490 kN (110 kip) universal testing machine with a 51 mm (2.1 in.) gauge length extensometer to measure strain. For the column ties the yield point in the stress-strain profile was taken as the 0.2% offset, and the results from Shrestha (2019) can be found in Table A6.1.4.

Table A6.1.4 – Tensile Test Results of #10M (#3) Steel Bars (after Shrestha 2019).

Yield Strength, MPa (ksi)	Yield Strain (με)	Tensile Strength, MPa	Ultimate Elongation (%)
386 (56)	1,923	583 (86)	27.78

Tensile tests were conducted on the remaining steel reinforcement by cutting 457 mm (18 in.) coupons from spare bars and delivered to a nearby testing facility to validate the mill certifications of the manufacturer. The testing facility used the 0.2% offset method for the yield strength and tested bars in accordance with ASTM A370-20. The results of the tests can be viewed in Table A6.1.5. All remaining bars were Grade 60.

Table A6.1.5 – Tensile Test Results on the Reinforcing Steel

Bar Size	Bar Type	Tensile Strength, MPa (ksi)	Yield Strength, MPa (ksi)	Elongation in 4D (%)	Reduction of Area (%)	Original Gauge Diameter, mm (in.)
#13M, #4	Tie	738 (107)	552 (80)	26	66	6.4 (0.252)
#13M, #4	Footing	614 (89)	372 (54)	28	56	6.4 (0.252)
#32M, #10	Column/ Starter	758 (110)	490 (71)	21	49	12.8 (0.503)

A6.1.3 TITANIUM ALLOY BARS

Because the Titanium Alloy Bar (TiAB) spirals remained elastic during the tests conducted by Shrestha (2019), They were able to be reused for the three specimens. Shrestha (2019) used a sample from the stock of unused TiAB was tested to validate the mill certified properties. The results of the test indicated that the mill certified properties were accurate; therefore, the mill certified properties were used as the actual properties for the #10M (#3) TiAB ligaments and the #16M (#5) TiAB spirals. The tensile properties of the TiAB spirals used be Shrestha (2019) can be found in Table A6.1.6.

Table A6.1.6 – Tensile Test Results on TiABs.

TiAB Bar Type	Tensile Strength, MPa (ksi)	Yield Strength, MPa (ksi)	Elongation 4D (%)	Reduction of Area (%)
Ligament	1126 (163.3)	1037 (150.4)	21	55
Spiral	1010 (146.5)	920(133.4)	19	50

A6.1.4 SOIL SIMULANT

Soil was simulated for Tests 1-7 with FOAMULAR® 1000 Extruded Polystyrene (XPS) Rigid Foam Insulation. All of the tests used 4 – 50.8 mm (2 in.) thick layers of foam for the subgrade. For Tests 1, 3, and 4 with foam embedment 3 – 50.8 mm (2 in.) thick layers were used on the north and south face on the footings. The manufacturer reports minimums of 689 kPa (100 psi) compressive strength and 965 kPa (140) psi flexural strength on their website: commercial.owenscorning.com. Shrestha (2019) completed cyclic compressions tests on 3 cylindrical test samples measuring 96.5 mm (3.8 in.) in diameter and 152 mm (6 in.) in depth. Figures A6.1.1, A6.1.2, and A6.1.3 display the tests results and Table A6.1.7 displays a summary of critical information from the tests.

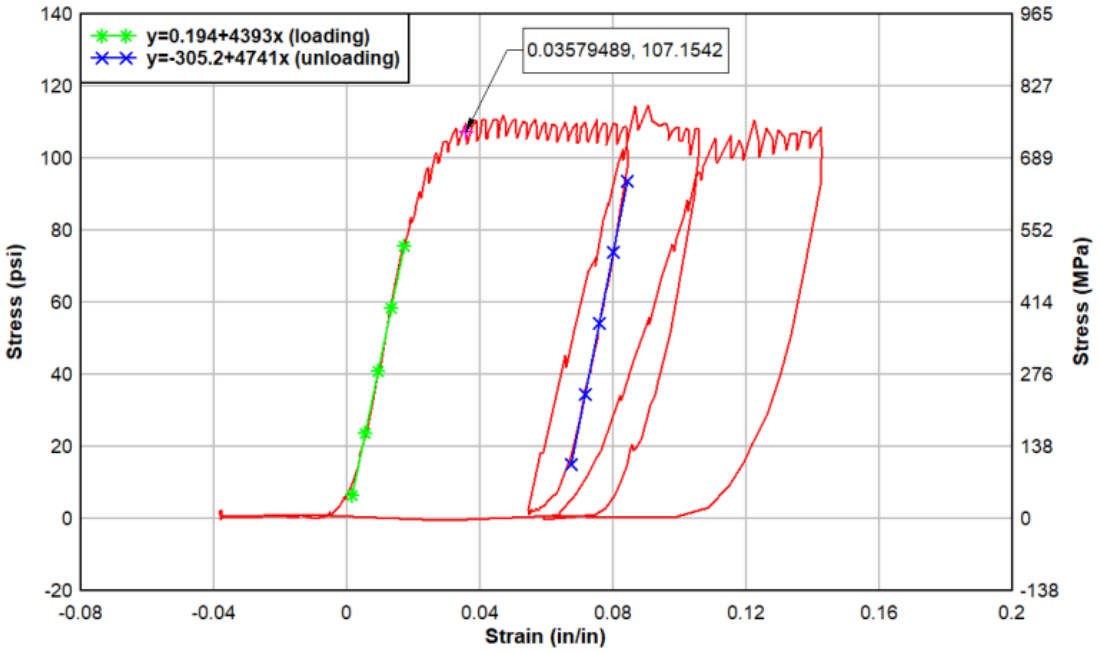

Figure A6.1.1: Shrestha (2019) Compression Test Result, Foam Cylinder 1.

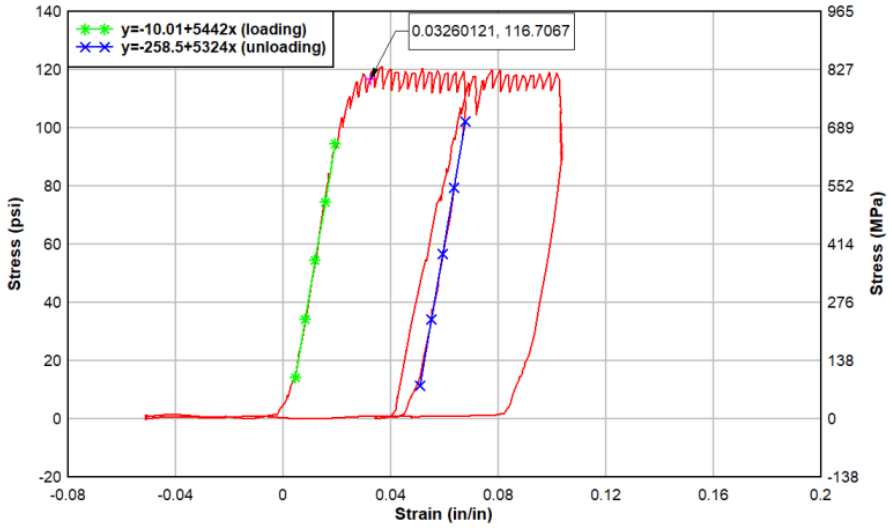

Figure A6.1.2: Shrestha (2019) Compression Test Result, Foam Cylinder 2.

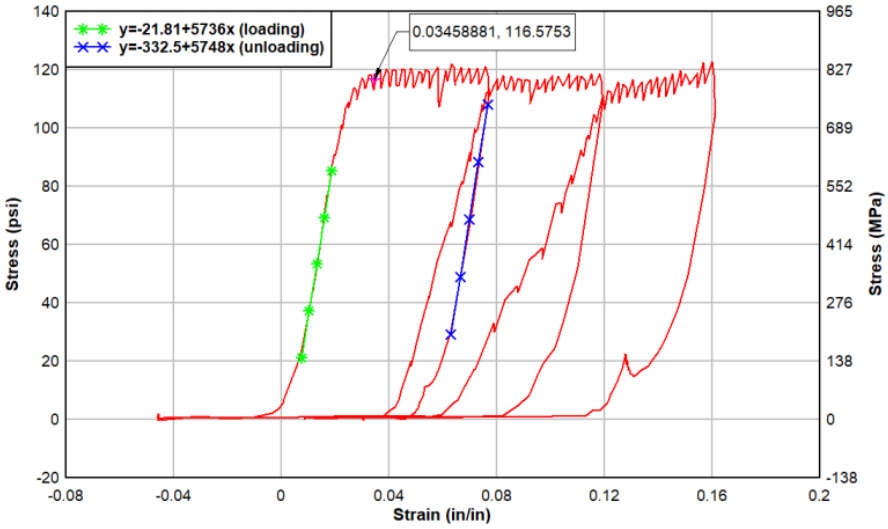

Figure A6.1.3: Shrestha (2019) Compression Test Result, Foam Cylinder 3.

Table A6.1.7 – Summary of Foam Compression Test Results (reported by Shrestha 2019).

Foam Cylinder	Surface Area, mm^2 ($in.^2$)	Yield Strength, Mpa (ksi)	Peak Stress, kPa (psi)	Strain (%)
1	7135 (11.06)	30.3 (4.39)	738 (107)	3.58
2	7090 (10.99)	37.5 (5.44)	807 (117)	3.26
3	7155 (11.09)	39.6 (5.74)	793 (115)	3.14

PROPERTY	TEST METHOD[3]	400	600	1000
Thermal Resistance, R-Value (180 days) minimum, hr•ft²•°F/Btu (RSI, °C•m²/W) @ 75°F (24°C) mean temperature	ASTM C518	5.0 (0.88)	5.0 (0.88)	5.0 (0.88)
@ 40°F (4.4°C) mean temperature		5.4 (0.95)	5.4 (0.95)	5.4 (0.95)
@ 25°F (-3.9°C) mean temperature		5.6 (0.99)	5.6 (0.99)	5.6 (0.99)
Long-Term Thermal Resistance, LTTR-Value,[4] minimum hr•ft²•°F/Btu (RSI, °C•m²/W) @ 75°F (24°C) mean temperature	CAN/ ULC S770-03	5.0 (0.88)	5.0 (0.88)	5.0 (0.88)
Compressive Strength,[5] minimum psi (kPa)	ASTM D1621	40 (276)	60 (414)	100 (689)
Flexural Strength,[6] minimum psi (kPa)	ASTM C203	90 (621)	120 (828)	150 (1035)
Water Absorption,[7] maximum % by volume	ASTM C272	0.3	0.3	0.3
Water Vapor Permeance,[8] maximum perm (ng/Pa•s•m²)	ASTM E96	1.1 (63)	1.1 (63)	1.1 (63)
Dimensional Stability, maximum % linear change	ASTM D2126	2.0	2.0	2.0
Flame Spread[9, 10]	ASTM E84	10	10	10
Smoke Developed[9, 10]	ASTM E84	175	175	175
Oxygen Index,[9] minimum % by volume	ASTM D2863	24	24	24
Service Temperature, maximum °F (°C)	—	165 (74)	165 (74)	165 (74)
Linear Coefficient of Thermal Expansion, in/in/°F (m/m/°C)	ASTM E228	3.5×10^{-5} (6.3×10^{-5})		

2 Properties shown are representative values for 1-inch-thick material, unless otherwise specified.
3 Modified as required to meet ASTM C578.
4 R means the resistance to heat flow; the higher the value, the greater the insulation power. This insulation must be installed properly to get the marked R-value. Follow the manufacturer's instructions carefully. If a manufacturer's fact sheet is not provided with the material shipment, request this and review it carefully. R-values vary depending on many factors, including the mean temperature at which the test is conducted and the age of the sample at the time of testing. Because rigid foam plastic insulation products are not all aged in accordance with the same standards, it is useful to publish comparison R-value data. The R-value for FOAMULAR® & FOAMULAR® NGX™ XPS insulation is provided from testing at mean temperatures of: -4°C (25°F), 4.4°C (40°F), and 24°C (75°F) and aging techniques of 180-day real-time aged (as mandated by ASTM C578) and accelerated aging "Long-Term Thermal Resistance" (LTTR) per CAN/ULC S770-03. The R-value at 180-day real-time age and 75°F mean temperature is commonly used to compare products and is the value printed on the product.
5 Values at yield or 5% deflection.
6 Properties shown are representative values for 2-inch-thick material, unless otherwise specified. Value at yield or 5%, whichever occurs first.
7 Data ranges from 0.00 to value shown due to the level of precision of the test method.
8 Water vapor permeance decreases as thickness increases.
9 These laboratory tests are not intended to describe the hazards presented by this material under actual fire conditions.
10 Data from Underwriters Laboratories Inc.® classified. See Classification Certificate U-197.

Figure A6.1.4: FOAMULAR® 1000 material properties as reported by manufacturer, Owens Corning (owenscorning.com/en-us/insulation/products/foamular-400) accessed on 7/19/2022).

A6.1.5 BONDING EPOXY

The epoxy used to bond the #10M (#3) TiAB spirals and the #16M (#5) TiAB ligaments was Hilti HIT-RE 500 V3. The following information from the manufacturer's website: hilti.com provides the material specifications used:

- Bond strength per ASTM C882-13A: 10.8 MPa (1.56 ksi) for a 2 day cure time, and 11.7 MPa (1.69 ksi) for a 14 day cure time.
- Tensile strength per 7 day ASTM D638-14: 49.3 MPa (7.15 ksi)
- Nominal bit diameter: 12.7 mm (1/2 in.) for #10M (#3) bar, 19 mm (3/4 in.) for #16M (#5) bar

- Effective minimum embedment: 60 mm (2-3/8 in.) for #10M (#3) bar, and 76 mm (3 in.) for #16M (#5) bar

A6.1.6 3D NUMERICAL SIMULATIONS OF EMBEDDED COLUMN-FOOTING SPECIMENS TO DEVELOP EQUIVALENT LATERAL EARTH PRESSURE-INDUCED SPRING STIFFNESS

Previous research has emphasized the importance of accurately capturing soil-structure interaction when analyzing embedded footings. The response of the footing to applied loads is directly influenced by the behavior of the surrounding soil, necessitating careful consideration of the lateral earth pressure distribution on the vertical faces of the footing anticipated during rocking and its simulation in large-scale experiments. In this study, we adopted a practical approach to simulate soil behavior in the large-scale experiments conducted in the structural laboratory. To represent the soil-structure-interaction arising from lateral earth pressures, a series of springs were installed on the side walls of the footings, perpendicular to the direction of the lateral load (Figure A6.1.5). These springs served as a simplified representation of the soil, with their stiffness playing a crucial role in replicating realistic responses during the experimental tests as described in Section 7.

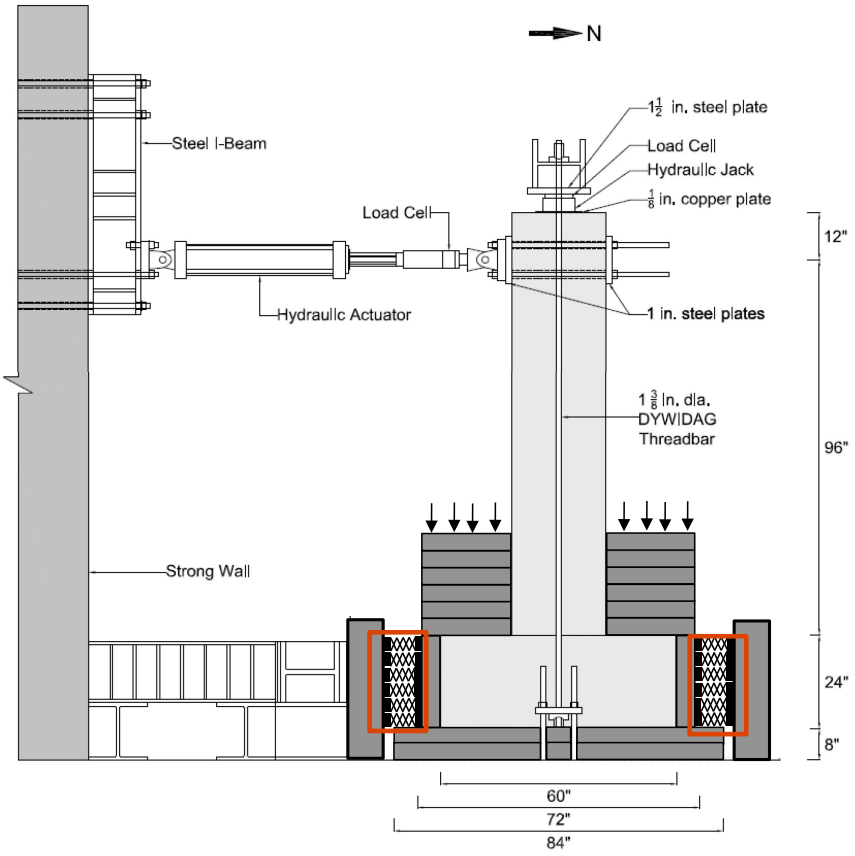

Figure A6.1.5: Possible experimental setup envisioned to be deployed in the structural laboratory on full-scale column-footing specimens with the springs indicated in the red boxes.

To investigate the behavior of an embedded footing under lateral load, we performed 3D numerical soil-structure-interaction simulations using FLAC3D similar to those described in Sections 5 and 6. Our aim was twofold: first, to understand the response of the footing to lateral load, and second, to determine the stresses exerted on the vertical soil-footing interface by the surrounding soil. Through these simulations, we captured the emergent stress distribution that is anticipated to be developed in response to a rocking foundation embedded in soil. The stresses calculated using the numerical simulations were then used to derive the equivalent spring stiffness for a finite tributary area on the vertical footing faces. These parameters were determined based on the relationship between stress and deformation, allowing us to simulate the soil behavior in the subsequent large-scale experiments.

The details of the numerical simulations conducted in this study are presented in Figure A6.1.6. These figures provide a comprehensive overview of the four cases considered for the simulations, each representing different scenarios of considering embedment. Figure A6.1.6a illustrates the case of the embedded footing in soil with no overburden pressure. In this scenario, the footing is directly in contact with the natural soil without any additional soil layer on top. Figure A6.1.6b depicts the case of the embedded footing in real soil with 2' of soil on top of the footing. This overburden soil layer represents a 12 kPa (250 psf) surcharge applied to the top of the footing. In Figure A6.1.6c, the embedded footing is shown with a 2' foam layer on top and a 12 kPa (250 psf) normal force is applied to the top of the foam. This configuration simulates the presence of a foam layer acting as a load-bearing element on the footing as this was considered as an alternative during design of the experiments presented in Section 7. Lastly, Figure A6.1.6d presents the case of the embedded footing in real soil without any overburden soil but with a 12 kPa (250 psf) normal force applied to the top of the foam layer surrounding the footing.

The soil and soil simulant were simulated using the linear elastic-perfectly plastic Mohr Coulomb constitutive model. Interface elements were deployed between vertical and horizontal soil-footing interfaces using the approach described in Sections 5 and 6.

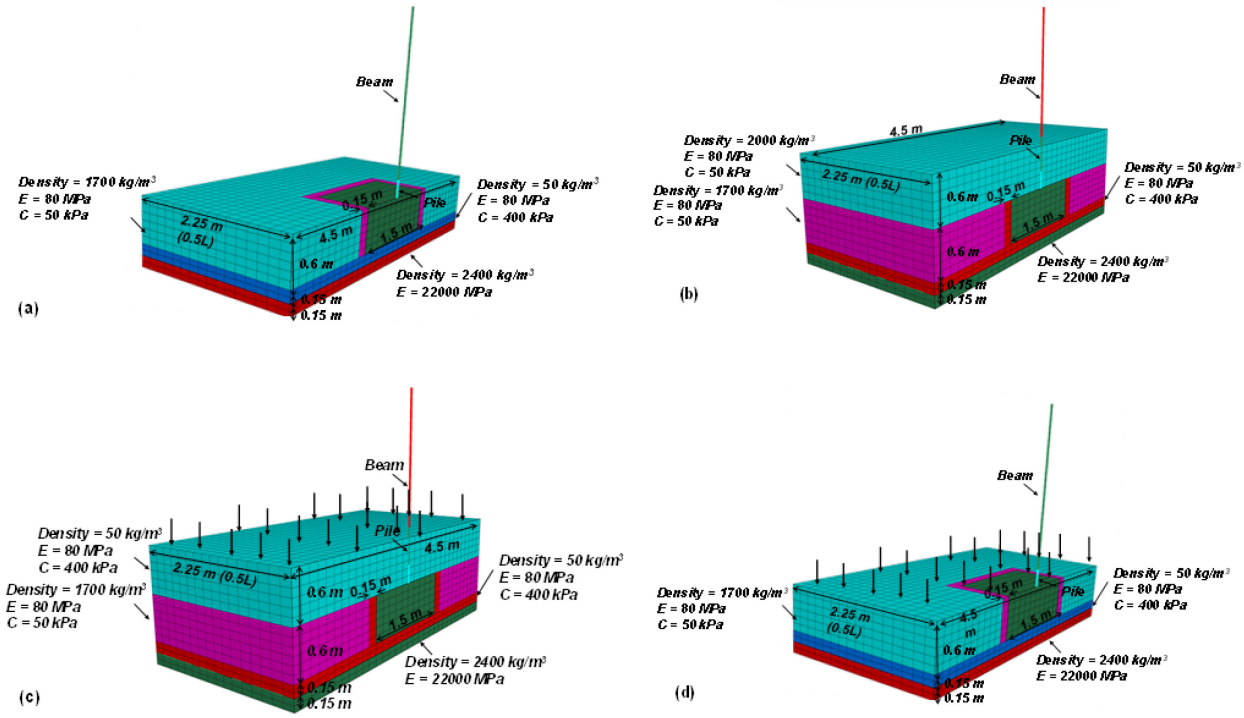

Figure A6.1.7: Numerical simulations considered for calculating spring stiffness for large scale experiments.

The forces measured along the vertical wall of the footing at the soil-footing interface are presented in Figure A6.1.8 for the four cases and are used to determine the stiffness of the springs used to simulate the soil behavior in the structural laboratory. Note that layer 0 starts at the bottom of the footing and represents 4 inches of tributary area, and Layer 5 corresponds to the topmost tributary area of the vertical footing face. Table A6.1.8 provides a comprehensive summary of the lateral forces measured along the footing wall and the corresponding calculated spring stiffness for each case. The measured forces along the wall of the footing slightly varied across the different scenarios, reflecting the influence of the soil conditions and external loads on the footing's response. As can be observed in Figure A6.1.8, the nonlinear response of the lateral earth pressure was simplified into a linear elastic-perfectly plastic representation for use in designing the actual springs used in the experiments. The calculated spring stiffness values ranged from 140 to 250 kips/in at different depths, indicating the varying levels of stiffness required to accurately simulate anticipated soil behavior. It should be noted that this selection of stiffness for springs should be made based on considerations of achieving a balance between accurately representing the soil behavior and practical feasibility within the experimental setup. Following an assessment of the simulations, the springs designed for use in the structural laboratory considered the results of Case 1, as noted in Section 7.2.6.2.

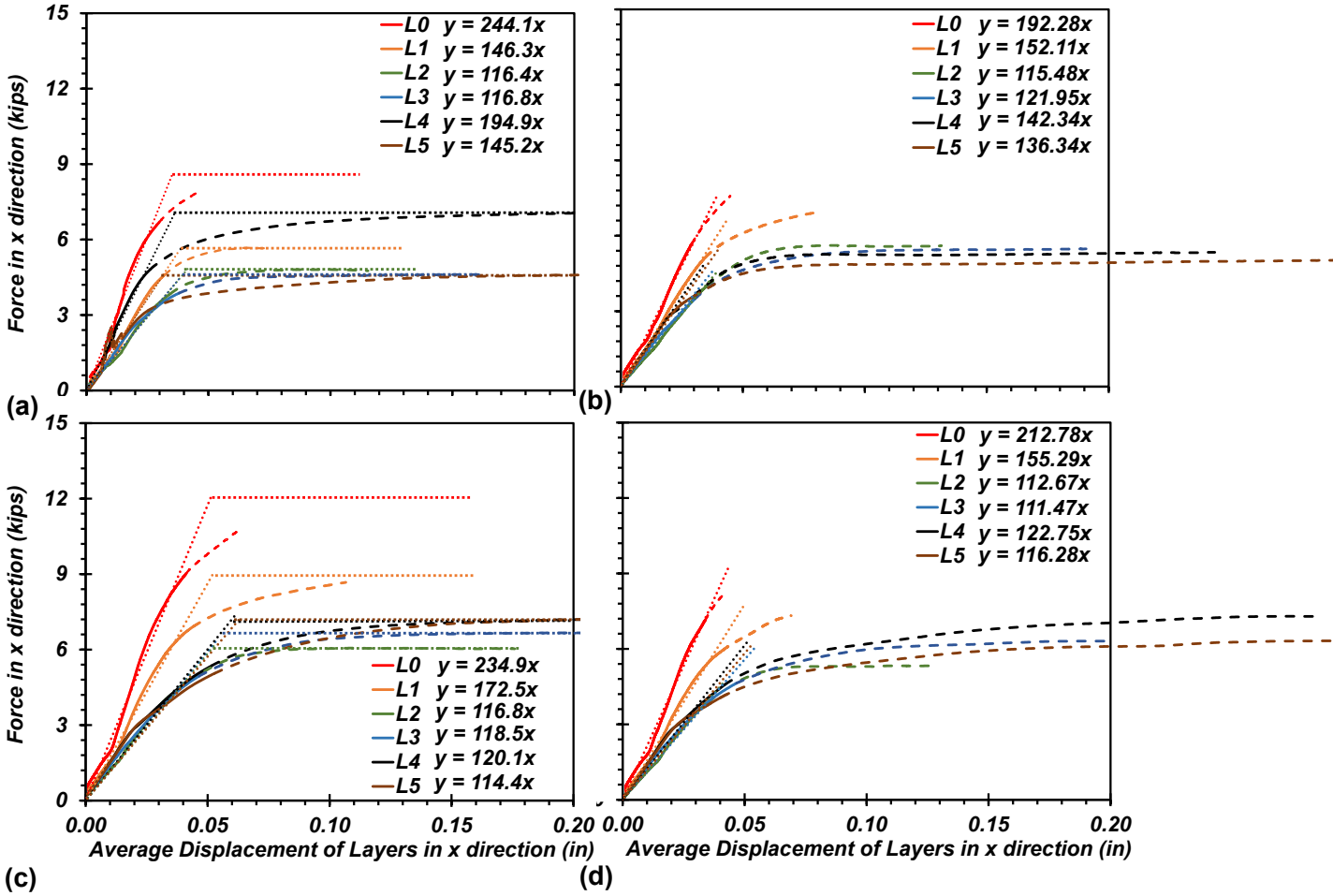

Figure A6.1.8: Lateral forces measured along the footing walls for: (a) an embedded footing in soil with no overburden pressure, (b) embedded footing in soil with 2' overburden soil on top equivalent to a 12 kPa (250 psf) surcharge, (c) embedded footing in soil with a 2' foam on top and 12 kPa (250 psf) normal force applied to the top of the foam, and (d) embedded footing in soil with no overburden soil but 12 kPa (250 psf) normal force applied to the top of the foam.

Table A6.1.8 – Summary of calculated spring stiffnesses for the four simulation cases.

Case 1: Embedded Footing in real soil with no overburden pressure			
Layer #	**Layer Thickness (in)**	**Spring Stiffness (kips/in)**	**Max Force (kips)**
L0 (Bottom layer)	4	244.1	8.6
L1	4	146.3	5.7
L2	4	116.4	4.8
L3	4	116.8	4.5
L4	4	194.9	7.0
L5 (Top Layer)	4	145.2	4.6

Case 2: Embedded Footing in real soil with 2' overburden soil on top equivalent to a 12 kPa (250 psf) surcharge applied to the top of the footing			
Layer #	**Layer Thickness (in)**	**Spring Stiffness (kips/in)**	**Max Force (kips)**
L0 (Bottom layer)	4	234.9	12.0
L1	4	172.5	9.0
L2	4	116.8	6.0
L3	4	118.5	6.7
L4	4	120.1	7.2
L5 (Top Layer)	4	114.4	7.2

Case 3: Embedded Footing in real soil with a 2' foam on top and 12 kPa (250 psf) normal force applied to the top of the foam			
Layer #	**Layer Thickness (in)**	**Spring Stiffness (kips/in)**	**Max Force (kips)**
L0 (Bottom layer)	4	212.8	9.6
L1	4	155.3	7.8
L2	4	112.7	5.4
L3	4	111.5	6.3
L4	4	122.8	7.0
L5 (Top Layer)	4	116.3	6.2

Case 4: Embedded Footing in real soil with no overburden soil but 12 kPa (250 psf) normal force applied to the top of the foam

Layer #	Layer Thickness (in)	Spring Stiffness (kips/in)	Max Force (kips)
L0 (Bottom layer)	4	192.3	9.4
L1	4	152.1	7.2
L2	4	115.4	5.7
L3	4	121.9	5.6
L4	4	142.3	5.6
L5 (Top Layer)	4	136.3	5.2

APPENDIX A6.2: SENSOR NAMING CONVENTIONS AND PLACEMENT

A6.2.1 STRAIN GAUGE NAMING CONVENTION

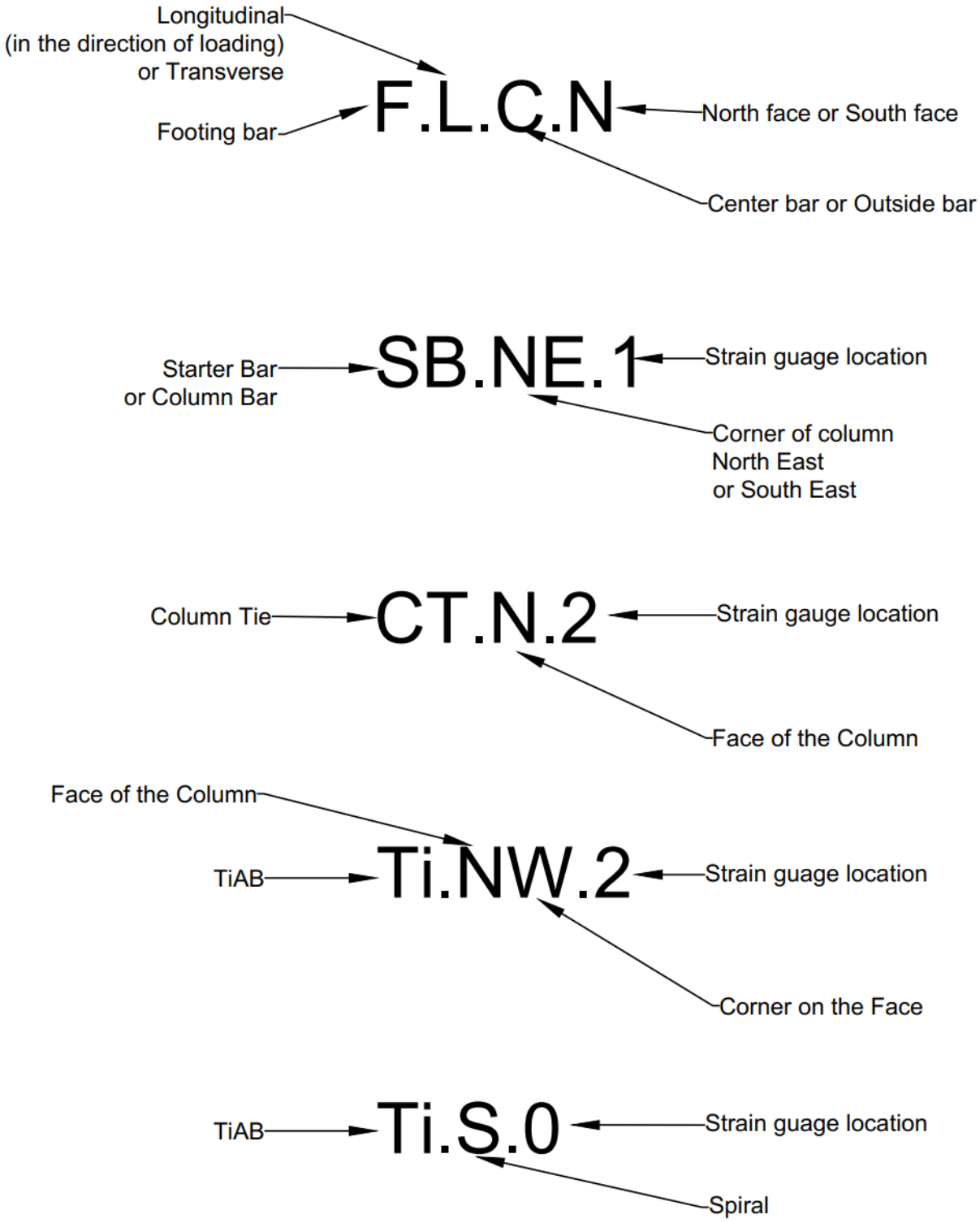

A6.2.2 STRAIN GAUGE SENSOR LOCATIONS

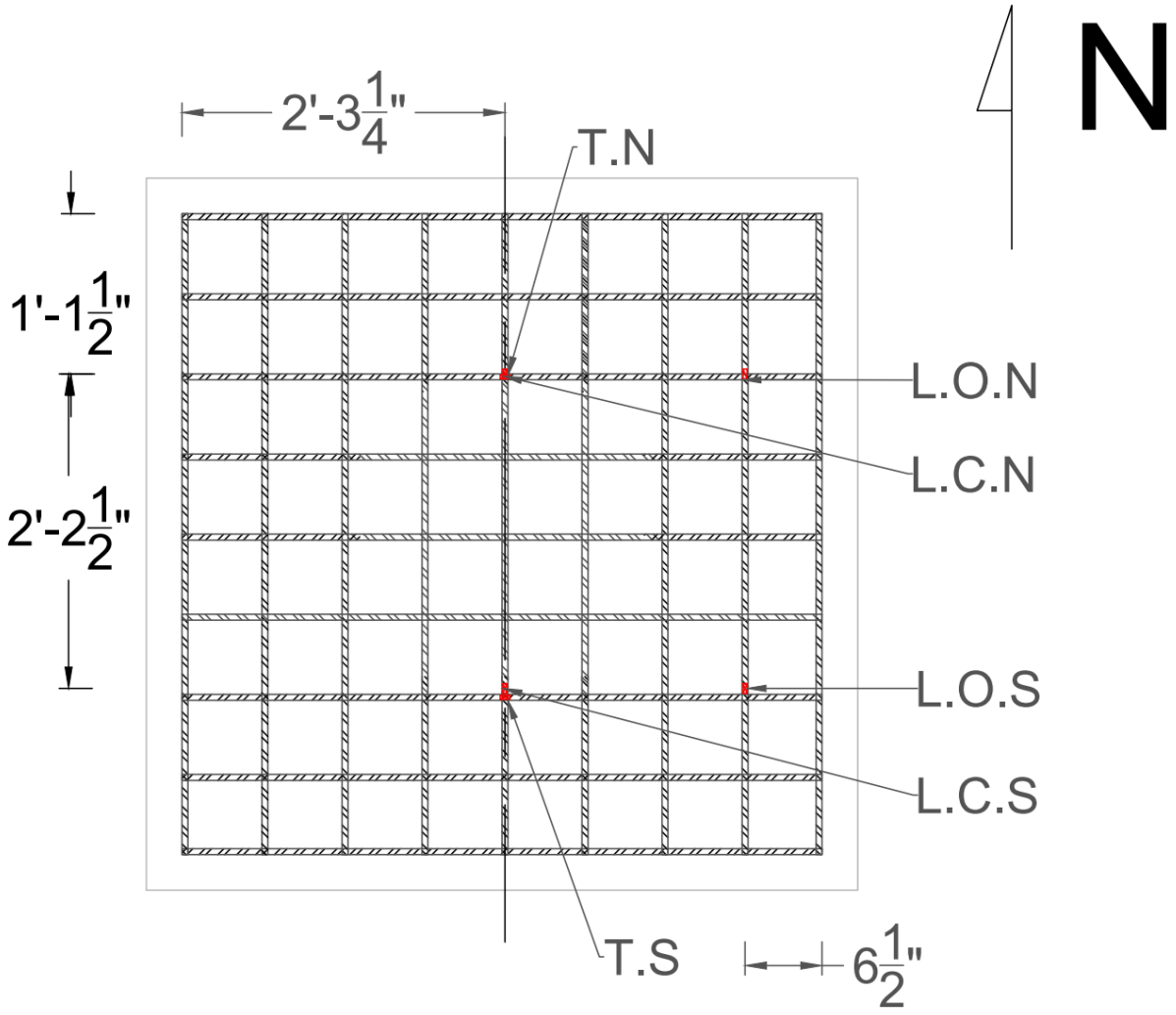

PLAN VIEW

Figure A6.2.1: Location of footing strain gauges.

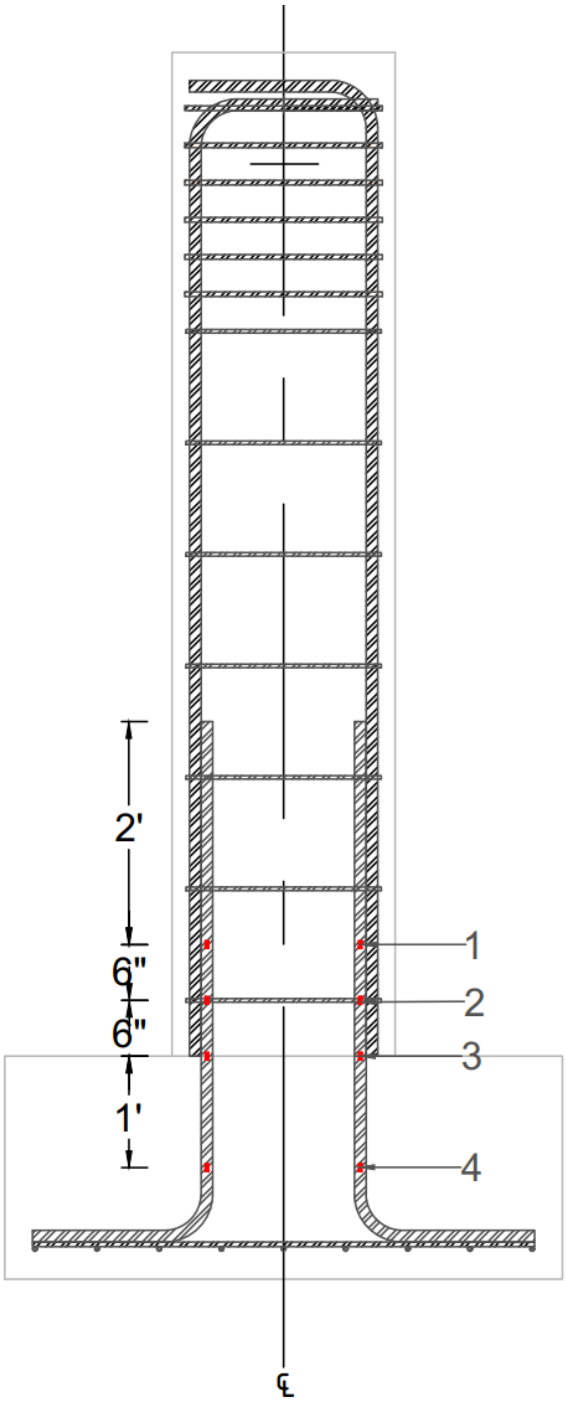

ELEVATION N-S

Figure A6.2.2: Starter bar strain gauge locations.

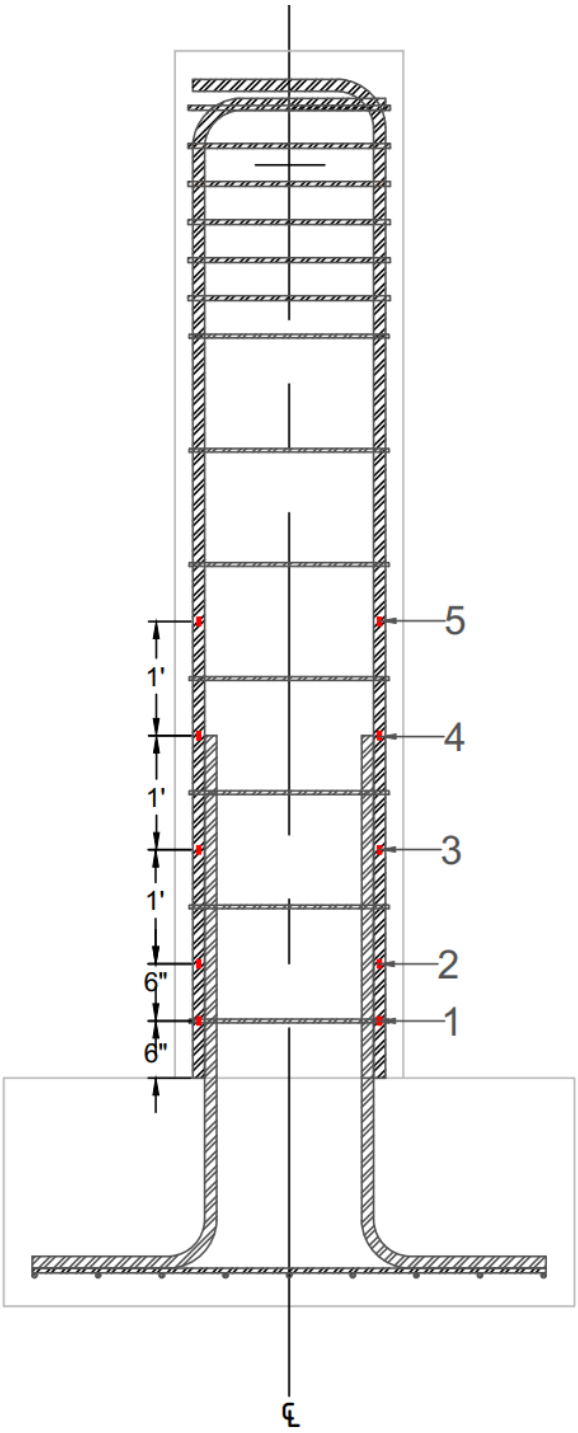

ELEVATION N-S

Figure A6.2.3: Column bar strain gauge locations.

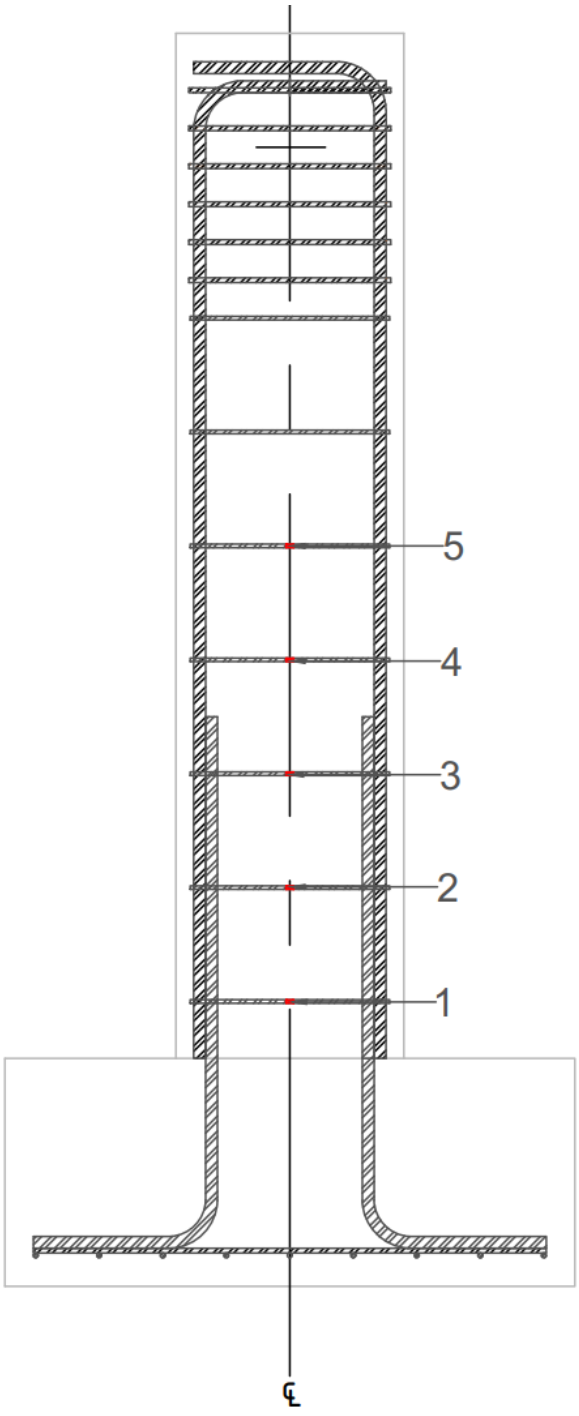

Figure A6.2.4: Column tie strain gauge locations on the east face.

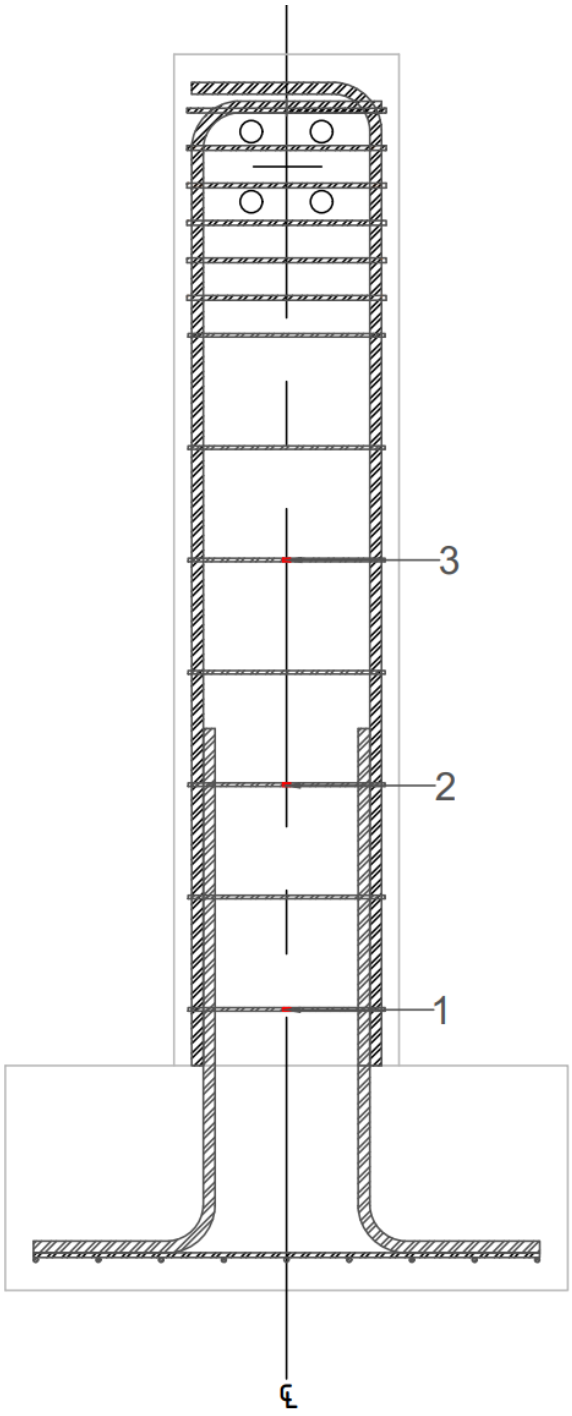

ELEVATION E-W

Figure A6.2.5: Column tie strain gauge locations on the north face.

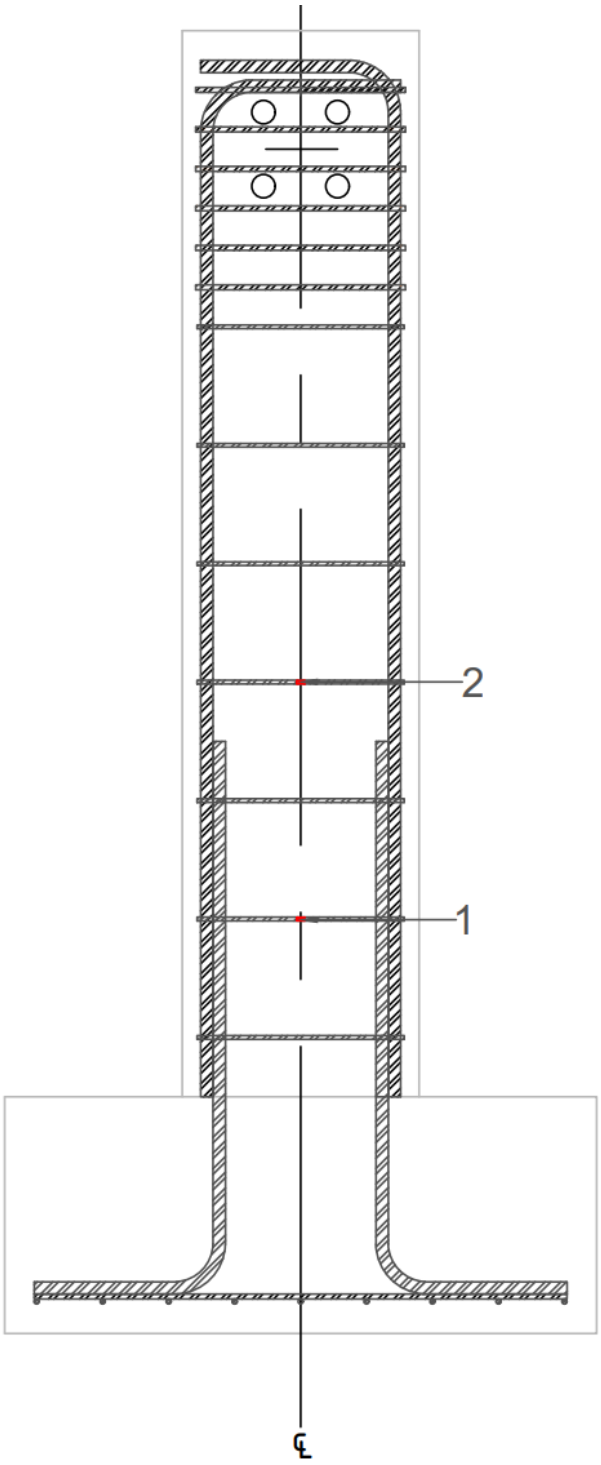

Figure A6.2.6: Column tie strain locations on the south face.

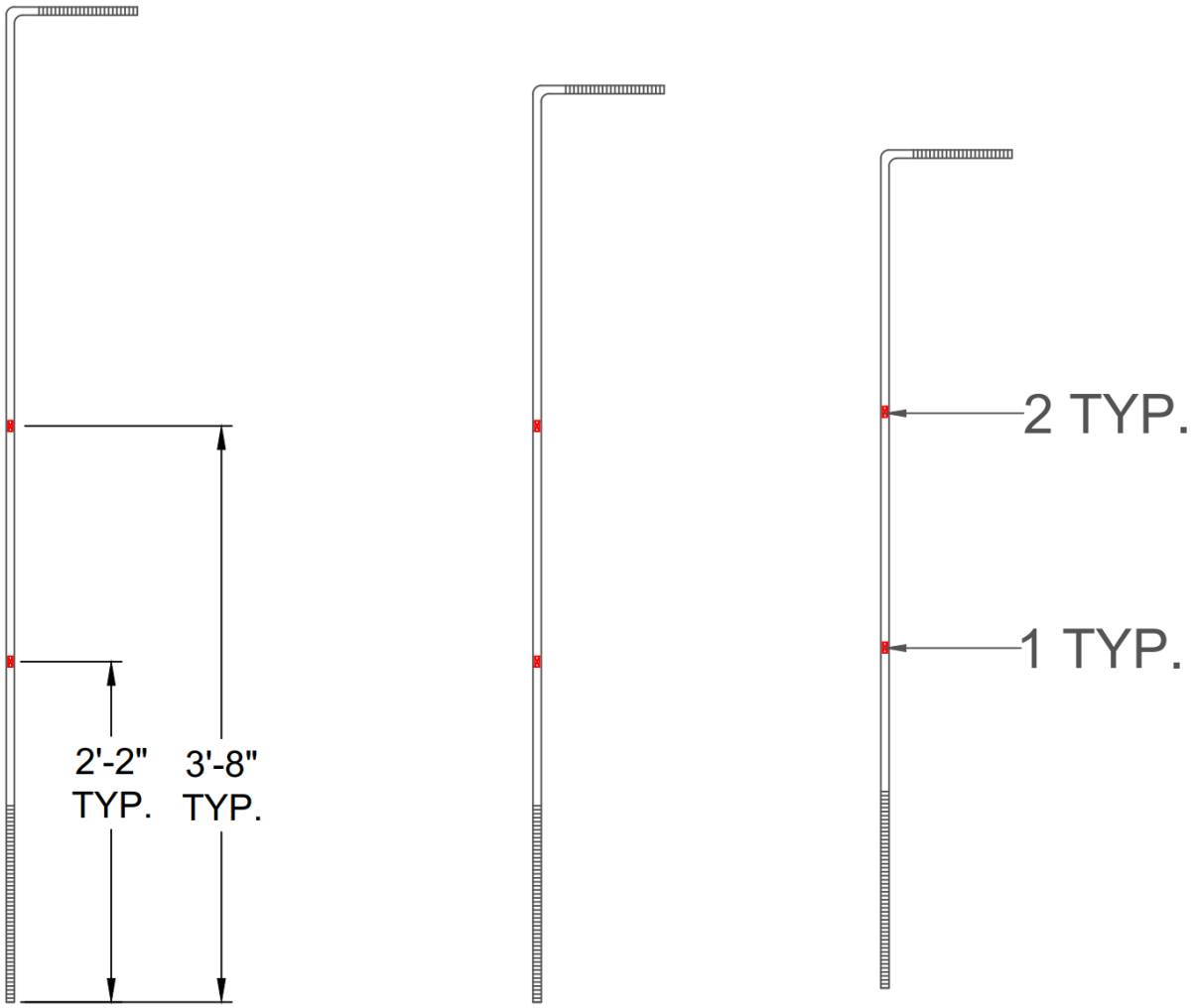

Figure A6.2.7: TiAB ligament strain gauge locations.

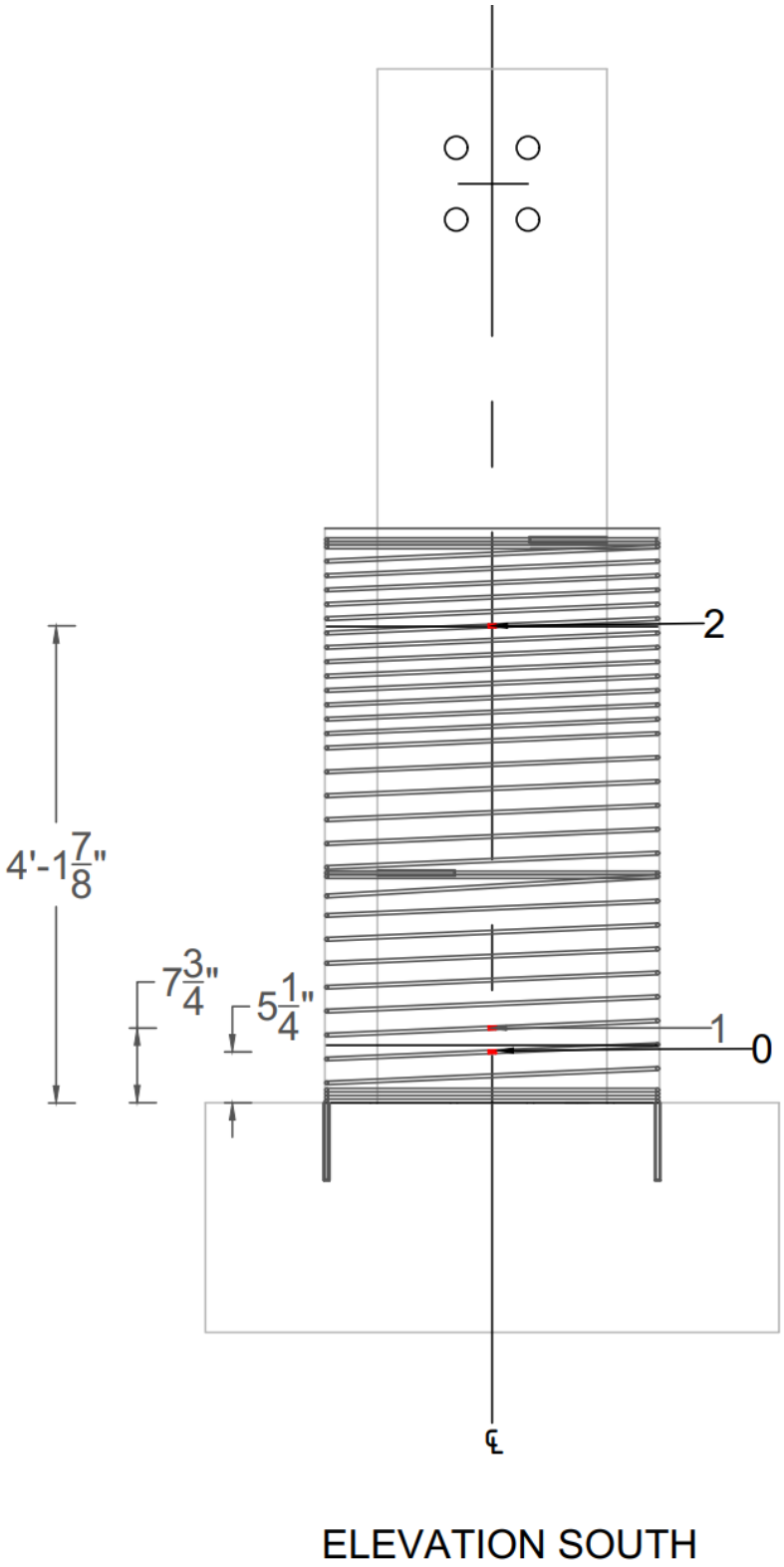

Figure A6.2.8: TiAB spiral strain gauge locations.

A6.2.3 STRING POTENTIOMETER SENSOR LOCATIONS

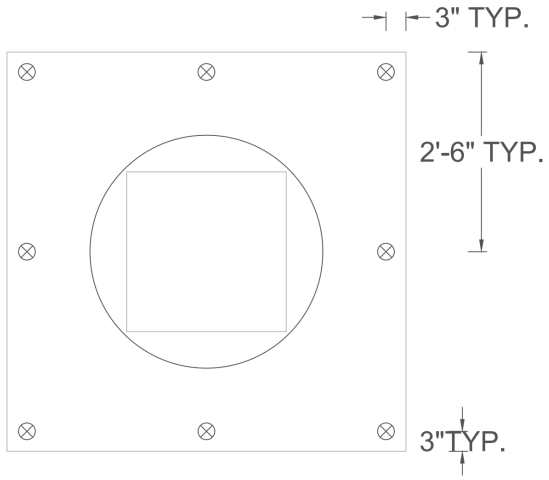

Figure A6.2.9: String potentiometer locations on the top of the footing.

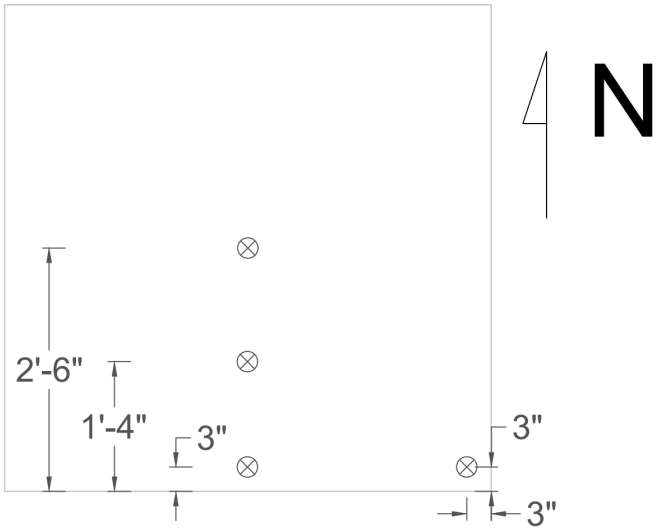

Figure A6.2.10: String potentiometers on the bottom of the footing.

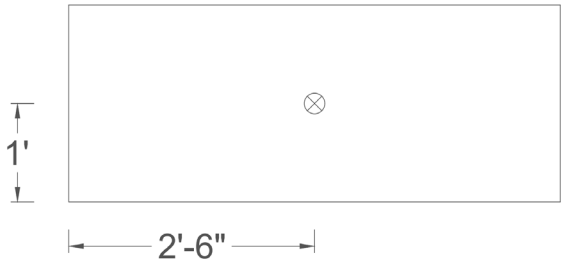

Figure A6.2.11: String Potentiometer locations on the east and west of the footing.

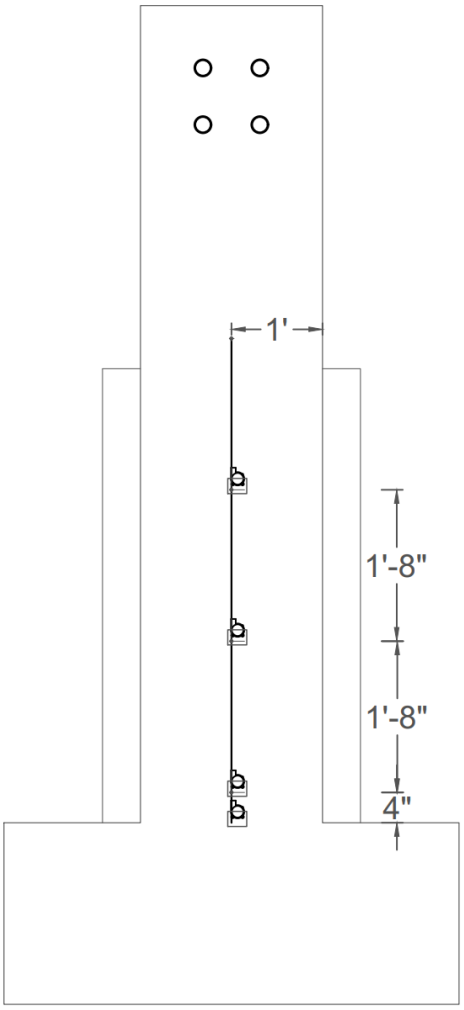

Figure A6.2.12: String potentiometer locations on the north and south face of the column.

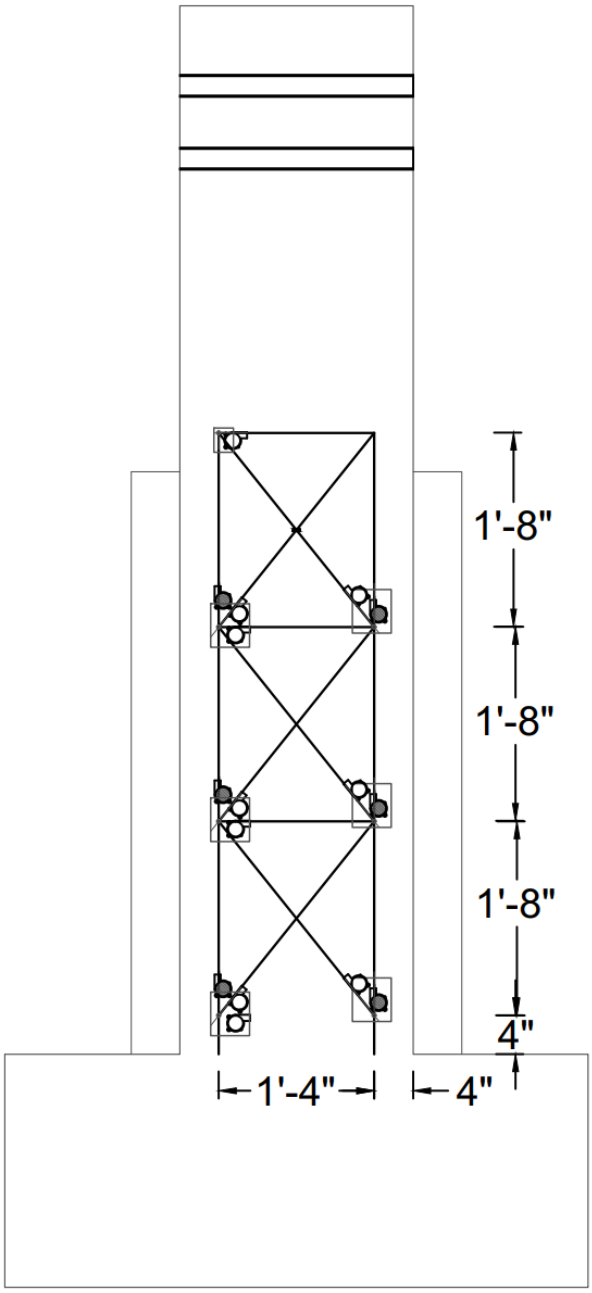

Figure A6.2.13: String Potentiometer locations on the west face.

APPENDIX A6.3: EXPERIMENTAL DATA FOR ALL TESTS REPORTED IN SECTION 6

A6.3.1 TEST 1 - SPECIMEN 1: COMPLETE RETROFIT WITH FOAM EMBEDMENT & SUBGRADE

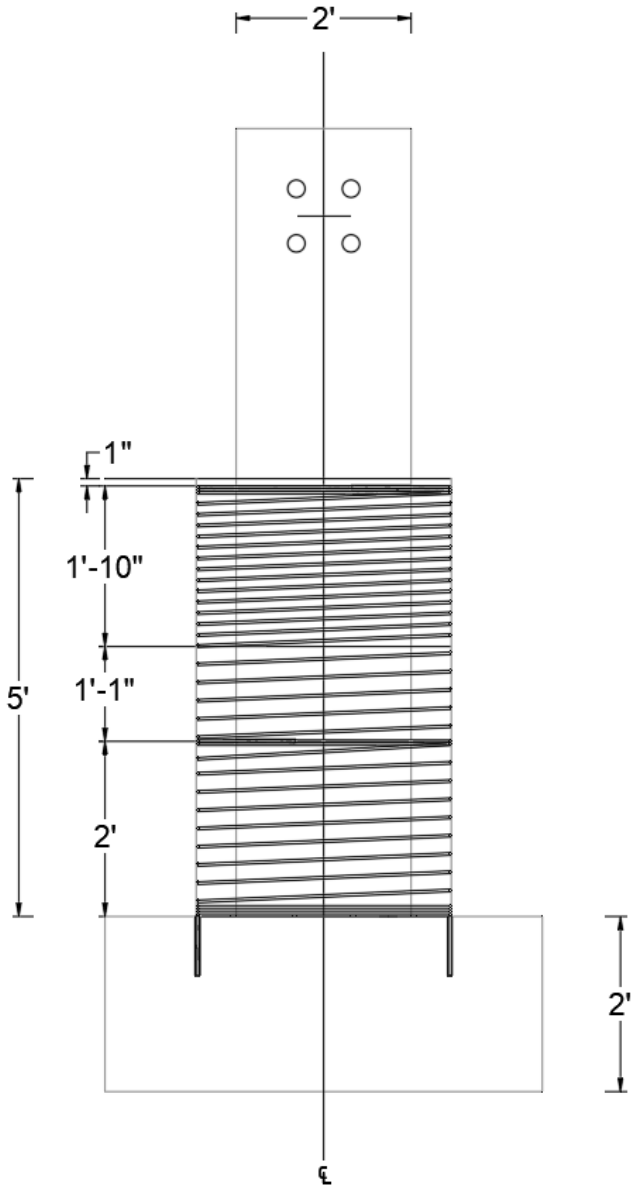

Figure A6.3.1.1: Elevation View of Specimen 1 used in Test 1.

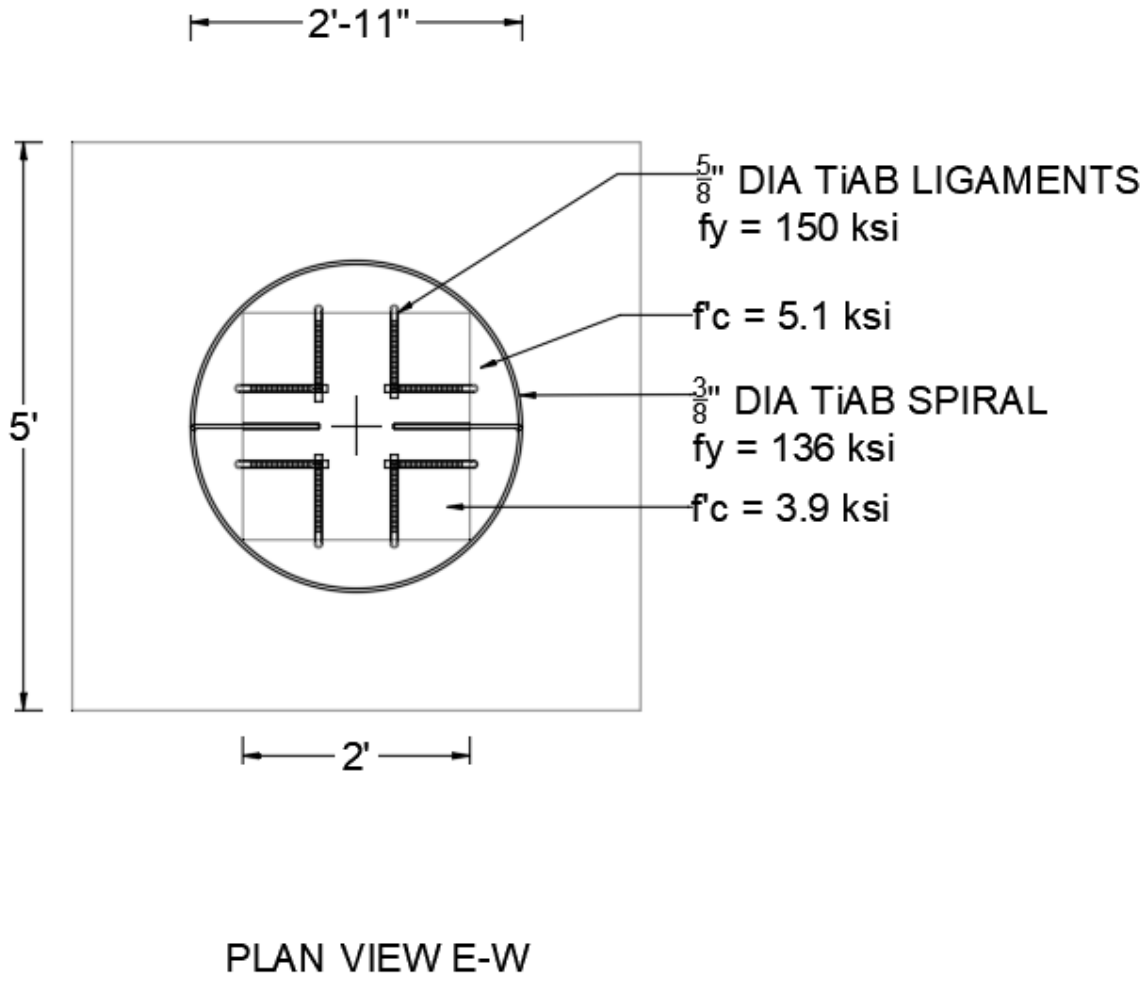

Figure A6.3.1.2: Plan View of Specimen 1 used in Test 1.

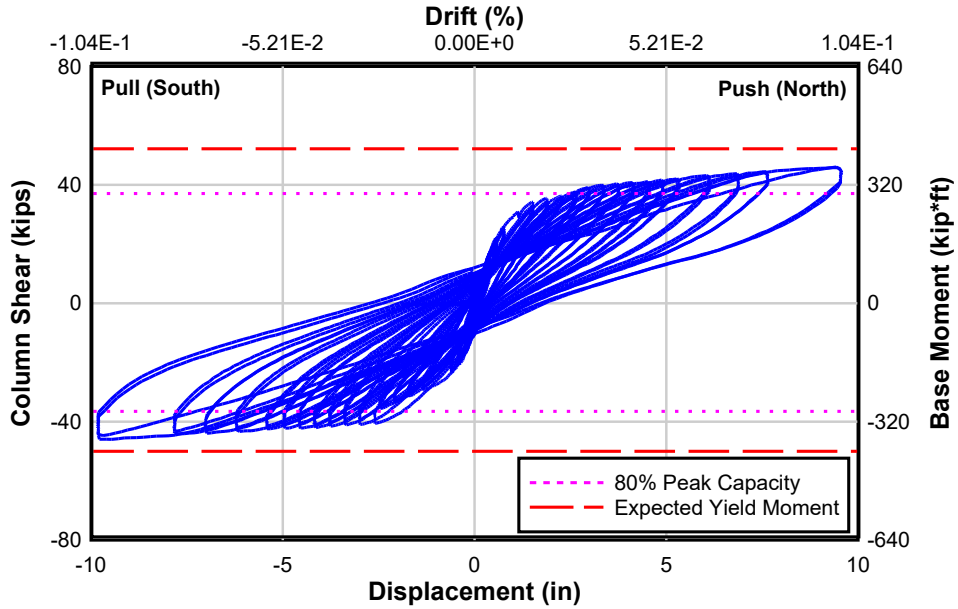

Figure A6.3.1.3: Overall Force Displacement Response – Test 1.

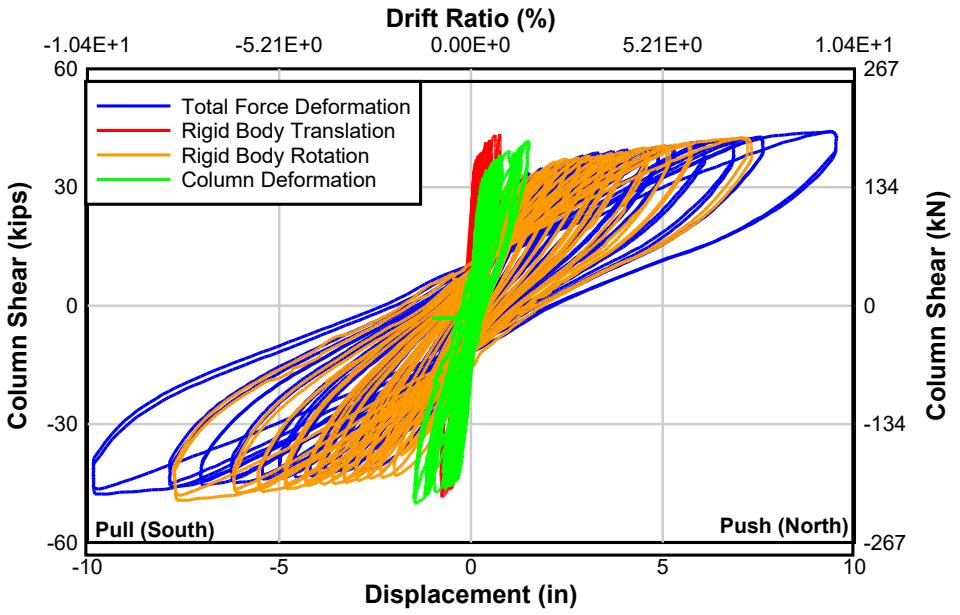

Figure A6.3.1.4: Component Contributions to Force Displacement – Test 1.

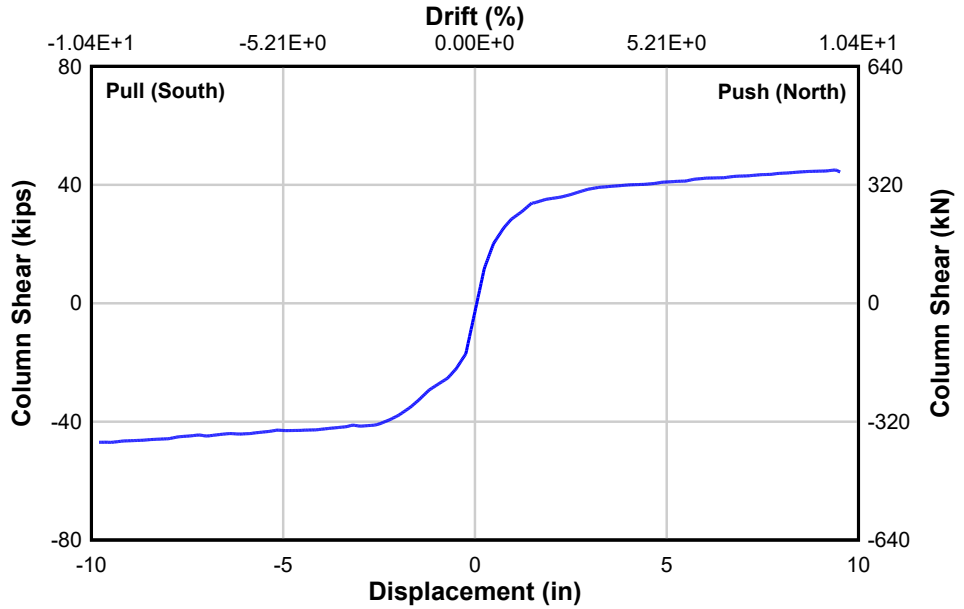

Figure A6.3.1.5: Overall Force Displacement Backbone Curve – Test 1.

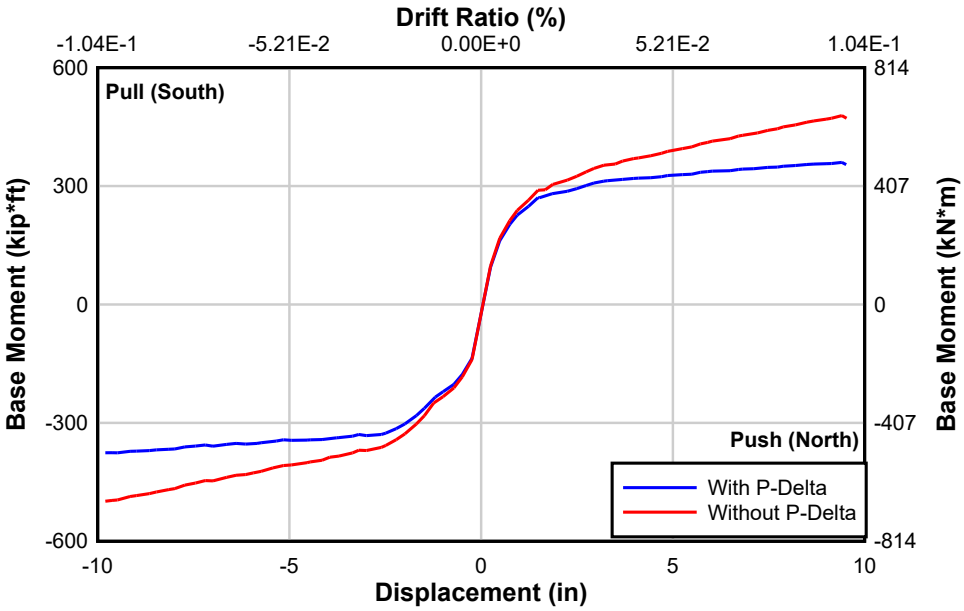

Figure A6.3.1.6: P-Delta Effects Backbone Curve – Test 1.

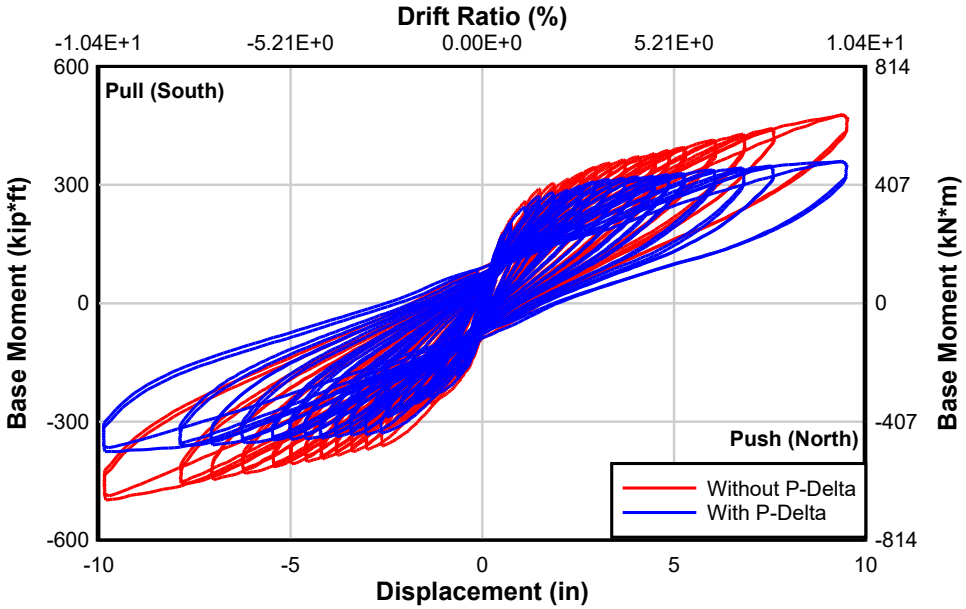

Figure A6.3.1.7: P-Delta Effects – Test 1.

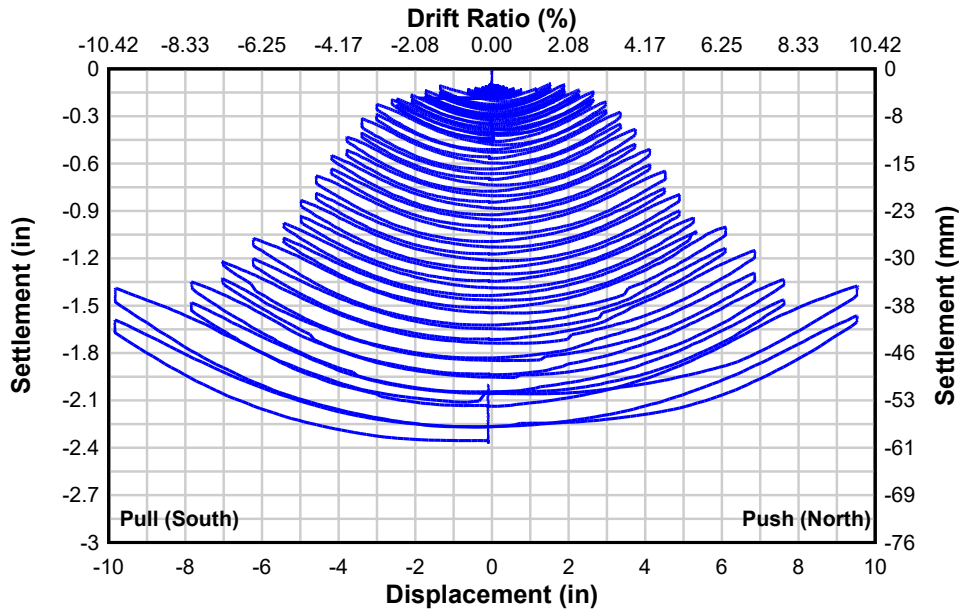

Figure A6.3.1.8: Settlement – Test 1.

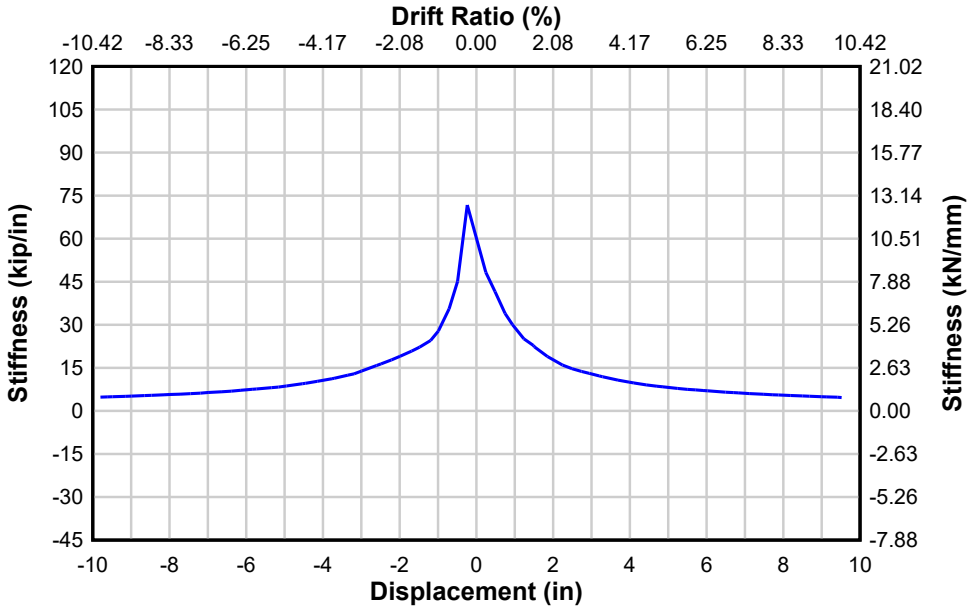

Figure A6.3.1.9: Evolution Secant Stiffness – Test 1.

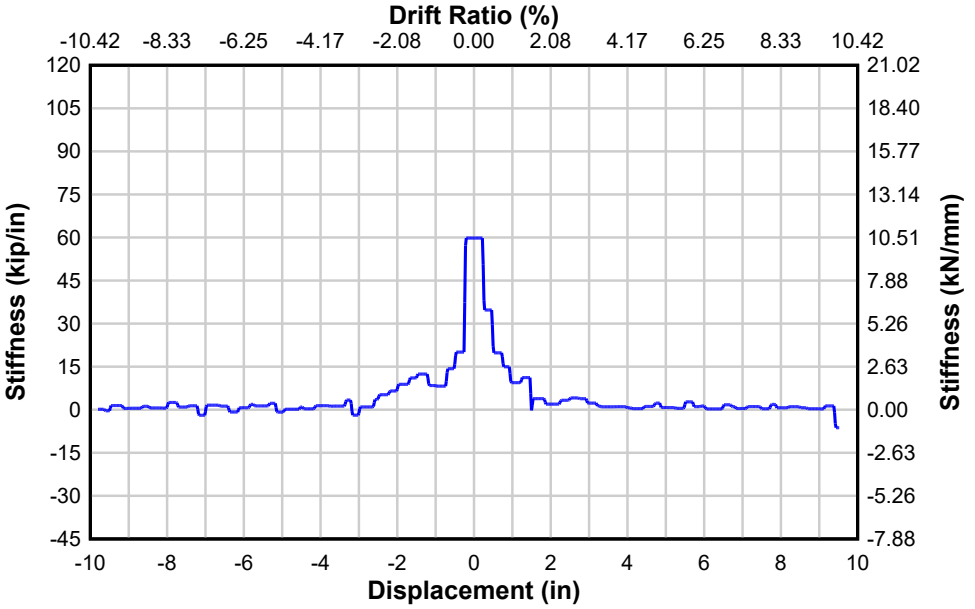

Figure A6.3.1.10: Evolution of Tangent Stiffness – Test 1.

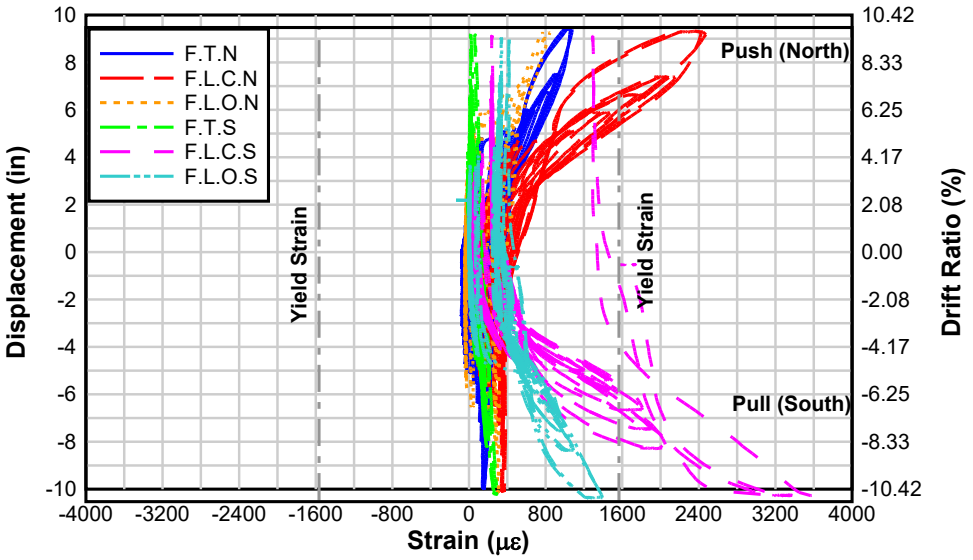

Figure A6.3.1.11: Footing Bar Strains – Test 1.

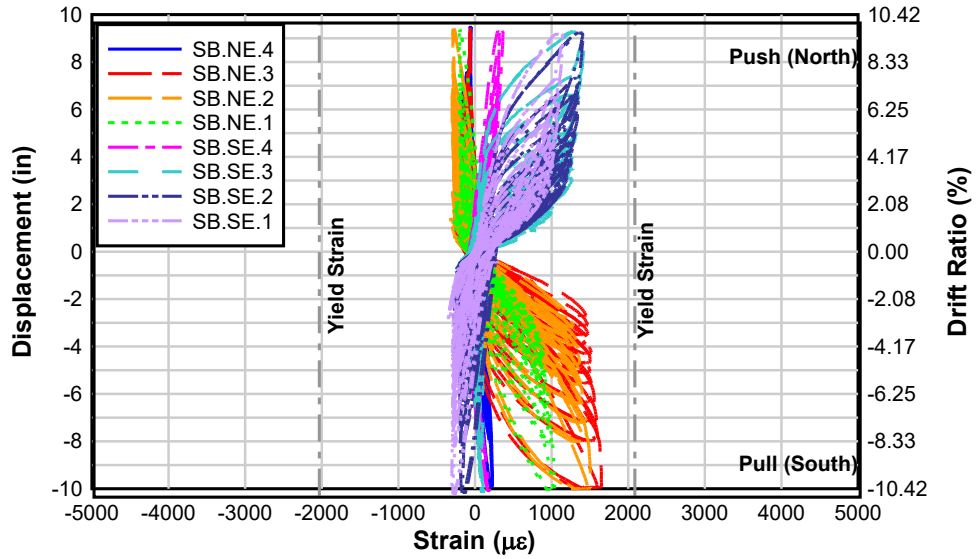

Figure A6.3.1.12: Starter Bar Strains – Test 1.

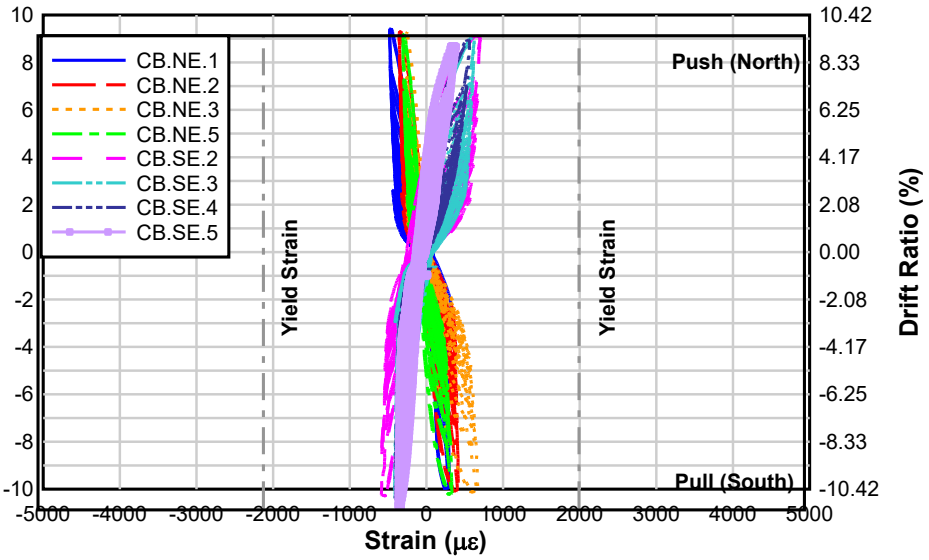

Figure A6.3.1.13: Column Bar Strains – Test 1.

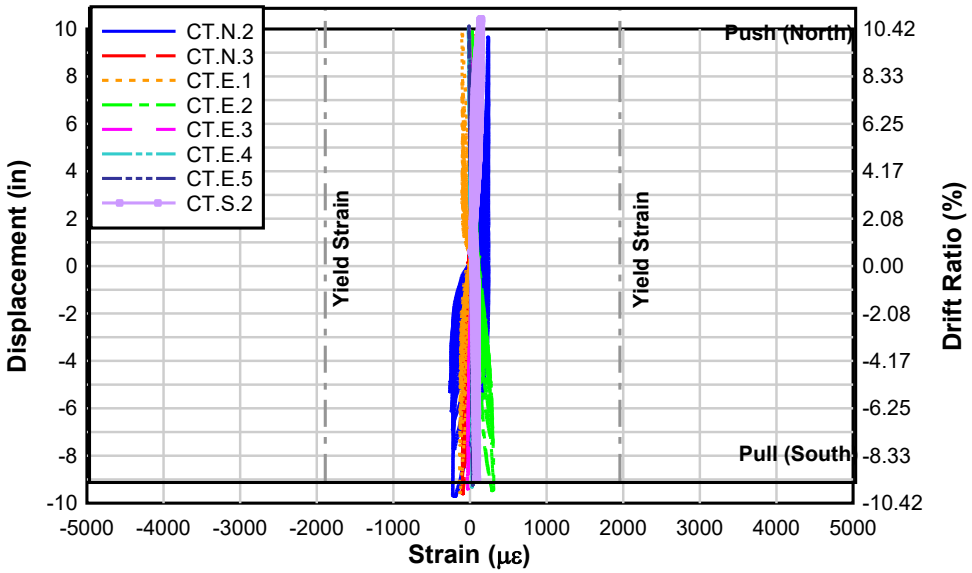

Figure A6.3.1.14: Column Tie Strains – Test 1.

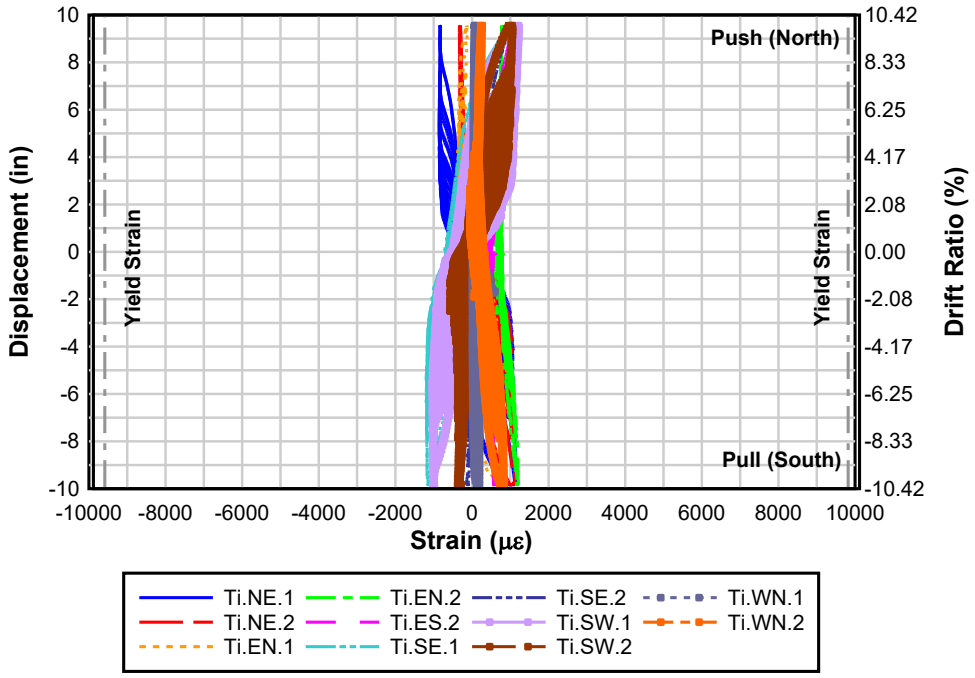

Figure A6.3.1.15: TiAB Ligament Strains – Test 1.

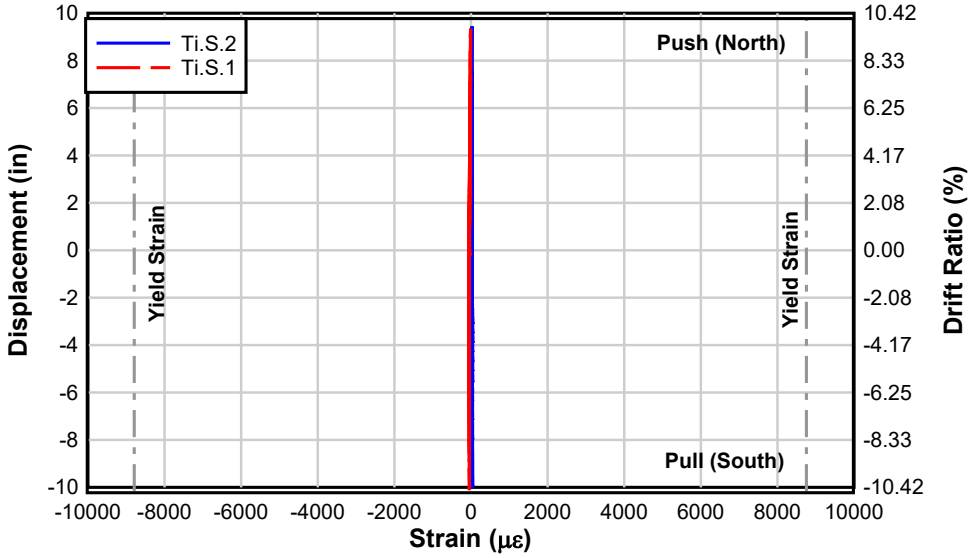

Figure A6.3.1.16: TiAB Spiral Strains – Test 1.

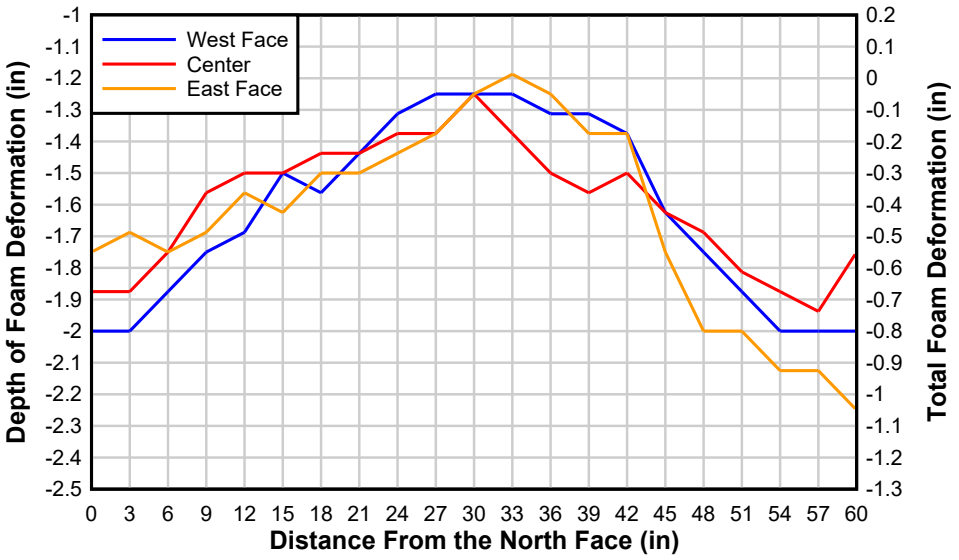

Figure A6.3.1.17: Soil Simulant Profile After Testing – Test 1.

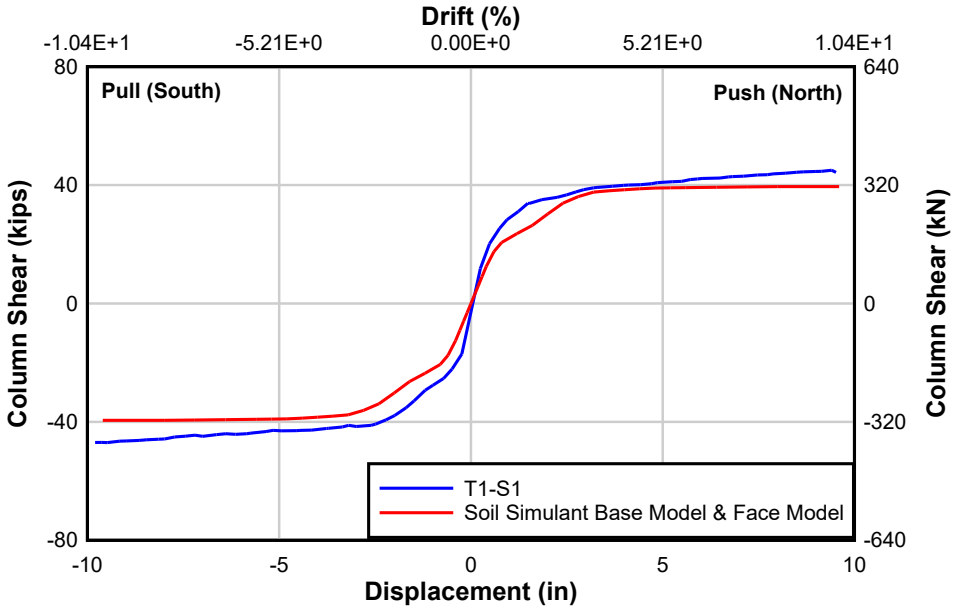

Figure A6.3.1.18: Soil Simulant Model Comparison – Test 1.

A6.3.2 TEST 2 - SPECIMEN 2: COMPLETE RETROFIT WITH NO EMBEDMENT & FOAM SUBGRADE

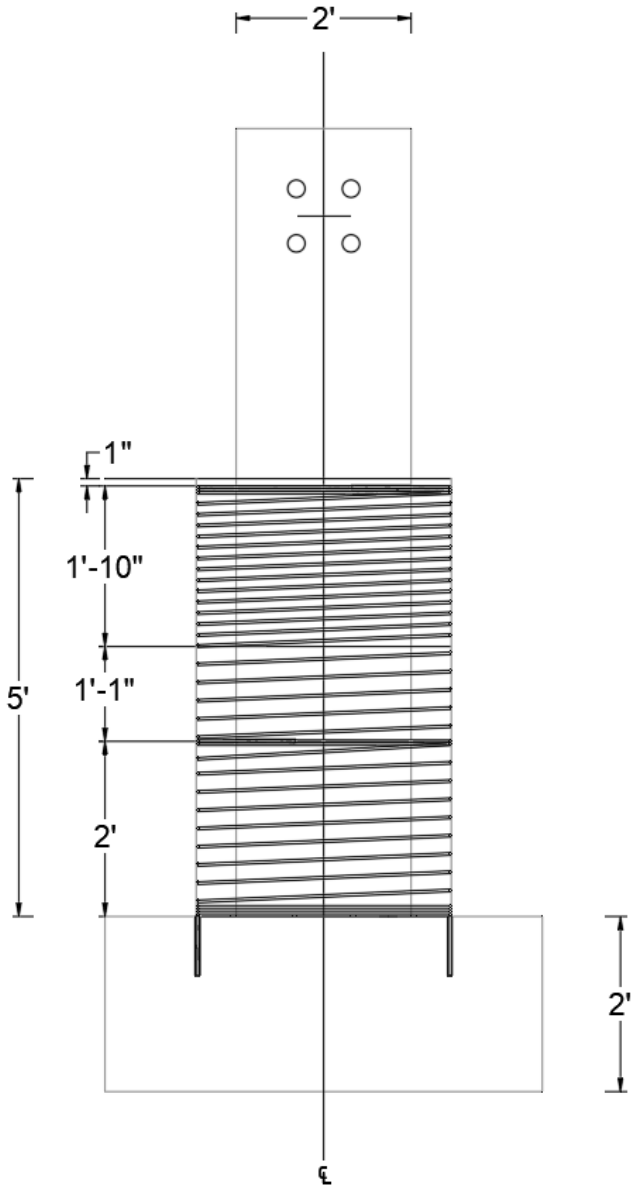

Figure A6.3.2.1 - Elevation View of Specimen 2 used in Test 2.

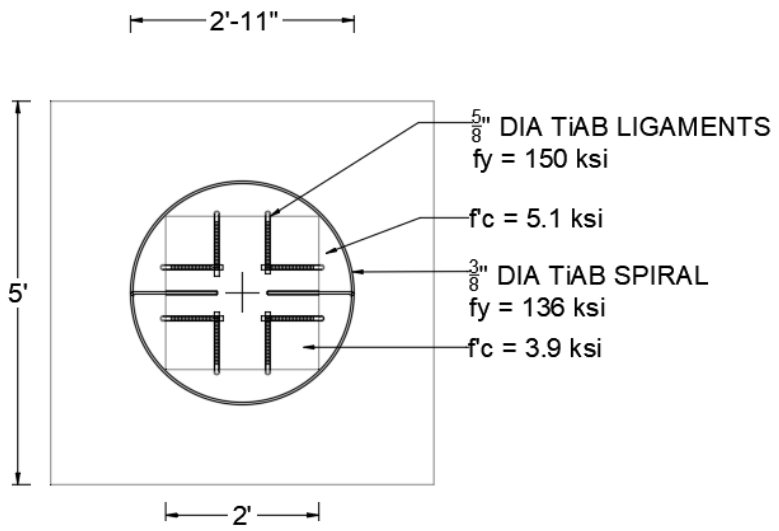

PLAN VIEW E-W

Figure A6.3.2.2: Plan View of Specimen 2 used in Test 2.

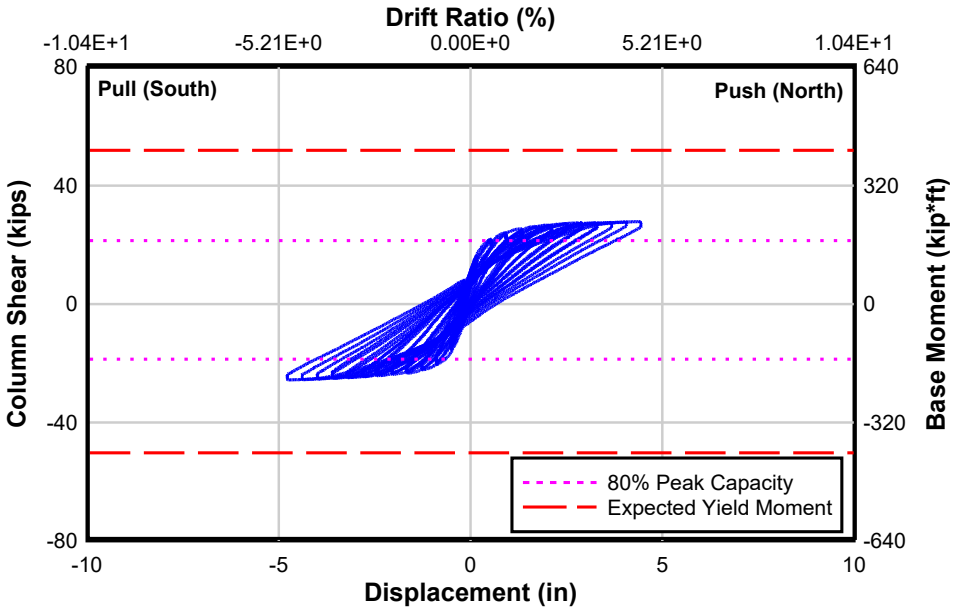

Figure A6.3.2.3: Overall Force Displacement Response – Test 2.

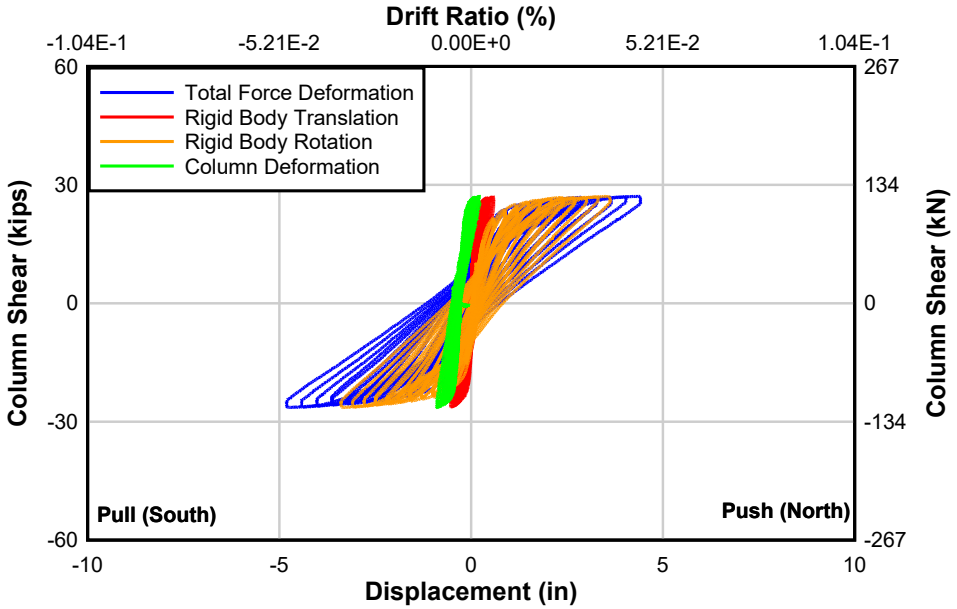

Figure A6.3.2.4: Component Contributions to Force Displacement – Test 2.

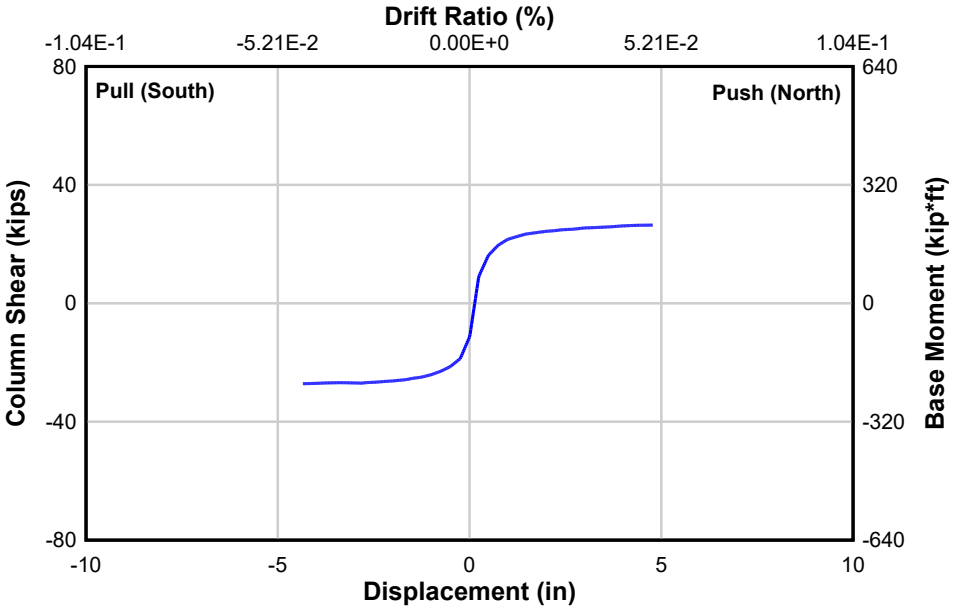

Figure A6.3.2.5: Overall Force Displacement Backbone Curve – Test 2.

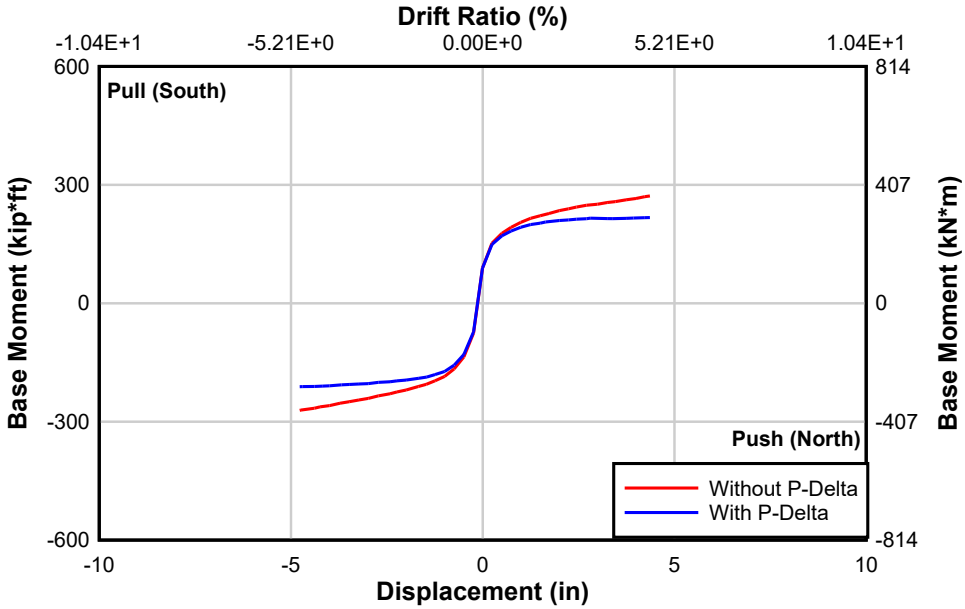

Figure A6.3.2.6: P-Delta Effects Backbone Curve – Test 2.

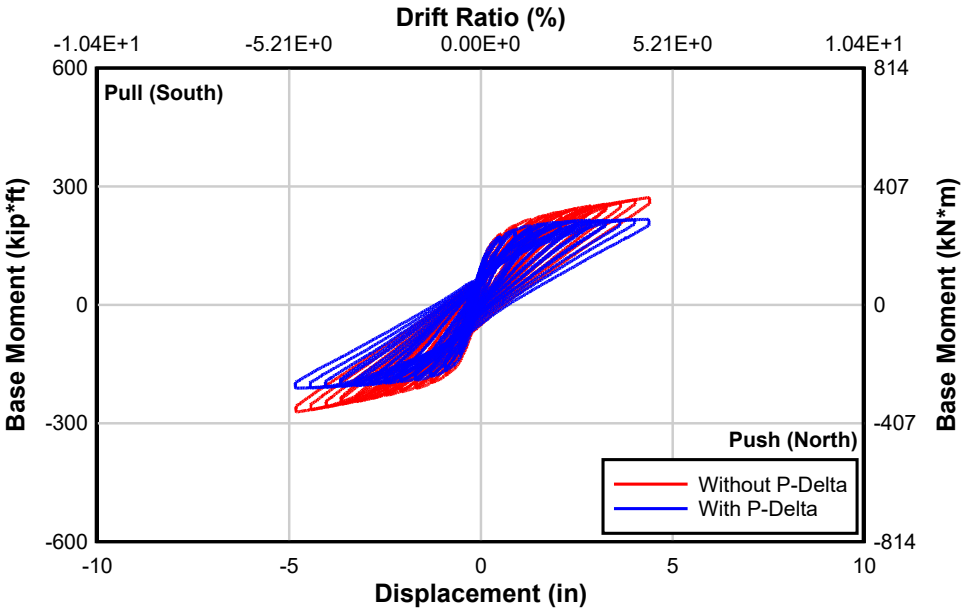

Figure A6.3.2.7: P-Delta Effects – Test 2.

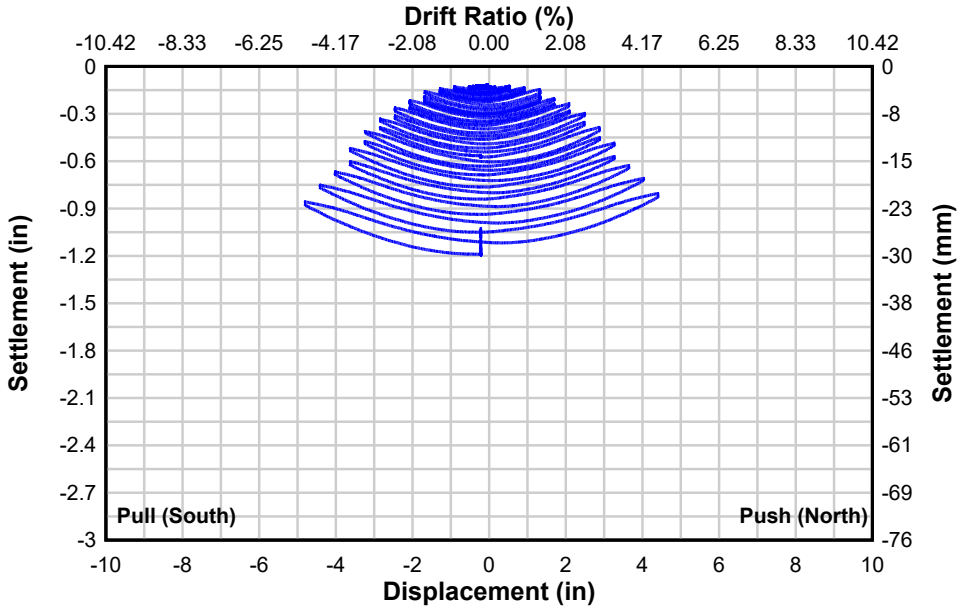

Figure A6.3.2.8: Settlement – Test 2.

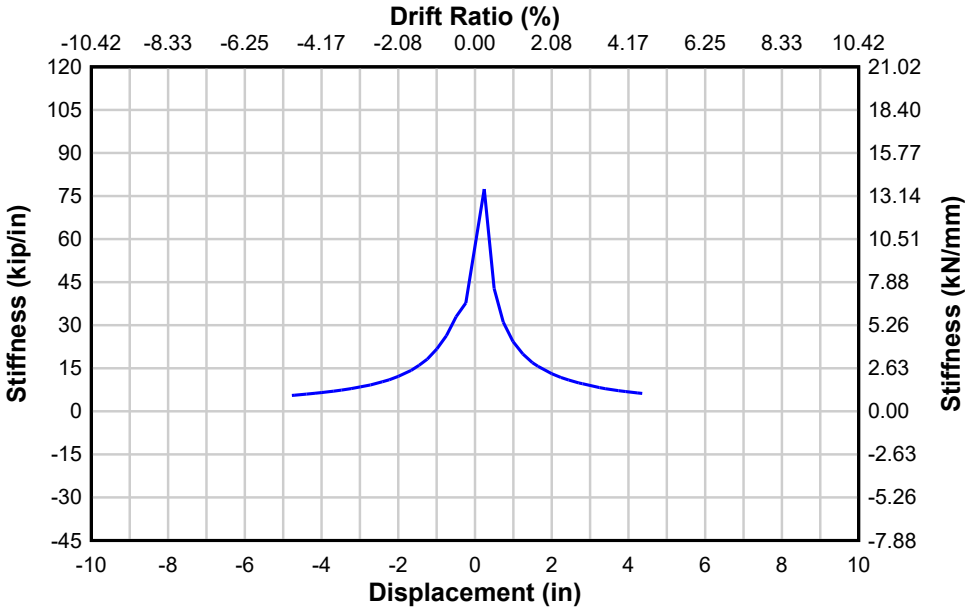

Figure A6.3.2.9: Evolution of Secant Stiffness – Test 2.

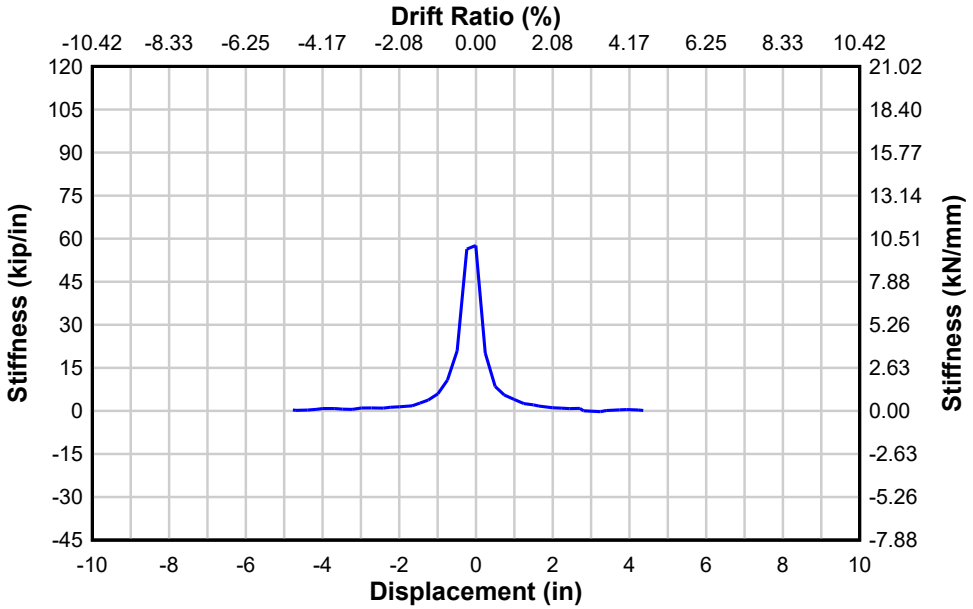

Figure A6.3.2.10: Evolution of Tangent Stiffness – Test 2.

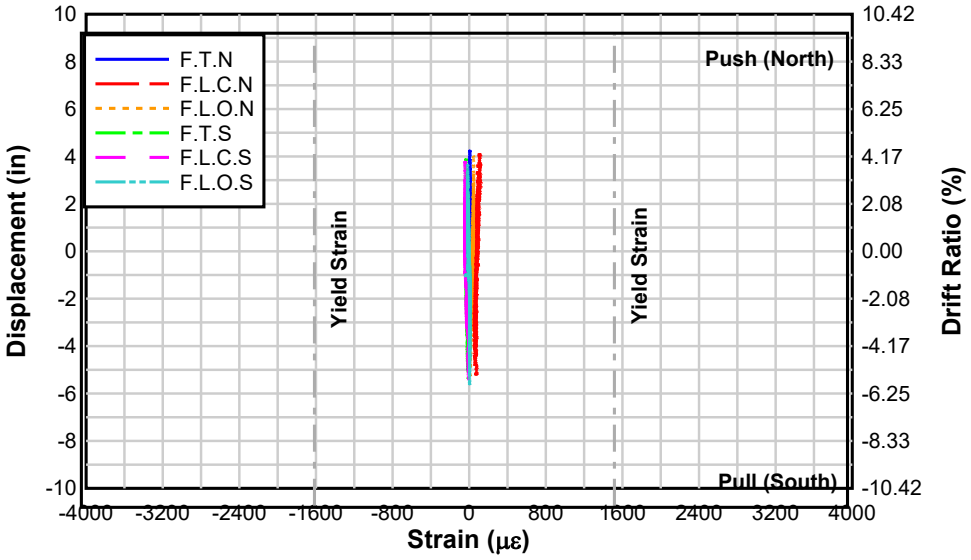

Figure A6.3.2.11: Footing Bar Strains -Test 2.

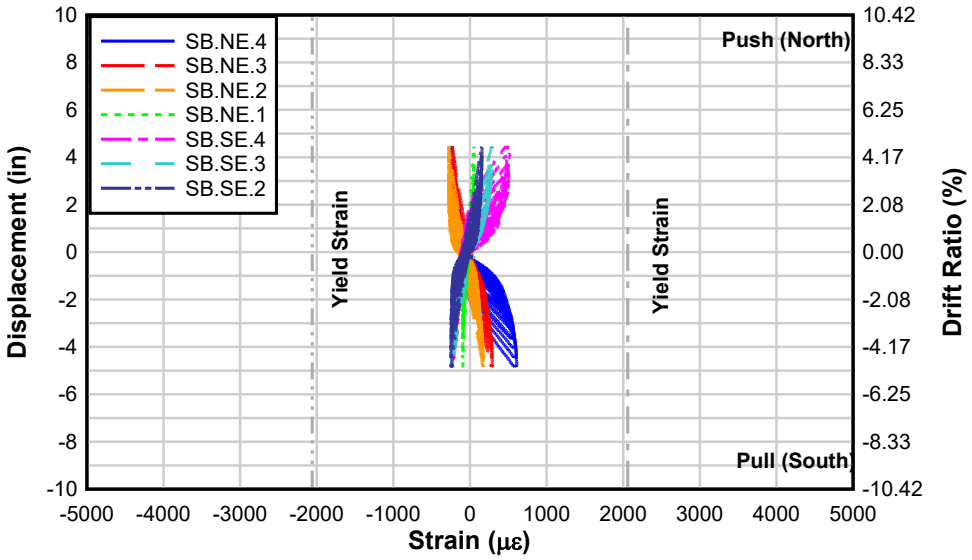

Figure A6.3.2.12: Starter Bar Strains – Test 2.

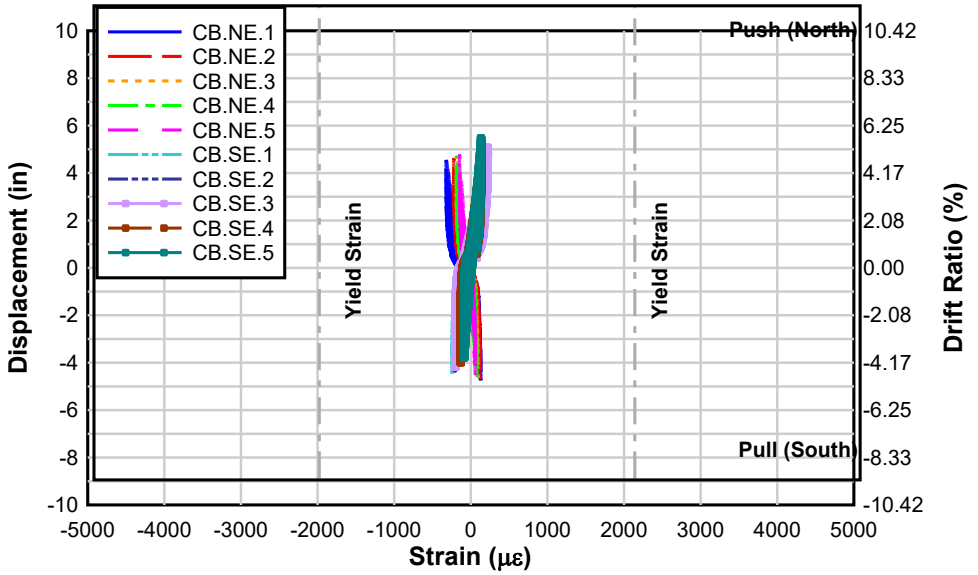

Figure A6.3.2.13: Column Bar Strains – Test 2.

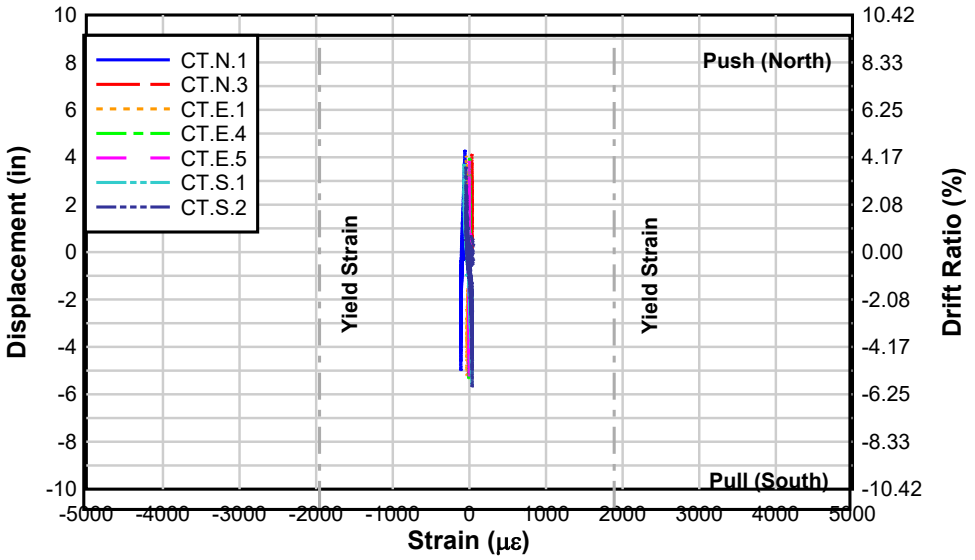

Figure A6.3.2.14: Column Tie Strain – Test 2.

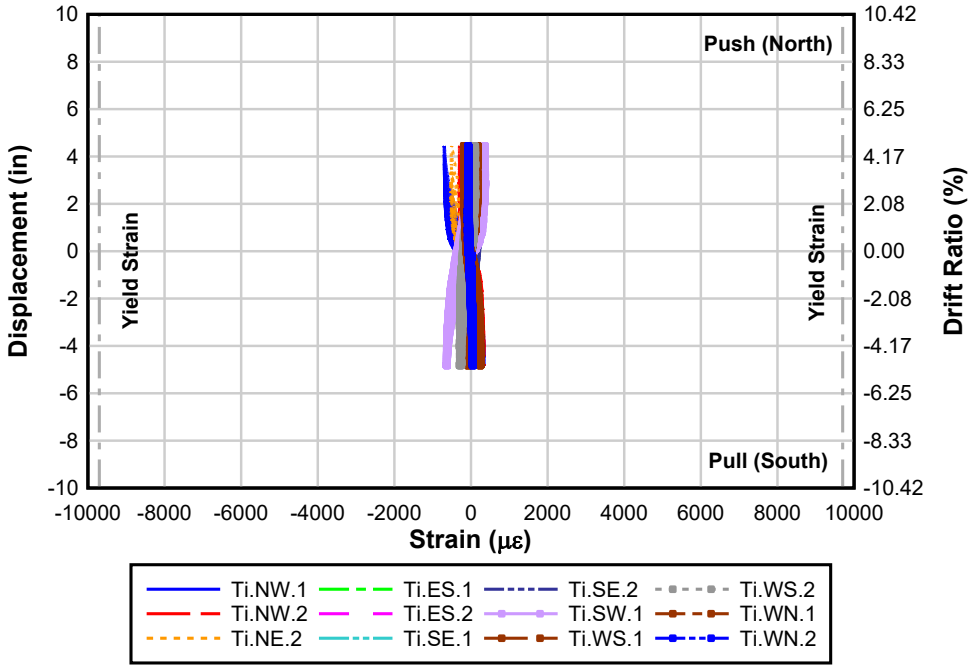

Figure A6.3.2.15: TiAB Ligament Strain – Test 2.

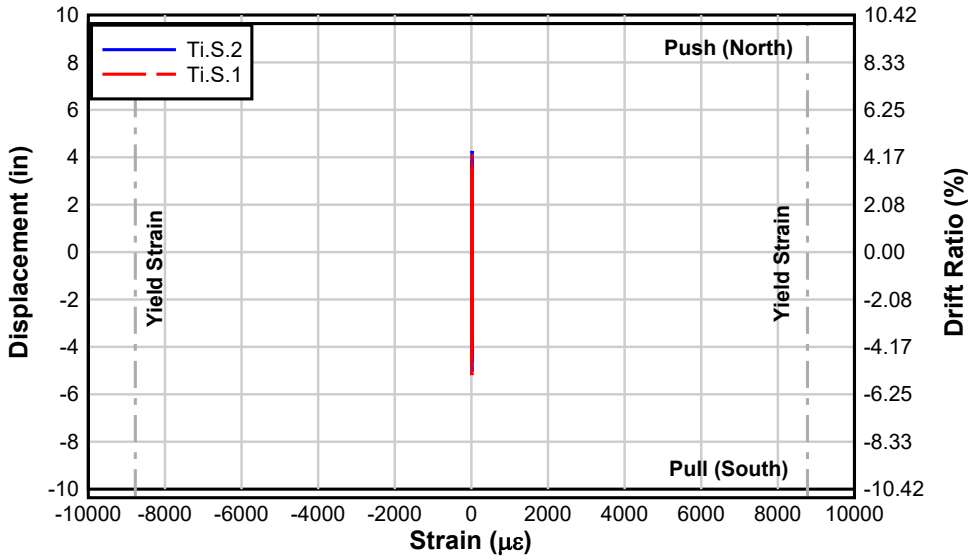

Figure A6.3.2.16: TiAB Spiral Strain – Test 2.

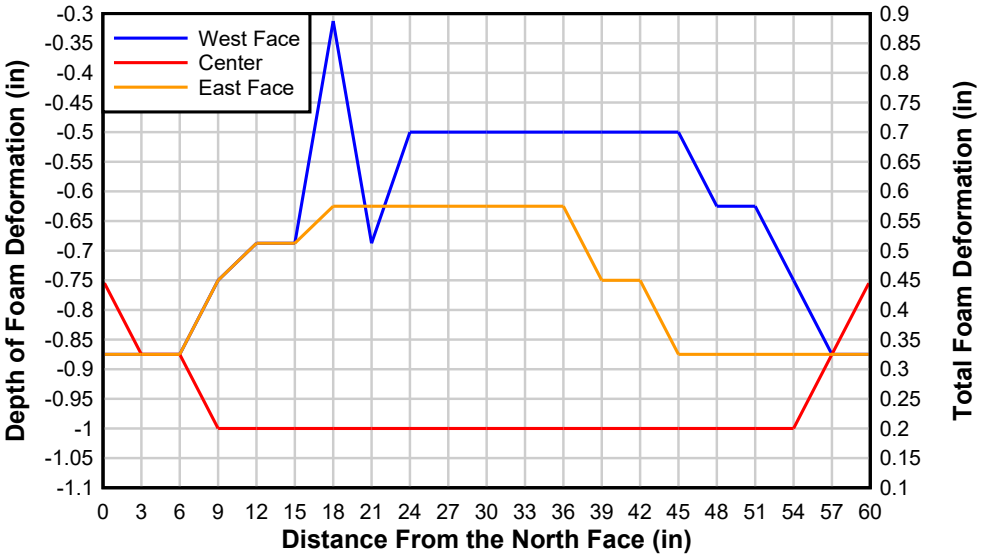

Figure A6.3.2.17: Soil Simulant Profile After Testing – Test 2.

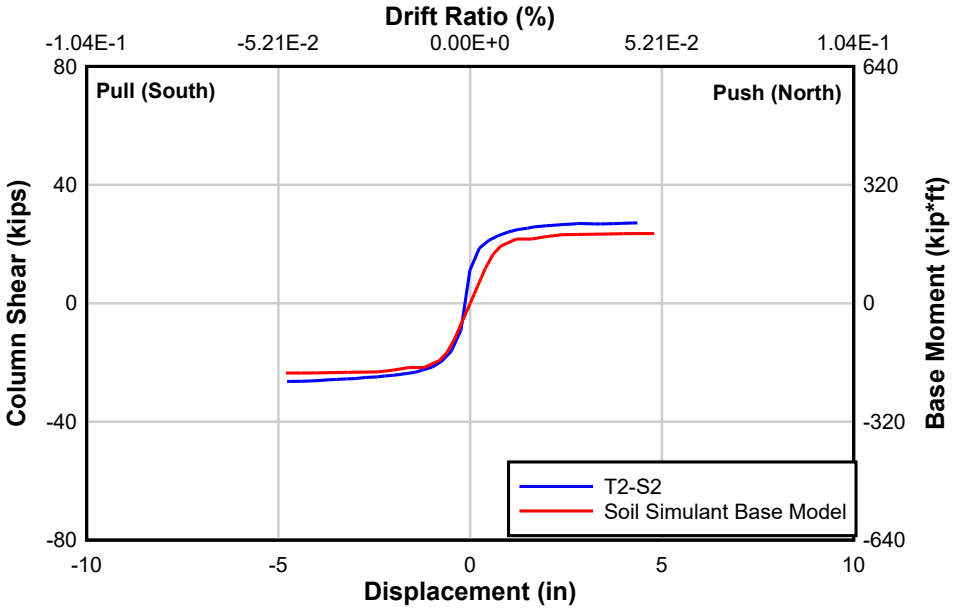

Figure A6.3.2.18: Soil Simulant Model Comparison -Test 2.

A6.3.3 TEST 3 – SPECIMEN 3: VINTAGE WITH FOAM EMBEDMENT, SUBGRADE, & 150 KIP AXIAL LOAD

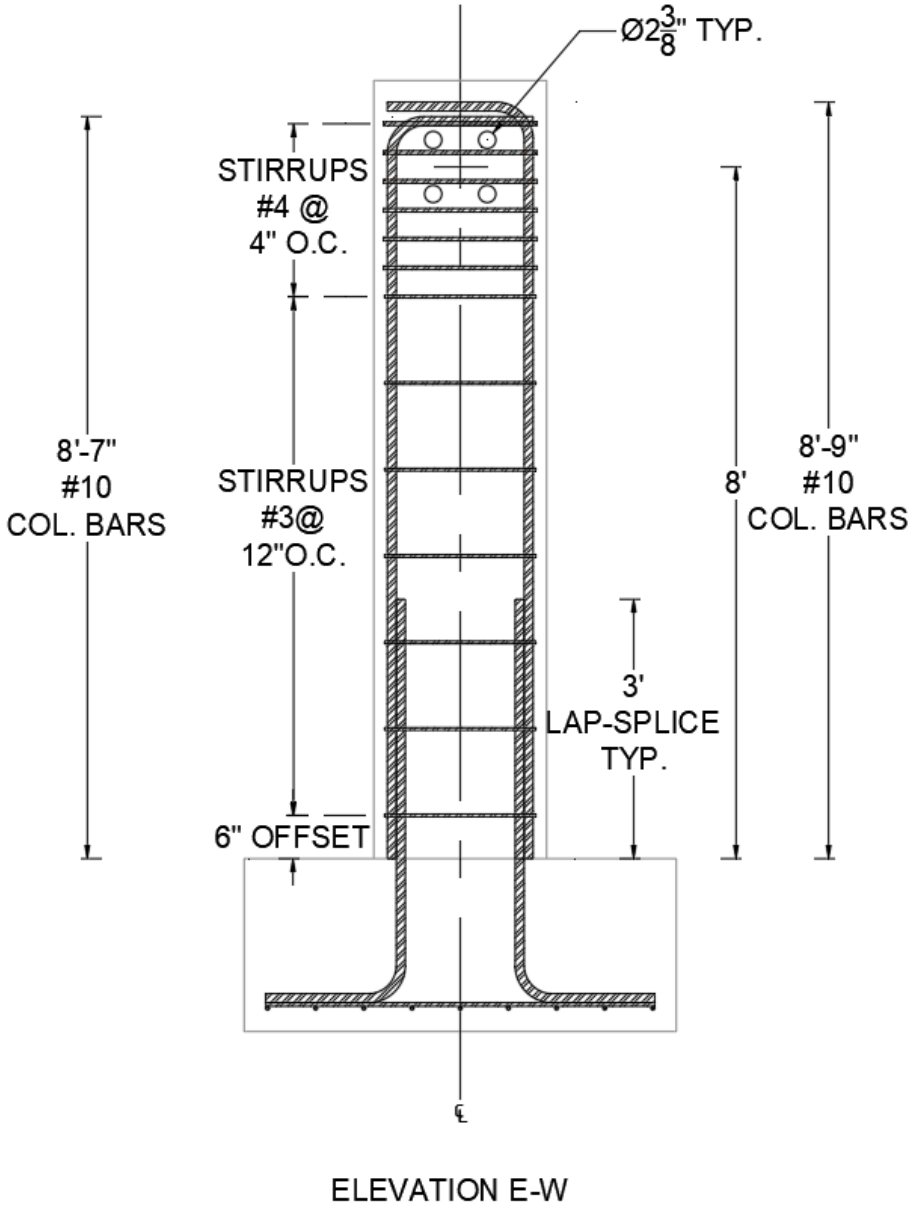

Figure A6.3.3.1: Elevation View of Specimen 3 used in Test 3.

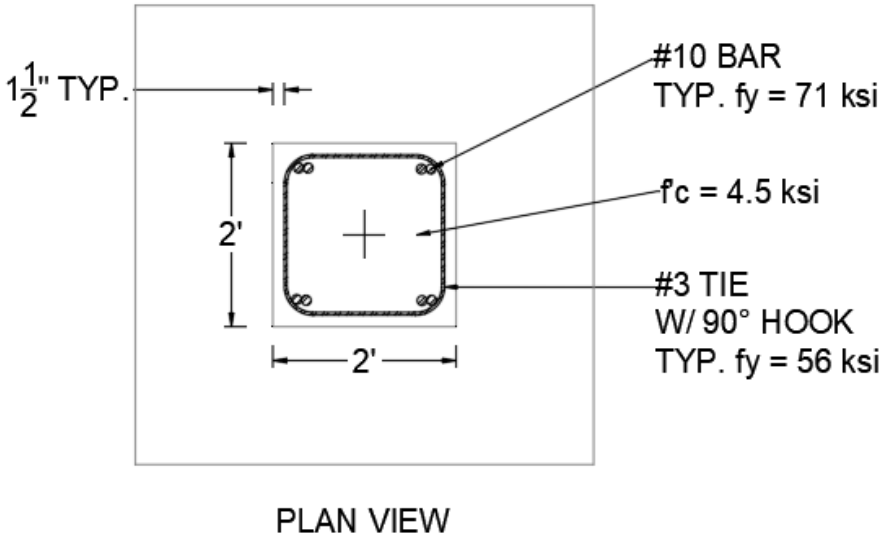

Figure A6.3.3.2: Plan View of Specimen 3 used in Test 3.

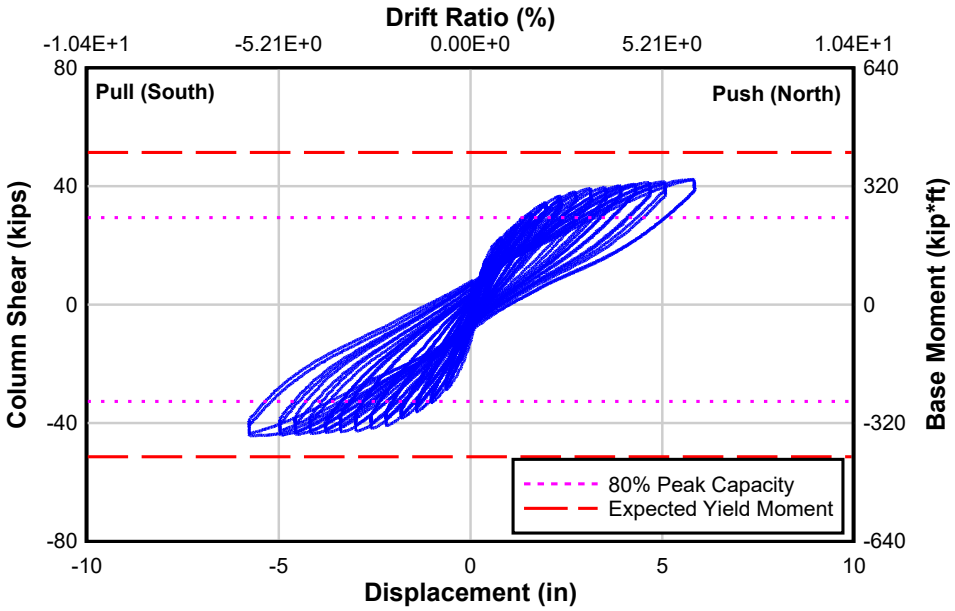

Figure A6.3.3.3: Overall Force Displacement Response – Test 3.

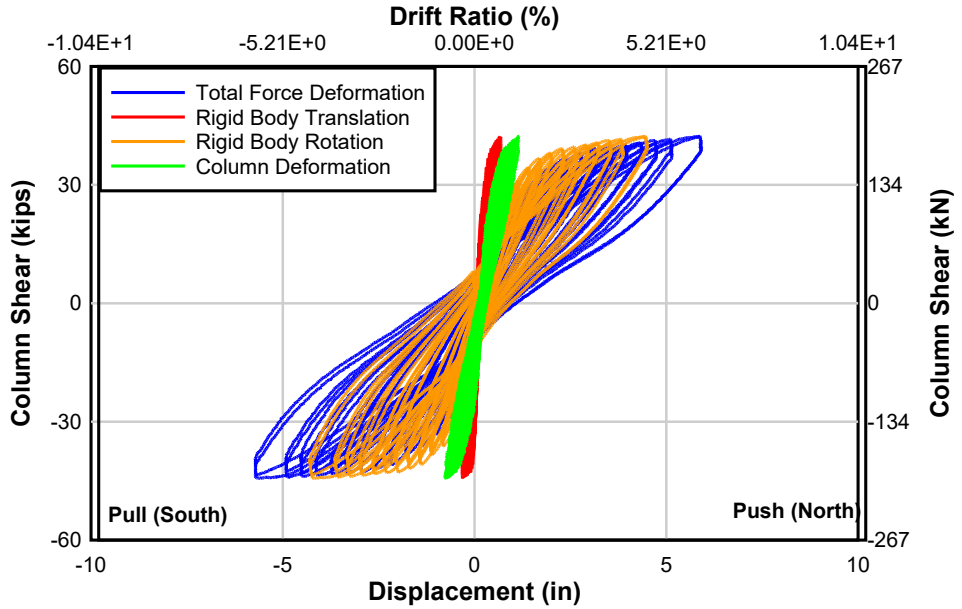

Figure A6.3.3.4: Component Contributions to Force Displacement – Test 3.

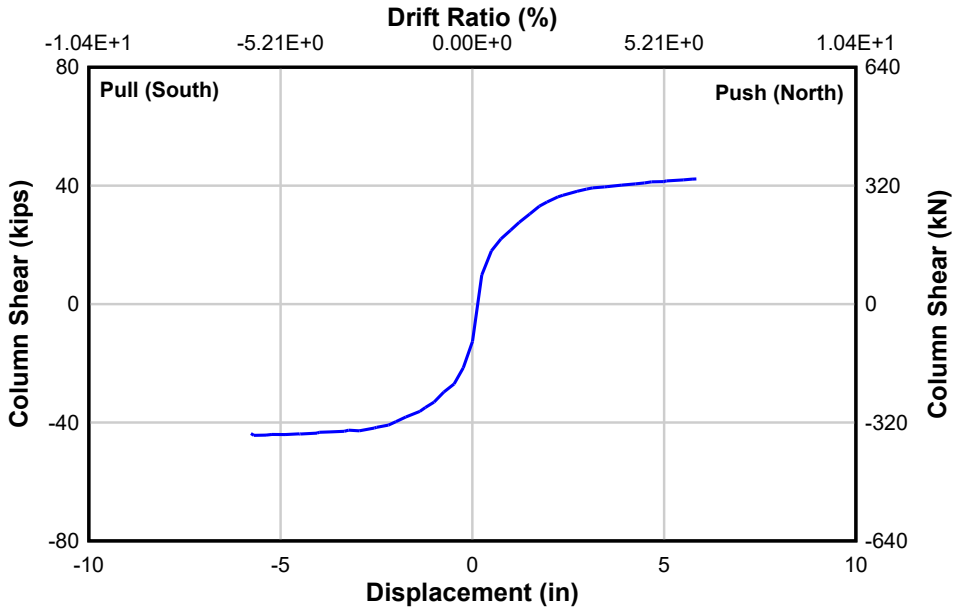

Figure A6.3.3.5: Overall Force Displacement Backbone Curve – Test 3.

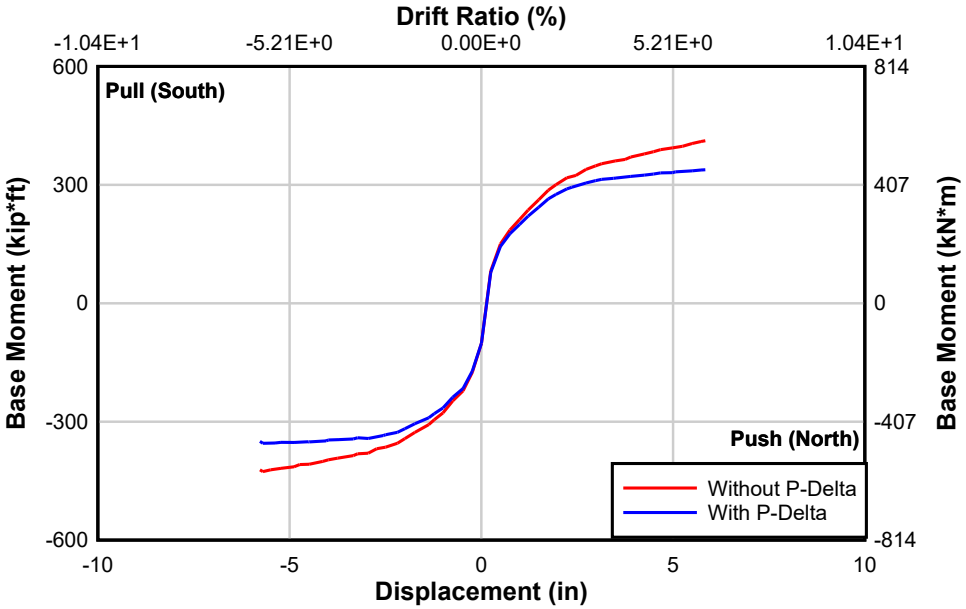

Figure A6.3.3.6: P-Delta Effects Backbone Curve – Test 3.

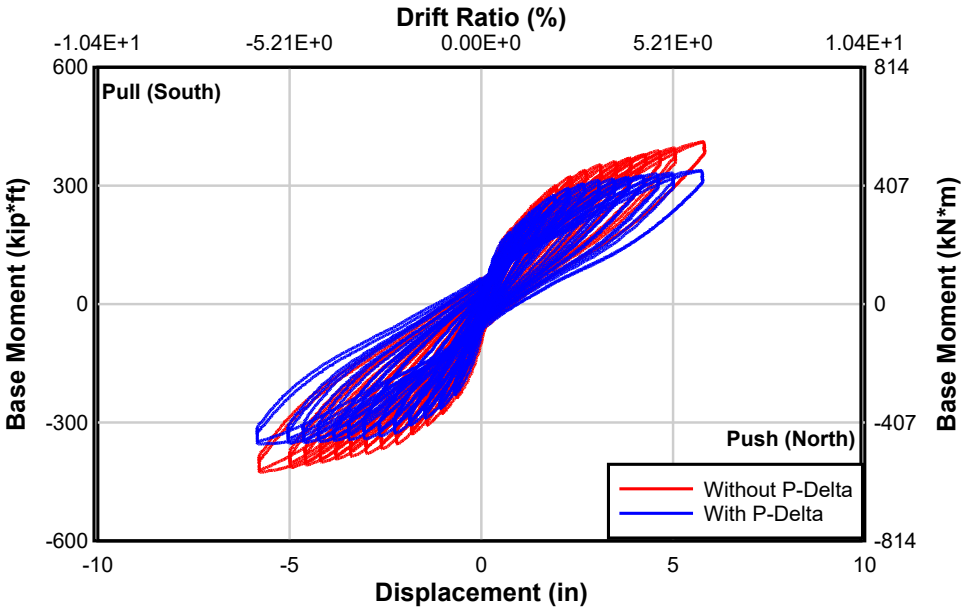

Figure A6.3.3.7: P-Delta Effects – Test 3.

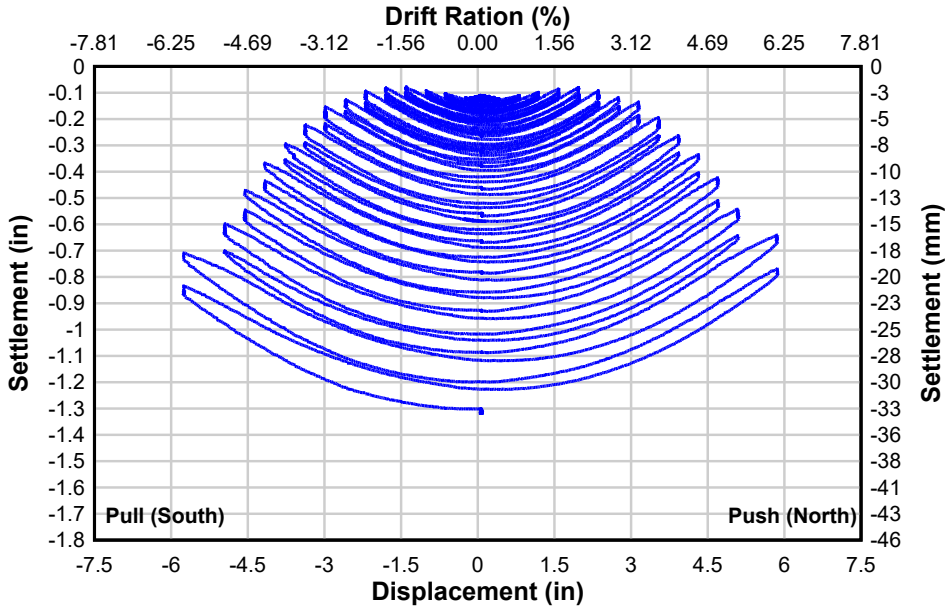

Figure A6.3.3.8: Settlement – Test 3.

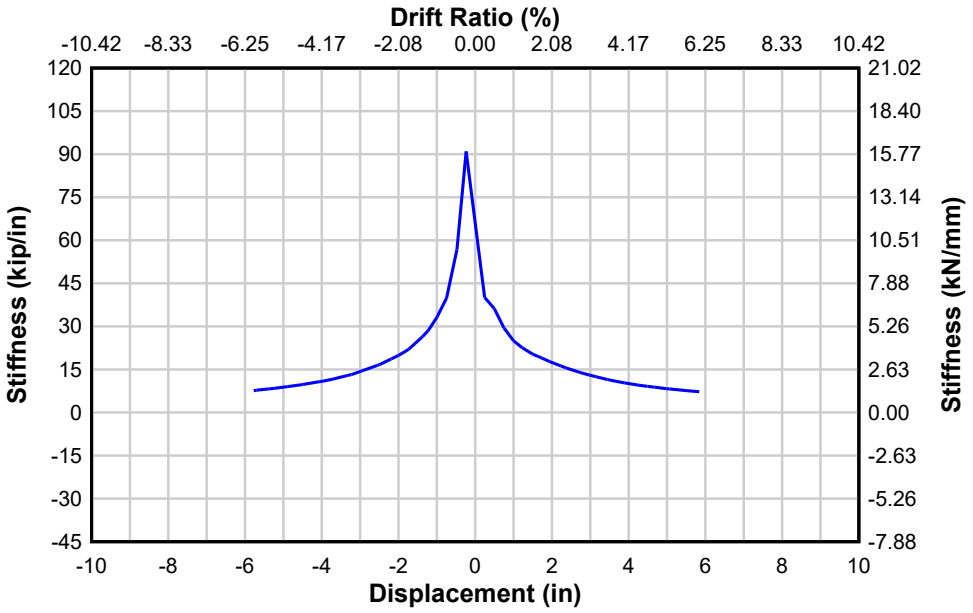

Figure A6.3.3.9: Evolution of Secant Stiffness – Test 3.

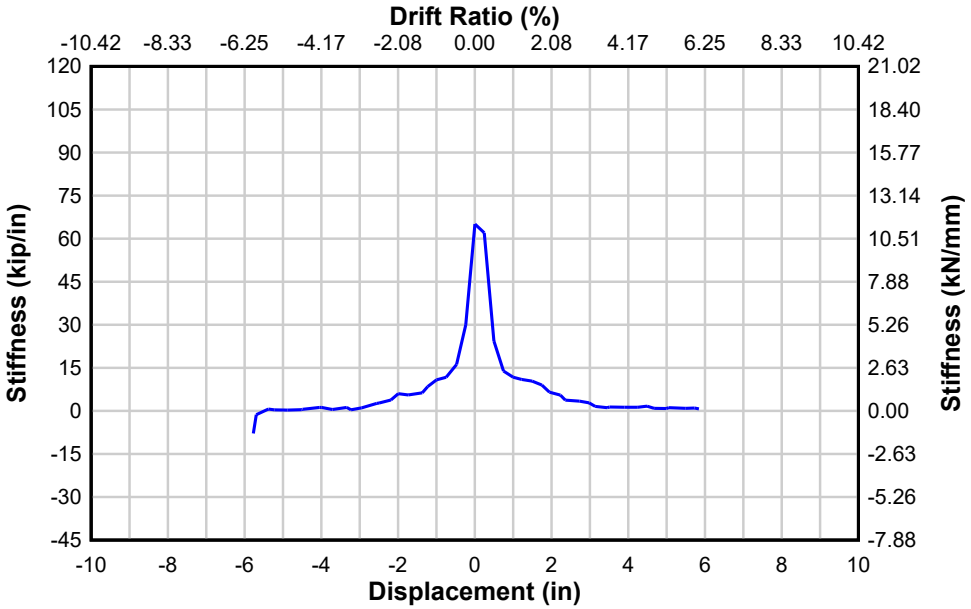

Figure A6.3.3.10: Evolution of Tangent Stiffness – Test 3.

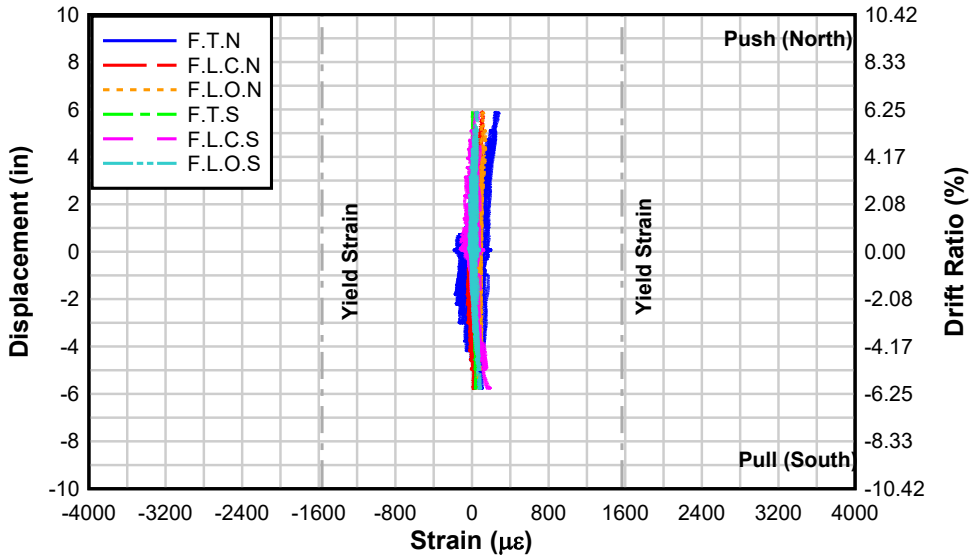

Figure A6.3.3.11: Footing Bar Strains – Test 3.

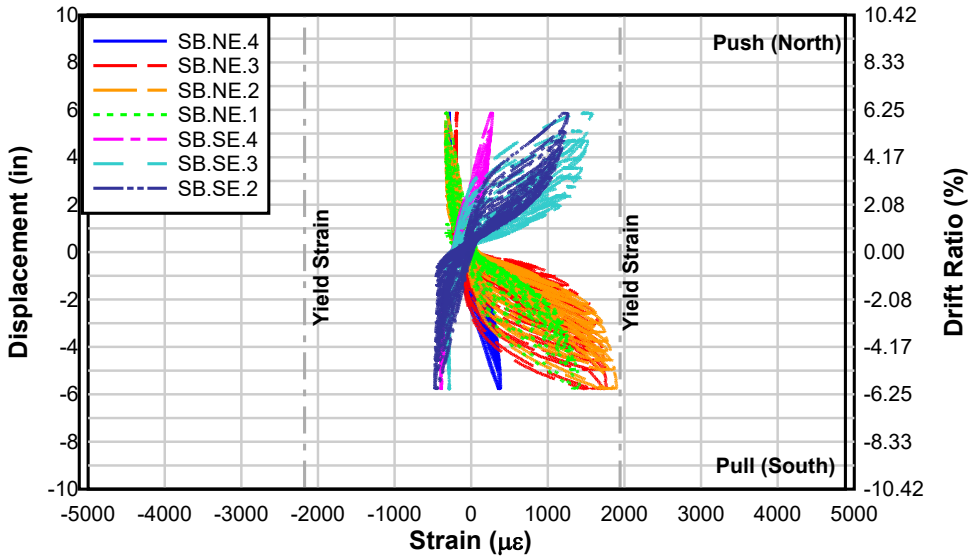

Figure A6.3.3.12: Starter Bar Strains – Test 3.

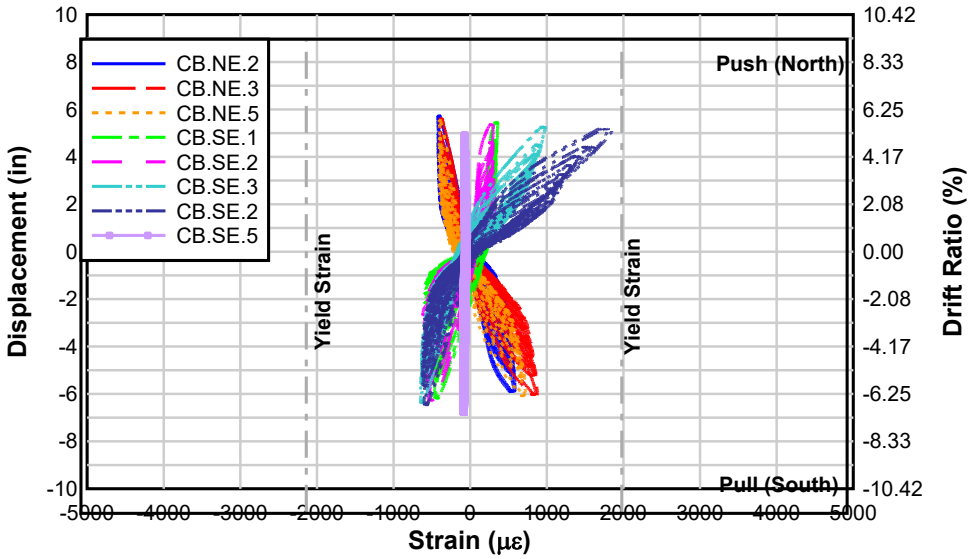

Figure A6.3.3.13: Column Bar Strains – Test 3.

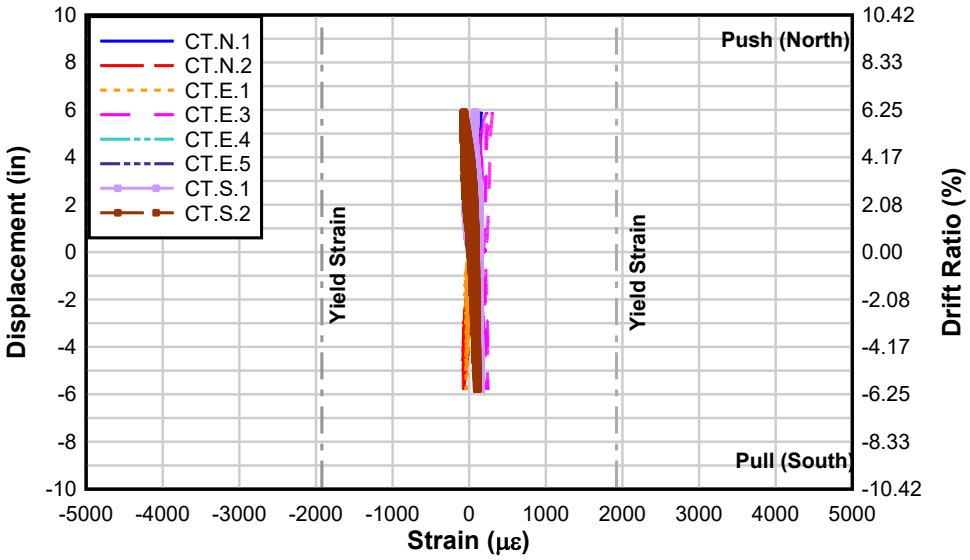

Figure A6.3.3.14: Column Tie Strains – Test 3.

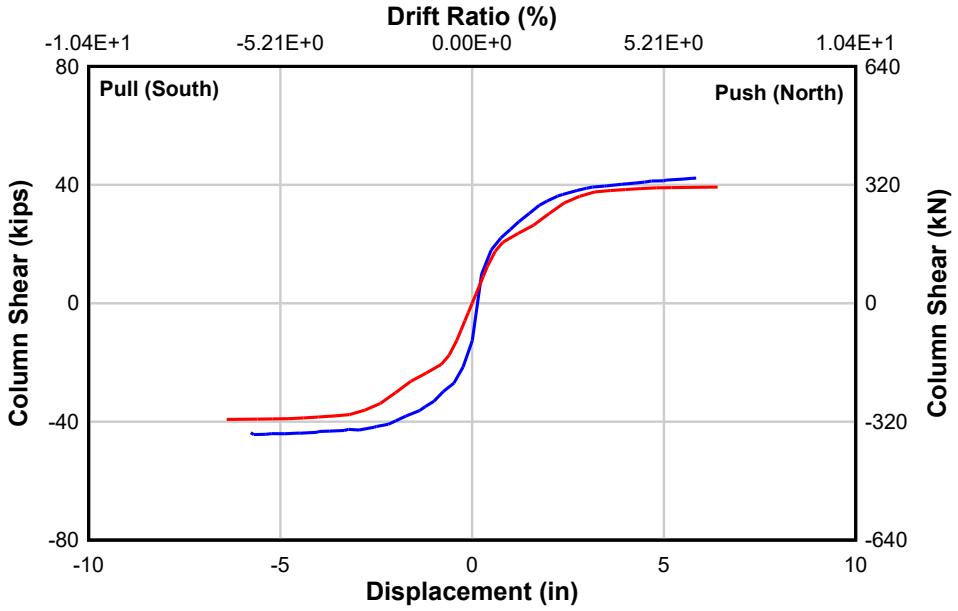

Figure A6.3.3.15: Soil Simulant Model Comparison – Test 3.

A6.3.4 TEST 4 – SPECIMEN 3: VINTAGE WITH FOAM EMBEDMENT, SUBGRADE, & 100 KIP AXIAL LOAD

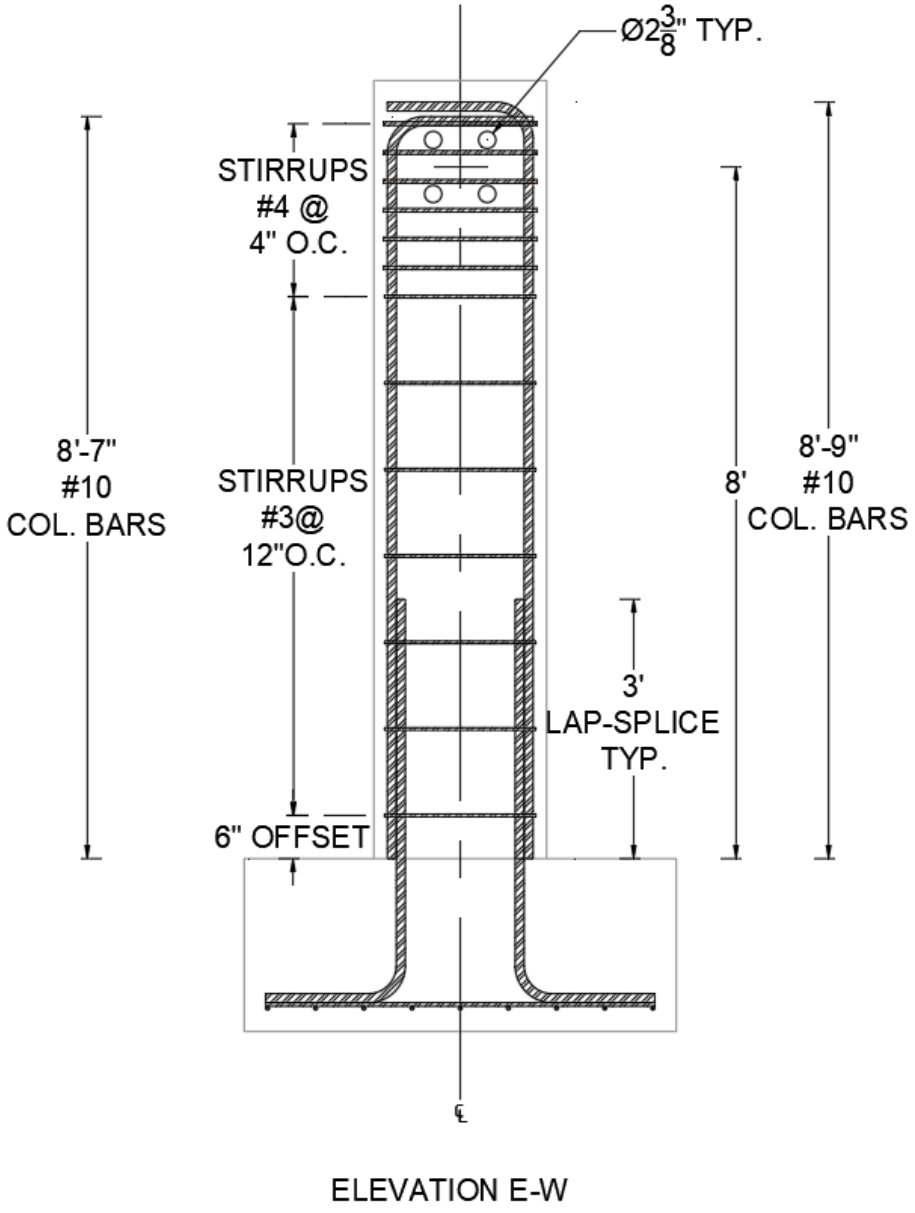

Figure A6.3.4.1 - Elevation View of Specimen 3 used in Test 4.

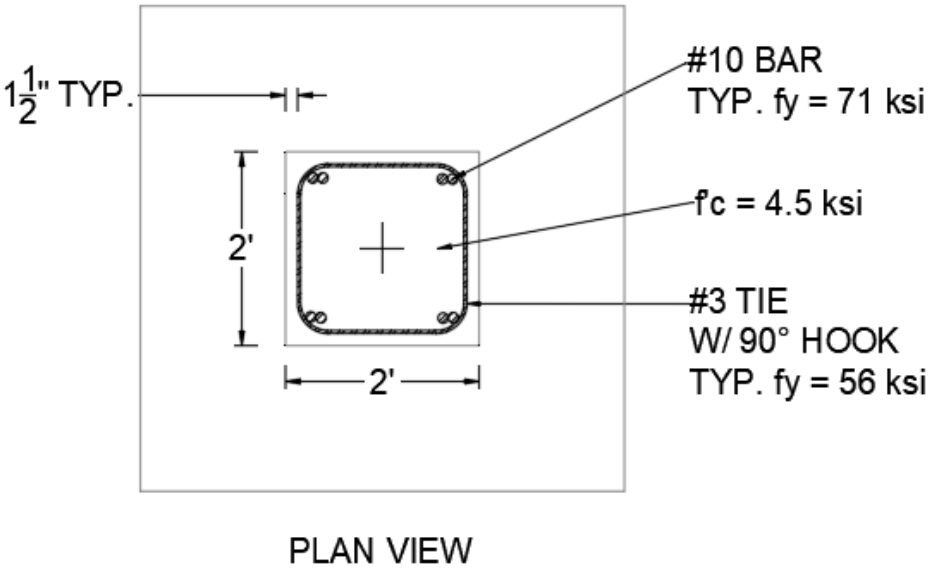

Figure A6.3.4.2 - Plan View of Specimen 3 used in Test 4.

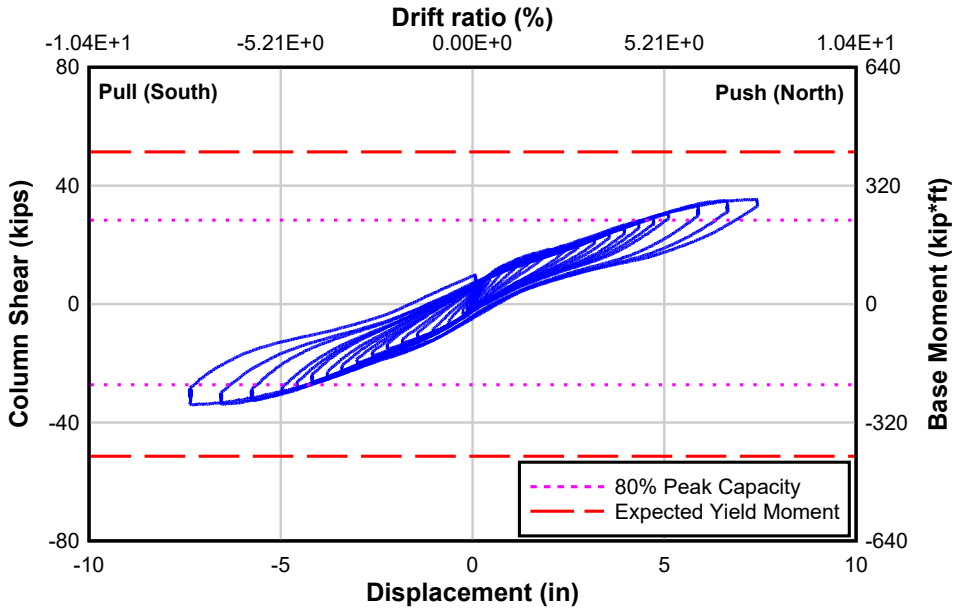

Figure A6.3.4.3: Overall Force Displacement Response -Test 4.

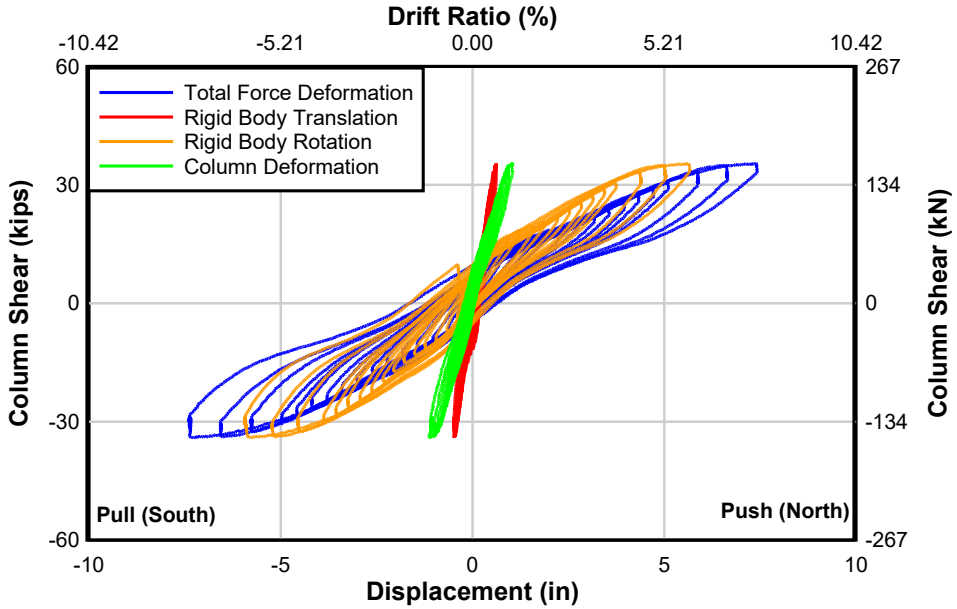

Figure A6.3.4.4: Component Contributions to Force Displacement – Test 4.

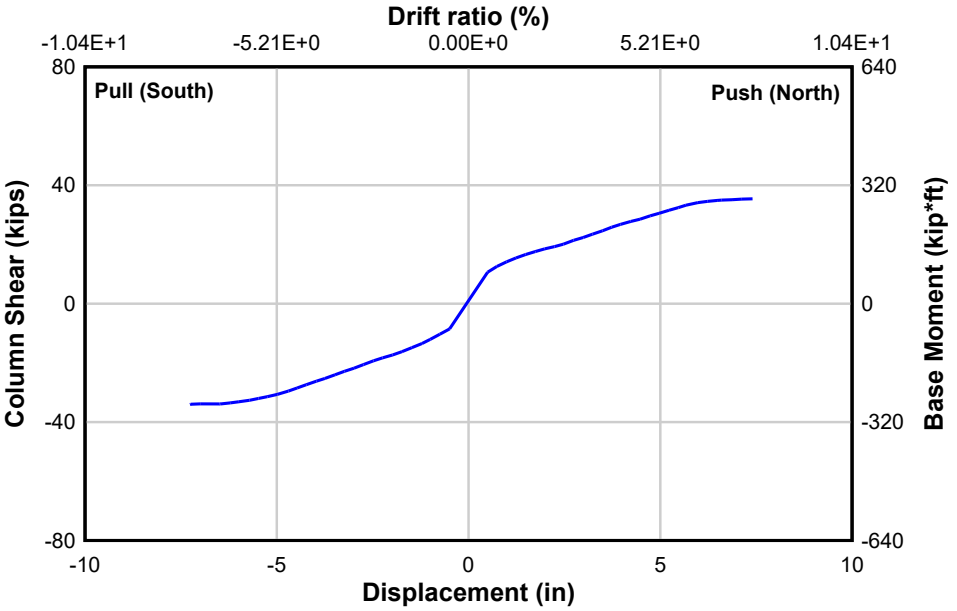

Figure A6.3.4.5: Overall Force Displacement Backbone Curve – Test 4.

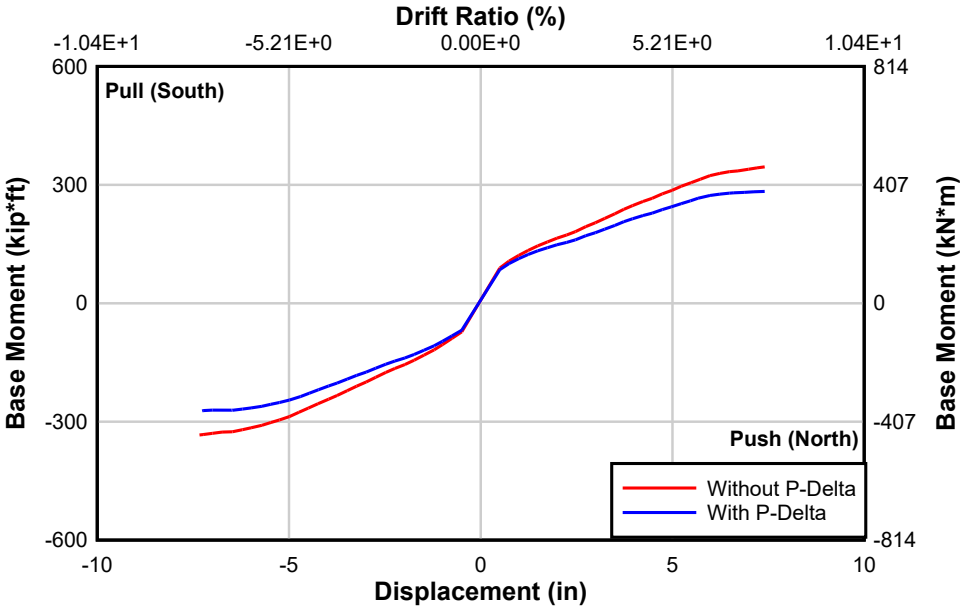

Figure A6.3.4.6: P-Delta Effects Backbone Curve – Test 4.

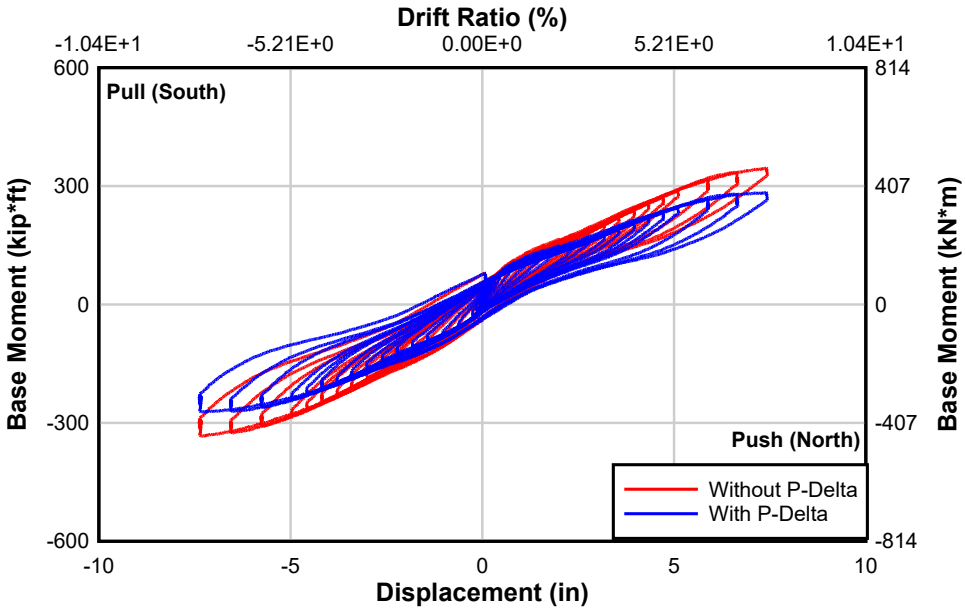

Figure A6.3.4.7: P-Delta Effects – Test 4.

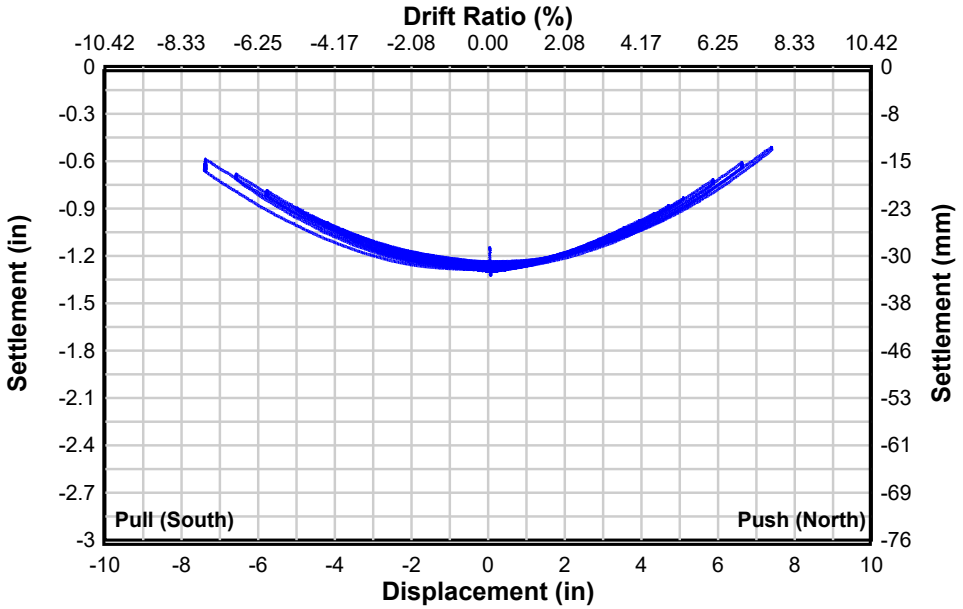

Figure A6.3.4.8: Settlement – Test 4.

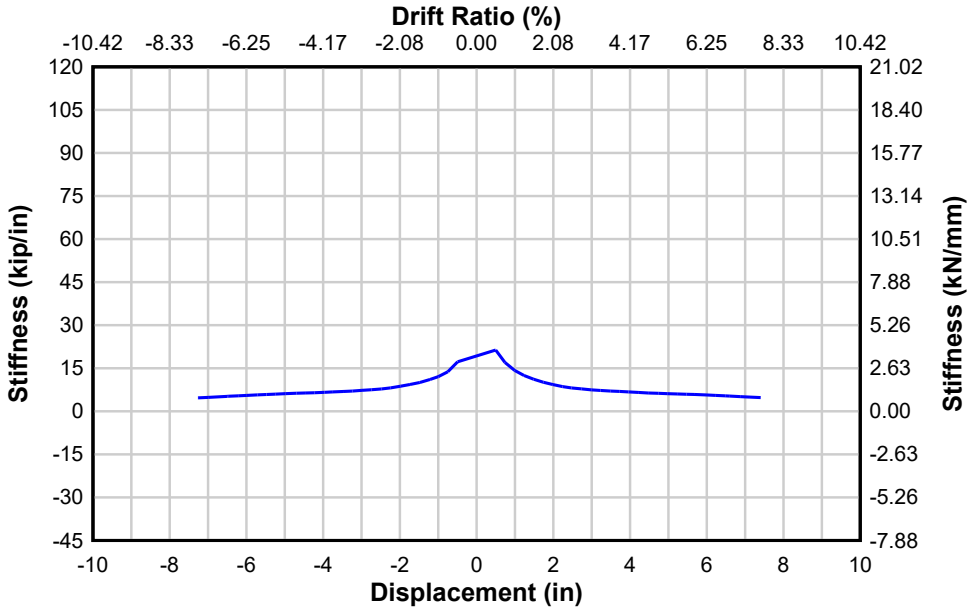

Figure A6.3.4.9: Evolution of Secant Stiffness – Test 4.

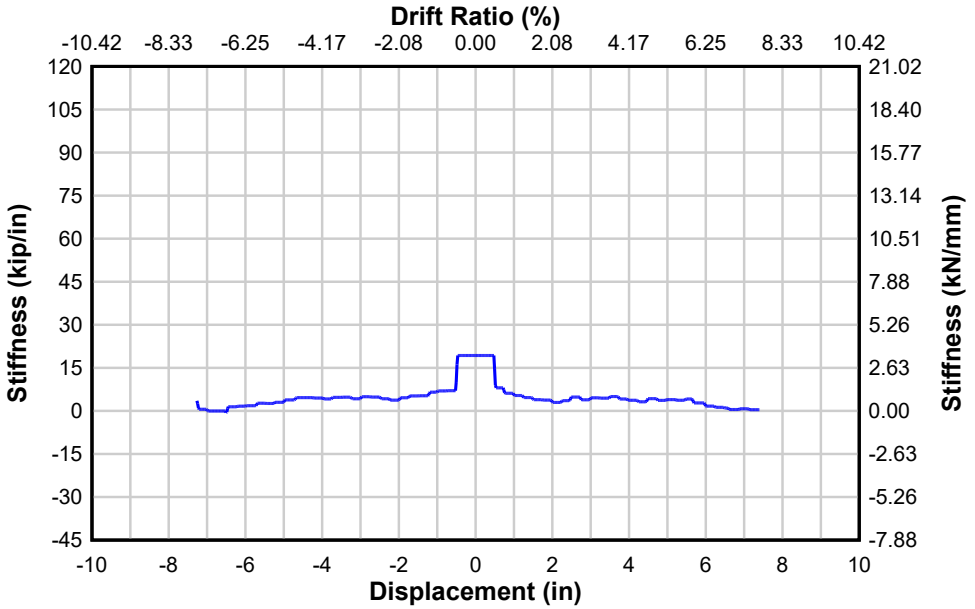

Figure A6.3.4.10: Evolution of Tangent Stiffness – Test 4.

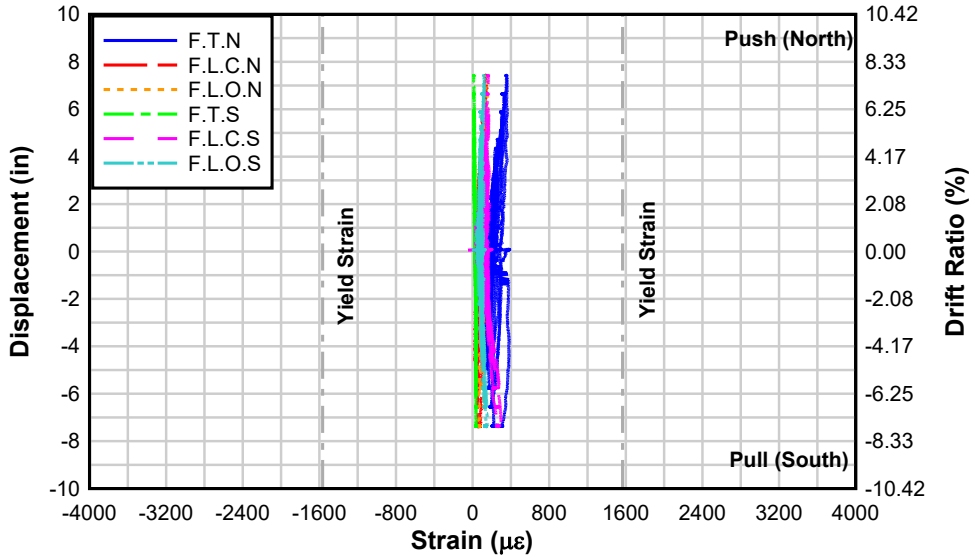

Figure A6.3.4.11: Footing Bar Strains – Test 4.

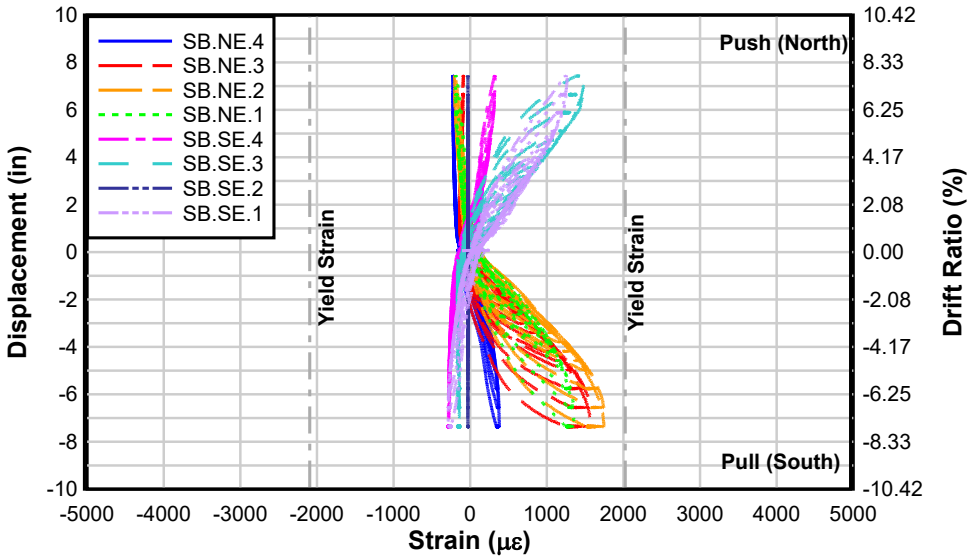

Figure A6.3.4.12: Starter Bar Strains – Test 4.

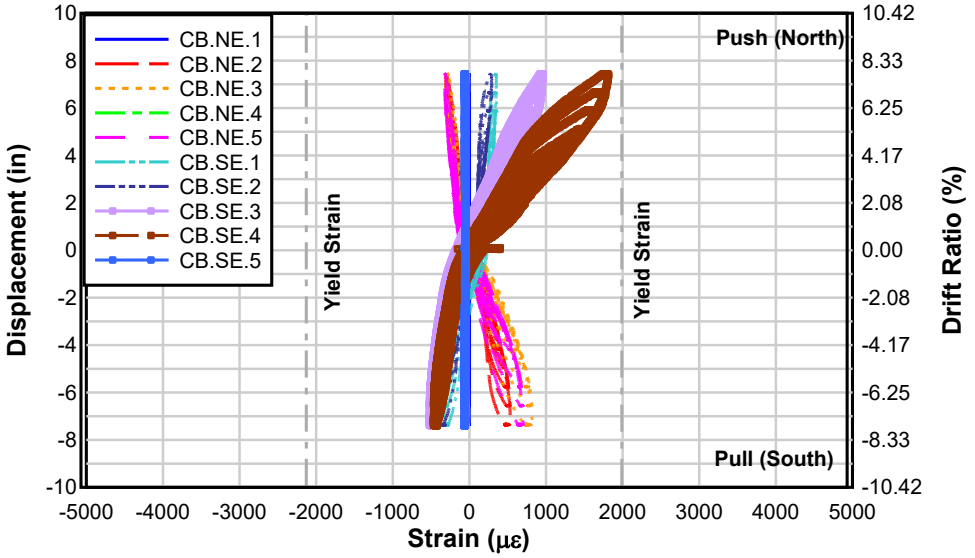

Figure A6.3.4.13: Column Bar Strains – Test 4.

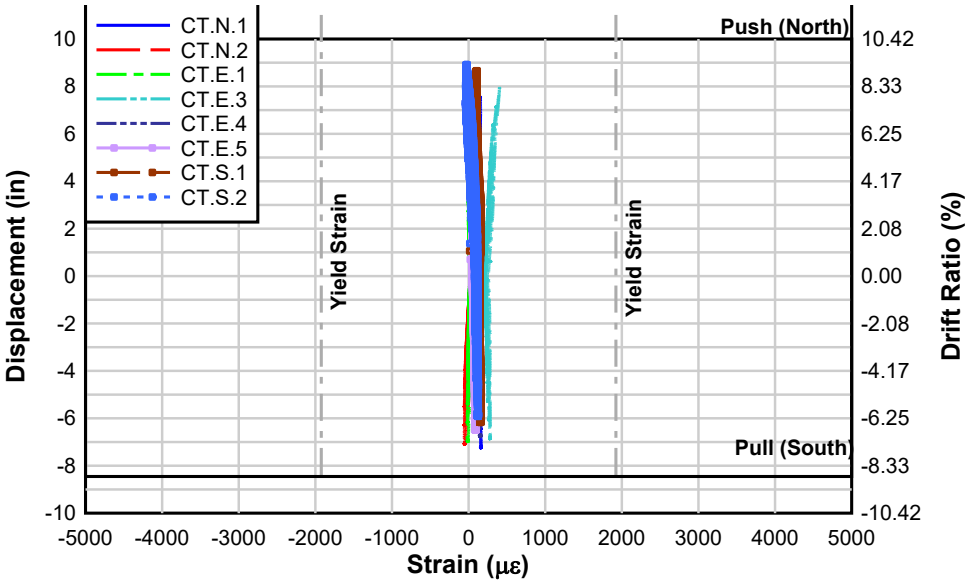

Figure A6.3.4.14: Column Tie Strains – Test 4.

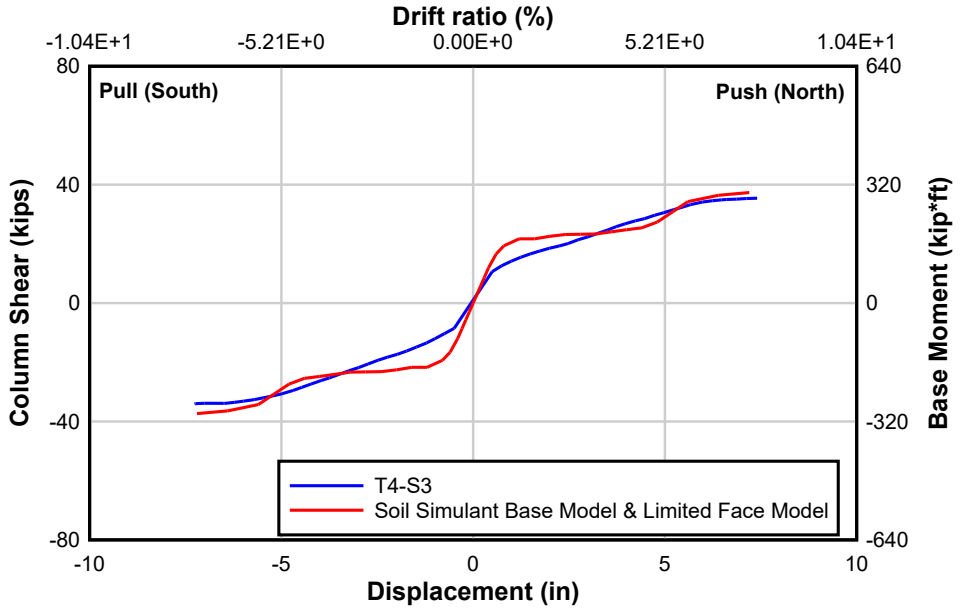

Figure A6.3.4.14: Soil Simulant Model – Test 4.

A6.3.5 TEST 5 – SPECIMEN 3 -VINTAGE FAILURE WITH FOAM SUBGRADE & STEEL EMBEDMENT

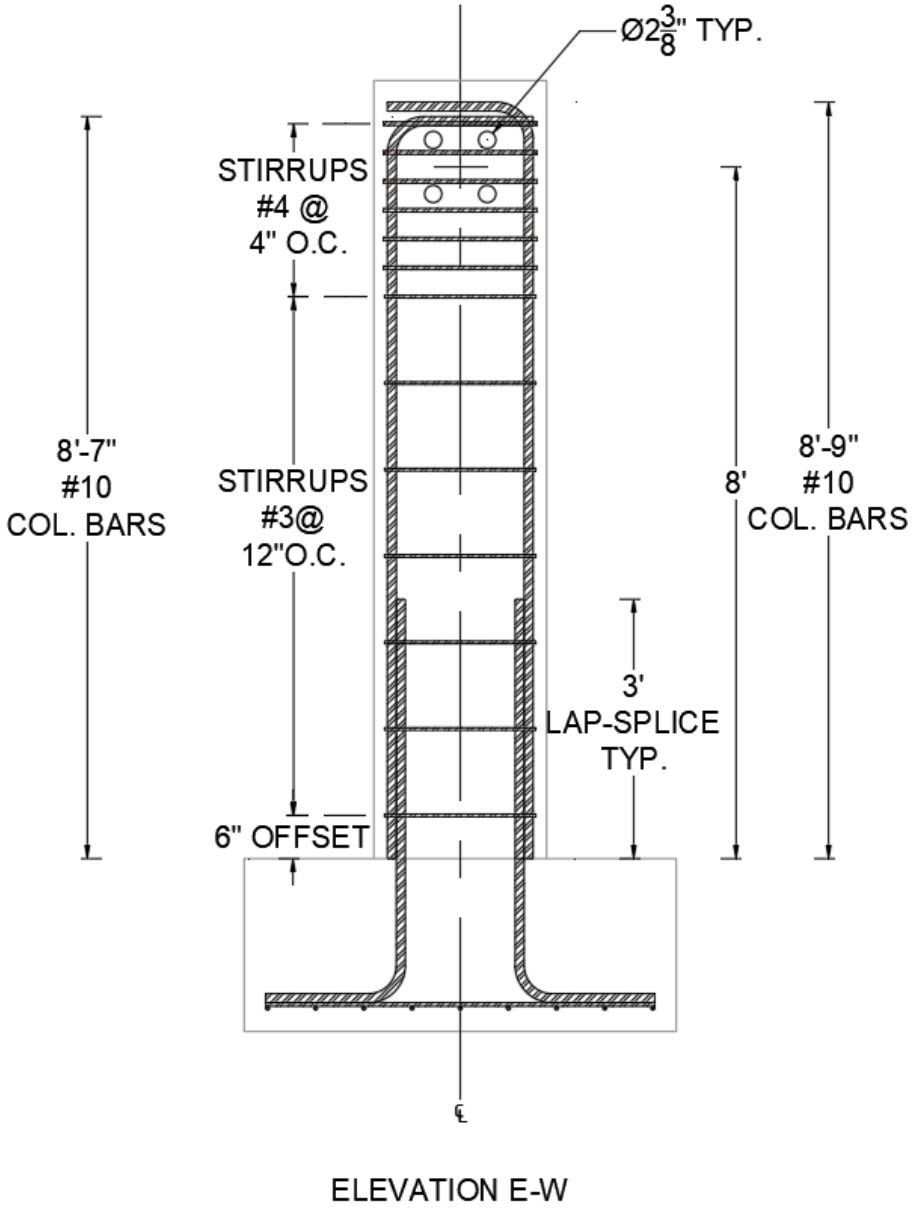

Figure A6.3.5.1 - Elevation View of Specimen 3 used in Test 5.

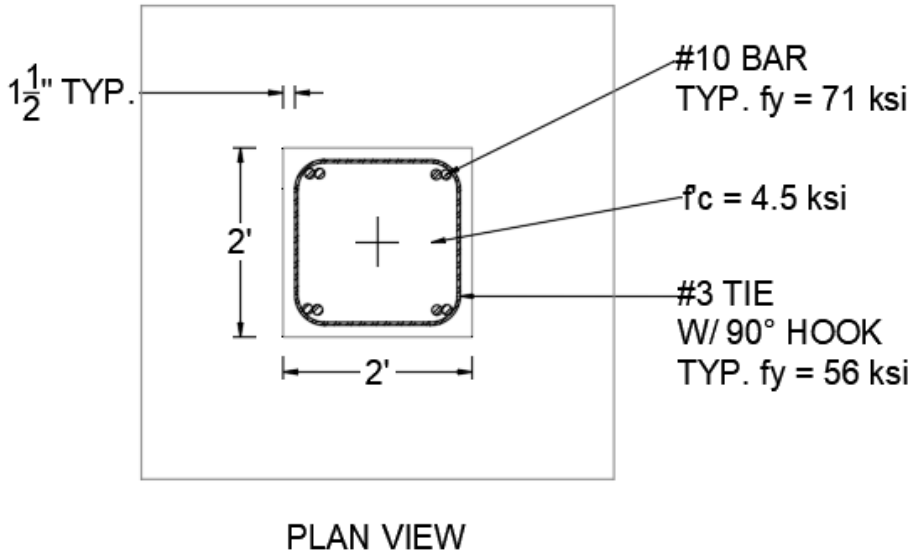

Figure A6.3.5.2 - Plan View of Specimen 3 used in Test 5.

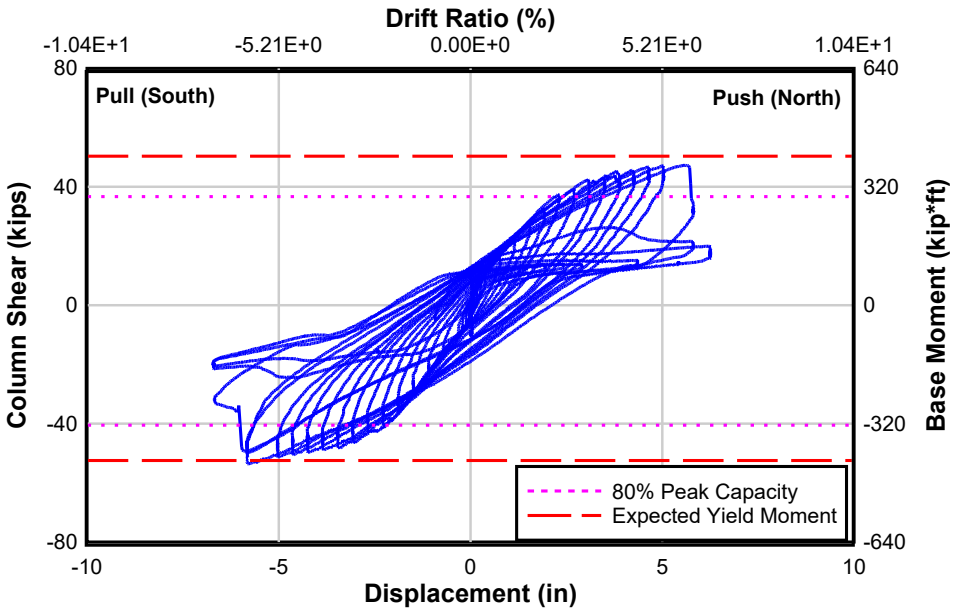

Figure A6.3.5.3: Overall Force Displacement Response – Test 5.

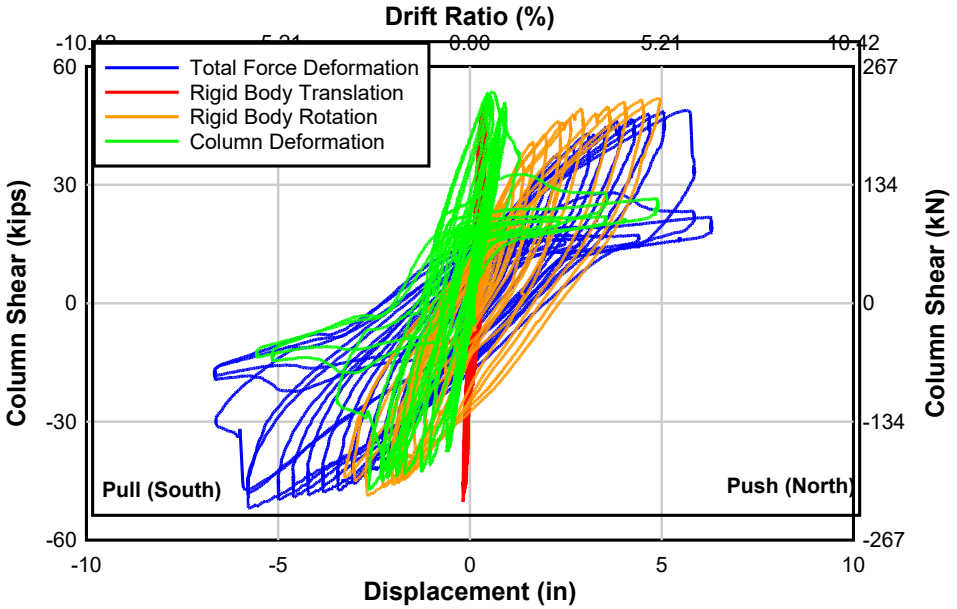

Figure A6.3.5.4: Component Contributions to Force Displacement – Test 5.

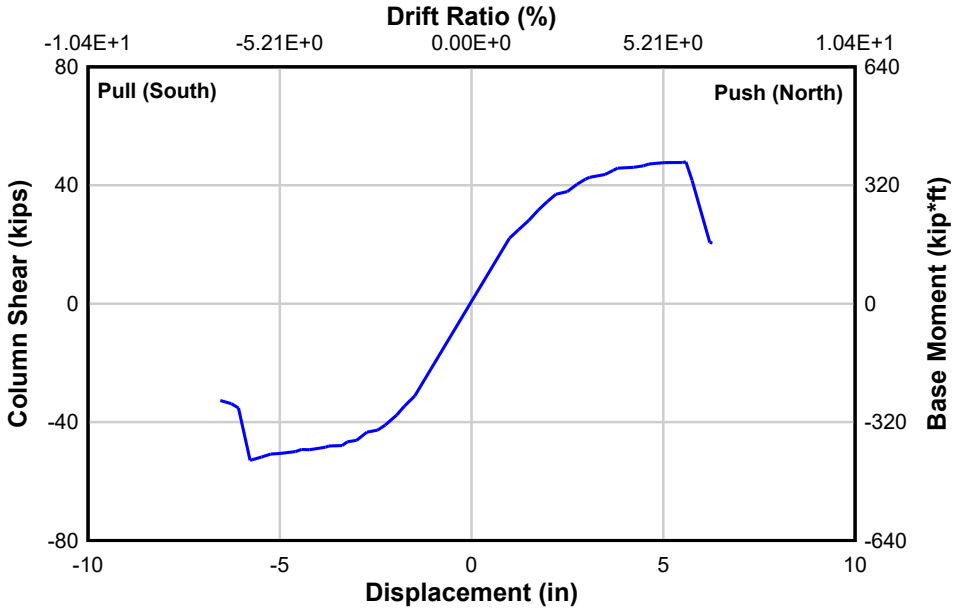

Figure A6.3.5.5: Overall Force Displacement Backbone Curve – Test 5.

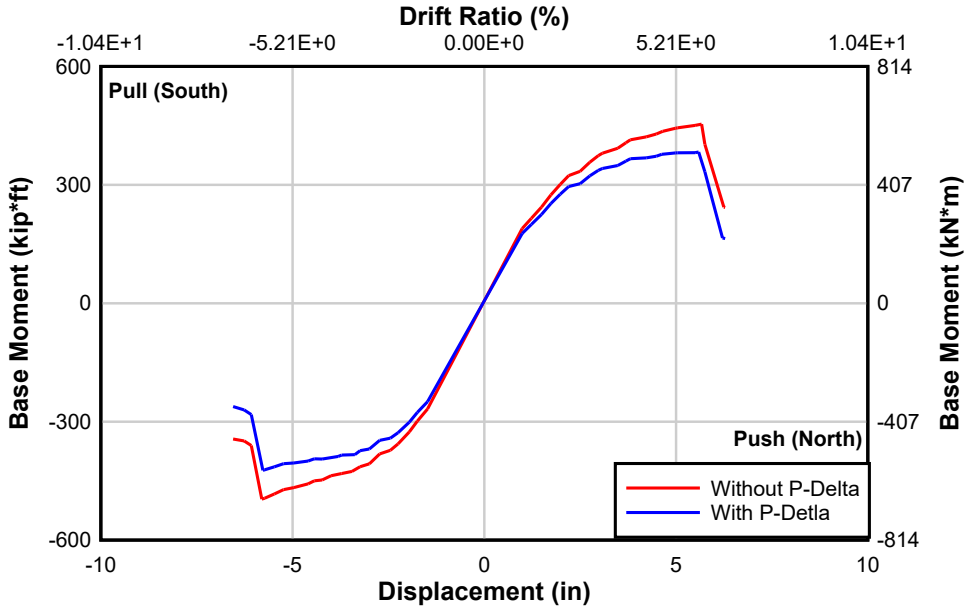

Figure A6.3.5.6: P-Delta Effects Backbone Curve – Test 5.

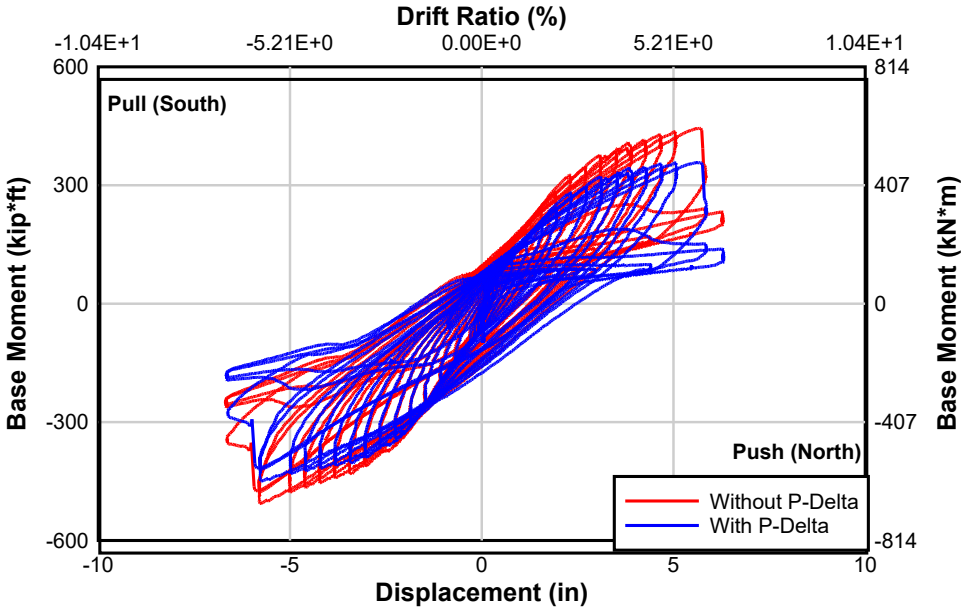

Figure A6.3.5.7: P-Delta Effects – Test 5.

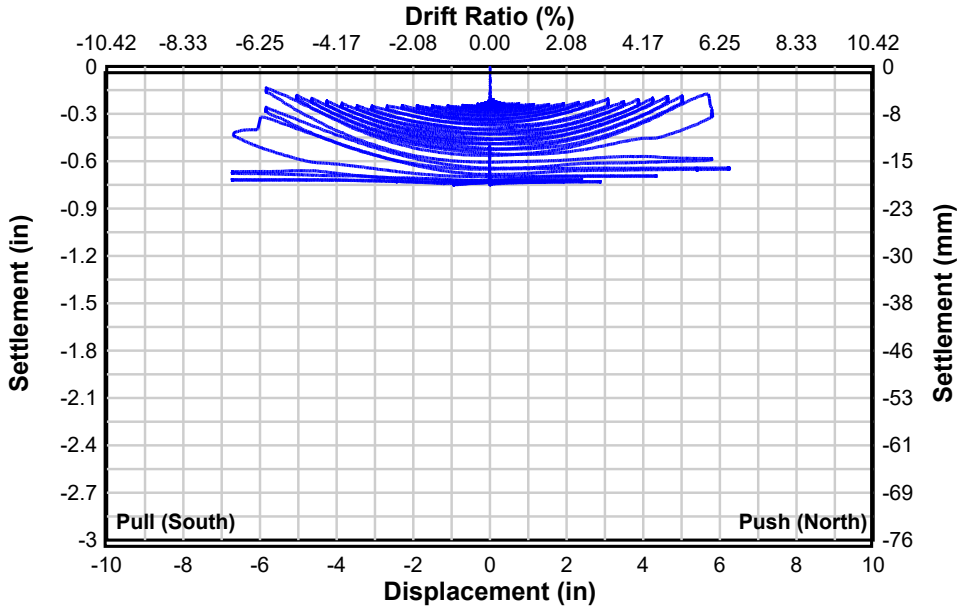

Figure A6.3.5.8: Settlement – Test 5.

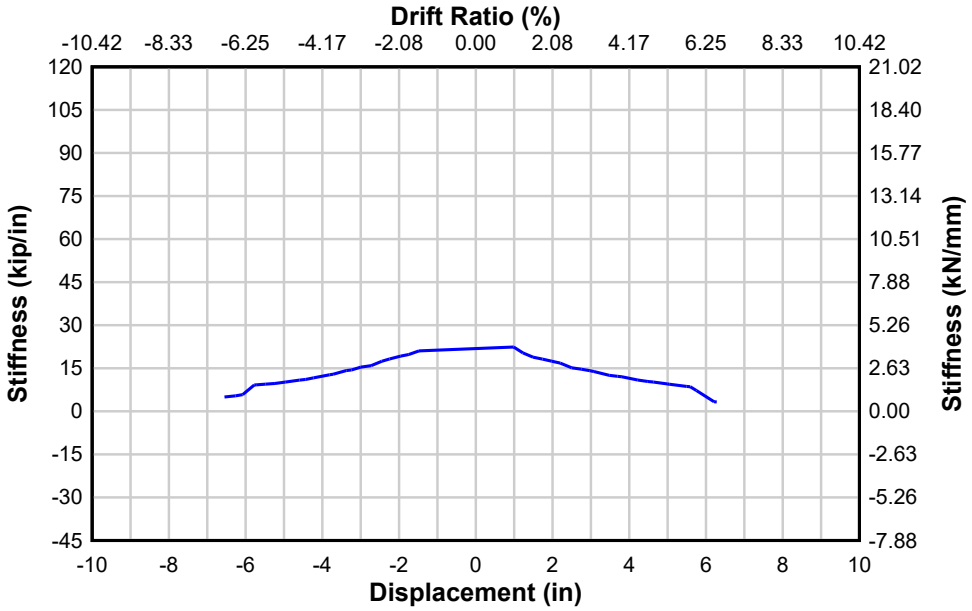

Figure A6.3.5.9: Evolution of Secant Stiffness – Test 5.

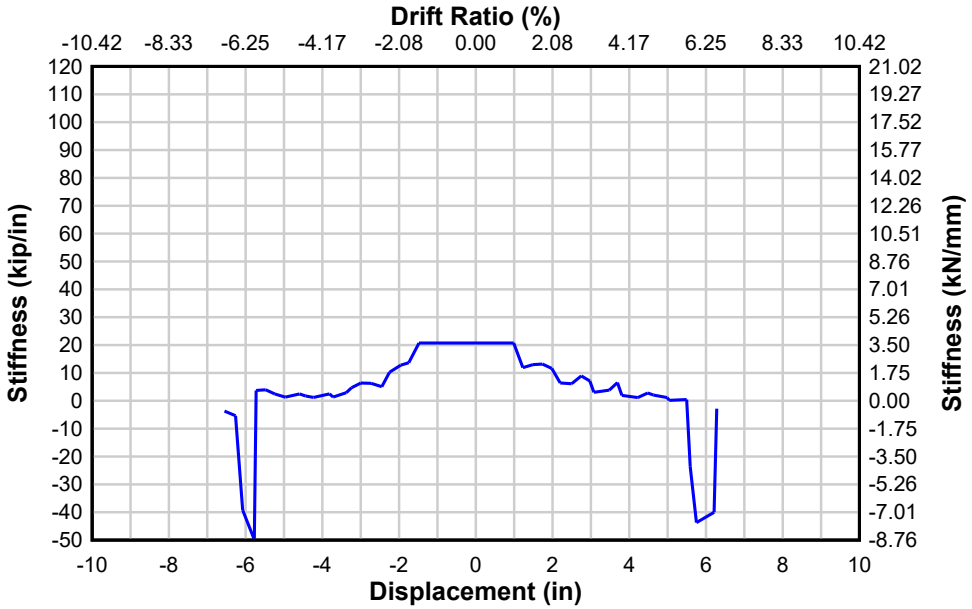

Figure A6.3.5.10: Evolution of Tangent Stiffness – Test 5.

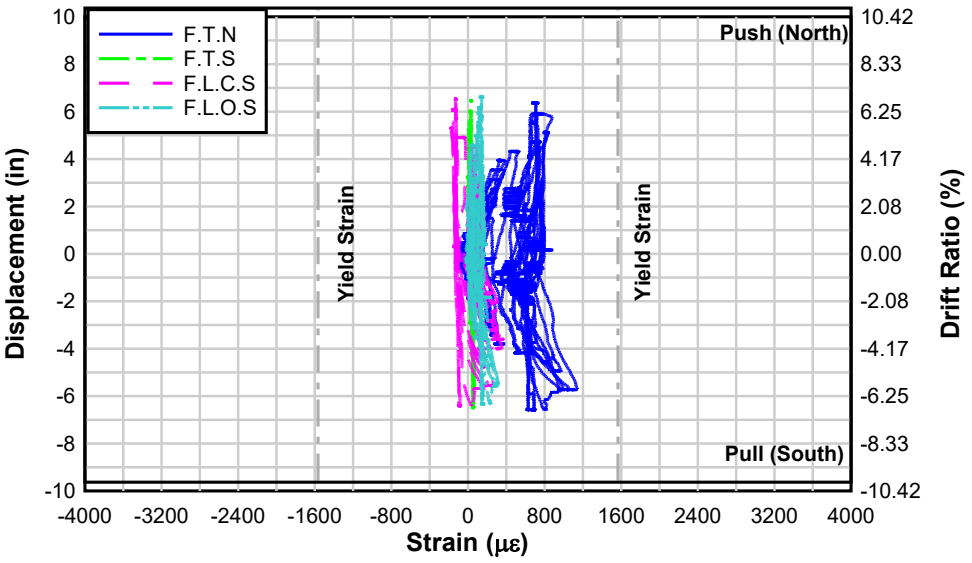

Figure A6.3.5.11: Footing Bar Strains – Test 5.

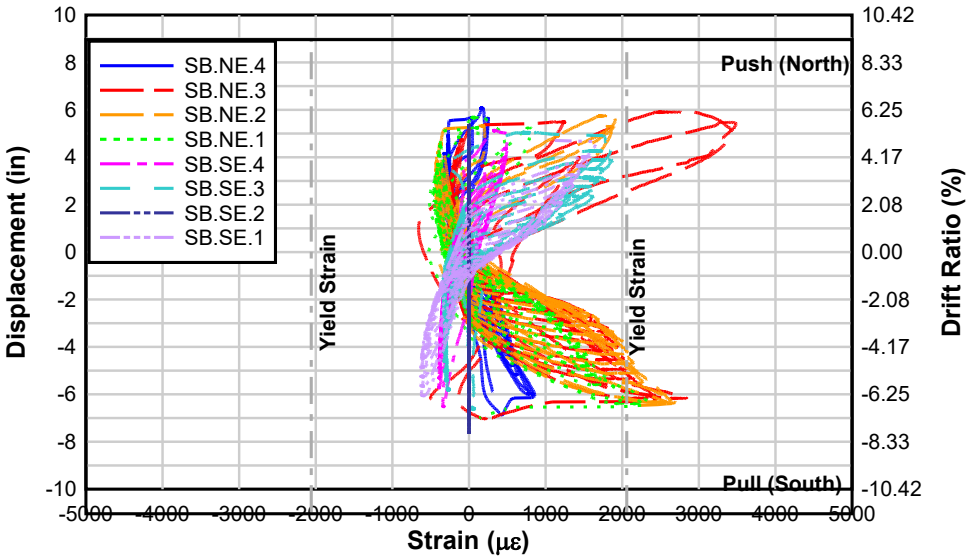

Figure A6.3.5.12: Starter Bar Strains – Test 5.

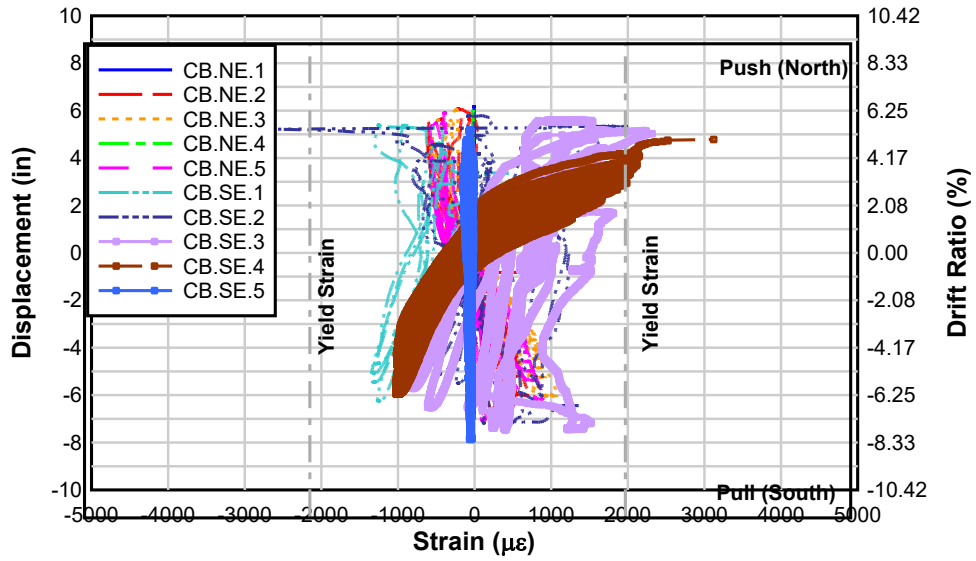

Figure A6.3.5.13: Column Bar Strains – Test 5.

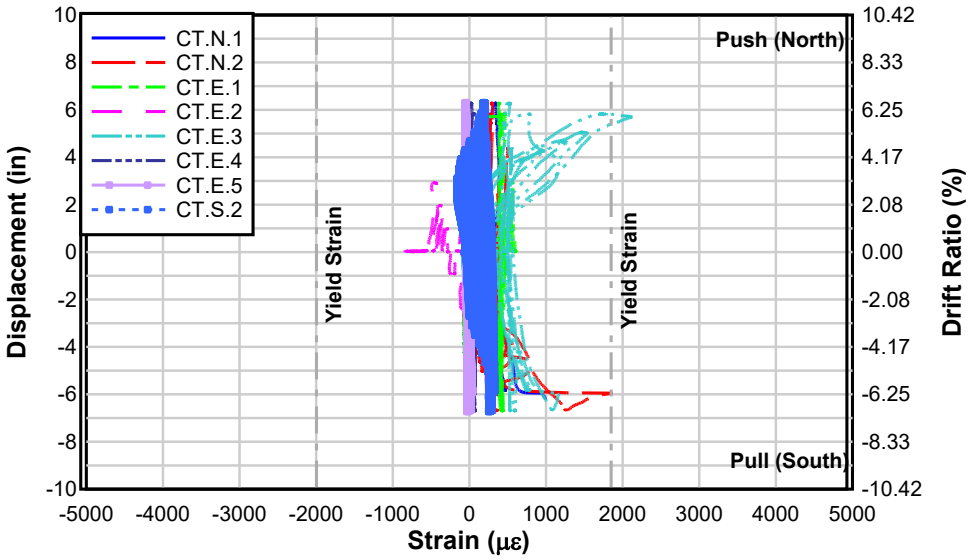

Figure A6.3.5.14: Column Tie Strains – Test 5.

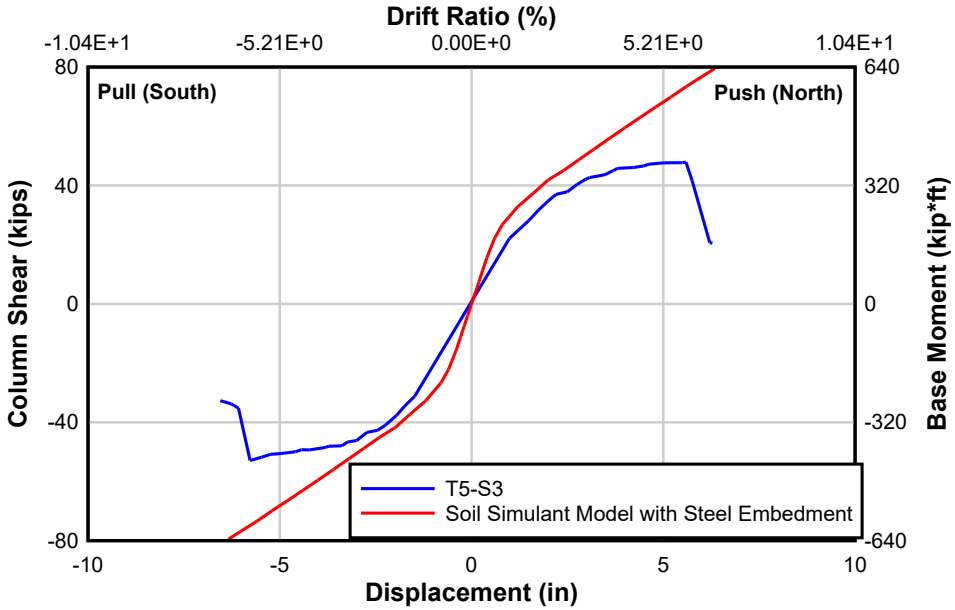

Figure A6.3.5.15: Soil Simulant Model: Test 5.

A6.3.6 TEST 6 – SPECIMEN 3: VINTAGE TIAB LIGAMENT RETROFIT WITH FOAM SUBGRADE & STEEL EMBEDMENT

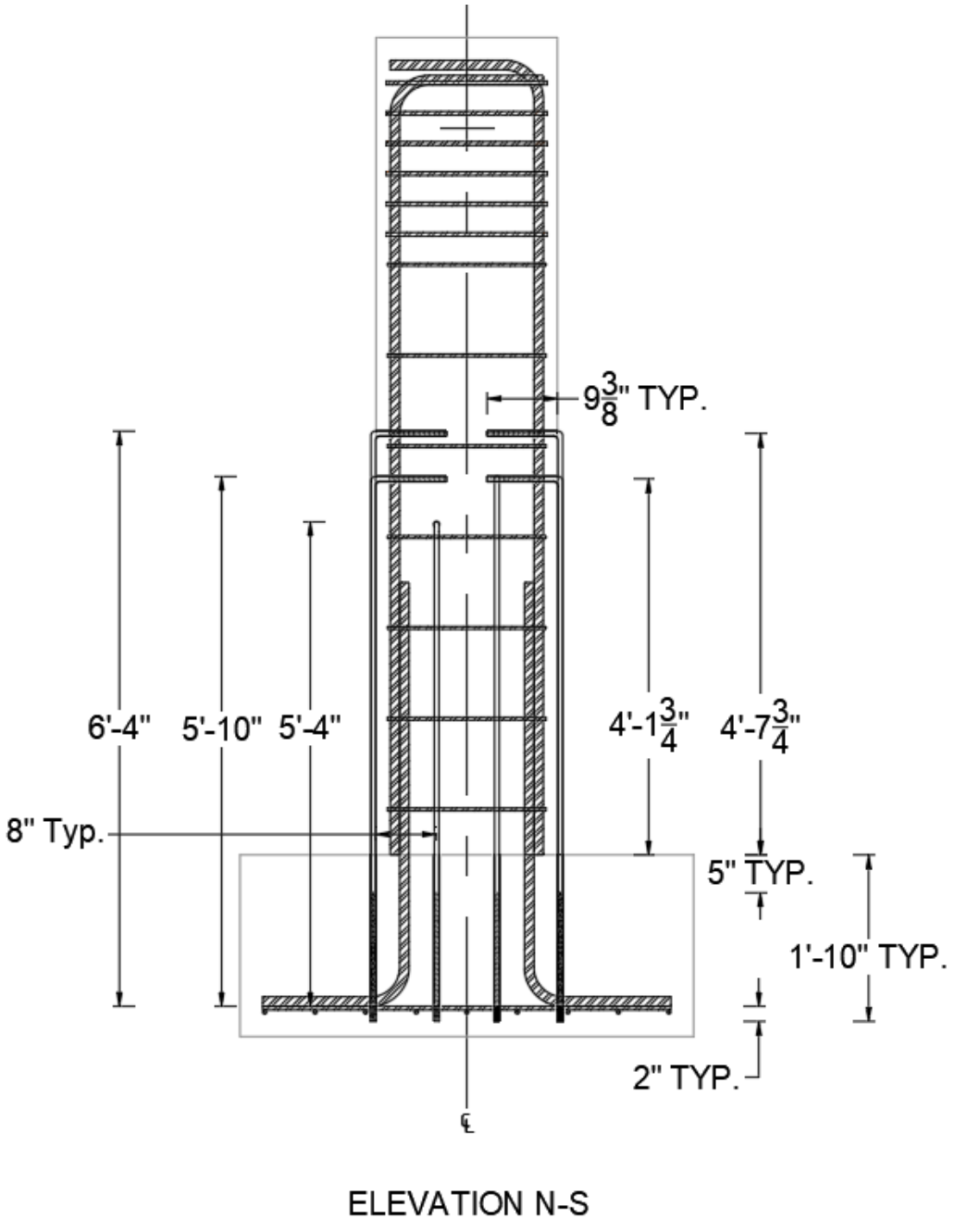

Figure A6.3.6.1 - Elevation View of Specimen 3 used in Test 6.

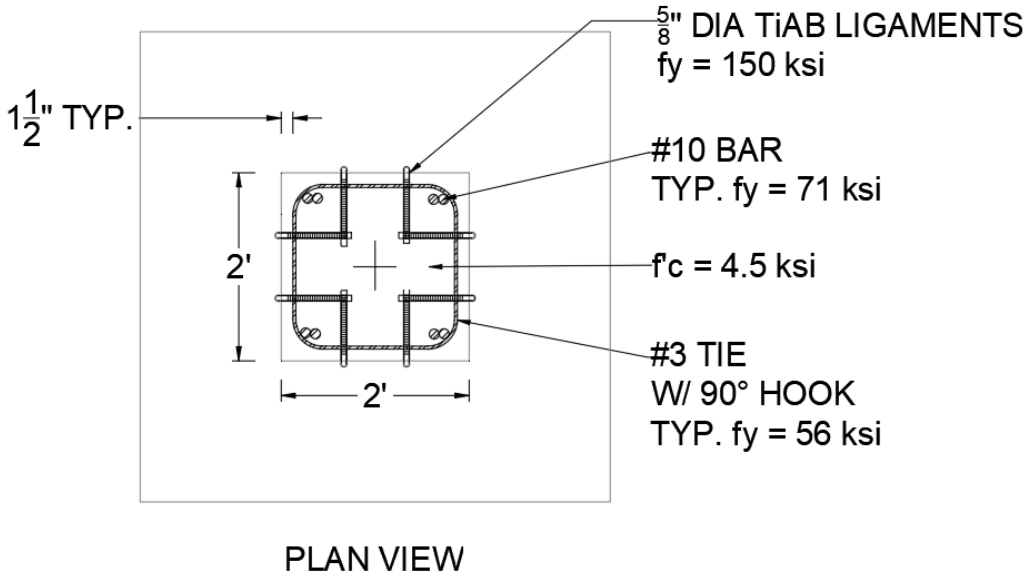

Figure A6.3.6.2 - Plan View of Specimen 3 used in Test 6.

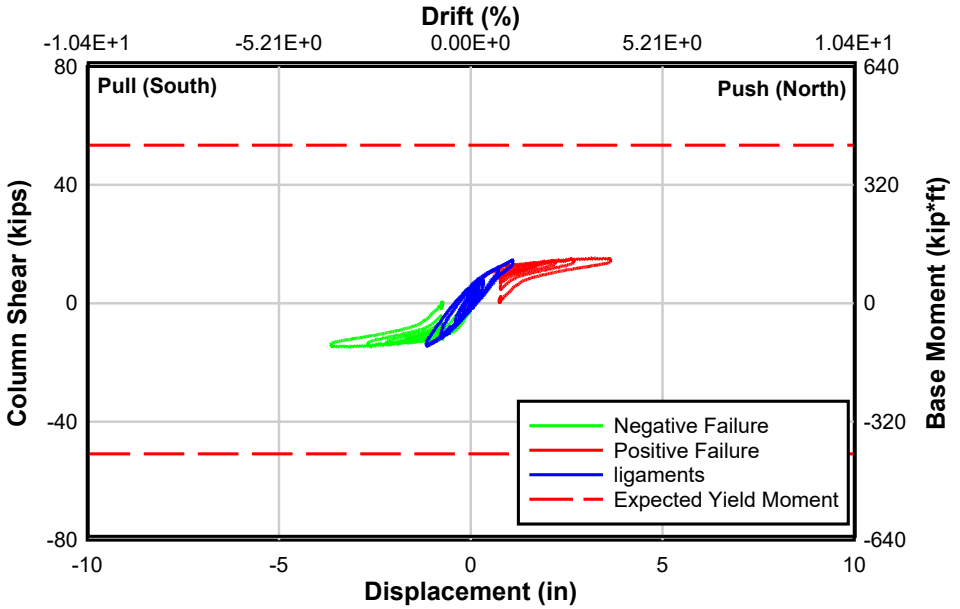

Figure A6.3.6.3: Overall Force Displacement Response – Test 6.

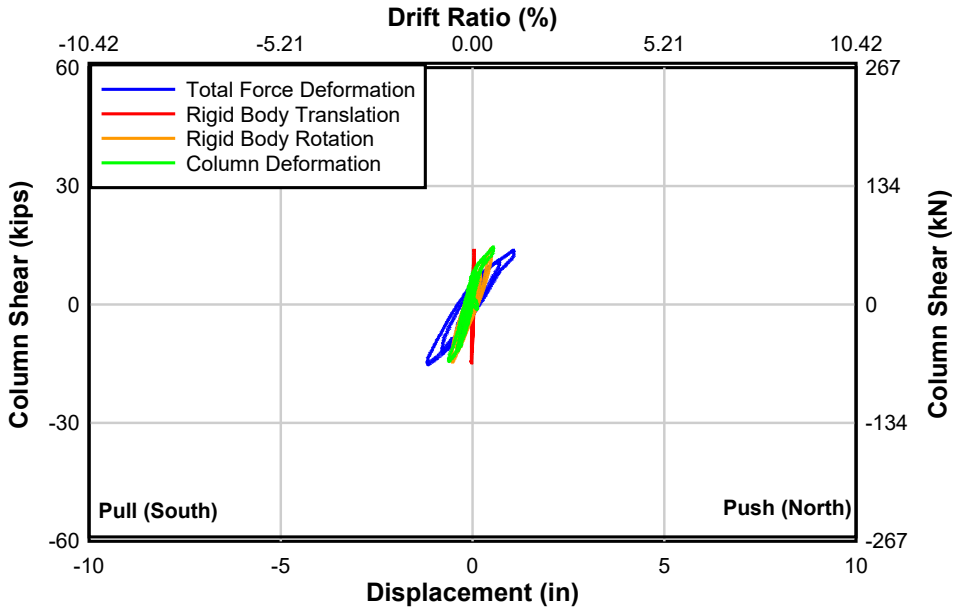

Figure A6.3.6.4: Component Contributions to Force Displacement – Test 6.

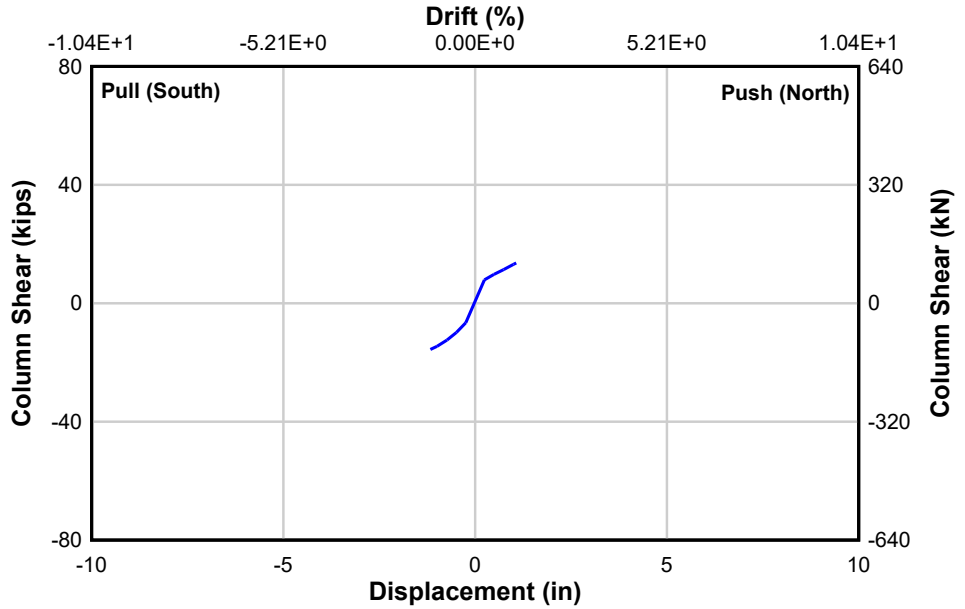

Figure A6.3.6.5: Overall Force Displacement Backbone Curve – Test 6.

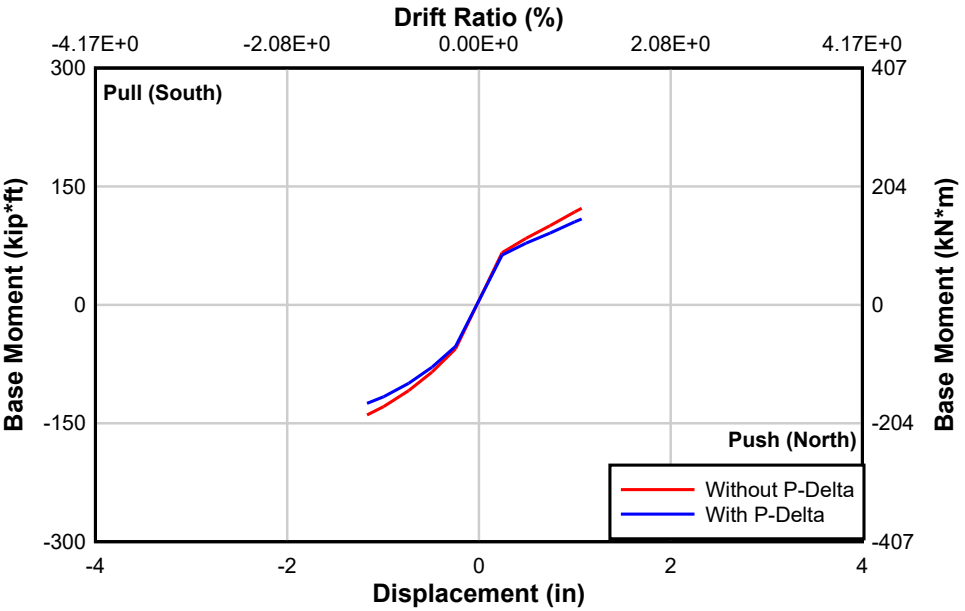

Figure A6.3.6.6: P-Delta Effects Backbone Curve – Test 6.

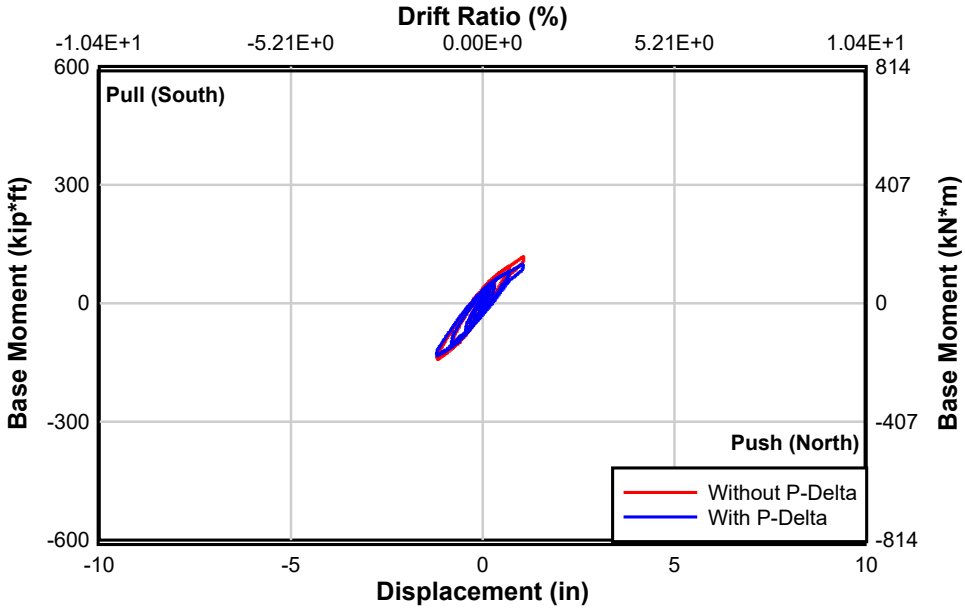

Figure A6.3.6.7: P-Delta Effects – Test 6.

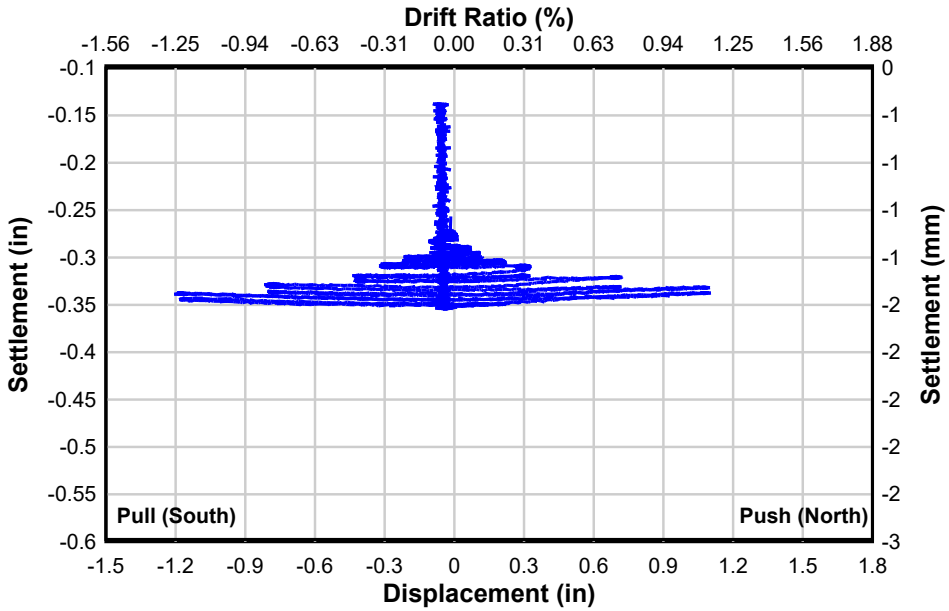

Figure A6.3.6.8: Settlement – Test 6.

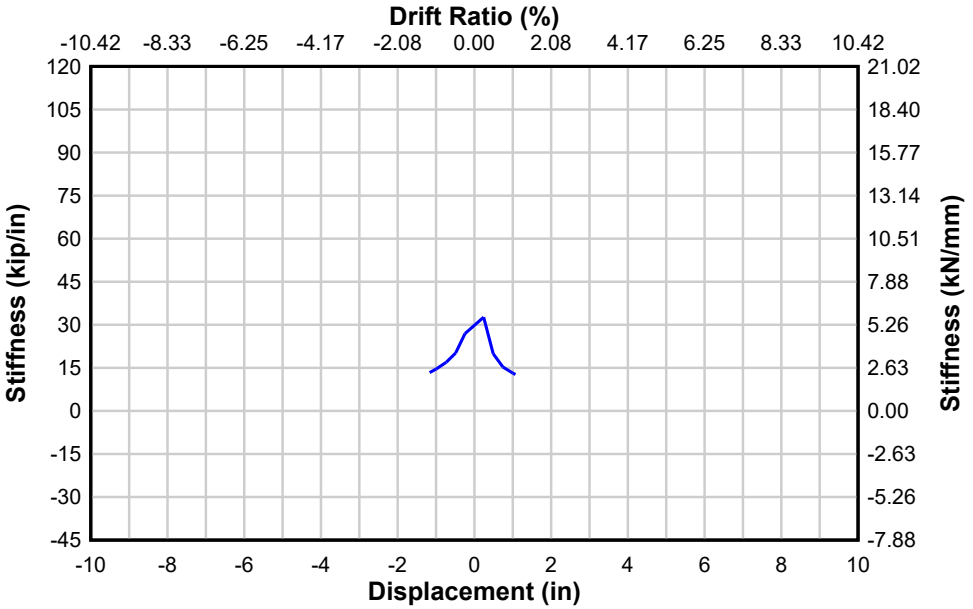

Figure A6.3.6.9: Evolution of Secant Stiffness – Test 6.

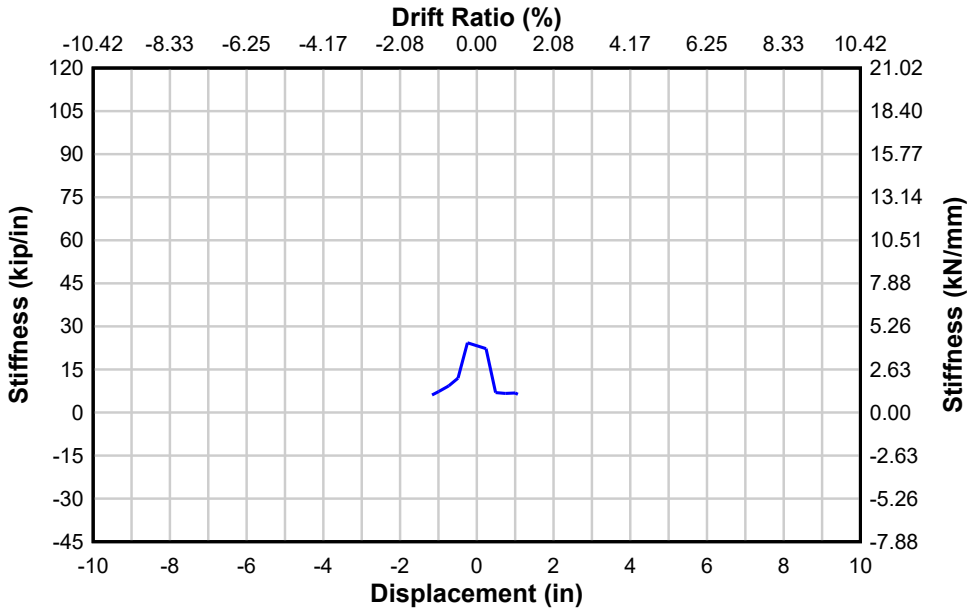

Figure A6.3.6.10: Evolution of Tangent Stiffness – Test 6.

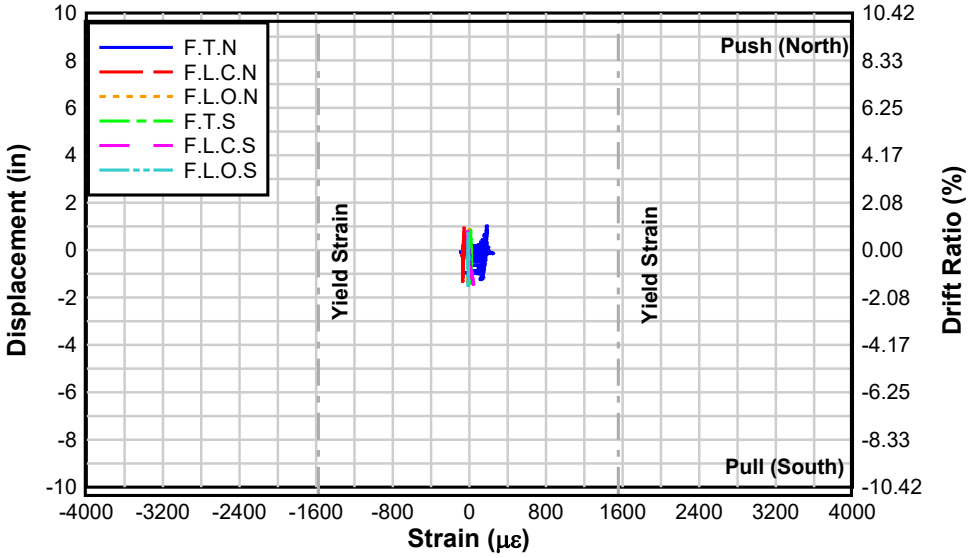

Figure A6.3.6.11: Footing Bar Strains – Test 6.

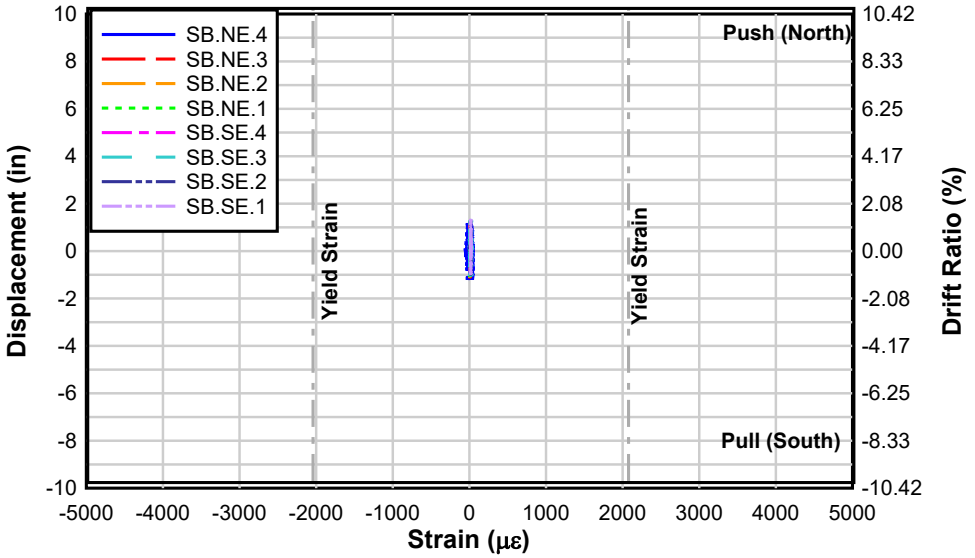

Figure A6.3.6.12: Starter Bar Strains – Test 6.

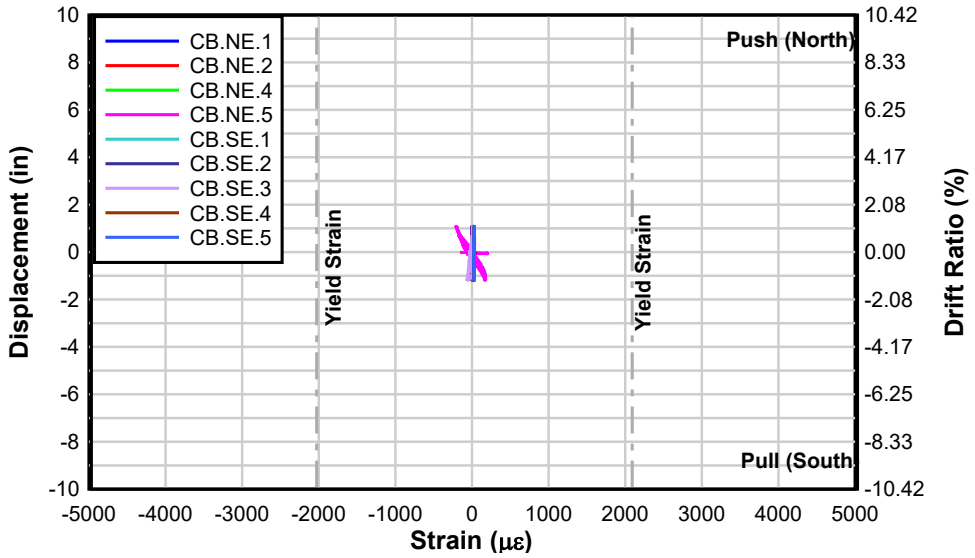

Figure A6.3.6.13: Column Bar Strains – Test 6.

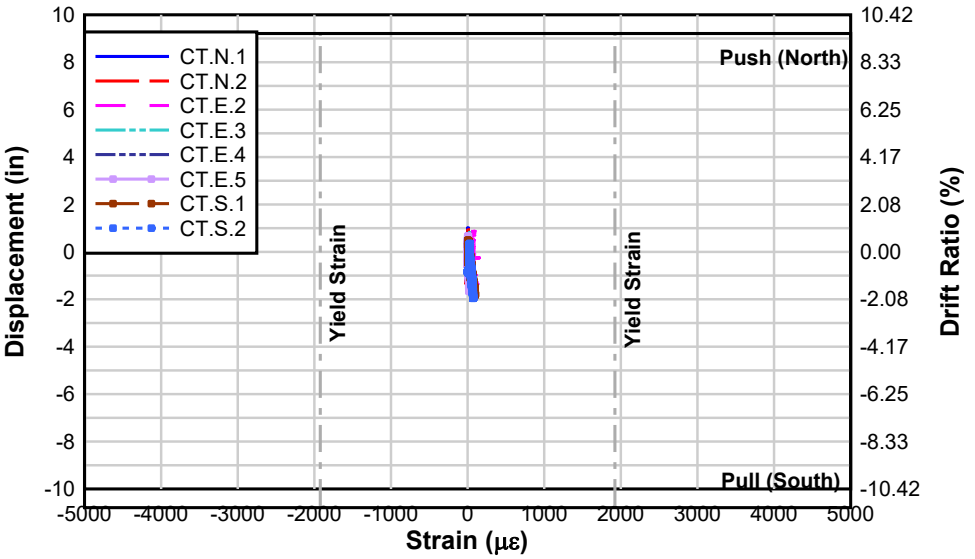

Figure A6.3.6.14: Column Tie Strains – Test 6.

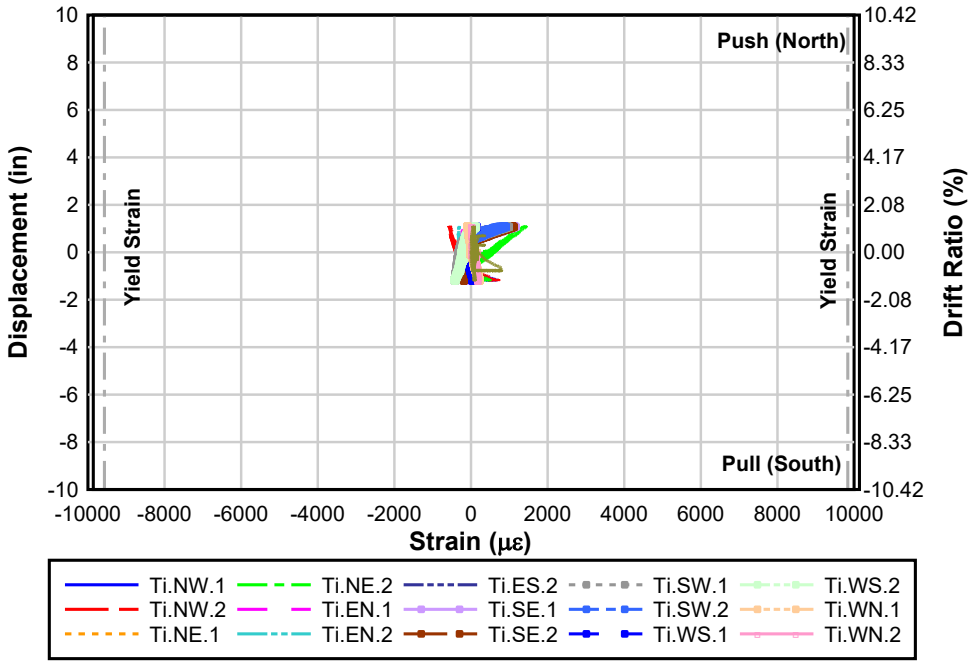

Figure A6.3.6.15: TiAB Ligament Strains – Test 6.

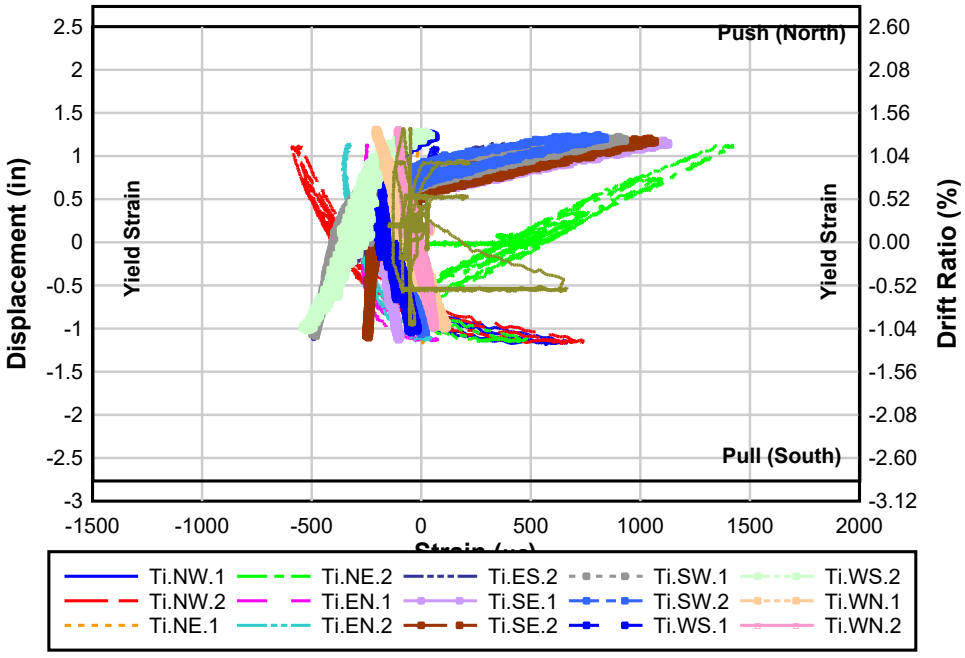

Figure A6.3.6.16: TiAB Ligament Strains Close Up – Test 6.

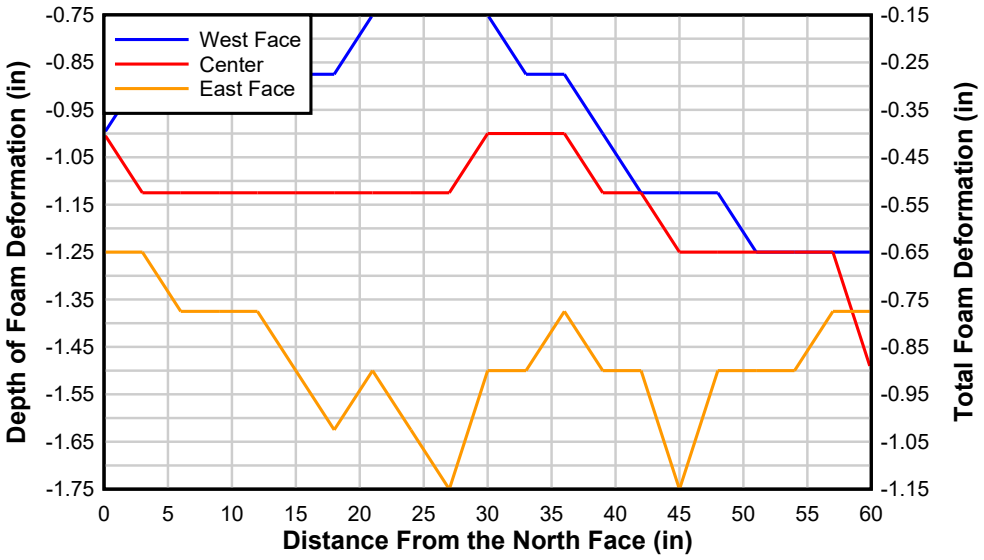

Figure A6.3.6.17: Soil Simulant Profile After Test 6.

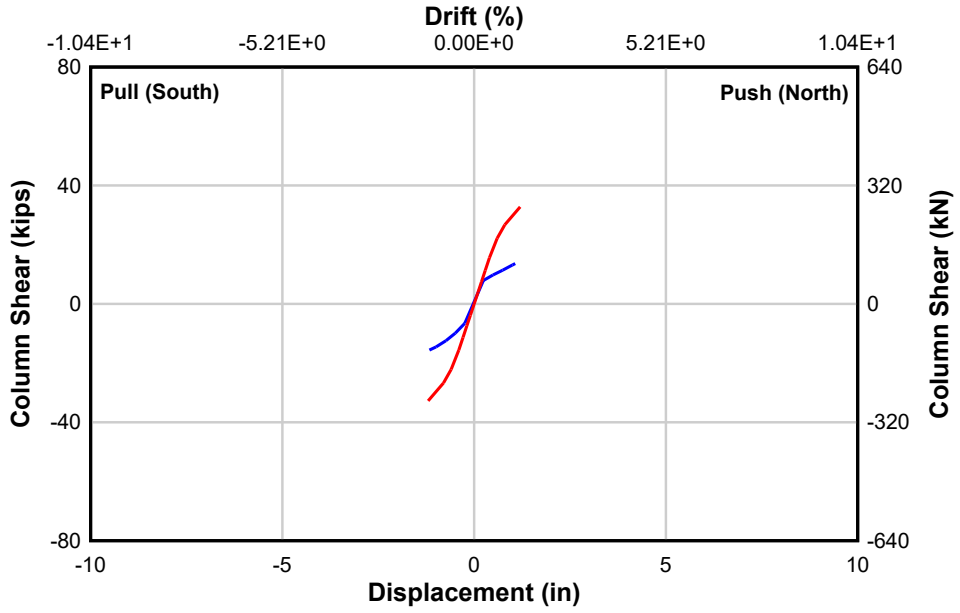

Figure A6.3.6.18: Soil Simulant Model Comparison – Test 6.

A6.3.7 TEST 7 – SPECIMEN 3: VINTAGE COMPLETE RETROFIT WITH FOAM SUBGRADE & STEEL EMBEDMENT

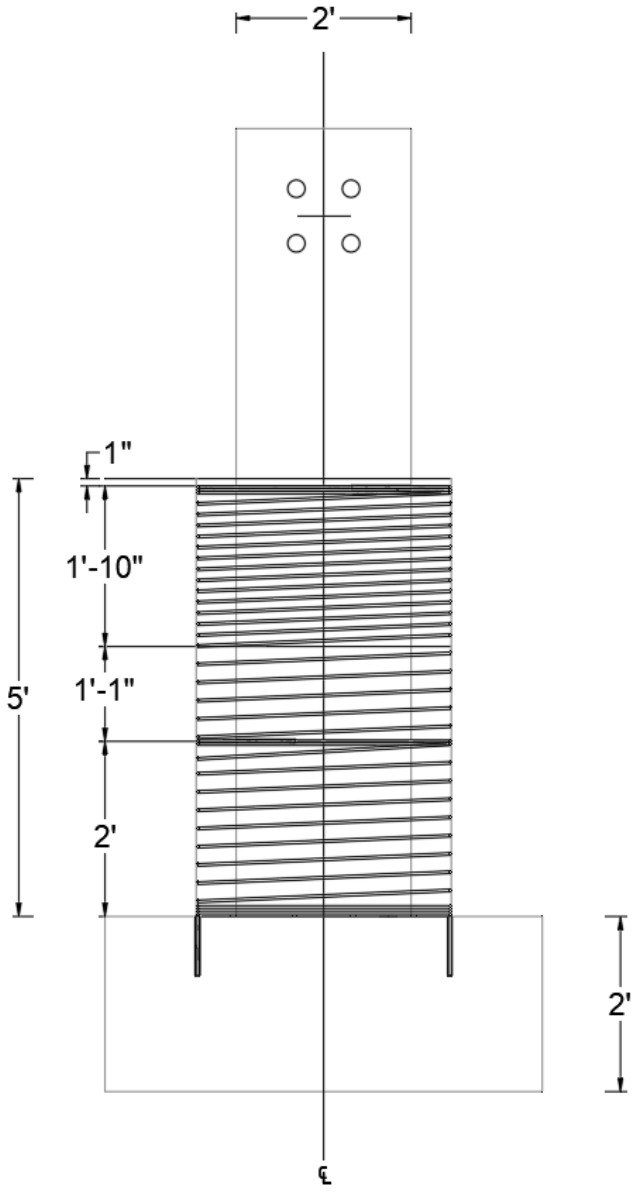

Figure A6.3.7.1: Elevation View of Specimen 3 used in Test 7.

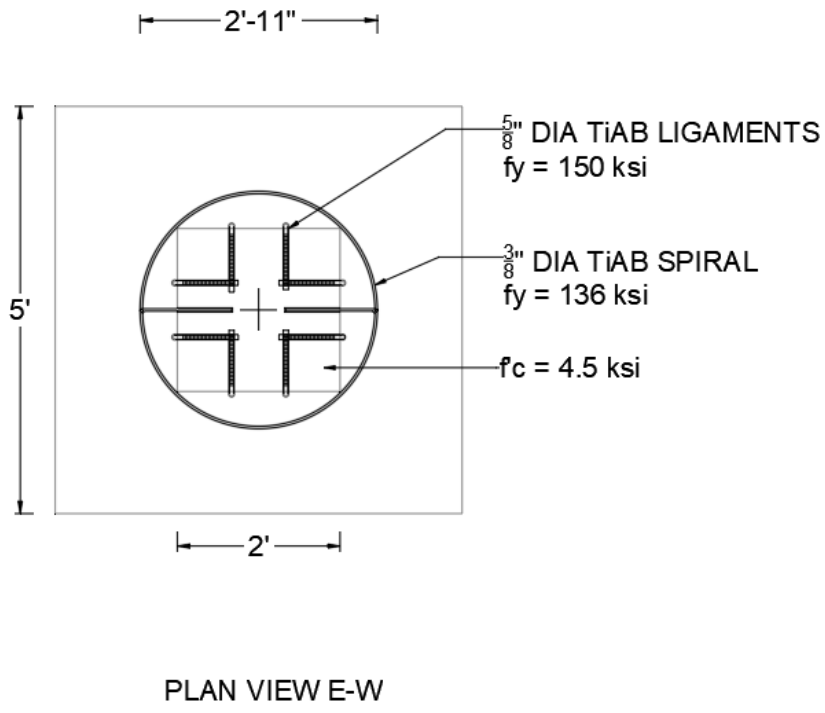

Figure A6.3.7.2: Plan View of Specimen 3 used in Test 7.

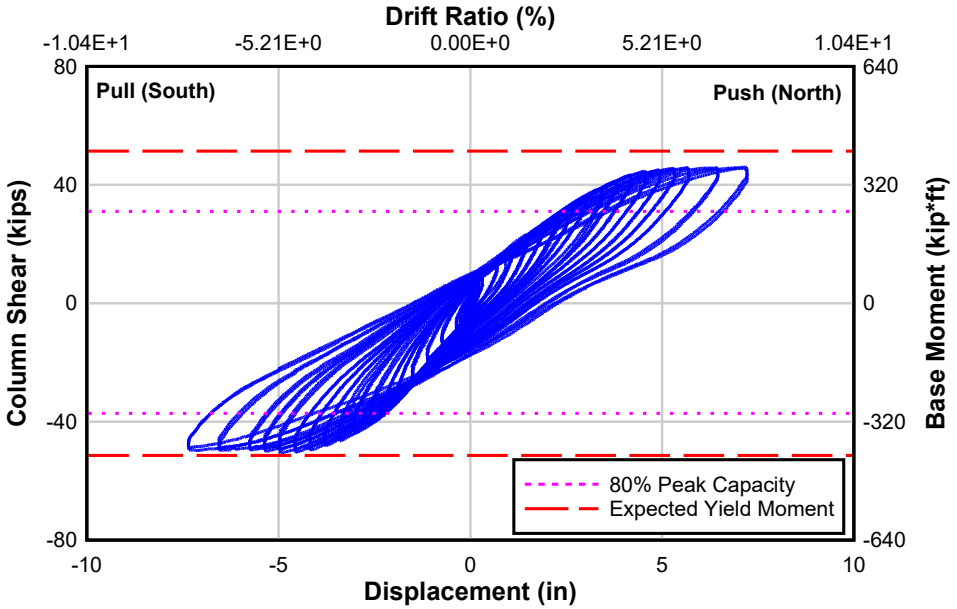

Figure A6.3.7.3: Overall Force Displacement Response – Test 7.

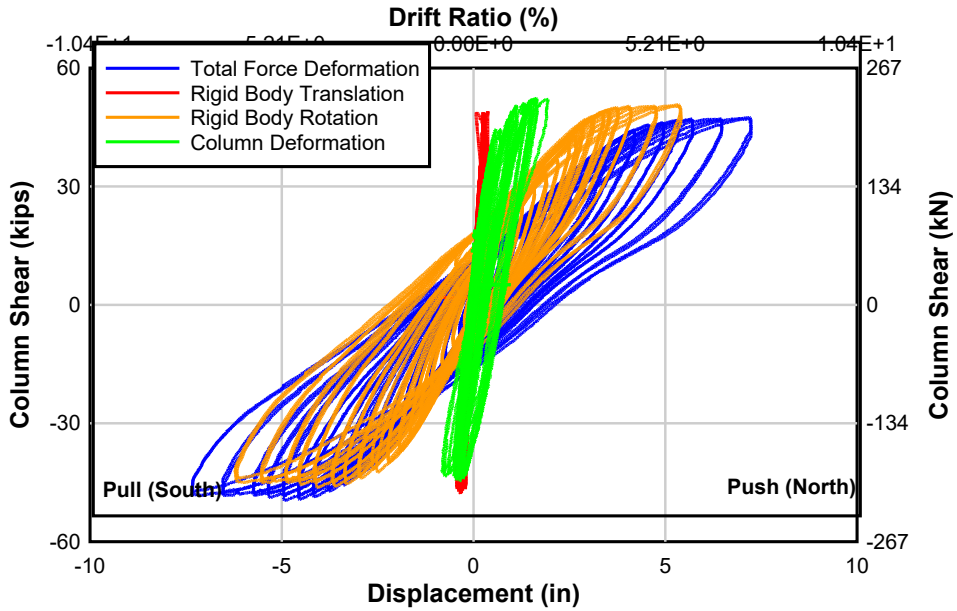

Figure A6.3.7.4: Component Contributions to Force Displacement -Test 7.

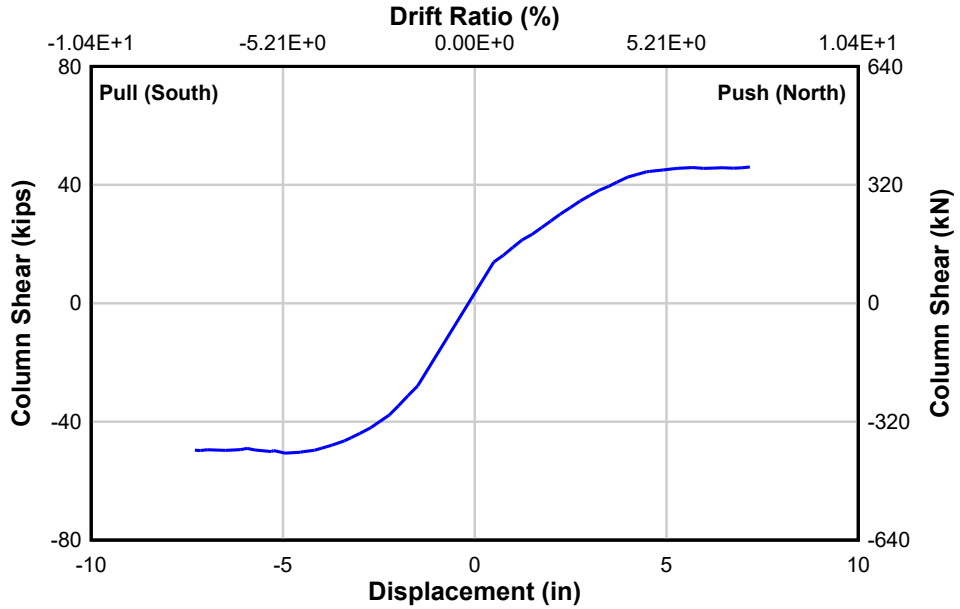

Figure A6.3.7.5: Overall Force Displacement Backbone Curve – Test 7.

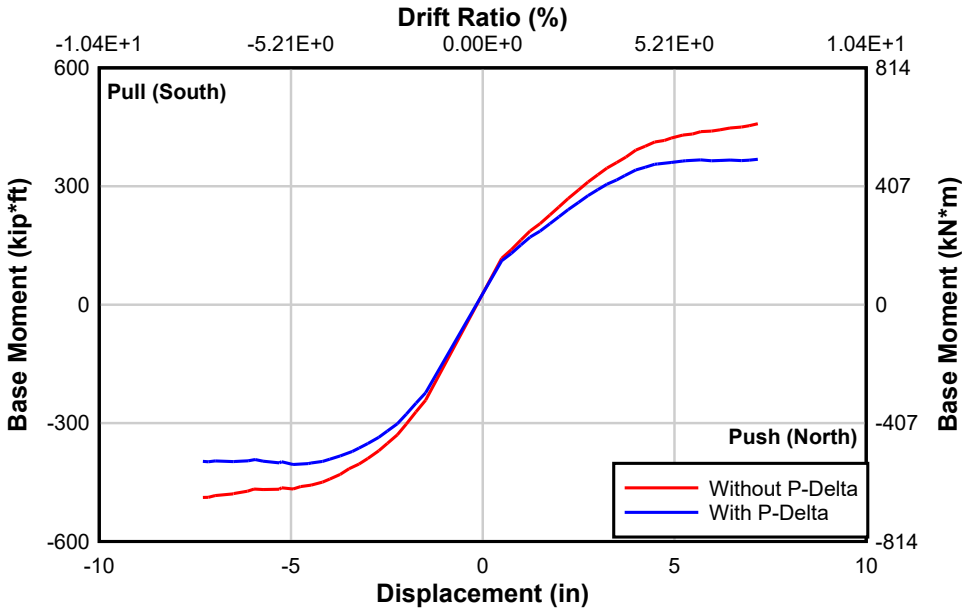

Figure A6.3.7.6: P-Delta Effects Backbone Curve – Test 7.

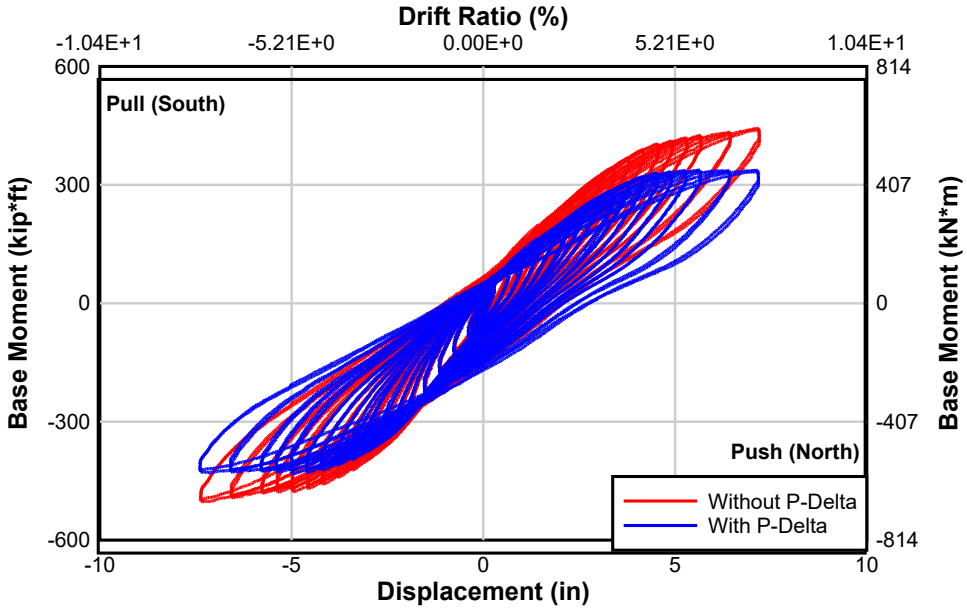

Figure A6.3.7.7: P-Delta Effects – Test 7.

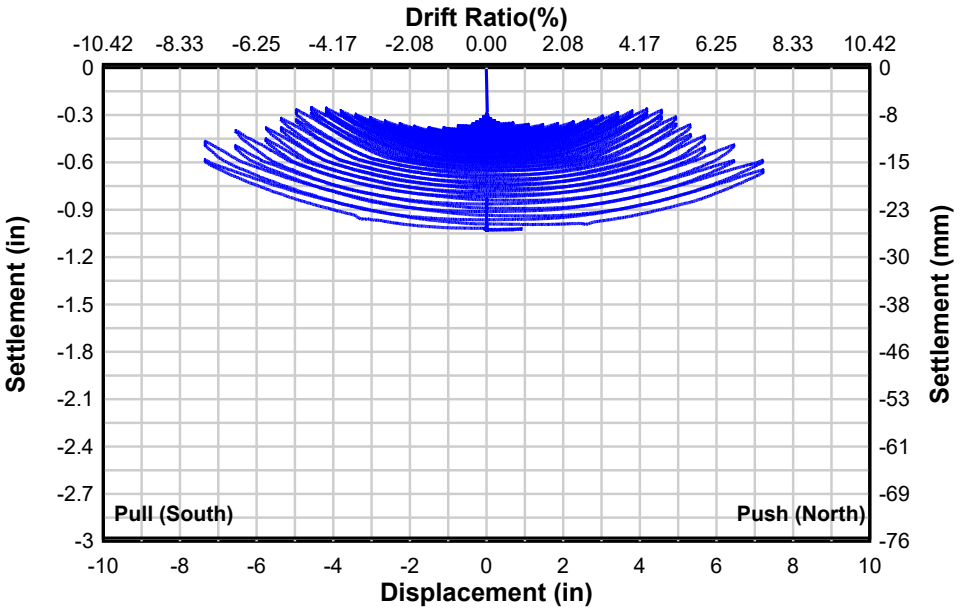

Figure A6.3.7.8: Settlement – Test 7.

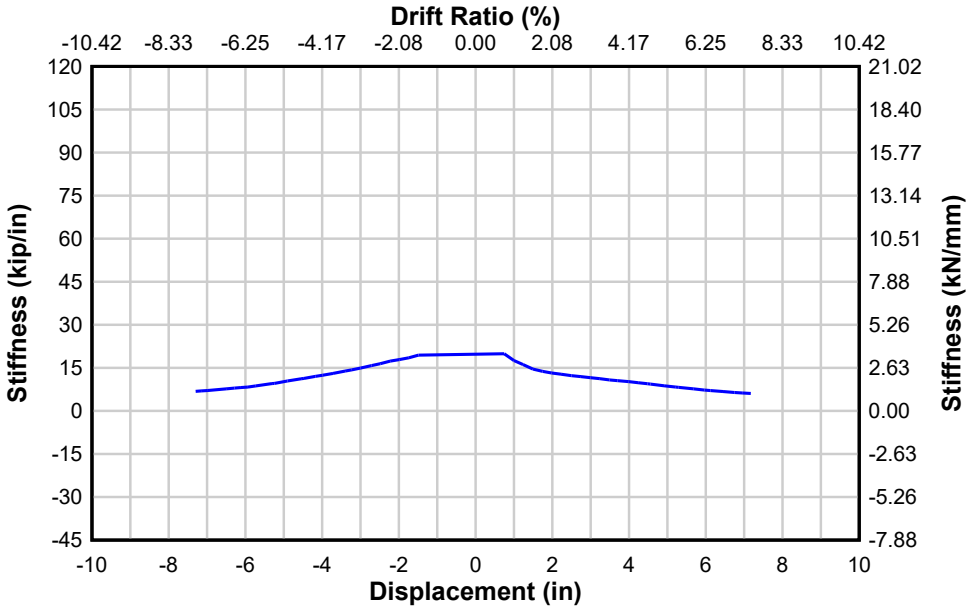

Figure A6.3.7.9: Evolution of Secant Stiffness – Test 7.

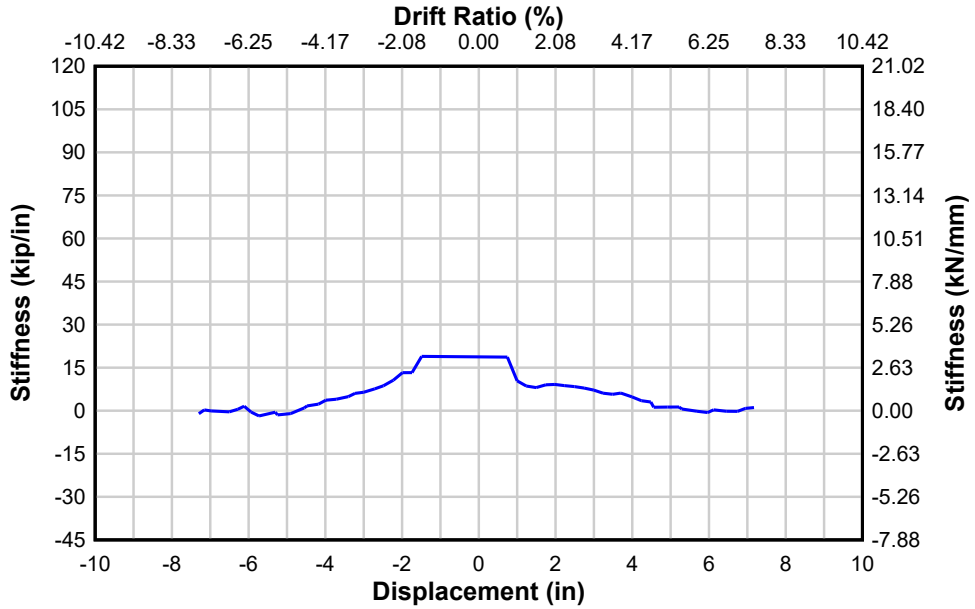

Figure A6.3.7.10: Evolution of Tangent Stiffness – Test 7.

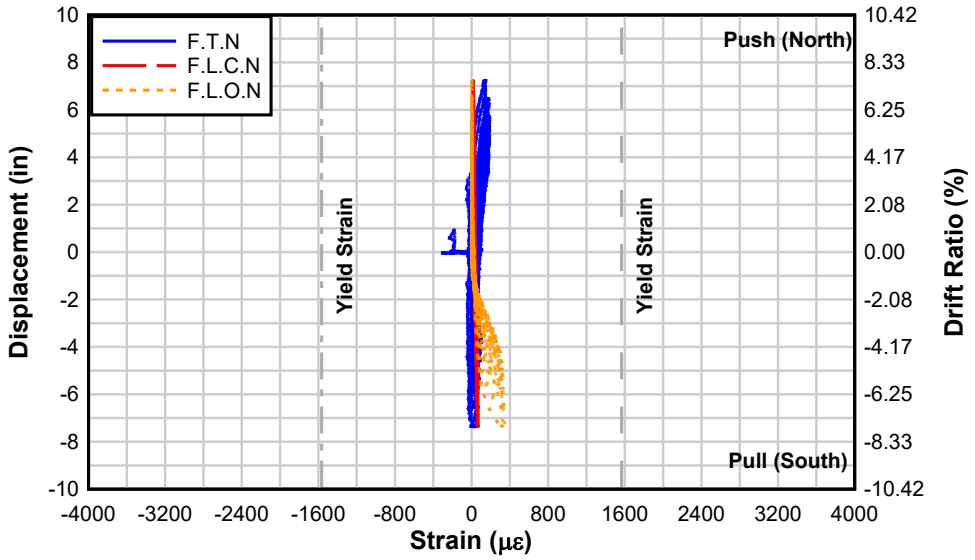

Figure A6.3.7.11: Footing Bar Strains – Test 7.

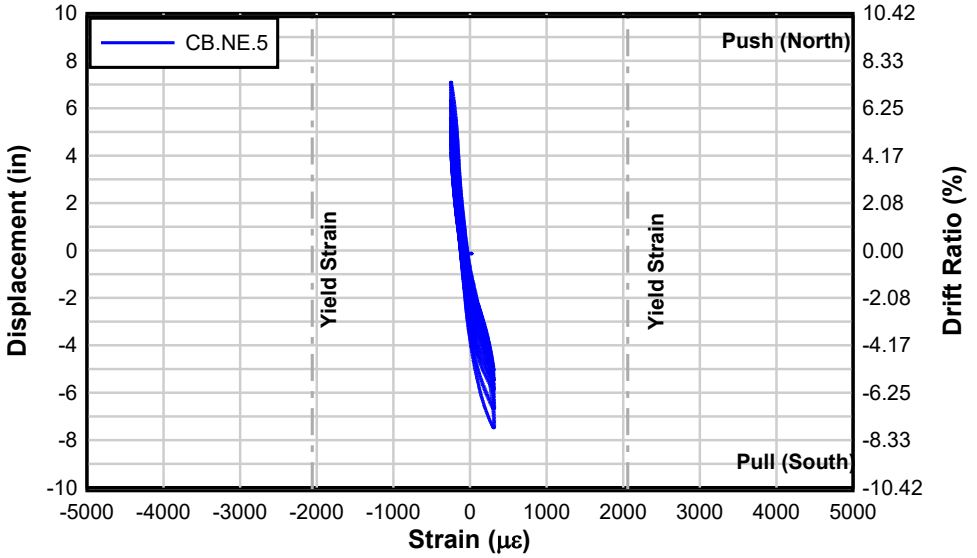

Figure A6.3.7.12: Column Bar Strains – Test 7.

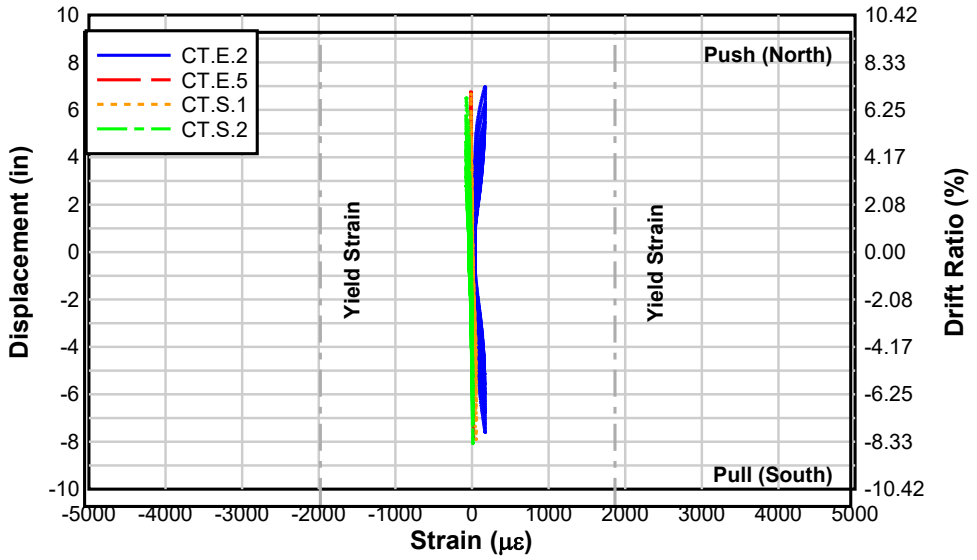

Figure A6.3.7.13: Column Tie Strains – Test 7.

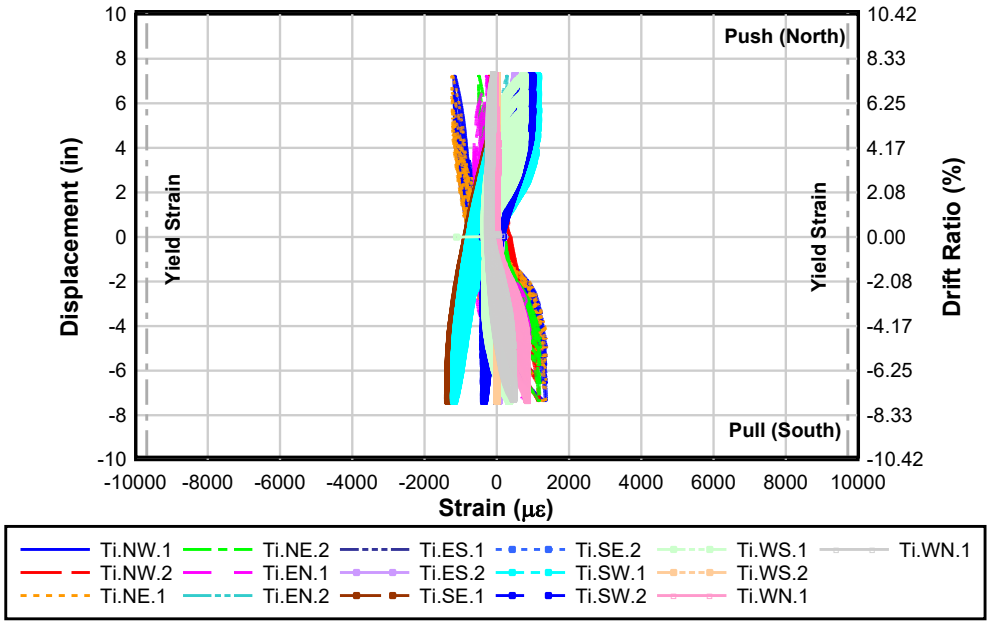

Figure A6.3.7.14: TiAB Ligament Strains – Test 7.

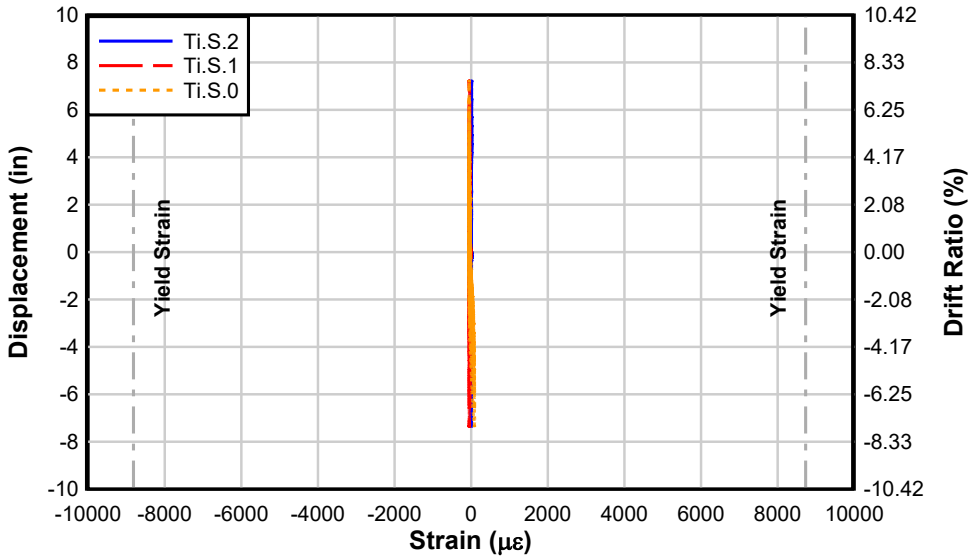

Figure A6.3.7.15: TiAB Spiral Strains – Test 7.

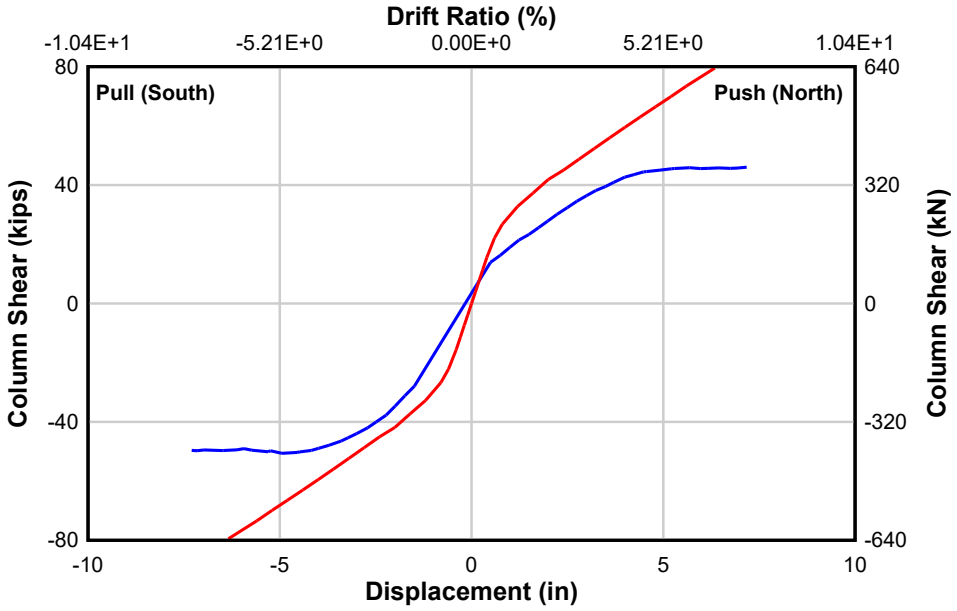

Figure A6.3.7.16: Soil Simulant Model Comparison – Test 7.

A6.3.8 TEST 8 – SPECIMEN 2: COMPLETE RETROFIT WITH TIED DOWN FOOTING

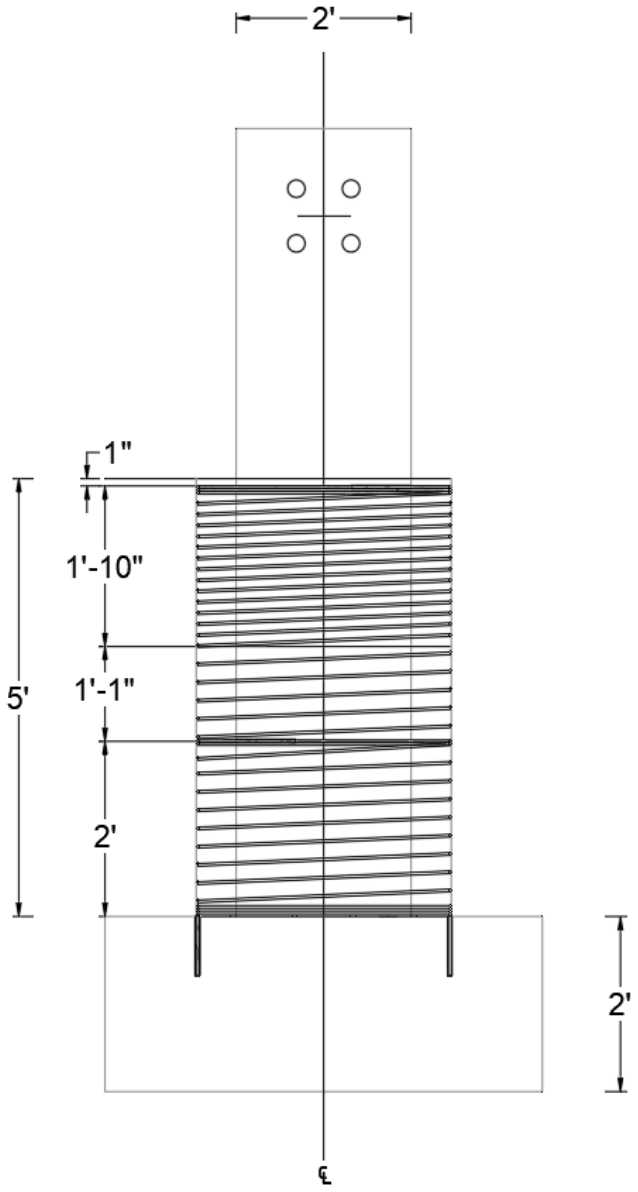

Figure A6.3.8.1: Elevation View of Specimen 2 used in Test 8.

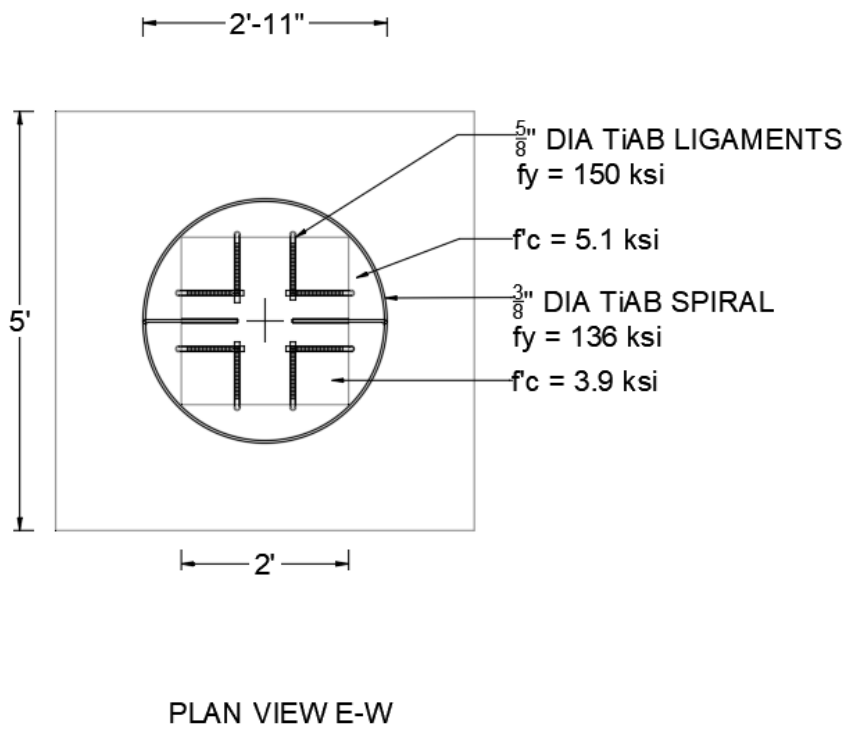

Figure A6.3.8.2: Plan View of Specimen 2 used in Test 8.

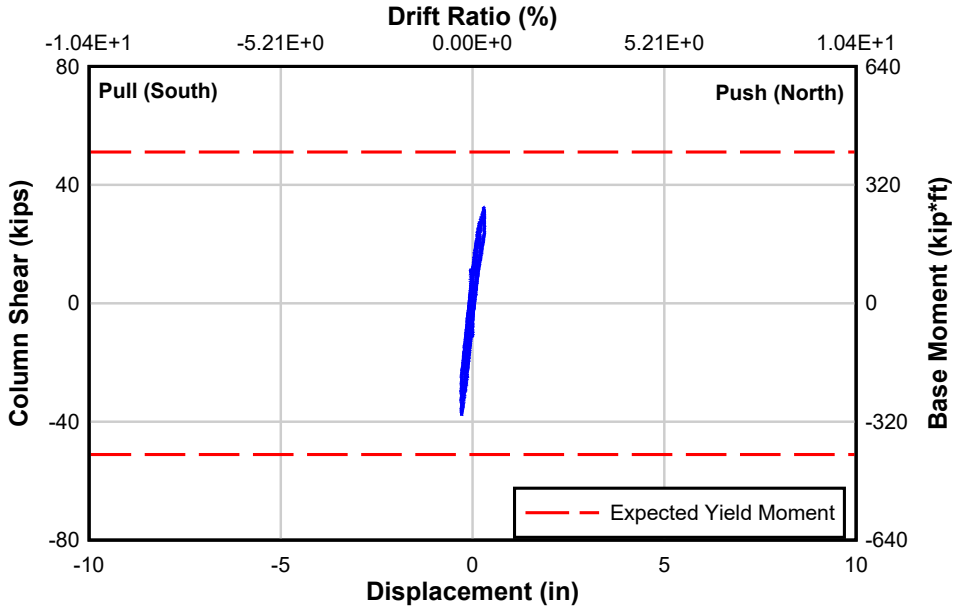

Figure A6.3.8.3: Overall Force Displacement Response Pre-failure – Test 8.

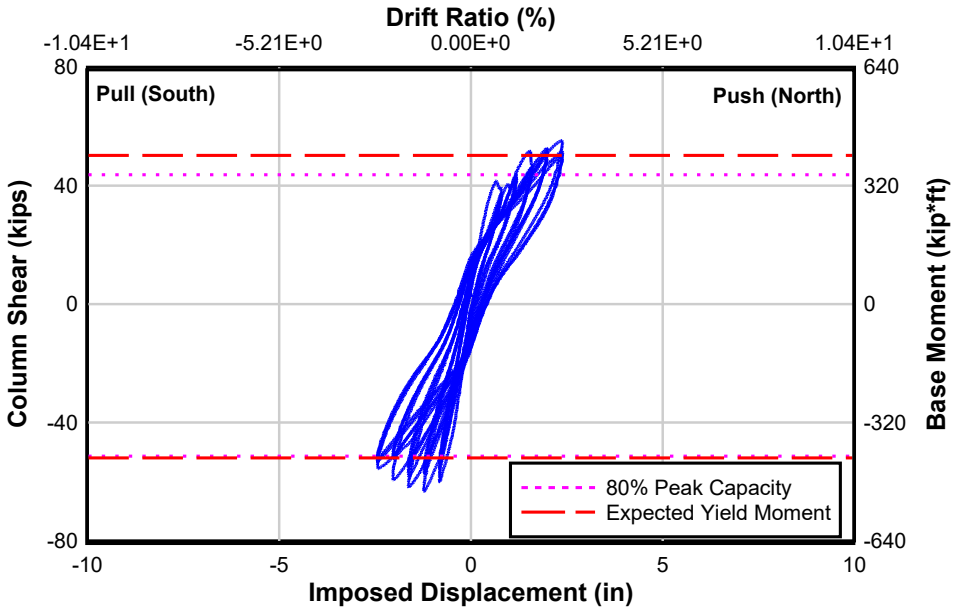

Figure A6.3.8.4: Overall Force Displacement Response Post-failure – Test 8.

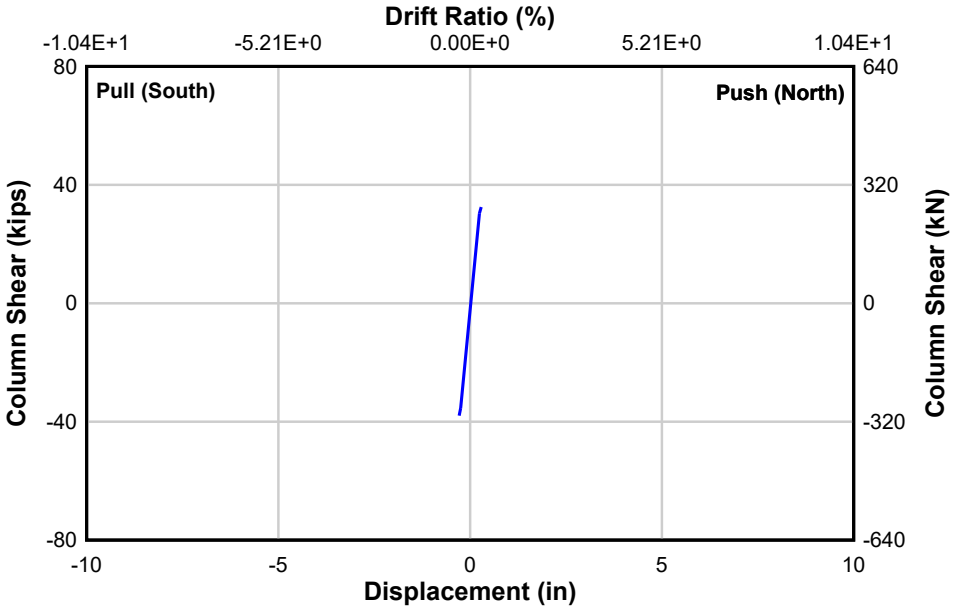

Figure A6.3.8.5: Overall Force Displacement Backbone Curve Pre-failure – Test 8.

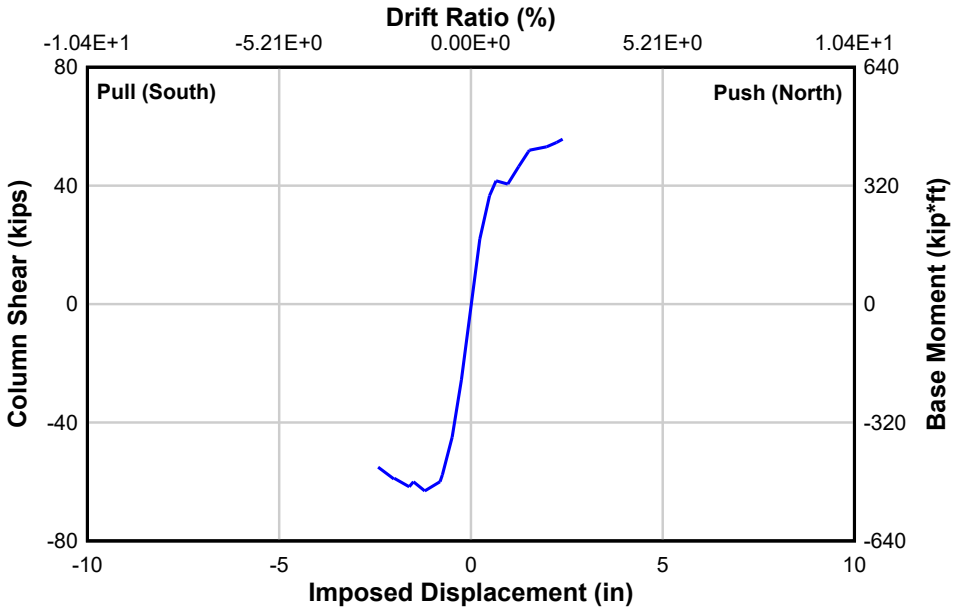

Figure A6.3.8.6: Overall Force Displacement Backbone Curve Post-failure – Test 8.

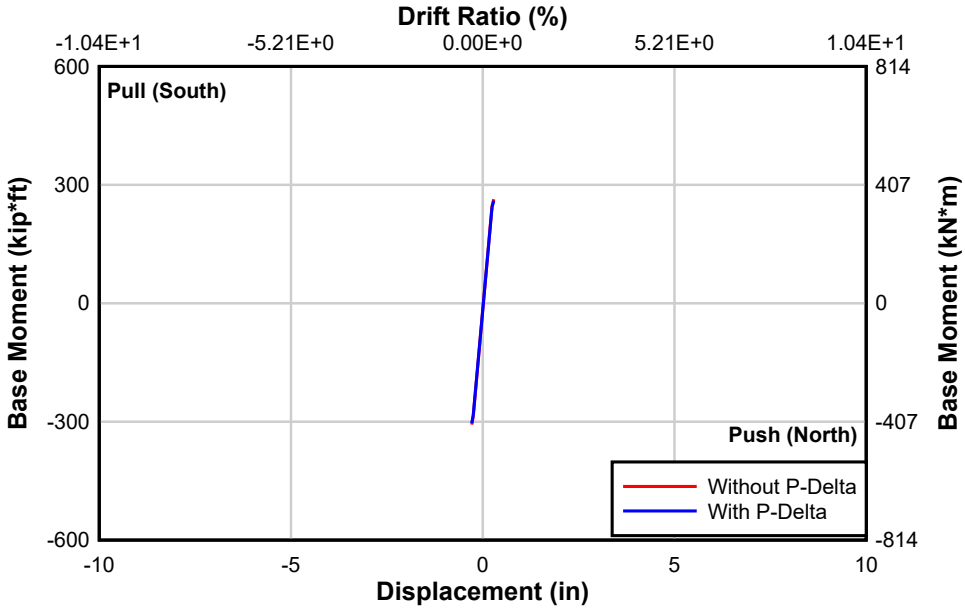

Figure A6.3.8.7: P-Delta Effects Backbone Curve Pre-failure – Test 8.

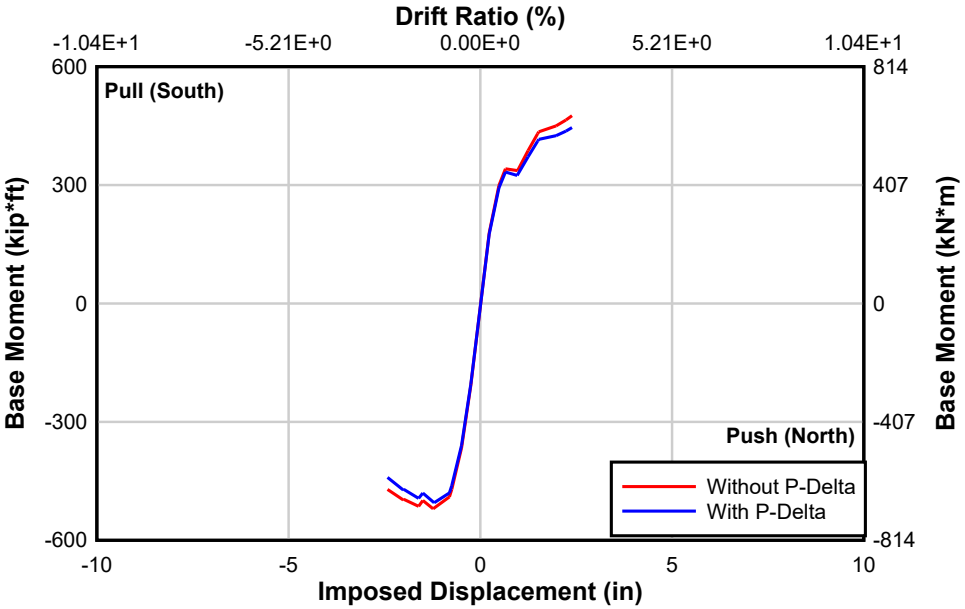

Figure A6.3.8.8: P-Delta Effects Backbone Curve Post-failure – Test 8.

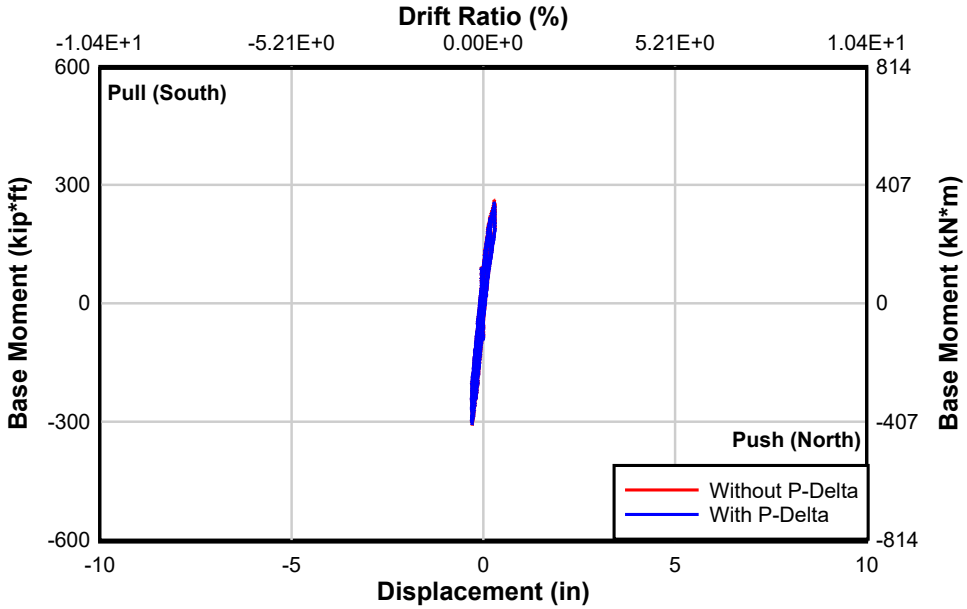

Figure A6.3.8.9: P-Delta Effects Pre-failure – Test 8.

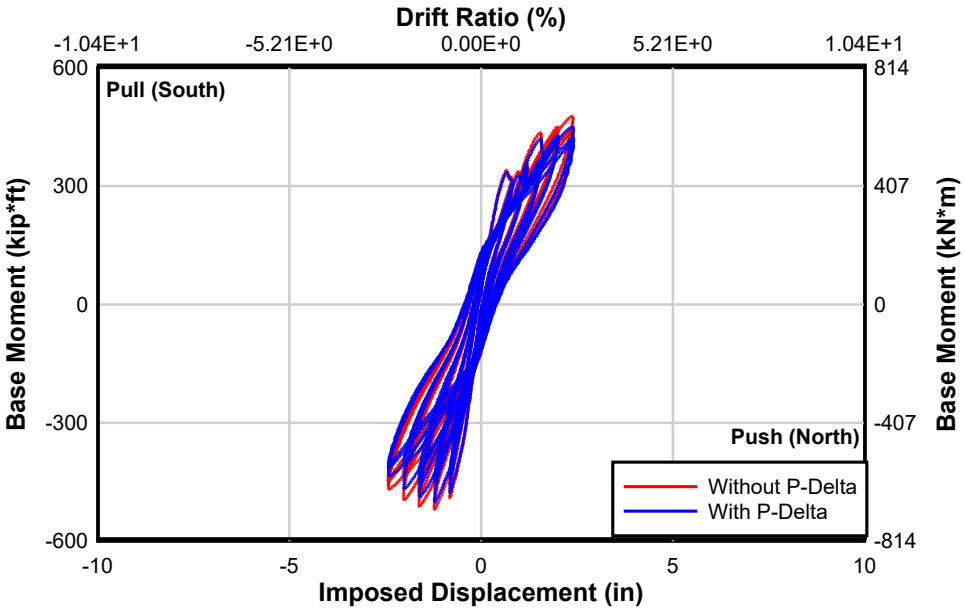

Figure A6.3.8.10: P-Delta Effects Post-failure – Test 8.

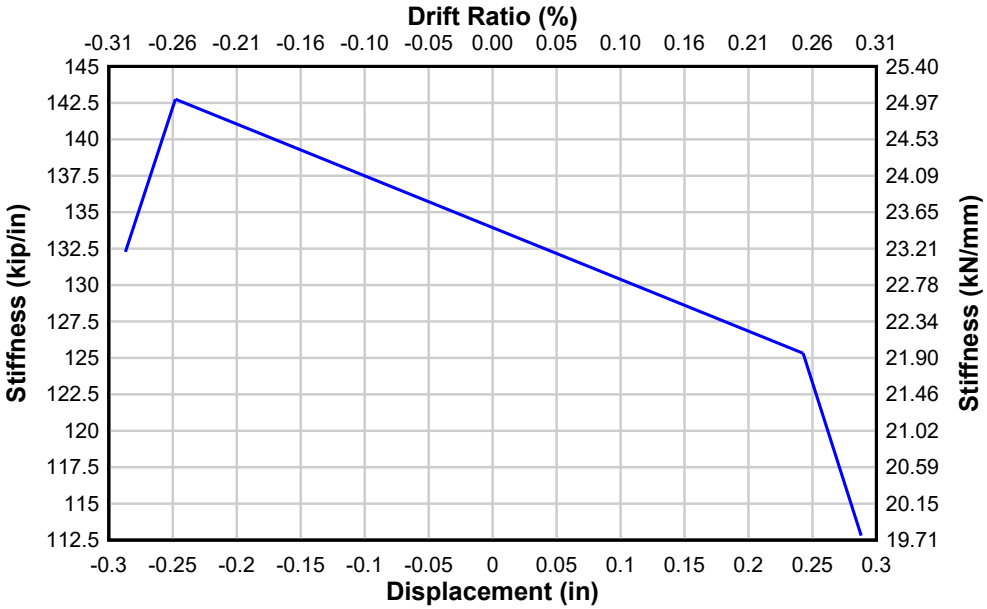

Figure A6.3.8.11: Evolution of Secant Stiffness Pre-failure – Test 8.

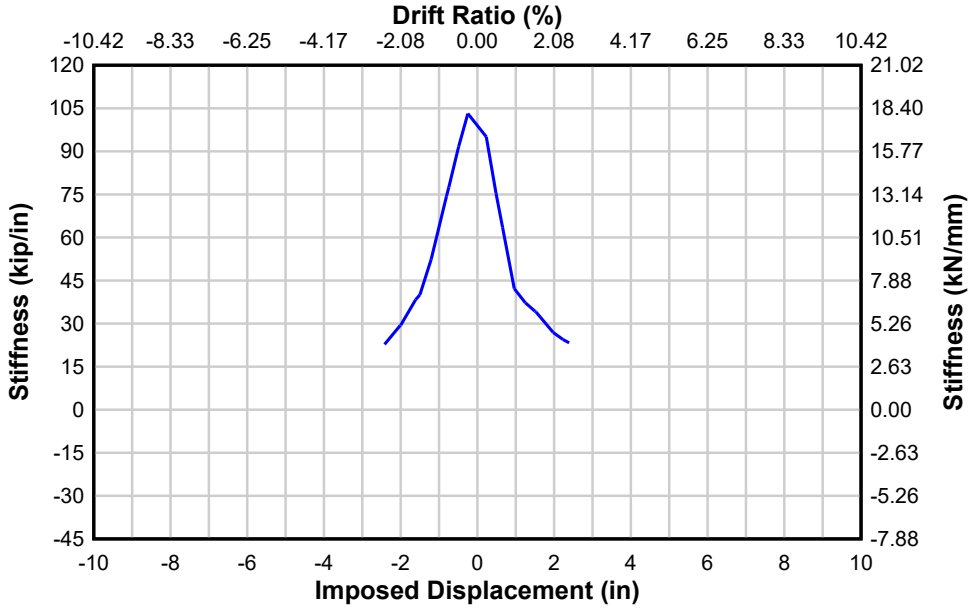

Figure A6.3.8.12: Evolution of Secant Stiffness Post-Failure – Test 8.

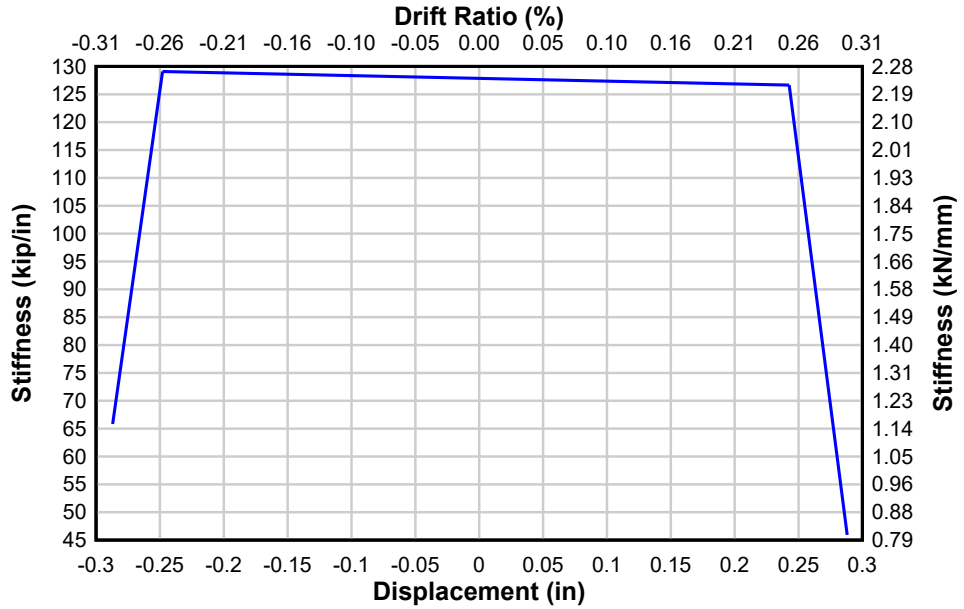

Figure A6.3.8.13: Evolution of Tangent Stiffness Pre-failure – Test 8.

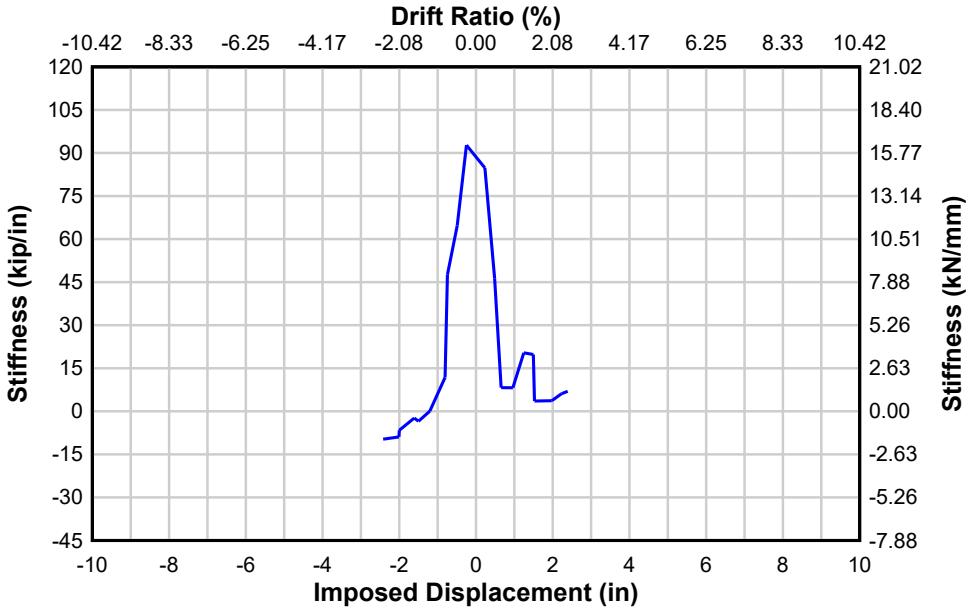

Figure A6.3.8.14: Evolution of Tangent Stiffness Post-Failure – Test 8.

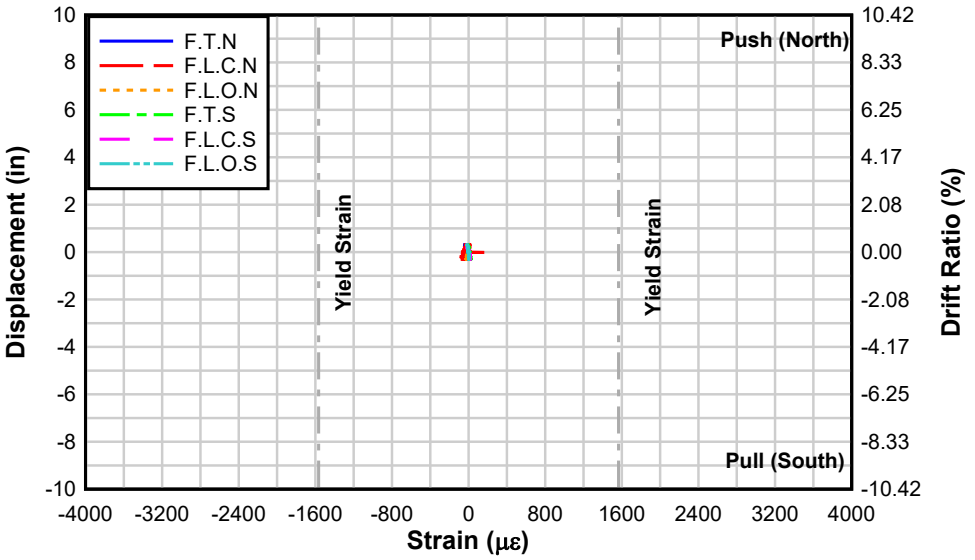

Figure A6.3.8.15: Footing Bar Strains Pre-failure – Test 8.

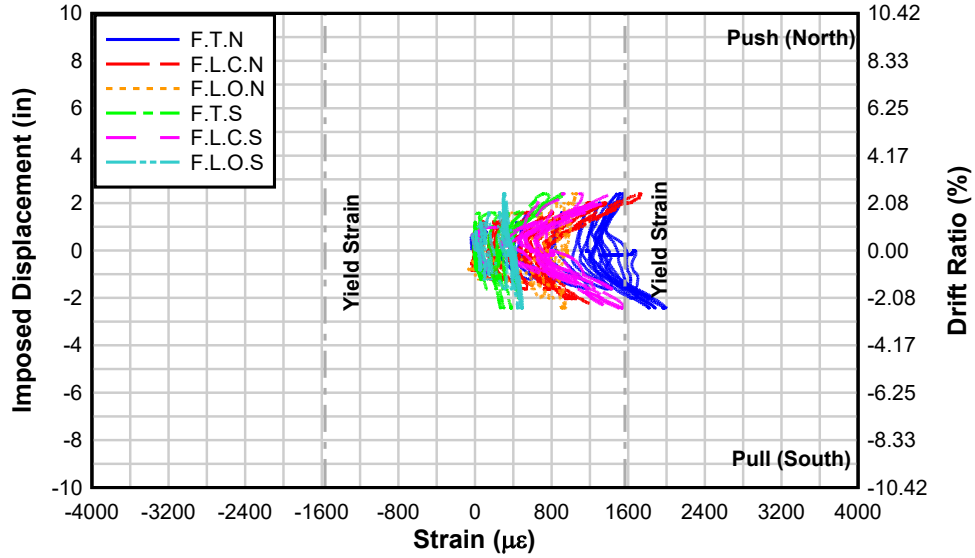

Figure A6.3.8.16: Footing Bar Strains Post-Failure – Test 8.

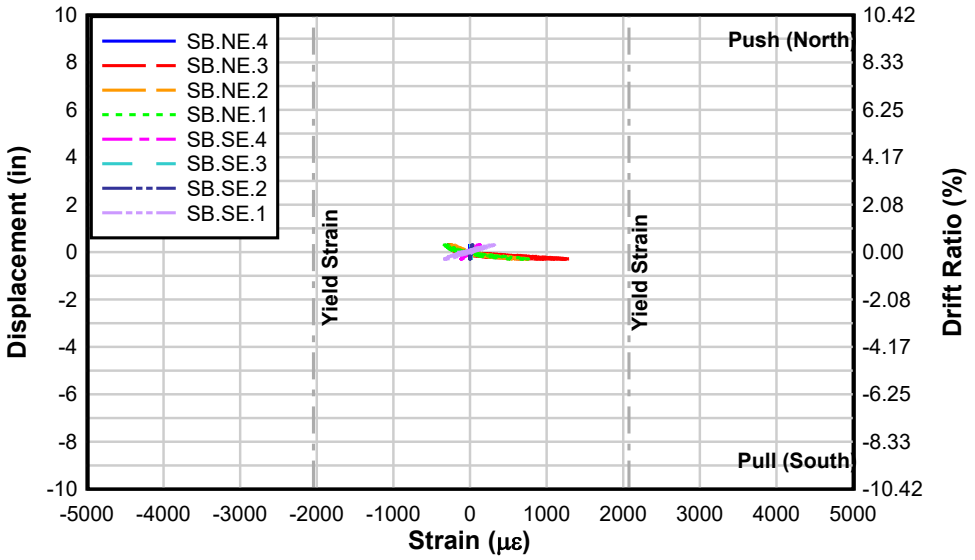

Figure A6.3.8.17: Starter Bar Strains Pre-failure – Test 8.

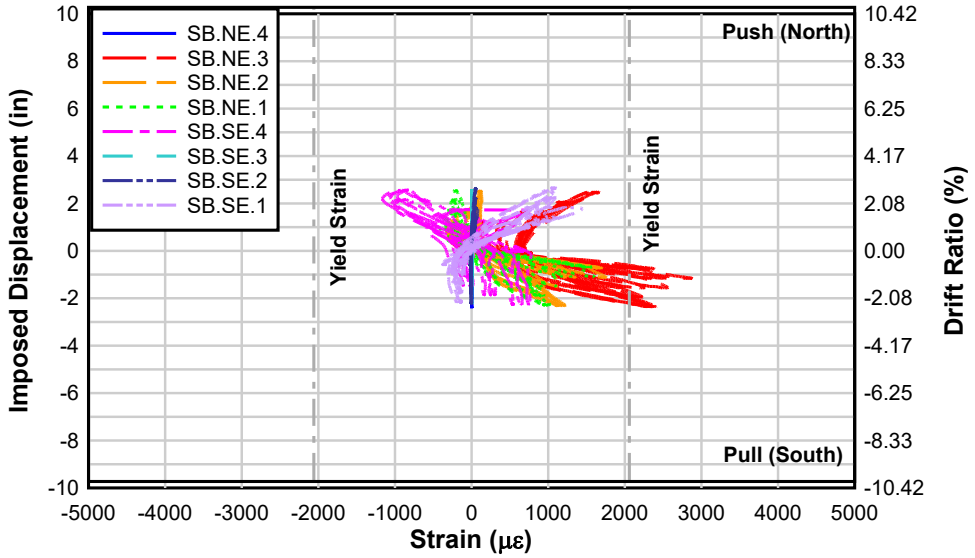

Figure A6.3.8.18: Starter Bar Strains Post-failure – Test 8.

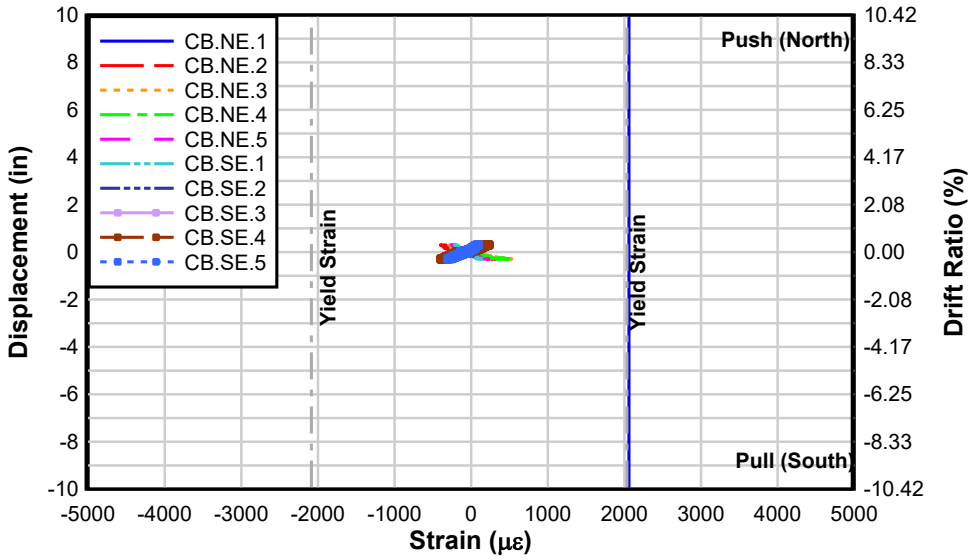

Figure A6.3.8.19: Column Bar Strain Pre-failure – Test 8.

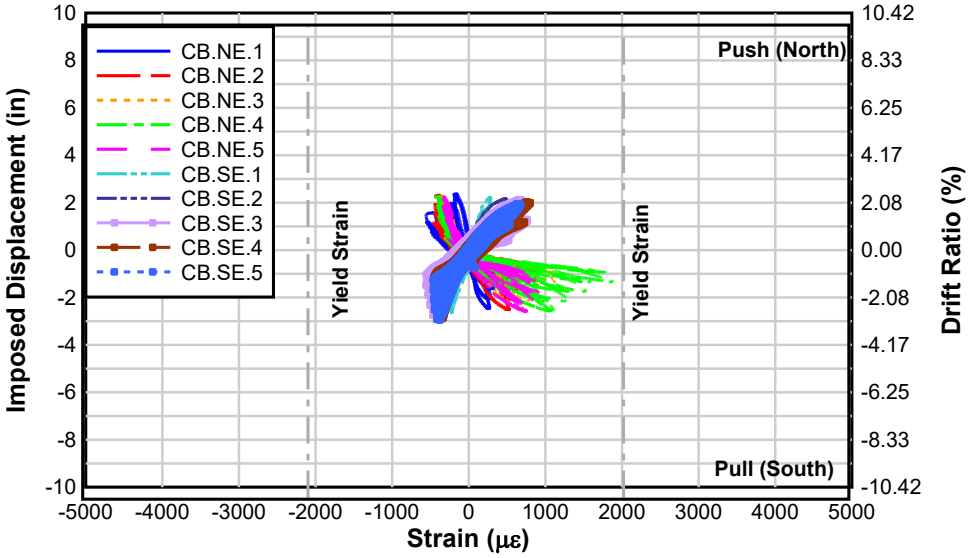

Figure A6.3.8.20: Column Bar Strain Post-failure – Test 8.

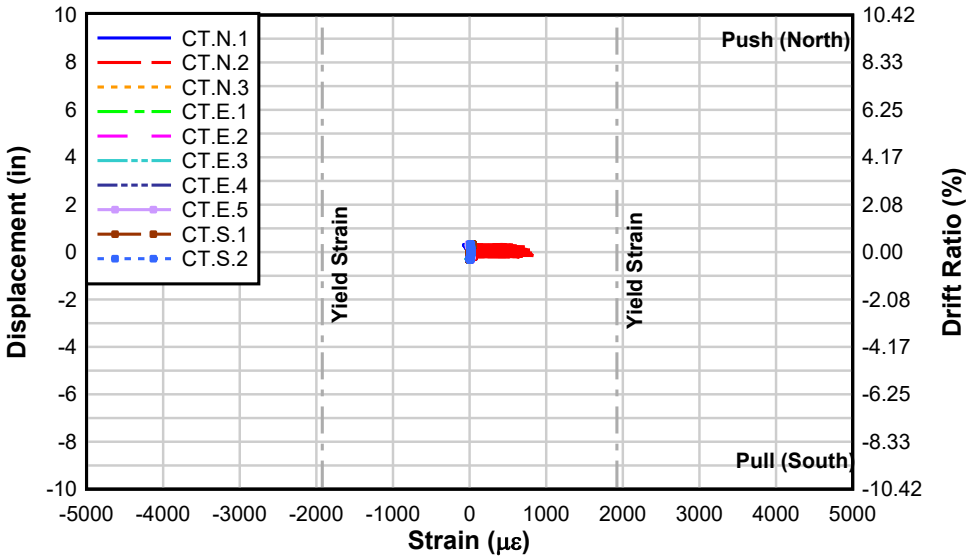

Figure A6.3.8.21: Column Tie Strains Pre-failure – Test 8.

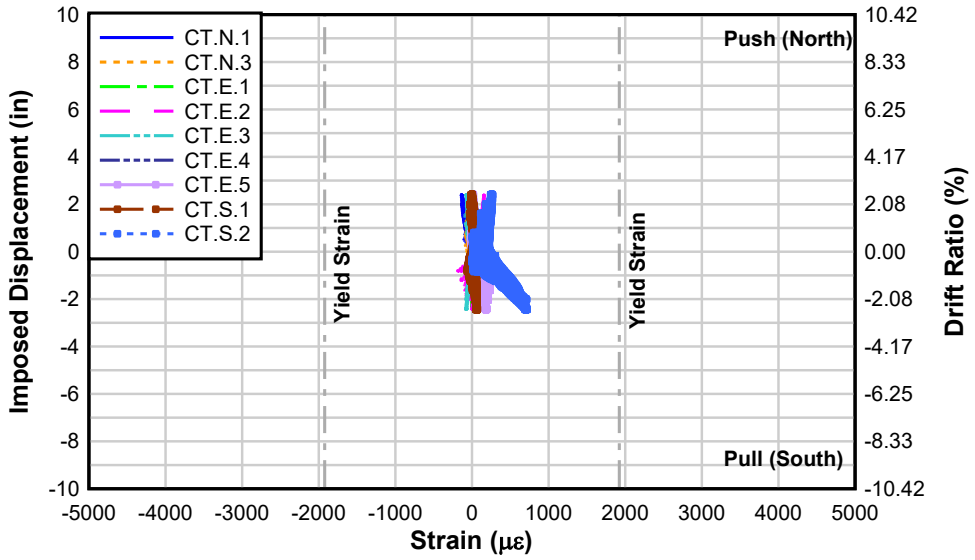

Figure A6.3.8.22: Column Tie Strains Post-failure – Test 8.

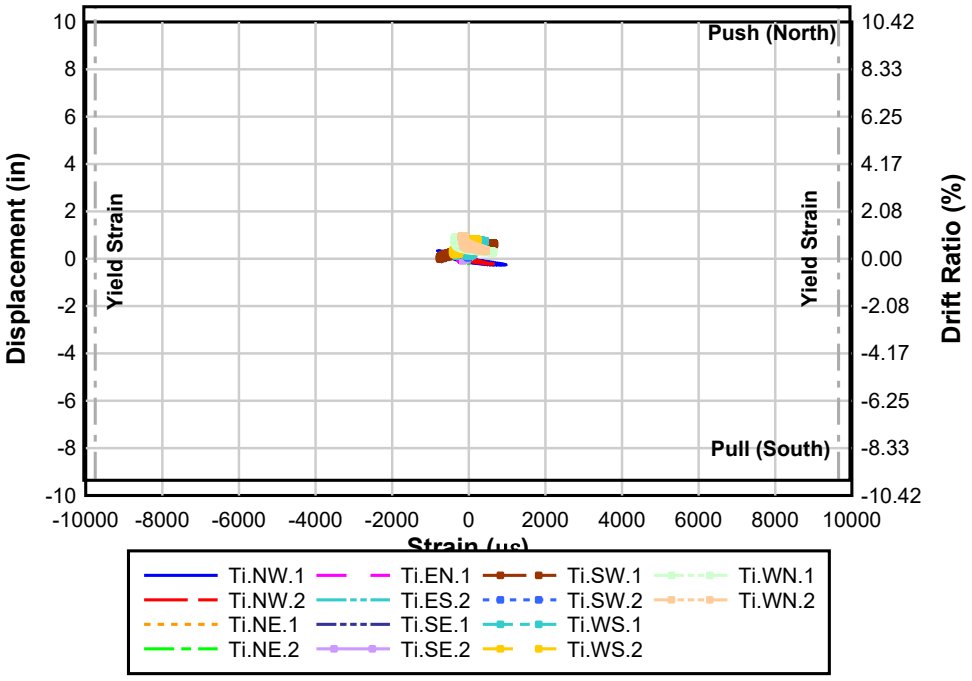

Figure A6.3.8.23: TiAB Ligament Strains Pre-failure – Test 8.

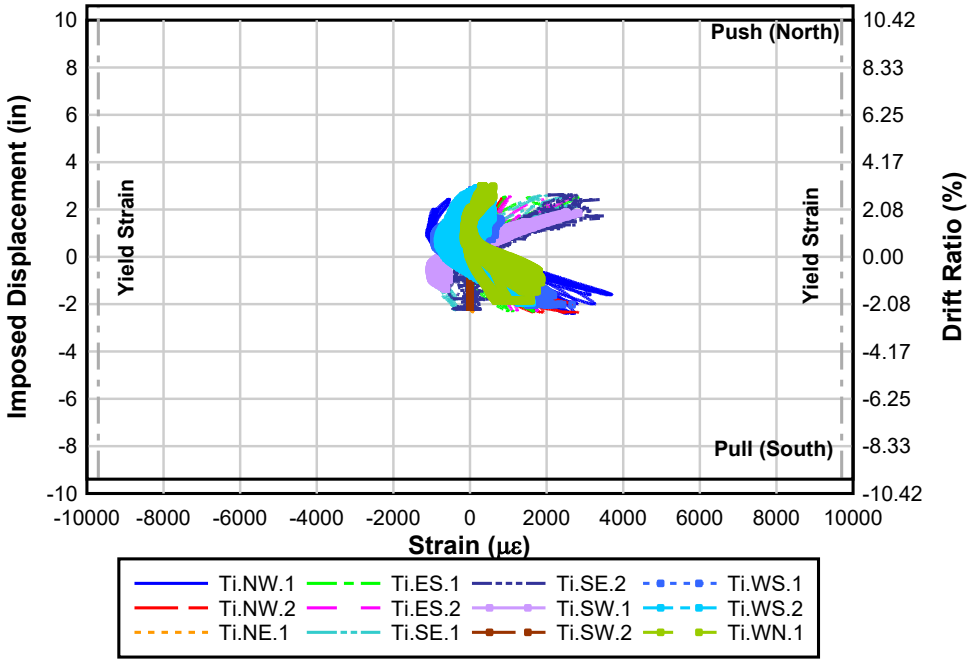

Figure A6.3.8.24: TiAB Ligament Strains Post-failure – Test 8.

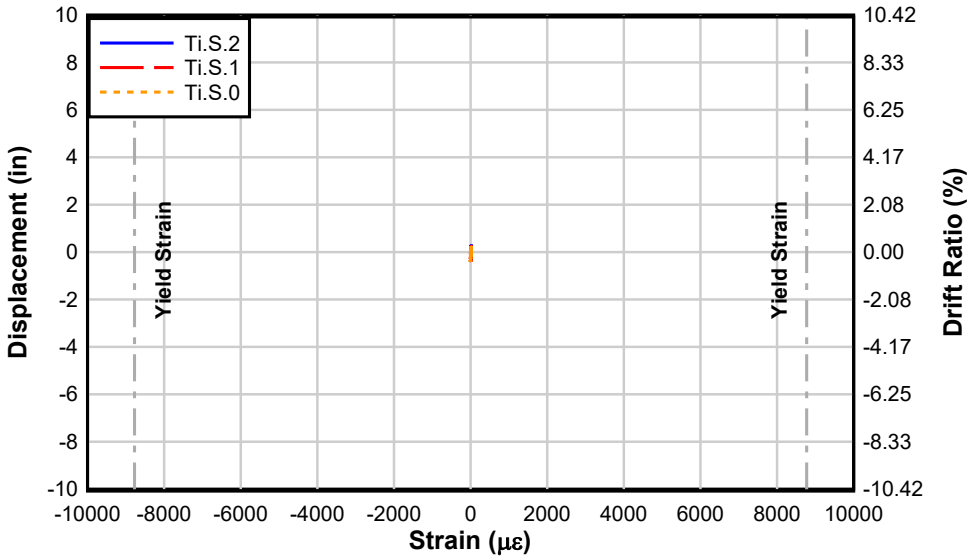

Figure A6.3.8.25: TiAB Spiral Strains Pre-failure – Test 8.

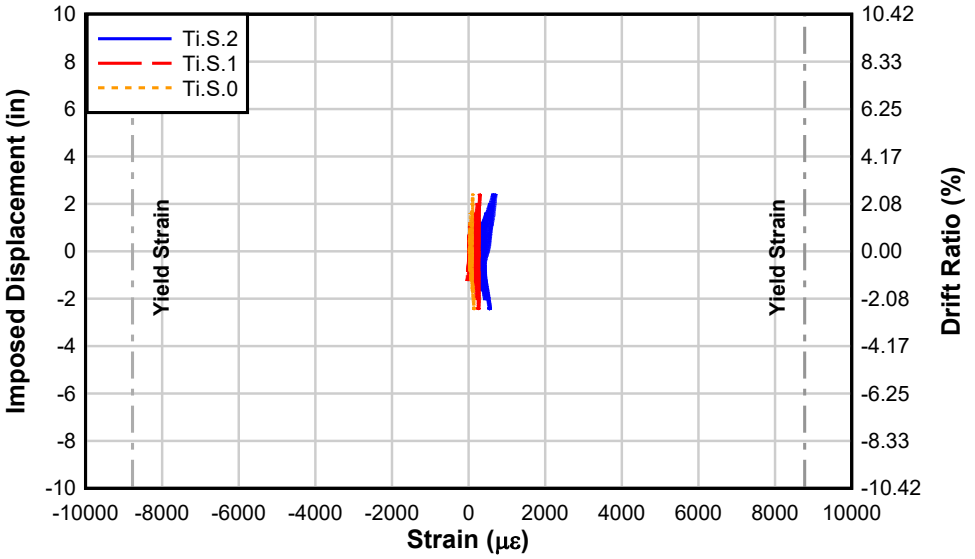

Figure A6.3.8.26: TiAB Spiral Strains Post-failure – Test 8.

A6.3.9 COMPARISON PLOTS

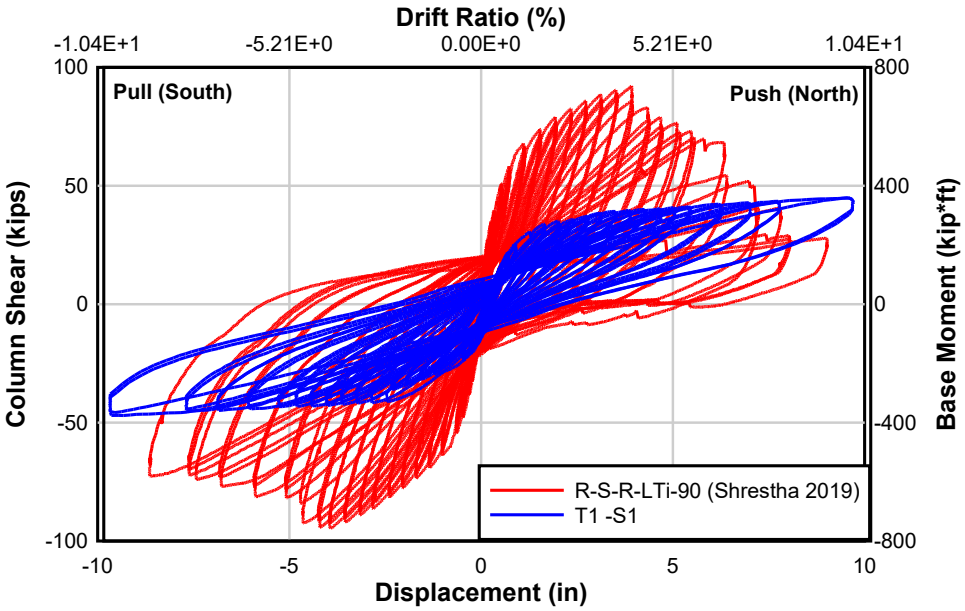

Figure A6.3.9.1: Comparison of Complete Retrofit SSI.

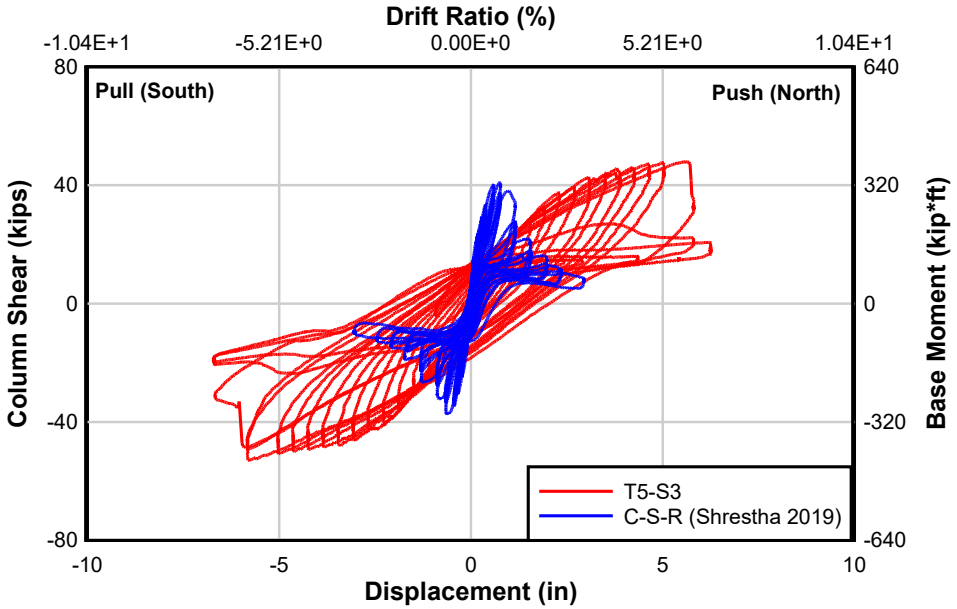

Figure A6.3.9.2 – Comparison of Vintage Column SSI.

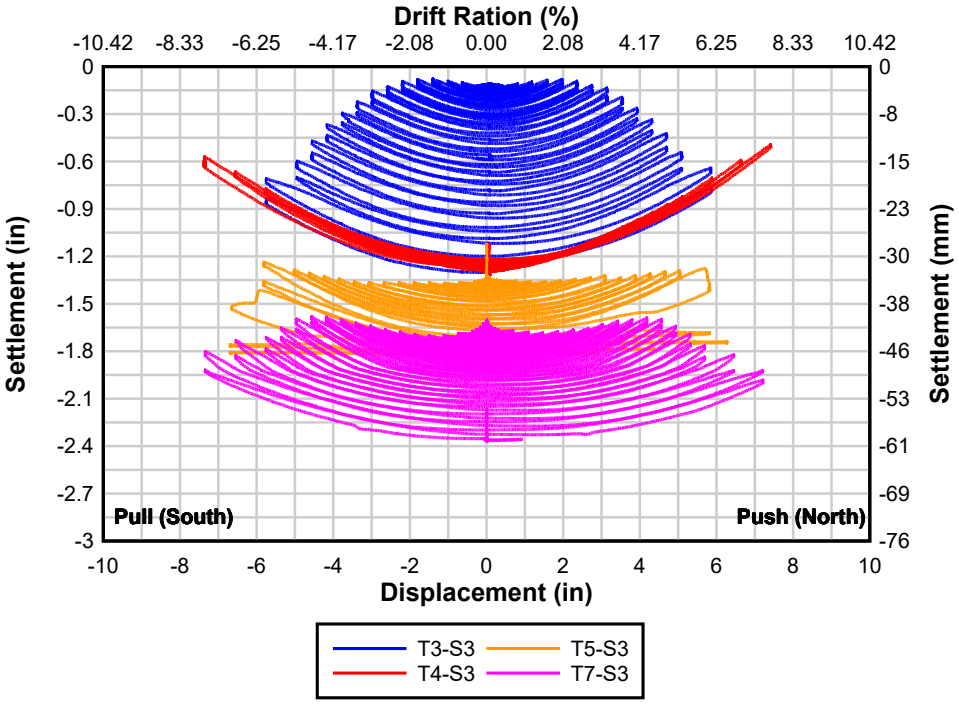

Figure A6.3.9.3: Subsequent Settlement Comparison.

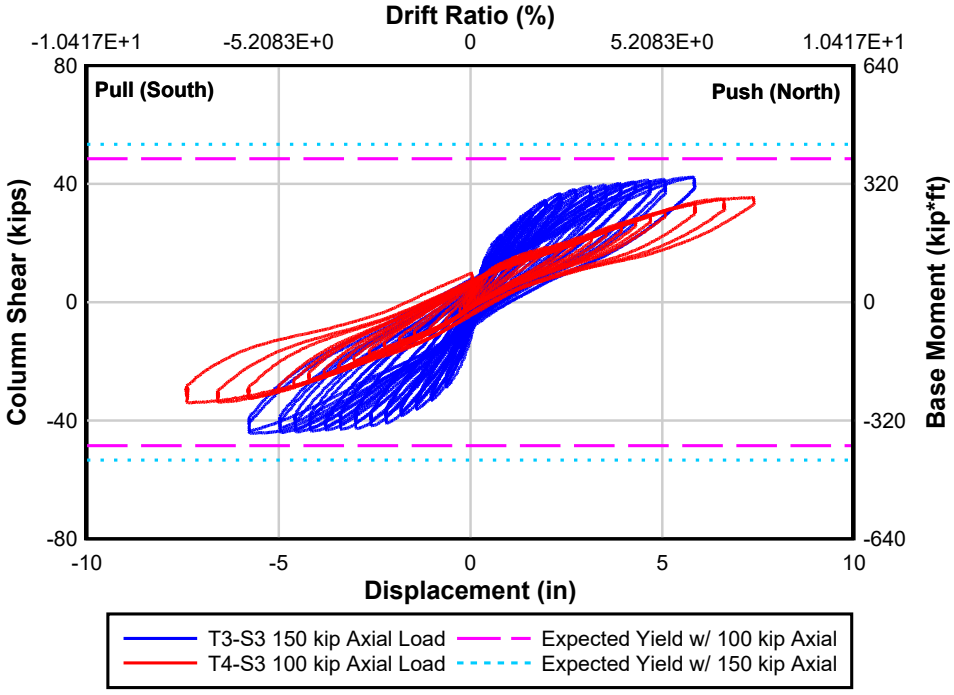

Figure A6.3.9.4: Effect of Axial Load.

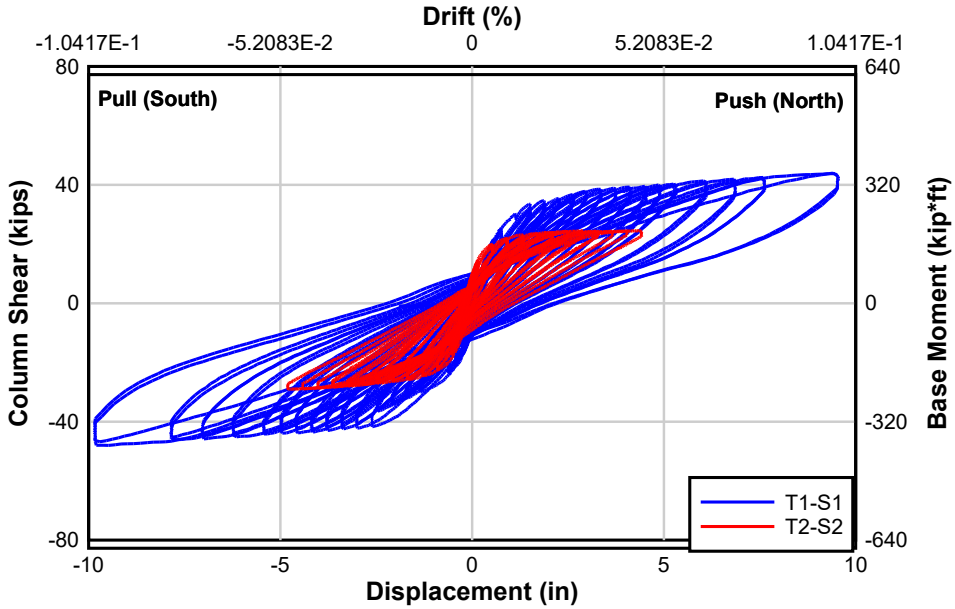

Figure A6.3.9.5: Effect of Embedment.

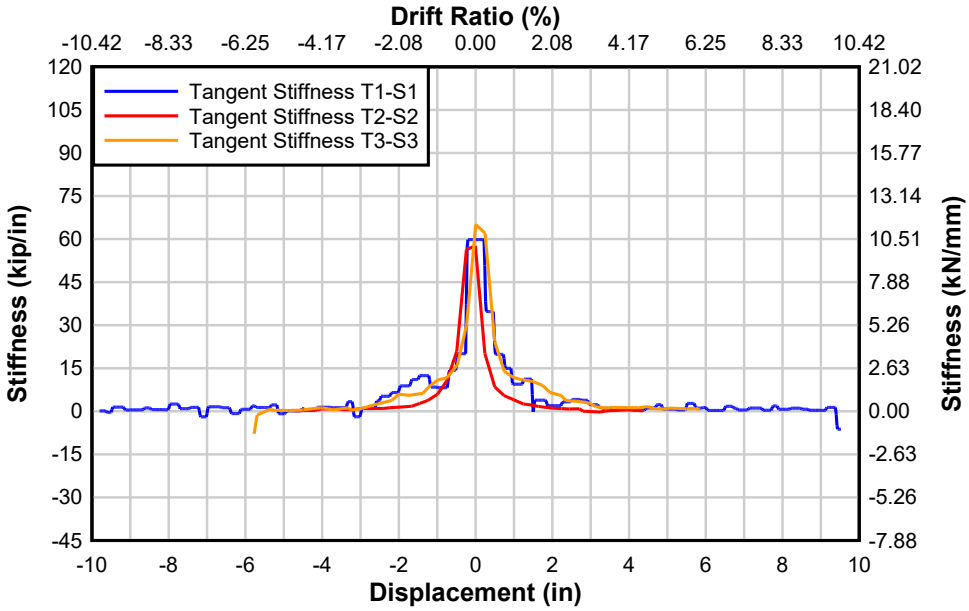

Figure A6.3.9.6: Tangent Stiffness Virgin Soil Simulant.

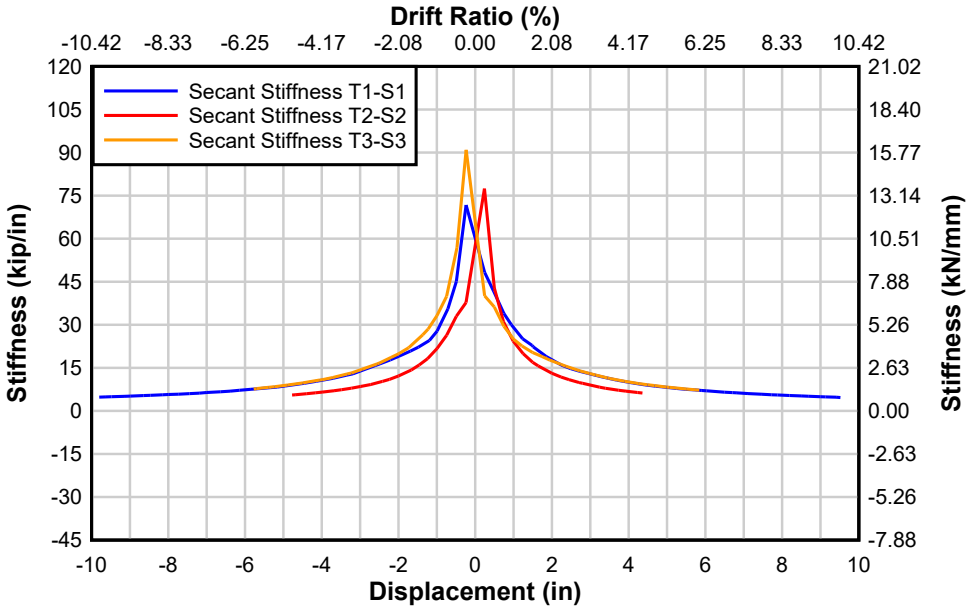

Figure A6.3.9.7: Secant Stiffness Virgin Soil Simulant.

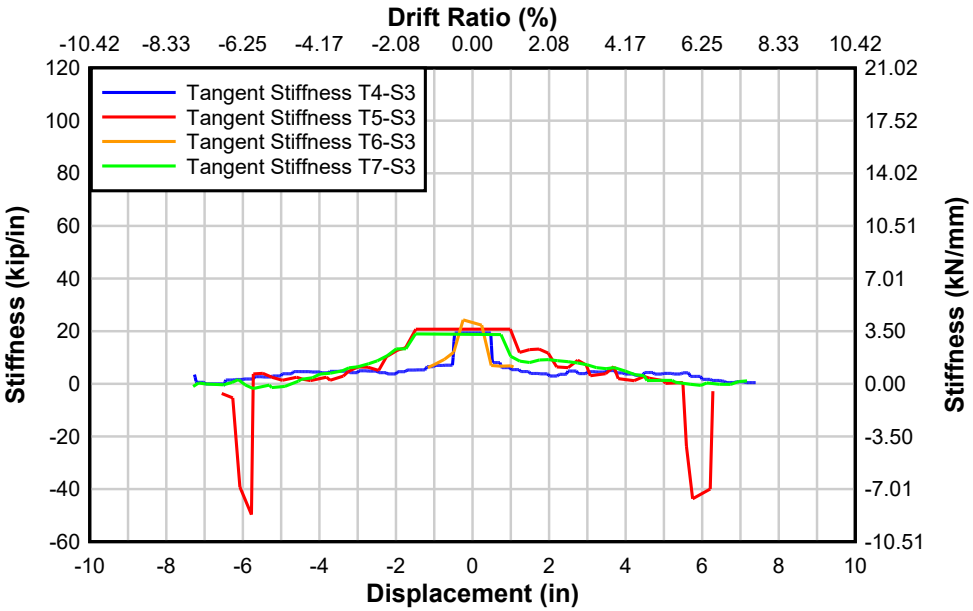

Figure A6.3.9.8: Tangent Stiffness of Failed Soil Simulant.

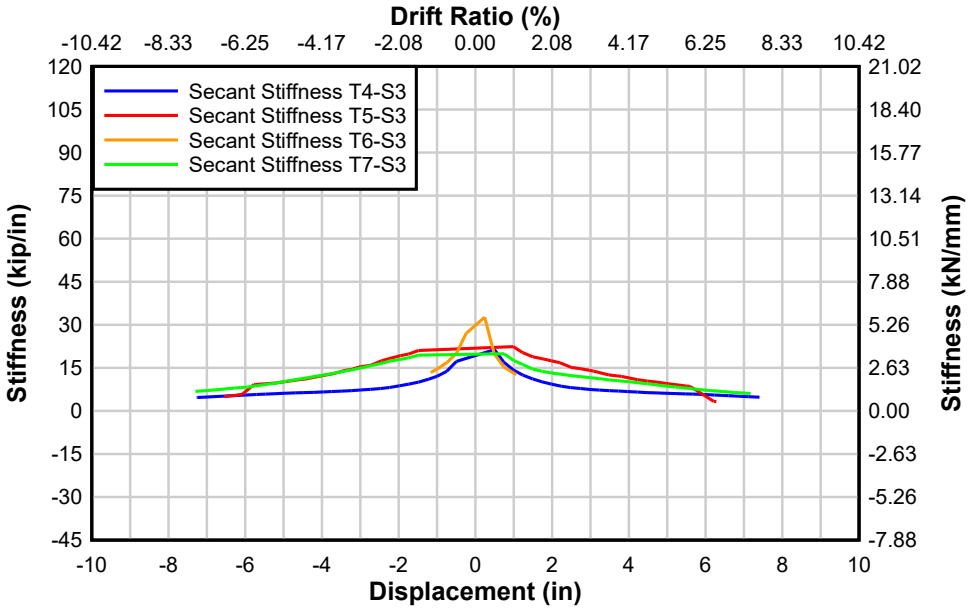

Figure A6.3.9.9: Secant Stiffness of Failed Soil Simulant.

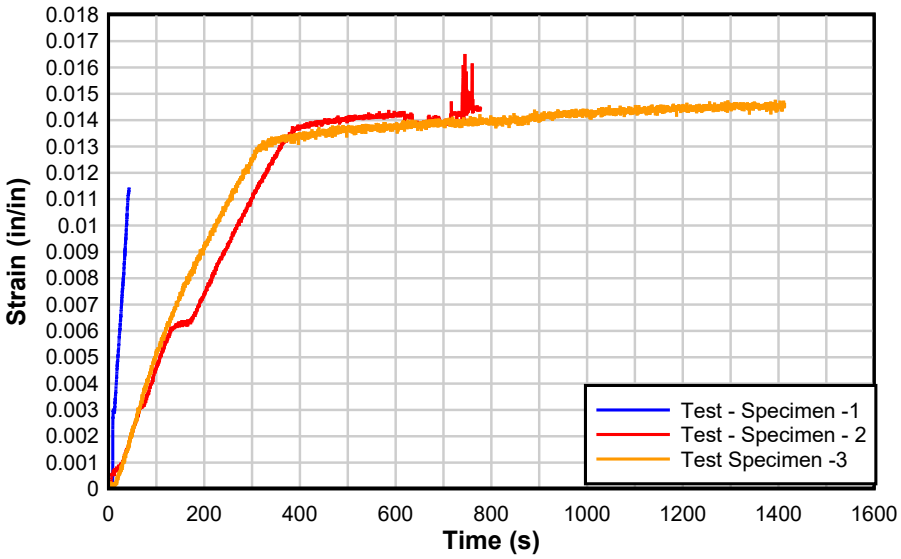

Figure A6.3.9.10: Strain Rate on Virgin Soil Simulant.

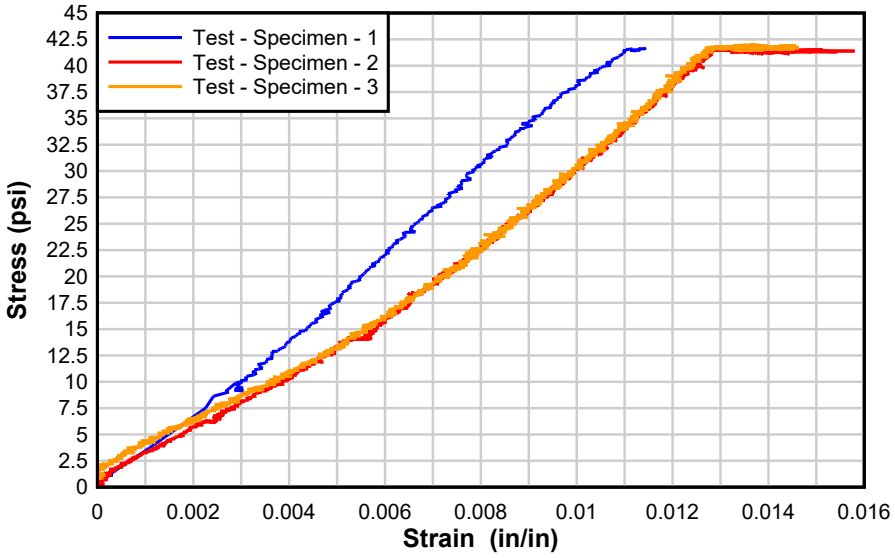

Figure A6.3.9.11: Bulk Engineering Stress-Strain Relationship on Virgin Soil.

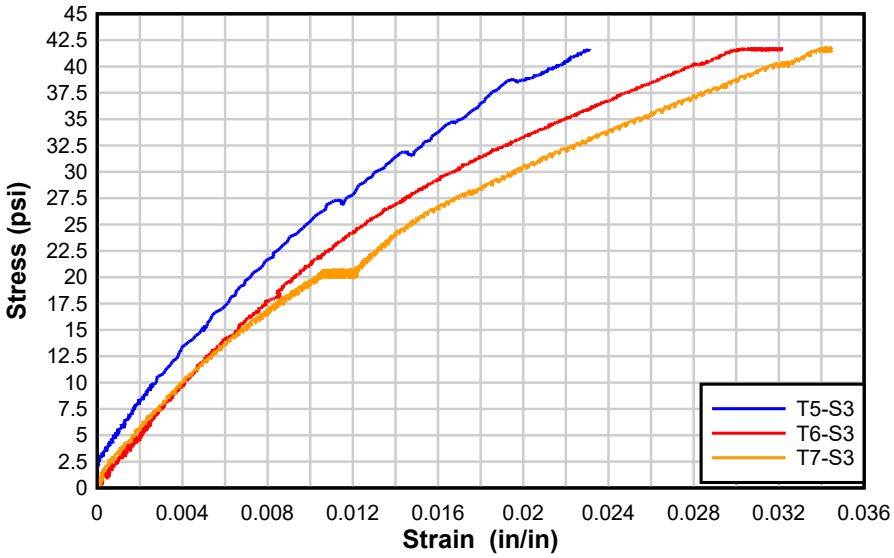

Figure A6.3.9.12: Bulk Average Engineering Stress-Strain Relationship on Failed Soil Simulant.

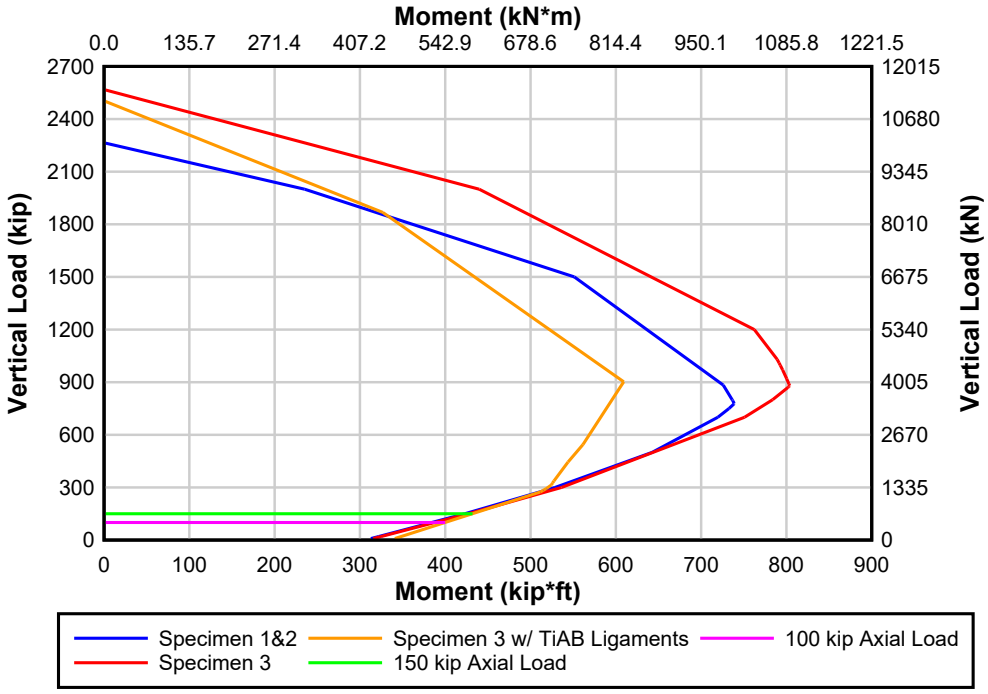

Figure A6.3.9.13: P-M Interaction Diagrams with As-Built Vintage Column Details.

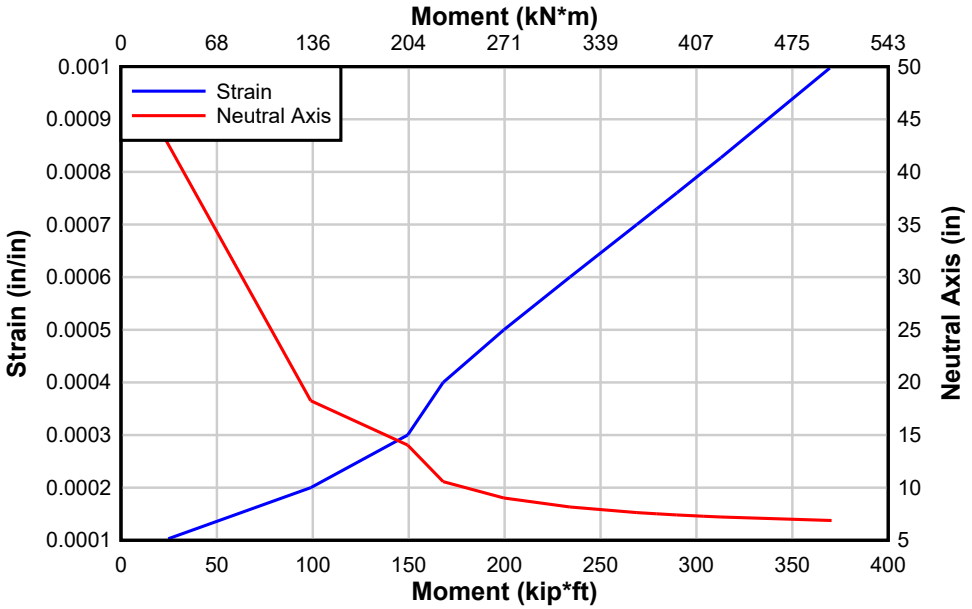

Figure A6.3.9.14: Expected moment strain as neutral axis varies.

APPENDIX A7.1: EXPERIMENTAL DATA FOR ALL TESTS REPORTED IN SECTION 7

A7.1.1 TEST 9 – S1: VINTAGE COLUMN WITH LIGAMENT AND SPIRAL RETROFIT, RESTRAINED FOOTING WITH RETROFIT

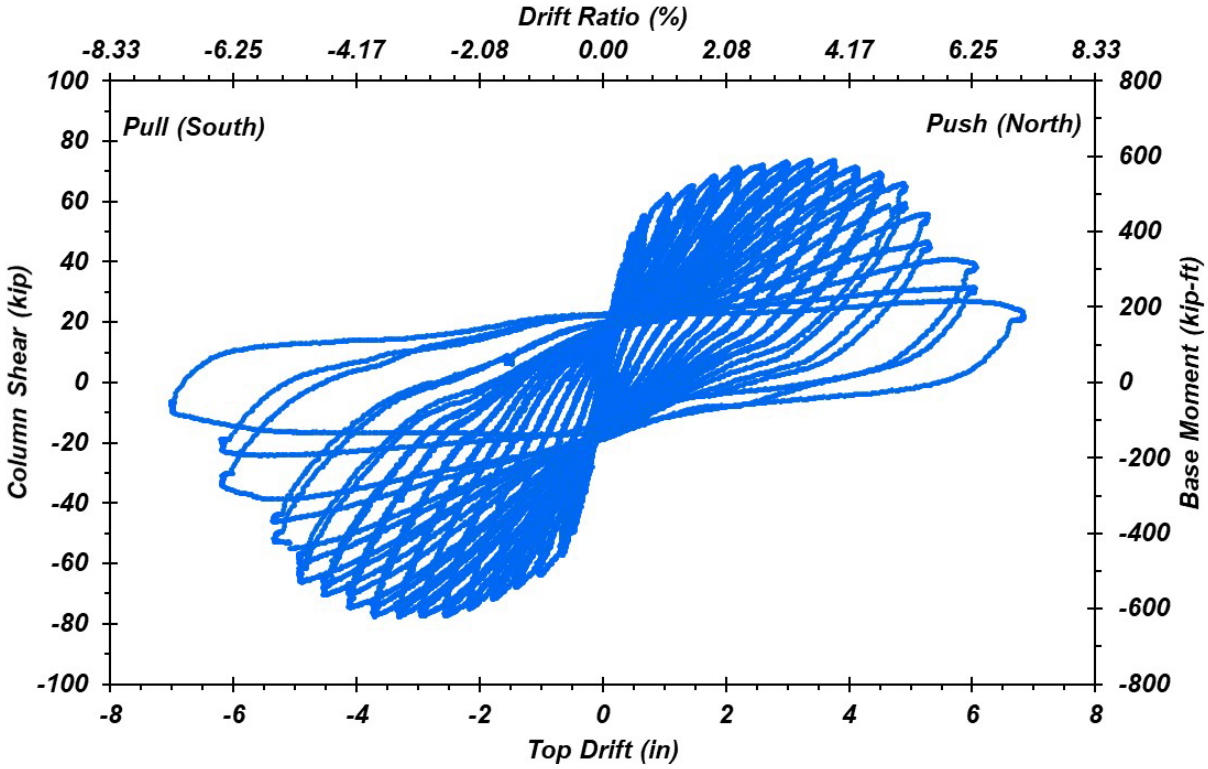

Figure A7.1.1.1: Overall force-displacement response, Test 9 – S1.

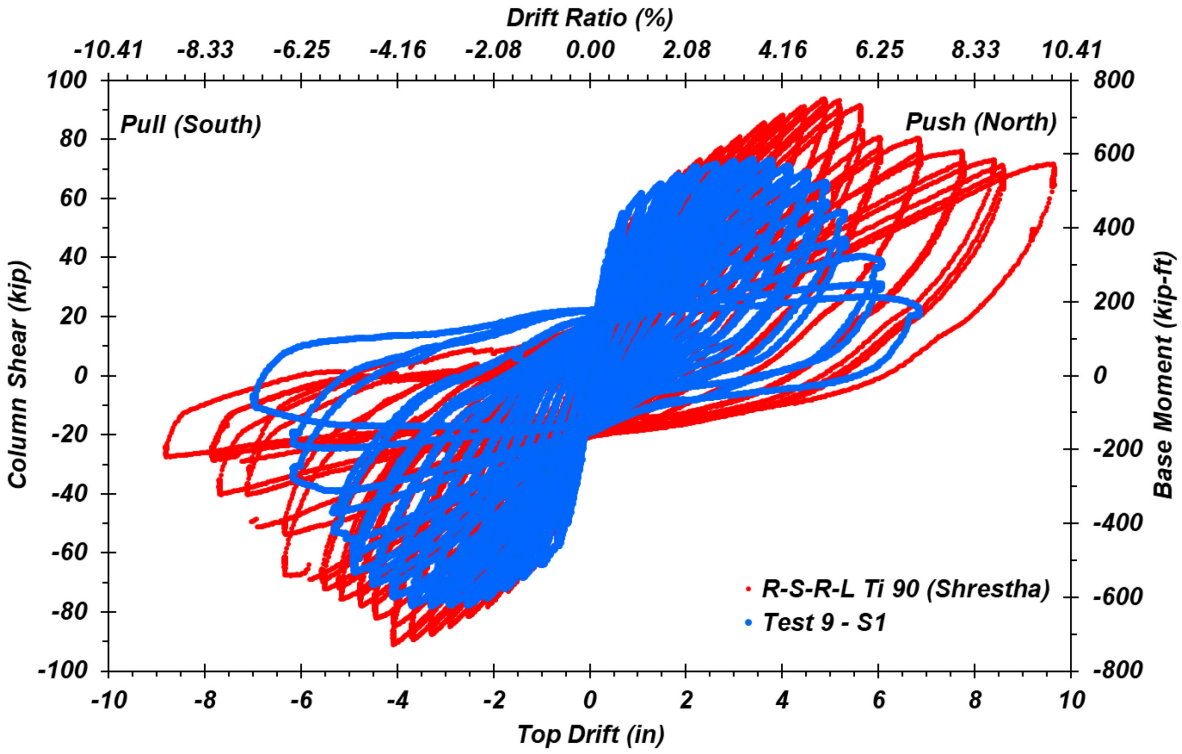

Figure A7.1.1.2: Load-drift comparison, Test 9 – S1 and R-S-R-L Ti 90 (Shrestha 2019).

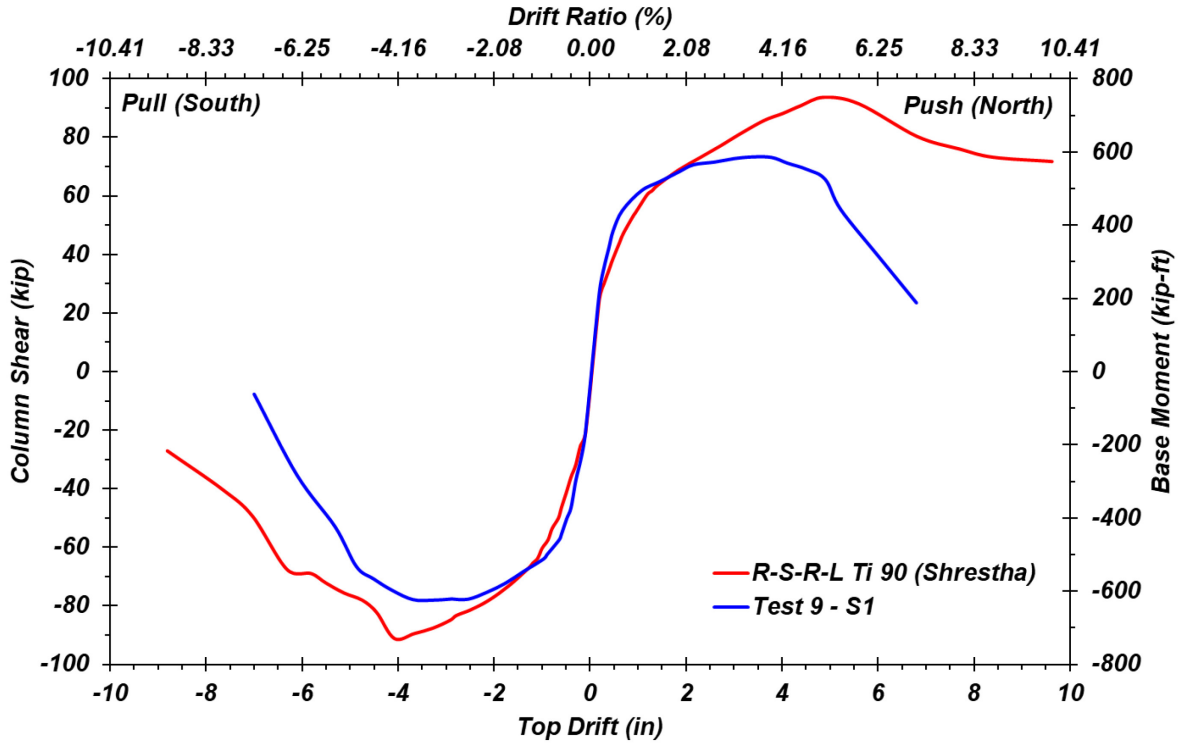

Figure A7.1.1.3: Backbone Curves, Test 9 – S1 and R-S-R-L Ti 90 (Shrestha 2019).

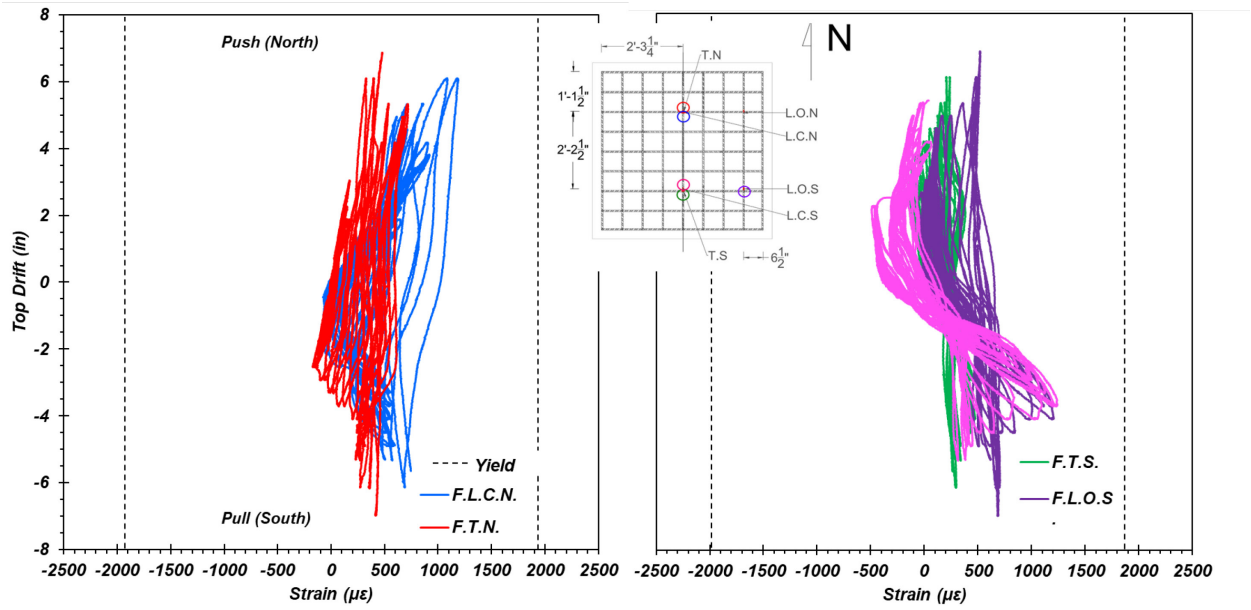

Figure A7.1.1.4: Footing bar strain-drift histories, Test 9 – S1.

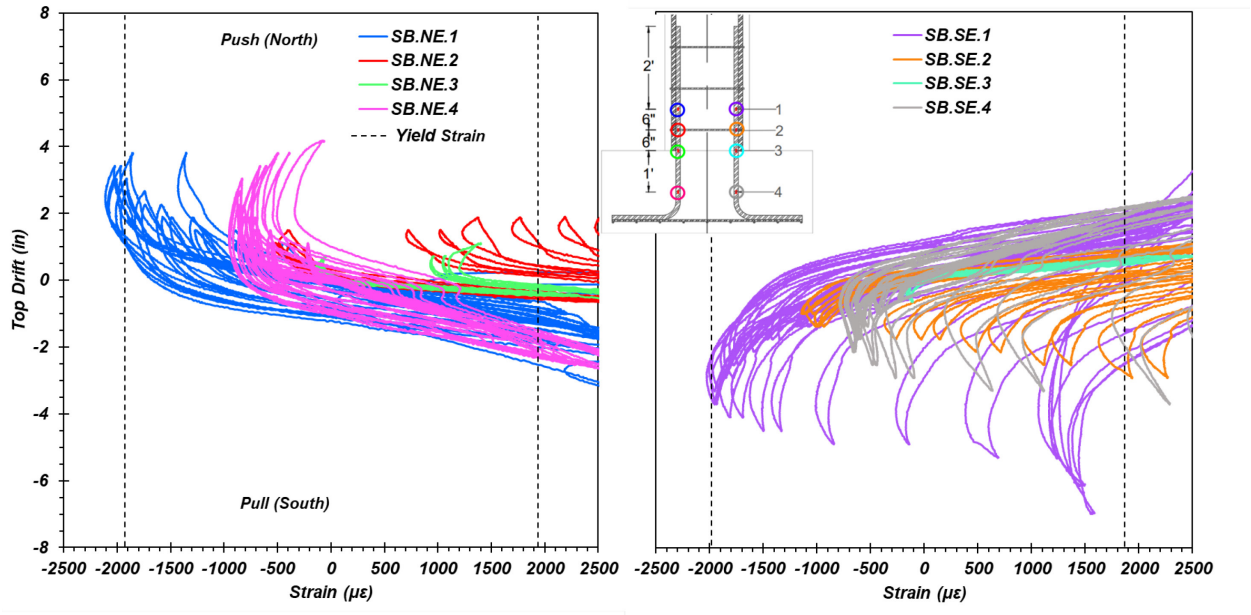

Figure A7.1.1.5: Starter bar strain-drift histories, Test 9 – S1.

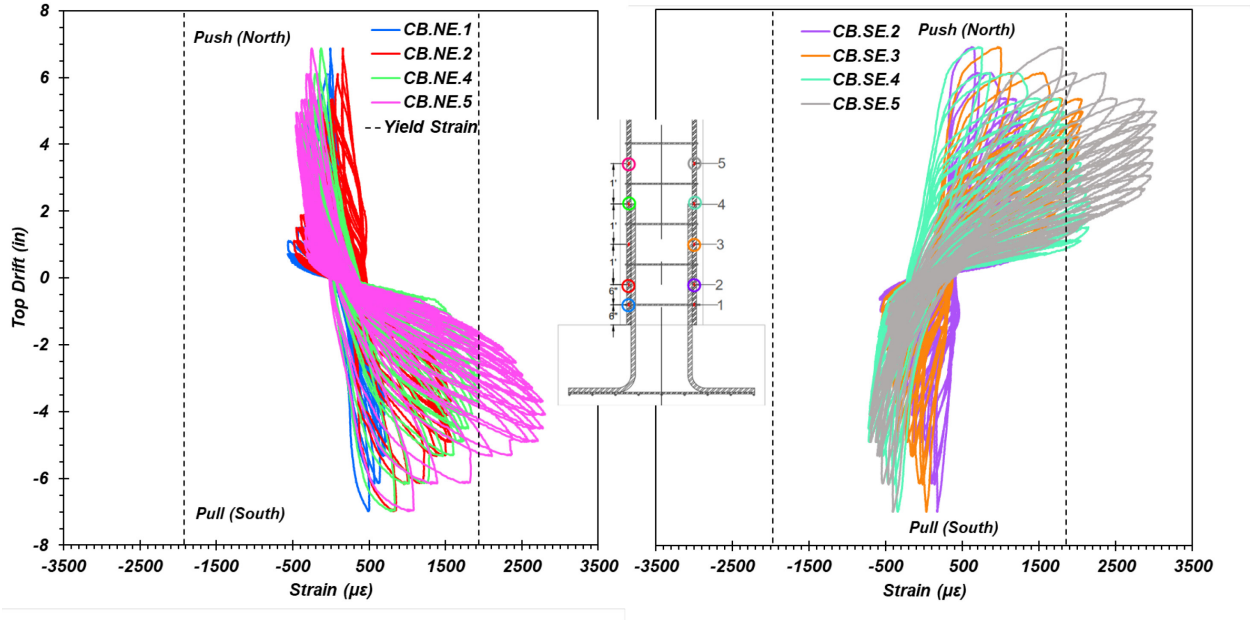

Figure A7.1.1.6: Column bar strain-drift histories, Test 9 – S1.

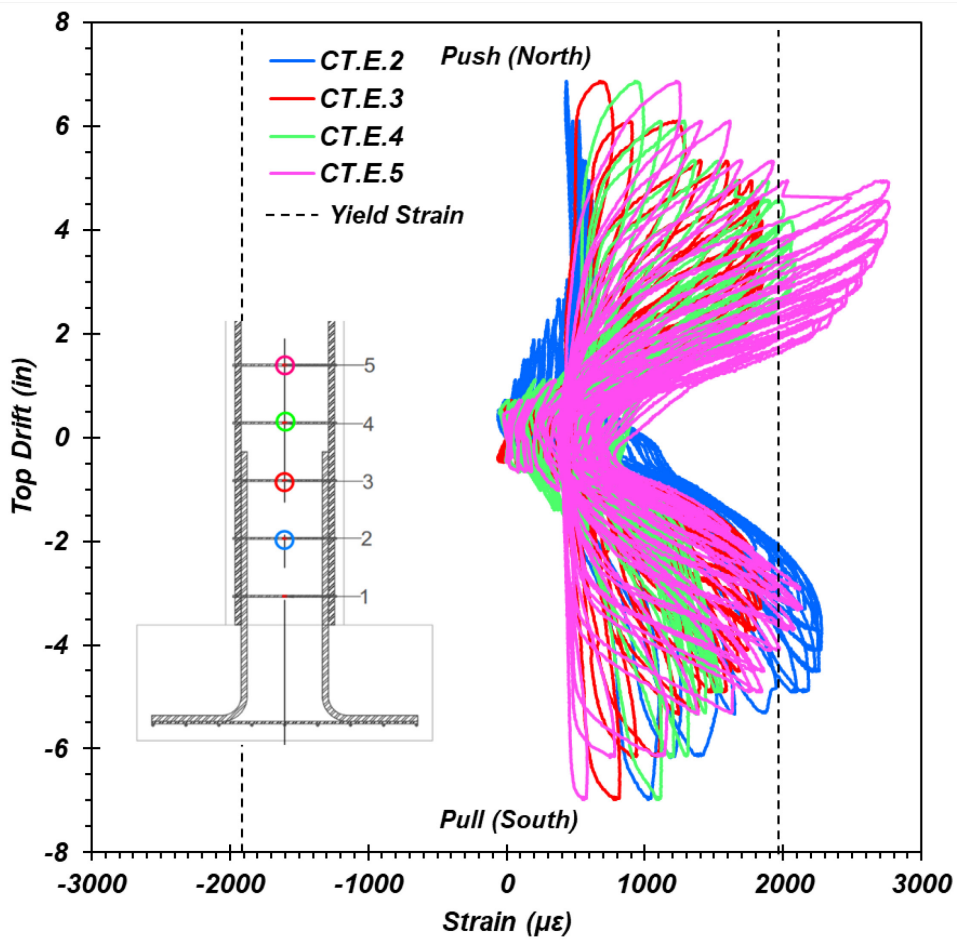

Figure A7.1.1.7: Column tie strain-drift histories, Test 9 – S1.

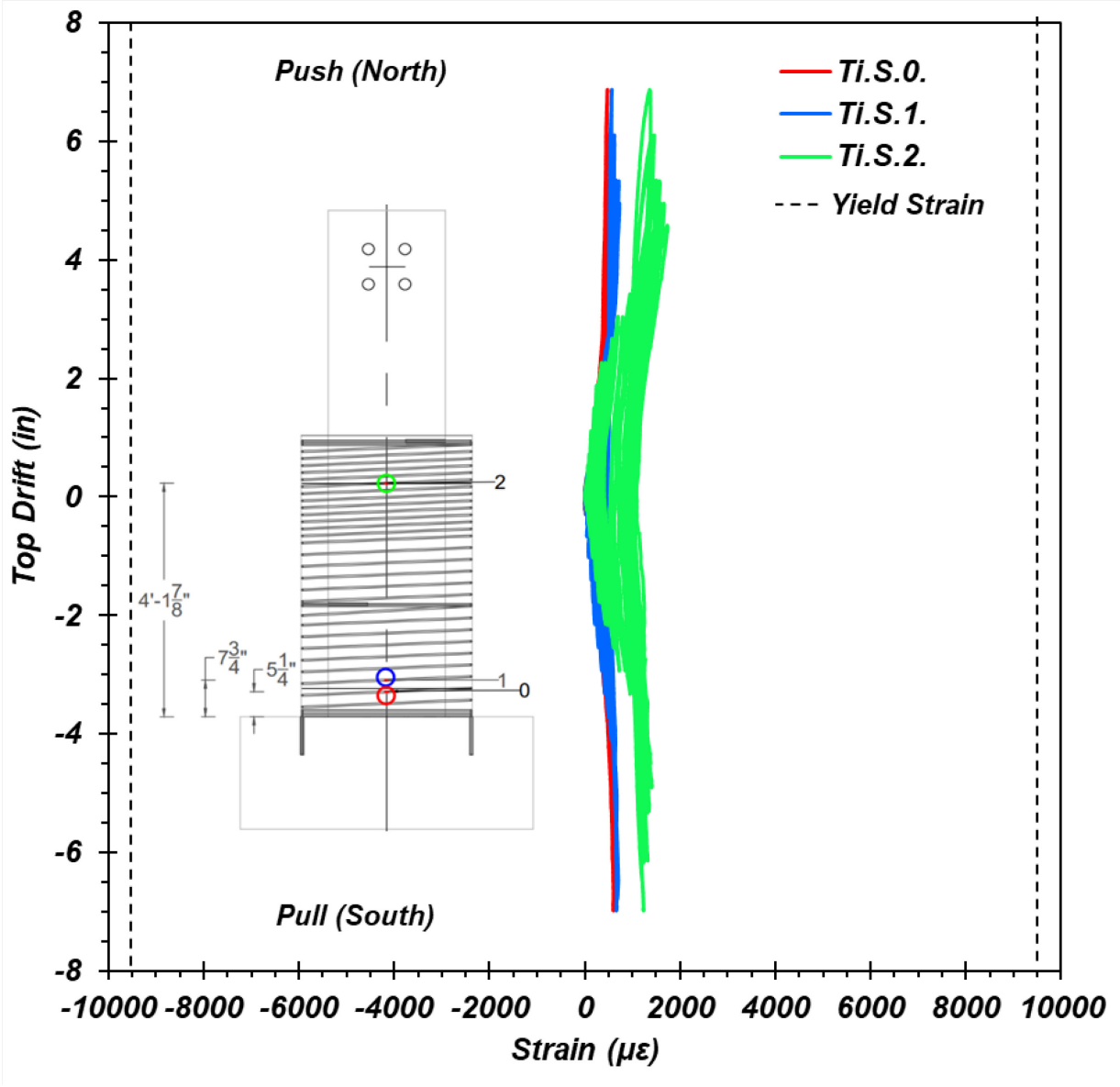

Figure A7.1.1.8: TiAB spiral strain-drift histories, Test 9 – S1.

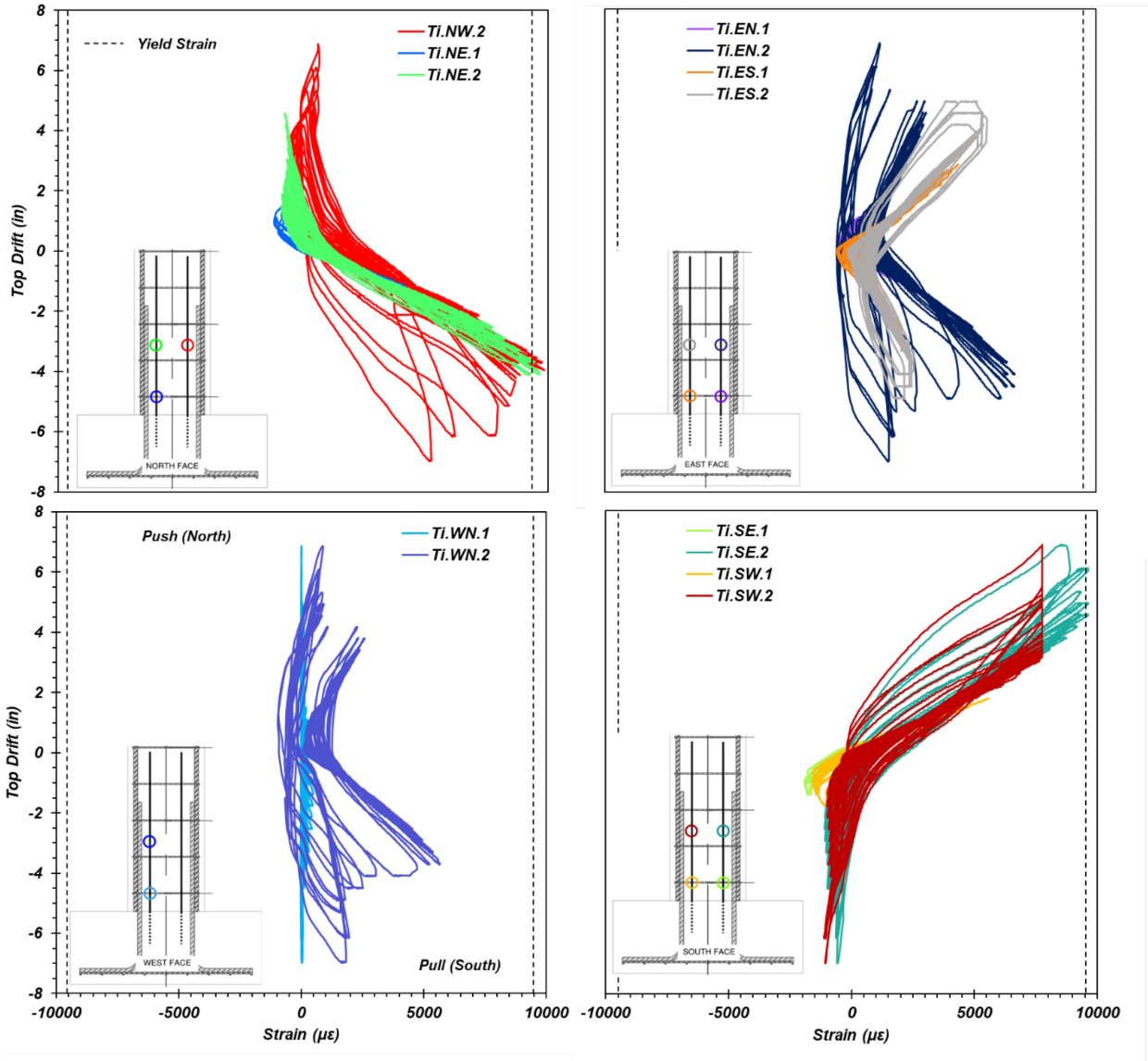

Figure A7.1.1.9: TiAB ligament strain-drift histories, Test 9 – S1.

A7.1.2 TEST 10 – S2: VINTAGE COLUMN WITH LIGAMENT AND SPIRAL RETROFIT, RESTRAINED FOOTING WITH ADDITIONAL RETROFIT

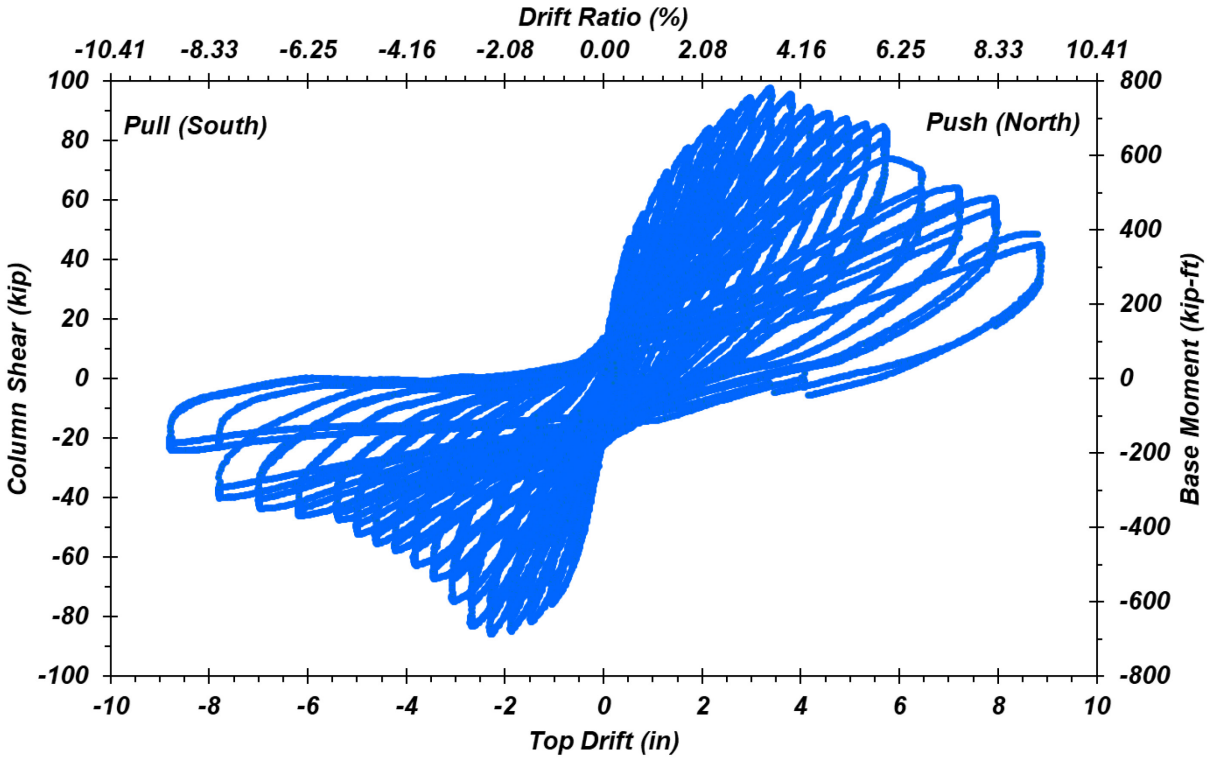

Figure A7.1.2.1: Overall force-displacement response, Test 10 – S3.

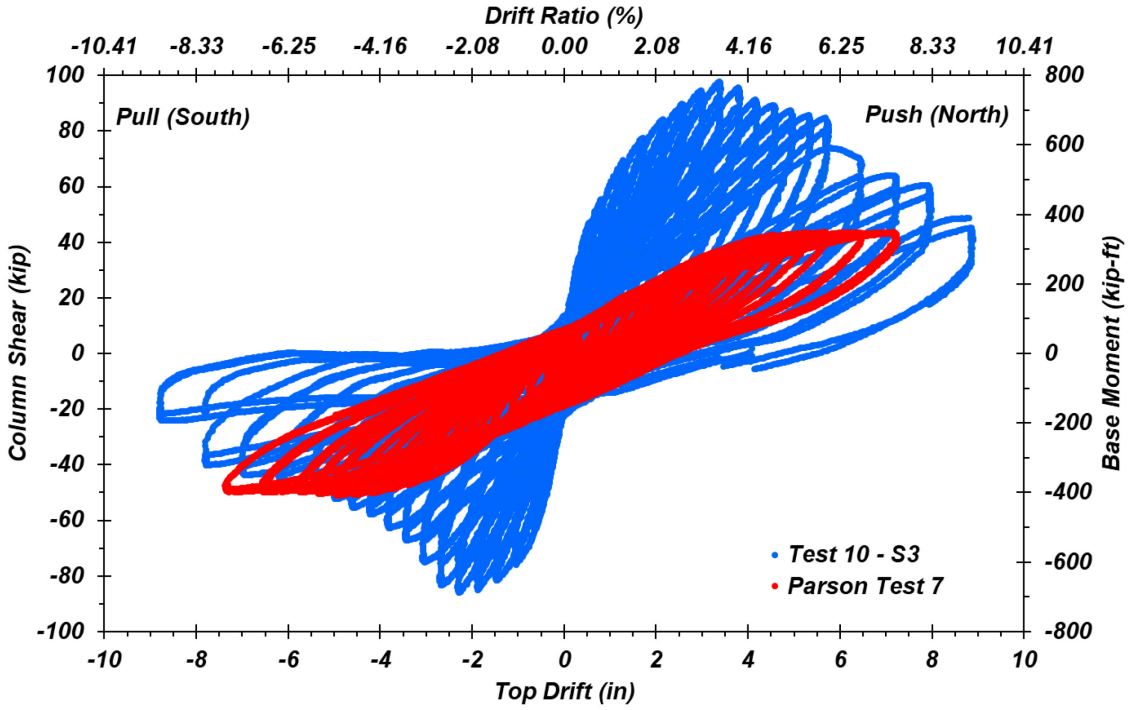

Figure A7.1.2.2: Overall force-displacement response comparisons: Test 7 – S3 (Appendix A6.3.7) and Test 10 – S3.

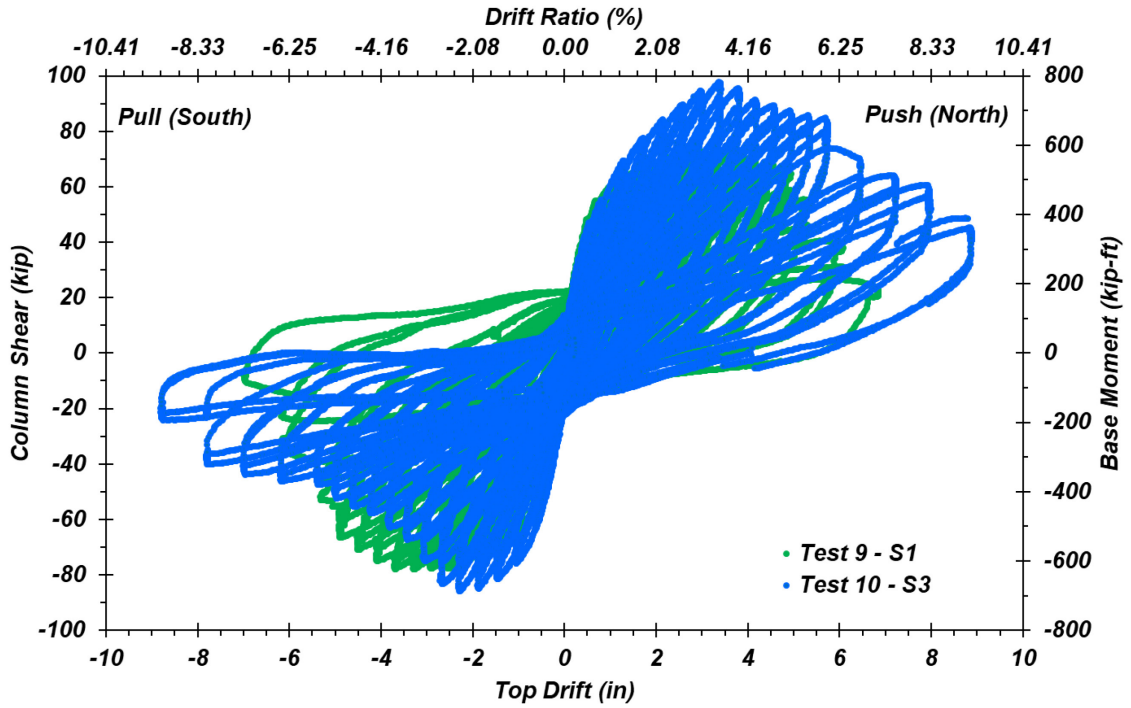

Figure A7.1.2.3: Overall force-displacement response comparisons: Test 9 – S1 and Test 10 – S3.

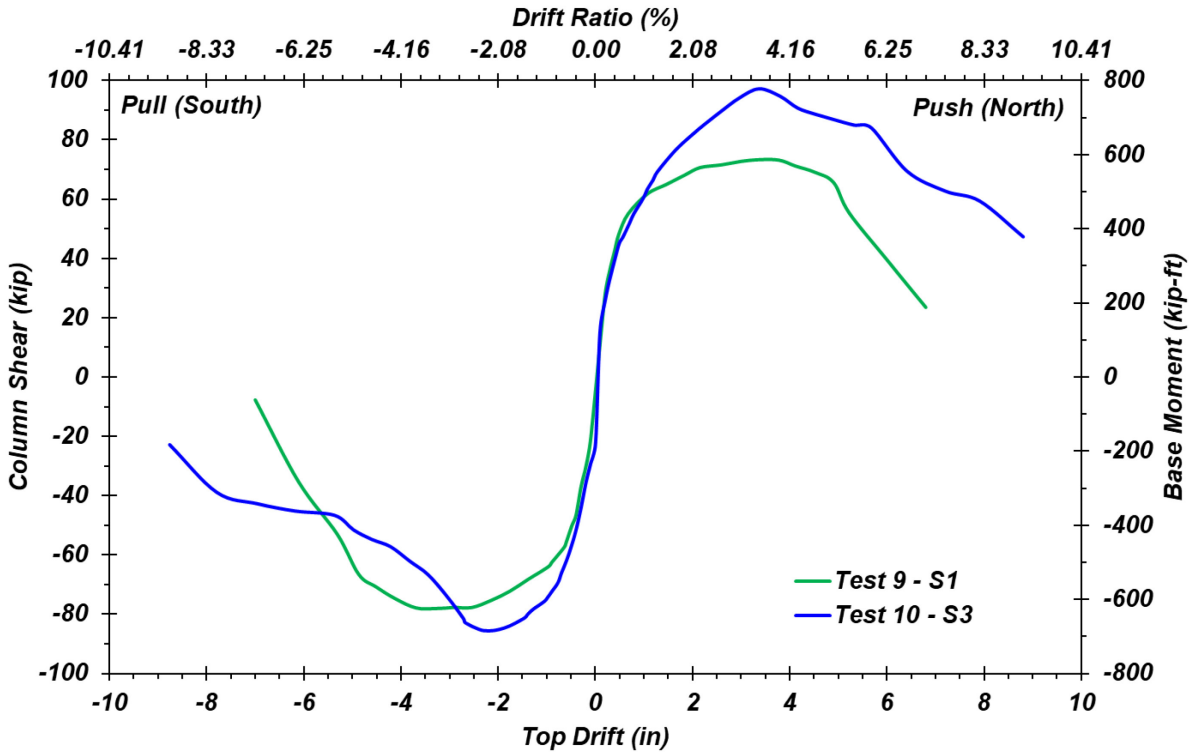

Figure A7.1.2.4: Backbone curve comparisons: Test 9 – S1 and Test 10 – S3.

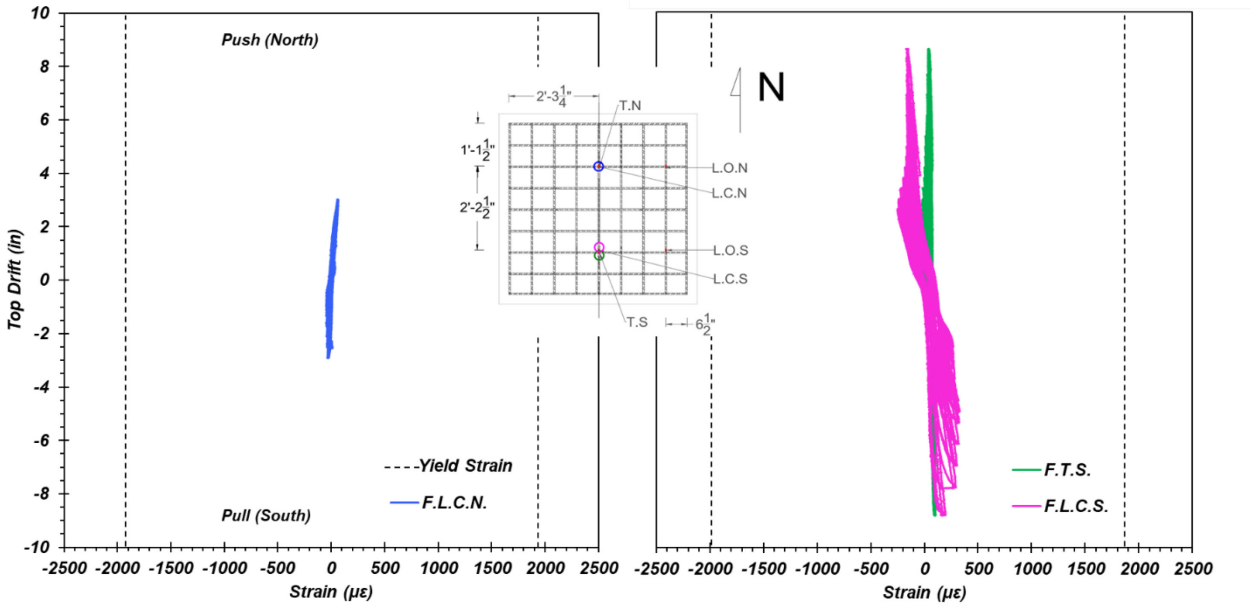

Figure A7.1.2.5: Footing bar strain-drift histories, Test 10 – S3.

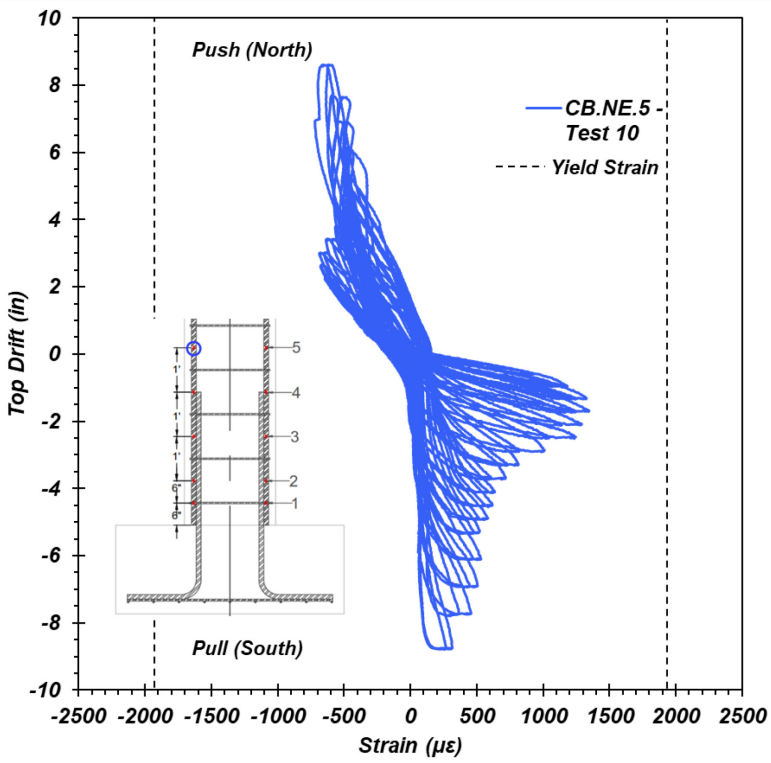

Figure A7.1.2.6: Column bar strain histories, Test 10 – S3.

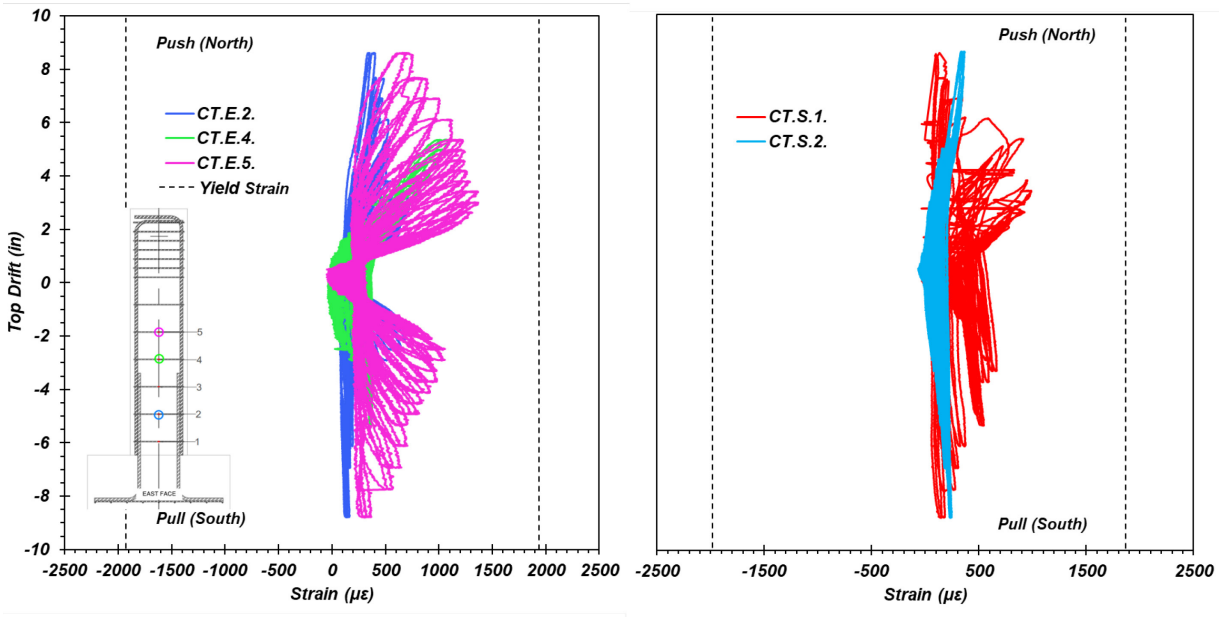

Figure A7.1.2.7: Column tie strain histories, Test 10 – S3.

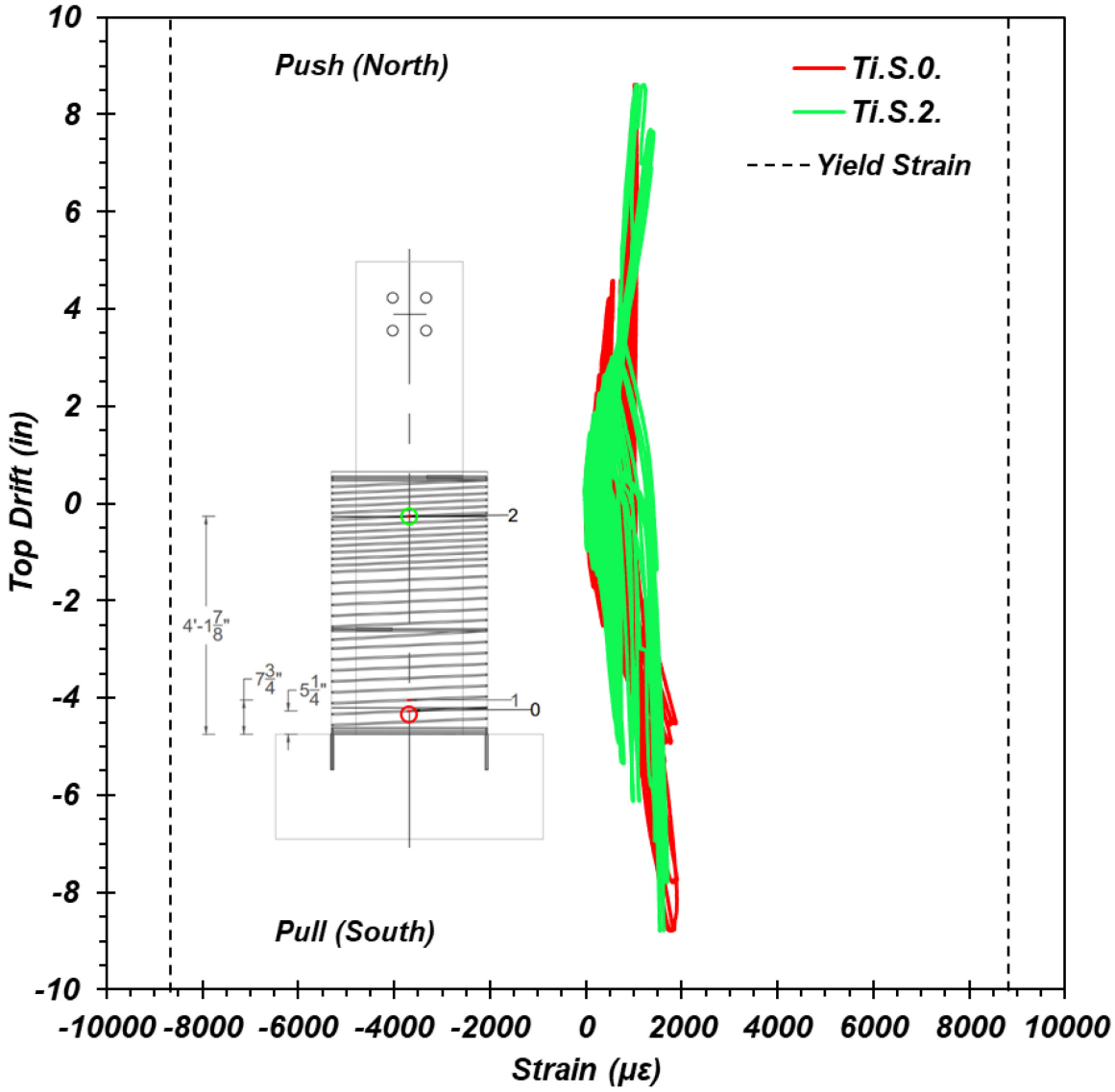

Figure A7.1.2.8: TiAB spiral strain histories, Test 10 – S3.

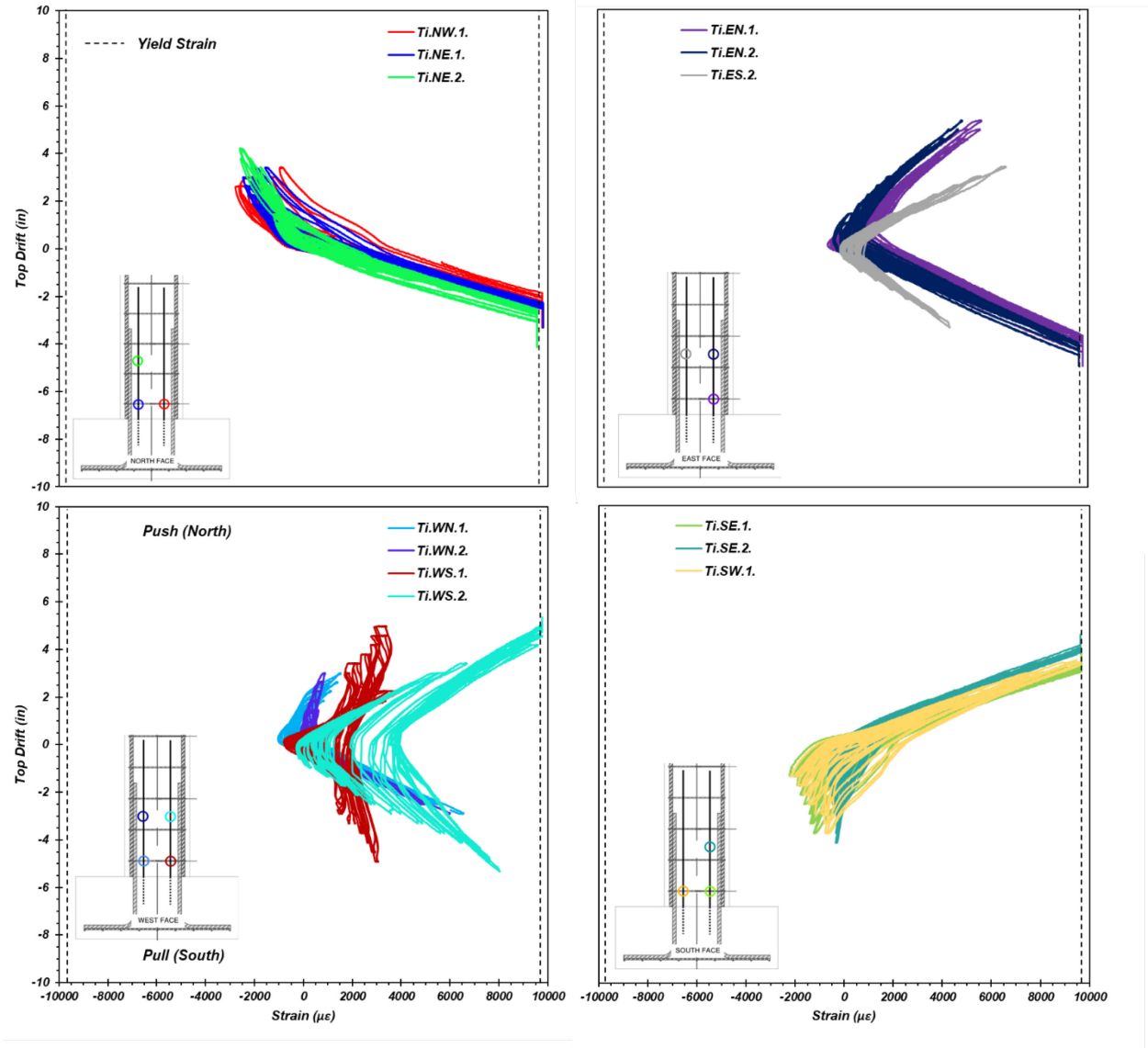

Figure A7.1.2.9: TiAB ligament strain histories, Test 10 – S3.

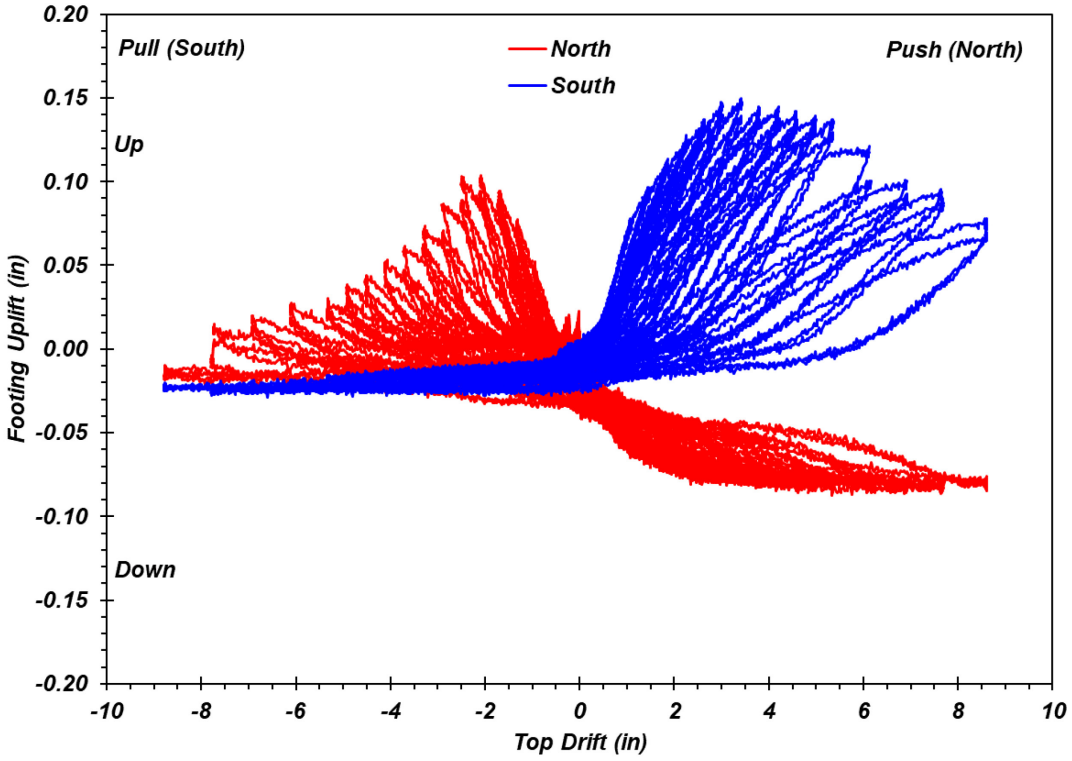

Figure A7.1.2.10: Vertical displacement of footing, Test 10 – S3.

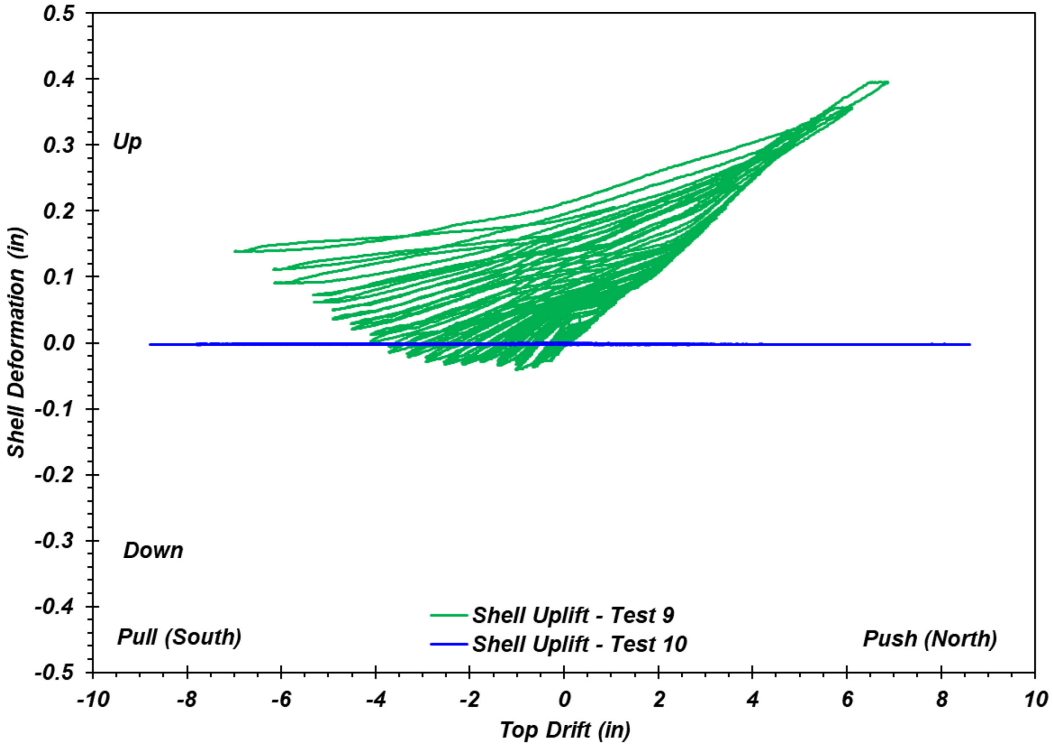

Figure A7.1.2.11: Shell uplift, Test 9 – S1 and Test 10 – S3.

A7.1.3 NOVEMBER 29TH SNAP-BACK TEST (F = 19.9 KN OR 4.48 KIP)

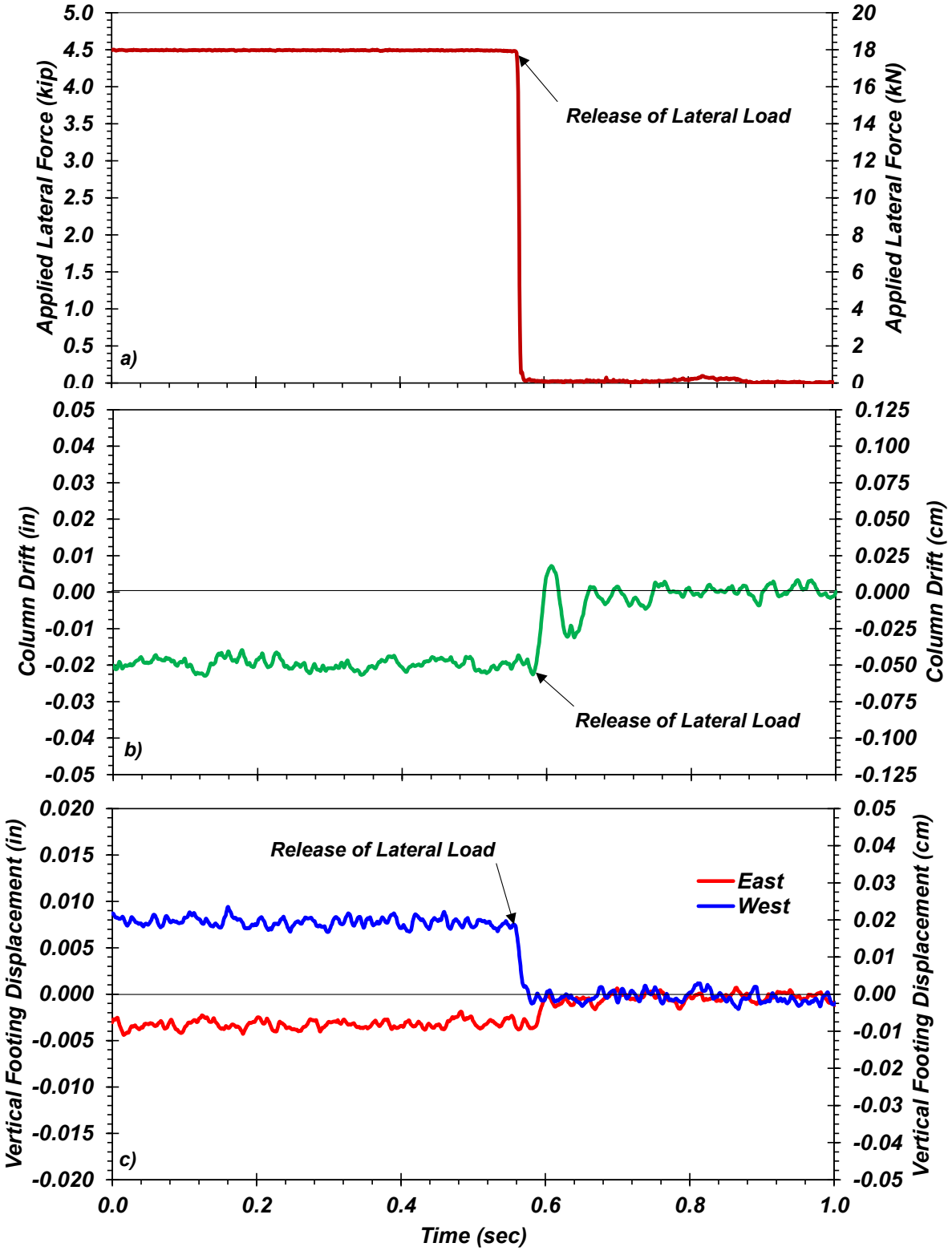

Figure A7.1.3.1: Overall rocking displacement.

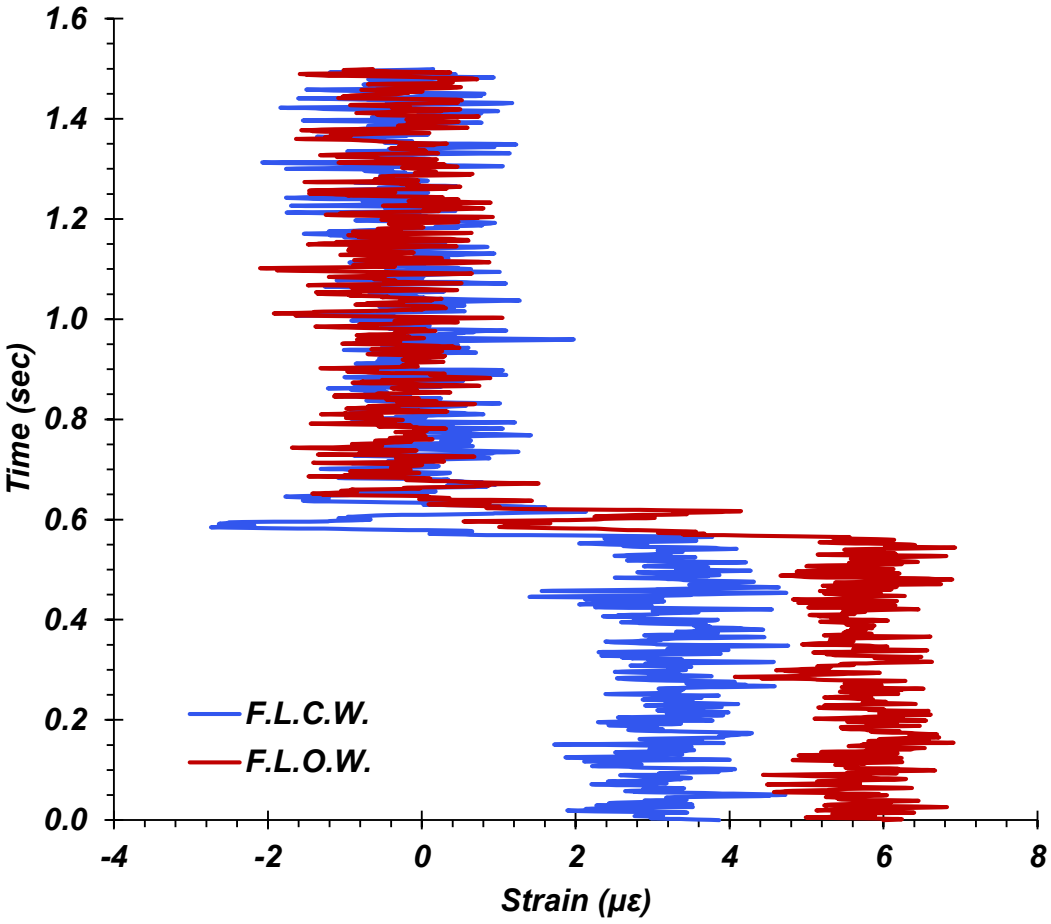

Figure A7.1.3.2: Footing bar strain histories.

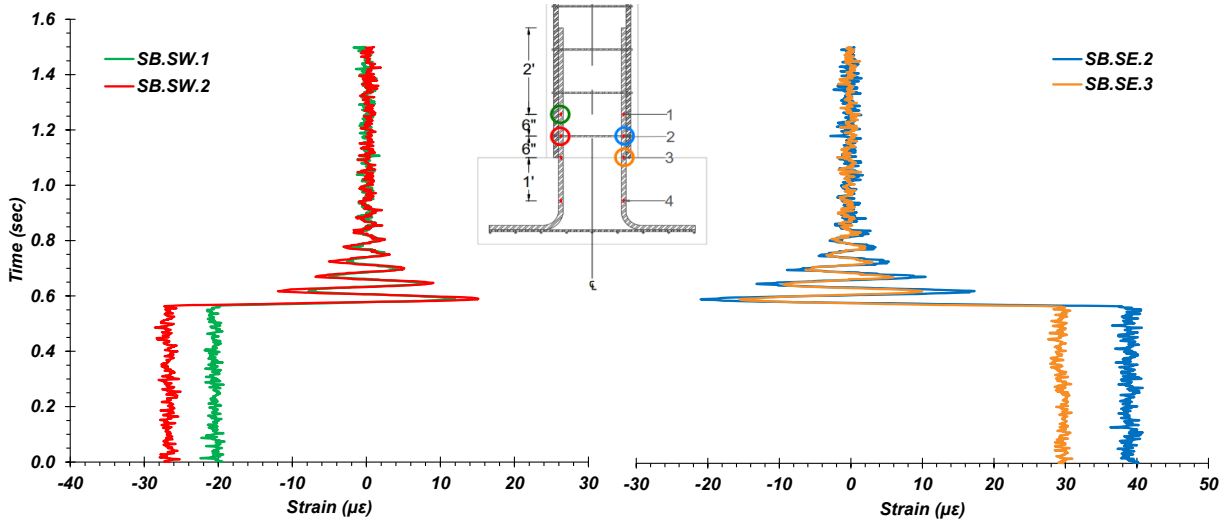

Figure A7.1.3.3: Starter bar strain histories.

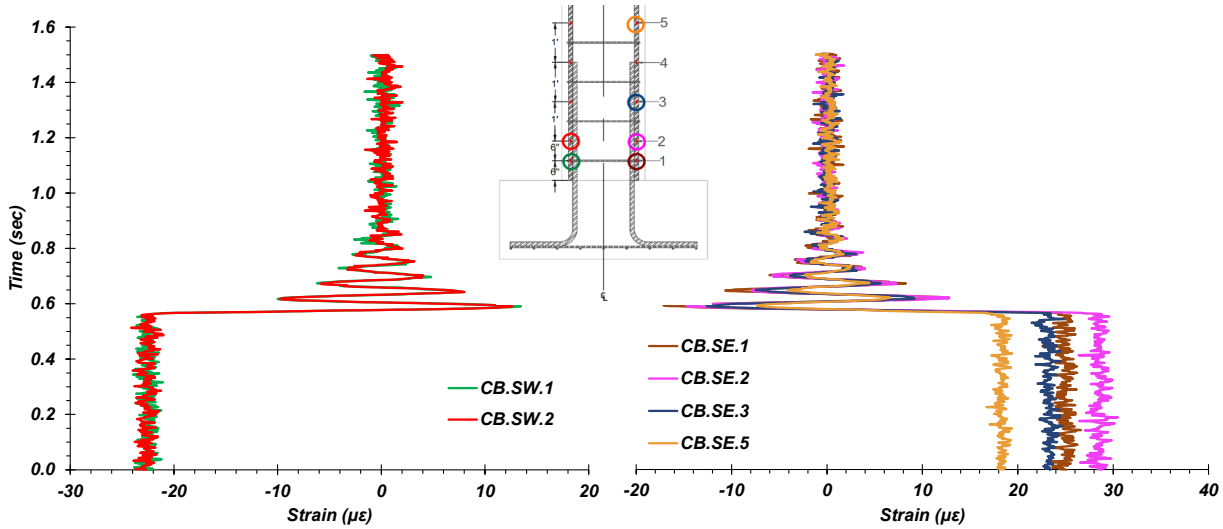

Figure A7.1.3.4: Column bar strain histories.

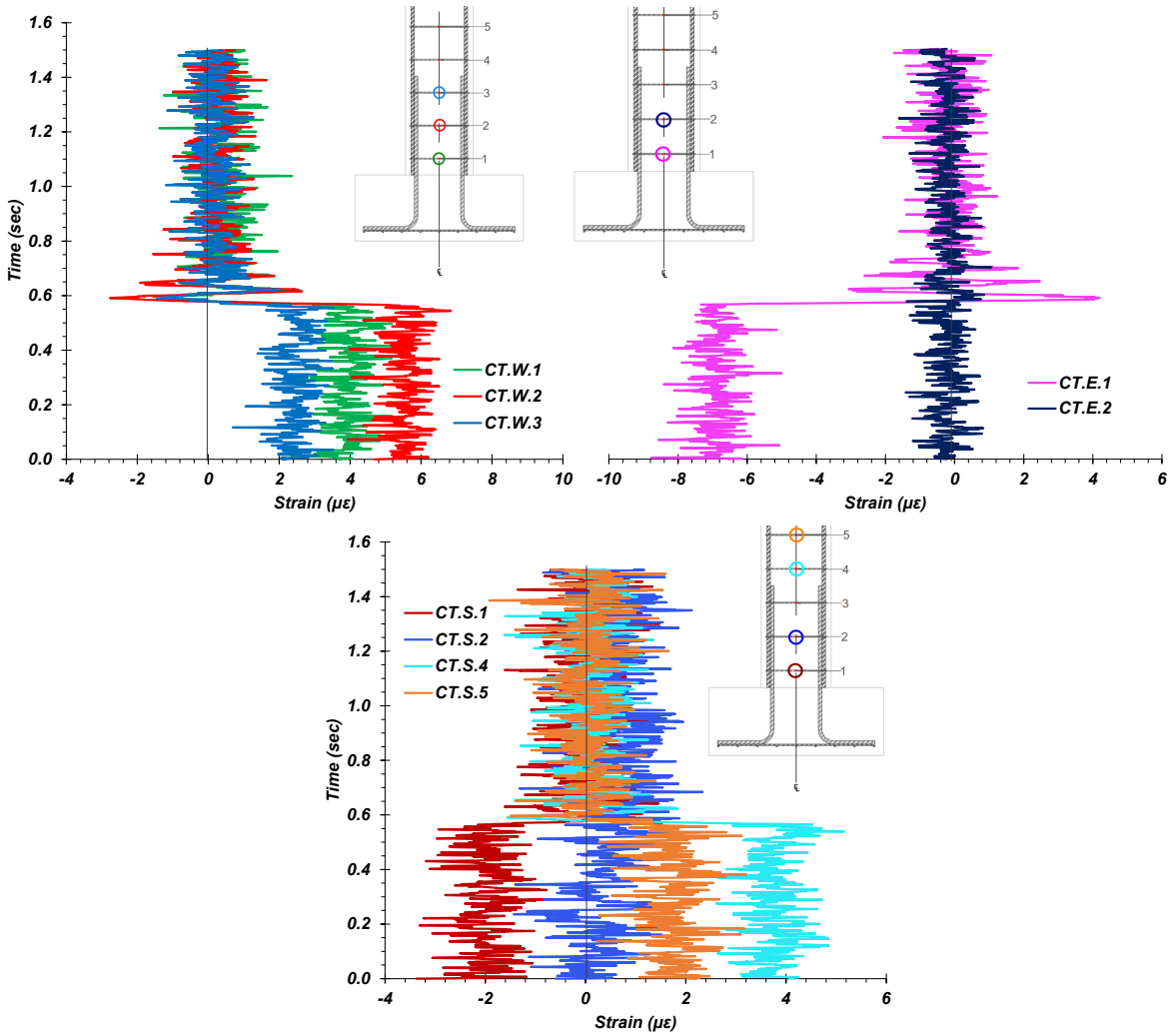

Figure A7.1.3.5: Column tie strain histories.

A7.1.4 DECEMBER 2ND SNAP-BACK TEST (F = 19.1 KN OR 4.34 KIP)

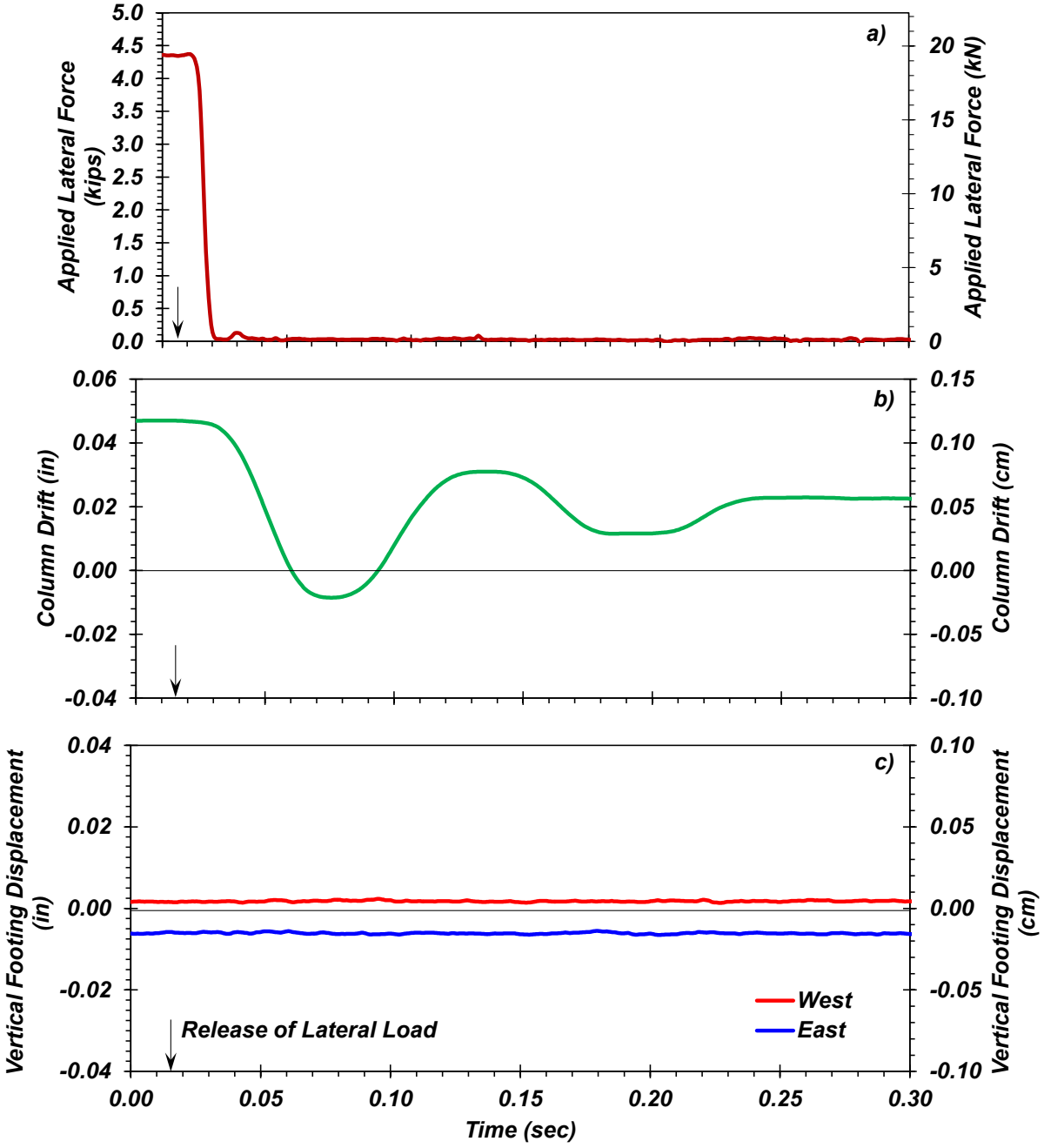

Figure A7.1.4.1: Overall rocking response.

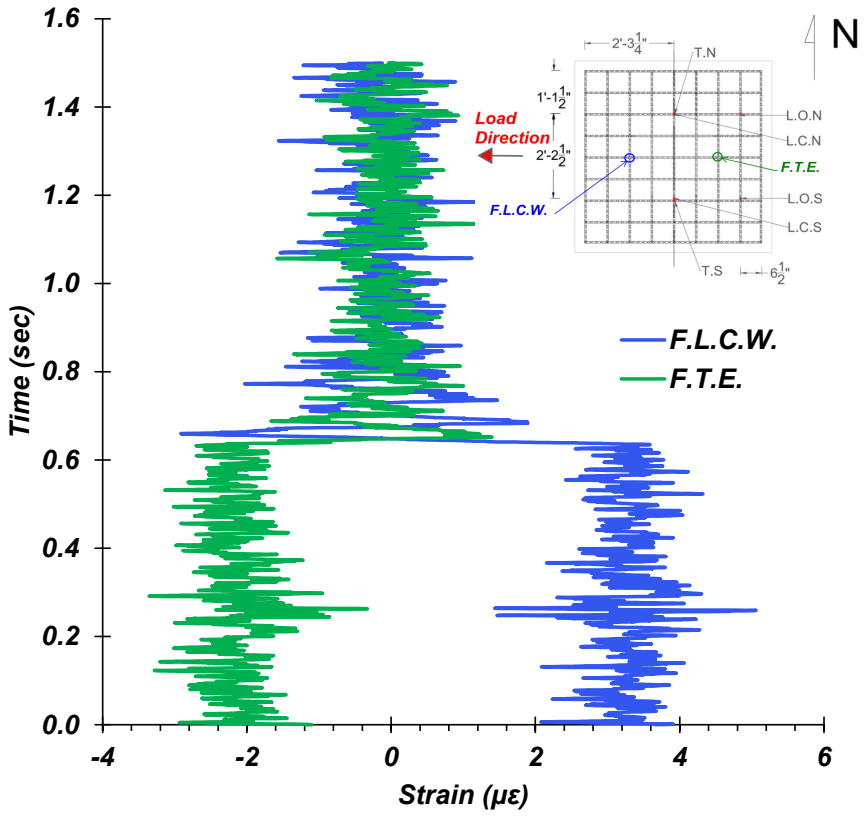

Figure A7.1.4.2: Footing bar strain histories.

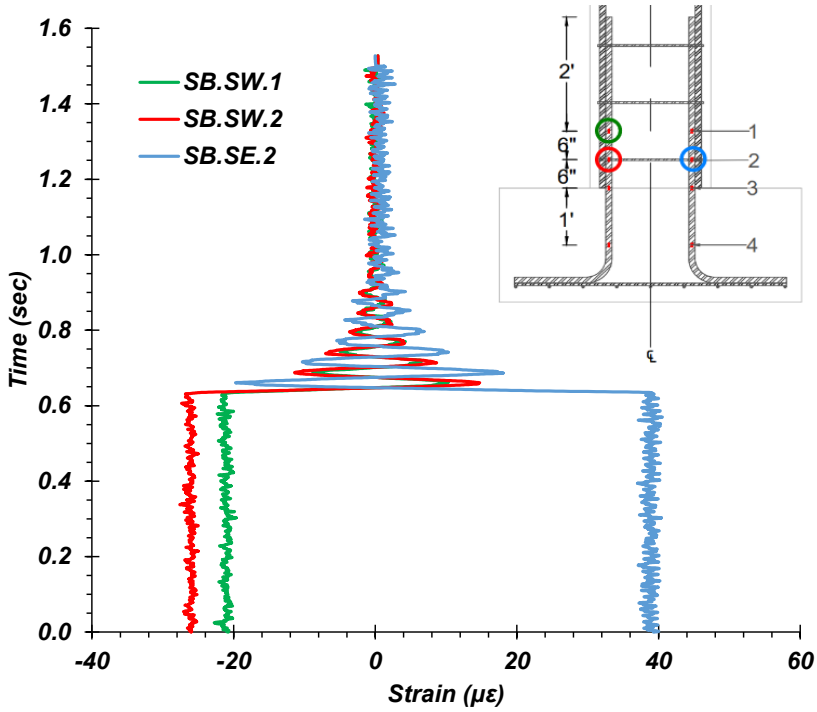

Figure A7.1.4.3: Starter bar strain histories.

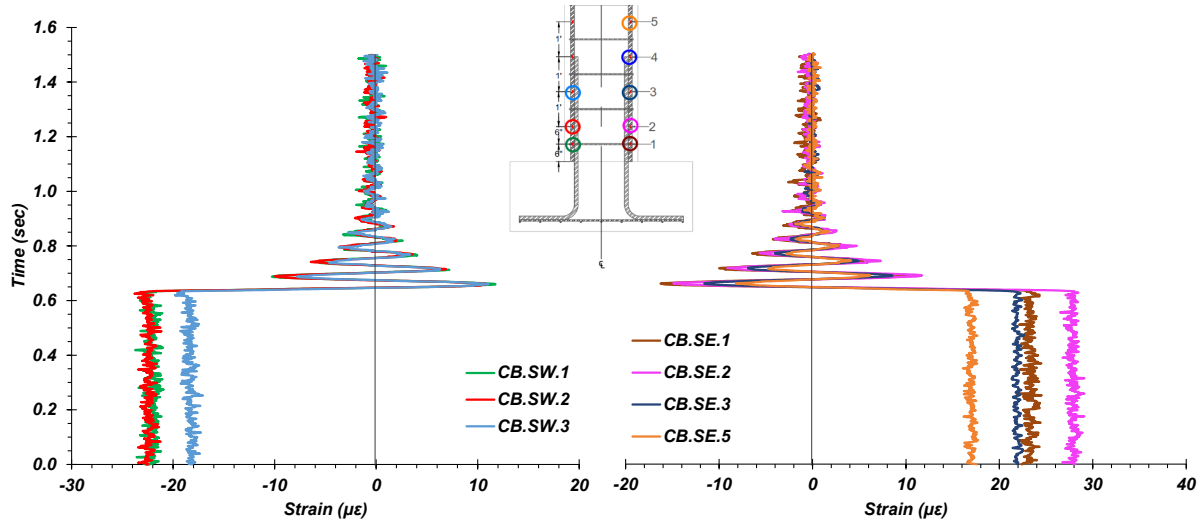

Figure A7.1.4.4: Column bar strain histories.

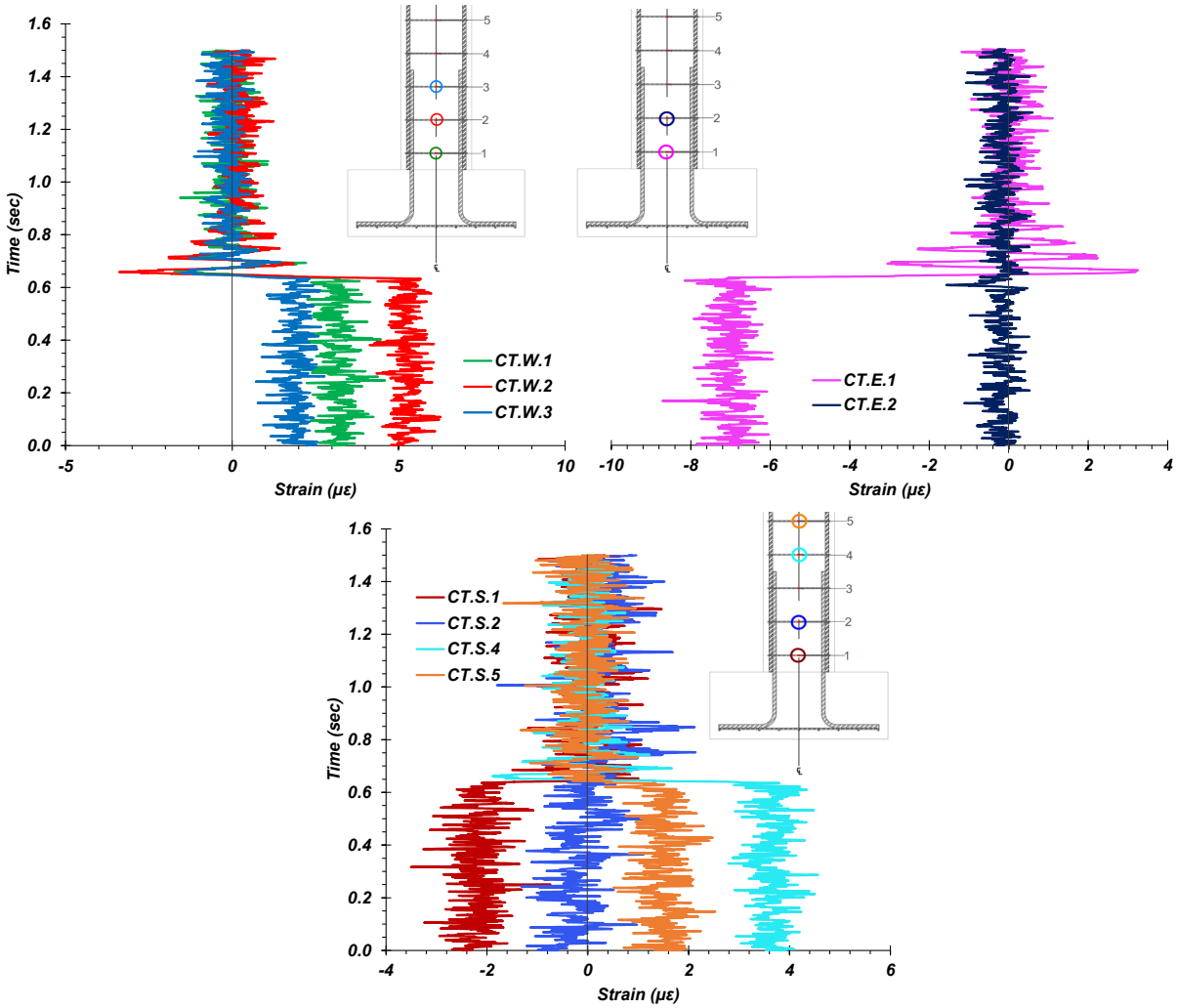

Figure A7.1.4.5: Column tie strain histories.

A7.1.5 DECEMBER 5TH SNAP-BACK TEST (F = 28.1 KN OR 6.32 KIP)

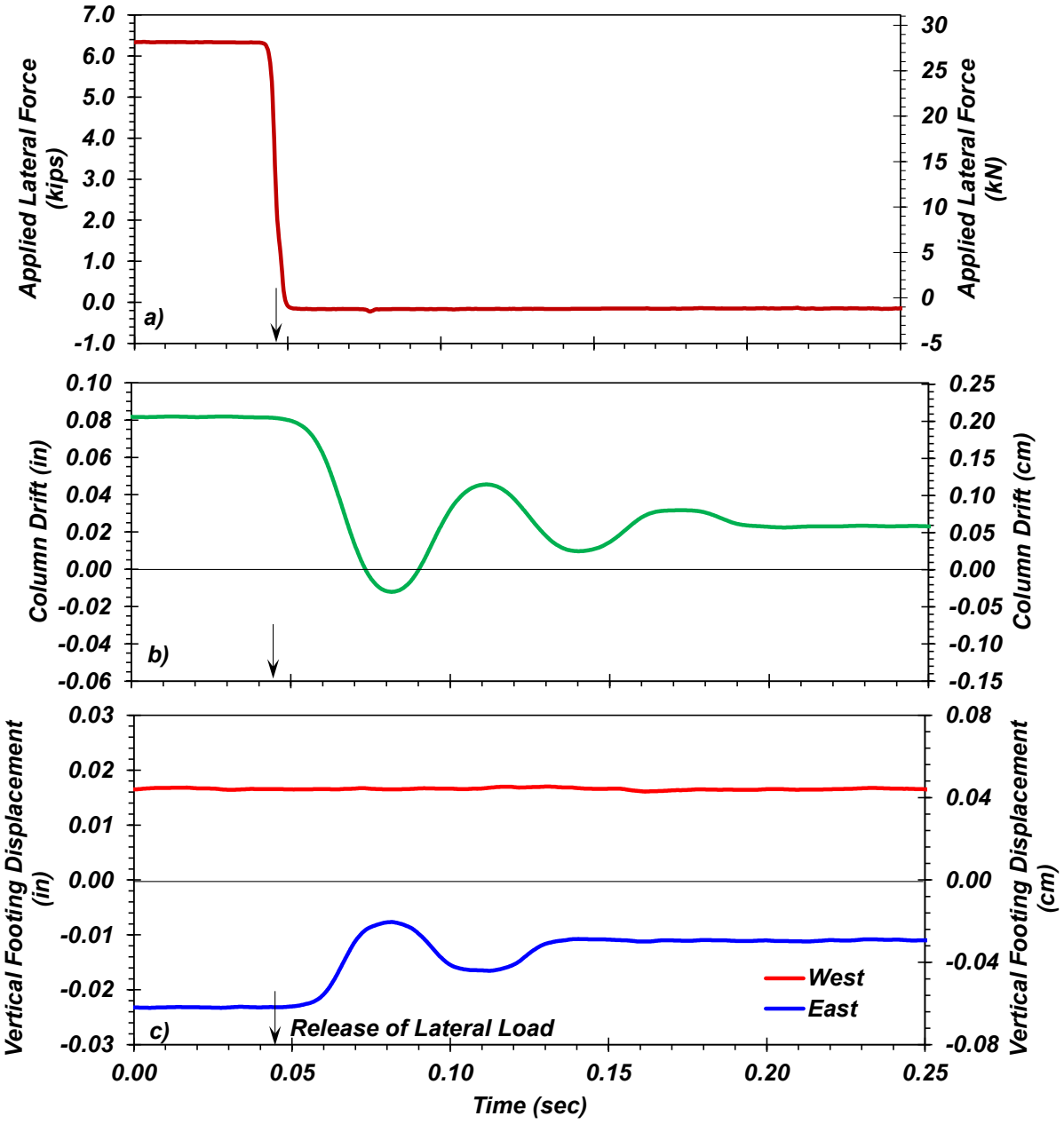

Figure A7.1.5.1: Overall rocking displacements.

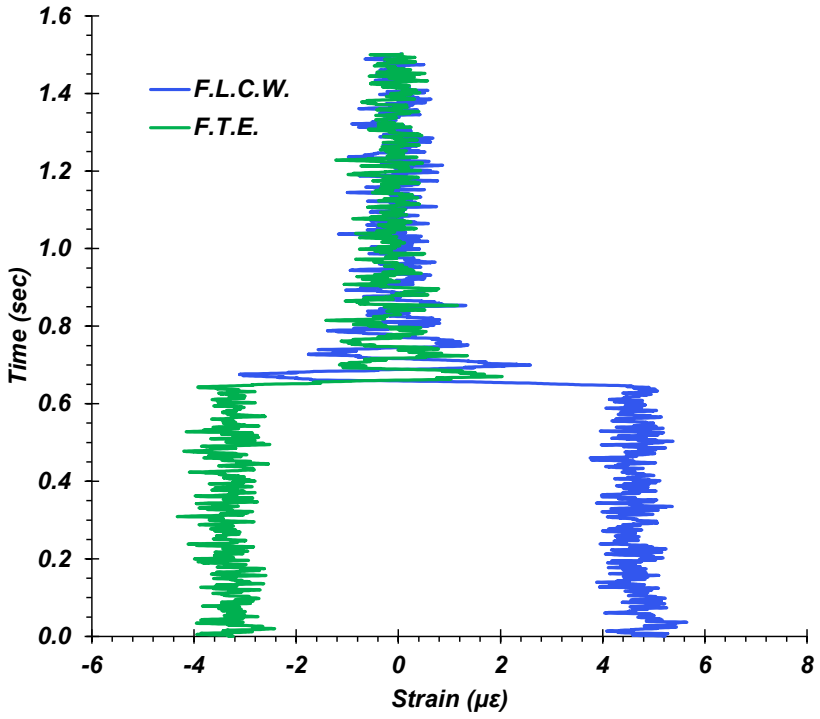

Figure A7.1.5.2: Footing bar strain histories.

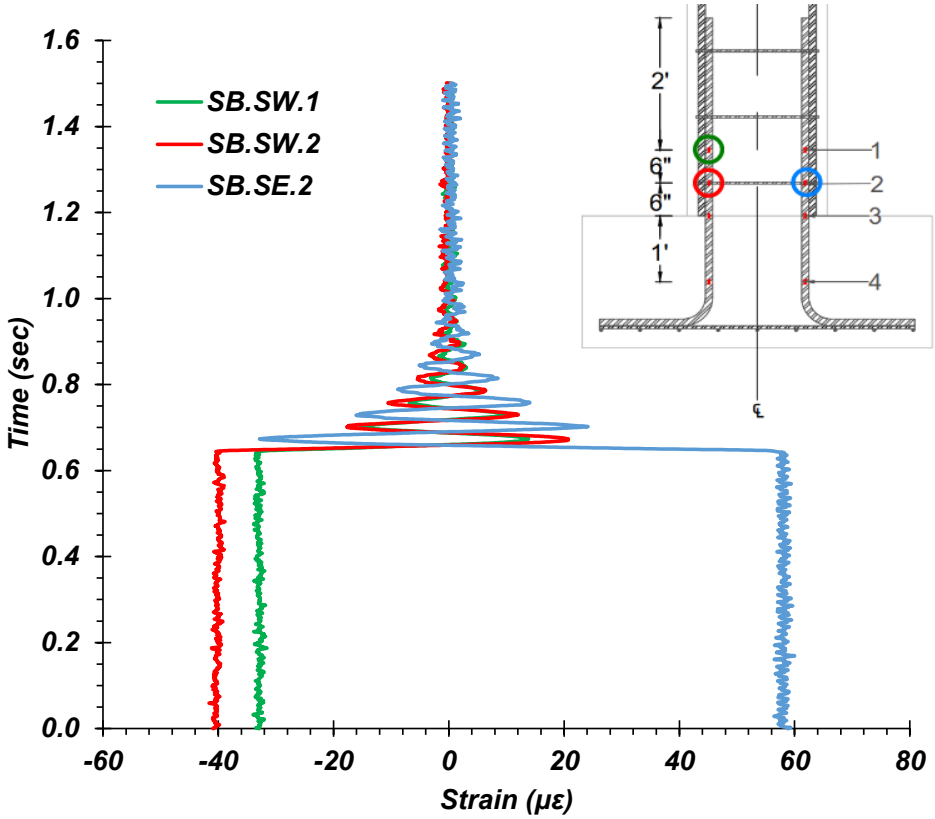

Figure A7.1.5.3: Starter bar strain histories.

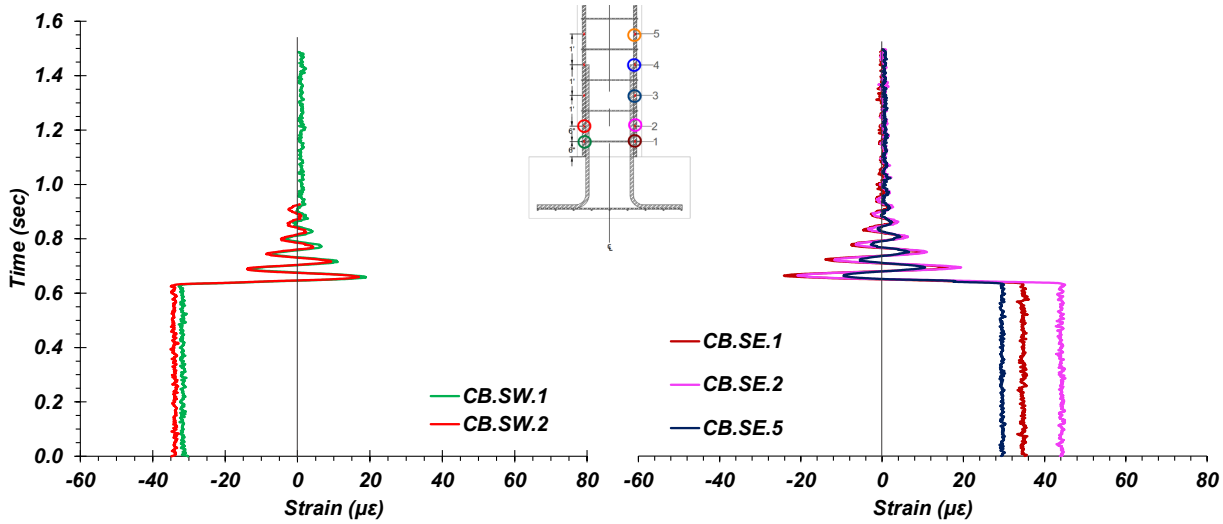

Figure A7.1.5.4: Column bar strain histories.

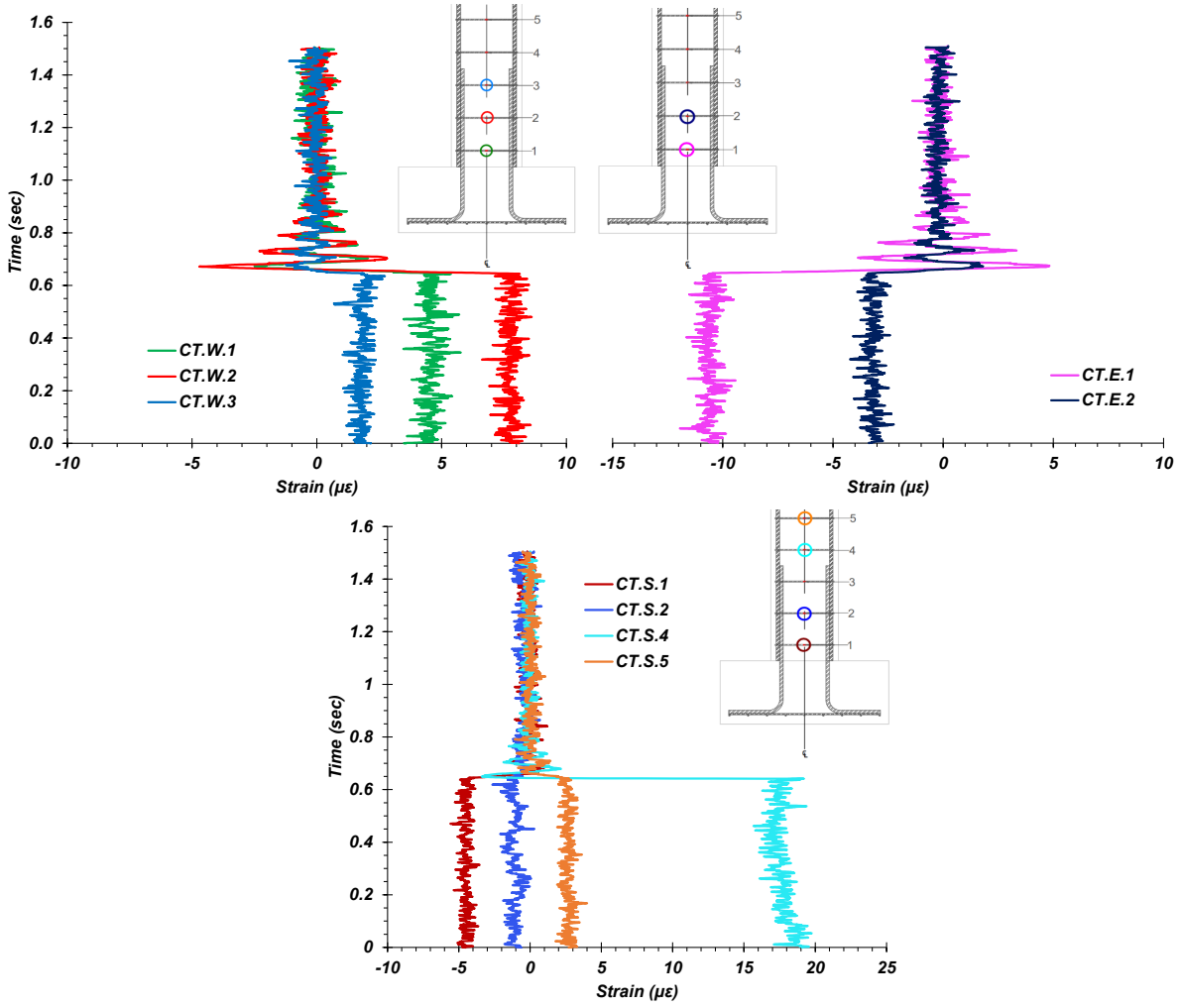

Figure A7.1.5.5: Column tie strain histories.

A7.1.6 MAY 22ND SNAP-BACK TEST (F = 28.9 KN OR 6.50 KIP)

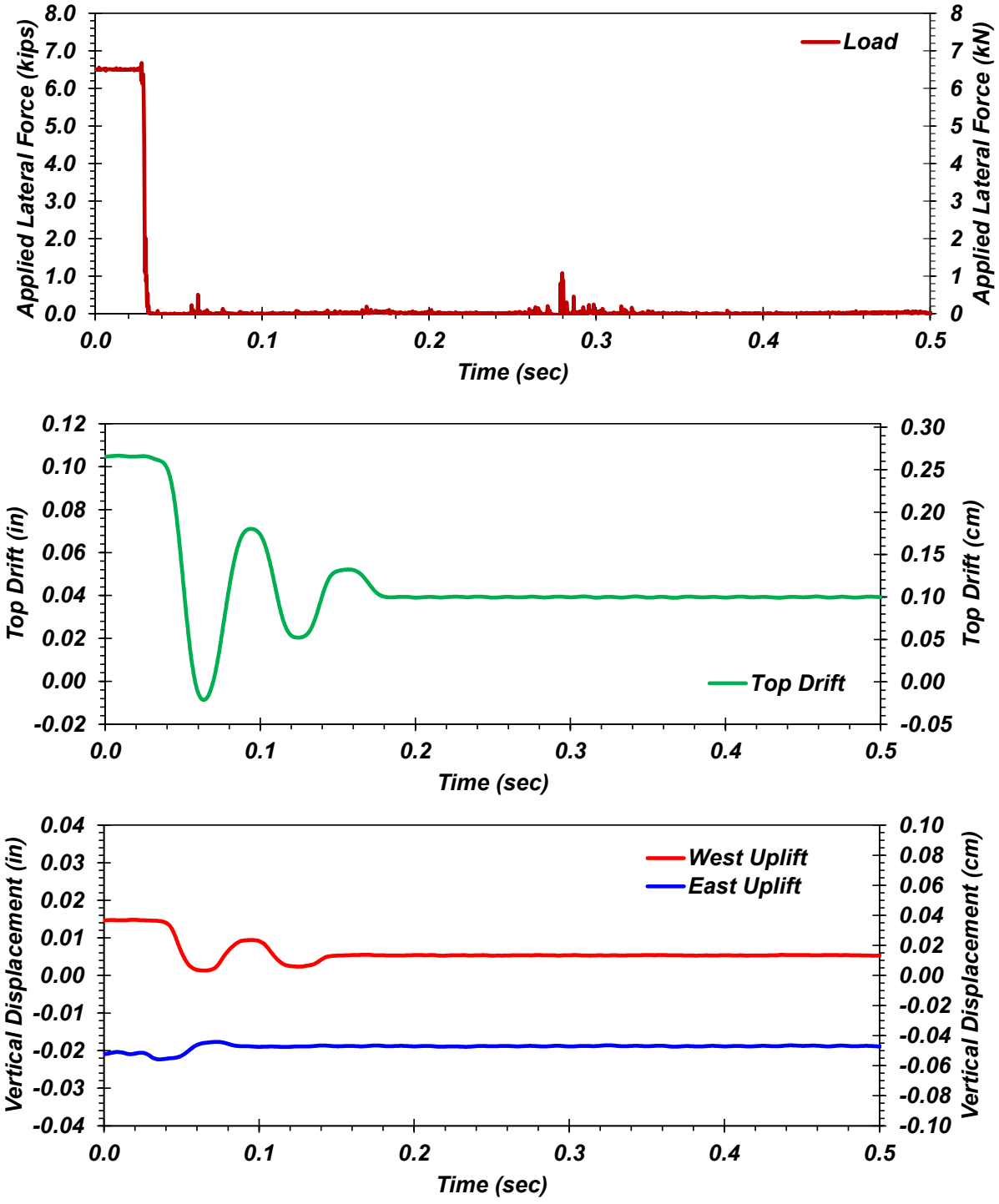

Figure A7.1.6.1: Overall rocking displacements.

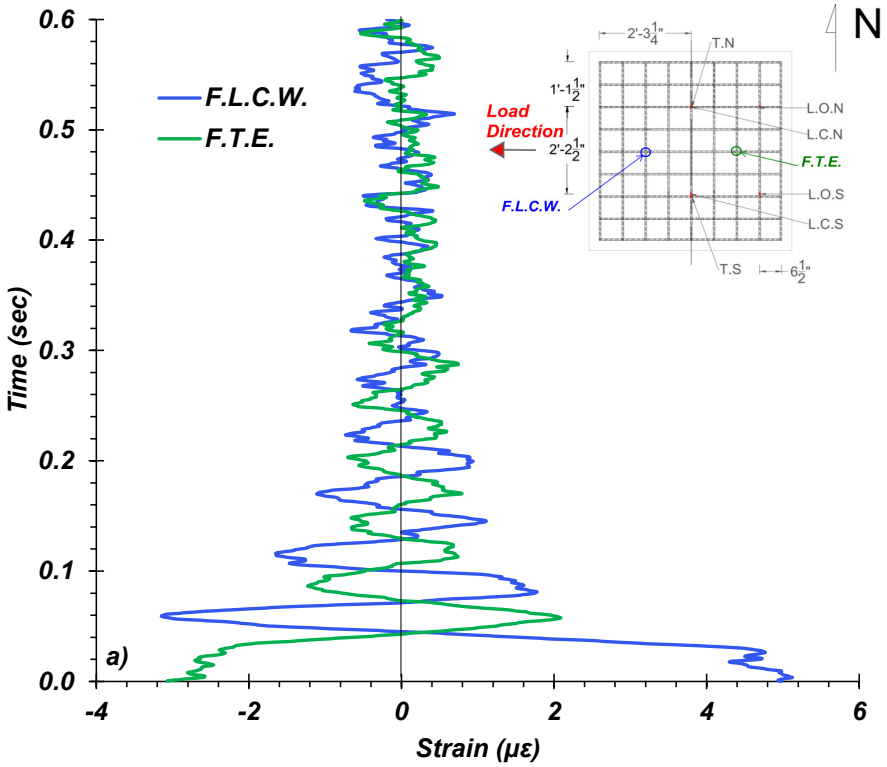

Figure A7.1.6.2: Footing bar strain histories.

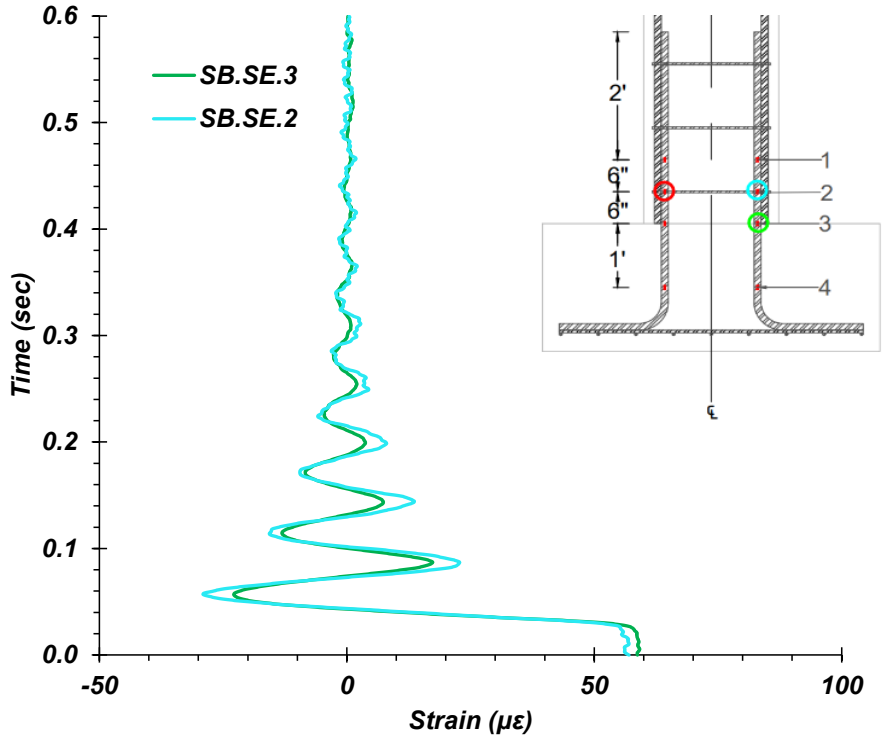

Figure A7.1.6.3: Starter bar strain histories.

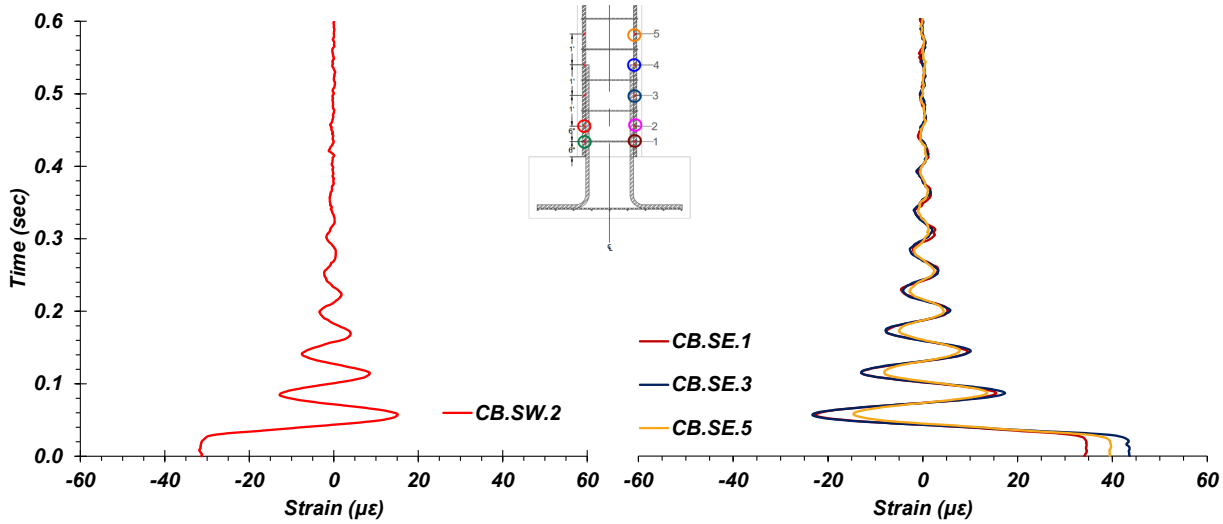

Figure A7.1.6.4: Column bar strain histories.

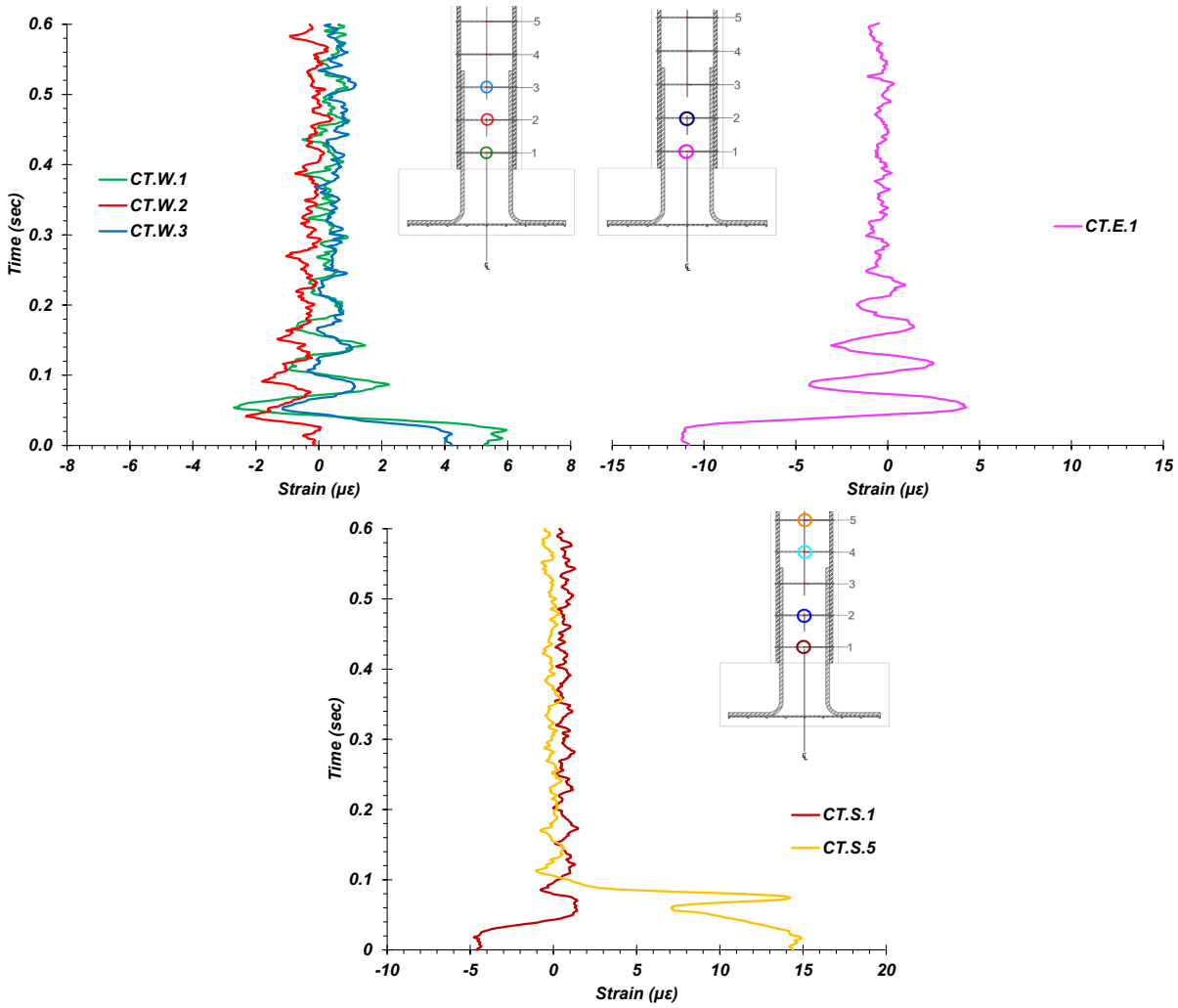

Figure A7.1.6.5: Column tie strain histories.

A7.1.7 MAY 22ND SNAP-BACK TEST (F = 38.6 KN OR 8.67 KIP)

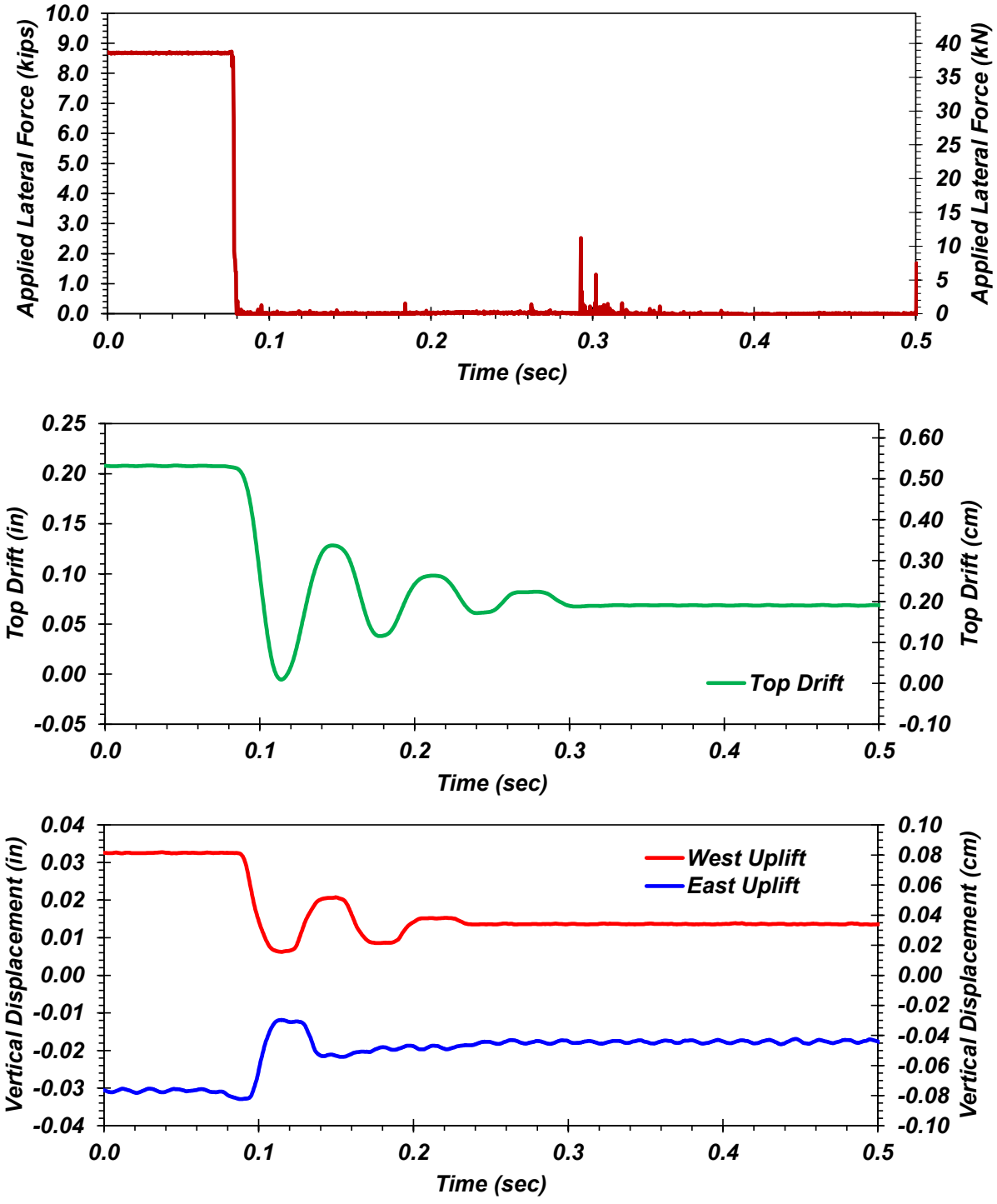

Figure A7.1.7.1: Overall rocking displacements.

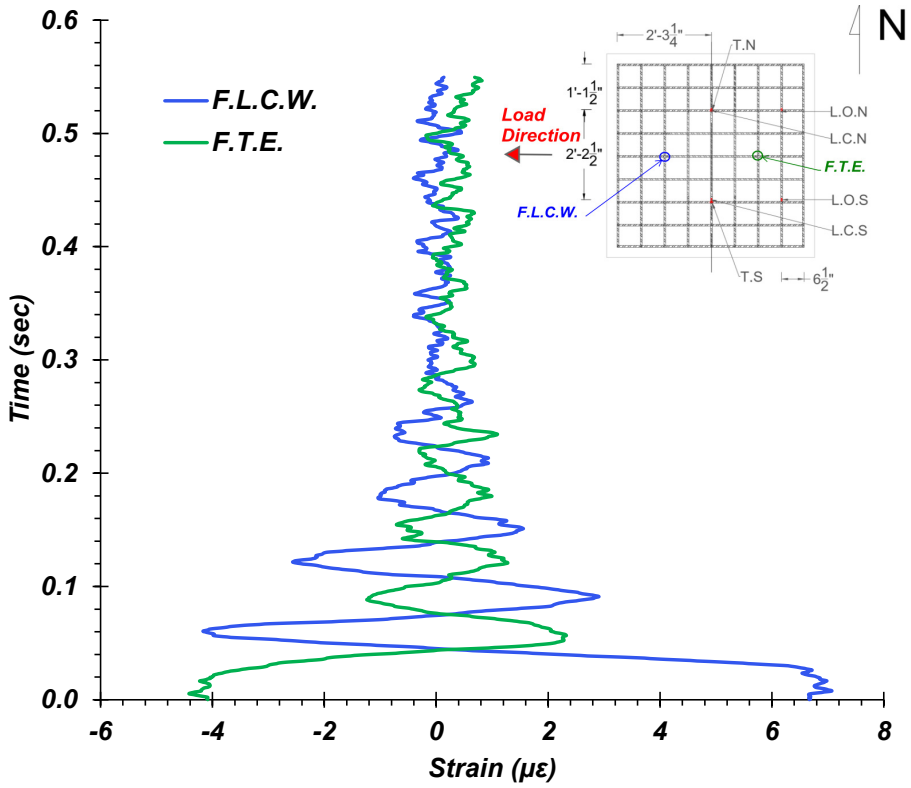

Figure A7.1.7.2: Footing bar strain histories.

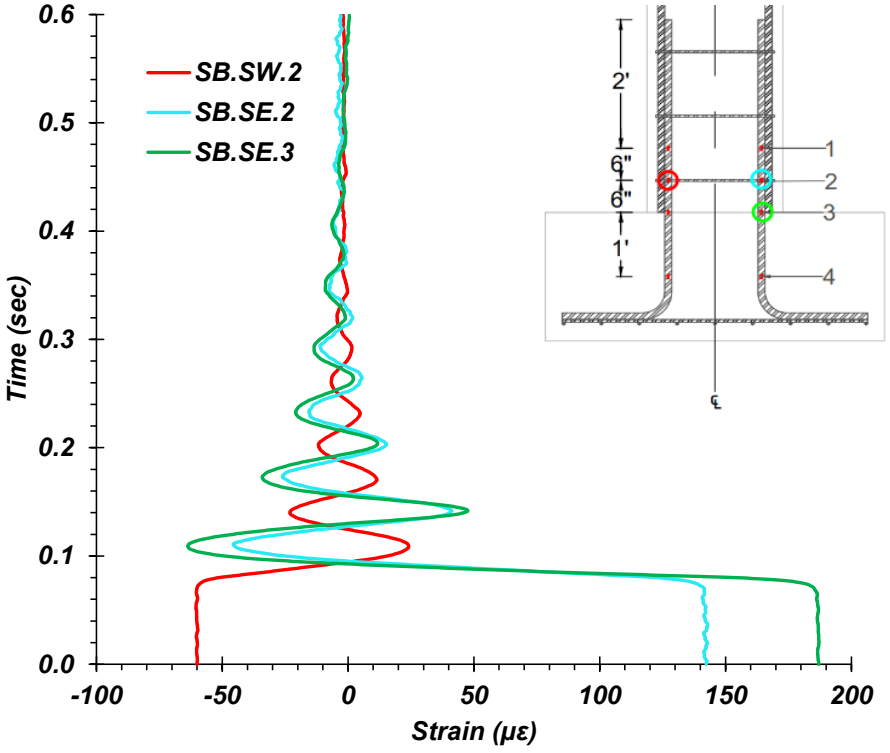

Figure A7.1.7.3: Starter bar strain histories.

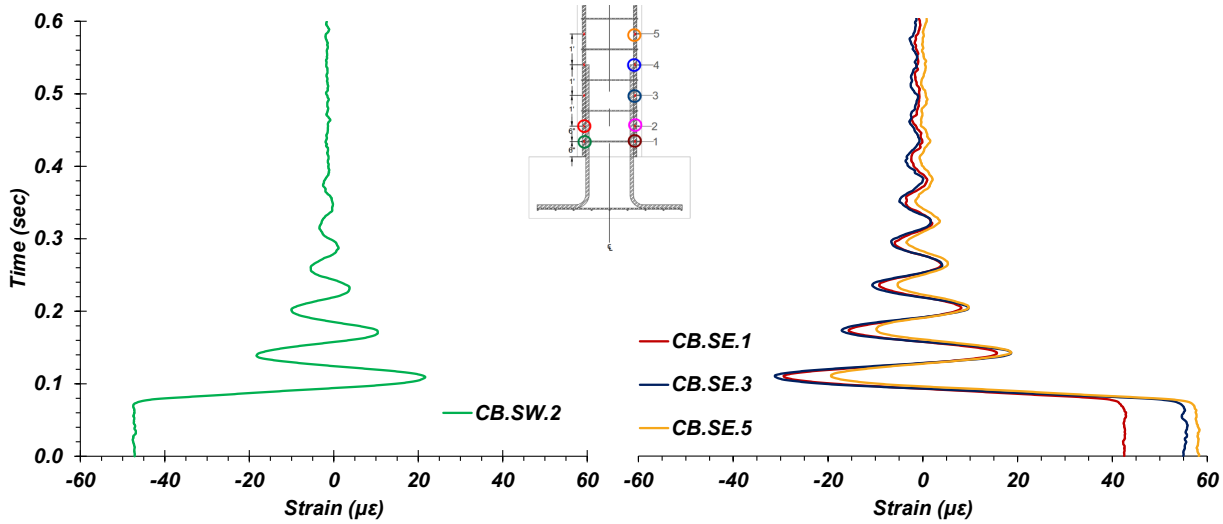

Figure A7.1.7.4: Column bar strain histories.

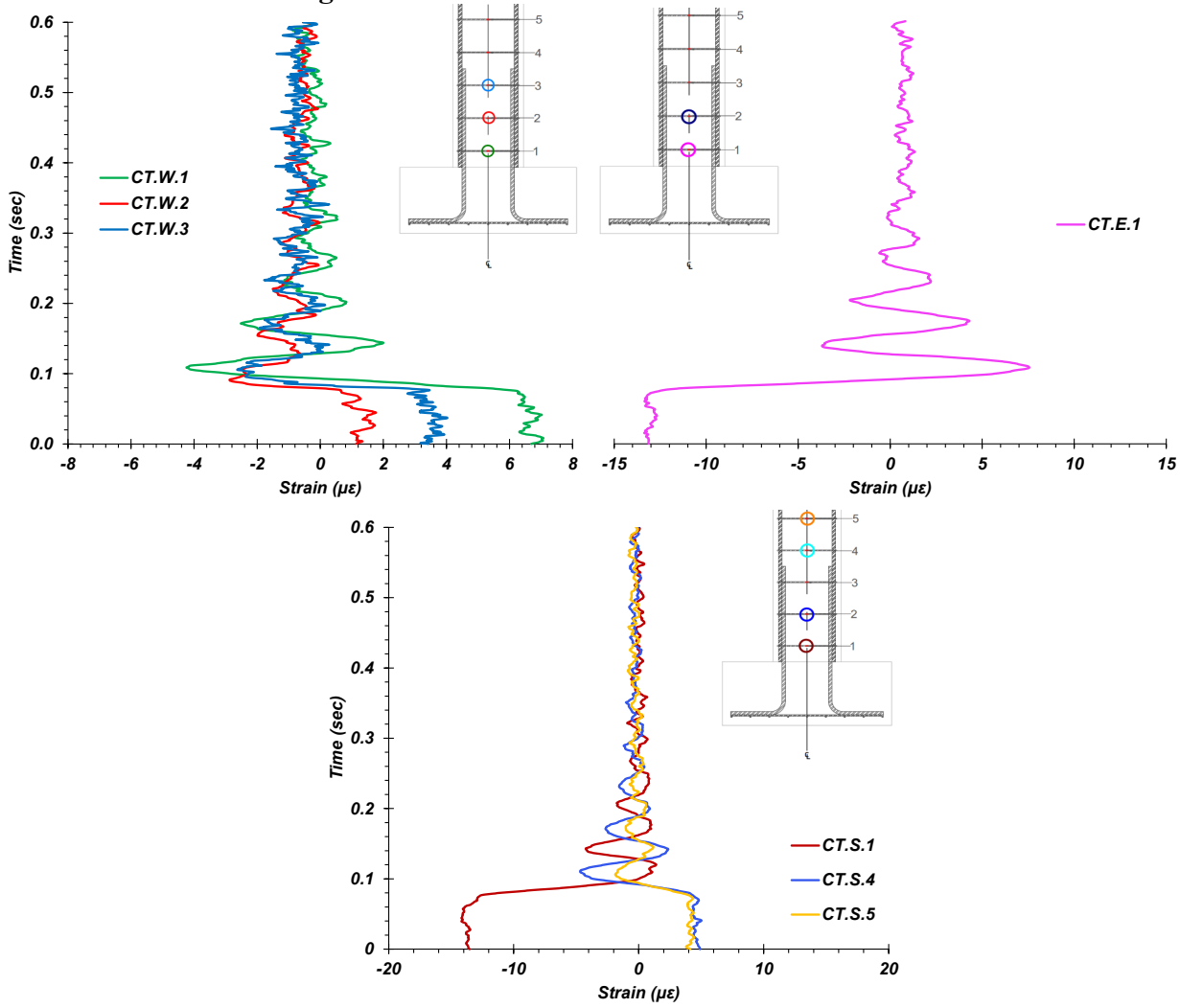

Figure A7.1.7.5: Column tie strain histories.

APPENDIX A7.2: STRAIN TIME HISTORIES IN SOIL SIMULANT BELOW THE FOOTING OF TEST 2 – SPECIMEN 2

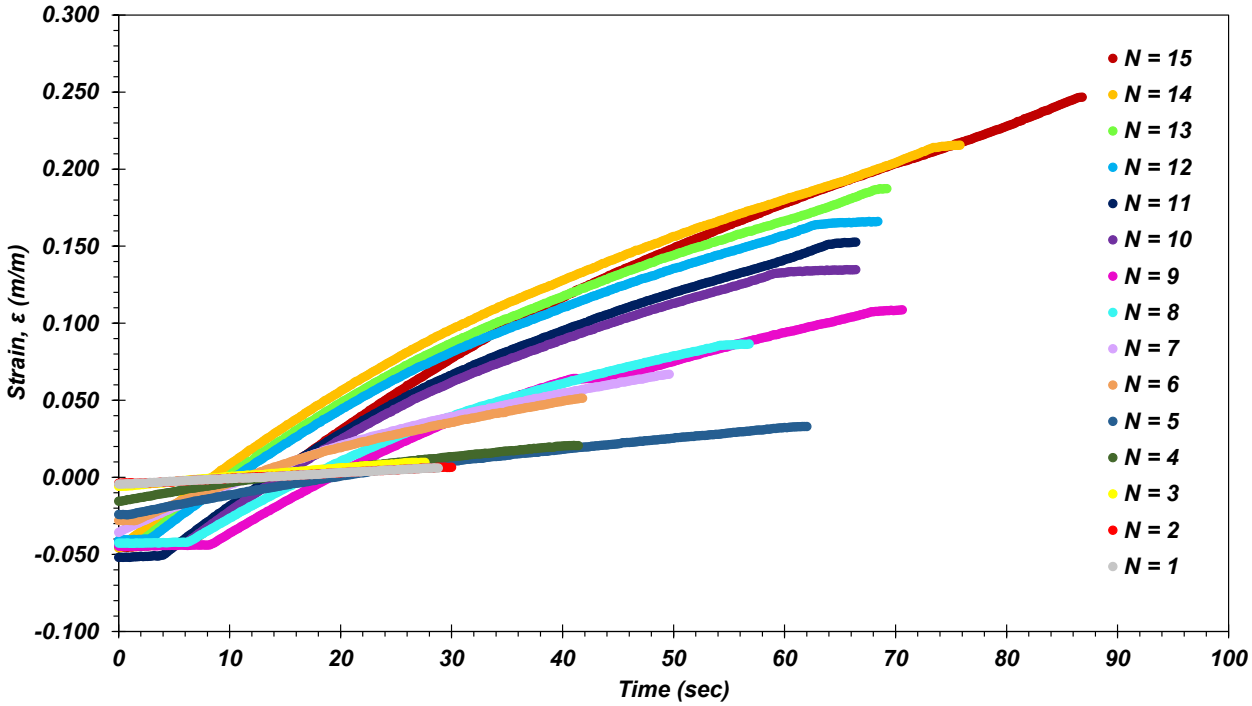

Figure A7.2.1: Strain-time histories observed during rocking at the edge of the footing for Test 2 – S2 for all fifteen unique cycles, where *N* = the cycle number.